Dynamic Failure of Composite and Sandwich Structures

SOLID MECHANICS AND ITS APPLICATIONS
Volume 192

Series Editors: G.M.L. GLADWELL
Department of Civil Engineering
University of Waterloo
Waterloo, Ontario, Canada N2L 3GI

Aims and Scope of the Series

The fundamental questions arising in mechanics are: *Why?*, *How?*, and *How much?* The aim of this series is to provide lucid accounts written by authoritative researchers giving vision and insight in answering these questions on the subject of mechanics as it relates to solids.

The scope of the series covers the entire spectrum of solid mechanics. Thus it includes the foundation of mechanics; variational formulations; computational mechanics; statics, kinematics and dynamics of rigid and elastic bodies: vibrations of solids and structures; dynamical systems and chaos; the theories of elasticity, plasticity and viscoelasticity; composite materials; rods, beams, shells and membranes; structural control and stability; soils, rocks and geomechanics; fracture; tribology; experimental mechanics; biomechanics and machine design.

The median level of presentation is the first year graduate student. Some texts are monographs defining the current state of the field; others are accessible to final year undergraduates; but essentially the emphasis is on readability and clarity.

For further volumes:
www.springer.com/series/6557

Serge Abrate • Bruno Castanié
Yapa D.S. Rajapakse
Editors

Dynamic Failure of Composite and Sandwich Structures

Springer

Editors
Serge Abrate
Department of Mechanical Engineering
and College of Engineering
Southern Illinois University
Carbondale, IL, USA

Bruno Castanié
INSA Toulouse
Institut Clément Ader
Toulouse Cedex 4, France

Yapa D.S. Rajapakse
Office of Naval Research (ONR 332)
Arlington, VA, USA

ISSN 0925-0042
ISBN 978-94-007-5328-0 ISBN 978-94-007-5329-7 (eBook)
DOI 10.1007/978-94-007-5329-7
Springer Dordrecht Heidelberg New York London

Library of Congress Control Number: 2012945626

© Springer Science+Business Media Dordrecht 2013
This work is subject to copyright. All rights are reserved by the Publisher, whether the whole or part of the material is concerned, specifically the rights of translation, reprinting, reuse of illustrations, recitation, broadcasting, reproduction on microfilms or in any other physical way, and transmission or information storage and retrieval, electronic adaptation, computer software, or by similar or dissimilar methodology now known or hereafter developed. Exempted from this legal reservation are brief excerpts in connection with reviews or scholarly analysis or material supplied specifically for the purpose of being entered and executed on a computer system, for exclusive use by the purchaser of the work. Duplication of this publication or parts thereof is permitted only under the provisions of the Copyright Law of the Publisher's location, in its current version, and permission for use must always be obtained from Springer. Permissions for use may be obtained through RightsLink at the Copyright Clearance Center. Violations are liable to prosecution under the respective Copyright Law.
The use of general descriptive names, registered names, trademarks, service marks, etc. in this publication does not imply, even in the absence of a specific statement, that such names are exempt from the relevant protective laws and regulations and therefore free for general use.
While the advice and information in this book are believed to be true and accurate at the date of publication, neither the authors nor the editors nor the publisher can accept any legal responsibility for any errors or omissions that may be made. The publisher makes no warranty, express or implied, with respect to the material contained herein.

Printed on acid-free paper

Springer is part of Springer Science+Business Media (www.springer.com)

Preface

The use of composite materials and sandwich construction in modern structures is increasingly rapidly. These structures are often required to operate in severe environments which include highly dynamic loading, requiring us to establish a better understanding of the dynamic response and failure of composite materials and composite and sandwich structures. This book is the result of a multi-year effort starting with the organization of the "Recent Advances in Dynamic Failures of Composite and Sandwich Structures" workshop held June 24–25, 2011, in Toulouse, France and organized by the Institut Clément Ader. Twenty experts from seven different countries were invited to present comprehensive view of a topic of their choice and submit extended abstract that were available at that meeting. Participation in that workshop struck a balance between academia and industry. Presenters were invited to extend their work to present a comprehensive overview of their chosen topic to be published in a book. After a lengthy process, this book became a reality and its 14 chapters each deal with a particular aspect of the general topic of dynamic failure of composite materials and sandwich structures.

The contents can be grouped into several categories according to the applications: marine structures, aerospace structures, transportation. The first five chapters deal with issues of concern for marine structures: hull slamming, underwater and in-air explosions and low velocity impacts. The next seven chapters deal with impacts on composite and sandwich structures in aeronautical applications. The last two chapters deal with the behavior of composite structures in vehicles subjected to crash.

The editors would like to thank all the participants of the workshop, the local organizers, the Institut Supérieur de l'Aéronautique et de l'Espace (ISAE) for hosting the event and INSA Toulouse for its support. We would also give special thanks to all the authors for their hard work and perseverance and to the publisher for their support and patience.

Y.D.S. Rajapakse
B. Castanié
S. Abrate

Contents

Hydroelastic Impacts of Deformable Wedges 1
Riccardo Panciroli

Blast Loading of Sandwich Structures and Composite Tubes 47
H. Arora, P.A. Hooper, and J.P. Dear

Interaction of Underwater Blasts and Submerged Structures 93
S. Abrate

Compressively Pre-stressed Navy Relevant Laminated and Sandwich Composites Subjected to Ballistic Impact 151
Eric Kerr-Anderson, Selvum Pillay, Basir Shafiq, and Uday K. Vaidya

Development of a Test to Simulate Wave Impact on Composite Sandwich Marine Structures 177
Peter Davies, Benoît Bigourdan, Dominique Choqueuse, Nicolas Lacotte, and Bertrand Forest

Damage Mechanisms and Energy Absorption in Composite Laminates Under Low Velocity Impact Loads 209
V. Lopresto and G. Caprino

Perforation of Composite Laminate Subjected to Dynamic Loads 291
Shirley Kalamis García-Castillo, Sonia Sánchez-Sáez, Carlos Santiuste, Carlos Navarro, and Enrique Barbero

Discrete Impact Modeling of Inter- and Intra-laminar Failure in Composites 339
Christophe Bouvet, Natthawat Hongkarnjanakul, Samuel Rivallant, and Jean-Jacques Barrau

High Velocity Hail Impact on Composite Laminates – Modelling and Testing 393
Robin Olsson, Rickard Juntikka, and Leif E. Asp

Discrete Modeling of the Crushing of Nomex Honeycomb Core and Application to Impact and Post-impact Behavior of Sandwich Structures 427
Bruno Castanié, Yulfian Aminanda, Jean-Jacques Barrau, and Pascal Thevenet

Foldcore Sandwich Structures and Their Impact Behaviour: An Overview 491
Sebastian Heimbs

Experimental and Numerical Study of Normal and Oblique Impacts on Helicopter Blades 545
J. Aubry, P. Navarro, I. Tawk, S. Marguet, J.F. Ferrero, S. Lemaire, and P. Rauch

Energy Absorbing Sacrificial Structures Made of Composite Materials for Vehicle Crash Design 577
G. Belingardi, S. Boria, and J. Obradovic

Composites and Dynamic Failures: Experimental and Numerical Solving Strategies and Solutions 611
Daniel Coutellier

Hydroelastic Impacts of Deformable Wedges

Riccardo Panciroli

Abstract This work investigates the slamming phenomenon experienced during the water entry of deformable bodies. Wedges are chosen as reference geometry due to their similarity to a generic hull section. Hull slamming occurs when a ship re-enters the water after having been partially or completely lifted out the water. There are three more cases commonly defined as slamming phenomena: bow-flare, wet-deck and green water slamming. These are all special cases of the general topic of water entry of a body. While the analysis of rigid structures entering the water has been extensively studied in the past and there are analytical solutions capable of correctly predicting the hydrodynamic pressure distribution and the overall impact dynamics, the effect of the structural deformation on the overall impact force is still a challenging problem to be solved. In fact, in case of water impact of deformable bodies, the dynamic deflection could interact with the fluid flow, affecting the hydrodynamic load. This work investigates the hull-slamming problem by experiments and numerical simulations of the water entry of elastic wedges impacting on an initially calm surface with pure vertical velocity. The objective is to determine an accurate model to predict the overall dynamics of the wedge and its deformations. More than 1,200 experiments were conducted by varying wedge structural stiffness, deadrise angle, impact velocity and mass. On interest are the overall impact dynamics and the local structural deformation of the panels composing the wedge. Alongside with the experimental analysis, numerical simulations based on a coupled Smoothed Particle Hydrodynamics (SPH) and FEM method are developed. Ranges of applicability of a simplified model neglecting the air are found. The results provide evidence of the mutual interaction between hydrodynamic load and structural deformation. It is found a simple criterion for

R. Panciroli (✉)
Alma Mater Studiorum, Università di Bologna, Viale del Risorgimento 2, 40136, Bologna, Italy
e-mail: riccardo.panciroli@unibo.it

S. Abrate et al. (eds.), *Dynamic Failure of Composite and Sandwich Structures*,
Solid Mechanics and Its Applications 192, DOI 10.1007/978-94-007-5329-7_1,
© Springer Science+Business Media Dordrecht 2013

the onset of fluid structure interaction (FSI), giving reliable information on the cases where FSI should been taken into account. The occurrence of ventilation and cavitation varying the impact parameters are also outlined.

1 Introduction

When a vessel sails in rough seas, its forefoot can rise above the water surface. As the vessel re-enters the water, impulsive pressures are imparted to the hull structure due to the relative motion of the sea and ship. In these cases the hull literally slams into the water surface. The duration of the slamming event is in the order of milliseconds. These loads might damage the entire ship or, because of their short duration, excite dynamic response of the local structure of the hull and cause vibrations. This work focuses on hull slamming; however, there are three more phenomena that are defined as slamming in marine applications: (1) the impact of the bow on water induced by the ship motions in waves, (2) the horizontal impact of steep waves or breaking waves on the ship hull and (3) the water impact induced by water run-up and green water on the deck.

1.1 Theoretical Studies

It is of major interest for engineers to find an analytical solution capable of providing the hydrodynamic load and the impact pressure during a slamming event, since it can be easily used during the design process. This section describes the analytical methods developed to study the water entry of rigid bodies.

The first analytical solution to solve the impact dynamics of rigid bodies entering the water was presented by Von Karman [1], who developed a formula capable to predict the maximum force acting on a rigid body entering the water, in order to make a stress analysis on the members connecting the fuselage with the floats of a seaplane. As example, to study the water entry of a rigid wedge, Von Karman considered a wedge of unit thickness, mass M, and deadrise angle β entering the water with initial velocity V_0. Von Karman's work is based on some simplification, i.e.: (1) inviscid and irrotational flow, (2) surface tension, gravity and structural elasticity effect neglected, (3) no air entrapped. In this method, as the body hits the water it is assumed that the mass of a half disk of water of radius r is moving with the wedge (as shown in Fig. 1), resulting in an added mass $m = \frac{\pi}{2}\rho r^2 = \frac{\pi}{2}\rho\frac{\xi^2}{tan^2(\beta)}\gamma^2$, where γ is a coefficient accounting for the water pile up at the intersection with the free surface that varies with the deadrise angle. The value of γ can be evaluated as suggested in [2], for example. In this model, velocity and acceleration of the body are given by:

$$\dot{\xi} = \frac{V_0}{1 + \frac{\pi}{2}\rho\frac{\gamma^2\xi^2}{Mtan^2(\beta)}} \quad ; \qquad \ddot{\xi} = \frac{\pi\rho\gamma^2}{MV_0tan^2(\beta)}\xi\dot{\xi}^3 \tag{1}$$

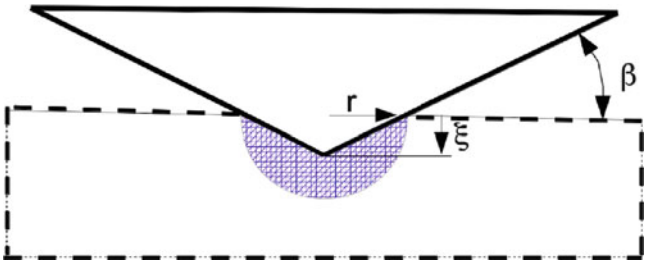


Fig. 1 Von Karman's momentum approach. Where β is the deadrise angle, ξ the penetration depth, r the wet distance from the wedge edge. The cross-hatched region represents a half disk of water of radius r moving with the wedge

In von Karman's model (Eq. 1), the impact force reaches its maximum value

$$F^* = \left(\frac{5}{6}\right)^3 \frac{V_0^2}{tan(\beta)} \sqrt{\frac{2\pi}{5}\rho M \gamma^2} \tag{2}$$

when the velocity is

$$\dot{\xi}^* = \frac{5}{6} V_0 \tag{3}$$

the penetration depth is

$$\xi^* = \sqrt{\frac{2M}{5\pi\rho\gamma^2}} tan(\beta) \tag{4}$$

and the time is

$$t^* = \frac{16}{15} \frac{\xi^*}{V_0} \tag{5}$$

Equation 2 shows that the maximum force increases with the square of the velocity and the square root of the mass of the wedge. F^* is inversely proportional to $tan(\beta)$ so that it decreases as β increases and it becomes infinite as the deadrise angle tends to zero. When β becomes small, r becomes very large, the added mass becomes infinite and the wedge stops instantly. Equation 3 shows that the velocity is 5/6 times the initial velocity when the force reaches its maximum. Equation 4 shows that the penetration depth at that particular instant is proportional to the square root of the mass and to $tan(\beta)$ ($tan(\beta) = 0$ implies no penetration). Combining Eqs. 4 and 5 gives

$$t^* = \frac{16}{15} \frac{\tan(\beta)}{V_0} \sqrt{\frac{2M}{5\pi\rho\gamma^2}} \tag{6}$$

This shows that the force reaches its maximum at a time that is inversely proportional to the initial velocity and increases with $tan(\beta)$. Figure 2 shows the overall acceleration and velocity of a wedge of 20 Kg per unit with entering the water at 4 m/s for various deadrise angles. It is shown that decreasing the deadrise angle from 30° to 5° leads to an increase of the maximum acceleration and a reduction of the characteristic time t^*.

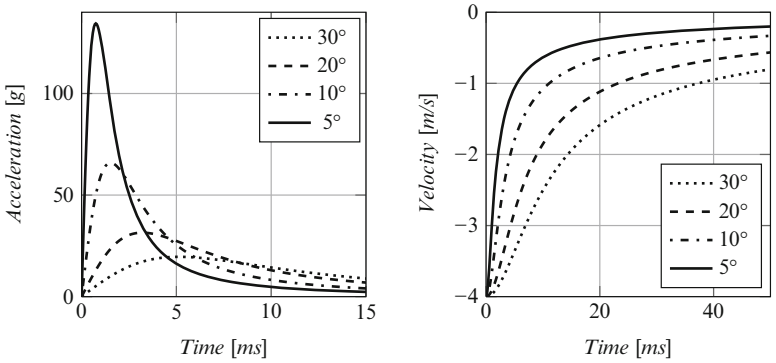


Fig. 2 Von Karman solution. Acceleration and Velocity of a wedge varying the deadrise angle β. Total wedge mass: 20 kg per unit width

Wagner [3] later extended Von Karman's method to predict the pressure distribution at the fluid/structure interface during the impact. In this model, the pressure along the wedge is given by:

$$\frac{p(x)}{\rho} = \ddot{\xi}\sqrt{r^2 - x^2} + \frac{\pi}{2}\frac{\dot{\xi}^2 r}{tan(\beta)\sqrt{r^2 - x^2}} - \frac{1}{2}\frac{\dot{\xi}^2 x^2}{r^2 - x^2} \tag{7}$$

Equation 7 shows that the pressure becomes infinite when β tends to zero and there is a singularity near the end when x tends to r. The maximum impact pressure p_{max} is obtained by defining $dp/dc = 0$ and assuming the acceleration of the body $\ddot{\xi}$ to be negligible. This gives

$$p_{max} = \frac{1}{2}\rho V^2 \left[1 + \frac{\pi^2}{4} cot^2\beta\right] \tag{8}$$

which occurs at the location

$$x = L\left[1 - \frac{4\tan^2\beta}{\pi^2}\right]^{\frac{1}{2}} \tag{9}$$

since p_{max} occurs some time t after the instant of impact t_0, V is used in Eq. 8 since it might not be the impact velocity V_0. At the keel of the wedge, $x = 0$. From Eq. 7, the impact pressure at that point is

$$p_{keel} = \frac{1}{2}\,\rho\, V^2\,\pi\, cot(\beta) + \ddot{\xi}\,\rho\, L \tag{10}$$

if $\ddot{\xi}$ can be neglected,

$$p_{keel} = \frac{1}{2}\,\rho\, V^2\,\pi\, cot(\beta) \tag{11}$$

These analytical models were developed for the analysis of the water entry of rigid bodies and are not capable of accounting for hydroelastic effects, since the changes of the fluid motion due to the structural deformation are not accounted. Thus, in the present work, Wagner and Von Karman solutions will be used to validate the numerical model in the case of slamming of rigid bodies, while the validated numerical model will be used to study the water entry of deformable wedges, since hydroelastic effects might appear.

Since Wagner developed the first analytical solution to evaluate the pressure during water-entry problems, much effort has been devoted to slamming problems, resulting in an impressive amount of papers: more than 200 papers were listed in the Ship Structure Committee report SSC-385 [4].

In the literature, many analytical methods extend Wagner's method to different shapes (e.g. [2, 5]) and are very effective when dealing with the water entry of simple-shaped structures impacting the surface with pure vertical velocity. However, these analytical models are limited to the analysis of simple-shaped bodies impacting onto a free and initially calm surface. Yettou [6] developed an analytical solution to symmetrical water impact problems, showing a very good agreement between experimental results and analytical solutions of the water entry of rigid wedges. Some of these solutions are even capable of accounting for oblique impacts (e.g. [7–9]). It is reported that there are particular conditions (entry velocity, deadrise angle and tilt angle) where the fluid detaches from the wedge apex (i.e. the keel) introducing difficulties in evaluating the pressure at the interface by analytical formulations. Chekin [10] concluded that there was only one unique combination of wedge angle and impact angle from which no separation of flow from the vertex would occur. For a given wedge and wedge orientation, any other impact angle would force separation. Defining U_0 the horizontal velocity and W_0 the vertical velocity, the ratio $\frac{U_0}{W_0}$ at which the flow separation appears is less for bodies of larger deadrise angles. For small asymmetric impacts, the cavity flow that generates at the apex during the water entry is very small. Furthermore, the flow that separates from the apex quickly re-attaches to the wedge. A symmetric body impacting with horizontal velocity will produce a flow similar to asymmetric impact with only vertical velocity when rotation about the x-axis is not allowed. In [7], Judge at al. performed experiments on wedges where asymmetry and horizontal impact velocity are present and compared the results with an analytical solution, showing good agreement for low angles of asymmetry and small ratios of horizontal to vertical impact velocity.

Some models are even capable of accounting for the coupling between the fluid motion and the structural deformation [11–15]. However, in order to fully describe impact forces and resulting structural response, other different phenomena (like trapped air, hydroelastic interaction, compressibility effects, and non-linear free surface mechanics) must be considered. These phenomena need further investigation. Accurate prediction methods for hydrodynamic loads are needed in order to reduce the probability of structural failure.

1.2 Hydroelastic Effects in Water Impact Problems

The analytical models developed for rigid bodies might not be used to study the water entry of deformable bodies since the structural deformation might change the hydrodynamic pressure and the impact dynamics due to hydroelastic effects. This section gives a brief review about the known methods to study hydroelasticity during slamming. Experimental, analytical and numerical approaches are presented.

Hydroelasticity is the dynamic interaction between water and a structure (sometimes called fluid-structure interaction). Water entry is only one example of it. Faltinsen in his review [16] on hydroelastic slamming show that it is common to use an equivalent pressure resulting in the same maximum strain in the structure reached during the dynamic event, but has no physical meaning and the resulting pressure load would be an order of magnitude smaller than the maximum physical pressure.

Due to the mutual interaction between the fluid motion and the structural deformation, the hydrodynamic loads that elastic bodies are subjected during the water entry might differ from the loads acting on rigid bodies [17]. The concept is that the impact pressure is related to the movement of the impact region with respect to the water [18]. In particular, as mentioned in [14], the evolution of the wetted body area in time is an important characteristic of the impact, which strongly affects the magnitude of the loads. Elastic structures with low deadrise angles are the most subjected to changes in the impact dynamics respect to rigid structures, since a small deflection of the structure might result in a big difference of the wetted surface and consequently the hydrodynamic load. Such problems are still difficult to analyze and compute.

Carcaterra and Ciappi [19] studied the water entry problem of elastic wedges simplifying the deformable wedge as two rigid plates connected by a rotational spring of constant stiffness. They show how the hydrodynamic force is affected by the deformation of the wedge. It was found that during the initial phase of the impact the deadrise angle decreases due to the structural deformation. When the deadrise angle becomes smaller, the wetted surface is increased and an increment of the hydrodynamic load, with respect to the rigid wedge case, is observed. When the wetted front crosses the center of gravity line, an opposite moment contribution arises that tends to contrast the deadrise decrement. Alternate closing and opening of the wedge was predicted. They showed that this phenomenon could be observed only if the natural period of oscillations is small compared to the characteristic time of application of the hydrodynamic force. They observed that the mass of the plates composing the wedges has an influence on the stresses at the beginning of the impact, when the inertia induces the deadrise angle to decrease, even if the hydrodynamic load itself is pushing the wedge to close and increase its deadrise angle. A similar effect was experimentally found by Arai and Miyanki [20].

Kapsenberg [21] reported that, in case of hydroelastic phenomena, the magnitude of the deformation of an elastic body might be lower than the one expected from classical beam theory and neglecting hydroelastic effects can, in an extreme case, result in an over-prediction of the deformation (hence the stress) by a factor of 10.

Several scientists [16, 20–29] investigated the water impact of elastic structures, showing that the the relative importance of the elasticity of the beam on the hydrodynamic force is governed by deadrise angle, panels thickness and impact velocity. Hydroelastic effects are relevant when the relative angle between the body and the surface of the fluid is small, and if the duration of the impact is short relative to the resonance period of the structure. Hirdaris and Temarel [30] suggest that particle-based methods, as other numerical methods, are expected to become increasingly used in the future, but currently suffer of lack of computational efficiency. Further studies and validations on its applicability to water entry problems are needed.

Many solutions of water-entry problems are available and many are very effective in dealing with the water entry of complex geometries, sometimes even considering oblique impacts (e.g. [7]), but most deal with rigid structures. To study more realistic situations, many numerical methods capable of coupling the fluid dynamics with the structural response have been used [11, 12, 15, 25, 31].

Seddon and Moatmedi [32] review the literature on the water entry problems for aerospace structures from 1929 to 2003 and show that very few efforts were made to develop solutions for non-vertical impacts, three-dimensional bodies, or deformable bodies. The majority of the work on these problems is experimental. They suggest that Smoothed Particle Hydrodynamics (SPH) can possibly be a tool to study these problems, but that a large amount of work is required to validate such models. One of SPH's major advantages is the ease of treating fluids presenting a free surface, together with the possibility to interact with FEM models, while its major limitation is the very expensive computational time due to the high number of particles needed to model the fluid, which limits its application to relatively small two dimensional models [33–36]. For example, in [35] 21 millions particles are needed to obtain results similar to Wagner's solution for the water entry of a rigid wedge. Anghileri et al. [37] used the SPH method to study the water entry of a rigid cylinder and a rigid wedge, showing a good prediction of the impact force.

Shao [38] performed a sensitivity analysis by refining the particle spacing. It was found that the spatial resolution can have a relatively large influence on the flow in the water splash-up region (the water entry produces a water jet piling up the wedge panels during impact, see e.g. [39]), but it has less influence on the falling velocity of the object and the fluid forces. The finer the particle resolution is, the better the detailed flow structures can be resolved, but at the cost of more computational time. For the pressure evaluation at the fluid/structure interface, many articles show results that are inaccurate and lack details, to the point that this technique cannot be considered to be fully suitable for this purpose [34–36]. In general, the pressure values suffer noise due to numerical fluctuations. An averaging therapy on the pressure field has been recently proposed in the literature (see i.e. [40]). Molteni and Colagrossi [41] proposed the introduction of a proper diffusive term in the continuity equation to increase the smoothness and the accuracy of pressure profile. They showed that this corrective method does not alter the match of the numerical solution with the analytical one. However, no fluid/structure interaction problems are treated in their study. Kapsenberg [21] reported that SPH

is numerically a very robust method and impressive results are obtained for very violent phenomena. However, work on verification of the results (convergence with respect to particle size and time step) is not yet at the level of the normal CFD. Kapsenberg also reports that the main problems related to the SPH method are difficulties in correctly reproducing the pressures wave propagation and a robust treatment of the fluid/structure interface, while computer requirements are an order of magnitude higher than for classic CFD methods.

During the water entry of flat-bottom structures with high velocity, air can be trapped in between the fluid and the structure. The next section describes this phenomenon.

1.3 Air Cushioning Effect in Water Entry

Trapping of air in the fluid during the water impacts is common in case of impact of flat-bottom structures [43]. This section describes its relieving effects on the maximum impact pressure.

In [44] two-dimensional impact tests of a rigid flat-bottom model indicates that the maximum impact pressure is nowhere near the theoretical infinitely large hydrodynamic pressure or near the theoretical acoustic pressure. With the assumption that no air is trapped in the fluid during the slamming event of a flat structure, an approximate value of the maximum impact pressure is [45]:

$$p_{max} = \rho c V_0 \tag{12}$$

where p is the pressure, ρ is the fluid density, c is the speed of sound in the fluid, and V_0 is the impact velocity. However, evidences resulting from investigations reveal that the impact of flat structures is cushioned by the presence of trapped air between the falling body and the water. If all the air is forced to escape during a flat-bottom drop, the air velocity must be infinite just before impact occurs. Consequently some air is trapped between the water and the structure: as the body approaches the surface of the water and the air cannot escape fast enough, the pressure deforms the surface of the water before contact is made. Then, a large air bubble is trapped under the body. This causes the impact pressure to be reduced. Air trapping is maximum for a flat-bottom structure, but it appears (with lower magnitude) for deadrise angles up to about 10°. The cushioning effect of the compressible air trapped between the impact body and the water surface reduces the impact pressure to about one-tenth of the acoustic pressure predicted by Eq. 12. Evidence from Chuang's investigation [18] supports the thesis that Wagner's hydrodynamic impact theory does not apply to the impact of wedge-shaped bodies with small deadrise angles. Furthermore, Chuang experiments showed that a deformable body affords considerable relief from the impact load.

1.4 Experimental Studies

This section introduces some of the experimental studies on the water entry found in the literature. Most of them investigate the water entry of stiff bodies. The major attention is given to the evaluation of the impact dynamics and the pressure at the fluid/structure interface (e.g. [37]). For example, Engle [46] studied the water entry of rigid wedges measuring the pressure at the fluid/structure interface. Results based on peak pressures at different impact velocities compared well with Wagner's theory. Some authors attempted to experimentally investigate the parameters affecting hydroelasticity during slamming. Several scientists [24–27] reported that the water entry of deformable bodies is affected by various parameters: stiffness of the structure, presence of entrapped air between the structure and the water surface. It reported that the ratio between the impact duration and the period of the first dry mode of vibration is the key factor in deciding when the analysis of the structural response should include elastic deformations.

Faltinsen [16,22] showed that, due to hydroelasticity, cavitation may occur since pressures becomes negative relative to atmospheric pressure during the second half of the first wet natural oscillation period; ventilation might also appear, i.e. air can be caught in an air pocket in the water leading the air flow to interact with the water flow. Recently Huera-Huarte [47] experimentally studied the hydrodynamic load on panels entering the water at speeds higher than 5 m/s and low deadrise angles, showing that for angles lower than 5° air entrapment is important and the analytical solutions tend to overestimate the hydrodynamic loads.

Results found in the literature show that there are particular conditions where hydroelastic, air entrapment, cavitation and ventilation phenomena might occur during slamming. However, a reliable tool to predict the occurrence and the magnitude of such phenomena is missing.

1.5 Scope of Present Investigation

As shown in the previous literature review, there are many complicating factors related to hydroelastic effects. Many authors concentrated on the experimental evaluation of the pressure variation due to the structural deformation during the water entry. The primary objectives of this work are:

- Experimentally evaluate the hydroelastic effects by experiments where the dynamic interaction between the structural deformation and the fluid motion is high.
- Develop a numerical model to study the water entry of deformable bodies which can correctly predict the overall impact dynamics and the impact-induced stresses and validate it by comparison with the experimental results.

This study presents an extended experimental campaign on the water entry of deformable wedges. Experiments investigate the water-entry of composite and aluminum flexible wedges varying thickness, deadrise angle and impact velocity. The objective is to develop a reliable formula capable of estimating the maximum stress reached during the water entry of deformable bodies.

Results of the impact-induced accelerations are compared with analytical solutions for rigid structures: assuming that the wedge is rigid, the impact dynamic can be evaluated by Von Karman's approach, while the pressure distribution along the edge can be determined using Wagner's formula. This pressure can be used to calculate the stresses in the panels provided that deflections remain small and do not induce changes in the fluid flow. This study examines cases where the deformation of the wedge is very large. This affects the fluid flow and consequently the pressure distribution along the edge, introducing hydroelastic effects. The impact-induced acceleration is recorded by an accelerometer while strain gauges located at various locations on the wedge measure the overall local deformations. Alongside with the experimental campaign, numerical simulations are developed by a coupled SPH/FEM numerical model and the computed structural deformations are compared with the experimental results.

This research initially validates the coupled FEM/SPH model by analyzing its capability to correctly reproduce the pressure waves propagation and the overall fluid motion. Later, it investigates the water-entry problems of rigid bodies, whose results are compared with Von Karman and Wagner's analytical solutions, showing that SPH is actually capable of correctly simulating the impact dynamics. The accuracy of the solution in terms of pressure at the fluid-structure interface was found to be highly influenced by various parameters like: element size, artificial bulk viscosity and non-reflecting boundary conditions. Once the solution method has been validated, the research moves to the investigation of hydroelastic effects on the impact dynamics and structural deformation. Numerical results are compared with experiments about water-entry of elastic wedges of varying thickness, deadrise angle and impact velocity.

Experimental results show that the relative importance of hydroelasticity is strictly related to the ratio between the time necessary for the structure to get completely wet during the water entry (also called wetting time) and the natural period of the structure. Numerical simulations reveal that SPH is actually capable of correctly replicating the structural deformations even for low mesh refinement. On the other hand a low refinement gives a poor approximation of the pressure distribution over the fluid/structure interface. However, this lack of accuracy seems to have negligible effect on the structural deformation.

Being able to model the fluid with a low mesh refinement means lower computational time which is, from the practical point of view, the most delicate point for the applicability of the SPH technique to full-scale three-dimensional simulations to be used for design purposes.

2 Experimental Set-Up

As shown in the previous sections, hydroelasticity in water-entry problems has been studied by many authors, both by experimental campaigns and by numerical simulations (e.g. [16,24,26,27,48]). However, their interest mostly focused on the analysis of the pressure at the fluid/structure interface rather than the structural deformation itself. Furthermore, all the structures used in the experiments are stiff and present very little structural deformation. Consequently, hydroelastic effects are low.

Instead, the experimental part of this work is not focusing on the impact pressure but on the structural deformation itself. An experimental apparatus was designed to perform slamming tests of wedges of various stiffness and to compare them with the theoretical results shown in the previous sections and numerical simulations. The time history of the hydrodynamic force applied on the wedge and the strains at several locations on the panel are measured. The design of the testing machine and the specimens was chosen in order to avoid air trapping effects, as described in Sect. 1.3.

2.1 Description of Models and Tests

A drop weight machine (Fig. 3) with a maximum drop height of 4.5 m was specially designed and built. The machine is composed by an aluminum frame 2 m long, 1.8 m wide and 6 m high, holding two prismatic rails guiding an aluminum sledge (Fig. 4). The rails have a maximum vertical run of 4.0 m so that the wedge can fall from various heights leading to different entry velocities. Teflon insets minimize the friction between the sledge and the prismatic rails. The sledge can hold wedges up to 350 mm long (per side) and 800 mm wide. The falling body hits the fluid at the center of a tank 1.2 m wide, 1.8 m long and 1.1 m deep. The tank was filled with

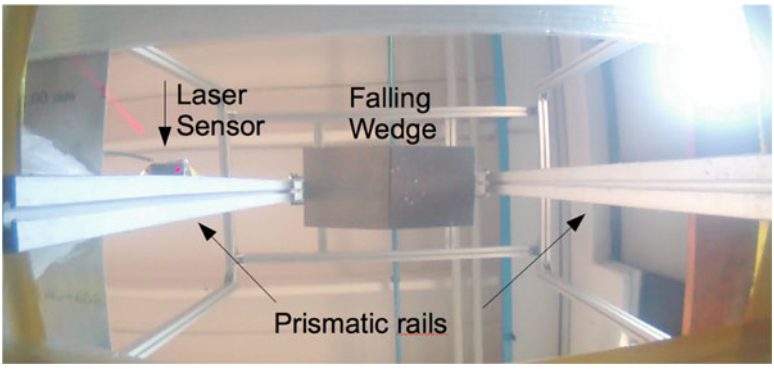


Fig. 3 Picture of the drop weight machine seen from the *bottom* of the water tank



Fig. 4 Picture of the sledge with an aluminum wedge mounted on it

water only up to 0.6 m to prevent the water waves generated during the impact to overflow. The drop heights, which are defined as the distance between the keel and the water surface, ranged from 0.5 to 3 m at 0.25 m increments.

Impact acceleration is measured by a *V-Link Microsrain* wireless accelerometer (± 100 g) located at the tip of the wedge. All reported accelerations are referenced to 0 g for the free-falling phase. The sampling frequency is set to its maximum of 4 kHz. Entering velocity is recorded by a laser sensor ($\mu\varepsilon$ ILS 1402) capturing the sledge position over 350 mm of ride at a frequency of 1.5 kHz with a definition of 0.2 mm. The entry velocity is obtained by the numerical differentiation of the position. The maximum impact height is 4 m, corresponding to a maximum impact velocity of 8.8 m/s. This maximum impact velocity cannot be reached during experiments due to the large wedge dimensions offering a high air resistance. Friction on the prismatic rails was found to be negligible compared to the air resistance.

One of the main requirements was to be able to easily test a high number of wedges with different stiffness and deadrise angle without having a large number of specimens. Thus, wedges were designed to be composed of two panels (Fig. 5) joined together on one side (keel) by a mechanism capable to change the deadrise angle smoothly from 0° to 50°. The impact angles were measured at rest with a digital level providing 0.1° resolution. Figure 6 shows a conceptual sketch of the wedge.

In nautical applications, composite hulls are usually made by panels whose edges are clamped to the main frame (a sketch of this configuration can be seen in Fig. 7). Locking all the edges of the panel has the effect of increasing the first natural frequency. However, the literature [16, 22–27] indicates that hydroelastic

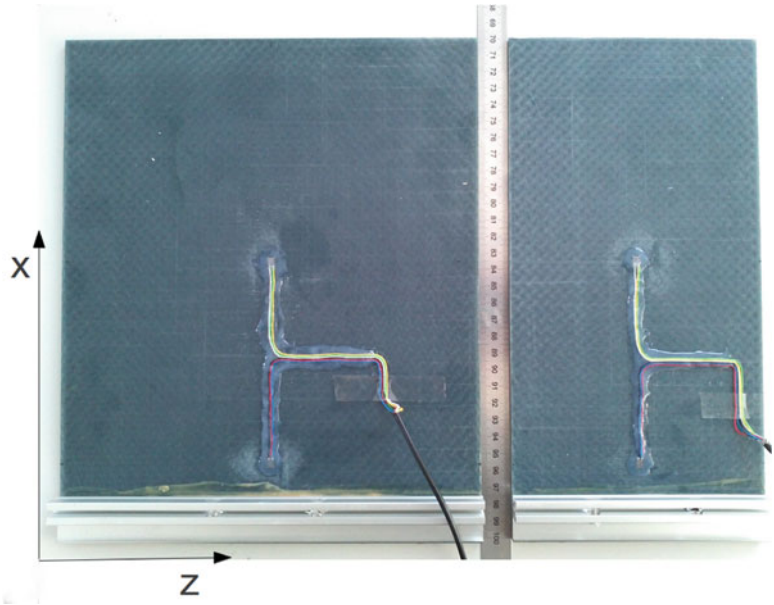


Fig. 5 Picture of two composite panels of different width: 250 and 150 mm

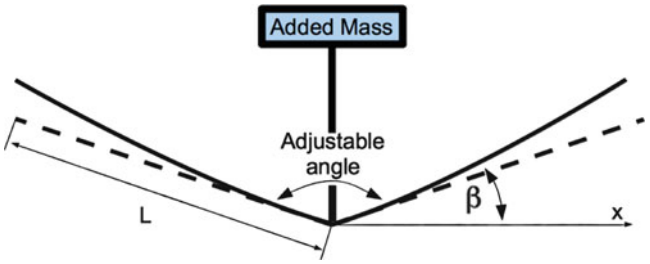


Fig. 6 Conceptual scheme of the wedge used for experiments. L panel length. β deadrise angle. *Dashed line*: undeformed panels, *solid line*: expected deformation during impact

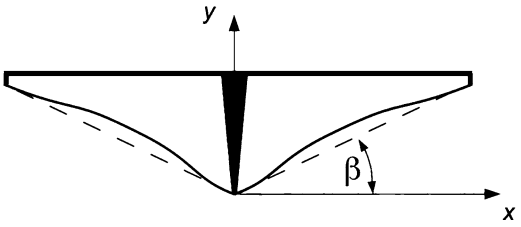


Fig. 7 Sketch of a wedge clamped on two sides. *Dashed line*: initial configuration, *solid line*: expected deformation during impact

effects increase while increasing the entry velocity and decreasing the ratio between the wetting time and the first natural frequency. This means that hydroelasticity is more likely to appear for structures having longer natural period. Consequently hydroelastic effects appear at lower impact velocity in case of flexible structures

Table 1 Plates material properties

Material	Abbr.	$E_1 = E_2$ (GPa)	ν_{12}	ρ(kg/m^3)
6068 T6	A	68	0.32	2,700
E-Glass (mat)/vinylester	V	20.4	0.28	2,050
E-Glass (woven)/epoxy	W	30.3	0.28	2,015

Table 2 First three dry natural frequencies of the panels used for experiments

Abbr.	Material	Thickness (mm)	$\omega_1, \omega_2, \omega_3$ (Hz)
A2	Aluminum	2	18.01 112.89 316.12
A4	Aluminum	4	36.03 225.79 632.24
V2	Fibreglass	2.0	9.77 61.22 171.44
V4	Fibreglass	4.0	19.73 123.67 346.29
W2	Fibreglass	2.2	19.69 123.40 345.54
W4	Fibreglass	4.4	37.80 236.94 663.44

than for stiff structures. From the experimental point of view there are two main advantages when using wedges with a longer first natural period:

- Experiments can be conduced at lower velocities
- Deformations are larger and consequently easier to measure

For these reasons, wedges are designed as two panels rigidly connected only at the keel edge. All the others edges are free to deform.

2.2 Specimens

Ref. [16] shows that hydroelasticity is influenced by the ratio between the wetting time and the panel's lower natural frequency. To vary the fundamental natural frequency of the panels, different stiffness to area density ratios are needed. Thus, aluminum (A), E-glass (mat)/vinylester (V) and E-Glass (woven)/epoxy (W) panels of various thickness (2 and 4 mm) were used. All wedges are made by two panels 300 mm long, but with two different width: 150 and 250 mm. Aluminum and Composite panels material properties are listed in Table 1. Composite panels were produced by VARTM by infusion of vinylester resin on E-Glass fibre mat, while the E-glass (woven 0°/90°)/epoxy panels were produced in autoclave.

All panels were equipped with two strain gauges per side, located at 25 and 120 mm from the reinforced tip, as shown in Fig. 5. The reinforced tip is 27 mm long and is used to connect the two panels to the aluminum sledge.

The position of the strain gauges was chosen on the basis of a dry modal analysis: they were placed far from the nodes (referred to the deformation) of the first three mode shapes, whose frequencies are listed in Table 2. Note that the nodal position referred to the strains are not the same one of the modal shapes, as visible in Fig. 8.

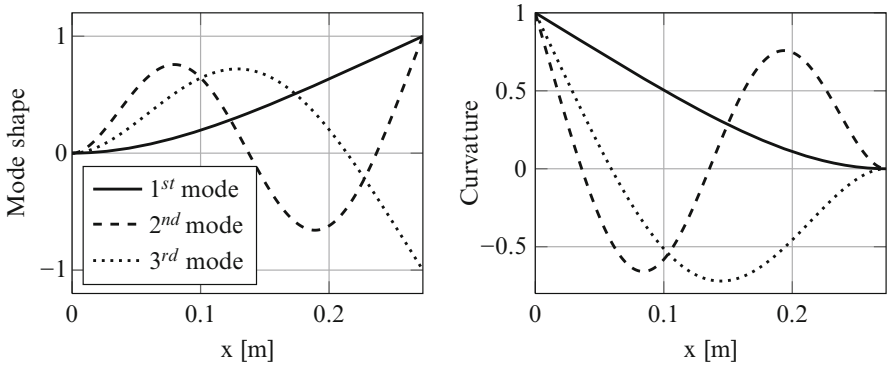


Fig. 8 Mode shapes of a dry panel (*left*) and curvature (*right*). The comparison of the two graphs shows that the position of the nodes is different. The location of the strain gauges was chosen as 25 and 120 mm from the clamped side

3 Experimental Results

For each combination of material, plate thickness, impact height and deadrise angle, experiments were repeated three times to guarantee the accuracy of the measures and to verify the repeatability of the tests. A total of more than 1,200 experiments have been conducted, only a few of these results are presented in this work. Figures 9 and 10 show the impact-induced deformations of composite wedge (W2) with deadrise angle of 30° entering the water at 2.77 and 6.28 m/s respectively. Each test case was repeated three times, showing a very good repeatability.

The response of the wedges in terms of structural deformation show different behavior varying the impact parameters: entry velocity, deadrise angle and stiffness to area mass ratio. In Fig. 9 the signals of the two strain gauges show smooth shape and their trend is similar, suggesting that the first mode of vibration dominates the structural deformation. A different behavior is recorded when the impact velocity is higher (Fig. 10), where the deformation recorded by the strain gauges located at the center of the plate follows the overall trend recorded by the first strain gauge but marked oscillations appears, suggesting that more than one mode shape is excited. Furthermore, it was observed that the maximum strain is not always recorded by the strain gauge located at 25 mm from the wedge tip, but for the most severe impacts (higher velocity and lower deadrise angle) the maximum value is recorded by the strain gauge located at 120 mm from the wedge tip. Figure 11 show the results of a composite wedge (W2) with deadrise angle of 30° entering the water with various impact velocities. Recorded accelerations show good repeatability. The scatter on the maximum acceleration recorded during the three repetitions is below $\pm g$ for all the impact cases.

Experiments show that the structural flexibility affects the acceleration during the water entry. It was found that: if the structural deflection is small, this has

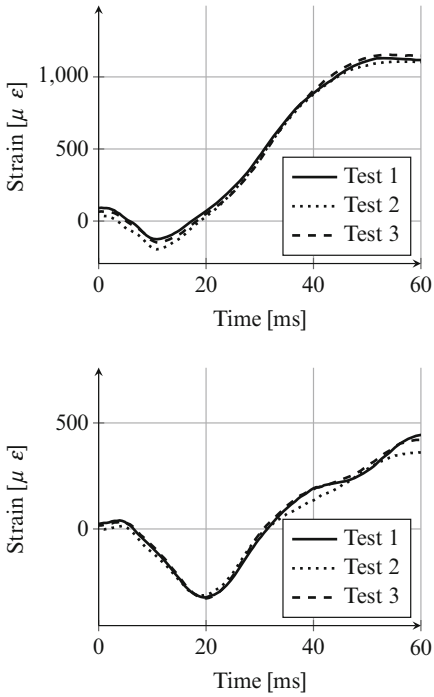


Fig. 9 Example of a composite (W2) wedge, 2 mm thick, $\beta = 30°$, $V_0 = 2.77$ m/s. Strain recorded at 25 mm (*top*) and 120 mm (*bottom*) from the wedge tip. Three repetitions of each impact case are shown, revealing extremely good repeatability

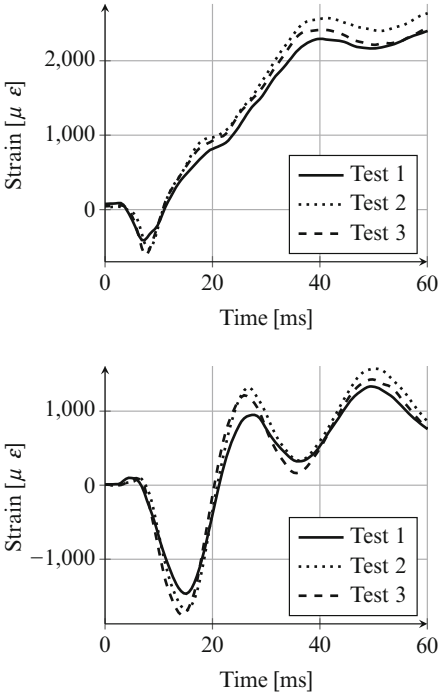


Fig. 10 Example of a composite (W2) wedge, 2 mm thick, $\beta = 30°$, $V_0 = 6.28$ m/s. Strain recorded at 25 mm (*top*) and 120 mm (*bottom*) from the wedge tip. Three repetitions of each impact case are shown, revealing extremely good repeatability

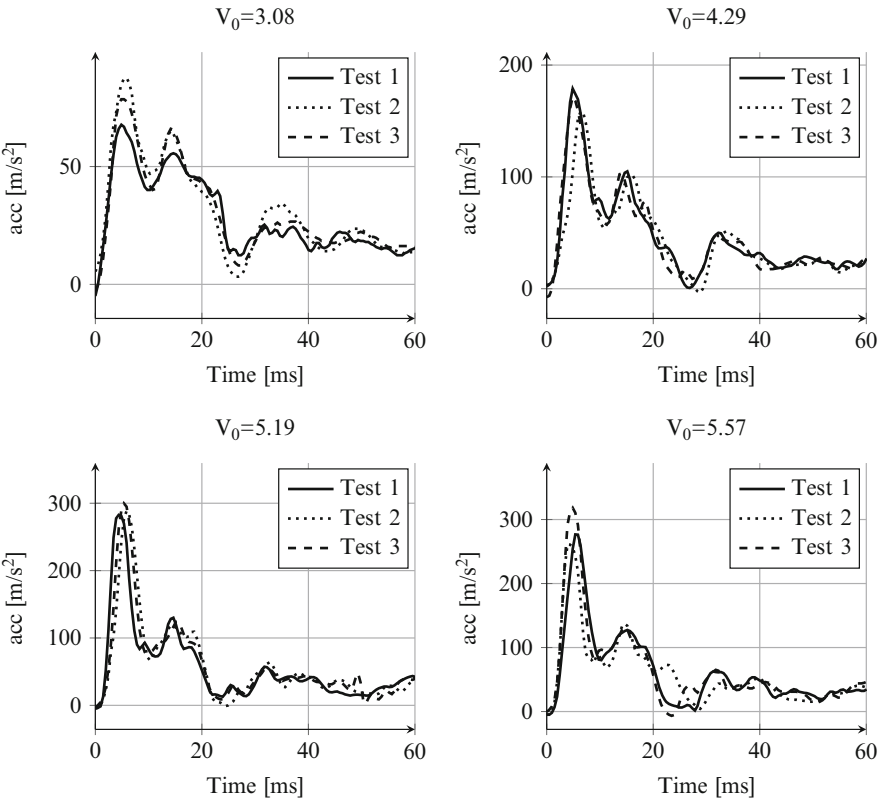


Fig. 11 Accelerations during the water entry of a wedge (W2) with deadrise angle $\beta = 30°$ entering the water at various impact velocities. Three repetitions of each impact case are shown, revealing extremely good repeatability

very little influence on the accelerations. While, if the structural deflection is high, accelerations show high oscillations if compared to to the water entry of a rigid body. As examples, Figs. 12 and 13 show the comparison between the solution for a rigid wedge (blue line) and the recorded accelerations of flexible wedges (black lines). The structural deformation is increasing as the impact velocity increases (left to right, top to bottom in the Figures) and as the deadrise angle decreases (the deadrise angle is reducing from Figs. 12 to 13). Looking the graphs in this order is evident that there is an increase of the oscillations in the accelerations as the structural deformation increases. Furthermore, while for low entry velocities and high deadrise angles the maximum acceleration is the same one as for the rigid case and the acceleration oscillations are low; as these oscillations increase, the maximum acceleration and the time this is reached moves from the rigid-body solution. In particular, the maximum acceleration lowers compared to the one experienced by rigid bodies.

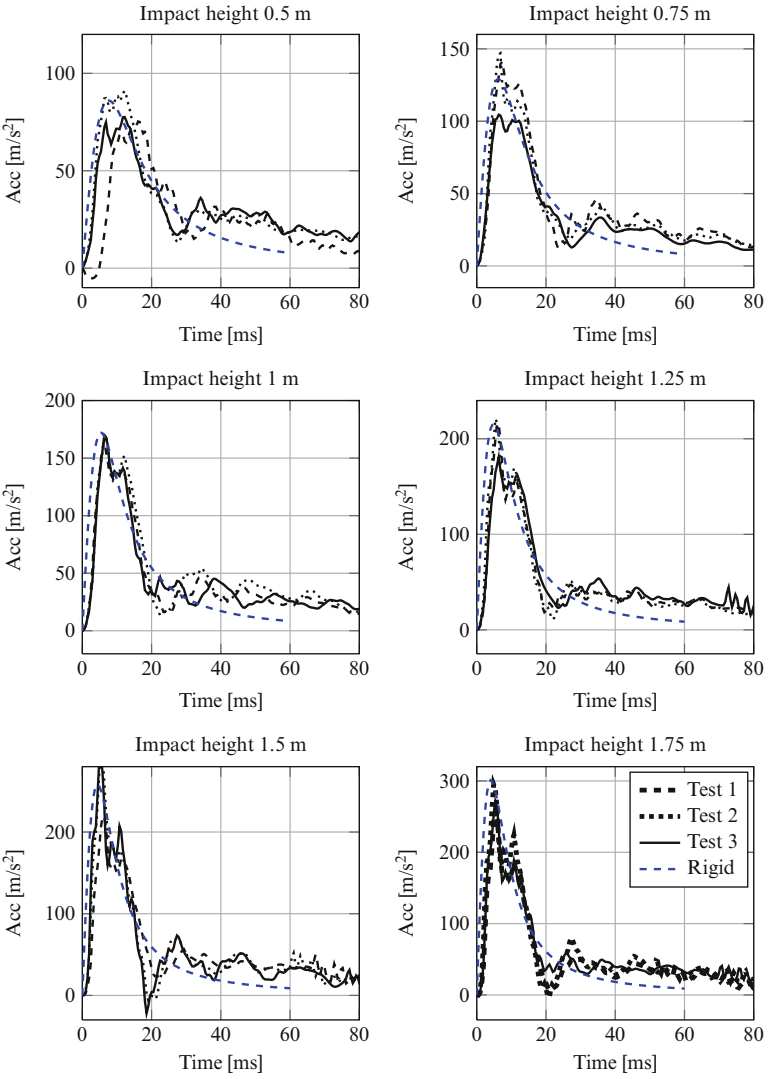


Fig. 12 Recorded accelerations of a composite wedge with $\beta = 25°$ impacting from various impact heights (three tests for each configuration, *black lines*) compared with the acceleration of a rigid wedge (*blue line*)

A secondary effect of hydroelasticity can be appreciated in the next graphs: Fig. 14 shows the recorded strains for a composite wedge (V2) with given deadrise angle presented as function of the drop height, while Fig. 15 shows the recorded strains for an aluminum wedge 2 mm thick presented as function of the deadrise angle for a given impact velocity. Figure 15 shows that the deformation in time is very smooth when the velocity is small (left plot on top), while the dynamic

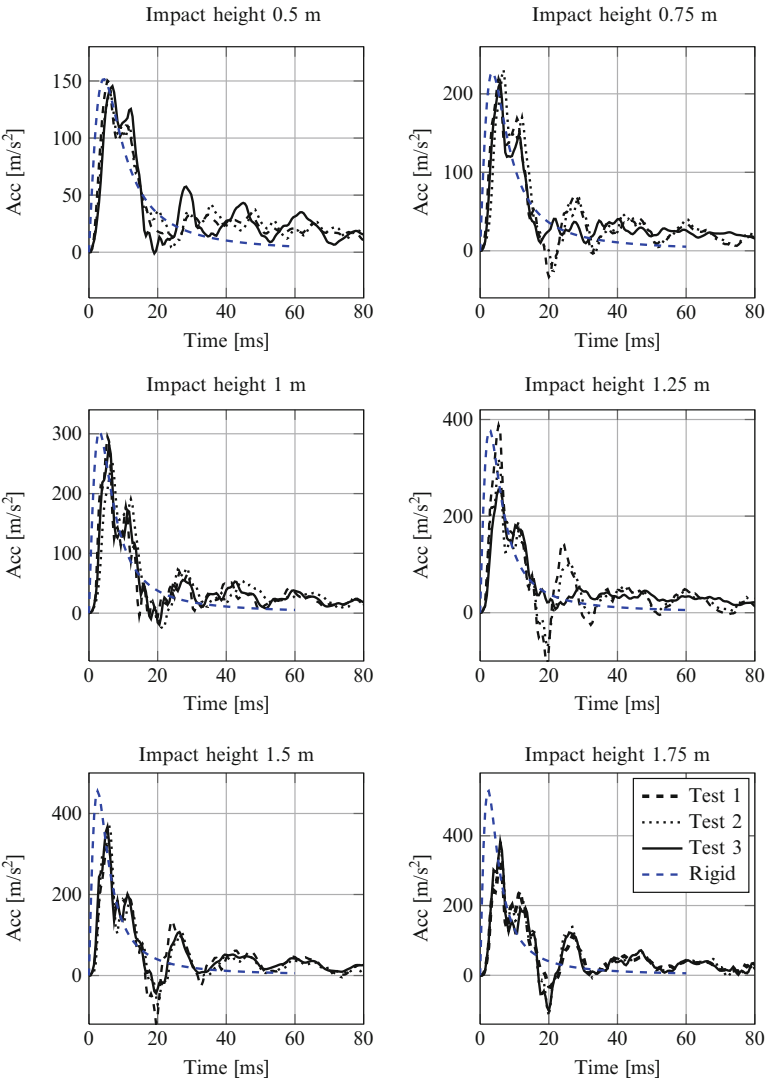


Fig. 13 Recorded accelerations of a composite wedge with $\beta = 15°$ impacting from various impact heights (three tests for each configuration, *black lines*) compared with the acceleration of a rigid wedge (*blue line*). An increasing dynamic response is clearly visible as the impact speed increases

response increases as the impact becomes more severe. The fourth plot (bottom, right) clearly shows this transition: the wedge with higher deadrise angle (35°, black full line) shows a smooth (almost sinusoidal) response; as the deadrise angle decreases oscillations appears. These results show that, as the impact becomes more severe, the dynamic response switches from a single-mode dominated response to a multiple-mode dominated deformation.

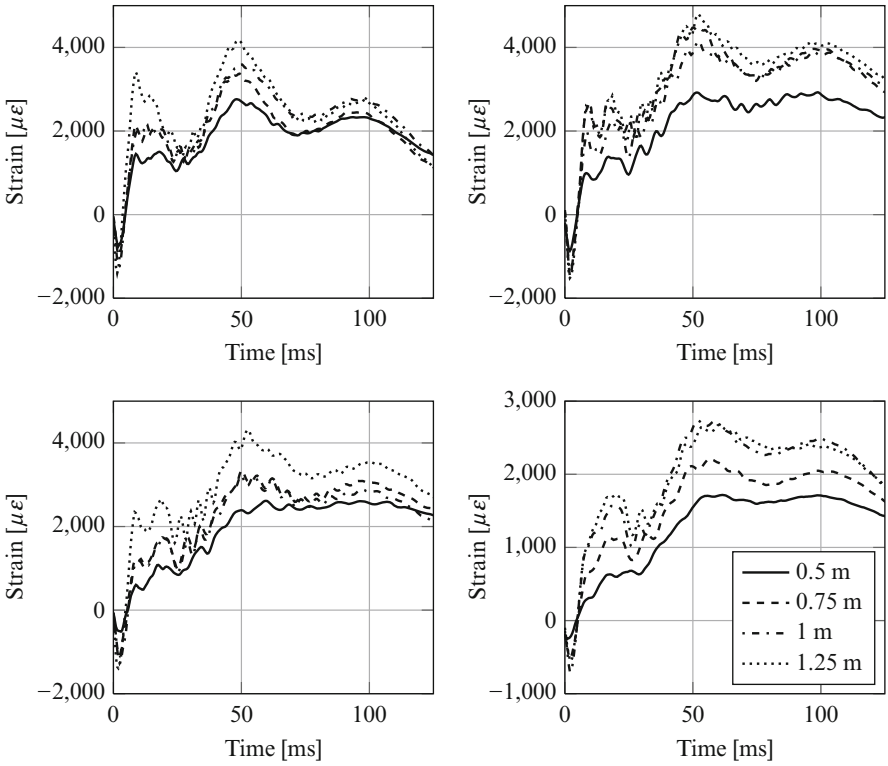


Fig. 14 Experimental recorded strains for various drop heights. Composite panel (V2), 2 mm thick. $\beta = 10^\circ$ (*top*, *left*), $\beta = 15^\circ$ (*top*, *right*), $\beta = 20^\circ$ (*bottom*, *left*), $\beta = 25^\circ$ (*bottom*, *right*)

Experiments show that in all the impact cases the strain measured by the strain gauge closer to the wedge apex initially assumes negative values. The strain is associated to the local curvature of the wedge, revealing that the panels are deforming downward at the very beginning of the impact. This deformation is opposite to the one induced by the impact pressure, that is pushing the wedge to deform upwards. This initial negative deformation has to be attributed to the effect of inertia: the hydrodynamic load acts on the wedge apex at first, to later spam on a larger area as the wedge enters the water. Furthermore, the maximum impact load is reached close to the beginning of the impact and rapidly decreases. Consequently, at first deformations are induced by the inertia of the panels that are being decelerated during the impact and consequently deform downward. As the wedge enters the water the hydrodynamic load covers a larger area and the deformation due to the pressure exceeds the deformation due to inertia, leading the strains to positive values.

Faltinsen [50] shows that, for local slamming-induced stresses, hydroelastic effects increase with decreasing deadrise angle β and increasing impact velocity V. Following a similar approach, we define a parameter R as the ratio between the

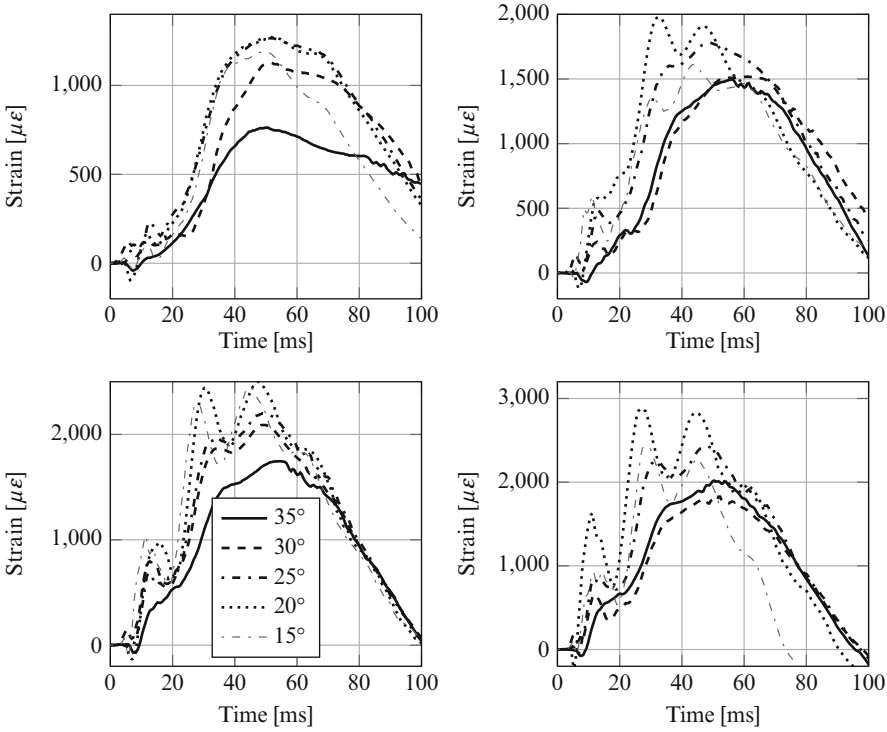


Fig. 15 Experimental recorded strains for various deadrise angle. Aluminium panel (A2), 2 mm thick. $V_0 = 3$ m/s (*top*, *left*), $V_0 = 4.2$ m/s (*top*, *right*), $V_0 = 5.2$ m/s (*bottom*, *left*), $V_0 = 6$ m/s (*bottom*, *right*)

wetting time and the lower natural period of the panel, where the wetting time was calculated by Wagner's approach. Figure 16 shows the non-dimensional recorded maximum strain $\frac{\epsilon_m EI tan(\beta)}{z_a V^2 \rho L^2}$ (as suggested in [50]) versus the parameter R. Where EI is the bending stiffness, z_a is the thickness and L is the panel length. Results of 2 mm thick panels are presented for various impact velocity, deadrise angle and material (blue marks: aluminum panels, red marks: composite panels (V), black marks: composite panels (W)). The non dimensional stress shows an increasing trend as the parameter R increases, to flatten once it reaches the unity value. This shows that hydroelastic effects (for the particular geometry studied) become important when the parameter R, which is proportional to the ratio between the wetting time and the first structural natural period, is lower than 1. In fact, in the range of $0 < R < 1$ the maximum strain is not proportional to V^2, as in quasi-steady-pressure loading, but decreases as the parameter R decreases. These results are similar to the one found by Faltinsen [16], whose model is based on the assumption of constant impact velocity and was not supported by experimental results.

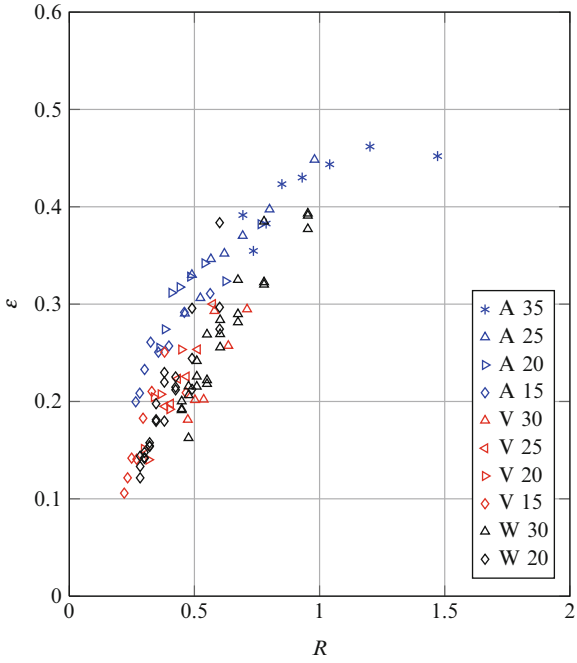


Fig. 16 Non-dimensional recorded maximum strain ϵ, presented as a function of a parameter R that is proportional to the ratio between the wetting time of a rigid wedge and the dry natural period of the panel [49]

4 Smoothed Particle Hydrodynamics (SPH)

A coupled FEM and SPH formulation available in the commercial FE code LS-Dyna was used to model the water entry of elastic wedges. In the following it is shown how the fluid is modeled and the validation of the SPH method to correctly study water entry problems. First, the SPH model is validated and optimized by comparison with analytical and numerical examples of simple problems. Then, the optimized model is used to study water impacts of elastic structures, comparing the numerical results with experiments.

4.1 Equation of State

To model the fluid, an equation of state (EOS) needs to be defined in LS-Dyna. In the literature the most used EOS is the Gruneisen model [51–53], which follows the formula:

$$p = \frac{\rho C^2 \mu \left[1 + \left(1 - \frac{\gamma_0}{2}\right)\mu - \frac{a}{2}\mu^2\right]}{\left[1 - (S_1 - 1)\mu - S_2 \frac{\mu^2}{\mu+1} - S_3 \frac{\mu^3}{(\mu+1)^2}\right]^2} + (\gamma_0 + a\mu)E \tag{13}$$

Table 3 Gruneisen model constants for water

C (m/s)	S_1	S_2	S_3	ρ (kg/m^3)	γ	a	E
1,480	2.56	1.986	1.2268	1,000	0.5	0	0

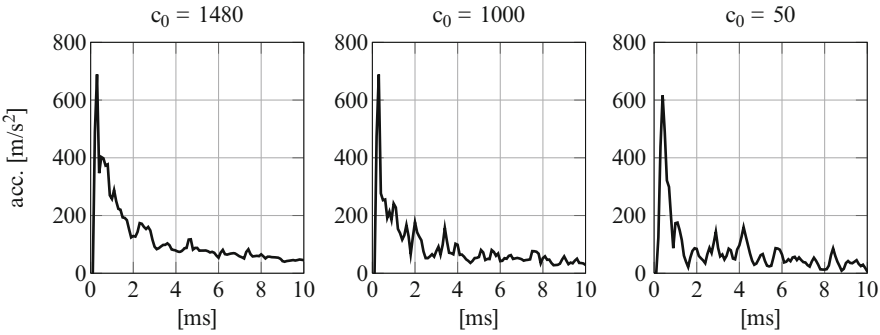


Fig. 17 Acceleration response of a wedge entering the water varying the bulk speed of sound. The acceleration shows increasing oscillations as the bulk speed decreases (*left* to *right*)

Where $\mu = \eta - 1$ (η is the ratio between initial an final density), C is the bulk speed of sound, ρ is the density of the fluid. There are many combinations for the constant that satisfy the water behavior. In this work we used the values presented in Table 3; values are taken from the literature [53].

By lowering the value of C it is possible to reduce the bulk speed of sound. A reduction in the pressure waves speed leads to an increase of the minimum time step needed for the solution and the consequent reduction of the computational time. Furthermore the traveling pressure waves take longer to reach the boundaries and reflect back towards the impactor, it is than possible to build a model where there are no reflected pressure waves during the entire solution time. A common value used in the literature for the waves speed is 80 m/s. The main disadvantage of this artifice is that, in case of slamming event, the quality of the impact dynamics get worse in terms of smoothness of acceleration and of the pressure distribution at the fluid/structure interface. For example, Fig. 17 shows the acceleration of a wedge entering the water at 4 m/s varying the bulk speed of sound (1,480, 1,000 and 80 m/s). Moving from the left graph to the right, as the bulk speed of sound decreases, the acceleration shows increasing oscillations.

To avoid this loss of quality it is necessary to increase the number of elements, increasing the computational time. For these reasons we preferred to use the real pressure wave speed of 1,480 m/s.

4.2 Validation of the Numerical Model

The numerical model should be capable of correctly predicting the fluid motion in order to replicate the impact dynamics of a body entering the water. At the same

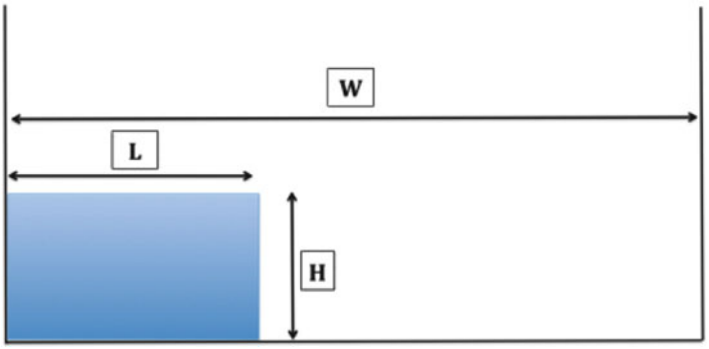


Fig. 18 Dam-break geometry. The *blue* region is the fluid, initially at rest, whose right boundary is suddenly removed to let the water occupy a larger tank. H = initial water depth, L = initial water length, W = water tank length once the boundary is removed

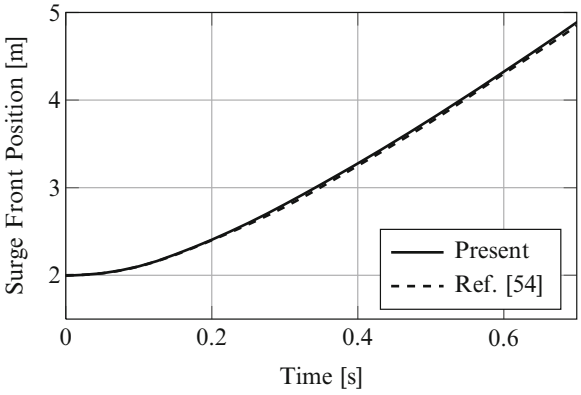


Fig. 19 Numerical solution of the surge front position vs. time. *Full line*: present solution. *Dashed line*: example from the literature [54]

time, the pressure distribution in the fluid should be accurate to guarantee the correct evaluation of the pressure at the fluid/structure interface. This section shows two models used to validate the numerical solution: the dam-break problem is used to validate its capability to treat the overall fluid motion, while the example of a water column subjected to a step load is used to evaluate the accuracy of the model when focusing on the pressure waves propagation.

The so called dam-break problem is often used in the literature as benchmark test to evaluate SPH accuracy ([40, 54–57]) in a two dimensional simulation of a water tank where a boundary is removed instantaneously to let the water to cover a larger tank (Fig. 18) where $f = 5.4\,\text{m}$, $L = 2\,\text{m}$ and $H = 1\,\text{m}$. The fluid is modeled by 180,000 particles and only the gravitational force is applied. Figure 19 shows the position of the front wave during time. Results about the water shape and the position of the surge front are in good agreement with those presented in the literature [40, 54–57]. However, while SPH seems to give accurate results for

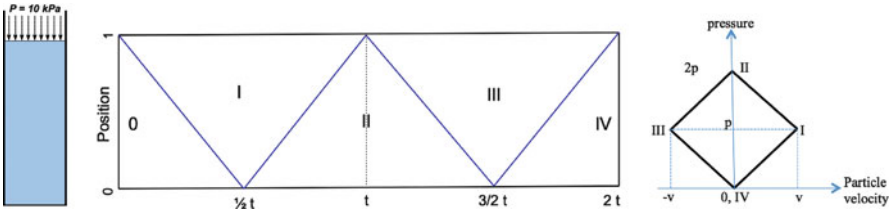


Fig. 20 *Left*: sketch of the water column loaded at the free surface by a constant pressure. *Center* and *right*: Lagrange diagram. Analytical solution for the reflection of a pressure wave during time

particles velocity and water flow, it seems not to correctly account for the pressure field, as it will be shown in the next example. In fact, as other numerical methods, SPH suffers noise in the pressure evaluation due to numerical fluctuations, leading to a poor definition of the pressure at the fluid/structure interface. This behavior is well known in the literature [58] and much effort is being spent on it. The most used technique to suppress these pressure fluctuations is the introduction of an artificial viscosity. Most of the work found in the literature focuses on the suppression of pressure oscillations in gases and solids [59–61]. To take into account the artificial viscosity [58,62], an artificial viscous pressure term q is added such that the pressure p of the ith particle is computed as:

$$p_i = p_i + q \tag{14}$$

where

$$q = \beta \cdot \rho \cdot h_i \cdot \dot{\epsilon}_{kk}^2 - \alpha \cdot c_0 \cdot \dot{\epsilon}_{kk} \tag{15}$$

where h_i is the minimum distance between the particles, α and β are the linear and quadratic coefficients and $\dot{\epsilon}$ is the strain rate. For gases the linear and quadratic terms are usually in the range $\alpha = 1.0 \div 4.0$ and $\beta = 1.5 \div 2.0$, while for solids $\alpha = 0.06$ and $\beta = 1.5$.

To study the influence of the artificial viscosity term for liquids, numerical results have been compared with an example considering a water column suddenly subjected to a uniform pressure load equal to 10 kPa on the free surface. An analytical solution to this problem is found assuming that it is governed by the one dimensional wave equation. Boundaries are fixed. Figure 20 shows the Lagrange diagram, which is divided in five regions, namely 0, I, II, III and IV. In region 0 and IV the pressure is null, in region I and III the pressure equals the applied pulse and in region II the pressure is twice the applied pulse. The related stress history at the top, bottom and middle of the water column is presented in Fig. 21. At the top, the pressure remains constant and obviously equals the applied pressure. At the bottom, pressure is zero until the first pressure wave reaches the boundary at time $1/2t$, when the wave is entirely reflected and the pressure becomes twice the incident pulse. Once the reflected wave reaches the top, at the time t, a second pressure wave of intensity equal to the applied pressure, but negative, is generated.

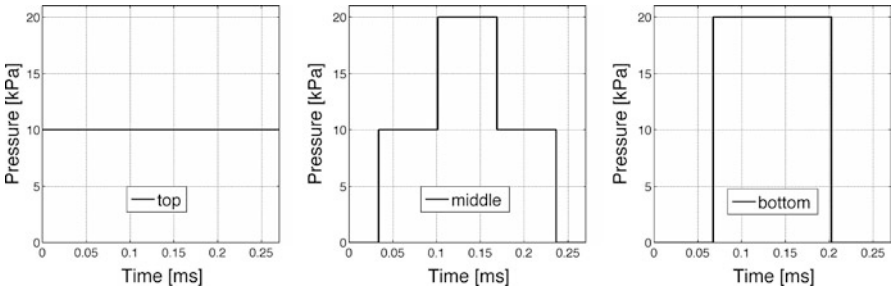


Fig. 21 Analytical solution of the pressure due to a wave propagation at the top (*left*), middle (*center*) and bottom (*right*) of a water column

This second wave reaches the bottom at time $3/2t$, it entirely reflects and the pressure at the bottom returns to zero. At the middle the pressure turns from zero to the applied pressure at time $t/4$, when the first wave pass through; the reflected wave arrives at time $3t/4$, switching the pressure to twice the applied pulse. The second (negative) wave arrives at $5t/4$, lowering the pressure again to the applied pressure, and the second reflected wave brings the pressure again to zero at time $7t/4$. In an ideal fluid this scheme continues infinitely with a period of $2t$.

Figure 22 shows the numerical results varying the linear bulk viscosity coefficient α of Eq. 15 (the quadratic term was found to have negligible effects) for a water column with particle spacing of 1 mm. The travelling wave theoretically switches the pressure value instantaneously without transitions. This behavior is difficult to reproduce numerically, since there is a transition between two different pressure regions which produces oscillations in the solution. This is known as Gibb's phenomenon and it occurs for most numerical methods unless some particular steps are taken to avoid it. These oscillations cannot be eliminated, but refining the particle size can reduce their duration and amplitude. The numerical results show that the artificial damping is effective for values as low as 0.2, and numerical fluctuations are entirely smoothed out for values of α greater than 0.5. These results show that the introduction of the artificial viscosity term lowers the pressure oscillations. However, in case of water-entry problems, the impact dynamics is negatively affected, as indicated by the results shown in Fig. 23. The graphs show the displacement and the velocity in time of a rigid wedge with a deadrise angle of 30° entering the water with an initial velocity of 4 m/s for various bulk artificial viscosity term. It is found that the higher the viscosity term, the higher the fluid resistance: the wedge decelerates more rapidly as the viscosity term increases, showing that α needs to be chosen as low as possible. For all the examples studied during this work α has been chosen to be lower than 0.2.

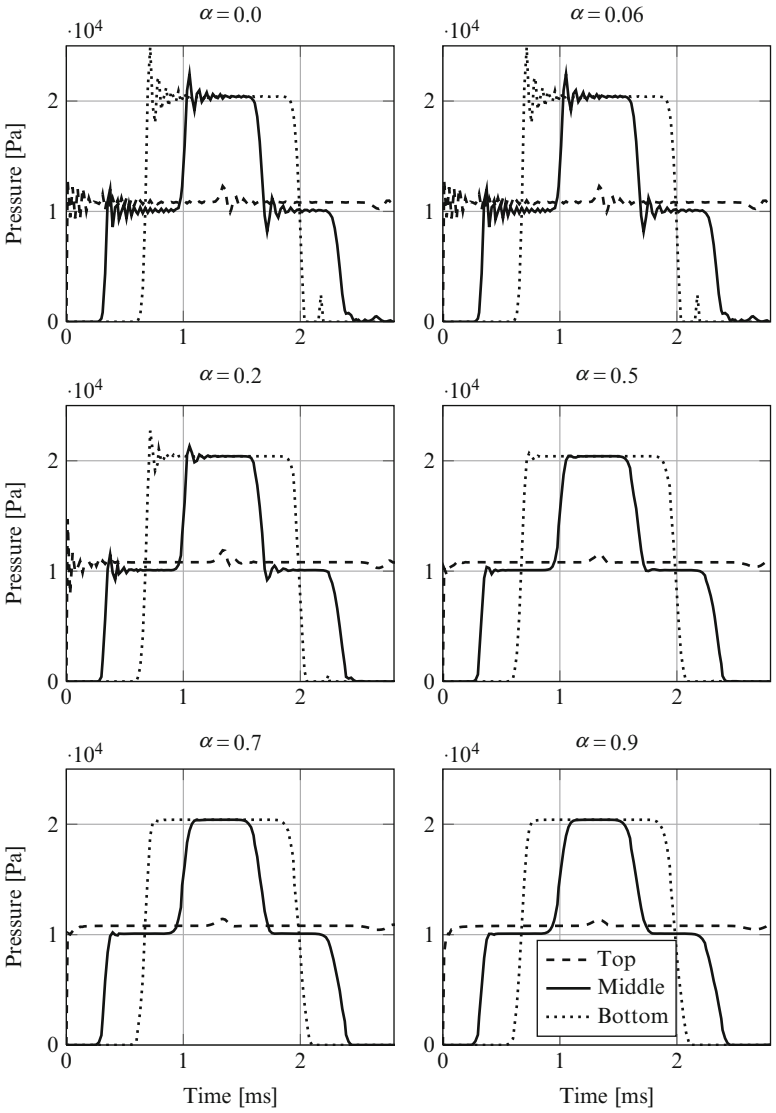


Fig. 22 Numerical pressure fluctuation reduction varying the linear artificial viscosity coefficient. *Dashed line*: top. *Full line*: middle. *Dotted line*: bottom of the water column

4.3 Non Reflecting Boundaries

In case of impacts on wide water surfaces, these can be considered as infinite since there are no reflected pressure waves travelling back to the impacting body. On the contrary, numerical solutions are necessarily affected by these reflected pressure

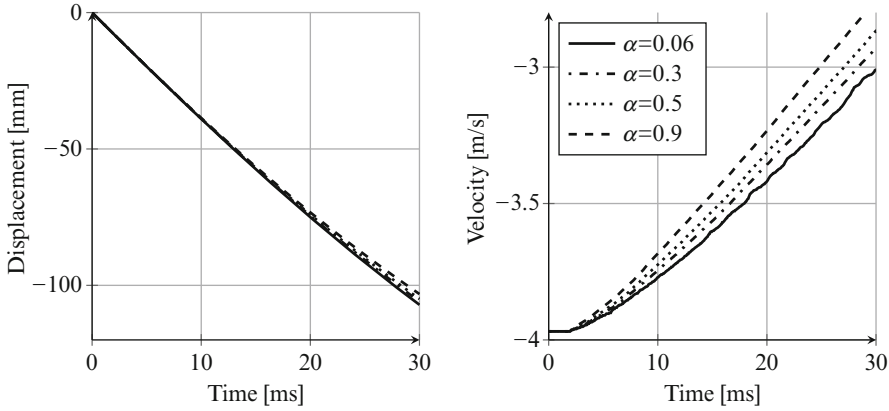


Fig. 23 Displacement and velocity during slamming of a rigid wedge entering the water with an initial velocity of 4 m/s varying the bulk artificial viscosity term α

waves, since to reduce the computational time it is necessary to limit the fluid domain. One of the most used technique to suppress the reflected pressure waves is to lower the speed of sound in the fluid (usually it is lowered from 1,480 to 80 m/s). As mentioned in Sect. 4.1, lowering the pressure waves speed permits to eliminate the reflected waves from the solution. However, since it is not always allowable to lower the sound speed, other techniques have to be used. In [63] Gong et al. proposed an improved boundary treatment capable to suppress wave reflection. They modeled the fluid with its real properties except for the last particles close to the boundary limits, whose sound speed has been reduced. This method presents the advantage of modeling the right fluid behavior together with the capability to entirely suppress the reflected pressure waves. Figure 24 shows the effect of the non reflecting boundaries in the case of a wave generated by the water entry of a cylinder: the pictures on top show a cylindrical pressure wave moving from the top to the bottom that, after 2 ms, is reflected in the case of rigid boundaries (on the right), while the non-reflcting boundaries (on the left) entirely absorbed it.

4.4 Comparison with Analytical Models

The optimized SPH model is now used to study the water entry of rigid wedges and its results are compared with those from the analytical models presented in Sect. 1.1. The model of the water entry of the wedge is based on the following main assumptions:

1. The fluid free surface is initially at rest;
2. Air is not included in the model. Air cushioning and air entrapment are consequently neglected;

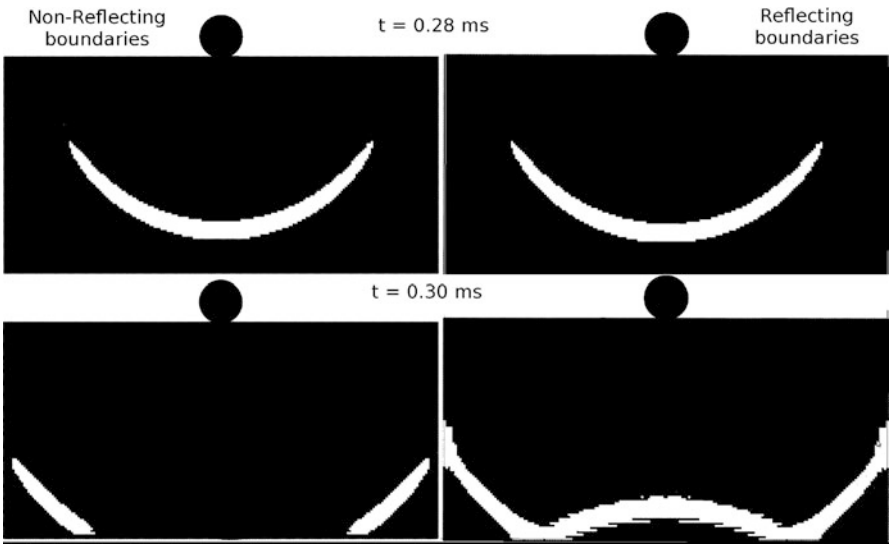


Fig. 24 Position of a pressure wave generated by the water entry of a cylinder before and after it reaches the boundaries: non-reflecting boundaries (*left*, the wave is absorbed) vs. rigid boundaries (*right*, the wave is reflected)

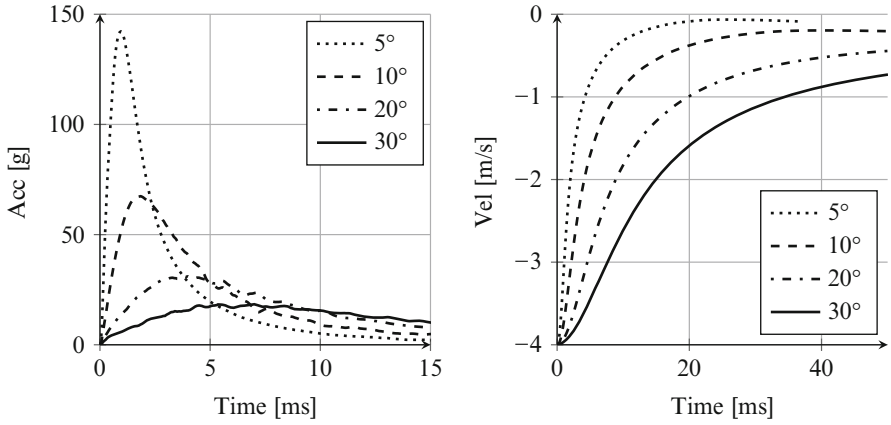


Fig. 25 Acceleration and velocity of a wedge varying the deadrise angle β. Total wedge mass: 20 kg per unit width. SPH simulations with rigid wedges

3. The wedge is assumed infinite along the z-axis (3D boundary effects are not included);
4. The problem is symmetrical with respect to the zy plane (y is the gravity direction, as in Fig. 6).

Figure 25 shows the SPH numerical results of the impact dynamics for rigid wedges of various deadrise angle entering the water at 4 m/s. The numerical results show a

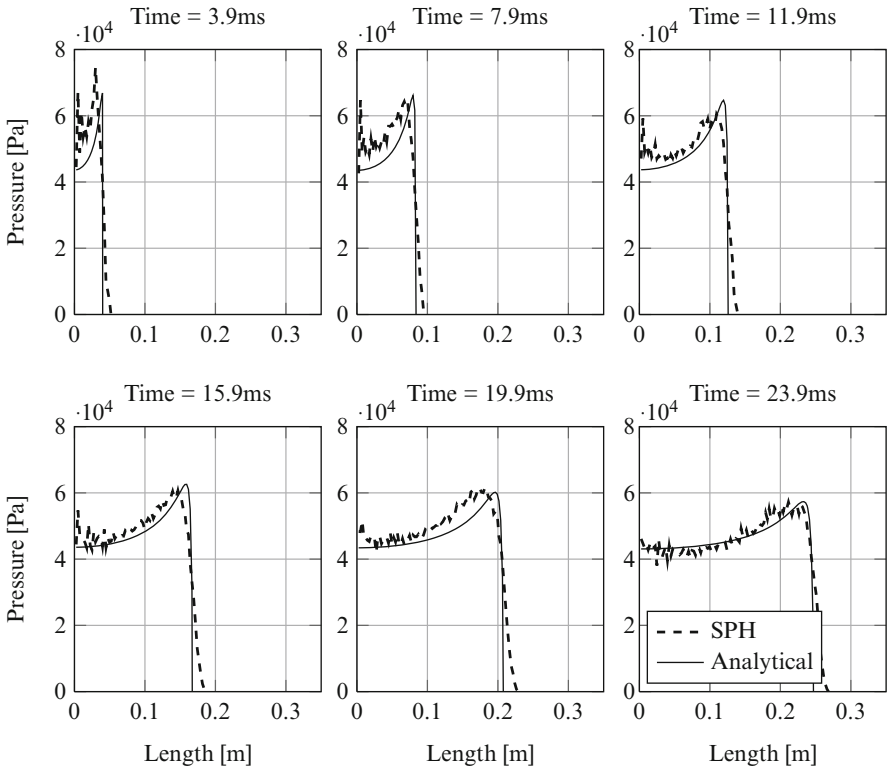


Fig. 26 Pressure in time at the fluid/structure interface for a wedge of 500 kg/m, deadrise angle 30° and initial velocity $V_0 = 4$ m/s. *Full line*: Wagner analytical solution. *Dashed line*: numerical results

good agreement with Von Karman's solution (Fig. 2) and Eqs. 2–6. The difference between the analytical and the numerical maximum impact force is always lower than 5% while the difference between the time the force peak is reached is lower than 15%.

Figure 26 shows the comparison of the pressure along the wedge between Wagner's solution and the numerical results for a wedge entering the water at 4 m/s with a deadrise angle of 30° and a mass per unit width of 500 kg/m. SPH results are in very good agreement with Wagner's solution except for the very initial contact time, since there are too few elements in contact to show a smooth pressure distribution at the interface. The maximum pressure value is reached at the beginning of the impact, and is constant for a given entry velocity and deadrise angle, while mass is affecting only the impact dynamics.

These results validate the SPH method and reveal that it is actually capable of predicting the impact dynamics and the pressure at the fluid/structure interface of rigid bodies entering the water. Thus, the SPH method will now be used for the analysis of water impacts of elastic structures, where analytical solutions are not available.

Table 4 Scheme of numerical simulations. The table shows the abbreviation of the various combination of material, thickness and entry velocity

	Material	Thickness (mm)	Impact velocity (m/s)
A2-4	Aluminum	2	4
A4-4	Aluminum	4	4
A2-2	Aluminum	2	2
A4-2	Aluminum	4	2
V2-4	Fibreglass	2	4
V4-4	Fibreglass	4	4
V2-2	Fibreglass	2	2
V4-2	Fibreglass	4	2

5 Elastic Wedges

The previous sections show that SPH is capable of modeling the impact dynamic and the pressure at the fluid/structure interface during the water entry of rigid wedges. In the following, elastic wedges are considered. The structural deformation might change the motion of the fluid introducing the so-called hydroelastic effects, causing the impact dynamics to differ from that of rigid wedges.

This section presents a parametric analysis of hydroelastic impacts of elastic wedges entering the water varying wedge flexural stiffness, impact velocity, deadrise angle and SPH particles size. Wedges are modeled as an ideally elastic aluminum (E = 70 GPa, $\nu = 0.3$, $\rho = 2{,}700\,\text{kg/m}^3$), or as an ideally elastic fibreglass mat composite ($E_1 = E_2 = 20$ GPa, $\nu = 0.3$, $\rho = 2{,}050\,\text{kg/m}^3$). To be able to compare wedges of different thickness, an added mass is applied to the tip of the wedge to reach a total mass of 20 kg per unit width in all analysis. Faltinsen [16] demonstrated that hydroelastic effects become important when

$$tan(\beta) \; < \; 0.25\, V \sqrt{\frac{\rho L^3}{E I}} \tag{16}$$

showing that the occurrence of hydroelastic effects depends on: impact velocity, deadrise angle and structural stiffness. In particular, the higher the impact velocity V, the lower the deadrise angle β and the higher the structure natural period T_1 is, the more important the hydroelastic effects are. To investigate the effect of hydroelasticity on the impact dynamics, wedges of different thickness were implemented: 2 and 4 mm, both for aluminum and fibreglass composite wedges. This way four different bending stiffness are considered: plates flexural stiffness compared to the stiffer one (aluminum 4 mm thick) are in the ratio of 1:1, 1:4, 1:8, 1:32. The effect of impact velocity has been also investigated. Table 4 shows the list of the numerical simulations campaign.

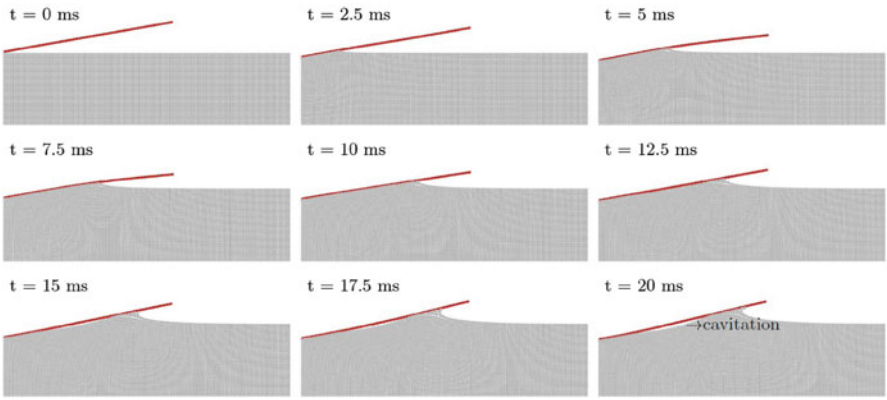


Fig. 27 Wedge deformation over time. 10° deadrise angle, 4 mm thick, 4 m/s initial velocity

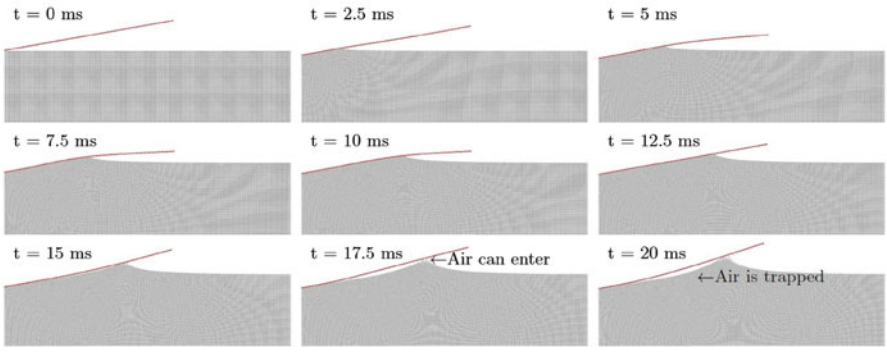


Fig. 28 Wedge deformation over time. 10° deadrise angle, 2 mm thick, 4 m/s initial velocity. Due to the structural vibrations some air might enter from the side and be trapped in the fluid

5.1 Hydroelastic Effects

Figures 27 and 28 show two examples of the water entry of deformable wedges. In the first one, an aluminum wedge 4 mm thick with deadrise angle of 10° is entering the water at 4 m/s. The second one shows the same example but the wedge thickness is 2 mm. Initially (up to 2.5 ms in these cases), the deformation of the wedge is low, so that it behaves like a rigid wedge. Then, the deformation of the wedge becomes important (≈5 ms) resulting into a mutual interaction between the fluid motion and the structural deformation. In this initial time of impact, the wedge is deforming downward due to its inertia. The wedge eventually reaches its maximum deformation (≈7.5 ms) and starts bending in the other direction (at ≈10 ms the wedge is in its neutral position, as shown in the central plot of Fig. 27). At this point, three events may happen:

1. The entire wetted portion of the wedge stays in contact with the water, and no air is entrapped in between the solid and the fluid. The fluid/structure interaction continues and the vibrations are damped by the fluid.
2. Along the wet part of the wedge the fluid tends to move away from the wedge, then pressure becomes negative and cavitation occurs, as shown in Fig. 27, from the seventh plot (when the impact time is 15 ms) and above.
3. The wedge detaches from the fluid and some air enters from the side. The air is eventually trapped in between the wedge and the fluid and an air cushion is generated, as shown in Fig. 28. In this case the interaction between the air flow and the fluid flow has to be taken into account.

In the cases studied, cavitation and ventilation phenomena appeared only in the cases of deadrise angle of 10° and initial velocity of 4 m/s (i.e. the most severe case). In all the other cases no fluid detachment was predicted.

An example of the effect of the structural deformation on the impact pressure in which no fluid detaches from the wedge and no air is trapped in the fluid during the impact is presented in Fig. 29. The plots show the comparison of the pressures over time of a rigid wedge vs. an elastic wedge (aluminum 2 mm thick) with deadrise angle of 30° and total mass of 20 kg/m entering the water at 4 m/s. It is found that the two solutions show extremely similar results at the beginning of the impact (until about 12 ms), when the impact pressure is higher. Pressures are similar until the panel has reached its maximum negative (leaded by the inertia) deformation. Once the wedge starts to deform in the opposite direction, the pressure eventually reduce to a lower value compared to the rigid case. Note that at this time the impact force is already in its descending phase and the maximum impact force has already been reached.

5.2 Impact Dynamics

This section presents a parametric study of the effect of fluid-structure interaction on the impact dynamics. Figures 30–32 show a parametric study varying the particle size of the numerical solutions of aluminum wedges 2 mm thick with deadrise angle of 10°, 20°, and 30° respectively, entering the water at 4 m/s. Since only vertical impacts are considered, one half of the wedge and water are modeled splitting the structure on its symmetry axis. Wedges side length is 300 mm while the fluid domain has been modeled as a tank 800 mm width and 600 mm height. Three particles sizes have been chosen for the simulations: 1 mm (*Fine model, 480,000 particles*), 2.5 mm (*Medium model, 192,000 particles*) and 5 mm (*Rough model, 48,000 particles*). The computation takes about 12 h to run in the case of fine model and only about 0.5 h for the rough model. Results show that the particle size is only slightly affecting the impact dynamics (velocity and acceleration are evaluated at the wedge tip). While velocity is computed correctly, the acceleration tends to present fluctuations increasing with the particle size, especially in the early stage of the impact. These

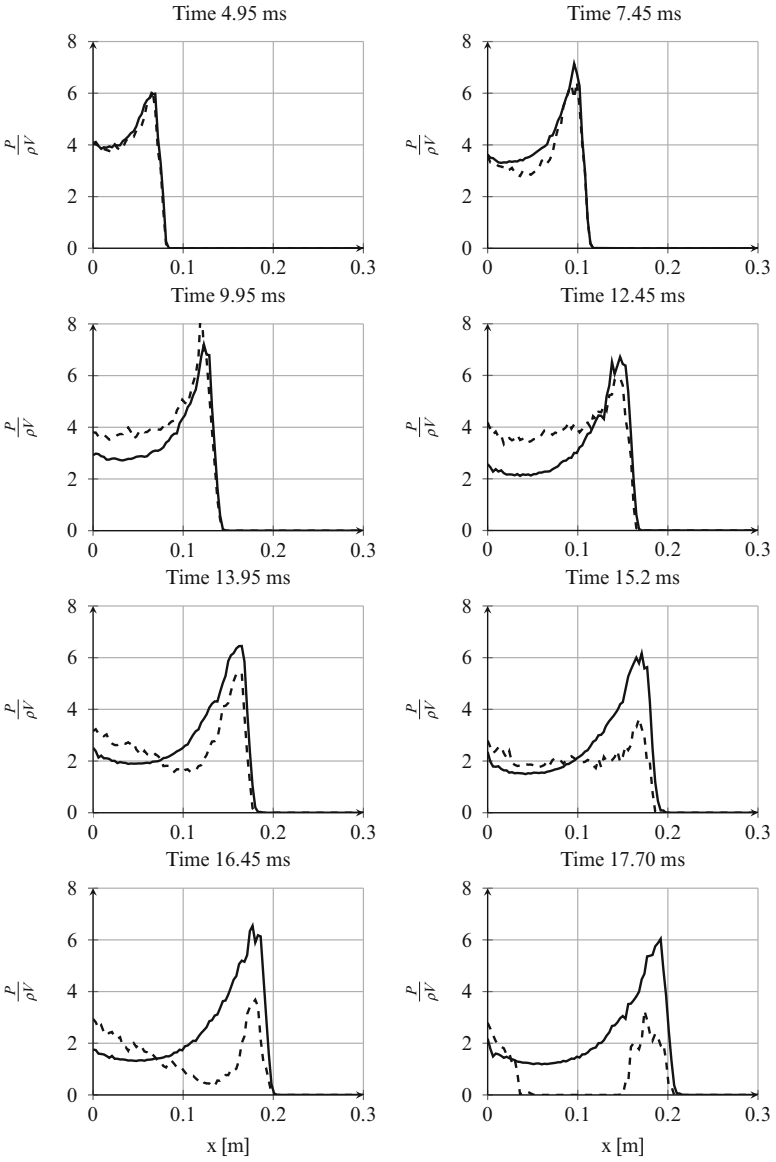


Fig. 29 Non-dimensional hydrodynamic pressure along the wedge over time. P is the hydrodynamic pressure, ρ is the density of the water and V is the instant velocity of the wedge. Deadrise angle 30°, mass 20 Kg/m. Comparison between rigid wedge (*solid line*) and elastic wedge (*dashed line*, aluminum wedge 2 mm thick). Results are similar at the beginning of the impact but diverges rapidly after 10 ms

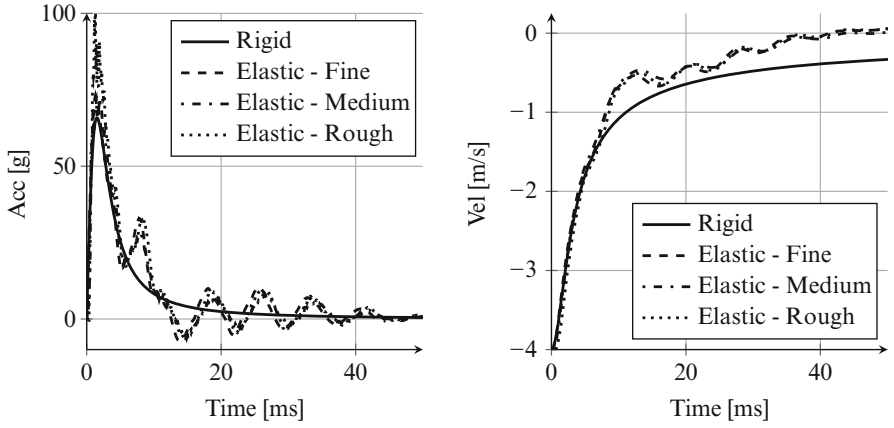


Fig. 30 Acceleration (*left*) and Velocity (*right*) of a wedge varying the particle size. Total wedge mass: 20 kg per unit width. Deadrise angle 10°. Comparison between the solution for a rigid wedge (*solid line*) and the simulation of a deformable wedge entering into a fluid modeled by three various particle sizes (*dashed lines*)

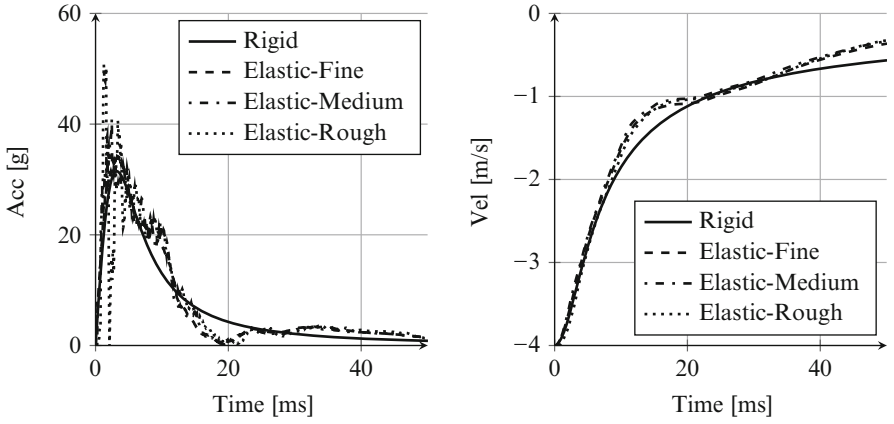


Fig. 31 Acceleration (*left*) and Velocity (*right*) of a wedge varying the particle refinement. Total wedge mass: 20 kg per unit width. Deadrise angle 20°. Comparison between the solution for a rigid wedge (*solid line*) and the simulation of a deformable wedge entering into a fluid modeled by three various particle sizes (*dashed lines*)

fluctuations increase with the deadrise angle. This behavior is due to the lower number of particles getting in contact with the wedge while raising the deadrise angle. Furthermore, the maximum acceleration is found to increase with the particle size due to the aforementioned fluctuations.

As expected from Faltinsen's [16] observations, the computed impact-induced acceleration are found to differ from the rigid case for all the deadrise angles investigated. Figures 30–32 show that the impact dynamic of the elastic wedges initially follows the solution for rigid structures until the maximum acceleration

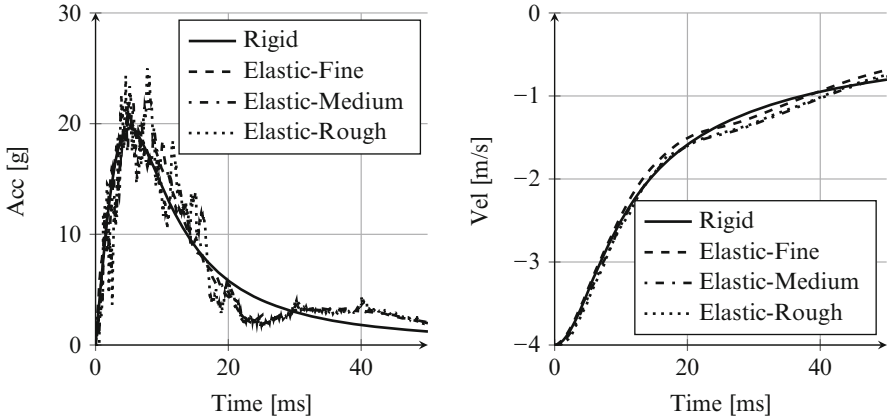


Fig. 32 Acceleration (*left*) and Velocity (*right*) of a wedge varying the particle refinement. Total wedge mass: 20 kg per unit width. Deadrise angle 30°. Comparison between the solution for a rigid wedge (*solid line*) and the simulation of a deformable wedge entering into a fluid modeled by three various particle sizes (*dashed lines*)

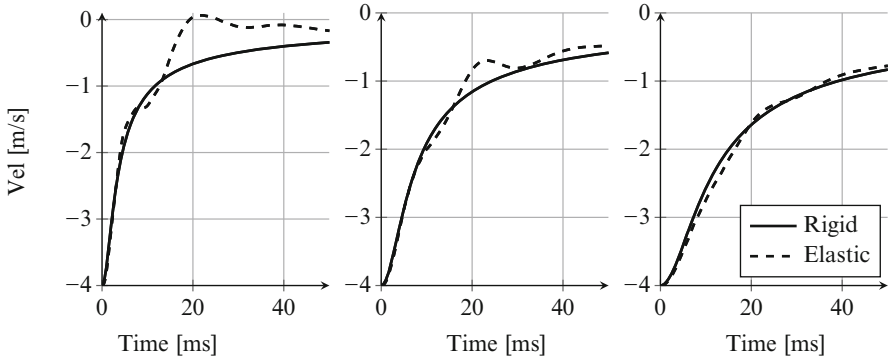


Fig. 33 Hydroelasticity effect on the impact dynamics of aluminum wedges 4 mm thick of different deadrise angles entering the water at 4 m/s. From *left* to *right*: 10°, 20°, 30° deadrise angle

is reached, to later differ due to oscillations whose magnitude increase as the maximum acceleration increases.

Figure 33 shows the comparison of the impact dynamics of elastic and rigid 4 mm thick aluminum wedges with different deadrise angles entering the water with an initial velocity of 4 m/s. As before, results are in accordance with Faltinsen's observations: hydroelasticity highly affects the impacts of wedges with deadrise angle from 5° to 20°, while the 30° behavior is close to the rigid wedge and very small hydroelastic effects appear. Figure 34 shows the same example but the wedges are entering the water at 2 m/s. In the cases of 20° and 30° deadrise angles fluid-structure interactions are small and elastic wedges behaves like the rigid wedges. Figures 35 and 36 compare the results for given deadrise angles and impact

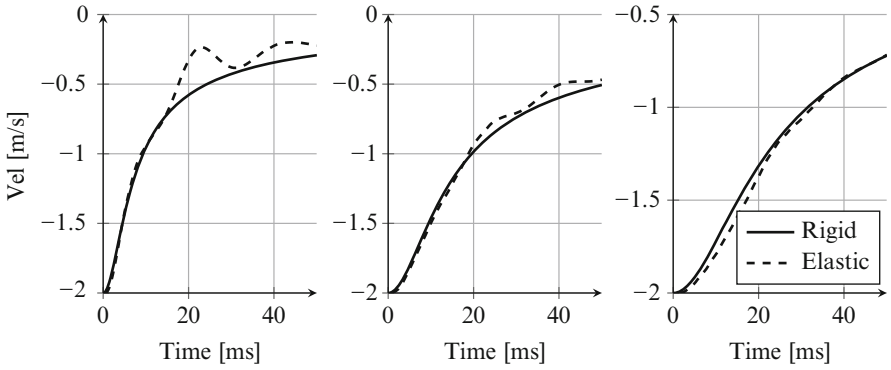


Fig. 34 Hydroelasticity effect on the impact dynamics of aluminum wedges 4 mm thick of different deadrise angles entering the water at 2 m/s. From *left* to *right*: 10°, 20°, 30° deadrise angle

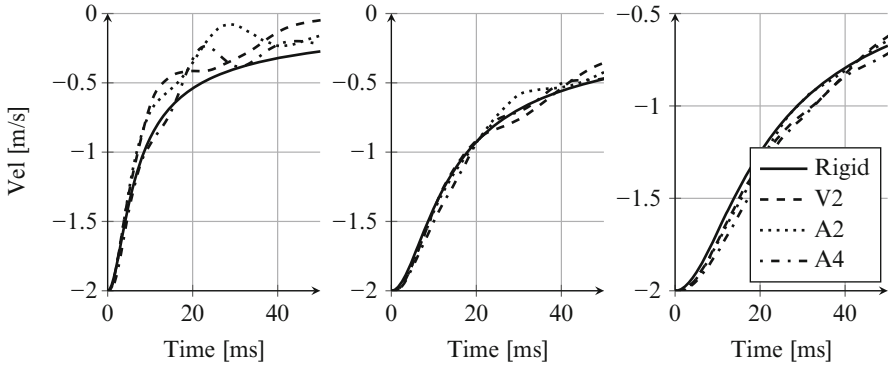


Fig. 35 Impact dynamics varying plate stiffness, deadrise angle from *left* to *right*: 10°, 20°, 30°, $V_0 = 2$ m/s

velocities varying the plate stiffness. Results are as expected: hydroelastic effects lower with increasing deadrise angles and plate stiffness, while they increase with the impact velocity. Further results about the importance of hydroelasticity on the structural deformation are presented in the next section, where a dependency of the structural response from the hydroelastic effect is shown.

5.3 Stresses Evaluation

It was shown in the previous section that increasing the particle size leads to an overestimation of the maximum acceleration due to oscillations in the computed acceleration, although the velocity is computed correctly. This section investigates the effect of the particle size on the stress computation.

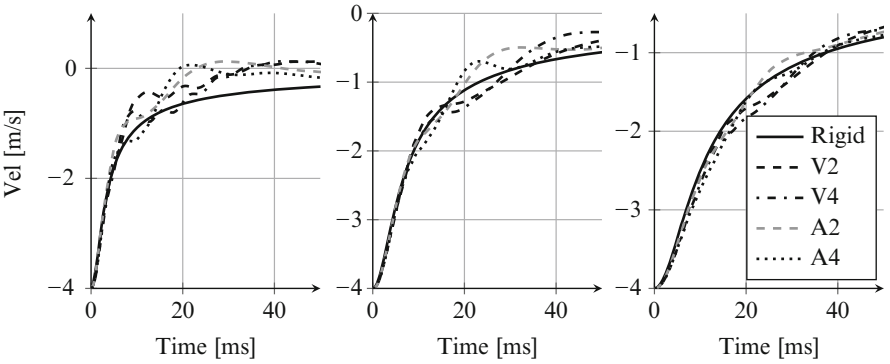


Fig. 36 Impact dynamics varying plate stiffness, deadrise angle from *left* to *right*: 10°, 20°, 30°, $V_0 = 4$ m/s

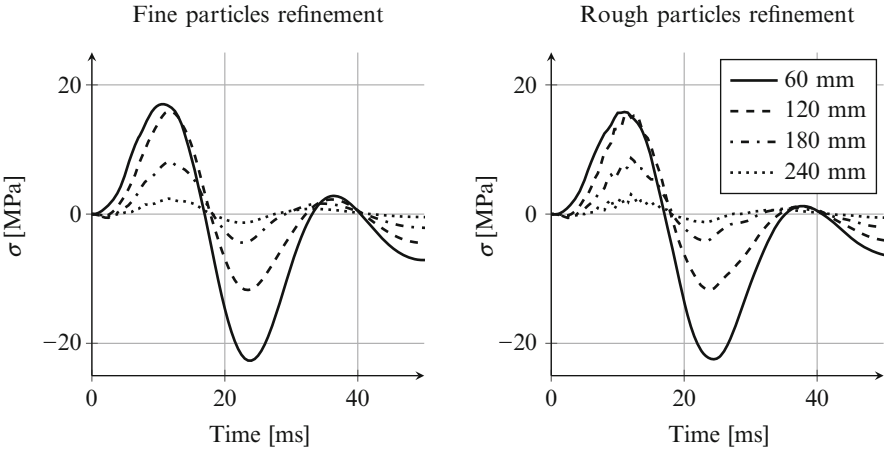


Fig. 37 Stresses at different distances from the wedge tip for fine and rough particle refinement. $\beta = 30°$, $V_0 = 4$ m/s

Figures 37 and 38 show the comparison of the stresses during time at different distances from the wedge tip in case of fine and rough particles refinement models. Results are definitely in good agreement, especially considering that the difference in the computational time between the fine particles model and the rough particles model is about 12 vs. 0.5 h. As mentioned before, the main disadvantage of increasing the particle size is that it becomes impossible to evaluate the pressure at the fluid/structure interface, however, this was found not to influence the evaluation of the structural deformation. The cases of 30° and 10° deadrise angles are shown, since these represent respectively the minimum and maximum influence of hydroelastic effects on the impact loads. In the first case, the wedge deformation is smooth with an almost sinusoidal shape, while moving to a more severe impact (lowering the deadrise angle from 30° to 10°) the stresses show high fluctuations, suggesting that more modes of vibrations superpose.

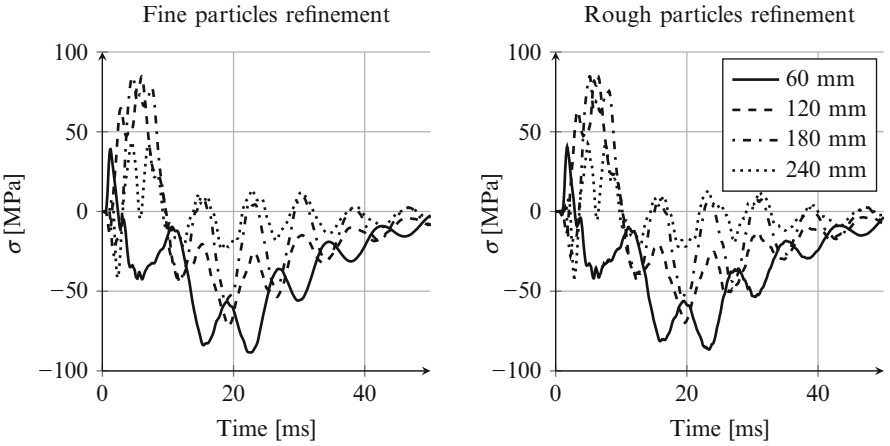


Fig. 38 Stresses at different distances from the wedge tip for fine and rough particle refinement. $\beta = 10°$, $V_0 = 4$ m/s

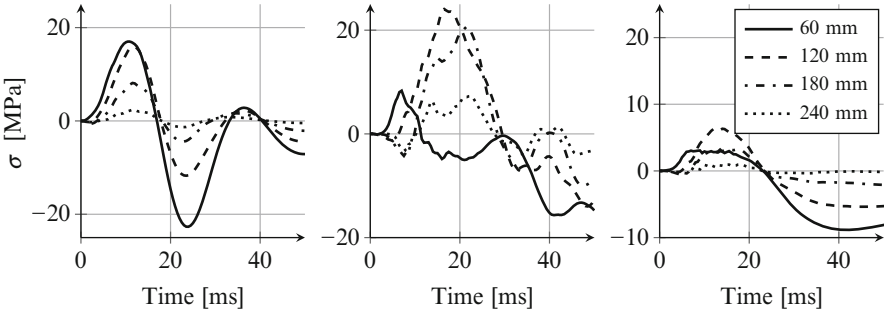


Fig. 39 Stresses at different distances from the wedge tip increasing the hydroelastic effect. A4-4 (*left*), A2-4 (*center*), V2-4 (*right*). $\beta = 30°$ ($V_0 = 4$ m/s)

Effects similar to the reduction of the deadrise angle are found by reducing the plate stiffness. Figure 39 shows a comparison of wedges with 30° deadrise angle and different stiffness entering the water at 4 m/s. Results show that moving from a stiffer plate (on the left, aluminum 4 mm thick plate) to a weaker plate (Fibreglass 2 mm thick, on the right), hydroelastic effects become more important and the deformations of the plate get more complicate since more vibrating modes superpose.

5.4 Influence of the Structural Deformation on the Impact Dynamics

As suggested in [16], the loading can be considered as quasi static if the loading period is significantly larger than the first natural period of the structure, otherwise

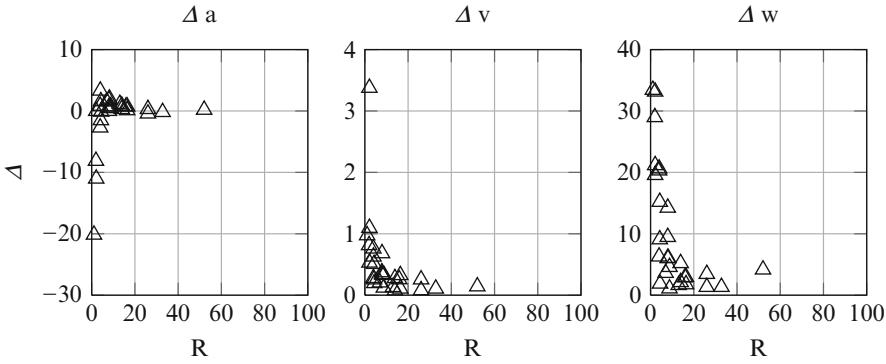


Fig. 40 Maximum impact dynamics variation between SPH results and Von Karman results. Acceleration a (m/s^2) (*left*), Velocity v (m/s) (*center*) and Displacement w (mm) (*right*)

hydroelastic effects might appear. Figure 40 shows the maximum variation with respect to Von Karman's results as function of the term R given by the ratio between the wetting time calculated as $\frac{tan(\beta)\cdot l}{v_0}$ and the first dry natural period of the structure calculated by the beam theory. β is the deadrise angle, v_0 is the impact velocity and l is the wedge side length. The numerical impact dynamics has been evaluated at the tip of the wedge. The calculation of the maximum variation between SPH and Von Karman results was calculated as:

$$\Delta a = max\left[a_{SPH}(t) - a_{th}(t)\right] \tag{17}$$

$$\Delta v = max\left[v_{SPH}(t) - v_{th}(t)\right] \tag{18}$$

$$\Delta w = max\left[w_{SPH}(t) - w_{th}(t)\right] \tag{19}$$

Results show that the impact dynamics differ from the Von Karman's analytical solution for values of R lower than 1, meaning that hydroelasticity needs to be taken into account when the wetting time is lower than the first structural dry natural period.

6 Comparison Between Experiments and Numerical Results

In the previous sections, experimental and numerical results were presented separately. In this section, the numerical results are compared with experiments.

Figures 41–43 show the comparison between experimental (blue lines) and numerical (red lines) results of the water-entry of elastic wedges. Figures 41 and 42 show the impact-induced stresses in an aluminum plate 2 mm thick with deadrise angle of 30° entering the water at 3 and 4 m/s. The numerical solutions compare well with the experimental results: stresses in time are well replicated both in terms of

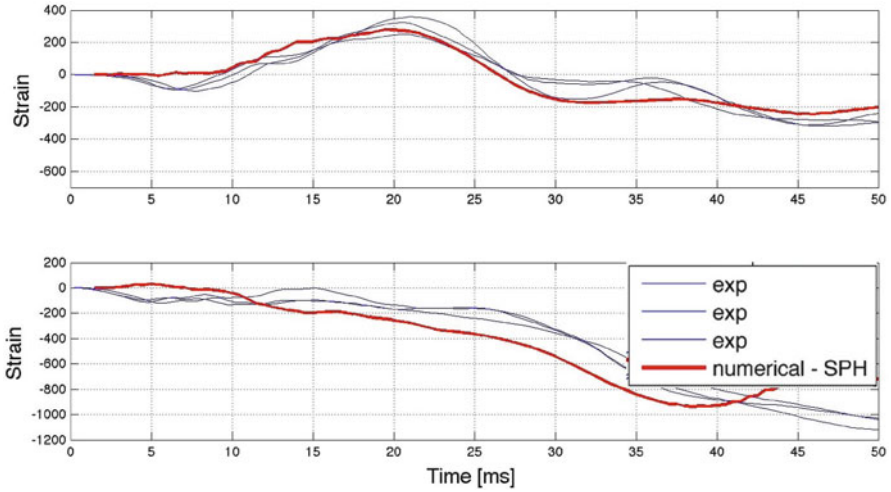


Fig. 41 Recorded strains and numerical solution of an aluminum wedge 2 mm thick, deadrise angle $\beta = 30°$. Initial velocity 3 m/s

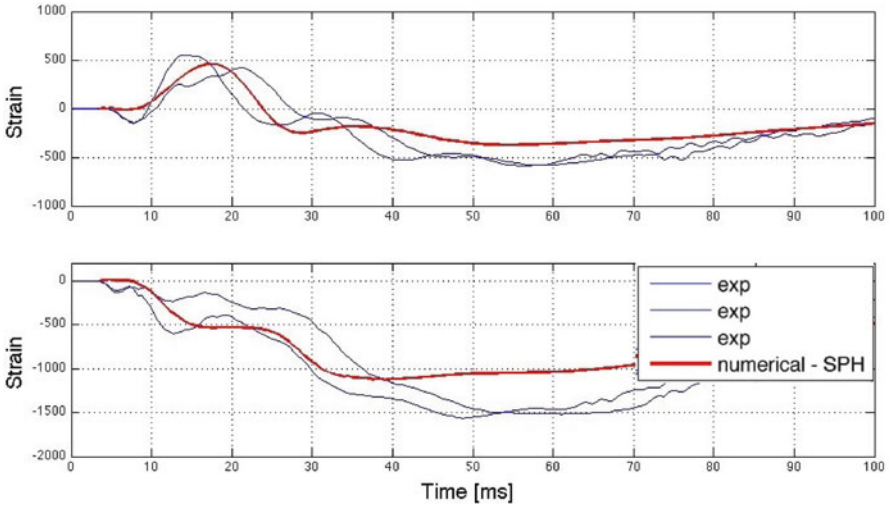


Fig. 42 Recorded strains and numerical solution of an aluminum wedge 2 mm thick, deadrise angle $\beta = 30°$. Initial velocity 4 m/s

maximum value and overall shape. This indicates that the simulations are correctly replicating the fluid/structure interaction in case of hydroelastic impacts. These results are particularly interesting considering that the panels are only 2 mm thick, deformations are consequently very high and the fluid motion is highly modified by the structure.

In Fig. 42 the numerical solution slightly differs from the experimentally recorded values after 40 ms of impact. This difference has to be attributed to

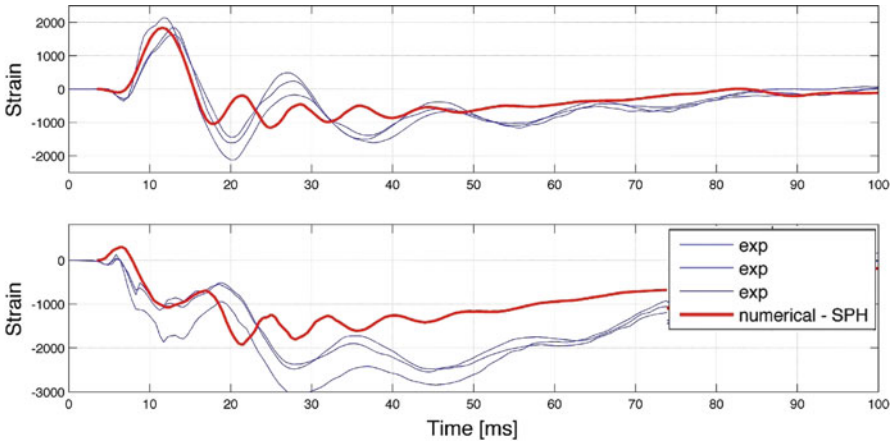


Fig. 43 Recorded strains and numerical solution of an aluminum wedge 2 mm thick, deadrise angle $\beta = 15°$. Initial velocity 5 m/s. Note that after 20 ms the experimental recorded strain show longer period of vibration compared to the numerical results

boundary effects: after 40 ms the entire wedge is wet and the water starts to overflow the panel from the side. To solve this problem the hydrodynamic loads acting on the free edge of the wedge have to be computed accurately. This can be done increasing the particle spatial resolution, with a consequent increase of the computational time. However, this problem is not on interest at this stage of the work.

Figure 43 shows the comparison between numerical and experimental results of an aluminum wedge 2 mm thick with deadrise angle of 15° entering the water at 5 m/s. In this case the numerical solution fits with the experiments only in the very first instants of the impact, approximately up to 20 ms. Later, the plates vibrates at higher frequencies in the numerical solution than in reality. In this simulation in fact the wedge detaches from the fluid and vibrates like in vacuum.

7 Conclusions

In this work, hydroelastic impacts of deformable wedges entering the water through free fall motion was studied numerically and experimentally. The water entry of rigid structures has been previously treated in the literature by other authors, however, on the contrary with their studies, this work investigates extremely flexible structures, introducing high hydroelastic effects. Furthermore, in opposition with what done in the literature, interest was pushed not only on the evaluation of the pressure at the fluid/structure interface but also on the overall structural deformation. Hydroelastic effects were studied as function of different parameters like: deadrise angle, impact velocity and plate stiffness to area mass ratio. In particular, it was found that hydroelastic effects lower increasing deadrise angle and plate stiffness,

while increase with the impact velocity. The relative importance of hydroelasticity was found to be governed by the ratio (R) between the wetting time and the natural period of the structure. For the particular geometry studied, hydroelasticity is important for values of R lower than 1.

The experiments were replicated by a numerical method. A coupled SPH/FEM model was used for the simulations and, validating the solutions with the experimental results, it was found that this model is actually capable of correctly modeling the fluid behavior and of predicting hydroelastic impacts, although a range of validity applies. For the cases studied, it was found that the structural deformation is not affecting the hydrodynamic pressure at the fluid/structure interface during the first instants of the impact: remarkable variations in the pressure at the fluid/structure interface appears only after the maximum impact force is reached. The presented SPH model was found to be able to simulate hydroelastic impacts if no air is trapped between the structure and the fluid. In fact, if (due to the structural deformation) air bubbles are trapped into the fluid during the impact, air cannot be neglected in the numerical model. By the numerical simulations it was also possible to better understand the mechanisms causing cavitation and air entrapment between the structure and the fluid due to hydroelastic effects.

Acknowledgements This research would not have been possible without the support and assistance of Prof. Serge Abrate, Prof. Giangiacomo Minak and Prof. Andrea Zucchelli, whose guidance and constant encouragement throughout the years will never be repaid enough.

Support from the Office of Naval Research (Grant n. N00014-12-1-0260) and the encouragement from the manager of the Solid Mechanics Program Dr. Yapa Rajapakse are gratefully acknowledged.

References

1. Von Karman TH (1929) The impact on seaplane floats, during landing. National Advisory Committee for Aeronautics, Washington, DC. NACA-TN-321
2. Mei X, Liu Y, Yue D (1999) On the water impact of general two-dimensional sections. Appl Ocean Res 21:1–15
3. Wagner H (1932) Uber Stoss-und Gleitvorgange an der Oberflache von Flussigkeiten. Z angew Math Mech 12(4):193–215
4. Daidola JC, Mishkevich V (1995) Hydrodynamic impact on displacement ship hulls: an assessment of the state of the art. Ship Structure Committee report SSC-385, NTIS PB96-129101
5. Korobkin A (2006) Second-order Wagner theory of wave impact. J Eng Math 58(1–4):121–139
6. Yettou E, Desrochers A, Champoux Y (2007) A new analytical model for pressure estimation of symmetrical water impact of a rigid wedge at variable velocities. J Fluids Struct 23(3):501–522
7. Judge C, Troesch A, Perlin M (2004) Initial water impact of a wedge at vertical and oblique angles. J Eng Math 48(3/4):279–303
8. Korobkin A (1988) Inclined entry of a blunt profile into an ideal fluid. Fluid Dyn 23(3):443–447
9. Riccardi G, Iafrati A (2004) Water impact of an asymmetric floating wedge. J Eng Math 49(1):19–39

10. Chekin B (1989) The entry of a wedge into an incompressible fluid. J Appl Math Mech 53(3):300–307
11. Qin Z, Batra R (2009) Local slamming impact of sandwich composite hulls. Int J Solids Struct 46(10):2011–2035
12. Korobkin A (2000) Unsteady hydroelasticity of floating plates. J Fluids Struct 14:971–991
13. Korobkin A, Khabakhpasheva T, Wu G (2008) Coupled hydrodynamic and structural analysis of compressible jet impact onto elastic panels. J Fluids Struct 24(7):1021–1041
14. Korobkin A, Guéret R, Malenica Š (2006) Hydroelastic coupling of beam finite element model with Wagner theory of water impact. J Fluids Struct 22(4):493–504
15. Iafrati A, Korobkin A (2008) Hydrodynamic loads during early stage of flat plate impact onto water surface. Phys Fluids 20(8):082104
16. Faltinsen O (2001) Hydroelastic slamming. J Mar Sci Technol 5(2):49–65
17. Korobkin A, Parau E, VandenBroeck J (2011) The mathematical challenges and modelling of hydroelasticity. Philos Trans Ser A Math Phys Eng Sci 369(1947):2803–2812
18. Chuang S (1970) Investigation of impact of rigid and elastic bodies with water. NSRDC report no. 3248
19. Carcaterra A, Ciappi E (2000) Prediction of the compressible stage slamming force on rigid and elastic systems impacting on the water surface. Nonlinear Dyn 21:193–220
20. Arai M, Miyanchi T (1998) Numerical study of the impact of water on cylindrical shells, considering fluid structure interactions. Dev Mar Technol 11:59–68
21. Kapsenberg G (2011) Slamming of ships: where are we now? Philos Trans Ser A Math Phys Eng Sci 369(1947):2892–2919
22. Faltinsen O (1997) The effect of hydroelasticity on ship slamming. Philos Trans R Soc A Math Phys Eng Sci 355(1724):575–591
23. Bereznitski A (2001) Slamming: the role of hydroelasticity. Int Shipbuild Prog 48(4):333–351
24. Carcaterra A (2004) Hydrodynamic shock of elastic structures impacting on the water: theory and experiments. J Sound Vib 271(1–2):411–439
25. Lu CH, HE YS, Wu GX (2000) Coupled analysis of nonlinear interaction between fluid and structure impact. J Fluids Struct 14:127–146
26. Peseux B, Gornet L, Donguy B (2005) Hydrodynamic impact: numerical and experimental investigations. J Fluids Struct 21(3):277–303
27. Scolan Y (2004) Hydroelastic behaviour of a conical shell impacting on a quiescent-free surface of an incompressible liquid. J Sound Vib 277(1–2):163–203
28. Charca S, Shafiq B, Just F (2009) Repeated slamming of sandwich composite panels on water. J Sandw Struct Mater 11(5):409–424
29. Charca S, Shafiq B (2009) Damage assessment due to single slamming of foam core sandwich composites. J Sandw Struct Mater 12(1):97–112
30. Hirdaris SE, Temarel P (2009) Hydroelasticity of ships: recent advances and future trends. Proc Inst Mech Eng Part M J Eng Marit Environ 223(3):305–330
31. Wu G (2004) Numerical simulation and experimental study of water entry of a wedge in free fall motion. J Fluids Struct 19(3):277–289
32. Seddon C, Moatamedi M (2006) Review of water entry with applications to aerospace structures. Int J Impact Eng 32(7):1045–1067
33. Stenius, I, Rosén A, Kuttenkeuler J (2011) Hydroelastic interaction in panel-water impacts of high-speed craft. Ocean Eng 38(2–3):371–381
34. Dalrymple RA, Rogers B (2006) Numerical modeling of water waves with the SPH method. Coast Eng 53(2–3):141–147
35. Oger G, Doring M, Alessandrini B, Ferrant P (2006) Two-dimensional SPH simulations of wedge water entries. J Comput Phys 213(2):803–822
36. Khayyer A, Gotoh H, Shao S (2008) Corrected Incompressible SPH method for accurate water-surface tracking in breaking waves. Coast Eng 55(3):236–250
37. Anghileri M, Castelletti L, Francesconi E, Milanese A, Pittofrati M (2011) Rigid body water impact: experimental tests and numerical simulations using the SPH method. Int J Impact Eng 38(4):141–151

38. Shao S (2009) Incompressible SPH simulation of water entry of a free-falling object. Int J Numer Methods Fluids 59:91–115
39. Battistin D, Iafrati A (2004) A numerical model for the jet flow generated by water impact. J Eng Math 48(3/4):353–374
40. Colagrossi A (2003) Numerical simulation of interfacial flows by smoothed particle hydrodynamics. J Comput Phys 191(2):448–475
41. Molteni D, Colagrossi A (2009) A simple procedure to improve the pressure evaluation in hydrodynamic context using the SPH. Comput Phys Commun 180(6):861–872
42. Geoffrey M, Smith PD (1995) Blast effects on buildings: design of buildings to optimize resistance to blast loading. T. Telford, London; American Society of Civil Engineers, New York
43. Korobkin A, Ellis AS, Smith FT (2008) Trapping of air in impact between a body and shallow water. J Fluid Mech 611:365–394
44. Chuang S, Milne D (1971) Drop tests of cone to investigate the three-dimensional effect of slamming. NRDC report no. 3543
45. Chuang S (1966) Slamming of rigid wedge-shaped bodies with various deadrise angles. NSRDC report 2268
46. Engle A (2003) A comparison of hydrodynamic impacts prediction methods with two dimensional drop test data. Mar Struct 16(2):175–182
47. Huera-Huarte FJ, Jeon D, Gharib M (2011) Experimental investigation of water slamming loads on panels. Ocean Eng 38(11–12):1347–1355
48. Lewis S, Hudson D, Turnock S, Taunton D (2010) Impact of a free-falling wedge with water: synchronized visualization, pressure and acceleration measurements. Fluid Dyn Res 42(3):035509
49. Inman D (1994) Engineering vibration. Vibration fundamentals and practice. Prentice Hall, Englewood Cliffs
50. Faltinsen O (1999) Water entry of a wedge by hydroelastic orthotropic plate theory. J Ship Res 43(3):180–193
51. Yupu G, Zhenhua Z, Wei C, Deping G (2008) Foreign object damage to fan rotor blades of aeroengine part II: numerical simulation of bird impact. Chin J Aeronaut 21(4):328–334
52. Brett J (1998) Numerical modeling of shock wave and pressure pulse generation by underwater explosion. Technical report, Department of Defence
53. Liu M, Liu G, Lam K (2002) Investigations into water mitigation using a meshless particle method. Shock Waves 12(3):181–195
54. Veen D, Gourlay T (2008) SPH study of high speed ship slamming. In: 3rd ERCOFTAC SPHERIC workshop on SPH applications, Lausanne
55. Khayyer A, Gotoh H, Shao S (2009) Enhanced predictions of wave impact pressure by improved incompressible SPH methods. Appl Ocean Res 31(2):111–131
56. Antoci C, Gallati M, Sibilla S (2007) Numerical simulation of fluid-structure interaction by SPH. Comput Struct 85(11–14):879–890
57. Marrone S, Antuono M, Colagrossi A, Colicchio G, Le Touzé D, Graziani G (2011) δ-SPH model for simulating violent impact flows. Comput Methods Appl Mech Eng 200(13–16):1526–1542
58. Johnson G (1996) Artificial viscosity effects for SPH impact computations. Int J Impact Eng 18(5):477–488
59. Nejad-Asghar M, Khesali AR, Soltani J (2007) Artificial viscosity in simulation of shock waves by smoothed particle hydrodynamics. Astrophys Space Sci 313(4):425–430
60. Mani A, Larsson J, Moin P (2009) Suitability of artificial bulk viscosity for large-eddy simulation of turbulent flows with shocks. J Comput Phys 228(19):7368–7374
61. Randles PW, Libersky LD (2000) Normalized SPH with stress points. Int J Numer Methods Eng 48(10):1445–1462
62. Selhammar M (1997) Modified artificial viscosity in smooth particle hydrodynamics. Astron Astrophys 325(2):857–865
63. Kai G, Hua L, Ben-long W (2009) Water entry of a wedge based on SPH model with an imporved boudary treatment. J Hydrodyn 21(6):750–757

Blast Loading of Sandwich Structures and Composite Tubes

H. Arora, P.A. Hooper, and J.P. Dear

Abstract This chapter reviews blast impact experimentation on glass fibre reinforced polymer (GFRP) and carbon-fibre reinforced polymer (CFRP) sandwich composite materials and laminate composite tubes. Explosive charges of 0.64–100 kg TNT equivalent were used during these air- and underwater-blast tests. The difference in response and damage inflicted from underwater- and air-blast loading was assessed from strain-field measurements and post-blast specimen analysis. Procedures for monitoring the structural response of such materials during blast events have been devised. High-speed photography was employed during the air-blast loading of GFRP and CFRP sandwich panels, in conjunction with digital image correlation (DIC), to monitor the deformation of these structures under shock loading. Failure mechanisms have been revealed using DIC and confirmed in post-test sectioning. The improved performance of composite sandwich structures with CFRP skins compared to GFRP equivalent constructions is demonstrated for air-blast experiments. Strain gauges were used to monitor the structural response of similar sandwich materials and GFRP tubular laminates during underwater shocks. The effect of the supporting/backing medium (air or water) of the target facing the shock has been identified during these studies. Mechanisms of failure have been established such as core crushing, skin/core cracking, delamination and fibre breakage. Strain gauge data supported the mechanisms for such damage. A transition in behaviour was observed in the sandwich panels when subject to an underwater blast as opposed to an air-blast load. Damage mechanisms notably shifted from distributed core shear failure originating from regions of high shear in air blast to global core crushing in underwater blast. The full-scale experimental results presented here will assist in the development of analytical and computational models. Furthermore, the research highlights the importance of boundary conditions with regards to blast resistant design.

H. Arora • P.A. Hooper • J.P. Dear (✉)
Department of Mechanical Engineering, Imperial College, London SW7 2AZ, UK
e-mail: hari.arora04@imperial.ac.uk; p.hooper07@imperial.ac.uk; j.dear@imperial.ac.uk

S. Abrate et al. (eds.), *Dynamic Failure of Composite and Sandwich Structures*,
Solid Mechanics and Its Applications 192, DOI 10.1007/978-94-007-5329-7_2,
© Springer Science+Business Media Dordrecht 2013

Keywords Air blast • Underwater blast • Shock • Sandwich structures • Composites

1 Introduction

The study reported here forms part of a programme to investigate the retention of integrity of composite structures subject to increasingly demanding conditions. When designing against such threats one has to consider the blast event (pressure wave), the surroundings (fluid medium and boundary conditions) and the component (material properties and construction). The research presented here focuses on air-blast loading of glass-fibre reinforced polymer (GFRP) and carbon-fibre reinforced (CFRP) sandwich composite panels and underwater-blast loading of GFRP sandwich composite panels and GFRP tubular laminates.

It is clear from the nature of an explosion that they can be very damaging to a structure and it is because of recent events, accidental or otherwise, that there has been a growth within this area of research [1]. When a shock wave reaches a structure there are typically three stages of response that a structure undergoes. The first stage is where compressive stress waves are transmitted from the front face to the back. In polymer foam core sandwich fibre reinforced polymer composites, as those of primary concern for this investigation, core crushing occurs as well as impulsive transverse shear reaction forces initiating from the clamped edges. The structure does not experience any global deflection in stage 1. Momentum and kinetic energy are transmitted globally to the plate at the end of stage 1 while the transverse shear strains propagate towards the middle of the structure. By stage 2 the load pressure pulse would have decayed to negligible magnitudes. Meanwhile the transverse shear stress waves cause the development of bending and shear deformations behind the wave front. There comes a point in stage 3 where the direction of those shear waves reverse causing a reversal of plate deflection (at the point of maximum central point deflection) and flexural oscillations begin [2]. There have been numerous investigations into blast loading of structures using open-air charges, buried charges and other apparatus. Several studies have investigated dynamic deformations due to explosive blast loading on plates. Neuberger [3, 4] highlighted several early studies, which classified failure modes of structures under impulse loading, from large inelastic deformation to tearing and shear failure at the supports. Neuberger also highlighted various studies investigating the scaling effects for comparison of similar blast events using different explosive mass or specimen distance to quantify material response. These studies observed the effect of air-blast [3] and buried charges [4] on clamped circular plates and the validity of scaled testing. Several earlier studies have also investigated the dynamic deformations due to explosive blast loading on plates. Menkes and Opat [5] classified failure modes of structures under impulse loading, from large inelastic deformation to tearing and shear failure at the supports. Nurick amongst others has conducted extensive studies over the years investigating various plate response to blast loading summarised in

reference [6]. For instance the types of failures described by Menkes and Opat have been investigated further by Nurick, Olsson et al. [7], in particular the significant effects of the boundary conditions for the purpose of predicting tearing in steel plates have been highlighted in reference [8].

Cantwell, Nurick and Langdon et al. have continued similar experimental investigations and analysis into composite behaviour under blast conditions [9–11]. In addition to explosive testing, shock tubes have been found to give a good and convenient option for shock/blast studies. The advantage of shock tubes is the controlled nature of the event produced, in addition to the event concentrating solely on the shock wave influence rather than any others inherent with blast situations e.g. burning. A shock tube consists of a long rigid cylinder, divided into a high-pressure driver section and a low pressure driven section, which are separated by a diaphragm. A shock is created by pressurising one section (high-pressure) until the pressure difference across the diaphragm reaches a critical value, resulting in the diaphragm rupturing. This rapid release of gas creates a shock wave, which travels down the tube and on to the test specimen [12]. Tekalur et al. [12–14] have experimentally studied the effect of blast loading using shock tubes and controlled explosion tubes loading on E-glass fibre based composites and other materials. Results suggested that the E-glass fibre composite experienced progressive damage during high-rate loading of the same nature as described in Hoo Fatt and Palla [2], with progressive front-face failure due to indentation followed by complete core collapse. These studies have been continually developed by the same research group to great effect, with many parameters being examined such as the distribution of blast energy during the impact process [15] and retention of integrity of sandwich structures due to blast loads [16].

Changing the medium used to carry the shock from a gas to a liquid (increasing the density) increases speed of sound and generates a significant rise in pressures produced by a blast event. It is for these and related reasons that underwater shocks and their interaction with surrounding submerged structures are of particular interest to the naval industry. When an explosion occurs underwater, there is an intense release of energy, high pressure and heat, similar to the air blast case. This is relieved by the formation of an intense (compressive) pressure wave, or shock wave, which radiates away from the source. However with an underwater explosion, there is also the formation of high-pressure gas bubble, which is formed by the expanding reaction products formed during the explosion. The pressure within this bubble is significantly higher than hydrostatic and therefore the bubble radius increases rapidly. However, due to inertial and other effects, the gas bubble expands too far until the hydrostatic pressure is greater than the pressure within the gas bubble. The bubble then contracts once more until it contracts too far. The pressure in the gas bubble then rises in pressure and emits a compressive pressure wave prior to expanding once more from this minimum. There are a series of overshoots and undershoots during this process until all the energy is dissipated in one way or another. The movement and dynamic behaviour of the bubble is influenced by a number of factors including the proximity to the air-water interface, other surfaces and turbulence [17]. In terms of energy released, approximately 47% goes towards the formation

and pulsation of the bubble and the remainder to the shock wave [18]. If stand-off distance can be assumed to be large, then the effect of the bubble can be ignored, and this seems to be the focus of most authors, highlighted by Panciroli and Abrate [19].

Conducting underwater explosive experiments is again a very high risk and high cost procedure. Moreover, considerable care is needed to instrument underwater explosive experiments to obtain the required high quality data. Therefore, different laboratory experimental techniques are employed by researchers. For example, the principle of a shock tube has been applied to water blast simulations using the water-hammer effect. Deshpande et al. [20] investigated the fluid structure interaction (FSI) of sandwich plates with steel face sheets and aluminium foam cores. A strong FSI effect was observed experimentally and a coupled finite element (FE) analysis was able to capture the measured degree of core compression unlike the decoupled analysis, which underestimated the degree of core compression. This illustrated the importance of FSI and having a coupled analysis during such events. This water hammer technique has been used elsewhere incorporating moiré shadow interferometry techniques to obtain full field out-of-plane deformation profiles by Espinosa et al. [21]. This method was also employed by LeBlanc and Shukla [22] with in-depth finite element (FE) analyses forming agreements in terms of damage generated in the composite laminates studied. Other effects of water pertinent to naval structures are shock focusing during impacts, water slamming and wave interactions. This phenomenon has been investigated within a comprehensive study of impulse loading on marine structures conducted by Ravichandran et al. [23].

The complexity of blast load conditions is significant and various aspects are being investigated every day with the aim of improving computational simulations and hence the design process for marine structures. This investigation aims to highlight the mechanisms of failure observed within commercially available naval materials and improve the understanding behind the sequence of events responsible for such damage. The main focus of this study is the blast response of composites and sandwich structures on a large scale but related research [24–27] has focussed on the impact performance of composites and sandwich structures.

Although a significant amount of work is being conducted over a range of scales and types of experimentation, as highlighted in this chapter already, suitable standards for scaling and test procedures have not been established. Therefore data that is most valuable to industry is full-scale explosive testing and will be of focus for this investigation. Methods of instrumentation and sample restraint for large-scale marine structures will also be of focus, highlighting the precautions required to implement the traditional instrumentation methods and more modern techniques currently in use in a number of related research areas.

2 Materials

There were three different types of sandwich composite panels and one type of composite tubular laminate evaluated; these are shown schematically in Fig. 1. The sandwich panels had GFRP skins or CFRP skins on two different SAN cores

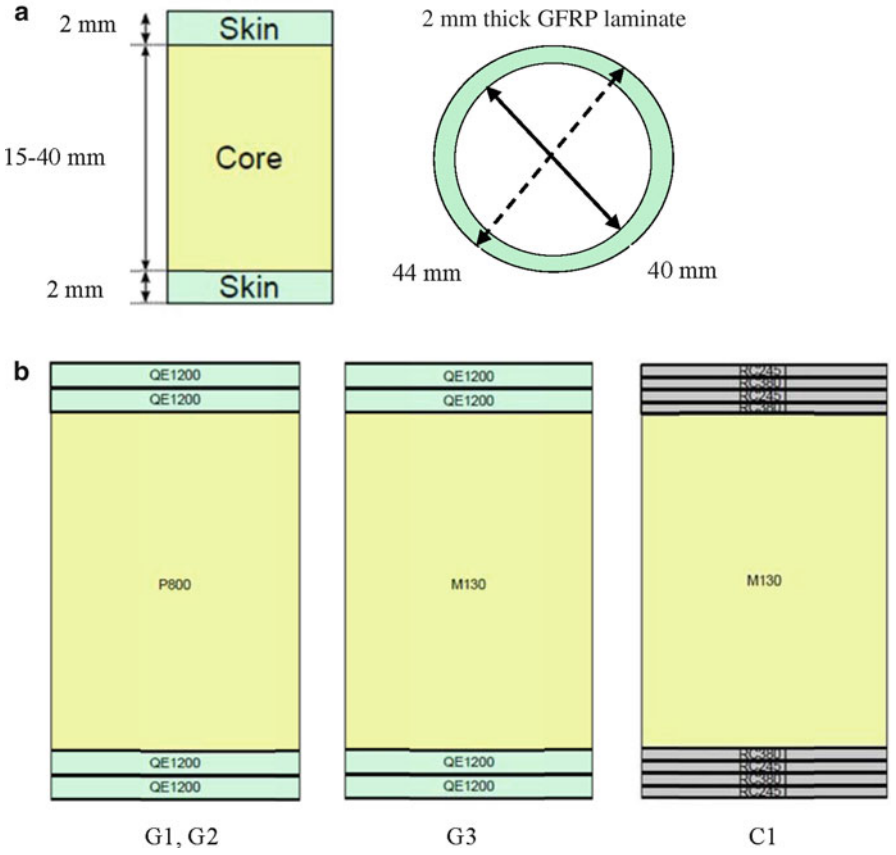


Fig. 1 Target constructions: (**a**) sandwich panels (*top left*) and tubular laminate (*top right*); (**b**) Sandwich panel skin lay ups for each type of panel tested: G1 & G2 (QE1200 glass skin with 40 mm P8 core and 30 mm P8 core respectively) – *left*; G3 (QE1200 glass skin with 25 mm M130 core) – *centre*; C1 (RC245T/RC380T carbon skins with 25 mm M130 core) – *right*

(P800 or M130). The GFRP-skinned sandwich panels were constructed using 2 plies of (0°/90°/±45°) E-glass quadriaxial skins with (manufacturer code QE1200) on SAN foam cores (manufacturer code P800 or M130) infused with an Ampreg 22 epoxy resin. Various core thicknesses were tested from 15 to 40 mm for air blast and underwater blast studies. The CRFP-skinned sandwich panels consisted of two repeat layers of two plies of 0°/90° carbon (code: RC245T) on two plies of ±45°carbon (code: RC380T) on a 25 mm thick SAN foam core (code: M130) and this was compared with GFRP-skinned sandwich panels consisting of 2 plies of (0°/90°/±45°) E-glass quadriaxial skins on a 25 mm thick SAN foam core (code: M130). All these sandwich constructions were infused with an Ampreg 22 epoxy resin. These different sandwich constructions are shown schematically in Fig. 1. A 3 mm thick panel made of mild steel (composition: EN-10025-2-05-S275JR-AR) was also tested for comparison with the 25 mm SAN foam-cored sandwich panels.

Comparisons can be made against the mild steel plate to compare conventional against more modern ship building materials and clarify what savings can be made, if any, on a weight-for-weight basis, for each sample construction. The GFRP and CFRP-skinned panels had equivalent mass per unit area, $\sim$17 kg/m^2. The steel plate also had a near equivalent mass per unit area as the composite sandwich panels, larger at $\sim$23 kg/m^2, and was included to demonstrate the advantages or otherwise of the composite sandwich construction over traditional engineering materials.

The exposed target areas for the air-blast and underwater-blast experiments were 1.6×1.3 m and 0.4×0.3 m respectively. The two different sized panels were designed to have a comparable aspect ratio. The larger panels, used for the air-blast, were to represent full-scale face-panels of comparable magnitude to real naval structures. Smaller samples were required for the underwater blast experiments to allow for sufficient rigid edge restraint/support during tests as well as manoeuvrability of the entire rig during test set-up. The smaller targets were used to keep the experiments within sensible bounds of the test facility in terms of the size of test pond, explosives used, desired maximum pressures and hence blast parameters (suitable guidelines for such underwater test designs are outlined in reference [28]). The process used to decide each of these factors started with the charge size, using a charge size and location in the test facility that minimised unwanted secondary pressure cycles from reflections etc. Secondly the size of the panel was chosen to allow sufficient damage to be inflicted by such a charge, whilst keeping manoeuvrability of appropriate test fixtures at a manageable level. The size of the panels (length to thickness ratio) was also chosen to keep the behaviour of the structure to that of a plate i.e. allow for typical bending response to occur. Typical aspect ratios of 6:1 ensure this, although as this reduces below 3:1, the amount of flexure experienced by the target becomes negligible. Given these targets are meant to simulate face-sheet material, bending is of greater interest than purely through-thickness stresses, which would dominate in a target of low aspect ratio. Sandwich materials were provided by SP Gurit manufactured by P.E. Composites. The comparison of GFRP-skinned and CFRP-skinned sandwich materials and the steel plate was only performed for the explosive air blast experiments. Only GFRP materials were employed for the underwater blast experiments.

The composite tube construction was 40 mm inner diameter, 44 mm outer diameter made from 8 H Satin weave 300 g/m^2 (excluding CYCOM® 919 epoxy resin impregnation) known as weave style US 7781. The tube was constructed from 9 plies of 7781 epoxy rubber toughened thermoset E-glass fabric. The fabric weave style was selected as the mechanical properties are similar in both the warp and weft directions, simplifying the construction process. The exposed target length was 0.3 m. This size of target was chosen to allow for both the cross-sectional/circumferential and axial (bending) deformation to be observed. Tubular laminates were sourced from Tri-Cast. Table 1 shows a summary of the material properties provided by the manufacturer.

Table 1 Summary of materials used in the GFRP & CFRP sandwich panels and tubular laminates

Material	QE1200	RC245T	RC380T	P800	M130	CYCOM 919-7781
Density (kg/m^3)	1,750	1,390	1,390	155	140	1,320
Tensile modulus (GPa)	17	49	11	0.14	0.084	27
Compressive modulus (GPa)	–	–	–	0.13	0.13	29
Tensile strength (MPa)	250	470	–	–	–	470
Compressive strength (MPa)	200	310	–	2.8	–	480
Shear modulus (MPa)	6,500	3,100	23,600	61	49	–
Tensile failure strain (%)	$\geq$1.5	–	–	–	–	$\geq$1.7

3 Experimental

3.1 Air Blast Loading of GFRP- and CFRP-Skinned Sandwich Panels

Six different sample configurations were evaluated. Five of the targets were sandwich composite panels with lay-ups, shown schematically in Fig. 1. One panel is made of mild steel. There were two sets of samples tested for two different investigations. One set focussed on the influence of core thickness on panel response to air blast as well as the effect of different stand-off of the air blasts on the panel response (Series A). The second set focussed on the influence of skin type on the sandwich panel response to air blast (Series B).

GFRP-skinned and CFRP-skinned sandwich panels were subject to full-scale air-blast loading to observe the deformation and damage development with typical marine constructions. An overview of the test configurations is shown in Fig. 2 (see Fig. 2a for air blast studies). Full-field displacement plots of the back face of the target were obtained for the duration of the blast event by employing high-speed photography in conjunction with digital image correlation (DIC) methods. Two high-speed video cameras (Photron SA3s) were positioned behind the 1.6×1.3 m speckled targets and sampled at 2,000 frames/s at full resolution ($1{,}024 \times 1{,}024$ pixels). This sampling frequency, required to suitably capture the event, was decided using a single degree of freedom model based on the procedure outlined by Biggs [29]. The time taken to reach maximum deflection for an air blast with say 2 bar peak shock pressure was established for each target to be within the region of 5 ms. Therefore by using the Photron SA3 cameras it was possible to operate at full resolution (keeping spatial resolution high), whilst capturing the images at a suitable rate (temporal resolution) for the DIC analysis to be conducted. These cameras were calibrated prior to testing to allow the recorded images to be processed in ARAMIS (produced by GOM mbH), the DIC software used to perform the image correlation calculations. A laser gauge was positioned on a steel beam mount as a secondary point measurement tool focussing on the centre of the panel, which sampled at

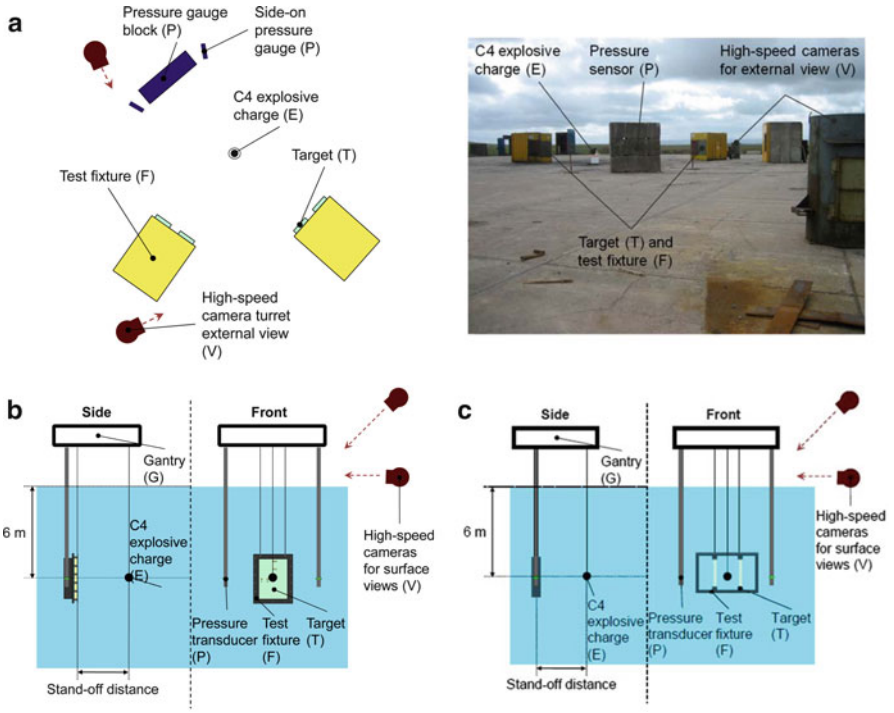


Fig. 2 Blast configurations showing schematic diagrams and images of the test set-up: (**a**) Air blast, (**b**) underwater blast of sandwich panels and (**c**) underwater blast of composite tubes. Featured in each diagram are: targets to be tested (T), sample fixtures (F), high-speed cameras and their relative locations (V), pressure sensor arrangements (P), gantry for the underwater tests (G) and C4 explosive charge (E)

2,000 Hz. The purpose of the laser gauge was to verify the results taken from the high-speed video recordings. Instrumentation is shown in Fig. 3 with the DIC set-up and laser gauge arrangement featured in Fig. 3a.

3.2 Air Blast Test Design and Other Instrumentation

Reflected pressure and static (side-on) pressure measurements were taken at the same stand-off distance from the charge as the target. High-speed video cameras were also positioned externally on the test pad, shielded in turrets, to capture front-face deformation as shown in Fig. 2a. For Series A, three GFRP-skinned targets were tested; two with a 40 mm thick core (denoted G1), one with a 30 mm core (denoted G2). The blast parameters used during the tests shown here were 30 kg C4 charge at a stand-off distance of 8 m and 14 m. The tests conducted at a 14 m stand-off distance (an equivalent peak shock pressure of approximately 2 bar) were

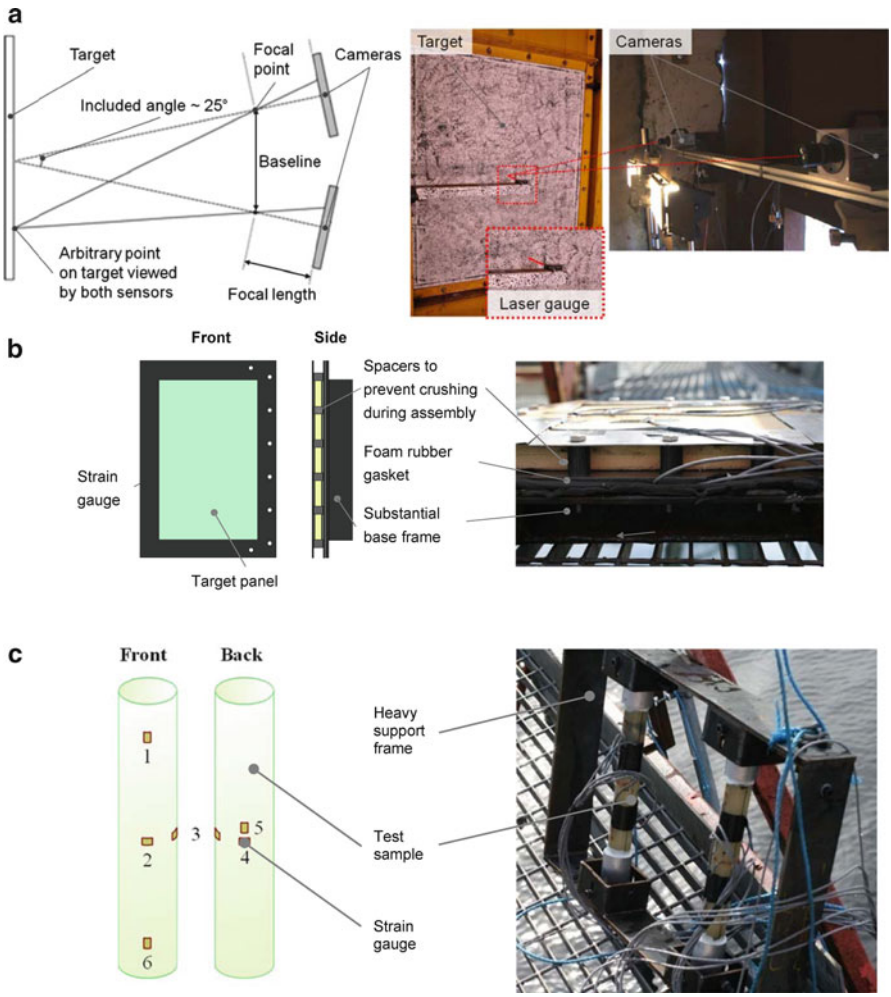


Fig. 3 Instrumentation: (**a**) Air blast featuring the DIC set-up and position of laser gauge; (**b**) Strain gauge arrangement for underwater blast loading of sandwich panels; (**c**) composite tubes

designed to take the panels to their elastic limit. The blast of 30 kg C4 at 8 m stand-off on G1 was designed to inflict damage on the target. For Series B, where skin comparison studies were conducted, one GFRP-skinned panel (denoted G3 with 25 mm core), one CFRP-skinned panel (denoted C1 with 25 mm core) and one steel plate (denoted S1) were evaluated. The blast parameters used during the tests shown here were 100 kg charges of Nitromethane (100 kg TNT equivalent) at a stand-off distance 14 m as this reduced stand-off correlated to the equivalent impulse which saw significant damage initiate in testing on Series A. FE simulations were conducted in ABAQUS to design the panel geometries, predicting the central peak deflections and peak surface strains below failure conditions (see Table 1).

3.3 Underwater Blast Loading of GFRP Sandwich Panels

GFRP sandwich panels were subject to underwater-blast loading to observe the deformation of the targets during the blast and damage sustained. A comparison can be made between the air and underwater blast cases as to differences in behaviour. Surface strain measurements were taken during the blast event using strain gauges positioned at 12 different locations. They were positioned along centre-lines of the panel face: three on the horizontal spaced evenly at 60 mm intervals from the centre and three on the vertical spaced evenly at 80 mm intervals 10 mm from the centre to avoid overlap of gauges. The other six gauges were positioned behind these locations on the rear face (shown in Fig. 3b). The strain gauges (and data acquisition hardware) chosen for this application was chosen specifically with the ability to monitor dynamic events (in terms of strain magnitude and strain rate). Once the gauges were bonded they were sealed in accordance to recommendations from engineers at Vishay Micro-Measurements to insulate from the environment and protect during impact, whilst maintaining a low profile and mass [30].

The panels were first bonded into a steel frame (3 mm thick mild steel). They were then bolted into a substantial base frame, comprising 10 mm thick mild steel, prior to testing. The base frame was designed to mitigate the effects of the blast wave wrapping around the target and interfering with its response to the incident wave acting on the front face. It also provided an enclosed volume behind the back-face of the panel to hold either air or water, which represents the conditions existing in a significant portion of a naval vessel. Thirdly it provided a weighty structure on its edges to replicate the boundary conditions experienced by a similar panel on the hull of a ship (from the support framework). A rubber foam gasket was used to create a seal for the backing fluid and to minimise the damage caused to the cables connected to the strain gauges on the rear face. Steel tube spacers were used to avoid crushing of the core material of the test panels, when bolted into the heavy base frame.

3.4 Underwater Blast Loading of GFRP Tubular Laminates

GFRP tubes were subject to underwater blast loads to assess how a tubular structure, a curved geometry, responds to such loads. Eight tubes were tested, seven filled and sealed with air inside (AF) and one with water (WF). One set of AF and WF tubes were paired to investigate the effect of the filling medium on the response of the tubes. The remainder of the air-filled tubes were tested in pairs and subjected to progressively increasing shock pressures to observe the damage inflicted on such constructions over a range of shock pressures. The sites thought to experience high principal stress during loading are at the ends of each tube on the front face (aligned square-on to the shock) and in the centre on the back face (this was also observed by [31] during similar aluminium shell trials). The two main motions observed during

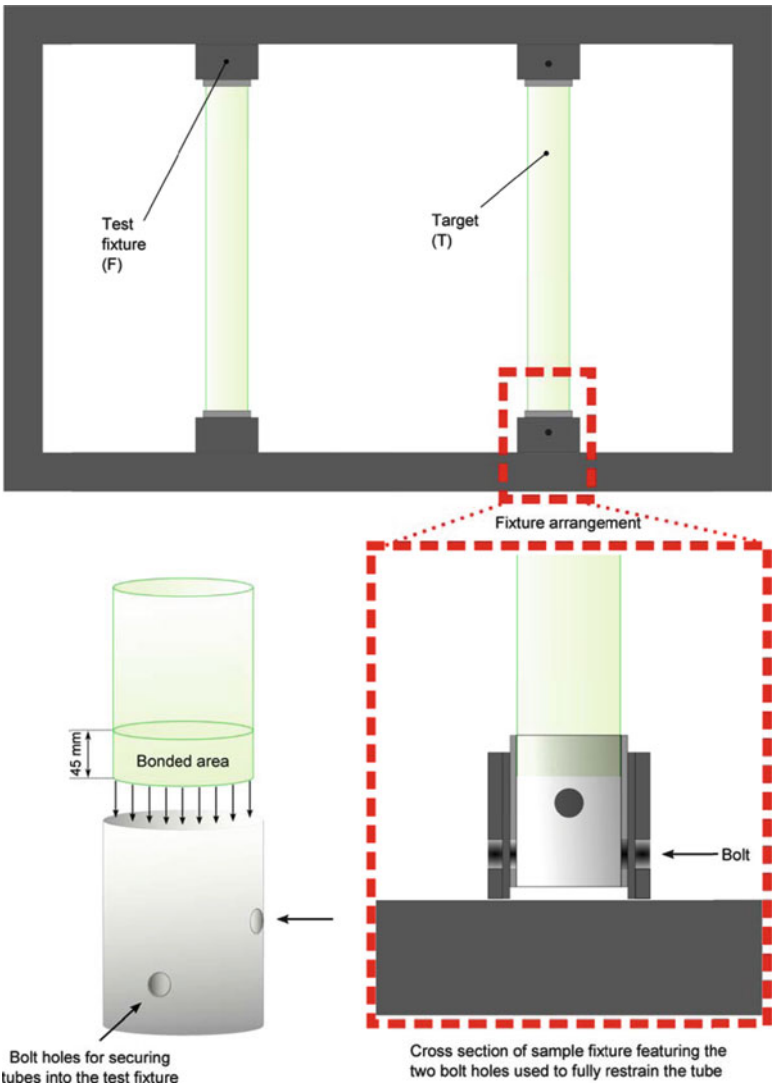


Fig. 4 Schematic of the assembly process of the test samples and the method used to attach the cylindrical samples in the test fixture

an underwater blast, bending and, what is commonly termed, breathing. These were deemed to be best observed by positioning three gauges axially, one at either end on the front and one at the centre on the back face, and three gauges circumferentially at the centre of the tube at 90° intervals (shown in Fig. 3c). The tubes were bonded into aluminium end-tabs and then bolted into a heavy steel frame, restraining the tube ends in all six degrees of freedom. This arrangement is shown in Fig. 4.

3.5 Underwater Blast Test Design and Other Instrumentation

High-speed video cameras were positioned on the test pad to capture the surface waves and disturbances during the blast from several angles. Static (side-on) pressure measurements were taken either side of the target using Neptune Sonar shock gauges. These were mounted on steel scaffold poles and lowered to the mid-height of the target. Details of the set-up are shown in Fig. 2b,c. Two panel targets were tested, one a 30 mm thick core (denoted G4) with air as the supporting fluid on the rear face and the other a 15 mm thick core (denoted G5) with water the supporting fluid. Blast parameters for the panel tests were 1 kg C4 charge at 6 m depth and a stand-off distance of 1.0 and 1.4 m respectively. These blasts were designed to cause significant damage to the targets to observe any trends regarding effects of backing fluid and differences between air-shock and underwater-shock regimes. The tubes were subject to a range of blast parameters, which involved using 0.5–1.0 kg C4 charges over a range of stand-off distances from 1.0 to 2.0 m at a 6 m depth. The details for specific tests will be mentioned alongside the results. The intention here was to also inflict significant damage to the tube structures, specifically, to observe progressive levels of damage in the air-filled tubes and highlight any effects of the filling medium on the observed response.

All positions of targets, charge and pressure sensors were verified using a submarine camera, prior to testing featured in Fig. 2b,c.

4 Results

4.1 Air Blast of GFRP-Skinned and CFRP-Skinned Sandwich Composite Panels

For Series A, two targets (G1 – GFRP-skinned with 40 mm core and G2 -GFRP-skinned with 30 mm core) were both initially subject to the same explosive charge (30 kg of C4) at the same stand-off distance (14 m). Figure 5 shows sample images taken from the high-speed videos positioned on the test pad. The shock wave is seen to arrive at the target 20 ms after detonation. This blast experiment was designed to take the panels to their elastic limit as stated in the Sect. 3.1. Figure 5 shows the test sample, with an arbitrary grid painted across it to enable ease of tracking the front-face deformation, held on the right-had side in the test fixture (the large yellow cubicle, with the second window on the left-hand side of the fixture blanked out with a steel plate).

Figures 6 and 7 give a direct comparison between the target sandwich panels, G1 (40 mm core) and target G2 (30 mm core) respectively, with regard to their response to a given air-blast load. It can be seen that increasing the core thickness lowers the amplitude of oscillations. This is due to the increased stiffness of the plate, resulting from the increased core thickness.

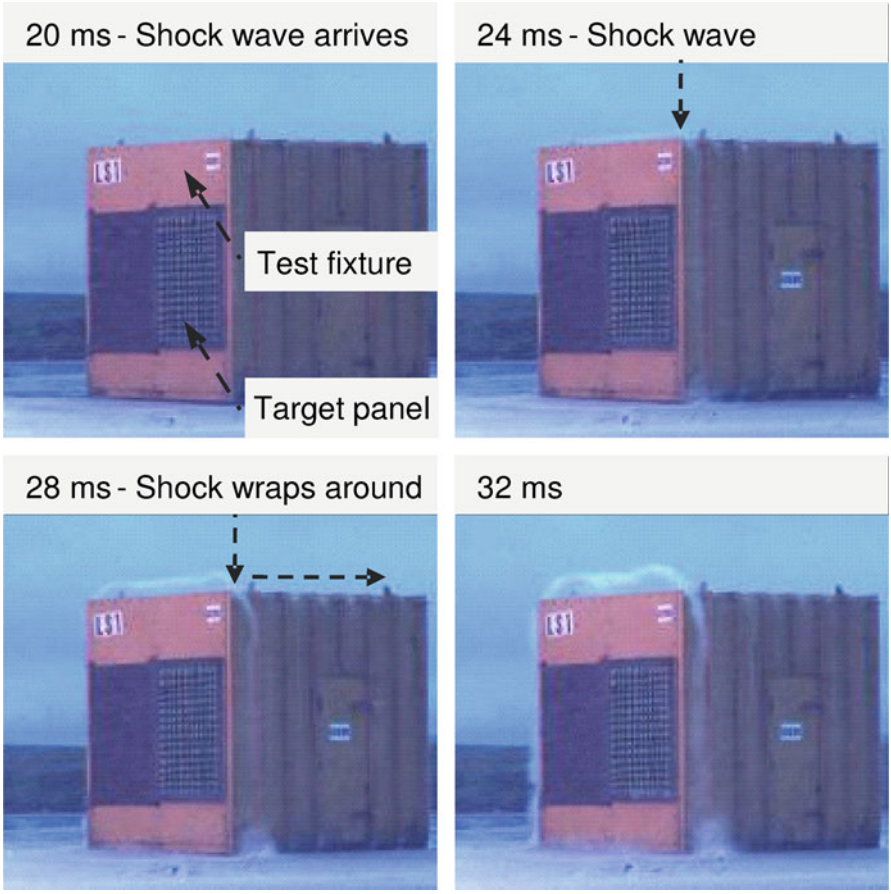


Fig. 5 Images of the shock wave impinging on the test sample (at 20 ms) and wrapping around the test cubicle thereafter (sandwich panel G1 with core thickness 40 mm and charge of 30 kg charge at stand-off of 14 m)

Figure 6 shows the central point deflection of G1 subjected to a recorded peak pressure of 2 bar (30 kg of C4 at stand-off of 14 m). The computed results from the image correlation are shown in the form of contour plots of out-of-plane displacement, principal strain and shear strain for the various times highlighted. It can be seen that the line from the left hand edge to the centre in the contour plots is the region of the specimen obscured by the laser gauge and its mount. This was employed to give an independent measure of central displacement in addition to DIC data. G1 was seen to deflect to a maximum distance out-of-plane of 63 mm (whilst Fig. 6 shows G2 deflected 78 mm). These deflection measurements agreed well with the laser gauge measurements for this single (central) point data, details to be discussed later in Sect. 5.1. The level of major principal strain peaked in the

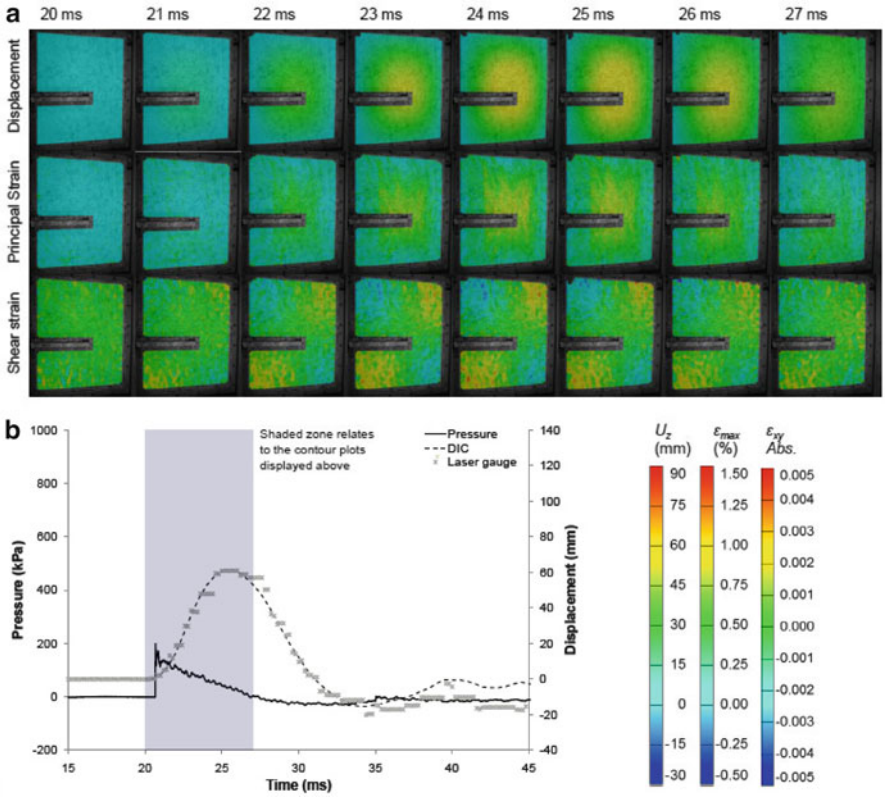


Fig. 6 Blast summary for 30 kg C4 at 14 m stand-off from G1 including: (**a**) DIC analysis and (**b**) a plot of pressure–time and displacement–time using both DIC and laser gauge centre point measurements. The DIC analyses features contour plots of out-of-plane displacement, maximum principal strain and shear strain, corresponding to various stages in the graphical plot. *The horizontal bar* visible in the contour plots (from the *left hand edge* to the *centre*) is the region of the specimen obscured by the laser gauge

region of 1% on the back face for G1. The G1 panel was deformed within a limit such that no visible damage was sustained. There were no obvious signs of damage shown within the DIC analysis for G1.

A similar response was exhibited in Fig. 7 for G2 with its reduced core thickness when subjected to a recorded peak pressure of 2 bar (30 kg of C4 at stand-off of 14 m). For G2, surface strains peaked at 1.25% and below the expected failure strains of the fibres. The lower limit (assuming a linear elastic relationship) for fibre strain to failure is 1.4% (as stated in Table 1). Signs were, however, observed within the DIC analysis that mild sub-surface core cracking had occurred. Early discontinuities in the major principal strain plots indicate possible detachment of the skin from the core i.e. possible cracking. This was confirmed upon sectioning of the panel after the blast.

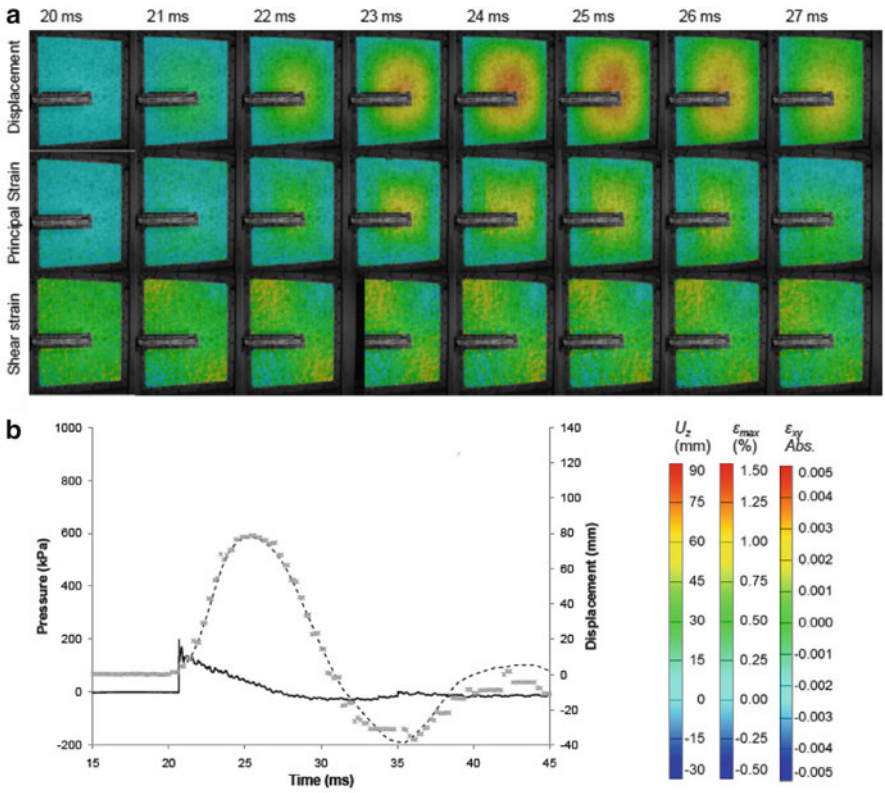


Fig. 7 Blast summary for 30 kg C4 at 14 m stand-off from G2 including: (**a**) DIC analysis and (**b**) a plot of pressure–time and displacement-time using both DIC and laser gauge centre point measurements. The DIC analyses features contour plots of out-of-plane displacement, maximum principal strain and shear strain, corresponding to various stages in the graphical plot. *The horizontal bar* visible in the contour plots (from the *left hand edge* to the *centre*) is the region of the specimen obscured by the laser gauge

As the DIC analysis agreed with predictions for peak elastic displacements of the targets due to a 2 bar shock pressure, and both the DIC analysis and visual inspection showed no visible skin damage to panel G1, it was decided that another panel of the same construction as G1 be subject to a more substantial blast to induce significant skin and core damage. This highlighted clearly the failure diagnostic capabilities of the DIC technique in this context. Blast parameters for this final air blast involved a 30 kg charge positioned at a reduced stand-off of 8 m from G1. Figure 8 shows the progressive deformation and eventual skin damage inflicted on G1 by the 8 bar pressure shock wave. A skin crack is seen to originate from the top left hand edge of the panel and propagate down that side of the target.

Figure 9 shows the measured reflected pressure as well as the central out-of-plane displacement during the blast event for G1 (GFRP-skinned with 40 mm core)

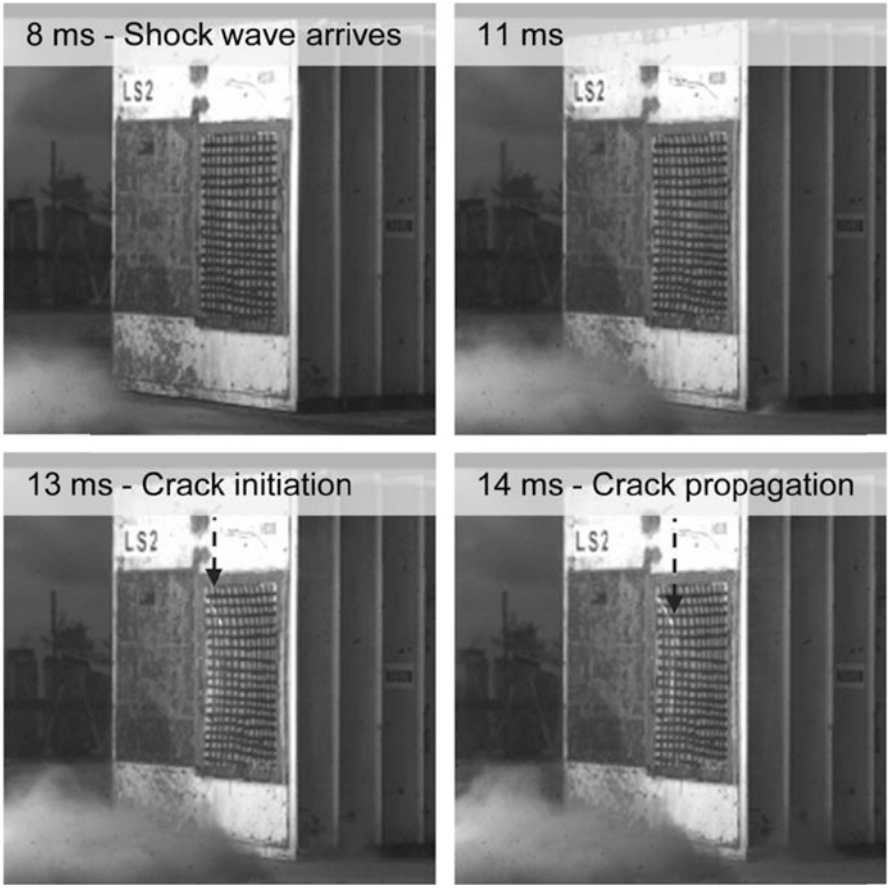


Fig. 8 Images of the shock wave impinging on the test sample (8 ms) causing deformation and front-skin damage thereafter (sandwich panel G1 with core thickness 40 mm and charge of 30 kg charge at stand-off of 8 m)

with at 30 kg charge at stand-off of 8 m. Comparing this plot of out-of-plane displacement to that shown earlier in Fig. 6, asides from the magnitude of peak out-of-plane displacement, immediately one can notice the difference in smoothness of the path taken during the first oscillation. Looking closely at the time period 12.5–13.5 ms, one can observe a flattening in the displacement curve near its maximum condition. This coincides with the time (13 ms) when the crack is observed to form in Fig. 8.

The peak out-of-plane displacement was 131 mm and strains peaked in the region of 3% prior to the crack developing. Upon post inspection, the front face sustained inter-laminar skin failure and front-ply fibre breakage whilst the core suffered a severe skin-to-skin crack (see Fig. 10). Towards the centre of the panel, the severity of the failure increased.

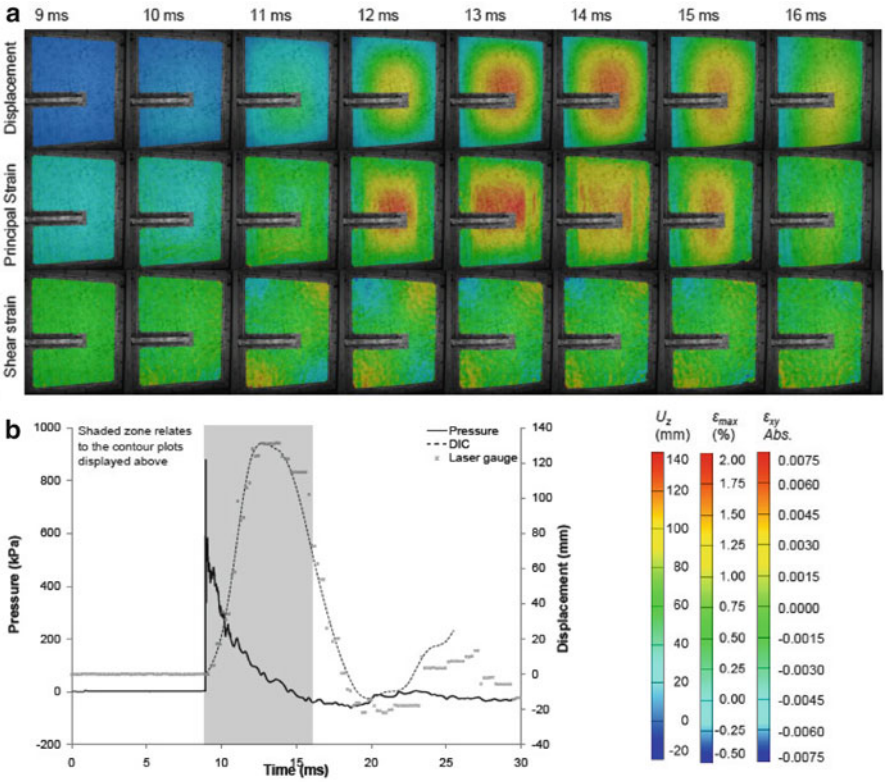


Fig. 9 Blast summary for 30 kg C4 at 8 m stand-off from G1 including: (**a**) DIC analysis and (**b**) a plot of pressure–time and displacement-time using both DIC and laser gauge centre point measurements. The DIC analyses features contour plots of out-of-plane displacement, maximum principal strain and shear strain, corresponding to various stages in the graphical plot. The horizontal bar visible in the contour plots (from the *left hand edge* to the *centre*) is the region of the specimen obscured by the laser gauge

For the series B experiments, glass-skinned and carbon-skinned sandwich panels were compared: G3 (GFRP-skinned with 25 mm core) and C1 (CFRP-skinned with 25 mm core). The air blast employed 100 kg charge Nitromethane at 14 m stand-off. The samples were tested side-by-side (in the same test fixture) to compare directly the response of the GFRP-skinned sandwich panel to the CFRP-skinned sandwich panels. The two types of panel had similar mass per unit area ($\sim$17 kg m^{-2}) with the constructions forming panels of the same thickness (same thickness of skins, 2 mm each, on the same thickness of core, 25 mm). The two types of panel provide a good comparison for observing the effect of skin configuration on blast mitigation. A sample of sheet steel (S1) was also tested under these conditions to provide a comparison against traditional naval engineering materials. Central point displacement, full-field contour DIC data and pressure data will be provided for the duration of the event.

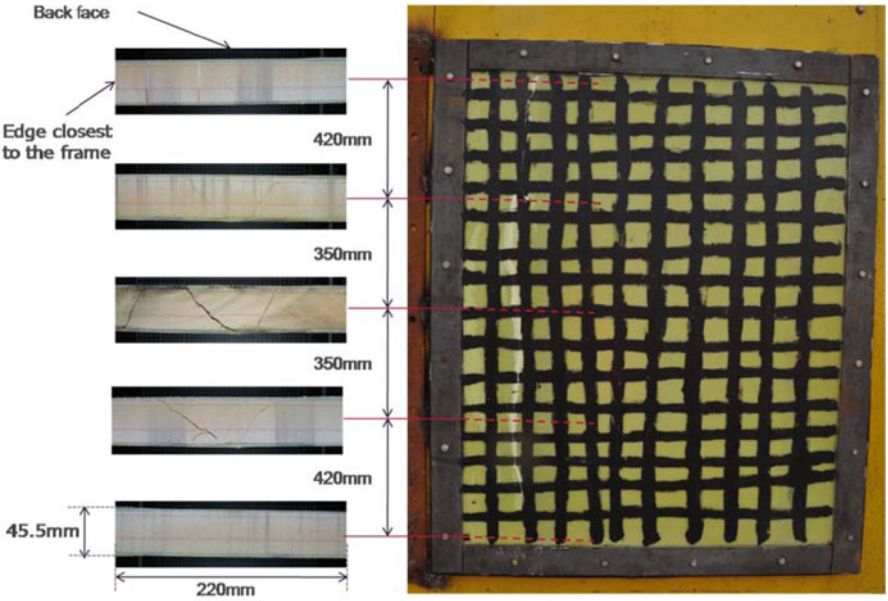


Fig. 10 Front face damage on G1: The whole panel with a clear crack down the *left-hand edge* of the panel (*right*), sectioned at regular intervals showing various failure mechanisms (*left*). This is for sandwich panel G1 – GFRP-skinned with core thickness 40 mm and charge of 30 kg charge at stand-off of 8 m

The 100 kg TNT at a 14 m stand-off blast was employed to give a severe comparison of CFRP-skinned composite sandwich panel (C1) with the GFRP-skinned composite sandwich panels (G3). The result for the experiment, forming the visible damage post-test, is presented below (for G3 and C1). Figure 11 shows the progressive deformation and eventual skin damage inflicted on the panel by the blast, where the peak overpressure was equal to 2.5 bar, corresponding to a 100 kg charge Nitromethane at 14 m stand-off. Unlike previous blast experiments, the overpressure or side-on pressure was measured rather than the reflected pressure. A skin crack is seen to originate from the top right hand edge of the panel at approximately 19 ms into the blast event and propagate down that side of the target.

Figure 12 shows a summary of the blast data recorded for G3 in this blast (100 kg Nitromethane at 14 m stand-off). From the graphical plot in this summary, around maximum out-of-plane displacement, the distortion (due to damage initiation and propagation) of the return stroke of the target is clear. Between the time period 19.0–22.0 ms, one can observe a flattening in the displacement curve around its maximum. This coincides with the time period over which the crack was observed to initiate and propagate in Fig. 11 from the top right-hand corner of the GFRP panel. Maximum deflection was found to be 140 mm and the strain peaked in the region of ∼1.6% prior to the crack developing.

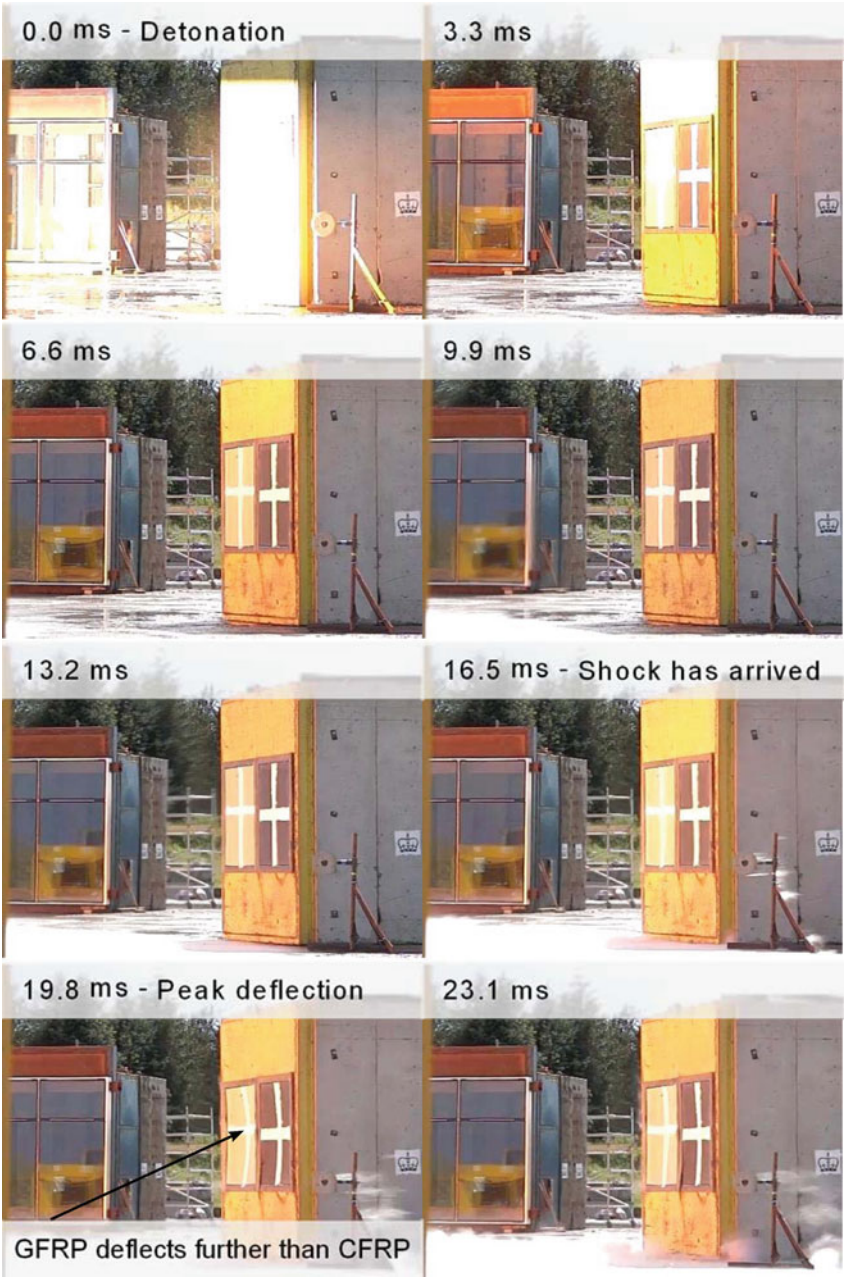


Fig. 11 Images of shock wave progression and front-face deformation of G3 and C1(GFRP-skinned sandwich panel G3 with core thickness 25 mm and CFRP-skinned sandwich panel C1 with core thickness 25 mm separately subject to 100 kg TNT equivalent charge at stand-off of 14 m). Images are shown from the detonation (0 ms) through the shock wave arrival at target (15 ms) until targets begin their first rebound. Exact time at which these event occur are not shown in the images (due to availability), therefore timings of interest are highlighted around those exact times

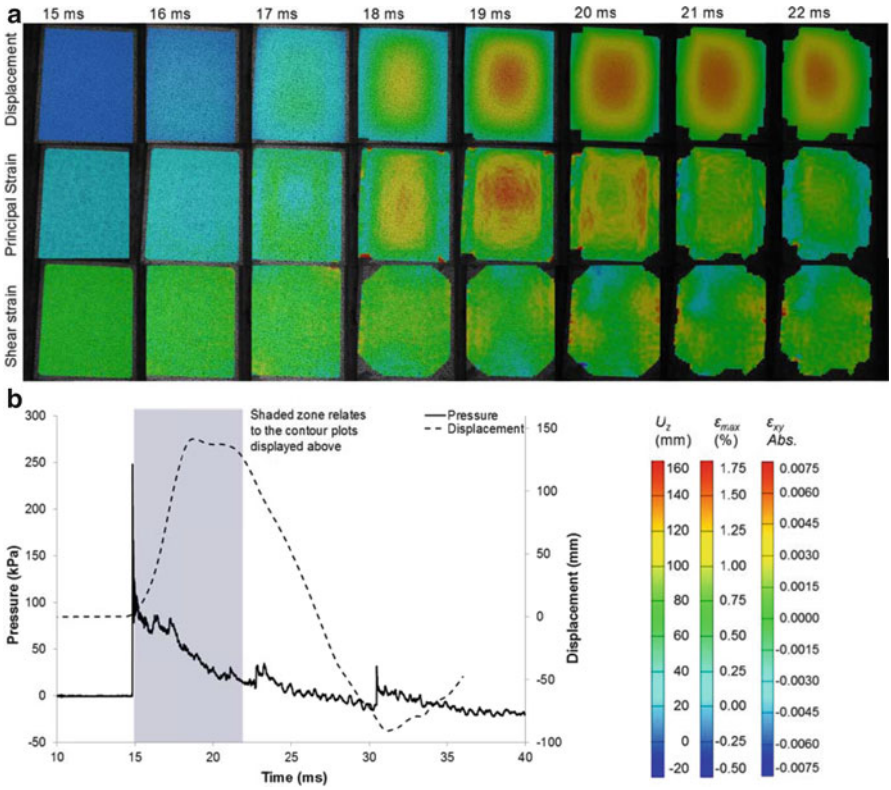


Fig. 12 Blast summary for 100 kg TNT equivalent at 14 m stand-off from G3 including: (**a**) DIC analyses and (**b**) a plot of pressure–time and displacement-time using both DIC and laser gauge centre point measurements. The DIC analyses features contour plots of out-of-plane displacement, maximum principal strain and shear strain, corresponding to various stages in the graphical plot

Comparatively C1, in Fig. 11, is observed to deflect noticeably less than G3. The two panels are subject to the same blast (recorded peak pressure of 2.5 bar and duration ca. 12 ms). There are of course asymmetry effects with regard to the load distribution, however in this case the support structure is completely symmetrical and the charge was positioned central to the test structure, therefore any asymmetry of loading can be assumed to be consistent for both targets. A considerable skin crack is seen to form in G3, however C1 formed no global failure similar to G3. A fine crack was observed to form towards one of the panel edges and the core shear failure was still observed to a similar severity as for G3. Figure 13 shows a summary of the blast data recorded for this blast (100 kg Nitromethane at 14 m stand-off). The carbon-skinned sandwich panel (C1) exhibits a greater resistance to the blast than glass-skinned sandwich panel (G3). The stiffer carbon skins minimise maximum deflection to 107 mm (compared to 135 mm for G3). The contour plots in Fig. 13 show a larger central region than G3. This is perhaps because more of the blast energy was distributed throughout the structure in C1, causing less severe but

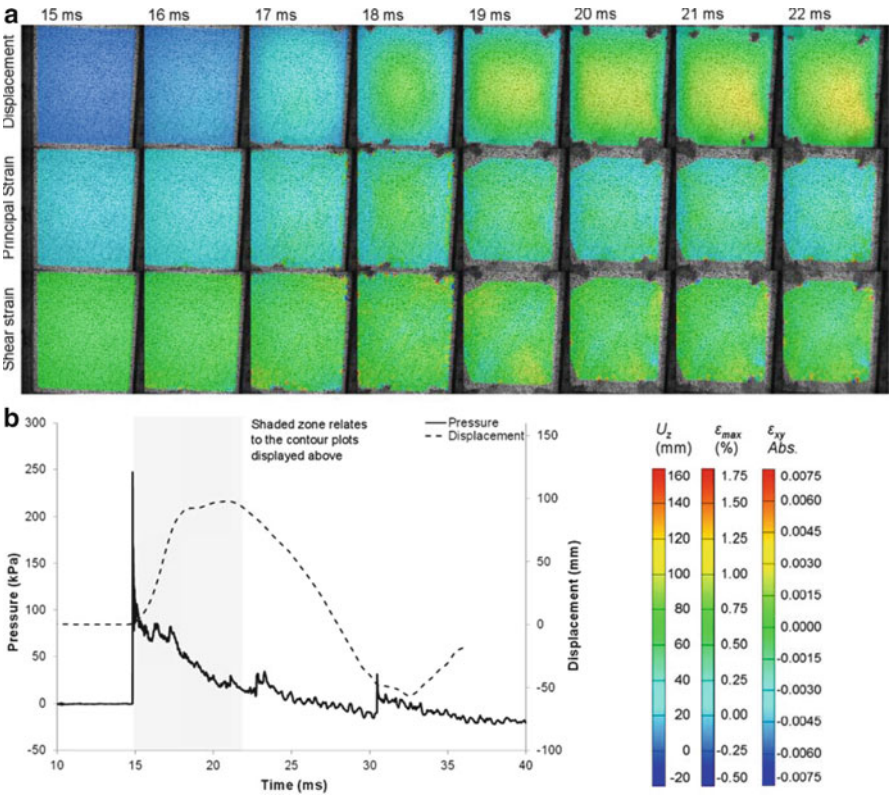


Fig. 13 Blast summary for 100 kg TNT equivalent at 14 m stand-off from C1 including: (**a**) DIC analyses and (**b**) a plot of pressure–time and displacement-time using both DIC and laser gauge centre point measurements. The DIC analyses features contour plots of out-of-plane displacement, maximum principal strain and shear strain, corresponding to various stages in the graphical plot

more widespread core cracking. Conversely G3 did not distribute the blast energy quick enough throughout the entire structure leading to a major localised failure of the skin and core. This type of damage mechanism (core cracking) accounts for the elongated return of C1 observed in Fig. 13. The time taken for the panel to return to its original position took an extra millisecond in the carbon panel compared to the glass panel. This extended response time absorbed the blast energy over a longer time period, resulting in a lower observed maximum deflection (107 mm) and maximum strain (∼0.8%) compared to G3.

Upon post inspection, the front face sustained inter-laminar skin failure and severe front-ply fibre breakage whilst the core suffered cracking from skin to skin but the rear skin remained intact. Figure 14a shows an overview of the damage observed by the two panels. The front skins were more severely damaged in the GFRP-skinned composite sandwich panels (G3). This is when compared to the CFRP-skinned sandwich panels (C1). For both panels the rear skins of the composite sandwich panel showed no visible damage. This was consistent with



Fig. 14 (**a**) Before and after images taken of the front face view of G3 and C1 after being subject to a charge of 100 kg TNT equivalent at stand-off of 14 m. (**b**) Images featuring the damage sustained by G3 and C1 after being blasted

previous air blast experiments in Series A. There was core damage present in G3 and C1 resulting from front skin failure and interlaminar failure between front skin and core. This damage initiated for G3 in transition regions from constraint to regions of deflection of the panel. This is where the stress state caused by the restraint and the impulsive loading, promotes failure initiation. The lack of sufficient distribution of energy lead to global propagation of the crack in the GFRP panels compared to the CFRP panels, which have small areas of skin cracking (which actually probably initiated from the stress concentration at the bolt hole, see Fig. 14b).

The other blast conducted during this set of experiments involved a mild steel plate (S1) of a near equivalent mass per unit area (∼23 kg/m^2) as per the GFRP and CFRP sandwich materials (∼17 kg/m^2) tested. This steel sheet was used to illustrate clearly the differences that exist between conventional construction materials and the latest style of naval constructions. Figure 15 shows the external view captured of the deformation process. There are similarities, from first impressions of the nature of deformation observed in terms of shape for instance. However further analysis of this footage and analysis of the DIC data uncovers distinct differences. Figure 16 gives a summary in the same fashion as for G3 and C1. From the plot in Fig. 15b there is an almost linear initial portion of response, however at around 20 ms the panel pulls out from six bolt holes. This dissipates a lot of energy (and relieves the intensity of the oncoming pressure wave providing clearing for the blast wave too), hence the sharp decrease gradient of the displacement-time plot. The curve is then seen to decrease in gradient steadily until it reaches a plateau, where all the momentum has transferred to plastic deformation of the steel sheet.

The contour plots in Fig. 16 only show the deformation within the time period shown for that of G3 and C1. This shows that the panel deformed significantly more than the sandwich structures. Moreover S1 folded and crumpled in the regions between the bolt holes where high shear stresses causing this crumpling to occur.

S1 had a peak deflection which was 270 mm, which is considerable more than GFRP and CFRP skinned sandwich panels. A deflection of approximately 120 mm was attained prior to bolt shear, which dissipated some energy and also relieved some of the blast pressure. Major principal strain peaks at approximately 1.1%. The damage sustained by S1 is featured in Fig. 17, showing the final deformed profile relative to its original at profile.

4.2 Underwater Blast Loading of GFRP Sandwich Panels

Two sandwich panel targets, G4 (GFRP-skinned with 30 mm core thickness) and G5 (GFRP-skinned with 15 mm core thickness), were subject to two different blast scenarios. There were two different impulses and two different sets of boundary conditions to explore the effect of the backing (or supporting) medium to the target's response. A 1 kg C4 explosive charge was set at the mid-height of the target 6 m below the surface of the water at a stand-off distance of 1 m for G4 with an air-pocket encapsulated behind the target. G5 had the 1 kg charge of C5 1.4 m away at the same depth but this time with water encapsulated behind the target. Although only a 1 kg charge was used this was still substantial given the transition from air blasting to underwater.

Surface effects propagating from the blast event were recorded and sample images are shown in Fig. 18. The sequence runs through the initial shock producing a spray at the surface at about 5 ms, which remains until the bubble begins to rise, forming a dome at the surface after the first 1,000 ms. This reaches a peak height of approximately 1 m prior to venting at 1,400 ms, throwing a large mass of water up in the air.

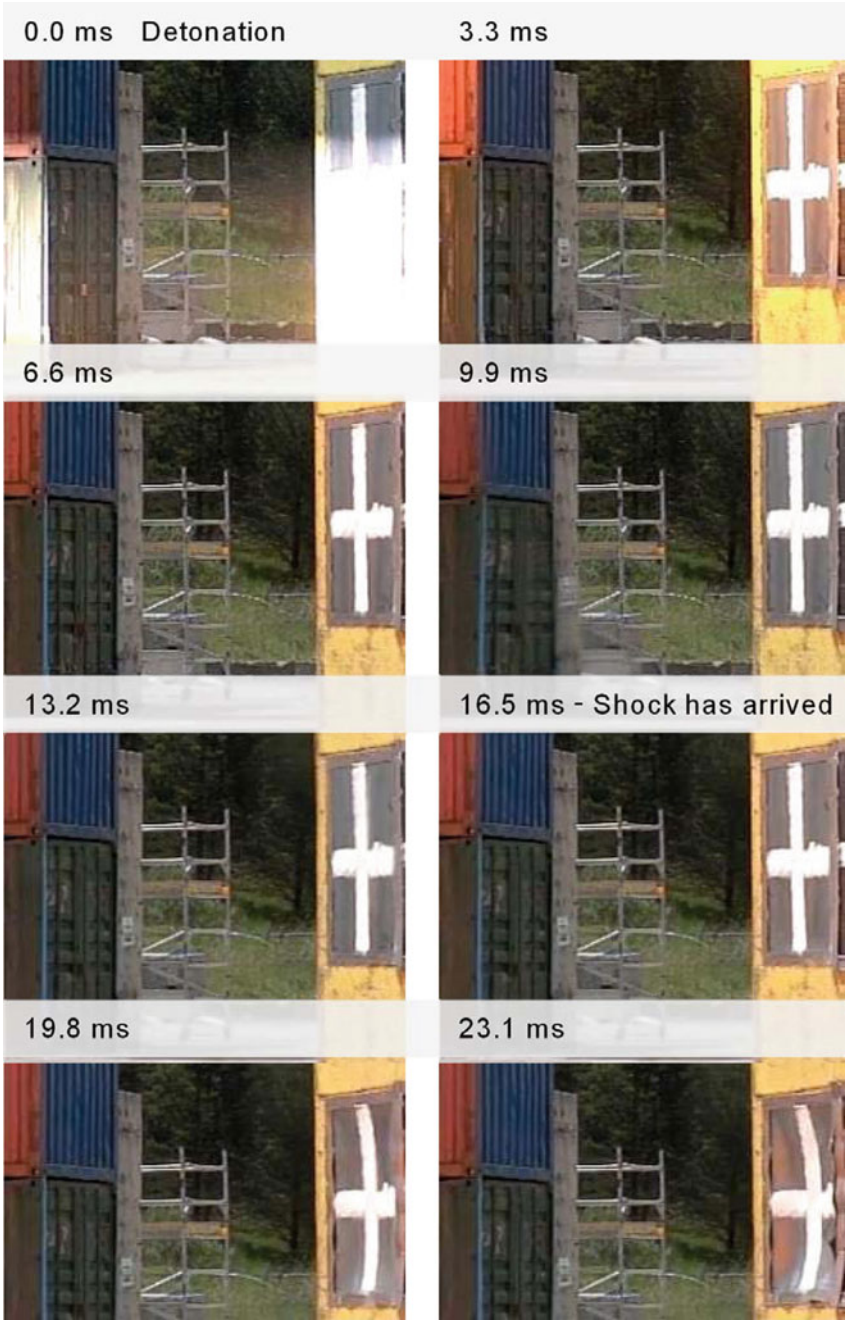


Fig. 15 Images of shock wave progression and front-face deformation of S1 (3 mm thick steel plate). Images are shown from the detonation (0 ms) through the shock wave arrival at target (15 ms) until targets begin their first rebound. Exact time at which these event occur are not shown in the images (due to availability), therefore timings of interest are highlighted around those exact times

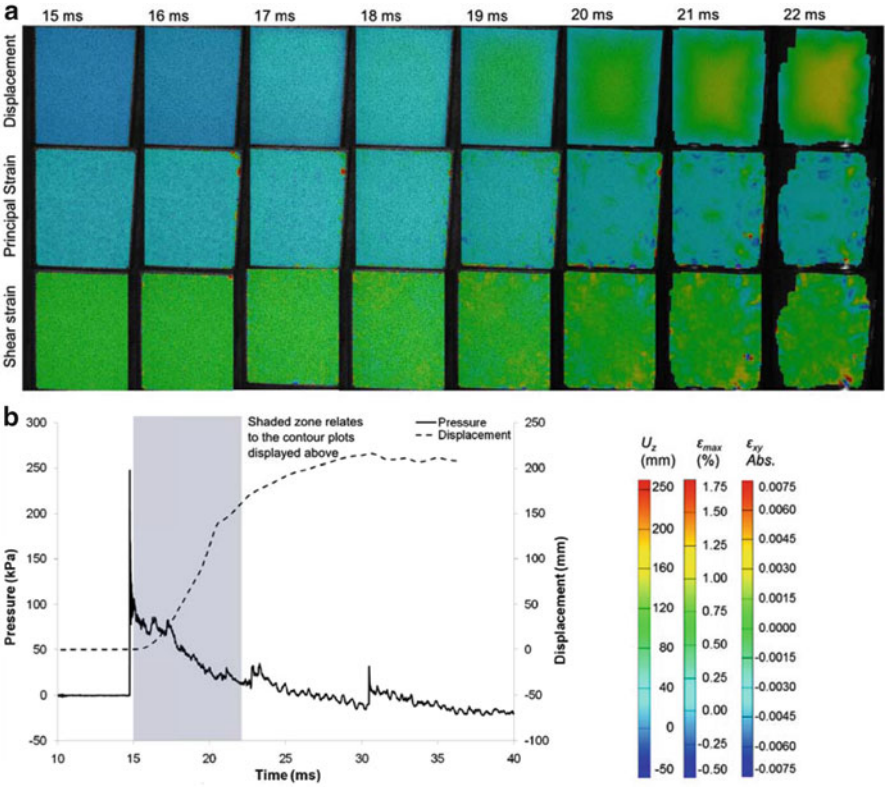


Fig. 16 Blast summary for 100 kg TNT equivalent at 14 m stand-off from S1 including: (**a**) DIC analyses and (**b**) a plot of pressure–time and displacement-time using both DIC and laser gauge centre point measurements. The DIC analyses features contour plots of out-of-plane displacement, maximum principal strain and shear strain, corresponding to various stages in the graphical plot

Blast pressures experienced by panels G4 (30 mm core) and G5 (15 mm core) peaked at a shock pressure of 430 bar (1 kg of C4; 6 m depth; stand-off 1 m; panel air-backed) and 300 bar (1 kg of C4; 6 m depth; stand-off 1.4 m; panel water-backed) respectively. The two pressure–time traces are shown in Fig. 19 for the two blast scenarios, illustrating the ferocity of the blast event, note that the strain gauge data will be restricted to the initial response also highlighted in Fig. 19. Figure 20 shows an example of all strain gauge data for G5. These pressures are very high shock pressures to subject the test panels to and it resulted in significant damage sustained by the targets. The air-backed G4 had its core crushed to half the original thickness (*16 mm* core thickness reduction) by the shock. There were initial surface strains in the region of 3% and once the panel membrane response began, surface strains of around 1% remained causing severe cracks to form within the skins along the panel edges. This is evident in Fig. 14.

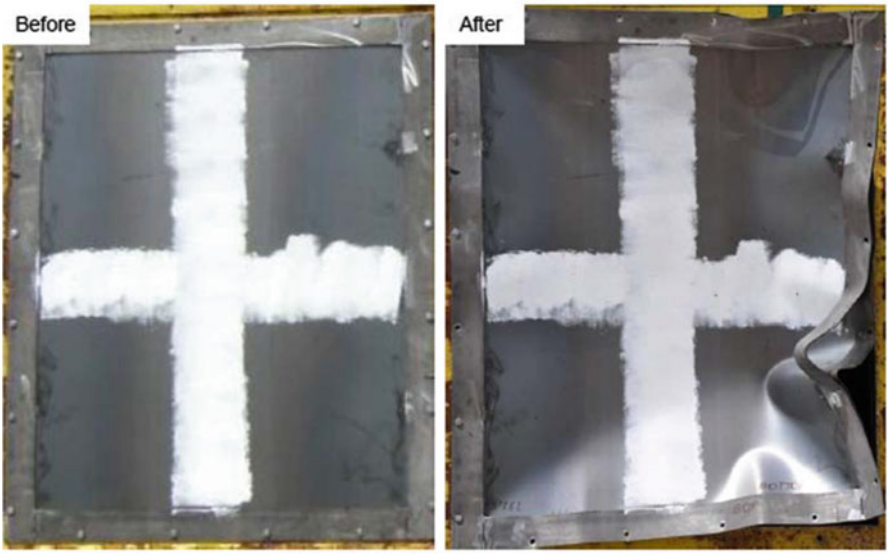


Fig. 17 Before and after images taken of the front face view of S1 after being subject to a charge of 100 kg TNT equivalent at stand-off of 14 m

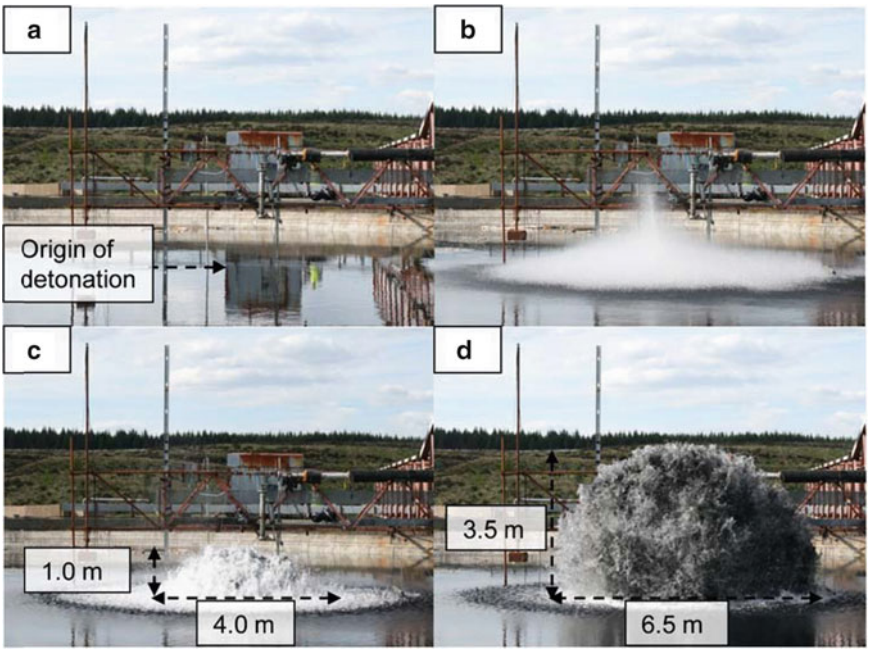


Fig. 18 Images of the event taken from the edge of the pond of the water surface. Different stages of the blast event are shown: (**a**) Prior to detonation with various aspects of the set-up highlighted; (**b**) Initial shock wave reaching the surface of the water causing a spray of water to form at the surface; (**c**) Bubble migrating upwards forming a dome on the surface of the water (at ∼1,000 ms); (**d**) the bubble venting to the atmosphere throwing a mass of water into the air (at ∼1,400 ms)

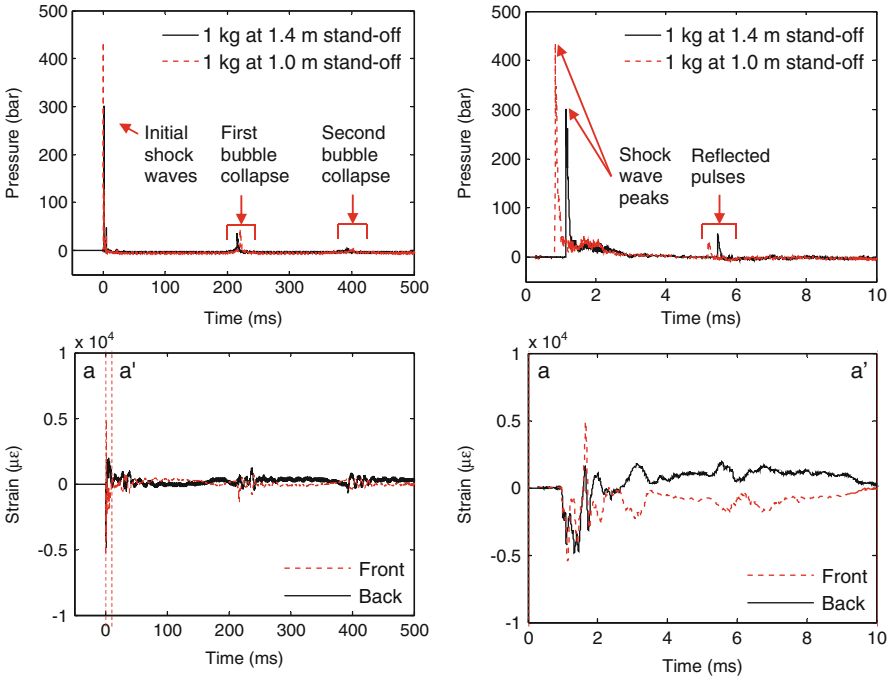


Fig. 19 Pressure–time traces for 1 kg blasts at stand-offs of 1.0 and 1.4 m: the entire event including the first bubble pulse at ∼200 ms (*top left*); and initial shock pressure including reflected shock at ∼5 ms (*top right*). Sample strain gauge data of the panel response is given over these time periods for strain gauge position 1 (as shown in Fig. 3), front and back face, of the water backed-panel G5 (15 mm core thickness) when subjected to the 1 kg charge C4 at 1.4 m stand-off

The water supporting the rear face of panel G5 was observed to dampen the overall response of the panel during the blast. The large strains observed in G4 were not observed in G5 due to the fact that the water medium supported the panel and restrained its response to the blast. Typical flexural response of the plate under a distributed transient pressure load was not observed. This is why surface strains generally remained low over the entire target area of G5 (water-backed) in comparison to the blast on G4 (air-backed), where strain magnitude rose towards the centre of the target. The fact that G5 experienced a decreased impulse was irrelevant; the change in the response characteristics is what has occurred. Figure 20 shows that strains peaked at ±0.6% on the front face and −0.6% on the back face of G5. Each face initially went into a state of compression, forcing the sandwich panel inwards on itself. After this, typical oscillatory motion ensued with strains of ±0.2% resulting. There was no visible damage to the skins after the blast; however, the 15 mm thick core suffered significant crushing as shown in Fig. 21c (7 mm core thickness reduction). This was again in the region of 50% core thickness reduction this time for a peak shock pressure of 300 bar (130 bar lower than that observed for G4) and an impulse of 4.82 bar ms (compared to 6.41 bar ms for G4). The

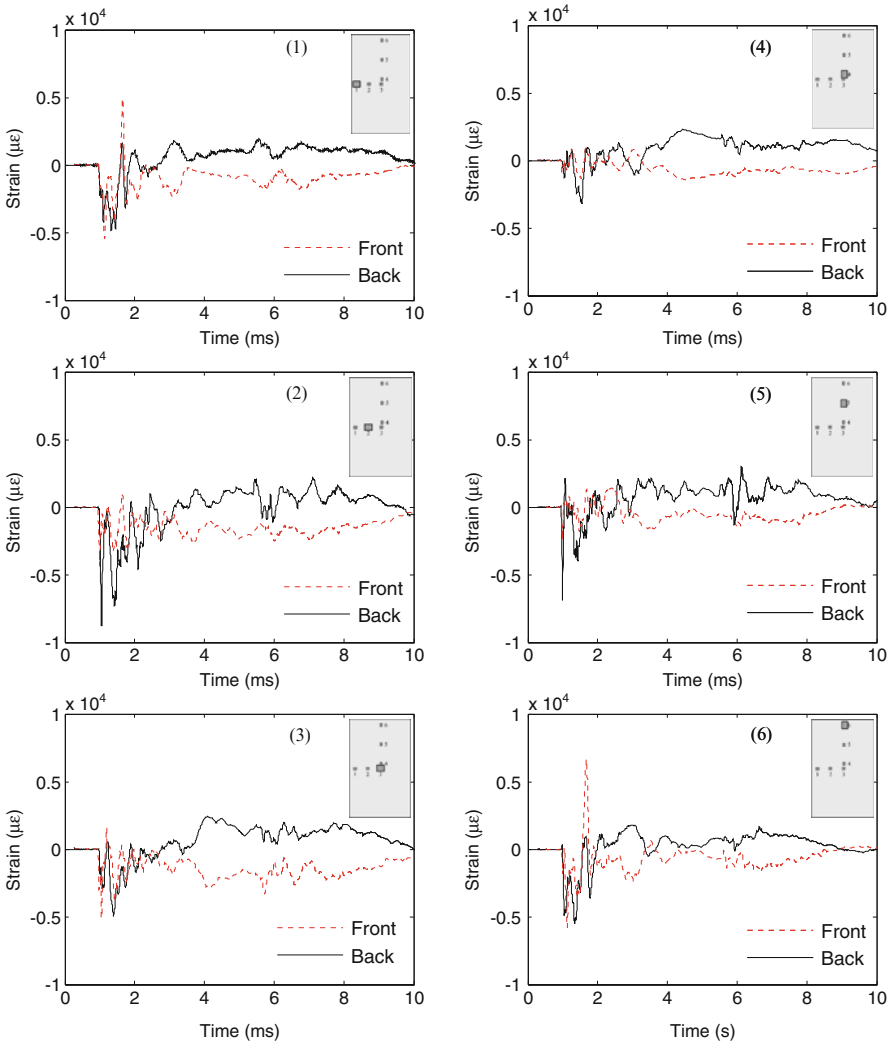


Fig. 20 Sample strain gauge data displayed for G5 (core thickness 15 mm) sandwich composite panel with water on the front and back face (300 bar; 1 kg of C4; 6 m depth; stand-off 1.4 m). Data is displayed for the first 10 ms for each gauge position (numbered as shown in Fig. 3)

two panel responses for G4 and G5 were compared in Fig. 21, the difference in strain magnitude is highlighted as well as the effect of the backing medium with the water-backed G5 (see Fig. 21a) experiencing lower surface strains compared to the air-backed G4 (see Fig. 21b). Moreover the characteristic response of a plate due to impulsive loads was captured by the strain gauge data for the air-backed G4 illustrated in Fig. 21c. The plate experienced an initial compression near the top edge of the panel whilst the central region remained in tension as evident in the strain gauge response shown in Fig. 21b.

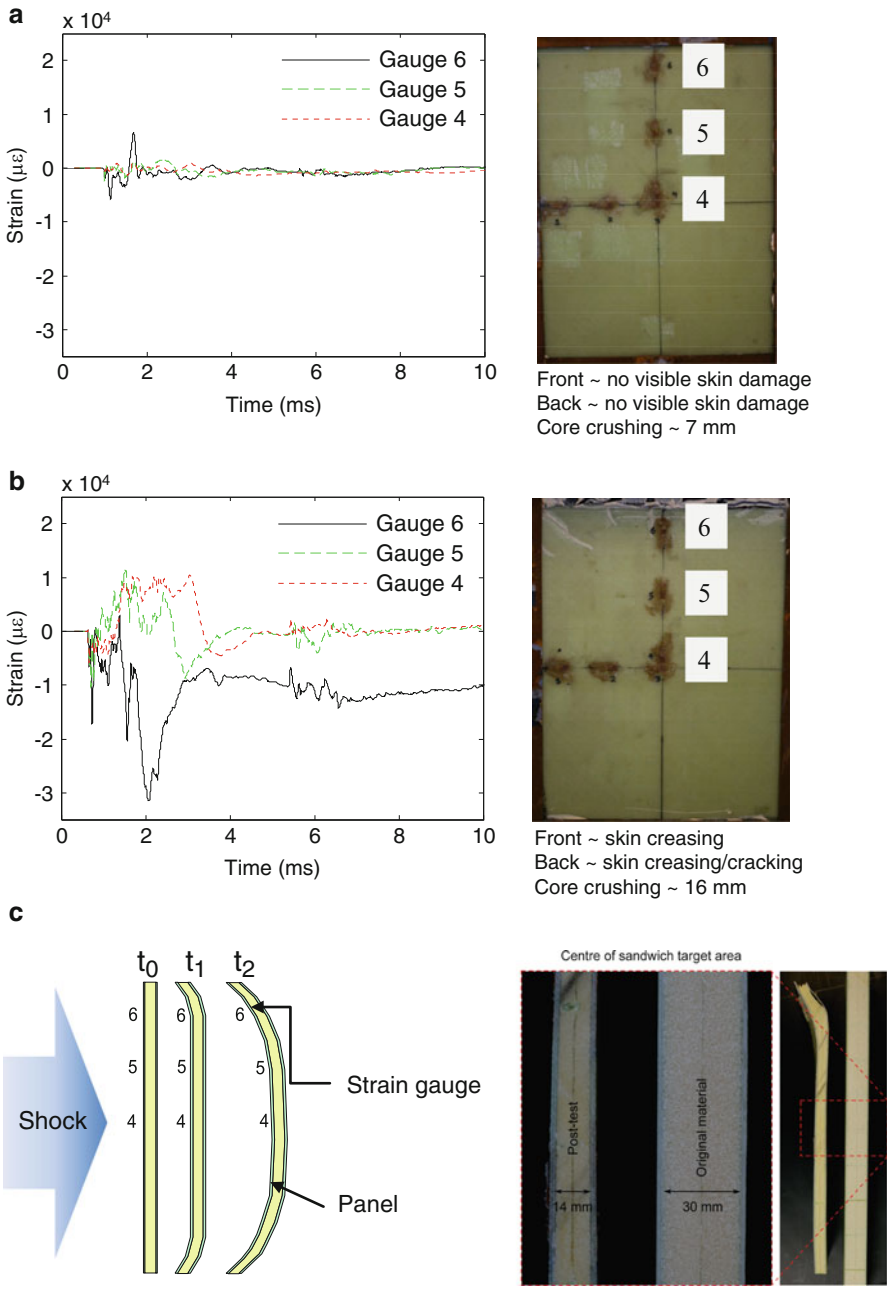


Fig. 21 Comparison of underwater blast response of sandwich panels tested: The first 10 ms of strain gauge data is displayed for gauge positions 4–6 (numbered as shown in Fig. 3) for: (**a**) water-backed sandwich panel G5 (core thickness 15 mm) with shock: 300 bar (1 kg of C4; 6 m depth; stand-off 1.4 m); (**b**) air-backed sandwich panel G4 (core thickness 30 mm) with shock: 430 bar (1 kg of C4; 6 m depth; stand-off 1.0 m); (**c**) diagrammatic representation and sectional views (before and after shock loading) of G4

4.3 Underwater Blast Loading of GFRP Tubular Laminates

4.3.1 Progressive Shock Loading of GFRP Tubular Laminates

Figure 22 shows the combined pressure time traces for each underwater blast on composite tubular laminates of air-filled (AF) design. Peak pressures ranged from 180 to 400 bar for a range of blast parameters from 0.5 kg C4 explosive charge at a 2.0 m stand-off distance at a 6 m depth to a 1.0 kg charge at 1.0 m stand-off distance at the same depth. Figure 16 shows the combined results for the progressive loading of these tubular laminates. The 180 bar blast produced no visible skin damage to the targets with the surface strains sufficiently low to form an agreement with this observation. The 240 bar blast proved to be the threshold for damage evolution with surface strains reaching 1%. The tubes were then tested at a peak shock pressure of 350 bar and visible damage was inflicted on the targets with axial cracks forming along the front facing side of the sample as strains reached 1.5%. In the final test the tubes were taken beyond their limit, where complete shear failure was observed for a peak shock pressure of 400 bar. Similar signs of axial cracking were observed in this final sample (as for the blast of 350 bar) evident from the remains at the end-tabs featured in Fig. 23 prior to the entire gauge length shearing off at the supports.

4.3.2 Effect of Filler Fluid on Tubular Laminate Response

One tube of each air filled (AF) and water filled (WF) design were subject to 350 bar peak shock load caused by a 1 kg C4 charge at 1.4 m stand-off at 6 m depth (pressure–time history shown previously in Fig. 22). There is the initial compression/collapse of the tube inwards at its centre prior to the oscillatory squashing motion. However when these traces in gauges 2–4 for AF are compared to WF (see Fig. 24), there is a marked difference in response. Using water as the filler fluid causes a damped the amplitude of response, reducing peak strains from 1.5% in AF to 0.5% in WF (see gauge position 4 recording the fluctuation in hoop strain on the back facing side of the tube in Fig. 24).

The tubes were both subject to a pressure of 350 bar (there were two independent recordings of pressure either side of the targets). The damage sustained by AF relative to WF was apparent with no visible damage observed for WF whereas AF shown in Fig. 25 shows axial cracking, most likely caused by shear failure during the circumferential crushing phase of the sample deformation causing cracks to initiate.

5 Discussion and Analysis

These sandwich composite structures, although very simple in construction, provided significant blast resistance to shock loading. They sustained a pressure loading of 2 bar in air without resulting in a catastrophic failure. The back face of the panel

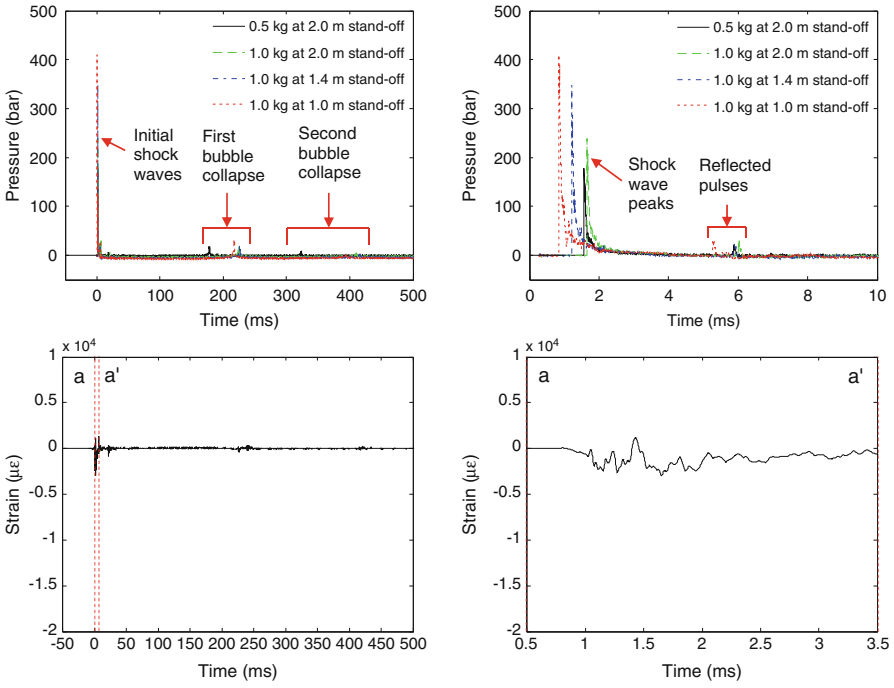


Fig. 22 Pressure–time traces for 0.5–1.0 kg blasts at stand-offs of 1.0–2.0 m: the entire event including the first bubble pulse at ∼200 ms (*top left*); and initial shock pressure including reflected shock from the water surface at ∼5–6 ms (*top right*). Sample strain gauge data of the tubular laminate response is given over these time periods for strain gauge position 1 monitoring axial strain (as shown in Fig. 3) of the air-filled A1 when subjected to the 1 kg charge C4 at 1.4 m stand-off

still remained intact after deflecting 80 mm. The transition to underwater studies showed different energy absorbing and failure mechanisms. Core crushing and skin fibre breakage was observed but not complete skin-to-skin failure when subjected to peak shock pressures of 450 bar. The tubes represented an alternative geometry and the variable of filler medium (water or air) proved to influence the response greatly.

5.1 Air Blast Loading of GFRP-Skinned & CFRP-Skinned Sandwich Composite Panels

A summary of the key results and observations from the air-blast loading of GFRP-skinned & CFRP- skinned sandwich panels is given in Table 2. For the Series A experiments, comparing the response of G1 (40 mm core thickness) and G2 (30 mm core thickness) it was shown that the influence of increasing the core thickness lowered the amplitude of oscillations. Increasing the core thickness increases the second moment of area of the panel and the equivalent flexural rigidity, *D*.

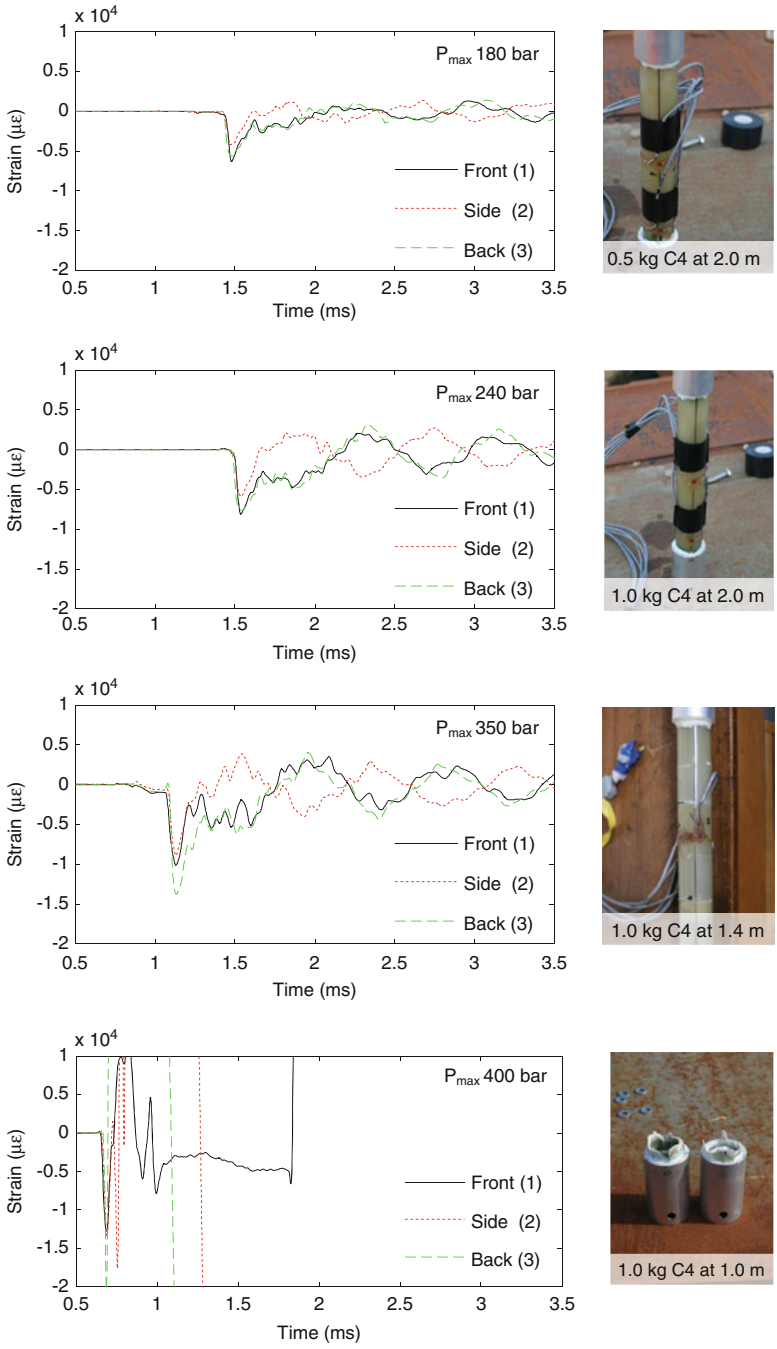


Fig. 23 Shock loading of composite tubes with max shock pressure increasing from 180 to 400 bar

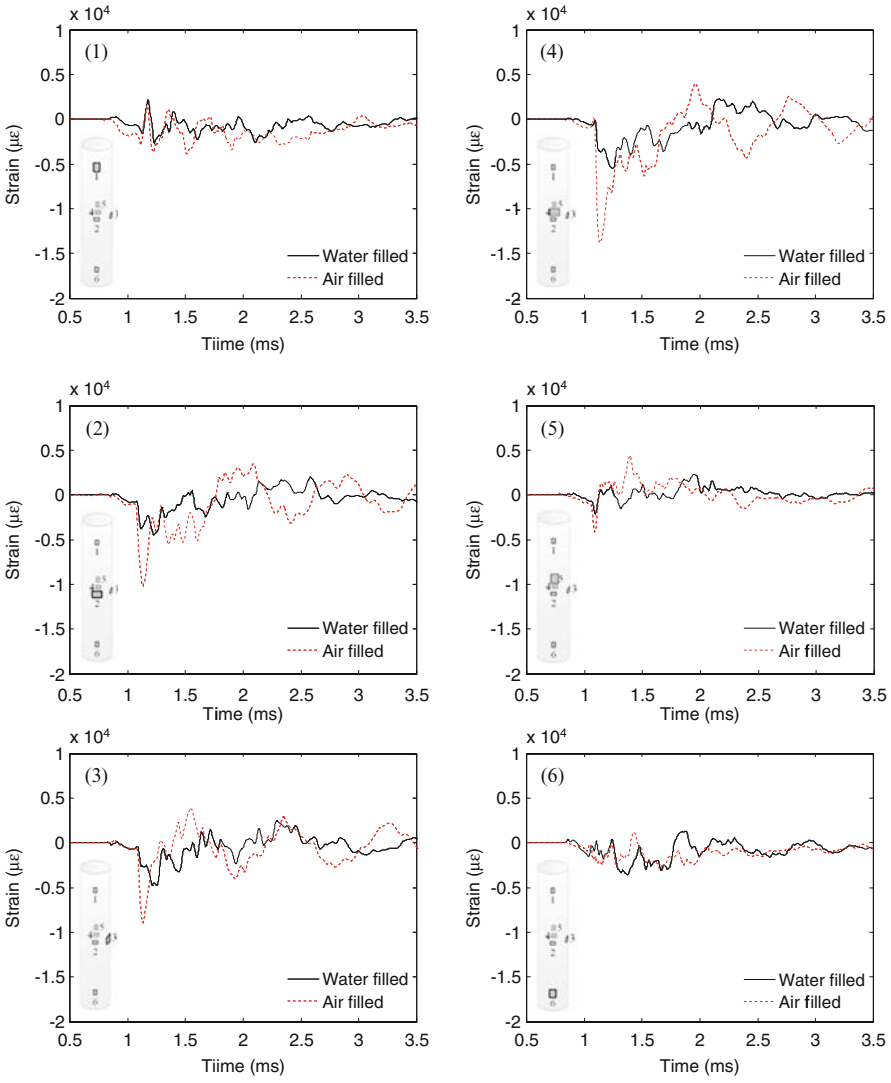


Fig. 24 Strain gauge data is displayed for the first 3.5 ms with peak shock pressure of 350 bar (1 kg C4; depth 6 m; stand-off 1.4 m) for each gauge position on tubes AF and WF, each plot shows the corresponding data for AF (air filled) and WF (water filled) at that particular location

According to [32] D is proportional to the square of the core thickness in sandwich materials. Therefore increasing the core thickness increased the stiffness of the panel and this provided for smaller peak amplitude of displacement. G1 was seen to deflect to a maximum distance out-of-plane of 63 mm whilst G2 deflected 78 mm. The first period of oscillation differed by only 10% between the two targets. Referring also to [29] discussing the response of a fully clamped panel to a uniformly distributed load,

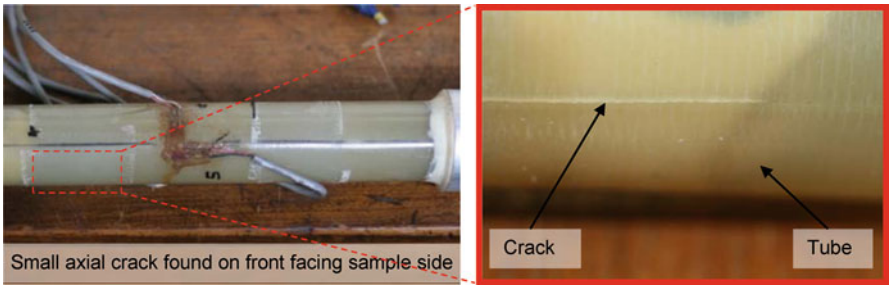


Fig. 25 Post-test images of the AF tube (peak shock pressure of 350 bar) featuring axial cracking near one end (*left*) and a zoomed in view of the crack formed during the blast (*right*)

the equivalent single degree of freedom spring constant of the panel is proportional to D. Combining this stiffness term with the mass term, the natural frequency can be determined. Therefore the period of oscillation was reduced for the thicker core, G1, given the stiffness term increased more significantly than the mass term, in this case by 10%, which was observed when referring to Figs. 6 and 7.

The second G1 panel was tested with the 30 kg charge at 8 m, it can be seen when Figs. 6 and 9 are compared that G1 deflected over twice as much as during the blast at 14 m. The increased pressure (2–8 bar peak shock pressure) and impulse (0.43–1.25 bar ms) caused a more severe response from the target. There is a deviation from static analysis where, the response of a structure to an applied load will be expected to be proportional. These load cases discussed in this paper are highly rate dependent and the structural response is nonlinear. Furthermore introducing damage (and transient boundary conditions) can affect the energy absorbing mechanisms in action and therefore the amount of energy transferred to momentum in the plate.

In terms of damage when the second G1 panel was subject to a stronger blast a skin crack formed on the front face of the target. Employing DIC was a powerful tool for damage detection during the blast. The major principal strain fields generated can tell a great deal about what is happening to the structure. Referring to Fig. 9 it is clear that there is a build up of high-strain of around 3% in the central region until a point, where there is a split in the strain field, with some strain relief appearing in a narrow region down the right-hand side of the panel. This region of stress relief indicates a region of separation between the core and skin (where the skin is unsupported by the core), resulting in the load concentrating on the edges of this (cracked-core) region on the skin. The levels of strain observed in the skin along these edges peaked at 1.8%. Further analysis in Fig. 26 displays the deformed profile of the width of the panel. Out-of-plane displacement of a horizontal central section was taken within the ARAMIS post-processing software and plotted over regular time intervals for the duration of the initial response. It shows the panel deflecting in a symmetrical manner during its inward stroke, up until the point of maximum deflection occurring at 12.5 ms. It is clear that a failure (or change in structural balance) has occurred within the panel, causing an asymmetric rebound profile of the panel at 15.5 ms.

Table 2 Summary of each air-blast conducted on GFRP- and CFRP-skinned sandwich panels highlighting the peak pressures, peak strains and visible damage

Sample code	Skin lay-up, core thickness (mm)	Charge size (kg), Stand-off distance (m)	Peak pressure (bar), duration (ms)	Peak strain (%)[a]	Damage	Notes
G1	2× QE1200, 40 P800	30 kg; 14 m	2 bar; 6 ms	1	No visible damage	No damage detected in DIC analysis
G2	2× QE1200, 30 P800	30 kg; 14 m	2 bar; 6 ms	1.25	No visible skin damage, some mild core cracks	Mild signs of damage visible in DIC
G1	2× QE1200, 40 P800	30 kg; 8 m	8 bar; 5 ms	3	Severe skin and core cracking (no crushing)	Definite signs of damage shown in DIC as well as in post inspection
G3	2× QE1200, 25 M130	100 kg; 14 m	2.5 bar; 12 ms	1.6	Severe skin and core cracking	DIC confirms appreciable defection and shows damage to front skin and core
C1	2× RC245T & RC380T, 25 M130	100 kg; 14 m	2.5 bar; 12 ms	0.8	Slight skin crack; less severe but more widespread core cracking	DIC shows reduced deflection and minimal damage

[a] Strain measurements were taken from the back face of the target

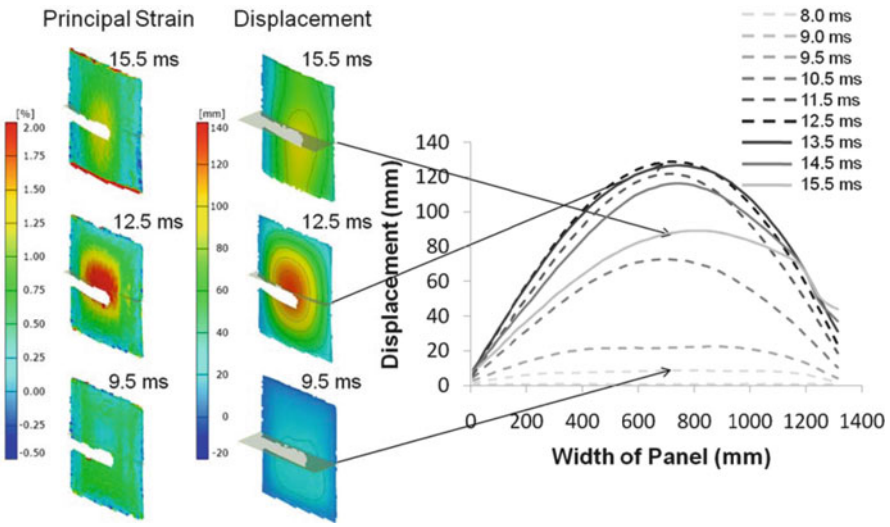


Fig. 26 Displacement data taken across a horizontal section running through the point of maximum deflection for panel G1 (core thickness 40 mm) during blast loading (30 kg at 8 m stand-off). Data displayed for several time intervals from 8 ms after detonation. *Dotted lines* show displacement profile up to maximum deflection and *solid lines* show subsequent return

This reinforces the notion of a complete core shear failure, resulting in complete crack propagation from face-to-face down a significant portion of the panel. The first 1.5 ms (8.0–9.5 ms) of response show the flat central area of the panel progressing, which is characteristic to impulsive loading situations. After 1.5 ms, there is a faint region of stress-relief on one edge of the panel due to crack initiation causing separation between the skin and core (locally). Now it can be accounted for due to the exaggerated bending stresses experienced in the early stages (around the square wave front) where the radius of curvature in the bend is significantly lower. The reason for the crack developing preferentially on one side rather than the other is due to the uneven loading experienced and the asymmetry in support conditions. The cubicle design is such that one edge of the composite sandwich panel leads to free air and one edge leads to the centre of the cubicle and so the magnitude of impulse deteriorates on one side relative to the other. This cubicle design also leads to an effectively more rigid support along the edge of the cubicle compared to the central support. For the ideal case (with the same support and loading all around the panel) cracks would be forming from all four corners causing a square section of the panel to crack. However, once one crack forms, stress relief dictates that another is unlikely to form without sustained or increased loading. Once the crack formed in the core the front (and back) skins were left unsupported by the core and therefore the strains concentrated on the edges of this core crack and this lead to skin fibre breakage. Sectioning confirmed that failures had occurred, specifically the core crack, which propagated through from face-to-face of the core (see Fig. 10). However, the DIC analysis did pick up the separation of skin and

core, also highlighted in the blast on G2 to an extent, confirmed with sectioning. With appropriate experience, DIC can be a very powerful tool for monitoring the structural integrity of various materials and identifying damage mechanisms occurring even when subject to extreme load cases such as these.

For the series B experiments, with the GFRP-skinned sandwich panels (G3), there was a uniform forward (positive) stroke, however, due to the compromised integrity of the skin and core, there was an augmented return stroke. It is also apparent that there are more uniform support conditions achieved with the use of two panels side by side. This was the aim of this test fixture, to avoid or minimise the bias on strain distributions. Although this was achieved the location of the failure occurred on one side of the target. The core crack seemed to initiate in the early stages again at ∼1.5 ms after impact, 16.5 ms after detonation. As stated previously, the higher bending stresses cause shear cracks to initiate in the early stages of the G3 & C1's deformation cycles. However, since the GFRP-skinned panel provides less resistance to the shock wave impact, the severity of damage increases faster than in the CFRP-skinned panel. Furthermore, the average velocity of the target deformation is 40 m/s in G3 compared to 25 m/s in C1. In the case of G3 this lead to fibre breakage all along this crack at the point of peak deflection. In the CFRP target, C1, distributed the blast energy more effectively through the panel and responded with a greater resistance to the impact. It gained in less kinetic energy too, which was sustained on the rebound strike without any global skin failures. Once the centre of the target reached maximum displacement the remaining momentum carried the edges of the panel forward, unrestrained due to the loss in integrity of the core, leading to this flattening out observed of the deformed profile after the maximum displacement is reached.

Finally, S1 is analysed to give a direct comparison to the GFRP and CFRP sandwich panels. The steel plate exhibits the classic impulsive behaviour, with the central flattened region. This blast caused bolt shear to occur on one side causing the bias on the deformed profile. The plate was moving at an average velocity of 25 m/s at the point of bolt shear, causing a jump in the central point velocity (up to 31 m/s). Then this remaining tail of the pressure pulse and momentum of the plate causes the plate to continue with large plastic deformations. The steel plate is heavier than the composite sandwich panels, therefore these velocities of deformation and magnitudes of deflection are considerable from a blast mitigation point of view.

5.1.1 Accuracy of Data Reported by DIC Compared to Laser Gauge Measurements

As stated previously, point data on the targets was taken from the DIC analysis and compared to the measurements recorded by a laser gauge for verification purposes (see Fig. 27). Data was taken from the point where the laser gauge was targeting, which was precisely identified in the raw images. There was good agreement, with a $<1\%$ error until maximum deflection, between the two sets of measurements as shown in Fig. 27a.

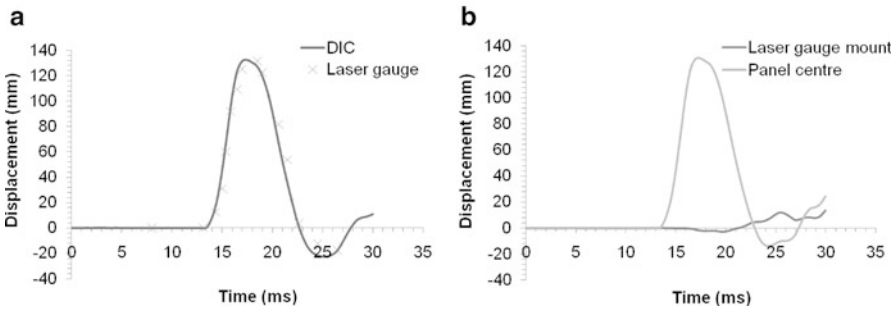


Fig. 27 Comparison of the central point displacement measured by the laser gauge and that recorded by the DIC analysis. The data shown is from the 30 kg at 8 m stand-off air-blast on G1: (**a**) analysis of the same point deflection during the blast measured by the DIC analysis and by the laser gauge; and (**b**) point data taken from the DIC analysis showing the relative movement of the laser gauge mount to its original target point on the panel

During the blast event, there reaches a point in time where the laser gauge (visibly) began to move and the data it was recording became compromised. The steel beam structure, comprising the mount for the laser gauge, flexed and vibrated after the (primary) target response reached peak deflection. To clarify when the laser gauge began to move, the steel beam itself was speckled and computed for its movements. It can be seen from Fig. 27b that the position of the laser gauge begins to move at the point where the panel is reaching its maximum deflection. This data shows qualitatively where the reliability of the data deteriorates. After this stage the laser gauge begins to flex and rotate (observed in the video recording) and so the validity of its results breaks down, since it was not at its original start position nor was it pointing at the same point. This exercise indicated a close agreement of the two systems for point displacement measurements until the point of maximum deflection. Therefore the validity of the measurements taken using DIC techniques under such extreme conditions can be taken to be true (provided vibrations of the cameras can be kept to a minimum). Provisions of heavy based tripods, held down with auxiliary weighting, supporting the cameras isolated on rubber mounts ensured minimal vibration transmission until the target's first period of oscillation completed. To be conservative within this analysis, the DIC data is accepted until the first rebound. All data presented and discussed is taken from within this period.

5.2 Underwater Blast Loading of GFRP Sandwich Composite Panels

As shown earlier with post-test images, significant damage was sustained by each target. Key observations and results are summarised in Table 3. The air-backed panel G4 (30 mm core thickness) had its core crushed to half the original thickness by the

shock with pressure 430 bar (duration is stated in Table 3 as a duration of the peak, in this case 0.2 ms, and as a duration of the tail of the shock wave, which decays at a much slower rate than the initial stage, here the tail duration is 3.2 ms). By the time typical membrane response began, excessive surface strains remained in the region of 1% causing cracks to form within the skins along the panel edges. The front surface strain measurements for gauges 4–6 are displayed in Fig. 21. From gauge 6 positioned at the top edge of the panel, it is clear that the panel bent, deformed around its edge, causing the 2–3% strains observed on the surface in that region. Comparing the strains across that length from edge to centre it is clear that after the initial compression, the centre moves into tension (unlike the panel edges), causing a possible third order mode shape of flexural response. In other words the typical impulsive shape of deformation shown previously for the air-blast trials was present, where a square profile deforms outwards upon impact prior to parabolic oscillations. The resulting visible front-face damage concentrated around the top edge is shown previously in Fig. 21. Although the initial shock can be assumed to act uniformly over the entire face, the bubble pulse would mainly have affected the top edge, given the first bubble minimum would have occurred 0.9 m above the site of the charge (calculations taken from [33]). This can account for the discrepancy of visible damage sustained by the top edge, since nearly half the explosive energy released by the charge contributes towards the pulsation of the bubble and this would have been imparted predominantly on the top edge of the panel.

For the water-backed shock loading of G5 thickness, by the shock with pressure 300 bar, it was shown that each face initially went into a state of compression, forcing the sandwich panel inwards on itself. This can be due to a number of reasons, namely, the panel being forced backwards against a mass of water and, due to the small time period and the fact that the water is encapsulated within the base-frame, this caused an initial crushing effect (on the target) as there was insufficient means for the water to vent out of the frame (seals). This caused an increased through-thickness stress on the panel compared to when the panel is backed by air, resulting in the highly compressed core. The edges of the panel peaked into tension on both faces, perhaps as a response to the compression of the core or superposition of surface stress waves at the boundary edge. After this, typical oscillatory motion ensued with strains of $\pm 0.2\%$ resulting. There was no visible damage to the skins after the blast due to the relatively low surface strains experienced. The 15 mm thick core however was crushed to nearly half its original thickness due to this pressurising effect. The difference between the two underwater blasts in terms of peak shock pressure and the backing medium meant that for the lower peak shock pressure the same relative core thickness reduction was experienced, simply due to the fact that the backing medium was denser. This phenomenon was verified in another set of trials where two targets of same thickness were subject to the same peak shock pressure with only the backing medium the variable. The air backed panel sustained more skin damage but less core crushing due to the nature of the fluid medium supporting the skins.

Table 3 Summary of each underwater blast conducted on GFRP sandwich panels highlighting the peak pressures, peak strains and visible damage

Sample code	Skin lay-up, core thickness (mm)	Charge size (kg), Stand-off distance (m)	Peak pressure (bar), duration (ms)	Peak strain (%)[a]	Damage	Notes
G4	2× QE1200, 15	1.0, 1.4 (water-backed panel)	300 bar 0.2 ms (peak) 3.0 ms (tail)	±0.6/−0.6	Severe core crushing but no visible skin damage	Water was present behind panel ~ squashing the panel during the blast
G5	2× QE1200, 30	1.0, 1.0 (air-backed panel)	430 bar 0.2 ms (peak) 3.2 ms (tail)	−3/−1[b]	Severe core crushing and skin cracking	Air was present behind panel ~ unsupported

[a] Strain measurements are shown for the front and back face of the target

[b] Strain gauges lost the recording after the initial impact caused a given state of strain (compression)

5.3 Underwater Blast Loading of GFRP Tubular Laminates

The results are summarised in Table 4 for both the progressive loading of GFRP tubular laminates as well as the experiments to observe the effect of the filler medium.

5.3.1 Progressive Shock Loading of GFRP Tubular Laminates

This set of blasts produced progressive damage on the tube constructions from no visible damage to complete shear failure, when subjected to peak shock pressures of 180–400 bar. For the blast of 0.5 kg at 2 m producing a peak shock pressure of 180 bar, 0.1 ms duration, the gauge data indicated mild bending response with opposing axial strain gauges recorded signals that were out-of-phase with each other i.e. one in tension when the other is in compression; and initial breathing action hoop strains were all in compression (−0.6%). After this (0.5 ms after impact) the tube response reverts to an oscillatory squashing motion (front/back strain gauges were out-of-phase with side strain gauges), see Fig. 16 for hoop strain data.

This air filled (AF) construction was tested to a peak shock pressure of 240 bar, 0.1 ms duration, (1.0 kg at 2 m stand-off). This blast resulted in larger amplitude of strains of similar characteristics to the previous blast (0.5 kg at 2 m). Strains peaked at 0.8% across the range of gauges. There were generally only mild signs of possible damage with chalky patches appearing on the tube surfaces (mild matrix cracking). This was the threshold for damage for this construction. The AF tube was then subject to a peak pressure loading of 350 bar, 0.1 ms duration, (1.0 kg at 1.4 m stand-off), which resulted in axial cracks forming at the front ends of the tubes. The characteristic response of the tube was again similar to that those tested previously with strain peaking at 1.5%, highlighted in Fig. 16. The final blast, 1 kg at 1 m stand-off, on AF tubes exceeded the blast limit of the tube construction when subject to a peak pressure of 400 bar, 0.2 ms duration. From the strain data in Fig. 16 it is clear that the tubes response was insufficient to absorb the energy imparted on it in a quick enough period. The strain gauge recordings implied an initial compression inwards, with the front face circumferential gauge holding at 0.5% strain, prior to the ends of the tube shearing away from the fixed end-tabs, terminating all recordings within the first 5 ms.

5.3.2 Effect of Filler Fluid on Tubular Laminate Response

All common modes of response expected by tube structures to underwater shocks were present as mentioned in the previous section of analysis: circumferential reduction/expansions (breathing) and elliptical oscillations (squashing) as illustrated in Fig. 28. The tubes represent an alternative geometry to the flat panels. The initial shock wave wraps around the cylindrical geometry, causing an inward compression. After the pressure of the surrounding fluid reduces the energy gone into deforming

Table 4 Summary of each underwater blast on GFRP tubular laminates highlighting the peak pressures, peak strains and visible damage

Sample code	Charge size (kg), Stand-off distance (m)	Peak pressure (bar), duration (ms)	Peak strain (%)[a]	Damage	Notes
AF	0.5, 2.0	180 bar 0.1 ms (peak) 2.4 ms (tail)	−0.2/0.3/±0.2	No visible damage	Elastic oscillations
AF	0.5, 2.0	180 bar 0.1 ms (peak) 2.4 ms (tail)	−0.6/–0.6/–0.4	No visible damage	Elastic oscillations
AF	1.0, 2.0	240 bar 0.1 ms (peak) 2.3 ms (tail)	−0.4/0.4/±0.3	Some surface fibre damage visible	Elastic oscillations but subsurface damage to laminate
AF	1.0, 2.0	240 bar 0.1 ms (peak) 2.3 ms (tail)	−0.7/–0.8/–0.5	Some surface fibre damage visible	Breathing motion clearly observed with larger amplitude strains
AF	1.0, 1.0	400 bar 0.2 ms (peak) 3.0 ms (tail)	±1/+ve/+ve[b]	Complete shear failure at the ends of the tube	The central section began to respond prior to fracture at ends
AF	1.0, 1.0	400 bar 0.2 ms (peak) 3.0 ms (tail)	±1/3/±1[b]	Complete shear failure at the ends of the tube	The central section began to respond prior to fracture at ends
AF	1.0, 1.4	350 bar 0.1 ms (peak) 2.3 ms (tail)	−1/–1.5 −1	Axial cracking at front face ends of tubes	Hoop strains dominated with larger amplitude of strains
WF	1.0, 1.4	350 bar 0.1 ms (peak) 2.3 ms (tail)	±0.3/−0.5 −0.4	No visible damage	Filler fluid damped the strains experienced

[a] Strain measurements are shown for the front, back and side of each tube

[b] Strain gauges lost the recording after the initial impact caused a given state of strain (tension)

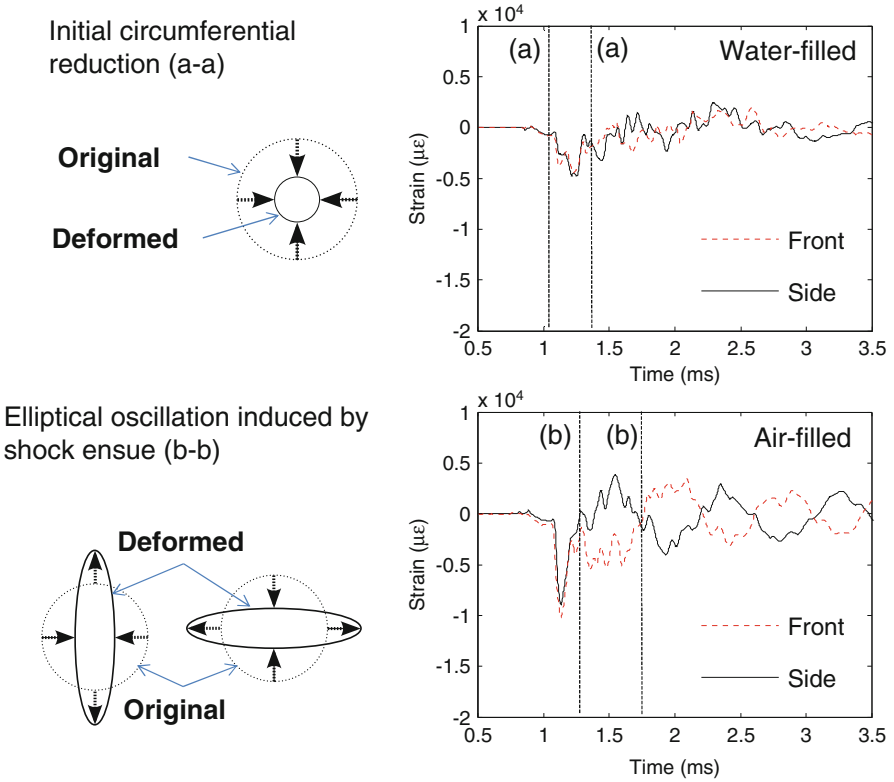


Fig. 28 Diagram illustrating the two main modes of deformation observed, breathing (*top left*) and elliptical oscillation or squashing (*bottom left*) as the relative magnitudes of strain observed in both tube cases, water filled (*top right*) and air-filled (*bottom right*)

the tube in this manner is released in the mode of oscillatory vibrations with the dominant mode in the form of a circumferential squashing motion. These two modes of vibration were the most dominant of those observed during these trials, however, the most significant result to emerge from this trial is the fact that the backing fluid (filler fluid) made considerable savings with regard to damage sustained by the tube structures (visible in Fig. 25). The denser filler medium (water) made the tube effectively more rigid and reduced the magnitude of surface strains experienced and hence damage sustained. Figure 24 shows that the water filled tube experienced surface strains of half the magnitude of those experienced by the air-filled tube. To analyse this further, having a denser filler medium also dampens the vibrations quicker. After a few milliseconds, the strains in the air-filled tube are still greater than even the maximum strain experienced by the water filled tube. Moreover the water-filled tube seems to also resist the elliptical/squashing mode of vibration clearly observed with the air-filled tube. This is due to the fact that the tube needs to compress the filler medium to oscillate between tension/compression when going

through this squashing motion and the energy required to compress the denser filler medium is too great. Therefore the energy is dissipated within the water filler medium and in mild residual surface vibrations in comparison to the air-filled tube which freely vibrates with large magnitude of strains >1% (highlighted in Fig. 28).

6 Conclusions

These sets of blast data have shown the capabilities of simple composite constructions to resist blast loads. Both conventional (strain gauges) and more advanced (high-speed DIC) strain monitoring techniques were employed to monitor the deformation of the targets during the blasts. Various aspects of blast events have been highlighted by these studies such as the ferocity of these explosions, the damage they can inflict as well as how boundary conditions can affect the outcome in terms of damage sustained and how these boundary conditions can play more of an important role in blast mitigation than material design.

These experiments were conducted on commercially available marine constructions, on a large scale (target length scales in the range of 0.3–1.6 m) against actual explosive charges (0.64–100 kg TNT equivalent charge weights). These experiments differ from others investigating blast/shock impact on such materials, due to the style of tests approaching a real simulation of in-service conditions (large-scale targets subject to explosions both in-air and underwater).

During the underwater blast experiments the sandwich panels were subject to pressures over 100 times greater in magnitude in less than a tenth of the period of time than those experienced during the air-blast experiments. During the air-blast experiments, back-face skins (and front-face skins generally) maintained their form without tearing/cracking. However during the underwater blasts, the cores experienced considerable crushing (up to 50%) and the skins experienced very large strains, causing fibre breakage on both faces (with strains exceeding 3%) when the targets were backed by air. The effect of having water as a backing medium reduced the surface strains experienced and hence damage incurred by the skins but increased the relative crushing observed in the core. Tube structures were tested and the effect of the filler/backing medium was again apparent with the water filled tube reducing surface stains by 60% in some regions. The sample data is limited for traditional statistical analysis of sample response (no repeat experimentation). This is due to the fact that the samples used were full-scale (up to 1.3 m × 1.6 m for air blasts) and restrictions were in place with respect to the consumables required to manufacture them. However, within the small sample of tests conducted, verification of the data collected for the air-blasts was achieved to some extent using two techniques for point measurement and for the underwater-blasts using multiple gauge arrangements, giving confidence in the quality of data recorded.

The main findings in summary are:

- DIC was successfully employed during full-scale air-blast experiments to capture the damage progression in sandwich structures.

- CFRP-skinned sandwich panels exhibited less damage and deformation than equivalent GFRP-skinned sandwich panels when subject to explosive air blast.
- There is a difference in response of GFRP sandwich panels to air-blast (30 kg at 8–14 m) and underwater-blast loading (1.0 kg at 1.0–1.4 m) due to the different pressure–time signatures: peak shock pressures of 2–8 bar (6 ms duration) to 300–430 bar (0.2 ms duration).
- Damage mechanisms changed from front-face skin damage and core shear cracking for air blast to severe core crushing (up to 50%) and skin fibre-breakage for underwater blast.
- Damage and response of tubes subjected to underwater blast varies according to whether the tubes are filled with air or water, with the air-filled tubes sustaining longitudinal cracking compared to no visible damage on the water-filled tube subject to the same blast load.
- All experiments, on blast loading of GFRP and CFRP-skinned composite structures, highlighted the importance of boundary conditions on the structural response and damage sustained by the structure, in terms of both location and nature of damage caused by a blast.

Acknowledgements Much appreciated is the strong support received from Dr Yapa Rajapakse of the Office of Naval Research (ONR N00014-08-1-1151) in particular for Hari Arora. We also acknowledge the Metropolitan Police and CPNI for use of the test cubicles and other equipment, GL Industrial for the use of their facilities and support on site, SP Gurit for provision of materials and GOM mbH for access to latest DIC equipment during the air-blast trials and Shouhua Chen and Paolo Del Linz for help with analysis of DIC and other experimental results.

References

1. Ambrosini RD, Jacinto AC, Danesi RF (2001) Experimental and computational analysis of plates under air blast loading. Int J Impact Eng 25(10):927–947
2. Hoo Fatt MS, Palla L (2009) Analytical modeling of composite sandwich panels under blast loads. J Sandw Struct Mater 11(4):357–380
3. Neuberger A, Peles S, Rittel D (2007) Scaling the response of circular plates subjected to large and close-range spherical explosions. Part I: air-blast loading. Int J Impact Eng 34(5):859–873
4. Neuberger A, Peles S, Rittel D (2007) Scaling the response of circular plates subjected to large and close-range spherical explosions. Part II: buried charges. Int J Impact Eng 34(5):874–882
5. Menkes SB, Opat HJ (1973) Tearing and shear failure in explosively loaded clamped beams. Exp Mech 13(11):480–486
6. Nurick GN, Martin JB (1989) Deformation of thin plates subject to impulsive loading – a review. Part II: experimental studies. Int J Impact Eng 8(2):171–186
7. Nurick GN, Olsson MD, Fagnan JR (1993) Deformation and rupture of blast loaded square plates – predictions and experiments. Int J Impact Eng 13(2):279–291
8. Gelman ME, Nurick GN, Marshall NS (1986) Tearing of blast loaded plates with clamped boundary conditions. Int J Impact Eng 18(7–8):803–827
9. Nurick GN, Simmons MC, Cantwell WJ, Langdon GS, Lemanski SL, Schleyer GK (2007) Behaviour of fibre-metal laminates subjected to localised blast loading: Part I experimental observations. Int J Impact Eng 34:1202–1222

10. Langdon GS, Simmons MC, Cantwell WJ, Lemanski SL, Nurick GN, Schleyer GK (2007) Behaviour of fibre-metal laminates subjected to localised blast loading: Part II experimental observations. Int J Impact Eng 34:1223–1245
11. Cantwell WJ, Langdon GS, Nurick GN (2005) The blast response of novel thermoplastic-based fibre-metal laminates some preliminary results and observations. Compos Sci Technol 65: 861–872
12. Tekalur SA, Shivakumar K, Shukla A (2008) Mechanical behavior and damage evolution in E-glass vinyl ester and carbon composites subjected to static and blast loads. Compos Part B Eng 39(1):57–65
13. Tekalur SA, Bogdanovich AE, Shukla A (2009) Shock loading response of sandwich panels with 3-D woven E-glass composite skins and stitched foam core. Compos Sci Technol 69(6):736–753
14. Tekalur SA, Shukla A, Shivakumar K (2008) Blast resistance of polyurea based layered composite materials. Compos Struct 84(3):271–281
15. Wang EH, Shukla A (2010) Analytical and experimental evaluation of energies during shock wave loading. Int J Impact Eng 37(12):1188–1196
16. Jackson M, Shukla A (2011) Performance of sandwich composites subjected to sequential impact and air blast loading. Compos Part B Eng 42(2):155–166
17. Cole RH (1948) Underwater explosions. Princeton Univ. Press, Princeton
18. Hetherington JG, Smith PD (1994) Blast and ballistic loading of structures. Butterworth Heinmann, Oxford/Boston
19. Panciroli R, Abrate S (2009) Dynamic response of sandwich shells to underwater blasts. In: ICCM 17, IOM Communications, Edinburgh
20. Deshpande VS, Heaver A, Fleck NA (2006) An underwater shock simulator. P R SocA Math Phys Eng Sci 462(2067):1021–1041
21. Espinosa HD et al (2009) Performance of composite panels subjected to underwater impulsive loading. In: ONR 2009 solid mechanics program, UMUC, Maryland
22. LeBlanc J, Shukla A (2010) Dynamic response and damage evolution in composite materials subjected to underwater explosive loading: an experimental and computational study. Compos Struct 93(3):1060–1071
23. Ravichandran G, Bhattacharya K, Colonius T, Dimotakis PE, Gharib M, Ortiz M, Rosakis AJ, Shephard JE (2009) Muri on mechanics and mechanisms of impulse loading, damage and failure of marine structures and materials. In: Rajapakse JY (ed) ONR solid mechanics program 2009. UMUC, MD
24. Arora H, Hooper PA, Dear JP (2011) Dynamic response of full-scale sandwich composite structures subject to air-blast loading. Compos Part A 42:1651–1662
25. Bland PW, Dear JP (2001) Observations on the impact behaviour of carbon-fibre reinforced polymers for the qualitative validation of models. Compos Part A 32(9):1217–1227
26. Dear JP, Lee H, Brown SA (2005) Impact damage processes in composite sheet and sandwich honeycomb materials. Int J Impact Eng 32(1–4):130–154
27. Dear JP, Brown SA (2003) Impact damage processes in reinforced polymeric materials. Compos Part A 34(5):411–420
28. Rajendran R, Paik JK, Lee JM (2007) Of underwater explosion experiments on plane plates. Exp Tech 31(1):18–24
29. Biggs JM (1964) Introduction to structural dynamics. McGraw-Hill Book Company, New York
30. Deegan M (2010) Personal communication, Vishay Measurements Group, UK
31. Kwon YW, Fox PK (1993) Underwater shock response of a cylinder subjected to a side-on explosion. Comput Struct 48(4):637–646
32. Gibson LJ, Ashby MF (1997) Cellular solids, structure and properties, 2nd edn, Cambridge solid state science. Cambridge University Press, Cambridge
33. Reid WD (1996) The response of surface ships to underwater explosions. Department of Defence, Defence Science and Technology Organisation, Melbourne

Interaction of Underwater Blasts and Submerged Structures

S. Abrate

Abstract This chapter examines the interaction of shock waves generated by underwater explosions and submerged structures. Cylindrical shells filled with air, water, or a liquid with a different speed of sound are considered and the specific issue considered is the prediction of the position of the various wave fronts as a function of time. This is a challenging problem for both analytical and numerical approaches due to the sharp discontinuities, the complex shapes of these wave fronts and their numbers. A simple ray tracing procedure is developed to predict the exact position of all the wave fronts. It provides great insight into the physics of the problem and explains the evolution of the shape of the various fronts and the formation of singularities. Applications to the medical field are also presented.

Keywords Underwater blast • Explosion bubble • Shock wave • Wave front • Diffraction

1 Introduction

This chapter deals with the effect of underwater explosions on submerged marine structures and more specifically with the interaction of blast wave with those structures. Underwater explosions have been studied for a long time and much of what is known about the physics of the problem is summarized in a book published by Cole [1] in 1948. These explosions generate a shock wave that propagate through the water at the speed of sound and a large gas bubble that oscillates and migrates towards the free surface. With nearby explosions, a structure will be subjected to both effects and the interaction can be quite complex. As a rule of thumb, if the

S. Abrate (✉)
Department of Mechanical Engineering and Energy Processes, Southern Illinois University, Carbondale, IL 62901-6603, USA
e-mail: abrate@engr.siu.edu

S. Abrate et al. (eds.), *Dynamic Failure of Composite and Sandwich Structures*, Solid Mechanics and Its Applications 192, DOI 10.1007/978-94-007-5329-7_3,
© Springer Science+Business Media Dordrecht 2013

distance between the bubble and the structure is always larger than three times the maximum radius of the bubble, their interaction can be neglected. Then, the structure is subjected to the effect of the shock wave only.

The next section will review some basic knowledge about underwater explosions and empirical equations used to predict the pressure pulse generated at a point given the mass of the explosive charge and the stand-off distance. The same data can be used to predict the size of the explosion bubble, its frequency of oscillation, and how fast it migrates towards the surface. Some charts are presented to show the effects of the governing parameters and show the order of magnitudes of the quantities predicted by these equations. Section 3 introduces the propagation of waves in solids, liquids, and their interfaces. It covers body waves, surface waves such as Rayleigh waves, Scholte-Stoneley waves, Franz waves, and wave propagation in wave guides as described by the Rayleigh-Lamb theory and various beam, plate and shell theories. Section 4 describes the interaction of between shock waves and submerged structures on a short time scale and on a longer time scale. It shows how shock waves can excite waves propagating along the interface with the water, how it can lead to cavitation, and how the wave is transmitted to the inside of a fluid-filled shell.

Many studies present analytical and numerical approaches for predicting the interaction of a shock wave with submerged cylindrical or spherical shells. While these approaches can generate the response at any point in the fluid or on the surface of the shell, previous studies typically presented plots of pressure versus time or transverse velocity versus time at only a few points around the circumference of the shell. It is then difficult to understand the physics of the problem. Recently, some investigators presented results showing the complex interaction between the shock wave and the structure with many wave fronts that travel, change shape, and sometimes exhibit singularities. Obtaining accurate results numerically for the entire domain is a challenging task and the interpretation of those results can be difficult. Section 5 presents a brief overview of the literature and a simple geometrical approach based on ray tracing for predicting the position of all wave fronts at any given time. It is particularly useful in predicting the shape of certain wave fronts as singularities occur on ray caustics. It also provides valuable insight in cases of liquid-filled shells and particularly when the speed of sound inside in different than that in the outside fluid.

Section 6 shows how the approach developed here can be applied to the analysis of two problems in the medical field: (1) Shock Wave Lithotripsy (SWL) a noninvasive procedure for kidney stone removal; (2) Traumatic Brain Injury (TBI) caused by impact and blast loading.

2 Underwater Explosion in an Infinite Domain

Underwater water explosions generate both a shock wave that decays rapidly with time and an oscillating and migrating explosion bubble (Fig. 1). As the charge is detonated, a pressure pulse is generated. The rise time is very short and it decays

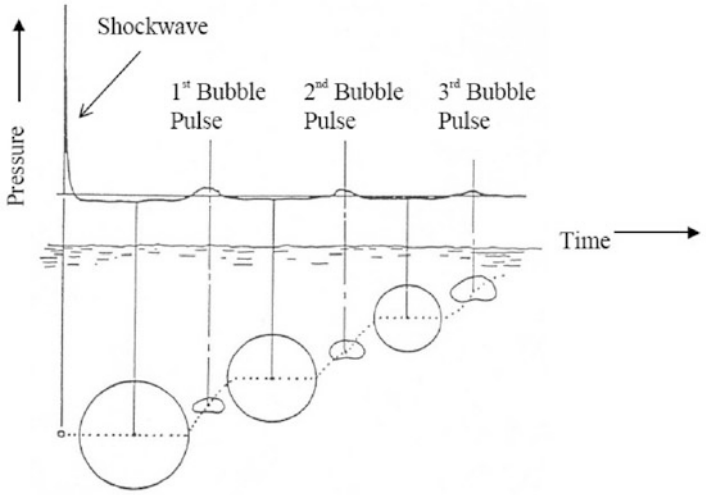


Fig. 1 Shockwave and bubble generated by an underwater blast

rapidly. The pressure wave is called a shock wave because, for high explosives, the pressure raises almost instantly to a maximum pressure at the wave front. This is in contrast with other cases of explosions where the pressure has a finite rise time like the pressure wave generated by the failure of a pressure vessel. This shock wave propagates at the speed of sound over long distances and can cause damage to structural panels but, generally, it does not transfer enough momentum to induce overall deformation of the ship.

Pritchett [2] describes the formation of an explosion bubble for an uncased spherical charge of conventional high explosive such as TNT initiated at the center. As the detonation front expands through the charge, the explosive material it goes through undergoes a chemical reaction and releases energy. The detonation wave speed is typically in the 6,000–7,000 m/s range. As it reaches the surface of the charge and proceeds into the water, the chemical reaction is complete and Y, the total energy released by the explosion, is proportional to the product of Q, the mass of the charge, and q, the energy released per unit mass of the explosive. For TNT, $q = 4.2 \times 10^6$ J/kg. Initially, about half of the energy is contained in the shockwave propagating in the water and the other half is in the gas bubble as kinetic energy and heat. Near the original charge, the nonlinear shock dissipates energy in the water in the form of heat. After the shock wave has travelled 10–15 radii from the origin, this dissipation process is over. Hunter and Gears [3] give a simple rule to estimate the size of the near field where the wave front propagates at speeds that are substantially higher than the acoustic wave propagation. The size of the near field should be twice the maximum radius of the bubble which is approximately 15 times the radius of the charge. Therefore, acoustic wave propagation speed near 1,500 m/s occurs beyond 30 charge radii.

Figure 1 shows the evolution of the pressure in time in which we note a first pulse due to the passage of the shockwave and a series of smaller pulses due to the

periodic collapse of the explosion bubble. This figure also shows that the bubble radius periodically reaches a maximum and shrinks or collapses to a minimum while migrating towards the water surface. The migration appears to stop while the bubble radius reaches a maximum and restart once it starts shrinking again. Explosion bubbles oscillate with very low frequencies and can induce whipping of nearby structures and induce severe damage.

2.1 Scaling of Underwater Explosions

Over the years many experimental studies have been conducted over the years and empirical formulas have been developed to characterize the evolution of the free-field pressure behind the shock wave in terms of the mass of the explosive charge and the stand-off distance. Formulas are also available for prediction the evolution of the explosion bubble. The formulas discussed in this section are called scaling equations or similitude equations.

2.1.1 Scaling of the Shock Wave

Following the arrival of the shock wave, the pressure p at a given point decreases exponentially

$$p(t) = p_o e^{-t/t_o} \tag{1}$$

Analysis of experimental results [4] show that the maximum pressure p_o and the characteristic time t_o depend on the ratio $Q^{1/3}/R$ where Q is the mass of the explosive charge and R is distance R from the explosion (also called the stand-off distance). Following Cole [1],

$$p_o = K_1 \left(\frac{Q^{1/3}}{R}\right)^{A_1}, \quad t_o = K_2 Q^{1/3} \left(\frac{Q^{1/3}}{R}\right)^{A_2} \tag{2}$$

where Q is expressed in kg, R in m, p_o in MPa and t_o in ms. K_1, K_2, A_1, and A_2 are constants obtained from experiments. For trinitrotoluene (TNT), these constants are $K_1 = 52.4$, $A_1 = 1.18$, $K_2 = 0.084$, $A_2 = -0.23$. The experiments of Murata et al. [5] indicate that the pressure in both the initial pressure pulse and the bubble pulse follow Eq. (2). As the stand-off distance increases, the maximum pressure p_o decreases (Fig. 2) and the time t_d increases (Fig. 3). Both p_o and t_d increase when Q, the mass of the charge, increases.

Many other expressions are available for scaling of underwater explosions. The mass of the explosive can be written as $Q = (4/3)\pi\rho_E a^3$ where ρ_E is the density of the explosive and a is the equivalent spherical radius of the charge. Then, the term

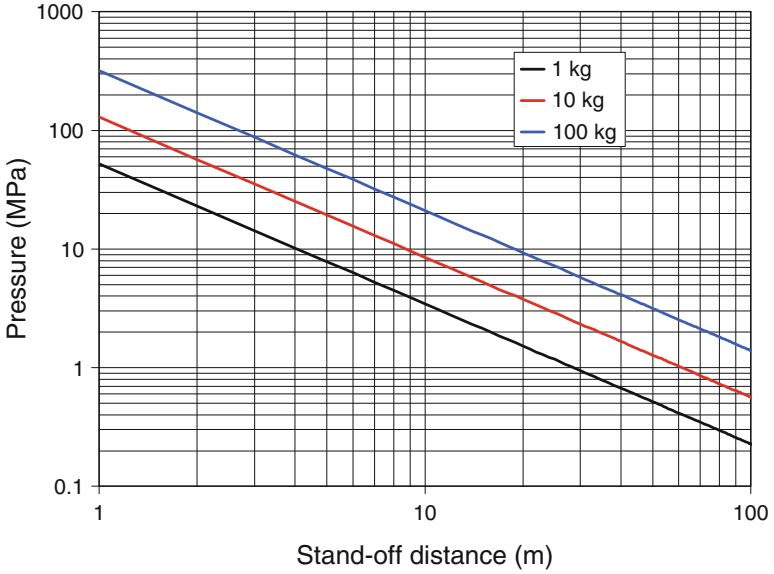


Fig. 2 Maximum pressure during underwater explosion as a function of standoff distance and mass of the charge

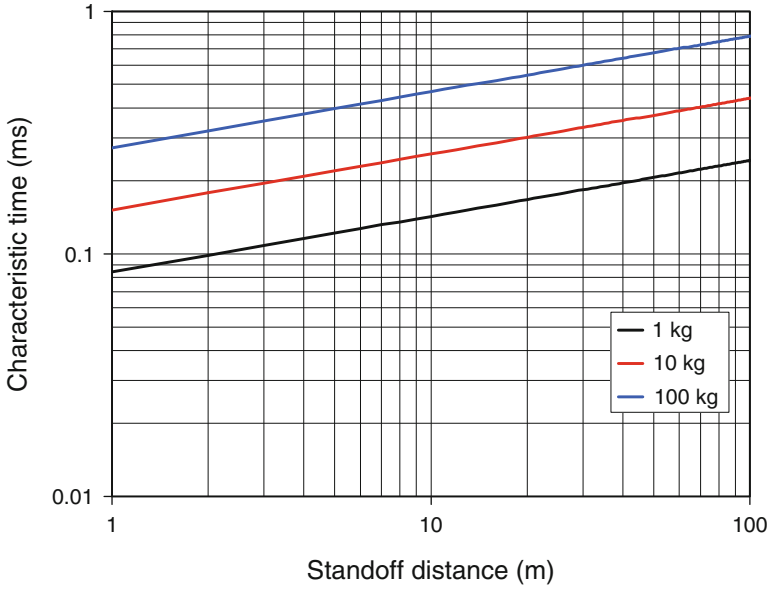


Fig. 3 Characteristic time for underwater explosion as a function of standoff distance and mass of the charge

$Q^{1/3}/R$ in Eq. (2) is proportional to a/R, the ratio of the radius of the charge and the stand-off distance. Some authors write Eq. (2) in terms of a/R. In Refs. [37, 38] Eq. (1) is written as

$$p = P_c\,[a/R]^{1/A}\,f(\tau) \tag{3}$$

in terms $\tau = \nu_c\,(a/R)^B\,t/a$ and four constants P_c, ν_c, A, and B. It can be shown that τ in this expression is equal to t/t_o in Eq. (1). Then, the function $f(\tau)$ is taken to be

$$f(\tau) = e^{-\tau} \qquad \text{when} \quad \tau \le 1 \tag{4}$$

and

$$f(\tau) = 0.8251\,e^{-1.338\,\tau} + 0.1749\,e^{-0.1805\,\tau} \qquad \text{when} \qquad 1 < \tau \le 7 \tag{5}$$

Combining Eqs. (3) and (4), we recover Eq. (1) which is said to be valid until the end of the expansion phase of bubble ($\tau = 1$). Equation (5) covers the oscillation phase of the bubble. Equations. (3, 4 and 5) were used by Kalavalapally et al. [6, 7]. Van der Schaaf [8] found that the pressure varies according to Eqs. (1) and (2) when $t < t_o$ but observed a decay slower than exponential at larger times. The pressure was approximated by

$$p(t) = \begin{cases} p_o e^{-t/t_o} & \text{for} \quad t \le t_o \\ p_o t_o\,/\,(t.e) & \text{for } t_o \le t \le nt_o \\ 0 & \text{for} \quad t > nt_o \end{cases} \quad p_o e^{-t/t_o} \tag{6}$$

with n between 5 and 10.

Empirical Eqs. (1 and 2) are widely used to predict the main characteristics of the shock wave generated by underwater explosions. A few new studies serve as reminders that the expressions are used to fit experimental results and slight improvements are always possible. Figures 1, 2 and 3 give general trends and orders of magnitudes for the maximum pressures and characteristic times.

2.1.2 Scaling of the Explosion Bubble

The bubble consists of high-pressure, high-temperature gases generated by the explosion that initially expands. Because of inertia, the bubble over-expands, the pressure inside the bubble becomes less than that of the surrounding water and it collapses. Similarly, as the bubble shrinks, the pressure inside eventually becomes larger than the pressure outside and the bubble will expand again. This new expansion will generate a new but less severe shock wave. This oscillation cycle repeats several times but decays rapidly. In addition, the bubble tends to move up

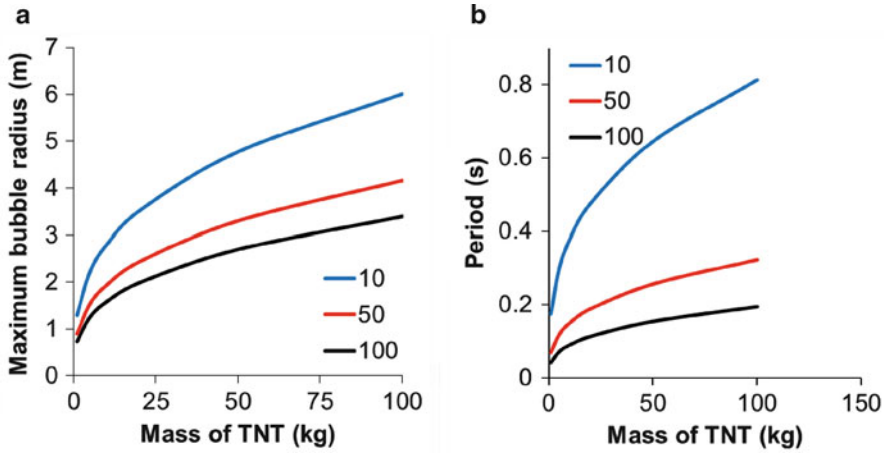


Fig. 4 Oscillating explosion bubble as a function of the explosive charge for three values of the charge depth: 10, 50, 100 m. (**a**) Maximum radius; (**b**) Period of the first bubble oscillation

towards the surface. Bubble pulsations can lead to significant pressure impulses on nearby ship hulls. The maximum bubble radius and the first bubble oscillation period are given by

$$R_{max} = K_3 \ (Q/Z_o)^{1/3} \tag{7}$$

and

$$T = K_4 \ \left(Q^{1/3}/Z_o^{5/6}\right) \tag{8}$$

where $Z_0 = D + 9.8$ is the total static pressure at the location of the explosive, $K_3 = 3.50$ and $K_4 = 2.11$ (Reid [9]). Equation (8) was obtained by curve fitting of experimental results by Arons et al. [10] who examined the periods of the first eight oscillations of the gas bubble. A different constant K_4 was given for each period. Chapman [11] validated Eq. (8) with $Z_0 = D + 10.1$ for $80 < Z < 6{,}700$ m. In several references [12–14] the maximum radius is calculated using (Fig. 4)

$$R_{max} = 3.38 \left(\frac{Q}{D + 10}\right)^{1/3} \tag{9}$$

In the example taken from Vernon [15], with a 227 kg charge of TNT at 45 m, Eq. (2) predicts that $p_o = 4.957$ MPa and $t_o = 0.811$ ms. Equations (7, 8) predict a maximum bubble radius $R_{max} = 5.62$ m and a first oscillation period $T = 0.458$ s while with Eq. (9) the maximum radius is slightly different: $R_{max} = 5.42$ m. The period of the oscillation bubble is in good agreement with Vernon's results. The period of the oscillation bubble (0.458 s) is much larger than the characteristic time of the shock wave (0.811 ms).

Equations (7, 8) give the period and maximum radius of the explosion bubble for its first oscillation. Snay [16] extended these formulas to give the period and maximum radii for all subsequent oscillations. Leybourne [17] suggested that the bubble oscillations period should vary according to

$$T_i = K_4 \left(Q^{1/3}/Z_o^{5/6}\right)/i^{1/2} \tag{10}$$

Pulsation periods are often close to bending frequencies of ships and can cause large amplitude heave and whipping motion. Vernon [15] showed how to determine the far-field acceleration of the fluid, the forces acting on the ship, and the ship's response. When the gas bubble is close to a submarine or a ship hull, this bubble may collapse onto the hull and produce a high speed water jet with water velocities of 130–170 m/s [18].

For TNT, the migration of the gas bubble between the location of the explosive to the location at the time of the first minimum bubble radius is given by [18]

$$m = \frac{12.2}{D + 9.8} Q^{1/2} \tag{11}$$

For 1,000 kg TNT charge at a depth of 60 m, the bubble moves up by 6.24 m during the first bubble oscillation. The ratio between the initial radius R_o and the maximum bubble radius R_m is given empirically by [13]

$$R_o/R_m = 0.0327\, D^{1/3} \tag{12}$$

Relationships between energy, period and maximum radii for two consecutive cycles [19]

$$\frac{E_{n+1}}{E_n} = \left(\frac{T_{n+1}}{T_n}\right)^3 = \left(\frac{R_{m,n+1}}{R_{m,n}}\right)^3 \tag{13}$$

where E is the sum of the potential energy and the kinetic energy of the system. Typically, T_2/T_1 and $R_{m,2}/R_{m,1}$ are approximately equal to 0.70.

2.2 Oscillations of the Explosion Bubble

The period of oscillations can be estimated using a formula attributed to Rayleigh [19, 20] or Willis [21, 22]

$$T = 1.83\, R_{max} \left(\frac{\rho}{p_\infty - p_v}\right)^{1/2} \tag{14}$$

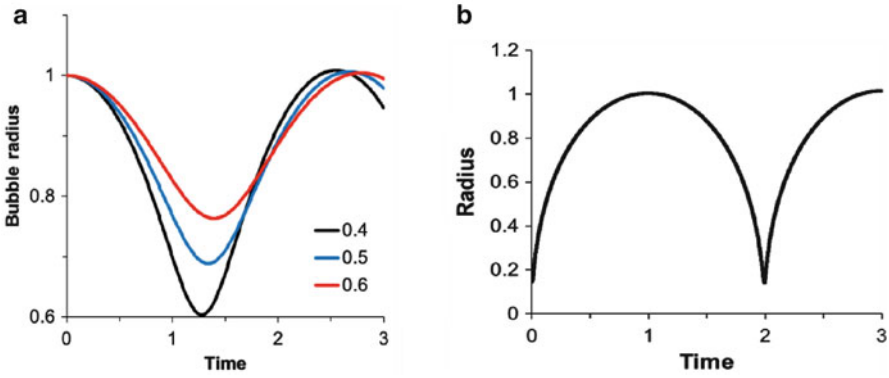


Fig. 5 (**a**) Non-dimensional bubble radius versus non-dimensional time for three values of the parameter ε and $\gamma = 4/3$; (**b**) Oscillations of an explosion bubble with $\varepsilon = 103.36$, $\gamma = 1.25$ and $\xi_0 = 0.1467$

where $p_\infty = p_{ATM} + \rho gh$ is the reference pressure at the hydrostatic depth h far away from the bubble, p_{ATM} is the atmospheric pressure (1 bar), g the acceleration due to gravity and ρ is the fluid density. The vapor pressure p_v is a function of the temperature of the bubble wall only and is assumed to be small ($p_v \sim 2$ kPa at 20°C) and is often neglected [19]. Equation (15) is consistent with Eq. (8) since from Eq. (7), $(Q/Z_0)^{1/3} = R_{max}/K_3$ and after substitution into Eq. (8), $T = \frac{K_4}{K_3}\frac{R_{max}}{Z_o^{1/2}}$. Neglecting p_v, $p_\infty = \rho g Z_0$ and finally, $T = \sqrt{g}\frac{K_4}{K_3} R_{max}(\rho/p_\infty)^{1/2}$. Using the values of K_3 and K_4 given above and $g = 9.81$ m/s^2, gives $\sqrt{g}\, K_4/K_3 = 1.888$.

First derived by Lamb [23] and usually attributed to Rayleigh [20], the Rayleigh-Plesset equation governing the oscillation of spherical bubbles is

$$\ddot{\xi}\xi + 1.5\dot{\xi}^2 - \varepsilon(\xi_o/\xi)^{3\gamma} + 1 = 0 \tag{15}$$

where $\xi = R/R_{max}$ is the dimensionless radius of the bubble and ξ_0 is its initial value. The parameter ε is the ratio between p_b, the initial pressure inside the bubble, and $p_\infty - p_v$. Integrating Eq. (15) numerically for $\gamma = 4/3$ and $\varepsilon = 0.4$, 0.5 and 0.6, the results shown in Fig. 5a show that the radius decreases progressively until it a minimum value is reached at time T/2 and then bounces back. This example taken from Ref. [24], shows the typical behavior for a cavitation bubble for which ε is small. Lee et al. [19] considered an explosion bubble with much higher value of ε. For that case, the results in Fig. 5b indicate that the bubble collapses abruptly at the end of the first cycle. Afanasiev and Grigorieva [24] used the following approximate relation for the minimum non-dimensional radius

$$R'_{min} \approx \frac{3\varepsilon}{1 + 3\varepsilon - \varepsilon^{3/2}} \tag{16}$$

Extensive research on the oscillation of bubbles in a liquid have considered various complicating factors: (1) bubbles are not necessarily spherical and do not remain spherical as they collapse [25–27]; (2) the Rayleigh-Plesset model predicts undamped oscillation of the gas bubble because the surrounding fluid was assumed to be incompressible [28] and, assuming that surrounding water is governed by the wave equation [29] damping of the bubble oscillations was predicted and excellent agreement with experimental results was obtained [28]; (3) with a model accounting for the effects of the pressure inside the bubble, the water depth, and the compressibility of the surrounding fluid [30], the empirical relations for the maximum bubble radius and the bubble collapse time (Eqs. 7 and 8) are recovered.

2.3 Other Types of Explosives

The preceding equations were developed for TNT explosions. For other types of explosives, it is possible to use the same equations after calculating the equivalent TNT charge Q_{TNT} as follows

$$Q_{TNT} = Q_{exp}\, H_{exp}/H_{TNT} \tag{17}$$

where Q_{exp} is the mass of the explosive used, H_{TNT} is the heat of detonation of TNT, and H_{exp} is the heat of detonation of the explosive used [31]. $H_{TNT} = 4.520 \times 10^3$ kJ/kg [32].

3 Wave Propagation in Solids and Fluids

Wave propagation in elastic solids is treated in details in several books [33–36]. Brekhovskikh [37] describes the propagation of waves in layered media. Viktorov [38] focused on Rayleigh and Lamb waves. Lighthill [39] and Whitham [40] discuss waves in fluid and Brekhovskikh and Lysanov [41] cover the more specialized topic of ocean acoustics. This section discusses wave propagation in bulk solids, along the surface of a solid, and along the interface between a solid and a liquid. Finally, some basic results concerning propagation of elastic waves in elastic layers and the connection between elasticity theory and plate theories are presented.

3.1 Wave Propagation in Unbounded Solids

The equations of motion for an elastic solid are

$$\sigma_{ji,\,j} = \rho \ddot{u}_i \tag{18}$$

in terms of the stress components σ_{ij} and the displacement u_i. For an orthotropic material, the stress strain relations can be written as

$$\begin{Bmatrix} \sigma_{11} \\ \sigma_{22} \\ \sigma_{33} \\ \sigma_{23} \\ \sigma_{31} \\ \sigma_{12} \end{Bmatrix} = \begin{bmatrix} C_{11} & C_{12} & C_{13} & 0 & 0 & 0 \\ C_{12} & C_{22} & C_{23} & 0 & 0 & 0 \\ C_{13} & C_{23} & C_{33} & 0 & 0 & 0 \\ 0 & 0 & 0 & C_{44} & 0 & 0 \\ 0 & 0 & 0 & 0 & C_{55} & 0 \\ 0 & 0 & 0 & 0 & 0 & C_{66} \end{bmatrix} \begin{Bmatrix} \varepsilon_{11} \\ \varepsilon_{22} \\ \varepsilon_{33} \\ \varepsilon_{23} \\ \varepsilon_{31} \\ \varepsilon_{12} \end{Bmatrix} \tag{19}$$

in material principal coordinates. The strain–displacement relations are

$$\begin{aligned} &\varepsilon_{11} = u_{1,1}, \quad \varepsilon_{22} = u_{2,2}, \quad \varepsilon_{33} = u_{3,3}, \\ &\varepsilon_{23} = u_{2,3} + u_{3,2}, \quad \varepsilon_{31} = u_{3,1} + u_{1,3}, \quad \varepsilon_{12} = u_{1,2} + u_{2,1} \end{aligned} \tag{20}$$

The material behavior is defined by three elastic moduli (E_1, E_2, and E_3), three shear moduli (G_{12}, G_{13}, and G_{23}), and three Poisson's ratios (ν_{12}, ν_{13}, and ν_{23}). With these nine parameters, the stiffness coefficients are

$$C_{11} = E_1 (1 - \nu_{23}\nu_{32}) / \Delta, \quad C_{22} = E_2 (1 - \nu_{31}\nu_{13}) / \Delta, \quad C_{33} = E_3 (1 - \nu_{12}\nu_{21}) / \Delta$$

$$C_{21} = E_2 (\nu_{12} + \nu_{13}\nu_{32}) / \Delta, \; C_{31} = E_3 (\nu_{13} + \nu_{12}\nu_{23}) / \Delta, \; C_{32} = E_3 (\nu_{23} + \nu_{13}\nu_{21}) / \Delta$$

$$C_{12} = E_1 (\nu_{21} + \nu_{31}\nu_{23}) / \Delta, \; C_{13} = E_1 (\nu_{31} + \nu_{21}\nu_{32}) / \Delta, \; C_{23} = E_2 (\nu_{32} + \nu_{31}\nu_{12}) / \Delta$$

$$C_{44} = G_{23}, \quad C_{55} = G_{13}, \quad C_{44} = G_{12},$$

with $\Delta = 1 - \nu_{12}\nu_{21} - \nu_{23}\nu_{32} - \nu_{31}\nu_{13} - 2\nu_{12}\nu_{23}\nu_{31}$.

3.1.1 Dilatational Waves

First, consider the case where u_1 is the only non-zero displacement and an arbitrary pulse is moving in the x_1-direction with a velocity c_1. Then, u_1 can be written as

$$u_1 = f(x_1 - c_1 t) \tag{21}$$

where f is an arbitrary function. Then, $\varepsilon_{11} \neq 0$, $\varepsilon_{22} = \varepsilon_{33} = \varepsilon_{23} = \varepsilon_{31} = \varepsilon_{12} = 0$, and the first equation of motion (Eq. 18) becomes

$$C_{11}\, u_{1,11} = \rho \ddot{u}_1 \tag{22}$$

which is the one-dimensional wave equation. Substituting Eq. (21) into Eq. (22) gives the wave velocity

$$c_1 = \sqrt{C_{11}/\rho}. \tag{23}$$

Using the same approach, if u_2 is the only non-zero displacement and the wave front is moving in the x_2-direction with a velocity c_2. With $u_2 = f(x_2 - c_2 t)$, ε_{22} is the only non-zero strain component and the second equation of motion becomes

$$C_{22}\, u_{2,22} = \rho \ddot{u}_2 \tag{24}$$

and the velocity of dilatational waves in the x_2-direction is

$$c_2 = \sqrt{C_{22}/\rho} \tag{25}$$

Similarly, if u_3 is the only non-zero displacement and the wave front is moving in the x_3-direction with a velocity c_3. With $u_3 = f(x_3 - c_3 t)$, ε_{33} is the only non-zero strain component and the third equation of motion becomes

$$C_{33}\, u_{3,33} = \rho \ddot{u}_3 \tag{26}$$

and

$$c_3 = \sqrt{C_{33}/\rho} \tag{27}$$

This shows that for orthotropic materials, for dilatational waves propagating in the material principal directions, the equations of motion uncouple and three different wave velocities are obtained (Eqs. 23, 25 and 27). For isotropic materials, the wave velocity is the same in all directions and is given by

$$c = \sqrt{\frac{E(1-\nu)}{\rho(1+\nu)(1-2\nu)}} \tag{28}$$

With this type of body waves where a planar wave front propagates in an unbounded solid, behind the wave front the body is in a state of plane strain. For a thin rod under axial stress, the material is in a state of plane stress and the stress strain relation is Hooke's law ($\sigma = E\varepsilon$). In that case, waves propagate in the axial direction with the velocity

$$c_o = \sqrt{E/\rho} \tag{29}$$

which is sometimes called the rod velocity. For steel, Poisson's ratio is 0.3 so, using the last two equations we find that $c/c_o = 1.160$ which is a significant difference.

3.1.2 Shear Waves

When u_1 is the only non-zero displacement and the wave front is moving in the x_2-direction with a velocity c_4. Then, u_1 can be written as

$$u_1 = f(x_2 - c_4 t) \tag{30}$$

where f is an arbitrary function. Then, $\varepsilon_{12} \neq 0$, $\varepsilon_{11} = \varepsilon_{22} = \varepsilon_{33} = \varepsilon_{23} = \varepsilon_{31} = 0$, and the first equation of motion becomes

$$G_{12}\, u_{1,22} = \rho \ddot{u}_1 \tag{31}$$

which is the one-dimensional wave equation. Writing Eq. (30) as $u_1 = f(\eta)$ where $\eta = x_2 - c_4 t$, we find that $u_{1,22} = f''$ and $\ddot{u}_1 = c_4^2 f''$ where a prime indicates a derivative with respect to η. Substituting into Eq. (31) gives the shear wave velocity $c_4 = \sqrt{G_{12}/\rho}$. Similarly, when u_1 is the only non-zero displacement and the wave front is moving in the x_3-direction with a velocity c_5. Then, u_1 can be written as $u_1 = f(x_3 - c_5 t)$. ε_{31} is the only non-zero strain and substituting into the first equation of motion gives $c_5 = \sqrt{G_{13}/\rho}$. When $u_2 = f(x_3 - c_6 t)$, substituting into the second equation of motion gives $c_6 = \sqrt{G_{23}/\rho}$.

Substituting $u_2 = f(x_1 - c_4 t)$, $u_3 = f(x_1 - c_5 t)$, or $u_3 = f(x_2 - c_6 t)$ into the equations of motion will also give the three shear wave velocities

$$c_4 = \sqrt{G_{12}/\rho},\ c_5 = \sqrt{G_{13}/\rho},\ c_6 = \sqrt{G_{23}/\rho} \tag{32}$$

For an isotropic material the three shear moduli are the same so the three shear wave velocities are the same.

3.2 Surface Waves

The body waves discussed in the previous subsection reflect after reaching a boundary of the solid. There are also several types of waves that propagate along the surface of the body. Here we recall some basic results for three types of surface waves: Rayleigh waves, Scholte-Stoneley waves, and Franz waves. Rayleigh waves are disturbances that propagate along the surface of a solid with amplitudes that decay exponentially with depth. In this section we recall existing results for the c_R, phase velocity of Rayleigh waves, and approximate expressions that show that those waves propagate at speeds that are slightly lower than the phase velocity of bulk shear waves in the solid. At the interface between a liquid and a solid, Rayleigh waves can be excited by an incident wave in the fluid. These waves propagate along the interface with a velocity c_R and radiate back into the fluid. They are called leaky Rayleigh waves.

Stoneley waves are waves that propagate along the interface between two solids with amplitudes that decay exponentially away from the interface. When the interface separates a solid from a fluid these waves are called Scholte-Stoneley waves or simply Scholte waves. Such waves are observed during the interaction of an underwater blast and a structure.

For curved bodies such as spheres and cylinders, the surface of the body is divided into an illuminated region that can be reached by the incident wave and a shadow region. Franz waves (or creeping waves) start from the edges of the illuminated region, propagate into the shadow zone following the curvature of the body and then radiate in a tangential direction. These waves propagate in the fluid at the speed of sound in the fluid.

3.2.1 Rayleigh Waves

In a solid, Rayleigh waves [42] are surface waves in which the motion is localized in a thin layer near the surface with a thickness approximately equal to twice the wavelength of the wave [33]. The horizontal and vertical components of the motion are 90° out of phase and the trajectories of the particles are ellipses with a major axis perpendicular to the surface. The amplitude of these waves decay exponentially with the distance from the free surface and c_R, the speed of Rayleigh waves, is the solution of the equation

$$\left(2-\frac{c_R^2}{c_T^2}\right)^2 = 4\sqrt{1-\frac{c_R^2}{c_T^2}}\sqrt{1-\gamma\frac{c_R^2}{c_T^2}} \tag{33}$$

where $\gamma = \mu/(\lambda+2\mu)$. The phase velocity of Rayleigh waves c_R is slightly lower than the phase velocity of transverse waves (shear waves) c_T and it depends of Poisson's ratio. A good approximation for the phase velocity of Rayleigh waves is given by

$$c_R = c_T \ (0.862 + 1.14\nu)/(1+\nu) \tag{34}$$

used by Jagnoux and Vincent [43], or the following approximations

$$c_R = c_T \ (0.87 + 1.12\,\nu)/(1+\nu) \quad c_R = \left(\frac{0.44+K}{0.58+K}\right)^{1/2} c_T \tag{35-a,b}$$

given by Viktorov [38] and Royer and Clorennec [44] respectively where $K = \nu/(1+\nu)$. Many other such approximations can be found in the literature [e.g. 45–58].

When the solid surface is in contact with a fluid, the Rayleigh wave propagating along the surface of the interface induces waves in the fluid. In this case, the wave is called a leaky Rayleigh wave or a generalized Rayleigh wave. The motion of

particles near the interface is elliptical in both the fluid and the solid. Leaky Rayleigh waves are used for ultrasonic imaging of surface defects in materials [43]. They also are observed during the diffraction of a shock wave by an elastic solid.

Considering a solid immersed in water, a wave propagating in the water at a speed $c_1 = 1{,}498$ m/s at an incident angle i_1 will generate two waves in the solid with phase velocities c_2 and c_3 and their respective angles i_2 and i_3. In addition, for the proper value of i_1, Rayleigh waves will propagate along the surface ($i_R = 90°$) with a velocity c_R. According to Snell's law,

$$\frac{\sin i_1}{\sin i_k} = \frac{c_1}{c_k} \tag{36}$$

where $k = 2,3$ for bulk waves and $k = R$ for Rayleigh waves. For steel $E = 210$ GPa, $\rho = 7{,}850$ kg/m^3 so $c_2 = 3{,}208$ m/s for shear waves and $c_3 = 5{,}172$ m/s for longitudinal waves. Using Eq. (34), for a Poisson's ratio of 0.3, the velocity of Rayleigh waves is $c_R = 0.9262\, c_2 = 2{,}971$ m/s compared to 2,990 m/s in [43]. Equation (36) indicates that $i_2 = 90°$ when $\sin i_1 = c_1/c_R$ or $i_1 = 30.3°$. The incident wave in the fluid excites Rayleigh waves for an incident angle of $\theta_R = 30°$.

The amplitude of leaky Rayleigh waves decays rapidly with the distance travelled along the solid-water interface because of energy radiation into the liquid. This is in contrast with the propagation of Rayleigh waves on the surface of a solid in air where no such attenuation takes place.

Neuenschwander et al. [59] showed that the phase velocity of leaky Rayleigh waves should be between that of the Rayleigh wave in air and that of the transverse wave in the solid $c_R \leq c_{LR} \leq c_T$. The experiments of Goodman, Bunney and Marshall [60] showed that when an acoustic beam reaches the surface of a cylinder at an angle θ_R, leaky Rayleigh surface waves are generated, as in the case of a plate, and the amplitude of the portion of that wave radiated in the fluid is maximum when the receptor is located at an angle θ_R from the radial direction. The measured velocity of θ_R the Rayleigh wave was 3,280 m/s for a solid aluminum cylinder in water and the measured θ_R angle 28°.

Formulas such as (33, 34, 35-a,b) for calculating the velocity of Rayleigh waves were derived assuming that the surface of the solid was flat. Several authors examined how the curvature of the surface of a cylinder affected the speed of Rayleigh waves. According to Szilard [61], on circular cylinders, Rayleigh waves propagate in the circumferential direction with a velocity

$$c = c_R \left(1 + \frac{\lambda}{2\pi R}\right) \tag{37}$$

where c_R is the velocity on a flat surface, λ is the wavelength and R is the radius of the cylinder. The analysis of Jin, Wang and Kishimoto [62] indicated that

$$c = c_R \left(1 + 0.4822\, \frac{\lambda}{2\pi R}\right) \quad c = c_R \left(1 - 1.1429 \frac{\lambda}{2\pi R}\right) \tag{38-a,b}$$

in the circumferential and axial directions respectively. These three formulas show that the effect of curvature become negligible when the wavelength is short compare to the radius of curvature.

Experiments conducted by Bunney et al. [63] showed that as a solid cylinder is progressively made hollow, the circumferential acoustic waves that can be excited change from having characteristics of Rayleigh waves to having the characteristics of Lamb waves. It is also possible to excite both Rayleigh- and Lamb-type waves [64–68].

3.2.2 Scholte-Stoneley Waves

Disturbances propagate near a free surface (Rayleigh waves) but also near the interface between two half-spaces. Stoneley [69] pointed out the existence of a wave propagating along the interface between two elastic solids. In this case, the amplitudes decrease with x_2 away from the interface $x_2 = 0$. The geophysicist Scholte [70] described a particular case of the Stoneley wave when one of the solid becomes a fluid. This wave, called the Scholte-Stoneley wave, has its energy mainly localized in the fluid and, if the viscosity of the media is negligible, it propagates without attenuation [71]. The wave is of maximum intensity at the interface and decreases exponentially away from the interface into both the fluid and the solid medium. Near the interface, particles move on elliptical trajectories. In the solid, the major axis of the ellipses are perpendicular to the interface while in the water they are parallel to the interface.

Considering a fluid–solid interface where the fluid being located above the interface and the solid below the interface ($x_2 < 0$), the phase velocity of the Stoneley wave is determined from the algebraic equation [72]

$$\left(\frac{\rho_1}{\rho_2} b_{2L} + b_1\right) r^4 - 4 b_1 r^2 - 4\, b_1\, (b_{2L} b_{2T} - 1) = 0 \tag{39}$$

where

$r = c_s/c_{2T}$, $b_1 = \left(1 - \frac{c_s^2}{c_1^2}\right)^{1/2}$, $b_{2L} = \left(1 - \frac{c_s^2}{c_{2L}^2}\right)^{1/2}$ and $b_{2T} = \left(1 - \frac{c_s^2}{c_{2T}^2}\right)^{1/2}$. c_s is the phase velocity of the Stoneley wave, c_1 is the speed of sound in the fluid, c_{2L} and c_{2T} are the phase velocities of longitudinal and transverse waves in the solid. Meegan et al. [73] indicate that for several common examples of water-solid examples, the velocity of Scholte waves are only slightly lower than the speed of sound in water except for the sandstone-water example. The maximum phase velocity of the Scholte-Stoneley wave is approximated by

$$c_s = (1 - \varepsilon)\, c_f \tag{40}$$

where c_f is the speed of sound in the fluid and ε is a given by

$$\varepsilon = \frac{1}{8}\left(\frac{\rho_f}{\rho} \frac{c_f^2\, c_L^2}{c_T^2\, \left(c_L^2 - c_T^2\right)}\right)^2 \tag{41}$$

in terms of ρ_f, the density of the fluid, ρ, the density of the solid, and the longitudinal and transverse wave velocities in the solid c_L and c_T [71]. Therefore, Scholte-Stoneley wave the maximum speed of is usually slightly lower than the speed of sound in the fluid.

Experiments [74] showed that, at a water-glass interface, the Rayleigh wave is strongly attenuated while the Scholte wave (theoretically undamped) is weakly attenuated. The phase velocities were 3,091 m/s for the leaky Rayleigh wave and 1,488 m/s for the Scholte wave. The phase velocities for bulk waves in the glass were $c_L = 5{,}712$ m/s and $c_T = 3{,}356$ m/s. Surface waves at a plexiglass-water interface were also studied. In that example, the density of plexiglass is 1,190 kg/m^3, $c_L = 2{,}692$ m/s, $c_T = 1{,}407$ m/s and the predicted velocity of the Scholte wave is $c_S = 1{,}067$ m/s while the speed of sound in water is 1,500 m/s. This configuration is called a soft solid–fluid configuration because $c_T < c_W$. In this case, a bulk wave with a wave speed of 1,407 m/s was observed during experiments but no Rayleigh wave was detected. This is attributed to the fact that the acoustic velocity of water is larger than the transverse velocity of Plexiglass. When the same plexiglass is immersed in pure ethanol with a density of 790 kg/m^3 and an acoustic velocity of 1,115 m/s, a leaky Rayleigh wave with a phase velocity of 1,377 m/s was observed along with a Scholte wave with a velocity of 1,011 m/s. Weng and Yew [75] showed that underwater explosions generate Scholte-Stoneley surface waves at the interface between the water and an ice cover.

A review of the acoustics of shells [76] discusses the dispersion curves for Lamb waves on free plates and for fluid-loaded plates. For plates with one-sided water loading, a Scholte-Stoneley wave called the A wave appears. It is due to the fluid loading and is largely water-borne. When the plate is loaded with one fluid on one side and a different fluid on the other side, there are two Scholte-Stoneley waves [77].

Experimental results from short-pulse of scattering of water-immersed thin-walled cylindrical shells filled with air, water or alcohol [78] provide evidence of the existence of two Scholte-Stoneley waves for double fluid loading. Since the speed of sound is 1,480 m/s in water and 1,200 m/s in alcohol, the two Scholte-Stoneley waves could be clearly distinguished in the back scattering signals. Bao, Raju, and Uberall [79] also studied a submerged cylindrical shell with a different fluid inside.

Uberall et al. [66] presented an overview of the dispersion curves for Lamb waves and Scholte-Stoneley waves on thin, water-loaded and evacuated shells made of aluminum, stainless steel and tungsten carbide. Kim and Ih [80] determined the dispersion curves for the Scholte-Stoneley and Lamb waves of boron-aluminum composite shells immersed in water analytically and experimentally. Maze and co-workers [81, 82] studied the propagation of Scholte-Stoneley waves on submerged cylindrical shells.

3.2.3 Franz Waves

Franz [83] first showed that the scattering of waves by a cylinder immersed in water consist of a specular reflection and two waves with velocities lower that the

free-wave velocity in water that circumnavigate the cylinder one in the clockwise and one in the counterclockwise direction (Bunney, Goodman and Marshall [63]). The first experimental evidence of those waves that Franz called creeping waves was provided by Barnard and McKinney [84]. In the experiments conducted by Neubaeur [85, 86], the speed of creeping waves around a cylinder submerged in water was 99% of the speed of sound in water.

Ahyi et al. [87] first presented shadowgraphs of the interaction of an incident wave with a cylinder submerged in water. Figures clearly show the incident wave, the specularly reflected wave, the creeping wave and both symmetric and anti-symmetric Lamb waves. Further experimental visualization results for creeping waves were provided by Latard et al. [88] for scattering by a glass sphere. Neubauer [89] presented experimental results and graphical methods for determining the shape of the reflected wave front, the creeping wave front and the wavefront produced by leaky Rayleigh waves during the diffraction of acoustic waves by an elastic cylinder. When the incident ray becomes tangent to the cylinder, a creeping wave is generated that travel in part around the circumference of the cylinder and then radiate into the water in the tangential direction. Keeping a constant travel time, the tip of the vector representing the final radiation into the water generates the wave front for the creeping wave.

Theoretical analyses of creeping wave were conducted by Überall, Doolittle, and McNicholas [90], Ugincius [91] and Ugincius and Uberall [92].

3.3 Lamb Waves

In an infinite elastic layer in which the top and bottom surface are stress free, two families of waves results from the combination of dilatational and shear waves reflecting from the free surfaces and Rayleigh waves propagating along these surfaces. These waves are usually called Rayleigh-Lamb waves or Lamb waves and for long wavelengths the lowest modes correspond to extensional or bending waves predicted by plate theories.

Wave propagation in isotropic solids can be studied in a more general way starting with the equations of motion (Eq. 18), the stress–strain relations

$$\sigma_{ij} = \lambda\, \varepsilon_{kk}\, \delta_{ij} + 2\mu\varepsilon_{ij} \tag{42}$$

where λ and μ are the two Lame constants of the material, and the strain–displacement relations

$$\varepsilon_{ij} = \left(u_{i,j} + u_{j,i}\right)/2 \tag{43}$$

Using Helmholtz's representation, the displacements can be written in terms of a scalar potential ϕ and a vector potential $\bar{\psi}$ so that

$$\bar{u} = \overline{\nabla\phi} + \bar{\nabla}\, x\, \bar{\psi} \tag{44}$$

so that the three components of the displacement vector are

$$u_1 = \frac{\partial \phi}{\partial x_1} + \frac{\partial \psi_3}{\partial x_2} - \frac{\partial \psi_2}{\partial x_3}$$

$$u_2 = \frac{\partial \phi}{\partial x_2} + \frac{\partial \psi_1}{\partial x_3} - \frac{\partial \psi_3}{\partial x_1}$$

$$u_3 = \frac{\partial \phi}{\partial x_3} + \frac{\partial \psi_2}{\partial x_1} - \frac{\partial \psi_1}{\partial x_2} \tag{45}$$

Substituting into the equations of motion gives

$$(\lambda + 2\mu)\ \nabla^2 \phi - \rho \ddot{\phi} = 0 \tag{46}$$

$$\mu \nabla^2 \bar{\psi} - \rho \ddot{\bar{\psi}} = 0 \tag{47}$$

These two equations are satisfied when the phase velocities for the longitudinal and transverse waves are

$$c_L = \sqrt{(\lambda + \mu)/\rho} \quad \text{and} \quad c_T = \sqrt{\mu/\rho} \tag{48}$$

These are the same velocities obtained in Sect. 3.1.

Lamb [64] studied the propagation of harmonic waves in isotropic layers. When the motion is restricted to the x_1-x_2 plane, Eq. (47) become

$$\frac{\partial^2 \phi}{\partial x_1^2} + \frac{\partial^2 \phi}{\partial x_2^2} = \frac{1}{c_L^2} \frac{\partial^2 \phi}{\partial t^2} \quad \frac{\partial^2 \psi}{\partial x_1^2} + \frac{\partial^2 \psi}{\partial x_2^2} = \frac{1}{c_T^2} \frac{\partial^2 \psi}{\partial t^2} \tag{49}$$

For harmonic waves of the form

$$\phi = \Phi(x_2)\ \exp[i(kx_1 - \omega t)]\ \psi = \Psi(x_2)\ \exp[i(kx_1 - \omega t)] \tag{50}$$

there are two types of modes: (1) symmetric modes for which $\Phi = A_2 \cos(px_2)$ and $\Psi = B_1 \sin(qx_2)$; (2) anti-symmetric modes for which $\Phi = A_1 \sin(px_2)$ and $\Psi = B_2 \cos(qx_2)$ where $p^2 = \frac{\omega^2}{c_L^2} - k^2$ and $q^2 = \frac{\omega^2}{c_T^2} - k^2$. Relationships between the frequency ω and the wave number k are obtained by considering the boundary conditions on the top and bottom surfaces ($x_2 = \pm h$): $\sigma_{22} = \sigma_{12} \equiv 0$ which give

$$\frac{\tan(qh)}{\tan(ph)} = -\frac{4k^2 pq}{\left(q^2 - k^2\right)^2} \text{ and } \frac{\tan(qh)}{\tan(ph)} = -\frac{\left(q^2 - k^2\right)^2}{4k^2 pq} \tag{51}$$

for the symmetric and anti-symmetric modes respectively. These equations are known as the Rayleigh-Lamb equations. In the literature, the symmetric modes are

designated as S_o, S_1, S_2, ... in order of increasing frequency. The anti-symmetric modes are designated as A_o, A_1, A_2, ... For long wavelengths ($k \to 0$) the first symmetric mode (S_o) called the "extensional mode" travels at the "plate velocity". In this regime the plate stretches in the direction of propagation and contracts correspondingly in the thickness direction. At higher frequencies, the phase velocity converge towards the Rayleigh wave velocity. The first axisymmetric mode (A_o) called the "flexural mode".

Osborne and Hart [65] obtained the dispersion curves of a steel plate in contact with water, an extension of Lamb's work for plates in air. The dispersion relations for cylindrical shells in air and in water were determined analytically and experimentally by Uberall et al. [66, 67]. Experimentally determined dispersion curves for A_o modes are given by Cheeke et al. [68].

4 Interactions Between Shock Waves and Submerged Structures

This section discusses two important points in our geometrical acoustics approach to the study of shock wave interactions with submerged structures. First we examine how underwater shock waves generate other types of waves as they interact with the shell and the fluid inside. A basic approach is presented for generating the position of the various wave fronts. Then we examine the evolution of the pressure on both faces of a plate loaded by an underwater shock wave. This example brings out significant differences in the response between two important practical cases in which the back face is contact with air or in contact with water. It is shown that for water-backed plates, the incident pulse appears to propagate through as if the plate was not there. This apparent transparency property is used in Sect. 5 to analyze shock wave interactions with cylindrical shells.

4.1 Initial Response of a Plate to a Shock Wave

This subsection discusses how underwater blasts excite surface waves and Lamb waves in submerged plates and shells. Previous studies providing direct experimental evidence of this phenomenon are reviewed and an example is given to illustrate how a simple geometrical approach can be used to predict the position of the various wave fronts as a function of time. Only a few studies are dealing with close-in explosions. An overview of the current state of knowledge is presented here.

4.1.1 Shock Wave Generates a Rayleigh Wave on the Surface of a Thick Plate

The propagation of leaky Rayleigh waves and Scholte waves at the interface of a liquid and an elastic solid has been studied extensively because of potential applications. Scholte waves are used to determine the properties of marine sediments down to hundreds of meters below the seafloor [93, 94], to detect objects buried in the seabed [95], to measure the thickness thin gold layer deposited on a silicon wafer [96], to size inaccessible parts of industrial structures [97] for example. Leaky Rayleigh waves are used extensively in non-destructive testing [98].

Interface waves can be excited by explosions or transient forces applied on the interface [99–101] or by implosions [102]. In the following example, surface waves at the interface between a thick glass plate and water are excited by a cylindrical wave generated by a transducer. In the experiments of Fu et al. [103], a cylindrical wave is emitted from a source S located in water domain in the upper half of the plane and glass occupies the lower half-space. The speed of sound in the water is taken to be 1,480 m/s. For glass, the density is 2,530 kg/m^3, the phase velocity of longitudinal waves is 5,690 m/s, the phase velocity of transverse waves is 3,460 m/s and the Rayleigh wave velocity is 3,180 m/s. The source is located 10 mm above the glass-water interface and the position of the various wave fronts after 12.5 μs is shown in Fig. 6. The incident wave is a circle of radius 18.5 mm centered at S. The reflected wave R is a circle centered at a point S′ symmetrically located below that interface. Figure 6 shows that, as the incident wave reaches the solid surface, a new wave front H called the head wave is created. In this example, the plate is quite thick so bending deformations are not induced. However, Rayleigh surface waves propagate along the interface and radiate back into the water. In a solid, Rayleigh waves are surface waves in which the motion is localized in a thin layer near the surface with a thickness approximately equal to twice the wavelength of the wave. The amplitude of Rayleigh waves decays exponentially with the distance from the free surface. A good approximation for the phase velocity of Rayleigh waves is

$$c_R = c_T \, (0.862 + 1.14\nu) \, /(1 + \nu) \tag{52}$$

where, for an isotropic solid, $c_T = \sqrt{G/\rho}$ is the phase velocity of shear waves in terms of the shear modulus G and the density ρ. When $\nu = 0.3$, $c_R = 0.926\, c_T$.

For the example in Fig. 6, a Rayleigh wave will be excited when the incident angle θ_i is such that the transmitted angle $\theta_t = 90°$ so that the reflected wave propagates along the interface. Using Snell's law,

$$\sin\theta_i \,/\, \sin\theta_t = c_f \,/\, c_R \tag{53}$$

we find that this angle is 27.74°. The solid-borne Rayleigh wave propagates along the interface at a speed c_R and then radiates back into the water at a 27.74° angle from the vertical to form what is called a head wave with a straight wave front at a 27.74° angle from the interface (Fig. 6).

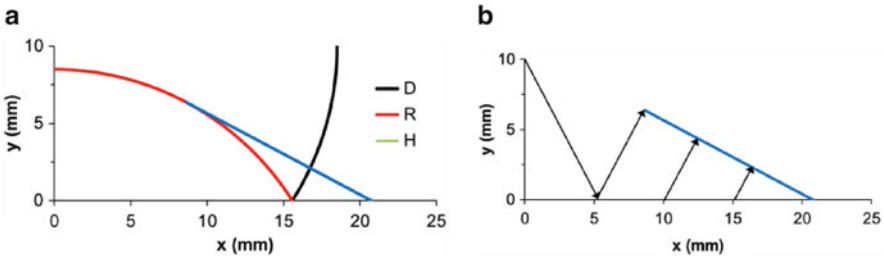


Fig. 6 Interaction of a shock wave generated by a transducer located at (0, 10) with a thick glass plate ($y < 0$). (**a**) Direct wave D, reflected wave R and a head wave H; (**b**) Rayleigh waves generated by an incided wave making a 27.74° with the vertical, travels along the interface ($y = 0$) and radiates back into the water ($y > 0$) at an angle of 27.74°

In this type of problem it the elastic solid is called soft if its shear wave velocity is smaller than the speed of sound in the liquid. Such a "soft solid–fluid" interface is found in the case of Plexiglas–water and PVC–water interfaces [74] and soft sea floors [101]. On the other hand, a "hard solid–fluid" configuration refers to a case in which speed of sound in the fluid is smaller than the shear velocity of the solid material as in the case of a glass-water interface. Theoretical and experimental investigations [74, 99–101] established that leaky Rayleigh waves do not propagate along a soft solid- fluid interface and in that case only a Scholte-Stonely surface wave propagates along the interface. Data from the propagation of Scholte waves is used to characterize the properties of sediments.

Alkier [104] showed that, at a critical incidence angle, an acoustic pulse can excite internally guided longitudinal stress waves in a submerged plate. In the case of an aluminum plate with a longitudinal wave velocity $c_L = 5.45 \times 103$ m/s immersed in water with water with $c_w = 1{,}484$ m/s, the critical angle obtained from Snell's law is $\theta_c = \sin^{-1}(c_w/c_L)$ or $\theta_c = 15.79°$ in this case.

4.1.2 Shock Waves Excite Lamb Waves in a Thin Plate

Leaky Lamb waves are used extensively in non-destructive evaluation [98]. There are other uses of this type of waves. For example, Bingham et al. [105] describe an approach using the propagation of Lamb waves to detect the presence of limpet mines on ship hulls. Ahyi et al. [87] presented experimental results for 1 mm thick steel plates in water subjected to a shock wave. In that case, both symmetric and anti-symmetric Lamb waves are excited and radiate back into the water. Ahyi et al. also considered 1 mm thick steel plates with water on both sides. Then, on the opposite side of the plate there is a wave front for the transmitted wave that is the mirror image of the reflected front R in Fig. 6 and the wave fronts corresponding to Lamb waves propagating along the plate.

4.1.3 Close-in Explosion

Wardlaw and Luton [106] described the fluid–structure interactions occurring when a charge explodes near a plate. Numerical analyses of close-in explosions near rigid surfaces, homogeneous plates, and sandwich plates are discussed in [107–110]. Similar studies for explosions inside water filled cylinders are presented in [106, 109, 111]. In all of these studies the explosion is modeled as a small initial cavity subjected to a given pressure. The initial shock wave propagates towards the structure, reflects, and interacts with the cavity. During the short duration of these simulations, the cavity representing the explosion bubble deforms very little due to the low frequency of the bubble oscillations

4.2 Long Term Response of a Plate to an Underwater Explosion

Here four related examples are considered in order to gain some insight into the dynamic response of plates subjected to impulsive loading. First we consider a plate subjected to a pressure pulse applied directly on the surface. When the time is much larger than the travel time through the thickness of the plate, the plate can be assumed to be rigid. In the second example, a semi-infinite solid is in contact with water and the loading consists of a pressure pulse propagating through the water. The pressure at the interface is the sum of the incident and reflected pulses and depends on the mechanical impedances of the water and the solid. In the third example, the semi-infinite solid is replaced by a plate of finite thickness in contact with air on the other side. In the fourth example, the plate is in contact with water on both sides.

4.2.1 Free Plate Subjected to a Pressure Pulse

Considering an infinite plate of thickness subjected to a step pressure on the left and free on the right, the Lagrange diagram of Fig. 7a shows the reflections of elastic waves from the two surfaces. In that figure the non-dimensional time $\bar{t} = t\,c/h$ is plotted versus the non-dimensional position $\bar{x} = x/h$ where h is the thickness of the plate, and c is the speed of sound in the material. Using the method of characteristics, we find that the particle velocity on the right face increases in a stair-case manner (Fig. 7b). The non-dimensional velocity is defined as $\bar{v} = v.\,\rho c/p_o$ where ρ is the density of the material and p_o is the suddenly applied pressure. If the plate is considered as a rigid body, the velocity of the plate is directly proportional to time ($\bar{v} = \bar{t}$) and the figure shows that the rigid body approximation is adequate for times much larger that h/c, the travel time through the thickness.

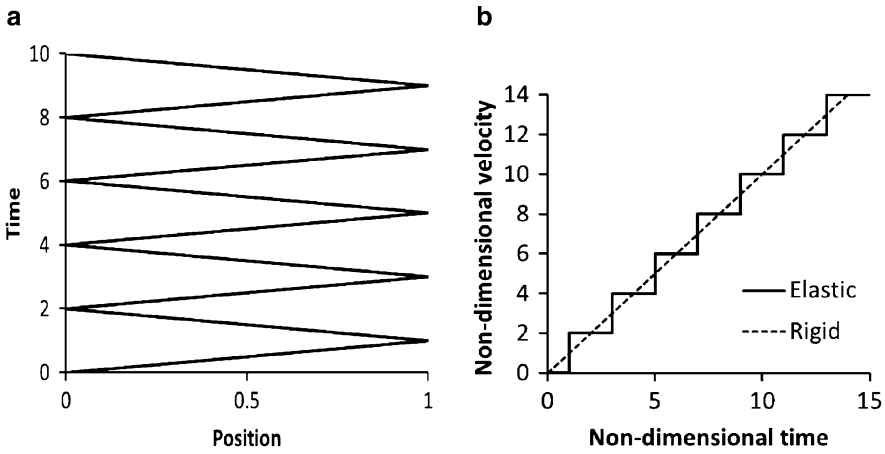


Fig. 7 Short term response of a plate subjected to step pressure pulse (**a**: Lagrange diagram; **b**: non-dimensional plate velocity versus time)

Considering the plate as a rigid body with a density ρ, a thickness h, and a surface area A that is completely free and subjected to a pressure pulse p(t) applied directly to its front face. V is the velocity at the end of the pulse, ρhA V is the linear momentum at the end of the pulse, and $I = \int p\, dt$ is the pressure impulse (per unit area). The impulse-momentum relation states that the momentum at the end of the impulse is equal to the applied impulse. Therefore, the velocity is

$$V = I / \rho h \tag{54}$$

When the plate is subjected to a step pressure, the impulse increases linearly with time. Equation (54) predicts that the velocity V also increases linearly with time as indicated by the dashed line in Fig. 7b. The rigid body approximation is adequate for times much larger that h/c, the travel time through the thickness. The kinetic energy of the plate is

$$T = \frac{1}{2}\rho h V^2 = \frac{1}{2}\rho h\left(\frac{I}{\rho h}\right)^2 = \frac{1}{2}\frac{I^2}{\rho h} \tag{55}$$

This equation indicates that the kinetic energy absorbed by the plate increases with the square of the impulse and is inversely proportional to the mass per unit area. For a given impulse, a heavy plate absorbs less kinetic energy than a light plate.

Fleck and Deshpande [112] describe the response of metallic sandwich structures to blast loading into three phases: in Phase I the applied impulse results in a uniform velocity of the first facesheet, Phase II corresponds to the crushing of the core material and phase III overall bending and stretching deformations of beam occurs.

Given the magnitude of the impulse I, Eq. (54) was used to determine the velocity of the front facesheet at the end of phase I [112]. Equation (55) is used without derivation by Pan and Watson [113]. It shows that the kinetic energy absorbed is proportional to the square of the impulse and inversely proportional to the mass per unit area. Therefore, for a given impulse, a heavier plate absorbs less kinetic energy than a lighter plate. We also note that the impulse is the quantity of interest regardless of the shape of the pressure versus time curve.

4.2.2 Wave Interaction at the Interface Between Water and a Solid

Underwater blasts generate shock waves that propagate through water before reaching the surface of a solid structure and reflecting off of that surface. The pressure at the water-solid interface is shown to be different from that of the incident pulse.

Figure 8a shows the one-dimensional problem of a pulse impinging on a water-solid interface with a normal incidence. The Lagrange diagram (Fig. 8b) shows the time-position domain is divided into three regions. Initially both the water domain ($x < 0$) and the solid ($x > 0$) are a rest (region O in the figure). Region I is the incident pulse and after the pulse reaches the interface the water and the solid have the same stress T (positive in compression) and particle velocity v (Region II). From the stress-velocity diagram (Fig. 8c) it can be easily shown that

$$T_2 = \frac{2z_s}{z_s + z_w} T_1 \tag{56}$$

where T_1 is the stress in region I, T_2 is the stress in region II, z denotes the mechanical impedance and the subscripts s and w refer to the impedance of the solid and the water respectively.

The speed of sound in water is approximately 1,500 m/s and the density 1,000 kg/m^3 so its mechanical impedance $z_w = 1.5 \times 10^6$ kg/m^2/s. For steel, with a modulus of elasticity of 210 GPa, a Poisson's ratio of 0.3 and a density of 7,850 kg/m^3, Eq. (28) predicts a speed of sound of 6,001 m/s. The mechanical impedance of steel $z_s = 47.11 \times 10^6$ kg/m^2/s is much larger than that of water and the ratio T_2/T_1 predicted by Eq. (56) is 1.938 which is very close to 2. Therefore, it is often said that upon reflection from a steel surface the pressure suddenly doubles as if that surface were rigid. Considering a typical composite material with a transverse modulus of 10.30 GPa and a density of 1,500 kg/m^3, the speed of sound is approximately 2,620 m/s, $z_s = 3.931 \times 10^6$ kg/m^2/s and from Eq. (56) we find that $T_2/T_1 = 1.448$. Therefore, the mechanical impedance of the composite material is closer to that of the water a much different behavior occurs: the pressure does not double as the wave reflects from the surface.

Considering a 5 mm thick steel plate in contact with air on the right hand side, the response to a step pressure wave is such that the pressure on the wet side decays

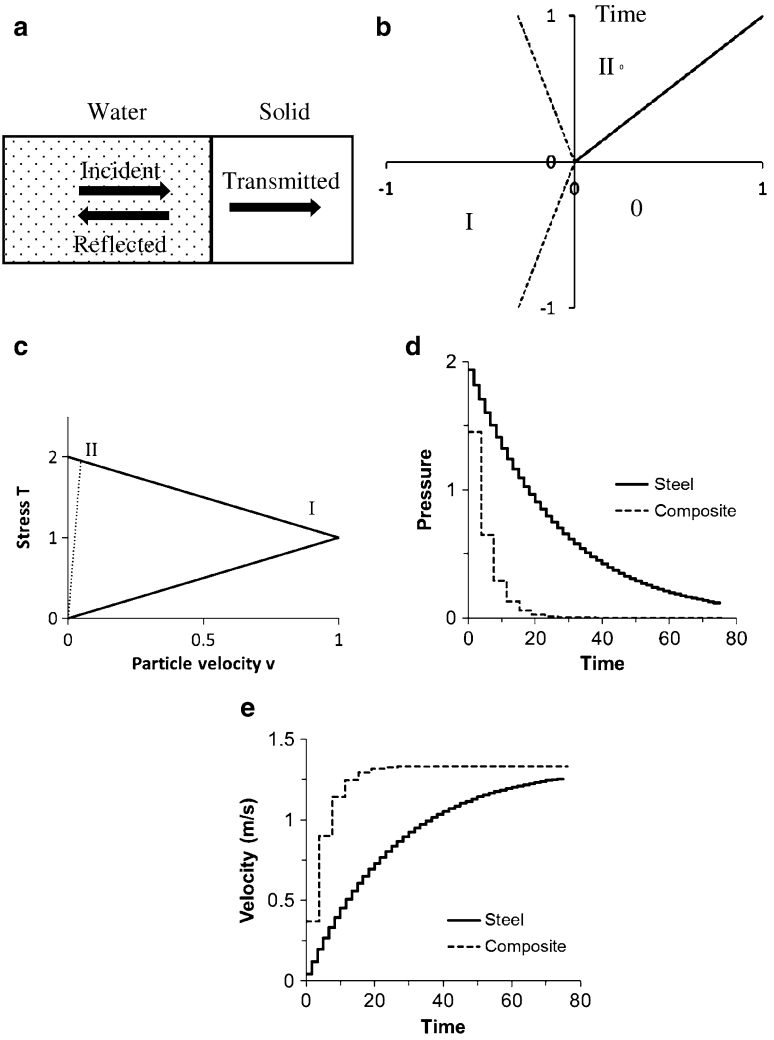


Fig. 8 Reflection and transmission of an incident wave at a fluid–solid interface. (**a**) Reflected and transmitted waves at a water-solid interface; (**b**) Lagrange diagram showing the incident wave in the fluid being reflected from the interface $x = 0$ and the transmitted wave in the solid ($y > 0$); (**c**) Stress velocity diagram where the slope of the *solid lines* is the impedance of water and the slope of the *dashed line* is the impedance of the solid; (**d**) Interface pressure (MPa) versus time (μs) for 5 mm thick air backed plates made out of steel or composite materials; (**e**) Interface velocity versus time (μs) for 5 mm thick air backed plates made out of steel or composite material

progressively to zero (Fig. 8d) and the velocity of that face increases progressively towards an asymptotic limit (Fig. 8e). The small steps in those curves are due to wave reflections inside the plate. For a 5 mm thick composite plate, the response is quite different as shown on these figures. Both the pressure and the velocity change

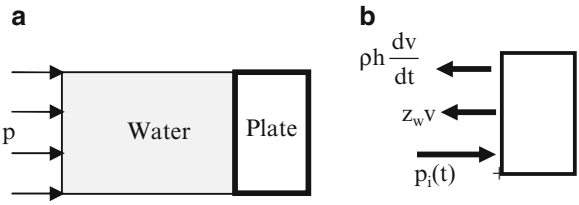


Fig. 9 One dimensional model of an air-backed plate (ABP) subjected to an incident pressure pulse (**a**: general configuration, **b**: Free body diagram of the plate)

more rapidly in a few large steps. These examples show that the response to an incident pulse transmitted through water is different than when the pressure pulse is applied directly to the plate. The response of a composite plate is significantly different because its mechanical impedance is much lower than that of steel.

4.2.3 Dynamic Response of an Air-Backed Plate to a Shock Wave

Now consider an exponentially decaying pulse $\left(p_i = p_o\, e^{-t/t_d}\right)$ propagating towards an air-backed plate (Fig. 9). Considering a unit area of the plate as a rigid body, two external forces are applied: one is caused by the incident and reflected waves $(p_i + p_r)$ and the other is due to the motion of the plate $(z_w v)$. The inertia force is equal to ρh, the mass per unit area, times the acceleration dv/dt. As discussed above, $p_r = p_i\,(2z_s)/(z_s + z_w)$ and, if the impedance of the solid is much larger than that of water, $p_r \approx p_i$.

Applying Newton's law, gives the equation of motion originally derived by Taylor [114] in 1941

$$\rho h \frac{dv}{dt} + z_w v = 2p_o\, e^{-t/t_d} \tag{57}$$

Solving Eq. (57) gives the velocity of the plate

$$v = \frac{2p_o}{z_w}\left(e^{-t/t_d} - e^{-t/t_o}\right) \Big/ \left(1 - \frac{t_o}{t_d}\right) \tag{58}$$

where the mechanical impedance $z_w = \rho_w c_w$ is the product of the density of the water and the speed of sound in the water. The constant $t_o = \rho h/z_w$ is called by Kirkwood the damping time of the plate (see Kennard [115]). The total pressure on the wet face of the plate is

$$\tilde{p} = 2p_o\, e^{-t/t_d} - z_w\, v = 2p_o \left(-\frac{t_o}{t_d} e^{-t/t_d} + e^{-t/t_o}\right) \Big/ \left(1 - \frac{t_o}{t_d}\right) \tag{59}$$

This pressure becomes zero for time t_m when $-\frac{t_0}{t_d} e^{-t_m/t_d} + e^{-t_m/t_0} = 0$ which gives

$$t_m = \frac{t_d}{\frac{t_d}{t_o} - 1} \ln \frac{t_d}{t_o} \tag{60}$$

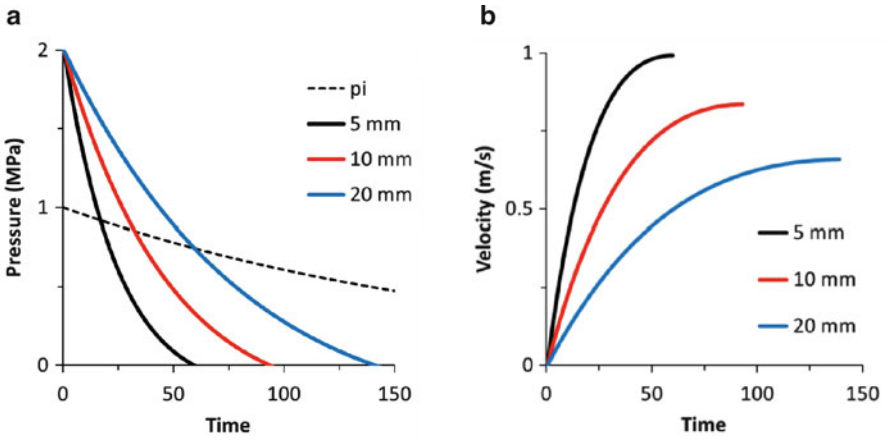


Fig. 10 Air-backed steel plate subjected to exponential pulse with $p_o = 1$ MPa, $t_o = 200$ μs. Pressure on the wet side of the plate and velocity as a function of time (μs) for three values of the thickness h

The velocity of the plate at that time is

$$v = \frac{2p_o}{z_w} e^{-t_m/t_d} = \frac{2p_o}{z_w} \left(\frac{t_d}{t_o}\right)^{1/\left(1-\frac{t_d}{t_o}\right)} \tag{61}$$

Figure 10 shows results for a steel plate obtained assuming that the density of steel is 7,850 kg/m^3, the density of water is 1,000 kg/m^3, the speed of sound is 1,500 m/s, $p_o = 1$ MPa, and $t_o = 200\,\mu s$. On the wet surface of the plate, the pressure becomes negative once t exceeds the value t_m predicted by Eq. (60) which defines the limit of the model. Figure 10 shows that this cavitation occurs shortly after the plate velocity reaches its maximum.

The loss of contact with the fluid implies that the impulse I_o is not fully applied to the plate. The impulse transmitted to the plate is given by

$$I = \xi I_o \tag{62}$$

where $\xi = \psi^{\psi/(1-\psi)}$ and $\psi = t_d/t_o$. Kambouchev et al. [116, 117] extended Taylor's model to the case of explosions in air. In that case, the reflection coefficient for the shock wave reflecting from the front face of the plate varies between 2 and 8 instead of 2 for underwater explosions. In the work of Kennard [115] and Dawson and Sullivan [118], the plate rests on an elastic foundation.

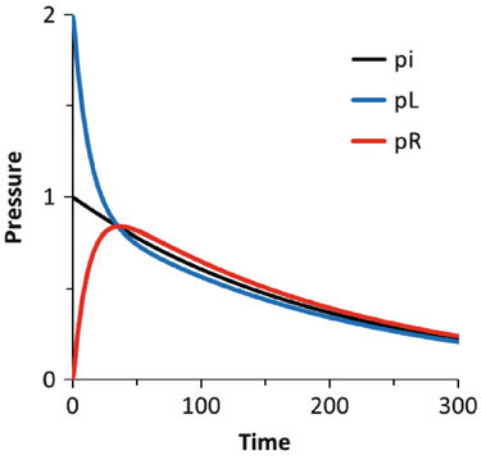


Fig. 11 Water-backed steel plate subjected to exponential pulse with $p_o = 1$ MPa, $t_o = 200$ μs. Incident pressure p_i and pressures on the *left* and *right* sides of the plate as a function of time (μs) for a thickness h = 5 mm

4.2.4 Water Backed Plates

The back face of the plate could also be in contact with water and in that case we will have a Water Backed Plate (WBP) as opposed to the Air backed Plate (ABP) previously considered. Both ABP and WBP were studied in [109, 111, 119, 120].

Equation 57 was developed for an air-backed plate, for a water backed plate, the mechanical impedance z_w should be replaced by $z'_w = 2\,z_w$ to account for the fact that there is water on both sides of the plate. The pressure on the back face is obtained by multiplying the plate velocity by the impedance z_w. With the same parameter used for the ABP, we consider a 5 mm thick WBP steel plate assuming that the density of steel is 7,850 kg/m^3, the density of water is 1,000 kg/m^3, the speed of sound is 1,500 m/s, $p_o = 1$ MPa, and $t_0 = 200$ μs. Figure 11 shows a very different behavior: after approximately 35 μs the pressures on both the left and the right surfaces of the plate are nearly identical to the incident pulse. For this reason, it is sometimes said that the plate is almost "transparent" to the wave. There is a reduction in the maximum amplitude and, while the incident wave is a shock wave since it rises instantly from zero to its maximum pressure, the pressure pulse on the left rises progressively. It can also be seen that the pressure on the left surface remains positive.

5 Shock Wave Interactions with Submerged Shells

5.1 Previous Studies

The effect of shock waves on submerged cylindrical or spherical shells has been studied for many years because of naval applications. Without attempting an exhaustive review, we note the analytical approaches of Huang and co-workers

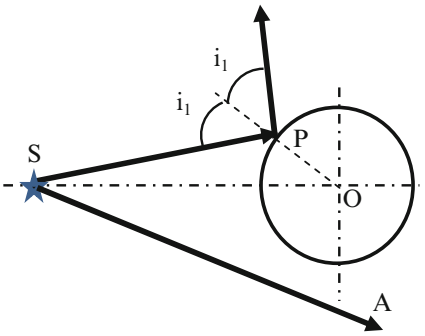


Fig. 12 Geometry of the problem. The explosion source S is located at a distance D = 5R to the *left* of a cylindrical shell of radius *R*. Lines *ST1* and *ST2* define the illuminated and shadow regions of the shell

[121–130], Payton [131], Tang and Yen [132], the analytical and numerical analyses in [133–139] and the experimental results of Hung et al. [140, 141]. In these references, pressure, velocity or acceleration at a few points around the shell is plotted as a function of time. Ref. [131] gives one figure showing the position of various wave fronts at one particular instant. Detailed studies of the interaction of shock waves with submerged cylindrical shells showing the progression of the various wave fronts as a function of time were presented by Iakovlev [142–153], Leblond et al. [154–158], Hasheminejad [159–161], and others [162–164].

5.2 Interaction of a Cylindrical Wave with an Evacuated Shell

Considering the interaction of a shock wave with a submerged air-filled cylindrical shell, this subsection presents an approach to determine the position of several wave fronts in the surrounding water. Wave fronts due to the direct, reflected and creeping waves propagating in the water and those due to waves radiated in the fluid because of the motion of the shell are determined using a ray tracing procedure.

With the geometry used in Iakovlev [142–153], a cylindrical shell of radius R is subjected to a cylindrical shock wave emanating from a source located at a distance D = 5R from the axis of the shell (Fig. 12). From the source S, drawing two lines ST_1 and ST_2 tangent to the surface of the shell, defines the illuminated region T_1LT_2 and the shadow region T_1RT_2 of the shell. In the fluid, the region delimited by the two tangents and located to the right of the arc T_1RT_2 is called the shadow zone.

The shock wave propagates in all directions at the speed of sound in the water. The direct wave front, undisturbed by the presence of the shell, is a circle of radius r centered at S and SA is a typical ray (Fig. 13). The shock wave interferes with the shell when r > D-R. Then, rays reaching a point P in the illuminated region is reflected so that the reflected angle i_2 is equal to the incident angle i_1 and the total length SP + PB = SA = r. The wave fronts for the direct wave and the reflected wave labeled D and R in Fig. 14 are drawn using this ray tracing procedure. Following

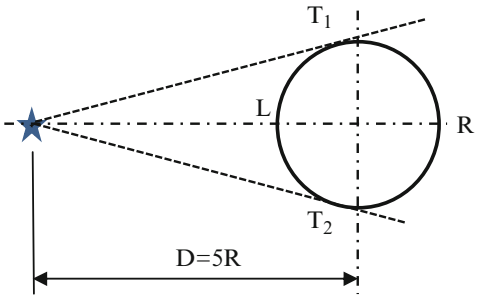


Fig. 13 Generation of a direct wave front by rays not interfering with the shell (ray *SA*) and reflected wave fronts (ray *SPB*)

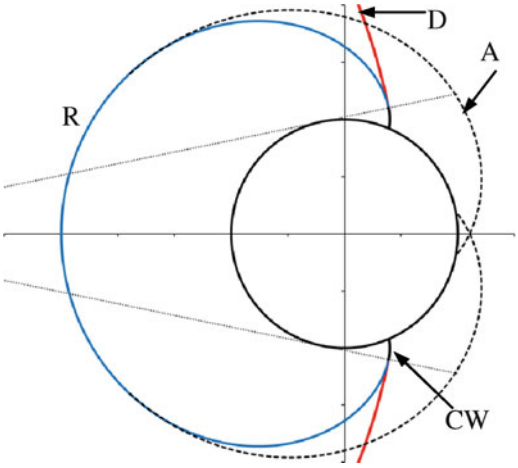


Fig. 14 Wave fronts generated by the interaction of a cylindrical shock wave and a cylindrical air-filled shell for d/R = 1.5 (*D* Direct wave, *R* reflected wave, *CW* creeping wave, *A* anti-symmetric radiated wave)

the same convention as in [142–153] we define the penetration distance d = r-D + R and plot the position of the various wave front for d/R = 1.5 as in Ref. [147]. The D and R wave fronts meet along the tangents from the source to the shell. The curve joining that point to the surface of the shell is the wave front for the creeping waves in the shadow zone.

Creeping waves also known as Franz waves propagate in the shadow zone as the speed of sound in the fluid. As illustrated in Fig. 15, starting from the tangent point T1, a creeping wave propagates along the circumference and then radiates into the fluid in a tangential direction. The total length $ST_1 + T_1Q + QC$ is equal to r. When $T_1Q = 0$, the creeping wave meets the direct wave and reflected wave fronts and when $ST_1 + T_1Q = 0$, it reaches the surface of the shell.

The shock wave excites the propagation of waves in the shell along the circumferential direction. The lowest symmetrical and anti-symmetrical modes are excited. Anti-symmetrical modes tend to propagate at speeds near that of shear waves in a solid. In the calculations we assume a shear wave speed $c_2 = 3{,}100$ m/s in steel and a speed of sound of 1,480 m/s in water. Figure 16 shows an incident

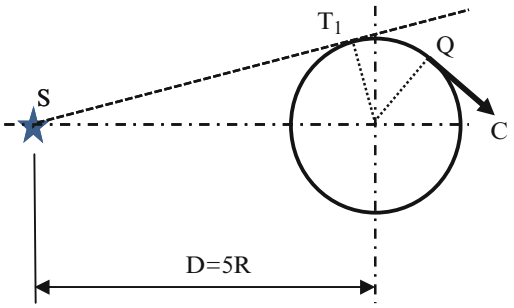


Fig. 15 Ray tracing procedure for creeping waves in the shadow region of cylindrical shell

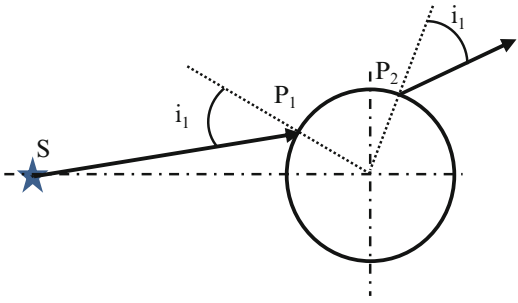


Fig. 16 Ray tracing procedures for waves caused by oscillations of the shell

ray SP1 making an angle i_1 with the radial direction. If this ray excites waves propagating in the circumferential direction, that is with a refracted angle i_2 of 90°, according to Snell's law, the critical angle for exciting the oscillations of the shell wall is given by

$$\sin i_1 = c_1 / c_2 \tag{63}$$

which gives a value of 28.52° in this case. Then, anti-symmetric waves in the shell propagate along the circumference with a velocity c_2 (arc P_1-P_2 in Fig. 16) and radiate back into the fluid at an angle i_1 as shown. The total length $SP_1 + P_1P_2 (c_2/c_1) + P_2D$ is equal to r, the radius of the direct wave front. The two radiated wave fronts shown in Fig. 14 are drawn using this ray tracing procedure. Symmetric modes for the shell tend to propagate at speeds near that of longitudinal waves in a solid: about 5,000 m/s for steel. The same procedure can be used to obtain those wave fronts.

The procedure presented here yield results that are in excellent agreement with those of Ref. [146] for this particular example and can be applied successfully to examples from [142–164]. The four types of wave fronts shown in Fig. 14 are predicted accurately without having to solve a complex fluid–structure interaction problem. Another advantage is that it brings insight into the physics of the problem. With a numerical approach, the interpretation of the results is not always clear.

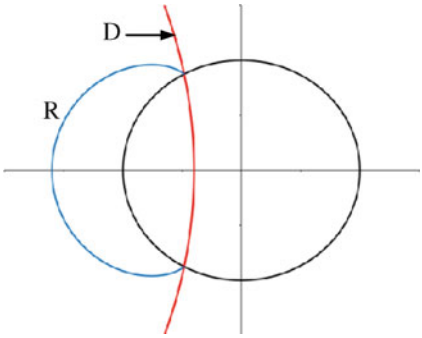


Fig. 17 Interaction with a fluid-filled cylindrical shell. Sonic case: $d/R = 0.6$, $c_2/c_1 = 1$. Direct and reflected wave fronts

5.3 *Interaction of a Cylindrical Wave with a Fluid-Filled Shell: Sonic Case*

Considering the interaction of a shock wave generated by an underwater explosion with a submerged cylindrical shell, we examine the case in which the liquid inside the shell is the same as the liquid surrounding it ($c_2/c_1 = 1$). Since the shell is filled with a liquid, waves will propagate through the inside fluid, they will in part reflect from the inside surface of the shell and inpart be transmitted back into the outside fluid. Therefore, there will be several new wave front in addition to those discussed in Sect. 5.2.

In Fig. 17, $d/R = 0.6$ and the shell is "transparent" to the direct wave in the sense that the wave front propagates through as if the shell was not there. The position of the wave front for the reflected wave is not affected by the presence of the inside fluid. Rays emanating from the source S do not reflect from the inside surface of the shell until the direct wave reaches the tangent point T1 (Fig. 12). This occurs when $r = \sqrt{D^2 - R^2}$ or $r = R\sqrt{24}$ for the present geometry. In other words, internal reflections will occur when

$$\frac{d}{R} > \sqrt{\frac{D^2}{R^2} - 1} - \left(\frac{D}{R} - 1\right) \tag{64}$$

In this case, $D/R = 5$ so we must have $d/R > \sqrt{24} - 4 = 0.89898$ for waves to reflect from the inside of the shell.

For a larger value of the d/R ratio ($d/R = 1.7$), we also note the presence of creeping waves in the outside fluid and of an additional wave front in the inside (Fig. 18). This new wave front is due to the reflection of rays from the inside surface of the shell. It is called R_1 because the rays reflect from the inside surface only once. This wave front has a cusp singularity and it starts where the direct wave crosses the shell (Fig. 18b). That figure also indicates that the R_1 wave front does not meet the CW wave front as they cross the shell.

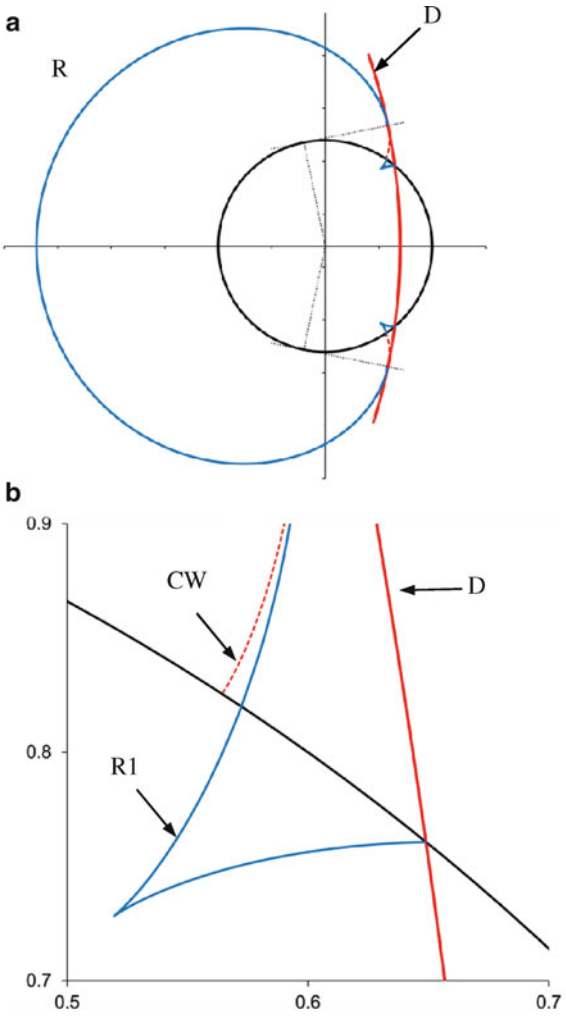


Fig. 18 Interaction with a fluid-filled cylindrical shell. Sonic case: $d/R = 1.7$, $c_2/c_1 = 1$. (**a**) general view; (**b**) expanded view

The R_1 wave front is drawn as indicated in Fig. 19. For a given value of the angle θ, the distances SA and AE are given by

$$SA = R\sqrt{\frac{D^2}{R^2} + 1 - 2\frac{D}{R}\cos\theta} \quad AE = 2R\cos(\gamma)$$

where $\gamma = \sin^{-1}\left(\frac{D}{SA}\sin\theta\right)$ is the angle between both SA and AE and the radial direction. The distance from E to the center of the center of the shell given by

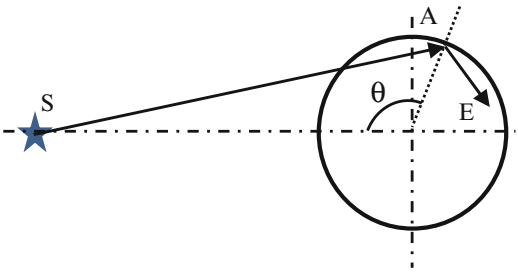


Fig. 19 Ray tracing procedure for the first reflected wave front R_1

$$OE = R\sqrt{1 + \left(\frac{D}{R} - 1 + \frac{d}{R}\right)^2 - 2\left(\frac{D}{R} - 1 + \frac{d}{R}\right)\cos(\gamma)}$$

when $D/R = 5$ and $d/R = 1.7$, $OE \leq 1$ when $94.3^o \leq \theta \leq 130.5^o$. With this construction, when $78.46^o \leq \theta \leq 94.3^o$, point E is located outside the shell which means that this reflected ray has reached the inside surface of the shell and has been in part transmitted into the outside fluid and in part reflected back inside. The R1 wave front outside the shell is seen to meet the CW and D wave fronts along ST_1, the tangent to the circle. The wave front corresponding to the second reflection from the inside of the shell is too small to be drawn on this figure.

When $d/R = 2.2$, the size of the two R_1 wave fronts became larger and joined together and we note the presence of two additional wave fronts labeled R_2 (Fig. 20). R_2 indicates that those wave fronts are obtained by considering rays that reflect from the inside surface of the shell twice. R_2 wave fronts start where the R_1 wave fronts cross the shell. Figure 20b shows how the R_1 front meets the CW and D fronts in the outside fluid. The R_2 front follows the same pattern in the outside fluid but that part is not drawn here to keep the figure legible.

When $d/R = 2.9$, the R_1 wave fronts are no longer singular (Fig. 21). In that case, two R_3 wave fronts also appear and we see that the R_1 wave fronts are connected to two R_2 wave fronts which in turn are connected to the R_3 wave fronts. The R_3 wave fronts do not quite reach the CW front which indicates that there are R4 fronts which are not shown here because they are very small. Results shown in Figs. 19, 20 and 21 for cases where $d/R = 1.7$, 2.2, and 2.9 are in excellent agreement with those shown by Iakovlev et al. [143].

Figure 22 shows that inside the shell, the first reflected rays form a caustic in the upper right quadrant. That figure also shows that the singular points of the R_1 wave fronts are located on that caustic when $d/R = 1.7$ and 2.2. For $d/R = 2.9$, there is no singular point since the wave front goes beyond the caustic. Similarly, Fig. 23 shows the caustic generated after two reflections from the inside surface and the R_2 fronts for $d/R = 2.2$, 2.9, and 4.21. All three of these wave fronts have a singular point located on the caustic.

Results in Figs. 24 and 25 are in good agreement with those in Iakovlev et al. [143].

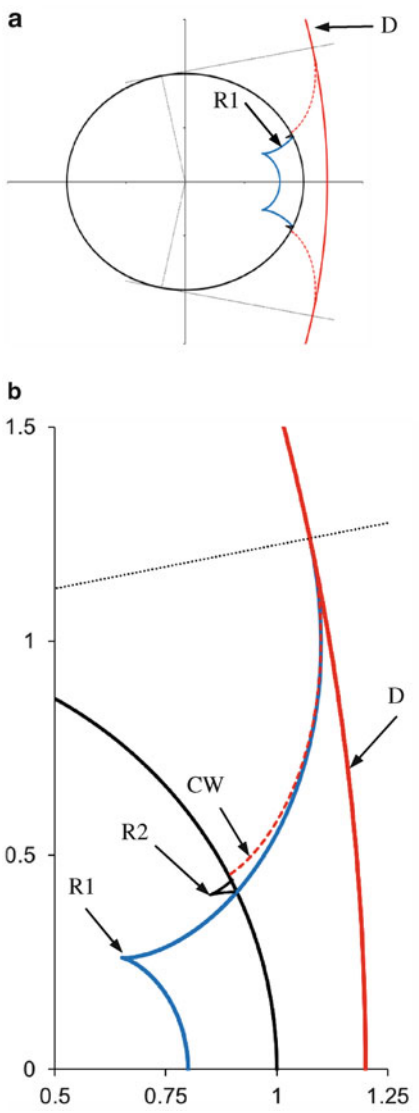


Fig. 20 Interaction with a fluid-filled cylindrical shell. Sonic case: d/R = 2.2, $c_2/c_1 = 1$. (**a**) general view; (**b**) expanded view

5.4 Interaction of a Cylindrical Wave with a Fluid-Filled Shell: Subsonic Case

When waves propagate slower in the inside fluid than in the outside ($c_2/c_1 < 1$) fluid different phenomena occur. In the present example, $c_2/c_1 = 0.43$. Figure 26 shows a different shape for the direct wave inside the shell compared to Fig. 17. This reflects

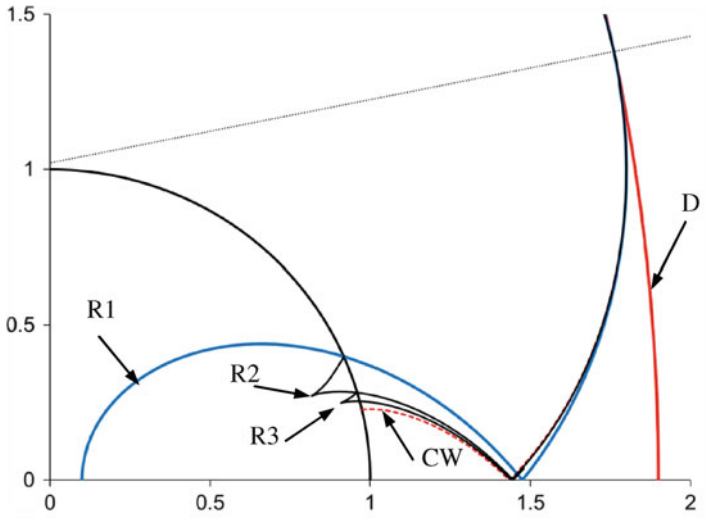


Fig. 21 Interaction with a fluid-filled cylindrical shell. Sonic case: $d/R = 2.9$, $c_2/c_1 = 1$

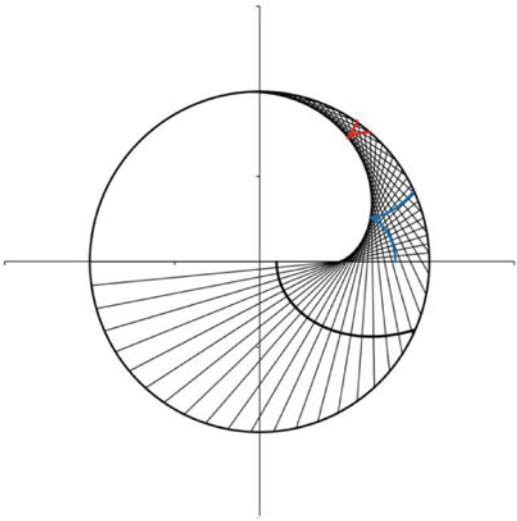


Fig. 22 Caustic and R_1 reflected wave fronts for $d/R = 1.7$ (*red*), 2.2 (*blue*), 2.9 (*black*). Sonic case, $c_2/c_1 = 1$

the fact that waves propagate at slower speeds inside. From Fig. 27 we find that, for a given angle θ, the angles α, i_1 and i_2 are given by

$$\alpha = \tan^{-1}\left[\sin\theta \,/\left(\frac{D}{R} - \cos\theta\right)\right],\ i_1 = \theta + \alpha,\ i_2 = \sin^{-1}\left(\frac{c_2}{c_1}\sin i_1\right) \qquad (65)$$

The penetration distance is $AF = \frac{c_2}{c_1} R\left\{\frac{D}{R} - 1 + \frac{d}{R} - \sqrt{\frac{D^2}{R^2} + 1 - 2\frac{D}{R}\cos\theta}\right\}$.

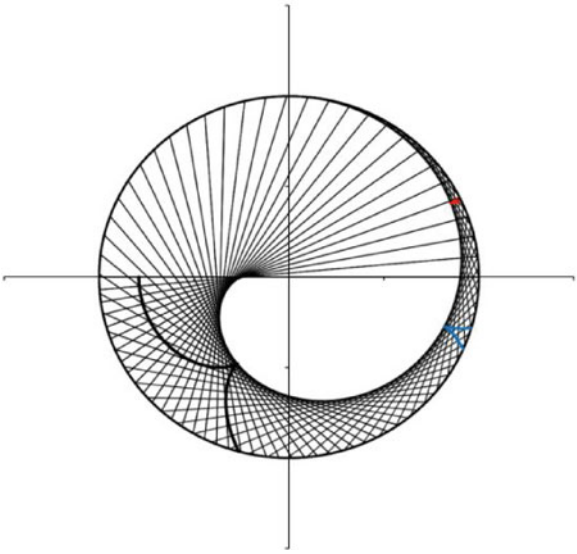


Fig. 23 Caustic and R_2 reflected wave fronts for $d/R = 2.2$ (*red*), 2.9 (*blue*), 4.21 (*black*). Sonic case, $c_2/c_1 = 1$

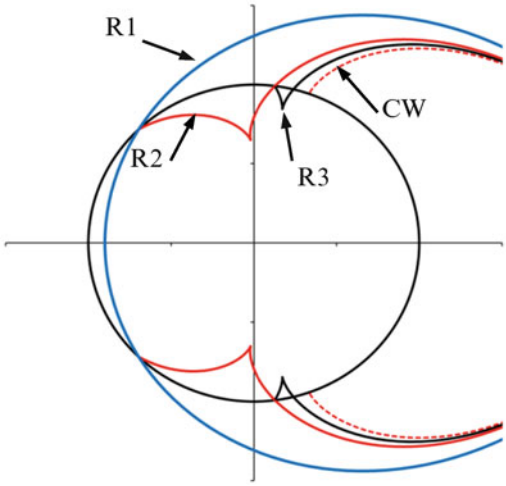


Fig. 24 Interaction with a fluid-filled cylindrical shell. Sonic case: $d/R = 3.9$, $c_2/c_1 = 1$. First three reflected wave fronts (R1: *blue*, R2: *red*, R3: *black*) and CW front (*dashed red line*) when

In Fig. 28, the line AF is extended until F reaches the inside of the shell. That is, until $AF = 2 \cos(i_2)$. It shows that direct rays do not reach the entire volume inside the shell and they also form a caustic in the upper right quadrant. This results in direct wave fronts that do not reach the shell when $d/R > 0.8990$ and in some cases cusp singularities occur on the caustic. When $d/R = 4.21$ this wave front is singular since it reaches the caustic. The DWI start reflecting from the inside surface when $d/R > 2\ c_1/c_2 = 4.651$. We also note that these wave fronts all start on the ray emanating from the tangent point T1 in Fig. 12.

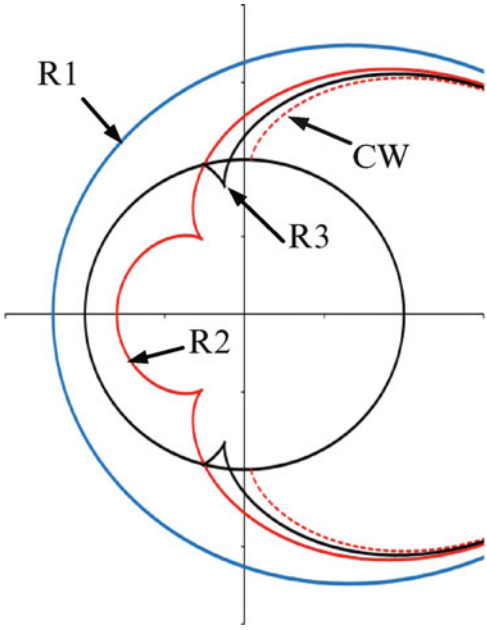


Fig. 25 Interaction with a fluid-filled cylindrical shell. Sonic case: d/R = 4.20, $c_2/c_1 = 1$. First three reflected wave fronts (R1: *blue*, R2: *red*, R3: *black*) and CW front (*dashed red line*)

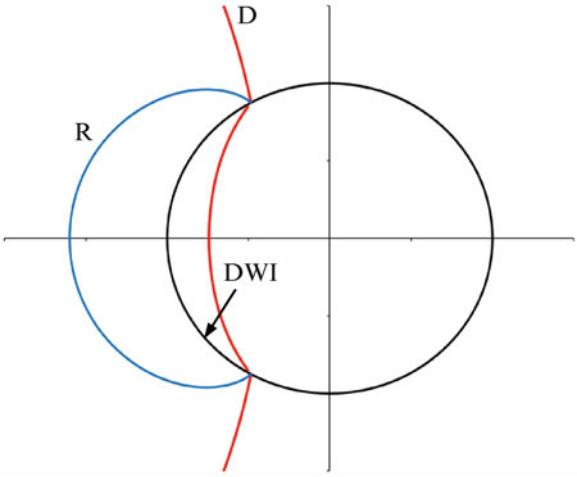


Fig. 26 Interaction with a fluid-filled cylindrical shell. Subsonic case: d/R = 0.6, $c_2/c_1 = 0.43$

The creeping wave propagating around the outside circumference of the shell has a 90° angle of incidence relative to the radial direction. According to Snell's law this wave is transmitted to the inside fluid at an angle given by

$$i_2 = \sin^{-1}(c_2/c_1)$$

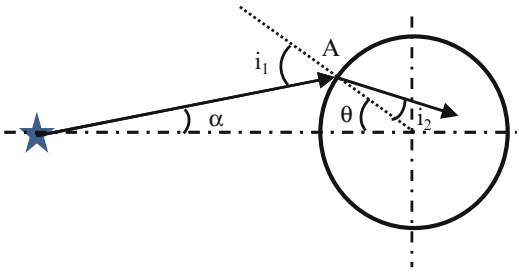


Fig. 27 Ray tracing procedure for direct wave inside when $c_2/c_1 \neq 1$

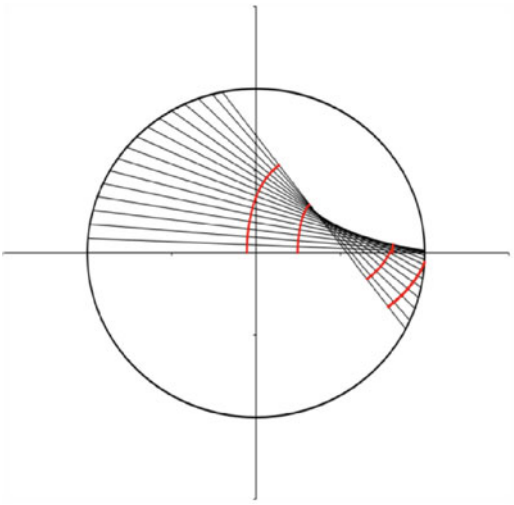


Fig. 28 Interaction with a fluid-filled cylindrical shell. Subsonic case: $c_2/c_1 = 0.43$. Direct rays inside the shell and corresponding wave fronts for d/R = 2.2, 2.9, 4.21, and 4.7

In the present example, $c_2/c_1 = 0.43$ so $i_2 = 25.5°$. Figure 29 shows that a ray from the source S to the tangent point T1, followed by a creeping wave from T1 to an arbitrary point P on the circumference is followed by a ray PG in the inside fluid. The total length ST1 + T1P + PG.c2/c1 is equal to the radius of the direct wave in the outside fluid. The wave front generated by this creeping wave after it is transmitted to the inside fluid is labeled CWI. This CWI wave front connects smoothly to the DWI (Fig. 30).

Rays generating the CWI wave front make an angle $i_2 = \sin^{-1}(c_2/c_1)$ with the radial direction. Their envelope is the circle of radius Rc_2/c_1 shown in Fig. 31. The dashed line in that figure starts from the tangent point T1 and makes an angle i_2 with the radial direction. It can be shown that the CWI wave front starts on the line AB when $0.89890 < d/R < 5.0982$. That wave front is smooth when $0.89890 < d/R < 2.9986$ and becomes singular when $2.9986 < d/R < 5.0982$ as shown in Fig. 31.

When d/R = 2.9, the top and bottom creeping wave fronts cross each other as they circumvent the shell on the outside, and same occurs for the CWI wave

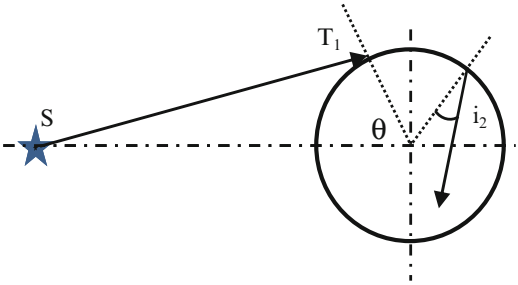


Fig. 29 Interaction with a fluid-filled cylindrical shell. Subsonic case. Ray tracing procedure for creeping waves inside (CWI)

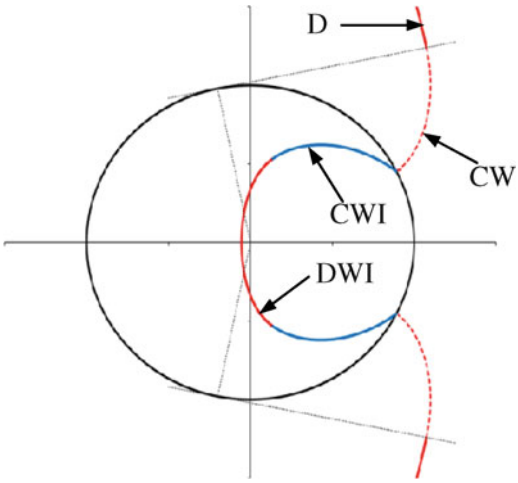


Fig. 30 Interaction with a fluid-filled cylindrical shell. Subsonic case: d/R = 2.2, $c_2/c_1 = 0.43$

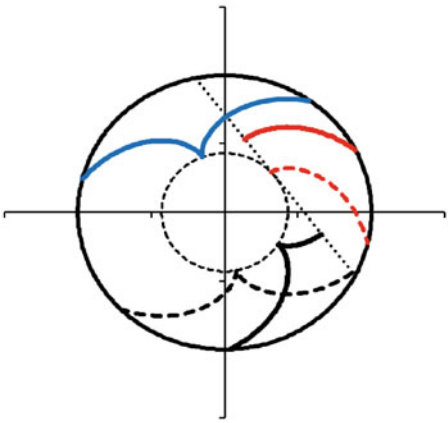


Fig. 31 Interaction with a fluid-filled cylindrical shell. Subsonic case: $c_2/c_1 = 0.43$. CWI wave fronts and related caustic

fronts inside the shell (Fig. 32). d/R = 4.21 both DWI and CWI wave fronts have cusp singularities (Fig. 33) as already indicated in Figs. 28 and 31. After a single reflection from the inside of the shell, rays form the pattern shown in Fig. 34 where it can be seen that the wave fronts are restricted to a small region and that a caustic is formed in the lower left quadrant.

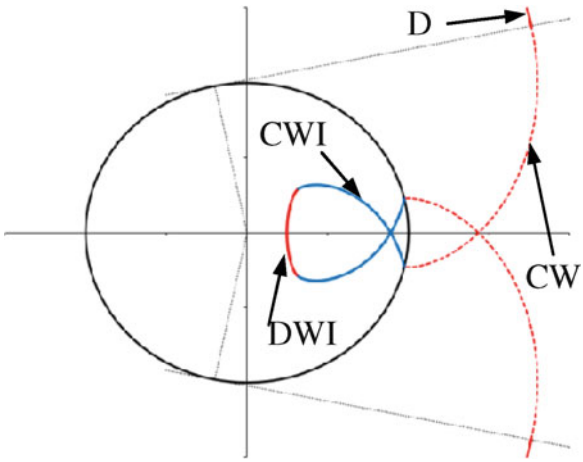


Fig. 32 Interaction with a fluid-filled cylindrical shell. Subsonic case: d/R = 2.9, $c_2/c_1 = 0.43$

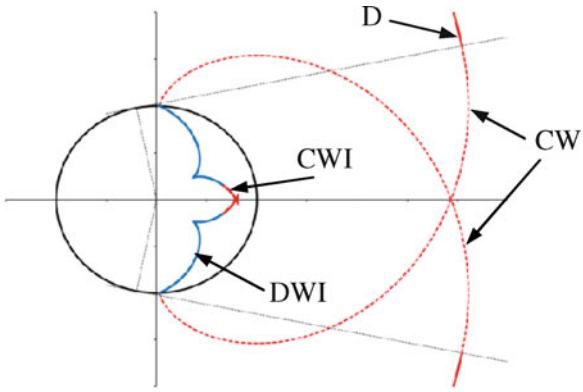


Fig. 33 Interaction with a fluid-filled cylindrical shell. Subsonic case: d/R = 4.21, $c_2/c_1 = 0.43$

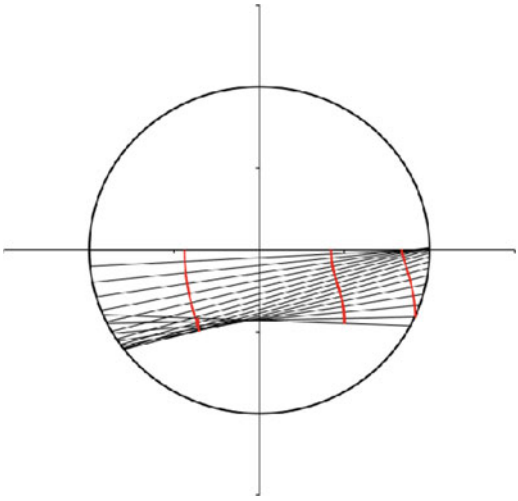


Fig. 34 Interaction with a fluid-filled cylindrical shell. Subsonic case: $c_2/c_1 = 0.43$. R1 caustic and wave fronts for several values of d/R

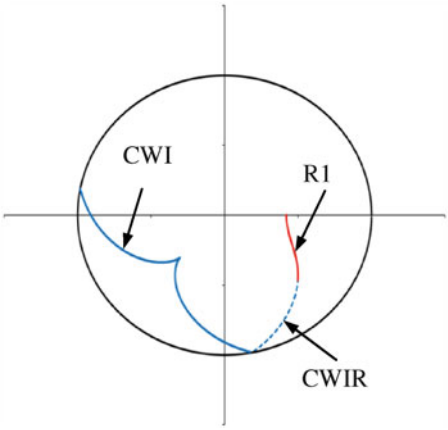


Fig. 35 Interaction with a fluid-filled cylindrical shell. Subsonic case: d/R = 6, $c_2/c_1 = 0.43$

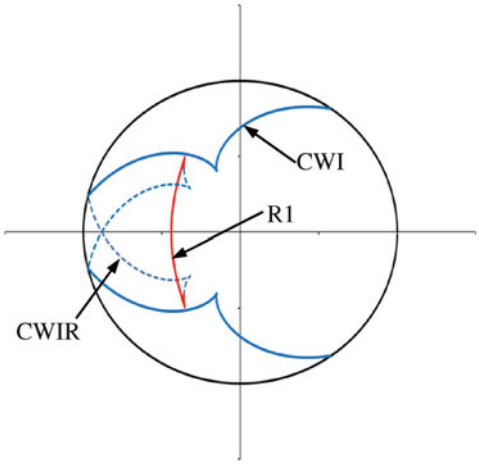


Fig. 36 Interaction with a fluid-filled cylindrical shell. Subsonic case: d/R = 8, $c_2/c_1 = 0.43$

When d/R = 6 we notice three types of wave fronts (Fig. 35): the CWI wave front, the portion of the CWI wave front that is reflected from the inside surface of the shell, and the R1 wave front previously shown in Fig. 34. Figure 35 only shows wave fronts generated by initial rays starting above the horizontal axis. Initial rays below that axis generate three more wave fronts that are mirror images of those shown on the figure. They are not shown in order to keep the figure simple. On the other hand, Fig. 36 shows both sets wave fronts are drawn for d/R = 8. In this case the reflected CWI wave fronts also have a singularity and they cross along the horizontal axis. The R1 wave front also has a singularity as indicated in Fig. 34 and it meets the CWI wave front at that singular point.

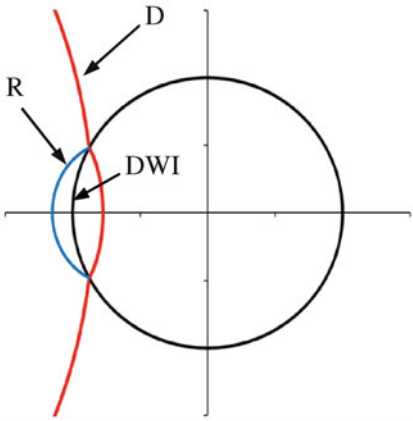


Fig. 37 Interaction with a fluid-filled cylindrical shell. Supersonic case: $d/R = 0.15$, $c_2/c_1 = 1.5$

5.5 *Interaction of a Cylindrical Wave with a Fluid-Filled Shell: Supersonic Case*

A different behavior is observed when the speed of sound is higher inside the shell than outside ($c_2/c_1 > 1$). In this example, $c_2/c_1 = 1.5$. The main result is that rays traveling though the inside fluid generate new wave fronts in the outside fluid.

First, using the construction shown in Fig. 27, we find that the refracted angle $i_2 = 90°$ when the incident angle $i_1 = 41.8°$ and that occurs when $\theta = 34.15°$ and $d/R = 0.2100$. When $d/R < 0.21$, wave fronts for the direct wave outside and the direct wave inside meet as they both reach the shell as shown in Fig. 37 when $d/R = 0.15$. Waves propagate faster inside the shell. When $d/R > 0.21$, the two wavefronts (DWO and DWI) no longer meet along the circumference of the shell as shown in Fig. 38 for $d/R = 0.6$. We find that, for this particular example ($D/R = 5$, $d/R = 0.6$), when $32.045° < \theta < 34.15°$ refracted rays reach the inside of the shell and generate refracted rays in the inside fluid and transmitted rays outside (Fig. 37). The incident ray SA makes an angle i_1 with the radial direction while AB makes an angle i_2 with that direction. At B, the reflected ray BC makes an angle i_2 with the radial direction while the transmitted ray BD is at an angle i_1. Snell's law relates the angle i_2 to i_1. When $\theta = 34.15°$, the transmitted wave front meets the reflected wave front on a line making a 41.8° angle with the radial direction at point A.

Figure 38 shows another wave front for rays traveling through the inside fluid and out into the outside fluid but the R1 reflected front is too small to be clearly visible (Fig. 39). However it is clearly visible when $d/R = 1.0$ (Fig. 40). The IO wave front is seen to start from where the R1 wave front starts and it joins smoothly with the reflected wave front R. When $d/R = 1.4$ the direct rays have all reached the back of the shell and have reflected to give a R1 wave front inside and in the outside fluid the two IO fronts shown in Figs. 38 and 40 merged together (Fig. 41).

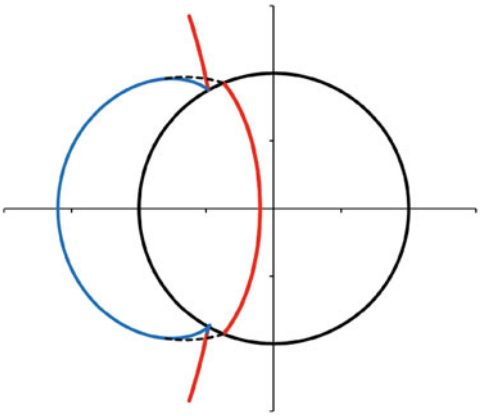


Fig. 38 Interaction with a fluid-filled cylindrical shell. Supersonic case: d/R = 0.6, $c_2/c_1 = 1.5$

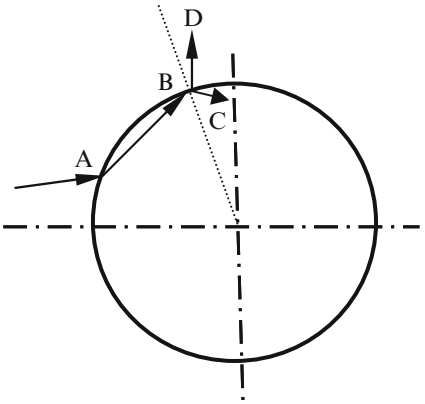


Fig. 39 Construction of transmitted wave front (T) and reflected wave front R1 for supersonic case

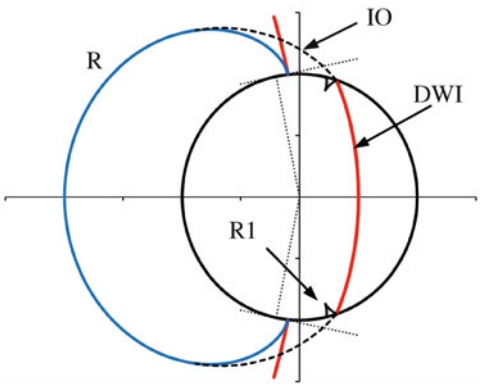


Fig. 40 Interaction with a fluid-filled cylindrical shell. Supersonic case: d/R = 1.0, $c_2/c_1 = 1.5$

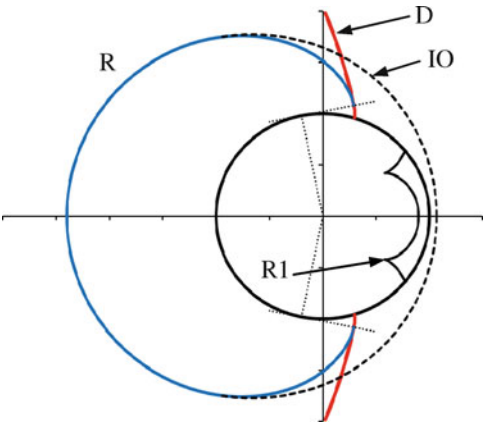


Fig. 41 Interaction with a fluid-filled cylindrical shell. Supersonic case: d/R = 1.4, $c_2/c_1 = 1.5$

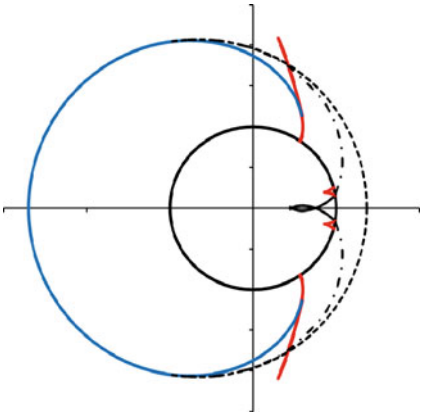


Fig. 42 Interaction with a fluid-filled cylindrical shell. Supersonic case: d/R = 1.7, $c_2/c_1 = 1.5$

For d/R = 1.7, R_2 wave fronts corresponding to two reflections from the inside of the shell are seen in the inside fluid (Fig. 42). A second wave front labeled IO2 initiates from the start of the R2 front and then joins smoothly with the IO front. When d/R = 2.4, the same pattern is observed (Fig. 43) and in addition we see a third IO front starting from the end the R2 wave front inside. The end of R2 is also the beginning of R3 which is not shown on the figure because it is too small. In Fig. 43, the R1 front does not have a singularity. Results in Figs. 38, 40, 41, 42 and 43 are in good agreement with those shown in Fig. 9 of Iakovlev [145].

The evolution of the shape and size of the R1 wave fronts can be seen in Fig. 44. When d/R = 1.0, 1.4, and 1.7 the wave front has a singularity when it reaches the caustic formed by the reflected rays. For d/R = 2.4, the R1 front is smooth.

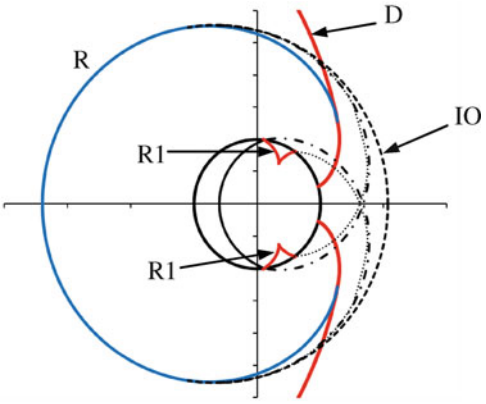


Fig. 43 Interaction with a fluid-filled cylindrical shell. Supersonic case: d/R = 2.4, $c_2/c_1 = 1.5$

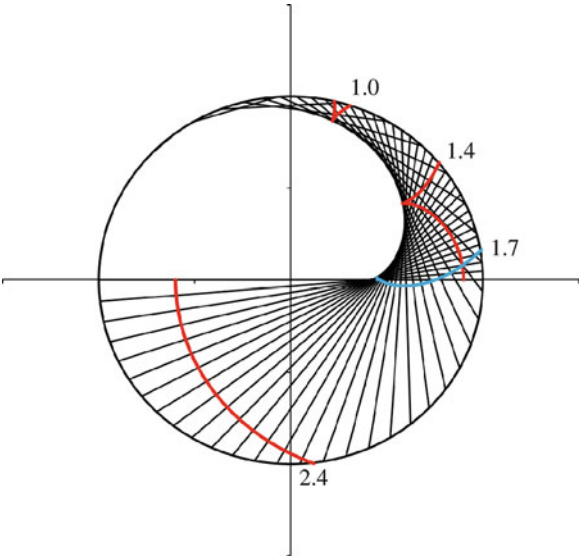


Fig. 44 Rays after one reflection from the inside of the shell, caustic, and wave fronts for several values of d/R, $c_2/c_1 = 1.5$

6 Related Problems

The approach developed to study shock wave interactions with submerged structures can be applied to other areas. This section describes how it can be applied to better understand a commonly used medical procedure called lithotripsy and to understand the development of traumatic brain injury (TBI) caused by impacts and explosions.

6.1 Lithotripsy

Shock wave lithotripsy (SWL) is a noninvasive procedure for kidney stone removal that was introduced in the United States in 1984. An overview of SWL is given by Bailey et al. [165, 166]. The device used for this procedure is called a extracorporeal shock wave lithotripter and it has three main components, a shock wave source, a method of acoustically coupling shock waves to the patient, and an imaging system for targeting. Lithotripters produce decaying pulses that can be described by the expression introduced by Friedlander for explosions in air

$$p = p_o \left(1 - \frac{t}{t_o}\right) e^{-\alpha\, t/t_o} \tag{66}$$

where t_o is the duration of the positive phase, p_o is the maximum pressure, and α indirectly defines the magnitude of the negative phase. Typically, a positive pressure spike with a duration of 1 μs followed by a 5 μs duration, negative pressure trough. Peak positive amplitudes range from 15 to 150 MPa and negative pressures are in the -8 to -15 MPa range. Typically, 2,000–4,000 shock waves are administered at a rate between 0.5 and 2 Hz. With this procedure, the shock waves break up the kidney stones.

Dahake et al. [167, 168] studied the interaction of shock waves with 22 mm cylinder made out of plaster immersed in water. Plaster is used to simulate kidney stones and, in that material, longitudinal waves propagates with velocity $c_L = 3.3$ mm/μs and shear waves with $c_s = 1.75$ mm/μs. The speed of sound in water is $c_w = 1.5$ mm/μs. Using the method developed in the present study we consider a source located 90 mm to the left of the cylinder.

Figure 45a shows the position of the shock wave in the water 6 μs after it has reached the cylinder. Inside the solid cylinder waves propagate faster than in the water and Fig. 45 shows four wave fronts inside. As a ray reaches the surface of the water it generates both a compressional wave PP and a shear wave PS in the cylinder (Fig. 45b). Some PP rays reach the surface of the cylinder and are reflected generating a PPP wave and PPS wave (Fig. 45c, d).

As the PP rays reach the surface of the cylinder, the reflected rays form a caustic (Fig. 46). The PPP wave front has a fold type singularity and that singularity occurs on the caustic.

After 8 μs, the PP wave front disappears and the PPP and PPS wave front have changed shape as shown in Fig. 47. The PPs wave front becomes singular as it reaches its caustic (Fig. 48).

The present approach gives precise prediction for the position of the various wave fronts which is difficult to obtain using numerical approaches such as the finite difference method used by Dahake et al. [168] for example. Several other authors have studied the propagation of shock waves in kidney stones [169–171].

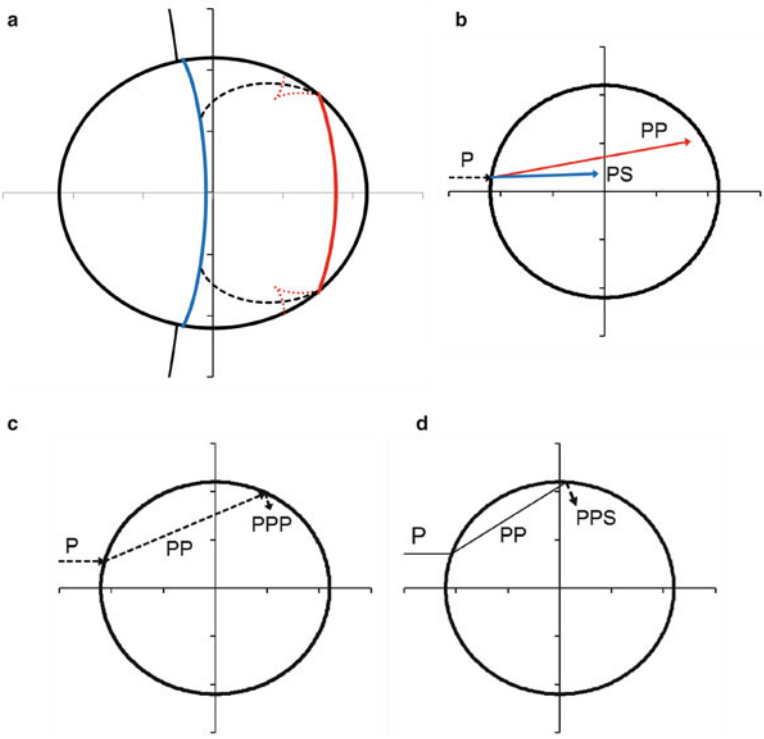


Fig. 45 Lithotripsy. Interaction of water borne shock wave with a plaster cylinder. (**a**) wave fronts for t = 6 μs; (**b**) Ray tracing procedure for the direct compression (*PP*) and shear wave (*PS*) fronts; (**c**) Ray tracing procedure for the PPP front; (d) Ray tracing procedure for the PPS front

6.2 Traumatic Brain Injury

Many articles have been devoted to the study of impacts on the human head. Young [172] modeled the head as a spherical fluid-filled shell. In the impact model, the head makes contact with a surface though a nonlinear spring representing the local deformation according to Hertz's contact law. That nonlinear spring acts in series with a linear spring that accounts for the deformation of the shell. Using this model, closed form solutions were obtained for the impact duration and the maximum impact force. The response of the fluid inside the shell is expected to remain hydrostatic if the duration of the impact is larger than 4 times the period of the first n = 2 spheroidal mode of the shell [172]. Analyses of the natural frequencies and mode shapes of fluid-filled spherical shells are found in [173–175].

A simple analysis for understanding the propagation of waves through the brain is provided by Babbs [176, 177]. In this model, an elastic bar is impacting a rigid surface with an initial velocity. Elastic waves propagate along the bar, reflect from the free end and return towards the impact point. The dynamic response

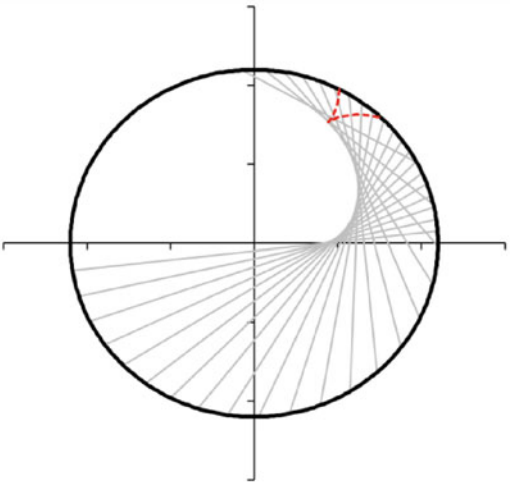


Fig. 46 Lithotripsy. Interaction of water borne shock wave with a plaster cylinder. 6 μs

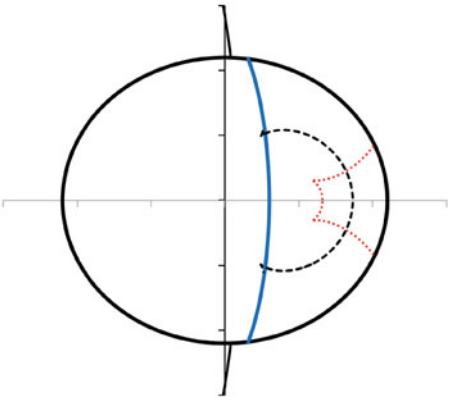


Fig. 47 Lithotripsy. Interaction of water borne shock wave with a plaster cylinder. The PS, PPP, and PPS wave fronts 8 μs after the shock wave has reached the cylinder

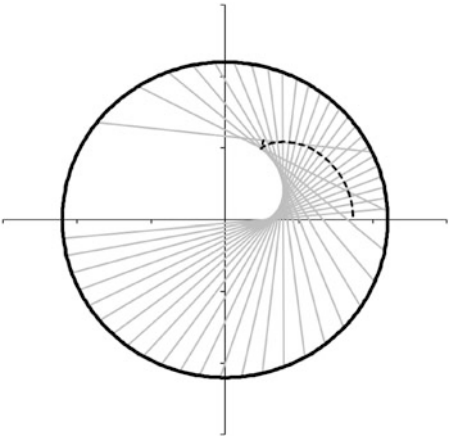


Fig. 48 Lithotripsy. Interaction of water borne shock wave with a plaster cylinder. Caustic and PPS wave front for t = 8 μs

of a fluid-filled spherical shell subjected to a radial impulsive load was studied analytically by Engin [178] in order to predict both skull fracture and brain damage. This model was extended by Kenner and Goldsmith [179, 180]. Finite element models of a human head subject to an impact force were developed by many authors including Engin et al. [181] who produced many contour plots for pressure levels inside the brain at different times.

A number of studies [e.g. 182, 183] used numerical simulations to study the role of blast wave interactions with the human head in producing traumatic brain injury. Grujicic et al [184] used a six layer one-dimensional model to simulate the effect of blasts on the head of a soldier wearing a helmet with polyurea suspension pads. The six layers are: a layer of air, a Kevlar-phenolic layer representing the helmet shell, a layer of polyurea, the skull, the cerebro-spinal fluid and the cerebrum. The objective is to assess the ability of polyurea to mitigate the effects of blast loading and, in turn, to reduce the possibility for TBI. A full three-dimensional analysis of this problem [185] showed the propagation of waves through the brain and through the skull at a faster speed. Simulations of blast waves with human head wearing a helmet can also be found in [186].

7 Conclusion

This chapter presented an overview of the physics of underwater explosions and wave propagation in solids and along fluid–structure interfaces. A geometrical approach is used to study the shock wave interactions with submerged structures and predict the position of wave fronts as a function of time. This simple approach gives a whole field view of these interactions and brings insights that are difficult to gain from numerical simulations. Several examples are presented for interactions with fluid-filled cylindrical shells and the method accurately predicted the evolution of complex patterns with many wave fronts. Singularities in some wave fronts were explained in terms of caustics formed by the rays generating these wave fronts. Singularities occur when the wave front reaches the caustic and singular points are located on the caustic. The method is shown to apply to other problems in the medical field.

Acknowledgements This work was supported by grant from the Office of Naval Research. The advice and encouragement of the program manager Dr. Y.D.S. Rajapakse are greatly appreciated.

References

1. Cole RH (1948) Underwater explosions. Princeton University Press, Princeton
2. Pritchett JW (1971) An evaluation of various theoretical models for underwater explosion bubbles. DTIC report AD Number: AD0737271
3. Hunter KS, Geers TL (2004) Pressure and velocity fields produced by an underwater explosion. J Acoust Soc Am 115(4):1483–1496

4. Arons AB (1954) Underwater explosion shock wave parameters at large distances from the charge. J Acoust Soc Am 26(3):343–346
5. Murata K, Takahashi K, Kato Y (1999) Precise measurements of underwater explosion phenomena by pressure sensor using fluoropolymer. J Mater Process Technol 85(1–3): 39–42
6. Kalavalapally R, Penmetsa R, Grandhi R (2006) Multidisciplinary optimization of a lightweight torpedo structure subjected to an underwater explosion. Finite Elem Anal Des 43:103–111
7. Kalavalapally R, Penmetsa R, Grandhi R (2009) Configuration design of a lightweight torpedo subjected to an underwater explosion. Int J Impact Eng 36:343–351
8. Van Der Schaaf P (1992) Underwater shock in the far-field from a distribution of charges. DTIC report Number ADA253458
9. Reid WD (1996) The response of surface ships to underwater explosions. Report DSTO-GD-0109
10. Arons AB, Slifko JP, Carter A (1948) Secondary pressure pulses due to gas globe oscillation in underwater explosions I. Experimental data. J Acoust Soc Am 20(3):271–276
11. Chapman NR (1988) Source levels of shallow explosive charges. J Acoust Soc Am 84(2): 697–702
12. Klaseboer E, Khoo BC, Hun KC (2005) Dynamics of an oscillating bubble near a floating structure. J Fluid Struct 21(4):395–412
13. Wang C, Khoo BC (2004) An indirect boundary element method for three-dimensional explosion bubbles. J Comput Phys 194(2–4):451–480
14. Zhang AM, Yao XL, Yu XB (2008) The dynamics of three-dimensional underwater explosion bubble. J Sound Vib 311(3–5):1196–1212
15. Vernon TA (1986) Whipping response of ship hulls from underwater explosion bubble loading. Technical memorandum 86/255, Defence Research Establishment Atlantic, pp 1–41
16. Snay HG (1962) Underwater explosion phenomena: the parameters of migrating bubbles. Technical report NAVORD 4185, U.S. Naval Ordnance Laboratory, White Oak, MD
17. Leybourne AE (1990) An extension of underwater explosive models to include the high frequency transients following pulse maxima. Math Comput Model 14:771–775
18. Reid WD (1996) The response of surface ships to underwater explosions. DSTO report DSTO-GD-0109
19. Lee M, Klaseboer E, Khoo BC (2007) On the boundary integral method for the rebounding bubble. J Fluid Mech 570:407–429
20. Rayleigh JW (1917) On the pressure developed in a liquid during the collapse of a spherical cavity. Philos Mag 34(3):94–98
21. Willis HF (1941) Underwater explosions: the time interval between successive explosions. British Report, WA-42-21
22. Chahine GL (1977) Interaction between an oscillating bubble and a free surface. J Fluids Eng Ser I 99:709–716
23. Lamb H (1923) The early stages of a submarine explosion. Philos Mag 45:257–265
24. Afanasiev KE, Grigorieva IV (2006) Numerical investigation of three-dimensional bubble dynamics. J Eng Math 55:65–80
25. Best JP (2002) The effect of non-spherical collapse on determination of explosion bubble parameters. DSTO report DSTO-RR-0238
26. Best JP, Kucera A (1992) A numerical investigation of non-spherical rebounding bubbles. J Fluid Mech 245:137–154
27. Klaseboer E, Khoo BC (2006) A modified Rayleigh-Plesset model for a non-spherically symmetric oscillating bubble with applications to boundary integral methods. Eng Anal Bound Elem 30(1):59–71
28. Keller JB (1980) Some bubble and contact problems. SIAM Rev 22(4):442–458
29. Keller JB, Kolodner II (1956) Damping of underwater explosion bubble oscillations. J Appl Phys 27:1152–1161
30. Geers TL, Park CK (2005) Optimization of the G&H bubble model. Shock Vib 12(1):3–8

31. Beshara FBA (1994) Modelling of blast loading on aboveground structures—I. General phenomenology and external blast. Comput Struct 51(5):585–596
32. Krauthammer T (2008) Modern protective structures. CRC Press, Boca Raton
33. Achenbach JD (1973) Wave propagation in elastic solids. North-Holland, Amsterdam
34. Ewing EW (1957) Elastic waves in layered media. McGraw-Hill, New York
35. Graff KF (1975) Wave motion in elastic solids. Ohio State University, Columbus
36. Miklowitz J (1978) The theory of elastic waves and waveguides. North Holland Pub. Co., Amsterdam
37. Brekhovskikh LM (1980) Waves in layered media. Academic Press, New York
38. Viktorov IA (1967) Rayleigh and lamb waves. Plenum Press, New York
39. Lighthill J (2001) Waves in fluids. Cambridge University Press, Cambridge
40. Whitham GB (1974) Linear and nonlinear waves. Wiley, New York
41. Brekhovskikh LM, Lysanov IP (2003) Fundamentals of ocean acoustics, AIP series in modern acoustics and signal processing. Springer, New York
42. Rayleigh JW (1889) On the free vibrations of an infinite plate of homogeneous isotropic elastic matter. Proc Lond Math Soc 1–20:225–234
43. Jagnoux P, Vincent A (1989) Ultrasonic imaging by leaky Rayleigh waves. NDT Int 22(6):329–346
44. Royer D, Clorennec D (2007) An improved approximation for the Rayleigh wave equation. Ultrasonics 46:23–24
45. Li XF (2006) On approximate analytic expressions for the velocity of Rayleigh waves. Wave Motion 44:120–127
46. Nkemzi DW (2008) A simple and explicit algebraic expression for the Rayleigh wave velocity. Mech Res Commun 35(3):201–205
47. Nkemzi DW (1997) A new formula for the velocity of Rayleigh waves. Wave Motion 26(2):199–205
48. Ogden RW, Vinh PC (2004) On Rayleigh waves in incompressible orthotropic elastic solids. J Acous Soc Am 115(2):530–533
49. Vinh PC (2010) On formulas for the velocity of Rayleigh waves in prestrained incompressible elastic solids. J Appl Mech 77(2):1–9, Article Number: 021006
50. Vinh PC, Giang PTH (2010) On formulas for the Rayleigh wave velocity in pre-strained elastic materials subject to an isotropic internal constraint. Int J Eng Sci 48(3):275–289
51. Rahmana M, Michelitsch T (2006) A note on the formula for the Rayleigh wave speed. Wave Motion 43:272–276
52. Vinh PC, Malischewsky PG (2008) Improved approximations of the Rayleigh wave velocity. J Thermoplast Comp Mate 21(4):337–352
53. Vinh PC, Malischewsky PG (2007) An improved approximation of Bergmann's form for the Rayleigh wave velocity. Ultrasonics 47(1–4):49–54
54. Vinh PC, Malischewsky PG (2007) An approach for obtaining approximate formulas for the Rayleigh wave velocity. Wave Motion 44(7–8):549–562
55. Vinh PC, Malischewsky PG (2006) Explanation for Malischewsky's approximate expression for the Rayleigh wave velocity. Ultrasonics 45(1–4):77–81
56. Vinh PC, Ogden RW (2004) On formulas for the Rayleigh wave speed. Wave Motion 39(3):191–197
57. Vinh PC, Ogden RW (2004) Formulas for the Rayleigh wave speed in orthotropic elastic solids. Arch Mech 56(3):247–265
58. Vinh PC, Ogden RW (2005) On the Rayleigh wave speed in orthotropic elastic solids. Meccanica 40(2):147–161
59. Neuenschwander J, Schmidt T, Luthi T, Romer M (2006) Leaky Rayleigh wave investigation on mortar samples. Ultrasonics 45:50–55
60. Goodman RR, Bunney RE, Marshall SW (1967) Observation of circumferential waves on solid aluminum cylinders. J Acoust Soc Am 42:523–524
61. Szilard J (1982) Ultrasonic testing—non-conventional testing techniques. Wiley, New York

62. Jin F, Wang Z, Kishimoto K (2005) Basic properties of Rayleigh surface wave propagation along curved surfaces. Int J Eng Sci 43(3–4):250–261
63. Bunney RE, Goodman RR, Marshall SW (1969) Rayleigh and lamb waves on cylinders. J Acoust Soc Am 46(5b):1223–1233
64. Lamb H (1917) On waves in an elastic plate. Proc R Soc Lond Seri A 93(648):114–128
65. Osborne MFM, Hart SD (1945) Transmission, reflection, and guiding of an exponential pulse by a steel plate in water. I. Theory. J Acoust Soc Am 17(1):1–18
66. Uberall H, Ahyi AC, Raju PK, Bjorno IK, Bjorno L (2002) Circumferential-wave phase velocities for empty, fluid-immersed spherical metal shells. J Acoust Soc Am 112(6): 2713–2720
67. Uberall H, Bjorno IK, Bjorno L (2000) Dispersion of circumferential waves on evacuated, water-loaded spherical steel shells. Ultrasonics 37(10):673–675
68. Cheeke JDN, Li X, Wang Z (1998) Observation of flexural lamb waves (Ao mode) on water-filled cylindrical shells. J Acoust Soc Am 104(6):3678–3680
69. Stoneley R (1924) Elastic waves at the surface of separation of two solids. Proc R Soc Lond Ser A 106:416–420
70. Scholte JGJ (1956) On seismic waves in a spherical earth. Koninklijk Nederlands Meteorologisch Instituut, Commun, No. 65, The Hague, pp 1–55
71. Jenot F, Ouaftouh M, Duquennoy M, Ourak M (2005) Interferometric detection of acoustic waves at air-solid interface. Applications to non-destructive testing. J Appl Phys 97, 094905
72. Kaufman AA, Levshin AL (2005) Acoustic and elastic wave fields in geophysics, vol 3. Elsevier, ISBN 04445 19556, 97804445 19559
73. Meegan GD, Hamilton MF, Il''inskii YA, Zabolotskaya EA (1999) Nonlinear Stoneley and Scholte waves. J Acoust Soc Am 106:1712–1723
74. Glorieux C, Van de Rostyne K, Nelson K, Gao W, Lauriks W, Thoen J (2001) On the character of acoustic waves at the interface between hard and soft solids and liquids. J Acoust Soc Am 110(3), Pt. 1, 1299–1308
75. Weng X, Yew CH (1990) The leaky Rayleigh wave and Scholte wave at the interface between water and porous sea ice. J Acoust Soc Am 87(6):2481–2488
76. Uberall H (2001) Acoustics of shells. Acoust Phys 47(2):115–139
77. Bao XL, Franklin H, Raju PK, Überall H (1997) The splitting of dispersion curves for plates fluid-loaded on both sides. J Acoust Soc Am 102(2):1246–1248
78. Sessarego J-P, Sageloli J, Gazanhes C, Uberall H (1997) Two Scholte–Stoneley waves on doubly fluid-loaded plates and shells. J Acoust Soc Am 101(1):135–142
79. Bao XL, Raju PK, Überall H (1999) Circumferential waves on an immersed, fluid-filled elastic cylindrical shell. J Acoust Soc Am 105(5):2704–2709
80. Kim JY, Ih JG (2003) Scattering of plane acoustic waves by a transversely isotropic cylindrical shell – application to material characterization. Appl Acoust 64(12):1187–1204
81. Maze G, Leon F, Ripoche J et al (1995) Nature of Scholte interface waves on cylindrical-shells. Acustica 81(3):201–213
82. Maze G, Léon F, Ripoche J, Überall H (1999) Repulsion phenomena in the phase-velocity dispersion curves of circumferential waves on elastic cylindrical shells. J Acoust Soc Am 105(3):1695–1701
83. Franz W (1954) Uber die Greenschen Functionen des Zylinderus und der Kugel. Z. Naturforsch 9A, 705–716
84. Barnard GR, McKinney CM (1961) Scattering of acoustic energy by solid and air-filled cylinders in water. J Acoust Soc Am 33(2):226–238
85. Neubauer WG (1968) Experimental measurement of “creeping” waves on solid aluminum cylinders in water using pulses. J Acoust Soc Am 44(1):298–299
86. Neubauer WG (1968) Experimental observation of three types of pulsed circumferential waves on solid aluminum cylinders. J Acoust Soc Am 44(4):1150–1152
87. Ahyi AC, Pernod P, Gatti O et al (1998) Experimental demonstration of the pseudo-Rayleigh (A(0)) wave. J Acoust Soc Am 104(5):2727–2732

88. Latard V, Merlen A, Preobazhenski V, Ahyi AC (1999) Acoustic scattering of impulsive geometrical waves by a glass sphere in water. Appl Phys Lett 74(13):1919–1921
89. Neubauer WG (1969) Pulsed circumferential waves on aluminum cylinders in water. J Acoust Soc Am 45(5):1134–1144
90. Überall H, Doolittle RD, McNicholas JV (1966) Use of sound pulses for a study of circumferential waves. J Acoust Soc Am 39(3):564–578
91. Ugincius P (1968) Creeping-wave analysis of acoustic scattering by elastic cylindrical shells. NWL technical report TR-2128
92. Ugincius P, Oberall H (1968) Creeping wave analysis of acoustic scattering by elastic cylindrical shells. J Acoust Soc Am 58(1025–1035):1968
93. Nguyen XN, Dahm T, Grevemeyer I (2009) Inversion of Scholte wave dispersion and waveform modeling for shallow structure of the ninetyeast ridge. J Seismol 13(4):543–559
94. Stoll RD, Bautista EO, Akal T (1996) Generating interface waves using a freely falling, instrumented source. IEEE J Oceanic Eng 21(4):452–457
95. Kotenkoff C, Lacoume JL, Mars M (2005) Multicomponent seismo-acoustic surface waves beamforming for undersea buried object detection. Oceans 2005 Europe International Conference, Brest, France, June 20–23, 2005. Oceans 2005 – Europe, vols 1 and 2, pp 769–774
96. Lefevre F, Jenot F, Ouaftouh M, et al (2010) Laser generated guided waves and finite element modeling for the thickness gauging of thin layers. Rev Sci Instrum 81(3), Article Number: 034901
97. Jenot F, Ouaftouh M, Duquennoy M et al (2005) Sizing of structures by laser ultrasonics using air-solid interface waves. Rev Prog Quant Nondestruct Eval 760:305–312
98. Su Z, Ye L (2009) Identification of damage using lamb waves: from fundamentals to applications. Springer, London
99. Zhu JY, Popovics JS, Schubert F (2004) Leaky Rayleigh and Scholte waves at the fluid–solid interface subjected to transient point loading. J Acoust Soc Am 116(4):2101–2110
100. Zhu JY, Popovics JS (2006) Analytical study of excitation and measurement of fluid–solid interface waves. Geophys Res Lett 33(9), Article Number: L09603
101. Luke BA, Stokoe KH (1998) Application of SASW method underwater. J Geotech Geoenviron Eng 124(6):523–531
102. Herber R, Grevemeyer I, Exner O et al (1998) An implosive seismoacoustic source for seismic experiments on the ocean floor. Mar Geophys Res 20(3):239–247
103. Fu D, Liu L, Chen Y, Zhu G (2001) Phase difference and interference between reflected cylindrical wave and head wave at a liquid/solid interface. Chin Sci Bull 46(18):1556–1560
104. Alkier KW (1978) Underwater acoustic backscattering and echo structure characteristics for a thin stiffened plate. J Acoust Soc Am 63(3):704–708
105. Bingham J, Hinders M, Friedman A (2009) Lamb wave detection of limpet mines on ship hulls. Ultrasonics 49(8):706–722
106. Wardlaw AB, Luton JA (2000) Fluid–structure interaction mechanisms for close-in explosions. Shock Vib 7(5):265–275
107. Xie WF, Young YL, Liu TG et al (2007) Dynamic response of deformable structures subjected to shock load and cavitation reload. Comput Mech 40(4):667–681
108. Young YL, Liu Z, Xie W (2009) Fluid–structure and shock-bubble interaction effects during underwater explosions near composite structures. J Appl Mech 76(5):1–10
109. Xie W, Liu Z, Young YL (2009) Application of a coupled Eulerian–Lagrangian method to simulate interactions between deformable composite structures and compressible multiphase flow. Int J Numerical Methods Eng 80(12):1497–1519
110. Liu Z, Young YL, Motley MR (2010) Transient response of partially-bonded sandwich plates subject to underwater explosions. Shock Vib 17(3):233–250
111. Xie WF, Young YL, Liu TG (2008) Multiphase modeling of dynamic fluid–structure interaction during close-in explosion. Int J Numer Methods Eng 74(6):1019–1043
112. Fleck NA, Deshpande VS (2004) The resistance of clamped sandwich beams to shock loading. J Appl Mech 71(3):386–401

113. Pan YG, Watson A (1998) Effect of panel stiffness on resistance of cladding panels to blast loading. J Eng Mech 124(4):414–421
114. Taylor GI (1941) The pressure and impulse of submarine explosion waves on plate. Cambridge University Press, Cambridge
115. Kennard EH (1941) Report on Underwater Explosions. David Taylor Model Basin Underwater Explosion (UNDEX) Research, Oct; Office of Naval Research (ONR, 1950)
116. Kambouchev N, Noels L, Radovitzky R (2006) Nonlinear compressibility effects in fluid–structure interaction and their implications on the air-blast loading of structures. J Appl Phys 100(6), Article Number: 063519
117. Kambouchev N, Radovitzky R, Noels L (2007) Fluid–structure interaction effects in the dynamic response of free-standing plates to uniform shock loading. J Appl Mech 74: 1042–1045
118. Dawson RL, Sullivan GM (1995) A theoretical investigation of the effect of structural stiffness in underwater shock wave loading using the plane wave approximation. J Appl Mech 62(1):260–262
119. Liu Z, Young YL (2008) Transient response of submerged plates subject to underwater shock loading: an analytical perspective. J Appl Mech 75(4), Article Number: 044504
120. Motley MR, Young YL. Liu Z (2011) Three-dimensional underwater shock response of composite marine structures. J Appl Mech 78(6), Article Number: 061013
121. Huang H (1969) Transient interaction of plane acoustic waves with a spherical elastic shell. J Acoust Soc Am 45(3):661–670
122. Huang H (1970) An exact analysis of the transient interaction of acoustic plane waves with a cylinder elastic shell. J Appl Mech 37:1091–1099
123. Huang H (1971) Early time interaction of spherical acoustic waves and a cylindrical shell. J Acoust Soc Am 50(3):885–891
124. Huang H, Wang YF (1971) Early-time interaction of spherical acoustic waves and a cylindrical elastic shell. J Acoust Soc Am 50(3B):885–891
125. Huang H, Lu YP, Wang YF (1974) Transient interaction of spherical acoustic waves, a cylindrical elastic shell, and its internal multidegree-of-freedom mechanical system. J Acoust Soc Am 56(1):4–10
126. Huang H (1975) Scattering of spherical pressure pulses by a hard cylinder. J Acoust Soc Am 58(2):310–317
127. Huang H (1979) Transient response of two fluid-coupled spherical elastic shells to an incident pressure pulse. J Acoust Soc Am 65(4):881–887
128. Huang H (1979) Transient response of two fluid-coupler cylindrical elastic shells to an incident pressure pulse. J Acoust Soc Am 46:513–518
129. Huang H, Gaunard GC (1998) Transient diffraction of a plane step pressure pulse by a hard sphere: neoclassical solution. J Acoust Soc Am 104(6):3236–3244
130. Huang H (1981) Interaction of acoustic shock waves with a cylindrical elastic shell immersed near a hard surface. Wave Motion 3(3):269–278
131. Payton RG (1960) Transient interaction of an acoustic wave with a circular cylindrical shell. J Acoust Soc Am 32:722–729
132. Tang SC, Yen DHY (1970) Interaction of a plane acoustic wave with an elastic spherical shell. J Acoust Soc Am 47(5):1325–1333
133. Lai WH (2007) Transient dynamic response of submerged sphere shell with an opening subjected to underwater explosion. Ocean Eng 34(5–6):653–664
134. Lam KY, Zhang ZJ, Gong SW, Chan ES (1998) The transient response of a two-layered elastic cylindrical shell impinged by an underwater shock wave. Compos Part B Eng 29(6):673–685
135. Lam KY, Zhang ZJ, Gong SW, Chan ES (1998) The transient response of submerged orthotropic cylindrical shells exposed to underwater shock. Compos Struct 43(3):179–193
136. Li J, Hua H (2009) Transient response of an orthotropic cylindrical shell to an underwater explosive loading. J Reinf Plast Comp 28(14):1747–1762
137. Li J, Hua H (2009) Transient interaction of a plane acoustic wave with an elastic orthotropic cylindrical shell. Thin-Walled Struct 47(3):335–345

138. Li J, Hua H (2009) Transient vibrations of laminated composite cylindrical shells exposed to underwater shock waves. Eng Struct 31(3):738–748
139. Hu G, Xia F, Li J (2010) The transient responses of two-layered cylindrical shells attacked by underwater explosive shock waves. Compos Struct 92(7):1551–1560
140. Hung CF, Hsu PY, Hwang-Fuu JJ (2005) Elastic shock response of an air-backed plate to underwater explosion. Int J Impact Eng 31(2):151–168
141. Hung CF, Lin BJ, Hwang-Fuu JJ, Hsu PY (2009) Dynamic response of cylindrical shell structures subjected to underwater explosion. Ocean Eng 36(8):564–577
142. Iakovlev S, Dooley G, Williston K, Gaudet J (2011) Evolution of the reflection and focusing patterns and stress states in two-fluid cylindrical shell systems subjected to an external shock wave. J Sound Vib 330(25):6254–6276
143. Iakovlev S, Gaudet J, Dooley G, MacDonald B (2010) Hydrodynamic fields induced by the shock response of a fluid-filled submerged cylindrical shell containing a rigid co-axial core. J Sound Vib 329(16):3359–3381
144. Iakovlev S, Mitchell M, Dooley G (2011) Modeling two-fluid response of thin elastic shells. Int J Num Methods Fluids 65(11–12):1389–1406
145. Iakovlev S (2009) Interaction between an external shock wave and a cylindrical shell filled with and submerged into different fluids. J Sound Vib 322:401–437
146. Iakovlev S (2008) Interaction between a submerged evacuated cylindrical shell and a shock wave – part I: diffraction-radiation analysis. J Fluids Struct 24:1077–1097
147. Iakovlev S (2008) Interaction between a submerged evacuated cylindrical shell and a shock wave-part II: numerical aspects of the solution. J Fluids Struct 24(7):1098–1119
148. Iakovlev S (2007) Radiation by a submerged cylindrical shell in response to an external non-stationary acoustic pulse. Can Acous Acoustique Canadienne 35(3):168–169
149. Iakovlev S (2007) Submerged fluid-filled cylindrical shell subjected to a shock wave: fluid–structure interaction effects. J Fluids Struct 23(1):117–142
150. Iakovlev S (2006) External shock loading on a submerged fluid-filled cylindrical shell. J Fluids Struct 22(8):997–1028
151. Iakovlev S (2004) Influence of a rigid coaxial core on the stress–strain state of a submerged fluid-filled circular cylindrical shell subjected to a shock wave. J Fluids Struct 19(7):957–984
152. Iakovlev S (2003) Interaction of a spherical shock wave and a submerged fluid-filled circular cylindrical shell. J Sound Vib 255(4):615–633
153. Iakovlev S (2002) Complex shock loading on submarine oil pipelines. Can Acous Acoustique Canadienne 30(3):88–89
154. Leblond C, Sigrist JF, Iakovlev S (2008) A semi-analytical approach to the study of the transient acoustic response of cylindrical shells. Can Acous Acoustique Canadienne 36(3):166–167
155. Leblond C, Iakovlev S. Sigrist JF (2010) A fully elastic model for studying submerged circular cylindrical shells subjected to a weak shock wave. Proceedings of the ASME pressure vessels and piping conference, Prague, Czech Republic, 26–30 July 2009, vol 4, pp 557–564
156. Leblond C, Iakovlev S, Sigrist JF (2009) A fully elastic model for studying submerged circular cylindrical shells subjected to a weak shock wave. Mecanique Industries 10(3–4):275–284
157. Leblond C, Sigrist JF (2010) A versatile approach to the study of the transient response of a submerged thin shell. J Sound Vib 329(1):56–71
158. Sigrist JF, Leblond C (2008) A semi-analytical approach for the modelling of acoustic shock wave-elastic submerged shell interaction. Application to the pre-design of submarine hulls. Mecanique Industries 9(6):543–550
159. Hasheminejad SM, Abbasion S, Mirzaei Y (2011) Acoustic pulse interaction with a submerged functionally graded material hollow cylinder. Acoust Phys 57(1):20–35
160. Hasheminejad SM, Bahari A, Abbasion S (2011) Modelling and simulation of acoustic pulse interaction with a fluid-filled hollow elastic sphere through numerical Laplace inversion. Appl Math Model 35(1):22–49
161. Hasheminejad SM, Abbasion S, Bahari A (2010) Time domain computation and visualization of shock induced sound fields for a doubly fluid-loaded hollow cylinder. Comput Struct 88(19–20):1077–1091

162. A-man Z, Wen-shan Y (2011) Yao XL NUMERICAL simulation of underwater contact explosion. Appl Ocean Res 34:10–20
163. Panahi B, Ghavanloo E, Daneshmand F (2011) Transient response of a submerged cylindrical foam core sandwich panel subjected to shock loading. Mater Des 32(5):2611–2620
164. Feuillade C (2004) Animations for visualizing and teaching acoustic impulse scattering from spheres. J Acoust Soc Am 115(5):1893–1904
165. Bailey MR, McAteer JA, Pishchalnikov YA, Hamilton MF, Colonius T (2006) Progress in lithotripsy research. Acous Today 2:18–29
166. Bailey MR, Khokhlova VA, Sapozhnikov OA et al (2003) Physical mechanisms of the therapeutic effect of ultrasound – (a review). Acoust Phys 49(4):369–388
167. Dahake G, Gracewski SM (1997) Finite difference predictions of P-SV wave propagation inside submerged solids. II. Effect of geometry. J Acoust Soc Am 102(4):2138–2145
168. Dahake G, Gracewski SM (1997) Finite difference predictions of P-SV wave propagation inside submerged solids. I. Liquid–solid interface conditions. J Acoust Soc Am 102(4): 2125–2137
169. Cleveland RO, Tello JS (2004) Effect of the diameter and the sound speed of a kidney stone on the acoustic field induced by shock waves. Acous Res 5(2):37–43
170. Cleveland RO, Sapozhnikov OA (2005) Modeling elastic wave propagation in kidney stones with application to shock wave lithotripsy. J Acoust Soc Am 118(4):2667–2676
171. Sapozhnikov OA, Maxwell AD, MacConaghy B et al (2007) A mechanistic analysis of stone fracture in lithotripsy. J Acoust Soc Am 121(2):1190–1202
172. Young PG (2003) An analytical model to predict the response of fluid-filled shells to impact – a model for blunt head impacts. J Sound Vib 267(5):1107–1126
173. Young PG (2002) A parametric study on the axisymmetric modes of vibration of multi-layered spherical shells with liquid cores of relevance to head impact modeling. J Sound Vib 256(4):665–680
174. Engin AE, Liu YK (1970) Axisymmetric response of a fluid-filled spherical shell in free vibrations. J Biomech 3(1):11–22
175. Engin AE (1969) Vibrations of fluid-filled spherical shells. J Acoust Soc Am 46(1B):186–190
176. Babbs CF (2005) Brain motion and deformation during closed head injury in the presence of cerebrospinal fluid. J Mech Med Biol 5(2):277–306
177. Babbs CF (2006) A new biomechanical head injury criterion. J Mech Med Biol 6(4):349–371
178. Engin AE (1969) The axisymmetric response of a fluid-filled spherical shell to a local radial impulse – a model for head injury. J Biomech 2(3):325–341
179. Kenner VH, Goldsmith W (1973) Impact on a simple physical model of the head. J Biomech 6(1):1–11
180. Kenner VH, Goldsmith W (1972) Dynamic loading of a fluid-filled spherical shell. Int J Mech Sci 14(9):557–568
181. Engin AE, Liu YK (1970) Axisymmetric response of a fluid-filled spherical shell in free vibrations. J Biomech 3(1):11–16
182. Taylor PA, Ford CC (2009) Simulation of blast-induced. Early-time intracranial wave physics leading to traumatic brain injury. J Biomech Eng (6) 061007, DOI 10.1115/1.3118765
183. Moore DF, Jerusalem A, Nyein M et al (2009) Computational biology – modeling of primary blast effects on the central nervous system. NeuroImage 47:T10–T20
184. Grujicic M, Bell WC, Pandurangan B et al (2010) Blast-wave impact-mitigation capability of polyurea when used as helmet suspension-pad material. Mater Des 31(9):4050–4065
185. Grujicic M, Bell WC, Pandurangan B et al (2011) Fluid/structure interaction computational investigation of blast-wave mitigation efficacy of the advanced combat helmet. J Mater Eng Perform 20(6):877–893
186. Nyein MK, Jason AM, Yu L et al (2010) In silico investigation of intracranial blast mitigation with relevance to military traumatic brain injury. Proc Natl Acad Sci USA 107(48): 20703–20708

Compressively Pre-stressed Navy Relevant Laminated and Sandwich Composites Subjected to Ballistic Impact

Eric Kerr-Anderson, Selvum Pillay, Basir Shafiq, and Uday K. Vaidya

Abstract Assembled structures such as ship decks, walls, and masts are often times under different degrees of pre-stress or confinement. Structural composite integrity can be compromised when subjected to impacts from events such as wave slamming, tool drops, cargo handling, and ballistic fragments/projectiles. It has been shown by several researchers that when a highly pre-stressed structure is subjected to impact, the damaged area and impact response changes. The main focus of this study was the impact of compressively pre-stressed structures which can also be considered as compression-during-impact. The results showed that for various laminate configurations, there was a compressive pre-stress threshold above which impact damage caused more damage than witnessed in typical compression after impact (CAI) tests. Both fiberglass and carbon laminates pre-stressed to higher than 30% of ultimate compressive strength, failed from impact at 300 m/s; but the carbon laminates developed shear cracks above 10% of the ultimate compressive strength. The work is of benefit to naval and other composite designers to be able to account for failure envelopes under complex dynamic loading states, i.e. pre-stress and impact for various composite configurations.

Book chapter for paper presented at Office of Naval Research (ONR) Workshop/Conference, June 23–24, 2011, Instit Clement Ader (ICA), Toulouse, France, Organized by – Serge Abrate, Bruno Castanié and Yapa D.S. Rajapakse.

E. Kerr-Anderson • S. Pillay • U.K. Vaidya (✉)
Materials Processing and Applications Development (MPAD) Composites Center,
Department of Materials Science & Engineering, University of Alabama at Birmingham,
Birmingham, AL 35294, USA
e-mail: uvaidya@uab.edu

B. Shafiq
Department of Engineering, University of Puerto Rico at Mayaguez,
Mayaguez, PR, USA

S. Abrate et al. (eds.), *Dynamic Failure of Composite and Sandwich Structures*,
Solid Mechanics and Its Applications 192, DOI 10.1007/978-94-007-5329-7_4,
© Springer Science+Business Media Dordrecht 2013

Keywords Sandwich composites • High velocity impact • Pre-stress • Compression

1 Introduction

Composite structures continue to replace steel structures on naval vessels in order to create lighter and often more cost effective structures. Fiberglass offers operational accessibility that steel and aluminum cannot compete with due to the near elimination of maintenance costs. Steel naval vessels must undergo extensive inspection and maintenance regiments each year while in a corrosive marine environment. Attempts have been made to reduce the weight of some steel naval vessels by replacing steel components with aluminum, which resulted in costly maintenance and replacement. The high cyclical swaying loading provided by ocean waves caused severe stress corrosion to develop in the aluminum structures. Large cracks formed over short periods of time which resulted in fracture. An additional drawback of aluminum has been the drastic structural strength loss during fires. Fiberglass naval vessels have been widely used as minecountermeasure vessels in which typical construction methods included the use of a framed single skin design, an unframed monocoque design, and a sandwich hull utilizing a thick polyvinyl chloride (PVC) foam core. The 73 m long Visby class corvette was the first naval ship to incorporate large amounts of carbon fiber into its hull which is comprised of a hybrid carbon and glass fiber polymer laminate covering a PVC foam core. Some designs range in weight savings between 20 and 60%. The reduction of weight allows for better performance in the form of speed or reduced fuel consumption. The reduction of weight also provides additional cargo or payload capacity. Other benefits include radar and magnetic transparency; yielding stealthier ships less susceptible to prevalent magnetic mine attacks [1]. A comprehensive understanding is required to establish optimal weight savings in terms of damage caused by blast waves, ballistic impact, and fire. This study examined the synergistic effect of compressive pre-stress and impact to determine if load bearing structures would be able to withstand ballistic impact.

Laminated and sandwich composites are susceptible to impact damage from events such as tool drops, wave impacts, bullets/fragments, and log debris strikes to name a few [1–3]. The impact damage typically follows a conical profile illustrated in Fig. 1 primarily in the form of matrix cracking, fiber breakage and delamination in a laminated composite.

The well-defined impact regimes for laminated composites are – low velocity impact (LVI), intermediate velocity impact (IVI), high velocity impact (HVI), and hyper velocity impact (HPI) [2–4]. LVI covers the broadest forms of impact usually involving a large mass (1–10 kg) impacting at relatively low velocities (<10 m/s). LVI events represent accidental tool drops, cargo falling, or other non-static loading scenario. IVI events typically occur between 10 and 100 m/s which range from rock debris to lower energy fragments. HVI or ballistic impact typically involves small mass projectiles, such as a 2 g 7.62 mm diameter steel sphere, traveling at high

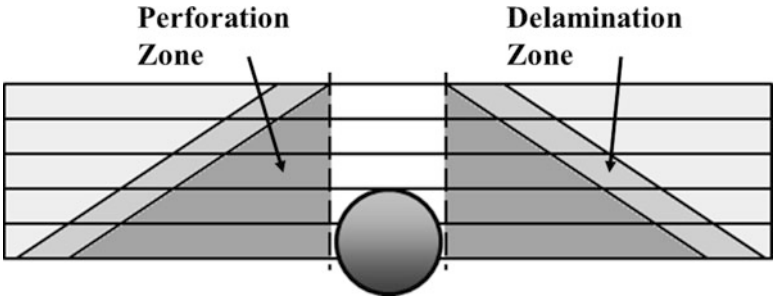


Fig. 1 Energy absorbing failure modes of ballistic impact on woven laminated composite structures

velocities (>100 m/s). HVI events include ballistic impacts, fragment, shrapnel, and debris impact [5]. HPI represents small mass meteorites impacting at velocities in excess of 2,000 m/s. The differences between the four classes are based on impact velocity, mass, and contact area which translates into imparted strain and momentum exchange deformation.

For a normal impact event with constant mass and contact area, the impact force, damage evolution, resultant strains and stresses of the target laminate are highly dependent on the impactor velocity. LVI to a laminate may cause out-of-plane deflection, but minimal fiber breakage. Most damage in this mode is in the form of matrix shearing between lamina, i.e. delamination. As the impact velocity increases, the delaminated area extends outward in a conical shape from the point of impact through the thickness to the distal face and fiber breakage may be more prevalent. The lowest velocity at which the entire thickness delaminates and the projectile penetrates the laminate is called the ballistic limit or V_{50}. As the velocity is increased further, the initial layers of material begin to shear and delamination begins afterwards, which in effect shifts the conically shaped delamination zone to an inverse funnel. If the laminate is sufficiently rigid, a high enough impact velocity causes a shear plug, leaving a relatively clean hole with little or no delamination [2–4]. It has also been observed that the conical delamination angle for a globally rigid laminate is much less than that of a somewhat flexible laminate.

Compression after impact (CAI) is one of the standard test methods to determine residual strength after impact [6–8]. It is a means to determine the compressive strength after an impact event. There have been three main CAI fixtures developed by NASA, Boeing, and Airbus. The NASA CAI test utilizes a sample with dimensions 10–12.5 × 7 × 0.25 in. for low velocity impact after which the sample is trimmed to 10–12.5 × 5 × 0.25 for compression testing [6]. The NASA fixture has no accommodation for thickness variation and uses a large amount of material. The Boeing fixture, which has been adopted as ASTM D 7137 [7], requires test samples 6 in. long by 4 in. wide and a thickness between 4 and 6 mm. The Boeing test fixture allows the most sample dimension flexibility as the thickness can be adjusted, but it provides only a simply supported contact on all edges. The side supports have a knife edge support to allow bending while the top and bottom clamps are square to

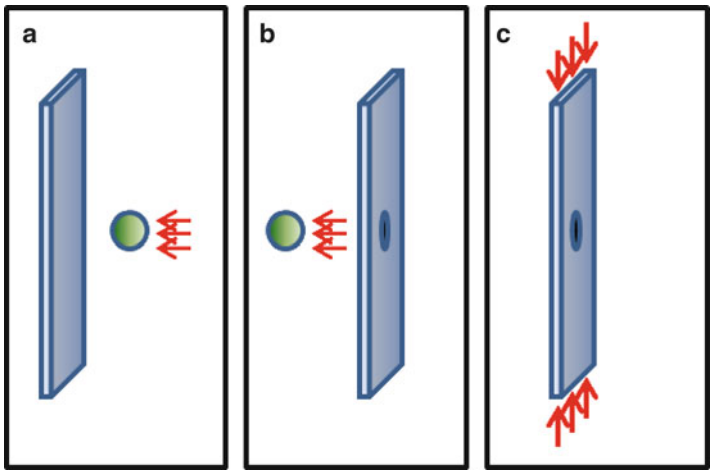


Fig. 2 Standard compression after impact (CAI) test; (**a**, **b**) sample is impacted, and (**c**) impacted sample is compressed to failure

prevent brooming. The top and bottom supports are not clamped but press fit at best. The Airbus CAI fixture utilizes a sample with dimensions 6 in. × 4 in. × 4 mm, and allows for a fully clamped top and bottom while providing a simply supported side constraint. There is no accommodation for thickness variation, but the Airbus fixture does incorporate the top support into the main fixture to force alignment, which is not accounted for with the Boeing CAI fixture. Additionally there have been some scaled up versions of the Boeing CAI test fixture to accommodate samples up to 10.5 × 10.5 in. and with longer aspect ratios as much as 17 × 4 in. [8]. All CAI data in this study was obtained using a CAI fixture consistent with ASTM D 7137 specifications. The samples are large enough to account for the damage area caused by the impact event, the sides of the sample are simply supported, and the ends are supported to prevent brooming. Figure 2 below illustrates the process of obtaining a CAI test result.

With the CAI test method, samples are impacted (Fig. 2a, b) and compressed to failure in a CAI fixture (Fig. 2c). Since no in-plane load is applied until after the impact event, no synergistic effects between impact and compression can be extrapolated from the CAI test. However, structural components are under pre-load during an impact event, which is the reason for observation of pre-stress effects during impact.

Assembled structures such as ship decks and walls are oftentimes under different degrees of compression pre-stress or confinement [9]. When a pre-stressed structure is subjected to impact, this condition can be considered as compression-during-impact (CDI). Although this is a more complex test to conduct, the results are more representative of in-field condition. Figure 3 shows the difference between CAI and CDI.

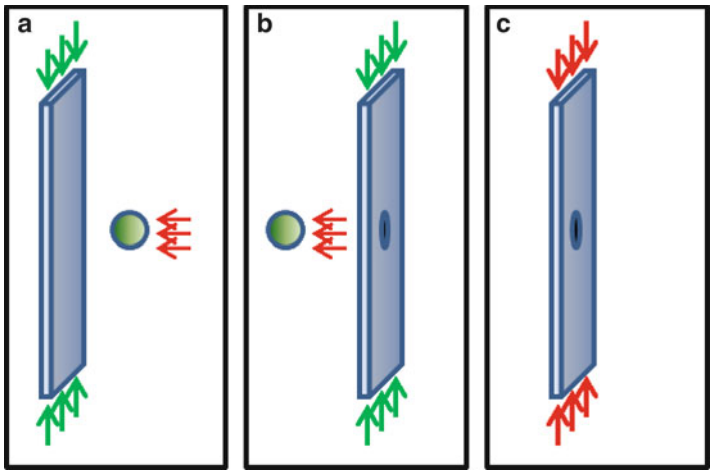


Fig. 3 Pre-stressed compression during impact (CDI) test method – (**a**) pre-stress is applied; (**b**) pre-stressed sample is impacted, and (**c**) impacted sample is compressed to failure

CDI testing involves compressing a sample prior to impact (Fig. 3a), impacting the sample (Fig. 3b), and compressing the damaged sample to failure in the CAI fixture (Fig. 3c). For both methods step (c) is the same.

Since structural composite materials are susceptible to impact events, it is important for design purposes to characterize the extent of damage caused by impact. Naval designers must be able to account for failure envelopes under a complex loading state. Several researchers have examined the residual strength after impact event to accommodate the loss in structural properties due to any anticipated impact from service use. The methods used to obtain design allowables have included residual flexural strength after impact (FAI), tensile strength after impact (TAI), compression strength after impact (CAI), strain energy density calculations, and impact under pre-stressed conditions.

Testing of impact under pre-stressed conditions requires 5× more samples than CAI testing and requires an additional 20 min per sample for installation and pre-stressing. It is preferable to have experiments replicate service conditions as close as possible to ascertain synergistic effects of loading and impact, which can be otherwise missed from post-testing an impacted sample under tension, compression, or flexure.

Lamination theory is adequate to predict failure in tension and flexure for most laminated systems [10, 11]. However, compressive strength for composite laminates has been more difficult to characterize, because models are idealized, and require difficult to attain properties. For example, it has been reported that in-plane compressive strength of a composite material can be less than a tenth of the in-plane tensile strength [11–13]. Most fiber reinforcements have a small fiber diameter (8–22 μm) to obtain enhanced tensile, bending, and torsional properties. Smaller diameters are detrimental to compressive loading. Since classical Euler buckling is directly related to the second moment of inertia, each small diameter fiber has a

very low buckling strength when compared to its tensile strength. When loaded in compression, the fibers begin to buckle and compress the matrix. The fibers begin to fail when the matrix yields and a critical buckling radius is reached.

2 Impact of Laminated Composites

There have been numerous studies of impact on composite structures. Several models have been implemented based on analytical methods [14–27]. Naik et al. [5] explored the shift in energy absorbing mechanisms when altering the impact velocity of a projectile. They confirmed that the highest amount of energy is absorbed at the ballistic limit, and proposed a momentum exchange model. Hazell et al. [24] reported that even at very high velocities (1,825 m/s) there appeared to be an asymptotic maximum delamination area threshold. Several studies have reported the impact face distortion caused at the impact contact area. In some cases, this distortion affects through the thickness profile [5, 16, 22–27].

In a pre-stress composite laminate, the momentary geometrical distortion caused by a point impact can cause it to behave differently due to the local strains causing geometrical distortion. The compressive buckling load is lower due to the increased out of plane deflection. Several approaches used to enhance compression performance under impact include:-increasing interfacial strength, increasing matrix yield strength, or decreasing the global deflection with ribbing or other reinforcing methods.

One of the main methods used to determine laminate properties after an impact event is to use a standard tensile, compression, or flexural test on impacted samples. Trudel-Boucher et al. [28] examined the effects of LVI damage on the residual flexural and tensile strengths of 3.5 mm thick cross-ply glass fiber/polypropylene composites. They observed that damage progressively increased as the impact energy increased, and at the highest impact energy of 9 J plastic deformation resulted in residual curvature. They also reported that both the normalized flexural strength and modulus decreased linearly with respect to the impact energy. Applying flexure on the non-impacted side resulted in higher flexural strength, but resulted in a pronounced drop in flexural modulus. This indicated that compression was a limiting factor for flexural strength.

Trudel-Boucher et al. [28] also showed that the normalized tensile strength was not affected until an impact energy greater than 5 J was reached, after which it decreased. The tensile modulus was not affected by the level of impact damage. O'Higgins et al. [29] suggested that insight into the damage evolution for impacted tensile specimens can be obtained from investigating the crack initiation and growth in an open hole tension test. It was seen that cracks propagated transversely from the hole until failure. It was also seen that the stress concentration decreased as higher levels of damage were attained, which resulted in higher open hole tensile

strength. Craven et al. [30] modeled a carbon/epoxy multi-directional laminate with pre-existing damage patterns under tensile loading and observed its effect on the tensile stiffness. It was found that both delamination and fiber fracture cracks must be taken into account to determine residual tensile properties. Cui et al. [31] modeled a T300/BMP-316 laminate in which tensile specimens were subjected to LVI prior to applying tensile load to capture the effect of actual damage instead of crack concentrations. The transverse crack forms at the boundaries of the delaminated zone and then propagates outward until failure. The error associated with this method for both damage area and residual tensile strength was less than 10%.

3 Residual Strength of Laminated Composites

There have been numerous studies on the residual compressive strength after impact of composite laminates, because impact damage can reduce the residual compressive strength to as low as one tenth the ultimate strength for carbon/epoxy and one third for E-glass/epoxy laminates. Several authors have shown that decrease in compressive strength is directly correlated to the impact damage area. Since the impact damage area is highest at the ballistic limit, the compressive strength decreases as a function of impact velocity, and reaches an asymptotic value at the ballistic limit. CAI samples are first impacted which forms the frustum shaped damage area associated with non-pre-stressed impact shown in Fig. 1. The impact damage causes a stress concentration to form with the applied compressive load at the edge of the delaminated area perpendicular to the applied load. It has been shown that a linear elastic fracture mechanics approach can be used to determine limiting loads that cause crack growth [2, 32]. Shear cracks propagate outward from the point of impact quickly to the edge of the delaminated area, then slowly continue to propagate until catastrophic failure occurs. Gillespie Jr. et al. [33] showed that stitching of sandwich panels and cross-ply laminates created marginal improvements in the CAI strength. Zhou et al. [34, 35] examined preconditioned laminates with embedded films to replicate delamination damage. Oval, rectangular, and circular delaminations were created at multiple locations through the thickness of the laminate. Comparisons were made between open hole, impact damaged and preconditioned residual compressive strengths.

Several authors have researched the CAI strength of sandwich composites, where several additional failure modes occur associated with the core. Williams et al. [36] used a modified CAI fixture and CFRP laminates containing hollow glass fibers filled with uncured resin. Samples were impacted, subjected to a curing cycle to heal the damaged area, and residual strengths were obtained using a CAI test. The study concluded that an impacted laminate could retain a majority of its original strength via this method. Aoki et al. [37] showed that hygrothermal conditions can drastically affect the CAI strength. The wet samples had a lower T_g than dry samples, and when CAI was conducted above the T_g of the matrix, compressive properties dramatically

decreased. This study indicated that the yield strength of the matrix has a dominant effect on the compressive strength of a laminate.

4 Strain Rate Sensitivity

When characterizing damage caused by an impact event, the determination of strain rate sensitivity for a material is critical. Daniel et al. [38], Xiao et al. [39], and Brown et al. [40] have conducted strain rate sensitivity studies on composite laminates and observed that, as the strain rate increases, the modulus and strength increase, but the strain to failure decreases. LS-DYNA's MAT 162 [41] utilizes strain rate sensitive strength and modulus functions as given by:

$$\{S_{RT}\} = \{S_0\}\left(1 + \frac{C_{Rate}\ln\{\dot{\bar{\varepsilon}}\}}{\dot{\varepsilon}_0}\right) \tag{1}$$

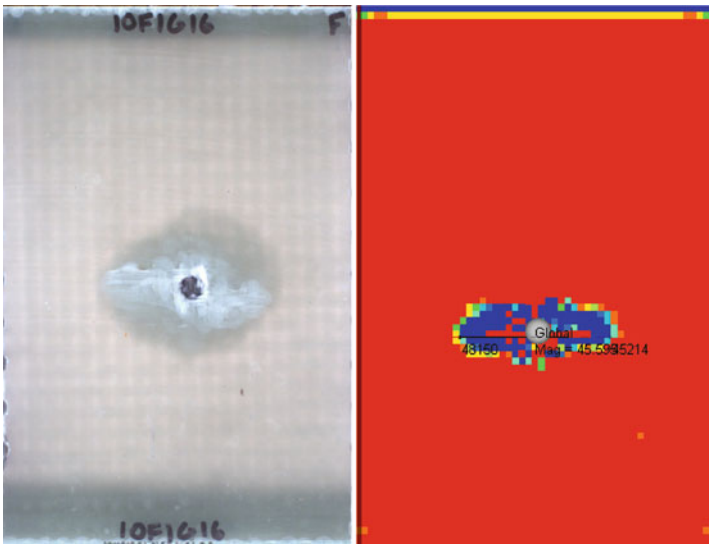
$$\{E_{RT}\} = \{E_0\}\left(1 + \frac{C_{Rate}\ln\{\dot{\bar{\varepsilon}}\}}{\dot{\varepsilon}_0}\right) \tag{2}$$

where the rate coefficient is a user defined input used to fit data regressions. Based on the work done by Matzenmiller et al. [42], this method is important for pre-stressed materials, because although the initial loading is quasi-static the impact event and initial failure upon impact is a dynamic event. As discussed by Abrate [2], the shear, compressive, and tensile waves produced at an impact site repeatedly travel back and forth through the laminate, prior to any distortion. When failure takes place, the recoil force causes damage at a higher strain rate than the loading rate. The result of which is a laminate failing at a lower strength than anticipated from standard residual strength test methods. Preliminary studies by the authors have shown that the strain sensitivity functions of MAT 162 can be used to effectively model the impact under compression damage as shown below in Figs. 4 and 5.

The resultant front face damage area of a fiberglass laminate pre-stressed to 190 MPa impacted by a 2 g 7.62 mm diameter steel sphere at 120 m/s had an 8.8% error between the experiment and model, for the front face crack length.

5 Impact Under Pre-load

Several researchers examined impact while under a pre-load. These investigations include – analytical models, FEA, biaxial loading under impact, compression under impact, torsion/shear under impact, flexure under impact, and tension under impact. Sun and Chattopadhyay [43] studied central impact of a mass on a simply supported plate. They analytically determined that the contributions of pre-



Figs. 4 and 5. Pre-stressed impact damage area of experimental (*Left*) compared with the finite element analysis (*Right*)

stressed tension on an impacted composite reduced the deflection, bending stress, shear force, and energy absorption due to impact. Rossikhin and Shitikova [44] used a ray series approximation and linearized Hertzian contact deformation to analytically determine the effect of in-plane compressive pre-stressed orthotropic circular plates under normal low velocity impact. It was analytically shown that a compressive pre-stress will soften the impact response and cause greater out-of-plane deflection. It was shown that shear locking occurs at the compressive critical magnitude, which attenuates the transverse shear wave similar to Landau attenuation witnessed in highly compressed gases. Zheng and Binienda [45] analyzed laminated plates which were simply supported and impacted using a linearized elastoplastic contact law and shear deformable plate theory. The contact force history was not affected by prestress, but it was found that pre-stress significantly affected the out-of-plane deflection. Pre-tension reduced the deflection and pre-compression increased deflection. Rossikhan and Shitikova [46] went on to determine the impact response generalized non-dimensional equations for transversely isotropic plates with compressive pre-stress. It was found that as the compressive force increased due to impact, the shear wave was attenuated. The concentrated absorbed energy was closer to the impact site which caused more damage. The studies showed that additional compressive pre-stress caused more deflection and less contact force.

Schoeppner and Abrate [22] examined the Air Force Research Laboratory (AFRL) database and found that for AS4/3501-6 graphite/epoxy laminates subjected to a tensile pre-load up to 2,400 $\mu\varepsilon$ and impacted up to 4.2 m/s caused no significant difference in the delamination threshold limit. Khalili et al. [47] used

Sveklo's elastic contact theory to determine analytical results for an impact under both uniaxial and biaxial tensile pre-stress. It was determined that the maximum impact force increased and central deflection increased as the tensile pre-load increased. For the unidirectional carbon fiber laminate analyzed, the transverse pre-stress caused more of the aforementioned effects than the longitudinal pre-stress. Biaxial pre-stress resulted in the most impact force increase and central deflection decrease. Garcia-Castillo et al. [48] conducted a study in which the ballistic limit of 1.5 mm thick aluminum samples was determined in the unloaded and 38% pre-loaded tensile state. There was no discernible difference in the ballistic limit, but it was witnessed that the pre-loaded samples catastrophically failed upon impact while the unloaded samples did not fail.

Minak et al. [49, 50] investigated carbon fiber epoxy cylinders which were pre-stressed in torsion prior to LVI. They reported that the torsional pre-load did not change the delamination initiation though it aids in the delamination propagation. High torsional pre-load resulted in more delamination propagation, lower critical buckling loads, and lower residual torsional strength. Catastrophic failure resulted in some cases. Mizukawa et al. [51] created a fixture which allowed torsion and bending to be applied to thin walled tubes while being impacted by a drop tower. They found that there was a synergistic effect between the apparent torsional stress and apparent bending stress when under impact. Kepler and Bull [52] conducted tests on sandwich panels subjected to global bending while ballistically impacted. They found that under applied bending loads, the impact caused catastrophic shear cracking that was non-existent without the applied bending. Kulkarni et al. [53] conducted a drop tower study on plain woven fiberglass samples which were pre-stressed by pressurizing the distal side of the laminate up to 0.9 MPa. No discernible difference was witnessed in the range of pre-stress tested.

Robb et al. [54] conducted drop tower studies on biaxially pre-loaded chopped E-glass polyester laminates. It was found that the most damage, least contact force, and least contact duration were caused in a biaxially loaded tension/compression state. Tensile pre-stress caused stiffening while compressive pre-stress caused softening. Whittingham et al. [55] tested carbon fiber epoxy laminates under realistic biaxial pre-stressed loads witnessed in the field. It was found that within the realistic biaxial pre-stressed state, no discernible difference was witnessed. Mitrevski et al. [56] examined the effect of impactor shape on the biaxially pre-stressed impact of E-glass/polyester laminates. As the contact surface of the impactor shifts from cylindrical to spherical to conical, the maximum deflection and absorbed energy increased. At the levels of pre-tensioned biaxial impact tested, no discernible differences of damaged area were observed. Garcia-Castillo et al. [57] conducted studies on woven glass/polyester laminates subjected to high velocity normal impact under both uniaxial and biaxial tensile pre-stress. It was determined that the biaxially preloaded samples had a slightly higher ballistic limit, but for the range of preload tested there were no discernible differences in the energy absorbing terms of primary yarn, secondary yarn, kinetic energy cone, delamination, and matrix cracking. Loktev [58] studied spherical impact on a pre-stressed orthotropic Uflyand-Mindlin plate using a Legendre polynomial and Laurent series expansion. It

was determined that pre-tensioned samples had a higher contact force and duration, while the pre-compressed laminates had a lower contact force and duration. A positive pre-stressed moment caused a stiffening response and dramatically reduced the contact duration.

Finite element model (FEM) analysis has been conducted on the impact response on pre-stressed laminates. Mikkor et al. [59] used PAM-CRASH to analyze ballistic failure of pre-stressed laminates. Their findings show that at higher tensile pre-stress, failure occurs higher than a critical impact velocity. Choi et al. [60, 61] examined in-plane pre-stress with the FEM method and experimental results to determine that tensile pre-stressed caused a faster impact response while compressive pre-stress induced a slower response. Ghelli and Minak [62] studied the effect of membrane pre-loads through FEA. It was shown that tensile pre-load increased the peak stress while the compressive pre-load reduced the peak impact stress.

Herzl Chai [63] conducted LVI testing on stiffened carbon/epoxy panels pre-stressed in compression. A 0.5 in. diameter aluminum sphere impacted the pre-stressed laminates up to 400 fps. It was determined that shear cracks leading to catastrophic failure developed at 30% of the ultimate compressive strength. Equations were derived based on a strain energy density analysis which accurately modeled the failure phenomenon of impact under compression. McGowen and Ambur [64] conducted compressive pre-stressed impact on graphite/epoxy sandwich panels with honeycomb cores. Similar results were achieved as Chai in which pre-stressed samples caused failure upon impact at high levels of pre-stress. Zhang et al. [65] also compressed laminates prior to impact and found that failure can result if the compressive pre-stress is too high during impact. Varying buckling shapes at impact were compared. Herszberg and Weller [66] conducted studies for impact under compressive pre-loads on stitched and unstitched carbon/epoxy laminates. Catastrophic failure was also found at high pre-stress levels when impacted. Stitching was found to dramatically reduce the impact damage area, though it had no effect on the penetration velocity or catastrophic failure thresholds. Heimbs et al. [67] impacted compressively pre-stressed carbon/epoxy laminates and observed catastrophic failure witnessed by the aforementioned researchers. The quasi-isotropic laminates exhibited damage reshaping as pre-stressed conditions increased. Additionally LS-DYNA was used to corroborate the results. Pickett et al. [68] conducted a study using a significantly longer sample to apply in-plane compressive pre-stress during drop tower impact. The carbon/epoxy laminates exhibited transverse cracks when impacted at high pre-stress. PAM-CRASH was used to validate the witnessed failure modes.

Wiedenman and Dharan [69] investigated samples of G10 glass of varying thicknesses compressed to different levels and penetrated with a 5.56 mm projectile with the equivalent of an M4 carbine. A CAI fixture and portable MTS load frame were used to apply in-plane compressive load. It was found that the combination of impact and compressive strain was much more detrimental than that of impact alone. They also observed a delamination reshaping to damage more of the structure perpendicular to loading and shear kink band formation due to impact. There was no account for the increased deflection which would be present in thinner samples.

The authors found good agreement when using the model presented by Starnes et al. [70].

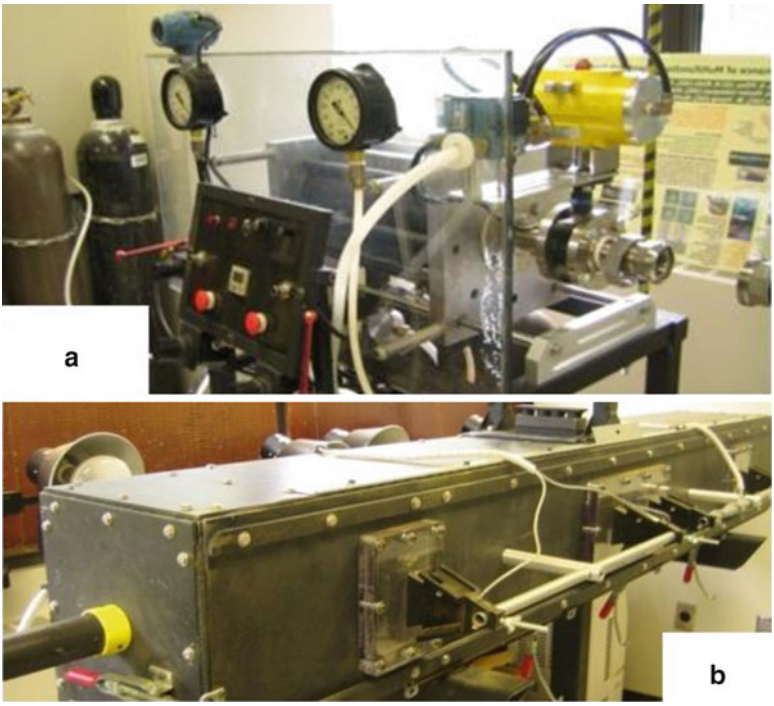
The database for complex loading of polymer matrix composites is sparse. Predictive models have been implemented with some success to help fill the gap for the lack of test data, but to truly understand the failure strength of a laminate configuration a large amount of exploratory testing must be conducted. Testing conducted closest to the service loading witnessed at failure would yield more accurate failure thresholds and allow existing models to be supplemented. The work done on pre-stressed composites by the authors provides additional insight into failure modes that could be witnessed by structural composites subjected to an impact event. By understanding the failure mechanisms and failure thresholds, improved predictive models can be developed for use by naval designers. The value to naval designers would be the reduction of required safety factors by removing some of the uncertainty associated with complex loading. A reduced safety factor would allow for an optimized structure, which by further reducing vessel weight would result in increased naval vessel performance.

6 CDI Fixture Design

For the purpose of evaluating realistic residual strength after impact, studies were conducted by the authors to characterize the synergistic effect of impact under pre-stressed in-plane compression for woven glass/vinyl ester (VE) composite laminates. The ballistic impact equipment used was a custom built gas gun allowing for spherical ball rounds up to 12.7 mm (0.5 in.) diameter to be fired up to 350 m/s. The equipment illustrated in Figs. 6 and 7 and 7 uses compressed helium to propel a machined foam sabot housing a projectile down the barrel [71]. The sabot breaks apart when it strikes the stripper plate and the projectile continues to propel to the sample. Velocity measurements were attained from two sets of Oehler Model 35 proof chronographs with the Oehler Skyscreen III photo detectors.

The compression during impact (CDI) fixture used to conduct pre-stressed testing was designed, machined, and manufactured in-house, see Fig. 8. The CDI fixture fits inside the capture chamber dimensions of 304 mm × 292 mm × 100 mm ($12'' \times 11.5'' \times 4''$).It is completely replaceable when required, and effectively applies uniform, in-plane compressive loads of up to 300 kN. Load is applied with a 30 t low-clearance hydraulic cylinder as shown in Figs. 8 and 9. The hydraulic cylinder used was a manually operated unit retrofitted with both a psi gage and a pressure transducer which allowed monitoring of the applied load before and after impact.

All of the components of the CDI fixture are attached with bolts. The fixture was designed so that the hydraulic cylinder was placed outside the capture chamber, and a load transfer block is used to both apply load to the sample and mimic the clamped end condition used in the CAI test fixture. The samples are constrained in-plane by two adjustable ½" plates shown in Fig. 9, which allowed a slip-fit to be



Figs. 6 and 7 Gas Gun (**a**) and (**b**) Capture Chamber

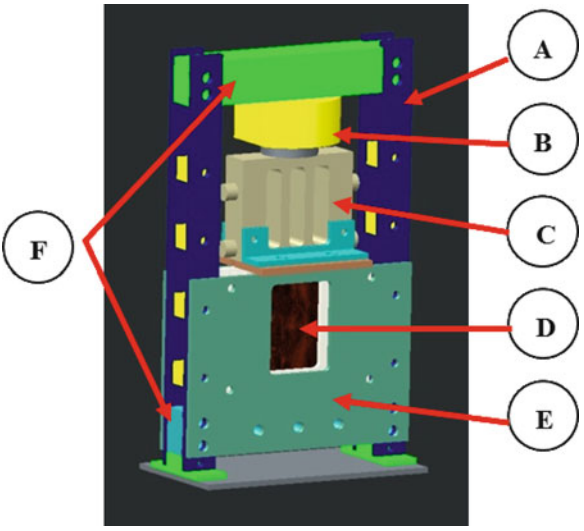


Fig. 8 CDI fixture. A: *vertical* support bars, B: hydraulic cylinder, C: load transfer block, D: sample, E: *front* and *back* support plates, F: *top* and *bottom* support bars

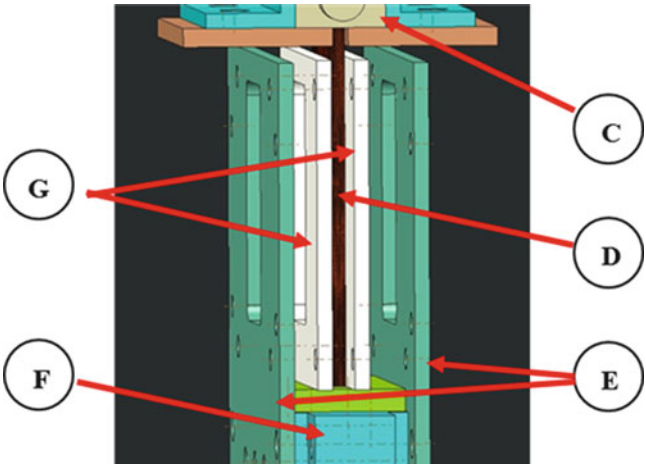


Fig. 9 *Side view* of CDI fixture – C: load transfer block D: sample, E: *front* and *back* support plates, F: *bottom* support bar, and G: inner slip-fit support plates

achieved. The bottom and top support bars are made from 2 in. square steel bars, and an exchangeable contact plate is used to provide for testing flexibility.

7 Procedure and Material

Samples were made via a VARTM process and machined to $4'' \times 6''$ rectangular samples for CDI testing. Samples were installed in the CDI fixture and a load was applied. The sample was given at least 30 s to relax prior to impact. All samples in this study were impacted with a 0.3 in. steel sphere weighing 2 g at velocities ranging from 75 to 350 m/s. After impact, the load was released, back-lit photography was adopted, and samples were compressed to failure in an ASTM CAI fixture. Samples tested included 6 mm thick woven orthotropic E-glass/VE laminates, 4.2 mm thick woven orthotropic E-glass/VE laminates, 6.2 mm thick quasi-isotropic E-glass/VE laminates, sandwich panels made of 3.1 mm thick quasi-isotropic E-glass/VE face sheets with a 50.8 mm thick HP 130 divinyl cell foam core, and 3.4 mm thick orthotropic carbon fiber/VE laminates.

8 Results and Discussion

The effect of compressive pre-stress on the residual strength of a 6 mm thick E-glass/VE composite laminate is shown in Fig. 10 [72]. Each series represents the level of in-plane compressive pre-stress the laminate was subjected to when im-

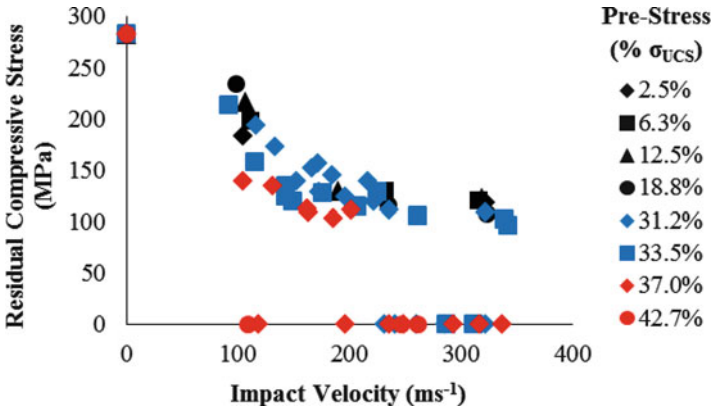


Fig. 10 Effect of compressive pre-stress on residual strength after impact

pacted. Five samples tested in accordance with the Combined Loading Compression (CLC) ASTM D6641 [73] yielded an ultimate compressive strength, σ_{UCS}, of 377 (±40) MPa.

At higher loading levels (31.2, 33.5, 37.0, and 42.7% σ_{UCS}), samples failed compressively when impacted at velocities higher than 225 m/s. These samples are displayed along the x-axis of Fig. 10, since their residual strength was zero. These samples failed because the impact event damaged enough material where the remaining cross-sectional area was unable to sustain the applied load. The effect of changing the geometrical loading of compression due to the instantaneous out of plane distortion caused by the impact event causes this failure. The point at 0 m/s was determined from baseline compression tests of unimpacted samples using the CAI fixture. The baseline compressive strength found using the CAI fixture was 280 MPa, which was much less than the ultimate compressive strength obtained from CLC testing. The CLC fixture [73] utilizes a much shorter span length of 12.7 mm and larger grip lengths of 64 mm in comparison to the CAI fixture [7] which has a span length of roughly 137 mm and grip lengths of 8 mm. The CAI fixture does not adequately constrain samples to be used for determining ultimate compressive strength.

Statgraphics [69] was utilized to determine empirical best-fit regression. The correlation was in found to fit the form:

$$\sigma_{Residual} = 0.75\sigma_{UCS} - B\sqrt{(V_{Impact})} \tag{3}$$

The model indicates that the residual compressive strength can be derived by subtracting from the compressive ultimate strength, B, times the square root of the impact velocity. The coefficient B which is unique to each loading level is derived from the constituents of the sample and the amount of pre-stress. Each regression passed an ANOVA analysis with a 95% confidence level. The comparison of these

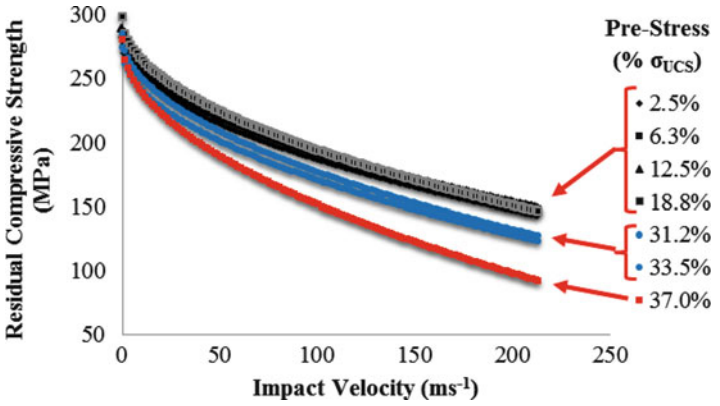


Fig. 11 Effect of pre-stress on residual strength after an impact (regression line comparison)

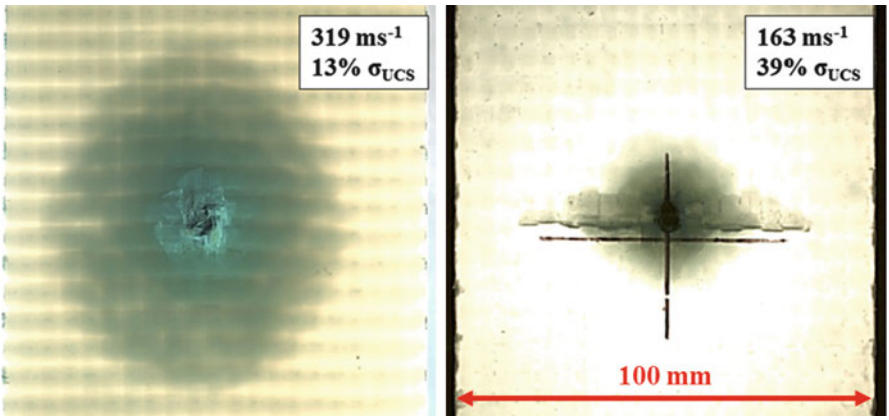
regressions, as seen in Fig. 11, indicated that there is little statistical difference in the first four loading levels. Residual strength decreased as the loading increased in the range of 31% up to 37%, which implied that there was an increase in transverse cross-sectional damage.

Regressions were only plotted up to 225 m/s due to the failure witnessed at higher impact velocities. The pre-stress level of 42.7% was not plotted, because all samples failed due to impact. This drop in residual strength was observed to be due to an impact induced shear crack (IISC) on the front face of the laminate. The IISC was similarly seen in studies by Kepler et al., Chai, and Wiedenman et al. [48, 59, 65]. The length of the IISC increased with increase in impact velocity as illustrated in Figs. 12 and 13. It was also observed that as the IISC increased in length, the delamination area increased. With increase in IISC, an additional conical delamination zone develops whose base is in the front face of the composite. This base is elliptical in nature following the profile of the IISC. For nominally thick laminates – such as 4 mm or greater for woven glass/VE, the total delamination area resembles a distorted yo-yo or an hourglass on its side.

The damage evolution resulting in a set of glass/VE laminates from increasing the impact velocity and compressive pre-stress is shown in Fig. 14. The lighter images are back-lit samples showing the delamination damage. The darker images are front lit samples showing the formed IISC. All pictures are at the same magnification. Impact velocity increases from top to bottom, and compressive pre-stress increases from left to right in the figure.

The formation of an IISC is clearly visible for the higher pre-stressed samples, and failure can be seen at high compressive pre-stress and at higher loading combinations.

By plotting the residual strength as a function of the length of the compression initiated crack in Fig. 15, a strong correlation is obtained linking the front face crack length to a decrease in the residual strength (i.e. cross-sectional area). A further



Figs. 12 and 13 Development of a front face crack due to high pre-stress. (*Left*) displays a typical conical delamination zone; (*Right*) shows a developing conical delamination zone with the addition of an IISC on the Front Face

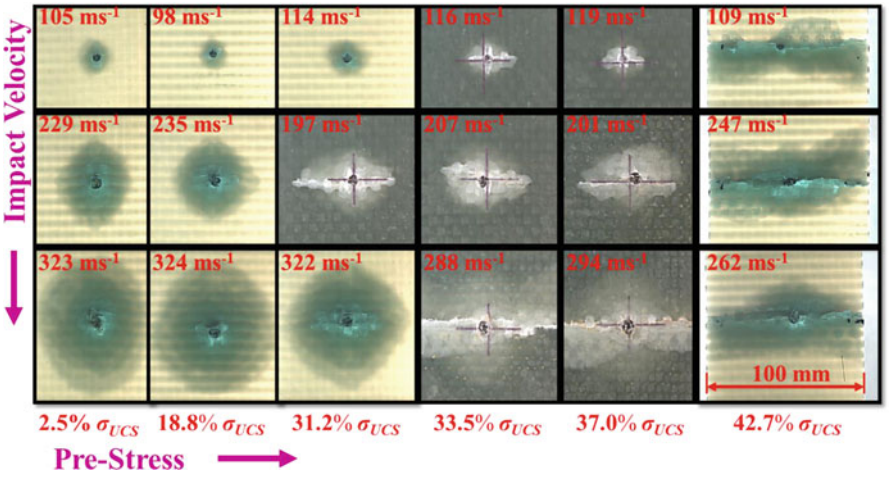


Fig. 14 Evolution of damage from increased compressive pre-stress during ballistic impact

ANOVA analysis validated the correlation. When the crack length becomes too large, the sample fails in compression.

Since the crack length directly correlates with the residual strength, it is inferred that a front face crack denotes damage throughout the thickness of the composite. Figure 16 shows the samples failed due to impact. Failure was caused by a compressive pre-stress, but it was also observed that the synergistic effect of pre-stress and impact was more detrimental. Failure mode envelopes are observed in which typical conical damage occurs, an IISC is formed, and that IISC extends far

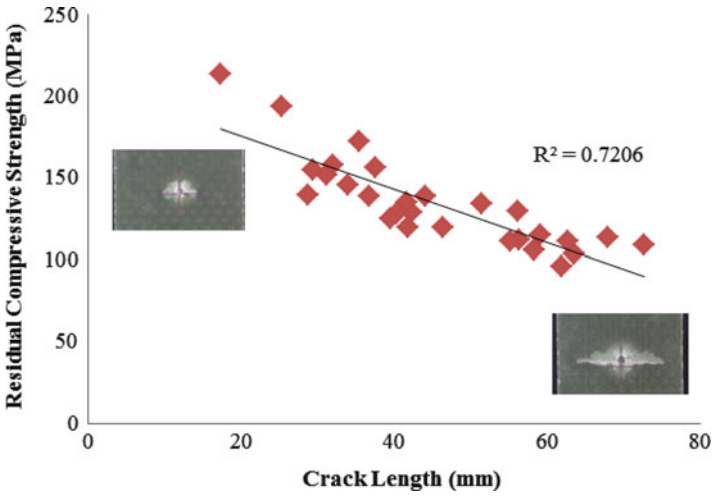


Fig. 15 Effect of front face IISC length on residual strength

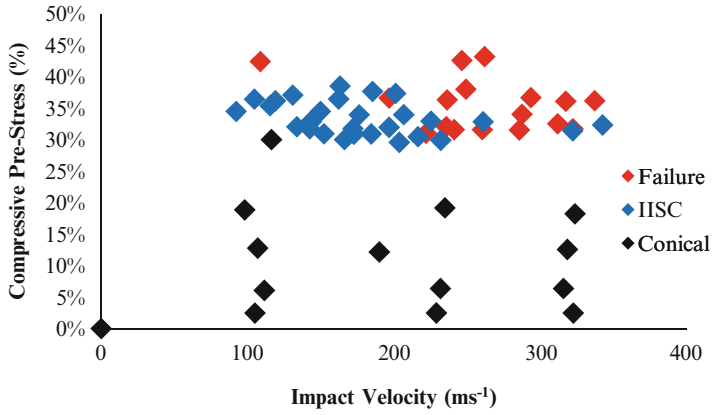


Fig. 16 Effect of compression and impact on failure mode type

enough to cause failure. The data from Fig. 16 is used to create failure threshold envelopes shown in Fig. 17.

These envelopes can be used to determine when it is safe to use predictive models for conical delamination, when additional safety factors may be needed, and when failure will occur.

Figure 18 is a contour plot displaying the combined effect of compression and impact on the residual compressive strength attained from CAI testing. Combined with the results from Figs. 11, 12,13, 14, 15 and 16, it is seen that more transverse damage in the form of an IISC is created as a laminate is impacted under higher

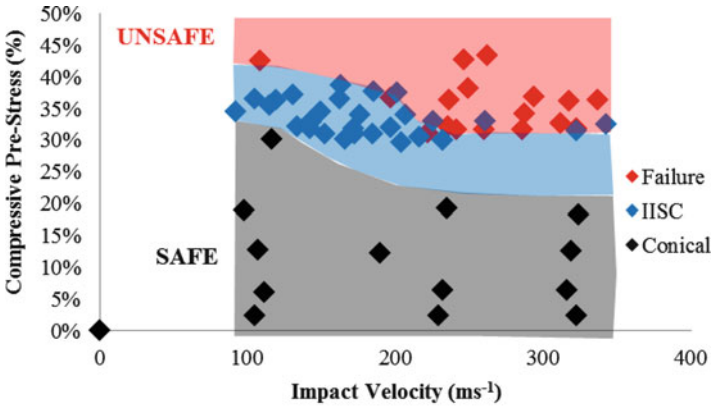


Fig. 17 Failure threshold envelopes

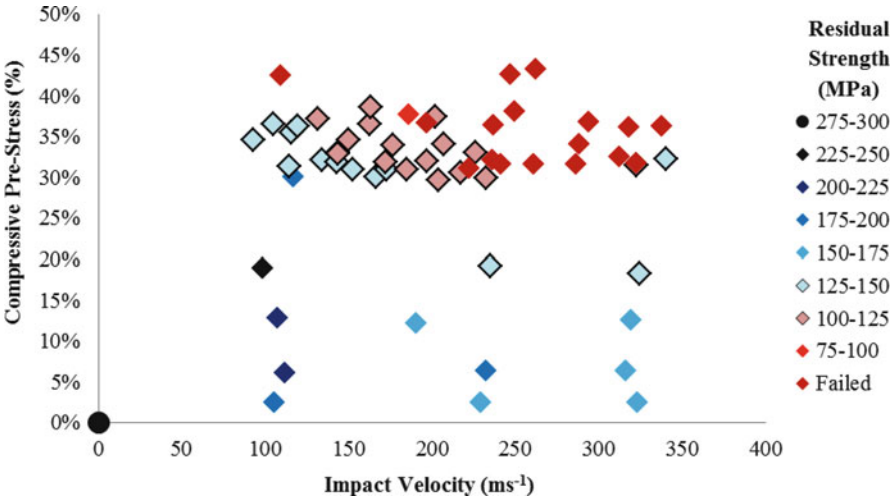


Fig. 18 Synergistic effect of compression and impact on the residual compressive strength of damaged GFRP

compressive pre-stress. For an impact velocity of 100 m/s, Fig. 18 displays that at low levels of compression there is very little change in the residual strength, but as the pre-stress is increased the residual strength reduces. Correlating these results with Fig. 17, it can be seen that the reduction in residual strength is directly linked with the formation of an IISC. The impact velocity also has a strong effect on the length of such a shear crack and the residual strength of the GFRP laminate.

Likewise, the penetration chart below in Fig. 19 designates the observed penetration of the compressed laminates. It was observed that for the samples tested thus far, none of the samples were fully penetrated at the tested impact velocities.

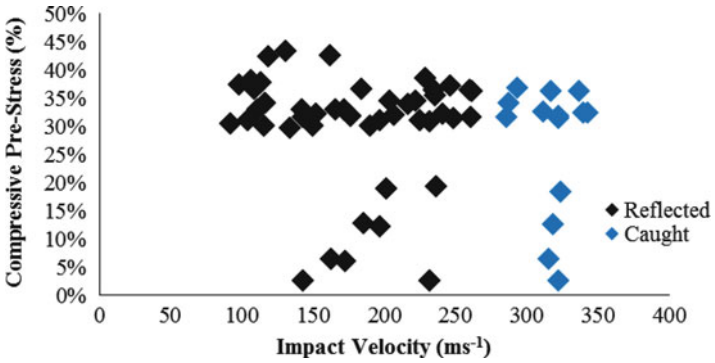


Fig. 19 Penetration chart for 100 mm × 150 mm (4″ × 6″) samples based on pre-stress and impact velocity

It may be noted that partial penetration only occurred at higher velocities. Based on the initial results, penetration does not seem to be effected by the synergistic effect of compression and impact indicating that the IISC formation occurs prior to penetration. Naik et al. have shown that the friction force between projectile and laminate absorbs significant amount of energy [5]. If the IISC had formed after penetration, more energy would be absorbed from the increased friction forces when pre-stress was applied and the ballistic limit decreases.

Similar studies have been conducted for other data sets including a 4.2 mm thick woven orthotropic E-glass/VE laminates, 6.2 mm thick quasi-isotropic E-glass/VE laminates, sandwich panels made of 3.1 mm thick quasi-isotropic E-glass/VE face sheets with a 50.8 mm thick HP 130 divinyl cell foam core, and 3.4 mm thick orthotropic carbon fiber/VE laminates [70]. The failure threshold envelopes associated with each of these data sets are shown below in Fig. 20.

The failure threshold envelopes remain relatively the same for E-glass/vinyl ester laminates. The carbon fiber data set showed a significant reduction in relative failure strength when compared to the E-glass fiber data set, which can be attributed to strain rate sensitivity associated with carbon fibers. Figure 21 shows the difference in damage evolution for the various data sets.

There was little difference between damage resulting in seven and ten layer orthotropic configurations. The ±45° contribution in the quasi-isotropic laminate displays damage biasing in both the delamination and IISC. The quasi-isotropic sandwich panel showed a more unique failure mode showing biased delamination and a thicker IISC.

Since the compressive modulus of the laminate facesheets and foam core differ and they are bound by a weaker interface, some barreling or tendency towards barreling occurs during loading. When the front laminate is impacted and penetrated, it is adequately supported by the core and associated impact deformation/delamination is reduced. The load carried by the delaminated front face is transferred to the surrounding undamaged material and the back laminate. The projectile is also

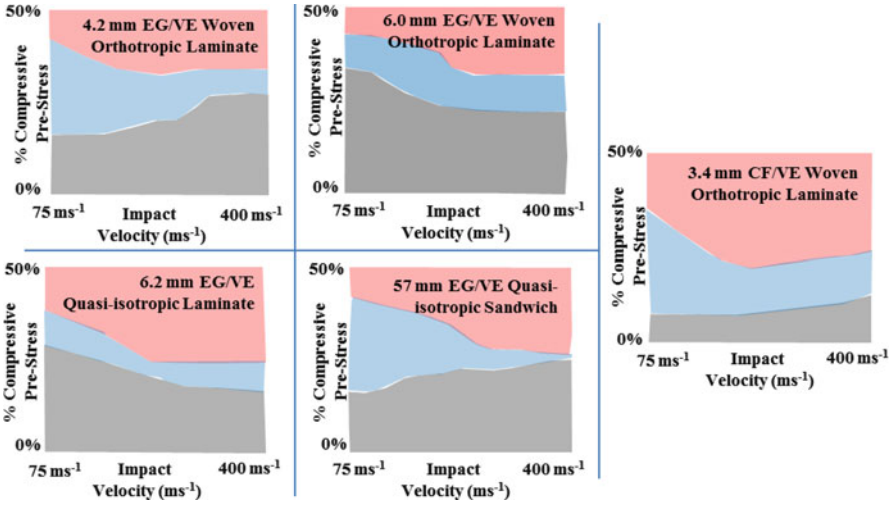


Fig. 20 Comparison of the failure threshold envelopes for various laminate configurations

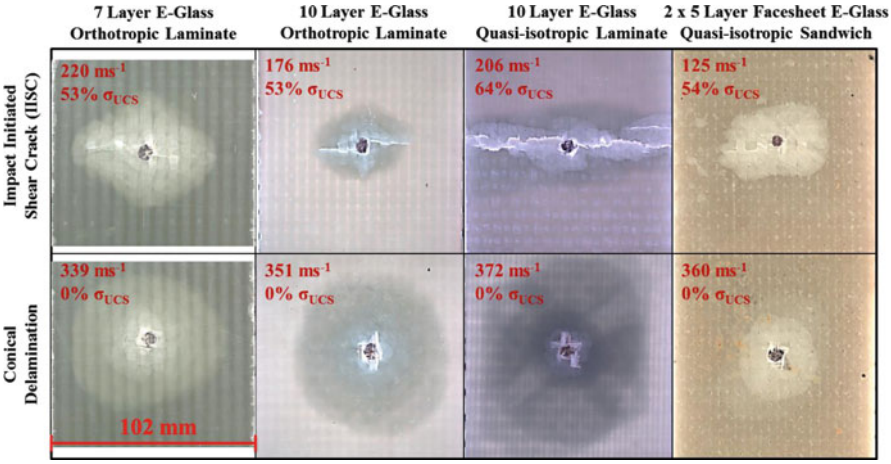


Fig. 21 Damage evolution effect of laminate configuration

significantly slowed down from penetrating the front facesheet. When the back facesheet is impacted, the projectile is moving slower which produces more damage if slightly less than the ballistic limit. The back facesheet is under a locally higher pre-stress due to the loss of structural integrity of the front facesheet. The back facesheet is also not supported by anything other than the interface and is essentially a five layer thick laminate with a much lower buckling load than the sandwich panel. All of these conditions lead to large delamination on the back facesheet. The structural failure associated with the back face damage is then passed back to the front which will force shear cracks to propagate if the stress concentration is

too high. Sandwich panels offer some of the most beneficial aspects for structural composites, but the addition of a foam core has many unintended consequences that must be accounted for during design.

It should be noted that many factors affect both compression and impact of composite structures to cause uncertainty. The information presented is intended as a guide to designers of what to expect to see when a structure is loaded too high and impacted. Considerable additional testing is required to be able to use such a threshold diagram for design purposes. The general trends have been established and presented by this and other works. Various factors have to be taken into account, such as percent strain, some span to thickness ratio, and percent ultimate stress to establish standard design guidelines for laminates impacted during compression.

9 Conclusion

This study provided some insights into the failure modes and safety thresholds of navy relevant composites in regards to ballistic impact when subjected to different degrees of in-plane compressive pre-stress. It was observed that beyond a threshold combination of impact velocity and degree of pre-stress, the shape of the damage changes from circular to elliptical leading to catastrophic damage. Failure was witnessed using the impact under compression test method which was not accounted for by standard CAI test methods. Failure envelopes for the combined effects of pre-stress and impact have been developed for orthotropic glass/vinyl ester laminates, quasi-isotropic glass/vinyl ester laminates, quasi-isotropic glass/vinyl ester sandwich composites, and carbon/vinyl ester laminates. Although the testing of the CFRP system was sparse, it indicated that a GFRP system would be better suited to structural application in compression, subject to ballistic impact. Since the ultimate compressive strength of a composite system is dependent on thickness, boundary conditions, and lay-up, it is difficult to pinpoint a safety threshold, but in this case the safety threshold for the orthotropic GFRP was 30% σ_{UCS}, quasi-isotropic GFRP was 40% σ_{UCS}, quasi-isotropic GFRP sandwich panel was 40% σ_{UCS}, and the orthotropic CFRP was 15% σ_{UCS}. Based on these results, the weight savings would not justify the use of the more expensive CFRP system for structural composites in an environment of ballistic threat. A significant amount of work is left to be done in this field relating to effectively modeling the residual strengths of pre-stressed impact for composite structures. A framework has been established to conduct such testing, but at present a constitutive model is yet to be developed.

Acknowledgements We are grateful to support from the ONR Solid Mechanics program managed by Dr. Yapa D.S. Rajapakse, Office of Naval Research. Some aspects of the compression fixture for crashworthiness studies were funded through the Department of Energy, Graduate Automotive Technology Education (GATE) program and we gratefully acknowledge this support.

References

1. Mouritz AP et al (2001) Review of advanced composite structures for naval ships and submarines. Compos Struct 53(1):21–42
2. Abrate S (1998) Impact on composite structures, 1st edn. Cambridge University Press, Cambridge
3. Vaidya UK (2011) Impact response of laminated and sandwich composites. Courses Lect Int Cent Mech Sci 526:97–192
4. Bartus SD, Vaidya UK (2005) Performance of long fiber reinforced thermoplastics subjected to transverse intermediate velocity blunt object impact. Compos Struct 67(3):263–277
5. Naik NK, Shrirao P (2004) Composite structures under ballistic impact. Compos Struct 66 (1–4):579–590
6. NASA reference publication 1092 (1983) Standard tests for toughened resin composites. Langley Research Center, Hampton, Washington, DC: National Aeronautics and Space Administration pp 1–6
7. ASTM D 7137 (2005) Standard test method for compressive residual strength properties of damaged polymer matrix composite plates. American Society for Testing and Materials, West Conshohocken
8. Adams D (2007) Testing tech: compression after impact testing. High-Performance Composites Nov: 4–6
9. Critchfield M, Judy T, Kurzweil A (1994) Low-cost design and fabrication of composite ship structures. Mar Struct 7(2–5):475–494
10. Chamis CC, Lewis Research Center (1984) Simplified composite micromechanics equations for strength, fracture toughness, impact resistance and environmental effects. Lewis Research Center, Cleveland, NASA TM-83696
11. Agarwal BD, Broutman LJ, Chandrashekhara K (2006) Analysis and performance of fiber composites, 3rd edn. Wiley, Hoboken
12. Greenwood JH, Rose PG (1974) Compressive behaviour of kevlar 49 fibres and composites. J Mater Sci 9(11):1809–1814
13. Piggott MR (1981) A theoretical framework for the compressive properties of aligned fibre composites. J Mater Sci 16(10):2837–2845
14. Jones R et al (1993) Assessment of impact damage in composite structures. Department of Defence, Defence Science Technology Organisation, Aeronautical Research Laboratory, Fishermens Bend
15. Riedel W et al (2006) Hypervelocity impact damage prediction in composites: Part II—experimental investigations and simulations. Int J Impact Eng 33(1–12):670–680
16. Morye SS et al (2000) Modelling of the energy absorption by polymer composites upon ballistic impact. Compos Sci Technol 60(14):2631–2642
17. Li CF et al (2002) Low-velocity impact-induced damage of continuous fiber-reinforced composite laminates. Part I. An FEM numerical model. Compos Part A 33(8):1055–1062
18. He T, Wen HM, Qin Y (2007) Penetration and perforation of FRP laminates struck transversely by conical-nosed projectiles. Compos Struct 81(2):243–252
19. He T, Wen HM, Qin Y (2008) Finite element analysis to predict penetration and perforation of thick FRP laminates struck by projectiles. Int J Impact Eng 35(1):27–36
20. Tabiei A, Aminjikarai SB (2009) A strain-rate dependent micro-mechanical model with progressive post-failure behavior for predicting impact response of unidirectional composite laminates. Compos Struct 88(1):65–82
21. Aymerich F, Dore F, Priolo P (2008) Prediction of impact-induced delamination in cross-ply composite laminates using cohesive interface elements. Compos Sci Technol 68(12): 2383–2390
22. Schoeppner GA, Abrate S (2000) Delamination threshold loads for low velocity impact on composite laminates. Compos Part A 31(9):903–915

23. Duan Y et al (2006) A numerical investigation of the influence of friction on energy absorption by a high-strength fabric subjected to ballistic impact. Int J Impact Eng 32(8):1299–1312
24. Hazell PJ, Appleby-Thomas G (2009) A study on the energy dissipation of several different CFRP-based targets completely penetrated by a high velocity projectile. Compos Struct 91(1):103–109
25. Fujii K et al (2003) Effect of characteristics of materials on fracture behavior and modeling using graphite-related materials with a high-velocity steel sphere. Int J Impact Eng 28(9): 985–999
26. Sevkat E et al (2009) A combined experimental and numerical approach to study ballistic impact response of S2-glass fiber/toughened epoxy composite beams. Compos Sci Technol 69(7–8):965–982
27. Gama BA, Gillespie JW (2008) Punch shear based penetration model of ballistic impact of thick-section composites. Compos Struct 86(4):356–369
28. Trudel-Boucher D et al (2003) Low-velocity impacts in continuous glass fiber/polypropylene composites. Polym Compos 24:499–511
29. O'Higgins RM, McCarthy MA, McCarthy CT (2008) Comparison of open hole tension characteristics of high strength glass and carbon fibre-reinforced composite materials. Compos Sci Technol 68(13):2770–2778
30. Craven R et al. (2009) Buckling of a laminate with realistic multiple delaminations and fibre fracture cracks using finite element analysis. ICCM Int Conf Compos Mater
31. Cui H-P, Wen W-D, Cui H-T (2009) An integrated method for predicting damage and residual tensile strength of composite laminates under low velocity impact. Comput Struct 87(7–8):456–466
32. Elder DJ et al (2004) Review of delamination predictive methods for low speed impact of composite laminates. Compos Struct 66(1–4):677–683
33. Gillespie JW, Monib AM, Carlsson LA (2003) Damage tolerance of thick-section S-2 glass fabric composites subjected to ballistic impact loading. J Compos Mater 37(23):2131–2147
34. Zhou G, Rivera LA (2007) Investigation on the reduction of in-plane compressive strength in thick preconditioned composite panels. J Compos Mater 41(16):1961–1994
35. Zhou G (2005) Investigation for the reduction of in-plane compressive strength in preconditioned thin composite panels. J Compos Mater 39(5):391–422
36. Williams GJ, Bond IP, Trask RS (2009) Compression after impact assessment of self-healing CFRP. Compos Part A Appl Sci Manuf 40(9):1399–1406
37. Aoki Y, Yamada K, Ishikawa T (2008) Effect of hygrothermal condition on compression after impact strength of CFRP laminates. Compos Sci Technol 68(6):1376–1383
38. Daniel IM et al (2011) Characterization and constitutive modeling of composite materials under static and dynamic loading. AIAA J 49(8):1658–1664
39. Xiao JR, Gama BA, Gillespie JW (2007) Progressive damage and delamination in plain weave S-2 glass/SC-15 composites under quasi-static punch-shear loading. Compos Struct 78(2):182
40. Brown KA et al. (2007) Modelling the impact behaviour of thermoplastic composite sandwich structures. In: 16th International Conference on Composite Materials, ICCM-16 – "A Giant Step Towards Environmental Awareness: From Green Composites to Aerospace", July 8, 2007 – July 13, 2007. International Committee on Composite Materials, Kyoto, Japan
41. LSTC, Ls-dyna user manual 971, May 2007
42. Matzenmiller A, Lubliner J, Taylor RL (1995) A constitutive model for anisotropic damage in fiber-composites. Mech Mater 20(2):125–152
43. Sun CT, Chattopadhyay S (1975) Dynamic response of anisotropic laminated plates under initial stress to impact of a mass. J Appl Mech 42(3):693
44. Rossikhin YA, Shitikova MV (2006) Dynamic stability of a circular pre-stressed elastic orthotropic plate subjected to shock excitation. Shock Vib 13(3):197–214
45. Zheng D, Binienda WK (2008) Analysis of impact response of composite laminates under prestress. J Aerosp Eng 21(4):197–205

46. Rossikhin YA, Shitikova MV (2009) Dynamic response of a pre-stressed transversely isotropic plate to impact by an elastic rod. J Vib Control 15(1):25–51
47. Khalili SMR, Mittal RK, Panah NM (2007) Analysis of fiber reinforced composite plates subjected to transverse impact in the presence of initial stresses. Compos Struct 77(2): 263–268
48. García-Castillo SK, Sánchez-Sáez S, Barbero E (2011) Behaviour of uniaxially preloaded aluminium plates subjected to high-velocity impact. Mech Res Commun 38(5):404–407
49. Minak G et al (2010) Residual torsional strength after impact of CFRP tubes. Compos Part B Eng 41(8):637–645
50. Minak G et al (2010) Low-velocity impact on carbon/epoxy tubes subjected to torque – experimental results, analytical models and fem analysis. Compos Struct 92(3):623–632
51. Mizukawa K et al (1985) Impact strength of thin-walled composite structures under combined bending and torsion. Compos Struct 4(2):179–192
52. Kepler JA, Bull PH (2009) Sensitivity of structurally loaded sandwich panels to localized ballistic penetration. Compos Sci Technol 69(6):696–703
53. Kulkarni MD, Goel R, Naik NK (2011) Effect of back pressure on impact and compression-after-impact characteristics of composites. Compos Struct 93(2):944–951
54. Robb MD, Arnold WS, Marshall IH (1995) The damage tolerance of GRP laminates under biaxial prestress. Compos Struct 32(1–4):141
55. Whittingham B et al (2004) The response of composite structures with pre-stress subject to low velocity impact damage. Compos Struct 66(1–4):685–698
56. Mitrevski T et al (2006) Low-velocity impacts on preloaded GFRP specimens with various impactor shapes. Compos Struct 76(3):209–217
57. García-Castillo SK et al (2009) Impact behaviour of preloaded glass/polyester woven plates. Compos Sci Technol 69(6):711–717
58. Loktev AA (2011) Dynamic contact of a spherical indenter and a prestressed orthotropic uflyand–mindlin plate. Acta Mech 222(1–2):17–25
59. Mikkor KM et al (2006) Finite element modelling of impact on preloaded composite panels. Compos Struct 75(1–4):501–513
60. Choi I-H et al (2010) Analytical and experimental studies on the low-velocity impact response and damage of composite laminates under in-plane loads with structural damping effects. Compos Sci Technol 70(10):1513–1522
61. Choi I-H (2008) Low-velocity impact analysis of composite laminates under initial in-plane load. Compos Struct 86(1–3):251–257
62. Ghelli D, Minak G (2010) Numerical analysis of the effect of membrane preloads on the low-speed impact response of composite laminates. Mech Compos Mater 46(3):299–316
63. Chai H (1982) The growth of impact damage in compressively loaded laminates. PhD Dissertation. California Institute of Technology, Pasadena
64. McGowan DM, Ambur DR (1999) Structural response of composite sandwich panels impacted with and without compression loading. J Aircr 36(3):596–602
65. Zhang X, Davies GAO, Hitchings D (1999) Impact damage with compressive preload and post-impact compression of carbon composite plates. Int J Impact Eng 22:485–509
66. Herszberg I, Weller T (2006) Impact damage resistance of buckled carbon/epoxy panels. Compos Struct 73(2):130–137
67. Heimbs S et al (2009) Low velocity impact on CFRP plates with compressive preload: test and modelling. Int J Impact Eng 36(10–11):1182–1193
68. Pickett AK, Fouinneteau MRC, Middendorf P (2009) Test and modelling of impact on pre-loaded composite panels. Appl Compos Mater 16(4):225–244
69. Wiedenman N (2006) Ballistic penetration of compressively loaded composite plates. J Compos Mater 40(12):1041–1061
70. Starnes JH Jr, Rose CA (1997) Nonlinear response of thin cylindrical shells with longitudinal cracks and subjected to internal pressure and axial compression loads. In: Proceedings of the 1997 38th AIAA/ASME/ASCE/AHS/ASC Structures, Structural Dynamics, and Materials Conference. Part 4 (of 4), AIAA, Kissimmee, FL, 7–10 Apr 1997

71. Bartus SD(2006) Simultaneous and sequential multi-site impact response of composite laminates. PhD dissertation. University of Alabama at Birmingham, Birmingham
72. Vaidya U, Kerr-Anderson E, Pillay S (2010) Effect of pre-stressing and curvature on e-glass/vinyl ester composites, In: Proceedings mechanics of composite materials, College Park, MD
73. ASTM D 6641(2001) Standard test method for determining the compressive properties of polymer matrix composite laminates using a combined loading compression (clc) text fixture

Development of a Test to Simulate Wave Impact on Composite Sandwich Marine Structures

Peter Davies, Benoît Bigourdan, Dominique Choqueuse, Nicolas Lacotte, and Bertrand Forest

Abstract Wave impact is a potentially damaging load case not only for fast ships and racing yachts but also for wave energy devices and signal buoys. This chapter describes the development and analysis of a test designed to simulate the response of composite and sandwich marine structures subjected to wave impact. First a brief overview of previous work on impact of composites and sandwich materials is given, and existing tests to study wave slamming are discussed. The development of a medicine ball test is then described, and examples of results from tests on various sandwich panels are given. Finally, the evolution from a qualitative to a quantitative test is described, FE modelling is discussed and examples of results are given.

Keywords Impact • Slamming • Sandwich • Modeling • Core damage • Wave energy

1 Introduction

Impact damage is one of the most frequent causes of failure of marine structures, which are subjected to severe loadings in a hostile environment. Polymer matrix composites are particularly sensitive to impact, and for this reason many studies have focused on this topic. Impact response can be very complex, even for isotropic materials, including material rate effects combined with local and global structural behaviour. The orthotropic nature of composites makes their response even more difficult to predict, as the contributions of fibres and matrix to in-plane and through-thickness properties multiply the input data and can result in unexpected coupling

P. Davies (✉) • B. Bigourdan • D. Choqueuse • N. Lacotte • B. Forest
Materials and Structures group, Brest Centre, IFREMER (The French Ocean Research Institute), Brest Centre, 29280 Plouzané, France
e-mail: peter.davies@ifremer.fr; benoit.bigourdan@ifremer.fr; dominique.choqueuse@ifremer.fr; nicolas.lacotte@ifremer.fr; bertrand.forest@ifremer.fr

S. Abrate et al. (eds.), *Dynamic Failure of Composite and Sandwich Structures*, Solid Mechanics and Its Applications 192, DOI 10.1007/978-94-007-5329-7_5,
© Springer Science+Business Media Dordrecht 2013

effects. However, it is essential that predictive tools be developed, as impact damage may occur in most composite applications and particularly in the marine structures of interest here.

Marine composites have traditionally been mainly glass fibre reinforced thermosets (polyester, vinyl ester and epoxy for example), used either alone or as the facings on sandwich structures. The fibres are usually found in the form of weaves and chopped strand mat, although some stitched multi-axial reinforcements are used [1]. Sandwich cores include polymer foams, balsa wood and honeycomb. In the past marine composites have generally been manufactured by hand lay-up, though more recently infusion techniques have been adopted for some applications. There has also been an increase in interest in carbon fibre reinforcement for marine structures. This is widely used in racing yachts but some military ships, notably the Swedish Navy *Visby* vessel, have also adopted carbon as it has been shown that the resulting weight gains can be significant [2, 3].

The particular type of loading which will be discussed here is wave impact. This is a rapid pressure pulse applied to a floating structure, either due to the fast displacement of a vessel which encounters waves or the loading of moored structures by breaking waves. It is important for many floating bodies, including buoys and wave energy recovery systems, but the work described here was started over 15 years ago to study impact damage observed on racing yachts. This resulted in large areas of honeycomb sandwich crushing and there was no test available at the time which simulated this damage. A simple "medicine ball" drop test was therefore developed, which produced exactly this type of damage, and allowed materials to be compared in the search for better damage resistance. The test was subsequently improved, instrumentation was added and numerical modeling was performed. This chapter provides an overview of that development, with some hitherto unpublished results from recent tests on sandwich materials.

2 Previous Work on Impact of Marine Composites and Sandwich

There is a vast literature on the impact behaviour of composite materials. The aim here is not to provide a comprehensive review, several review papers and books provide an overview of impact on composite materials [4–6], but simply to give some examples of what has been done specifically to study marine composites and sandwich materials.

2.1 Impact on Marine Composites

If we focus on impact tests on composites used in marine structures the amount of data available reduces significantly. While impact on carbon reinforced composites



Fig. 1 Example of drop weight impact test on a thick composite tube

and definition of their damage tolerance has been a key issue in the development of aircraft materials, marine composites have received much less attention. The majority of published studies have concentrated on flat panels. Sutherland and Soares have published several papers of this type, in which they examine impact damage in woven glass and chopped strand mat reinforced polyester composites by extensive testing [7–9]. A particularity of this type of material is their low damage threshold compared to aeronautical materials. The authors describe the appearance of delaminations at very low incident energies followed by fibre damage in these low stiffness materials. Other authors have provided test data and numerical modeling of plates with woven reinforcement and underlined the need for a full 3D model to capture the response of thick plates [10].

Concerning impact on more complex composite structures; there has been some work on tubes [11–14], both thin walled, such as those used in cooling and firewater applications on ships and offshore platforms, and thick walled such as those for underwater applications to resist external pressure, Fig. 1.

2.2 Impact on Marine Sandwich Materials

Published work describing impact on marine sandwich materials, mostly foam or balsa cored materials with glass reinforced facings, is also quite limited. There was a concerted effort to characterize foam core sandwich materials in the 1980s and

1990s, particularly in Scandinavia, as PVC foam core sandwich materials were adopted there for both military and high speed passenger vessels, first with glass composite facings then with carbon reinforced skins [15–17]. Some of the data generated are available, but much has remained confidential. Other navies also studied foam core sandwich and described testing including underwater explosion tests [18].

One specific aspect of importance when considering the behaviour of sandwich materials is the influence of loading rate on foam core properties. This will be discussed again below in the modelling section, but some test data have been published. Initially it was the material suppliers who provided information on rate effects [19, 20], but subsequently other values became available [21, 22]. There is generally a trend towards higher modulus and strength but lower ductility as loading rate is increased. For example, the compressive yield strength of a 250 kg/m^3 PVC foam and 90 kg/m^3 balsa wood were shown to double when the strain rate was increased from quasi-static rates (10^{-4} s^{-1}) to rates on the order of 10^3 s^{-1} [22]. In contrast, a 100 kg/m^3 PVC foam displayed only a small elevation in uniaxial compressive strength (about 30%) for the same increase in strain rate.

Several authors have described the impact response of sandwich beams and panels and this has been a popular topic at recent conferences on sandwich structures. Figure 2 shows a typical drop test set-up. For example, Mines and colleagues have presented test and modelling results for foam cored sandwich with glass facings [23, 24]. Balsa cored materials have also been studied [25].

As marine materials have evolved from traditional hand lay-up glass reinforced composites to higher performance infused and carbon fibre reinforced materials the distinction between marine and non-marine composites has become less well-defined. Many studies not specifically mentioning marine applications, some of which were nevertheless performed within ONR programmes, are then relevant. For example, Schubel et al. [26] have presented results for foam cores with carbon reinforced facings. They proposed a quasi-static indentation test to simulate low velocity impact. Zenkert et al. studied similar materials [27], used in the Swedish *Visby* corvette, and showed how different types of damage affected mechanical properties in order to establish non-destructive inspection procedures. Other Swedish work has focussed on fatigue behaviour of foam core sandwich [28].

Honeycomb sandwich materials have received much more attention, as they are used in aircraft and aerospace structures, e.g. [29–32], and detailed models have been presented [33].

For a more complete review the reader is referred to reference [5].

There has been surprisingly little work to examine the influence of the environment on impact strength of marine sandwich materials. Cantwell and colleagues have examined how water affects toughness of balsa wood sandwich materials [34] and Weitsman and other authors have studied foam sandwich. The latter have shown that water can improve foam toughness but degrade interfacial fracture energy [35–38].

Finally in this brief overview of impact on marine sandwich materials Ulven and Vaidya have published an original study of the influence of fire damage on impact



Fig. 2 Foam core sandwich panel, laboratory scale drop test

behaviour [39]. The resistance of composite materials to fire often limits the use of these materials, both for passenger vessels and offshore oil and gas structures, and has received considerable attention [40–44]. Sandwich materials have hardly been studied however, and more work is needed to quantify how fire affects properties such as impact resistance.

Larger scale tests on sandwich materials are expensive, and are rarely performed, but an example of a high energy (120 kJ) impact on a sandwich floor is shown in Fig. 3 [43]. This test was designed to demonstrate the energy absorbing capability of sandwich materials for an offshore platform floor application and two designs, both passing the offshore fire resistance requirements, were studied. Containers weighing up to 4 t were dropped onto the sandwich materials from heights up to 3 m.

Other large scale tests have been performed to qualify foam filled polymer signal buoys, Fig. 4 shows an example in which a buoy suspended from a crane was impacted against a concrete wall to verify the float structure, as an acceptance test for a new design.

These large scale tests are very useful to demonstrate new concepts but for more routine testing smaller scale tests are needed. In the next sections the development of a small scale test for wave impact will be described.



Fig. 3 Large energy (120 kJ) impact test on sandwich floor for offshore application



Fig. 4 Buoy acceptance impact test

3 Background to Wave Impact Test Development

The tests described above provide some information on the sensitivity of marine composites and sandwich materials to a local, rigid impact. However, in discussions with naval architects and designers it became apparent that such tests do not represent the repeated interaction between waves and racing yacht structures, and the resulting damage observed after wave impact is not local perforation but core crushing or shear failure over large areas. Wave impact includes a large range of impacts, from the repeated slamming on the bottom of high speed craft such as surface effect ships (SES) to the loading of signal buoys, and the severity and duration of the impacts will depend on the geometry and ocean conditions. There have been a number of attempts to simulate this type of impact loading. Much of the published work in this area has been directed at fast passenger vessels and has focussed on elastic wedges entering the water, following classic work by Wagner in the 1930s. Since then various other authors have described hull slamming, caused by impacts between a running marine vessel and the water, see for example Sellars [44], Bishop et al. [45], Mizoguchi and Tanizawa [46], and Faltinsen [47–49]. In most cases, this loading is the result of a series of pitch and heave motions that force a part of the hull to come out of water and then re-enter it. The generated load is typically characterized by very short-durations (a few milliseconds), acting on a small surface and resulting in high peak pressure. The impact can cause severe local damage to boat hulls, which may subsequently propagate by fatigue.

In the recent ISO procedure for dimensioning hull structures [50] a full size impact test is suggested to validate new designs. Such tests are performed occasionally (e.g. [51], Fig. 5) but this is clearly a very expensive option.

Valuable data can of course also be obtained by instrumenting composite boats directly, and there are examples of this approach in the published literature (e.g. [52–54]). However, in order to exploit these data correctly it is essential to have the corresponding loading conditions, and this requires an extensive, synchronized instrumentation package.

One of the difficulties in using glass fibre reinforced composite structures is that their stiffness is lower than that of steel, so the impact behaviour of a deformable structure must be analysed [55]. This results in considerable modelling complexity, and so in order to determine peak pressures emphasis has been placed on testing. Extensive studies were performed at DNV in the 1990s using drop tests, to examine how pressure varies during impact of composite sandwich structures on water [56, 57]. These involved large prismatic sandwich samples, 2 m wide and 1.5 m long, with a 30° dead rise angle and 50 mm thick ductile PVC foam. They were dropped on a guide trolley from heights up to 7 m into a fjord. Core shear strains were measured by implanted strain gage pairs at ±45°.

Smaller scale models have been used in drop tests by other authors to obtain slamming response data. For example, Charca and Shafiq used a free drop symmetric wedge slamming system to examine the influence of energy level (161–779 J)

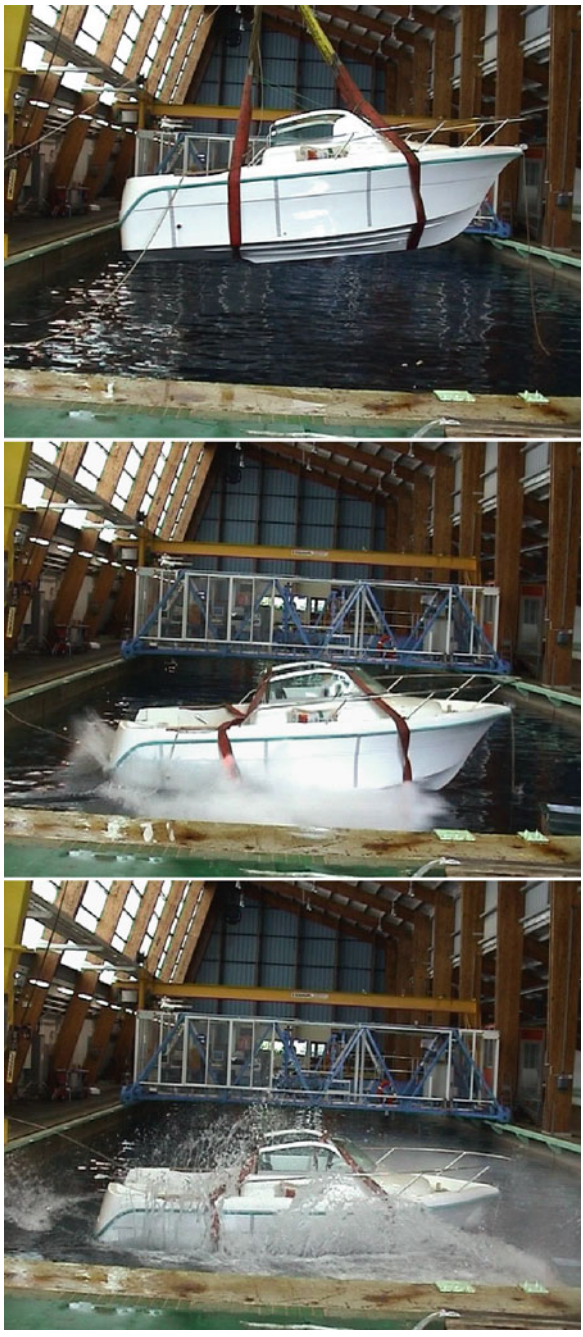


Fig. 5 Example of instrumented motorboat drop test [47]

and dead-rise angle (0–45°) on damage in polyurethane foam core sandwich specimens [58].

Reichard used a pressure loading test set-up to study a range of sandwich panels under static and dynamic loading [59]. He noted that beam test results do not relate well to panel damage, and concluded that finite element modelling was not able to predict the strength of sandwich panels with resilient cores.

Tveitnes et al. [60] proposed an original test rig using a motor drive, to generate constant velocity water entry of wedges. However, they measured dynamic noise with their set-up which limited the accuracy of results.

Huera-Huarte and Gharib have proposed a slingshot apparatus recently [61], which uses a bungee cord to project $(0.3 \times 0.3)\text{m}^2$ samples into water at impact velocities over 5 m/s. They instrumented the panel support system rather than the specimens to simplify specimen preparation.

In another recent publication Panciroli et al. [62] describe some of the results from a large experimental study (more than 1,200 experiments) in which aluminium and fibreglass wedges equipped with strain gauges and an accelerometer were dropped along guide rails onto water.

Appropriate instrumentation is essential in these tests in order to maximize the information from each test. In another recent study a PVC foam core sandwich panel was instrumented with three fibre optic sensors. Strains were recorded by Bragg gratings at 16 points along the fibres when the panel was dropped into a wave tank [63]. Measured surface strains were found to be linearly dependent on impact speed. In that study the fibre optic sensors were bonded onto the panel surface, but such sensors can be integrated in the composite during manufacture.

Another recent paper describes a test set-up in New Zealand specifically designed to examine controlled velocity impacts of panels on water [64–66]. Specimens are fixed to a hydraulic ram and pushed into water. This provides interesting data and in particular the influence of loading rate on core properties can be evaluated. Tests on honeycomb and foam core showed that the foam materials were significantly stronger in shear when loaded dynamically (at rates up to 540 mm/s) than at pseudo-static loading rates [65]. However, these tests require a large, complex, dedicated test machine.

There is clearly a need for a simpler wave impact test, allowing different core and facing combinations to be rapidly evaluated, and this was the initial motivation for the study described here. A need for an impact test with a deformable impacter was identified, which could simulate pressures of 20 t/m^2 or more on full thickness samples. The latter is important as analysis of scaling of impact events in composite materials is not straightforward. Various studies have presented results from scaling studies on composites based on non-dimensional parameters, e.g. [9, 67, 68], but in a sandwich material for which the core is rate dependent these may be impossible to satisfy.

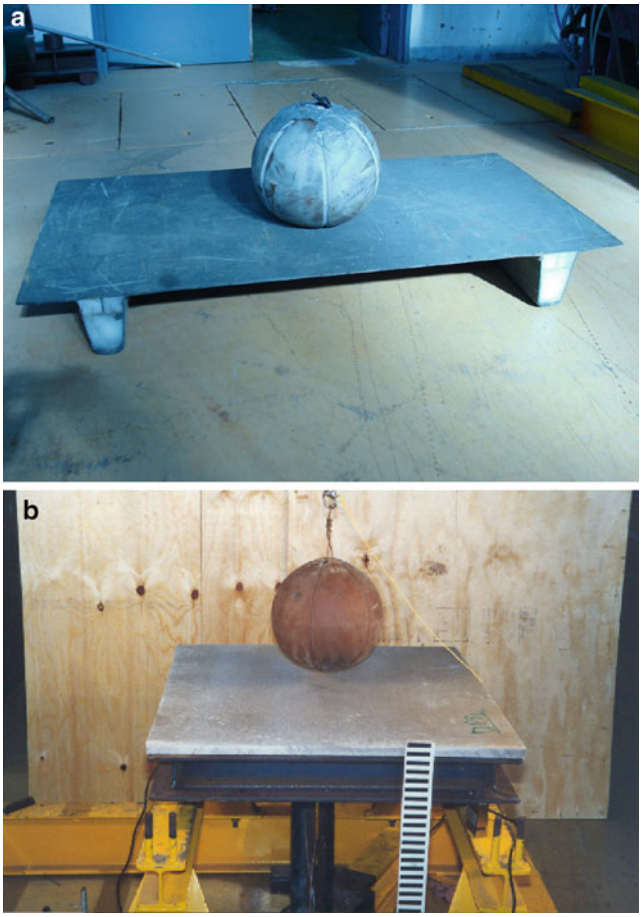


Fig. 6 Initial test fixtures, no instrumentation (**a**) initial test set-up, (**b**) panel simply supported on steel frame

4 Development of an Original Wave Impact Test

The original idea for the test developed here was suggested by the late Hubert Desjoyeaux of the CDK boatyard in Brittany, during discussions following extensive damage to the monohull racing yacht of Jean-Luc Van Den Heede. The aim was to try to reproduce the damage with a laboratory test. A simplified test was performed in 1995 during material selection for *PRB*, a racing monohull, in collaboration with the architects Finot-Conq. The stiffened panels to be tested were initially placed with the stiffeners directly on the floor, Fig. 6a. Later sand-filled boxes were placed below the panel to reduce stiffener damage.

A medicine ball, filled with sand and weighing 18 kg, was dropped from increasing heights until damage was observed. Some panels were instrumented with

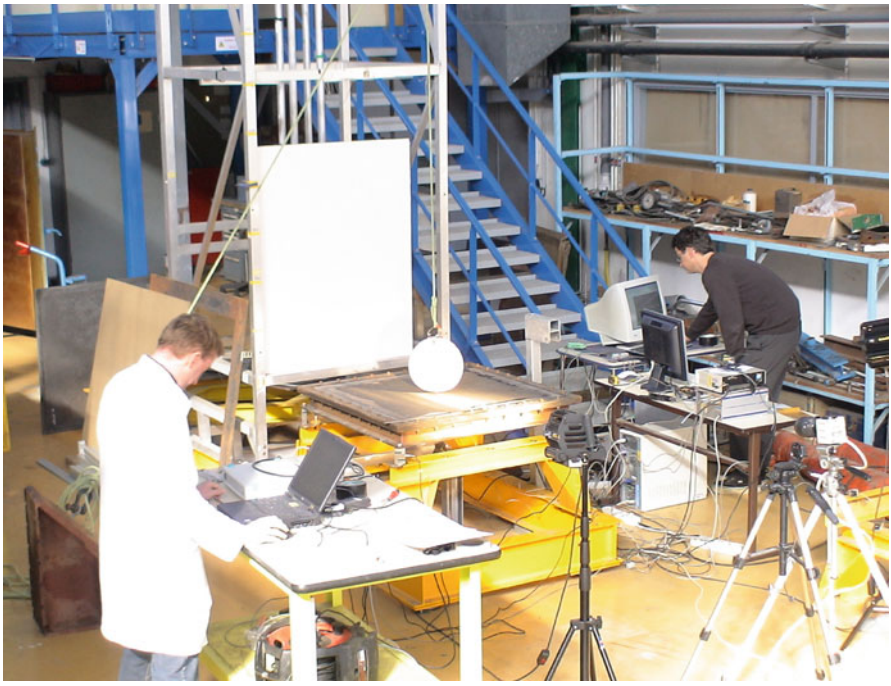


Fig. 7 Current instrumented medicine ball test set-up, with high speed camera

strain gages to measure strains during impact. The results from these first tests, some of which were presented in reference [43], showed significant differences in the responses of stiffened monolithic and sandwich panels. More important, the damage observed, particularly crushing of foam cores over a large area, was very similar to that seen on damaged yacht hull sandwich structures, suggesting that the test might be useful in material comparisons. The first tests therefore concentrated on simply comparing different material options. However, subsequently, as more instrumentation was added and boundary conditions were improved, Fig. 6b, the scope was widened to include FE modeling with the aim of using results to help in defining scantlings.

5 Instrumented Test Set-Up

The current test set-up is shown in Fig. 7, more details can be found in [69].

The 0.9×0.9 m^2 test panel is rigidly fixed to a steel frame, bolts are tightened with a torque wrench to ensure repeatable boundary conditions. Wooden inserts are placed in the sandwich sample around its perimeter to avoid local damage, Fig. 8a. Two laser transducers measure displacements of the panel center and the frame, Fig. 8b, four load cells below the frame measure the reaction forces, Fig. 8c.



Fig. 8 (**a**) Square section wooden insert to reinforce exterior of panel in boundary region, (**b**) panel removed to show laser transducer which records central displacement, (**c**) load cells at corners of panel

Strain gauges are bonded to the lower face of the panel. All the measurements are recorded by two high speed data acquisition systems for post-treatment. A high speed digital camera records the ball shape during impact, while a standard digital camera records rebound height. Pressure sensitive paper has also been used to record maximum pressure [69] but results will not be presented here.

6 Examples of Test Results

Various test campaigns have been performed using this test set-up over the last 15 years, both for material suppliers and racing teams. The two most extensive test series were performed for the *Groupama* team, for their multi-hull developments, and for *BMW-Oracle* in collaboration with the HDS design group before the 2010

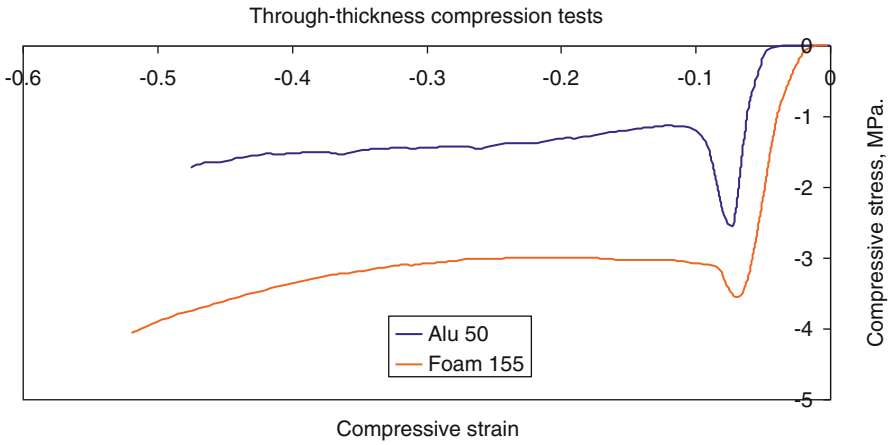


Fig. 9 Examples of through-thickness compression stress–strain plots for samples cut from panels with foam (155 kg/m^3) and honeycomb (50 kg/m^3) cores. (Plots offset from origin for clarity)

Table 1 Core shear properties (manufacturers' data)

Sandwich material	Density kg/m^3	Shear modulus, MPa	Shear strength, MPa
Flexcore aluminium honeycomb	50	90/220	0.7/1.2
Flexcore aluminium honeycomb	66	118/300	1/1.8
SAN foam	155	65	2.1
SAN foam	220	101	3.1

Values in 2 directions for honeycomb

Americas Cup series. Some results have been published previously [69–71] and have shown how through-thickness reinforcement (z-pins) can significantly enhance impact resistance.

In this chapter examples of results for two types of sandwich panel, both with 0.6 mm thick 0/90/±45° carbon/epoxy facings on 20 mm thick core, will be presented. The first is an isotropic polymer foam core (SAN, known as Corecell™), the second is an anisotropic aluminium honeycomb (Flexcore™). For both materials two densities have been studied, 155 and 220 kg/m^3 for the foam and 50 and 66 kg/m^3 for the honeycomb. Table 1 presents the nominal shear properties of the different materials, and Fig. 9 shows their through-thickness compression behaviour. The latter were measured in tests according to ASTM C365 on coupons cut from the panels at a loading rate of 10 mm/min.

There is a large load drop after buckling of the honeycomb cells, whereas the foam crushing is more gradual.

In the following sections examples of results are given for these materials. First measured impact loads are shown, followed by displacements and strains. Then

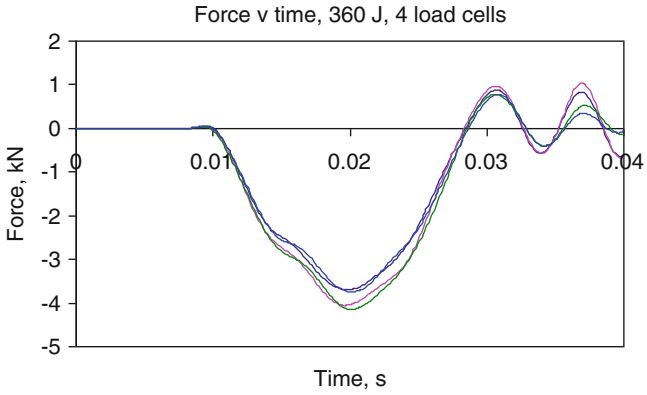


Fig. 10 Load-time plots, aluminium honeycomb 50 kg/m^3 core

examples of high speed camera images are given, to illustrate how the medicine ball deforms during the impact. Finally some images showing the damage incurred will be discussed.

6.1 Impact Loads

Loads are measured by four load cells in the corners of the panel. Figure 10 shows an example of the loads measured by the four load cells during a 360 J impact on a 50 kg/m^3 density aluminium core panel.

The loads measured are very significant, the impacting medicine ball weighs 18 kg and the total load recorded is over 15 kN. Using these recordings together with pressure sensitive paper and images of the deformed shape of the ball it was established that peak pressures of several tens of tons per m^2 could be generated at drop heights up to 6 m.

The impact lasts about 20 ms under these conditions, for most of the tests the duration was in the range from 15 to 25 ms. It is not easy to obtain measured data from racing yachts, in order to determine whether these durations are representative of what the structure sees in service. However, Casari measured the shear strains in a racing monohull during navigation and peak recordings were observed to last about 25 ms [72].

6.2 Displacements and Strains

Figure 11 shows examples of the maximum values of central panel displacements and central strains recorded during impacts at increasing energies on 66 kg/m^3

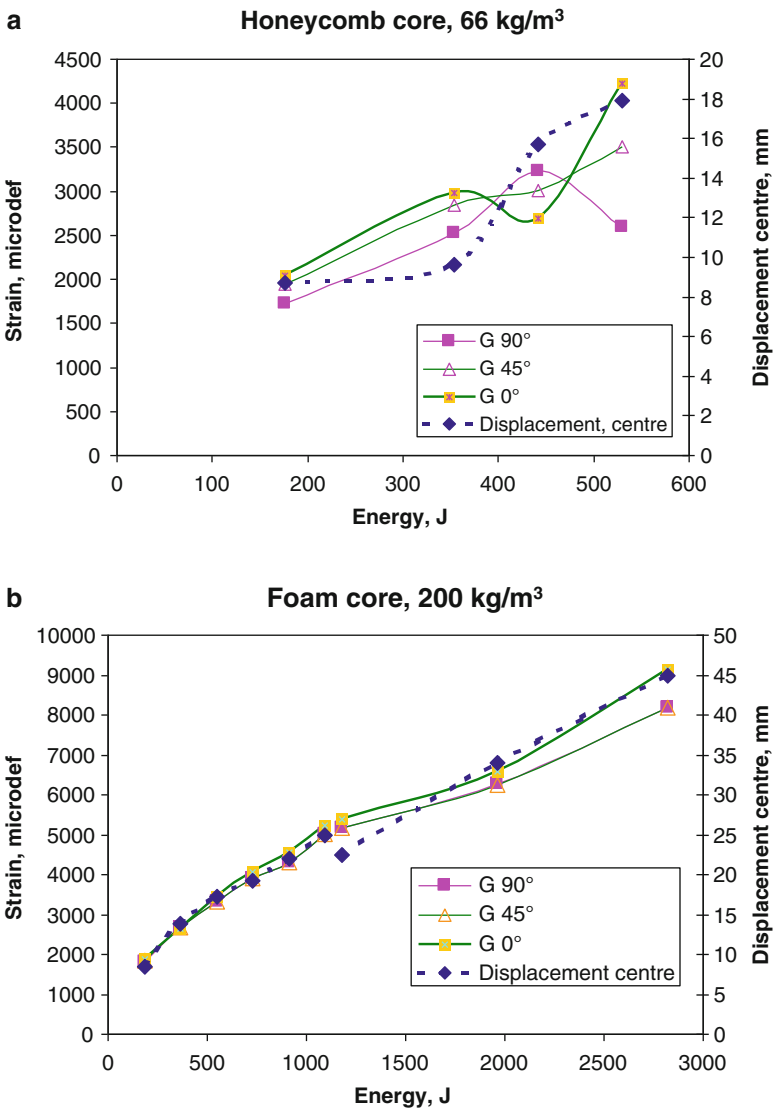


Fig. 11 Examples of measured maximum central displacements and strains measured by three strain gauges for (**a**) 66 kg/m^3 honeycomb, (**b**) 220 kg/m^3 foam core panel, versus impact energy

aluminium honeycomb (Fig. 11a) and 220 kg/m^3 foam core panels (Fig. 11b). Strains and displacements increase with impact energy. The strains differ slightly in the three directions for the honeycomb core panel as it is not isotropic, the 90° direction is stiffer. Above 360 J the order of the strains switches and central displacement increases, suggesting that core damage has occurred. This is discussed in more detail later.

Nine tests have been performed to produce the foam core plot. At the highest energies the displacements are quite large and strains are around 0.9%. The three strain gauges show similar values, this is a quasi-isotropic lay-up, and the core is isotropic. At these strain levels the panel facings are probably damaged. However the panel was still intact at the end of this test series. It is interesting to note that there is a discontinuity in the displacements at around 1,000 J. This corresponds to a change in medicine ball, from 18 to 40 kg, and the larger ball does not produce quite the same displacement as the lighter one though the strains are quite similar. This suggests that there is a small influence of the filler material, changing from sand to lead pellets changes not only the weight but also the ball stiffness, so fixing equal energy and weight is not sufficient to completely define these soft impacters.

6.3 High Speed Camera Images

The use of a high speed camera (500 images per second here) enables the change in shape of the medicine ball to be quantified throughout the impact event, Fig. 12.

The ball, initially circular, flattens considerably during the impact. One concern during the first tests was that the filler materials inside the ball, sand or metal pellets, would bed in during impacts and not be reproducible. However, repeat tests with the same energy have been performed several times and no significant differences have been measured.

6.4 Impact Damage

Damage appears at different energy levels for the different cores and densities. Table 2 summarizes the results.

The results from these tests indicate that sandwich panels with aluminium honeycomb cores of 50 and 66 kg/m^3 density resist impact energies up to 270 and 550 J respectively before core shear damage.

Identical sandwich panels with Corecell foams of 155 kg/m^3 density support much higher energy impacts, up to 1,580 J, before skin damage occurs. It was not possible to damage the 220 kg/m^3 foam core panels even with a repeated impact at 3,200 J. If we normalize these results with respect to the panel weights, Fig. 13, we see that in spite of their higher weight the foam core panels provide very significant increases in damage resistance.

Figure 14a shows the damage in the aluminium honeycomb core. This is a section through the center of the panel (produced by high pressure water jet cutting to limit further damage in preparation of the section). The center of the panel is at the right

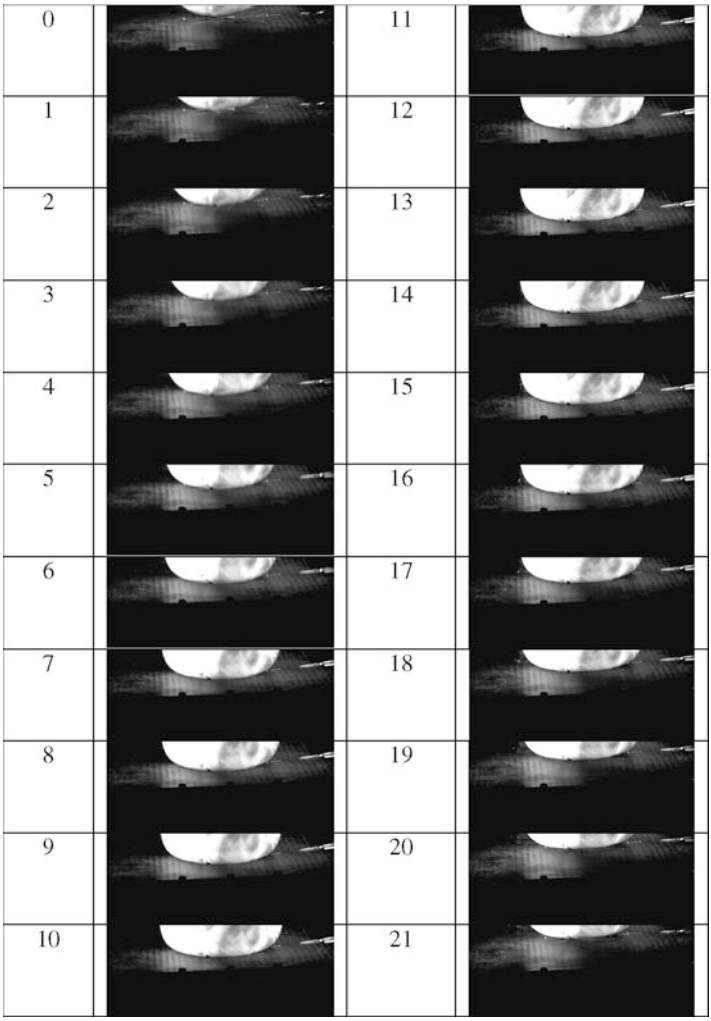


Fig. 12 Examples of images recorded during impact (2 ms between each image)

Table 2 Damage observed in sandwich panels with increasing impact energy

Sandwich material	Density kg/m^3	Energy at first damage, J	Type of damage
Honeycomb	50	270	Core shear
Honeycomb	66	550	Core shear
Foam	155	1,580	Upper skin failure
Foam	220	>3,200	No damage detected

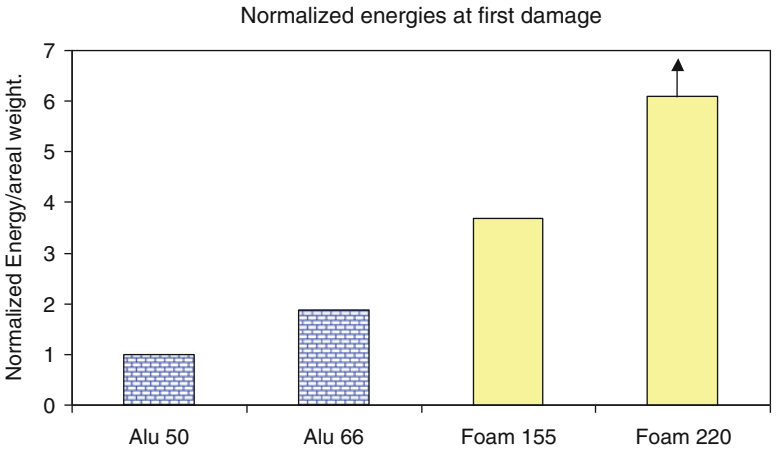


Fig. 13 Energy to first damage divided by panel weight, normalized with respect to 50 kg/m^3 aluminium honeycomb energy

of the photo and there is a highly sheared region at the center of the photo. At this impact energy a circular shear failure is produced, and the central part of the panel is extruded downwards a few millimeters when this occurs.

Figure 14b shows the failure of the foam core sandwich upper facing. Here the damage includes a 45° facing crack and a region close to the corner of the frame where the facing has buckled and debonded from the core.

6.5 Repeated Impact

While single wave impacts can cause damage, repeated impact may also result in a progressive accumulation of damage leading to failure. Although this test in its present form was not designed to apply large numbers of repeated impacts, some tests have been performed to examine whether repeating impacts at energies below the values resulting in damage would lead to failure. Figure 15 shows two examples of results. For the aluminium honeycomb, Fig. 15a, there was no significant strain change after ten impacts. For the foam core however, loaded to higher facing strains, the central strain (the value on the lower facing in the middle of the panel measured at 45° in the frame diagonal direction) appeared to increase with the number of impacts though no visible damage was detected.

There has been very little experimental work on repeated impact damage in sandwich materials and this is an area which would benefit from further study. Charca et al. presented some results for a foam core sandwich recently [73]. Scatter in results was high but they showed slamming energy versus lifetime curves with an exponentially decreasing trend.

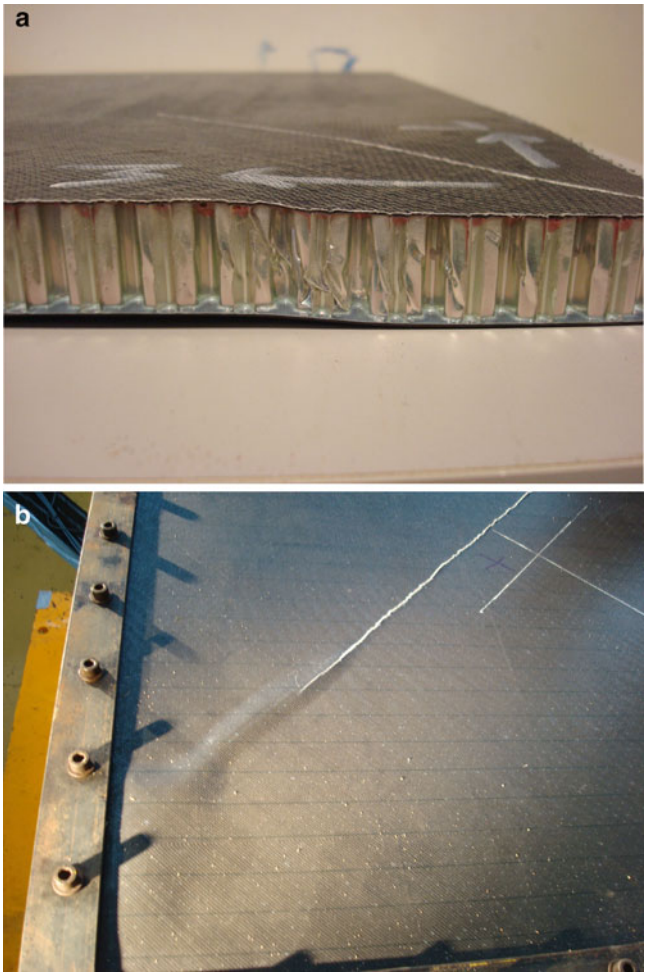


Fig. 14 Damage observed in sandwich panels, (**a**) aluminium honeycomb, 50 kg/m^3 section through panel center, (**b**) 155 kg/m^3 foam core sandwich panel upper surface facing

7 Modelling

There has been renewed interest in modelling of the slamming behaviour of composite sandwich structures recently, and the ONR has encouraged several original studies [61, 62, 74]. Here, in order both to validate the test and to analyze the results, some dynamic numerical modeling has been performed, using the finite element method with implicit time integration. This provides the medicine ball deformations during impact, the variations of the pressure field during impact in both temporal and spatial fields, and the resulting strains in facings and sandwich cores. It has allowed the influence of boundary conditions to be studied and is now providing a tool on which to base the optimization of impact resistance.

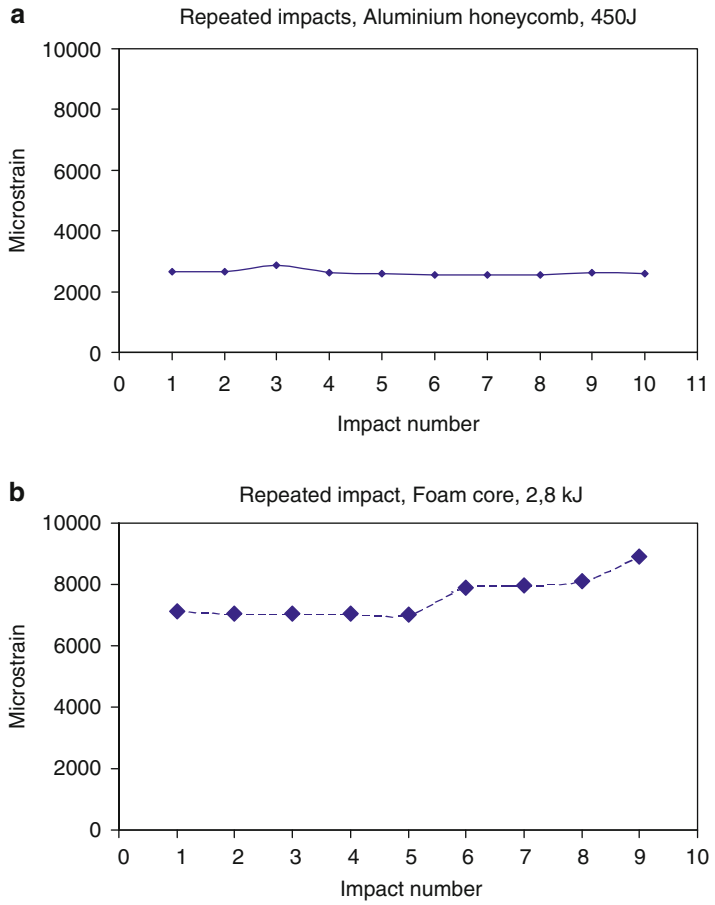


Fig. 15 Examples of strains recorded at the center of the panel lower facing after repeated impacts, (**a**) aluminium 66 kg/m^3, (**b**) foam 220 kg/m^3

7.1 Example of FE Model

Figure 16 shows one of the numerical models developed, using the ADINA version 8.5.0 finite element software [75]. Due to symmetries, only one quarter of the ball and panel is meshed.

It is important to represent the medicine ball correctly: The envelope of the ball is modelled here using quadratic shell elements with an isotropic linear elastic material model, the sand in the ball using quadratic three-dimensional elements with a non-linear Mohr-Coulomb material model. Various models were examined for the sand in a preliminary study, from linear elastic to advanced geo-technical models [76–80]. Different sand models with equivalent Young's modulus gave practically

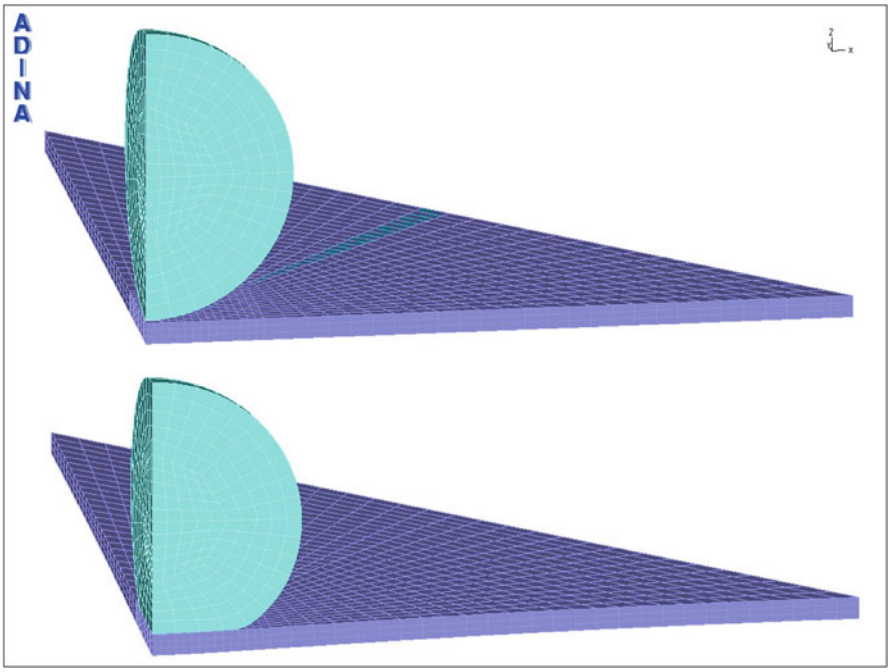


Fig. 16 FE mesh just before impact (*upper*) and at maximum displacement (*lower*) for a 184 J (1 m drop) impact on 155 kg/m^3 foam core sandwich panel

the same values of maximum stress in the panel. However, the cohesion and friction angle parameters in the Mohr-Coulomb model affect the strain rate, the impact area and the unloading phase (rebound).

7.2 Sandwich Panel Input Data

For the sandwich panel, the skins are modelled using quadratic multi-layered shell elements with an orthotropic linear elastic material model. The cores are represented using quadratic three-dimensional elements with an orthotropic linear elastic material model for the honeycomb, an isotropic model for the foam. The contact between the panel and the ball is assumed to be frictionless, and is controlled by a constraint function method [76]. The sandwich panel is perfectly clamped on its edges. A very small structural damping is introduced using Rayleigh factors to stabilize the vibrations.

A major problem in modeling impact on sandwich structures is establishing the appropriate material properties. The approach used here was to run the model with quasi-static manufacturers' data obtained from the standard ASTM shear (C297) and compression (C365) tests, in order to obtain an estimate of strain rates, then to verify by testing the influence of those rates on the core properties and to re-calculate the response. Figure 17 shows an example. In Fig. 17a the result from a

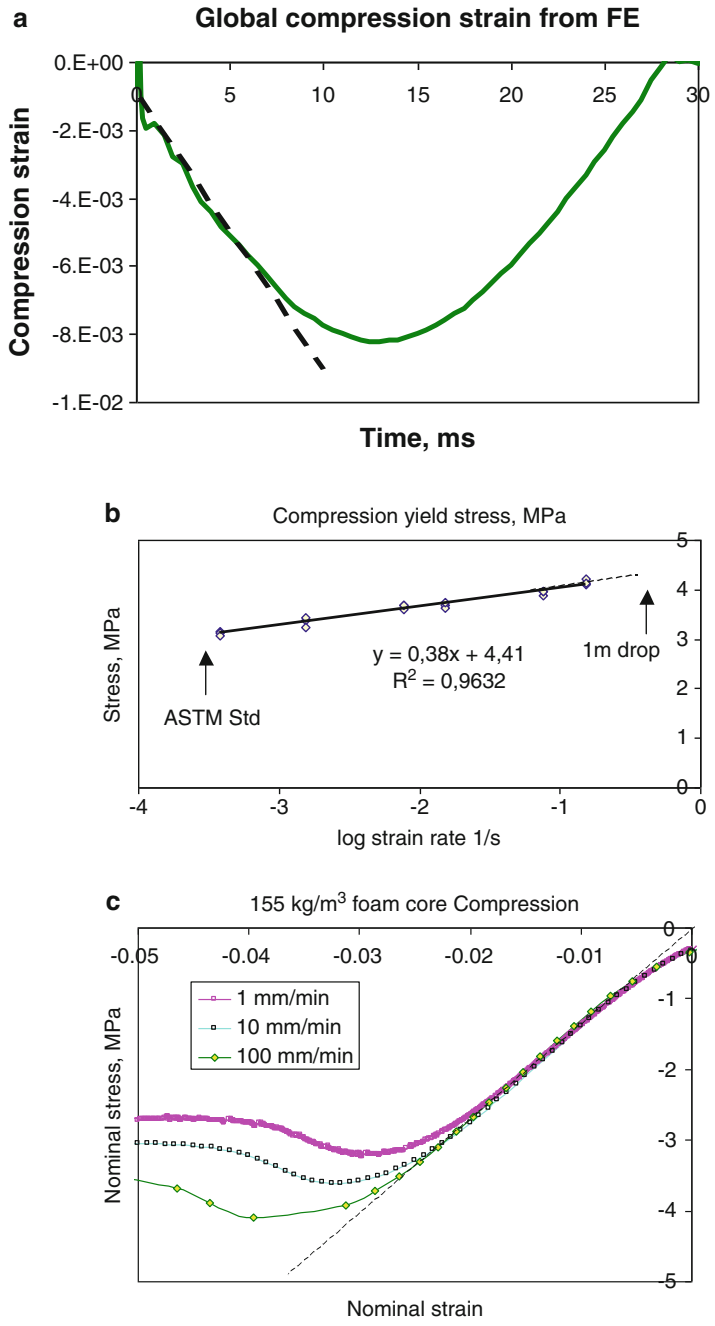


Fig. 17 155 kg/m^3 foam core sandwich. (**a**) Example of calculated compressive strain in core versus time for 1 m drop, (**b**) compression yield stress versus loading rate, (**c**) examples of compression test stress–strain plots for different loading rates

model using the manufacturer's quasi-static core properties for the 155 kg/m^3 foam core panel (Table 1) for a 1 m 18 kg drop are shown. This gives the maximum compression strain below the impacter versus impact time, shown by the dotted line, estimated to be around 0.8 s^{-1} here. This is much faster than the loading rate in the ASTM test. Compression tests were then performed on samples cut from one of these panels at increasing loading rates and Figs. 17b, c show results. It was not possible with the machine available to reach 0.8 s^{-1} but there is a clear linear trend on this semi-logarithmic plot. For this material there is a small increase in foam compression yield stress with increasing strain rate (Fig. 17b). However, over this range the compression modulus remains constant (Fig. 17c).

In the present case, the actual strain rate seen by the core in the panel during a 1 m drop (Fig. 17a) is much higher than that used in quasi-static testing. However, as the modulus of this high density foam does not change at this loading rate the only influence of rate is the higher yield stress, which postpones the onset of yield. For lighter foam cores the modulus can increase with rate and this must then be taken into account in the model.

8 Test-Modelling Comparison

Figure 18 shows an example of results from modelling together with measured results for the same impact on the 155 kg/m^3 foam core sandwich panel. In this example a triaxial 0°/90°/45° strain gauge was bonded to the lower surface of the

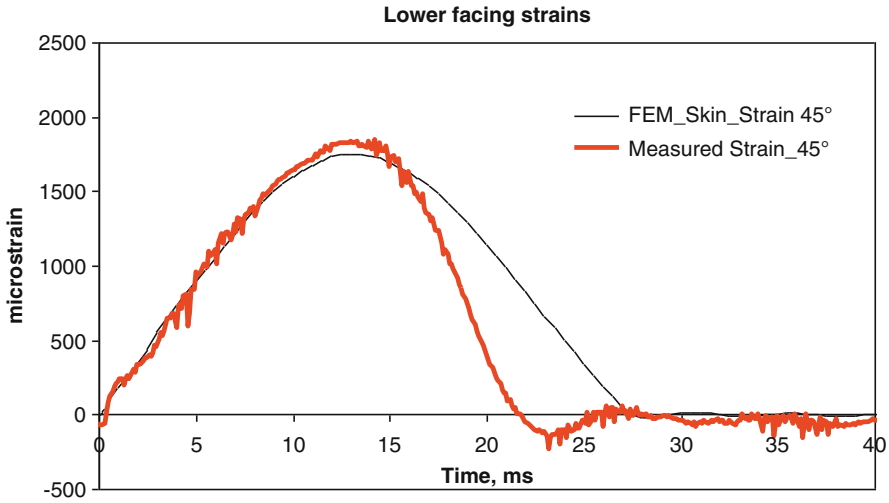


Fig. 18 Test-Model correlation, lower surface composite facing center strain at 45°, 155 kg/m^3 foam core panel, 1 m impact, 18 kg ball

Table 3 Model material input data

Element		Model	Mechanical properties	Other values
Ball	Envelope	Modeled using 9 node shell elements (thickness 1 mm).	E = 10 MPa	Density 1,200 kg·m^{-3}
		Behavior model: isotropic elastic material	Poisson's ratio 0.2	
	Sand	Modeled using 27 node 3D elements	E = 3.5 MPa	Friction angle 30° Dilatation angle 4°
		Behavior model : Mohr-Coulomb	Poisson's ratio 0.3	Cohesion 0
				Density 1,610 kg·m^{-3}
Sandwich panel	Facings	Modeled using 9 node multilayered shell elements (thickness 0.6 mm).	Ply properties:	Density 1,400 kg·m^{-3}
		Behavior model : orthotropic elastic material	$E_1 = 130$ GPa	
			$E_2 = 5$ GPa	
			$G_{12} = 3$ GPa	
			$G_{13} = G_{23} = 2$ GPa	
			$\nu_{12} = 0.02$	
	Core	Modeled using 27 node 3D elements.	E = 186 MPa	Density 155 kg·m^{-3}
		Behavior model : isotropic elasto-plastic material	Poisson's ratio 0.208	
			Yield stress 2.77 MPa	
			Tangential modulus 93 MPa (arbitrary)	

sandwich in the center of the panel. Strain gauges at 0° and 90° were parallel to the panel edges, the 45° gauge is in the reinforcement fibre direction. Table 3 shows all the material properties used in the model.

The model predicts the strains during the drop quite well, but the measured rebound response is not symmetrical. There is an additional mechanism occurring when the sand-filled ball rises, which requires further study. Nevertheless, stresses and strains can be calculated in both facings and in the core. Figure 19 shows an example of the calculated shear stresses in the core for the same test case.

The maximum core shear stresses measured here for a 1 m drop are around 1 MPa, less than 50% of the static core shear strength (Table 1).

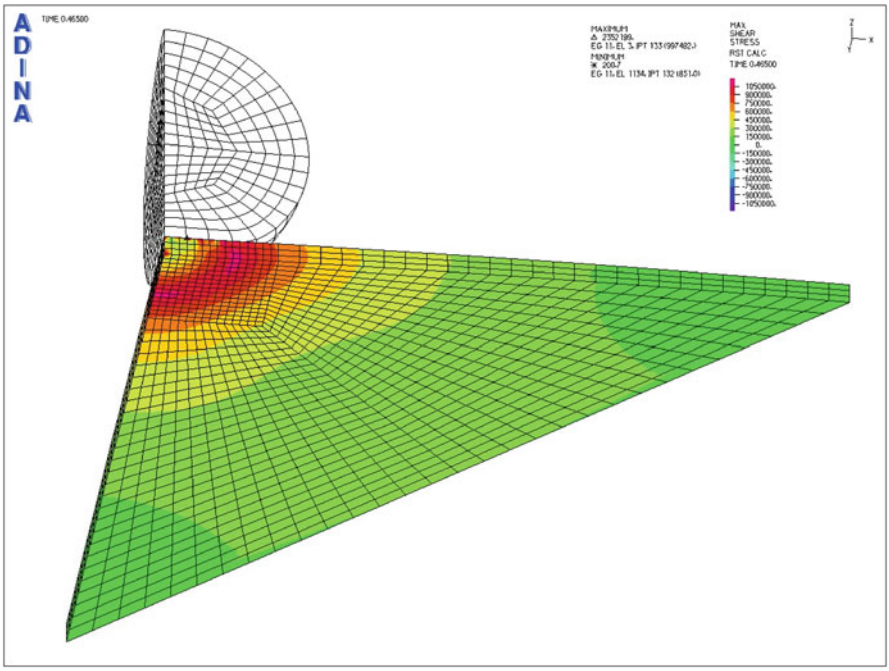


Fig. 19 Maximum core shear stresses, 155 kg/m^3 foam core panel, 1 m impact, 18 kg ball, viewed from underneath

Table 4 Mesh refinements

	Mesh 3	Mesh 2	Mesh 1	Mesh used	Mesh 0
Degrees of freedom	60,431	71,463	90,233	128,909	137,951
Contact equations	121	121	121	121	121
Shell elements (panel facings)	920	920	1,296	2,070	2,250
3D elements (panel core)	920	1,380	1,944	3,105	3375

The FE mesh sensitivity was studied for this example. Different mesh refinements were examined, both for the ball and the sandwich panel. Table 4 shows the different panel meshes examined. Figure 20a, b show the least and most refined meshes employed.

It was found that when the calculation was run with the different meshes the central displacement was identical for all of them. The central strain varied a little however, Fig. 20 shows the results. The mesh selected was chosen as further refinement did not change the calculated strains.

This model allows potential damage mechanisms to be studied, and the influence of material and test parameters on impact response can be evaluated. An example of the influence of varying the core material is shown below.

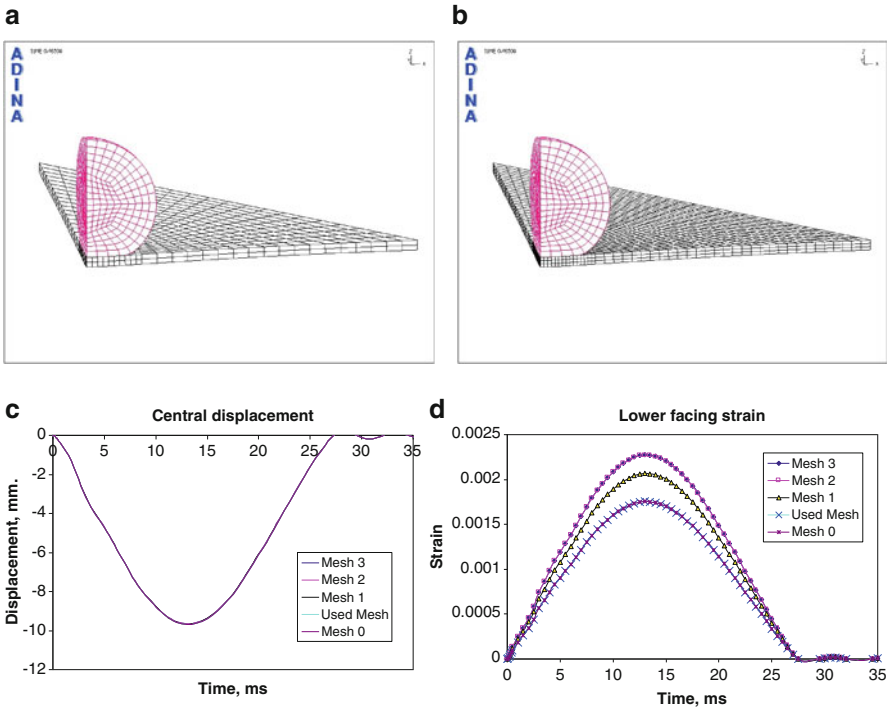


Fig. 20 Influence of mesh size on central displacement and strain. (**a**) Least refined (*mesh 3*) and (**b**) most refined mesh studied. Influence of mesh size on (**c**) central displacement, (**d**) central lower facing 45° strain, 155 kg/m^3 foam core panel, 1 m impact, 18 kg ball

Table 5 SAN foam core property input data

Density (kg/m^3)	100	155	220
E (MPa)	90	186	330
G (MPa)	44	77	121
τ yield stress, MPa	1.27	2.77	5.16

Foam cores of 100, 155 and 220 kg/m^3 density have been modelled for the same 1 m 18 kg drop. Table 5 shows the core properties used in the model, and Fig. 21 shows the central displacements plotted versus impact time.

Here increasing the core density results in lower central displacements, though more than doubling the density, only results in a 25% reduction in displacement.

9 Future Work

The majority of the tests performed to date have involved flat panels. However, the response of features such as stiffeners to impact is also of considerable importance, as stiffener debonding can jeopardize the integrity of marine structures.

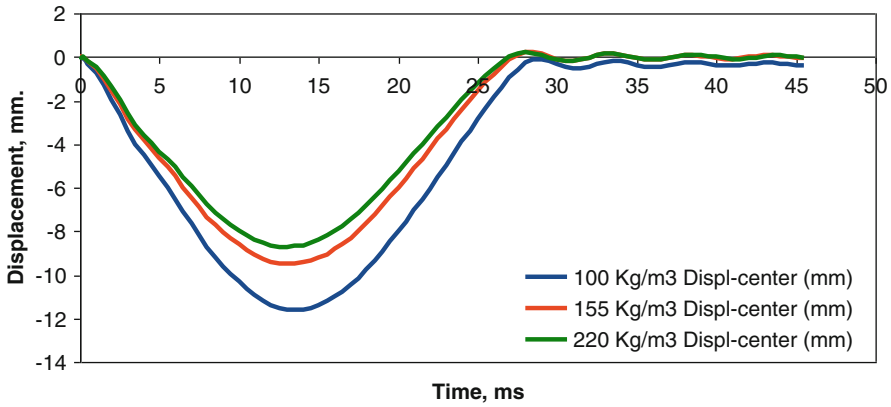


Fig. 21 Influence of core density on central displacement

Fig. 22 Example of stiffened test panel for impact test



Some preliminary tests have been performed, Fig. 22, but adapting the test to provide useful information on the response of such complex details is not straightforward.

A combination of modeling and test iterations is needed to avoid introducing unrealistic damage simply due to the interaction between the stiffener ends and test boundary conditions.

Most of the original work on wave impact was related to fast ships. However, there is considerable current interest in renewable marine energy, and various devices are being proposed to capture wave energy. These are required to remain in service for 20 years or more in severe environments [81] and wave impact resistance will clearly be critical for such structures.

A recent example was provided by van Paepegeem et al. [82], who presented finite element calculations of the mechanical response of composite floating point absorbers designed to recover wave energy, supported by small-scale and large-scale experimental tests. The large-scale tests simulated the repeated wave impacts under yearly storm conditions and the survival under extreme storm conditions. They showed that while the deformability of their structure enabled it to withstand the slamming loads, the conventional design of such structures [83] would have required a much thicker composite structure.

There is likely to be renewed interest in this type of loading in the near future and more research is needed to understand the limits of the energy absorbing potential of composite and sandwich structures.

10 Conclusions

This chapter describes the development of a test to study the response of composite and sandwich panels to a distributed impact, in order to produce similar damage to that observed in racing yachts subjected to repeated wave loading.

A medicine ball drop test was initially developed to provide qualitative data. The main advantage of this approach, compared to large scale boat section tests or special slamming test machines used elsewhere, is simplicity. Different material combinations can be rapidly compared. The test was then instrumented and refined, to enable test parameters to be recorded, and this has allowed modelling work to be validated. The next step is to use this modeling tool to optimize the sandwich panels in order to improve impact resistance.

There are three points which suggest that this may be a useful addition to the range of tests available to characterize composite sandwich structures. First, the damage observed on lightweight foam and nomex honeycomb structures damaged during service, namely crushing of the sandwich over a large area, is reproduced by the test. This is not achieved with conventional rigid impacters. Second, the loading pressures attained during medicine ball impacts are of the same order of magnitude, tons per square meter, as the values used in design of racing yachts. And third, the loading durations in these tests, typically tens of milliseconds, are similar to those recorded on racing yachts during wave impact events.

These wave impact studies were initially confined to fast ship design, but recent developments in wave energy capture are generating renewed interest in this type of loading.

References

1. Davies P (2012) Marine composites. In: Nicolais L, Borzacchiello A (eds) Wiley Encyclopedia of Composites. Wiley, Oxford
2. Lonno A, Hellbratt SE (1989) Use of carbon fibre in a 63m high-speed vessel for the Swedish Navy. In: Proceedings of the 3rd international conference on sandwich construction, Southampton
3. Hellbratt S-E (2003) Experiences from design and production of the 72 m CFRP-sandwich corvette visby. In: Proceedings of the 6th international conference on sandwich construction. CRC Press, Fort Lauderdale, pp 15–24
4. Cantwell WJ, Morton J (1991) The impact resistance of composite materials – a review. Composites 22(5):347–362
5. Abrate S (1998) Impact on sandwich structures. Cambridge University Press, Cambridge
6. Reid SR, Zhou G (eds) (2000) Impact behaviour of fibre-reinforced composite materials and structures. Woodhead Publishing, Cambridge
7. Sutherland LS, Soares CG (1999) Effects of laminate thickness and reinforcement type on the impact behaviour of E-glass/polyester laminates. Compos Sci Technol 59(15):2243–2260
8. Sutherland LS, Soares CG (2006) Impact behaviour of typical marine composite laminates. Compos Part B 37:89–100
9. Sutherland LS, Soares CG (2007) Scaling of impact on low fibre-volume glass–polyester laminates. Compos Part A 38(2):307–317
10. Johnson HE, Louca LA, Mouring S, Fallah AS (2009) Modelling impact damage in marine composite panels. Int J Impact Eng 36(1):25–39
11. Alderson KL, Evans KE (1992) Low velocity transverse impact of filament-wound pipes: part 1. Damage due to static and impact loads. Compos Struct 20:37–45
12. Alderson KL, Evans KE (1992) Failure mechanisms during the transverse loading of filament-wound pipes under static and low velocity impact conditions. Composites 23(3):167–173
13. Curtis J, Hinton MJ, Li S, Reid SR, Soden PD (2000) Damage, deformation and residual burst strength of filament-wound composite tubes subjected to impact or quasi-static indentation. Compos Part B 31:419–433
14. Gning PB, Tarfaoui M, Collombet F, Riou L, Davies P (2005) Damage development in thick composite tubes under impact loading and influence on implosion pressure: experimental observations. Compos Part B 36(4):306–318
15. Gullberg O, Olsson K-A (1990) Design and construction of GRP sandwich ship hulls. Mar Struct 3(2):93–109
16. Remen W (1992) The use of FRP sandwich. In: Davies P, Lemoine L (eds) Proceedings of the nautical construction with composite materials, Paris, Dec, Ifremer editions, pp 432–439
17. Bull PH, Edgren F (2004) Compressive strength after impact of CFRP-foam core sandwich panels in marine applications. Compos Part B 35(6–8):535–541
18. Hall DJ, Robson BL (1984) A review of the design and materials evaluation programme for the GRP/foam sandwich composite hull of the RAN minehunter. Composites 15(4):266–276
19. Feichtinger KA (1991) Test methods and performance of structural core materials – IIA-Strain rate dependence of shear properties. Composites 1(Jan-Feb):37–47
20. Van Gellhorn E, Reif G (1992) Think dynamic – dynamic test data for the design of dynamically loaded structures. In: Proceedings of the 2nd sandwich constructions conference, Gainesville, Florida, USA, pp 541–557
21. Davies P, Baizeau R, Wahab A, Pecault S, Collombet F, Lataillade J-L (1998) Determination of material properties for structural sandwich calculations: from creep to impact loading. In: Vautrin A (ed) Mechanics of sandwich structures. Kluwer Publishers, Dordrecht
22. Tagarielli VL, Deshpande VS, Fleck NA (2008) The high strain rate response of PVC foams and end-grain balsa wood. Compos Part B 39(1):83–91
23. Mines RAW, Worrall CM, Gibson AG (1994) The static and impact behaviour of polymer composite sandwich beams. Composites 25(2):95–110

24. Mines RAW, Alias A (2002) Numerical simulation of the progressive collapse of polymer composite sandwich beams under static loading. Compos Part A 33(1):11–26
25. Atas C, Sevim C (2010) On the impact response of sandwich composites with cores of balsa wood and PVC foam. Compos Struct 93(1):40–48
26. Schubel PM, Luo J-J (2005) Daniel IM low velocity impact behavior of composite sandwich panels. Compos Part A: 36(10):1389–1396
27. Zenkert D, Shipsha A, Bull P, Hayman B (2005) Damage tolerance assessment of composite sandwich panels with localised damage. Compos Sci Technol 65:2597–2611
28. Zenkert D, Burman M (2009) Tension, compression and shear fatigue of a closed cell polymer foam. Compos Sci Technol 69:785–792
29. Herup EJ, Palazotto AN (1997) Low velocity impact damage initiation in graphite/epoxy/nomex honeycomb sandwich plates. Compos Sci Technol 57:1581–1598
30. Andersen T, Madenci E (2000) Experimental investigation of low velocity impact characteristics of sandwich composites. Compos Struct 50:239–247
31. Meo M, Vignjevic R, Marengo G (2005) The response of honeycomb sandwich panels under low velocity impact loading. Int J Mech Sci 47:1301–1325
32. Heimbs S, Schmeer S, Middendorf P, Maier M (2007) Strain rate effects in phenolic composites and phenolic impregnated honeycomb structures. Compos Sci Technol 67:2827–2837
33. Bouvet C, Castanié B, Bizeul M, Barrau JJ (2009) Low velocity impact modelling in laminate composite panels with discrete interface elements. Int J Solids Struct 46(14–15):2809–2821
34. Cantwell WJ, Scudamore R, Ratcliffe J, Davies P (1999) Interfacial fracture in sandwich laminates. Compos Sci Technol 59(14):2079–2085
35. Li X, Weitsman J (2004) Sea-water effects on foam-cored composite sandwich lay-ups. Compos Part B 35(6–8):451–459
36. Veazie DR, Robinson KR, Shivakumar K (2004) Effects of the marine environment on the interfacial fracture toughness of PVC core sandwich composites. Compos Part B 35(6–8): 461–466
37. Avilés F, Aguilar-Montero M (2010) Mechanical degradation of foam-cored sandwich materials exposed to high moisture. Compos Struct 92(1):122–129
38. Kolat K, Neşer G, Özes C (2007) The effect of sea water exposure on the interfacial fracture of some sandwich systems in marine use. Compos Struct 78(1):11–17
39. Ulven CA, Vaidya UK (2006) Post-fire low velocity impact response of marine grade sandwich composites. Compos Part A 37(7):997–1004
40. Croquette J, Baudin M (1992) Commonly used composite materials: fire behaviour. In: Davies P, Lemoine L (eds) Proceedings of the nautical construction with composite materials, Paris, Dec, Ifremer editions, pp 287–297
41. Mouritz AP, Feih S, Kandare E, Mathys Z, Gibson AG, Des Jardin PE, Case SW, Lattimer BY (2009) Review of fire structural modelling of polymer composites. Compos Part A 40(12):1800–1814
42. Mouritz AP, Mathys Z (1999) Post fire mechanical properties of marine polymer composites. Compos Struct 47:643–653
43. Choqueuse D, Baizeau R, Davies P (1999) Experimental studies of impact on marine composites. In: Proceedings of the ICCM12, Paris
44. Sellars FH (1976) Water impact loads. Mar Technol 13(1):46–58
45. Bishop R, Price WG, Tam PKY (1978) On the dynamics of slamming. Trans R Inst Nav Archit 120:259–280
46. Mizoguchi S, Tanizawa K (1996) Impact wave loads due to slamming – a review. Ship Technol Res 43:139–154
47. Faltinsen OM (1990) Sea loads on ships and offshore structures. Cambridge University Press, Cambridge
48. Faltinsen OM (2000) Hydroelastic slamming. J Mar Sci Technol 5:49–65
49. Faltinsen OM, Chezhian M (2005) A generalized wagner method for three-dimensional slamming. J Ship Res 49(4):279–287

50. ISO/FDIS 12215–5 (2006) Hull construction – scantlings – part 5: design pressure for monohulls, design stresses, scantlings determination
51. Baur P, Roy A, Casari P, Choqueuse D, Davies P (2004) Structural mechanical testing of a full-size adhesively bonded motorboat. Proc J Eng Marit Environ I Mech E Part M 218:259–266
52. Baley C, Cailler M (1992) Experimental and numerical behaviour of the structure of a 7.7 m sailing boat at sea. In: Proceedings of international conference on nautical construction with composite materials. IFREMER publication, Paris, pp 423–431. ISBN 2905434449
53. Aksu S, Price WG, Suhrbier KR, Temarel P (1993) A comparative study of the dynamic behaviour of a fast patrol boat travelling in rough seas. Mar Struct 6(5–6):421–441
54. Manganelli P, Wilson PA (2001) An experimental investigation of slamming on ocean racing yachts. In: Proceedings of the 15th Chesapeake sailing yacht symposium, Chesapeake Bay, Maryland, USA
55. Qin Z, Batra RC (2009) Local slamming impact of composite sandwich hulls. Int J Solids Struct 46:2011–2035
56. Hayman B, Haug T, Valsgard S (1991) Response of fast craft hull structures to slamming loads. In: Proceedings of the FAST'91, Trondheim, Norway, pp 381–388
57. Hayman B, Haug T, Valsgard S (1992) Slamming drop tests on a GRP sandwich hull model. In: Proceedings of the 2nd conference on sandwich construction, EMAS, Gainesville, Florida, USA
58. Charca S, Shafiq B (2010) Damage assessment due to single slamming of foam core sandwich composites. J Sandw Struct Mater 12:97–112
59. Reichard RP (1992) Pressure loading of FRP panels for marine structures. In: Proceedings of the international conference on nautical construction with composite materials. IFREMER Publication, Paris, pp 231–245
60. Tveitnes T, Fairlie-Clarke AC, Varyana K (2008) An experimental investigation into the constant velocity water entry of wedge shaped sections. Ocean Eng 35:1463–1478
61. Huera-Huarte FJ, Gharib DJM (2011) Experimental investigation of water slamming loads on panels. Ocean Eng 38:1347–1355
62. Panciroli P, Abrate S, Minak G, Zucchelli A (2012) Hydroelasticity in water entry problems: Comparison between experimental and SPH results. Compos Struct 94(2):532–539
63. Jensen AE, Havsgard GB, Pran K, Wang G, Vohra ST, Davis MA, Dandridge A (2000) Wet deck slamming experiments with a FRP sandwich panel using a network of 16 fibre optic Bragg grating strain sensors. Compos Part B 31:187–198
64. Downs-Honey R, Erdinger S, Battley M (2006) Slam testing of sandwich panels. SAMPE J 42(4):47–55
65. Battley MA, Lake SE (2007) Dynamic performance of sandwich core materials. In: Proceedings of the International Conference on Composite Materials (ICCM16), Kyoto, Japan
66. Battley M, Allen T, Pehrson P, Stenius I, Rosen A (2010) Effects of panel stiffness on slamming responses of composite hull panels. In: Proceedings of the International Conference on Composite Materials (ICCM-17), Edinburgh
67. Morton J (1988) Scaling of impact loaded carbon fiber composites. AIAA J 26(8):989–994
68. Swanson SR (1993) Dynamic and scaling effects in impact of composite structures. In: Proceedings of the International Conference on Composite Materials (ICCM9), vol 5, Madrid, pp 291–298
69. Baral N, Cartié DDR, Partridge IK, Baley C, Davies P (2010) Improved impact performance of marine sandwich panels using through-thickness reinforcement: experimental results. Compos Part B 41(2):117–123
70. Davies P, Choqueuse D, Bigourdan B, Devaux H, Robert S (2010) Wave impact resistance of racing yacht composites. JEC Mag 59:28–29
71. Davies P, Choqueuse D, Bigourdan B, Baral N, Cartié DDR, Partridge IK, Baley C (2010) Pinned foam core sandwich for improved damage tolerance of racing multi-hull yachts. In: Proceedings of the International Conference on Composite Materials (ICCM-17), Edinburgh
72. Lolive E, Davies P, Casari P (2005) Loading rate effects on foam cores for marine composite structures. In: Proceedings of the ICCS, Aalborg, Denmark

73. Charca S, Shafiq B, Just F (2010) Repeated slamming of foam core composite sandwich panels on water. In: Proceedings of the International Conference on Composite Materials (ICCM-17), Edinburgh
74. Das K, Batra RC (2011) Local water slamming impact on composite sandwich hulls. J Fluid Struct 27:523–551
75. ADINA theory & modeling guide. Report ARD 08–7. ADINA R&D, Inc. February (2008)
76. Bathe K-J (1996) Finite element procedures. Prentice-Hall, Englewood Cliffs
77. Ling HI, Callisto L, Leshchinsky D, Koseki J (2007) Soil stress–strain behavior: measurement, modeling and analysis. In: A collection of papers of the geotechnical symposium in Rome, Springer Solid Mechanics and its Applications, vol 146, 16–17 Mar 2006
78. Cameron DA, Carter JP (2009) A constitutive model for sand based on non-linear elasticity and the state parameter. Comput Geotech 36(7):1219–1228
79. Delfosse-Ribay E, Djeran-Maigre I, Cabrillac R, Gouvenot D (2004) Shear modulus and damping ratio of grouted sand. Soil Dyn Earthq Eng 24(6):461–471
80. Blázquez R, López-Quero S (2006) Generalized densification law for dry sand subjected to dynamic loading. Soil Dyn Earthq Eng 26(9):888–898
81. Bahaj AS (2011) Generating electricity from the oceans. Renew Sustain Energy Rev 15(7):3399–3416
82. Blommaert C, Van Paepegem W, Dhondt P, De Backer PG, Degrieck J, De Rouck J, Vantorre M, Van Slycken J, De Baere I, De Backer H, Vierendeels J, De Pauw P, Matthys S, Taerwe L (2010) Large scale slamming tests on composite buoys for wave energy applications. In: Proceeding of the 17th International Conference on Composite Materials (ICCM17), Edinburgh
83. Det Norske Veritas (DNV) Classification notes no. 30.5, environmental conditions and environmental loads, section 6, wave and current loads, March 2000

Damage Mechanisms and Energy Absorption in Composite Laminates Under Low Velocity Impact Loads

V. Lopresto and G. Caprino

Abstract An extensive study of the behaviour of composite laminates subjected to dynamic loads was carried out by the authors many years in order to understand the complex mechanisms of damage initiation and propagation under low velocity impact loads. A review of the main results is hereafter presented.

The problem is that many parameters are involved in an impact and the induced damage is very complex and not always visible. The present research efforts were undertaken to supply semi empirical and analytical models for the prediction of the impact response in terms of load curve, damage, involved energies and forces, independently of the particular laminate, its thickness and stacking sequence, matrix type and content, fibre type and architecture, fibre orientations and impact conditions such as tup and support diameter, load speed.

Experimental tests were carried out on different material systems varying the initial kinetic energy until the complete penetration. This allows the study of the start and propagation of the failure modes. From the load-deflection curves recorded, all the impact parameters involved like first failure and maximum load and energy, absorbed and penetration energy, were obtained. The influence of the thickness and stacking sequence so that the composite system, constrain condition and tup diameter on the impact parameters was evaluated. Destructive and non-destructive techniques were adopted to investigate the failure modes and the observed damage was correlated to the relative energies.

The analysis highlighted the importance of the penetration energy, U_p. An elastic solution available for circular isotropic plates loaded at the centre was modified to model the indentation and applied to the prediction of the load-displacement curve necessary to know the energy that cause the first failure. Interestingly, the force

V. Lopresto (✉) • G. Caprino
Department of Materials and Production Engineering, University of Naples Federico II,
P.le Tecchio 80, 80125 Naples, Italy
e-mail: lopresto@unina.it

S. Abrate et al. (eds.), *Dynamic Failure of Composite and Sandwich Structures*,
Solid Mechanics and Its Applications 192, DOI 10.1007/978-94-007-5329-7_6,
© Springer Science+Business Media Dordrecht 2013

required for damage initiation under form of delamination was found to increase at the increasing of the thickness, t, following a power law whose exponent is very close to 1.5 of the contact law.

1 Introduction

Due to their brittleness and anisotropy, composite laminates are particularly sensitive to low velocity impact damage caused by accidental loadings imparted during fabrication or in service. This has lead to many studies concerning impact dynamics [1–4], mechanisms of failure initiation and propagation [4–8] and the correlation between impact energy, damage and residual material properties [4, 5, 9–12].

In some cases, parameters such as the maximum force achievable for an assigned energy level or the energy required to penetrate the body, are of major interest. The body panels of car, truck and rail vehicles must be designed in order to prevent penetration by foreign objects of known mass and velocity so that it becomes very useful to know the penetration energy. The absorbed energy is very important, for example, in Formula 1 race cars where it is necessary that the mechanical shock is not transferred to the human body. At the aim to ensure the driver's safety in high speed crashes, lightweight laminated composites are designed to absorb the race car's energy and limit the decelerations on the human body. In this field, in fact, the extreme racing speeds may lead to severe accidents with high amounts of energy involved.

In the design of metallic aeronautical structures, medium and high-velocity impact phenomena are of major concern, due to the danger of flying debris during the take-off and landing operations, and bird strike in cruising. For composite components, also low-velocity impact must be taken into account, because even a tool dropping on the structure during fabrication or maintenance activity can induce severe damage, resulting in a significant strength loss.

In aerospace structures, it is very important to correlate the internal damage that can occur during an impact such as delamination, fiber failure, matrix cracking to the residual properties of the structure. In particular, delamination is the most critical one since it causes significant loss in compression strength that represent the most severe load causing failure for buckling.

Delamination is a crack in the resin rich area between two adjacent layers. It was observed that delamination occurs after a threshold energy has been reached in presence of matrix crack [13]. Even if there is a common agreement on the mechanisms of initiation and growth of this failure during an impact event [8, 14, 15], a general approach for predicting this damage mechanism is absent. The complexity of the stresses in the vicinity of impacted point complicates the analysis. For example, Ref. [14] showed that delamination growth was governed by interlaminar longitudinal shear stress (σ_{13}) and transverse in-plane stress (σ_{22}) in the layer below the delaminated interface and by the interlaminar transverse shear stress (σ_{23}) in the layer above the interface.

A dangerous aspect is the difficulty to detect damage by visual inspection. A composite can severely damage without any external sign. The only external indication of an impact is the indentation, the plastic deformation due to the contact, left by the impactor on the laminate surface. It has brought to the concept of "Barely Visible Impact Damage" (BVID), usually adopted in the design of aeronautical structures: for adequate safety, a minimum laminate strength is required in the presence of a barely visible indentation. For an ease inspection operations, the ideal composite for aeronautical applications should exhibit an easily detectable visible indentation when a small internal damage area, resulting in a negligible strength loss, has been induced by an accidental impact.

It is important to find a relationship between external and internal damage at the aim to investigate about the residual properties without destroy the structure.

An extensive study of the behaviour of composite laminates subjected to dynamic loads was carried out by the authors many years in order to understand the complex mechanisms of damage initiation and propagation under low velocity impact loads. A review of the main results is here presented at the final aim to give useful information to predict the residual strength. In the first sections, the load-displacement curve recorded during each experimental tests carried out varying the initial kinetic energy, were studied at the aim to obtain information about the impact behaviour of the specimens: some characteristic points were individuated to correspond to the evolution of the inner damage. In correspondence of these points, the first failure and maximum load, the correspondent energies, the absorbed and penetration energy were calculated. After that, the influence of the thickness and stacking sequence, matrix type and content, fibre type and architecture, fibre orientations and impact conditions like tup and support diameter, load speed is investigated to find semi empirical and analytical models for the prediction of the impact response in terms of load curve, damage, involved energies and forces. The internal and external damage was investigated through destructive and non destructive testing.

Another topic again obscure at this time is the way through which the initial energy of the impactor is introduced into the target. In a non-perforating impact, a part of this energy is stored elastically, and can be easily measured. Particular attention is dedicated, in Sect. 3.4, to the elastic energy that causes the first failure, generally found as delamination. At the aim to predict this critical value, it is necessary to accurately describe the load curve and to know the critical force resulting in the first failure. At this scope, a non-linear solution available for isotropic materials [16] was modified and it was revealed valid to accurately shape the elastic portion of the load curve and to predict the contact force corresponding to delamination initiation and the related energy. The results show a very reasonable agreement with the theory.

An indentation law, allowing for the prediction of the impact energy from the depth of indentation, was assessed and presented in Sect. 3.6. This law has a general applicability, being scarcely affected by the fibre type and orientations, and matrix type. The indentation was found to be a function of the impact energy through the perforation one that represent the kinetics initial energy necessary to

completely penetrate the laminate and obtained as the area under the complete load curve at penetration [17]. The latter becomes a fundamental parameter to be known at the aim to have information about the impact energy that cause the strength loss [9, 18–20]. The complex failure mechanisms that can occur in a laminate under low velocity impact load and their complex interaction must be taken into account too. The impact tests revealed that, for a given fibre areal weight, U_p was independent of the reinforcement architecture and stacking sequence and of the extend of the delamination. U_p increases more than linearly with thickness times fibre volume fraction, confirmed in [21–23]: the dependence found for CFRP and GFRP laminates is well described by a power law having exponent 1.5 and 1.35 respectively. This is discussed in Sect. 3.7.

The dependence of the residual strength on the impact energy and the possibility to predict the residual properties of the composite structures from indentation depth measurements by a minimum of experimental tests is included in the successive section.

Efforts were done, and the results are presented in Sect. 3.9, at the aim to establish a correlation between the damage occurring in a composite as a consequence of low-velocity impact and the energy dissipated during the impact phenomenon. To investigate about the damage progression as a function of impact energy, ply-by-ply delamination and fibre breakages revealed by destructive tests were measured. A previous model, based on energy balance considerations, was applied to understand the experimental results, together with an original method of data reduction, allowing for the isolation of the maximum energy portion due to indentation and vibrational effects.

The damages were observed by visual analysis, as well as by deplying some of the specimens: delamination was found between layers equally oriented too.

2 Materials and Experimental Methods

During the history of the present experimental research, a large variety of samples (Table 1) were tested under very different tests conditions. Most of them concerned carbon fibre laminates made of prepreg with fibres T400/HMF 934 epoxy resin under form of tape and fabric with different fibre areal weights, stacking sequences and thicknesses. The thickness varied in the 1–4 mm range that is generally considered for applications. Quasi-isotropic panels with $\{[(0, 90)/(\pm 45)]_s\}_n$ stacking sequence, $n = 1$ to 4, were fabricated by hand lay-up and autoclave cured at 177 °C under 0.7 MPa pressure. The fibres were under form of plain weave fabric 193 g/m^2 in areal weight. The specimens were labelled as F in the text. The stacking sequence $[(0, 90)_n/+45_n/-45_n]_s$ was adopted too for the same presented material and technology (FT label). The fibre content by volume was $V_f = 0.55$. Moreover, rectangular graphite/epoxy panels, labelled as T30, T60 and T45, made of carbon/epoxy T400/934 tape were fabricated with different lay-ups, $(\pm 30)_{2s}$,

Table 1 Materials tested in the present work

ID	Material	Lay up	t (mm)	V_f (%)	D_t (mm)	D_s (mm)
F	T400/HMF 934	$\{[(0, 90)/(\pm 45)]_s\}_n$ n = 1 to 4	0.96–3.85 (1–4)	55	12.7, 16, 19.8	40, 50
FT	T400/HMF 934	$[(0, 90)_n/+45_n/-45_n]_s$	0.95–3.80 (1–4)	55	6–19.8	50, 100
T30	T400/HMF 934	$(\pm 30)_{2s}$	1.2	55	6–19.8	50
T60	T400/HMF 934	$(\pm 60)_{2s}$	1.2	55	6–19.8	50
T45	T400/HMF 934	$(\pm 45)_{2s}$	1.2	55	6–19.8	50
SMC	–	–	1.7–7	30	6–20	40–100
(C50/50)	E-glass/epoxy	$(0/90)_n$ n = 5–16	0.7–2.4	60	6–20	50–100
(C90/10)	E-glass/polyester	$(0/90)_n$ n = 4–8	1.2–4.2	35	6–20	50–100
G	E-glass fabric 295 g/m^2 in areal weight and Cycom 7701 epoxy resin	$[(0,90)_n/(+45,-45)_n]_s$ n = 1 to 4	0.96–3.85	55	16, 19.8	50

$(\pm 60)_{2s}$, and $(\pm 45)_{2s}$, resulting in laminate nominal thickness t = 1.2 mm. The fibre content in the cured laminates was about 55% by volume, and the total fibre areal weight 1.16 Kg/m^2. Three basic laminae, namely a sheet moulding compound and labelled as "SMC" hereafter, an E-glass cloth/epoxy with 50% fibre in the warp and 50% fibre in the weft direction (C50/50), and an E-glass cloth/polyester with 90% fibre in the warp and 10% fibre in the weft direction (C90/10), were used to obtain additional composite plates tested in the present campaign. The fibre volume fraction V_f was 0.30, 0.60, and 0.35, respectively, and the nominal thickness of a single cured layer 0.6, 0.15, and 0.3 mm. For each material system, panels different in thickness were fabricated stacking together different numbers of layers. In the C50/50 and C90/10, the layers were laid to obtain 0/90 balanced laminates having a total of 50% fibre along the 0° and the 90° directions. The panels were cured under press according to the resin supplier specifications, and from them square specimens, 150 mm in side, were cut by a diamond saw.

Also GFRP prepreg made of plain-weave E-glass fabric 295 g/m^2 in areal weight and Cycom 7701 epoxy resin were used to fabricate square plates 300 × 300 mm cured by a stamp forming process between hot press plates at 120 °C of temperature and 2 bar of pressure for about 2 h. The stacking sequence was $[(0,90)_n/(+45, -45)_n]_s$, with n = 1 to 4, and the corresponding nominal thicknesses *t* varied in the range 0.96 mm to 3.85 mm. The fibre volume fraction was about 55%. The specimens cut are labelled as G in the text.

From the panels, square and rectangular specimens were cut by a diamond saw and subjected to the experimental tests. They were supported on steel plates with a circular opening 40, 50 or 100 mm in internal diameter, D_s in the last

column of Table 1, or on a rectangular window 150×100 mm suggested by the EN6038, respectively. All the low-velocity impact tests were carried out on a Ceast Fractovis MK4 instrumented falling weight testing machine, equipped with a DAS 8000 digital acquisition system. Specimens were struck at their centre using hemispherical steel indentors with diameters $D_t = 12.7$, 14.9, 16 or 19.8 mm. To prevent multiple impacts, the tup was caught on the rebound by a brake available in the test apparatus.

A first series of tests, to obtain and record the force-displacement (F-d) curve at perforation, was carried out using a mass $M = 10.6$ kg falling from a 1 m height. From the F-d curves recorded for each panel, the penetration energy was evaluated. The different energy levels were produced by suitably combining the drop height and three masses ($M = 3.6$, 5.6, 7.6 kg) available in the testing machine. In all, at least five impact tests were performed for each experimental condition.

Additional tests carried out on a MTS RT/50 universal testing machine in displacement control statically loading the specimens, had the scope to investigate about the influence of the loading speed and the possibility to study the impact phenomenon by static conditions. The adopted supports and impactors were the same of the dynamic tests. The stroke speed was fixed at 0.1 mm/min.

All the involved energies were evaluated by numerical integrations as the area under the load-displacement curves recorded. The force values were evaluated directly on the load curve. The indentation resulting from the indentor-material contact was measured by a micrometric dial gauge and the measurements were performed following the EN6038 standard.

After impact, each specimen was visually inspected to ascertain eventual visible damage. The coupons were, then, inspected by an ultrasonic (UT) pulse-echo immersion testing technique and, after a transversal cut suggested by the NDE results, analysed by an optical microscope, Leitz, in order to identify damage modes.

Some of the E-glass specimens struck with $D_t = 19.8$ mm were subjected to a deeply technique too. First of all, after impact, since glass fibres are transparent, the extent of the projected delaminated area was obtained exploiting the translucent appearance of the material: the damage zone was highlighted by an intense light source on the back of the specimens, and photographed; then, the projected damage area was measured by an image analyzer and related to the specimen thickness and the impact energy. In order to study the ply-by-ply damage extent and type, a small hole 1 mm in diameter was drilled in correspondence of the impact point of the selected specimens. The aim was to ease the penetration of the liquid into the interlaminar cracks. The specimens were immersed in blue ink bath for 1 h until the projected delaminated area was completely darkened by the ink; then, they were dried for a suitable time of about 2 h, and carefully thermally deplied with the help of moderate heating; finally, the resin was burnt away and the delaminated area in correspondence of each interlaminar surface was measured, and the in-plane length of broken fibres within each ply was evaluated by optical microscopy at low magnification.

3 Experimental Observations

3.1 Load-Displacement Curve

The load-displacement curve recorded during a low velocity impact at complete penetration contains useful information about the failure process: it is possible to observe, characteristic points related to the behaviour of the material under dynamic loads. Despite differences in thickness, material and architecture, these curves showed some features common to all laminates [24, 25]. Figure 1 shows a schematic view of a typical load-displacement curve with several characteristic points. In Fig. 2, four different curves recorded during low velocity impact tests on

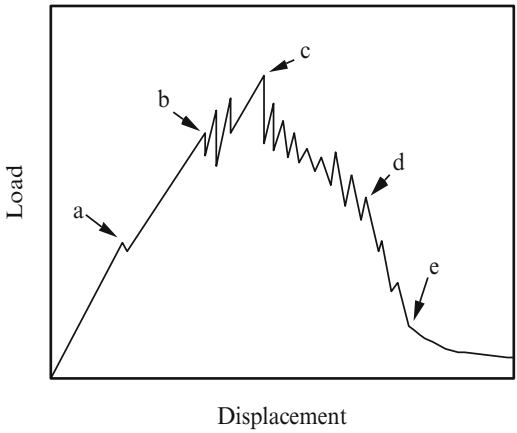


Fig. 1 Schematic view of the impact load displacement curve at penetration

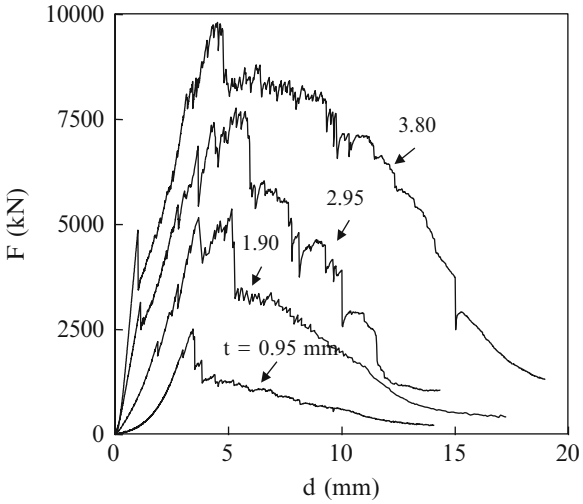


Fig. 2 Load curves for different thickness: mat. FT from Table 1; $D_s = 19.8$ mm

CFRP laminates (FT from Table 1), one for each different thickness, are collected. Despite the difference in thickness, some common features were noted.

Up to point "a" in Fig. 1, the curve shows no evidence of damage developing inside the material. In this diagram a linear trend is observed initially as the displacement increases.

However, a different behaviour between thin (less than eight layers) and thick laminates was observed as showed in Fig. 2 where the initial rigidity of the laminates increases with increasing t. The thinnest plates display an evident non-linear response under very low displacement values (less than 2 mm in Fig. 2), due to large displacements [26].

At the end of the elastic phase a load drop, clearly visible when the material thickness is sufficiently high, is noted (point "a" in Fig. 1). This is difficult to appreciate for the lowest thickness where the load remained substantially constant with increasing the displacement or a different slope is evidenced, with only negligible oscillations. However, in both thin or thick laminates, a local rigidity variation happens, denoting damage inside the laminate.

The successive drop of the load is an indication of damage initiation in the form of fibre breakage, and/or damage propagation in the form of matrix cracking and delamination, fibre breakage, and fibre/matrix debonding and pull out (point b on the curve). Matrix cracks in the resin pockets, are commonly believed to be the first type of damage during an impact [26, 27] and the presence of matrix cracks does not dramatically affect the overall laminate stiffness during an impact event [25, 28]. However, matrix cracks represent the initiation point for delamination [14, 18, 29, 30] and fibre break that dramatically change the local and the global stiffness of the composites and influence the load–time response [31]. All the energy that exceed the latter is used for the propagation of the damages. Of course, all these failure modes lead to a reduction in the residual strength of the impacted panels [25]. After first failure, the load increases again, although the laminate rigidity is reduced. Then, a series of load drops, resulting in oscillations in the force-displacement curves, are noted to correspond to extensive failures in the fibres and in the resin along the laminate thickness.

In the range "b" – "d", the different damage propagate through all the layers that are progressively broken, until (point "d") the complete perforation. The term "perforation" is used here to indicate that there is at least one fracture surface in each layer, so a light beam can pass through the laminate. The slope of the F-d curve begins to decrease rapidly when the material perforation occurs.

The maximum force (point "c" in Fig. 1) was generally achieved between points "b" and "d" even if for the thickest laminates (twelve layers or more), the point b was often found coincident to point d that means that the first significant fibre failure often happens at maximum force [24].

The decrease in the contact load between "d" and "e" is about the penetration process. Finally, beyond point "e" the contact force decreases slowly: the cylindrical impactor slides along the penetrated sample and the energy is dissipated by friction. The penetration energy, the difference between the initial and residual kinetic energy

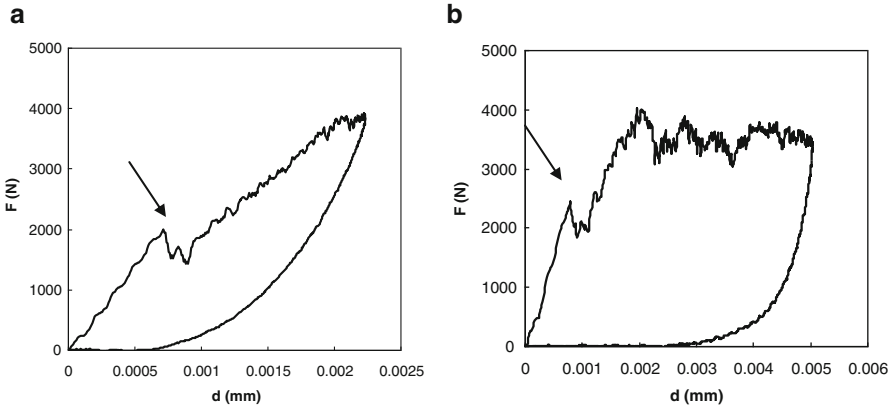


Fig. 3 Load-displacement curve of a 3 mm non penetrated carbon fibre laminate. (**a**) impact energy level U = 5 J; (**b**) impact energy level U = 15 J

of the projectile, necessary to completely penetrate the laminate and given by the area under the load-displacement curve at penetration, is conventionally calculated at point "e".

Both Figs. 1 and 2 deal with cases in which complete perforation occurs. In case of non-perforating impacts, at some point the projectile reaches a maximum displacement and then the displacement decreases during unloading (Fig. 3). After the first load drop (arrows in Fig. 3), the unloading part is different from the loading one since a part of the energy is stored inside the material for the damage formation. In Fig. 3, in fact, where the curve refers to a specimen loaded by 15 J of impact energy, it is possible to note a larger area respect to Fig. 3 where the same laminate was impacted by a lower energy, U = 5 J, that caused less damage. The first load drop signalled by the arrow in Fig. 3 is generally due to delamination that was found the only damage when the 3 mm specimen was impacted with 5 J of energy. A higher impact energy of 15 J caused the propagation of the damage along the thickness in correspondence of a nearly constant load.

Since the similar shape of the curves in Fig. 2, a scaling coefficient was adopted to overlap the curves: by scaling the force according to the coefficient 1.5, the same force-displacement curves sensibly converge to a single master curve, the displacements are held unchanged (Fig. 4). Therefore, the contact force varies according to $t^{1.5}$. All the curves were normalised for the thickness 3.06 mm (16 layers laminate). In this way, as it will be hereafter discussed, the dependence of the first failure load, maximum force, energy at maximum force and penetration energy on the thickness can be easily established. By using a scale parameter in the design of experiments for impact damage the number of experimental tests can be reduced.

Other investigators [21] have also used a scaling parameter, able to predict the force-displacement curve exhibited by thick laminates, obtained using the force-displacement curve recorded in testing thin samples. From the experimental data,

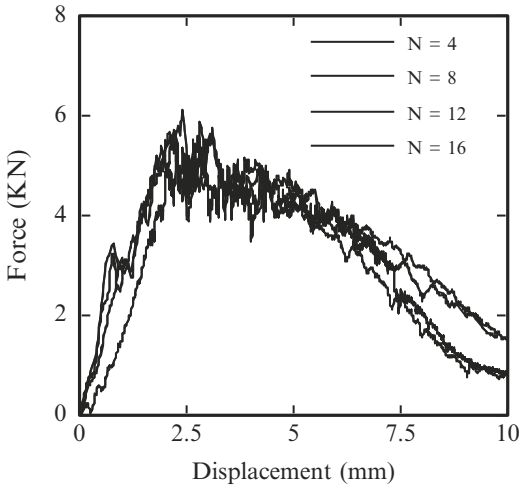


Fig. 4 Superposition of the force-displacement curves for the different thicknesses. *N* number of layers

concerning composite plates having thicknesses in the range 3.3–8.3 mm, all the curves were reduced to a master curve, by scaling both the force and the displacement through power laws. The best scaling exponent for forces was 1.2, whereas the best exponent for the displacements was 0.35. Considering that energy is the area under the force-displacement curve, it was concluded [21] that the penetration energy varies to the power of 1.55 with increasing the plate thickness. It is very similar to the exponent 1.5 found in this work.

Carefully observing the curves in Fig. 4, the superposition does not hold in the very early stage of contact because, as it will be demonstrated, the energy in correspondence of delamination initiation does not increase according to a power law. After perforation, the superposition is satisfying for the 4 and 8 layers laminates and for the 12 and 16 layers composites denoting a drastic change in the failure modes after perforation for the two different groups of thickness.

3.2 Force at Damage Initiation

In this section the effect of several parameters on the damage initiation force is studied. Those parameters are: the laminate thickness, the diameter of the impactor, and the size of the plate. The trends observed are compared with prediction from simple models.

Laminate thickness strongly affect the contact force history. The influence of material thickness on the force at damage initiation, F_i, was first evaluated. The importance in predicting the first failure load is due to the fact that it represents a threshold for the formation of a damage that is not always possible to individuate on the load curve. This force was here evaluated in correspondence of the first load drop

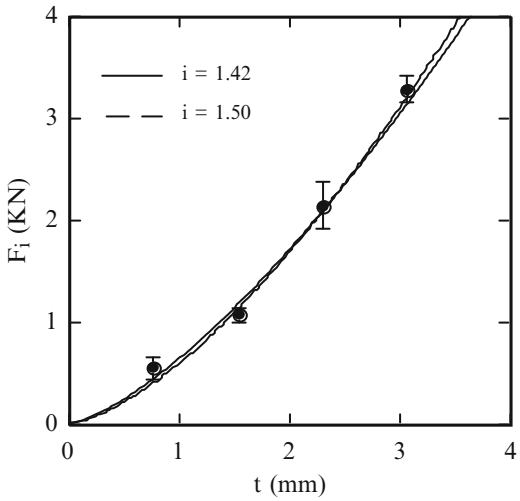


Fig. 5 Force for damage initiation, F_i, against specimen thickness, t

or the change in slope on the ascending portion of the load *vs* displacement curve (point "a" in Fig. 1). The data were obtained loading CFRP specimens made of T400 fibres and HMF 934 epoxy resin having $\{[(0, 90)/(\pm 45)]_s\}_n$ stacking sequence, with $n = 1$ to 4, resulting in nominal thicknesses varying in the range 1–4 mm (F in Table 1). It was found that F_i follows a power law as a function of the thickness, with the exponent coincident with the exponent of the contact law.

Studying the contact between a rigid sphere and a laminate some researchers [32–35] demonstrated the successful application of the elastic contact law [36]. In Fig. 5, F_i is plotted against the specimen thickness, t, for the data obtained here.

The following expression:

$$F_i = F_{io} \cdot t^i \tag{1}$$

was revealed adequate to describe the F_i trend (continuous line in Fig. 5). From the best-fit curve, the values $F_{io} = 0.64$ KN/mm^i and $i = 1.42$ were obtained, for F_i given in KN.

According to the Hertzian contact law [36], the radius R of the contact zone is given by:

$$R = k \cdot \sqrt[3]{D_t \cdot F} \tag{2}$$

where k is a constant only depending on the material elastic constant [36], F is the applied load and D_t the impactor diameter.

For a circular plate loaded at the centre, the shear stresses in the thickness direction around the point of load application are dependent on the applied load, rather than on the flexural moment. In fact, the evaluation of the shear force per unit length of arc along a circle of given radius only involves equilibrium considerations.

A shear induced failure develops when the average shear stress τ along the thickness direction at the periphery of the contact zone achieves a critical value, proportional to the interlaminar shear strength $\bar{\tau}$ of the material:

$$\tau = k' \cdot \bar{\tau} \tag{3}$$

where k′ is a constant.

From equilibrium considerations, considering the cylindrical shape along the thickness in correspondence of the contact zone, it results that the average shear stress τ along the specimen thickness at the boundary of the contact zone is:

$$\tau = \frac{F}{2\pi R t} \tag{4}$$

where t is the laminate thickness. It is necessary to underline that this is an approximate formula since τ is not the maximum value but the mean value along the thickness.

If the shear stress is responsible for delamination initiation, from Eq. (2) and (4) F_i was calculated as:

$$F_i \propto (\bar{\tau} \cdot t)^{1.5} \tag{5}$$

where $\bar{\tau}$ is the interlaminar shear strength of the material.

A good agreement between the exponent of Eqs. (1) and (5), related to the experimental value (i = 1.42) and the expected one from the contact law, was respectively found. It is possible to better appreciate the agreement between experiments and theory in Fig. 5 where the dashed line was drawn putting i = 1.5 in Eq. (1), and F_{io} =0.60 KN/mm$^{1.5}$ by the best fit method. In this way, a simple failure criterion uniquely based on shear stresses would be able to calculate the critical load for delamination initiation.

Matrix cracks are believed to be the first type of damage during impact. It has been shown by Sjoblom et al. [28] that the presence of matrix cracks does not dramatically affect the overall laminate stiffness during an impact. It was demonstrated that [30, 37, 38] an interaction between matrix cracking and delamination initiation exists. Matrix crack tips act as starting points for delaminations and fibre breaks and the latter two damages can dramatically change the local and or global stiffness of the composite laminate and effect the load-time response [31]. Delamination propagate starting from intralaminar cracks was found in particular in thin laminates [38–41] where the membrane contribution is significant. In the following figures, low (a) and high (b) magnification micrograph of loaded quasi-static (Fig. 6) and dynamic (Fig. 7) beam showing the matrix and delamination cracks resulting from quasi-static bending are reported [38]. The same was confirmed here by the authors: for example, in Figs. 8 and 9 a central part and a magnification of the central thickness of a micrograph showing delamination starting from cracks in the resin pocket and connected by intralaminar cracks in the FT laminate 2 mm in thickness (Table 1), is reported.

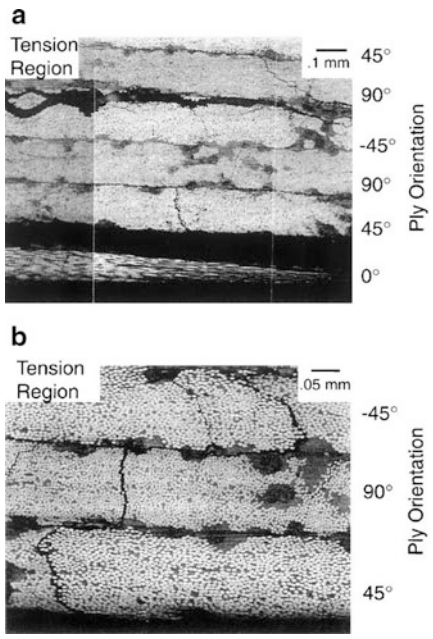


Fig. 6 Low (**a**) and high (**b**) magnification micrograph of the tested quasi-static beam showing the matrix and delamination cracks from quasi-static bending

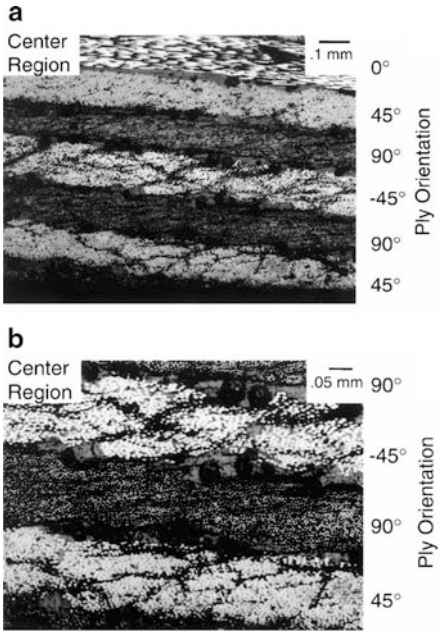


Fig. 7 Low (**a**) and high (**b**) magnification micrograph of the dynamically tested beam showing matrix and delamination cracks. V = 34.9 m/s

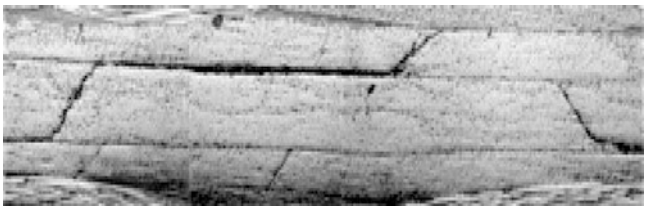


Fig. 8 Micrograph showing delamination starting from cracks in resin pocket and connected by intralaminar cracks in FT laminates (Table 1), t = 2 mm

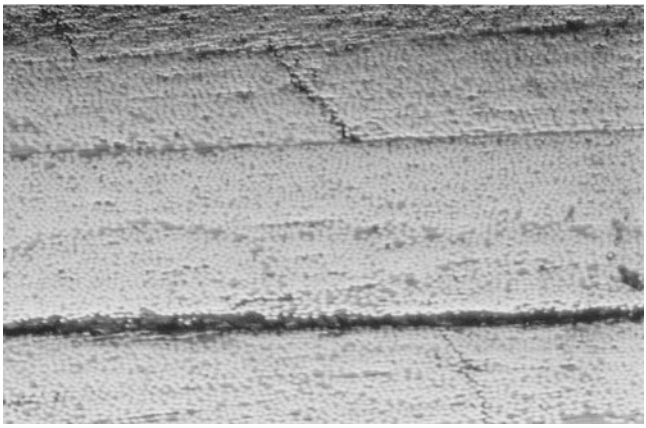


Fig. 9 Magnification of the central part of a micrograph showing delamination starting from cracks in resin pocket and connected by intralaminar cracks in FT laminates (Table 1), t = 2 mm

As accepted by a large number of authors [14, 30, 42, 43], the evolution of the damage in a composite laminate subjected to a concentrated force is driven by intralaminar tensile and shear cracks occurring in the layers farther from and nearer to the contact point. From these cracks, delaminations were found to be generated at interfaces between plies with different orientations, mainly propagating in the direction of the fibres in the lower ply, and extending the more, the larger is their distance from the contact point. These mechanisms were, here, observed only in the thinnest laminates. By deplying GFRP laminates, for $t > 0.96$ mm, delamination was found between layers with the same orientation too, in agreement with [44, 45]. In particular, for $t = 2.88$ mm the maximum extent of interlaminar fractures was found at the midplane between layers having the same orientation.

Extensive delamination was also found without macroscopic evidence of intralaminar cracks in the thick laminates. This confirms that in thick plates shear stresses play a main role for delamination initiation [39–42, 46]. In [39–41, 46], the problem of the delamination initiation was investigated in depth. A difference between thin and thick laminates was found. In the thin laminates the bending

is predominant whereas the shear stresses predominates in the thick ones and delaminations without intralaminar cracks evidence were found at the mid plane.

Sjoblom [47] proposed a simple model for the calculation of F_i based on the hypothesis that the first failure happens when the shear stress τ along the direction of the thickness attains a characteristic critical value τ_c. Taking into account also the effect of the tup diameter, D_t, from the contact law, [47], F_i was calculated as follow:

$$F_i = \frac{(2\pi\tau_c)^{1.5} D_t^{0.75}}{k_c^{0.5}} \tag{6}$$

where k_c is the local rigidity. From Fig. 2 the first load drop becomes lower and lower at the decreasing of laminate thickness since most of energy is stored to the bending phase.

Combining Eqs. (2), (3) and (4), F_i is easily obtained as [48]:

$$F_i = \delta D_t^{0.5} t^{1.5} \tag{7}$$

where:

$$\delta = \left(2\pi \cdot k \cdot k' \cdot \overline{\tau}\right)^{1.5} \tag{8}$$

dependent on τ_c and k_c.

Equation (7) is coincident with Eq. (5), except for the fact that in the latter the influence of the tup diameter is not explicit.

Of course, Eq. (7) is expected to lose its validity when the first failure takes place in the back layer of the laminate. In this case, since the flexural moment depends on the support diameter, the phenomenon should be strongly affected by this parameter.

In Fig. 10 the term $F_i/D_t^{0.5}$ is plotted against the thickness, t: all the data about the FT laminates converge to a single curve irrespective of the tup diameter and the velocity (some data are, in fact, from static tests). Only in the case of small thickness of $t = 0.95$ mm loaded by a large indenter diameter, $D_t = 19.8$ mm, the superposition is not verified (circle in Fig. 10). In this case the flexural rigidity is low (low thickness) whereas the first failure load is relatively high since the large tup diameter. The curvature at first failure is so large and this impairs the model on which Eq. (7) relies.

The continuous line is drawn by Eq. (7). The constant value of 0.152 KN/mm^2 was calculated best fitting all the experimental data except the one, the triangle symbol in the circle in Fig. 10, that does not follow the general trend.

For the thinnest laminate supported on the fixture 50 mm in diameter and loaded with the 12.7 mm tup diameter it was not clearly apparent from the curve the first load drop, so that only the non-destructive analysis was able to approximately detect the first failure point. The same difficulty was not found when the 19.8 mm tup diameter was adopted, without varying the support diameter (arrow in Fig. 11).

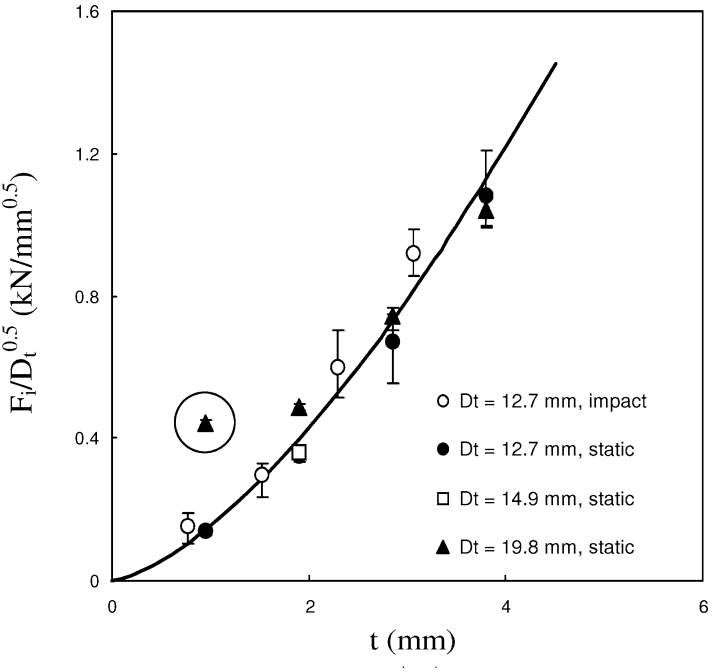


Fig. 10 Effect of the laminate thickness, t, and tup diameter, D_t, on the first failure load, F_i. Mat.: FT (Table 1)

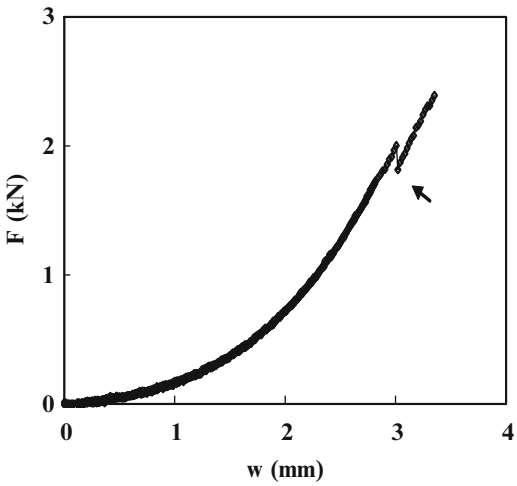


Fig. 11 Load-deflection curve at first failure t = 0.95 mm and a tup diameter D_t = 19.8 mm. Support diameter D = 50 mm

One of the hypotheses on which Eq. (7) relies is that the first failure is independent on the support diameter, being uniquely determined by the shear stresses, rather than by the normal stresses associated with the flexural moment.

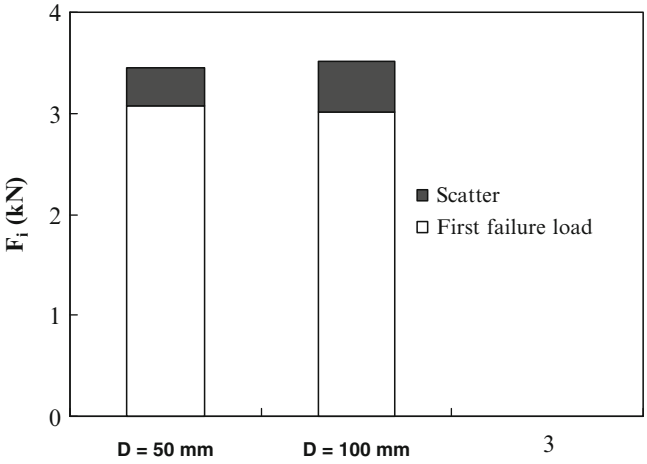
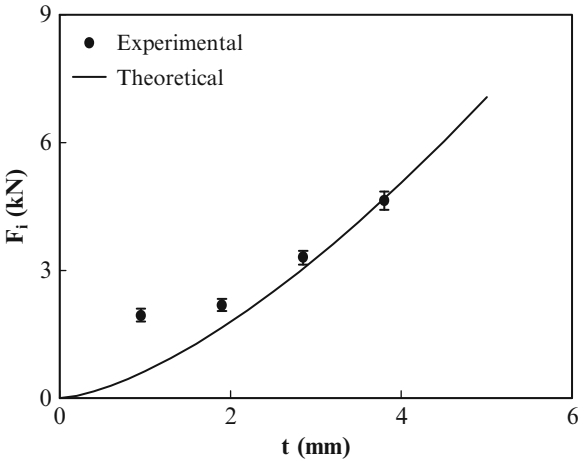


Fig. 12 Effect of the support diameter, D_s, on the first failure load, F_i. Plate thickness t = 2.85 mm; tup diameter D_t = 19.8 mm. Mat.: FT laminates (Table 1)

Fig. 13 First failure load, F_i, vs plate thickness, t, for a tup diameter D_t = 19.8 mm. Support diameter D_s = 50 mm



In Fig. 12, the first failure loads recorded in the tests carried out by adopting D_s = 50 mm and D_s = 100 mm for t = 2.85 mm and D_t = 19.8 mm are compared. The load inducing first failure is actually the same, independently of the support diameter which confirms the assumption made.

Comparing Eqs. (1) and (7) and accounting for the tup diameter (D_t = 12.7 mm), the δ value of 0.142 kN/mm^2 is immediately calculated from F_{io} = 0.507 kN/mm$^{1.5}$. Then, from Eq. (7) the critical load F_i was calculated as a function of t with D_t = 19.8 mm (continuous line in Fig. 13).

From the comparison of theory with the experimental data, the agreement is quite good for thick laminates whereas for thinner plates the predicted trend diverges from the actual one. An explanation of this occurrence is given hereafter.

Eq. (2), from which the first failure criterion is derived, is rigorously valid for a sphere impinging a flat plate. When the real plate is loaded with an increasing force, its curvature increases accordingly, so that Eq. (7) falls in defect. In particular, the actual contact area becomes larger than predicted from Eq. (7) [36]. As a consequence, the average shear stress (Eq. 4) decreases and the critical load F_i increases. This effect is more evident for thin than for thick plates, since their higher deflection for a given applied force. This explain why F_i is higher than expected for the thin laminates in Fig. 13. On the other hand, from the theory of Hertzian contact, the error in using Eq. (7) rapidly increases with increasing D_t. Therefore, the validity of this equation is anticipated to hold within a higher range of plate thicknesses for lower tup diameter values. This can justify the agreement between theory and experiments in Fig. 13.

From Eq. (7), the first failure load for the plates with $t = 1.9$ mm loaded by a 14.9 mm tup diameter was calculated, obtaining $F_i = 1.44$ kN. From three tests carried out on $D_s = 50$ mm, the mean value $F_i = 1.38$ kN, in good agreement with the theoretical prediction, was obtained. This result seems to confirm that the usefulness of Eq. (7) is retained if the tup diameter is small enough. When the scope of the test is the material characterisation in terms of δ, small tup and support diameters, and high plate thicknesses should be used to avoid large deflections of the plate, favouring the applicability of Eq. (7).

The simple dependence of the first failure on the specimen thickness independently of the tup diameter is in a complete agreement with the results published in [27] where about 350 specimens different in thickness and laminations and made of three different types of basic laminae were examined at the aim to investigate about the first failure load. The first failure load was found to vary with the laminate thickness to the 3/2 power too. The same was predicted by other investigators [47, 49–52]. Moreover, in [42] where the impactor diameter and the boundary conditions were fixed, F_i was found to be dependent on $t^{1.5}$ and the critical shear strength was found to be a constant value for the specific material system even if the laminates are made of laminae with different orientations.

3.3 Energy at Damage Initiation

Since the energy, rather than force, is the input datum in impact, one of the most important objectives in approaching the problem of impact is the possibility to predict the energy level in correspondence of which the first damage begins to develop. In what follow, the main factors affecting the absorbed energy at damage initiation are examined and from the results an analytical model is developed. The model allows the calculation of the first failure energy assuming that the total energy is shared in two parts, one of which stored in flexure, and the other in the material volume close to the contact zone.

The main energy absorbing mechanisms can be partitioned into, U_{flex}, the energy stored by the plate in bending; U_{ind}, is absorbed due to the localised contact deformation; some energy is dissipated through vibrations. It is difficult to separate the irreversibly absorbed energy that contributes to damage initiation and propagation. Many authors [53–56] have shown that, for sufficiently low velocity impact, that means up to 10 m/s [10, 28, 52, 57], the behaviour of carbon fibre reinforced plastics is independent of the loading rate, so that the dynamic response can be simulated by static tests. The energy dissipated by vibrations is negligible, and the flexural displacement w_o can be modelled by strength-of materials formulae. The same does not happen for GFRP laminates [58, 59] since the viscoelastic nature of the glass fibres.

Therefore, it can be assumed that, in a low velocity impact, the penetration of CFRPs energy is the sum of two components: one related to the flexure of the panel, and the other related to failure modes. A composite plate subjected to a transverse load absorbs energy by deformation and creation of damage zone. The material deformation occurs first and the panel absorbs energy through flexural deformation. This part of energy has been identified by elastic energy, U_{flex}. It is expected that the capacity to store elastic energy increases as the panel dimensions increase, since the flexural deformation will be larger, or when it is less constrained at the supports. In addition, plate deflections are proportional to the bending rigidities which in turn are proportional to the cube of the plate thickness [60] so that the decrease of the thickness has the same effect of the increase the panel dimension. In these cases, the structural rigidity became lower, provided the failure modes remain unchanged. U_i represents the limit energy below which no damage is present in the laminate. Energies supplied higher than U_i, are useful for damage initiation and propagation at perforation.

With these hypotheses, the energy absorbed by the material at the point of delamination initiation is given by:

$$U_i = \int_0^{w_t^*} F dw_t \tag{9}$$

where F is the applied load, $w_t = w_o + w_i$ where w_i is the indentation, w^*_t is the critical deflection at first failure, and

$$w_0 = K_f \frac{F}{D} \tag{10}$$

with K_f a constant depending on the boundary conditions and D the flexural rigidity, which for an orthotropic circular clamped plate can be calculated as the elements D_{ij} of the [D] matrix, through the relationship available in [16].

For the contact law, the following relationship holds:

$$F = K_{ind} \cdot w_i^{1.5} \tag{11}$$

Substituting w_o and w_i from Eqs. (10), (11) in Eq. (9) and integrating, it was possible to obtain U_i as:

$$U_i = \frac{K_f F_i^2}{2D} + \frac{2F_i^{5/3}}{5K_{ind}^{2/3}} \tag{12}$$

where the first and the second term on the right represent U_{flex} and U_{ind}, respectively.

From Eqs. (12) and (1):

$$U_i = \frac{K_f \cdot F_{io}^2 \cdot t^{2i}}{2D} + \frac{2F_{io}^{5/3} \cdot t^{5i/3}}{5K_{ind}^{2/3}} \tag{13}$$

From lamination theory, it can be verified that, for all the laminates taken into account:

$$D = K_D \cdot t^3 \tag{14}$$

with K_D a constant.

Since the dependence of F_i on the laminate thickness can be predicted very well by a power law having exponent $i = 1.5$ (see dashed line in Fig. 5), in the following this value will be adopted for simplicity. In fact, this assumption is in agreement with the hypothesis of contact law, underlying Eq. (13) (see Eq. (11)). Accounting for this and combining Eq. (13) and Eq. (14), it is finally found:

$$U_i = \frac{K_f \cdot F_{io}^2}{2K_D} + \frac{2F_{io}^{5/3} \cdot t^{2.5}}{5K_{ind}^{2/3}} \tag{15}$$

Therefore, according to Eq. (15), U_{flex} should be independent of the thickness, t, whereas U_{ind} should vary with $t^{2.5}$.

In Fig. 14, the measured U_i is plotted against t. It was found to increase rapidly with increasing the thickness of the laminate.

Plotting the data in Fig. 14 against $t^{2.5}$ as predicted from Eq. (15), the experimental points fall with excellent agreement along a solid straight line having equation:

$$U_i = 0.318 + 0.047t^{2.5} \tag{16}$$

with U_i in J and t in mm. From this equation, the U_{flex} is 0.318 J (dashed line in Fig. 14). This energy could be calculated from the first term on the right of Eq. (12), knowing that, for a clamped plate loaded by a concentrated force at the centre, the constant K_f is given by [16]:

$$K_f = \frac{R^2}{2\pi} \tag{17}$$

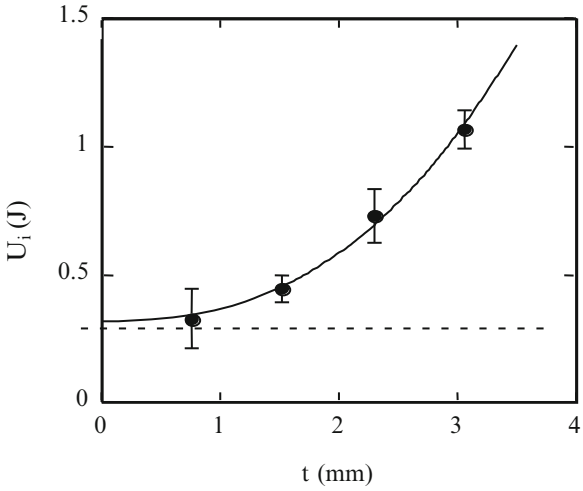


Fig. 14 Energy for damage initiation, U_i, against specimen thickness, t. Mat.: F (Table 1)

where R is the plate radius.

In [32], a different value of the constant affecting the second term on the right of Eq. (16) (0.016 KN/mm$^{1.5}$) is calculated from Eq. (15). The poor agreement with the experimental value found here (0.047 KN/mm$^{1.5}$) is due to fact that the resin type or the fibre form (fabric in the present case, unidirectional in [32]) play a major role in lowering the local rigidity of the material. Consequently, the relative importance of the flexural energy (dashed line in Fig. 14) dramatically changes as a function of the thickness: for very low t values, almost all the impact energy just before delamination initiation is stored in flexure; on the contrary, when $t = 3.1$ mm or more the energy is mainly accumulated in the material volume close to the contact area.

It was possible to separate the energy at delamination initiation into two major contributions: one accounting for flexural deformation and the other for local deformation. The latter part becomes more and more important as far as the specimen thickness increases, so that it cannot be neglected for thick laminates.

3.4 Prediction of the Load Versus Displacement Curve

An important question to be answered in studying impact on composite laminates is the energy U_i required to cause first failure. In fact, while up to U_i the original material strength is retained, beyond this limit a residual strength being the lower the larger the imparted energy is.

In order to calculate the elastic energy stored in a plate at first failure, two conditions must be met: (a) the load-deflection curve must be described accurately;

(b) the critical force (or deflection) resulting in first failure must be evaluated correctly. The latter point was already successfully discussed. In what follows, the first topic will be treated and the equations for the prediction of U_i will be derived.

The study of the elastic response of composite structures is made intricate by many phenomena, among which the in-plane and along-the-thickness anisotropy are the most relevant. The bending-stretching coupling effects [61, 62], as well as the shear contribution to the deformation [63, 64], can considerably complicate the analytical development too. It was possible to simplify the study by introducing the fact that, when the impact velocity is low (up to 10 m/s), the static and dynamic response are similar [53–55], so that vibrational effects can be neglected and static tests can be adopted to simulate the impact behaviour. This assumption will be maintained along all this section, so that the vibratory effects will be disregarded. Nevertheless, in the first part of the impact phenomenon, before first failure occurs, the plate can be bent significantly and so, the non-linear effects deriving from the large deflections (thin laminates or large support diameter) become evident [65, 66]. When the tup displacement is adopted to find the load-deflection curve, the contact law must be included in the analysis.

Static tests simulating the dynamic ones and low velocity impact tests were carried out on anisotropic, simply supported and clamped circular plates made of graphite fibre reinforced plastic laminates of various thicknesses, 0.95, 1.90, 2.85 and 3.80 mm (TF in Table 1). According to $[(0, 90)_n/+45_n/-45_n]_s$ stacking sequence, n = 1 to 4, the plates were loaded at the centre by a hemispherical tup 12.7 mm in diameter. Two basic prepreg laminae, made of T400 fibres and HMF 934 epoxy resin, were used: in one, the fibres reinforcement was a plain weave fabric with a 193 g/m^2 in areal weight; in the other, the reinforcement was unidirectional with a 145 g/m^2 in areal weight.

The square plates 70 mm in side cut from the panels, were simply supported on a steel plate having a circular opening 50 mm in diameter. Some tests were stopped when sudden load drops were observed on the curve, clearly indicating significant damage development in the specimen; others were interrupted at predetermined load levels to investigate about the damage evolution.

3.4.1 Theory and Results

In performing both static and impact tests on composite plates, the tup displacement is often assumed to measure the plate deflection even if, in the case under study, the local deformation due to the contact between the indentor and the plate surface (Fig. 15) must be accounted for.

In Fig. 15, w_i is the local indentation, w_o the plate deflection and w_t the overall tup displacement given by the sum of w_i and w_o:

$$w_t = w_o + w_i \tag{18}$$

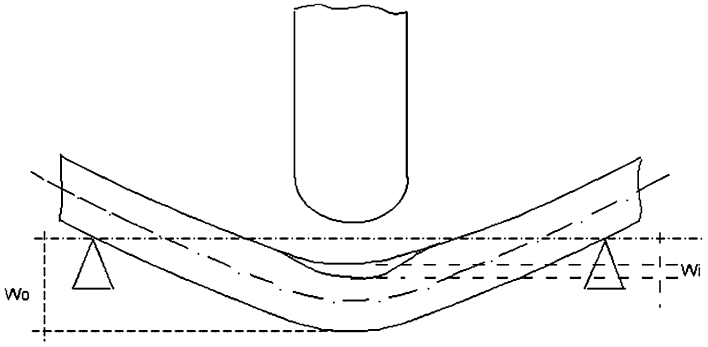


Fig. 15 Indentation due to the local contact tup-plate. w_i: local indentation; w_o: plate deflection

Simple strength-of-materials solutions are available in the literature, giving the deflection w_{ol} of circular isotropic plates subjected to small displacements. For instance, for a clamped plate loaded at the centre by a concentrated force F [16]:

$$w_{ol} = B \cdot \frac{F \cdot R^2}{E \cdot t^3} = \frac{F R^2}{16\pi D} \tag{19}$$

where R is the plate radius, $B = 1/16\pi$ a constant and $D = Et^3$ its flexural rigidity.

Unfortunately, the applicability of Eq. (19) to an anisotropic composite plate is not straightforward, since a laminate suffers the well known bending-stretching coupling effects [61, 62]. Moreover, the shear stresses arising along the thickness, whose effect is not taken into account in developing Eq. (19), can contribute considerably to w_{ol} [63, 64]. Finally, thin composite plates may be bent significantly before first failure occurs, overcoming the linear regime, within which Eq. (19) preserves its validity. The linear relationship between load and deflection, predicted by Eq. (19), is rapidly loosen with increasing the ratio of the deflection to the plate thickness, t. For sufficiently large values of this ratio, a higher-order theory, accounting for large displacements, must be addressed in order to accurately describe the elastic response of the structure [16]. Therefore, it is expected that, in general, w_o will not coincide with w_{ol}.

A closed-form, approximate solution for the large deflection of circular isotropic plates loaded at the centre is yielded in [16]:

$$\alpha D w_o + \beta E t w_o^3 = \frac{F R^2}{\pi} \tag{20}$$

α, β are two constants depending on the boundary conditions and E the elastic modulus of the material. In the case of clamped edge, $\alpha = 16$. The β value is strongly dependent on the possibility of the clamping device to prevent the radial displacement of the plate edge. If it is completely free, $\beta = 0.295$, whereas in the case of immovable edge $\beta = 0.650$ is readily obtained from the data in [16].

From Eqs. (19) and (20), it is easily to verify that $w_{ol} = w_o$ when the deflection is small, so that the cubic term on the left of Eq (20) is negligible compared to the linear one. The cubic term physically derives from the strain of the middle plane of the plate that is small when the deformation is small; as far as deformation increases, this phenomenon becomes more and more important and it must be accounted for in the analysis of large displacements.

Hoping that the validity of Eq. (20) could be retained at least for quasi-isotropic laminates exhibiting a moderate flexural anisotropy, its form was adopted in [67] as a starting point to model the load-displacement of composite plates. The E value in the equation, governing the stretching of the middle plane, was substituted by the in-plane modulus of the laminate. Recognizing that all the terms of the [D] matrix for a laminate can be expressed in the general form:

$$D = D_u t^3 \tag{21}$$

where D_u is representative of the flexural behaviour of the laminate, Eq. (20) was reduced to the following expression:

$$\frac{w_o}{t} + A\left(\frac{w_o}{t}\right)^3 = B\frac{F R^2}{E t^4} \tag{22}$$

with:

$$A = \frac{\beta E}{\alpha D_u} \tag{23}$$

$$B = \frac{1}{\pi\alpha} \tag{24}$$

From Eq. (18), also the local deformation w_i occurring at the tup-plate contact point must be known, if the overall displacement of the impactor is wanted. Rewriting Eq. (1) as a function of the local indentation [32]:

$$F = k_i (w_i)^{3/2} \tag{25}$$

useful in calculating the indentation w_i (Fig. 15).

In the field of small deflections, combining Eqs. (19), (18) and (25), the following relationship:

$$w_t = B \cdot \frac{F \cdot R^2}{E \cdot t^3} + \left(\frac{F}{k_i}\right)^{2/3} \tag{26}$$

is obtained. Equation (26) is valid only in the field of small displacements, since Eq. (19) suffers the same limitation.

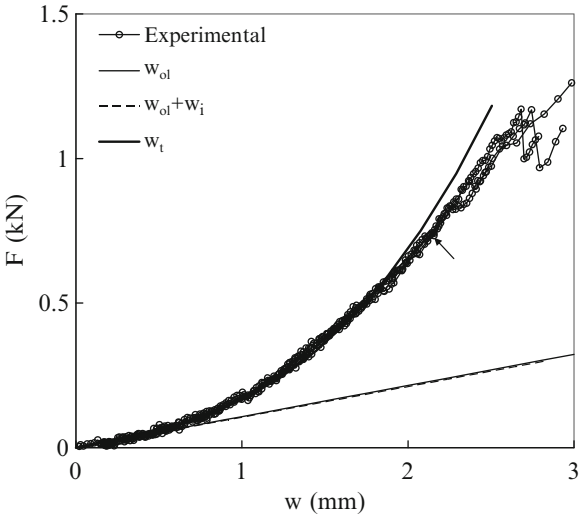


Fig. 16 Experimental load-deflection curves and theoretical predictions for the specimens with t = 0.95 mm

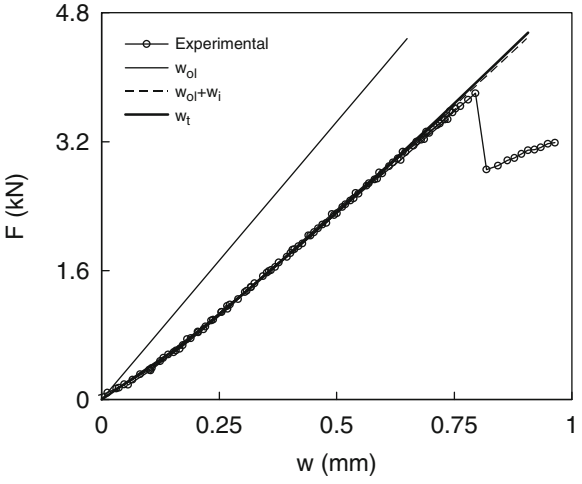


Fig. 17 Experimental load-deflection curves and theoretical predictions for the specimens with t = 3.80 mm

In Figs. 16 and 17, plots of the recorded load-displacement curves are shown for the lowest and the largest plate thickness tested, respectively. Apart some low-frequency oscillations, due to the dynamic effects, a divergence from the linear regime is observed in Fig. 16, with the plate rigidity increasing with increasing deformation. At a sufficiently high load (arrow in Fig. 16), high-frequency oscillations superpose to the fundamental frequency: this is a macroscopic effect of the first failures occurring in the laminate, revealed by the ultrasonic analysis, consisting of intralaminar cracks and delamination. Afterwards, both the load and the rigidity rise anew, until a clear load drop, denoting more pronounced failure phenomena, is recorded.

An increase in rigidity is present also in the first part of the curve in Fig. 17 even if, comparing Figs. 16 and 17, it is evident that the deviation from linearity is much more limited when a thick laminate is examined. This is expected from Eq. (22), according to which the effect of nonlinearity is more and more remarkable as the ratio of the deflection to the specimen thickness increases. Interestingly, it is confirmed that the first failure is much easier to detect from the load-displacement curve of the thick plate, resulting in a sharp load drop.

The continuous straight lines in Figs. 16 and 17 are the predictions of the load-deflection curves obtained on the basis of Eq. (19), i.e. simply assuming a linear behaviour without local indentation. Although the agreement between theory and experiments is good in the very early stage of loading in Fig. 16, the linear approximation results in an unacceptable error as soon as the deformation increases. Instead, for the thickest plate the theoretical prediction based on Eq. (19) results in a significant overestimation of the rigidity.

In order to assess the model presented, Eq. (25), to take into account the effect of non linearity, it is necessary to know the constants A and B/E in Eq. (22), and k_i in Eq. (25). To obtain B/E and k_i, use of Eq. (26) was made, together with an original method of data reduction, which was applied to the very early, linear portion of the load-displacement curve pertaining to $t = 3.80$ mm. The values $B/E = 1.27 \times 10^{-2}$ GPa^{-1} and $k_i = 34.9$ kN/mm$^{3/2}$ (C.V. $= 4.3\%$) were found here and adopted to evaluate $A = 0.56$ by best-fitting the load-displacement curve for $t = 1.90$ mm. The measured value of B/E was adopted in all the calculations hereafter. Some previous data, witnessing the physical consistency of the constants found, were recalled. In [32], values of k_i in the range 31.8–36.8 kN/mm$^{3/2}$, in excellent agreement with k_i evaluated here, were obtained. It was also shown that k_i is unaffected by the boundary conditions and specimen geometry, depending exclusively on the material and tup radius.

The dashed lines in Figs. 16 and 17 were drawn using the previous experimental values for B/E and k_i to calculate the quantity $(w_{ol} + w_i)$, even if they represent the predictions deriving from the hypotheses of linear elasticity and local indentation. Comparing these lines with the continuous straight ones previously discussed, it clearly emerges the role of local deformation w_i in determining the overall plate deflection. For the thinnest plates (Fig. 16), the two lines are practically coincident, indicating a negligible effect of the indentation whereas, the gap between the two curves increases with increasing the plate thickness. In Fig. 17, in fact for the laminate 3.80 mm thick the gap between the two curves is considerable. These results are qualitatively anticipated since large local deformations require high loads, which only thick plates can withstand without exceeding the elastic field.

However, from the comparison between Figs. 16 and 17, Eq. (26) tends to underestimate the force values for a fixed deflection value, with an error rapidly increasing with decreasing t resulting in an analytic solution unacceptably inaccurate for the thinnest plates (Fig. 16).

The thick solid curves in Figs. 16 and 17 represent the theoretical predictions from Eqs. (22) and (18), i.e. taking into account all the factors involved in the

deformation of the laminates. In the case of the 3.80 mm thick plates (Fig. 17), the non-linearity effect due to the cubic term in Eq. (22) is very small, as witnessed by the negligible difference between the dashed and the thick continuous curves. The influence of non-linearity increases with the decrease of the thickness, and it is very evident for the thinnest plate (Fig. 16). In any case, the load-deflection curve is modelled with great accuracy by theory as also confirmed by the data concerning the laminates of intermediate thicknesses, not shown here for brevity.

In conclusion, at this point it is possible to say that about the possibility to predict the first part of the load curve, for thin plates, the effect of indentation on the overall deflection can be neglected, whereas the cubic component in Eq. (22) plays a major role in determining the plate response; at the increasing of the thickness, the influence of the cubic component in Eq. (22) becomes lower and lower, whereas the effect of indentation on the deflection becomes relevant.

In what discussed above, generated under quasi-static conditions, demonstrated that Eq. (22) alone is not capable to efficiently describe the plate behaviour. The reason was found in the local indentation w_i occurring at the indentor-material contact point, which markedly affects the response of the structure, especially when large thicknesses are involved.

Three constants, A, B and k_i, were experimentally determined to solve the problem of the prediction of the elastic behaviour of a plate under dynamic conditions.

Further experimental support to the previous theoretical model was provided in subsequent works, where [67] the load-displacement curves deriving from both static and low-velocity impact tests on fabric laminates were predicted accurately. The possibility to reduce to two the number of unknown constants, yet achieving a reasonably good agreement between theory and experiments, was also discussed.

A modified version of the solution proposed above for quasi statically loaded tape laminates was developed in [67] for fabric laminae (F in Table 1) subjected to low-velocity impact. The formula (Eq. 22) was modified, to take into account the tup displacement associated with indentation. It is shown that the number of unknown constants can be reduced to two, yet achieving a good agreement between theory and experiments. Further, the relative importance of indentation and large displacements in affecting the load-displacement curve is assessed.

From the results, the analytical model accurately describes the actual elastic behaviour of the plates, provided two of the constants appearing in it are experimentally determined. The results discussed about thin and thick laminates were confirmed.

By the best fit method, the local rigidity $k_i = 12.0$ kN/mm$^{3/2}$ was obtained by Eq. (26) and from the curves recorded for the thickest plates. This value is about one third-one fourth compared with those found above and in [32, 68] for CFRP laminates made of tape laminae. This is due to the fabric architecture of the present composites, possibly playing a role in lowering k_i. The previous k_i was adopted as a constant independent of the laminate thickness [32].

Table 2 Plate thicknesses adopted for the various support diameters, D_s, and tup diameters, D_t

	D (mm)	
D_t (mm)	50	100
12.7	A	
14.9	1.90	
19.8	A	2.85

Legend: *A* All thicknesses

3.4.2 Influence of Support and Impactor Diameter. Development About First Failure Energy

Since the good results obtained for the prediction of the elastic part of the load curve, it is possible to proceed at the prediction of the elastic energy stored at first failure in a circular composite plate. The previous model is developed here to take explicitly into account the tup diameter, and is coupled with a previous formula [24] which is aimed at the prediction of the first failure load. From the two models, a formula for the calculation of the energy stored at first failure as a function of the test and material parameters is derived. Only when both the deflection at first failure and the tup diameter are large enough, the first failure load is significantly underestimated. The contribution of the different mechanisms of energy storage to the total energy at first failure is identified by the study of the analytical model. At the end, an analytical expression for the evaluation of the energy will be obtained.

The experimental tests were carried out on carbon fibre reinforced plastic laminates (FT in Table 1) of various thicknesses, which were simply supported at the periphery and loaded using two different supports, $D_s = 50$ mm and $D_s = 100$ mm, and three indentor diameters, $D_t = 12.7$ mm, 14.9 mm, and 19.8 mm. Table 2 shows the matrix of the experimental conditions adopted.

Some tests were stopped when sudden load drops were observed, others at predetermined load levels. After mechanical tests, each specimen was visually inspected and was then non-destructively evaluated by ultrasonic C-scan. Some of the samples were also sectioned, polished, and microscopically observed.

The results show that the elastic model, which takes into account the non-linearity due to the large displacements and the local indentation, is very accurate in shaping the load-deflection curve up to the first failure point. Also the predicted load and energy at first failure are in good agreement with the corresponding measured values. Both theory and experiments demonstrate that the critical load is independent of the support diameter in the range examined (50–100 mm), whereas it increases with increasing the plate thickness and the indentor diameter.

Comparing Eqs. (25) and (7), the influence of D_t on the local rigidity is clear:

$$k_i = \delta \cdot (D_t)^{1/2} \tag{27}$$

Knowing the k_i value for a given tup diameter, the corresponding local rigidity for another D_t value can be calculated.

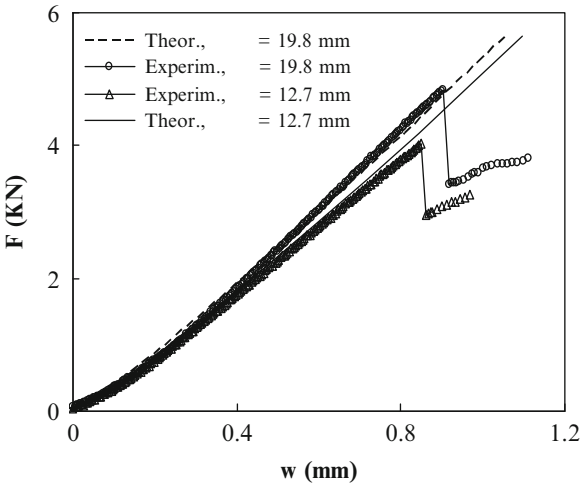


Fig. 18 Load-deflection curves for two different tup diameters, D_t. Plate thickness t = 3.80 mm. Support diameter D_s = 50 mm

For a given laminate and fixed boundary conditions, A and B/E will not change when the tup and support diameter are varied. k_i is a function of D_t through Eq. (27). Therefore, this equation can be used to calculate the appropriate value of the local rigidity for a given tup diameter, starting from k_i value found in the first part of this paragraph for the FT laminates of 34.9 kN/mm$^{3/2}$.

The effectiveness of Eq. (18) was already verified for different plate thicknesses. Hereafter the dependence of the elastic behaviour on D_s and D_t is estimated. Since the local rigidity was shown to be more evident when the flexural rigidity of the laminate is high, the support diameter $D_s = 50$ mm and the plate thickness t = 3.80 mm were adopted to verify the influence of the indentor diameter on the plate response.

From Fig. 18 (open symbols), the lower the tup diameter is, the lower the overall plate rigidity that is given by the rigidity of the plate plus the local rigidity, in qualitative agreement with Eq. (27).

The effect of the tup diameter within the range of D_t values considered is only moderate (Fig. 18). In the same figure, the theoretical predictions based on the analytical model are also plotted. The comparison between theory and experiments demonstrates an excellent agreement until the first failure point. The results obtained using Eq. (27) is interesting since some data was presented [32], showing that Eq. (27) does not model the effect of the tup diameter precisely.

The analytical prediction was successful used also to model the first part of the curve obtained using the support diameter $D_s = 100$ mm and tup diameter $D_t = 19.8$ mm. It is possible to conclude that the model is very accurate in describing the elastic behaviour of the laminate, accounting for the effect of thickness, as well as the influence of the support diameter and tup diameter.

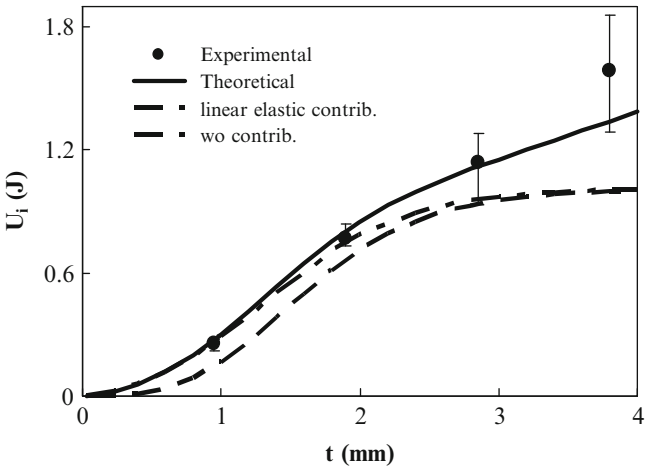


Fig. 19 First failure energy, U_i, against laminate thickness, t. Support diameter D = 50 mm; tup diameter D_t = 12.7 mm. Mat.: FT (Table 1)

Combining Eqs. (22), (25), and (9), and solving the integral, the following equation is obtained:

$$U_i = \frac{2 \cdot E \cdot w_o^{*2} \cdot t}{B \cdot D^2} \cdot \left(t^2 + A \cdot \frac{w_o^{*2}}{2} \right) + \frac{2 \cdot k_i \cdot w_i^{*5/2}}{5} \tag{28}$$

where the asterisk indicates the components of the deflection when $F = F_i$.

From Eq. (28), the first failure energy U_i as a function of the laminate thickness was calculated for the case D = 50 mm, D_t = 12.7 mm, and plotted (continuous line) in Fig. 19. The solid symbols are the experimental data, and show a very reasonable correlation with theory except for the thickest plates. In this case, the slight divergence of the actual trend from the expected one immediately before the load drop (Fig. 18) results in underestimating the actual energy storage capability of the material.

Looking at Fig. 19, the experimental data trend is well represented by a straight line but this should be misleading in the interpretation of the results in particular because the line does not pass through the origin, violating the boundary conditions.

The dashed line in Fig. 19 represents the energy associated with the linear elastic part of w_o, calculated through the analytical model. The dash-and-spot line is the portion of U_i due to w_o. Therefore, from the comparison of the two curves the effect of the cubic component of w_o on the stored energy is evidenced. As witnessed by the trend of the dash-and-spot and continuous line in Fig. 19, when high thicknesses are concerned, the importance of the energy correlated to the contact law cannot be neglected.

The model presented in Eq. (15) to explain the energy stored at first failure in fabric reinforced, quasi-isotropic CFRP laminates of different thicknesses, yielded consistent results. However, constant k_i values far lower than expected from

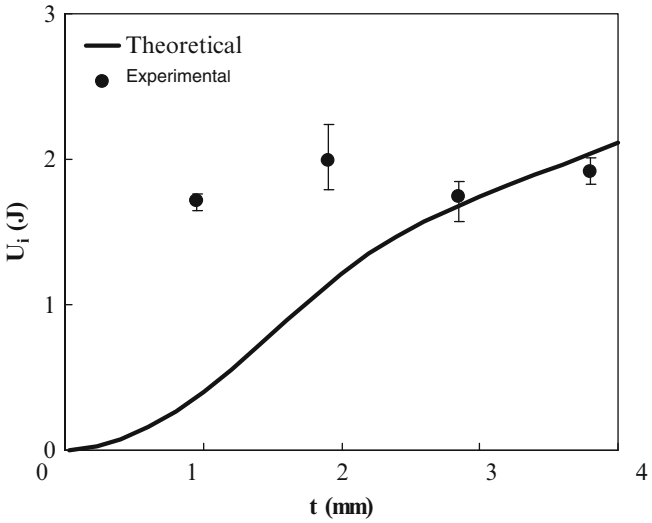


Fig. 20 First failure energy, U_i, against laminate thickness, t. Support diameter D = 50 mm; tup diameter D_t = 19.8 mm. Mat.: FT (Table 1)

previous works [32] were obtained through the energy data. The present results indicate that a reason for the poor correlation is the effect of non-linearity correlated with the cubic component of the deflection.

To add further confidence in the effectiveness of theory, the first failure energy for the case $D_s = 50$ mm, $D_t = 14.9$ mm was also evaluated through the present theoretical model. It was obtained $U_i = 0.91$ J, practically coincident with the measured value $U_i = 0.92$ J. The experimental results (symbols) and the analytical prediction (curve) of the first failure energy as a function of t for the case $D_s = 50$ mm, $D_t = 19.8$ mm are reported in Fig. 20. The agreement between theory and experiments is good only for a thickness $t \geq 2.85$ mm, whereas it is poor for the thinnest plates. This is not surprising, considering the effect of the plate curvature under loading on F_i, noted in Fig. 13. The interesting finding from Fig. 20 is that, especially when the plate is thin, the deformation can give a major contribution to its capacity of energy storage before first failure.

In Fig. 21, the influence of the support diameter on U_i is seen, where the data referring to a tup diameter $D_t = 19.8$ mm and $t = 2.85$ mm are also plotted as solid symbols, and the continuous line represents the corresponding prediction. Also in this case, the agreement between theoretical estimates and experimental results is satisfying. Of course, the increase in U_i with increasing D_s is due to the decrease in rigidity, together with the fact that the critical load remains the same, whichever D_s (Fig. 12).

For D_s values approaching zero, the accuracy of the present analytical model is expected to fail: in this case, the plate diameter becomes comparable with its thickness, so that the contribution of the shear deformation to the elastic behaviour, not considered here, becomes significant [33, 34].

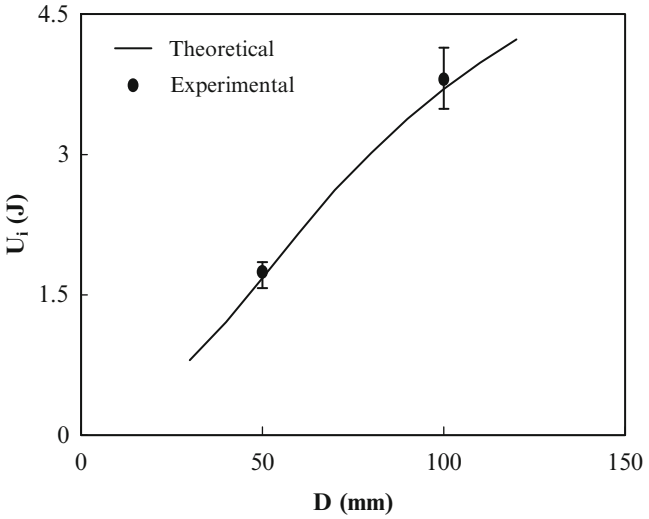


Fig. 21 Effect of the support diameter, D_s, on the first failure energy, U_i. Mat.: FT (Table 1)

According to Eq. (28), U_i is made of the sum of three terms associated with the linear and cubic components of the deflection and indentation, respectively. Consequently, the relative importance of the different mechanisms of energy storage at first failure can be appreciated if four constants, A and B/E in Eq. (22), k_i in Eq. (25), and δ in Eq. (7), are known.

The closed-form formula proposed and developed, aiming to predict the non-linear elastic behaviour of the plate, is successful in modelling the effect of both the support diameter and the indentor diameter on the elastic response. The first failure load is independent of the support diameter whereas it is a strong function of the tup diameter. Increasing the indentor diameter results in an increase in the critical load but this law is violated when the curvature caused by the applied load is significant compared to the indentor diameter.

3.4.3 Failure Energy of Glass-Fibre-Reinforced Plastic Panels

The above presented model was hereafter applied to predict the critical energy at first failure of simply supported circular glass-fibre-reinforced plastic laminates made of glass fabric/epoxy prepreg (G in Table 1). Four panel thicknesses, keeping the stacking sequence unchanged, and two tup diameters, $D_t = 16$ mm and $D_t = 19.8$ mm, were employed to verify the influence of these parameters on the elastic behaviour and first failure conditions of the material. Selected specimens was burnt away, and optical microscopy at low magnification was used to reveal possible reinforcement fracture. The experimental results were used to assess the same model proposed (Eq. 22) in the case of low velocity, large mass impact

on CFRP. The calculated values were in reasonably good agreement with their experimental counterparts. Only for the thickest laminate, the model yielded a far conservative estimate of the critical energy at first fibre failure, due to the deviation of the experimental load-displacement curve from the theoretical trend.

Through Eqs. (18), (22) and (25), the F-d curve is easily drawn: assigning a F value, w_o and w_i are calculated through Eqs. (22) and (25), respectively, then Eq. (18) gives w_t.

Accounting for Eqs. (18), (22), (25) and (7), Eq. (9) provided Eq. (28).

It is important to observe that Eq. (7), based on a stress approach rather than the more popular model proposed by Davies and Zhang [51]:

$$F_i = \pi \sqrt{\frac{8Et^3 G_{IIc}}{9(1-\nu^2)}} \tag{29}$$

deriving from energy considerations and successful in predicting delamination initiation for many quasi-isotropic laminates [51, 69, 70], was used in this work to calculate F_i. In Eq. (29), G_{IIc} is the Mode II delamination toughness, ν is the Poisson's ratio considered quasi-isotropic in the analytical development.

According to both Eqs. (7) and (29), F_i linearly increases with increasing $t^{3/2}$ whereas contrary to Eq. (29), Eq. (7) predicts a dependence of the threshold load on the tup diameter, not appearing from Eq. (29). Some experimental results supporting the increase of F_i with increasing D_t, in agreement with Eq. (7), were presented in [71].

In correspondence of the load drop in the force-displacement curve, fibre failure appeared at the back face of the laminate, as confirmed by optical microscopy after resin burning. Consequently, the load arrowed in Fig. 22 recorded for thin plates was attributed to fibre failure and is indicated by the symbol F_f hereafter.

In correspondence of the point signalled by the arrow in Fig. 23, obtained on thick plates, some irregularities, giving rise to a sawtooth appearance similar to the one observed in thin laminates, were noted. From visual analysis after tests, the knee signalling the departure from linearity was associated with delamination, and the abscissa of the corresponding load, F_d, was conventionally evaluated from the intercept of the two straight lines (dashed lines in Fig. 23) best fitting the approximately linear trend of the load-displacement curve before and beyond the knee, respectively. The maximum contact force preceding the sawtooth portion of the load-displacement curve (arrow in Fig. 23), associated with fibre failure, was also recorded.

Effect of Speed and Mass

The energy U in the impact tests was changed by varying not only the mass, but also the falling height (i.e. the tup velocity). This allowed to verify whether the parameters relevant to the impact phenomenon are rate-dependent or mass-dependent.

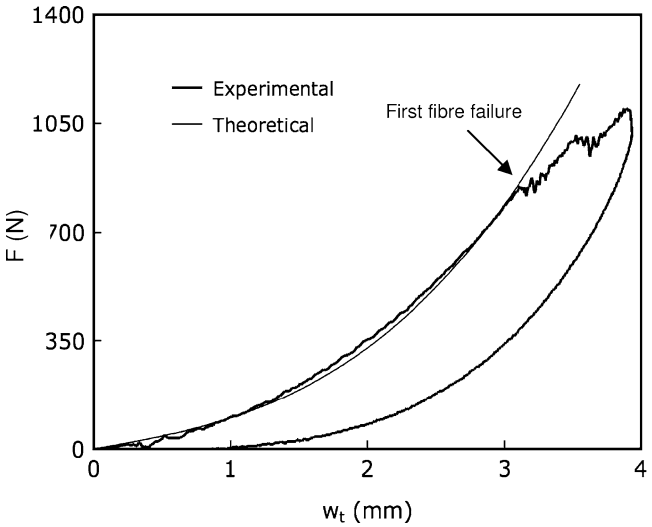


Fig. 22 Typical load-displacement curve recorded for the GFRP panels of thickness t = 0.96 mm. Indentor diameter D_t = 16 mm. Impact energy U = 1.68 J

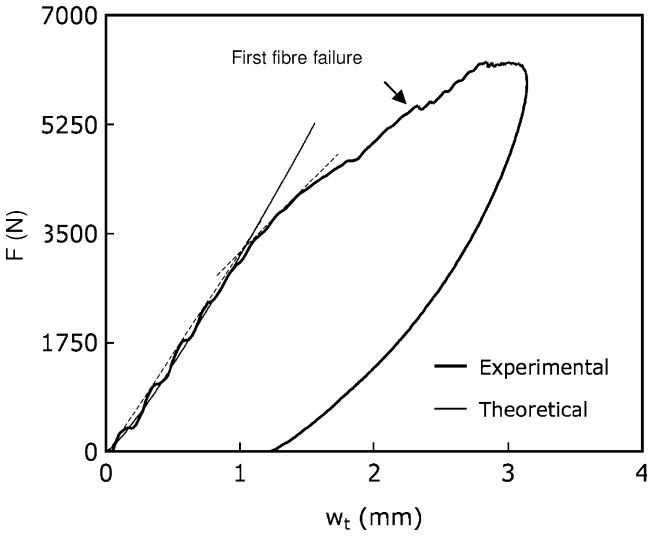


Fig. 23 Typical load-displacement curve recorded for the GFRP panels of thickness t = 3.84 mm. Indentor diameter D_t = 16 mm. Impact energy U = 12.2 J

Figure 24 shows the measured delamination load, F_d and the associated energy, U_d versus the impact energy, U, for t = 3.84 mm and D_t = 16 mm. They are, both, negligibly influenced by the impact energy and mass in the range adopted. The same was concluded by the examination of the shape of the overall F-d curves that is the same whichever the speed and mass.

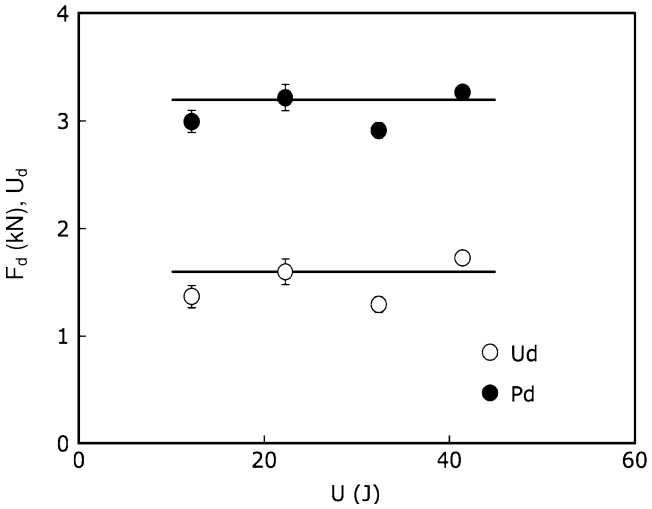


Fig. 24 Delamination load, F_d, and associated energy, U_d, against impact energy, U. Indentor diameter $D_t = 16$ mm. Panel thickness $t = 3.84$ mm

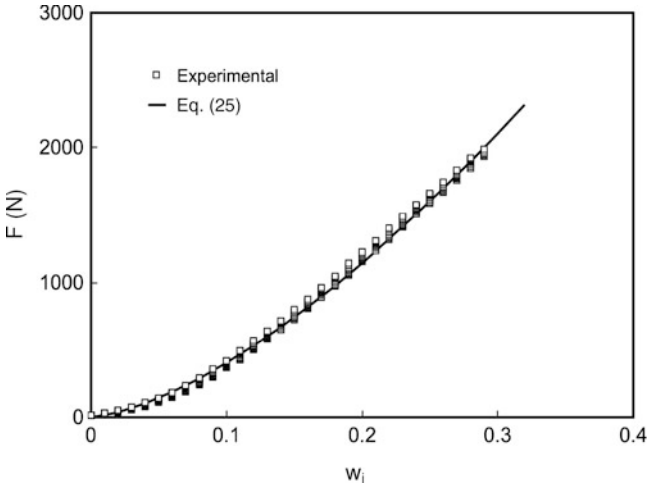


Fig. 25 Contact force, F, against indentation, w_i

To predict the load-displacement curve in the elastic phase through Eqs. (18), (22) and (25), the constants A, B/E, α must be known. As previously specified, α was directly measured through indentation tests, (results in Fig. 25). The solid line in Fig. 25 was drawn by Eq. (25), where $\alpha = 2.95$ KN/mm^2 was calculated by best fitting the experimental data. The good agreement between theory and experiments indicates that the contact law is effective in describing the phenomenon under study.

The values $A = 0.30$, $B/E = 1.73 \times 10^{-2}$ GPa^{-1} were obtained by a numerical technique based on the best-fit method, using the elastic portion of all the load-displacement curves. The A value is very near to that (0.27) valid for a simply supported, circular isotropic panel loaded at the centre [16] whereas it was previously found to hold 0.56, when CFRP laminates characterized by a low anisotropy ratio were tested. On the other hand, assuming $B = 0.55$ (isotropic materials), an unrealistically high E value, $E = 31.8$ GPa, larger than the elastic modulus (22–25 GPa) of the basic layer along the warp and weft directions, is calculated from B/E.

By substituting in Eqs. (18), (22) and (25) the values of the constants previously specified, the theoretical load-displacement curves were calculated and compared with the experimental ones (thin lines in Figs. 22 and 23). The correlation is outstanding at low displacements, indicating the effectiveness of the solution proposed in representing the elastic response of the panels. Beyond a given contact force, the experimental curves diverge from the calculated ones, denoting different damages.

According to theory, the effect of D_t on the overall shape of the elastic portion of the load curve is the more important, the thicker the laminate is. However, even for $t = 3.84$ mm, the effect of the tup diameter is hardly observable in the cases examined in this work: although not shown in Fig. 23 to avoid crowding of data, the thin line in the figure was hardly distinguishable from the one pertaining to $D_t = 19.8$ mm. It was confirmed by the results of the experimental tests.

Assessment of the Force Model

The open symbols in Fig. 26 are the measured F_d, whereas the full points in the same figure are the F_f values, plotted against panel thickness. Two different symbols have been used to distinguish the two impactor diameters, the vertical bars denote standard deviation. Both F_d and F_f increase steadily with increasing t and for a given t, a larger D_t results in a higher value of the first failure force.

From Eq. (7), the F_d data associated with the two tup diameters in Fig. 26 should converge to a single master curve, if the quantity $F_d/D_t^{0.5}$ is reported on the ordinate axis. In Fig. 27 the results in Fig. 26 have been rearranged according to this procedure: it shows that this actually occurs, supporting the effectiveness of Eq. (7) in modelling the influence of the tup diameter on F_d. More interestingly, the same law seems to be valid also for F_f. This result is not expected: the hypotheses on which Eq. (7) relies concern the distribution of the through-the-thickness shear stresses [10], which govern delamination initiation and propagation. The same assumptions are hardly acceptable for the normal stresses, responsible for fibre failure.

The solid and dashed lines in Fig. 27 graphically represent Eq. (7), in which the constant δ was calculated by best fitting the F_d and F_f data, respectively, obtaining $\delta = 105$ MPa (delamination) and $\delta = 200$ MPa (fibre failure). With these values in Eq. (7), the curves in Fig. 26 were drawn: they follow with sufficient accuracy the experimental results.

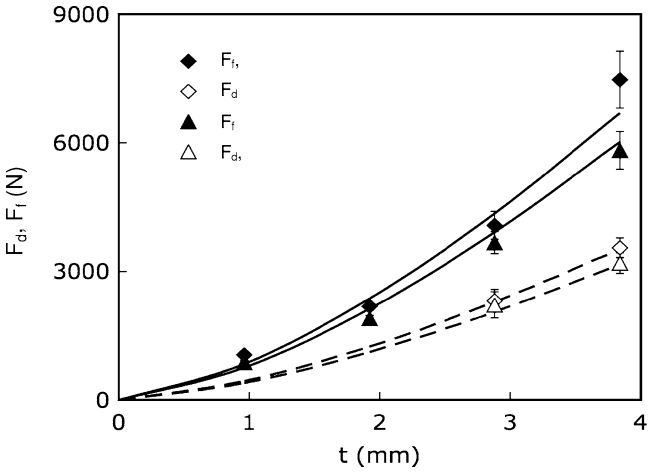


Fig. 26 Critical loads for delamination initiation, F_d, and fibre failure, F_f, vs panel thickness, t, for the two impactor diameters D_t used: open symbols $D_t = 16$ mm; full symbols $D_t = 19.8$ mm. Mat.: G (Table 1)

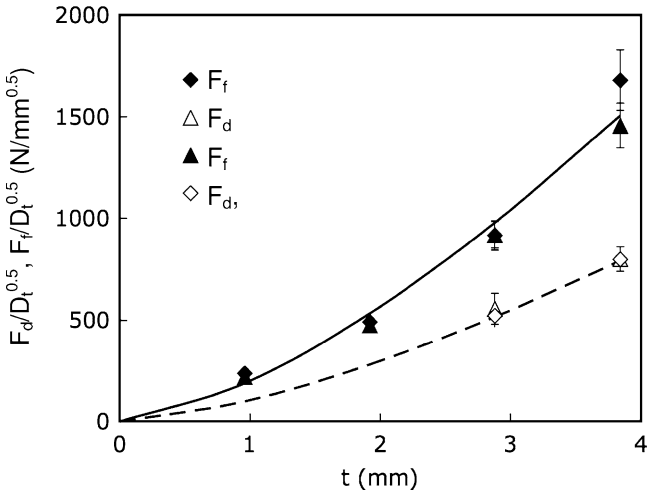


Fig. 27 $F_d/D_t^{0.5}$ and $F_f/D_t^{0.5}$ ratios versus panel thickness, t

First Failure Energy

The solid symbols in Fig. 28 represent the experimental energy at first fibre failure (yielded by the force-displacement curves in correspondence of F_f) against t for the two D_t adopted. The open symbols in the same figure are the energy U_d at delamination initiation. An increasing function of both laminate thickness and indentor diameter was found.

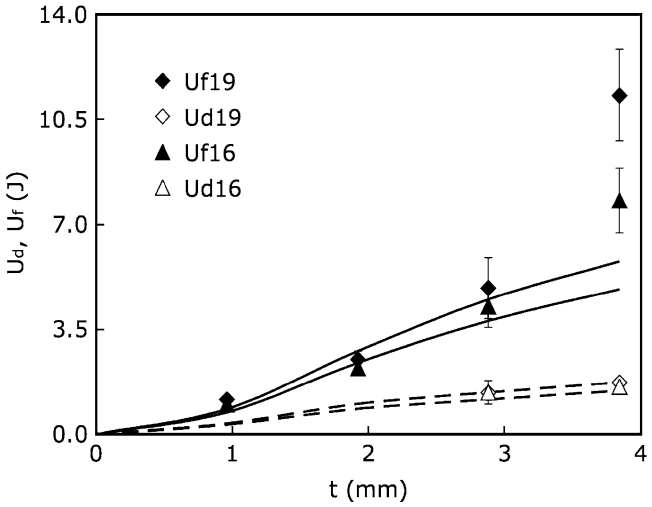


Fig. 28 Energies for delamination initiation, U_d, and first fibre failure, U_f, against panel thickness, t, for the two impactor diameters D_t used. open symbols $D_t = 16$ mm; full symbols $D_t = 19.8$ mm. Mat.: G (Table 1)

The curves in Fig. 28 were obtained by the theoretical predictions of the critical energies based on Eq. (28), in which the appropriate values of F_i ($F_i = F_d$, $F_i = F_f$) where inserted to obtain the corresponding energies ($U_i = U_d$, solid lines; $U_i = U_f$, dashed lines). The theory strongly underestimates U_f for $t = 3.84$ mm. It was anticipated, because of the knee in the load-displacement curves of the thickest panels, not taken into account by theory, bringing to an underestimation of the critical displacement at first fibre failure, w_f (Fig. 29). In the other cases, the theoretical model predicts with reasonable accuracy the experimental results also for the 2.88 mm thick panels, despite the existence of the knee in the load-displacement curve. The incongruence is explained by the fact that, as noted previously, the deviation from the theoretical elastic behaviour induced by delamination occurrence was negligible in this case.

From theory, the energy for delamination initiation in the 1.92 mm thick laminates is $U_d = 0.85$ J and $U_d = 1.01$ J for the two different impactors $D_t = 16$ mm and $D_t = 19.8$ mm, respectively. Unfortunately, impact tests at so low energy levels could not be carried out. Only a limited number of tests were performed setting $U \approx 1.5$ J using both the impactor diameters. Delaminated areas in the range 20–25 mm^2 were revealed by the visual inspections, whereas no evidence of fibre damage was yielded by the analysis after resin burning. This observation confirms that matrix damage is introduced in the material well before U_f is reached and the small extent of delamination suggests a stable growth, explaining the difficulty to individuate the occurrence of this mode of damage from the analysis of the load-displacement curve.

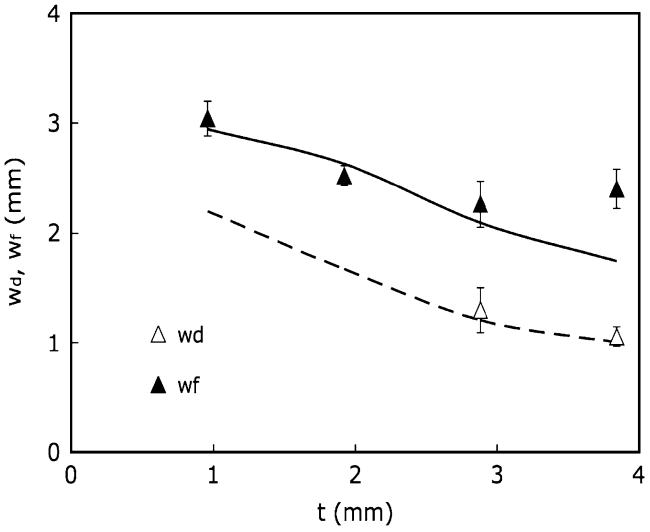


Fig. 29 Critical displacements at delamination initiation, w_d, and at first fibre failure, w_f, versus panel thickness, t. Tup diameter $D_t = 16$ mm. Curves: theoretical predictions

Final Considerations

A strategy suggested to easily determine the four constants appearing in the presented model (Eq. (22)) consists of two impact tests to be performed on a thick and a thin laminate, respectively. At low displacements, the cubic component of displacement for a thick laminate is negligible, while the effect of indentation is to take into account; these are the best conditions for measuring B/E and k_i from the load-displacement curve through the suggested procedure. On the contrary, the influence of indentation on the load curve of a thin laminate is insignificant whereas the membrane effect is evident, thus allowing for the evaluation of A. At the end, if the threshold load F_i is recorded from at least one of the two curves, also the constant δ is immediately obtained.

The present model does not account for the shear component of deflection, whose importance becomes more relevant the higher the ratios E/G (with G being the through-the-thickness shear modulus of the laminate) and t/D are, and the lower the indentor diameter is [52, 57]. The evaluation of the inaccuracy deriving from this approximation is not easy, because the shear stiffness is a function of contact area, which increases with the increasing of the applied load. To roughly estimate the maximum error made in the examined case, the data concerning the thickest panels and the lowest tup diameter were considered and the contact area pertaining to the maximum load experienced at the elastic limit was calculated through the equation provided in [12]. The shear and flexural stiffness were estimated, assuming typical values for the laminate elastic constants: the shear stiffness was found to be approximately ten times the flexural stiffness, resulting in a 9% error in the prediction of critical energy.

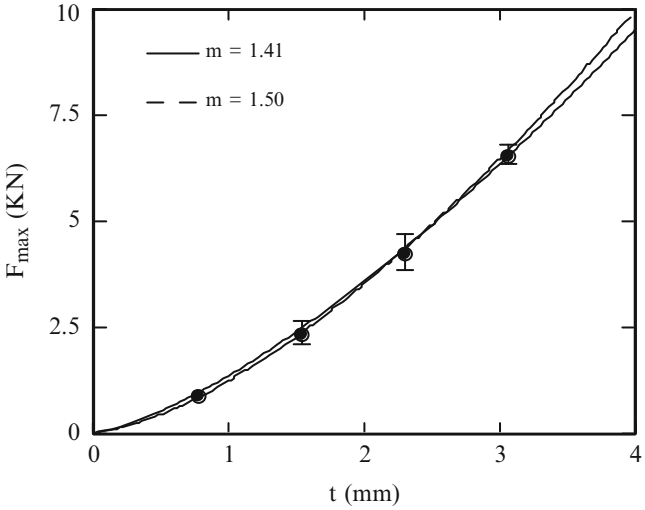


Fig. 30 Maximum contact force, F_{max}, against laminate thickness, t. Mat.: F (Table 1)

However, at the end, the discussed model is revealed to be able to accurately shape the elastic portion of the load-displacement curve, even when the laminate is so thin to exhibit an evident nonlinearity correlated with membrane effects It is able to predict the contact force corresponding to delamination initiation by a power law, in which a single parameter must be measured; the energy for delamination initiation, so that the energy at first fibre failure are well predicted by the model.

3.5 Maximum Force and Energy

The maximum contact force, F_{max}, could represent an important parameter in predicting the impact behaviour of composite laminates. Different authors [34, 72, 73], have noted that the failures in a laminate are force dependent rather than energy dependent. For this reason, it is necessary to understand how parameters such as specimen thickness can influence its value.

It was found that also F_{max}, follows a power law as a function of the thickness, with the exponent very similar to the exponent of the contact law. The same holds for the maximum energy, U_{max}.

In Fig. 30, the maximum load, F_{max}, measured on F carbon fibre laminates (Table 1) made of T400 fibres and HMF 934 epoxy resin, is plotted against the four specimen thickness, t, obtained with the following stacking sequence $\{[(0, 90)/(\pm 45)]s\}_n$ n = 1 to 4.

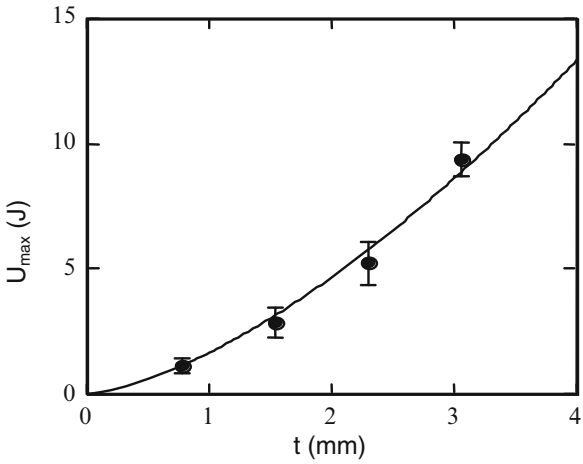


Fig. 31 Energy in correspondence of the maximum force, U_{max}, against laminate thickness, t

The continuous line is the best-fit power law, given by the equation:

$$F_{max} = F_{maxo} \cdot t^m \tag{30}$$

where $F_{maxo} = 1.35$ KN/mm^m, $m = 1.41$.

The values of the exponents i in Eq. (1) and m in Eq. (30) are very similar. This suggests that a strict correlation exists between the delamination initiation and the failure mechanisms resulting in the load drop just after the maximum force. If this is the case, the possibility to model F_{max} should critically depend on the ability to describe the first failure phenomena.

Also in Fig. 30 the experimental data were fitted by a power law having exponent 1.5 (dashed line), resulting in $F_{maxo} = 1.25$ KN/mm$^{1.5}$: the two curves are very close with each other. It could mean that, as already discussed about the first failure load, the importance of the contact law is deviced in determining the main laminate failure as well. There is in fact no difference in the prediction in adopting a power law having exponent 1.5.

The energy correlated to the maximum contact force presented above, U_{max}, was measured and plotted in Fig. 31 against the specimen thickness, t.

The continuous line in Fig. 31 is the best-fit power law having equation:

$$U_{max} = U_{maxo} \cdot t^n \tag{31}$$

with $U_{maxo} = 1.62$ J/mm^n, $n = 1.52$. Even the exponent n in Eq. (31), is very near to 1.5 that means that, considering Eqs. (30) and (31), an approximately linear correlation between the maximum force and the corresponding energy exists (Fig. 32).

In conclusion, the importance of the contact law is devised in determining the main laminate failure as well.

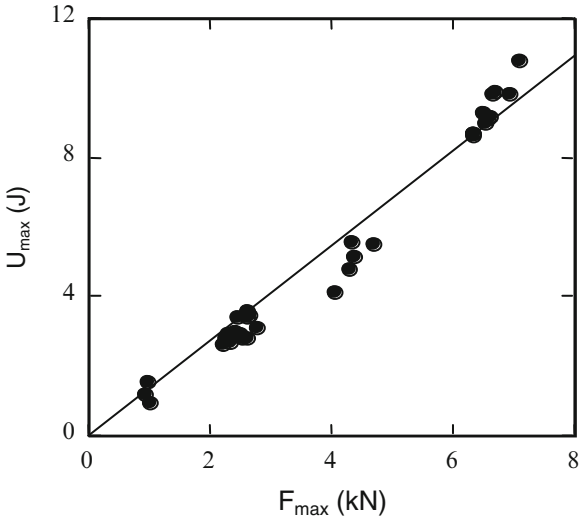


Fig. 32 Energy in correspondence of the maximum force, U_{max}, against maximum force, F_{max}

3.6 Indentation

With composite materials, it is difficult to detect impact damage by visual inspection even when considerable strength and rigidity losses have occurred. The external indication of an occurred impact is the indentation, the local deformation under the impactor the more pronounced the thicker the laminate is. It leads to the concept of 'barely visible impact damage' (BVID): at the aim to guarantee adequate safety, it is required an assigned minimum strength in the presence of a barely visible indentation generally fixed at 0.3 mm of depth. However, there is no common agreement on its value. This section considers the permanent indentation of laminated composites. In the development of mathematical models for the analysis of the impact dynamics, contact laws are needed to relate the dent depth to the impact energy and the residual strength to the dent depth.

After the impact tests carried out at different low energy levels when no perforation occurs, the specimens were taken away from the impact machine and a small permanent indentation depth, the only sign visible on the surface, was measured by a micrometrical dial gage. The measurements were carried out after the unloading phase of the impact tests when the impactor is not in contact with the material anymore and on the specimen there isn't any load. The indentation obtained in this way is the local permanent deformation due to the local contact load. Its trend was studied as a function of impact energy. The results obtained together with the experimental data available in the literature [65], were used to correlate the permanent indentation to the impact energy. A formula, modelling the residual tensile strength decay as a function of impact energy, is used to correctly predict the residual strength. Combining the indentation model and the residual strength model, a closed form model, explicitly correlating the residual strength and the indentation depth, is obtained.

Table 3 Details of the laminates tested in [65]

Material System	Symbol	Lay-up	Thickness (mm)	U_p (J)
T400 Fabric/934	F4	$[(0,90)/(\pm 45)]_s$	0.764	5.0
T400 Fabric/934	F8	$[(0,90)/(\pm 45)]_{2s}$	1.528	13.1
T400 Fabric/934	F12	$[(0,90)/(\pm 45)]_{3s}$	2.292	26.4
T400 Fabric/934	F16	$[(0,90)/(\pm 45)]_{4s}$	3.056	39.4
T400 Fabric/934 + SC[a]	SDF	$[(0,90)/(SC)/(0,90)/(SC)/(\pm 45)_2/(0,90)_2/(\pm 45)_2/(0,90)]$	3.751	29.9
T400 Fabric/934 + SC[a]	SEF	$[(0,90)/(SC)_2/(0,90)/(\pm 45)_2/(0,90)_2/(\pm 45)_2/(0,90)]$	3.751	30.1
T400 Fabric/934 + SC[a]	SIF	$[(0,90)/(\pm 45)_2/(0,90)/(SC)]_s$	3.560	18.9
AS-4 Tape/PEEK	A8	$(0/45/90/-45)_s$	1.056	19.2
AS-4 Tape/PEEK	A24	$(0/45/90/-45)_{3s}$	3.168	30.0

[a]SC = SynCore®

3.6.1 Relationship Between Dent Depth and Impact Energy

In [65] low velocity impact tests were carried out follow the same experimental methods used here on laminates different in thickness, lay-up, and material system (Table 3): some of the laminates were under sandwich form, obtained by the insertion of one of two layers of a syntactic foam (Syncore®), 1.016 mm in nominal thickness each one, at predetermined locations along the plate thickness. For the sandwiches, the impact happened on the first layer in Table 3, so that for SDF and SEF the foam was very near to the material-tup contact zone.

The measured indentation was plotted against U for all the laminates examined (Fabric (F) type, Sandwich (S) type, and AS-4 tape (A) type composites). The indentation rate was found to increase with increasing impact energy and for given energy and material system, the dent depth is the higher, the lower the plate thickness is. In Fig. 33, the results obtained on F laminates were reported for example.

SDF and SEF had approximately the same behaviour, different from what exhibit by SIF, when sufficiently high energy levels are adopted. The latter result was unexpected since, according to the contact law, a higher indentation should be expected from SDF and SEF sandwich plates, due to the presence of the unreinforced core near to the impact surface. However, the maximum indentation depth is comparable to the specimen thickness indicating extensive failure phenomena in the material. Therefore, the experimental test conditions in [65] involved contact forces well beyond the limit within which law can be reasonably applied. For a fixed impact energy, a higher indentation is found for F8 compared to SIF. The two systems were made by the same type and number of layers, except for the presence of core in the SIF structure so, the effect of core in preventing indentation is evident.

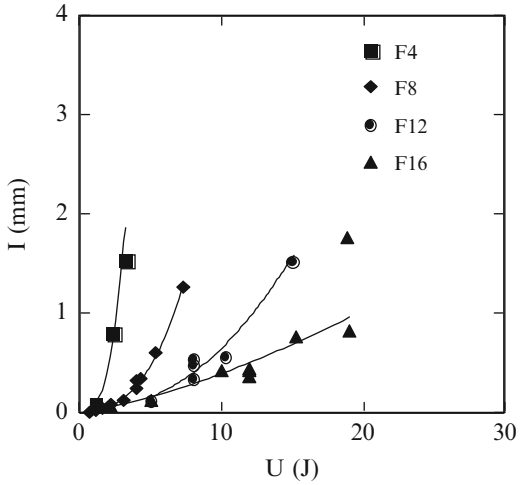


Fig. 33 Indentation, I, vs impact energy, U, for T400 fabric/934 laminates [65]. Mat.: F (Table 1)

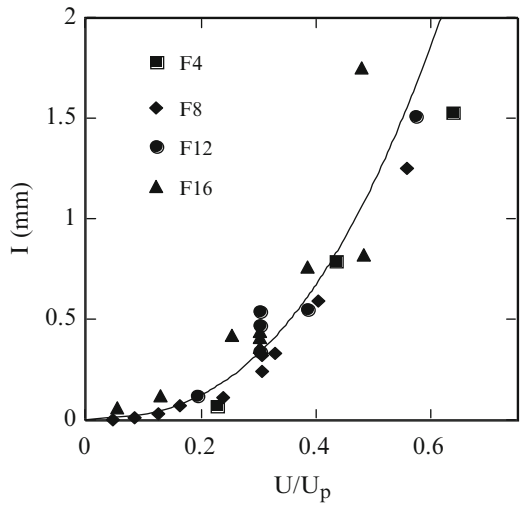


Fig. 34 Indentation, I, against non-dimensional impact energy, U/U_p (T400 fabric/934 laminates from [65])

In [65], the penetration energy U_p for all the laminates in Table 3 was evaluated (see last column in Table 3) as the area under the force-displacement curve up to the point in correspondence of which there is a marked decrease in slope and the cylindrical shaft supporting the tup hemispherical nose began to slide against the walls of the hole resulting from impact, dissipating energy by friction. In Fig. 34, the same data plotted in Fig. 33 are shown against the non-dimensional energy U/U_p. All the indentation data concerning a single material system, irrespective of the actual thickness, follow a master curve. It happens also for all the sandwich panels, despite the different location of the core, and the AS-4 tape (A) type system.

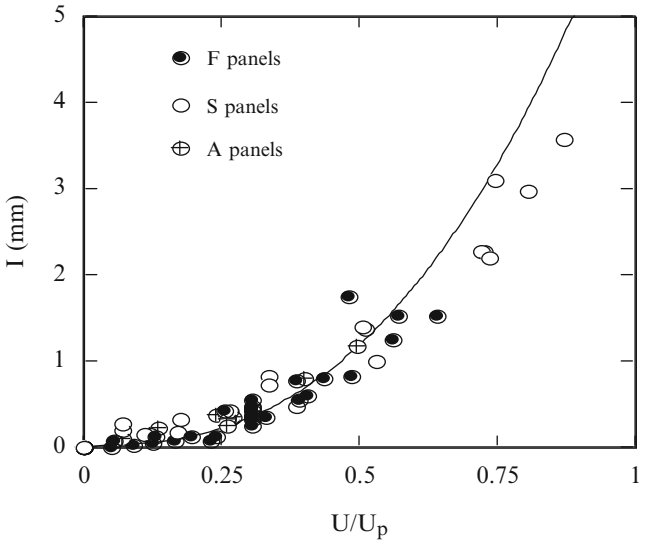


Fig. 35 Indentation depth, I, vs non-dimensional energy, U/U_p (Data from [65])

In Fig. 34, the power law equation:

$$I = I_o \cdot \left(\frac{U}{U_p}\right)^{\beta} \tag{32}$$

best fits all the F specimens experimental points, the values $I_o = 6.77$ mm and $\beta = 2.535$, resulting in the solid line in Fig. 34, were experimentally obtained.

In Fig. 35 all the indentation data of the material systems under attention are compared. It was found that the correlation between the data points and the curve found for the F type material is reasonable, demonstrating that the same equation can be used, independently of the actual material system, when an approximate evaluation of the non-dimensional energy is wanted. Equation (32) is very useful to calculate the impact energy from indentation measurement if the penetration energy U_p for a given laminate is known. However, looking better in Fig. 35, the agreement between theory and experimental trend is very good up to impact energy of about 60% of the penetration one. After that, the prediction overestimates the S panels behaviour.

Similarly to what above described about low-velocity impact, more data from quasi static tests on the same fabrics labeled as F4, F8, F12 and F16, were collected. It was also found that the rate of increase in indentation (Fig. 36) increases with the indentor energy and I strongly depends on the panel thickness, being the higher the thinner is the laminate, for a fixed energy level.

As already done previously, the data in Fig. 36 were then plotted against U/U_p (Fig. 37). As already observed for the dynamic case, all the points converge to a

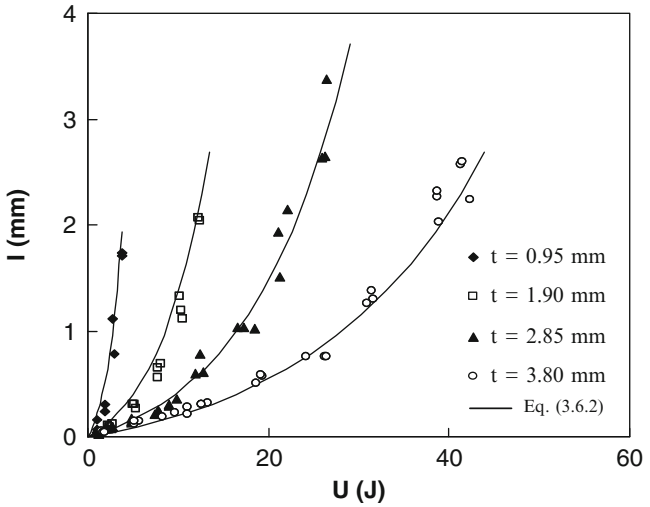


Fig. 36 Measured indentation, I, against impact energy, U

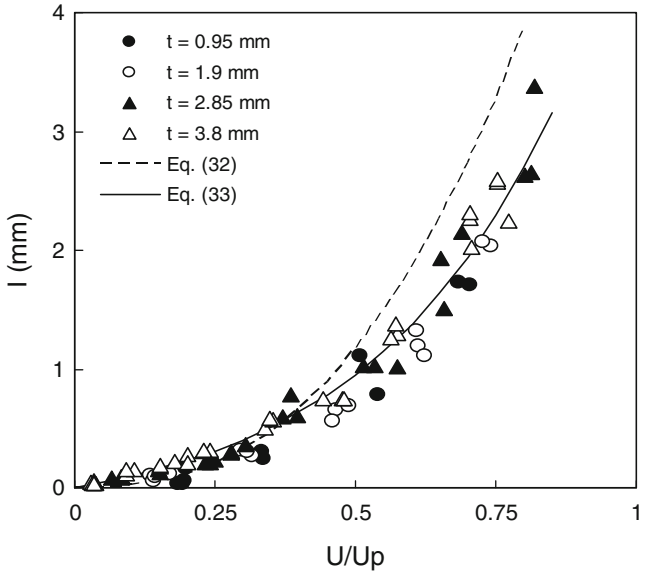


Fig. 37 Indentation, I, against non-dimensional energy, U/U_p

single master curve, indicating that the influence of the thickness disappears when the non-dimensional energy is used as the independent parameter.

The dashed line in Fig. 37, is the curve obtained from Eq. (32) best fitting the experimental data taken in [65] about impact tests carried out on T400/934 fabric laminates obtained above. Up to $U/U_p \cong 0.4$ the agreement is reasonable but

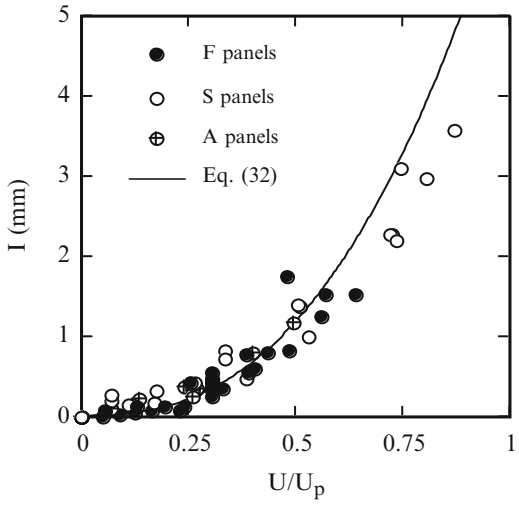


Fig. 38 Indentation, I, against non-dimensional energy, U/U_p, for the laminates from Table 3

the predicted indentation is higher than the measured values beyond this limit. To understand whether the discrepancy reflects the effect of loading speed, or material, or whether some other reason can be given to explain the phenomenon noted, in Fig. 38 the indentation data generated in [65] for the T400/934 fabric laminates (black circle), were reported. The best-fit curve calculated above and plotted in Fig. 37 (continuous line) is also shown in Fig. 38 for comparison purposes: a good fitting of the data was observed.

In Fig. 38 the data previously shown about the sandwich structures made of T400/934 fabric and Syncore® syntactic foam and the quasi-isotropic laminates made of AS-4 tape/PEEK are also reported. It was confirmed what discussed above about some deviation of that points giving the possibility to assert that the constants appearing in Eq. (32) could be mildly dependent on the specific material under examination.

All the points in Figs. 37 and 38 are collected in Fig. 39 where, contrary to what speculated above, a single indentation law actually holds for all the laminates considered, irrespective of the loading rate, fibre type and architecture, matrix type: once again, all the points converge to a single curve if plotted against the non dimensional energy, even if they showed different trends when plotted against the impact energy U since the dependence on the thickness and the particular material system. It seems that even the boundary conditions scarcely affect the relationship between I and U/U_p since the quite different constraint conditions previously adopted for the impact tests (plates clamped, support diameter 40 mm) from here where the plates were simply supported and the support diameter is 50 mm.

The dashed line in the figure represents the best-fit curve obtained calculating the constants appearing in Eq. (32) from all the points in Fig. 39. It is evident that again Eq. (32) is able to fit well the data up to about $U/U_p \cong 0.6$, beyond which it unacceptably underestimates indentation.

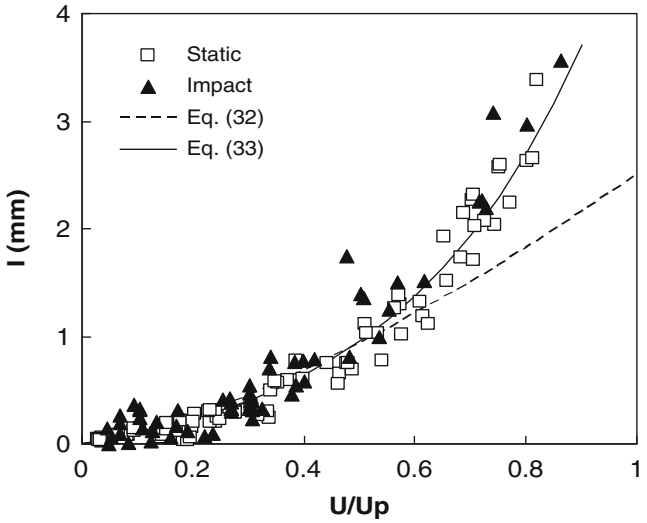


Fig. 39 Indentation, I, against non-dimensional energy, U/U_p, for both static and dynamic cases

The following expression, satisfying the boundary condition $U/U_p = 0 \Rightarrow I = 0$, was found to better correlate I and U/U_p:

$$I = k \cdot \left(10^{\gamma \cdot \frac{U}{Up}} - 1\right) \tag{33}$$

k, γ are two constants. From what here above asserted, these constants are expected to be negligibly affected by the particular laminate and matrix type.

Plotting Eq. (33) in a log scale (Fig. 40), it results in a straight line having slope γ useful to obtain the k value from the best fit method.

The k value was varied until the straight line best fitting the data passed through the origin. In this way, the values $k = 0.288$ mm and $\gamma = 1.269$ were obtained. The continuous lines in Figs. 36, 37, 39 and 40 were drown using Eq. (33): a good correlation between the new indentation model and the experimental data can be appreciated.

The most important conclusion is that, if U_p is known, the impact energy that cause a given indentation can be obtained from the measurement of the indentation depth. The found indentation law (Eq. 33) seems to have a quite general applicability, being scarcely affected by the fibre type and orientations, matrix type and clamping conditions.

Since the importance of the absorbed energy, U_a, in determining impact damage evolution, the same procedure applied above was followed considering U_a instead of the impact energy.

The impact energy, U, is related to the absorbed one, U_a through the penetration energy. In Fig. 41 the non dimensional value, U_a/U_p, is plotted against the ratio

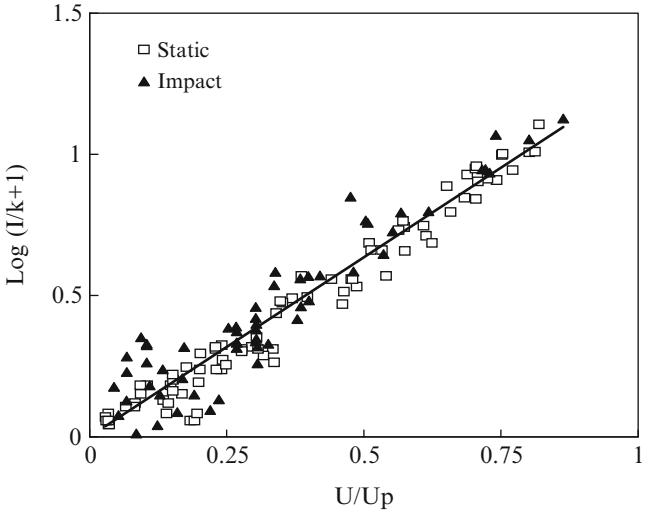


Fig. 40 Calculation of the constants in Eq. (33)

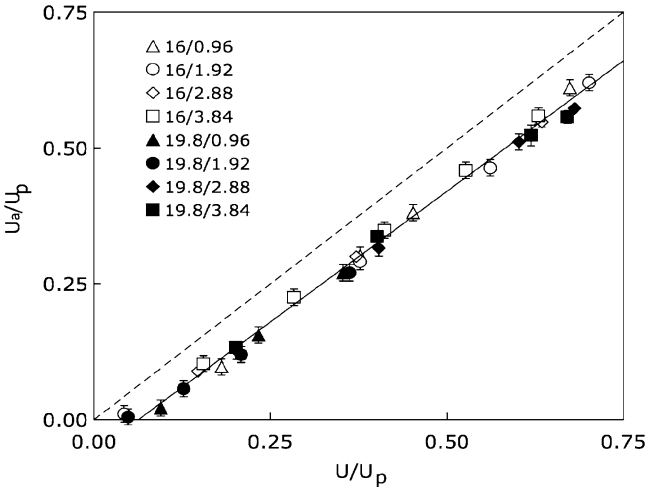


Fig. 41 Non dimensional absorbed energy, U_a/U_p, vs non dimensional impact energy, U/U_p. Mat.: G (Table 1)

U/U_p for E GFRP laminates, $[(0,90)_n/(+45,-45)_n/(+45,-45)_n/(0,90)_n]$, with $n = 1$ to 4: the vertical bars denote standard deviation and the symbols are identified by the label "A/B", where A stand for the tup diameter and B for the panel thickness in mm. All the data follow a single linear trend, irrespective of the panel thickness and impactor diameter. Only two points on the left at very low non-dimensional impact energy seems to have a deviation from linearity.

Sutherland and Guedes Soares in [74] observed a bi-linear trend between the absorbed energy plotted against the impact one, U, on GFRP laminates made of different woven roving architectures, thicknesses, and resins. They found a correspondence between the knee of the bilinear trend and the onset of fibre damage. The knee in the present case, should be located in the range $U/U_p = 0.08$ to 0.11.

Discarding the two points on the left, the solid best-fit straight line in Fig. 41 has equation:

$$\frac{U_a}{U_p} = 0.962\frac{U}{U_p} - 0.0609 \tag{34}$$

From the results, both the constants in Eq. (34) substantially hold whichever t and D_t. The virtual non-dimensional energy U_o/U_p corresponding to $U_a/U_p = 0$, represented by the intercept of the straight line with the x-axis, was calculated: $U_o/U_p = 0.063$. Therefore, would the linear relationship hold also at very low energy values, a perfect elastic impact should occur when the initial energy is about 6.3% or lower of the perforation one.

The dashed line in the same figure represents the condition for which all the available energy is absorbed and has equation $U_a/U_p = U/U_p$. Since the elastic portion of the non-dimensional impact energy, U_{el}/U_p, is given by $U_{el}/U_p = (U-U_a)/U_p$, the vertical distance of the generic experimental point from this line is given by U_{el}/U_p. With this in mind and considering that the slope of the continuous line is 0.962, very close to 1, it is possible to conclude that, beyond U_o, the elastic energy negligibly increases with increasing impact energy. U_e is nil at perforation that means that close to the perforation, the linear relationship in Fig. 41 will be violated.

At the increasing of impact energy, U, a part lower and lower of the initial energy is stored elastically, compared to the absorbed energy. This is clear in Fig. 42 where the data shown in Fig. 41 have been rearranged, plotting U_a/U against U/U_p. From Eq. (34) the following relationship for the solid line was obtained:

$$\frac{U_a}{U} = 0.962 - 0.0609\frac{U_p}{U} \tag{35}$$

From the figure it is clear that, at very low impact energy, a considerable portion of the impact energy is transferred back to the tup. Even when U is 25% of the perforation energy, about 71% of the energy is absorbed; at $U/U_p = 0.75$, only 12% of the energy is employed for rebound.

What above presented for glass fibre was done for carbon fibre reinforced plastic too.

In [74] the energy absorbed in low-velocity impact tests on GFRP laminates made of different woven roving architectures, thicknesses, and resins was plotted against U a linear trend similar to the one found here was observed for high values of the impact energy, U, whereas, at lower U a new straight line, with a lower slope,

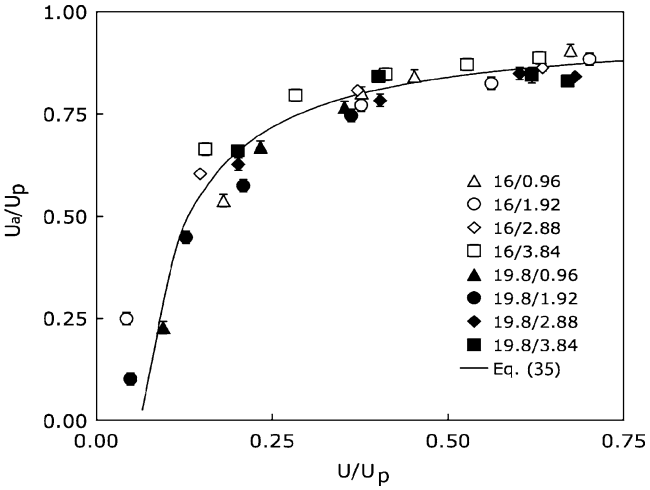


Fig. 42 Non dimensional absorbed energy, U_a/U_P, vs non dimensional impact energy, U/U_p

was necessary to effectively fit the experimental data. On the base of the analysis of the failure modes, the point of intersection of the two straight lines was found to coincide with the onset of fibre damage.

In a previous paper [24], low-velocity impact tests were carried out on CFRP T400/HMF 934 fabric laminates with the stacking sequence $\{[(0, 90)/(\pm 45)]_s\}_n$, with $n = 1$ to 4, and the thicknesses in the rang 0.76 and 3.01 mm with a hemispherical tup 12.7 mm in diameter. Some of the data from [24] were analyzed anew in this contest, the absorbed energy was evaluated, and its non-dimensional value U_a/U_p was plotted against U/U_p in Fig. 43. It is immediately clear in this figure the bi-linear trend highlighted by Sutherland and Guedes Soares [74], where the knee was associated with the onset of fibre damage. The latter would occur for $U \ 0.2U_p$ much earlier for the GFRP previously studied. The fact that in Fig. 43 the straight line fitting the data located beyond the knee seems to pass through the point (1,1) suggests that the linear trend is preserved until perforation.

Plotting the indentation depth values, I, against the absorbed impact energy, U_a, as already observed for impact energy, U, for a given energy, the dent depth increases monotonically with increasing U_a and it is the larger, the thinner is the panel and the lower is the tup diameter. The effectiveness of Eq. (33) in which the impact energy, U, is substituted by the absorbed energy, U_a, is really appreciated. The same indentation model previously presented (Eq. 33) assessed for the absorbed energy instead of the impact one, give the same good results. It was expected since the linear variation of U_a/U_p with U/U_p.

In Fig. 44, all the indentation data concerning GFRP (open triangles) and CFRP (full circles) are collected. Despite the scatter affecting the experimental data, it is obvious that GFRP laminates exhibit a larger indentation, for a fixed value of

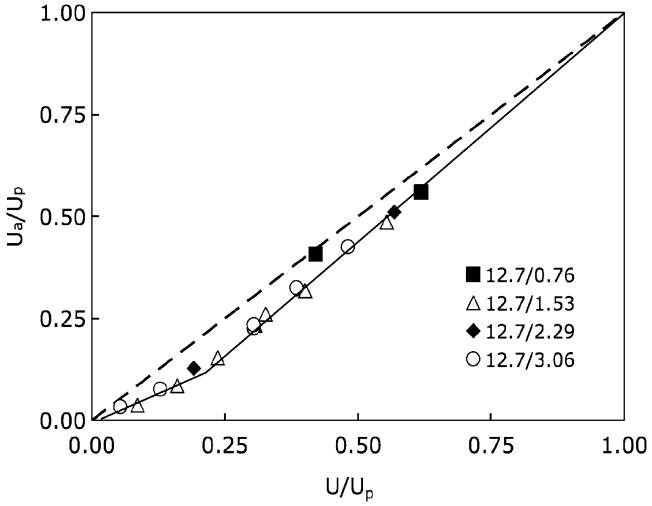


Fig. 43 Non dimensional absorbed energy, U_a/U_p, versus non dimensional impact energy, U/U_p. Material: CFRP [24]

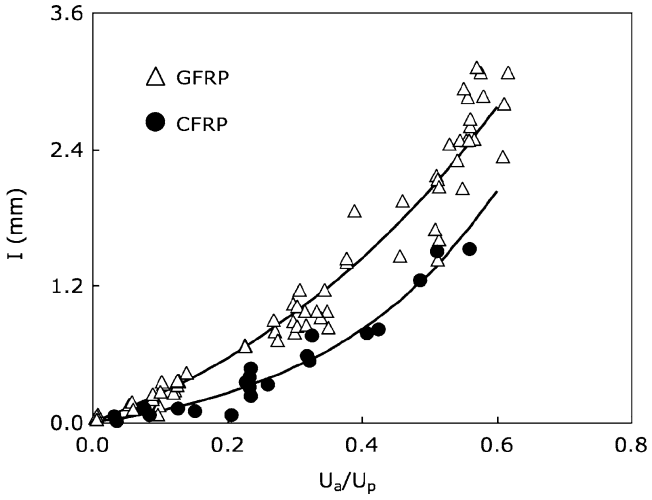


Fig. 44 Indentation, I, against non-dimensional absorbed energy, U_a/U_p, for CFPR (*full circle*) and GFRP (*open triangle*)

the non-dimensional absorbed energy. So, when the same indentation is measured on GFRP and CFRP systems, the latter absorbs a higher portion of energy, if the perforation energy is assumed as a benchmark.

The prediction model was revealed valid also considering U_a instead of U. In order to calculate the impact energy, U, or the absorbed one, U_a, from indentation measurements through Eq. (32) or (33), it is necessary to know the penetration energy, U_p, for a given laminate.

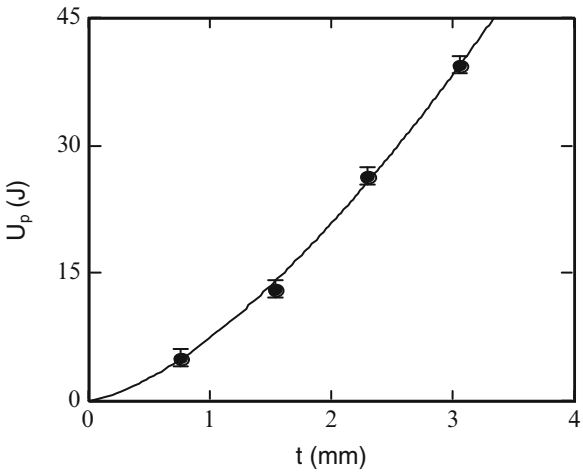


Fig. 45 Penetration energy, U_p, vs laminate thickness, t, for F laminates made of T400 fabric/934 layers [24]

3.7 Penetration Energy

This section deals with the prediction of the penetration energy, the difference between the initial and residual kinetic energy of the projectile during impacts resulting in complete perforation. The factors affecting the penetration energy of a composite material are examined.

For a given fibre type, the penetration energy is substantially influenced by the total fibre volume and tup diameter, whereas other factors, such as resin type and content, fibre architecture, stacking sequence and orientations, play a secondary role. An empirical power law equation proposed by the authors, is assessed on the basis of experimental results. Results indicate that the exponent of the power law is independent of the material considered, being practically the same for graphite fibre, as well as glass fibre reinforced plastics, and even for an isotropic material as polycarbonate, prone to extensive plastic yielding before final failure.

3.7.1 Effect of Laminate Thickness and Projectile Diameter

It is important to find a general formula to calculate the energy necessary to the indentor to completely perforate the laminate. The factors mainly affecting the energy under attention were first reviewed. In [23], the data in [24] for the F fabric laminates T400 fibres and HMF 934 epoxy resin having $\{[(0, 90)/(\pm 45)]_s\}_n$ stacking sequence, with n = 1 to 4, labelled as F in Table 1, were examined. The dependence of U_p on the laminate thickness is well described by the following power law:

$$U_p = U_{po} \cdot t^p \tag{36}$$

with $U_{po} = 7.33$ J/mm^p and p = 1.50, represented by the solid line in Fig. 45.

In [75, 76], the penetration energy for a given laminate was found to linearly increase with increasing t (i.e. fibre areal weight) but data from [17, 19, 21–23, 77] have demonstrated that doubling t or D_t results in more than doubling the energy absorbing capacity of the panel. So, the dependence for CFRP laminates could be well described by a power law having exponent 1.5 [17, 21]. Adopting the same law to fit the trend of data concerning GFRP [77], an exponent ≈1.35 was obtained.

However, before going on to develop the power dependence of U_p on t obtained with tests carried out in the present research, the experimental results obtained here together with data from the literature were utilized. The difficulty in comparing the various available data published derives from the fact that many factors, both internal and external, can affect the energy absorbing capacity of these materials. The most important ones are the matrix type and content, fibre type, architecture and orientation, laminate thickness and stacking sequence, the panel geometry and dimensions, the constraint conditions and the impactor geometry.

In [78], Babic and co-workers from the results of low-velocity impact tests on glass fibre reinforced plastics (GFRP) with different thicknesses and volume fraction of reinforcement, found that the scatter in the measured penetration energy was lower when U_p was plotted against the panel thickness, t, times fibre volume fraction, V_f, rather than against the actual thickness. The same was found in [22, 23], where different carbon fibre reinforced plastics and glass fibre reinforced plastics, were considered, respectively. The product $(t \times V_f)$ practically coincides with the total fibre thickness proportional to the total fibre areal weight, negligibly the void content. In [17], the authors obtained consistent results calculating U_p on the basis of the fibre areal weight alone. Therefore, what was found seems to indicate that the total fibre content plays a fundamental role in affecting the penetration energy and that not only the resin content, but also its type negligibly affects the penetration energy. In [22] six different types of resin were used to fabricate quasi-isotropic GFRP laminates subjected, then, to dynamic loads: very little differences in behaviour were observed. Bibo and Hogg [23] studied also the problem of the effect of fibre architecture on the penetration energy on quasi-isotropic laminates with different spatial distribution of reinforcement employing different forms of glass fibres (unidirectional, quadriaxial warp-knit fabric and eight-harness satin weave). For a fixed fibre areal weight, U_p revealed to be practically independent of the reinforcement architecture and stacking sequence although the delamination extent was quite limited in some cases and considerable in some others, indicating that the energy associated with delamination is negligible compared to the overall penetration energy.

The insensitivity of U_p to the fibre architecture was confirmed in [77], where the energy absorbing capability of an in-plane isotropic sheet-moulding compound was shown to be the same as that of fabric laminates with the same fibre areal weight. This confirms the importance of the total fibre content and in addition supports the hypothesis that fibre orientation play a secondary role in determining the penetration response of a composite, at least when the anisotropy ratio is not too high like for quasi-isotropic laminates. This hypothesis is confirmed in [21], where Delfosse and Poursartip used different indenter diameters on two types of

graphite/epoxy laminates. The first one was quasi-isotropic, whereas the second had 40% of the fibres oriented in the 0-direction. The penetration energy increases with increasing the impactor diameter but for a given indenter diameter, the two composites exhibited the same U_p value. This indicates that, at least when the anisotropy ratio is not too high, also the fibre orientations play a secondary role affecting the penetration energy of a laminate and the main parameters remain the fibre type and areal weight.

Moreover, the penetration energy of $(\pm 30)_{2s}$, and $(\pm 45)_{2s}$ tape CFRP laminates was successfully calculated on the basis of the test results deriving from quasi-isotropic fabric laminates taking into account only the total fibre thickness and not the fibre orientation.

In [53], penetration tests were carried out on different forms of glass fibres (unidirectional, non-crimp fabric and eight-harness satin) utilised to fabricate quasi-isotropic laminates with different spatial distribution of reinforcement. The results demonstrated that the penetration energy is scarcely affected by the reinforcement architecture and spatial distribution, if the total fibre volume remains unchanged.

The dependence of U_p on D_t is not so clear yet. In [21], where some data concerning CFRP were presented, it was concluded that a power law having exponent 0.7 could be adequate to describe the trend of CFRP but completely different conclusions were highlighted in [77], where the power law best fitting the experimental points had exponent 1.38 for GFRP. Taking into account the latter case, it was noted that the effect of both the thickness and the impactor diameter on the penetration energy could be modelled by power laws having very similar exponents.

The results suggest that the parameter controlling the penetration energy is the product $(t \cdot D_t)$.

The reinforcement plays a major role in determining the impact response also for GFRP. In [78], in fact, the U_p of all the data about GFRP deriving from specimens having different matrix content converge to a single master curve when plotted against the total fibre thickness obtained as the thickness times fibre volume fraction. Looking at what obtained by the authors [77], the quantity $(t \cdot V_f \cdot D_t)$ seems to be a parameter useful to compare on a common basis data obtained on GFRPs with different resin contents and different impactor diameters. To demonstrate what asserted, the penetration energy data generated on GFRP recalled above and described in the materials paragraph, are plotted against $(t \cdot V_f \cdot D_t)$ in Fig. 46. Despite the differences in fibre architecture and orientations, the data about three different materials tested approximately follow the same curve, confirming the conclusions in [78], where the negligible importance of the matrix on the energy absorption capacity of GFRP was noted.

The power law in Fig. 46 has equation:

$$U_p = K \cdot \left(t \cdot V_f \cdot D_t\right)^{\alpha} \tag{37}$$

and with $K = 0.90$ and $\alpha = 1.30$ is useful in calculating the penetration energy of a glass fibre reinforced plastic, irrespective of the fibre architecture and orientations,

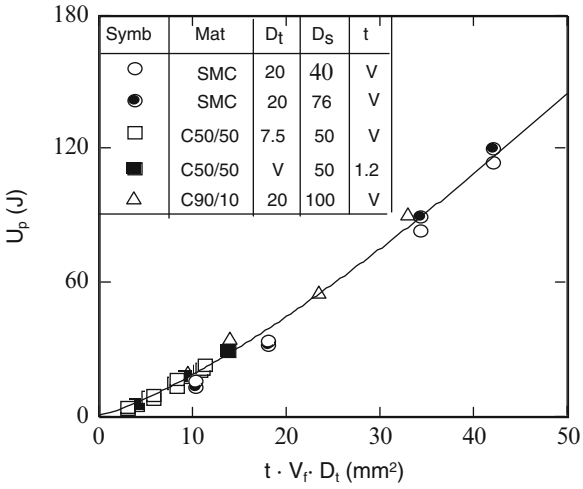


Fig. 46 Penetration energy, U_p, versus total fibre thickness times tup diameter, $t \cdot V_f \cdot \cdot D_t$. Table: dimensions in mm; D_s = support diameter; V = variable

and resin type. By examining the effect of each variable separately, it was found that U_p varied as a power function of each variable, the exponent being nearly the same. This suggested that U_p varies as in Eq. (37) where K and α are two experimental constant. The α value was found approximately equal to 1.3 independently of the examined variable.

This relationship is expected to be valid only for quasi-isotropic laminates and, as in the present case, the elastic energy stored in the structure is negligible compared to the energy expended in penetrating the material.

To demonstrate that relatively small variations in the matrix content do not affect considerably the penetration energy [23, 78], Eq. (36) can be expressed in the following form:

$$U_p = U_{po}^* \cdot W^p \tag{38}$$

where U_{po}* and p are two constant and W designates the total areal weight of fibre (proportional to the total fibre thickness), that is useful if the penetration response of laminates different in matrix content must be compared. In Fig. 47, the data of penetration energy measured on SDF, SEF, SIF and A laminates reported in Table 3, were plotted against W.

Plotting the F type laminates data from Table 3 showed in Fig. 45, as a function of W, by the best-fit power law the value $U_{po}^* = 7.22$ (valid when W is expressed in Kg/m^2) was found (Fig. 45) and used to draw the solid line in Fig. 47. As expected, S type and A type laminates follow a different trend respect to the F laminates ones and the AS-4/PEEK system seems to be less efficient than T400/934 in preventing penetration whereas, interestingly, the sandwiches showed a better impact response, for a given fibre areal weight. The latter demonstrates that the constants in Eq. (38) must be appropriately evaluated when sandwich structures are considered.

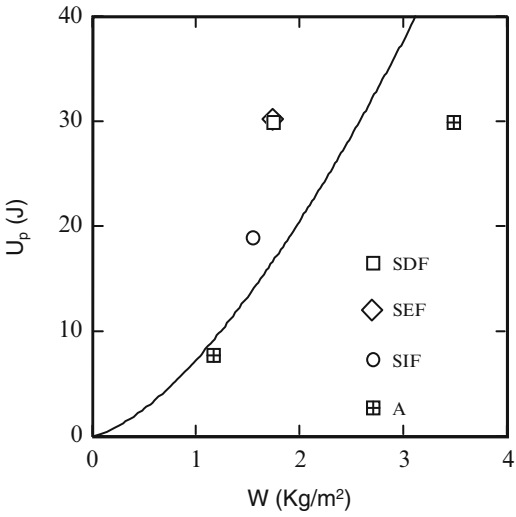


Fig. 47 Penetration energy, U_p, against fibre areal weight, W, for different laminates examined in [65]

The indentation law previously discussed (Eq. (32)) was used to demonstrate that the continuous line drown in Fig. 47 should be valid for a wide class of laminates based on the T400/934 system. Considering the Eq. (38) the following relationship was obtained:

$$I = I_o \left(\frac{U}{U_{op}^* \cdot W^p} \right)^{\beta} \tag{39}$$

in which the constants found for T400 fabric/934 are used to calculate the indentation as a function of impact energy for the $(\pm 30)_{2s}$, $(\pm 60)_{2s}$, and $(\pm 45)_{2s}$ laminates tested, made of T400 tape/934. The comparison between theory and experiments is carried out in Fig. 48, and the correlation between the experimental data and theoretical predictions is outstanding, whichever the actual laminate considered. This supports the idea that the constants in Eq. (38) are independent of both reinforcement architecture and fibre orientations.

In Table 4, a sufficiently large variety of carbon fibres (in Table 5 the mechanical properties are reported), matrix types, laminate lay-ups and thicknesses, constraint conditions, and penetrator diameters is covered. The support type is specified in the sixth column, through the code Annn/D, where "A" is the type of support (B = beam, Φ = circular plate, S = square plate), "nnn" is a number indicating the support dimensions, in mm (for beams, the length), and "D" is the type of constraint (S = simply supported, C = clamped).

The data presented indicate that the proposed formula has a quite wide applicability and can be probably further simplified, allowing a simple comparison of different materials.

In Fig. 49, in fact, the dependence on the total fibre thickness of all the laminates in Table 4 is shown on a log-log scale and results in a linear trend which slope

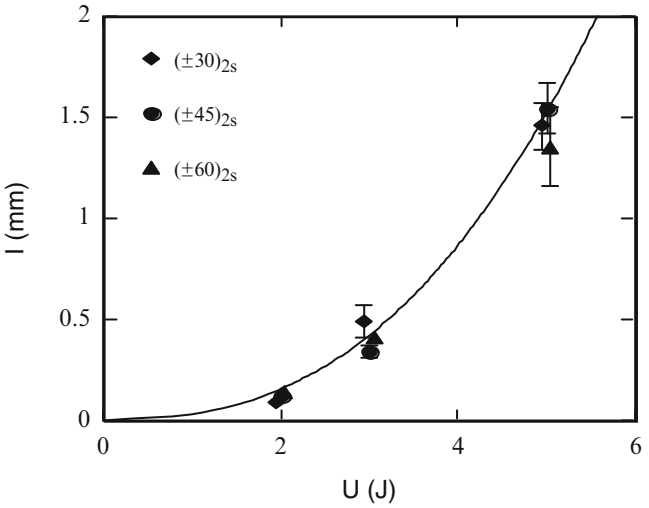


Fig. 48 Indentation, I, vs impact energy, U, for $(\pm\theta)_{2s}$ laminates made of T400 tape/934

Table 4 Carbon fibre reinforced plastic laminates tested at penetration

Ref.	Symb.	Material	Lay-up	t (mm)	Support	D_t (mm)
[18]	■	XAS/Epoxy, Tape	$(\pm45)_{ns}$	0.5 ÷ 4	B50/S	6
	♦	XAS/Epoxy, Tape	$(0, \pm45)_{ns}$	1.0 ÷ 2.0	B50/S	6
	●	XAS/Epoxy, Tape	$(\pm45)_{ns}$	0.5 ÷ 2.0	Φ120/C	6
[21]	◪	AS4/PEEK/LC[a], Tape	$(-45/0/45/90)_{ns}$	1.0 ÷ 3.0	Φ40/C	20
	◭	AS4/PEEK/HC[b], Tape	$(-45/0/45/90)_{ns}$	1.0 ÷ 3.0	Φ40/C	20
	◩	AS4/PPS/LC, Tape	$(-45/0/45/90)_{ns}$	1.0 ÷ 3.0	Φ40/C	20
	◹	AS4/PPS/HC, Tape	$(-45/0/45/90)_{ns}$	1.0 ÷ 3.0	Φ40/C	20
	◆	T650/PPS/Radel, Tape	$(-45/0/45/90)_{ns}$	2.0	Φ40/C	20
	◆	T800H/Epoxy, Tape	$(-45/0/45/90)_{ns}$	2.0	Φ40/C	20
[52]	□	T400/Epoxy, Fabric	0, ±45, 90	0.8 ÷ 3.1	Φ40/S	12.7
[57]	◇	AS4/Epoxy, Tape	$(0/90)_{5s}$	3.0	S127/S	12.7
	○	AS4/Epoxy, Fabric	$(0, 90)_{10s}$	2.2	S127/S	12.7
[58]	△	IM7/Epoxy, Tape	$[(0/90)_{22}0]_s$	6.4	Φ76/C	12.7
	⊞	IM7/Epoxy, Tape	$(90/\pm45/0)_{6s}$	6.8	Φ76/C	12.7
	◈	IM7/Epoxy, Tape	$[(0/45/90/-45)_{s2}/0/45/90]_s$	6.6	Φ76/C	12.7
	⊕	IM7/Epoxy, Tape	$[(0_2/\pm45)_{s2}/0_2/+45/-45_2/+45]_s$	6.4	Φ76/C	12.7
	▽	IM7/Epoxy, Tape	$[(02/\pm45)_{s2}/\pm45/0]_s$	6.5	Φ76/C	12.7
	▷	IM7/Epoxy, Fabric	$[(0/45)_9/45]_s$	6.4	Φ76/C	12.7

Legend: [a]*LC* low crystallinity [b]*HC* high crystallinity

Table 5 Mechanical properties of the fibre

Type	Modulus (GPa)	Strength (GPa)	Elongation (%)
XAS	234	***	***
AS4	221	4.0	1.6
T650	290	5.0	1.7
T800	294	5.5	1.9
T400	254	4.5	1.8
IM7	276	5.4	1.8

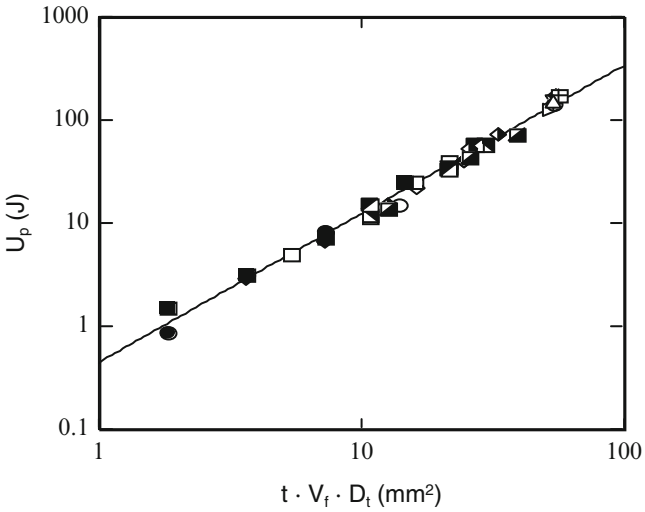


Fig. 49 Log-log plot of the penetration energy, U_p, vs $(t \cdot V_f \cdot D_t)$

(continuous lines each one for each different tup diameter) is unaffected by the particular D_t value. This is in agreement with Eq. (37), assuming a power law relationship between U_p and fibre thickness, and an exponent α dependent just on the material.

The values of the constants were found by the best–fit method providing $K = 0.45$ J/mm$^{2\alpha}$ and $\alpha = 1.44$ (continuous line in Fig. 49).

However, the analysis of the graph on a linear scale (Fig. 50) revealed an underestimating of the energy absorbing capacity at high values of the abscissa.

Also in [79], where a penetration model was developed in order to predict U_p as a function of the target thickness and specimen dimensions, a good agreement between theory and experiments was found up to 4 mm of thickness whereas the agreement was poor when an 8 mm thick laminate was considered. From microscopic observations of the failure modes during penetration and the energy associated with each ones or drawn from the literature, by sectioning and polishing the thick specimens, a substantial difference in failure modes was found between thin and thick laminates. Probably the validity of the model fails when thick composites were considered.

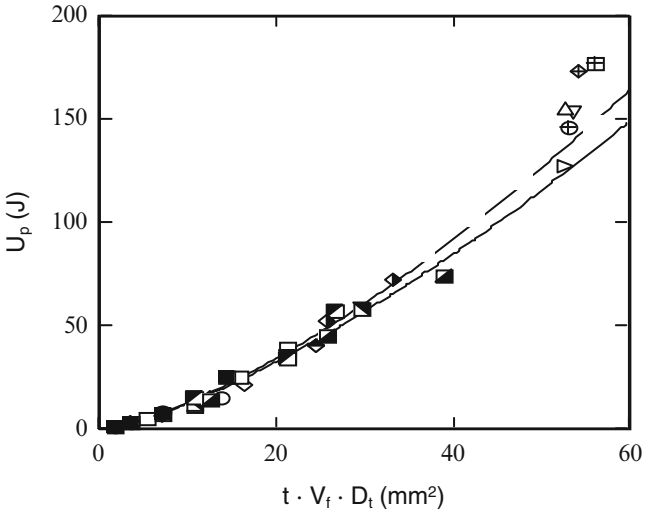


Fig. 50 Linear plot of the penetration energy, U_p, vs ($t \cdot V_f \cdot D_t$)

Here, it is not possible to know if high values of the abscissa are correlated with large tup diameters or thick laminates. However, all the points characterised by a high ($t \cdot V_f \cdot D_t$) value are about laminates of about 6.5 mm thickness and a change in failure modes can possibly explain the poor correlation between theory and experiments. The hypothesis is strengthened by the fact that, similarly to what found by Cantwell and Morton [79], also Eq. (37) tends to underestimate the penetration energy when the laminate thickness is high.

The values of the constants in Eq. (37) were, so, calculated anew only for the points characterised by ($t \cdot V_f \cdot D_t$) values lower than 40 mm^2, and 0.49 and 1.40 were found for K and α respectively. They are represented by the dashed line in Fig. 50.

The same was done on other material systems (GFRP and PC) and the similar results lead to the possibility to assume a single α value to describe the penetration energy trend. In this way, it could be simple to applied Eq. (37) since the parameter K could be used to rank different materials on the basis of their energy absorbing capacity provided the anisotropy ratio is not too high. The latter limitation is due to the fact that 0° composites are prone to transverse intralaminar failures, which can alter significantly the mechanisms of energy absorption under impact.

In Fig. 51 the best-fit straight line obtained for GFRP data discussed above is reported on a log-log scale together with the dashed line from Fig. 50 to allow a direct comparison of the energy absorbing capacity of GFRP and CFRP: glass fibres are superior with respect to graphite fibres even if the two straight lines tend to cross each other at high ($t \cdot V_f \cdot D_t$) values. The latter denote a better behaviour of CFRP when large tup diameters are used. The crossover point is well beyond the range of the experimental points available and it is a result of extrapolation. Since it

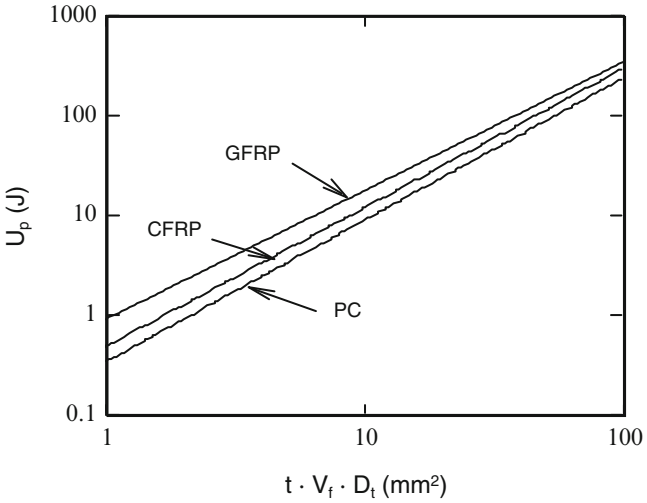


Fig. 51 Comparison of the energy absorbing capacity

is not clear whether the difference in α values between CFRP and GFRP is actually significant or it is only due to the data scatter, additional experimental data will be hereafter discussed, indicating that Eq. (37) can be possibly applied to a large class of materials and further simplified in form.

In [80], low velocity impact tests were performed on polycarbonate (PC) and GFRP panels supported on circular rings, and the influence of panel thickness and penetrator diameter on the penetration energy was examined. The energy absorption modalities were very different: in GFRP, in fact, as usually found in the literature for composite materials [21, 65, 75, 80–82], most of the energy was associated with the propagation of failure phenomena taking place beyond the onset of damage. On the contrary, PC exhibited an extensive permanent indentation, exclusively responsible for energy absorption. The energy associated with crack propagation after the maximum load was negligible: a fast propagation of cracks generated in correspondence of the contact point was observed witnessed by the sudden drop in the contact force down to zero.

The same procedure presented above was repeated for PC considering the measured panel thickness instead of the product $t \cdot V_f$. Once again the validity of Eq. (37) was clear, despite the marked differences in the mechanisms of energy absorption between PC and composites: the superposition of the points referring to different thicknesses and different tup diameters was very satisfactory.

The values of the constants K and α were calculated as previously done also for PC, obtaining $K = 0.35$ J/mm$^{2\alpha}$ and $\alpha = 1.42$. The continuous, best-fit straight line obtained for PC was reported in Fig. 51 for comparison purposes and the values of the constants calculated for the three materials considered in this paper are collected in Table 6.

Table 6 Values of the constants in Eq. (37)

Material	K (J/mm$^{2\alpha}$)	α
CFRP	0.49	1.40
GFRP	0.90	1.30
PC	0.35	1.42

Table 7 Values of the constants K best fitting the experimental results for given values for α

Material	α	K (J/mm$^{2\alpha}$)
CFRP	1.30	0.67
	1.42	0.45
GFRP	1.30	0.90
	1.42	0.59
PC	1.30	0.56
	1.42	0.35

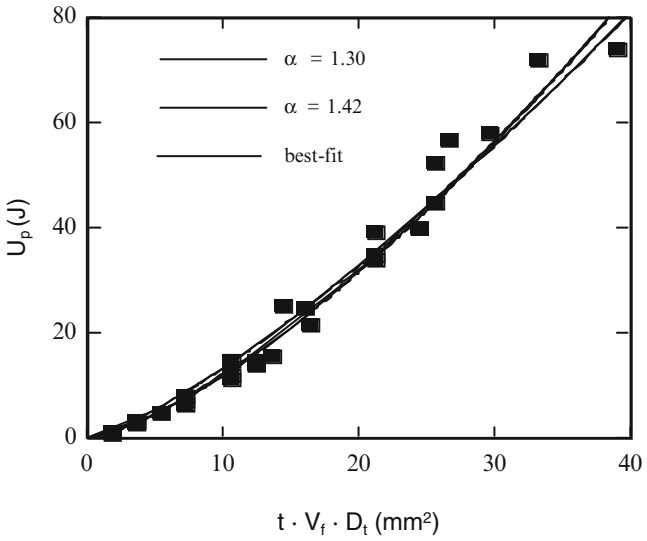


Fig. 52 Effect of the α value on the prediction capability of Eq. (37). Material: CFRP

The very similar α values raises the question whether this parameter is actually material dependent, or rather it can be considered a constant of general applicability. At this aim, the minimum and maximum α values found ($\alpha = 1.30$ and 1.42) were alternatively fixed for all the materials and the related K values, best-fitting the experimental points were calculated and reported in Table 7.

The results are graphically shown in Fig. 52 for CFRP: the curves concerning a single material are very close with each other, so that the scatter in the experimental data does not allow to judge which of them is the most efficient in predicting penetration energy. The same was found for GFRP and PC. The assumption that

a single α value has a general applicability cannot be rejected. However, if this was the case, the application of Eq. (37) would be straightforward, and the parameter K alone could be used to rank different materials on the basis of their energy absorbing capacity.

3.7.2 Effect of Projectile Velocity

To ascertain the effect of loading speed on the penetration energy, static and dynamic impact tests were carried out on C50/50 and SMC (Table 1), with the same impactor and support diameter. A strong dependence of the energy absorbing capability of GFRP on the speed was found, approximately doubling when the loading speed increases from 2 mm/min to about 7 m/s. The discussed influence about flat GFRP panels has been observed by many researchers [58, 83, 84] whereas other data [53, 58] show that laminates made by graphite fibre are practically insensitive to loading speed. The sensitivity of GFRP to velocity reflects, so, the well known and discussed viscoelasticity of glass fibres and it is independent of the matrix behaviour. At this point, the same model about the prediction of the penetration energy was assessed also in the case of static tests demonstrating that the penetration energy is substantially unaffected by the loading speed. The latter and what previously said about indentation indicate that impact tests can be substituted by static tests if the response of a CFRP laminate in terms of indentation and penetration is under study.

From the results obtained, the authors [19] noted that small samples do not necessarily behave like an in-service component under impact conditions. Conversely, if the scope of a testing procedure is the material characterisation, the elastic energy absorbed by the specimens should be minimised. This suggests the use of clamps at the supports, and the lowest in-plane dimensions allowing a free development of the damage. Interestingly, from the results of a limited amount of tests carried out at high speed clamping the plates between circular rings 120 mm in diameter [19], the penetration energy was found coincident with what given by the beam tests, and at low velocity U_p was only slightly higher. Additional data about two different types of circular GFRP panels were discussed [77]: only a moderate increase in the penetration energy was found at the increase of the support diameter in the range 40 mm to 100 mm, although one of the laminates was quite thin (1.2 mm) and the plates were simply supported. From the previous results, it can be reasonably thought that, when specimen dimensions are up to about 120 mm, the elastic energy is low and test conditions adequate to yield a sufficiently accurate value of the material penetration energy are achieved.

Experimental evidence and theoretical justification of this behaviour was given in [19], where the authors performed penetration tests at both low and high velocity on CFRP using a simply supported beam configuration and varying the beam length. The penetration energy showed an increase well described by a simple analytical model that take into account the elastic deformation of the material. Additional data in this direction was discussed about GFRP panels [77]: a little increase in

the penetration energy of about 10% was found passing from 40 to 100 mm of the support diameter since the elastic energy to bend the panel up to the maximum load also increases, contributing to the overall energy stored by the structure. However, it is reasonable to think that up to about 120 mm of the specimen dimensions, the test conditions are adequate to yield accurate values of the penetration energy since in comparison the elastic energy is low and lower at increasing of the thickness.

3.7.3 Literature Survey

As a confirmation of the results found in this work, an extensive literature research is hereafter presented.

In [22, 23, 78], low-velocity impact tests were carried out on glass and carbon fibre reinforced plastics (GFRP and CFRP) having different thickness and volume fraction of reinforcement finding that the precision in the measured penetration energy was higher when U_p was plotted against the panel thickness, t, times fibre volume fraction, V_f, rather than against the actual thickness. The product $(t \cdot V_f)$ represents the total fibre thickness proportional to the total fibre areal weight. Therefore, the results obtained in literature seem to indicate that, for a given laminate, the total fibre content is the main parameter affecting penetration energy. It means that not only the resin content, but also its type negligibly affects the penetration energy. This was demonstrated in [22] where six types of resin, including a toughened epoxy, amorphous and semi-crystalline PEEK, and amorphous and semi-crystalline PPS, were used to fabricate quasi-isotropic GFRP laminates: little differences in impact behaviour were observed on the basis of matrix type.

Different forms of glass fibres (unidirectional, quadriaxial warp-knit fabric and eight-harness satin weave) were employed to obtain quasi-isotropic laminates with different spatial distribution of reinforcement [23]. The impact tests revealed that, for a given fibre areal weight, U_p was independent of the reinforcement architecture and stacking sequence and of the extend of the delamination, quite limited in some of the cases but considerable in some others. The latter could indicate that the energy associated with delamination phenomena is negligible compared to the overall penetration energy.

Additional data confirming the insensitivity of U_p to the fibre architecture can be found [77]: the energy absorbing capability of an in-plane isotropic sheet-moulding compound was shown to be practically coincident with that of the fabric laminates having the same fibre areal weight. Besides confirming the importance of the total fibre content, this result supports the hypothesis that the fibre orientations play a secondary role in determining the penetration response of a composite, at least when the anisotropy ratio is not too high. Also in what reported in [17, 21], the formula used for the calculation of the penetration energy involved the knowledge of the total fibre thickness, whereas the fibre orientations were not taken into account.

The penetration energy for a given laminate was first found to linearly increases with increasing t (i.e. fibre areal weight) [75, 76]. However, more recent data [17, 19, 21–23, 77, 78] demonstrate that U_p increases more than linearly with thickness. In particular, it was found that [17, 21], as already here demonstrated, the dependence of the penetration energy on the material thickness, t, for CFRP and GFRP laminates could be well described by a power law having exponent 1.5 and 1.35 respectively.

Also the impactor shape strongly influences U_p, which increases with increasing impactor dimensions. Most of the data available on this subject concern spherical indenters about 6–25.7 mm in diameter, although conically shaped and flat cylindrical tups have also been extensively used [4].

From the previous considerations, limiting the attention to spherical tups and a given fibre type, the most effective parameters in influencing U_p are the fibre areal weight and the impactor diameter, D_t. It is so necessary to establish a relationship correlating these quantities. It is very important to highlight the dependence of U_p on D_t. From Eqs. (36) and (37) confirmed by [17, 21], the effect of both the thickness and the impactor diameter could be modelled by power laws having practically the same exponent, it was suggested that the empirical relationship proposed here (Eq. 37) helps to predict the penetration energy. The experimental tests supported Eq. (37): all the data obtained substantially fall on a single master curve when plotted against the quantity ($t \cdot V_f \cdot D_t$) irrespective of the adopted tup diameter and fibre architecture and orientations. The formula proposed has a quite wide applicability with a typical value for α of about 1.4, and can be probably further simplified, allowing a simple comparison of different materials.

3.8 Residual Strength Model

Since the residual material properties after an impact are of primary concern in applying damage tolerance concepts, efforts were also made to correlate, analytically or experimentally, the residual strength and the impact energy and the damage mechanisms [9, 42, 85]. In literature some models have been proposed [9, 18–20] to predict the residual strength σ_c of a composite laminate after low velocity impact strength, as a function of the impact energy:

$$\frac{\sigma_c}{\sigma_o} = \sigma(U) \tag{40}$$

where σ_c and σ_o are the virgin and the material residual strength after impact, respectively.

Since an explicit form was found for the relationship between indentation depth and impact energy through the penetration energy (Eq. (32)), it is possible to predict the residual strength from indentation. If the compression strength is of concern, Eq. (40) can assume a complicated form, because of the effect of delamination on the failure modes precipitating final collapse.

Table 8 Experimental values of the constants $U_{\sigma o}$ and α in Eq. (41), and theoretical limit indentation, I_{lim}, beyond which a reduction in tensile strength is predicted

Laminate	$U_{\sigma o}$ (J)	α	I_{lim} (J)
$(\pm 30)_{2s}$	1.87	0.386	0.125
$(\pm 45)_{2s}$	1.97	0.267	0.143
$(\pm 60)_{2s}$	1.48	0.275	0.069

Even if models are available in the literature for the prediction of the residual strength, in this work, the formula proposed in [19] is assumed for the simplicity in the procedures required to evaluate the constants involved:

$$\frac{\sigma_c}{\sigma_o} = \left(\frac{U_{\sigma o}}{U}\right)^{\alpha} \tag{41}$$

σ_o is the virgin strength of the laminate, and $U_{\sigma o}$, α are two constants to be experimentally determined.

When $U = U_{\sigma o}$ the residual tensile strength equals the virgin material strength. $U_{\sigma o}$ physically represents the limit energy below which no strength reduction is found. Equation (41) predicts a monotonic decrease in the residual strength with increasing U. On the contrary, it is known that, beyond penetration, σ_c does not decrease further, remaining approximately constant or undergoing a small recovery. The previous considerations bring to the conclusion that Eq. (41) no longer holds for $U < U_{\sigma o}$ and $U > U_p$.

Noting that the reduction in tensile strength is dependent on the broken fibres, rather than on the delaminated area induced by impact, it was suggested [19] that $U_{\sigma o}$ could be directly measured as the area under the force-displacement curve up to the point of the first fibre breakage. This damage is often signalled by a sudden drop in the contact force (point b in Fig. 1).

Since the evidence of the first fibre failure in the force-displacement diagrams for all the laminates considered and labelled as T30, T60 and T45 in Table 1, the procedure proposed [19] for the calculation of the constants was followed also here. The $U_{\sigma o}$ values obtained for the materials tested are reported in Table 8.

The results that the $(\pm 30)_{2s}$ and $(\pm 60)_{2s}$ laminates exhibited a quite different $U_{\sigma o}$ was unexpected. They both should yield the same response to impact since the axial symmetry, being nominally identical.

The constant α appearing in Eq. (41) was evaluated for each laminate using the residual strength measured after a 7 J impact (last column in Table 8). At this energy value, no penetration was observed for the materials tested, so that the condition $U < U_p$, necessary to ensure the validity of Eq. (41), was fulfilled. Using the constants from Table 8 in Eq. (41), the continuous lines in Fig. 53 were drawn.

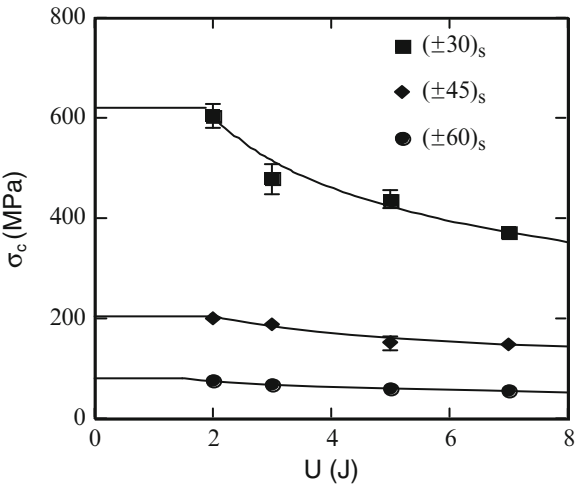


Fig. 53 Residual strength, σ_c, vs impact energy, U. *Black points*: test results. Solid lines: predictions on Eq. (41).

The correlation between the theoretical predictions and the experimental data (black symbols in Fig. 53) is very good, supporting the residual strength model.

Solving Eq. (39) for U, and substituting in Eq. (41), it results in:

$$\frac{\sigma_c}{\sigma_o} = \left[\frac{U_{\sigma o}}{U^*_{op} \cdot W^p} \left(\frac{I_o}{I} \right)^{1/\beta} \right]^{\alpha} \tag{42}$$

which yields the correlation wanted between I and σ.

For what previously shown in the indentation paragraph, the values $I_o = 6.77$ mm, $\beta = 2.535$, $U^*_{po} = 7.22$ J/(Kg/m^2)^p and $p = 1.50$, have a quite general applicability for laminates made of T400/934 layers, independently of the reinforcement architecture and fibre orientations. Taking this in mind, Eq. (42) becomes:

$$\frac{\sigma_C}{\sigma_O} = \left[\frac{U_{\sigma O}}{7.22 \cdot W^{1.50}} \left(\frac{6.77}{I} \right)^{\frac{1}{2.535}} \right]^{\alpha} \tag{43}$$

Contrary to the previous constants, here $U_{\sigma o}$ and α are characteristics of the specific laminate under concern, giving information on its resistance to first fibre breakage ($U_{\sigma o}$), and its sensitivity to impact damage in terms of residual strength (α).

Using Eq. (43) with the data in Table 8, the residual tensile strength for the three laminates tested having lay-ups $(\pm 30)_{2s}$, $(\pm 60)_{2s}$, and $(\pm 45)_{2s}$,was calculated as a function of the indentation I. The experimental data demonstrate a very reasonable agreement with theory, confirming the possibility to reliably predict the residual strength from the measured I value. In Fig. 54, it is shown for brevity only for the (±30) laminates but the same agreement with the same accuracy was found for the other orientations.

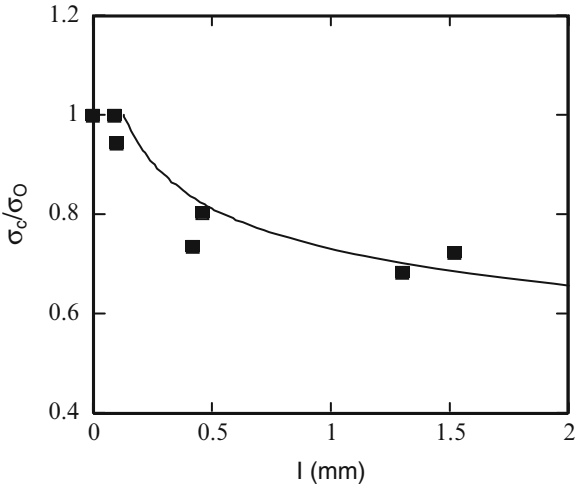


Fig. 54 Non-dimensional residual strength, σ_c/σ_o, against indentation, I, for $(\pm 30)_{2s}$ laminate

Solving Eq. (42) for $\sigma_c/\sigma_o = 1$, the limit value for I, I_{lim}, is obtained, under which no residual strength loss is expected:

$$I_{\text{lim}} = I_o \cdot \left(\frac{U_{\sigma o}}{U_{op}^* \cdot W^p} \right)^{\beta} \tag{44}$$

It is reported in the last column in Table 8 where it is observed that the initial strength decrease corresponds to an indentation level hardly detectable by visual inspection, especially for the $(\pm 60)_{2s}$ composite.

For a given laminate, Eq. (42) can be simplified in the form:

$$\frac{\sigma_c}{\sigma_o} = \left(\frac{I_o}{I_{\text{lim}}} \right)^{\gamma} \tag{45}$$

where:

$$\gamma = \frac{\alpha}{\beta} \tag{46}$$

Consequently, plotting on a log-log scale the residual strength data as a function of indentation for $I \geq I_{lim}$ results in a straight line providing a powerful tool for the calculation of the constants in Eq. (46), based on a minimum of experiments.

The analytical model evaluating the residual tensile strength as a function of indentation depth results in very reasonable agreement with the experimental data. In the particular case of a fixed laminate, the model becomes particularly simple, allowing the calculation of the material constants by a minimum of experimental tests.

It is important to note that, in some practice cases such as in aeronautics, impact damage strongly influences the design allowable in compression, rather than in tension. Therefore, the philosophy followed here could be usefully applied only if an analytical correlation similar to Eq. (41) should be found between the material compression strength and impact energy. Also the viscoelastic recovery of indentation during service, signalled by some researchers like in [86], deserves careful considerations and limits the applicability of the method to accidental damages produced during fabrication and control operations.

3.9 Energy Absorption Mechanisms and Damage: Correlation

The scope of this section is to establish a correlation between the damage occurring in a composite as a consequence of low-velocity impact and the energy dissipated during the impact phenomenon. Instrumented impact tests at different energy levels were at this aim carried out on glass fabric/epoxy laminates having different thicknesses (G in Table 1). To assess damage progression as a function of impact energy, ply-by-ply delamination and fibre breakages were measured by destructive tests deplying the specimens with the help of a heat source. A previous model [29], based on energy balance considerations, was applied for the interpretation of the experimental results. Some limitations in its applicability, supporting the present work, are emphasized. The contribution of fibre breakage and matrix damage to the irreversibly absorbed energy was found to be comparable at low impact energies; with increasing initial energy levels, delamination becomes predominant in determining energy dissipation.

3.9.1 Energy Absorbed by Fiber and Matrix Failures

It is important to understand the mechanisms of energy absorption in a laminate during low-velocity impact. Delfosse and Poursartip [29] tried to identify those mechanisms and correlated energy losses with observed failure modes. They carried out impact tests at different energy levels on two CFRP laminates, the first one (based on an IM6/937 material system) characterized by a brittle matrix, and the other (T800H/3900-2) by a ductile one. Following the authors, the absorbed energy, U_a, has two components, one, U_{dam}, necessary to create the damage, and the other, U_{dis}, dissipated through vibrations, heat, inelastic behaviour of the projectile or the supports, and so forth.

Since three types of damage are possible to occur in a laminate subjected to impact, and so the associated energies namely permanent indentation, U_{pi}, matrix damage (delamination and intraply splitting), U_m, and fibre breakage, U_f

$$U_a = U_{pi} + U_m + U_f + U_{dis} \tag{47}$$

On the other hand, it can be put:

$$U_m = G_m \cdot A_m \tag{48}$$

$$U_f = G_f \cdot A_f \tag{49}$$

where A_m is the total area of matrix damage, A_f the total area of broken fibres and G_m, G_f, are the energies required to create a unit damage area in the matrix and fibre, respectively.

The total delaminated area, A_m, was evaluated by pulse-echo ultrasonics together with destructive inspection whereas A_f, was measured thermally deplying the impacted panels after the resin was burnt off in a furnace.

Three-point bending tests were carried out to estimate G_f whereas the measurement of G_m was quite laborious, involving the selection of a range of impact energies giving rise uniquely to delamination damage, without fibre breakage: G_m was given by the slope of the straight line correlating U_a and A_m. However, this range of energies related only with delamination was very small (about 4.5 J) in the tough laminate, resulting in not accurated determination of G_m for the T800H/3900-2 system.

After the comparison between the absorbed energy deriving from matrix and fibre failure and the total absorbed energy [29], it was concluded that the contribution of the quantity ($U_{pi} + U_{dis}$) to U_a is negligible. In this case:

$$U_a \approx G_m A_m + G_f A_f \tag{50}$$

Delfosse and Poursartip found $G_m = 0.8$ KJ/m^2 and $G_m = 5.0$ KJ/m^2 for the brittle and the tough system, respectively. The fracture toughness value, G_{IIc} were obtained from quasi-static fracture toughness experiments, 0.75 KJ/m^2 and 2.0 KJ/m^2 and the big difference between G_m and G_{IIC} for the tough resin suggested that other damage mechanisms, not caught by the measured delaminated area, could contribute significantly to energy absorption mechanism.

Here, the main scope is to assess a method of data reduction able to overcome the difficulties previously highlighted.

After impact on the G laminates (Table 1), the projected delaminated area was obtained exploiting the translucent appearance of the material: the damage zone was highlighted by an intense light source on the back of the specimens; then, the photographed damaged area was measured by an image analyzer.

Moreover, in order to study the ply-by-ply damage extent and type, a central hole 1 mm in diameter was drilled in correspondence of the impact point of selected specimens. The latter were, then, immersed in black ink. Through the hole the liquid easily penetrated into the interlaminar cracks until the projected delaminated area was completely darkened by the ink; then, they were dried and carefully deplied with the help of moderate heating. The delaminated area in correspondence of each

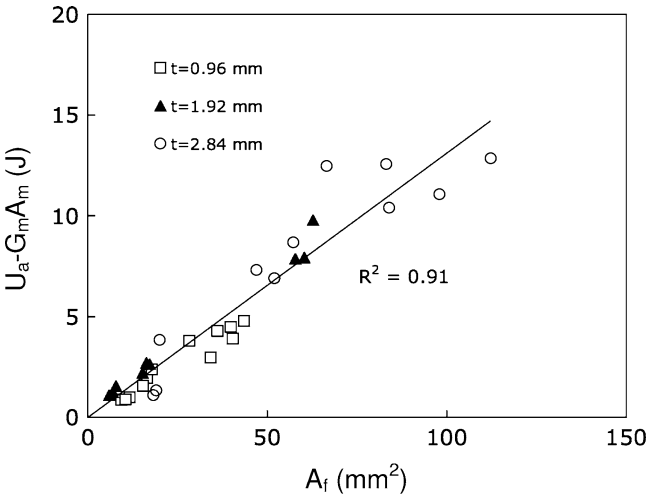


Fig. 55 Calculation of the upper bound value of unit energy for fibre breakage

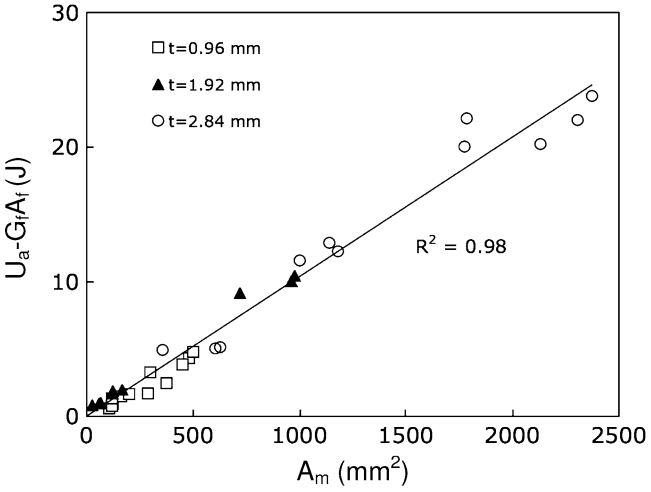


Fig. 56 Calculation of the upper bound value of unit energy for matrix damage

interlaminar surface was measured and the in-plane length of broken fibres within each ply was evaluated by optical microscopy at low magnification, following the procedure adopted by Delfosse and Poursartip [29].

If $(U_{pi} + U_{dis})$ in Eq. (47) is disregarded, it is possible to calculate G_f^u and G_m^l from the slope of the straight line passing through the origin in Figs. 55 and 56 where U_a-G_mA_m and U_a-G_fA_f obtained from Eqs. (47), (48), and (49), are reported against A_f and A_m respectively. The index "u" ("l") stand for an upper (lower) bound value. At the same way the $G_m{}^u$ and $G_f{}^l$ values can be obtained plotting A_m against

Table 9 Upper and lower unit energies bound values for matrix damage and fibre breakage

G_f^u (KJ/m^2)	G_f^l (KJ/m^2)	G_m^u (KJ/m^2)	G_{mf}^l (KJ/m^2)
131.0	126.3	10.1	10.4

U_a-G_fA_f. Tentative values was assumed for this quantity changing it until the best-fit straight line fitting the experimental data follows the expected trend. A lower limit of the absorbed energy, U_{amin}, was calculated considering the lower values of G_f and G_m.

The best-fit straight lines shown in the figures were drawn through all the data points. The straight lines fit reasonably well the experimental trends, supporting the applicability of the energy criterion proposed in [29].

In Table 9, the G_f^u, G_f^l,G_m^l, G_m^u values obtained from Figs. 55 and 56, are collected. It is possible to note that, in agreement with what find by Delfosse and Poursartip [29], the unit energy associated with fibre breakage is far higher than its matrix counterpart but the latter is about five times higher than what usually measured in a Mode II delamination test for a tough resin [87].

3.9.2 Delaminated Area and Broken Fiber Length

After impacting the G panels with two different impactor diameters, 19.8 and 16 mm, the extent of the projected delaminated area was obtained exploiting the translucent appearance of the material: the damaged zone was highlighted by an intense light source on the back of the specimens, photographed and the area was measured by an image analyzer. Two parameters, i.e. the projected delaminated area, A_p, the area of delamination as perceived from visual observation and the visible broken fibre length, d, were here assumed. The visible broken fibre length were obtained by measuring the length of the two lines along which fibre fracture was observed. Their mean value was, then, calculated. It is important to underline that A_p and d must not be confused with the corresponding ply-by-ply damage, with which the absorbed energy is conceivably correlated.

In Fig. 57, a typical impact damage visually observed on to the back face of the panel, where the classical visible diamond-shaped delaminated area attained its maximum dimensions, is shown. The axes coinciding with the warp-weft directions of the surface fabric layer (horizontal and vertical directions), is clearly visible. Besides, fibre fractures occur along two lines of length slightly lower than the major axes of delamination.

From Fig. 57, other cross fibre failures in the internal layers oriented at 45°, were also observed together with multiple delaminations occurring along the thickness suggested by a darker area fully contained in the projected delamination. These damages are not taken into account for A_p and d.

The behaviour of d and A_p with impact energy is shown in Figs. 58 and 59, respectively. Each point is related to a single measurement and the different symbols

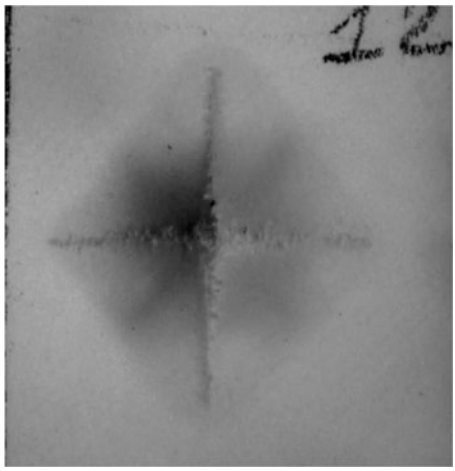


Fig. 57 Typical damage zone after impact. *Back surface*. Panel thickness t = 1.92 mm. Tup diameter D_t = 16 mm. Impact energy U = 15.8 J

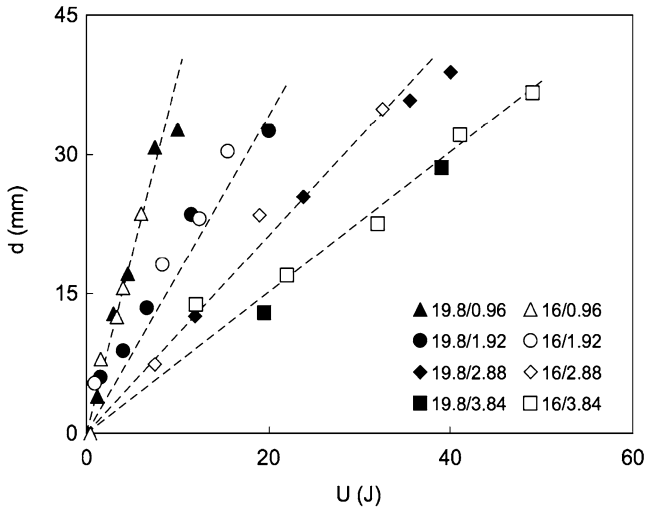


Fig. 58 Effect of the panel thickness, *t*, on the evolution of visible broken fibre length, *d*, at the increasing of impact energy, *U*. *Dashed lines*: Eq. (51)

are identified by the label "A/B", where A is the impactor diameter and B the panel thickness in mm.

It is clear that d and A_p are unaffected by the tup diameter and an increase was noted with decreasing the panel thickness, for a fixed value of the impact energy U. The visible broken fibre length vary linearly with U following the empirical equation (dashed lines in Fig. 58):

$$d = k\frac{U}{t^{\alpha}} \tag{51}$$

with $\alpha = 1.17$, $k = 3.66$ mm$^{(1+\alpha)}$/J.

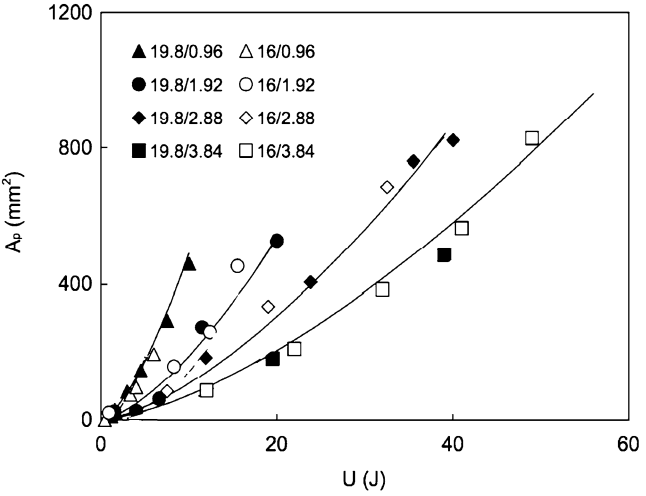


Fig. 59 Projected delaminated area, A_p, versus impact energy, U. *Solid lines*: Eq. (52)

The dependence of A_p on impact energy is represented by the relationship (solid lines in Fig. 59):

$$A_p = 14.71 \frac{U^{1.50}}{t^{1.38}} \tag{52}$$

providing A_p (in mm^2), if U (in J) and t (in mm) are known.

Equations (51) and (52) describe the role played by impact energy and laminate thickness in determining visual damage.

The study about the mechanisms of damage initiation and propagation was the primary focus of this part of the research. At the aim to find a simple impact parameter for the prediction of the delaminated area, the main factors causing delamination were here studied so that the possibility to correlate internal and external damage. As already said, there has been a considerable debate about the relative merits of using force and energy as a scale parameter for this impact damage. The approach based on impact force works well in different applications, especially when the onset of damage has to be determined for different plate or impactor geometry [47, 48] whereas Delfosse and Poursatip [29] showed that an energy-based approach can be more helpful in examining the extent of damage, beyond the onset.

On the base of what above asserted about the independence of the loading velocity [53–55], static tests were here carried out on rectangular carbon fibre reinforced plastic plates of four different thickness (T in Table 1). In order to verify the effect of the impactor, a number of impact tests were carried out varying the indentor diameter too. After the experimental tests, the specimens were subjected to non-destructive evaluation using an ultrasonic C-scan apparatus to investigate about the delamination extent. Moreover, some specimens were sectioned and observed by optical microscopy to confirm the US results.

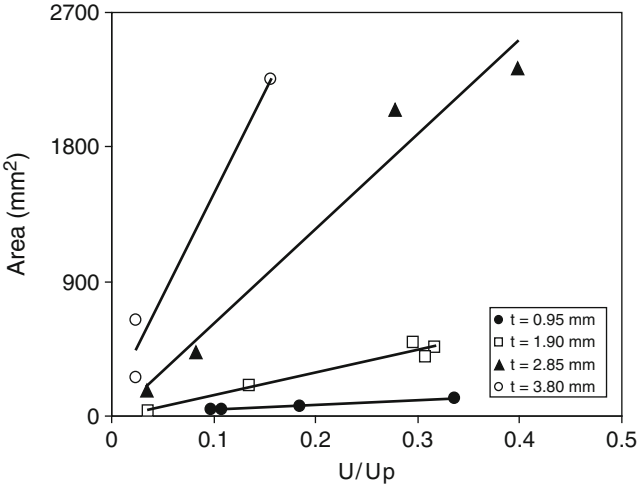


Fig. 60 Delaminated area versus non-dimensional energy, U/U_p, for laminates different in thickness, t

The most common parameter [25, 29, 42, 79, 88, 89], the impact energy considered the right one to evaluate the delaminated area is first investigated. However, the force approach was revealed in this case more interesting in collecting all the experimental data on a single master curve.

Discussion

The data presented refer to different material system, different thickness, different architecture, (unidirectional, fabric, cross ply, etc.) [79, 90, 91].

It could be interesting to find a way, as already done for the indentation, to obtain a single master curve for experimental data, about a specific material system, obtained in different test conditions, like different impactor, different thickness, different support diameter etc. A single master curve could also allow to know the threshold energy, given by the x intercept, below which no damage is present in the material.

With this in mind, the extension of the delaminated area against the non-dimensional energy U/U_p measured on the T laminates (Table 1), is shown in Fig. 60. The different symbols refer to the different thickness and the straight lines are drown to better understand the experimental data trend. First of all, it is important to note that the maximum energy level for each thickness is less than 40% of the penetration energy. This is due to the fact that the low energy range is the most interesting in aeronautical field because of the presence of a consistent internal damage correspondent to a not so evident external indentation. Moreover,

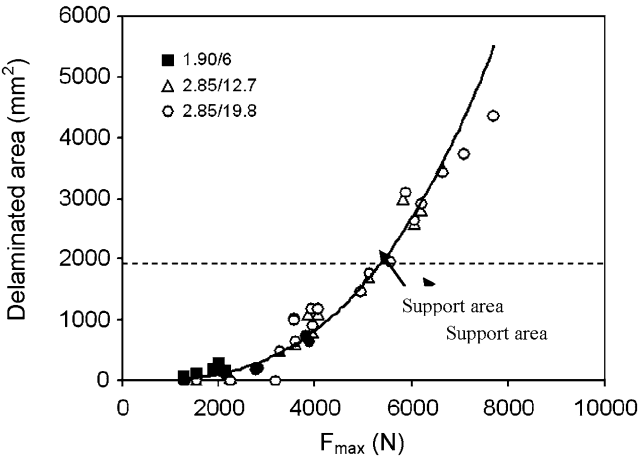


Fig. 61 Delaminated area versus impact load for laminates different in thickness

contrarily to what happens for the indentation, the experimental points are separated again. This means that the impact energy is not a simple parameter to adopt for the prediction of the delaminated area.

The fact already noted that the same energy level produces a larger delaminated area in thickest panels could be explained with the fact that the thickness laminates absorb the same energy with an higher load since the material rigidity increases with the thickness raised to the 3rd power. The latter suggests that the delaminated area can be related to the impactor-material contact load that could be used as a parameter to compare and to predict impact damages in structures from coupon tests [34]. Even if there is an open debate, the approach based on impact force works well in many applications, especially when the onset of damage has to be determined for different plates or impactor geometries [34, 49–51, 72, 73].

So said, the same experimental point from Fig. 60 are plotted in Fig. 61 against the maximum contact load, F_{max}: a single master curve was found and the damage is again larger the thicker the laminates are.

Support area

The continuous curve is the graphical representation of the following equation:

$$A = \eta \cdot F_{max}^{\beta} \tag{53}$$

where A is the delaminated area. The value of the two constants obtained by the minimum square method is $\eta = 3.13 \times 10^{-8}$ mm^2/N$^{\beta}$ and $\beta = 2.89$.

On the base of what found, the impact force could be used as a parameter to compare and to predict impact damage in structures from coupon tests [47].

4 Conclusion

Static and low velocity impact tests were carried out on different composite laminates in different tests conditions, at the main scope to supply more information about their behaviour under dynamic load conditions. The authors faced the very complex problem of the failure modes caused by an impact and tried to correlate them to the main parameters involved in the phenomenon at the aim to obtain semi empirical and analytical models for the prediction of the residual strength.

The main conclusions are listed in the following.

- The force required for damage initiation under form of delamination increases following a power law whose exponent is very close to 1.5 observed for the contact law. From the observation of the failure modes, this suggests that delamination is mainly due to shear stresses, which can be calculated by the contact law.
- The analysis highlighted the importance of the penetration energy in giving the possibility to predict the impact energy by a simple indentation measurement. The scope was the assessment of a simple model to correlate the indentation depth and the energies involved in the impact phenomenon. The model was found to have a quite general applicability: for a given fibre/resin system, the indentation depth is substantially independent of fibre type, architecture and orientations, laminate thickness and resin type and content, varying only as a function of the impact energy to the penetration energy ratio.
- The penetration energy can be predicted by an empirical equation: a power law with the exponent that is a constant, scarcely influenced by matrix type and content; the reinforcement architecture and orientations, and support diameter, play a minor role too in affecting U_p. The main parameter determining the energy absorption capacity is the total fibre thickness, proportional to the total areal weight of reinforcement and given by the product $(t \cdot V_f)$ of the panel thickness times the fibre volume fraction (Eq. (37)). This parameter was revealed useful in normalising impact data obtained under different test conditions.
- An analytical model evaluating the residual tensile strength as a function of indentation depth results in very reasonable agreement with the experimental data. The model allows the calculation of the material constants by a minimum of experimental tests.
- An elastic solution available for circular isotropic plates loaded at the centre was modified to model the indentation and applied to the prediction of the load-displacement curve. The analytical model accurately describes the elastic behaviour of the plates allowing to know the first failure energy. The prediction of the energy reveals that for thin plates, a large portion of the stored energy is correlated with the non-linear response of the plate deriving from the achievement of the large displacements regime and the indentation was negligible. The cubic component in Eq. (22) plays a major role in determining the plate response. This energy becomes negligible for thick plates (the influence of the

cubic component in Eq. (22) becomes lower and lower); the energy due to the local contact phenomena must be taken into account.
- The caused damages were observed by visual analysis, as well as by deplying some of the specimens: contrarily to what usually found, delamination was found between layers equally oriented too.

References

1. Sun CT, Liou WJ (1989) Investigation of laminated composite plates under impact dynamic loading using a three-dimensional hybrid stress finite element method. Comput Struct 33(3):879–884
2. Cairns DS (1991) Simple elasto-plastic contact laws for composites. J Reinf Plast Compos 10(4):423–433
3. Bucinell RB, Nuismer RJ, Koury JL (1991) Response of composite plates to quasi-static impact events. In: O'Brien TK (ed) Composite materials: fatigue and fracture. ASTM STP 1110., pp 528–549
4. Abrate S (1994) Impact on laminated composites: recent advances. Appl Mech Rev 47(11):517–544
5. Hong S, Liu D (1989) On the relationship between impact energy and delamination area. Exp Mech 29(2):115–120
6. Hull D, Shi YB (1993) Damage mechanism characterisation in composite damage tolerance investigations. Compos Struct 23:99–120
7. Hitchen SA, Kemp RMJ (1995) The effect of stacking sequence on impact damage in a carbon fibre/epoxy composite. Composites 26:207–214
8. Richardson MOW, Wisheart MJ (1996) Review of low-velocity impact properties of composite materials. Composites A 27A:1123–1131
9. Caprino G (1984) Residual strength prediction of impacted CFRP laminates. J Compos Mater 18:508–518
10. Cantwell WJ, Morton J (1991) The impact resistance of composite materials – a review. Composites 22(5):347–362
11. Cairns DS, Minuet PJ, Abdallah MG (1993) Theoretical and experimental response of composite laminates with delaminations loaded in compression. Compos Struct 25:113–120
12. Kim J-K, Mackay DB, Mai Y-W (1993) Drop-weight impact damage tolerance of CFRP with rubber-modified epoxy matrix. Composites 24(6):485–494
13. Choi HY, Downs RJ, Chang F-K (1991) A new approach toward understanding damage mechanisms and mechanics of laminated composites due to low velocity impact: part I-experiments. J Comp Mater 25:992–1011
14. Choi HY, Chang FK (1992) A model for predicting damage in graphite/epoxy laminated composites resulting from low-velocity point impact. J Compos Mater 26(14):2134–2169
15. Abrate S (1998) Impact on composite structures. Cambridge University Press, Cambridge
16. Timoshenko SP, Woinowsky-Krieger S (1959) Theory of plates and shells. McGraw-Hill, Singapore
17. Caprino G, Lopresto V (2000) The significance of indentation in the inspection of CFRP panels damaged by low-velocity impact. Compos Sci Technol 60:1003–1012
18. Chang FK, Choi HY, Wang HS (1990) Damage of laminated composites due to low velocity impact. In: 31st AIAA/ASME/ASCE/AHS/ASC structures, structural dynamics and Materials conference, Long Beach, CA, 2–4 April 1990, pp 930–940
19. Cantwell WJ, Morton J (1990) Impact perforation of carbon fibre reinforced plastics. Compos Sci Technol 38:119–141

20. Husman GE, Whitney JM, Halpin JC (1975) Residual strength characterisation of laminated composites subjected to impact loading. ASTM STP 568:92–113
21. Delfosse D, Poursartip A (1985) Experimental parameter study of static and dynamic out-of-plane loading of CFRP laminates. In: Proceedings of the 10th international conference on composite materials (ICCM10), Whistler, Canada, August 1985, pp V-583-590
22. Bibo G, Leicy D, Hogg PJ, Kemp M (1994) High-temperature damage tolerance of carbon fibre-reinforced plastics. Part 1: impact characteristics. Composites 25(6):414–424
23. Bibo GA, Hogg PJ (1998) Influence of reinforcement architecture on damage mechanisms and residual strength of glass-fibre/epoxy composite systems. Compos Sci Technol 58:803–813
24. Caprino G, Lopresto V, Scarponi C, Briotti G (1999) Influence of material thickness on the response of carbon-fabric/epoxy panels to low-velocity impact. Compos Sci Technol 59:2279–2286
25. Ghasemi Nejhad MN, Parvizi-Majidi A (1990) Impact behaviour and damage tolerance of woven carbon fibre-reinforced thermoplastic composites. Composites 21(2):155–168
26. Caprino G, Langella A, Lopresto V (2002) Elastic behaviour of circular composite plates transversely loaded at the centre. Composites A 33:1191–1197
27. Schoeppner GA, Abrate S (2000) Delamination threshold loads for low velocity impact on composite laminates. Composites A 31:903–915
28. Sjoblom PO, Hartness TM, Cordell TM (1988) On low-velocity impact testing of composite materials. J Compos Mater 22(1):30–52
29. Delfosse D, Poursatip A (1997) Energy-based approach to impact damage in CFRP laminates. Composites A 28A:647–655
30. Liu S, Kutlu Z, Chang FK (1993) Matrix cracking and delamination propagation in laminated composites subjected to transversely concentrated loading. J Compos Mater 27(5):436–470
31. Herup EJ, Palazotto AN (1997) Low-velocity impact damage initiation in graphite/epoxy/Nomex honeycomb-sandwiche plates. Compos Sci Technol 57(12):282–289
32. Yang SH, Sun CT (1982) Indentation law for composite laminates. In: Daniel I (ed) Composite materials: testing and design (sixth conference), ASTM STP 787, pp 425–449
33. Tan TM, Sun CT (1985) Use of statical indentation laws in the impact analysis of laminated composite plates. J Appl Mech 52(8):6–12
34. Jackson WC, Poe CC Jr (1993) The use of impact force as a scale parameter for the impact response of composite laminates. J Compos Technol Res 15(4):282–289
35. Abrate S (2001) Modeling of impacts on composite structures. Compos Struct 51:129–138
36. Timoshenko SP Strength of materials. McGraw-Hill, New York
37. Chang FK, Choi HY, Wang HS (1990) Damage of laminated composites due to low velocity impact. In: 31st AIAA/ASME/ASCE/AHS/ASC structures, structural dynamics and materials conference, Long Beach, CA, 2–4 April 1990, pp 930–940
38. Stout MG, Koss DA, Liu C, Idasetima J (1999) Damage development in carbon/epoxy laminates under quasi-static and dynamic loading. Compos Sci Technol 59:2339–2350
39. Gosse JH, Mori PBY (1988) Impact damage characterization of graphite/epoxy laminates. In: Proceedings of the 3rd technical conference of the American Society for Composites, Seattle, WA, pp 334–353
40. Tsai SW, Hahn HT (1975) Introduction to composite materials. Technomic Publishing Company, Lancaster
41. Hashin Z (1975) Failure criteria of unidirectional fiber composites. J Appl Mech 47:329–334
42. Liu S (1994) Quasi impact damage initiation and growth of thick-section and toughened composite materials. Int J Solids Struct 31(22):3079–3098
43. Siow YP, Shim PW (1998) An experimental study of low velocity impact damage in woven fiber composites. J Compos Mater 32(12):1178–1202
44. Kaczmerek H (1995) Ultrasonic detection of damage in CFRPs. J Compos Mater 29:59–95
45. Hosur MV, Murthy CRL, Ramamurthy TS, Shet A (1998) Estimation of impact-induced damage in CFRP laminates through ultrasonic imaging. NDT&E Int 31:359–374

46. Olsson R (2001) Analytical prediction of large mass impact damage in composite laminates. Composites A 32:1207–1215
47. Sjoblom P (1987) Simple design approach against low velocity impact damage. In: Proceedings of 32nd SAMPE symposium, Anaheim, CA, pp 529–539
48. Caprino G, Langella A, Lopresto V (2003) Prediction of the first failure energy of circular carbon fibre reinforced plastic plates loaded at the centre. Composites A 34:349–357
49. Zhang X (1998) Impact damage in composite aircraft structures-experimental testing and numerical simulation. Proc Inst Mech Eng 212(4):245–259
50. Davies GAO, Zhang X, Zhou G, Watson S (1994) Numerical modelling of impact damage. Composites 25(5):342–350
51. Davies GAO, Zhang X (1995) Impact damage prediction in carbon composite structures. Int J Impact Eng 16(1):149–170
52. Olsson R (1999) A review of impact experiments at FFA during 1986 to 1998. The Aeronautical Research Institute of Sweden, FFA TN 1999–08
53. Lesser AJ, Filippov AG (1991) Kinetics of damage mechanisms in laminated composites. In: International SAMPE symposium and exhibition, vol 36, part 1, pp 886–900
54. Crivelli Visconti I, Caprino G, Di Ilio A, Carrino L (1983) Impact tests on CFRP: a static-dynamic analogy. In: High performance composite materials – new applications and industrial production, acts of 4th international SAMPE conference-SAMPE Euro chapter, Bordeaux, 17–20 October 1983, pp 189–196
55. Lesser AJ, Filippov AG (1991) Kinetics of damage mechanisms in laminated composites. In: International SAMPE symposium and exhibition, vol 36, part 1, pp 886–900
56. Srinivasan K, Jackson WC, Hinkley JA (1991) Response of composite materials to low velocity impact. In: International SAMPE symposium and exhibition, vol 36, part 2, pp 850–862
57. Shivakumar KN, Elber W, Illg W (1985) Prediction of low velocity impact damage in thin circular laminates. AIAA J 23(3):442–449
58. Caprino G, Crivelli Visconti I, Di Ilio A (1984) Composite materials response under low-velocity impact. Compos Struct 2:261–271
59. Wu E, TSai CZ, Chen YC (1994) Penetration into glass/epoxy composite laminates. J Compos Mater 28:1783–1802
60. Zenkour AM, Mashat DS (2009) Exact solutions for variable-thickness inhomogeneous elastic plates under various boundary conditions. Meccanica 44(4):433–447
61. Agarwal BD, Broutman LJ (1980) Analysis and performance of fiber composites. Wiley, New York
62. Grediac M (1999) A procedure for designing laminated plates with required stiffness properties. Application to thin quasi-isotropic quasi-homogeneous uncoupled laminates. J Compos Mater 33:1939
63. Park JW, Kim YH (1999) Predictor-corrector procedure for displacements, stresses and their sensitivity coefficients in composite panels. J Compos Mater 33:1222
64. Wang CM, Reddy JN, Lee KH (2000) Shear deformable beams and plates. Elsevier, Amsterdam
65. Scarponi C, Briotti G, Barboni R, Marcone A, Iannone M (1996) Impact testing on composite laminates and sandwich panels. J Compos Mater 30(17):1873–1911
66. Lagace PA, Wolf E (1993). Impact damage resistance of several laminated material systems. In: 34th AIAA structures, structural dynamics and materials conference, La Jolla, CA, Pt. 4, pp 1863–1872
67. Lopresto V, Caprino G (2002) Elastic response of circular CFRP plates under low-velocity impact. In: Proceedings of ECCM10, 3–7 giugno 2002, Bruge, Belgio
68. Sun CT, Chen JK (1985) On the impact of initially stressed composite laminates. J Compos Mater 19:490–503
69. Davies GAO, Hitchings D, Wang J (2000) Prediction of threshold impact energy for onset of delamination in quasi-isotropic carbon/epoxy composite laminates under low-velocity impact. Compos Sci Technol 60:1–7

70. Cartiè DDR, Irving PE (2002) Effect of resin and fibre properties on impact and compression after impact performance of CFRP. Composites A 33:483–493
71. Lopresto V, Melito V, Leone C, Caprino G (2006) Effect of stitches on the impact behaviour of graphite/epoxy composites. Compos Sci Technol 66/2:233–239
72. Lagace PA, Williamson JE, Tsang PHW, Wolf E, Thomas SA (1993) A preliminary proposition for a test method to measure (impact) damage resistance. J Reinf Plast Compos 12(5):584–601
73. Poe Jr CC (1991) Relevance of impacter shape to non visible damage and residual tensile strength of a thick graphite/epoxy laminate. In: O'Brien TK (ed) Composite materials: fatigue and fracture, vol 3, ASTM STP 1110. American Society for Testing and Materials, Philadelphia, PA, pp 501–527
74. Sutherland LS, Guedes Soares C (2005) Impact on low fibre-volume, glass/polyester rectangular plates. Compos Struct 68:13–22
75. Wardle MW, Tokarsky EW (1983) Drop weight impact testing of laminates reinforced with Kevlar aramid fibres, E-glass and graphite. Compos Technol Rev 5(1):4–10
76. Hsieh CY, Mount A, Jang BZ, Zee RH (1990) Response of polymer composites to high and low velocity impact. In: Proceedings of the 22nd international SAMPE technical conference, 6–8 November 1990, pp 14–27
77. Caprino G, Lopresto V (2000) Factors affecting the penetration energy of glass fibre reinforced plastics subjected to a concentrated transverse load. In: ECCM–9, Brighton, 4–7 June 2000
78. Babic L, Dunn C, Hogg PJ (1989) Damage development and its significance in GRP subjected to impact. Plast Rubb Process Appl 12(4):199–207
79. Cantwell WJ, Morton J (1989) The influence of varying projectile mass on the impact response of CFRP. Compos Struct 13:101–104
80. Caprino G (1989) Results of instrumented drop-weight impact tests on polycarbonate and glass fibre reinforced plastics panels. Istituto Donegani internal report
81. Strait LH, Karasek ML, Amateau MF (1992) Effects of stacking sequence on the impact resistance of fiber reinforced thermoplastic toughened epoxy laminates. J Compos Mater 26(12):1725–1740
82. Chotard TJ, Benzeggagh ML (1998) On the mechanical behaviour of pultruded sections submitted to low-velocity impact. Compos Sci Technol 58(6):839–854
83. Wu E, Shyu K (1993) Response of composite laminates to contact loads and relationship to low-velocity impact. J Compos Mater 27(15):1443–1464
84. Wang H, Vu-Khanh T (1994) J Compos Mater 28:684
85. Cantwell WJ, Morton J (1990) An assessment of the residual strength of an impact-damaged carbon fibre reinforced epoxy. Compos Struct 14:303–317
86. Ilcewicz I (1997). Impact damage in composite structures. Polymer matrix composites, MIL-handbook 17
87. Davidson BD, Kumar M, Soffa MA (2009) Influence of mode ratio and hygrothermal condition on the delamination toughness of a thermoplastic particulate interlayered carbon/epoxy composite. Composites A 40:67–79
88. Scarponi C, Briotti G, Barboni R (1999) Reduction of tensile strength in angle-ply composite laminates due to low-velocity impact. J Reinf Plast Compos 18(1):63–85
89. Morton J, Godwin EW (1989) Impact response of tough carbon fibre composites. Compos Struct 13:1–19
90. Liu D (1988) Impact-induced delamination – a view of bending stiffness mismatching. J Compos Mater 22:674–692
91. Kumar P, Rai B (1993) Delaminations of barely visible impact damage in CFRP laminates. Compos Struct 23:313–318

Perforation of Composite Laminate Subjected to Dynamic Loads

Shirley Kalamis García-Castillo, Sonia Sánchez-Sáez, Carlos Santiuste, Carlos Navarro, and Enrique Barbero

Abstract This chapter focuses on the modeling of plain woven GFRP laminates under high-velocity impact. A brief review of the different approaches available in scientific literature to model the behavior of composite laminates subjected to high-velocity impact of low-mass projectiles is presented, and a new analytical model is proposed. The present model is able to predict the energy absorbed by the laminate during the perforation process including the main energy-absorption mechanisms for thin laminates: kinetic energy transferred to the laminate, fiber failure, elastic deformation, matrix cracking, and delamination.

The model is validated through comparison with experimental data obtained in high-velocity impact tests on plain woven laminates made from glass fiber and polyester resin, using different plate thicknesses. Moreover, a numerical model based on the Finite Element Method (FEM) was developed to verify the hypothesis of the analytical model. The model showed good agreement with experimental results for a laminate thickness between 3 and 6 mm. However, when the thickness reached 12 mm the model overestimated the residual velocity of the projectile.

The validated analytical model is used to analyze the contribution of the main energy-absorption mechanisms. For impact velocities lower than or equal to the ballistic limit, the main energy-absorption mechanisms are fiber elastic deformation and fiber failure, thus the impact behavior of the laminate is dominated by the stiffness and the strength of the plate. Meanwhile, for higher impact velocities, laminate acceleration is the main energy-absorption mechanism, and the behavior of the laminate is dominated by its density.

S.K. García-Castillo • S. Sánchez-Sáez • C. Santiuste • C. Navarro • E. Barbero (✉)
Department of Continuum Mechanics and Structural Analysis, University Carlos III of Madrid, Avda. de la Universidad 30, 28911 Leganés, Madrid, Spain
e-mail: ebarbero@ing.uc3m.es

S. Abrate et al. (eds.), *Dynamic Failure of Composite and Sandwich Structures*, Solid Mechanics and Its Applications 192, DOI 10.1007/978-94-007-5329-7_7,
© Springer Science+Business Media Dordrecht 2013

1 Introduction

Composite structures offer several advantages over traditional structures, such as high specific stiffness and strength. Nevertheless, composite materials have low strength under concentrated transversal loads [1, 2], such as those produced by an impact. Although composite structures are not designed as armor, during their service life they could be subjected to high-velocity impacts of low-mass fragments—for example, the impact of a fragment separated from the blades of the fan of a jet-engine against the fan cowl or the inlet. The effect of these impacts depends on many parameters, ranging from indentation to complete perforation of the structure.

The mechanical properties of a composite material are affected by the impact; frequently, extensive damage is caused, significantly reducing the load-bearing capability of the structure [3]. Also, although this damage can be internal and not detected visually, it could significantly compromise post-impact mechanical behavior [4]. Therefore, impact strength constitutes a critical design requirement in composite structures.

Despite years of extensive research using theoretical as well as experimental approaches on the impact behavior of composite laminates, a complete and validated methodology has not yet been developed. Many reviews treat this subject [3, 5–7] as do several recent works [8, 9].

Impulsive problems can be classified, depending on the speed of the projectile, into high- or low-velocity impacts. In a low-velocity impact, the stress waves reach the boundary of the structure and reflect several times during the impact; for this reason the response of the structure is global and is controlled by its geometry and boundary conditions. By contrast, at high velocity, the response of the structure is controlled by the stress-wave propagation through the thickness of the laminate, resulting in quite localized damage. The response of the structure is governed by the material properties in the area close to the impact and is essentially independent of the boundary conditions and the size of the structure.

No clear limit between high- and low-velocity impacts has been established, although researchers apply several definitions. One widely used defines 100 m/s as the minimum velocity for which an impact is considered high velocity [10]. However, some authors have even considered lower impact velocities of about 10 m/s [11]. Robinson and Davies [12] proposed a simple equation, $\varepsilon_c = v_0/c$, to estimate the transition impact velocity, above which stress waves are dominant. In this equation, v_0 is the impact velocity, c is the stress-wave propagation velocity, and ε_c is the failure strain of the composite. Typically, this formula, for epoxy-matrix composites, defines a transition velocity of around 10–20 m/s [4].

In a composite structure the characteristics of the high-velocity-impact process are controlled by the mechanical properties of the projectile and structure, the impact conditions (i.e. angle of the trajectory of the projectile), laminate configuration, geometry of the projectile, and plate thickness.

The damage generated on a laminated composite during a high-velocity impact is a complex phenomenon due to the many parameters involved [13]. Several failure mechanisms contribute to the absorption of the kinetic energy of the projectile. These mechanisms include failure of fibers, delamination, matrix cracking, shear plugging failure, etc.. Fiber failure is the ultimate damage mode, although the damage would appear in the form of matrix cracking, followed by delamination.

Some authors, studying the influence of impact velocity on the reduction of laminate strength, suggest that the greatest reduction is close to the perforation threshold [3]. This reduction could be related to the damage area, which is also greatest at the threshold [14]. Therefore, it is necessary to ascertain the perforation threshold, which is usually studied according to the ballistic-limit velocity.

The ballistic limit can be defined as the maximum velocity at which a particular projectile is expected to consistently fail to penetrate the component. This velocity can be determined by means of experimental tests or by theoretical models [15]. Usually this velocity is expressed in terms of probability as v_{50}, meaning that there is a 50% of probability of perforation [16]. To determine the ballistic limit from experimental data, many authors apply statistical techniques. This velocity depends primarily on laminate thickness and secondarily on projectile shape [17].

Several basic approaches are used to analyze the high-velocity impact problem on laminates: experimental, analytical, and numerical methods. Many works examine the impact behavior of composite laminates experimentally, a few recent examples of these being the references [14] and [18–22]. Numerical simulations have been successfully applied for modeling the perforation process of laminates subjected to ballistic impact [23–27]. These models allow in-depth studies of the perforation process, although they are time consuming. Also, many authors apply analytical models to determine the impact response of laminates [13, 22, 28–40]. The advantages of analytical models lie in their low computational cost and in their ability to explicitly describe the physical behavior of the laminate. Many of these papers have focused only on estimating the perforation velocity and less information can be found related to the energy absorbed by the different failure mechanisms.

The present work focuses on the perforation process of composite laminates subjected to high-velocity impact of low-mass fragments. An analytical model based on energy-conservation laws is proposed and validated, both analytically and numerically. This model is a modified and improved version of a previous one proposed by the authors [22, 39]. The previous model was applied to study the influence of the impact velocity and thickness in several energy-absorption mechanisms (fiber failure, elastic deformation, acceleration of the laminate, delamination, and matrix cracking) for glass-fiber-reinforced laminates.

The chapter is structured as follows. After this brief introduction, several theoretical models, analytical as well as numerical, used in the literature to analyze the behavior of laminate plates subjected to high-velocity impacts are summarized in Sect. 2. One analytical model based on energy-conservation laws is explained in depth in Sect. 3. This model was improved to include non-linear behavior of the laminate, and was formulated by a non-linear differential equation. The model was

validated with an experimental test and a numerical simulation; both are described in the Sect. 4. The influence of laminate thickness on the impact behavior and on the energy-absorption mechanisms and the applicability range of the analytical-model hypothesis are examined in Sect. 5. Finally, the main results are highlighted and some concluding remarks are given.

2 Modeling of High-Velocity Impact

This section briefly reviews the analytical approach to model the high-velocity impact behavior of laminates. Also, several failure criteria commonly used in the numerical modeling of this phenomenon are presented.

2.1 Analytical Modeling

An analytical method solves the basic equations of mechanics as well as simple constitutive relationships of the materials involved, taking into account the main physical aspect of the impact event. There are countless simplified analytical models for ballistic impacts, see Ben-Dor et al. [7] for a review of these models.

The high -velocity-impact analytical models can be divided into two groups. One group includes analytical models based on momentum equations and geometric considerations concerning the deformation of the laminate during impact. The analytical models of the other group are based on energy-conservation laws.

The models based on momentum equations and geometric considerations have been broadly applied in the modeling of woven fabric for armor applications. Many models can be found in the literature [28–31, 33, 40–42].

Taylor and Vinson [29] proposed a model that uses the plate theory and geometric consideration of the laminate deformation. The model was validated with experimental tests on woven laminates made from Kevlar® fabric.

Zhu et al. [30] divided the impact phenomenon into three consecutive phases: indentation, perforation, and exit. Five dissipative mechanisms were included in the model, indentation of the projectile nose, bulging at the laminate surface, fiber failure, delamination, and friction. Matrix cracking was disregarded in the model. The analysis was made by determining the total resistive force acting on the projectile due to each of these mechanisms. The authors applied laminate-plate theory to determine the global deflection. The model estimates residual velocity of the projectile, deflection, and ballistic limits. It was validated with experimental tests of Kevlar/polyester laminates subjected to high-velocity impacts.

Vinson and Walter [30] studied a carbon-fiber weave AS4/3501-6, using a model based on conical-shell theory and geometric considerations to predict the deformation of the panel and the displacement of the cone formed. Their model requires two tests to be made at different velocities to determine the relationship

between the strain, failure, and the impact velocity. With this model, they were able to predict the ballistic limit and the residual velocity.

Navarro [31] studied the impact in one fiber by an analytical model based on the one-dimensional wave-propagation theory. This model was later extended to unidirectional laminate adding the effect of the matrix as a dead weight. Only fiber failure was considered, while delamination and friction or other mechanisms were disregarded. In armor grade laminates, this is the main mechanism of energy absorption according to [43]. The model was validated with dry fabrics and woven laminates of aramid composites.

Wen et al. [33, 40] assumed that the deformation in the laminate is localized and that the pressure exerted by the projectile can be divided into two parts: a quasi-static part due to elastic-plastic deformation, and a dynamic part due to penetration velocity. This model enables the depth of penetration, residual velocity, and ballistic limits to be estimated. He et al. [44] applied the model to glass, Kevlar, and carbon laminates in order to study the influence of thickness at the ballistic limit. Two projectile geometries, truncated-projectile-nose and truncate-cone-nose were considered in the model [40].

Phoenix and Porwal [41] developed an analytical model based on membrane theory and studied a balanced fabric laminate struck by blunt-nosed projectiles. The model estimates the ballistic limit and residual velocity. On comparing the results of the model with experimental results from literature for Kevlar® and Spectra®, the authors reported good agreement.

One of the recent models based on the conservation of momentum was pro-posed by Mamivand and Liaghat [42], who studied the variation of the ballistic limit with areal density in a woven fabric made from Kevlar fibers. The model allows variation of spacing between laminas in order to study their effect on the ballistic limit.

On the other hand, the models based on energy-conservation laws consider that the kinetic energy of the projectile at impact should be consumed during the perforation process by the elastic deformation of the panel, by the failure process of the laminate (which includes several mechanisms), by friction and heating of the laminate, and by accelerating the panel after impact [13, 19, 20, 22, 32, 34–39, 45].

Moyre et al. [32] developed a simple model based on energy laws to estimate the ballistic limit. They considered that only the fibers directly in contact with the projectile fail, and that the other fibers are deformed only in the region affected by the stress waves generated by the impact. The energy loss of the projectile was subdivided into three terms: energy absorbed in tensile failure of the composite, energy converted into elastic deformation of the composite, and energy converted into the kinetic energy of the moving portion of the composite. The model was validated by experimental testing on woven laminates made from nylon, aramid, and polyethylene fibers.

A similar approach was used by Gu [34], who considered the same energy-absorption mechanisms. The failure of the laminate was estimated by the maximum-strain-failure criterion. This researcher carried out experimental tests on Twaron® and Kuralon® woven laminates to validate the model. The influence of

the strain rate in the mechanical properties of the laminates was studied, making tests at 1,500 s^{-1}.

Naik et al. [35–37] proposed an energy model based on that of Moyre et al. [32] to analyze the behavior of two-dimensional woven-fabric composites incorporating a greater number of energy-absorption mechanisms that can appear in these types of materials: cone formation, tensile failure of primary yarns, deformation of secondary yarns, delamination, matrix cracking, shear plugging, and friction during penetration. With the use of this model, the ballistic limit, contact duration, damage area, and energy absorbed by several mechanisms were predicted.

López-Puente et al. [38] proposed an energy model to study woven and tape laminates. This model was validated for carbon/epoxy laminates. Like the model of Naik, it considers different contributions to the energy absorbed by the panel (fiber failure, matrix cracking, and kinetic energy of the panel). It differs from the previous ones in using distance instead of time as an integration variable and in resolving the differential equation of the projectile velocity with perturbation techniques, enabling the analytic resolution of the equation and thereby providing a closed expression for the ballistic limit.

García-Castillo developed an energy model based on the proposals of Naik and Moyre to study laminate plates subjected to ballistic impact with and without in-plane preloads [22, 39, 45]. The model was also applied to study the impact behavior of composite spaced plates [46]. The model assumes that the plate absorbs the energy by three mechanisms: the elastic deformation of the fibers, the acceleration of the plate, and the generation of damage in the laminate. This damage may be due to the failure of fibers, delamination, and matrix cracking. This model was later used in a non-dimensional formulation to analyze the influence of several ratios in the ballistic behavior of thin laminates [19, 20].

The model of García-Castillo [22, 39] has been modified in this chapter to consider a general mechanical behavior of the woven laminate. This model is described in detail in Sect. 3. The model is used in this work to analyze the influence of laminate thickness and impact velocity on the contribution of the different energy-absorption mechanisms.

2.2 Numerical Modeling

To predict failure and damage evolution on composite laminates subjected to impact, numerical models based on Finite Elements have demonstrated their accuracy.

One approach to predict composite-damage onset and growth is the stress-failure criteria approach, used with the finite-element method to determine the stress in the laminate. The use of failure criteria has proved to be accurate for estimating failure under both static and dynamic conditions. Many sets of failure criteria can be found in the literature; see references [47, 48] or the more recent [49] for a review of this subject. Between 1998 and 2004, an international exercise was carried out to compare the most commonly used failure criteria under static conditions. The results

of this exercise were included in reference [50]. Despite these research efforts, a consensus on selecting the criterion to predict the composite failure has not been reached, especially to predict the out-of-plane failure and dynamic failure.

Although simple criteria such as the maximum-stress criterion or Tsai-Wu criterion have been used in several works, the complex nature of the damage of laminates requires more complex criteria to predict different failure modes (matrix cracking, fiber failure, delamination, etc.). The most common failure criteria used to analyze impact problems are those proposed by Hashin [51] and Hou et al. [52] the latter approach constituting a three-dimensional version of the Chang-Chang criteria [53]. Although both Hashin and Hou's criteria are expressed in terms of stresses by quadratic equations (Table 1), they consider different failure mechanisms and equations. Hashin failure criteria consider that there are four in-plane failure modes, i.e. fiber and matrix failure, under tensile and compression stress. Hou's criteria consider only three in-plane failure modes: fiber failure, matrix cracking, and matrix crushing.

The tensile failure of fiber is due to an accumulation of the breakage of the individual filaments, and when there are not enough intact filaments to support the load the lamina fail. Hou and Hashin criteria analyze fiber failure by a quadratic interaction of σ_{11}, σ_{12}, and σ_{13}. Some authors affirm that including shear stress to the fiber-breakage criterion may result in the underestimation of the laminate strength, and therefore they add a weighting factor to model the interaction between shear and tensile stress [54]. Other authors apply a maximum stress criterion for fiber failure in tension, assuming that the fiber failure under a three-dimensional state of stress occurs at the same stress as that which is acting under uniaxial stress [55]. The failure mechanism in the compression of the fibers is the accumulation of microbuckling in the individual filaments [56]. Many authors, including Hashin [51], apply a maximum stress or strain criterion for this mechanism. Hou uses the same equation in tension and compression. Another criterion, such as LarC [57, 58], includes fracture mechanic properties in this failure mechanism.

The mechanisms for matrix failure are more complex than fiber failure. Matrix failure is initiated by the nucleation of cracks at the fiber-matrix interface; these cracks grow along the lamina to coalesce into a critical fracture plane. There are many different expressions for matrix failure in tension, most of them assuming a critical fracture plane in the transverse direction. Hashin and Hou propose two different quadratic equations, involving the stress components acting in the plane of fracture. Other criteria include fracture mechanics expression in the equations. Compressive failure of the matrix is due to crushing. For matrix failure in compression the expressions are similar to that of the tension, involving the transversal components of the stress tensor. Due to the difficulty to identify the plane of fracture for the failure of the matrix in compression, Hashin proposes a quadratic interaction between stress invariants. Other criteria such as Puck and Schurmann [59] define the angle of the fracture plane, parallel to the fibers. This criterion needs several parameters without physical meaning and is difficult to determine, but it can nevertheless accurately reproduce the experimental results. Some criteria, such as those of Christensen [60], propose the same expression for matrix failure in tension and compression.

Table 1 Hou and Hashin failure-criteria formulation

Failure mode	Hou formulation	Hashin formulation
Fiber tension	$d_f^2 = \left(\frac{\sigma_{11}}{X_t}\right)^2 + \left(\frac{\sigma_{12}^2+\sigma_{13}^2}{S_L^2}\right)$	$d_{ft}^2 = \left(\frac{\sigma_{11}}{X_t}\right)^2 + \left(\frac{\sigma_{12}^2+\sigma_{13}^2}{S_L^2}\right)$
Fiber compression	$d_{fc}^2 = \left(\frac{\sigma_{11}}{X_c}\right)$	
Matrix cracking	$d_{mt}^2 = \left(\frac{\sigma_{22}}{Y_t}\right)^2 + \left(\frac{\sigma_{12}}{S_L}\right)^2 + \left(\frac{\sigma_{23}}{S_T}\right)^2$	$d_{mt}^2 = \left(\frac{\sigma_{22}+\sigma_{33}}{Y_t}\right)^2 + \left(\frac{\sigma_{12}^2+\sigma_{13}^2}{S_L^2}\right) + \left(\frac{\sigma_{23}^2-\sigma_{22}\sigma_{33}}{S_T^2}\right)^2$
Matrix crushing	$d_{mc}^2 = \frac{1}{4}\left(\frac{-\sigma_{22}}{S_T}\right)^2 + \frac{Y_c^2\sigma_{22}}{4S_T^2 Y_c} - \frac{\sigma_{22}}{Y_c} + \left(\frac{\sigma_{12}}{S_L}\right)^2$	$d_{mc}^2 = \frac{1}{Y_c}\left[\left(\frac{Y_c}{2S_T}\right)^2 - 1\right](\sigma_{22}+\sigma_{33}) + \left(\frac{\sigma_{22}+\sigma_{33}}{2S_T}\right)^2 + \frac{(\sigma_{23}^2+\sigma_{22}\sigma_{33})}{S_T^2} + \frac{(\sigma_{12}^2+\sigma_{13}^2)}{S_L^2}$

In addition to the intralaminar failure criteria, a delamination criterion has to be considered to predict the out-of-plane failure. A stress-failure criterion including through-the-thickness components of the stress tensor was used by several authors to predict delamination, using Eq. 1:

$$d_{del}^2 = \psi \cdot \left[\left(\frac{\sigma_{33}}{Z_T} \right)^p + \cdot \left(\frac{\sigma_{23}}{S_T} \right)^q + \left(\frac{\sigma_{31}}{S_L} \right)^r \right] \tag{1}$$

This criterion was proposed initially by Kim and Soni [61] and later modified by Brewer and Lagace [62], using a quadratic relationship (p, q and r equal to 2, and ψ equal to 1). Other authors assign a power unit at the stress σ_{33} [63, 64]. Some authors incorporate an empirical parameter ψ to adjust the damaged area [65]. With the same objective, Goyal et al. [66] propose to adjust the parameters q and r empirically. Hou et al. [52] modified their criterion, considering that compressive through-the-thickness stresses avoid delamination; they applied this criterion to model impact problems [52], using Eq. 2.

$$\begin{aligned} &\sigma_{33} > 0 \quad d_{del}^2 = \left[\left(\frac{\sigma_{33}}{Z_T} \right)^2 + \cdot \left(\frac{\sigma_{23}}{S_T} \right)^2 + \left(\frac{\sigma_{31}}{S_L} \right)^2 \right] \\ &\sigma_{33} < 0 \quad d_{del}^2 = 0 \end{aligned} \tag{2}$$

In some cases, this model can be applied between adjacent laminas of the laminate to improve the results, using a tuning parameter [65]. In the case of estimating the delamination associated with a free edge, average stresses integrated over a distance from the edge are applied [64, 67].

Stress criteria are useful to define damage onset, but not for modeling damage progression, especially the damage generated by delamination. These criteria have to be combined with degradation models of the laminate properties in order to estimate the failure [68]. Several degradation models have been proposed in the literature: instantaneous unloading, gradual degradation, and constant stress [69] (Fig. 1). In the instantaneous unloading, one or more of the elastic properties of the lamina or the stress components are set to zero or a small fraction of the original value once the criterion for each failure mode is verified [70]. Different residual values can be defined for each failure mechanism [71–73]. A sudden change in stiffness or stress can produce numerical instabilities in the simulation, and for this reason some authors introduce a smooth transition using an exponential factor [68]. For the constant stress model, the stress component related with each failure mechanism cannot be increased after the failure criterion is verified [74].

The gradual degradation models represent the accumulation of damage by one or more parameters that altered the stiffness matrix of the lamina [75] or the stress tensor. The evolution of this parameter is defined by Damage Mechanics theory and is usually linear [76] or exponential [77, 78]. This theory is based on the works of Kachanov [79] and Rabotnov [80] and was first applied to composites in the 1980s.

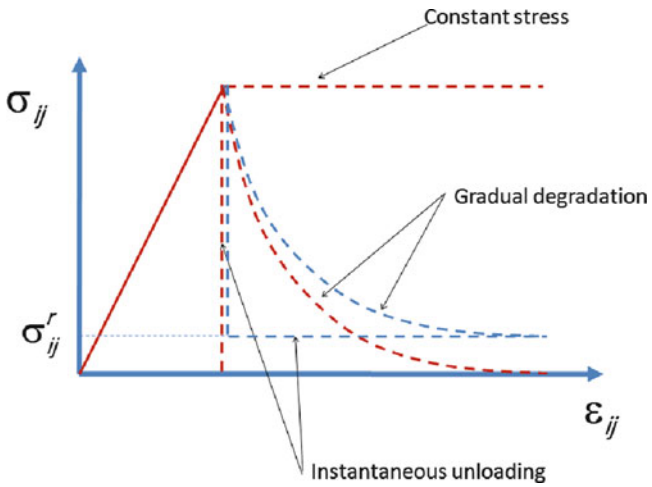


Fig. 1 Degradation models in laminates

Several anisotropic damage models are used to predict the time course of damage in laminates [81–84]. The final failure is assumed by defining an additional condition, typically a strain-failure criterion [85].

Although some authors suggest than Hashin criteria do not always fit the experimental tests [57], this criteria and Hou's criteria have the advantage of depending on parameters easily identifiable by conventional mechanical tests, unlike other criteria such as Puck or LarC. For this reason many authors apply variations of these models in several impact problems with different laminates [9, 23, 52, 86]. This methodology which combines failure criterion, degradation of the properties and final breakage condition is the most commonly used to model the failure of laminas [49]. For laminates, the same failure criteria as for laminas are applied, using *in situ* mechanical strengths. *In situ* properties are used because it has been verified experimentally that the mechanical behavior of a lamina inside a multidirectional laminate has greater mechanical strength than the same lamina in a unidirectional laminate [57]. This approach has been used with good results in impact problems on laminates at low- [85, 87] and high-velocity impacts [26, 39, 86–89].

3 Analytical Model Proposed

Many models are available to evaluate the impact behavior of laminates, those based on energetic criteria being the most widely used [13, 17, 19, 20, 22, 32, 35–39]. The present work presents an improved version of the model proposed by García-Castillo et al. [17, 22]. These models were validated experimentally and

numerically for plain woven laminates of GFRP. The García-Castillo model enables the determination of the residual velocity of the projectile, the ballistic limit, the contact time between the projectile and the laminate, and the contributions of several mechanisms to the absorption of the kinetic energy of the projectile. However, this formulation assumes a linear elastic behavior of the material.

The improved model was developed for any material behavior. In addition, this model is based on a differential formulation, for which the integration variable is the velocity at each time instant and it is the only unknown variable. The differential equation could be solved by any numerical method.

3.1 Hypotheses and Explanation

This model, developed for plain woven laminates of GFRP, is based on energy-conservation laws and considers three energy-absorption mechanisms: the elastic deformation of the fibers, the laminate acceleration, and the generation of damage in the laminate. This latter mechanism includes the failure of fibers and the matrix as well as damage by delamination.

For the formulation of this analytical model, the following hypotheses are considered:

- The projectile is spherical and perfectly rigid, and remains totally undeformable during the impact.
- The plain woven laminate is homogeneous and quasi-isotropic in the plane.
- The energy absorbed by shear plugging is negligible.
- The energy absorbed by friction between the laminate and the projectile, and the energy absorbed by heating the laminate are considered negligible, because the model considers that the laminate is thin.
- The velocities of longitudinal and transversal waves are constant in the laminate thickness.
- The energy absorbed by tensile failure of fibers and by elastic deformation of fibers is treated independently.
- The damage mechanisms by delamination and matrix cracking are considered.

To apply this model, it is necessary to know the constitutive equation of material studied, the density and thickness of laminate, as well as the mass and diameter of projectile.

3.2 Energy Absorption Mechanisms

The model assumes that the laminate absorbs energy by three mechanisms (Eq. 3): the elastic deformation of the fibers, the acceleration of laminate, and the generation of damage to the laminate.

$$E_{AB}(t) = E_{ED}(t) + E_{FL}(t) + E_{KL}(t) \tag{3}$$

where $E_{AB}(t)$ is the energy absorbed by laminate at each instant in time, $E_{ED}(t)$ is the energy absorbed by the elastic deformation of the fibers, $E_{KL}(t)$ is the energy absorbed by the acceleration of laminate, and $E_{FL}(t)$ is the energy absorbed by the generation of damage to the laminate.

The energy absorbed by the latter mechanism includes the failure of fibers, delamination, and matrix cracking, as can to be seen in Eq. 4.

$$E_{FL}(t) = E_{TF}(t) + E_{DL}(t) + E_{MC}(t) \tag{4}$$

where $E_{TF}(t)$ is the energy absorbed by fiber failure at each instant in time, $E_{DL}(t)$ is the energy absorbed by delamination, and $E_{MC}(t)$ is the energy absorbed by matrix cracking.

Equations 3 and 4, could be used to evaluate the behavior of the plain woven laminates of GFRP subjected to high-velocity impact. The expressions for calculating each of the terms in these equations are shown below.

3.2.1 Energy Absorbed by Laminate Acceleration

In the development of this model, it was assumed that the laminate and the projectile always make contact during the impact, and that a portion of laminate is accelerated. Since the laminate is considered thin, this model assumes a constant velocity through the laminate thickness. The energy absorbed by this mechanism can be written as:

$$E_{KL}(t) = \frac{1}{2} \cdot m(t) \cdot v(t)^2 \tag{5}$$

where $E_{KL}(t)$ is the kinetic energy at each instant in time, $m(t)$ is the mass of the accelerated portion of the laminate at each instant in time, and $v(t)$ is the velocity of the projectile and the accelerated portion of laminate at each instant in time.

The mass of the accelerated portion of laminate can be estimated as follows:

$$m(t) = \pi \cdot e \cdot \rho \cdot \left(R_T(t)\right)^2 \tag{6}$$

where e is the thickness of the laminate, ρ is the density of laminate, and $R_T\ (t)$ is the distance covered by the transversal wave. This distance is defined by Eq. 7.

$$R_T(t) = \int_0^t v_T \cdot dt \tag{7}$$

where v_T is the velocity of the transversal waves generated by the impact on the laminate. This velocity can be calculated using the expression proposed by Smith et al. [90]:

$$v_T = \sqrt{\frac{(1+\varepsilon_p)\cdot\sigma_r}{E}} - \int_0^{\varepsilon_p} \sqrt{\frac{1}{\rho}\cdot\left(\frac{d\sigma}{d\varepsilon}\right)}\cdot d\varepsilon \tag{8}$$

where ε_p is the strain corresponding to the yield point, σ_r is the mechanical strength of laminate, and E is the Young modulus of the laminate.

To calculate the derivative of the Eq. 8, $\left(\frac{d\sigma}{d\varepsilon}\right)$, it is necessary to know the constitutive equation of the material.

Therefore, the energy absorbed by laminate acceleration can be expressed by:

$$E_{KL}(t) = \frac{1}{2}\cdot\pi\cdot e\cdot\rho\cdot\left(\int_0^t\left(\sqrt{\frac{(1+\varepsilon_p)\cdot\sigma_r}{E}} - \int_0^{\varepsilon_p}\sqrt{\frac{1}{\rho}\cdot\left(\frac{d\sigma}{d\varepsilon}\right)}\cdot d\varepsilon\right)dt\right)^2\cdot v(t)^2 \tag{9}$$

This equation shows that energy absorbed by laminate acceleration is proportional to square of projectile velocity at each instant in time.

3.2.2 Energy Absorbed by Fibers

When a laminate is subjected to high-velocity impact, it is possible to identify two zones affected by the impact, as depicted in Fig. 2. Zone 1 is located below of projectile and this portion of laminate offers resistive force against penetration of the projectile. This model assumes that this region the fibers will fail under tension. Meanwhile, Zone 2 is the region located between the projectile diameter and the distance covered by the transversal waves. This model assumes that in this zone no failure occurs and the fibers are deformed elastically. Therefore, the energy absorbed by the fibers includes two absorption mechanisms: the energy absorbed by tensile failure of fibers, and the energy absorbed by elastic deformation of fibers.

Energy Absorbed by Tensile Failure of Fibers

In woven laminates, the fibers are grouped in assemblies called yarns, composed of several individual filaments. In this model, tensile failure is assumed to occur only in the yarns directly below the projectile, which offer resistive force against the penetration of the projectile (Fig. 2). The maximum strain criterion is assumed for the failure of the fibers.

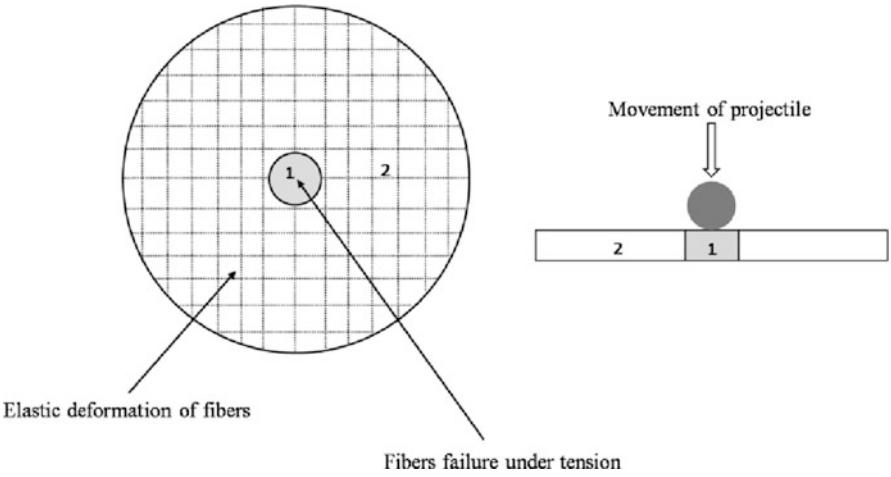


Fig. 2 Identification in a laminate of fibers that shows tensile failure and elastic deformation

It is assumed that the projectile diameter is smaller than the width of the yarn, so that the impact occurs only on one yarn. In addition, the depth of fiber failure in the thickness direction is equal to instant displacement of the projectile. Therefore, the energy absorbed by tensile failure of fibers during differential increment of time is:

$$d\,E_{TF}(t) = d\,w(t) \cdot B \int_0^z \left(\int_0^{\varepsilon_f} \sigma(\varepsilon) \cdot d\,\varepsilon \right) \cdot d\,z \tag{10}$$

where $dE_{TF}(t)$ is the energy absorbed by the tensile failure of fibers during an increment of time (dt), $dw(t)$ is the displacement of projectile during this increment, B is the width of the yarn, z is the through-thickness length of fibers failing under tension and it is equal to twice the distance covered by the longitudinal wave $R_L(t)$, $\sigma(\varepsilon)$ is the constitutive equation of laminate, and ε_f is the strain due to the attenuation of stress-waves, defined by following expression:

$$\varepsilon_f = \varepsilon_r \cdot b^{\frac{z}{B}} \tag{11}$$

where ε_r is the failure strain of the composite, and b is the stress-wave-transmission factor.

The attenuation of stress wave is generated mainly by the phenomenon of transmission and reflection of waves in an impacted material. As result of this phenomenon, the stress decreases with increasing transversal distance to the impact point.

The stress-wave-transmission factor is a constant and it is determined from stress-wave-attenuation study for each composite. This is a material property that depends

on the geometry of the fabric as well as mechanical and physical properties of the reinforcing material and the matrix. Usually the stress-wave-transmission factor is less than one [91].

The distance covered by the longitudinal wave generated by the impact on the laminate is defined by following equation:

$$R_l(t) = \int_0^t v_L \cdot dt \tag{12}$$

where v_L is the velocity of the longitudinal waves and is defined by Smith et al. [90]:

$$v_L = \sqrt{\frac{1}{\rho} \cdot \left(\frac{d\sigma}{d\varepsilon}\right)_{\varepsilon - \varepsilon_p}} \tag{13}$$

If Eq. 10 is divided by the time increment (dt), the energy absorbed by the tensile failure of fibers at each instant in time can be defined by the following equation:

$$\frac{d\,E_{TF}(t)}{dt} = \frac{dw(t)}{dt} \cdot B \int_0^x \left(\int_0^{\varepsilon_r \cdot b^{\frac{x}{B}}} \sigma(\varepsilon) \cdot d\varepsilon \right) \cdot dx \tag{14}$$

where $\frac{dw(t)}{dt}$ is the projectile velocity at each instant time, $v(t)$.

Integration of Eq. 14 gives:

$$E_{TF}(t) = \int_0^t \left(v(t) \cdot B \int_0^x \left(\int_0^{\varepsilon_r \cdot b^{\frac{x}{B}}} \sigma(\varepsilon) \cdot d\varepsilon \right) \cdot dx \right) \cdot dt \tag{15}$$

This last expression allows the energy absorbed by tensile failure of fibers of any woven laminate to be determined.

Energy Absorbed by Elastic Deformation of Fibers

The fibers deformed elastically during impact lie within the region affected by the transversal stress wave generated by the impact. This region is localized between the projectile diameter and the distance covered by the transversal waves (Fig. 2).

It is assumed that elastic deformation is a linear function of the radial position, from the impact point to the distance covered by the transversal wave, so that the fibers close to the impact point are subject to a deformation equal to the failure fibers by tension, whereas the fibers away from the impact point show a deformation equal to zero (Fig. 3).

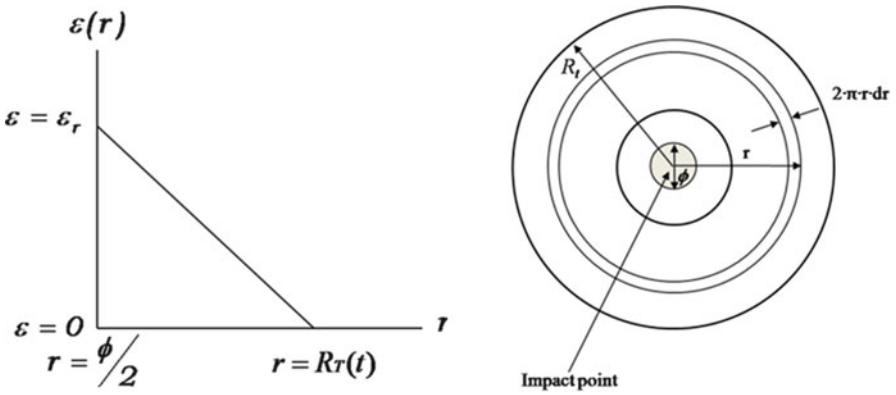


Fig. 3 Variation of the elastic deformation of fibers

Therefore, the following boundary condition for the variation of the strain is defined as:

$$\begin{aligned} r &= \varphi/2, \quad \varepsilon(\varphi/2) = \varepsilon_r \\ r &= R_T, \quad \varepsilon(R_T) = 0 \end{aligned} \tag{16}$$

where ϕ is the projectile diameter and $R_T(t)$ is the distance covered by the transversal wave.

The elastic deformation gives:

$$\varepsilon(r) = \frac{2 \cdot (R_T - r)}{2 \cdot R_T - \varphi} \cdot \varepsilon_r \tag{17}$$

The energy absorbed by elastic deformation of fibers was calculated from the area under the stress-strain curve of the material, using this integration:

$$E_{ED}(t) = \int_v \left(\int_0^{\varepsilon(r)} \sigma(\varepsilon) \cdot d\varepsilon \right) \cdot dv = \int_{\frac{\varphi}{2}}^{R_T(t)} \left(\int_0^{\varepsilon(r)} \sigma(\varepsilon) \cdot d\varepsilon \right) \cdot 2 \cdot \pi \cdot r \cdot e \cdot dr \tag{18}$$

This expression allows the energy absorbed by elastic deformation of fibers to be determined for any woven laminate.

3.2.3 Energy Absorbed by Damage Delamination and Matrix Cracking

In this work, it is assumed that the energy absorbed due to damage by delamination and matrix cracking are functions of distance covered by transversal waves on

the laminate. Moreover, fitting coefficients are used when considering non-circular damage on laminate. These coefficients are different in the case of delamination and in the matrix cracking.

The energy absorbed by delamination can be estimated by the following equation:

$$E_{DL}(t) = \alpha_{DL} \cdot \pi \cdot [R_T(t)]^2 \cdot G_{IICD} \tag{19}$$

where G_{IICD} is the critical dynamic-strain energy-release rate in mode II, and α_{DL} is the approximation coefficient of damage area.

The energy absorbed due to matrix cracking, can be calculated using the following equation:

$$E_{MC}(t) = \alpha_{MC} \cdot \pi \cdot [R_T(t)]^2 \cdot E_{MT} \cdot e \tag{20}$$

where E_{MT} is the energy absorbed by matrix cracking per unit volume, and α_{MC} is the approximation coefficient of matrix cracking.

3.3 Model Formulation

Given the energy conservation between two instants in time, such as an initial instant (t_0) and a generic instant (t):

$$E_0 = \frac{1}{2} \cdot m_p \cdot v_0^2 = E_T(t) = \frac{1}{2} \cdot m_p \cdot v^2(t) + E_{AB}(t) \tag{21}$$

where E_0 is the impact energy, m_p is the mass of projectile, v_0 is the impact velocity, and $E_T(t)$ is the total energy in the time.

In this work, it is assumed that during the perforation process the projectile and the laminate are in contact, and therefore the kinetic energy of system (laminate and projectile) is defined by the following equation:

$$\frac{1}{2} m_p \cdot v_o^2 = \frac{1}{2} \cdot m_p \cdot v(t)^2 + E_{AB}(t) \tag{22}$$

Then, the previous equation can be rewritten as:

$$\frac{1}{2} m_p \cdot v(t)^2 = \frac{1}{2} m_p \cdot v_o^2 - [E_{ED}(t) + E_{TF}(t) + E_{DL}(t) + E_{MC}(t) + E_{KL}(t)] \tag{23}$$

The total energy at a time instant (t) can be defined by the following equation:

$$\frac{1}{2} \left(m_p + m\,(t)\right) \cdot v(t)^2 = \frac{1}{2} m_p \cdot v_o^2 - E_{ED}(t) - E_{TF}(t) - E_{DL}(t) - E_{MC}(t) \tag{24}$$

The following equation can be formulated by deriving Eq. 24 and using the equations for each mechanism of absorption energy that were described above:

$$v(t)\cdot\frac{dv(t)}{dt}\left[m_p+m\,(t)\right]+\frac{1}{2}\cdot\frac{dm\,(t)}{dt}v(t)^2=$$
$$=-\frac{d}{dt}\left[E_{DL}(t)\right]-\frac{d}{dt}\left[E_{MC}(t)\right]-\left(v(t)\cdot\left[\frac{dE_{TF(t)}}{dt}\right]\right)-\frac{d}{dt}\left[E_{ED}(t)\right] \quad (25)$$

This last equation can be rewritten by defining two functions: g(t) and h(t). The first function $g(t)$ can be defined by the following equation:

$$g(t)=-\frac{d}{dt}\left(E_{ED}(t)+E_{DL}(t)+E_{MC}(t)\right) \quad (26)$$

The second function $h(t)$ is related to the energy absorbed by tensile failure and can be defined as:

$$h(t)=B\cdot E\int_0^{2\cdot R_l(t)}\left(\varepsilon_r\cdot b^{(2\cdot R_l(t)/B)}\right)^2\cdot dx \quad (27)$$

Finally, it is possible to define a differential equation, which allows the velocity of the projectile to be calculated. In this equation, all the energy-absorption mechanisms are included.

$$v(t)\cdot\left[m_p+m\,(t)\right]\cdot\frac{dv(t)}{dt}+\left[\frac{1}{2}\cdot\frac{dm\,(t)}{dt}\right]v(t)^2+h\,(t)\cdot v\,(t)=g(t) \quad (28)$$

where:

$$\frac{dm\,(t)}{dt}=\frac{1}{2}\cdot\pi\cdot V_T\cdot e\cdot\rho \quad (29)$$

Equation 28 is a non-linear differential equation that can be solved by any numerical method, with the initial conditions $v(0)=v_0$. From this equation the time course of projectile velocity, v(t), can be estimated.

The projectile displacement, w(t), can be calculated by the integration of the projectile velocity. Knowing the velocity of the projectile makes it possible to estimate the energy absorbed by each of the mechanisms. The integration of the Eq. 28 is stopped when either the plate is totally perforated or the projectile velocity is zero.

The condition for perforation is:

$$t=t_c,\quad w\,(t_c)=e,\quad v\,(t_c)=v_R \quad (30)$$

and the condition for non-perforation is:

$$t = t_c, \quad v\,(t_c) = 0 \tag{31}$$

where v_R is the residual velocity of projectile, and t_c is the contact time between the projectile and laminate during the impact.

In the first case, the projectile is stopped and therefore the impact energy is absorbed by the plate. In the second case, the laminate cannot stop the projectile, and the model can determine the residual velocity. In both cases, the energy absorbed by each mechanism can be calculated.

4 Model Validation

In this section, the proposed analytical model was validated through comparison with experimental tests in terms of residual velocity and ballistic limit. Also a numerical model was used to validate the hypotheses considered in the analytical model and the application range of these hypotheses.

4.1 Experimental Tests

To validate the analytical model, ballistic impact tests were performed under laminates made of E-glass/polyester woven plies. Table 2 shows the mechanical properties of the material.

Three laminate specimens with thicknesses of 3, 6, and 12 mm, were tested. This range of thickness was used to analyze the work limits of the analytical model. The dimensions of the specimens were 200 mm × 140 mm. This specimen size

Table 2 Mechanical properties of E-glass/polyester laminate [35, 45]

	Strain rate	
Mechanical properties	$\dot{\varepsilon} = 10^{-4}\text{s}^{-1}$	$\dot{\varepsilon} = 10^{3}\text{s}^{-1}$
Density (kg/m^3)	1980	
Young modulus (GPa)	10.13	15.20
Mechanical strength (MPa)	367.39	1102.00
Ultimate strain	0.0357	0.0725
Poisson ratio	0.16	–
Critical dynamic-strain energy-release rate in mode II (J/m^2)	3,000	
Wave-transmission factor	0.90	
Matrix-cracking energy per unit volume (J/m^3)	10^6	

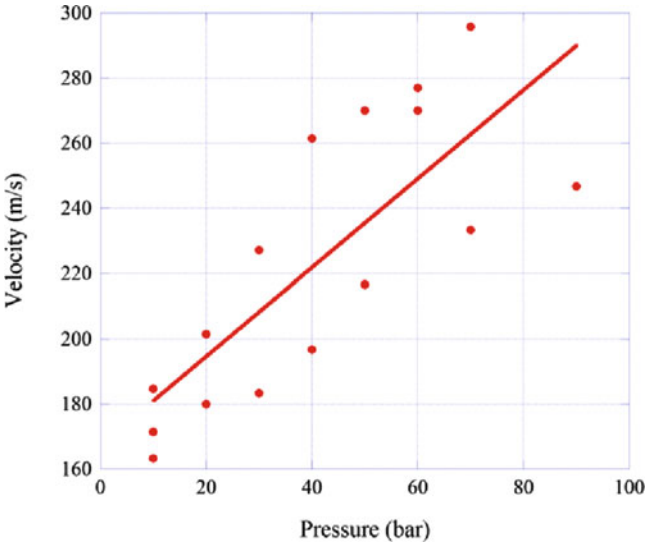


Fig. 4 Experimental correlation between gas-gun pressure and projectile velocity

guaranteed that the damage would not reach the edge of the specimen and therefore the boundary conditions did not influence the damage [45].

These experimental results were derived from previous works: impacts on laminates of thicknesses of 3 mm [22] as well as 6 and 12 mm [14].

4.1.1 Experimental Procedure

The experimental impact tests were made using an A1G + gas gun (manufactured by Sabre Ballistics). The specimens were impacted by spherical steel projectiles of 1.725 g in mass and 7.5 mm in diameter. Impact velocity was controlled by regulating the pressure in the system. To ascertain how much pressure was needed to reach a specific velocity, an experimental correlation between pressure and velocity of the projectile was estimated by numerous impact tests without specimens (Fig. 4).

This correlation was used to select the pressure to achieve the required impact velocity, from 80 to 780 m/s. Due to the wide range of impact velocities; two different types of gas were used: helium to achieve the highest velocities, and Stargon® (a mixture of argon, carbon dioxide, and oxygen) for the lowest velocities.

To measure the impact and residual velocity, different techniques can be found in the literature. Garcia-Castillo et al. [91] used a system made up of two frames, placed at the front and at the back of the specimen. Metal films were placed on each side of the frames, with a wire connecting these to an oscilloscope. When the projectile perforated the metal films, the oscilloscope recorded the time that the projectile took to go through the frame thickness, and it was possible to calculate the impact and residual velocity. Other researchers [92] used optical sensors, but the

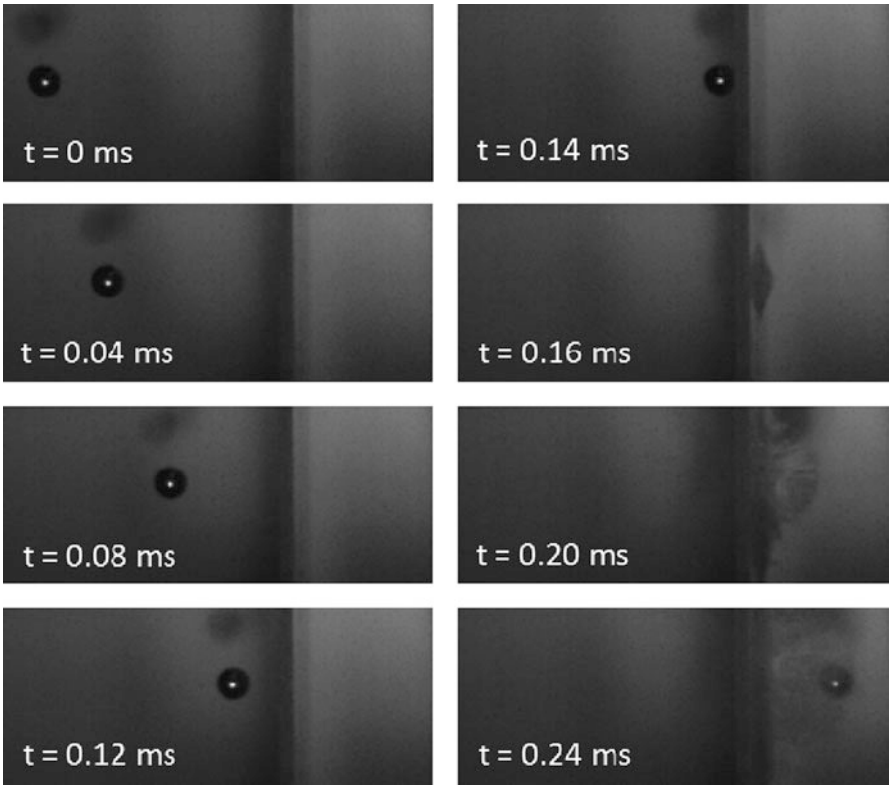


Fig. 5 Movement of the projectile before perforation and after perforation. Target: E-glass polyester plain woven laminate of 3 mm thick. Projectile: Steel projectile of 1.725 g in mass and 7.5 mm in diameter. Impact velocity: 354 m/s

measurement of the residual velocity was difficult due to shear plugs and because small particles can move the projectile ahead as it exits the other side of the laminate. Currently most researchers use a high-speed video camera [14, 93], due to its accuracy and reliability.

The impact tests used for validating the analytical model were recorded by a high-speed video camera (APX PHOTRON FASTCAM) with a data-acquisition system capable of taking up to 120,000 frames per second. For better recording quality, a high-intensity light source, model ARRISUN 12 plus, was used. A good resolution of the projectile path was achieved, as shown in Fig. 5, both in front and back face.

From the information provided by the camera, the impact and residual velocity was calculated, evaluating the distance travelled by the projectile in several consecutive frames (Fig. 6). The number of frames was selected according to a previous study to ensure an accurate estimation of the velocity [45].

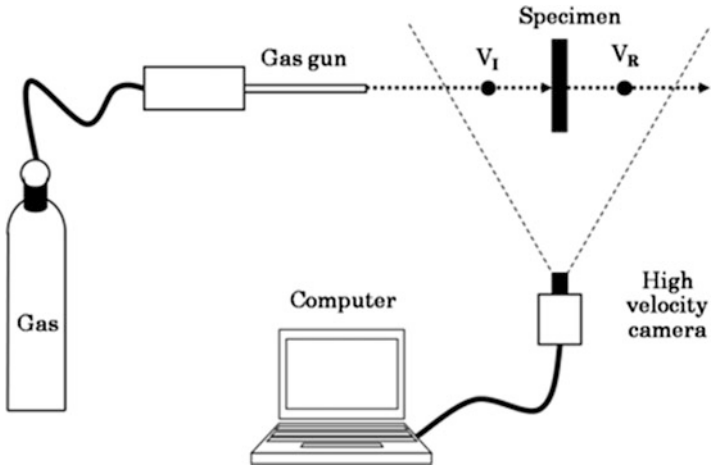


Fig. 6 Experimental device used in the impact tests

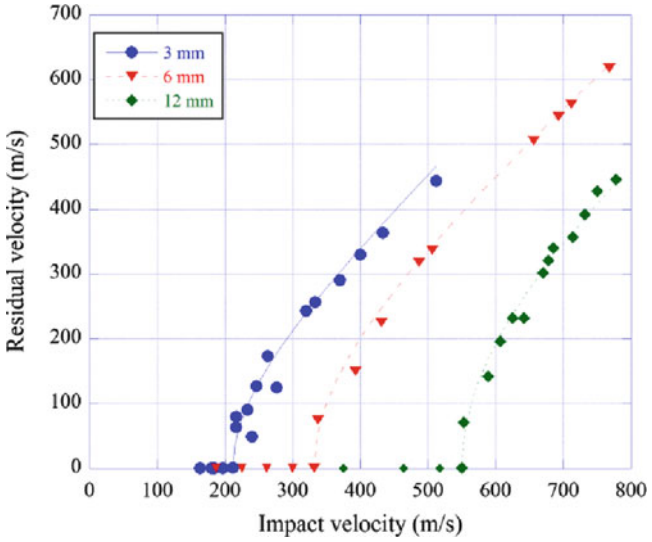


Fig. 7 Residual velocity vs. impact velocity for E-glass/polyester plain woven laminates, with thicknesses of 3, 6, and 12 mm, using a spherical projectile of 1.725 g in mass and 7.5 mm in diameter

4.1.2 Experimental Results

Figure 7 shows the relationship between the impact velocity and residual velocity for the specimen used in the model validation. The fitting curves shown in the figure were calculated using the Lambert-Jonas model which relates residual velocity to impact velocity by the following equation [94]:

Table 3 Experimental ballistic limit for E-glass/polyester plain woven laminates using a spherical projectile of 1.725 g in mass and 7.5 mm in diameter

Thickness of laminate (mm)	3	6	12
Ballistic limit (m/s)	212	332	550
p	2	2	2
A	1	0.9	0.8

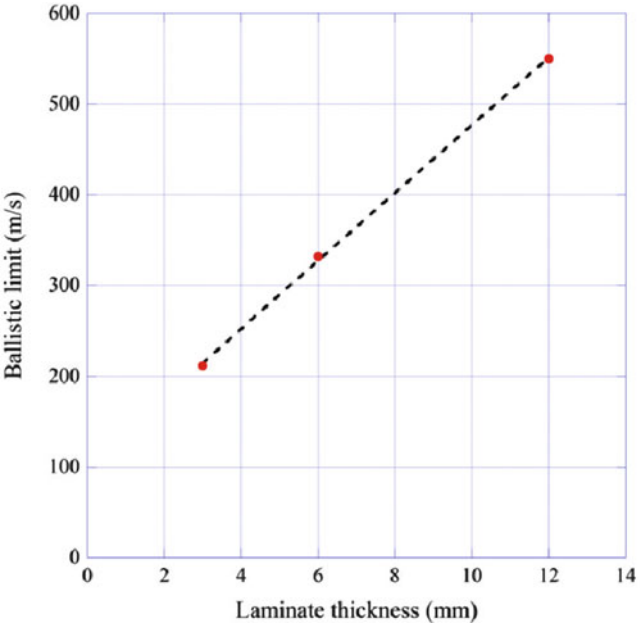


Fig. 8 Ballistic limit vs. laminate thickness for E-glass/polyester plain woven laminates impacted using a spherical projectile of 1.725 g in mass and 7.5 mm in diameter

$$v_R = A \cdot \left(v_0^p - v_{BL}^p\right)^{\frac{1}{p}} \tag{32}$$

where v_0 is the impact velocity of the projectile, v_{BL} the ballistic limit, v_R the residual velocity of the projectile, and A, p are empirical parameters.

It was not possible to calculate the ballistic limit in a deterministic way because there is an impact-velocity interval in which the structure may or may not be entirely perforated; in addition, the residual velocity of the projectile from the gas gun cannot be totally controlled. Therefore, the ballistic limit (Table 3) was estimated using Eq. 32 by a least-square fitting method.

The ballistic limit increased with the thickness of the laminates. In the 12-mm-thick laminate, the ballistic limit reached 2.6-fold that of the 3-mm thickness. A linear variation of ballistic limit with the thickness was found, as reflected in Fig. 8, where the data correlate well to a straight line (R^2 is 0.9994). This relationship can

be useful in estimating the ballistic limit of a laminate [19, 20]. Only two sets of experimental tests of a structure of the same material with two different thicknesses are required to calculate the ballistic limit for any thickness in the range considered. Linear relationships of this type have been found by others authors on Kevlar-fiber laminates using cylindro-conical projectiles [29], on carbon-fiber laminates using spherical projectiles [6], and on glass-fiber laminates with flat projectiles [33, 35].

4.2 Analytical Model

For the validation of the analytical model, it was applied to the experimental data described in the previous section.

The material used shows a linear-elastic behavior until failure. Therefore, the velocity transversal waves and longitudinal waves for this material can be simplified as follows.

The velocity of transversal waves, Eq. 8, yields:

$$v_T = \sqrt{\frac{(1+\varepsilon_r)\cdot\sigma_r}{E}} - \sqrt{\frac{E}{\rho}}\cdot\varepsilon_r \tag{33}$$

The velocity of longitudinal waves, Eq. 13, yields:

$$v_L = \sqrt{\frac{E}{\rho}} \tag{34}$$

The energy absorbed by laminate acceleration, Eq. 9, can be expressed by following equation:

$$E_{KL}(t) = \frac{1}{2}\cdot\pi\cdot e\cdot\rho\cdot V_T^2\cdot t^2\cdot v(t)^2 \tag{35}$$

The energy absorbed by tensile failure of fibers, Eq. 13, can be rewritten and can be expressed by the following equation:

$$E_{TF}(t) = \int_0^t \left(v(t)\cdot B \int_0^x \varepsilon_r^2\cdot b^{\frac{x}{B}}\,dx \right)\cdot dt \tag{36}$$

The energy absorbed by elastic deformation of fibers, Eq. 13, can be calculated with the following equation:

$$E_{ED}(t) = E\cdot e\cdot\pi\cdot\varepsilon_r^2 \int_{\frac{\varphi}{2}}^{R_T(t)} \left(\frac{2\cdot(V_T\cdot t - r)}{2\cdot V_T\cdot t - \varphi}\right)^2\cdot r\cdot dr \tag{37}$$

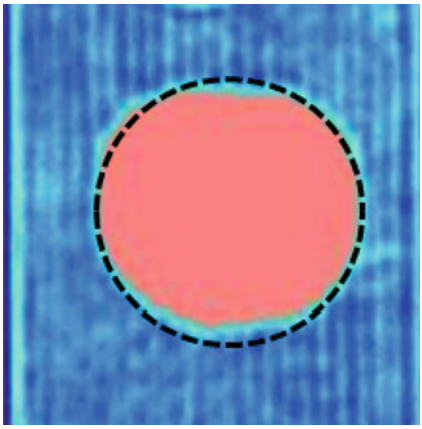


Fig. 9 C-Scan image of laminate of fibers glass-E and polyester subjected to impact with a steel spherical projectile of 7.5 mm of diameter 217 m/s at 217 m/s of velocity

To calculate the energy absorbed by delamination and matrix cracking the approximation coefficient of the damage area and the approximation coefficient of matrix cracking were determinate experimentally. A non-destructive inspection by C-Scan was carried out on all impacted laminates. All images obtained by C-Scan were approximately equal to a circular surface (Fig. 9). On each image four diameters were measured, which were used to estimate the damage area as a circle. Those results were compared with the results determinate by C-Scan and the difference was less to 1%. Therefore, the approximation coefficient of the damage area and the approximation coefficient of matrix cracking will be equal to one.

The equation used to calculate the energy absorbed by delamination is:

$$E_{DL}(t) = \pi \cdot V_T^2 \cdot t^2 \cdot G_{IICD} \tag{38}$$

and for the energy absorbed by matrix cracking is:

$$E_{MC}(t) = \pi \cdot V_T^2 \cdot t^2 \cdot E_{MT} \cdot e \tag{39}$$

Equation 28 was solved, using a finite-difference scheme. This model requires knowledge of the mechanical properties of the laminate (Young modulus, mechanical strength, ultimate strain, critical dynamic strain-energy-release rate in mode II), the density and thickness of the plate, as well as the projectile parameters (mass, and diameter) from Table 2.

4.3 Numerical Model

A finite-element model was developed to validate the analytical model proposed. Although the analytical model was validated by comparison with the experimental results, numerical modeling can provide information which is difficult to gain

experimentally. An FE model can be used to analyze failure modes during penetration, and thus the analytical-model hypothesis can be validated by comparison with numerical results.

The finite-element model used to analyze the laminate impact behavior was implemented in ABAQUS/Explicit. Since the influence of boundary conditions is negligible in high-velocity impacts, the FEM3D model included two solids: a projectile and a composite plate. As no plastic deformation was found in the projectile during the experimental test, linear elastic behavior was used for the steel projectile. Glass-fiber composite plates were modeled as linear elastic up to failure. A VUMAT subroutine was implemented to define anisotropic mechanical properties, a set of failure criteria and a procedure to degrade mechanical properties after failure.

4.3.1 Woven Composite Model

For a prediction of the failure of composite woven laminate, a modification of Hou's criteria [52] was applied. Hou's criteria were selected because they have been proved accurate to predict composite failure under impact loads [85]; moreover, Hou's criteria can be applied using only mechanical properties derived from characterization tests (Table 2).

Hou's criteria include three failure modes: fiber failure, matrix cracking, and matrix crushing (Table 1). Hou model was developed to predict the failure of composite tape plies, in which fibers are oriented in a single direction. However, a woven composite ply includes fibers in longitudinal (warp) and transverse (weft) directions, so that it was necessary to make some modifications. The matrix failure modes included in the Hou failure criteria considered that transverse loads are supported by the matrix. However, a woven laminate contains fibers in a transverse direction to support theses loads. Thus in this analysis, the fiber-failure criterion was applied to longitudinal and transverse directions [86].

Moreover, Hou included the criterion proposed by Brewer and Lagace [62] to predict delamination, Eq. 2. In total, five failure criteria were evaluated: fiber failure, which considers tensile and compressive fiber failure in longitudinal and transverse directions, and delamination, which applies only to normal tensile stress (Eqs. 40, 41, 42, 43, 44).

$$d_{f1}^2 = \left(\frac{\sigma_{11}}{X_t}\right)^2 + \left(\frac{\sigma_{12}^2 + \sigma_{13}^2}{S_{12}^2}\right) \quad \text{if } \sigma_{11} > 0 \tag{40}$$

$$d_{f1}^2 = \left(\frac{\sigma_{11}}{X_c}\right)^2 + \left(\frac{\sigma_{12}^2 + \sigma_{13}^2}{S_{12}^2}\right) \quad \text{if } \sigma_{11} < 0 \tag{41}$$

$$d_{f2}^2 = \left(\frac{\sigma_{22}}{Y_t}\right)^2 + \left(\frac{\sigma_{12}^2 + \sigma_{13}^2}{S_{12}^2}\right) \quad \text{if } \sigma_{22} > 0 \tag{42}$$

Table 4 Damage modes and corresponding stress update

Damage mode	Stresses updated
Fiber failure	$\sigma_{11} = \sigma_{22} = \sigma_{33} = 0$
	$\sigma_{12} = \sigma_{23} = \sigma_{13} = 0$
Delamination	$\sigma_{33} = \sigma_{23} = \sigma_{13} = 0$

$$d_{f2}^2 = \left(\frac{\sigma_{22}}{Y_c}\right)^2 + \left(\frac{\sigma_{12}^2 + \sigma_{13}^2}{S_{12}^2}\right) \quad \text{if } \sigma_{22} < 0 \tag{43}$$

$$d_{del}^2 = \left(\frac{\sigma_{33}}{Z_r}\right)^2 + \left(\frac{\sigma_{23}}{S_{23}}\right)^2 + \left(\frac{\sigma_{31}}{S_{31}}\right)^2 \quad \text{if } \sigma_{33} > 0 \tag{44}$$

Under a given load, the stresses at each integration point in the composite structure are computed in the material coordinate system. Then, the stresses are substituted in the failure criteria. If any failure occurs, the material properties at that point are degraded according to the mode of failure. A fiber failure results in the complete failure of the material at that point, whereas a delamination avoids only supporting stresses in a normal direction. To degrade the material properties, the stresses in the damaged area were reduced to close to zero, according to which the failure mode was achieved (Table 4).

A sudden drop of mechanical properties involves instability problems and lack of convergence during simulation so that it is necessary to develop a smooth transition between the stress values and zero. The stress components were corrected using the following equation:

$$\sigma_{ij}^{cor} = \sigma_{ij} \cdot \left(1 - \frac{2 - \exp^{S(d_i - 0.5)}}{2 - \exp^{\frac{S}{2}}}\right) \tag{45}$$

As the projectile can perforate a composite plate during impact, the model requires the use of a finite-element erosion criterion to avoid convergence problems due to distorted elements. The stresses on a finite element damaged drop to near zero while large deformations appear. These elements do not contribute to the stiffness or the strength of the plate, but they can cause instability problems. Maximum strain criteria were implemented in the VUMAT subroutine to remove the distorted elements: after each time increment the longitudinal strains (ε_{11}, ε_{22} and ε_{33}) are evaluated, and the element is removed if one of the strains reaches a critical value.

4.3.2 High-Velocity Impact Model

Three plates were simulated using the FE model corresponding to three plate thicknesses: 3, 6, and 12 mm. Only a quarter of the panel was modeled due to the symmetry of the problem (Fig. 10), and thus the plate dimensions in the model were 100×70 mm^2. Clamped boundary conditions were imposed to the external



Fig. 10 Finite-element models of high-velocity impact on composite woven laminates with thicknesses of 3, 6, and 12 mm

boundary of the plates, and an initial velocity was imposed on the projectile in order to reproduce the experimental tests.

A three-dimensional non-homogeneous mesh was used. Three-dimensional 8-node brick elements with reduced integration (C3D8R in ABAQUS) were used to mesh the composite plates, and three-dimensional 4-node tetrahedral elements (C3D4 in ABAQUS) to mesh the projectile. Successive space discretizations were carried out to evaluate the sensitivity of the mesh. Finally, the elements of the selected mesh for the composite plates had a characteristic size of 0.375 mm in the area close to the impact zone. 22,528, 45,296, and 90,592 elements were used to mesh the plates with thicknesses of 3, 6, and 12 mm, respectively. The projectile was meshed using 3,444 elements.

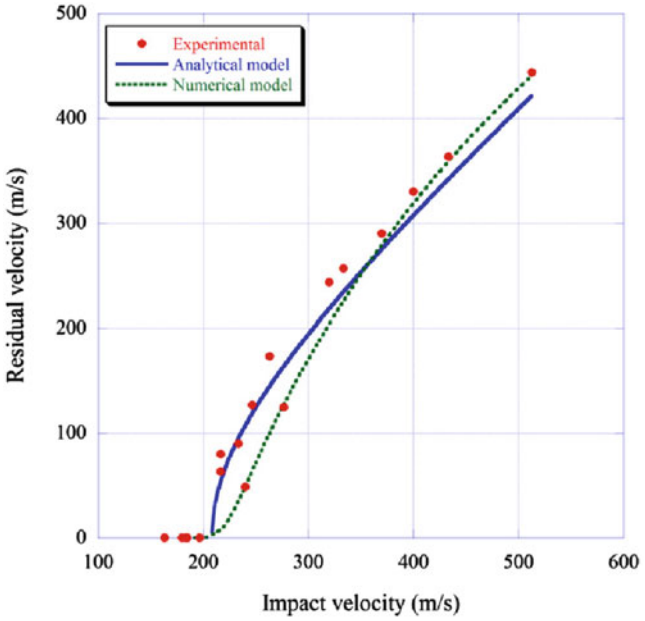


Fig. 11 Validation of analytical and numerical models. Residual velocity vs. impact velocity. Thickness = 3 mm

4.4 Comparison of Analytical, Numerical, and Experimental Results

To validate the analytical and FE models for further investigations, two variables were selected, residual velocity and ballistic limit. The residual velocity found in experimental test as a function of the impact velocity is compared to the model predictions in Figs. 11, 12, and 13.

Figure 11 shows the good correlation between experimental test and the analytical and numerical predictions for woven laminates having a thickness of 3 mm. At impact velocities close to the ballistic limit, small differences could be appreciated between FE model predictions and experimental results, but, as the impact velocity increased, the error diminished. The analytical model predictions proved extremely accurate.

Figure 12 also shows good agreement between analytical and numerical predictions and experimental results for 6-mm-thick laminates. For the highest impact velocities, the analytical model overestimated residual velocity but the error was lower than 10%. FE model predictions were in excellent agreement with the experimental results.

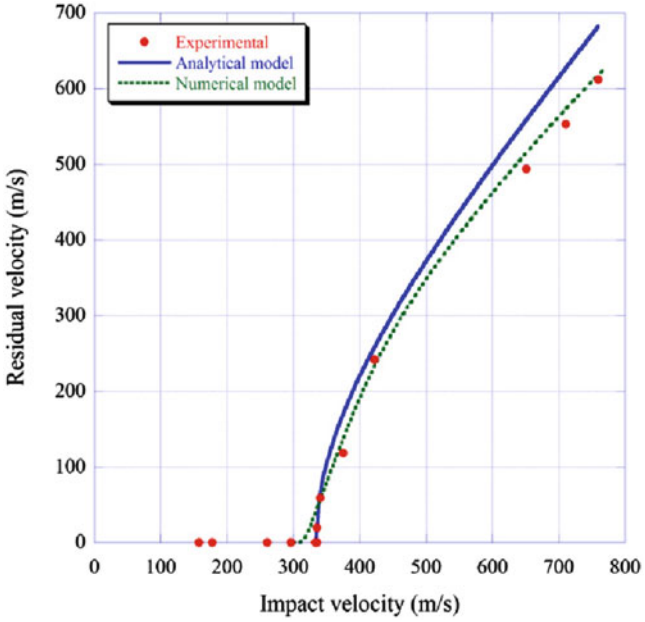


Fig. 12 Validation of analytical and numerical models. Residual velocity vs. impact velocity. Thickness = 6 mm

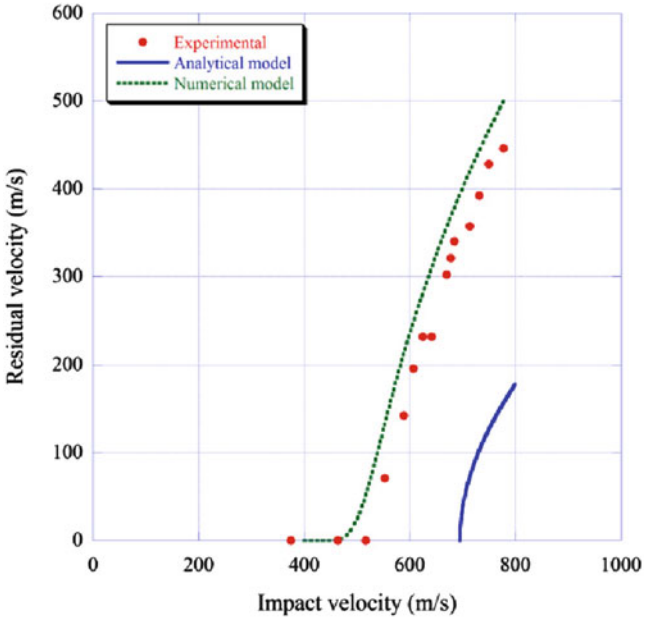


Fig. 13 Validation of analytical and numerical models. Residual velocity vs. impact velocity. Thickness = 12 mm

Table 5 Ballistic limit determined by the experimental test, analytical, and numerical models

	Ballistic limit (m/s)		
Laminate thickness (mm)	Experimental	Analytical model	Numerical model
3	212[1]	208	220
6	332[2]	352	320
12	550[2]	692	480

[1]From [22] [2]From [14]

Figure 13 shows the comparison between experimental data, numerical predictions, and analytical results for 12-mm-thick laminates. The FE model slightly overestimated residual velocity but predictions showed a good correlation with experimental results. On the contrary, the analytical model failed by a large amount in the prediction of residual velocity. The analytical model presented in this work assumes the hypothesis of thin laminates, and thus the validity of the model is limited to laminates with thickness up to 6 mm. This model cannot be applied to the 12-mm-thick laminate.

Table 5 shows the ballistic limit found in the experimental results and the predictions of numerical and analytical models. A good correlation between the FE model and experimental results can be observed for the three thicknesses. On the other hand, the analytical model accurately predicted the ballistic limit for laminates with 3 and 6 mm in thickness but failed in the prediction when the thickness was increased to 12 mm.

Figure 14 shows the ballistic limit as a function of laminate thickness determined by the experimental results and the numerical and analytical models. For thicknesses of between 3 and 6 mm, the numerical and analytical predictions agreed with experimental data. However, as laminate thickness increased, the analytical model predicted a ballistic limit higher than the experimental results. This overestimation was due to the invalidity of the hypothesis of thin laminates. In the case of thick laminates, it is necessary to incorporate other energy-absorption mechanisms such as friction and shear plugging. On the other hand, the FE model predicted a ballistic limit lower than experimental results, but numerical predictions are close to the experimental data.

According to these results, the analytical model proposed can be considered validated for a range of thicknesses up to 6 mm.

5 Results and Discussion

In this section the validated analytical model is used to analyze the contribution of the different energy-absorption mechanisms during high-velocity impact on woven GFRP laminates. The contribution of the energy-absorption mechanisms depends on the impact velocity and laminate thickness. For an analysis of the influence of

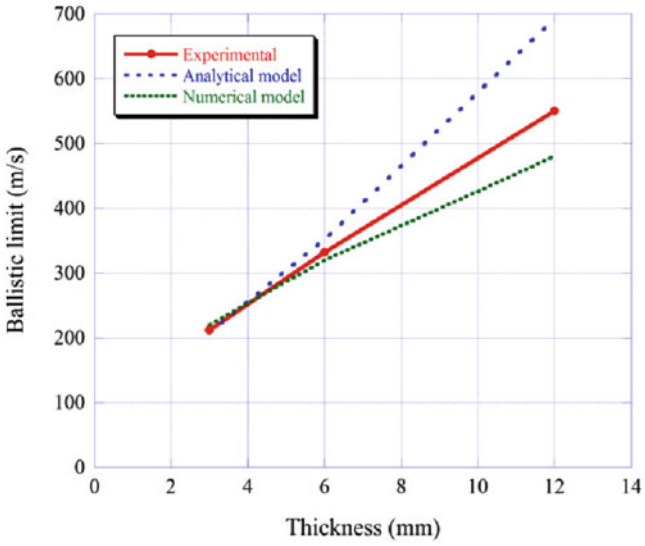


Fig. 14 Ballistic limit vs. laminate thickness. Experimental, numerical, and analytical results

these variables, three impact velocities were analyzed in detail for each laminate thickness. The impact velocities selected were: equal to, half, and double the ballistic limit. The FE numerical model was used to verify the results provided by the analytical model and to analyze the validity of the hypothesis assumed in the model.

5.1 Laminate Thickness Equal to 3 mm

Figures 15, 17, and 19 present the energy absorbed for each absorption mechanism as a function of the time during high-velocity impact on 3-mm-thick GFRP woven laminates. It should be notice that the fiber-failure energy-absorption mechanism considers the energy absorbed by the region of the laminate under the projectile section because the model assumes that all the fibers in this region fail. On the other hand, the elastic deformation mechanism considers the energy absorbed by the region of the laminate between the projectile radius and the distance covered by the transversal wave. During the first instants of the impact the distance covered by transversal wave is shorter than the projectile radius, and thus elastic deformation is zero. The time required by the transversal wave to cover a distance equal to the projectile radius depends on material properties and is independent of laminate thickness and impact velocity. Therefore, the time during which the elastic deformation is not considered is the same for every impact event analyzed (6 μs), see Figs. 15, 17, and 19.

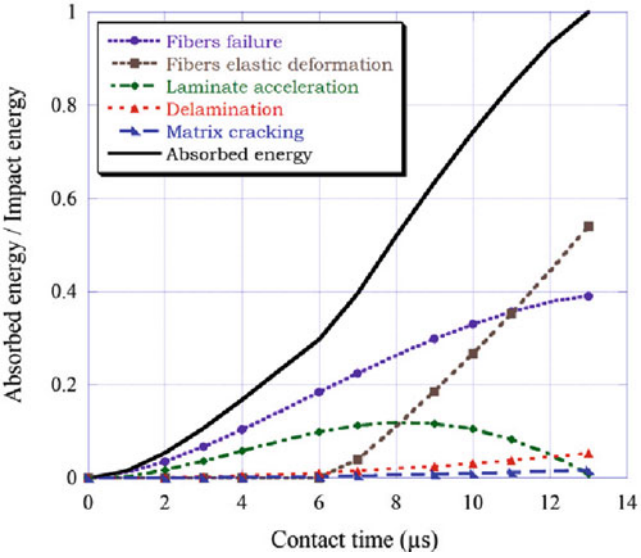


Fig. 15 Time course of the energy-absorption mechanisms at an impact velocity equal to 104 m/s (thickness 3 mm)

Figure 15 shows the time course of the energy-absorption mechanisms during impact for an impact velocity of 104 m/s (lower than the ballistic limit) on a 3-mm-thick laminate. In the first stage, fiber failure and laminate acceleration were the main energy-absorption mechanisms, while elastic deformation of the fiber was equal to zero. The energy absorbed by delamination and matrix cracking can be disregarded in comparison with the other energy-absorption mechanisms.

The numerical model confirms the analytical results (see Fig. 16). During the first stage (Fig. 16a), the laminate deformations are confined to the region under the projectile surface, thus energy is absorbed mainly by damage to the laminate due to fiber failure and the transference of kinetic energy to the elements of the composite by the projectile. Figure 16b reveals that the transverse wave covered a distance higher than projectile radius because the deformed elements are not confined under the projectile area. At this moment, the elastic deformation contributes to the energy-absorption process. Figure 16 shows that elastic deformations are clearly visible when the projectile is stopped. At the end of the event, for impact velocities lower than ballistic limit, the kinetic energy of the composite is zero because the projectile is stopped; on the other hand, elastic energy is stored in the laminate, being the main energy-absorption mechanism.

The results when the impact velocity is equal to the ballistic limit are similar to those found for lower velocities (Fig. 17). The main failure mechanisms in the first stage are fiber failure and laminate acceleration, fiber elastic deformation becoming the main mechanism at the end of the impact event. The numerical model also confirms the results found with the analytical model (Fig. 18). The distance covered

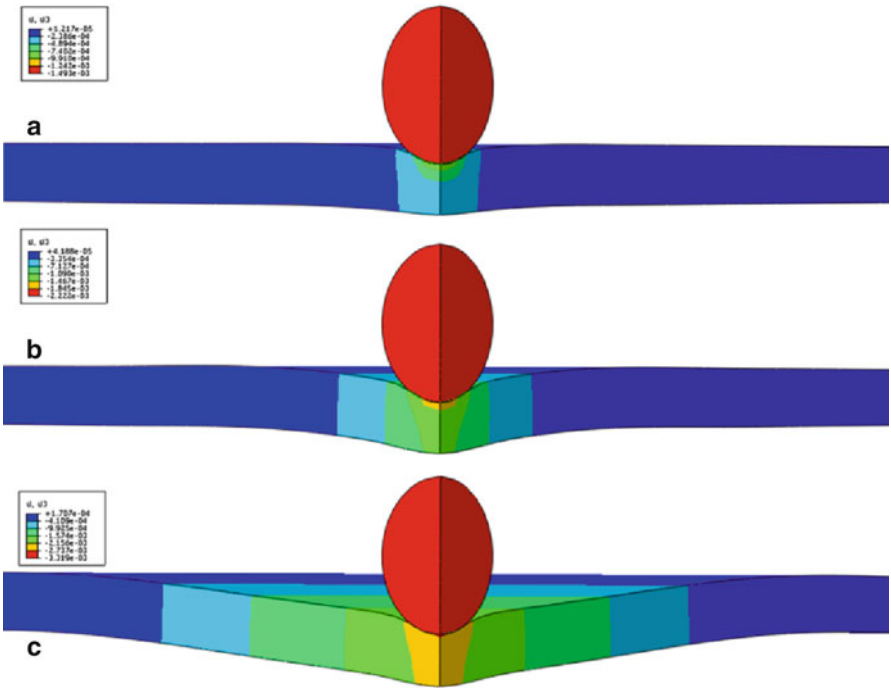


Fig. 16 Time course of the vertical displacement at an impact velocity equal to 104 m/s (thickness 3 mm). (**a**) t = 5 μs. (**b**) t = 10 μs. (**c**) t = 13 μs

by transverse wave was greater in comparison to the results found with lower impact velocities (Fig. 18c), but qualitatively the results for impact velocities equal to or lower than the ballistic limit are similar. These results have been mentioned by other authors [86], who determined that for impacts below the ballistic limit the main effect is bending.

When the impact velocity was higher than the ballistic limit the contribution of the energy-absorption mechanisms to the reduction of projectile velocity proved completely different (Fig. 19). During the first stage, the results were similar to those found for lower-impact velocity. The main mechanism was the kinetic energy transferred to the laminate, and fiber failure also contributed to the reduction of projectile velocity. However, the energy absorbed by fiber failure was limited by the strength of the material and, once fiber failure was achieved, the energy could not be absorbed by the failure mechanism or elastic deformations. Thus the main energy-absorption mechanism was laminate acceleration. These results were confirmed by FE model analysis (Fig. 20); that is, when fiber failure was achieved and the projectile perforated the laminate, elastic deformations were lower than those observed at an impact velocity equal to the ballistic limit.

According to these results, the main energy-absorption mechanisms for impact events with an impact velocity higher than the ballistic limit differed from those

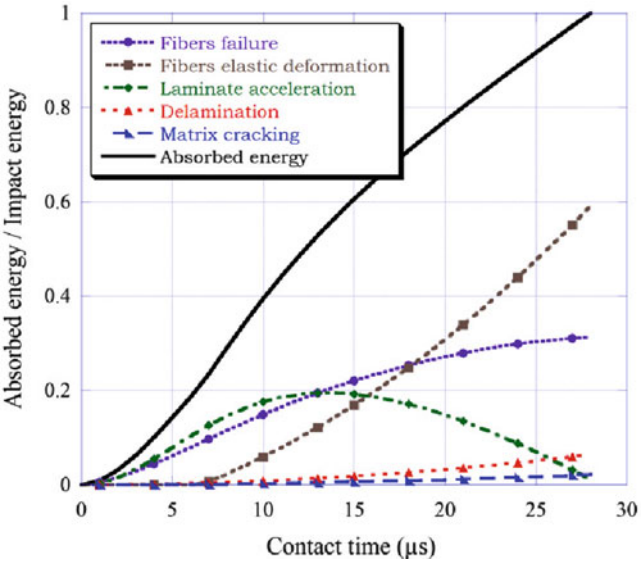


Fig. 17 Time course of energy-absorption mechanisms at an impact velocity equal to the ballistic limit (thickness 3 mm)

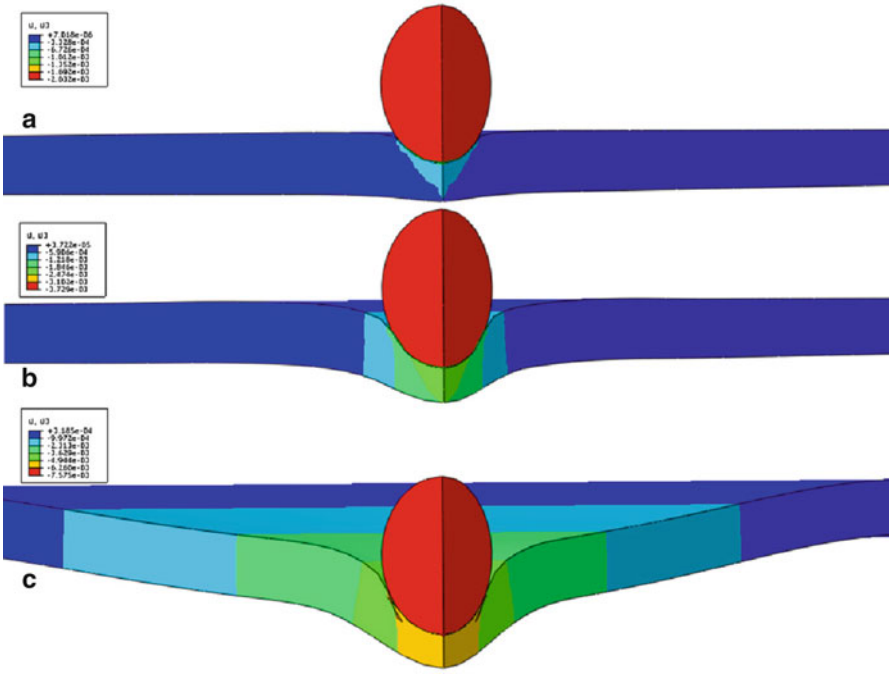


Fig. 18 Time course of vertical displacement at an impact velocity equal to ballistic limit (thickness 3 mm). (**a**) t = 5 μs. (**b**) t = 15 μs. (**c**) t = 28 μs

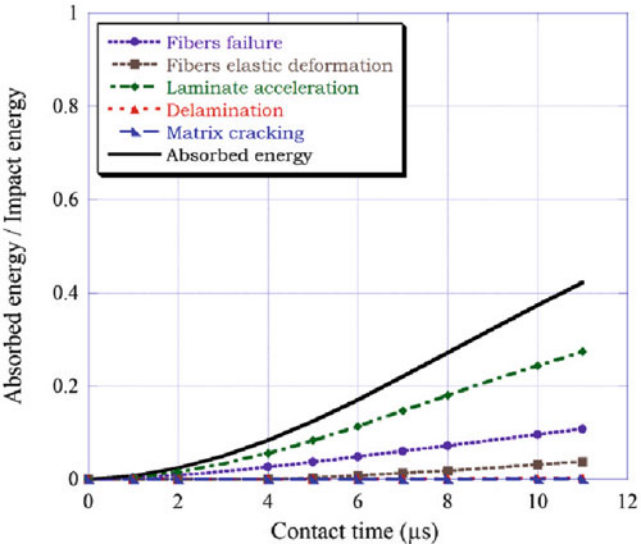


Fig. 19 Time course of energy-absorption mechanisms at an impact velocity equal to 416 m/s (thickness 3 mm)

found when the laminate was not perforated. When the woven laminate was not perforated, the main energy-absorption mechanisms were elastic deformation and fiber failure, and thus the behavior of the plate was governed by the strength and the stiffness of the material. On the other hand, for impact velocities higher than the ballistic limit, the main energy-absorption mechanism was the kinetic energy transferred to the laminate, and thus the behavior of the plate was dominated by the material density.

Although the energy absorbed by delamination can be neglected in comparison with other energy-absorption mechanisms, the analysis of this mechanism is worthy of investigation because the delaminated area is an important factor to predict residual strength of impacted specimens. For verification of the accuracy of the analytical model in the prediction of delamination, the damage area was measured by ultrasonic C-Scan. Figure 21 shows the damage area detected by C-Scan inspection in specimens receiving impacts at velocities equal to, lower than, and higher than the ballistic limit.

Figure 22 shows the extent of the damage area as a function of the impact velocity found in 3-mm-thick specimens. Two trends can be discerned for impact velocities lower or higher than the ballistic limit. When the impact velocity was lower than the ballistic limit, a linear relationship was found between the impact velocity and the damage area. The higher the impact velocity, the greater the damage area. The greatest damage area was found in specimens after impact at velocities close to the ballistic limit. On the other hand, when the woven laminate was perforated by the projectile, the damage area decreased with increasing impact velocity. The damage area tended towards a minimum equal to the projected surface area of the projectile.

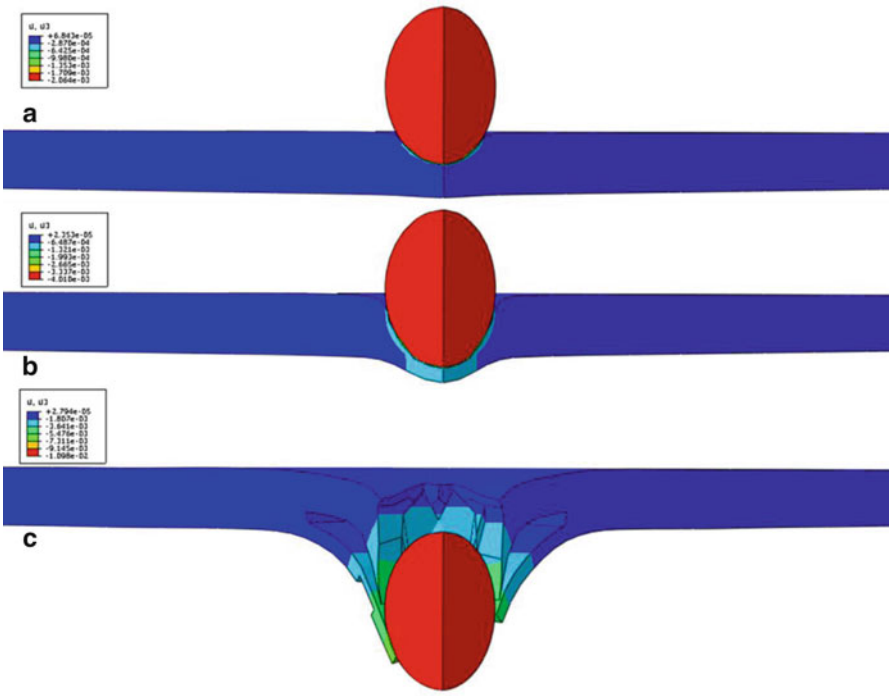


Fig. 20 Time course of the vertical displacement at an impact velocity equal to 416 m/s (thickness 3 mm). (**a**) t = 5 μs. (**b**) t = 8 μs. (**c**) t = 11 μs

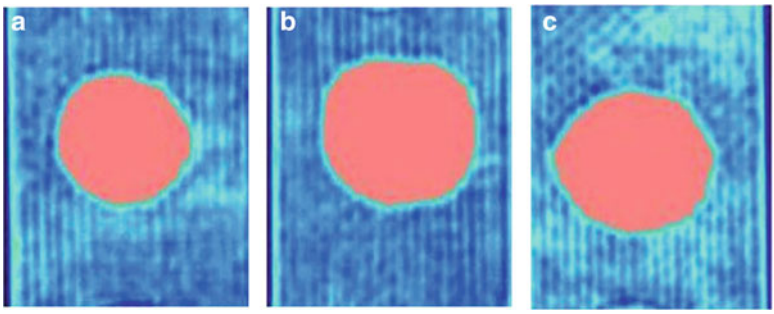


Fig. 21 Damage area visible in C-Scan ultrasonic inspection for impact velocities: (**a**) lower than the ballistic limit, (**b**) equal to the ballistic limit, and (**c**) higher than the ballistic limit

Analytical-model predictions for absorbed energy as a function of impact energy are shown in Fig. 23. The energy absorbed by delamination followed the same trend observed in the experimental tests: delamination increased with impact velocity, until the ballistic limit was reached. Then, delamination decreased with increasing impact velocity.

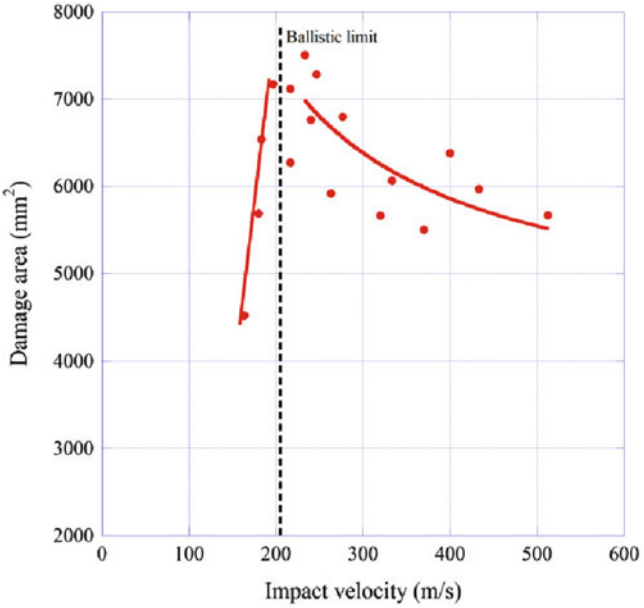


Fig. 22 Damage area as a function of impact velocity (thickness 3 mm)

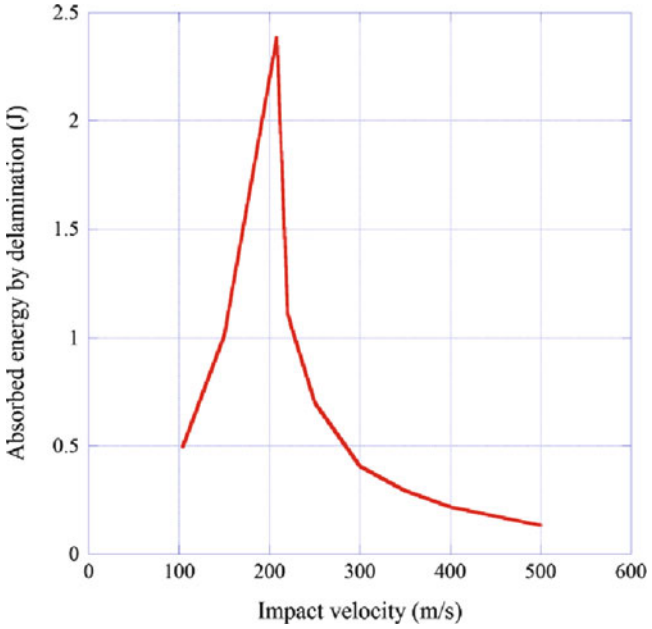


Fig. 23 Energy absorbed by delamination as a function of impact velocity (thickness 3 mm)

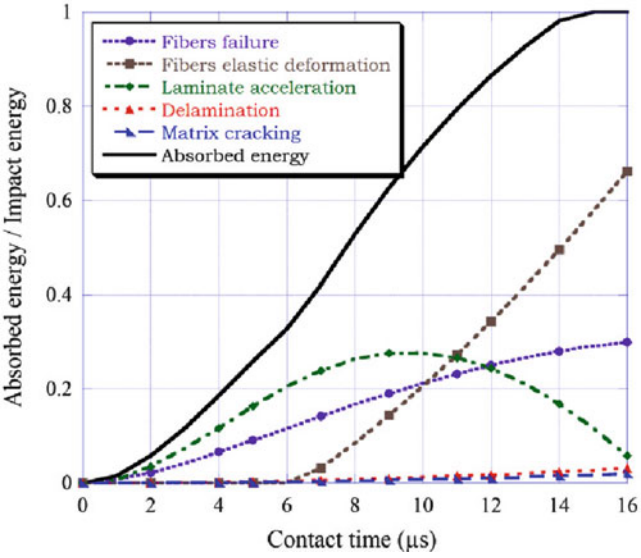


Fig. 24 Time course of energy-absorption mechanisms at an impact velocity equal to 176 m/s (thickness 6 mm)

5.2 Laminate Thickness Equal to 6 mm

The GFRP woven laminates with a thickness of 6 mm showed similar results to those found in the 3-mm-thick laminates (see Figs. 24, 25 and 26). Elastic deformation can be considered the main energy-absorption mechanism for impact velocities lower than the ballistic limit; however, its contribution can be neglected when the laminate is perforated. Fiber failure is the main energy-absorption mechanism related to the failure of the woven laminates, its contribution being significantly higher than that of delamination and matrix cracking. The contribution of fiber failure in the absorption of the projectile kinetic energy is noteworthy for impact velocities lower and higher than ballistic limit.

Laminate acceleration plays a major role in energy absorption for every impact velocity, but its contribution differs when the laminate is perforated or not. When the impact velocity is equal to or lower than the ballistic limit, part of impact energy is transferred to the laminate in the form of kinetic energy, and then the laminate displacement results in fiber failure and elastic deformation in the laminate. Thus, the kinetic energy of projectile and laminate are absorbed by the elastic deformation and the damage induced in the laminate. At the end of the impact event, the kinetic energy is reduced to zero and all the energy previously transferred to the laminate is absorbed by other mechanisms. For impact velocities higher than the ballistic limit, fiber failure and elastic deformations cannot absorb the total impact energy, and thus the transference of the kinetic to the laminate is the main energy-absorption

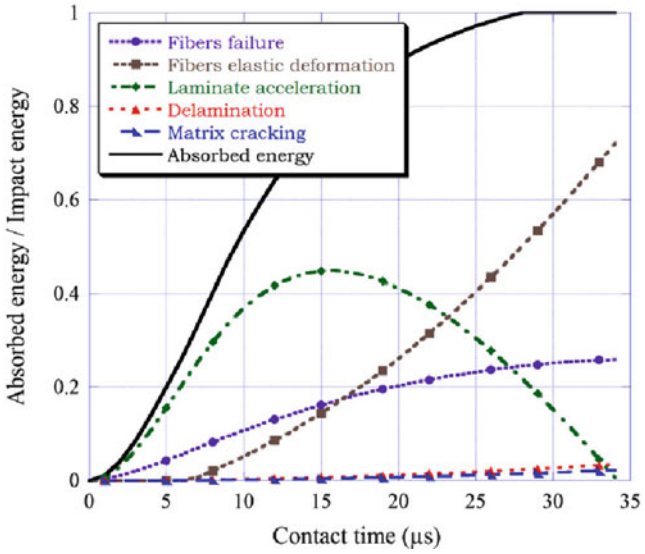


Fig. 25 Time course of energy-absorption mechanisms at an impact velocity equal to the ballistic limit (thickness 6 mm)

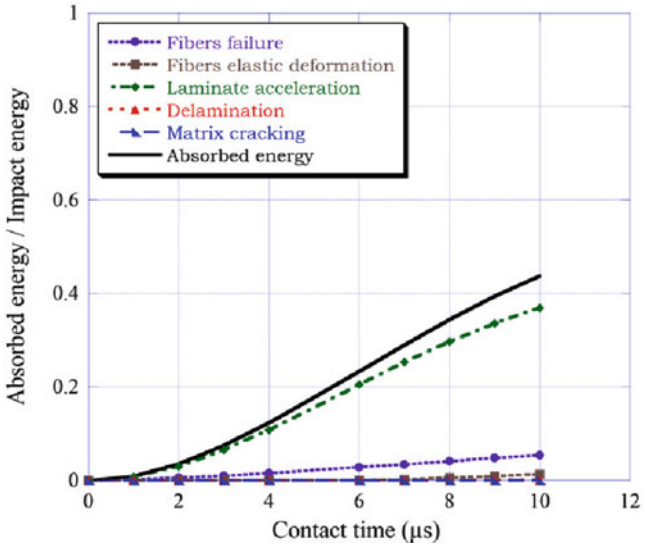


Fig. 26 Time course of energy-absorption mechanisms at an impact velocity equal to 704 m/s (thickness 6 mm)

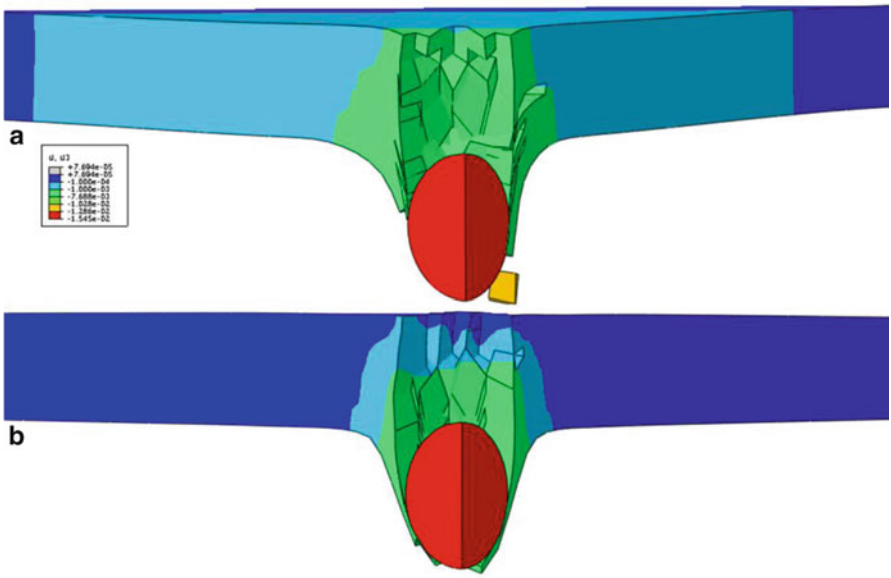


Fig. 27 Vertical displacement field after impact on 6-mm-thick laminates. (**a**) Impact velocity near the ballistic limit. (**b**) Impact velocity double the ballistic limit

mechanisms. Material density is the main parameter to govern the behavior of the plate under these impacts.

The analytical model showed excellent accuracy in predicting the residual velocity for all the impact velocities used for the 3-mm-thick laminates (Fig. 11). However, for impacts on 6-mm-thick laminates, the accuracy of the analytical model decreased for the highest impact velocity, as shown in the validation section (Fig. 12). The FE model was employed to analyze the reasons of this disagreement between experimental results and analytical-model predictions. Figure 27 shows the vertical displacement field for an impact velocity near the ballistic limit and an impact velocity double the ballistic limit. When the impact velocity was slightly higher than the ballistic limit (Fig. 27a), the displacements of the laminate corresponded to the deformations considered in the hypothesis of the analytical model. However, when the impact velocity was much higher than the ballistic limit (Fig. 27b), the deformations of the laminate were located in the region under the projectile surface. In this case, the hypotheses of the analytical model are not verified due to the presence of other energy-absorption mechanisms as shear failure. The FE model also considers the contribution of shear failure, and thus numerical results are in excellent agreement with the experimental data.

5.3 Laminate Thickness Equal to 12 mm

The analytical model assumes the hypothesis of thin laminates considering the formation of the acceleration of the laminate as the transverse wave advances. On the other hand, the analytical model considers several energy-absorption mechanisms, but neither shear failure nor friction forces are considered, nor the compression of the region directly below the projectile [34]. These hypotheses are valid for thin laminates, and in this work the results for laminates with thicknesses of 3 and 6 mm are in excellent agreement with the experimental data. However, when a thick laminate is subjected to high-velocity impact, these hypotheses cannot be assumed. Figure 28 shows the perforation process during impact at a velocity of 700 m/s on a 12-mm-thick laminate. The deformation of the laminate is located in the region under the projectile surface; the woven laminate is damaged by shear failure and only the elements which are in the projectile trajectory are eroded. The FE model considers this failure mode but numerical predictions do not agree well with the experimental tests. The residual velocity may be overestimated in the numerical predictions because friction between projectile and woven laminate was not considered in the FE model.

6 Summary and Conclusions

The high-impact-velocity behavior of woven laminates has been analyzed in this chapter. Experimental, numerical, and analytical approaches have been combined to gain a better understanding of the failure modes and energy-absorption mechanisms of GFRP plain woven laminates under high-velocity impacts.

Although this chapter does not seek to be an exhaustive compendium of simplified analytical models, several models have been briefly presented. Those based on energy-conservation laws have been applied successfully to estimate the residual velocity of the projectile and the ballistic limit. Also, a brief review is presented on numerical-model approaches based on the Finite-Element Method.

Moreover, an energy-based analytical model is presented. To assess the accuracy of these analytical models in the prediction of residual velocity and in the analysis of energy-absorption mechanisms, a study of the behavior of GFRP woven laminates under high-velocity impact was developed.

Experimental tests were performed to validate the precision of the analytical model in the prediction of residual velocity on GFRP woven laminates with different thicknesses. A FE model is described and applied to the validation of the hypothesis of the analytical model. The validity of the analytical model was verified through comparison with experimental and numerical results. The model proved valid for a wide range of impact velocities on thin laminates (up to 6 mm thick).

The influence of impact velocity and laminate thickness on the energy-absorption mechanisms was estimated from this model. According to these results the main

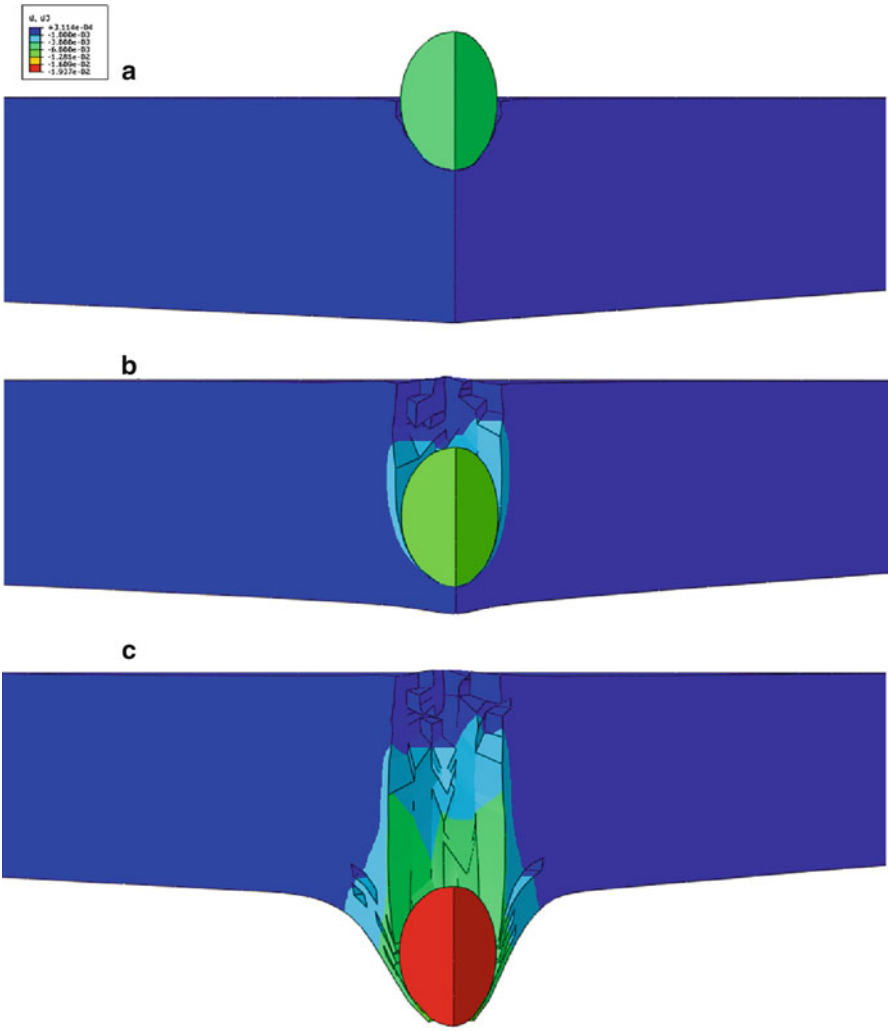


Fig. 28 Time course of the fiber-failure criterion at an impact velocity equal to 700 m/s (thickness 12 mm). (**a**) t = 5 μs. (**b**) t = 15 μs. (**c**) t = 22 μs

energy-absorption mechanisms for impact events with an impact velocity higher than the ballistic limit differs from those found when the laminate is not perforated. When a woven laminate is not perforated, the main energy-absorption mechanisms are elastic deformation and fiber failure, and thus the behavior of the plate is governed by the strength and stiffness of the material. On the other hand, for impact velocities higher than the ballistic limit, the main energy-absorption mechanism is the kinetic energy transferred to the laminate, and therefore the behavior of the plate is dominated by the material density.

The combination of experimental, numerical and analytical approaches has shown the limits of the hypothesis of the analytical formulation. These results can be used to develop new analytical approaches considering other energy adsorption mechanisms for thick laminates.

Acknowledgements The authors are indebted to the Spanish Comisión Interministerial de Ciencia y Tecnología (Projects TRA2007-66555) and Consejería de Educación de la Comunidad de Madrid (Projects GR/MAT/0498/2004 and IME-05-026) for the financial support of this work.

References

1. Koissin V, Skvortsov V, Krahmalev S, Shilpsha A (2004) The elastic response of sandwich structures to local loading. Compos Struct 63(3–4):375–385
2. Rizov V, Mladensky A (2008) Mechanical behaviour of composite sandwich structures subjected to low velocity impact – experimental testing and finite element modeling. Polym Polym Compos 16(4):233–240
3. Cantwell WJ, Morton J (1990) Impact perforation of carbon fiber reinforced plastic. Compos Sci Technol 38:119–141
4. Abrate S (1998) Impact on composite structures. Cambridge University Press, Cambridge
5. Abrate S (1994) Impact on laminated composites: recent advances. Appl Mech Rev 47(11):517–544
6. Kasano H, Abe K (1997) Perforation characteristics prediction of multi-layered composite plates subjected to high velocity impact. In: Proceedings of the ICCM-11, vol 2, pp 522–531
7. Ben-Dor G, Dubinsky A, Elperin T (2005) Ballistic impact: recent Advances in analytical modeling of plate perforation dynamic-a review. Appl Mech Rev 58:355–369
8. Menna C, Asprone D, Caprino G, Lopresto V, Prota A (2011) Numerical simulation of impact tests on GRFP composite laminates. Int J Impact Eng 38:677–685
9. Gama BA, Gillespie JW (2011) Finite element modeling of impact, damage evolution and penetration of thick-section composites. Int J Impact Eng 38:181–197
10. Navarro C (1997) Impact response and dynamic failure of composites and laminate materials. Key Eng Mat 141–143:383–402
11. Sjöblom PO, Hartness JT, Cordell TM (1988) On low-velocity impact testing of composite materials. J Compos Mat 22:30–52
12. Robinson P, Davies GAO (1992) Impactor mass and specimen geometry effects in low velocity impact of laminated composites. Int J Impact Eng 12(2):189–207
13. Naik NK, Shrirao P (2004) Composite structures under ballistic impact. Compos Struct 66:579–590
14. Buitrago BL, García-Castillo SK, Barbero E (2010) Experimental analysis of perforation of glass/polyester structures subjected to high-velocity impact. Mater Lett 64(9):1052–1054
15. Zukas JA, Nicholas T, Swift H, Greszczuk LB, Curran DR (1992) Impact dynamic. Krieger Publishing Company, Malabar
16. MIL-STD-662F Standard. V50 Ballistic test for armor. Department of Defense Test Method Standard
17. Ulven C, Vahadilla UK, Hosur MV (2003) Effect of projectile shape during ballistic perforation of VARTM carbon/epoxi composite panels. Compos Struct 61:143–150
18. Fujii K, Aoki M, Kiuchi N, Yasuda E, Tanabe Y (2002) Impact perforation behavior of CFRPs using high-velocity steel sphere. Int J Impact Eng 27:497–508
19. García-Castillo SK, Sánchez-Sáez S, Barbero E (2012) Nondimensional analysis of ballistic impact on woven laminate plates. Int J Impact Eng 29:8–15

20. Kim H, Welch DA, Kedward KT (2003) Experimental investigation of high velocity ice impacts on woven carbon/epoxy composite panels. Compos Part A Appl S 34:25–41
21. Johnson AF, Holzapfel M (2006) Influence of delamination on impact damage in composite structures. Compos Sci Technol 66:807–815
22. García-Castillo SK, Sánchez-Sáez S, Barbero E, Navarro C (2006) Response of pre-loaded laminate composite plates subject to high velocity impact. J Phys IV 134:1257–1263
23. Deka LJ, Bartus SD, Vaidya UK (2008) Damage evolution and energy absorption of E-glass/polypropylene laminates subjected to ballistic impact. J Mater Sci 43:4399–4410
24. Tan VBC, Ching TW (2006) Computational simulation of fabric armor subjected to ballistic impacts. Int J Impact Eng 32:1737–1751
25. He T, Wen HM, Qin Y (2008) Finite element analysis to predict perforation and perforation of thick FRP laminates struck by projectiles. Int J Impact Eng 35:27–36
26. Buitrago BL, Santiuste C, Sanchez-Saez S, Barbero E, Navarro C (2010) Modelling of composite sandwich structures with honeycomb core subjected to high-velocity impact. Compos Struct 92:2090–2096
27. Grujicic M, He T, Marvi H, Cheeseman BA, Yen CF (2010) A comparative investigation of the use of laminate-level meso-scale and fracture-mechanics-enriched meso-scale composite-material models in ballistic-resistance analyses. J Mater Sci 45(12):3136–3150
28. Taylor WJ, Vinson JR (1990) Modeling ballistic into flexible materials. AIAA J 28:2098–2103
29. Zhu G, Goldsmith W, Dharan CKH (1992) Penetration of laminated Kevlar by projectiles-II. Analytical model. Int J Solid Struct 29:421–436
30. Vinson JR, Walter JM (1997) Ballistic impact of thin-walled composite structures. AIAA J 35:875–878
31. Navarro C (1998) Simplified modelling of the ballistic behavior of fabrics and fiber-reinforced polymeric matrix composites. Key Eng Mat 141(1):383–399
32. Morye SS, Hine PJ, Duckett RA, Carr DJ, Ward IM (2000) Modelling of the energy absorption by polymer composites upon ballistic impact. Compos Sci Technol 60:2631–2640
33. Wen HM (2000) Predicting the penetration and perforation of FRP laminates struck normally by projectiles with different nose shapes. Compos Struct 49(3):321–329
34. Gu B (2003) Analytical modelling for the ballistic perforation of planar plain-woven fabric target by projectile. Compos Part B Eng 34:361–371
35. Naik NK, Shrirao P, Reddy BCK (2005) Ballistic impact behavior of woven fabric composite: parametric studies. Mater Sci Eng A Struct 472:104–116
36. Naik NK, Doshi AV (2005) Ballistic impact behavior of thick composite: analytical formulation. AIAA J 43:1525–1536
37. Naik NK, Shrirao P, Reddy BCK (2006) Ballistic impact behavior of woven fabric composites: formulation. Int J Impact Eng 32:1521–1552
38. Lopez-Puente J, Zaera R, Navarro C (2007) An analytical model for high velocity impacts on thin CFRPs woven laminated plates. Int J Solid Struct 44:2837–2851
39. García-Castillo SK, Sánchez-Sáez S, López-Puente J, Barbero E, Navarro C (2009) Impact behavior of preloaded glass/polyester woven plates. Compos Sci Technol 69:711–717
40. Wen HM (2001) Penetration and perforation of thick FRP laminates. Compos Sci Technol 61:1163–1172
41. Phoenix SL, Porwal PK (2003) A new membrane model for ballistic impact response and V50 performance of multi-ply fibrous systems. Int J Solid Struct 40:6723–6765
42. Mamivand M, Liaghat GH (2010) A model for ballistic impact on multi-layer fabric targets. Int J Impact Eng 37:806–812
43. Grujicic M, Bell WC, Arakere G, He T, Xie X, Cheeseman B (2010) A development of a meso-scale material model for ballistic fabric and its use in flexible-armor protection systems. J Mater Eng Perform 19(1):22–39
44. He T, Wen HM, Qin Y (2007) Penetration and perforation of FRP laminates struck transversely by conical-nosed projectiles. Compos Struct 81(2):243–252
45. García-Castillo SK (2007) Análisis de laminados de materiales compuestos con precarga en su plano y sometidos a impacto. PhD thesis, University Carlos III of Madrid

46. García-Castillo SK, Buitrago BL, Barbero E (2011) Behavior of sandwich structures and spaced plates subjected to high-velocity impacts. Polym Compos 32(2):290–296
47. Nahas NM (1986) Survey of failure and post-failure theories of laminated fiber-reinforced composites. J Compos Technol Res 8:138–153
48. Paris F (2001) A study of failure criteria of fibrous composite materials. Technical report: NASA-cr210661
49. Orifici AC, Herszberg I, Thomson RS (2008) Review of methodologies for composite material modeling incorporating failure. Compos Struct 86:194–210
50. Soden PD, Kaddour AS, Hinton MJ (2004) Recommendations for designers and researchers resulting from the world-wide failure exercise. Compos Sci Technol 64(3–4):589–604
51. Hashin Z (1980) Failure criteria for unidirectional fiber composites. J Appl Mech 47:329–334
52. Hou JP, Petrinic N, Ruiz C, Hallett SR (2000) Prediction of impact damage in composite plates. Compos Sci Tech 60(2):273–280
53. Chang F, Chang KA (1987) A progressive damage model for laminated composites containing stress concentrations. J Compos Mater 21:834–855
54. Zangani D, Robinson M, Gibson AG (2008) Energy absorption characteristics of web-core sandwich composite panels subjected to drop-weight impact. Appl Compos Mater 15:139–156
55. Foo CC, Chai GB, Seah LK (2008) A model to predict low-velocity impact response and damage in sandwich composites. Compos Sci Technol 68:1348–1356
56. Budiansky B, Fleck NA, Amaxigo JC (1998) On kink-band propagation in fiber composites. J Mech Phys Solid 46:1637–1653
57. Davila CG, Camanho PP (2003) Failure criteria for FRP laminates in plane stress. NASA/TM-2003-212663
58. Davila CG, Camanho PP, Rose CA (2005) Failure criteria for FRP laminates. J Compos Mater 39:323–343
59. Puck A, Schürmann H (1998) Failure analysis of FRP laminates by means of physically based phenomenological models. Compos Sci Technol 58:1045–1067
60. Christensen RM (1997) Stress based yield/fracture criteria for fiber composites. Int J Solid Struct 34:529–543
61. Kim RY, Soni SR (1986) Failure of composite laminates due to combined interlaminar normal and shear stresses. Composites '86: recent advances in Japan and the United States, pp 341–350
62. Brewer JC, Lagace PA (1988) Quadratic stress criterion for initiation of delamination. J Compos Mater 22(12):1141–1155
63. Tong L (1997) An assessment of failure criteria to predict the strength of adhesively bonded composite double lap joints. J Reinforce Plastic Composites 16:698–713
64. Lorriot TH, Marion G, Harry R, Wargnier H (2003) Onset of free-edge delamination in composite laminates under tensile loading. Compos Part B: Eng 34:459–471
65. Mahanta BB, Chakraborty D, Dutta A (2004) Accurate prediction of delamination in FRP composite laminates resulting from transverse impact. Compos Sci Technol 64:2341–2351
66. Goyal VK, Johnson ER, Dávila C (2004) Irreversible constitutive law for modeling the delamination process using interfacial surface discontinuities. Compos Struct 65:289–305
67. Zhang Z, Taheri F (2004) Dynamic damage initiation of composite beams subjected to axial impact. Compos Sci Technol 64:719–728
68. Maimi P, Camanho PP, Mayugo JA, Davila CG (2007) A continuum damage model for composite laminates: part I – constitutive model. Mech Mater 39(10):897–808
69. Sleight DW (1999) Progressive failure analysis methodology for laminated composite structures. NASA/TP-1999-209107
70. Chiu KD (1969) Ultimate Strength of laminated composites. J Compos Mater 3:578–582
71. Luo RK, Green ER, Morrison CJ (1999) Impact damage analysis of composite plates. Int J Impact Eng 22:435–447
72. Camanho PP, Matthews FL (1999) A progressive damage model for mechanically fastened joints in composite laminates. J Compos Mater 33:2248–2280
73. Papanikos P, Tserpes KI, Pantelakis SP (2003) Modelling of fatigue damage progression and life of CFRP laminates. Fatigue Fracture Eng Mater Struct 26:37–47

74. Hahn HT, Tsai SW (1974) On the behaviour of composite laminates after initial failures. J Compos Mater 8:288–305
75. Ghosh A, Sinha PK (2004) Dynamic and impact response of damaged laminated composite plates. Aircr Eng Aerosp Technol 76:29–23
76. Balzani C, Wagner W (2008) An interface element for the simulation of delamination in unidirectional fiber-reinforced composite laminates. Eng Fract Mech 75:2597–2615
77. Linde P, De Boer H (2006) Modelling of inter-rivet buckling of hybrid composites. Compos Struct 73:221–228
78. Sheikh AH, Bull PH, Kepler JA (2009) Behavior of multiple composite plates subjected to ballistic impact. Compos Sci Technol 69:704–710
79. Kachanov LM (1958) Time of the rupture process under creep conditions. Izvetia Akademii Naukk SSSR. Otdelenie Tekhnischeskich Nauk
80. Rabotnov YN (1968) Creep rupture. In: Proceeding of XII international congress on applied mechanic. Springer, Stanford
81. Talreja R (1987) Modeling of damage development in composite using internal variable concepts. Damage mechanics in composites, ASME Winter annual meeting, Boston
82. Ladeveze P, Ledantec E (1992) Damage modelling of the elementary ply for laminated composites. Compos Sci Technol 43:257–267
83. Matzenmiller A, Lubliner J, Taylor RL (1995) A constitutive model for anisotropic damage in fiber composites. Mech Mater 20:125–152
84. Barbero EJ, Lonetti P, Sikkil KK (2006) Finite element continuum damage modeling of plain weave reinforced composites. Compos Part B Eng 37:137–147
85. Santiuste C, Sánchez-Sáez S, Barbero E (2010) A comparison of progressive-failure criteria in the prediction of the dynamic. Compos Struct 92(10):2406–2414
86. Lopez-Puente J, Zaera R, Navarro C (2008) Experimental and numerical analysis of normal and oblique ballistic impacts on thin carbon/epoxy woven laminates. Compos Part A Appl S 39:374–387
87. Iváñez I, Santiuste C, Sánchez-Sáez S (2010) FEM analysis of dynamic flexural behavior of composite sandwich beams with foam core. Compos Struct 92(9):2285–2291
88. Ivañez I, Santiuste C, Sánchez-Sáez S, Barbero E (2011) Numerical modelling of foam-cored sandwich plates under high velocity impact. Compos Struct 93:2392–2399
89. Smith JC, McCrackin FL, Schiefer HF (1958) Stress-strain relationships in yarns subjected to rapis impact loading: 5 Wave propagation in long tensile yarns impacted transversally. J Res Nat Bur Stand 60:517–534
90. Roylance D (1980) Stress wave propagation in fibres: effect of crossovers. Fibre Sci Technol 13(5):385–395
91. García-Castillo SK, Sánchez-Sáez S, Barbero E (2011) Behaviour of uniaxially preloaded aluminium plates subjected to high-velocity impact. Mech Res Commun 38(5):404–407
92. Zee RH, Wang CJ, Mount A, Jang BZ, Hsieh CY (1991) Ballistic response of polymer composites. Polym Compos 12:196–202
93. Varas D, Zaera R, López-Puente J (2011) Experimental study of CFRP fluid-filled tubes subjected to high-velocity impact. Compos Struct 93(10):2598–2609
94. Kasano H (1999) Recent advances in high-velocity impact perforation of fiber composite laminates. JSME Int J A 42(2):147–157

Discrete Impact Modeling of Inter- and Intra-laminar Failure in Composites

Christophe Bouvet, Natthawat Hongkarnjanakul, Samuel Rivallant, and Jean-Jacques Barrau

Abstract The goal of this study is to initiate a "test-calculation dialogue" on low velocity/low energy impact tests in laminated composites. The different types of impact damage developing during an impact test, i.e. matrix cracking, fiber failure, interface delamination and permanent indentation, are simulated. The bibliography shows a general lack of detailed validation of impact modeling and the originality of this work is to use refined and complementary experimental data to build and validate a numerical model. The good correlation between the model and this refined experimental database gave us relative confidence in the model, despite a few non-standard material parameters.

Permanent indentation was particularly focused and studied. Then we propose an original scenario to create permanent indentation, with a debris blocking phenomenon in the matrix cracks, as well as the corresponding model. The fiber failure model was set up using an original formulation between the integration points of the volume element in order to dissipate a constant energy release rate per unit area. Finally the model was used to evaluate the distribution of the dissipated energy among the different damage types, and demonstrated an interesting distribution between fiber failure and delamination.

1 Introduction

Composite materials have been increasingly used in airframe and space applications in recent decades because of their advantageous characteristics, such as their low specific weight, enhanced mechanical strength, and high stiffness coefficient.

C. Bouvet (✉) • N. Hongkarnjanakul • S. Rivallant • J.-J. Barrau
INSA; UPS; Mines Albi; ISAE; ICA (Institut Clément Ader), Université de Toulouse, ISAE, 10, avenue Edouard Belin, 31055 Toulouse Cedex 4, France
e-mail: christophe.bouvet@isae.fr

S. Abrate et al. (eds.), *Dynamic Failure of Composite and Sandwich Structures*, Solid Mechanics and Its Applications 192, DOI 10.1007/978-94-007-5329-7_8,
© Springer Science+Business Media Dordrecht 2013

Nevertheless, during the structure's life, damage induced in these materials by impacts of minor and major objects, such as hail stones, runway debris or dropped tools, can drastically decrease the structure's life.

Low velocity impact is one of the most critical load factors for composite laminates. Indeed, for structures submitted to low energy impacts or small dropped objects drops, such as tools during assembly or maintenance operations, composite laminates reveal a brittle behavior and can undergo significant damage in terms of matrix cracks, fiber breakage or delamination. This damage is particularly dangerous because it drastically reduces the residual mechanical characteristics of the structure, and at the same time can leave very limited visible marks on the impacted surface [1].

This topic has been studied extensively in recent decades, but despite the large number of studies on composite impact, both experimentally [1–4 . . .] and numerically [5–8 . . .], a general lack of detailed validation of impact modeling exists in the literature. Currently the force-displacement curve, measured during impact, and the total delaminated area, measured by ultrasonic investigation, are correlated with numerical results. Nevertheless existing ultrasonic studies do not give accurate enough results to be able to observe the separation of each delaminated interface within the plate thickness. Therefore it is often difficult to evaluate the accuracy of the proposed models due to the lack of refined experimental data to compare them with.

This paper deals with the low velocity impact study on composite laminate, both experimentally, and numerically; although this paper is more particularly focused on modeling, an important experimental data base is used, on the one hand to verify this model on different impact conditions, on the other hand to build this model. This last point encompasses the originality of this work: using a large, refined experimental database on low velocity impact on composite laminate in order to build the proposed numerical model and in particular to choose the most appropriate way to simulate each observed damage type. Consequently some modeling types chosen in this paper are taken from conventional literature; for example the interfaces to simulate delamination damage, while we performed others ourselves, such as the "plastic-like" behavior of interfaces to simulate permanent indentation. This well-known approach can be summarized by the term "test-calculation dialogue" [9]. It enables us to better understand the experimental observations.

From an experimental view point, refined experimental investigations performed in the context of this paper, enabled us to accurately determine the different impact damage types. Conventional C-scans enabled us to determine delaminated interfaces; but in this study a particular choice of the stacking sequence and the performance of ultrasonic examination of impacted and non-impacted plate sides, led to a precise definition of each delaminated interface (Fig. 20a). This examination was also performed at different levels of impact energy, in order to evaluate the scenario of delamination formation (Fig. 27). The conventional image correlation enabled us to determine permanent indentation; but in this study the performance of this examination on impacted and non-impacted plate sides led to a precise definition of the plate deformation after impact (Fig. 19). Micrographic cuts were

performed in different planes, and after embedding the plate in resin, in order to precisely evaluate the impact damage and the phenomena responsible for permanent indentation (Fig. 12). This database of impact tests could enable other authors to evaluate and to improve their modeling on a well-documented case.

From the numerical viewpoint, a model was built in parallel with this experimental investigation to simulate as well as possible each observed damage type, i.e. matrix cracking, fiber failure and interface delamination. The inter-laminar damage, i.e. interface delamination, is conventionally simulated using interface elements based on fracture mechanics. Intra-laminar damage, such as matrix cracks, is conventionally simulated using interface elements based on failure criterion, but this failure criterion is not conventionally calculated: rather, it is measured in the neighboring volume elements to avoid stress concentrations. Theses interfaces also make it possible to simulate permanent indentation during impact unloading with nonconventional "plastic-like" behavior. And the fiber failure is simulated using conventional continuum damage mechanics, but with original formulation between the integration points of the element to dissipate a constant energy release rate per unit area. Then the model is used to study the effects of impact conditions, such as impact energy, boundary conditions, stacking sequence and impact velocity.

2 Bibliography and Outline

2.1 Permanent Indentation and Damage Tolerance Concept

The damage tolerance concept [10] was introduced in the seventies for civil aircraft structures and these requirements are expressed by the European certification JAR 25.571: "the damage tolerance evaluation of the structure is intended to ensure that should serious fatigue, corrosion or accidental damage occur within the operational life of the airplane, the remaining structure can withstand reasonable loads without failure or excessive structural deformation until the damage is detected". In the field of aeronautics, damage tolerance, for damage corresponding to impact loading, leads to dimensioning the structure according to impact detectability (Fig. 1): if the damage is not visibly detectable, i.e. when the impact indentation is less than barely visible impact damage (BVID), the structure must support the extreme loads and if the damage is detectable, i.e. when the impact indentation is bigger than BVID, another criterion must be considered, such as repair or change of the structure [11].

The BVID is defined as the minimum damage that can be detected by visual evaluation [1, 10]. In the field of aeronautics, it has been demonstrated that a permanent indentation between 0.25 and 0.5 mm is detectable during detailed visual inspection with a probability greater than 99% [12].

This concept of impact damage tolerance induces a very special design philosophy: the residual strength of the structure after impact depends on the impact damage [10] with the conventional conclusion that the greater the impact energy,

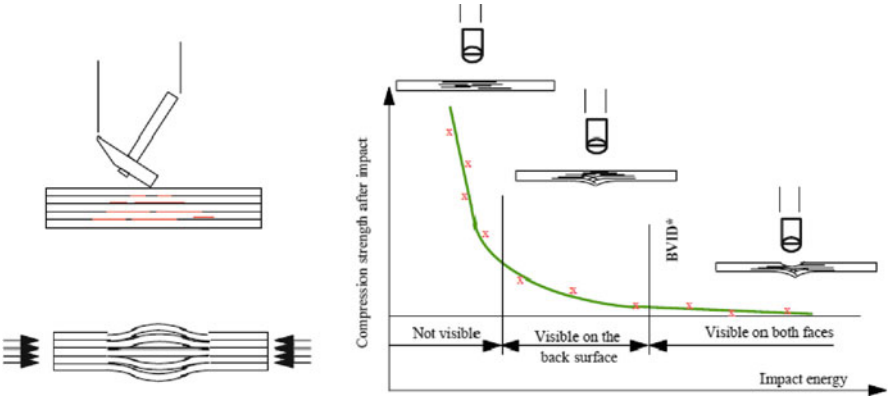


Fig. 1 Concept of impact damage tolerance: development of compression after impact, versus impact energy [10]

the greater the impact damage and consequently, the lower the residual strength. Therefore, if impact energy is known, the composite structure design is relatively conventional and the residual strength after impact should be greater than the required loads. This is for example the case for some aircraft locations where the impact energy is well known, due to statistical damage considerations. But in general, the impact energy is not known and is defined using the detectability concept. This detectability criterion makes it possible to define the BVID impact energy which is defined as the necessary impact energy to obtain a permanent indentation equal to BVID, although maximum impact energy (cut-off energy) is used to test each zone of the aircraft: consequently impact energy must not attain unreasonable values. Moreover, conventionally this BVID impact energy depends on the structure, such as material, stacking sequence, thickness, boundary conditions, or location of impact. For example, for a simple edge supported composite plate of constant thickness, the BVID impact energy will be different if the impact point is the plate centre or if it is near a supported edge.

Consequently, the optimization of a composite with the damage tolerance concept can be very complex. In particular, if this optimization is carried out using experimental tests, a large number of tests will be necessary, involving time consuming, expensive processes. For example, a series of each component is required to obtain the BVID impact energy at each impact location, and afterwards the residual strength, which has to be compared to required loads.

So the development of numerical tools is essential to the aerospace industry to optimize composite structures according to the damage tolerance concept. And the challenge is to simulate, with the same model, damage during impact and in particular permanent indentation, and the residual mechanical characteristics after impact, in order to be able to numerically optimize design of composite structures with impact damage tolerance.

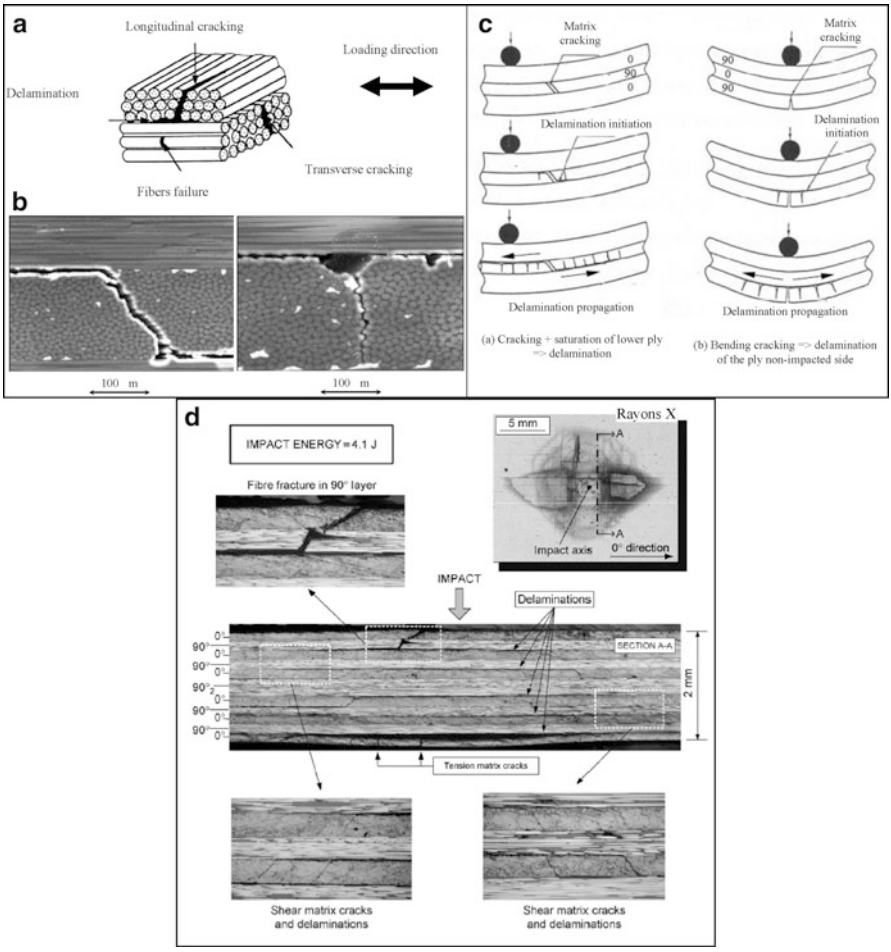


Fig. 2 Impact damage in UD composite: (**a**) different damage types [4], (**b**) damage photos [2], (**c**) principle diagram of interaction between intra- and inter-laminar damage [13] and (**d**) impact damage [14]

2.2 Impact Damage

A low velocity/low energy impact on a UD composite laminate induces three types of damage: matrix cracks, fiber fractures and delamination (Fig. 1) [2, 4, 13].

The first damage to appear is conventionally matrix cracking. When this damage grows, delamination quickly occurs. An interaction between these two damage phenomena is clearly visible during the impact tests (Fig. 2). This interaction is crucial to explain the very original morphologyof the delaminated interfaces

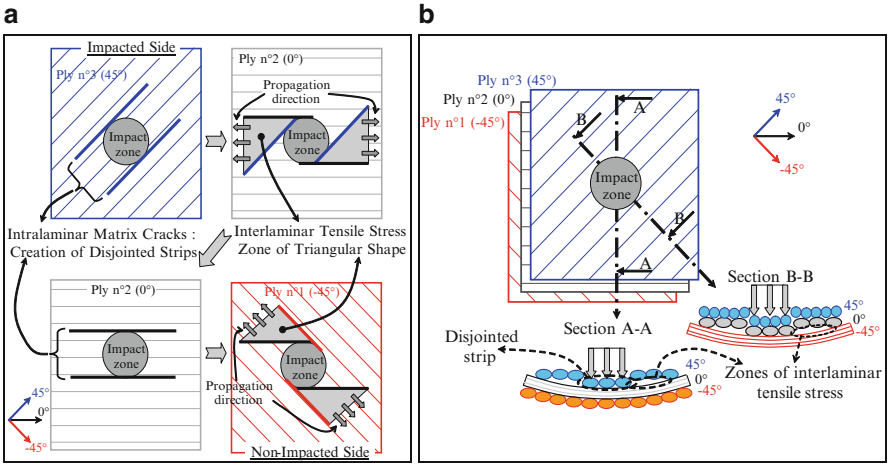


Fig. 3 Mechanism of delamination formation proposed by Renault [15]

in the thickness of the plate: a C-scan investigation shows delamination as twin triangles (Fig. 20) [8, 15] with a size growing from the impacted side to the non-impacted side.

This formation of twin triangles is illustrated by Renault [15] on a simple stacking sequence [−45, 0, 45] (Fig. 3). The impact damage begins with the development of matrix cracks in the impact zone below the impactor. These matrix cracks grow up during the loading in the fibers direction. Therefore, in each ply, a strip of fibers and resin disjoints and slides in the normal direction of this ply (z). This disjointed strip creates an inter-laminar zone of tension stress between two consecutive plies and can induce in this zone the formation of a delamination (Fig. 3a). The zone of tension stress, limited by the disjointed strips of the two adjacent plies, has triangular shape with a size growing from the impacted side to the non-impacted side. Figure 3b illustrates the inter-laminar zones of tension stress between the −45°/0° and 0°/45° plies.

This scenario enables us to illustrate some originalities of the impact damage morphology, such as delamination aligned with the fibers of the lower ply or the generally conical shape of delamination. However some questions remain subject to debate. For example, the type of delamination propagation modes (mode I, II or III) or the physical phenomenon responsible for permanent indentation are some of the numerous questions which are still largely open. To answer such questions, an impact finite element (FE) model has been created.

The key point for an impact model is interaction between intra-laminar damage, namely matrix cracks, and fiber failure, and inter-laminar damage, namely delamination. Some models in the literature [5–7, 16, 17] take into account this interaction due to explicit relations between the damage variables of matrix cracking in the ply and the damage variables of delamination between plies. Another way to

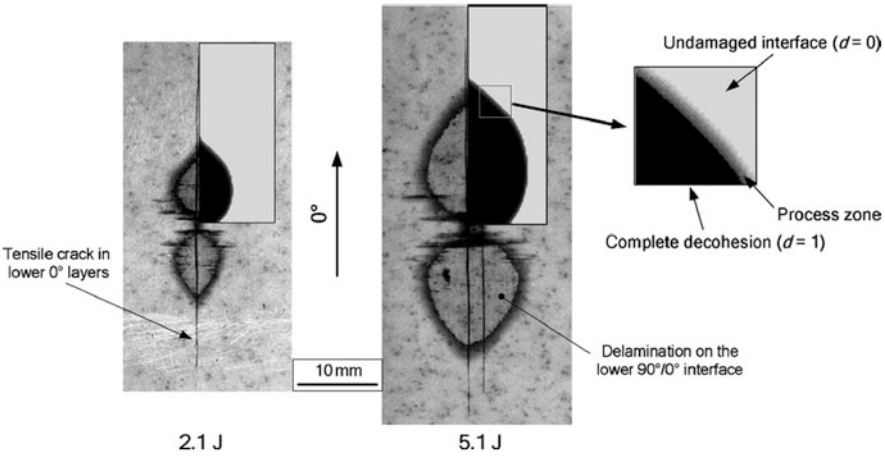


Fig. 4 Comparison of numerical predictions and experimental results [19]

model this interaction is to allow for the discontinuity created by matrix cracks, in order to naturally account for this interaction [5, 18, 19]. Indeed this discontinuity seems essential for the formation of impact damage [20] and should be modeled to correctly simulate this damage morphology.

2.3 Impact Modeling of Composite Laminate

Many authors have studied impact behavior of composite structures and their effects on residual strength, both experimentally [1–4 . . .], as well as numerically [5–8 . . .], but a lot of work is still needed to improve modeling of damage developing during impact on composite laminates and to numerically assess their residual mechanical characteristics in order to optimize their design. Therefore this short bibliography is not intended to be exhaustive, and the authors invite interested readers to consult review papers of Abrate [1], Davies and Olsson [21] or Wisnom [20], but only to show some modeling with different approaches.

For instance, a model proposed by Aymerich et al. [19] has simulated clustered ($[0_3/90_3]_S$ & $[90_3/0_3]_S$) and dispersed ($[0/90]_{3S}$) cross-ply laminates subjected to increasing levels of impact loads and have compared these numerical results to experimental observations. Cohesive interface elements have been used in 3D finite element models to simulate delamination but no matrix cracking is taken into account. They obtain a good correlation of the force-time histories, the sequence of damage events, the energy threshold and the size and shape of delamination. They conclude that initiation and growth of delamination are globally well reproduced in spite of a lack of simulation of the pre-existing matrix cracks in adjacent layers (Fig. 4).

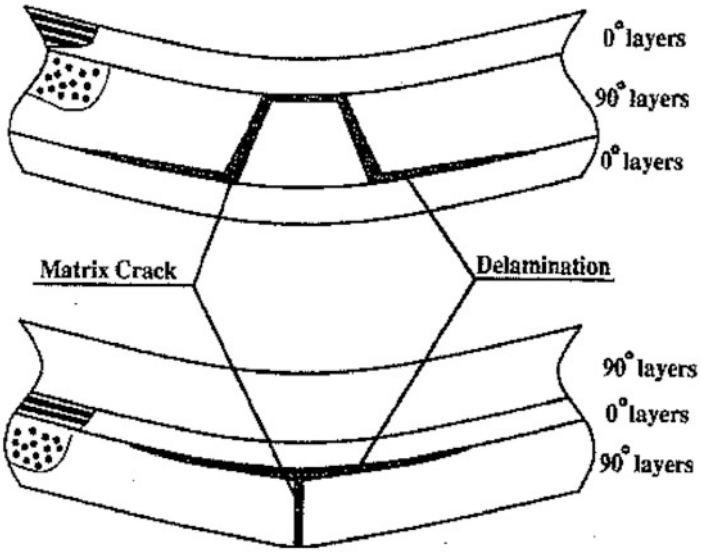


Fig. 5 Impact damage mechanisms. *Top*: delamination induced by inner shear cracks. *Bottom*: delamination induced by surface bending crack [6]

It is generally established in the literature [20, 22, 23] that matrix cracking seems to have a precursor role in delamination. Nevertheless Aymerich et al. conclude that the poor correlation between simulated and experimental delamination on the dispersed stacking sequence needs to be identified and in our opinion these discrepancies could be due to this lack of a matrix cracking model. For example, Choi and Chang [6] studied the onset of delamination during impact loading and showed a coupled criterion of delamination and matrix cracking is necessary to explain delamination. In particular, they introduced 2 types of delamination: delamination induced by inner shear cracks and delamination induced by surface bending cracks (Fig. 5).

They used a delamination criterion which decreases in the presence of matrix cracks and delamination is supposedly impossible without matrix cracking of the lower or upper ply. This idea is also used by Ladeveze et al. [24] who showed the coupling between inter-ply and intra-ply damage using a micro-mechanical model. Indeed they show that interface damage depends largely on matrix micro-cracking and local delamination (Fig. 6).

Moura and Gonçalves [7] have built an interface element with softening behavior to simulate delamination, as well as matrix cracking. These interface elements of matrix cracking are situated only where damage is detected during an experimental test, which is of course a limitation for a predictive model. The simulations are quite in accordance with experiments, although the delamination is overestimated and the matrix cracks underestimated.

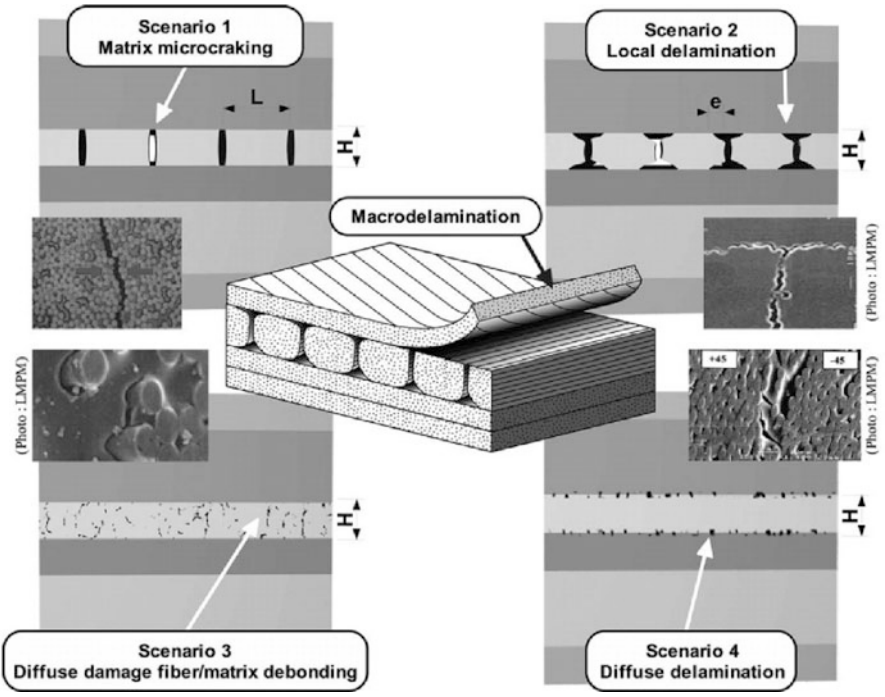


Fig. 6 The mechanisms of degradation on the micro-scale [24]

Zhang et al. [25] performed a similar study on $[0_4/90_4]_S$ carbon epoxy laminate plates. They showed that the modeling of the main matrix crack of the 0° ply, non-impacted side, is sufficient to obtain the correct size and shape of the delamination of the first interface non-impacted side. A previous study by Lammerant and Verpoest [26] have shown in the same way that the delamination shape depends primarily on the first matrix cracks and have concluded that the existence of matrix cracks cannot be disregarded when calculating delamination development.

So if the coupling between matrix cracking and delamination seems necessary to properly simulate delamination development during an impact, some numerical solutions seem possible. The coupling can be direct; the delamination criterion depends on the matrix cracking of the lower and upper plies, which induces a numerical exchange between delamination elements and matrix cracking elements. Or the coupling can be indirect by considering that the intra-ply damage representation is good enough to account for the intra-ply degradation and to naturally take this coupling into account. In general, this is the method adopted when matrix cracking is simulated using interface elements and this is the approach taken in the present work.

Nevertheless some numerical studies in the literature seem to give good correlation with experiments in spite of the lack of coupling between matrix cracking

and delamination. For example, Tita et al. [27] simulated low velocity impacts on thin composite laminates with complex stacking sequence $[45/-45/45/0/90]_S$ with uncoupled intra-ply and inter-ply damage models based on continuum damage mechanics. The simulation agrees relatively well with the experimental data, even if authors do not correlate the delaminated interfaces.

Johnson et al. [28] combined continuum damage mechanics for in-plane failure with interface elements based on the critical energy release rate for delamination. This model seems to correlate well with the dynamic response and the damage zone. Iannucci and Willows [29, 30] used interface elements to model delamination between plies, based on the critical energy release rate, and continuum damage mechanics to take into account intra-ply damage based on total energy dissipated for each damage mode. Afterwards this model was used to simulate impact on woven composite plate but due to computational constraints, the plate was only divided into two sub-laminates and only one delaminated interface could be obtained. Nevertheless, the numerical correlation with the experimental results seems relatively good.

Before finishing with this bibliography on low velocity impact modeling, and without performing a bibliography on models of compression after impact, Faggiani and Falzon's [17] work should be noted, because as far as we know, it is the only model in the literature used to simulate impact and compression after impact tests on a real structure. Indeed Faggiani and Falzon simulate the impact damage and the residual strength under compression of a stiffened composite panel. To do this, an intra-laminar damage model, based on continuum damage mechanics, is coupled with interface elements, based on the critical energy release rate. The permanent indentation after impact of the panel is also simulated using nonlinear shear formulation of the intra-laminar damage model. Faggiani and Falzon observe that this deformation should be significant in predicting the compression after impact response of the panel. The numerical correlation on time-force history, on damage shape and on residual strength seems to be good. Nevertheless insufficient knowledge of the real impact damage obtained experimentally makes it difficult to evaluate the reliability of this model. In particular the ultrasonic investigations (C-Scan) given in this study are not experimentally reproducible to determine the delaminated interface shapes and other experimental examinations, as micrographic cuts or subsequent inter-correlation using images during compression after the impact test, are needed to evaluate the reliability of the model. However this conclusion is generally valid for many models in the literature and experimental investigations of impact tests are often insufficient to evaluate the domain of their validity. Moreover this correlation, between numerical and experimental results is fundamental to drive a "test-calculation dialogue", i.e. to be able to validate a model through experimental results, as well as to better understand the experimental results via numerical results.

2.4 Outline

The goal of this study is to drive a "test-calculation dialogue" on the composite impact test. At the same time it is necessary to perform a refined experimental study of the different impact damage types, and to build a numerical model able to simulate these observations. Indeed the bibliography shows a general lack of detailed validation of impact modeling and an original aspect of the present study is to use refined, complementary experimental data to build and validate a numerical model. The experimental examinations are used, such as C-scans of impacted and non-impacted sides for different impact energy levels, micrographic cuts in different planes, evaluation of permanent deformation of the plate on impacted and non-impacted sides, or more standard force-displacement curves during impact.

The first section (Sect. 3) deals with the modeling principle of the different damage types developed during impact. The three most common damage types are simulated: matrix cracking, delamination and fiber failures. The modeling choices will be presented and explained using the experimental examinations and the bibliography results. In particular, original formulations are proposed for matrix cracking, fiber failure, and permanent indentation modeling.

The next section (Sect. 4) deals with the experimental validation. An impact reference case has been chosen to evaluate the accuracy of the proposed model. In practical terms, this step is interdependent with the previous section and multiple comparisons are necessary between the numerical results and the experimental observations: this is the "test-calculation dialogue" principle. Nevertheless, these two steps are separated in order to simplify the presentation. Subsequently, the model is used for a more in-depth analysis of the distribution of dissipated energy, or fracture modes of delamination, that cannot be directly estimated from experiments.

And the last section (Sect. 5) deals with numerical validation. Other experimental impact tests have been performed with different impact energy levels, different boundary conditions, different stacking sequences, or different impact velocities, in order to evaluate the influence of each of these parameters, and also to estimate the validity domain and limitations of the model.

Finally the conclusions will show the advantages of the "test-calculation dialogue" in building a numerical model able to represent the different experimental observations.

3 Modeling Principle

3.1 Introduction

This section deals with the presentation of the modeling principle of the different impact damage types developed during impact [31]. Intra-laminar damage, i.e. matrix cracks, is conventionally simulated using interface elements based on failure

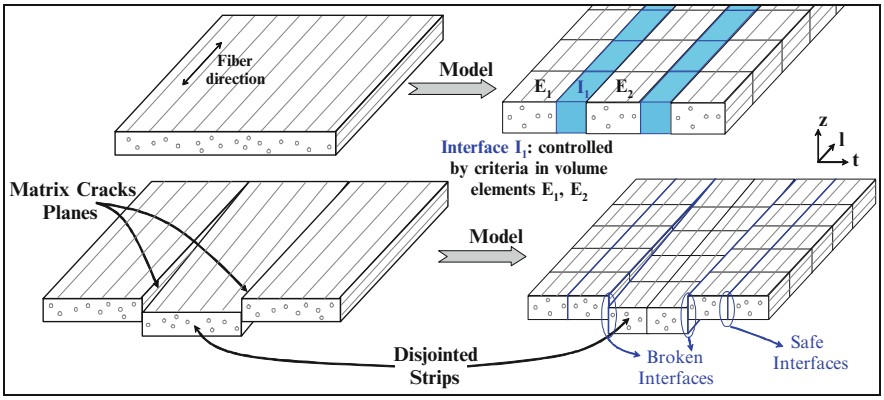


Fig. 7 Model of the ply meshed with longitudinal strips

criterion, but unlike the conventional approach, in our study, the fiber criterion is calculated in the neighboring volume elements to avoid stress concentrations. Fiber failure is simulated using conventional continuum damage mechanics, but with original formulation between the integration points of the 3D element to dissipate energy at a constant release rate per unit area. Inter-laminar damage, i.e. interface delamination, is conventionally simulated using interface elements based on fracture mechanics. And permanent indentation is modeled using the matrix cracking elements and an unconventional "plastic-like" behavior.

These modeling choices have been adopted in order to take into account the experimental observations. This is why some modeling choices are currently used in the literature, such as the inter-laminar interfaces to simulate delamination, and others are original, such as the "plastic-like" modeling of the matrix cracking interface elements to simulate permanent indentation.

3.2 Matrix Crack Modeling

Matrix cracking modeling should be able to simulate important matrix cracks as observed in the micrographs (Figs. 2b and 12) [1, 4, 20]. Moreover it should be able to simulate the interaction between matrix cracking and delamination damage which is a crucial point in impact damage formation. Then each ply is meshed separately using little longitudinal strips with one volume element in the ply thickness (Fig. 7).

Afterwards these little strips are connected together with zero-thickness interface elements normal to the transverse direction. These interface elements can account for matrix cracks in the thickness of the ply. Nevertheless this type of mesh presents some drawbacks:

- This mesh is complicated with uniform size in the impact zone. Nevertheless, it is possible to simulate an impact on a real structure using a multi-scale approach: the model described above for the area concerned with impact damage, and a conventional FE model for the remaining structure [32].
- This mesh can only simulate cracks occurring through the entire thickness of the ply and is not able to simulate small, diffusive matrix cracks. This means the propagation of matrix cracks within the ply thickness is assumed to be instantaneous. Then, if the ply thickness is not too great, the propagation of a matrix crack in the thickness takes place very quickly and its effect on the creation of the impact damage should remain local.
- This mesh can only simulate cracks normal to interfaces. However matrix cracks due to out-of-plane shear stress (τ_{tz}), are globally inclined at 45°. This hypothesis avoids the use of an overly complex mesh, and seems reasonable if the ply thickness is small compared to the laminate thickness.
- The mesh size imposes the maximum density of matrix cracks in the transverse direction of the ply. This drawback could seem very important but the presence of one matrix crack, i.e. of a broken interface, should unload the neighboring interfaces in the transverse direction and prevent their breaking. Indeed the matrix cracks, taken into account in this model, are only the largest ones, i.e. those running through the entire ply thickness, and not the little, diffuse matrix cracks. This means that the model does not take into account the network of little matrix cracks because the effect of these diffuse matrix cracks seems small compared to those running through the entire thickness.

Another consequence of this imposed maximum density of matrix cracks is the choice of the failure criterion. It would be interesting to use fracture mechanics, in addition to interface elements, to simulate the critical energy release rate [33]. But in this case, the mesh density, which is imposed a priori, induces the maximum energy possible to dissipate, except of course if the mesh is fine enough to simulate each crack. As it is not possible to simulate each matrix crack (Fig. 12) and very difficult to evaluate the maximum number of possible cracks, a model has been chosen without energy dissipation. The model ignores the energy dissipated by matrix cracking, even if a part of this energy should be included in the energy dissipated by delamination. Indeed, the DCB (Double Cantilever Beam) test, which is used to evaluate the critical energy release rate for delamination, is a comprehensive test taking into account all the damage types [34, 35]. Then the energy dissipated by the matrix cracks, accompanying the delamination, is taken into account. Nevertheless the consequence of this non dissipative model should be evaluated with other experimental tests. Another solution would be to use cohesive crack modeling to allow multiple matrix cracks per element, as proposed by Raimondo et al. [36].

Then the interface degradation is abrupt: if the material is safe, the stiffness of these matrix cracking interfaces is considered to be very high (typically 10^6 MPa/mm) and this stiffness is set to zero if matrix cracks exist. And this failure

is driven by standard criterion, similar to Hashin's criterion [37, 38], calculated in the neighboring volume elements:

$$\left(\frac{\langle \sigma_t \rangle^+}{\sigma_t^f}\right)^2 + \frac{{\tau_{lt}}^2 + {\tau_{tz}}^2}{\left(\tau_{lt}^f\right)^2} \leq 1 \tag{1}$$

Where σ_t is the transverse stress, τ_{lt} and τ_{tz} the shear stresses in the (lt) and (tz) planes, $<>+$ the positive value, σ_t^f the transverse failure stress and τ_{lt}^f the shear failure stress of the ply.

This conventional quadratic criterion [38] is written with stresses at each Gauss point of the two neighboring volume elements and the interface is broken when the criterion is reached at one of these points. This is an original point of the proposed model and can be considered as an average stress over a distance which depends on the mesh size. This mesh sensitivity will have to be studied further; this work is currently in progress.

3.3 Fiber Failure Modeling

For the fiber failures observed after impact (Fig. 12), there is no evidence of distributed fiber damage. Moreover due to the high critical energy release rate of fiber failure [39], it is necessary to dissipate this energy in the model. Additional interface elements could be used but would result in very complex meshing. Therefore, to avoid the use of such interfaces, fiber failure is taken into account using conventional continuum damage mechanics but with original formulation between the integration points of the element to produce a constant energy release rate per unit area. This approach can be compared to methods based on characteristic element length which makes possible mesh-size independent modeling [36, 40–42].

Therefore, to be able to produce the critical energy release rate due to fiber fracture per unit area of crack, the behavior laws of the eight integration points of a volume element are managed together. In this case, the law is written only in opening mode I (Fig. 8), but could be generalized with other fracture modes:

$$\int_V \left(\int_0^{\varepsilon^1} \sigma_l . d\varepsilon_l \right) . dV = S . {G_I}^f \tag{2}$$

Where σ_l (ε_l) is the longitudinal stress (strain), V (S) the volume (section) of the element, ε^1 is the strain of total degradation of the fiber stiffness (Fig. 8) and G_I^f the energy release rate in opening mode in fibers direction. It can be observed that volume elements with 8 Gauss points have been chosen to obtain good bending behavior with only one element in theply thickness.

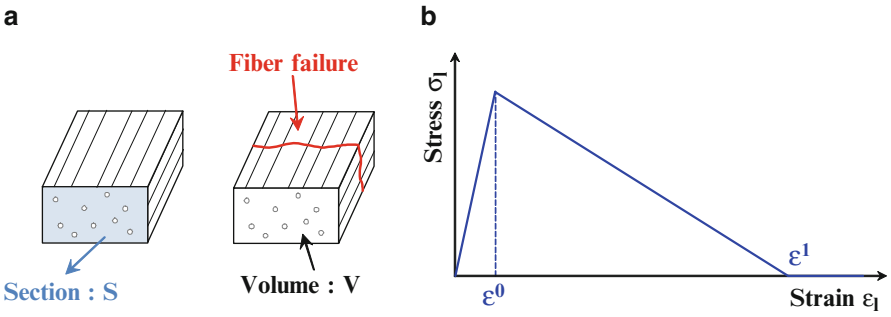


Fig. 8 Principle of fiber failure (**a**) and behavior law in the longitudinal direction (**b**)

Afterwards, the stiffness in fibers is degraded using a damage variable d_f:

$$\sigma_l = (1 - d_f).(H_{ll}.\varepsilon_l + H_{lt}.\varepsilon_t + H_{lz}.\varepsilon_z) \tag{3}$$

Where H_{ll}, H_{lt} and H_{lz} are the stiffness values in the longitudinal direction. And this damage variable is conventionally calculated according to the longitudinal strain in order to obtain a linear decrease of the longitudinal stress (Fig. 8) [42]:

$$d_f = \frac{\varepsilon^1.(\varepsilon_l - \varepsilon^0)}{\varepsilon_l.(\varepsilon^1 - \varepsilon^0)} \tag{4}$$

Where ε^1 is the strain of total degradation of the fiber stiffness calculated using the Eq. 2 and ε^0 is the strain of damage initiation.

Another originality of this fiber failure approach is to initiate the damage when the maximum of the longitudinal strains calculated at the element nodes reaches the fiber failure strain ε_l^f. The use of extrapolated strains at element nodes, rather than direct strain values at integration points, makes it easier to take into account the bending behavior of each ply with only one finite volume element in the thickness.

Moreover fiber failure due to compression or shear stress is not taken into account in this release of the model. Indeed this model has been based on a reference case (cf. Sect. 4) where these types of fiber failure does not seem appear. Nevertheless these failure types should be taken into account for other impact tests, such as impacts with different boundary conditions or with different stacking sequences (cf. Sect. 5). This work is currently in progress and could partially explain the discrepancies observed in these simulations.

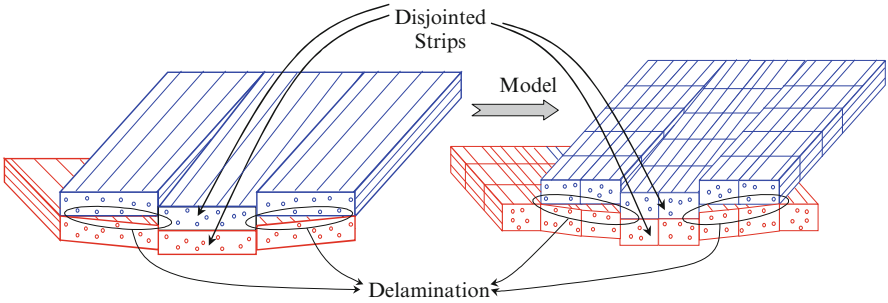


Fig. 9 Principle of the interface model between plies

3.4 Delamination Modeling

Delamination damage consists of important cracks between plies (Figs. 12 and 18) [6, 10, 13]. It is typically modeled with cohesive interface elements based on fracture mechanics [33, 43]. This modeling choice makes it possible to correctly take experimental observations into account and has been adopted in this study.

Then after the different plies are meshed with volume elements and matrix crack interface elements, two consecutive plies are joined using zero-thickness interface elements (Fig. 9). These delamination interface elements are conventionally softening interfaces [33, 43] of zero thickness driven by fracture mechanics. They are written in mixed fracture mode (mode I, II, III) to simulate the energy dissipated by delamination. Moreover the shearing (II) and tearing (III) fracture modes are combined and in the following, the term of mode II will be abusively used to name the fracture modes II and III. And in order to represent the overlap of 2 consecutive plies, the 0° and 90° plies are meshed with square elements and the 45° and −45° plies are meshed with diamond-shaped elements (Fig. 10).

Then, an equivalent displacement is written in order to simulate a linear coupling law between the fracture modes:

$$d_{eq} = \sqrt{\left(\langle d_I \rangle^+\right)^2 + \left(\frac{{d_I}^0}{{d_{II}}^0}.d_{II}\right)^2 + \left(\frac{{d_I}^0}{{d_{III}}^0}.d_{III}\right)^2} \tag{5}$$

Where d_I, d_{II} and d_{III} are the displacements respectively in the z, l and t directions, $\mathbf{d_I^0}$, $\mathbf{d_{II}^0}$ and $\mathbf{d_{III}^0}$ are the critical displacements respectively in the z, l and t directions, calculated according to failure stresses (Fig. 11):

$${d_I}^0 = \frac{{\sigma_I}^0}{{k_I}^0}; \quad {d_{II}}^0 = \frac{{\sigma_{II}}^0}{{k_{II}}^0}; \quad {d_{III}}^0 = \frac{{\sigma_{III}}^0}{{k_{III}}^0} \tag{6}$$

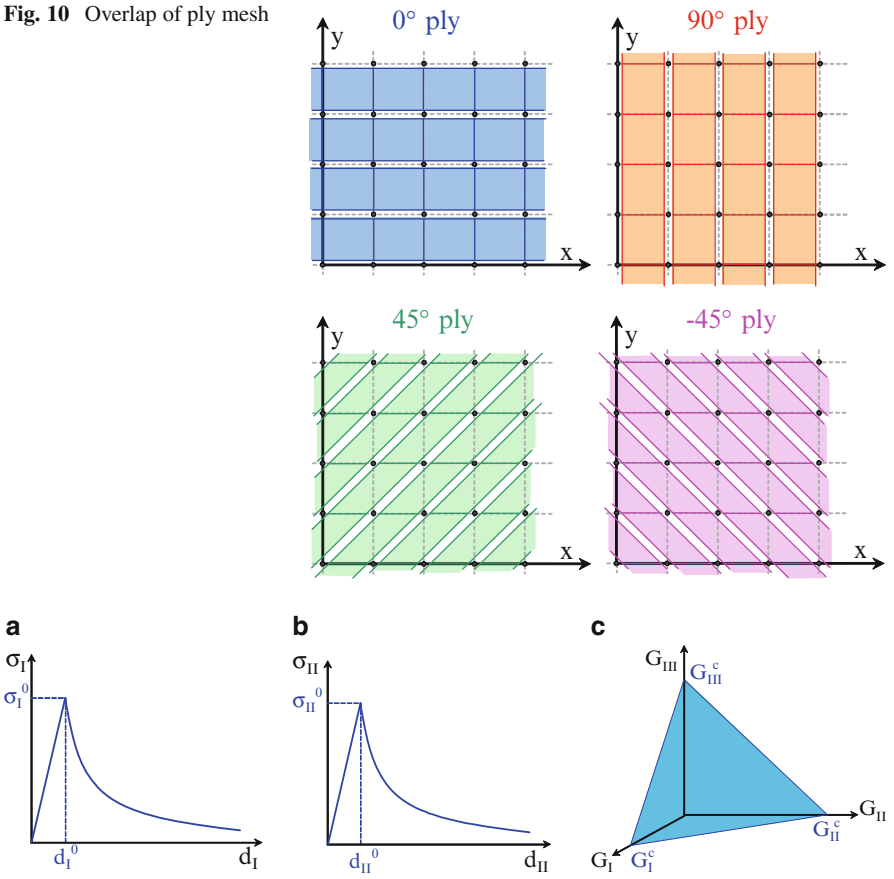


Fig. 10 Overlap of ply mesh

Fig. 11 Evolution of the stress-displacement curves in mode I (**a**) and II (**b**) and linear mixed fracture mode (**c**)

Where $\mathbf{k}_{\mathrm{I}}^{0}$, $\mathbf{k}_{\mathrm{II}}^{0}$ and $\mathbf{k}_{\mathrm{III}}^{0}$ are the stiffness values respectively in the z, l and t directions and σ_{I}^{0}, σ_{II}^{0} and $\sigma_{\mathrm{III}}^{0}$ are the critical stresses respectively in the z, l and t directions. And the 2 shear directions are assumed to be equivalent:

$$d_{III}{}^{0} = d_{II}{}^{0}; \quad k_{III}{}^{0} = k_{II}{}^{0}; \quad \sigma_{III}{}^{0} = \sigma_{II}{}^{0} \tag{7}$$

And to avoid additional material parameters, the critical stresses are assumed to be equal to the failure stresses of the ply:

$$\sigma_{I}{}^{0} = \sigma_{t}{}^{f}; \quad \sigma_{II}{}^{0} = \sigma_{III}{}^{0} = \tau_{lt}{}^{f} \tag{8}$$

Table 1 Material parameters

E_l^t (GPa)	E_l^c (GPa)	E_t (GPa)	ν_{lt}	G_{lt} (GPa)	σ_t^f (MPa)	τ_{lt}^f (MPa)
130	100	10	0.29	4.8	50	90
ε_l^f	G_I^d (N/mm)	G_{II}^d (N/mm)	G_I^f (N/mm)	ε_t^0	k_t (MPa/mm)	
0.016	0.5	1.6	133	0.02	10,000	

Then a decreasing exponential law is chosen to avoid the shock of the final fracture:

$$\begin{cases} \sigma_I = {\sigma_I}^0.\exp\left(-\beta.(d_{eq} - {d_I}^0)\right)\ \dfrac{d_I}{d_{eq}} \\ \sigma_{II} = {\sigma_{II}}^0.\exp\left(-\beta.(d_{eq} - {d_{II}}^0)\right)\ \dfrac{d_{II}}{d_{eq}}\dfrac{{d_I}^0}{{d_{II}}^0} \\ \sigma_{III} = {\sigma_{III}}^0.\exp\left(-\beta.(d_{eq} - {d_{III}}^0)\right)\ \dfrac{d_{III}}{d_{eq}}\dfrac{{d_I}^0}{{d_{III}}^0} \end{cases} \tag{9}$$

Where the coefficient β is determined to reproduce the energy release rate G_I^d in mode I under the stress-strain curve and G_{II}^d in mode II and III (Fig. 11):

$$\beta = \frac{1}{\frac{{G_I}^d}{{\sigma_I}^0} - \frac{{d_I}^0}{2}} \tag{10}$$

and the use of the same β coefficient for modes I, II and III imposes:

$${k_{II}}^0 = {k_{III}}^0 = \frac{\left({\sigma_{II}}^0\right)^2}{{G_{II}}^d}\left(\frac{1}{2} + \frac{1}{\beta.{d_I}^0}\right) \tag{11}$$

And the last undetermined coefficient ${k_I}^0$ (Table 1) is considered very high (typically 10^6 MPa/mm). It can be observed that a linear mixed mode of fracture is imposed (Fig. 11c) due to the choice of the equivalent displacement (Eq. 5).

This model adopted for delamination is often used in the literature [5, 20, 33] even if this expression (Eq. 5) is original. The definition of this equivalent displacement enables us to automatically compare all the possible mode ratios of displacement and how much energy should still be available to dissipate until total fracture occurs. Indeed during complex loading, with large variation in the mode ratio, it is not so easy with conventional formulation to evaluate this remaining energy to be dissipated [33, 44].

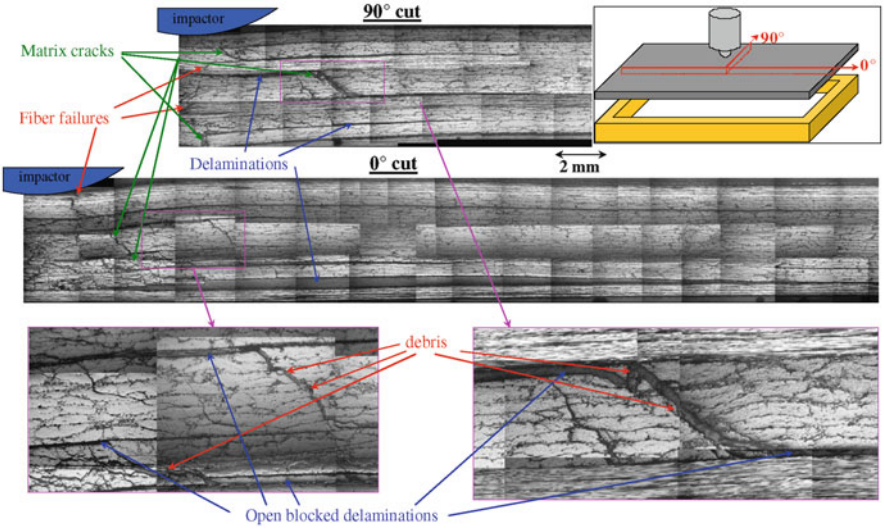


Fig. 12 Micrographic cuts after 25 J-impact

3.5 Permanent Indentation

Permanent indentation, i.e. the dent depth of the impact point, is a crucial aspect for the certification of composite structures with damage tolerance concepts [10–12]. Indeed the size of such an indentation determines whether impact damage can be detected or not. Moreover, in order to be able to use this model in the future to totally simulate impact damage tolerance design, permanent indentation has been taken into account through the intra-ply interfaces. Although some authors have worked on the permanent indentation phenomenon [3, 45–50], a lot of work is still necessary to physically understand this phenomenon and to correctly model it. Currently this residual deformation after impact is explained, for thermoset resin as epoxy, with "plasticity". Indeed this type of resin presents important permanent deformation after testing, particularly under shear stress [51], similar to plasticity deformation. But another phenomenon responsible for permanent indentation seems to be impact debris in 45° cracks through the ply thickness (Fig. 12) [52]. This phenomenon has been taken into account in the present model using an original "plastic-like" behavior in the matrix cracking elements.

In order to study the phenomenon of permanent indentation, laminated plate was cut after being embedded in resin to prevent relaxation (Fig. 12). These photos were taken after a 25 J-impact test on a UD laminate (cf. Sect. 4.1). In this photo, debris in the 45° matrix cracks seem to block their closure and to hold the adjacent delamination open. This phenomenon is schematically presented in Fig. 13 and could explain part of permanent indentation.

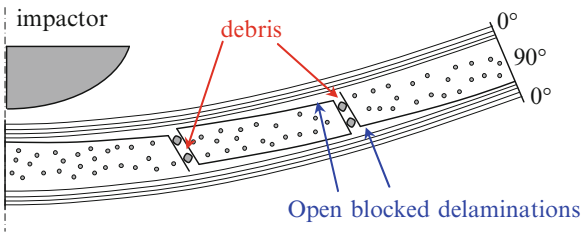


Fig. 13 Principle of producing permanent indentation

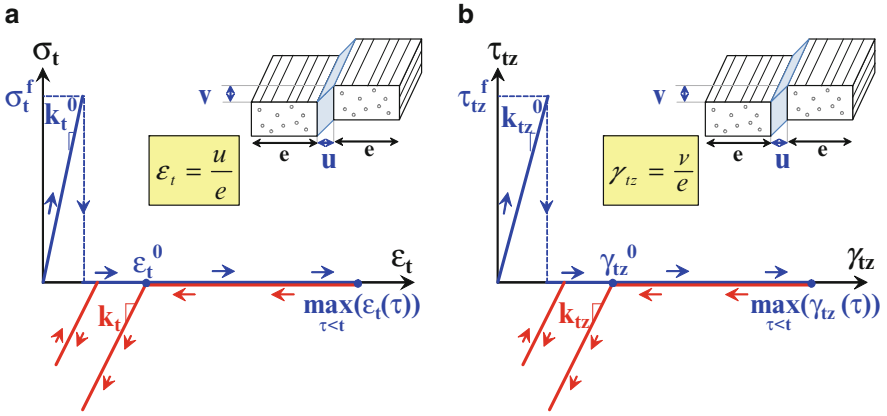


Fig. 14 Permanent indentation model in tension (**a**) and shear (**b**)

Nevertheless, this phenomenon cannot fully explain permanent indentation and other phenomena, such as "plasticity" or compaction of resin (due to initial porosity) or friction of delaminated interfaces, matrix cracks or fiber/resin debonding, may play a role. However the permanent indentation seems to a great extent to be due to the blockage of debris and this phenomenon was taken into account in the proposed model. To do this, a "plastic-like" model was introduced in the matrix cracking interfaces in order to limit their closure after failure under tension (σ_t) and out-of-plane shear (τ_{tz}) (Fig. 14):

$$\begin{cases} \varepsilon_t \geq \min\left(\max_{\tau\leq t}\left(\varepsilon_t(\tau)\right), {\varepsilon_t}^0\right) \Rightarrow \sigma_t = 0 \\ \varepsilon_t < \min\left(\max_{\tau\leq t}\left(\varepsilon_t(\tau)\right), {\varepsilon_t}^0\right) \Rightarrow \sigma_t = k_t.\left(\varepsilon_t - \min\left(\max_{\tau\leq t}\left(\varepsilon_t(\tau)\right), {\varepsilon_t}^0\right)\right) \\ \gamma_{tz} \geq \min\left(\max_{\tau\leq t}\left(\gamma_{tz}(\tau)\right), {\gamma_{tz}}^0\right) \Rightarrow \tau_{tz} = 0 \\ \gamma_{tz} < \min\left(\max_{\tau\leq t}\left(\gamma_{tz}(\tau)\right), {\gamma_{tz}}^0\right) \Rightarrow \tau_{tz} = k_{tz}.\left(\gamma_{tz} - \min\left(\max_{\tau\leq t}\left(\gamma_{tz}(\tau)\right), {\gamma_{tz}}^0\right)\right) \end{cases} \quad (12)$$

Where k_t and k_{tz} are the stiffness values of debris and ${\varepsilon_t}^0$ and ${\gamma_{tz}}^0$ the maximum dimensionless sizes (size divided by width) of these debris respectively in the normal direction and in shear.

If the crack is assumed at 45° in the (tz) plane these two stiffness values and debris sizes are equivalent and are assumed to be equal:

$$k_t = k_{tz}; \quad {\varepsilon_t}^0 = {\gamma_{tz}}^0 \tag{13}$$

Consequently, only two material parameters are necessary to take into account the phenomenon of permanent indentation. These two parameters are difficult to relate to conventional material parameters measured in conventional tests and are directly determined using the reference impact test (cf. Sect. 4). Therefore this evaluation process limits the predictive character of this model, and in particular for the part linked to permanent indentation. Other works are actually in progress in order to evaluate these parameters with other and simpler experimental studies. It can be observed that these two parameters are the only ones of this model which are directly determined in the impact test: all other values are obtained from conventional experimental tests described in the literature [34–36, 39, 42, 44, 53].

This no-closure model integrated into the interface elements of matrix cracking makes it possible to obtain a deformed shape of the plate, not only during impact but also after impact, and a permanent indentation (Fig. 17b). It can be observed that this permanent indentation modeling has little effect on damage morphology, in particular delamination, matrix cracks and fiber failure, but principally the deformed shape, and that a modification of the values of the 2 associated parameters does not affect significantly simulated delamination.

3.6 Conclusion of Modeling Principle

A numerical model has been elaborated in order to simulate the different impact damage types developing during impact. The three current damage types: matrix cracking, delamination and fiber failures, are simulated. The modeling choices have been determined by the experimental investigations and the bibliography results.

Compared to existing models of the literature, the main originalities of the model in order to simulate the observed damage are:

- the use of interfaces for matrix cracking, with a failure criterion calculated in the neighboring volume elements,
- the use of volume elements with original formulation at the 8 integration points to control fiber failure based on fracture mechanics,
- the use of cohesive elements with a “plastic-like” behavior to simulate permanent indentation.

4 Experimental Validation Using a Reference Case

4.1 Introduction

This section deals with experimental validation. An impact reference case has been chosen to evaluate the accuracy of the proposed model. As mentioned above, this step is not independent of the previous section and many comparisons of the numerical results and the experimental observations were required: this is the principle of the "test-calculation dialogue". However, these comparisons are not presented here for the purpose of simplicity.

Comparisons between experimental and numerical results were carefully performed using numerous refined experimental studies. The force-displacement and force-time curves were compared and show consistent agreement. The plate deformation numerically obtained after impact also compared well with micrographic cuts and with permanent deformation measured through image correlation. The numerically obtained delaminated interfaces were successfully compared with C-scan on the impacted and non-impacted sides of the plate.

Finally the model is used to highlight some experimental results. It enabled us to highlight the formation of delamination of the first interface on the non-impacted side or to evaluate the distribution of dissipated energy during an experiment. This work is the second step of the "test-calculation dialogue", i.e. to better understand the experimental results in comparison to the numerical results.

4.2 Experimental and Numerical Comparison

The proposed model is used to simulate an experimental impact test, considered as a reference case, on 100×150 mm^2 laminate plate manufactured with T700/M21 UD carbon/epoxy composite. This plate, with stacking sequence $[0_2, 45_2, 90_2, -45_2]_S$ is simply supported by a 75×125 mm^2 window (AITM 00-10) and impacted at 25 J with a 16-mm diameter 2-kg impactor of (Fig. 15). Only the half plate is meshed due to symmetry considerations, the boundary conditions are imposed due to contact with a fixed rigid body and the impactor is assumed to be non-deformable (Fig. 15c). The mechanical characteristics of this material and the material parameters used in this model are summarized in Table 1.

Where E_l^t (E_l^c) is the tension (compression) Young's modulus in the fiber direction, E_t is the Young's modulus in transverse direction, ν_{lt} is the Poisson's ratio, G_{lt} is the shear modulus. As mentioned above, it can be observed that the ε_t^0 and k_t are the only two parameters directly determined using the impact test: all other values come from conventional experimental tests in the literature [34–36, 39, 42, 44, 53].

The comparisons between experimental and numerical curves of impact force versus time and impactor displacement are illustrated in Fig. 16. A good correlation

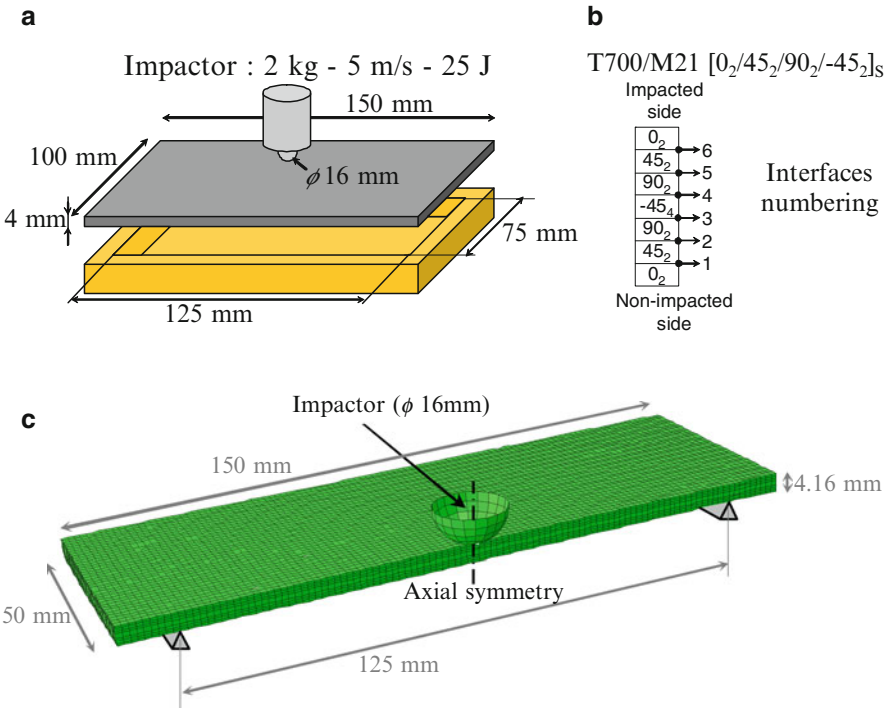


Fig. 15 Reference case: impact set up (**a**), draping sequence of the laminate (**b**) and finite element model (**c**)

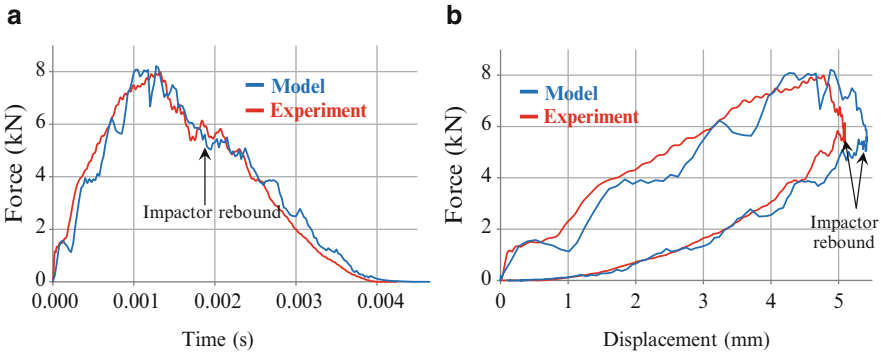


Fig. 16 Curves of force versus time (**a**) and displacement (**b**) obtained experimentally and numerically

is obtained between the experiment and model, demonstrating that the real impact damage is well account for in the numerical simulation. In particular the unloading is well simulated, while dissipated energy, corresponding to the area of the force-displacement curve, is correctly reproduced (Fig. 16b). The study of the dissipated

energy during an impact test is of primary interest because detailed knowledge of these parameters enables us to classify the different kinds of damage. For example, to design a more tolerant structure, it may be useful to favor a more dissipative damage phenomenon, inducing less effect on residual strength. This classification of energy dissipated by the different damage phenomena will be discussed in more detail in the next paragraph.

In Fig. 17a, the deformed shape of the plate, obtained numerically, is represented in three cut planes 0°, 45° and 90°. Of course, each cut angle corresponds to the ply orientation, therefore in the 0°, 45° and 90° cuts, the fiber directions of the 0°, 45° and 90° plies, respectively, are approximately horizontal in the plane of the diagram. This deformed shape is obtained for 1.9 ms, corresponding to the maximum displacement, about 6 mm, reached during the 25 J-impact. The displacement indicated in the figure is the z-displacement, corresponding to the normal direction. The displacement is maximum, corresponding also to the impactor stop, i.e. at null velocity before the rebound, but the force is decreased from its maximum value to about 1.3 ms. It is due to the numerous fiber failures developing in the plate's central zone below the impactor, inducing a decrease of the impact force from 8 to 6 kN.

Some major damage is clearly visible in Fig. 17a. For example, the first ply, non-impacted side, is clearly broken in the transverse direction, which is visible in the 90° cut. It can be also observed that, for an impact of 25 J, this ply is not broken in the fiber direction. This transverse crack corresponds to the conventional crack observed after impact on the non-impacted side [14]. Delamination is also observable, in the very large opening of the first interface, non-impacted side, on the 0° cut. The significant delamination of this interface is conventionally observed experimentally through C-Scan (Fig. 19). The central zone below the impactor is also severely damaged, as in the experiment (Fig. 12).

In Fig. 17b, the numerically obtained deformed shape of the plate after impact, is illustrated. This deformed shape is obtained for 4.3 ms, corresponding to the end of the impact test. At this time, corresponding to the impactor rebound, a weak oscillation is still present in the plate, but we have verified that deformation of the plate is very close to the permanent deformation reached after a longer time. At this time, the impact damage is still visible, even if most of the interfaces are partially closed.

Of course, the deformed shape of the plate, obtained during the impact test (Fig. 17a) cannot be compared with experimental data because it is nearly impossible to stop impact during the test to perform micrographic cuts. But the deformed shape of the plate, obtained after impact (Fig. 17b) can be compared with micrographic cuts (Fig. 18): the plate is cut in 0°, 45°, 90° planes and polished before examination with an optical microscope. Nevertheless, it is important to have the plate embedded in resin beforehand, to prevent the relaxation of the permanent indentation. In spite of this precaution, about 30% of the permanent indentation is relaxed during the specimen preparation. If we compare the experimental micrographic cuts with the numerical results, a good correlation is found. For example, the first interface, non-impacted side, remains open on the model, like in the experiment,

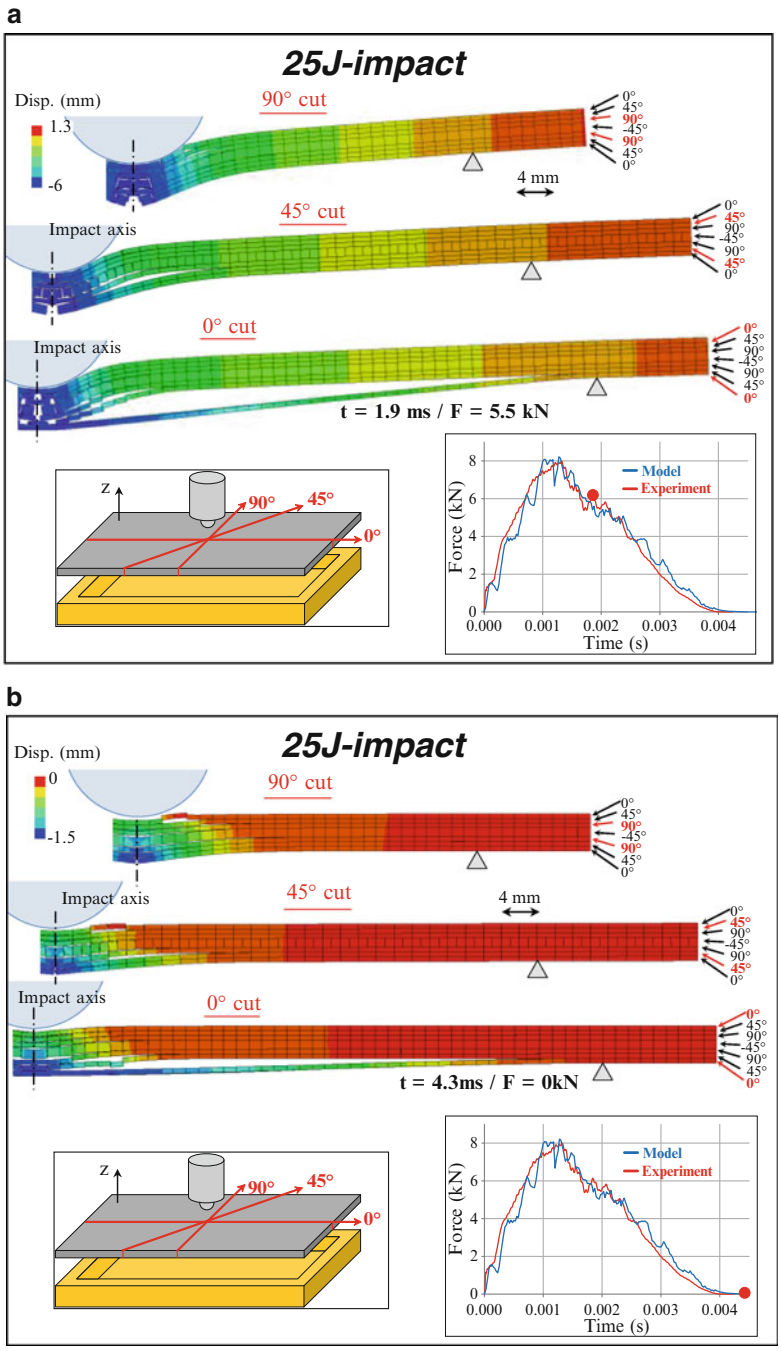


Fig. 17 Deformed mesh during 25 J-impact: (**a**) at maximum displacement – (**b**) after impact

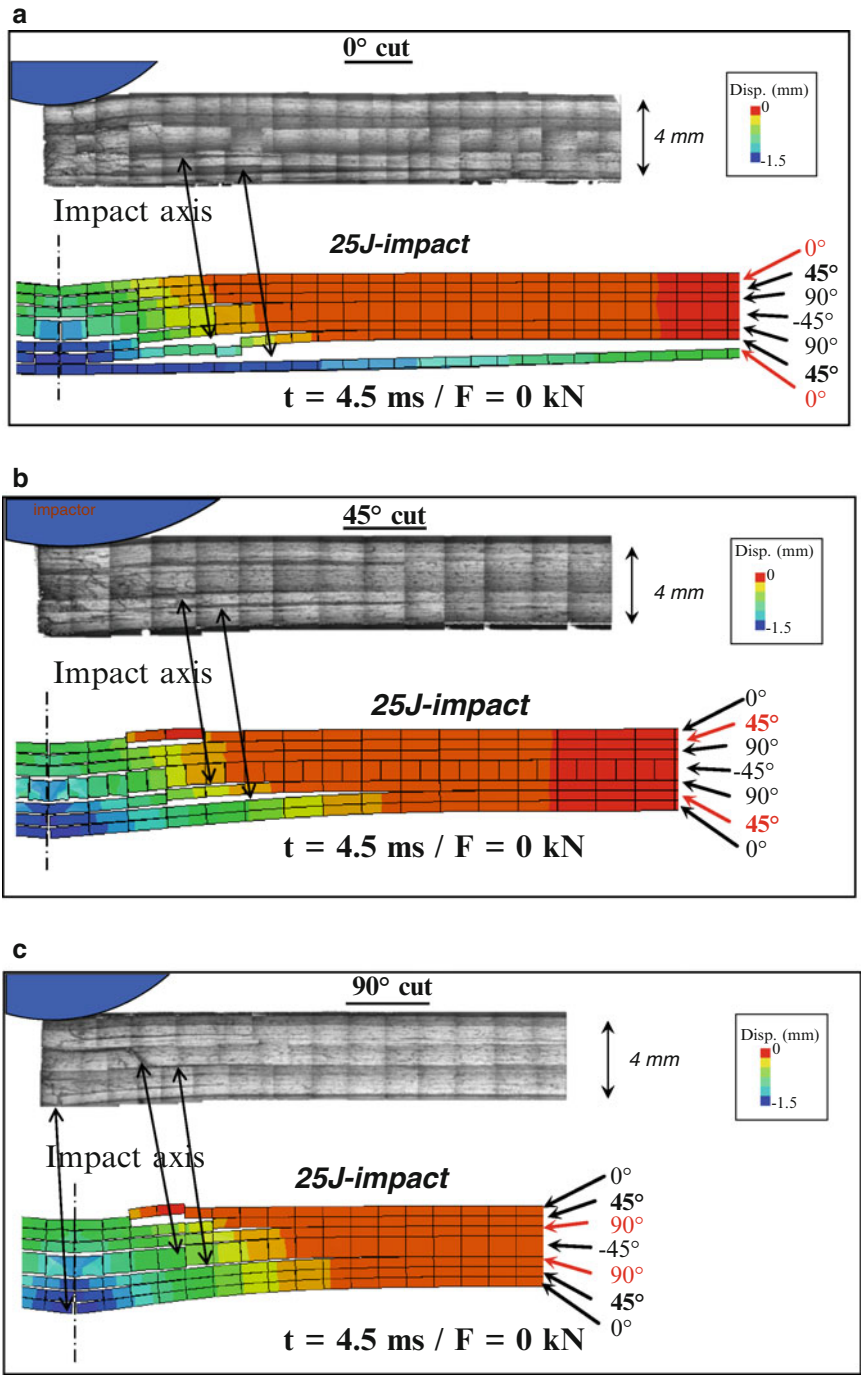


Fig. 18 Comparison between numerically and experimentally deformed shapes in the 0° (**a**), 45° (**b**) and 90° (**c**) planes

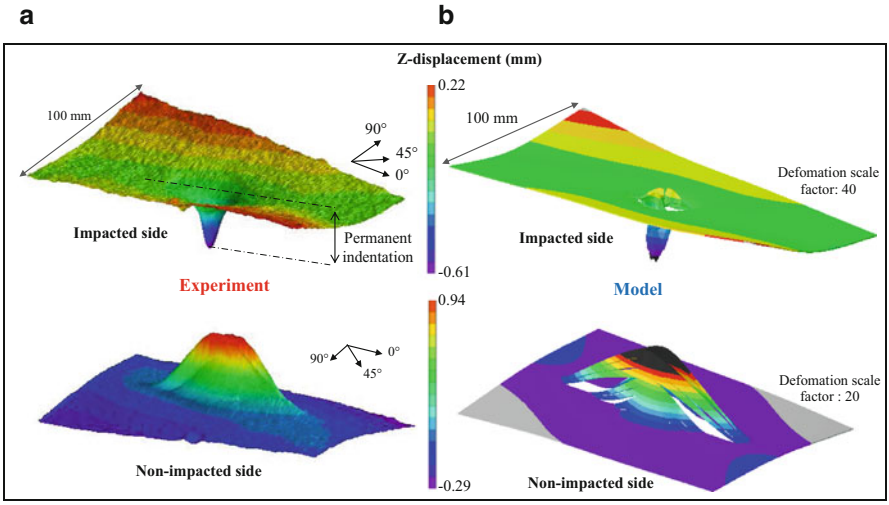


Fig. 19 Deformed plate after a 25 J-impact: experimental (**a**) and numerical (**b**) results

even if the opening is smaller in the experiment. Similar observations can be made on the 45° and 90° cuts. These differences can be explained partly by the relaxation of the experimental permanent indentation, which can be due to the cutting operation mentioned above, as well as due to the relaxation naturally observed after impact. Indeed a relaxation of about 30% is observed in the 48 h after impact [52] which is not taken into account by the model. Moreover the model of permanent indentation used is based on the debris blocking phenomenon and other phenomena such as resin "plasticity", and the relaxation of this "plasticity" are not taken into account.

Then the deformed plate resulting from the 25 J-impact was plotted on the impacted and non-impacted sides (Fig. 19). The experimental results were obtained with Vic3D image correlations and the numerical results were obtained from the finite element calculations. The permanent indentation is clearly visible on the impacted side, but is difficult to define because the plate is twisted. We chose to define it by the distance between the lowest line of the twisted plate and the lowest point of the plate, i.e. at the impact point. In this case, a value of about 0.5 mm is obtained. The plate shape after impact was accurately simulated by the numerical model, and in particular, the general twisted shape of the plate was reproduced. The orientation of the twisted shape, in the diagonal the nearest to the 45° ply, is due to the $[0_2, 45_2, 90_2, -45_2]_S$ draping sequence which induces a higher bending stiffness in this direction. In practical terms, the bending stiffness D_{11} is about 3.6×10^5 N·mm in the 45° direction compared to 1.8×10^5 N·mm in the −45° direction.

This twisted shape is also visible on the non-impacted side, in both the experimental and numerical results. Moreover the deformation of the impact point is larger than on the impacted side. For example, in the Z direction, the permanent indentation is about 1 mm compared to 0.5 mm on the impacted side. On the

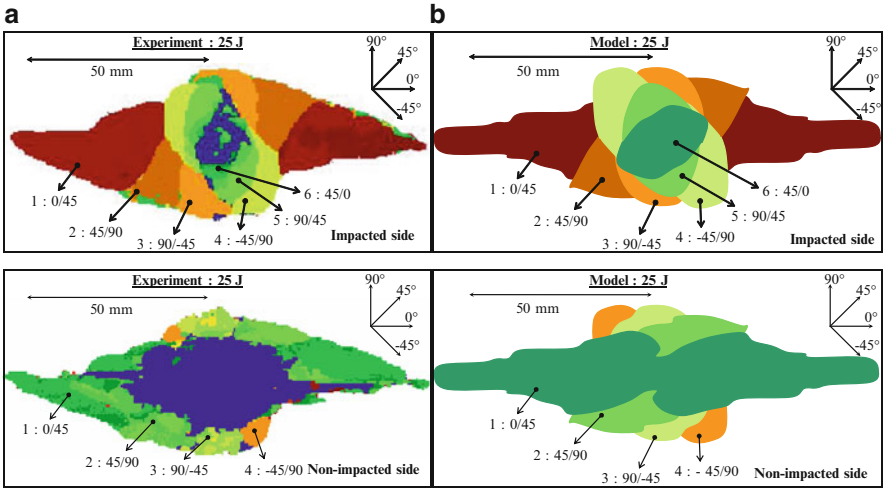


Fig. 20 Comparison between delaminated interfaces obtained experimentally (**a**) and numerically (**b**) from a 25J-impact test

non-impacted side, the terms of the impact point and the permanent indentation have been exaggerated to simplify the discussion. This higher indentation on the non-impacted side is due to the increased plate thickness in the impacted zone. This phenomenon is also visible in the micrographic cuts (Fig. 18), although it is lower, probably due to the cutting and polishing processes. It is generally simulated by the modeling but is amplified. Indeed, the black zone (Fig. 19b) represents Z-displacements above 0.94 mm, the highest experimental value, and the grey zone represents Z-displacements below −0.29 mm, the lowest experimental value obtained. Moreover the experimental and numerical scales are set to a constant and were correlated to half scale (green color). Moreover it can be observed on the numerically obtained, non-impacted side of the deformed shape, openings exist between consecutive fiber strips (white colored zone). These opening are artificial and due to the large deformation scale factor.

The deformed zone is also higher in the 0° plane of the non-impacted side, compared to the impacted side. This phenomenon is also generally simulated by modeling even if it is amplified.

In Fig. 20, delaminated interfaces obtained by calculation are compared to the experimentally obtained results, on the impacted and non-impacted sides. The accurate correlation between experimental and numerical results tends to confirm the relevance of the model, and in particular the model of interaction between inter and intra-laminar damage. As mentioned above, the shape of the delamination is closely linked to the interaction between matrix cracks and delamination [4, 6]. In particular, the orientation of delamination with the fibers of the lower ply or the special shape of the first interface of the non-impacted side are well simulated. Moreover this first delamination shape seems to be nearly separated into two parts,

as for the experimental results, although in the C-scan, the extensive matrix cracking of the first ply of the non-impacted side makes this observation difficult. To confirm this result, a comparison was performed between the delamination of the first numerically obtained interface and the C-Scan examination performed on the non-impacted side at different impact energy levels (Fig. 20).

This figure confirms the almost complete separation into two parts of this delamination which is clearly visible at 0.9 ms. This fact, which is coherent with the literature [1, 6, 15], is experimentally confirmed by the 17 J C-Scan, although this C-Scan involved a different test. In this figure (Fig. 21), the C-Scan was plotted at the point corresponding to 17 J of the 25 J test but is probably not the exact damage as shown at this point of the curve. Nevertheless the 17 J-point attained with a 17 J-impact or with the 17 J-point of a 25 J-impact are relatively close and the damage can be assumed to be equivalent. This delamination shape can be explained by the creation of a central conical shape at the beginning of the impact test below the impactor with high matrix cracking due to out-of-plane stresses (σ_{tz} and σ_{lz}). The delamination tends to be created on the boundaries of this cone and is not created just below the impactor (Fig. 23). This phenomenon can be highlighted by the illustration of the energy release rates in mode I, G_I/G_I^d and II, G_{II}/G_{II}^d, for each delaminated interface (Fig. 22).

It can be observed in this figure that mode II generally predominates, compared to mode I, except in a central zone around the impactor point. This zone can be assimilated to a conical central zone with its axis in the impact direction and with its higher diameter on the non-impacted side. It can be concluded that at the beginning of the impact test, the direct contact of the impactor with the laminate induces a conical shape with high matrix cracking due to out-of-plane stresses (τ_{tz} and τ_{lz}). These matrix cracks tend to separate a central cone which induces a beginning of delamination with a high rate of mode I (Fig. 22a). This scenario is coherent with the literature [1, 6, 15] which indicates a precursor role regarding the development of delamination and which assumes that the delamination development is principally related to mode I characteristics.

After this phase of delamination initiation, propagation of delamination is principally defined by mode II (Fig. 23b). This shearing fracture mode is due to high stresses in the lower ply of the interface in the fiber direction and explains the propagation direction of the delamination in the fiber direction of the lower ply.

Consequently, the "test-calculation dialogue approach" enabled us to define an appropriate model to accurately simulate an impact test and to take into account damage, such as matrix cracking, delamination, fiber failure or permanent indentation. Only two material parameters need to be identified on the reference impact test and the other ones are conventional material parameters. Nevertheless these two parameters only generate the simulated permanent indentation and scarcely modify delamination, matrix cracks or fiber failures. This model enabled us, in particular, to highlight formation of the delamination of the first interface on the non-impacted side and to explain its particular shape, partially separated into two parts. This result was determined by the creation of a central conical shape at the beginning of the

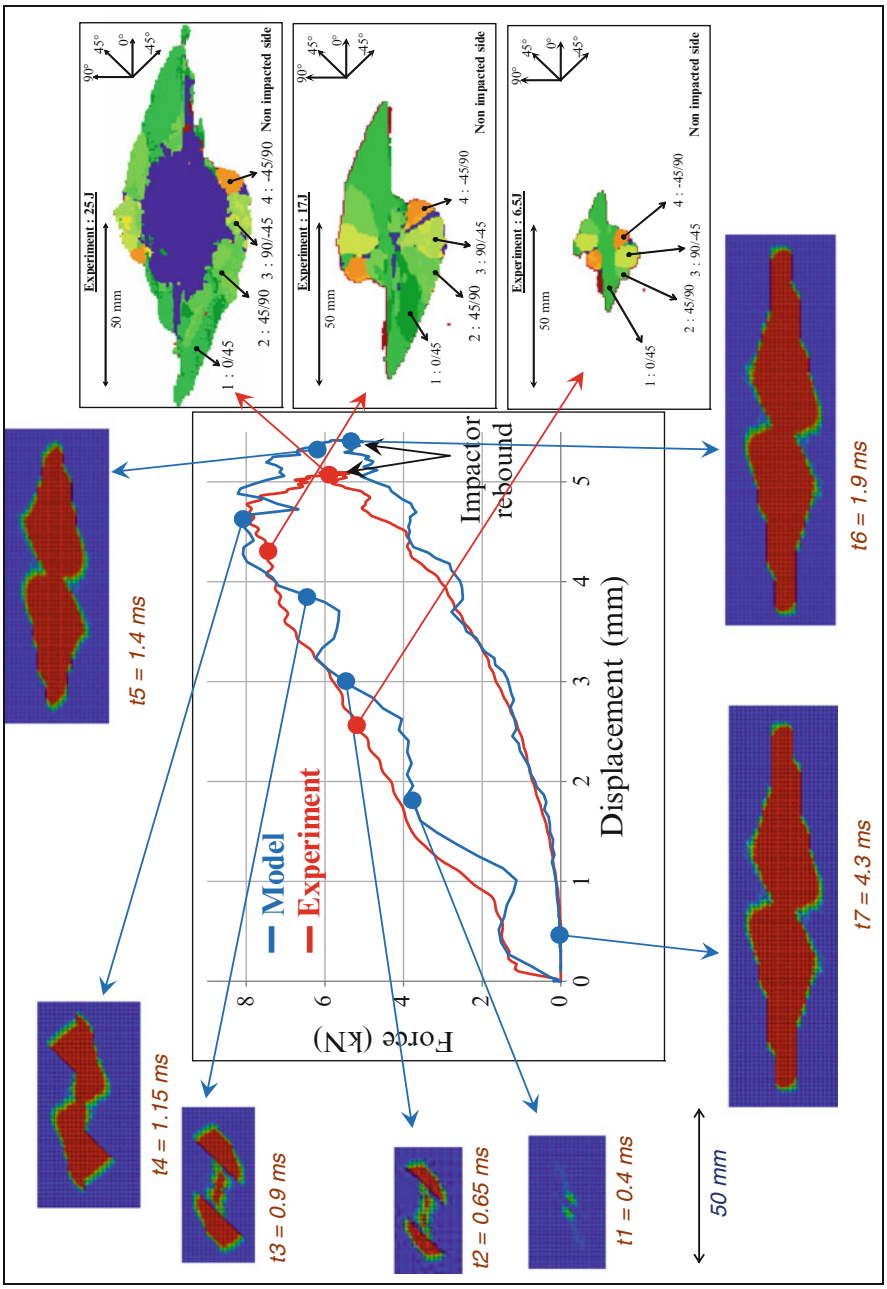


Fig. 21 Delamination of the first interface, non-impacted side, during a 25J-impact

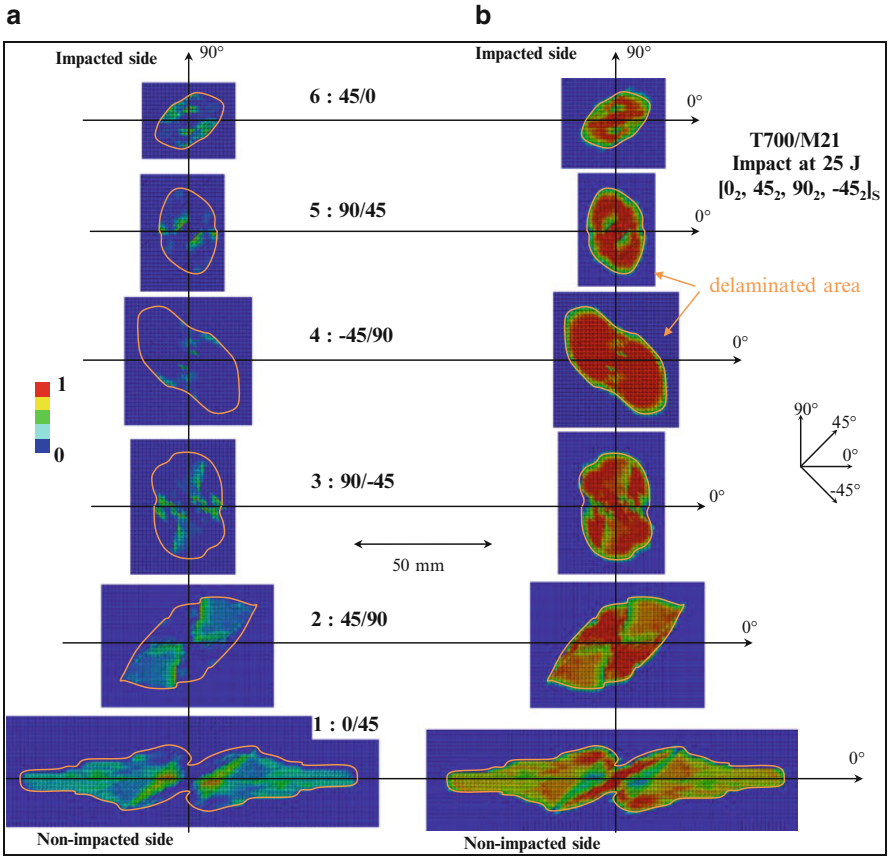


Fig. 22 Energy release rates in mode I, G_I/G_I^d (**a**), and II, G_{II}/G_{II}^d (**b**)

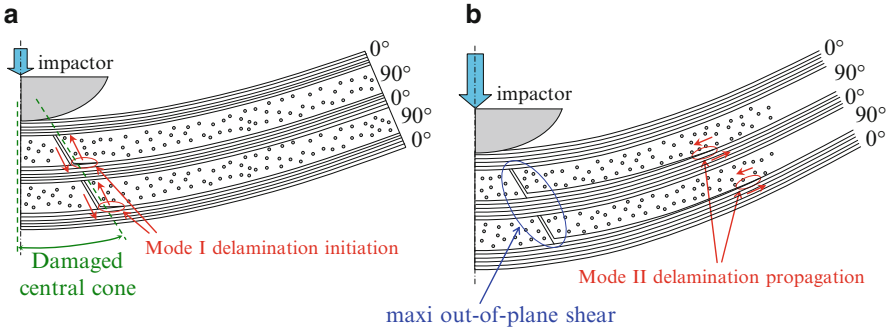


Fig. 23 Impact damage with creation of a severely damaged central conical shape: delamination initiation in mode I (**a**) and propagation in mode II (**b**)

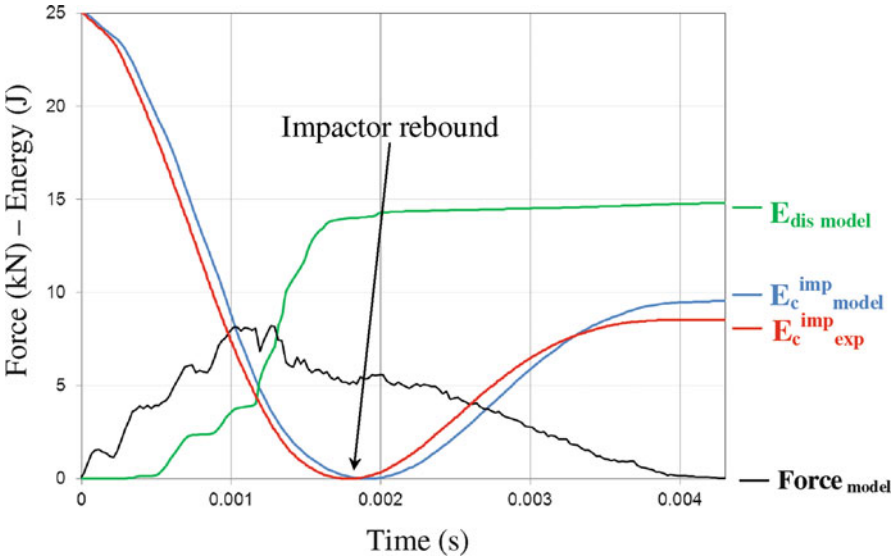


Fig. 24 Evolution of the dissipated energy during a 25J-impact

impact test, with high rate of opening fracture mode followed by propagation of delamination with high rate of shearing fracture mode.

4.3 Dissipated Energy

Afterwards, the model is used to evaluate the distribution of dissipated energy among the different damage phenomena. Figure 24 represents the evolution of the impactor kinetic energy, obtained numerically and experimentally.

The initial energy equals 25 J, drops to 0 J when the impactor stops and attains about 9 J after impact, corresponding to the rebound. A relatively good correlation is obtained between the experiment and the model. The numerically obtained dissipated energy is also illustrated. This energy starts at 0 J and reaches about 15 J after the impact. This final value is approximately equal to the difference between initial and final values of the experimentally obtained impactor kinetic energy:

$$E_{dis} \approx {E_c}^{init} - {E_c}^{fin} \approx 16.5\,J \tag{14}$$

Nevertheless in this approach, the final kinetic energy of the plate is disregarded and this hypothesis can be confirmed with numerical results:

$$at \quad t = 4.3\,ms, \quad {E_c}^{plate} \approx 0.05\,J \tag{15}$$

The evolution of the numerically obtained force is also illustrated (Fig. 25). It can be observed that the dissipated energy greatly increases during loading until the impactor stops and is almost constant after that. In this figure, the impactor arrest corresponds to zero kinetic energy. But the model also enables us to determine the origin of this dissipation, which can be divided into four phases (Fig. 25):

- The viscous dissipated energy E_{visc}. This dissipation is due to the conventional coefficients of viscosity in order to stabilize the explicit calculation. This energy remains relatively low and the viscosity coefficients have been decreased as soon as possible to avoid numerical problems.
- The dissipated energy by indentation E_{ind}. However this energy is stored, rather than dissipated! Indeed the energy dissipated by matrix cracking is almost null, due to the chosen criterion without damping. This choice of non-dissipative failure criterion is adopted to avoid excessively mesh-size dependant with dissipated energy. Indeed the density of matrix cracking, which can be taken into account by the model, is totally dependent on the mesh. But this drawback should be less than expected because the presence of one matrix crack should discharge the neighboring cracks, which emphasizes the large cracks, rather than the small, diffuse matrix cracks. In order to be more precise, the diffuse matrix cracking could be integrated by adding a continuum damage factor to the volume elements of the plies, as is usually done in the literature [19, 24]. However in this way, it is difficult to experimentally separate the diffusive matrix cracks from the large ones, i.e. those propagating through the entire ply thickness, and significantly influencing delamination. In this study, only the large matrix cracks are taken into account in order to avoid a more complex model, and as mentioned above, their dissipated energy is disregarded. In reality, it is difficult to evaluate what part of the dissipated energy comes from matrix cracking. Moreover a part of this dissipated energy should be included in the delamination value. Indeed the critical energy release rate of delamination is obtained from experimental tests, such as the double cantilever beam test, the mixed mode flexure test or the end notched flexure test which induce some matrix cracks [34, 35]. It is particularly true for multidirectional interfaces, i.e. when the angle between the two plies of the studied interface does not equal 0° (Fig. 26). And a part of this supplementary dissipated energy of a multidirectional interface should be due to supplementary matrix cracking; another part of this extra energy being due to bridging effects [34]. Consequently, E_{ind} is not energy dissipated in the matrix cracks but energy stored in the permanent indentation phenomenon: about half of this energy is stored in the matrix cracking interfaces, which are impeded from closing (Eq. 12), and half is stored in the volume elements which are always constrained after impact due to this non-closure phenomenon. Nevertheless this stored energy remains low compared to the energy dissipated by fiber failure and delamination.
- The energy dissipated by delamination E_{del}. This dissipation is due to the softening interface elements used to simulate delamination (Fig. 11) and is directly linked to the delaminated area.

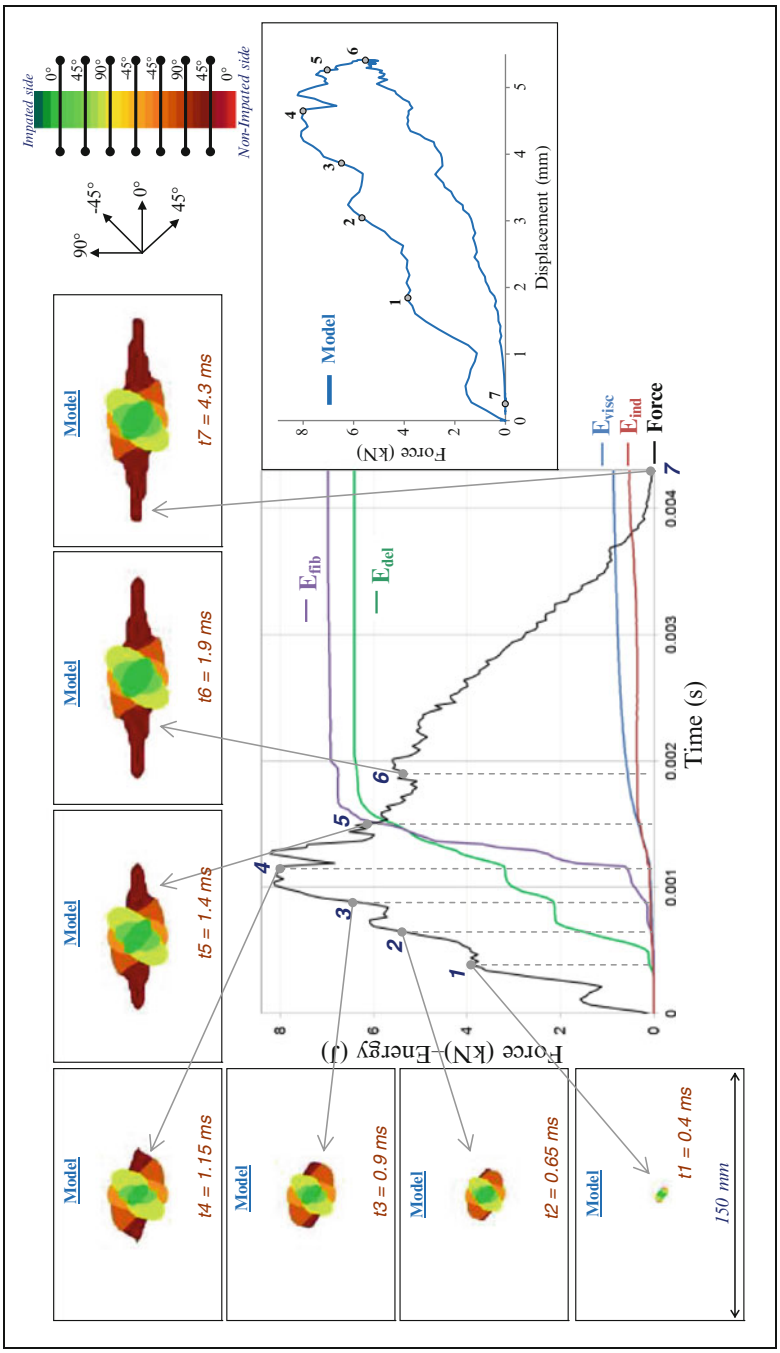


Fig. 25 Delamination during a 25J-impact and dissipated energy

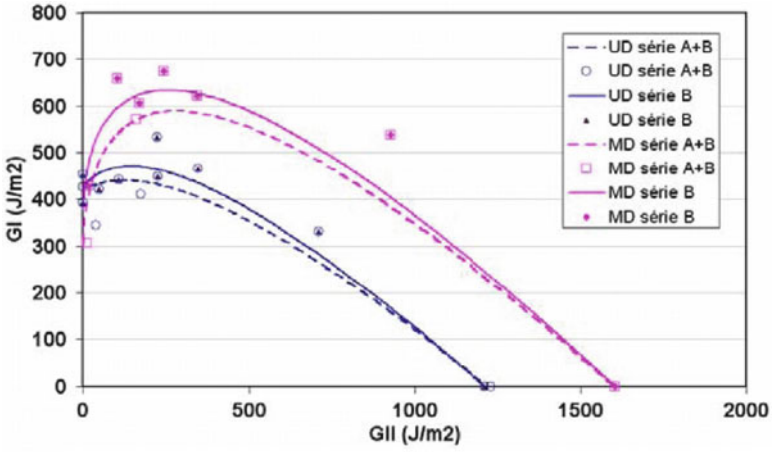


Fig. 26 Mixed mode of critical energy release rate for unidirectional (UD) and multidirectional (MD) interfaces [34]

- The energy dissipated by fiber failure E_{fib}. This dissipation is due to the softening behavior law of volume elements used to simulate fiber failure (Fig. 8) and is directly linked to the volume of broken fibers.

The origin of this dissipated energy is particularly interesting and highlights the damage scenario developing during impact. The first step is until point 1 (Fig. 25), no important damage is observed, only some matrix cracks, and the structure behavior is linear overall, with conventional oscillations due to dynamic loading. At point 1, the delamination begins to appear and increases with the impact force until point 4. Of course the greater the impact force, is the greater the delaminated area. A small decrease in plate stiffness is observed at point 1 due to this delamination. Before point 4, only a few fiber failures are observed and are not significant in the overall behavior of the structure. From point 4 and until point 6, the impact force decreases significantly due to fiber failure and the dissipated energy due to these fiber failures increases simultaneously. The effect of these fiber failures is clearly seen in the plate stiffness value. It is also during this step, between points 4 and 6, that the indentation energy increases, due to the blocking phenomenon of debris in the matrix cracking interfaces. Finally between points 6 and 7, no significant additional damage is observed.

At the end of the impact, the dissipated energy is divided into two nearly equal parts: delamination and fiber failure. Although it is due to random chance, since these two phenomena evolve very differently, and this conclusion could be different for another impact energy level.

Nevertheless these numerical results concerning the distribution of dissipated energy should be carefully taken into account due to the hypotheses adopted. For example, the dissipated energy in matrix cracking is not directly taken into account,

nevertheless part of this energy may be included in the delamination energy, more work is necessary to better understand the consequences of this hypothesis. For example, the dissipated energy due to fiber failure is only considered in the opening fracture mode (I) under tension stresses. This seems to be correct for this type of impact but with other conditions, shearing (II) and tearing (III) fracture modes, or fracture due to compression stresses, could be important (cf. Sect. 5). Finally, the stored energy due to permanent indentation may not be estimated accurately. Indeed the adopted model attributes greater importance to the blocking phenomenon of debris in matrix cracking on this indentation, and does not take into account the "plasticity" of the resin. Therefore, the corresponding stored and dissipated energy of this "plasticity" are not taken into account and should modify the dissipated energy distribution. Consequently, a model only represents a more complex phenomenon, therefore the use of this particular model to represent energy distribution should be carefully considered due to the difficulty of comparisons with the experimental results.

Consequently, this model's accuracy makes it possible to determine the distribution of dissipated energy among the different types of impact damage. In this 25 J-impact, the dissipated energy is divided into two nearly equal parts, the first one due to delamination and the other one due to fiber failure. Nevertheless these two types of dissipated energy develop quite differently: the delamination phenomenon begins first and increases slowly, while the fiber failure phenomenon begins later and increases rapidly. These developments can also be correlated with delamination and highlight the scenario of impact damage formation. These energy dissipation developments are very interesting, in particular because they are almost impossible to obtain experimentally.

4.4 Conclusion of Experimental Validation

The modeling of an impact reference case has made it possible to demonstrate the accuracy of the proposed model. The impact curves, such as force-displacement or force-time curves, the delaminated interfaces or the permanent deformation of the plate after impact were correctly simulated. This comparison was performed using numerous refined experimental studies and enables us to have relative confidence in this model.

Therefore the model can be used to more deeply analyze the behavior of materials during impact, such as the fracture modes involved in delamination or the distribution of dissipated energy. The most original aspect concerns the separation of the overall dissipated energy among the different damage types. For the reference impact case, the dissipated energy is divided into two equal parts, the first one due to delamination and the other one due to fiber failure. Nevertheless these two types of energy dissipate very differently and could give different results for other types of impact energy.

5 Effect of Impact Conditions

5.1 Introduction

This section deals with numerical validation. Different experimental impact tests have been simulated with different impact configurations and compared to experimental results.

The first test parameter is the impact energy used to set up the damage scenario during impact. Afterwards the effect of boundary conditions is studied and reveals some of the model's limits. Then the stacking sequence is changed to highlight other damage scenarios during impact. Finally the effect of impact velocity is studied in an attempt to separate the inertial effects from the strain rate effects.

These results show that engaging a "test-calculation dialogue" related to these supplementary experiments could contribute to enlarging the domain validity of the modeling. This work is currently in progress.

5.2 Effect of Impact Energy

The first effect studied is that of impact energy. Some of the impact tests have been performed, although only four particular impact tests are presented in detail. These four impact tests at 6.5, 17, 25 and 30 J have been simulated and compared to experiments. The correlation between delaminated interfaces and corresponding force-displacement curves is relatively close for the different types of impact energy (Fig. 27).

In this figure, due to an experimental problem the 17 J curve is not represented. This relatively good correlation is also visible on the curves of the delamination area and indentation versus impact energy (Fig. 28). In these figures, a supplementary impact test at 1.6 J is represented, but it did not induce a delaminated area, either experimentally or in simulation.

The model is the least accurate for 30 J and overestimates the damage. This could be due to the fiber failure model which could not correctly take into account the high impact damage near plate perforation, and other considerations should be modeled, such as shearing fracture mode of fibers, or removal of volume elements after fiber failure.

It is interesting to notice in the Fig. 28b, the strong increase of indentation for an impact of about 17 J. Based on the dissipated energy curve (Fig. 25), this phenomenon can be attributed to the apparition of fiber failures: when fiber failures appear, damage in the central zone below the impactor develops rapidly, inducing opening of matrix cracks, creation of debris blocking and increase of permanent indentation. This phenomenon is coherent with the experimental studies of Chen et al. [47] showing that permanent indentation increases suddenly when the first fiber failures are observed.

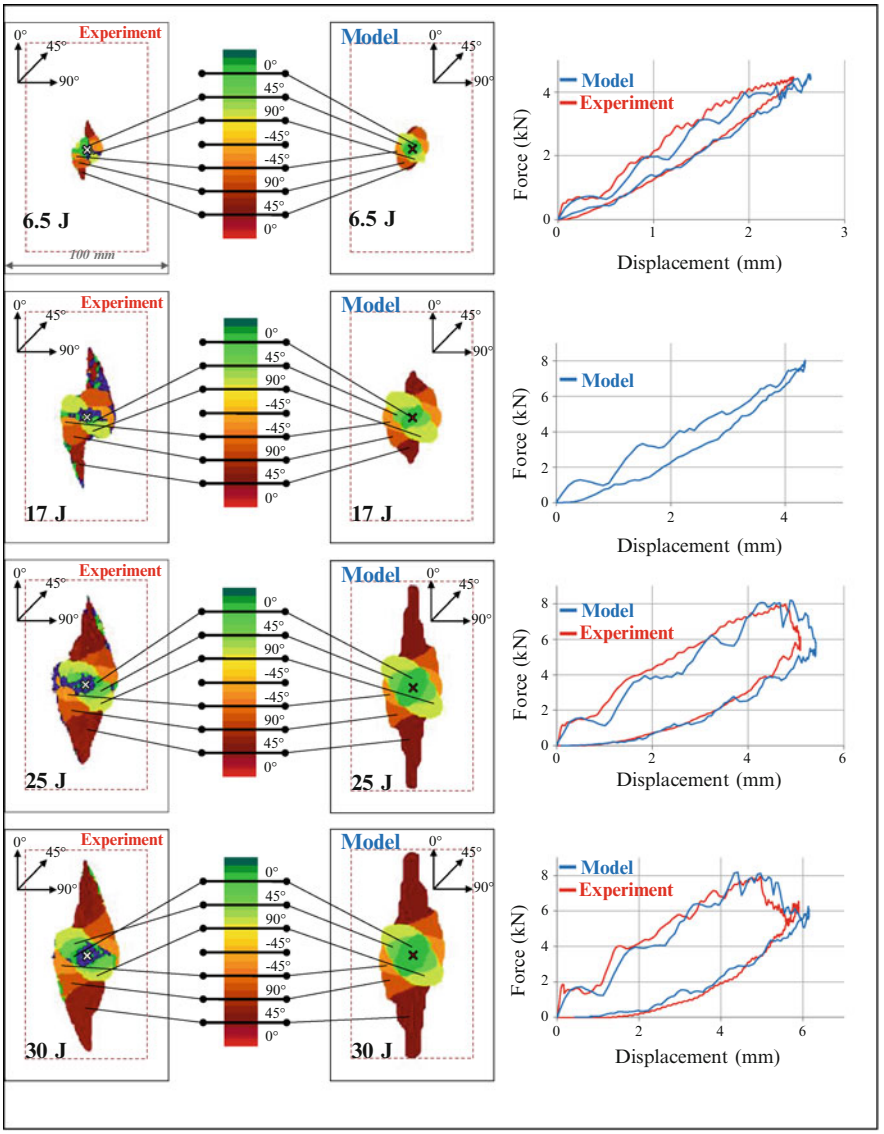


Fig. 27 Comparison between delaminated interfaces obtained experimentally and numerically for different types of impact energy

This phenomenon is interesting because it could make it possible to design composite structures more easily indented during impact by favoring fiber failure. Nevertheless, the effect of these fiber failures on compression after the impact test should be studied because it may play a precursor role on the final fracture under compression loads.

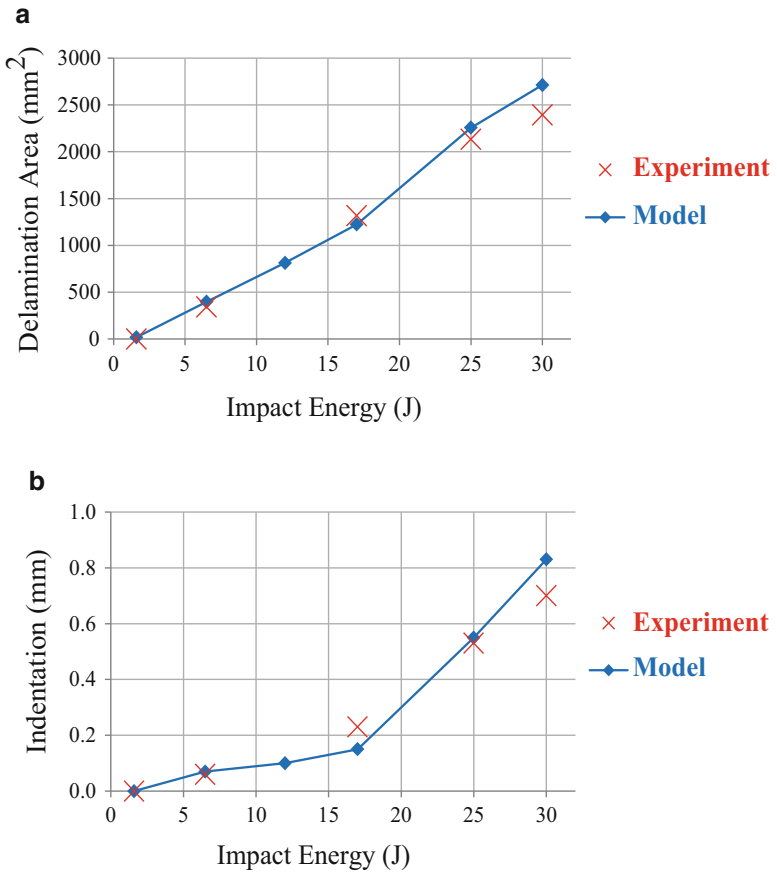


Fig. 28 Curves of delamination area (**a**) and permanent indentation (**b**) versus impact energy obtained experimentally and numerically

Consequently, the study of impact energy effects enables us to confirm the validity of this model with different damage sizes, and highlights the experimental results. For example, it enabled us to link the change in development of permanent indentation, versus impact energy, with the appearance of fiber failures which induce the large opening of a damaged central cone under the impactor and the creation of debris blocking.

5.3 Effect of Boundary Conditions

In order to evaluate the reliability of the model, the position of the impact point was moved from the centre (reference case) to a corner (Fig. 29), the plate being supported on the four edges as before (Fig. 15).

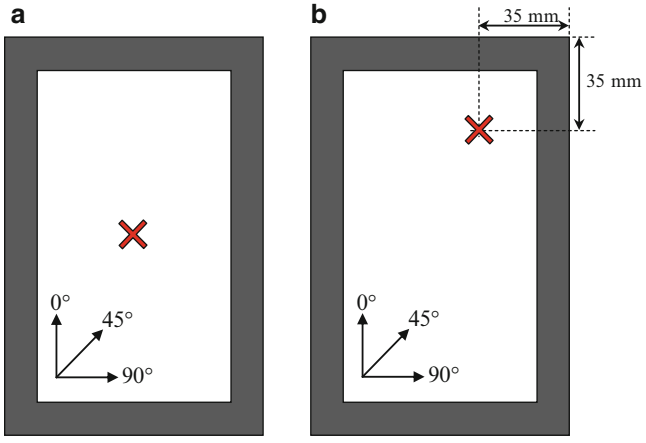


Fig. 29 Position of the impact point: reference case (**a**) and corner impact case (**b**)

This corner impact case enabled us to obtain different impact test boundary conditions with the same plate and experimental set up. This type of boundary condition is also interesting because it could be representative of an impact near a stiffener of a composite panel [17]. Indeed in a real composite structure, the stiffeners locally increase the structural stiffness and modify impact damage. And in order to validate a composite structure with impact damage tolerance, it is necessary to evaluate its residual strength whatever the impact location.

Finally, this case also enables us to obtain a non-symmetric situation, such as the delaminated areas (Fig. 30). This corner impact test was performed at 17 J and 25 J and is compared to the centre impact test at 25 J.

The comparison between the two experimental 25 J-impact tests shows that the maximum forces are similar at about 8 kN but the corresponding displacement is less for the corner impact test, at 3.5 mm versus 4.8 mm for the reference case. This is explained by the higher stiffness of the corner impact test due to the proximity of the impact point with the boundary condition. This higher stiffness is generally well reproduced by the model, although the stiffness decrease at 1.2 mm, due to delamination onset, is numerically overestimated. Moreover the load drop after the maximum load is delayed on the calculation compared to the experiment. This load drop can be attributed to fiber failure and an observation of the plate after impact shows fiber failures of the first ply on the non-impacted side (Fig. 31). This failure is observed only on the boundary condition and could be due to out-of-plane shear failure.

This type of fiber failure is not taken into account in the model and the numerically estimated load drop is due to tension fiber failure just under the impactor. Therefore, the model should be improved to be able to take into account this type of fiber failure due to out-of-plane shear stresses in order tobetter estimate

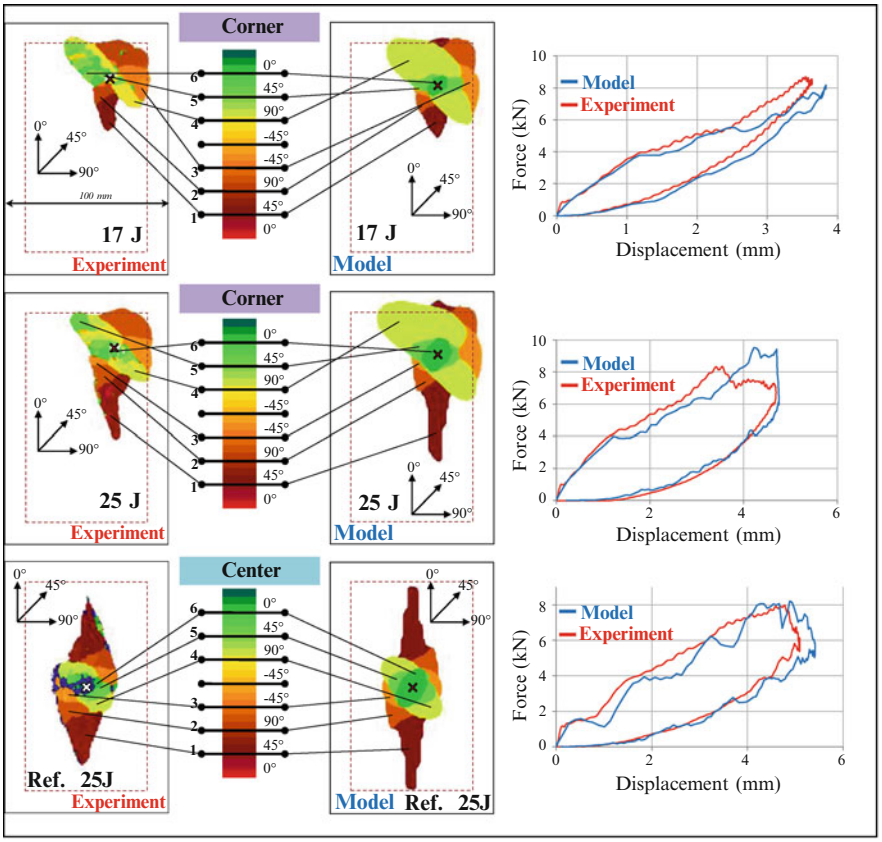


Fig. 30 Delaminated areas and force-displacement curves for corner impact case at 17 J and 25 J and reference case at 25 J

the load drop of this type of impact test. Of course this type of modeling of fiber failure exists in the literature [38, 40–42] and should be adapted to the present modeling.

In general the delaminated interfaces are accurately estimated by the model except at the top left of the impact point where the model forecasts the delamination of the fourth interface and the experiment shows mixed delamination of the fourth, fifth and sixth interfaces. This discrepancy could be due to the shear fiber failures mentioned above. In order to validate this hypothesis, a corner impact test at 17 J was performed. In this case, no fiber failure was observed non-impacted side and indeed a good correlation was obtained between the experiment and the model for the force-displacement curve. Again, the general delamination shapes are well simulated except at the top left of the impact point where the model does not forecast the delamination of the sixth interface. Moreover at this location, in observing the

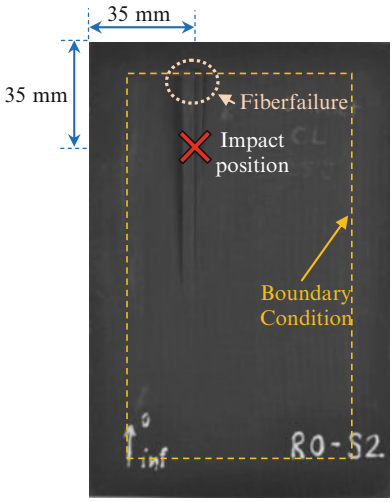


Fig. 31 Non-impacted side of the plate after 25 J corner impact test

experiments at 17 and 25 J, delamination jumps are seen between the first three interfaces on the impacted side. The reasons for this non-standard delamination are not very clear and more experimental studies are necessary to better explain it.

To conclude, modification of the impact point position showed that it is necessary to take into account the fiber failure under shearing and tearing fracture modes. Nevertheless modification of the impact point position also demonstrated the relatively accurate performance of the model with non-standard boundary conditions. Moreover this type of test is necessary to validate this model before it can be used to design a real composite structure, subject to impact at all points, and in particular near stiffeners.

5.4 Effect of Stacking Sequence

In order to evaluate the model's validity domain, laminated plates with different stacking sequences were impacted (Fig. 32). Three stacking sequences were studied and each sequence was tested with 0° ply both longitudinally and transversally. This resulted in 6 stacking sequences, but required the manufacture of only 3 plates, by varying the cuts. In order to facilitate the presentation, the two plates, rotated at 90° are named with the same letter (Table 2, i.e. C1/C2, D1/D2 . . .).

On Fig. 32, the delaminated areas and force-displacement curves, obtained numerically and experimentally, are illustrated. The correlations between the experiment and the model are acceptable. In practical terms, the shape of delaminated areas is qualitatively well simulated, but the projected delaminated areas are still overestimated (Fig. 33).

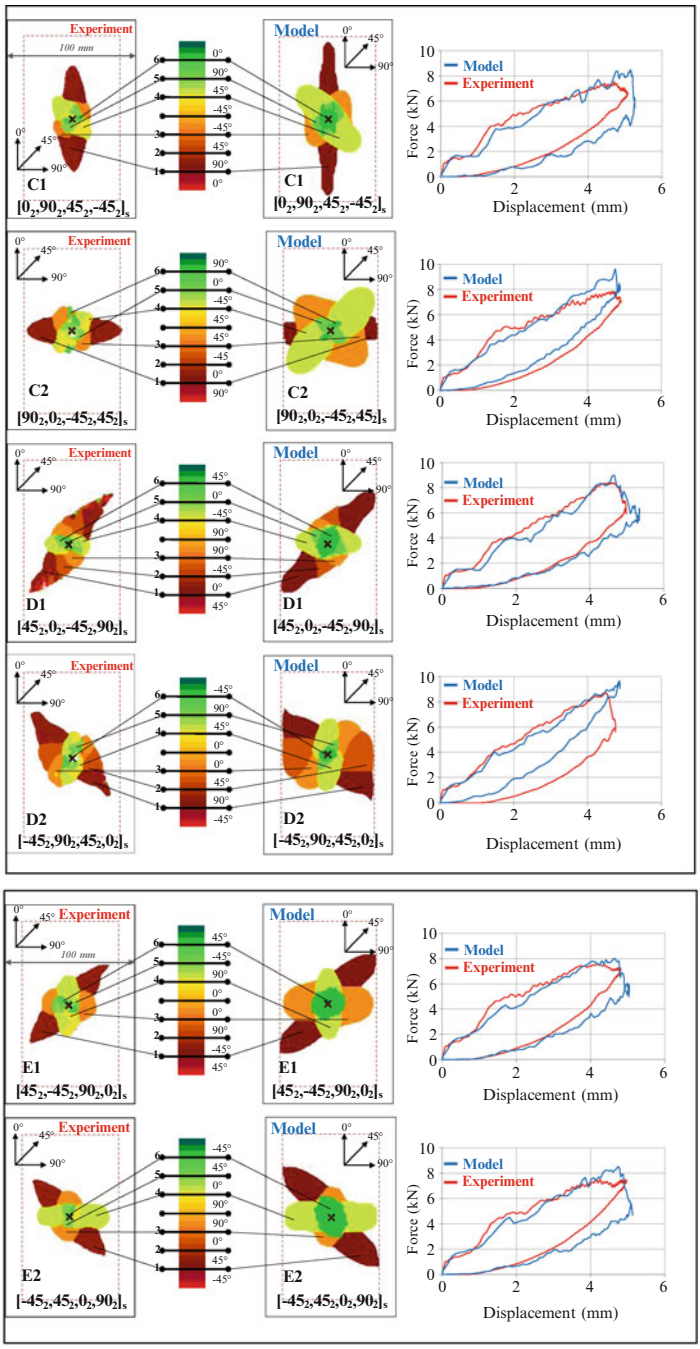


Fig. 32 Effect of stacking sequence on delaminated areas and force-displacement curves of 25 J-impact tests

Table 2 The different stacking sequences studied

Name	Stacking sequence	Remark
Ref	$[0_2, 45_2, 90_2, -45_2]_S$	
C1	$[0_2, 90_2, 45_2, -45_2]_S$	90°-rotation of C2
C2	$[90_2, 0_2, -45_2, 45_2]_S$	90°-rotation of C1
D1	$[45_2, 0_2, -45_2, 90_2]_S$	90°-rotation of D2
D2	$[-45_2, 90_2, 45_2, 0_2]_S$	90°-rotation of D1
E1	$[45_2, -45_2, 90_2, 0_2]_S$	90°-rotation of E2
E2	$[-45_2, 45_2, 0_2, 90_2]_S$	90°-rotation of E1

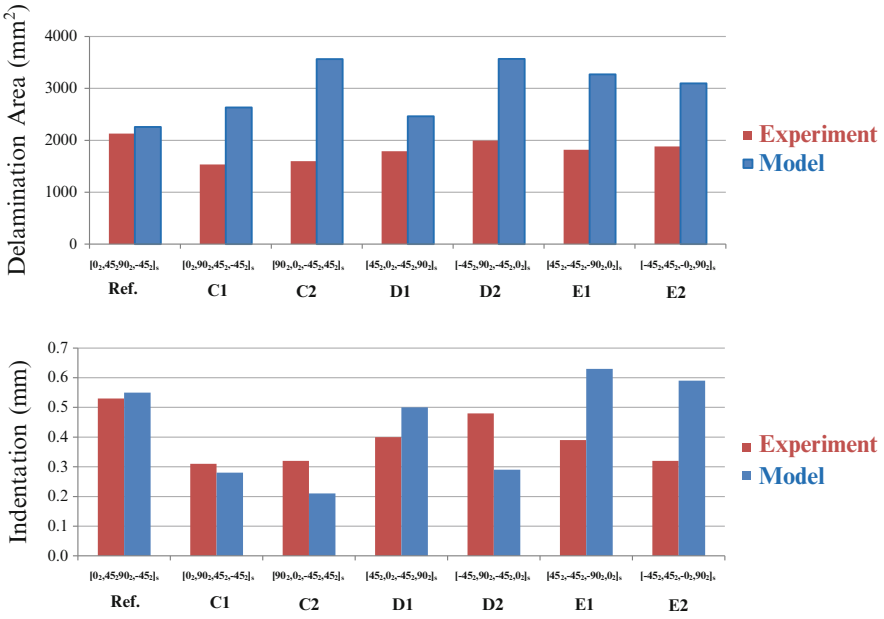


Fig. 33 Effect of stacking sequence on delaminated areas and indentation

This confirms that the model accurately takes into account the phenomenon of impact damage formation and in particular the interaction between matrix cracks and delamination but quantitative discrepancies of the projected delaminated areas highlight some problems. These discrepancies are also observed on the force-displacement curves. The D2 case is particularly interesting. In general, the model accurately simulates the delamination shapes, but the areas are highly overestimated and propagation is even arrested by the boundary conditions. This phenomenon is also observed on the force-displacement curve where a strong load drop is experimentally obtained but is not simulated. This load drop could be due to fiber failures which are not taken into account by the model, for example compression or shearing fractures. This hypothesis is confirmed by the delamination simulated before this experimental load drop (Fig. 34).

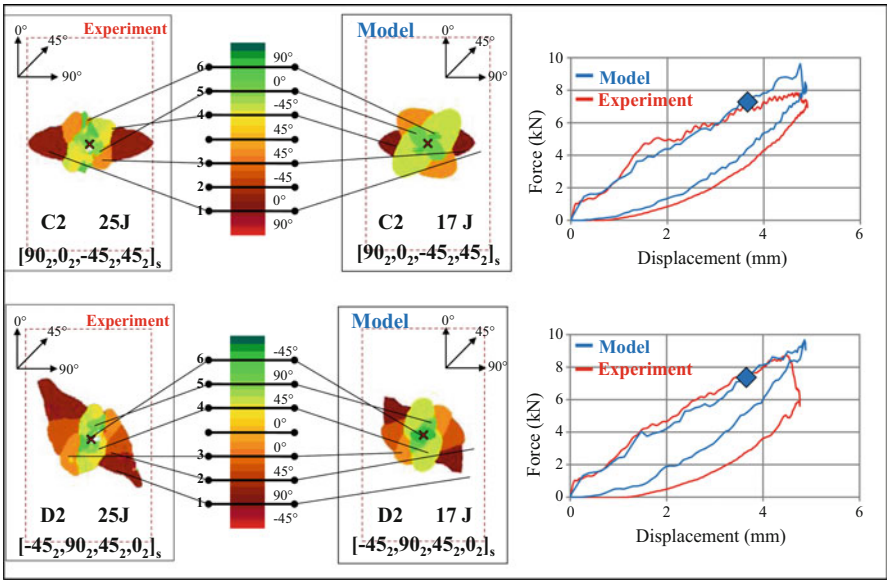


Fig. 34 Delaminated areas at 17 J during a 25 J-impact simulation (C2 and D2 cases)

In Fig. 34, delamination calculated for 3.8 mm-displacement (17 J) during a 25 J-impact simulation are illustrated and show a good correlation with experimental results, although the delamination of the first interface, on the non-impacted side is underestimated. This good match between experiment and modeling confirms that discrepancies at 25 J-impact could be due to the end of loading of the impact test, where the load is overestimated, due to fiber failures which the model does not take into account very well. This phenomenon is also observed in the case of C2 (Fig. 34), although here the load drop is less, which could be due to another type of fiber failure. And indeed on the impacted side of the C2 plate, a large crack of about 50 mm in the 0° direction is observed (Fig. 35), unlike the D2 plate where no crack is observed on impact side.

This crack of the top 90° ply could be due to bending of the plate during impact, which induces compression stresses at the top of the laminate. Moreover this plate is particularly sensitive to compression in the top of the laminate, because the 90° ply is in the short edge of the frame.

These problems of fiber failure modeling may also induce discrepancies in permanent indentation modeling (Fig. 33). Indeed the comparison between experimental and numerical results of permanent indentation shows some inaccurate estimates, in particular for E1 and E2 plates, although the general correlations are accurate. Nevertheless it is difficult to explain and to improve the permanent indentation model if fiber failure modeling problems are not solved and impact damage is not simulated accurately enough.

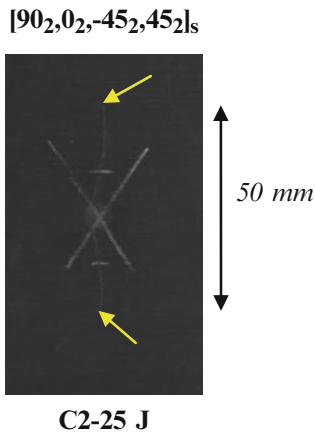


Fig. 35 Fiber failure in the case of C2 observed on impacted side

In conclusion, the modification of the draping sequence enabled us to confirm that the model is able to qualitatively simulate the formation of impact damage, but that other failure phenomena, such as fiber failure under shear or compression [38, 40–42], should be better taken into account. Nevertheless, the model seems to correlate well with experimental results, such as delamination or force-displacement curves, before significant fiber failures. These tests also enabled us to show that permanent indentation simulation needs to be improved, although the problems of fiber failure could be partially responsible for this discrepancy.

5.5 Effect of Impact Velocity

Subsequently, the effect of impact velocity was studied to evaluate the reliability of the model, as well as to attempt to separate inertial effects from material strain rate effects on impact damage. In this model, only inertial effects are taken into account and all material parameters are strain rate independent. The inertial effects of an impact test are schematically illustrated in Fig. 36 of Olsson's study [54]. Impact with low velocity and large mass presents quasi-static response, since impact with high velocity and small mass presents a local response controlled by wave propagation. And at the same time, the strain rate effect generally shows an increase in the material parameters with the strain rate [55] (Fig. 37) which induces generally less impact damage.

In Fig. 38, delamination and force-displacement curves are presented for 25 J-impact at 0.5, 5 and 50 m/s. In order to facilitate the discussion, the 0.5 m/s impact is called the static test, the 5 m/s impact is called the reference test, and the 50 m/s impact is called the high velocity test.

The difference between the static and reference impacts is very small, in particular for delamination. Nevertheless, oscillations of the force signal are conventionally

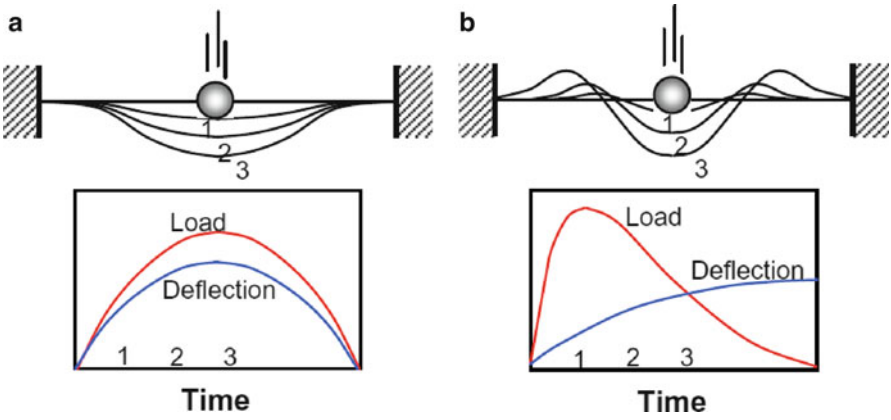


Fig. 36 Comparison of impacts with (**a**) large mass and low velocity and (**b**) small mass and high velocity [54]

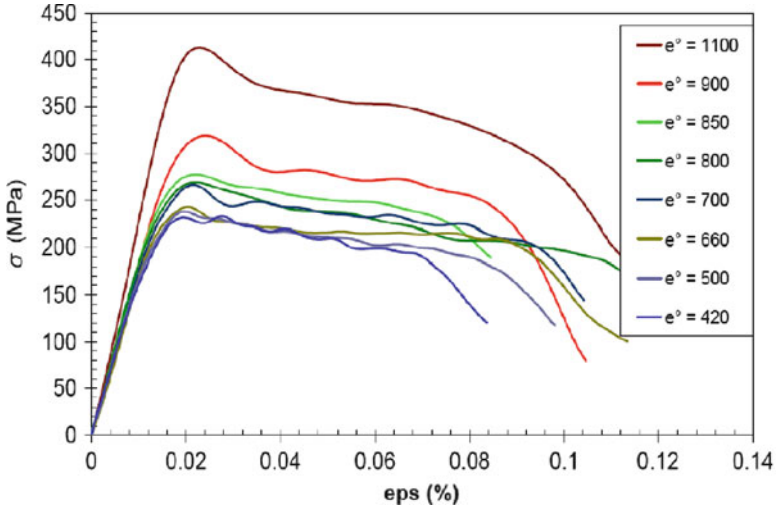


Fig. 37 Effect of strain rate on a compression of T800S/M21 $[\pm 45]_{3S}$ laminate [55]

observed in the reference impact, but not in the static case. The range of oscillations seems small enough to have a negligible effect on damage formation. This conclusion is coherent with certain articles in the literature [1, 56–58] where impact tests at velocities between 1 and 10 m/s are assumed to be equivalent to the static test (Fig. 39).

But this equivalence between static and impact tests, is not relevant for velocity greater than about 10 m/s, although this threshold is artificial and may depend on material, draping sequence, boundary conditions or impactor mass. With this model, impact damage simulated at high velocity is different and shows a more circular

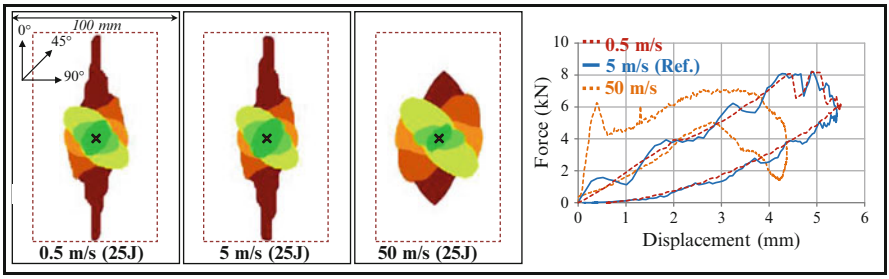


Fig. 38 Simulated effect of impact velocity

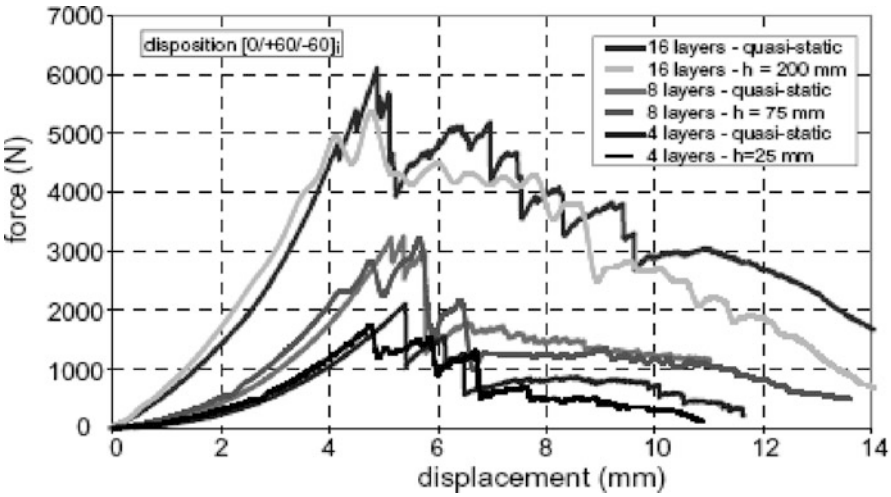


Fig. 39 Comparison between static and dynamic tests performed by Belingardi and Vadori [57]

shape, which is typical of high velocity impact damage, which decreases boundary condition effects compared to inertial effects (Fig. 36). Influence of impact velocity is also illustrated on the force-displacement curve (Fig. 38) where inertial effects are clearly visible for high velocity impacts. This high velocity curve shows that the first load peak at about 0.4 mm-displacement is conventionally due to the inertial effect and does not induce significant damage. Indeed, only some matrix cracks are observed in the impactor contact zone.

Finally experiments were performed at different impact velocities and compared to simulated results (Fig. 40):

- The quasi-static case is an indentation test performed on an electro-mechanical machine at about 10-4 m/s. This test is driven with imposed velocity up to a maximum displacement of about 5 mm, similar to the 25 J-impact test. This induces impact energy of about 23 J. This energy is imposed for the simulation and a small impact velocity of about 0.5 mm/s is chosen in order to avoid an

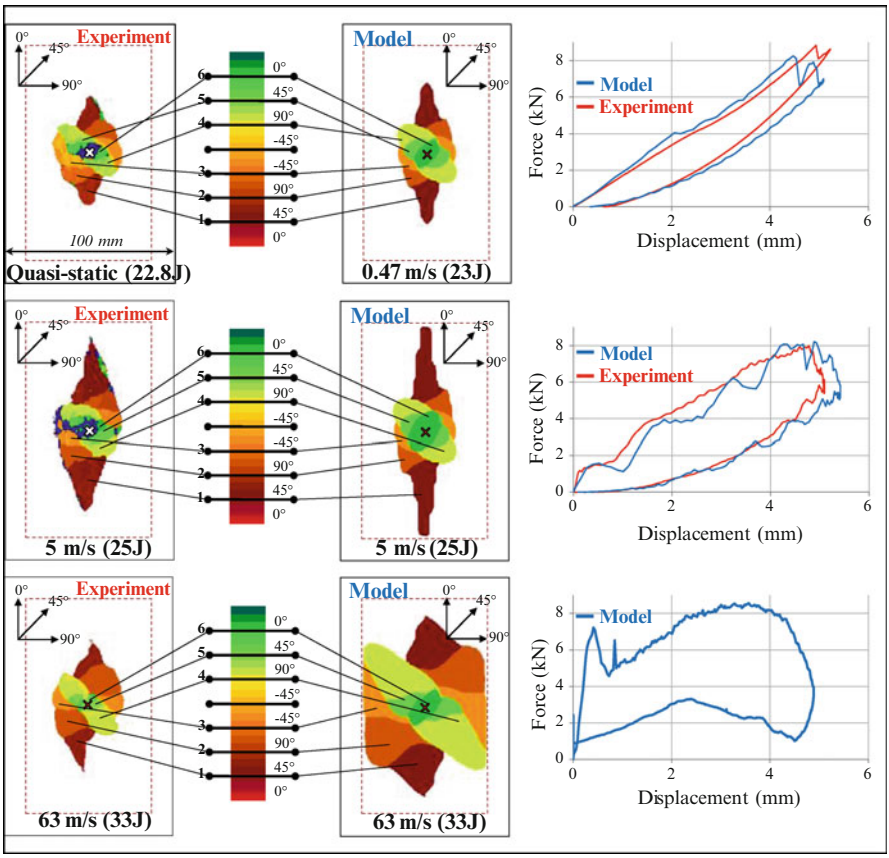


Fig. 40 Experimental and simulated effect of impact velocity and force-displacement curves

overly time-consuming calculation. Of course it has been verified that such a decrease in imposed velocity did not affect significantly the numerical result. A good correlation has observed between the experiment and the model, for delamination and force-displacement. The simulated load drop at about 4.5 mm-displacement is due to fiber failure under tension in plies of the lower half-plate.

- The 5 m/s-impact test is the reference impact test mentioned above. The satisfactory correlation between the experiment and the model has previously been discussed extensively.
- The 63 m/s experimental impact test used a gas gun, with the same boundary conditions and a steel ball of 16 mm-diameter and 34 g-mass. Unfortunately this experimental set up does not allow for precise control of the impact velocity and explains the difference between the required 50 m/s-velocity and the experimental velocity. Nevertheless a high speed camera is used to measure this velocity. Moreover this type of experimental set up does not allow for force

signal measurement during impact. Then only the force-displacement curve is represented on the other hand simulated and experimentally obtained delaminated interfaces are represented (Fig. 40). The correlation between experimental and numerical delamination shows that the delamination shapes are accurately simulated, but delaminated areas are overestimated. Once again, the model overestimates the delamination propagation at the end of impact test loading; experimentally obtained delamination data at 63 m/s compare favorably with delamination simulated at 50 m/s (Fig. 38). Again, as mentioned previously, delamination overestimation could be due to fiber failure which this model does not accurately take into account. Nevertheless, the lack of experimental force-displacement data does not support this conclusion, and the evolution of material parameters, such as delamination energy release rate or fiber failure strain, with the strain rate, should be taken into account.

To conclude, modification of impact velocity did not enable us to separate inertial effects from material strain rate effects, and the model needs to be improved to correctly simulate the effect of impact velocity and to be able to answer this question. Other high velocity experimental studies are also necessary to determine whether fiber failure is not accurately estimated. Nevertheless the equivalence between static and low velocity impact tests has been confirmed with this type of boundary conditions. Further studies are needed to validate this equivalence with other boundary conditions, in particular with less stiff boundary conditions.

5.6 Conclusion of Impact Conditions

The simulation of different experimental impact tests enabled us to demonstrate the domain validity of the model and to highlight certain effects of the impact conditions.

The study of the effect of impact energy made it possible to set up the damage scenario during impact and to show the fiber failure effect on permanent indentation. The modification of the boundary conditions and stacking sequence showed the importance of other types of fiber failure, such as shearing or compression, on damage creation. Finally the study of the effect of impact velocity failed to separate the inertial effects from the strain rate effects.

6 Conclusion

The goal of this work was to stimulate a “test-calculation dialogue” on the composite impact test. Therefore, it has been necessary to simultaneously carry out a refined experimental study of the different types of impact damage, and to build a numerical model able to simulate these observations. The accurate correlation of the model

with this refined experimental database enabled us to have relative confidence in this model, despite a few non-standard material parameters. Indeed the bibliography shows a general lack of detailed validation of impact modeling and the originality of this work is to use refined and complementary experimental data to build and validate a numerical model.

This approach enabled us to define an accurate model for impact, with some original points in modeling:

- An original scenario of permanent indentation with a phenomenon of debris blocking in the matrix cracks and the corresponding model were proposed. Cohesive interface elements of matrix cracking were used with a "plastic-like" behavior to simulate this phenomenon.
- A particular modeling of fiber failure was set up with original formulation between the integration points of the volume element in order to reproduce a constant energy release rate per unit area. The use of the strains extrapolated at nodes also to better account for the bending behavior of plies with only one element in the ply thickness.
- The model was then used for in-depth analysis of impact tests, which cannot be done directly from the experiments alone:
- Calculations were performed to evaluate the distribution of the dissipated energy between the different damage types. For the reference impact case, the dissipated energy is divided into two equal parts, the first related to delamination and the second related to fiber failure.
- The modeling of impacts at different energy levels enabled us to set up the damage scenario during impact. In particular the strong effect of fiber failure on the permanent indentation was demonstrated.

Finally, different configurations of impact were simulated to explore the validity domain and limitations of the model:

- The modeling of impacts with different stacking sequences showed the importance of fiber failure, under shear or compression solicitations - which are not yet taken into account in the model - on the impact damage morphology.

Finally significant work is still necessary to accurately simulate all the impact tests shown in this article, although this seems feasible. Moreover the impact model is only a first step, and the residual strength of the structure should also be numerically determined, in order to totally design a composite structure with impact damage tolerance and to optimize it. In addition, this type of model represents composite damage, observed in other kinds of loading, and could be used to simulate other dimensioning cases, such as pull-through [59], bearing of bolted composites or crashes.

References

1. Abrate S (1998) Impact on composite structures. Cambridge University Press, Cambridge
2. Petit S, Bouvet C, Bergerot A, Barrau JJ (2007) Impact and compression after impact experimental study of a composite laminate with a cork thermal shield. Compos Sci Technol 67:3286–3299
3. Zheng D, Binienda WK (2007) Effect of permanent indentation on the delamination threshold for small mass impact on plates. Int J Sol Struct 44(25–26):8143–8158
4. Eve O (1999) Etude du comportement des structures composites endommagées par un impact basse vitesse. Thèse de doctorat, Université de Metz
5. Allix O, Blanchard L (2006) Mesomodeling of delamination: towards industrial applications. Compos Sci Technol 66:731–744
6. Choi HY, Chang K (1992) A model for predicting damage in graphite/expoxy laminated composites resulting from low-velocity point impact. J Comp Mat 26(14):2134–2169
7. De Moura MF, Gonçalves SF (2004) Modelling the interaction between matrix cracking and delamination in carbon-epoxy laminates under low velocity impact. Compos Sci Technol 64:1021–1027
8. Guinard S, Allix O, Guédra-Degeorges D, Vinet A (2002) A 3D damage analysis of low-velocity impacts on laminated composites. Compos Sci Technol 62:585–589
9. Mulle M, Zitoune R, Collombet F, Robert L, Grunevald YH (2009) Embedded FBGs and 3-D DIC for the stress analysis of a structural specimen subjected to bending. Compos Struct 91:48–55
10. Rouchon J (1995) The fatigue and damage tolerance aspects for composite aircraft structures. Proceedings of ICAF symposium, Delft, The Netherlands
11. Alderliesten RC (2008) Damage tolerance of bonded aircraft structures. Int J Fati 31(6):1024–1030
12. Tropis A, Thomas M, Bounie JL, Lafon P (1994) Certification of the composite outer wing of the ATR72. J Aero Eng 209:327–339
13. Chang FK, Chang K (1987) A progressive damage model for laminate composites containing stress concentrations. J Comp Mat 834–855
14. Aymerich F (2008) Priolo, "Characterization of fracture modes in stiched and unstiched cross-ply laminates subjected to low-velocity impact and compression after impact loading". Int J Imp Eng 35:591–608
15. Renault M (1994) Compression après impact d'une plaque stratifiée carbone époxyde – Etude expérimentale et modélisation éléments finis associée. Rapport interne EADS CCR
16. Lopes CS, Camanho PP, Gürdal Z, Maimí P, González EV (2009) Low-velocity impact damage on dispersed stacking sequence laminates. Part II: Numerical simulations. Compos Sci Technol 69(7–8):937–947
17. Faggiani A, Falzon BG (2010) Predicting low-velocity impact damage on a stiffened composite panel. Compos Part A 41(6):737–749
18. Geubelle PH, Jeffrey S (1998) Baylor Impact-induced delamination of composites: a 2D simulation. Compos Part B Eng 29(5):589–602
19. Aymerich F, Dore F, Priolo P (2009) Simulation of multiple delaminations in impacted cross-ply laminates using a finite element model based on cohesive interface elements. Compos Sci Technol 69:1699–1709
20. Wisnom MR (2010) "Modelling discrete failures in composites with interface elements" Comp. Compos Part A Appl Sci Manufac 41(7):795–805
21. Davies GAO, Olsson R (2004) Impact on composite structures. Aero J 108:541–563
22. Aoki Y, Suemasu H, Ishikawa T (2007) Damage propagation in CFRP laminates subjected to low velocity impact and static indentation. Adv Mater 16(1):45–61
23. Borg R, Nilsson L, Simonsson K (2004) Simulation of low velocity impact on fiber laminates using a cohesive zone based delamination model. Compos Sci Technol 64:279–288

24. Ladeveze P, Lubineau G, Marsal D (2006) Towards a bridge between the micro- and mesomechanics of delamination for laminated composites. Compos Sci Technol 66:698–712
25. Zhang Y, Zhu P, Lai X (2006) Finite element analysis of low-velocity impact damage in composite laminated plates. Mater Des 27:513–519
26. Lammerant L, Verpoest I (1996) Modelling of the interaction between matrix cracks and delaminations during impact of composite plates. Compos Sci Technol 56:1171–1178
27. Tita V, Carvalho J, Vandepitte D (2008) Failure analysis of low velocity impact on thin composite laminates: experimental and numerical approaches. Compos Struct 83:413–428
28. Johnson HE, Louca LA, Mouring S, Fallah AS (2009) Modelling impact damage in marine composite panels. Int J Imp Eng 36:25–39
29. Iannucci L, Willows ML (2006) An energy based damage mechanics approach to modelling impact onto woven composite materials – part I: numerical models. Compos Part A 37:2041–2056
30. Iannucci L, Willows ML (2007) An energy based damage mechanics approach to modelling impact onto woven composite materials – part II: experimental and numerical results. Compos Part A 38:540–554
31. Bouvet C, Castanié B, Bizeul M, Barrau JJ (2009) Low velocity impact modeling in laminate composite panels with discrete interface elements. Int J Sol Struct 46(14–15):2809–2821
32. Ha-Minh C, Kanit T, Boussu F, Abdellatif I (2011) Numerical multi-scale modeling for textile woven fabric against ballistic impact. Compos Mater Sci 50(7):2172–2184
33. Mi Y, Crisfield MA, Davies GAO (1998) Progressive delamination using interface elements. J Compos Mater 32(14):1246–1272
34. Prombut P (2007) Caractérisation de la propagation de délaminage des stratifiés composites multidirectionnels. Thèse de doctorat, université de Toulouse
35. Prombut P, Michel L, Lachaud F, Barrau JJ (2006) Delamination of multidirectional composte laminates at 0°/theta° ply interfaces. Eng Fract Mech 7:2427–2442
36. Raimondo L, Iannucci L, Robinson P, Curtis PT (2012) A progressive failure model for mesh-size-independent FE analysis of composite laminates subject to low-velocity impact damage. Comp Sci Technol 72:624–632
37. Hashin Z, Rotem A (1973) A fatigue failure criterion for fiber-reinforced materials. J Compos Mater 7:448–464
38. Hashin Z (1980) Failure criteria for uni-directional fibre composites. J Appl Mech 47:329–334
39. Pinho ST, Robinson P, Iannucci L (2006) Fracture toughness of the tensile and compressive fibre failure modes in laminated composites. Compos Sci Technol 66:2069–2079
40. Bazant ZP, Oh BH (1983) Progressive Carck and band theory for fracture of concrete. Mater Struct 16:155–177
41. Lapczyk I, Hurtado JA (2007) Progressive damage modelling in fiber-reinforced materials. Compos Part A 38:2333–2341
42. Shi Y, Swait T, Soutis C (2012) Modelling damage evolution in composite laminates subjected to low velocity impact. Comp Struct 94(9):2902–2913
43. Yang Q, Cox B (2005) Cohesive models for damage evolution in laminated composites. Int J Fract 133:107–137
44. Pinho ST (2005) Modelling failure of laminated composites using physically-based failure models. PhD of the University of London
45. Guocai W, Jenn-Ming Y, Hahn HT (2007) The impact properties and damage tolerance of bi-directionally reinforced fiber metal laminates. J Mater Sci 42:948–957
46. Wardle BL, Lagace PA (1997) On the use of quasi-static testing to assess impact damage resistance of composite shell structures. J Reinf Plast Compos 16:1093–1110
47. Chen P, Shen Z, Xiong J, Yang S, Fu S, Ye L (2006) Failure mechanisms of laminated composites subjected to static indentation. Compos Struct 75:489–495
48. Nettles AT, Douglas MJ (2002) A comparison of quasi-static indentation testing to low velocity impact testing. ASTM, Composite Materials: testing, design and acceptance criteria 1416: 116–130

49. Chang DC, Khetan RP (1997) Surface damage of steel, aluminium and chopped-fiber composite panels due to projectile impact. J Reinf Plast Compos 3:193–203
50. Caprino G, Langella A, Lopresto A (2003) Indentation and penetration of carbon fibre reinforced plastic laminates. Compos Part B 34:319–325
51. Fiedler B, Hojo M, Ochiai S, Schulte K, Ando M (2001) Failure behavior of an epoxy matrix under different kinds of static loading. Compos Sci Technol 61:1615–1624
52. Abi Abdallah, Bouvet C, Rivallant S, Broll B, Barrau JJ (2009) Experimental analysis of damage creation and permanent indentation on highly oriented plates. Compos Sci Technol 69(7–8):1238–1245
53. HexPly M21 product data, Hexcel company, http://www.hexcel.com/Resources/DataSheets/Prepreg-Data-Sheets/M21_global.pdf
54. Olsson R (2010) Analytical model for delamination growth during small mass impact on plates. Int J Sol Struct 47:2882–2892
55. Ilyas M, Espinosa C, Lachaud F, Salaün M (2011) Modelling aeronautical composite laminates behaviour under impact using a saturation damage and delamination continuous material model. Key Eng Mater 452–3:369–372
56. Curtis J, Hinton MJ, Li S, Reid SR, Soden PD (2000) Damage, deformation and residual burst strength of filament-wound composite tubes subjected to impact or quasi-static indentation. Comp Part B 31:419–433
57. Belingardi G, Vadori R (2003) Influence of the laminate thickness in low velocity impact behavior of composite material plate. Compos Struct 61:27–38
58. Sjoblom PO, Hartnes TJ, Cordell TM (1988) On low velocity impact testing of composite materials. J Compos Mater 22:30–52
59. Adam L, Bouvet C, Castanié B, Daidié A, Bonhomme E (2012) Discrete ply model of circular pull-through test of fasteners in laminates. Comp Struct 94(10):3082–3091

High Velocity Hail Impact on Composite Laminates – Modelling and Testing

Robin Olsson, Rickard Juntikka, and Leif E. Asp

Abstract Hail impact on composite structures during flight occurs at high velocities and is a serious concern as it may cause matrix cracking, large internal delaminations, and eventually fibre fracture not visible on the impacted surface. The present paper gives an introduction to hail impact on composite laminates and an overview of experiments and modelling work on this topic, performed during several years at Swerea SICOMP. Ice balls of different sizes and velocities have been shot with an air gun on composite laminates of different thickness and reinforcement architecture. High speed photography and measurement of strain and deflection histories of the laminates have been used to validate the models developed. Models involve dynamic explicit finite element (FE) simulations with cohesive elements to allow for delamination in the laminate, and simplified but fast analytical models. The experimental response has also been compared with predictions from the FE model and the analytical models using various material models of the ice. FE models using a calibrated elastic–plastic ice model are capable of accurately predicting the response and delamination initiation, while the current analytical models are unable to simulate the initial part of the impact. A main conclusion is that delamination occurs at a very early stage of the impact (first 10–50 μs) where three-dimensional wave propagation and the initial elastic–plastic behaviour of the ice are important. Closed form models are capable of predicting the peak contact stresses at the first instance of contact, but further work is required to allow simulation of the decay of contact stresses observed in the FE simulations.

Keywords Hail impact • Composite • Laminates

R. Olsson (✉) • R. Juntikka • L.E. Asp
Swerea SICOMP AB, Box 104, SE-431 22 Mölndal, Sweden
e-mail: robin.olsson@swerea.se

R. Juntikka
FS Dynamics Sweden AB, Mölndalsv. 24, SE-412 63 Gothenburg Sweden

S. Abrate et al. (eds.), *Dynamic Failure of Composite and Sandwich Structures*,
Solid Mechanics and Its Applications 192, DOI 10.1007/978-94-007-5329-7_9,
© Springer Science+Business Media Dordrecht 2013

1 Introduction

1.1 Significance of Hail Impact

Hail and bird impact on engines and leading edges of wings and tail of aircraft in flight is a serious concern for designers due to the relatively high impact velocities. Impact by large birds is normally the most severe case, but will usually immediately be noticed and addressed. In contrast hail impact is relatively common, involves multiple impact sites and the resulting damage will in many cases remain undetected. A thorough, but fairly old review of the topic was given in [1]. Some examples of subsequent work may be found in [2]. The threat of hail impact on aircraft was recently addressed in a report to the European Aviation Safety Agency (EASA) [3]. Leading edges of aircraft are thus exposed to high velocity impact, but tend to be well protected and are rarely a part of the primary structure. Falling hail may cause severe damage to aircraft parked on ground, as the terminal impact velocity of large hail still is significant, Fig. 1, and the upper surfaces of fuselage and wings are less well protected against impact.

1.2 Effects of Hail Impact on Composite Structures

Impact damage is a particular concern for fibre reinforced composite laminates, which are sensitive to out-of-plane loading (e.g. impact) and may suffer extensive internal damage without any visible surface damage. The visibility is further reduced by impact of comparatively soft bodies like birds and ice, which produce less visible dents. Impact damage in composites typically involves cracks along

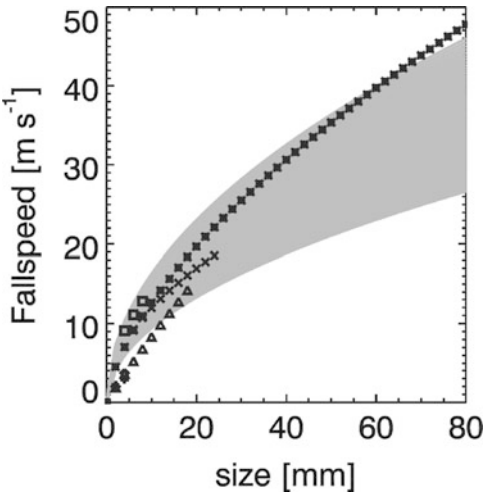


Fig. 1 Empirical (*symbols*) and theoretical (*grey range* for $0.5 < C_d < 1.5$) fall speeds for graupel and hail [3] © EASA. Reprinted with permission

the fibres (matrix cracks) and separation of plies (delamination), but may also involve fibre fracture, and may reduce the strength to 1/3 of the undamaged strength, particularly in compression [4].

The increasing use of composite materials in aircraft primary structures has caused a growing concern for the effect of hail impact on such structures. For this reason the aviation safety authorities FAA and EASA have initiated studies to define the threat of hail impact and its effect on structures, e.g. [3], with the aim to develop improved guidelines. Most work on hail impact has been focused on thin sheet metallic structures, while only a few studies have considered laminated composite structures.

Mahinfalah and Skordahl [5] compared the fatigue life of 2 mm quasi-isotropic carbon/epoxy laminates impacted by 25.4–38.2 mm diameter hail at the terminal velocity in free fall (∼45 m/s) and by 12.7 mm aluminium balls having the same kinetic energy. The ice balls caused no delaminations and no reductions in fatigue life of the laminates, while the aluminium balls caused noticeable reductions in the fatigue life. The damage inflicted by the aluminium balls was incorrectly contributed to their rigidity, but the main cause appears to have been that they were fired at a significantly higher velocity (71–139 m/s). It has been shown that delamination onset during small hard mass impact occurs at a specific threshold load [6] and that this load is virtually linearly proportional to the impact velocity, while the influence of impactor mass is negligible [7]. Hence, *the impact energy is not a relevant measure of impact severity*.

Kim and co-workers have performed extensive experimental studies and simulations of impact by artificial hail, focused on the impact response and resulting damage. The studies include quasi-isotropic layups of AS4/977 and AS4/8552 carbon/epoxy woven prepreg [8], quasi-isotropic layups of T800/3900-2 carbon/epoxy UD tape prepreg [9] and single lap joints with cross-ply carbon/epoxy UD tape prepreg [10]. Very similar delamination threshold velocities were obtained for the woven systems and for the UD-tape system.

Appleby-Thomas et al. [11] studied carbon/epoxy quasi-isotropic layups of a G0926/5 woven fibre system with an RTM-6 matrix, and a stitched triaxial NCF system with a 790 RTM matrix, manufactured using the RTM process. The plates were impacted using cylindrical ice impactors with a hemispherical front end and impacted plates were inspected using ultrasonic C-scan. The residual strength was evaluated in Compression After Impact (CAI) tests using a modified ASTM procedure, where the load only was applied over a portion of the specimen edge. Single and repeated impacts were performed to simulate the possibility of multiple hail impacts. It was found that repeated impacts resulted in a growing delamination area, essentially proportional to the cumulated energy. It is, however, hard to judge if the growth was a result of several impacts at a single point or due to several nearby impacts. Low velocity (drop-weight) impact tests [12] demonstrated that repeated impacts in a single location not causes further damage growth, while several neighbouring impacts result a superposition of delaminations for the corresponding single impacts. Appleby-Thomas et al. [11] found that the impact energy required to initiate delamination was higher for the woven architecture, and that the delamination areas and strength reductions typically were smaller for a given

energy level. A higher interlaminar toughness and less delamination is familiar from other studies of woven materials, but the two fibre architectures studied by Appleby-Thomas et al. are not directly comparable, due to differences in resin systems.

The current paper gives an overview of studies on hail impact on composites performed during 2005–2011 at Swerea SICOMP, mainly within various collaboration projects with Volvo Aero Corporation. The overview covers both previously presented work [13–15] and some previously unpublished work. This chapter is organised as follows; first an overview is given of the formation, properties and modelling of hail, secondly our experimental studies of hail impact on composite laminates are presented. This is followed by comparisons with the finite element (FE) simulations and analytical models developed at Swerea SICOMP. Finally, causes for disagreement between analytical models, FE models and experiments are discussed and areas for improvements are indicated.

2 Formation, Properties and Modelling of Hail

2.1 Hail Formation

By convention hail is defined as balls or irregular lumps of ice with a diameter of 5 mm or more [16]. Smaller pieces of ice of the same origin are called ice pellets. Smaller pieces of softer particles, typically 2–5 mm, are called snow pellets (graupel). The formation of hail is dependent on a rather specific type of weather system with strong updraft winds [17]. Strong updraft winds are present in a type of cloud called cumulonimbus ("thunderclouds"), which mostly appear in the summer. Clouds in general are created through condensation, which is related to the amount of water that air can sustain which in turn depends on temperature. The sun-warmed surface of the earth heats the surrounding damp air, which then expands and rises into the atmosphere. As it expands and cools it becomes saturated with water and eventually starts to precipitate creating tiny nuclei. Water droplets are then formed through condensation on these nuclei and small particles such as microorganisms, dust or pollen, thus making up the base of a cumulus cloud. Through combination of several cumuli a very strong, warm and humid updraft can be created with wind velocities of more than 160 km/h. This convection process creates thunderclouds which can expand over an altitude ranging from 2 to more than 15 km.

Within the thunderclouds the temperature will vary depending on the altitude, ranging from +10 to −60°C. At lower altitudes the cloud consists of droplets while at high altitudes the droplets form ice crystals. Within the given altitude interval an important phenomenon in cloud physics called super cooling occurs. Super cooling is a condition where drops of water can remain liquid at temperatures as low as −40°C. The presence of small particles in the super-cooling zone is the origin of hail formation through the fusion of droplets and the particles. The surrounding droplets, raindrops or soft hail build on the formed hail nuclei and the hail will gain altitude as the updraft increases and fall due to gravity. The dynamics of the storm

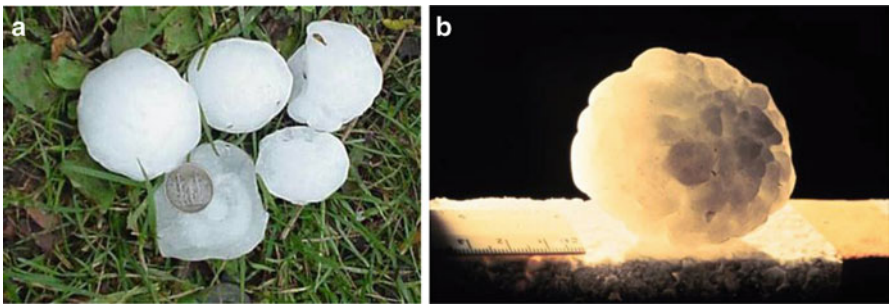


Fig. 2 Different types of hailstones; (**a**) Onion-layered [18]; (**b**) Fusion of several soft hail particles [19]

and the level of the updraft determine the continuation or the end of hail formation. If the updraft is below a certain level the hail will fall to the ground as rain or soft hail. However, if the updraft is sufficiently strong the hail particles continue to grow as they move up the continuously colder layers. Finally, when the updrafts can no longer support the weight of the hailstones or if they catch a downdraft they fall heavily to the ground, reaching speeds of up to 100 km/h for a 40 mm hailstone.

As mentioned, the hail grows either by fusion of hail nuclei and droplets, raindrops or soft hail. Depending on the growth process different hail types are formed. If the hail growth is mainly conducted within the region where super cooling is present the resulting hailstone becomes oblate spherical and "onion-layered", see Fig. 2a. This is particularly evident in larger hailstones. These layers usually alternate between opaque ice and clear ice. An opaque ice layer forms when the hailstone collects small, super cooled liquid droplets that freeze rapidly on impact, thereby trapping air bubbles within the ice and giving it a "milky" texture. This is called dry growth. When larger super cooled water drops impact on a hailstone, the freezing is slower, allowing the air bubbles to escape, and thus forming clear ice. This is called wet growth. The other type of hailstone is formed through fusion of snow pellets, thus forming a hailstone of irregular structure consisting of a number of small snow pellets (graupel), see Fig. 2b.

2.2 Mechanical Properties of Hail

It is rather difficult to find scientific investigations regarding mechanical properties of hail in the literature. There are some data on weight and dimensions of collected hailstones [3], but there appears to be a lack of direct tests of the mechanical properties of hail. As mentioned previously, the formation of hailstones can vary significantly, certainly giving varying mechanical properties of the hailstone. The structure of a hailstone depends on a number of variables present in the forming process such as droplet sizes, temperature, time of flight and level of updraft. It has been observed that hailstones may have an onion like structure, with layers of

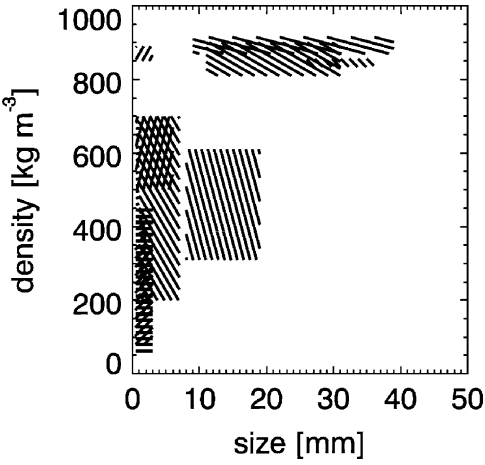


Fig. 3 Experimentally determined densities for graupel and hail [3] (© EASA. Reprinted with permission)

different density. The measured density of hail is in the interval of 300–900 kg/m^3, Fig. 3 [3]. The lower density is close to the maximum density of snow and the upper boundary is close to the density of clear ice. Due to the limited understanding of the properties of hail it is hereafter assumed that the worst-case hail impact scenario is represented by hailstones consisting of polycrystalline freshwater ice (clear ice).

The properties of ice has been an area of extensive research due to the need for relevant data in a wide variety of research areas, such as climatology, glaciology, avalanche research, comet research and studies of man-made structures in cold regions. Ice appears with a wide range of crystal structures, e.g. columnar-grained freshwater or saline (sea) ice, and random-grained polycrystalline freshwater ice (clear ice), which result in different degrees of anisotropy [20]. For extensive reviews, see e.g. [21] or [22].

In general ice is viscoelastic rather than elastic and the properties of ice strongly depend on temperature and loading rate [23–25]. Furthermore, the strength of ice is highly dependent on the hydrostatic stress component and the triaxial stress state [26]. Finally, there is a strong size effect, where the strength increases with decreasing size of the stressed volume, both in tension [23] and in compression [27]. Thus, a full characterisation of ice requires consideration of the type of ice, the temperature, loading rate and size effects for a wide range of stress states.

Polycrystalline freshwater ice (*clear ice*) is obtained by freezing water under ambient temperature and pressure, and has a hexagonal crystal structure with a density of around 900 kg/m^3. The structure results in a moderate anisotropy with a Young's modulus ranging from approximately 6 to 12 GPa along its most and least compliant direction respectively, and with a Poisson's ratio of around 0.33. Several studies have examined the properties of ice during uniaxial loading of ice cylinders with various aspect ratios. Experiments show a ductile behaviour in tension at low strain-rates and a brittle behaviour at intermediate and high strain-rates, Fig. 4 [21, 26]. Compressive stress–strain curves have shown ductile behaviour at low and

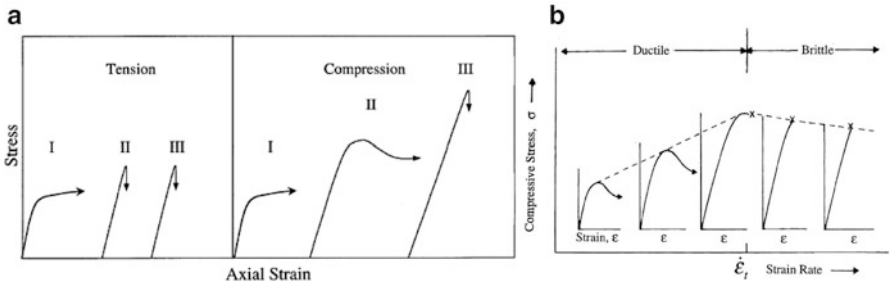


Fig. 4 Influence of strain-rate on the tensile and compressive stress–strain behaviour of ice. *I*, *II* and *III* denote low, intermediate and high strain-rate respectively. (**a**) [21] © Kluwer Academic Publisher. Reprinted with permission. (**b**) [26] © Elsevier. Reprinted with permission

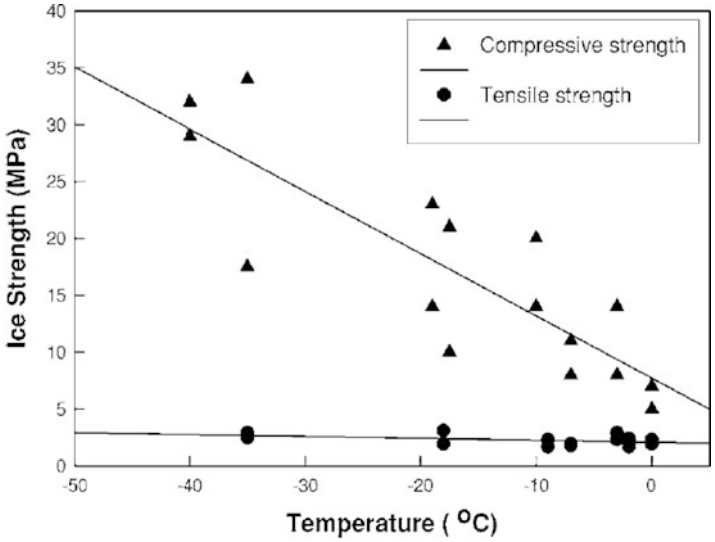


Fig. 5 Influence of temperature on compressive and tensile strength of ice [23] © Kluwer Academic Publisher. Reprinted with permission

intermediate strain-rates, but brittle behaviour at high strain-rates, Fig. 4. The compressive strength exhibits a relatively strong dependence of temperature, Fig. 5 [23] and strain-rate, Fig. 6, [24] whereas the tensile strength is much lower (about 1 MPa) and relatively insensitive to changes in temperature strain rate and temperature [23]. In general the compressive strength increases as the temperature decreases and/or the strain-rate increases. Some earlier studies indicated a decreasing compressive strength after a peak at a strain-rate of approximately 10^{-3}/s, which coincides with a transition from ductile to brittle behaviour, Fig. 4. These results are contradicted by later results in [24] obtained in the range 400–2600/s using a split Hopkinson

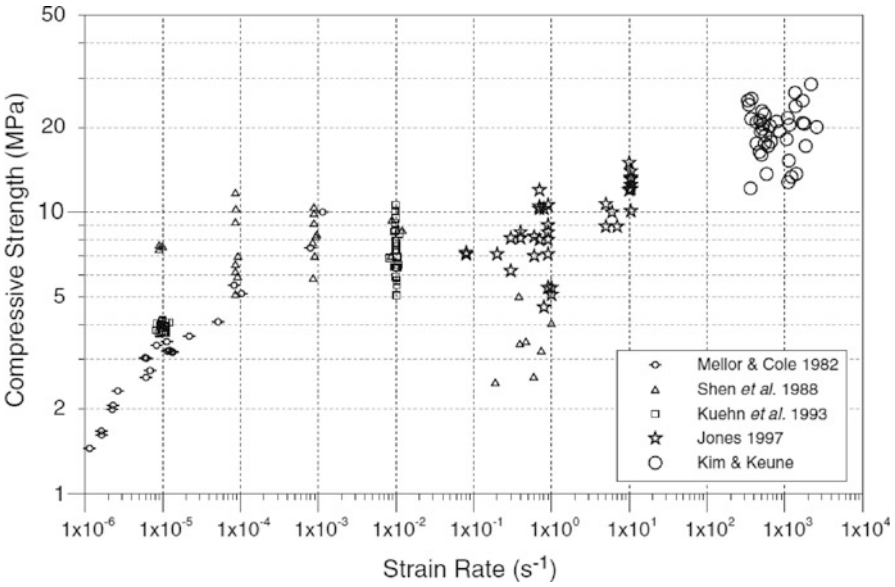


Fig. 6 Influence of strain-rate on the compressive strength of ice [24] © Kluwer Academic Publisher. Reprinted with permission

bar test, and by tests in [28] at strain rates of 10^{-3}–10^{-1}/s, where the compressive strength was fitted to a power-law of the form $\sigma = A\dot{\varepsilon}^m$, with $A = 8.9$ and $m = 0.15$.

The qualitative trends in Figs 5 and 6 have been confirmed by other studies, e.g. [29], but there is a large scatter in material data due to lack of standardised test specimens and evaluation methods. Thus a compressive strength of atmospheric ice as low as 1 MPa at −2°C and a strain rate 4.310^{-2}/s was found in [30].

Sea ice is anisotropic (results from vertical growth direction), contains salt and has a larger porosity. The strength appears to be somewhat lower than the polycrystalline freshwater ice in hail, although the qualitative influence of temperature and strain rate is similar. Thus, [31] found a tensile strength of 0.61 MPa at −5°C and 0.75 MPa at −20°C, both tested at 10^{-3}/s. The compressive strength increased from 4.67 MPa at −5°C to 8.24 MPa at −20°C, both tested at 10^{-3}/s.

The increasing strength at lower temperatures appears to be a combined effect of an increasing stiffness and increasing failure strains. Table 1 provides a comparison of reported Young's moduli and failure strains of two different types of ice. It should be noted that the properties of freshwater ice were calculated using the crosshead displacement, which indicates that the true modulus and failure strain might be substantially closer to the values reported for sea water.

As mentioned earlier, the strength of ice is strongly dependent of the strain rate and applied stress state, which is also indicated by the large differences in tensile and compressive strength. Impact of spherical ice balls will result in a triaxial stress

Table 1 Reported Young's modulus and failure strain of freshwater ice and sea ice

Property	Freshwater ice[a]		Sea ice[b]	
Density, ρ [kg/m^3]	~900		865	
Tensile Young's modulus [GPa]			6.6	−5°C;10^{-3}/s
			7.3	−20°C;10^{-3}/s
Compressive Young's modulus [GPa]	1.6[c]	−10°C;4.10^{-4}/s	6.2	−5°C;1.10^{-2}/s
	2.8[c]	−33°C;4.10^{-4}/s	7.5	−20°C;1.10^{-2}/s
Compressive failure strain [%]	0.50[c]	−10°C;4.10^{-4}/s	0.07	−5°C;1.10^{-2}/s
	0.64[c]	−33°C;4.10^{-4}/s	0.12	−20°C;1.10^{-2}/s

[a][29]
[b][31]
[c]Based on cross-head displacement

Table 2 Material properties assumed in evaluation of the analytical model

Ply properties of assumed carbon/epoxy material		Quasi-brittle ice [32]	
Density, ρ_c [kg/m^3]	1,520	Density, ρ_i [kg/m^3]	846
Longitudinal Young's modulus, E_{11} [GPa]	133	Young's modulus, E_i [GPa]	9.19
Transverse Young's moduli, $E_{22} = E_{33}$ [GPa]	10.0	Poisson's ratio, ν_i	0.33
Poisson's ratio, $\nu_{12} = \nu_{13}$	0.27	Yield strength, σ_Y [MPa]	10.3
Transverse Poisson's ratio, ν_{23}	0.44	Hardening modulus, E_{pl} [GPa]	6.89
In-plane shear moduli $G_{12} = G_{13}$ [GPa]	4.8	Bulk modulus, K_i [GPa]	8.99
Transverse shear modulus, G_{23} [GPa]	3.5	Plastic failure strain, ε_{plF} [%]	0.35
Transverse tensile strength, T [MPa]	50	Ultimate stress, σ_F [MPa]	34.4
Shear strength, S [MPa]	75	Tensile failure pressure, p_i	−4.0
Interlaminar tensile toughness, G_{Ic} [J/m^2]	421		
Interlaminar shear toughness, $G_{IIc} = G_{IIIc}$ [J/m^2]	1,420		

state, where the constitutive behaviour may differ significantly from the behaviour in uniaxial compression.

A practical approach to determine the constitutive parameters for the triaxial stress state during impact is to shoot ice balls on instrumented plates or flat load cells, and to use dynamic FE simulations to fit an appropriate constitutive model to the experimental results. This approach was used in [32] where hail impact experiments were performed on composite plates using manufactured ice balls with a temperature of −17°C. The experiments were simulated using the explicit software programme LS-Dyna 3-D employing material type 13, elastic–plastic with failure. Basic material inputs were collected from the literature but certain values for input, such as hardening modulus etc., were parametrically determined by comparing the numerical simulations with the experimental data. The simulation results were consequently in very good agreement with experiments. The resulting material properties have been listed in the right part of Table 2. The current authors successfully applied a similar approach during modelling of in-house experiments [14]. Key parameters of the material model were determined through a factorial parameter study and were fitted to a few benchmark tests, but the model details are commercially confidential.

According to [32] measurements of the adiabatic shock Hugoniot curves (pressure–volume relationship) of ice in [33] showed that an extremely large pressure (23.5 GPa) is required to cause a phase change from solid to liquid states. In the context of ice projectiles, there is insufficient confinement to allow such large pressure build-up. Therefore impacting ice is not expected to undergo phase change.

2.3 Manufacture of Artificial Hail

Various approaches have been used to manufacture ice samples. Kim and Kedward [32] produced monolithic and layered ice balls by using spherically shaped two-part moulds. The layered ice is slightly tougher than monolithic ice and was manufactured to simulate hail with a spherically layered "onion-like" structure. Due to manufacturing difficulties the layered ice balls were produced with flat layers of equal thickness through the diameter. When firing the ice spheres towards panels the impacting direction was aligned normal to the flat layers. Kim et al. [8] simply used a spherical split mould having a filling hole and after filling them up with water, the spheres were kept frozen at a temperature of −26°C. Arakawa and Maeno [29] compacted fine ice particles in a vessel at 7 MPa and 0°C at a pressure of 100 Pa below that of the atmosphere, which resulted in samples that were almost bubble free. A more than sophisticated way of the manufacturing procedure is the method used in [30]. They used a wind tunnel where they installed an aluminium collector, which they sprayed with water droplets using a water nozzle. The aim of the work was to investigate the influence of different atmospheric conditions on the mechanical properties of atmospheric ice. Weiss and Schulson [34] used presieved seeds and distilled, deionised and degassed water. An aluminium rectangular mould was filled with fragments of one size of ice in order to control the grain size, and was then evacuated at 0°C over 3 h. Afterwards, the water was passed slowly through the mould and the ice-water mixture was frozen radially inward using cooling plates at −5°C attached to the sides of the mould. The resulting porosity was low (<0.2%). To receive a reasonably low porosity in freezing ice resembling clear ice it seems to be sufficient to use a mould and freeze the samples in under-pressure conditions.

2.4 Influence of Impactor Shape

The type of ice and shape of impactors typically used in hail impact tests can affect the representativeness of these tests compared to a "real-life" impact. Combescure et al. [35] performed a series of high and low velocity impact tests on a rigid support and flexible aluminium plates using flat or conical impactors made of monocrystalline and polycrystalline ice. In cases of conical (or inclined flat) ice

impactors, the failure mode was always by cleavage while fine fragmentation was found for flat impactors. For a given impact velocity, the permanent deformation of the aluminium plates was greater in cases involving fragmentation, i.e. for flat impactors, which appear to represent a "worst-case" scenario as far as the impactor shape is concerned. Increasing velocity resulted in increased permanent deformation of the aluminium plates and smaller ice fragments.

A characteristic of ice impact is that the fragmentation of the impactor results in a large area of the impacted component being affected by the dynamic loading. The deflection of ice fragments instantly after impact was investigated in [36]. Impact tests of spherical ice impactors of several diameters were performed on rectangular plates, which could be tilted to offer different incident angles. The authors report that at the moment of impact, fragments from the front of the ball form a low density chaotic cloud which then evolves into a higher density, disk shaped cloud. The deflection angle was insensitive to the incident impact angle or impactor diameter and was relatively shallow ($\sim$1°–2°) with respect to the impacted surface. It was found that the cloud travels at a velocity close to the tangential impact velocity while preserving a disk shape.

2.5 Material Models for Hail

Various material models have been developed for numerical modelling of hail. The elastic–plastic model with brittle failure in [32] has already been mentioned. A modified version of this model was used by the current authors [14]. A more advanced ice model was developed in [37], as a part of the NASA investigations after the disaster with the space shuttle "Columbia". The model accounted for independent failure stresses in tension and compression, strain rate sensitivity of the flow stress, the ability of the failed ice to continue to carry hydrostatic stress and use of an Eulerian mesh, but did not consider effect of temperature. It was noted that consideration of the lower failure stress in tension would be of particular importance for non-spherical impactors, where the failure is no longer entirely controlled by compressive stresses. The model was based on interpolation of tabulated experimental data rather than on analytical relations for an assumed material model. A good agreement was shown for a range of different impacts on fixed load cells. Comparisons with alternative ice models were limited but it was noted that the model was able to successfully predict the fragmentation during impact by ice cylinders, in contrast to an elastic–plastic model of the type used in [32] and [14], which had been tuned for pressure dominated stress states during impact by ice spheres.

Chuzel et al. [38] developed a material model for ice and compared it to data from tests at low strain rates ($\leq$50/s) in [35]. The model is based on an isotropic damage model for concrete which assumes a linear elastic behaviour before failure initiation and uses an exponential softening law to handle progressive damage. The damage model features independent damage variables in tension and compression

and a regularization scheme for mesh objectivity. The model was implemented in LS-DYNA and used with an SPH formulation. It correlated well with results in [35], even though the SPH grid appears rather coarse to accurately capture the different wave features appearing during impact.

A material model for ice was also developed in [39], but the model was not applied to impact simulations. The model uses a continuum damage approach to model the brittle behaviour of ice and includes a plastic response with strain rate dependency. The model was implemented in an explicit FE code and used with standard solid elements. Failure locus for biaxial loading was predicted and in good agreement with experimental data. The model was also verified on three point bend tests but no correlation with experimental data was presented.

The developments in [38] and [39] indicate that accounting for the brittle cracking through progressive damage is important for the modelling of the ice material. Both models are based on models used for concrete, and even though the model in [39] includes features specific to the ice material (e.g. plasticity and strain rate), the physical basis of the models is rather unclear. To handle mesh objectivity a regularization scheme was used in [39]. However, both the regularization value and the characteristic length needs to be adjusted for a given mesh configuration, which can cause problem for irregular meshes and also raise the question of the actual fracture energy being spent to progress damage.

3 Experiments

3.1 Aims and Content

The experimental studies of ice impact have been conducted in close collaboration with Volvo Aero Corporation in Sweden. Most of these studies have been linked to investigations of candidate composite materials for outlet guide vanes (OGV) in the FP6 VITAL project [40]. One of the aims of this project was to demonstrate the possibility to use polymer composites in structural components of jet engines for future passenger aircraft. Based on the impact threat expressed by the aero engine manufacturers in the VITAL project the OGV must sustain normal impacts from 50 mm diameter ice at velocities exceeding 100 m/s (normal to the OGV). The experimental investigations aimed to compare and judge the merits of different composite materials and fibre architectures for their impact resistance to realistic threats from hail and runway debris.

3.2 Specimens

Several different composite materials were impacted using ice spheres and/or stones:

Table 3 Material properties of carbon/vinylester NCF assumed for predictions in Fig. 22

Ply properties of carbon/vinyl ester NCF	
Density, ρ_c [kg/m^3]	1,520
Young's moduli, 0° or 90° plies, E_{11} [GPa]	100 [a]
Young's moduli, ±45° plies, E_{11} [GPa]	116 [a]
Out-of-plane Young's modulus, $E_{22} = E_{33}$ [GPa]	7.6 [a]
Poisson's ratio, ν_{23}	0.31 [a]
In-plane Poisson's ratio, $\nu_{12} = \nu_{13}$	0.36 [a]
In-plane shear moduli $G_{12} = G_{13}$ [GPa]	2.9 [a]
Transverse shear modulus, G_{23} [GPa]	2.9 [a]
Transverse tensile strength, T [MPa]	50 [b]
Shear strength, S [MPa]	75 [b]
Interlaminar tensile toughness, G_{Ic} [J/m^2]	577 [c]
Interlaminar shear toughness, $G_{IIc} = G_{IIIc}$ [J/m^2]	1,152 [c]

[a][41]
[b]Assumed
[c][42]

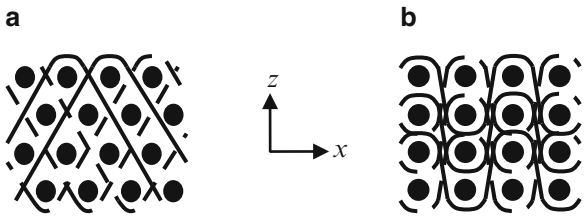


Fig. 7 Architecture of tested 3D weaves: (**a**) Angle interlock (AI), (**b**) Layer-to-layer interlock (LTL)

1. Quasi-isotropic $[0°/90°/45°/-45°]_{s3}$ non-crimp fabric (NCF) carbon fibre/vinyl ester (Norpol DION 9500–501) laminates of thickness 5.4 mm. The preform was a biaxial carbon fibre NCF (Devold AMT LT450 and DB450, 205 g/m^2 in each direction).
2. Quasi-isotropic non-crimp fabric (NCF) carbon fibre/epoxy laminates with nominal thickness 4 and 6 mm.
3. Orthotropic plain weave (PW) AS7-J/RTM6 carbon fibre/epoxy laminates with nominal thickness 4 mm.
4. Orthotropic 3D weave, angle interlock (AI) AS7-J/RTM6 carbon fibre/epoxy with nominal thickness 5 mm.
5. Orthotropic 3D weave, layer-to-layer interlock (LTL) AS7-J/RTM6 carbon fibre/epoxy with nominal thickness 4 mm.

The properties of material 1 are listed in Table 3. The weave reinforced composites were orthotropic and contained only fibres in the 0°/90° directions. The two 3D weaves (angle and layer-to-layer interlocks) are schematically depicted in Fig. 7, and were selected to achieve two laminates with considerably different shear stiffness.

All laminates were made by vacuum infusion of a resin into dry fibre preforms and had a fibre volume fraction between 50 and 55%. Measured and predicted homogenised in-plane and out-of-plane tensile properties for the different materials are listed in Table 4.

Table 4 Predicted homogenised in-plane properties for the various laminates

Property	CF/Vinyl ester NCF	CF/epoxy NCF	AI 3D weave	LTL 3D weave
Density, ρ [kg/m^3]	1,530 [a]	1,520[a]	1,510[c]	1,495[c]
Fibre volume fraction, v_f	55[a]	55[a]	50[c]	55[c]
Young's modulus, x-direction, E_x [GPa]	≈39[a]	≈52[a]	79[b]/25[c]	97[b]/96[c]
Young's modulus, y-direction, E_y [GPa]	≈39[a]	≈52[a]	51[b]	51[b]
Young's modulus, z-direction, E_z [GPa]	≈7.6[a]	≈10[a]	16[b]	12[b]
Shear modulus, G_{xy} [GPa]	≈16[a]	≈20[a]	6.2[b]	6.1[b]
Shear modulus, G_{yz} [GPa]	2.9[a]	4.1[a]	5.2[b]	4.9[b]
Shear modulus, G_{xz} [GPa]	2.9[a]	4.1[a]	13.7[b]	6.2[b]
Poisson's ratio, x-y-plane, ν_{xy}	0.36[a]	0.31[a]	0.04[b]	0.06[b]
Poisson's ratio y-z-plane, ν_{yz}	0.31[a]	0.34[a]	0.24[b]	0.34[b]
Poisson's ratio x-z-plane, ν_{xz}	0.31[a]	0.34[a]	0.71[b]	0.42[b]

[a]Based on available ply data and laminate theory
[b]Predicted by manufacturer, using textile software
[c]Measured [43]

The properties of the NCF laminates are based on laminate theory and experimental data from unidirectional NCF specimens. The predicted properties of the 3D weaves were provided by the manufacturer and were based on their own in-house software for textiles. Tensile tests in the x-direction indicated that the properties of the LTL weave were accurately predicted, while the properties of the AI weave appear to be severely overestimated. The discrepancy between predicted and measured properties of the AI weave laminates are partly or fully explained by microscopy observations which indicated significant matrix cracking after curing. Inability of the software to accurately predict matrix dominated properties may, however, also have contributed to the discrepancy. Note that the laminates from multidirectional NCF material will be somewhat orthotropic in flexure, and that the degree of flexural orthotropy is influenced by the thickness and stacking sequence.

Specimen types 1 and 2 had dimensions 250×250 mm, with a free window of 200×200 mm, while specimens 3–5 had length 150 mm and width 100 mm. The length direction is assigned the x-coordinate and the width direction the y-coordinate. During cross sectioning of the 3D weave reinforced plates the directions of the warp and weft directions in relation to the x- and y-directions of the plates during testing were confirmed, as indicated in Fig. 7.

3.3 Impact Testing

The laminates were cut into plates and impacted in the high-speed gas gun impact equipment at Luleå University of Technology in Sweden. The current paper is limited to experiments using 34 and 48 mm diameter ice spheres. Similar tests were also performed with 6 mm diameter runway stones and have been briefly described

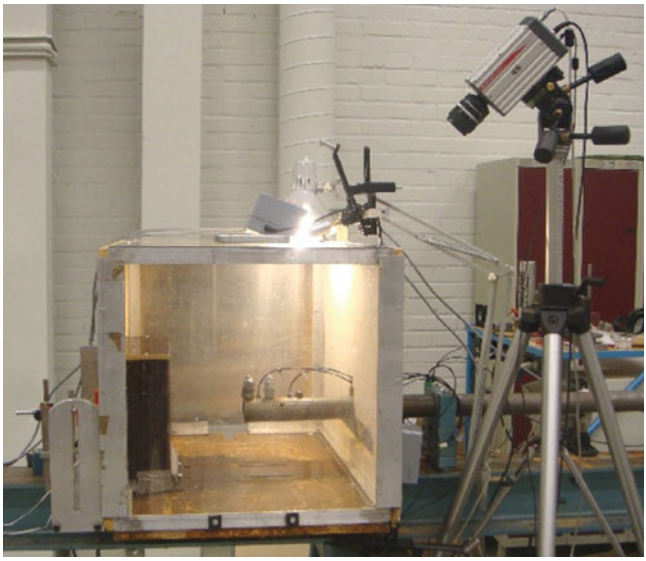


Fig. 8 Complete test setup [14]

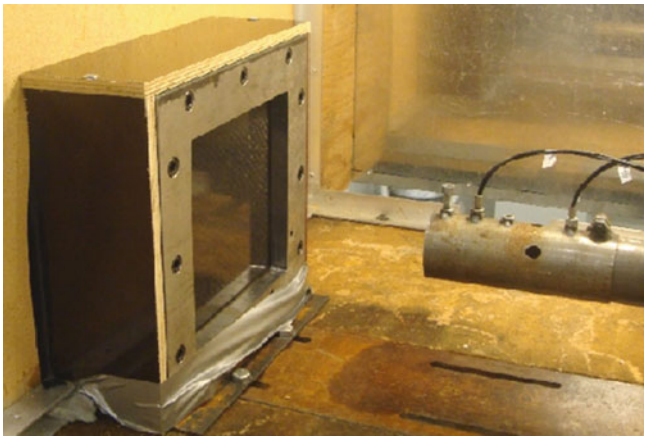


Fig. 9 Steel rig with plate and pipe end [14]

in [13]. The experiments were followed by a fractographic investigation consisting of visual inspection, ultrasonic C-scan analysis, optical microscopy and Scanning Electron Microscopy (SEM).

The gas gun consisted of a compression tank connected to a steel pipe approximately 5 m long with an inner diameter of 52 mm. The end of the pipe was placed inside a box where the plates were fastened approximately 200 mm from the pipe end using a steel rig, see Figs. 8 and 9.

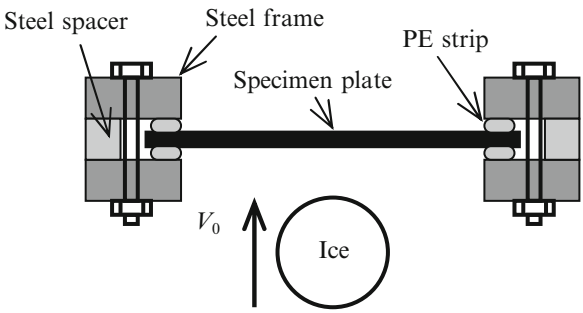


Fig. 10 Centre cross-section of the steel rig, view from above [14]



Fig. 11 Moulded ice ball [14]

The steel rig was made of three parts, front and back plates, width and height 300 and 20 mm thick with a steel spacer in between. The plates were mounted in the rig using steel bolts with a plexi-glass strip in front and a polyethylene (PE) strip in the back of the plates, see Fig. 10. The polymer strips were 5 mm thick and the clamping was made to compress the PE strip approximately 1 mm. The open window measured 200×200 mm with a radius of 10 mm in the corners.

Ice balls with different diameters, $\phi = 25$ to 48 mm, were manufactured by filling fresh tap water in squash balls and plastic balls, and allowing air to escape during a period of about 1 week. Subsequently the water was frozen slowly at a temperature of about -2°C. Thereafter the temperature was lowered to -10°C, which was maintained until testing. The moulded ice balls deviated somewhat from perfect spheres but were of rather high quality in terms of absence of cracks, see Fig. 11, although there were indications of a limited amount of micro-cracks close to the plastic mould filling hole. The mass and average diameter of each ice ball were measured prior to launch using a scale and a caliper, giving an average density of $\rho_{ice} = 970$ kg/m^3.

A low density cylindrical foam plug (sabot) was used to push the ice balls down the pipe using compressed air. The foam plugs were used to soften the acceleration

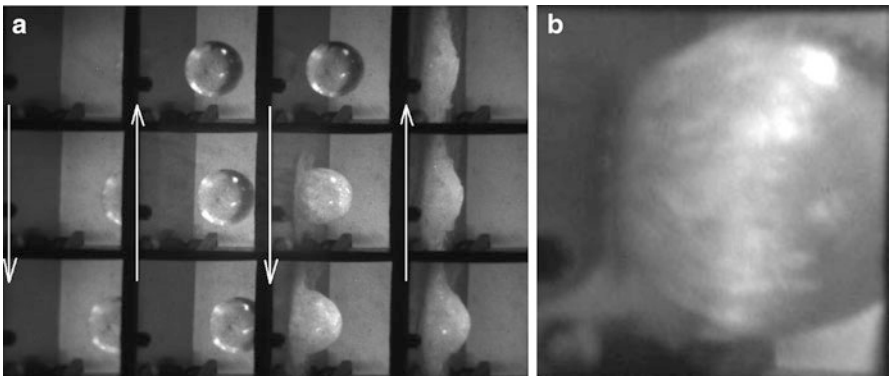


Fig. 12 Pictures captured by high speed camera. (**a**) Impact event [13] © Elsevier. Reprinted with permission, (**b**) Pressure wave in the ice [14]

and protect the ice. The impact speed was measured using two laser sensors placed at a specific distance between each other close to the pipe end, see Fig. 9.

Centre displacements of the plate and ice impact velocity were recorded for all materials tested (see Sect. 3.2). For the NCF laminates strain gauges (Kyowa KFRP-2-120-C1-3L1M3R, 2 mm gauge length, 120 Ω) were also applied on the back of the plates, one in the centre and one 50 mm off centre. Both were applied in the direction of the surface ply direction to increase the ability for measurement after initiation of matrix cracks. The strains were registered using a half bridge amplifier with a bandwidth of 100 kHz. The deflections and strains were registered using a sampling frequency of 1 MHz. The impact events were recorded using high speed video (MotionPro X3 Plus, Red Lake) using a sampling frequency of approximately 6,000 frames per second. After impact an ultrasound equipment (Sonatest 380 M with Sonatest 5 MHz/0.5 in. probe) was used to monitor damage initiation (delamination) in the plates.

3.4 Experimental Results

In the experiments, a pressure wave forms at the point of contact and moves towards the back of the ice ball. The wave creates micro cracks which suddenly transforms the ice from a solid body to a body made up of small ice particles. A small rise in the strain response can be seen just prior to when the equator of the ball reaches the plate, which is probably related to the momentum of the ball. Figure 12 illustrates the impact scenario. The pictures in Fig. 12a should be read from the first column on the left going down, second column going up etc. Figure 12b shows a snapshot of the pressure wave (white band) travelling from the impact point.

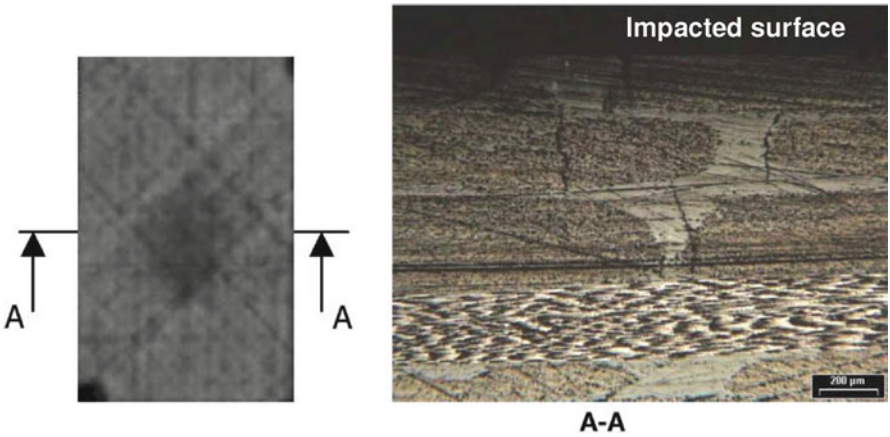
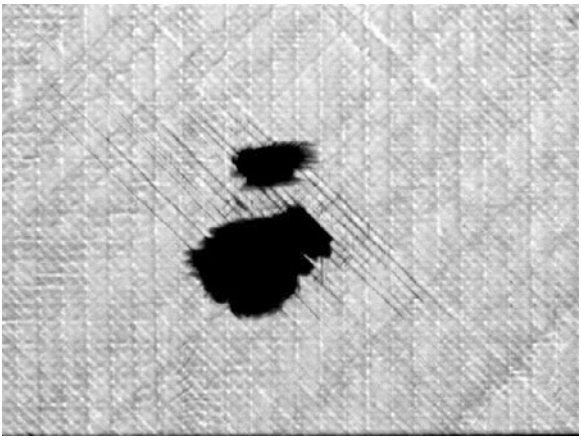


Fig. 13 Matrix cracks at the impact point. Ultrasound image and polished cross-section of an NCF laminate [13] © Elsevier. Reprinted with permission

Fig. 14 Ultrasound image of damage after impact



Investigations of the impacted plates show a typical damage initiation and progression response. When the damage threshold velocity is exceeded, damage appears as transverse matrix cracks at the impact point, see Fig. 13. As the impact velocity increases delaminations appear, growing in size as the velocity increases, see Fig. 14.

Interlaminar delaminations typically appear for a laminated composite material. For the 3D-weaves other damage types generally appear as well, such as fibre tensile breakage, fibre kinking and fibre-matrix debonding see Figs. 15 and 16.

Figure 17 gives a comparison of the visually detected damage for the 2D plain weave and the two 3D weaves at different normalised impact velocities. Subsequent

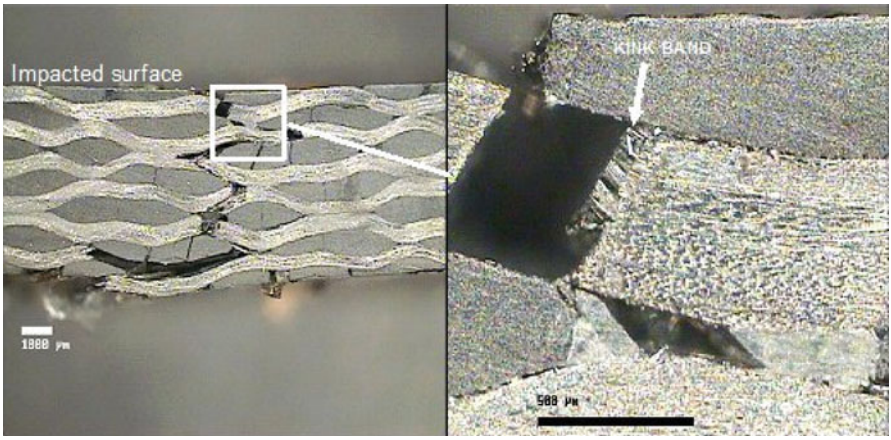


Fig. 15 Damage in 3D angle interlock (AI) weave

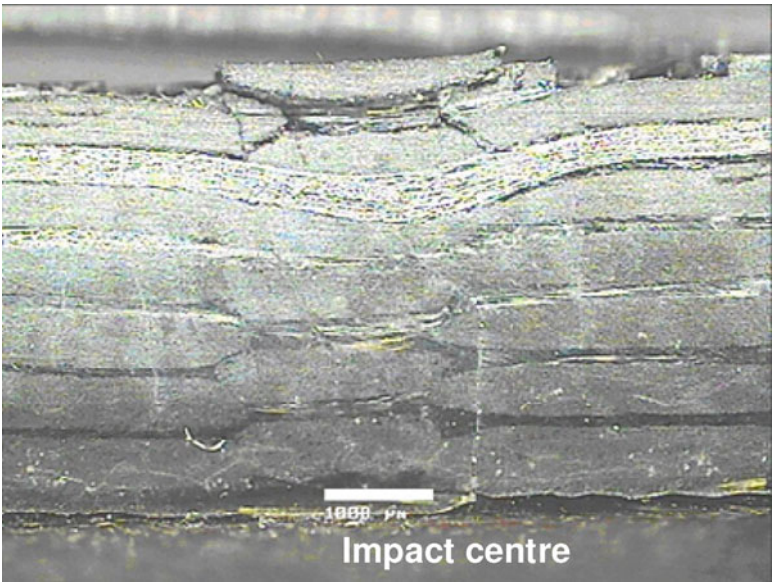


Fig. 16 Damage in 3D layer-to-layer (LTL) interlock weave

C-scans have been included together with arrows indicating the corresponding velocity, and show that large delaminations were present well before visible damage. The velocity range where delamination was detected by C-scan in the reference NCF-system has also been included for comparison. It is noted that delaminations in the woven laminates were present at much lower velocities than in the NCF

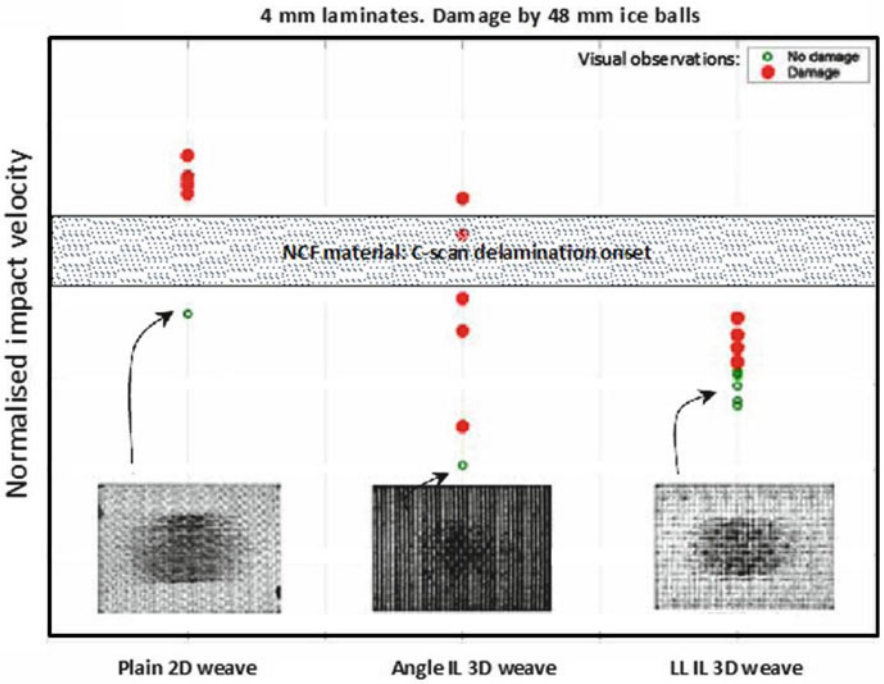


Fig. 17 Comparison of damage in NCF and weaves at different normalised impact velocities

laminates. The more extensive damage may partly be explained by the fact that fractography indicated that the fibre-matrix adhesion not was optimal for the woven laminates, which were based on a different fibre/matrix system than the NCF laminates. Nevertheless, all woven laminates contained a common fibre/matrix system and it is noted that an *increasing* degree of fibres in the thickness direction, i.e. the progression from 2D Plain Weave via Layer-To-Layer interlock 3D weave to Angle Interlock 3D weave, resulted in a *decreasing* damage threshold velocity. The extensive damage in the angle interlock system appears to have been caused by excessive deformation of the fibre bundles during the RTM process and by extensive matrix cracking after curing, which were observed on micrographs prior to testing. The matrix cracks are reflected by the black bands in the C-scan, which are present outside the delamination zone of the angle interlock 3D weave in Fig. 17.

The centre strain gauge readings (NCF material), Fig. 18a, show an initial peak corresponding to the first impact, and a second peak due to the arrival of the major flexural wave after reflection at the boundaries. Figure 18b illustrates a typical behaviour for the strain gauge located 50 mm off-centre.

The response illustrated in Fig. 18a indicates that the delamination threshold velocity is controlled by the peak load (peak centre strain) occurring just after the

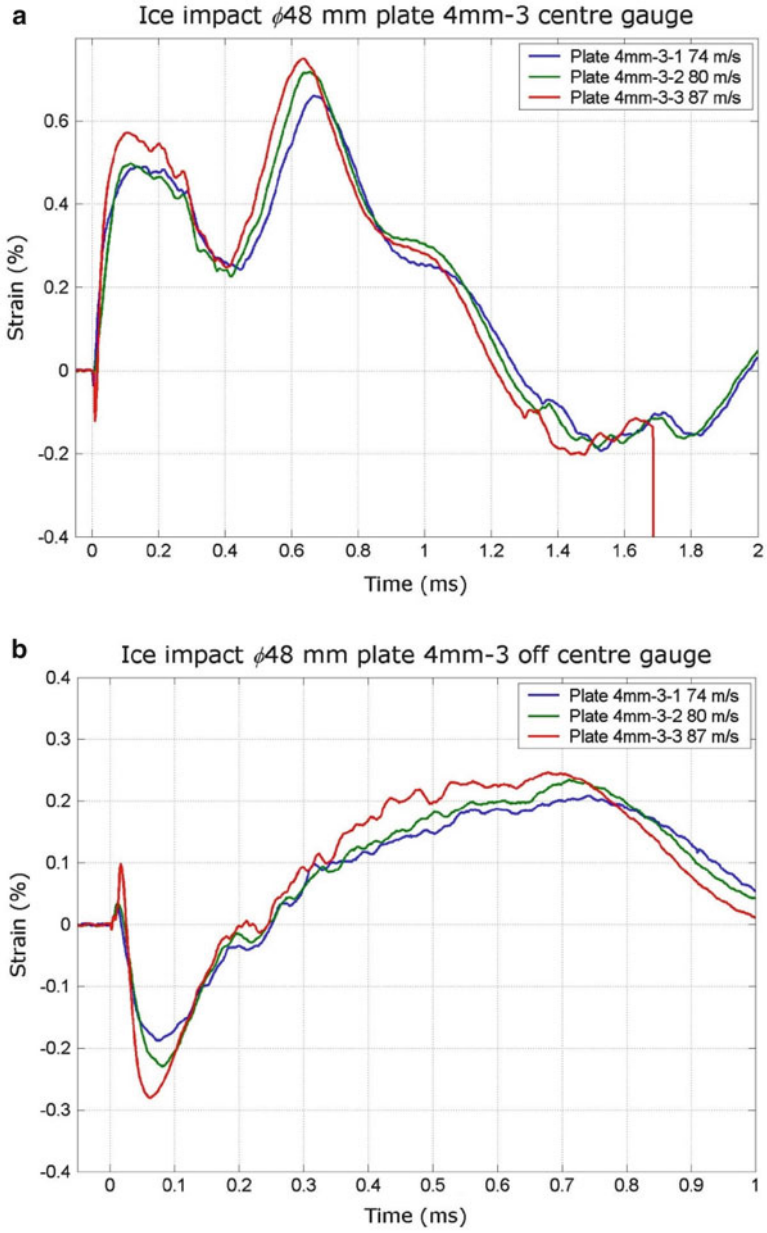


Fig. 18 Experimental strain history from ice impact. Strain response at (**a**) the centre and (**b**) off-centre

initial linear response. The FE simulations and previous analytical work [44], show a very strong link between the contact load and local flexural strains. Hence, the centre strain history also gives an indication of the impact load history.

4 Finite Element Simulations

The numerical modelling part was divided into calibrating the ice material model and predicting the threshold velocity for initiation of damage (delamination). All calculations were carried out using LS-Dyna.

The calibration of the ice material model was performed by choosing a representative material model and a parameter fitting procedure. The model is similar to the elastic–plastic ice model used in [32]. Two experiments were chosen to calibrate the model, one using a ϕ34 mm ice ball and one using a ϕ48 mm ice ball. The velocity in both tests was beneath the delamination initiation threshold velocity. A factorial parameter study was performed to identify how the material model parameters influenced the impact response. The factorial study was followed by a fitting of the parameters to the experimental results.

The plate was modelled using layered thick shell elements for the plate and Smooth Particle Hydrodynamics (SPH) for the ice ball. Four layers of thick shell elements (6 plies in each element layer) with full 3D stress updating were used through the thickness of the plate. Figure 19 illustrates the FE model.

For prediction of delamination initiation and growth a layer of solid cohesive elements of thickness $t_{coh} = 0.01$ mm was included in the centre of the laminate, where the highest shear stresses are expected. The cohesive elements (LS Dyna no. 138) allow for mixed mode tensile-shear interaction using bilinear cohesive laws with linear softening after failure initiation. Hence, each material is modelled by the

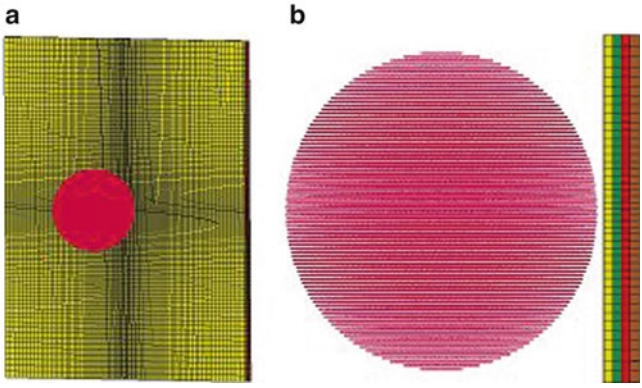


Fig. 19 FE model of the ice impact: (**a**) complete model, (**b**) close up of the ball and the centre of the plate [14]

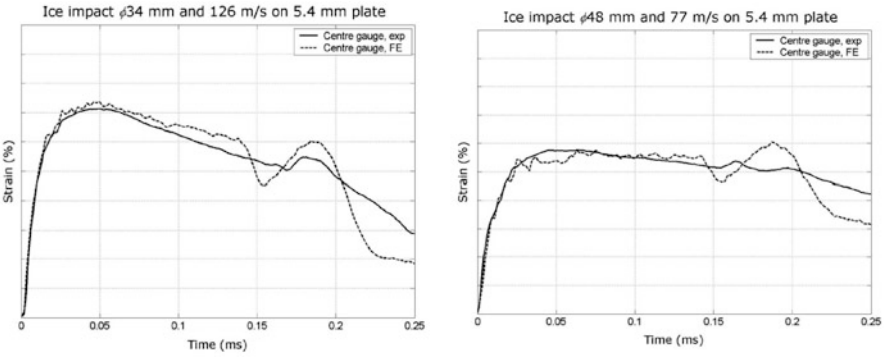


Fig. 20 Comparison of strain response between experiment and FE simulation after calibration of the ice material model [14]

interlaminar toughness values G_{Ic} and G_{IIc} (G_{IIIc} is assumed equal to G_{IIc}), and the interlaminar tensile strength T and shear strength S. The corresponding normal (EN) and tangential (ET) stiffness of the cohesive element were set to $EN = E_{33}/t_{coh}$ and $ET = G_{13}/t_{coh}$. Interlaminar toughness and strength were either based on published data or on available in-house experimental data.

The computational approach is demonstrated here on the quasi-isotropic carbon/vinyl ester NCF laminate (specimen type 1). The material properties used in the analysis were listed in Table 3. Further details on the experiments may be found in [14].

The modelling of the damage initiation threshold velocity was performed for four different ice ball diameters, ϕ25, ϕ34, ϕ40 and ϕ48 mm. Experimental results were only available for the ϕ34 and ϕ48 mm ice ball impacts, the other two were performed to give a more thorough comparison with the analytical model. The result of the calibration of the ice material model is shown in Fig. 20. The fidelity of the ice model is also supported by the ability to capture the stress wave in the ice and the subsequent microcracking, c.f. Figs. 12 and 21.

The predicted delamination threshold velocities, and corresponding experimental results, for the 5.4 mm carbon fibre/vinyl ester biaxial NCF laminates are given in Fig. 22. Further details and material data on these experiments can be found in [14]. The delamination threshold velocity was found by gradually increasing the impact velocity until delaminations were detected using ultrasonic equipment. In this case only two panels were available for testing and the tests with the 48 mm diameter ice ball were interrupted before the delamination threshold velocity was reached. A good agreement between predictions and experiments has, however, also been found in simulations performed in more extensive confidential studies of quasi-isotropic carbon/epoxy NCF laminates of different thickness.

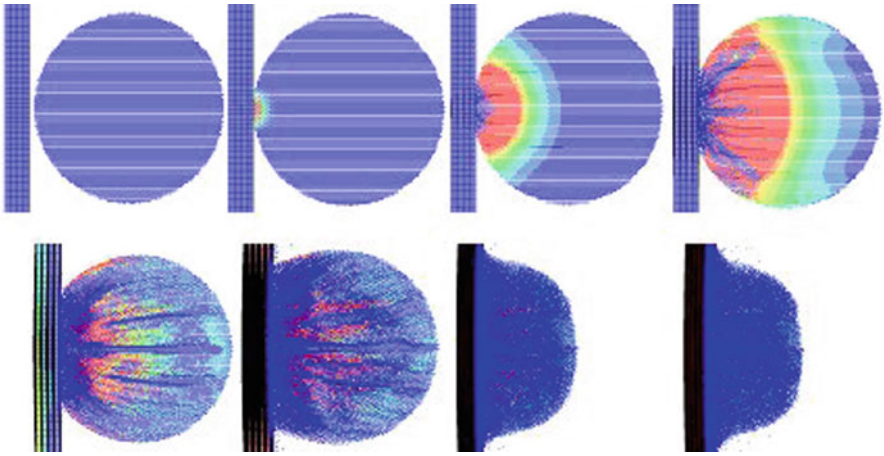


Fig. 21 Pictures from FE simulation of the Ø48 mm ice impact [14]

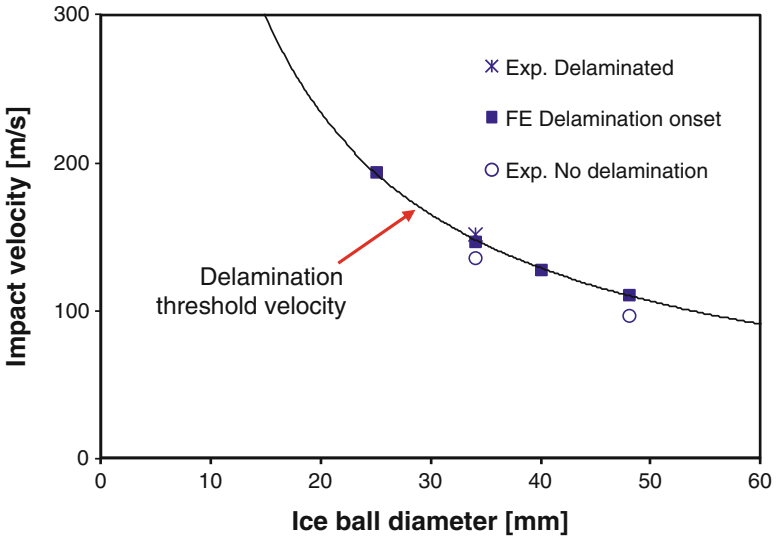


Fig. 22 Comparison between FE predictions of delamination onset and experimental observations for a 5.4 mm carbon/vinyl ester NCF laminate [14]

5 Analytical Models

5.1 Impact Response Up to Delamination Onset

An analytical response model was developed for fast numerical simulation of hail impact [15]. The model is based on a model for small mass impact on thin

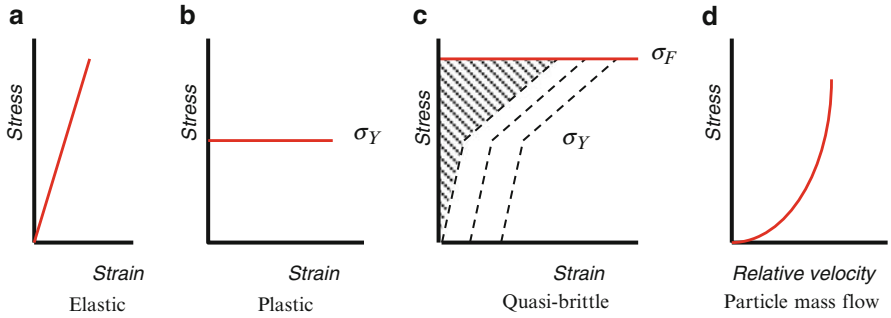


Fig. 23 Material models considered in the analytical impact model

orthotropic plates [45], which has been modified to account for a finite contact area and various constitutive models for the impactor. The underlying assumptions of the model are as follows:

- The plate region affected by impact through flexural and shear waves is smaller than the total size of the plate
- The contact area is much smaller than the affected region of the plate
- Through-the-thickness waves do not affect the contact behaviour (i.e. quasi-static contact applies).

Four different material models were considered for the ice ball; (a) fully elastic, (b) ideally plastic, (c) quasi-brittle, (d) mass flow of particles, Fig. 23. Failure of the quasi-brittle material was assumed to occur as a sequence of brittle failures at the ultimate failure stress σ_F. Figure 23c illustrates a sequence of elastic–plastic loading curves (dashed) with brittle failure at σ_F, and the corresponding simplified material model (solid line), together with the neglected initial behaviour (shadowed area). For the particle cloud no cohesive forces are present and the contact pressure is equal to the dynamic pressure from the mass flow against the plate, Fig. 23d.

For comparison with FE simulations a 48 mm diameter ice ball impacting the centre of a plate with dimensions $200 \times 200 \times 6.15$ mm was considered. The plate considered consists of carbon/epoxy NCF material with the layup $(45/0/-45/90)_{3s}$. A mode II interlaminar toughness $G_{IIc} = 1{,}420$ J/m^2 was assumed, [46]. The quasi-brittle ice model was based on the data in [32]. The material properties assumed for the composite plies and the quasi-brittle ice are listed in Table 2. For the composite plies index 1 refers to the fibre bundle direction, 2 and 3 to the in-plane and out-of-plane directions transverse to fibre bundles. For the ideally plastic ice E_{pl} was set to 0.001 GPa and ε_{plF} to 1,000.

The approach α ("indentation") between the impactor and plate may be expressed through the displacements w_i of the ice impactor and w_p of the plate centre, which are given as follows [45]:

$$\alpha = w_i - w_p = \underbrace{V_0 t}_{\substack{\text{Free impactor}\\ \text{movement}}} \underbrace{- \frac{1}{M}\int_0^t F(\tau)\,(t-\tau)\,d\tau}_{\text{Impactor retardation}} \underbrace{- \int_0^t \frac{F(t)}{8\sqrt{mD^*}}\frac{2}{\pi}\arctan\left[\frac{(t-\tau)\,S^*}{\sqrt{mD^*}}\right]d\tau}_{\text{Plate bending deflection}} + \underbrace{\int_0^{t-t_0} \frac{F(t)\,d\tau}{2\pi\,S^*\,(t-\tau)}}_{\text{Plate shear deflection}} \tag{1}$$

where V_0 is the impact velocity, M is the impactor mass, F is the resulting contact load, m is the mass per unit area of the plate, D^* is an effective bending stiffness of the plate, S^* is a corresponding shear stiffness, t is time, t_0 is a time correction accounting for finite contact area and τ is dummy integration variable. The time constant t_0 and the effective bending and shear stiffness D^* and S^* of orthotropic laminates are given by the following expressions:

$$D^* \approx \sqrt{D_{11}D_{22}(1+\eta)/2} \quad \text{where} \quad \eta = (D_{12}+2D_{66})\Big/\sqrt{D_{11}D_{22}}$$
$$S^* \approx \sqrt{A_{44}A_{55}} = \sqrt{K_{yz}G_{yz}h\;K_{xz}G_{xz}h} \qquad t_0 = R\alpha\sqrt{m/D^*}/4 \tag{2}$$

where D_{ij} and A_{44}, A_{55} are the bending and transverse shear stiffnesses according to laminated plate theory, K_{ij} are shear factors (≈5/6), h is the plate thickness, and R is the radius of the impactor (ice ball).

The contact load may be obtained from the following relation [15]:

$$F = p_{av}\pi\,c^2 \qquad \text{where} \begin{cases} c^2 = R\alpha & \text{for elastic contact} \\ c^2 = 2R\alpha - \alpha^2 & \text{for plastic contact} \end{cases} \tag{3}$$

where c is the contact radius. The contact radius for plastic conditions is obtained from a purely geometrical relation, assuming no material pile up at the contact edge.

The average contact pressure p_{av} is given by the following expressions [15]:

Elastic material	Plastic material
$p_{av} = \frac{4}{3\pi}Q_\alpha\sqrt{\alpha/R}$	$p_{av} = 2.8\sigma_Y$
Quasi − brittle	Particles
$p_{av} = \sigma_F$	$p_{av} = \frac{1}{2}\rho_i\left(V_0 - \dot{w}_p\right)^2$

(4)

where Q_α is an effective contact modulus, σ_Y is the yield stress, σ_F is the ultimate compressive strength and $\dot{w}_p$ is the deflection velocity of the plate at the point of impact. All cases, except the elastic, have more or less uniform contact pressure

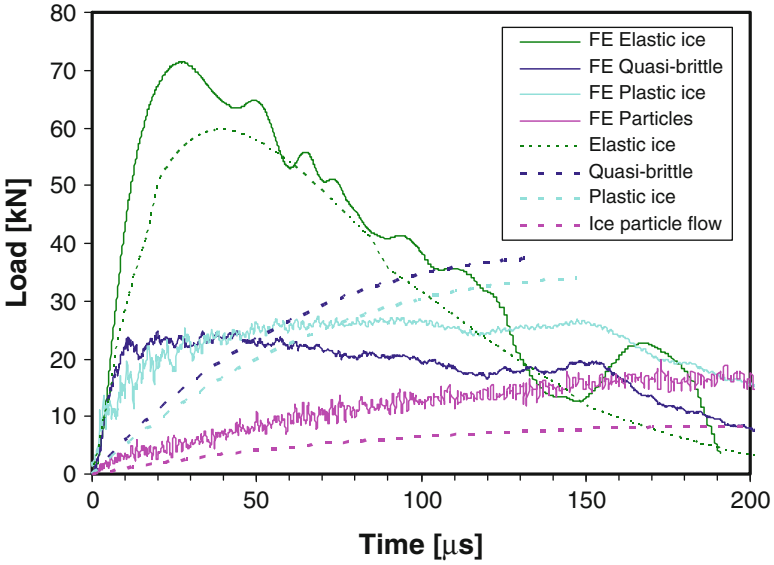


Fig. 24 Effect of various ice models during 117 m/s impact on elastic plate [15]

distributions. The average contact pressure for plastic contact is based on empirical findings by Tabor in 1951 from experiments with rigid hemispheres indenting ideally plastic plates, and a later theoretical study [47] which also demonstrated that the contact stress under ideally plastic contact is relatively *uniform*. By inserting Eq. (3) in Eq. (1) we obtain an integral equation for the indentation α. This equation may be written on a dimensionless form and solved numerically in a stepwise fashion, as described in [45].

Figure 24 gives a comparison of the analytically predicted load histories and the corresponding FE-simulations for a 48 mm diameter ice ball impacting the 6.15 mm thick plate at 117 m/s. According to the FE simulations this was just below the delamination threshold velocity for a quasi-brittle impactor but all analyses were performed assuming a fully elastic plate, i.e. without allowing damage growth. The FE load history is based on the resultant force of the FE contact elements. Figure 24 illustrates that the impact load predicted by FE initially is much higher than predicted analytically. For the homogeneous ice models this effect gradually dies out but for the particle flow the load enhancement appears to prevail through the entire impact, presumably as this is a continuous sequence of separate impacts.

5.2 Model for Delamination Onset

Delamination growth in composite laminates is typically generated by coalescence of shear cracks which appear at fairly low loads and grow under an increasing load

until the delamination threshold load is reached. Contact with a crushing ice ball causes a fairly uniform contact pressure, p_{av}. In this case the midplane (maximum) shear stress at a radius a is given by the following expression:

$$\tau_{mid} = \frac{3}{2}\frac{p_{av}\pi a^2}{2\pi\, ah} \quad \Leftrightarrow \quad \tau_{mid}^2 = \frac{9}{16}\frac{p_{av}a}{h}\frac{F\,(a\,/c\,)^2}{\pi\, ah} = \frac{9}{16\pi}\frac{p_{av}F\,\bar{a}^2}{h^2} \tag{5}$$

where $\bar{a} = a\,/c$

The critical contact force F_{sc} for shear cracking at a radius a at a given shear strength τ_c is obtained by the expressions:

$$\begin{aligned} F_{sc} &= \tfrac{16\pi}{9}(\tau_c h\,/\bar{a}\,)^2\,/\,p_{av} \qquad \text{for } \bar{a} = a\,/c \le 1 \\ F_{sc} &= \tfrac{16\pi}{9}(\tau_c h)^2\bar{a}\,/\,p_{av} \qquad \text{for } \bar{a} = a\,/c \ge 1 \end{aligned} \tag{6}$$

Expressions for the critical load for delamination growth were provided in [15] and are as follows:

$$\begin{aligned} &\bar{a} = \infty : F_{dth} = C\,F_{d1F} \quad \text{where} \quad C = 1.213 \quad \text{and } F_{d1F} = \pi\sqrt{32DG_{IIc}\,/3} \\ &\bar{a} \gg 1 : F_{dth} \approx C\,F_{d1F}\cdot\sqrt{w\,(c=0)\,/w\,(c\neq 0)} \\ &1 \le \bar{a} \approx 1 : F_{dth} \approx F_{d1F}\sqrt{12}\,/\bar{a} \\ &\bar{a} < 1 : F_{dth} = F_{d1F}\,2\,/\left(1-\bar{a}^2\right) \end{aligned} \tag{7}$$

The first expression is based on the closed form solution in [6], while the fourth expression is based on a closed form solution in [48]. The second and third expressions are based on perturbations of the first and fourth expression, as described in [15]. By comparison of Eqs. (5) and (6) it is obvious that shear cracks will initiate at the edge of the contact area ($\bar{a}$=1) and will grow inwards and outwards until the critical load for delamination growth is reached. Subsequent delamination growth inwards and outwards will occur under a decreasing load. The process is illustrated in Fig. 25, where the curve for delamination growth outside the contact radius has been obtained by a simple curve fit to data points were the perturbation solutions are considered valid. For the quasi-brittle ice the quasi-static ultimate stress of $\sigma_F = 35$ MPa results in an analytically predicted delamination load of about 38 kN, which is significantly higher than the FE prediction of 24 kN.

6 Causes for Discrepancies Between FE-Simulations and Simplified Analytical Models

To understand the reasons for the discrepancy between the analytical predictions and the FE-simulations the spatial distribution and time histories of the contact pressure in the FE model were examined in detail. The stresses were also compared

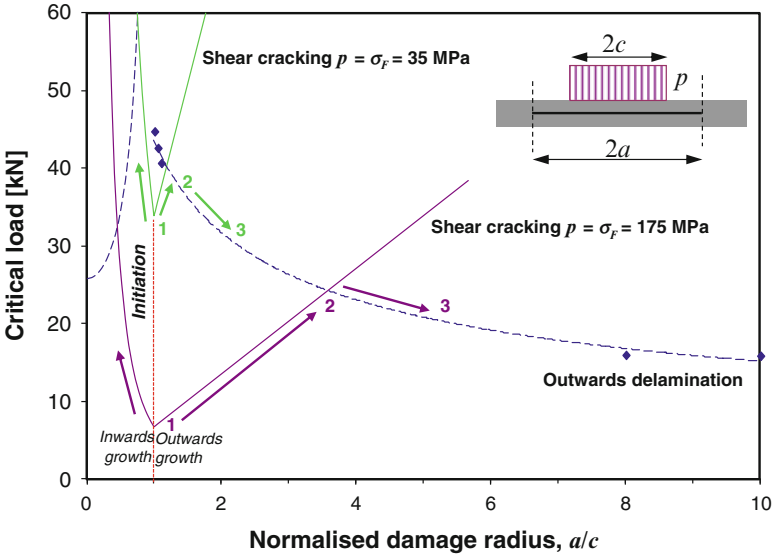


Fig. 25 Critical loads for shear cracking (*solid lines*) and delamination growth (*dashed lines*) under uniform local pressure by quasi-static crush stress (35 MPa) and initial stress peak (175 MPa)

with the expected average stress, given by the impact load divided by contact area. The contact stresses predicted by the SPH model were essentially "white noise", although the average stress was in fair agreement with the average stress expected from the load history. For this reason, the stresses at the top surface of the solid shell elements were used for *prediction* of the contact stresses. The LS Dyna thick shell elements with only 2D plane stress update resulted in very low stresses in poor agreement with the expected contact stress, while elements with full 3D stress updating produced stresses in good agreement with the expected contact stress. Figure 26 shows the pressure distribution predicted by the latter elements at some different times, and illustrates that there is a significant variation in the pressure distribution. Further analysis is ongoing to clarify if these fluctuations are due to numerical problems or due to actual wave phenomena. It is noted that the contact stresses after 40 μs are in good agreement with the $\sigma_F = 34.4$ MPa predicted by the material model, while the stresses initially are much higher.

Figure 27 illustrates the contact pressure histories at three different distances (x) from the impact centre during impact with a quasi-brittle material. It is noted that the high initial contact pressures gradually approach the quasi-static value of σ_F assumed in the analytical model. The initial stress peak may be explained by propagation of through-the-thickness waves. The stress amplitude can be approximated by the following expression for one-dimensional elastic wave propagation after an impact between two cylindrical elastic bodies [15]:

$$p_{in} = p\,(t = 0) = \sqrt{\rho_p E_{pz}}\, V_0 \,/\, \left(1 + \rho_p \,/\, \rho_i\right) \tag{8}$$

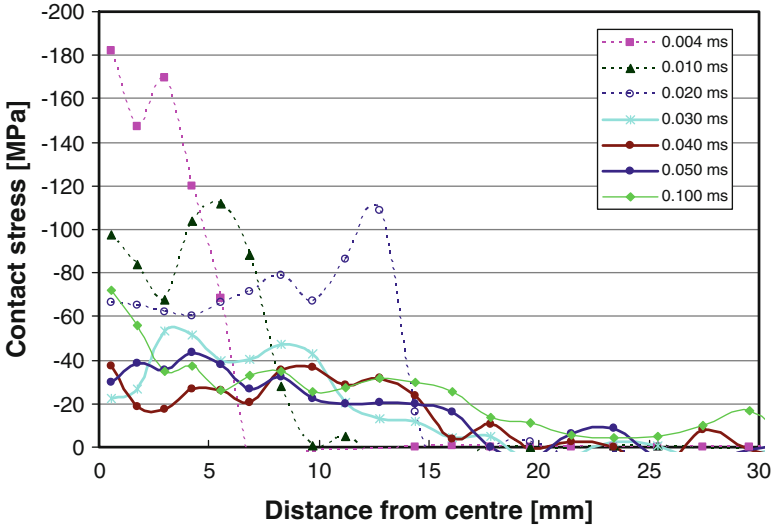


Fig. 26 Contact stress distributions at $V_0 = 117$ m/s for quasi-brittle material [15]

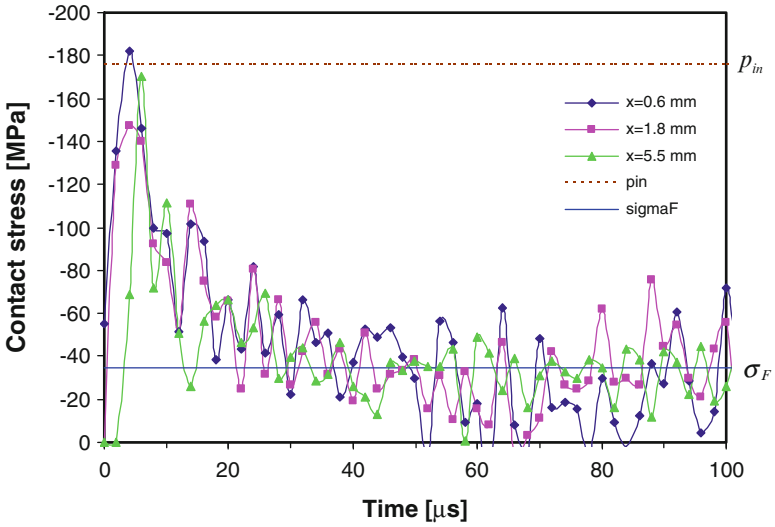


Fig. 27 Decay of contact stresses with time during 117 m/s impact with quasi-brittle impactor (x is distance from impact centre) [15]

where ρ_p and ρ_i are the densities of the plate and impactor and E_{pz} is the out-of-plane Young's modulus of the plate. The predicted initial peak pressure p_{in} has been included in Fig. 27, which demonstrates that Eq. (8) gives a fairly accurate prediction of the initial pressure peak.

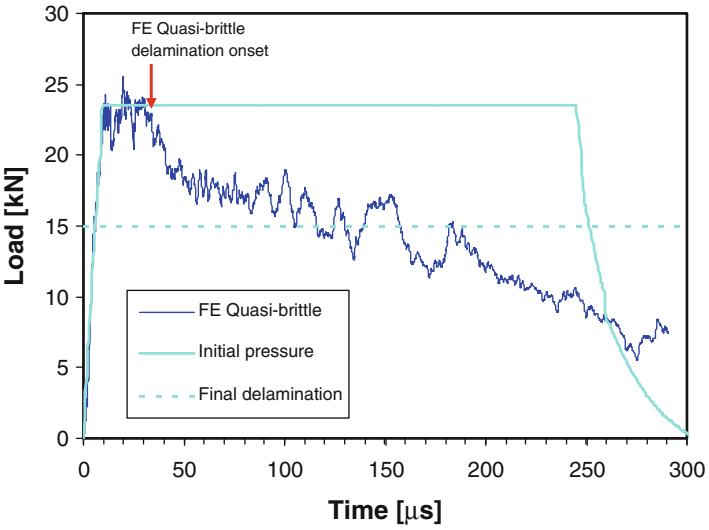


Fig. 28 FE-simulation and upper and lower analytical bounds for the load history with quasi-brittle ice impacting at 118 m/s (delamination onset)

The comparatively low contact pressure during ice impact results in higher delamination threshold loads than for equally sized metal impactors. For a uniform pressure equal to the initial stress peak (p_{in}) the delamination threshold load indicated by Fig. 25 is about 24 kN, which is followed by delamination growth at a decreasing load.

Figure 28 illustrates analytical simulation of delamination using a modified material model, assuming a uniform contact pressure equal to the initial stress peak (pin) until unloading occurs, and a load limited by a delamination threshold value of 24 kN. The initial response is in good agreement with the FE-simulation, which appears to gradually approach the load for quasi-static delamination growth, but the analytical model is unable to model the gradual decay in the load associated with the decreasing contact pressure (c.f. Fig. 27) and delamination growth (c.f. Fig. 28). It may be concluded that an accurate analytical model for hail impact would require incorporation of the initial contact pressure peak and the subsequent decay in contact pressure, as well as delamination initiation criteria considering the effect of a finite contact area.

7 Discussion and Conclusions

It may be concluded that the predicted response to hail impact on composite laminates is strongly influenced by the corresponding material model and by three-dimensional wave propagation during the initial phase of the impact. More reliable predictions of damage initiation and growth require development in several areas.

Reliable physically based models must be developed to account for the influence of anisotropy, strain rate, temperature and triaxial stress state for the stiffness and strength of ice under loading conditions relevant to hail impact during flight. This requires both a more thorough review of existing literature on ice behaviour and complementary experiments.

Detailed three-dimensional FE analysis is required for the initial phase of the impact to study the effect of out-of-plane waves and of the heterogeneous structure of laminates. Accurate prediction of the resulting damage also requires models for intralaminar and interlaminar damage growth in each ply and interface of the laminate.

Improved analytical models should be developed by incorporation of the influence of through-the-thickness waves on the initial contact pressure peak and its subsequent decay, as well as appropriate failure criteria to account for a finite contact area. The aim of these models should be to incorporate key mechanisms, while keeping the models sufficiently simple to be useful for preliminary design.

The methods should first be applied to hail of different size impacting plates with a range of different material systems, layups and thickness and validated by accompanying experiments. Subsequently the methods need to be extended to more complex geometries, e.g. leading edges and engine components. Finally the approach should be demonstrated by analysis and testing of a number of realistic components.

Acknowledgements Significant parts of the experimental work presented in this paper were funded by the VITAL project (FP6 Contract VITAL AIP4-CT-2004-012271). Further experimental studies have been funded through direct contracts from Volvo Aero Corporation (VAC), and we are grateful for the cooperation with Dr Fredrik Edgren, Dr Niklas Jansson and Mr Anders Sjunnesson at VAC. Further numerical and analytical studies have been funded by the internal competence development funds of the Swerea Group. Parts of the update on recent literature on hail impact have been provided by Dr Renaud Gutkin.

References

1. Souter RK, Emerson JB (1952) Summary of available hail literature and the effect of hail on aircraft in flight. NACA TN 2734. NACA, Washington, DC
2. Anghileri M, Castelletti L-ML, Invernizzi F, Mascheroni M (2005) A survey of numerical models for hail impact analysis using explicit finite element codes. Int J Impact Eng 31: 929–944
3. Field PR et al (2009) Hail threat standardisation. Research project EASA.2008/5, EASA
4. Davies GAO, Olsson R (2004) Impact on composite structures. Aeronaut J 108(1089):541–563
5. Mahinfalah M, Skordahl RA (1998) The effects of hail damage on the fatigue strength of a graphite/epoxy composite laminate. Compos Struct 42:101–106
6. Olsson R, Donadon MV, Falzon BG (2006) Delamination threshold load for dynamic impact on plates. Int J Solids Struct 43(10):3124–3141
7. Olsson R (2003) Closed form prediction of peak load and delamination onset under small mass impact. Compos Struct 59(3):340–348

8. Kim H, Welch DA, Kedward KT (2003) Experimental investigation of high velocity ice impacts on woven carbon/epoxy composite panels. Compos Part A 34:25–41
9. Rhymer J, Kim H, Roach D (2012) The damage resistance of quasi-isotropic carbon/epoxy composite tape laminates impacted by high velocity ice. Compos Part A 43(7):1134–1144
10. Park H, Kim H (2010) Damage resistance of single lap adhesive composite joints by transverse ice impact. Int J Impact Eng 37:177–184
11. Appleby-Thomas GJ, Hazell PJ, Dahini G (2011) On the response of two commercially-important CFRP structures to multiple ice impacts. Compos Struct 93(10):2619–2627
12. Östman P, Levin K (1994) On the character of neighbouring low energy impact damages in carbon fibre composites. Advanced structural fiber composites-proceedings. Topical sympos. III 8th CIMTEC-World Ceramics Cong. & Forum on New Material. Techna, Faenza, pp 615–622
13. Asp LE, Juntikka R (2009) High velocity impact on NCF reinforced composites. Compos Sci Technol 69:1478–1482
14. Juntikka R, Olsson R (2009) Experimental and modelling study of hail impact on composite plates. Paper F7:4. In: Proceedings of the 17th international conference on composite materials, Edinburgh
15. Olsson R, Juntikka R (2010) Validation of analytical model for hail impact on composite laminates. Paper 137. In: Proceedings 14th European conference on composite materials, Budapest
16. AMS Glossary (2012) http://amsglossary.allenpress.com/glossary. Accessed 29 Mar 2012
17. Wikipedia (2012) Hail. http://en.wikipedia.org/wiki/Hail. Accessed 29 Mar 2012
18. NOAA (2012) National weather service, St. Louis, MO Weather Forecast Office. http://www.crh.noaa.gov/lsx/?n=10_18_2004. Accessed 22 May 2012
19. NOAA (2012) NOAA Photo Library, NOAA Central Library; OAR/ERL/National Severe Storms Laboratory (NSSL). http://www.photolib.noaa.gov/htmls/nssl0001.htm. Accessed 22 May 2012
20. Ralston TD (1980) Yield and plastic deformation of ice crushing failure. In: Pritchard RS (ed) Sea ice processes and model. IAHS-AISH, pp 234–245
21. Schulson EM (1999) The structure and mechanical behavior of ice, featured overview. JOM 51:21–27. www.tms.org/pubs/journals/JOM/9902/Schulson-9902.html. Accessed 29 Mar 2012
22. Cole DM (2001) The microstructure of ice and its influence on mechanical properties. Eng Fract Mech 68(17–18):1797–1822
23. Petrovic JJ (2003) Review mechanical properties of ice and snow. J Mater Sci 38:1–6
24. Kim H, Keune JN (2007) Compressive strength of ice at impact strain rates. J Mater Sci 42:2802–2806
25. Shazly M, Prakash V, Lerch BA (2009) High strain-rate behavior of ice under uniaxial compression. Int J Solids Struct 46:1499–1515
26. Schulson EM (2001) Brittle failure of ice. Eng Fract Mech 68(17–18):1839–1887
27. Masterson DM, Frederking RMW (1993) Local contact pressures in ship/ice and structure/ice interactions. Cold Reg Sci Technol 21:169–185
28. Jones SJ (1997) High strain-rate compression tests on ice. J Phys Chem B 101(32):6099–6101
29. Arakawa M, Maeno N (1997) Mechanical strength of polycrystalline ice under uniaxial compression. Cold Reg Sci Technol 26:215–229
30. Druez J, Nguyen DD, Lavoie Y (1986) Mechanical properties of atmospheric ice. Cold Reg Sci Technol 13:67–74
31. Cox GFN, Richter JA, Weeks WF, Mellor M (1983) A summary of the strength and modulus of ice samples from multi-year pressure ridges. In: Third international symposium on offshore mechanics and arctic engineering. New Orleans
32. Kim H, Kedward KT (2000) Modeling hail ice impact damage initiation in composite structures. AIAA J 38:1278–1288

33. Schroede RC, McMaster WH (1973) Shock-compression freezing and melting of water and ice. J Appl Phys 44:2591–2594
34. Weiss J, Schulson EM (1995) The failure of fresh-water granular ice under multiaxial compressive loading. Acta Metall Mater 43:2303–2315
35. Combescure A, Chuzel-Marmot Y, Fabis J (2011) Experimental study of high-velocity impact and fracture of ice. Int J Solids Struct 48(20):2779–2790
36. Guégan P, Othman R, Lebreton D, Pasco F, Villedieu P, Meyssonnier J, Wintenberger S (2011) Experimental investigation of the kinematics of post-impact ice fragments. Int J Impact Eng 38(10):786–795
37. Carney KS, Benson BJ, DuBois P, Lee R (2006) A phenomenological high strain rate model with failure for ice. Int J Solids Struct 43(25–26):7820–7839
38. Chuzel Y, Combescure A, Nucci M, Ortiz R, Perrin Y (2010) Development of hail material model for high speed impacts on aircraft engine. In: 11th international LS-Dyna users conference
39. Sain T, Narasimhan R (2011) Constitutive modeling of ice in the high strain rate regime. Int J Solids Struct 48:817–827
40. VITAL (2009) http://cordis.europa.eu/projects/rcn/94198_en.html. Accessed 22 May 2012
41. Edgren F, Soutis C, Asp LE (2008) Damage tolerance analysis of NCF composite sandwich panels. Compos Sci Technol 68(13):2635–2645
42. Compston P, Jar P-YB (1998) Comparison of interlaminar fracture toughness in unidirectional and woven roving marine composites. Appl Compos Mater 5:189–206
43. Holmberg A, Lundmark P (2006) Composites based on 2-D and 3-D textile preforms. CR 06–013 (Confidential report). Swerea SICOMP, Piteå, Sweden
44. Olsson R (1992) Impact response of orthotropic composite laminates predicted from a one-parameter differential equation. AIAA J 30:1587–1596
45. Olsson R (2010) Analytical model for delamination growth during small mass impact on plates. Int J Solids Struct 47(21):2884–2892
46. Jain LK, Dransfield KA, Mai Y-W (1998) On the effects of stitching in CFRPs–II. Mode II delamination toughness. Compos Sci Technol 58:829–837
47. Biwa S, Storåkers B (1995) An analysis of fully plastic Brinell indentation. J Mech Phys Solids 43:1303–1333
48. Davies GAO, Robinson P, Robson J, Eady D (1997) Shear driven delamination propagation in two dimensions. Compos Part A 28:757–765

Discrete Modeling of the Crushing of Nomex Honeycomb Core and Application to Impact and Post-impact Behavior of Sandwich Structures

Bruno Castanié, Yulfian Aminanda, Jean-Jacques Barrau, and Pascal Thevenet

Abstract In this chapter, an original method for modeling the behavior of sandwich structures during and after impact is proposed and validated. It is based on the demonstration that Nomex honeycomb behaves in a post-buckling mode very early and that compression forces are taken up by the corners or vertical edges of the honeycomb cells in the same way as they are in the stiffeners in aircraft structures. Thus it is possible to represent the honeycomb discretely by a grid of springs located at the six corners of hexagonal cells. This approach represents the phenomenon of indentation on honeycomb alone or on sandwiches very well. This approach provides an understanding of how the sandwich and the core behave under compression after impact. An original criterion based on a local core crush is tested and validated to compute the residual strength. To consider the bending response of sandwich structures, a multi-level approach is also proposed.

Keywords Impact • Sandwich • Compression after impact

1 Introduction

In this first section, the general context of the study will be presented first, followed by a brief literature survey. Finally, the scope of the study will be explained.

B. Castanié (✉) • J.-J. Barrau
INSA, ISAE, Mines-Albi, UPS; ICA (Institut Clément Ader), Université de Toulouse, 135 Avenue de Rangueil, 31077 Toulouse, France
e-mail: bruno.castanie@insa-toulouse.fr

Y. Aminanda
Mechanical Engineering Department, IIUM, Jl. Gombak, P.O. Box 10, 50728 Kuala Lumpur, Malaysia

P. Thevenet
EADS Innovation Works, 12 rue Pasteur, BP 76, 92152 Suresnes Cedex, France

S. Abrate et al. (eds.), *Dynamic Failure of Composite and Sandwich Structures*, Solid Mechanics and Its Applications 192, DOI 10.1007/978-94-007-5329-7_10,
© Springer Science+Business Media Dordrecht 2013

1.1 Background

Sandwich structures consist of two skins, having high mechanical properties, and a lightweight core, which separates the skins. The quality of the skins-core assembly is intrinsically linked to the mechanical characteristics of the core. When the thickness of the core is increased, the bending stiffness and critical load prior to buckling increase significantly while the total mass of the sandwich structure remains small. However, the mechanical properties of the core are low, which leads to weakness of the sandwich structure in terms of its ability to withstand impact loading and local buckling. Therefore, despite their obvious advantages, the application of sandwich structures in aircraft is developing only gradually. It seems that they are reserved only for secondary structures in commercial aircraft. In the case of military helicopters (Eurocopter Tiger and NH90), almost the whole structure is made of sandwich materials and the utilization of composite reaches approximately 90%. The sandwich seems optimum for weakly loaded, non-pressurized structures and its current application as primary structure is limited to business jets (for example the Raython Premier).

With the increasing number of aircraft in service, impacts happen more often and incident management requires more sophisticated, less conservative and faster tools than the existing ones, which are based mainly on experimental data. In practice, when an incident occurs somewhere in the world, the manufacturer must be able to decide quickly if the aircraft can continue flying as it is, or if a repair should be performed or if a subunit has to be changed. The study presented in this paper is constrained to acquire the efficiency of an industrial tool. The ultimate goal is to develop a comprehensive maintenance loop. The work is divided into four main phases:

- Step 1: 3D imaging and measurement of the damage shape at the location of impact.
- Step 2: Reverse engineering by using the available data to reconstruct the projectile shape.
- Step 3: Simulation of the impact and computation of the residual strength of the structure.
- Step 4: Decision on whether the impacted part needs to be repaired or changed before flight clearance can be obtained from the authorities, or whether the aircraft needs to be grounded, or if the structure remains safe for several flights without any repairs.

The research work presented in this chapter is related to the development of step 3. It will be limited to aeronautical types of sandwich structures as defined by Guedra-Degeorges [1] where the maximum thickness of the composite skin is around 3 mm and the core is made of Nomex honeycomb. In the general case, the impact occurs during maintenance visits or ground operations. These impacts can be considered as low energy/low velocity and they are the only type of impact considered in this chapter. In the following chapter, a brief literature review of this type of impact will be presented.

1.2 Literature Survey

Many significant articles have been published since the late 1980s [2–8]. The research has focused on the identification and characterization of the damage to the laminated skins (delamination and fiber breakage) and the cores (crushing located under the impact area). The effects of boundary conditions and different combinations of materials for skin and core have also received attention. The various material combinations studied experimentally up to 1998 can be found in a comprehensive review by S. Abrate [9].

Although the issue of core crushing was identified in this period, relatively few studies investigated the behavior of core made from a honeycomb type of structure and subjected to compressive loading. And most of the works have studied the capability of honeycomb core made from aluminum alloys to absorb the energy [10–12]. The damage mechanism of honeycomb core under compression has been observed as the formation of lobes during loading and the lobes have been correctly modeled using plastic hinge theory. However, it appears clearly that this methodology cannot be applied to the Nomex honeycomb selected for this study. In this study, only low-velocity/low-energy impacts will be considered. The experiments conducted in our laboratory and in EADS IW facilities show that, for this type of impact acting on the aircraft type of sandwich structure, an equivalence of behavior between dynamic and static indentation can be considered. The same observations have been reported in numerous earlier papers as mentioned in [8, 13, 14].

The advantage of employing static tests is their simplicity of implementation and the low dispersion of test results. The first mathematical model proposed to identify the indentation on a sandwich structure used the Hertz contact law [9]. Analytical models based on beams or plates and supported by elastic foundations have been developed by some authors. The oldest approaches were based on the theory of elasticity, which had very limited application in practice [9]. Swanson [15], Soden [16] and Olsson [17] have proposed analytical models using a perfect plastic foundation to simulate honeycomb core behavior. In Soden's model [16], linear kinematics was considered and, as for Olsson's model [17], a large displacement was employed.

However, these models are of limited interest for our study because of the plastic deformation of the metallic skin and crushing of the core during indentation [1–8]. Also, the honeycomb is damaged even at very low impact energy. Therefore, understanding the damage mechanism is the key point in any attempt to model the indentation on a sandwich structure. The damage mechanism is very complex, involving the phenomena characterized by the appearance of folds and different fractures on the hexagonal honeycomb cells. That is why some authors have used a global constitutive behavior law by considering the core as continuum material (e.g. [18–20]). Only recently, due to greater computing capabilities and the higher stability of explicit computation strategy, finite element analysis models have been successfully developed to simulate the damage mechanism of Nomex honeycomb core [21]. However, the models require a complex method of parameter

identification to obtain the micro-mechanical properties of Nomex. The FEA models developed are themselves difficult to implement and require substantial computing time, which makes them unsuitable candidate tools for quick maintenance purposes. Therefore, this study focuses first on phenomenological observations of the crushing of Nomex honeycomb core in order to identify and explain its mechanisms and then propose a relevant model.

1.3 Scope of the Study

The state of the art shows that there are only two methods for modeling the crushing of honeycomb cores. The first one uses continuum and global laws and is easy to implement. The second one aims to represent the core finely, even distinguishing the aramid paper and the surface layers of phenolic resin of the Nomex paper [22]. The first approach hides a number of behaviors of the honeycomb structure, while the second succeeds in satisfying the aeronautics-related context of this study but at huge computational cost.

For these reasons, the study focuses first on the phenomenological observation of the crushing of Nomex honeycomb core in order to identify and explain its mechanisms and then propose a relevant model.

Structural effects, such as post-buckling behavior, will be identified and this will allow the core to be modeled by a grid of nonlinear springs. This "third way" of modeling is called discrete modeling or the discrete approach in this chapter. From this analysis, in Sect. 3, the discrete approach is used to model the indentation and impact of sandwich structures with metallic skins. This approach will then be extended to the problems of residual indentation and compression after impact in Sect. 4. The final section will provide a review and point out some perspectives.

2 Analysis of the Crushing of Honeycomb Core

In order to propose a relevant model for Nomex honeycomb, the study starts with an understanding and description of the mechanical phenomena involved in crushing as a failure mode for this type of structure. In this chapter, first, micromechanical analysis is presented qualitatively. The result of the study shows that it is possible to reason analogically with folding phenomena found for the damage mechanism on a tube structure subjected to compression loading, where the crushing is mainly controlled by the geometry of the cells.

A series of tests is performed on different honeycomb materials, which will help to identify the influential parameters and to propose a scenario for the mechanism of folding. The observations of the test lead us to propose a model where honeycomb can be represented by an array of springs. Each spring is located at the position of a vertical edge of the honeycomb cells. The proposed analytical model, which

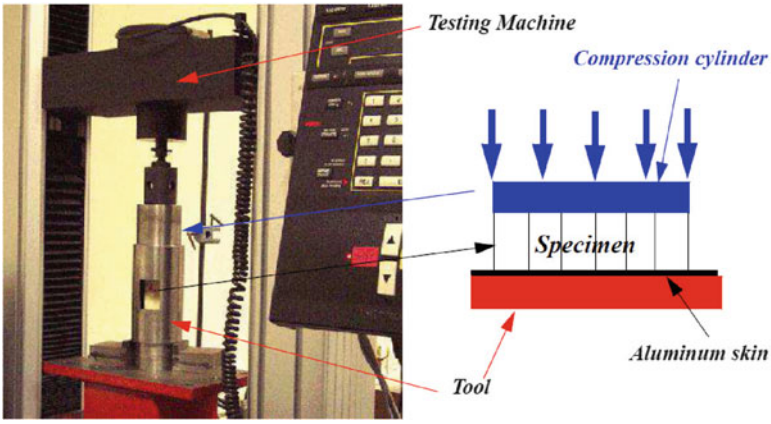


Fig. 1 Test procedure for compression of honeycomb cores

is based on test observations, will be validated by comparison with the results of indentation tests using hemispherical and conical projectiles. The limitations of the model are identified for a cylindrical projectile. A conclusion will be drawn to end the section.

2.1 Phenomenological Analysis

2.1.1 Qualitative Analysis of Crushing

The specimens made from Nomex (HRH 10-3/16-4) were carefully cut into rectangular shapes containing a total of 100 cells. The specimens were subjected to uniform compression loading using the procedure described in Fig. 1 by controlling the displacement speed at 0.5 mm/min, which is equivalent to quasi-static compression loading. Thirteen points on the force-displacement curve were selected for further examination.

Nomex honeycomb is a two-component material by its method of manufacture. The phenolic resin is mainly on the surface of an aramid paper. The first pictures in the elastic part (points 1,2,3,4 Fig. 2) show that the phenolic resin breaks throughout the height of the honeycomb (Fig. 3). Breaking occurs up to the maximum force in the force-displacement curve (point 5 and Fig. 4). After the maximum force is reached, the first fold is observed. Subsequently, the first fold flattens and a second fold appears (point 8, Fig. 5). The failure modes appear more and more complex, with tearing and local debonding (Fig. 6).

It is now interesting to refer to the literature on crushing and especially on folding mechanisms of tubes [23–27]. The folding of Nomex honeycomb does not occur symmetrically relative to the cell center. Effectively, the folding follows a

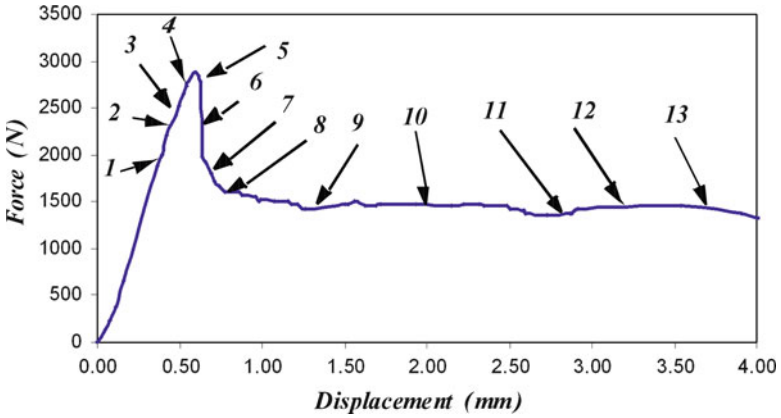


Fig. 2 Observation points during uniform compression loading

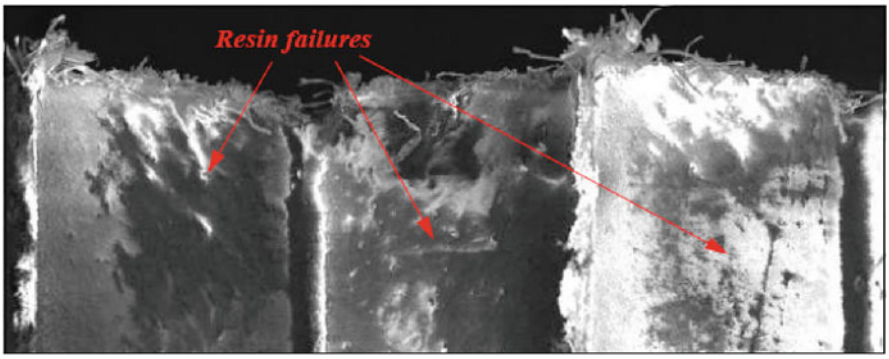


Fig. 3 Picture at point 2, view of resin failures

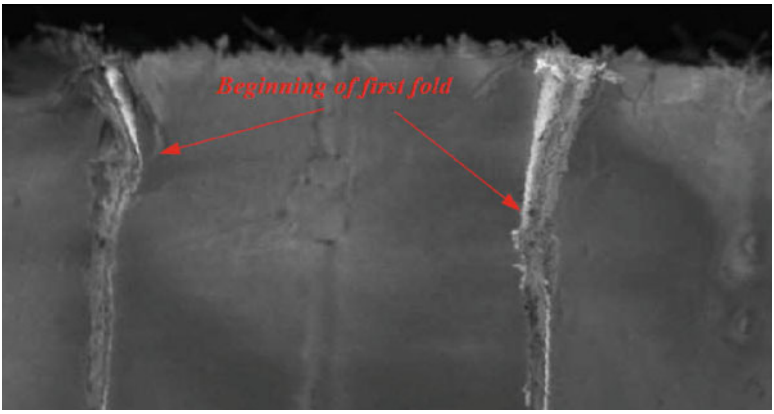


Fig. 4 Picture at point 5, appearance of first fold

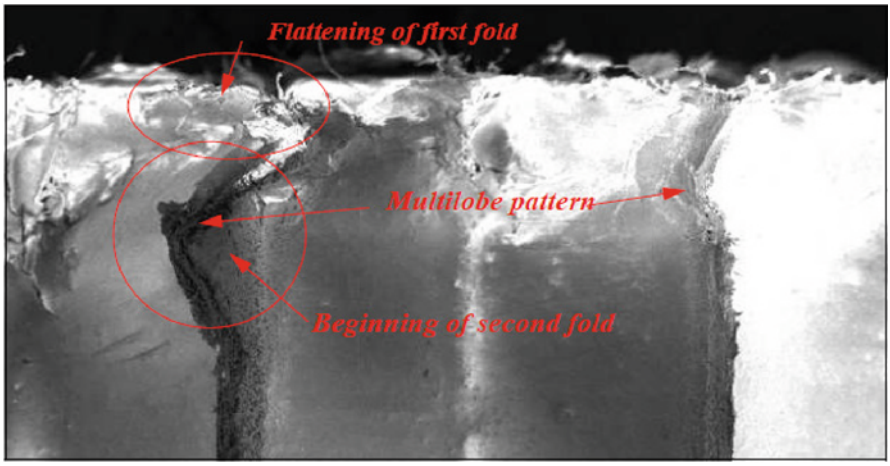


Fig. 5 Picture at point 8. Continuation of folding

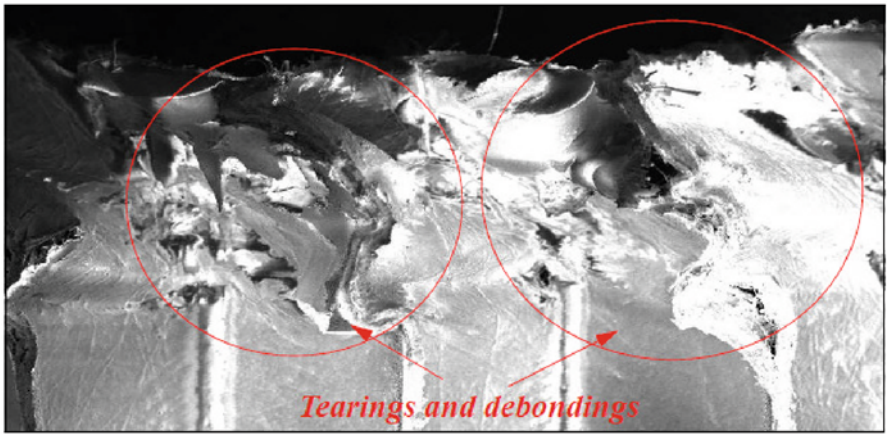


Fig. 6 Picture at point 11, damages in the honeycomb

non-axisymmetrical form or multi-lobe mode. The term is taken from Enboa Wu and Wu-Shung-Jiang's work [25] where the experiments were performed on a hexagonal tube subjected to compression loading. The multi-lobe folds depend on the tube diameter-to-thickness ratio [25–27]. During the crushing, the first folds flatten and new folds appear in relation to the force in the area called a "plateau" on the force-displacement curve.

The comparison between folding length (H) and eccentricity factor (m) as defined in Fig. 7, observed using an electron microscope and calculated using the "tube in compression" theory proposed by Singace [23], is shown in Table 1. The factor m is obtained by minimizing the strain energy of the folding and does not depend on the materials, diameter of the tube, or N. Its value is found to be 0.642 [23].

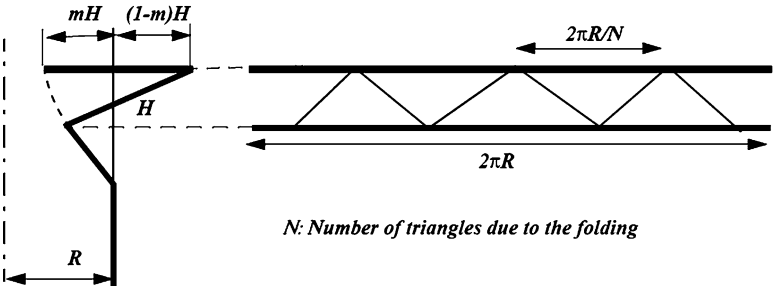


Fig. 7 Definition of factors m and H [23]

Table 1 Comparison between test and theory of folding

	Test	Calculation
Eccentricity factor (m)	0.65	0.64
Folding length (H) (mm)	0.667	0.518

To determine H, the following equation is used:

$$\frac{H}{t} = \frac{\pi}{N} \tan\left(\frac{\pi}{2N}\right) \frac{R}{t}. \tag{1}$$

where t is the thickness of the tube and R its radius.

It is difficult to determine the length of the fold on the pictures obtained from the electron microscope because the images are not very clear. To determine the length of the fold H using the formula (Eq. 1) given by Singace [23], the number N is taken equal to 6 (corresponding to the six faces of the honeycomb) and radius (R) is equal to the outer radius of the cell. The test results are similar to the calculation, which shows that the folding of the Nomex honeycomb also obeys the geometric laws. In addition, from a qualitative point of view, the phenomenon of folding occurs at various size scales and is similar for different honeycomb materials. For example, Fig. 8 shows the folding of individual cells of wood (the phenomenon is identical for the cells of foams). Figure 9 shows the folding of corrugated cardboard and Fig. 10 the folding of a steel tube subjected to compression loading.

In this subsection, the folding phenomena of Nomex honeycomb have been observed. It has been shown that complex failure modes are involved. By looking at the research related to other crushing mechanisms, it has been proved that crushing is controlled by the geometry of the honeycomb cell. Qualitative observation also shows that the phenomenon is similar for different cell sizes and materials of the honeycomb. Therefore, for a more detailed understanding of the crushing mechanism of Nomex honeycomb subjected to compression loading, it is possible to use different materials and sizes of honeycomb core. This reasoning by analogy is proposed in the next part.

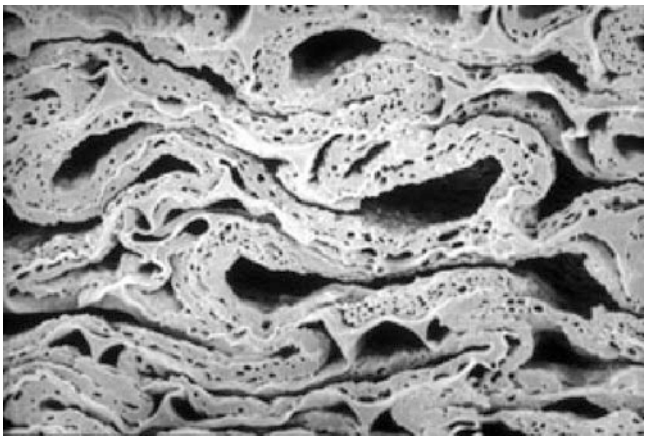


Fig. 8 Crushing of a wood cell

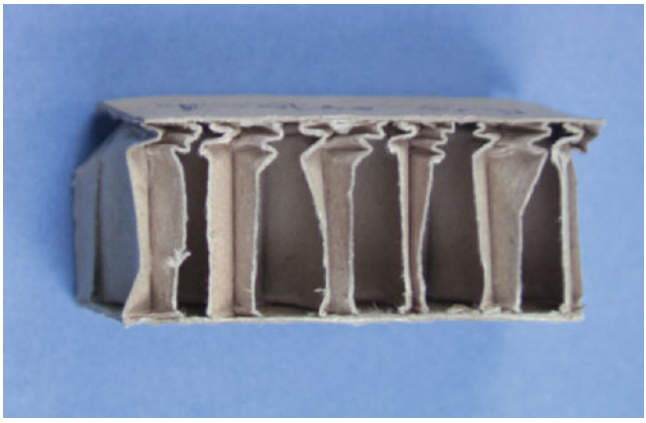


Fig. 9 Crushing of corrugated cardboard

2.1.2 Identification of the Folding Mechanisms

Compression tests were conducted on honeycomb blocks. A honeycomb made of drawing paper with a cell size of 35 mm was made manually in the laboratory. Aluminum honeycomb with a cell size of 6 mm and Nomex honeycomb, cell size 5 mm, were used to complete the test series. The tests used an Instron machine with a compression speed of 0.5 mm/min to obtain a quasi-static test. Each honeycomb tested (Table 2) was composed of two specimen types: with either two honeycomb faces or only one face glued to Plexiglas skins. The local boundary conditions were thus different, which will highlight the importance of this point. Finally, for each test, the force/displacement curves were plotted and the folding mechanism during the test on the drawing-paper honeycomb was filmed as shown in Fig. 11.

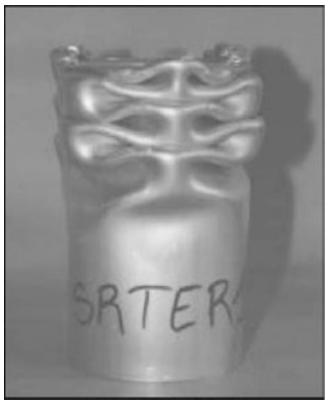


Fig. 10 Crushing of steel tube (Reproduced from [23])

Table 2 Specimens for uniform compression tests

Material	Drawing paper	Nomex	Aluminum
Cell size (mm)	35	5	6
Number of cells	11	36	10
Specimen dimension (mm^2)	140×140	35×35	25×25
Thickness (mm)	0.58−0.34		0.12
Height (mm)	45−22.5	15	45−15
Number of skins	1 or 2	1 or 2	1 or 2
Number of specimens	8	4	6

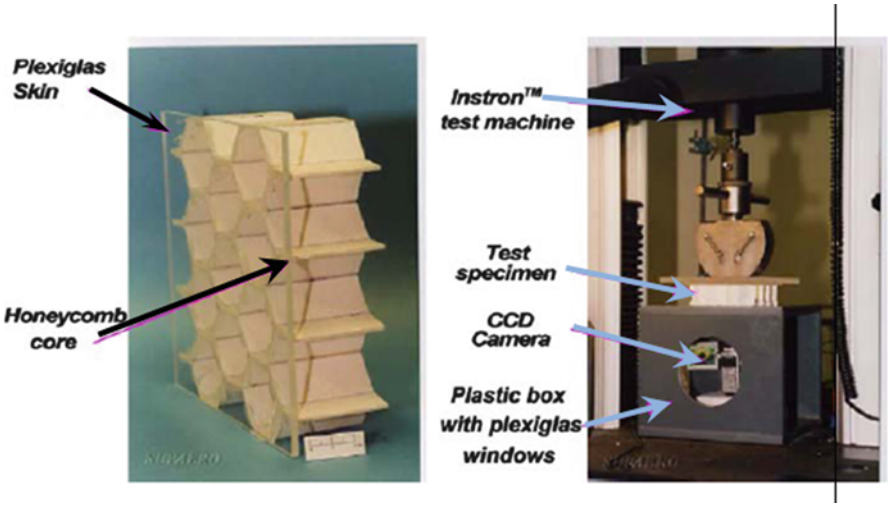


Fig. 11 Test specimen and test rig

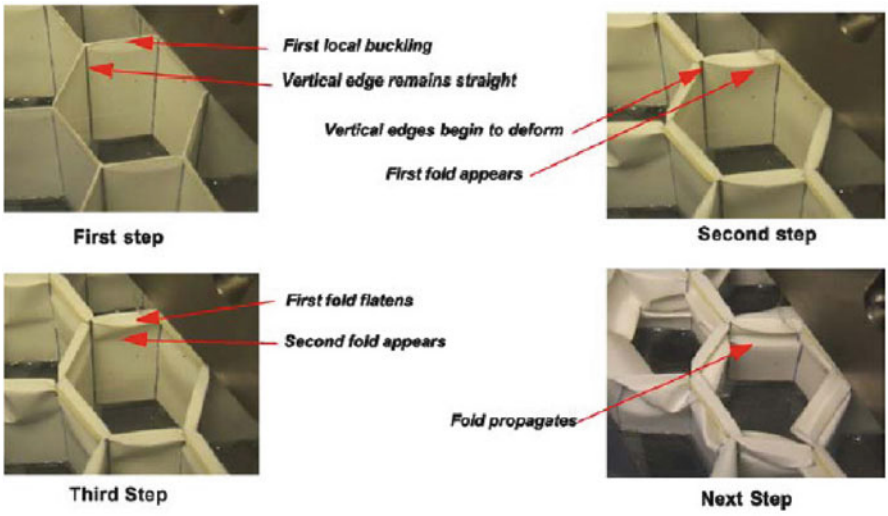


Fig. 12 Folding mechanism in the drawing paper honeycomb specimen

The mechanism of deformation observed on drawing-paper honeycomb with only one skin was as follows (Fig. 12).

First step: Initiation of the first fold.
Local buckling appeared on the free face of the honeycomb (without the Plexiglas skin). In this step the cell vertical edges remained straight. The simply supported boundary conditions authorized local rotation of the free face and seemed to be the origin of this folding initiation.

Second step: Flatness of the first fold and appearance of the second.
In this step, the folding increased gradually and the vertical edge started to deform. During the first folding process, the second fold also started to form. The folds made propagated alternately on one side then the other of the cell wall. During folding, interpenetrating local tears and local separations could be observed on the vertical edge.

Third step: Flattening of the second fold and appearance of the third.
In this step the second fold was flattened and, simultaneously, the third fold appeared. In the same manner, it was observed that the vertical edge either tore or fell apart and the honeycomb vertical edges were deformed according to the symmetrical or anti-symmetrical folding at their three walls. Then, the same mechanism was reproduced at lower height.

Next steps: Successive the honeycomb folding.
Folding and flattening followed one another in the same way as previously. The folding mechanism was the same for all drawing-paper honeycomb specimens. The honeycomb height and density (thus wall thickness) did not influence the mechanism described. The same observations were made for the aluminum and

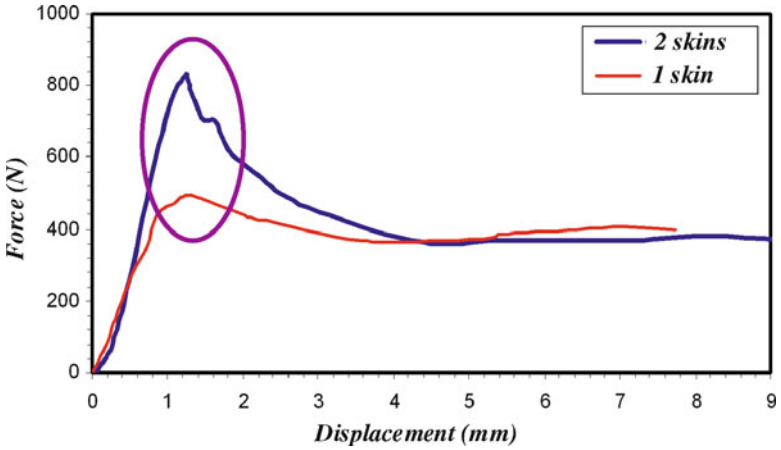


Fig. 13 Compression laws for the drawing-paper honeycomb specimens

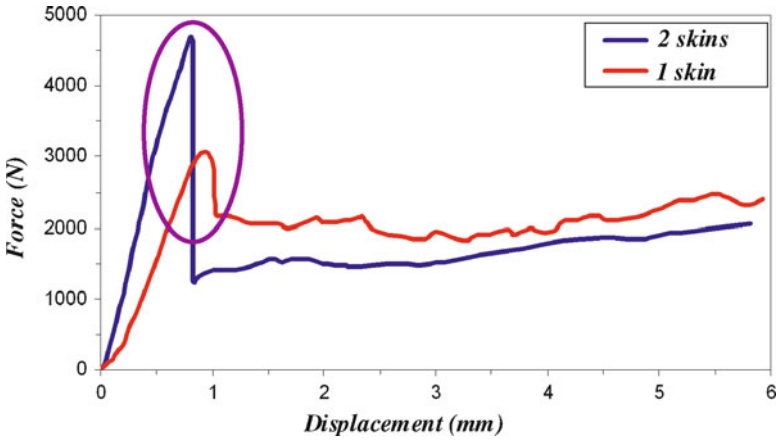


Fig. 14 Compression laws for the Nomex honeycomb specimens

Nomex honeycomb. However, the fold shape differed for each material: rounded for aluminum and with sharp angles for Nomex. This difference of shape can be attributed to the different plasticity of the materials. For the tests using specimens with two skins, folding occurred randomly through the honeycomb height but was never located near the skins. The final deformation pattern of the specimens is presented in reference [28].

The force–displacement curves of the honeycombs tested under uniform compression are given in Figs. 13, 14, and 15 for the different materials and for specimens with one or two skins.

The classic response [12] can be observed for all the cases. The behavior is elastic at the beginning of indentation until a critical load is reached. After the peak load, a

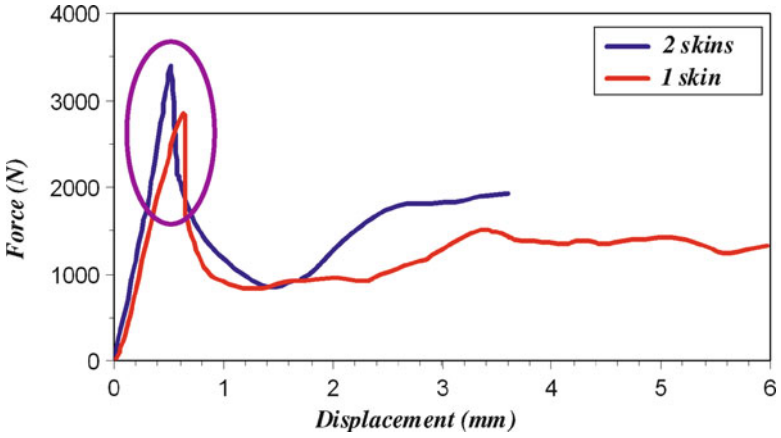


Fig. 15 Compression laws for the aluminum honeycomb specimens

sharp drop in load is observed, especially for two-skin specimens. It corresponds to the beginning of vertical edge deformation. The force decreases to reach a plateau, which corresponds to the succession of fold forming and results in densification of the honeycomb. The critical load for the two-skin specimens is always larger than that for one skin. It seems that there is an analogy with global buckling theory where the critical load is higher for clamped boundary conditions than for the simply supported one. The load drop is sharper for the Nomex honeycomb than for the drawing paper and the aluminum ones. This can be explained by the properties of their respective materials. In fact, the phenolic resin at the surface of the Nomex honeycomb cell wall breaks at the same time as the first fold occurs, which reduces the strength of the cell significantly. In the case of the aluminum honeycomb, a plastic hinge is formed at the fold angle, giving higher residual strength and less abrupt behavior. Another important fact to note is that, for aluminum honeycomb, the maximum peak load is almost the same for one- or two-skin specimens, which is not the case for paper or Nomex material. This highlights the importance of boundary conditions for "soft core materials".

To confirm these interpretations, an implicit finite element model (SAMCEF™ software) of a Nomex honeycomb hexagonal cell was made (see Fig. 16). The honeycomb was made from Aramid paper impregnated with phenolic resin that was then polymerized. This heterogeneous material was rendered homogeneous numerically with $E_{Vertical} = 2{,}341$ MPa, $E_{Horizontal} = 3{,}065$ MPa, $G = 800$ MPa, $\nu = 0.4$. The orders of magnitude of these characteristics were obtained theoretically and they were then used for linear numerical computation on several honeycomb models that fit the elastic stiffness of the experimental test. Once the material characteristics had been found, linear buckling was computed. In the case of the "one-skin" specimen, the first buckling mode was an earlier buckling of the hexagonal cell wall. The same was observed experimentally. Moreover, the deformed shape of this mode clearly showed how the fold was initiated. Also, the buckling force corresponding to this

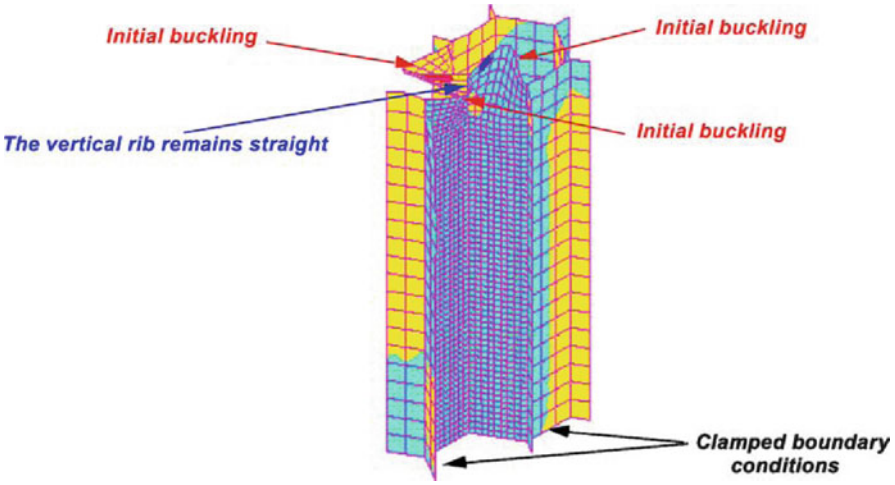


Fig. 16 Initial buckling mode of a Nomex hexagonal cell under uniform compression

mode was about 20–50% of the critical force observed in testing. The numerical analyses seem to confirm the interpretation of the test results. Since the buckling phenomenon appeared very early in the cell walls made from soft material, it can be assumed that the vertical edges of cells control the crushing behavior. Moreover this observation has already been reported by Wierzbicky [12], who proposed an analytical model for the aluminum honeycomb. Finally, some tests on single edges made of aluminum alloy or glass fibers [28] have demonstrated that, from a qualitative point of view, the compression-displacement curve is almost the same (linear response, peak load and plateau area).

This experimental study and some numerical investigations show that the overall crushing mechanism of the honeycomb structures is linked almost solely to the early buckling of cell walls and the response of the cell edge. These observations lead us to make an analogy with the post-buckling of a stiffened structure. This will be detailed in the next subsection and will lead to a proposal for the discrete modeling of honeycomb core. This approach will be validated on indentation tests on Nomex honeycomb core alone.

2.1.3 Analogy with Buckling of Stiffened Structures and Discrete Modeling

Since local buckling occurs early, the honeycomb structure works in a post-buckling mode and an analogy can be made with stiffened thin structures under compression loading such as can be found in aircraft structures (Fig. 17).

The stiffeners in honeycomb are the vertical edges, each of which is formed by the intersection of three thin cell walls. When the skin buckles, the compressive

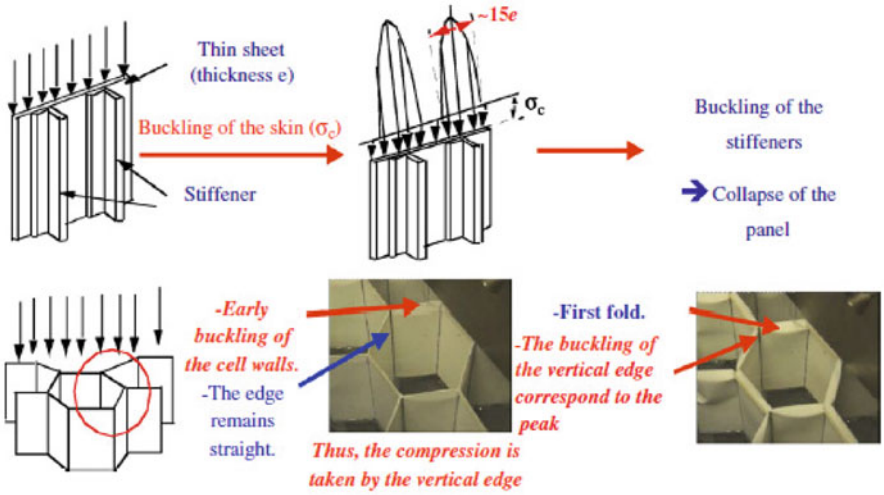


Fig. 17 Analogy with the buckling of stiffened panels

stress in the skin cannot be more than the buckling stress and the excess of compression loading is therefore taken up by the stiffener and a portion of the skin located near the stiffener with an equivalent half-width equal to 15 times the skin thickness [29, 30]. By analogy, for the honeycomb cell, the compression is mainly taken by the vertical edges since the buckling of the walls occurs earlier. Then the collapse of the stiffened structure corresponds to the global buckling of the stiffeners. In the case of honeycomb, there is no collapse but rather folding. The previous analysis shows that only the cell edge plays an important role from a structural point of view. This reasoning leads to the hypothesis that Nomex honeycombs under a crushing force behave like a juxtaposition of cell vertical edges and it is possible to model them by a grid of vertical nonlinear springs located at the angles of the hexagons (see Fig. 18). The compression law can be determined by a uniform compression test. To determine this law, a Nomex honeycomb with 100 cells was carefully selected by cutting the specimen to preserve the vertical edges on its sides. The force–displacement curve obtained in the test was divided by 240 (number of vertical edges) to obtain the force–displacement behavior law of one vertical edge [28].

The modeling proposed in Fig. 18 implies the following assumptions:

1. *External loading is taken mainly by the vertical edges of the honeycomb structure.*
2. *The vertical edges behave independently.*
3. *The contact between honeycomb and impactor is assumed to be perfect, which means that the honeycomb in contact with the indenter follows the indenter shape during crushing.*

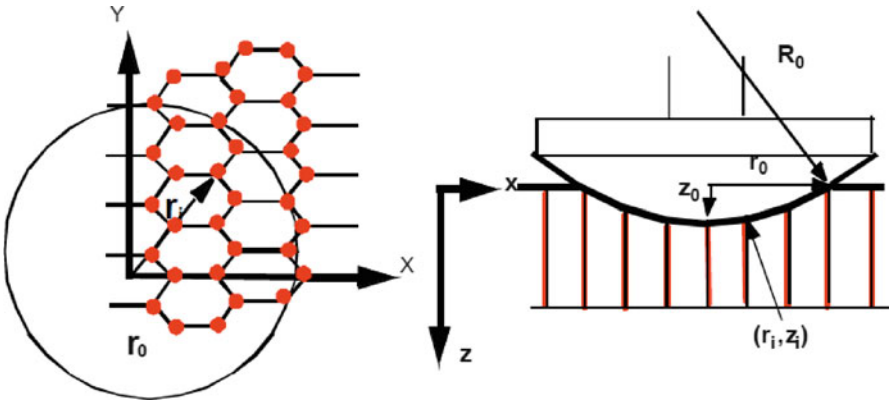


Fig. 18 Principle of honeycomb modeling

By making this assumption and using a polynomial function to discretize the compression law of one vertical edge, it is possible to propose an analytical model to compute the contact law. The computation steps (for a spherical indenter case) are the following:

1. *Computation of polar radius (r_i) of the vertical edges.*
   Since the vertical edges are regularly distributed, their distance is a function of the diameter of the honeycomb cell. At the beginning of contact, the indenter is considered to be at the center of a cell. The problem becomes symmetrical and only a quarter model is considered for the computation.
2. *Computation of the damaged surface radius (r_0) when impactor crushes down to z_0.*
   The value r_0 is calculated as a function of z_0 and R_0 (indenter radius) by using the following equation:

$$r_0 = \sqrt{\left(R_0{}^2 - (R_0 - z_0)^2\right)} \tag{2}$$

3. *Computation of the penetration of each vertical edge (z_i).*
   The penetration of the vertical edges under the damaged surface ($r_i < r0$) is calculated using the following equation:

$$z_i = \sqrt{R_0{}^2 - r_i{}^2} - R_0 + Z_0 \tag{3}$$

4. *Computation of the reaction force of each vertical edge (F_i).*
   Knowing the penetration of each vertical edge (z_i) obtained by the previous calculation, the reaction force for each edge i (F_i) is obtained using the curve of its behavior law found as in the previous subsection (Fig. 14, two skins).

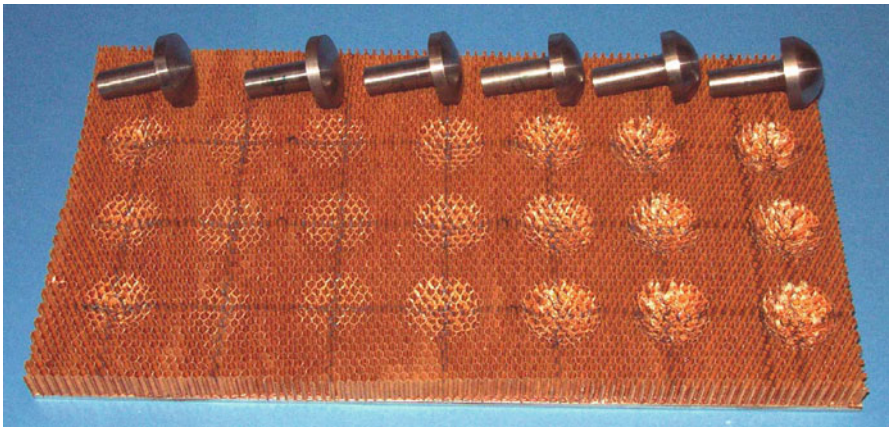


Fig. 19 Indentation tests on Nomex honeycomb alone with spherical indenters of different radii and a conical indenter

5. *Computation of indentation force.*
This is the sum of the reaction forces on each of the vertical edges:

$$F = \sum F_i \tag{4}$$

To obtain a complete law of indentation force versus indentation crushing, the same step is computed for several increments z_0 of indenter displacement.

2.2 Validation of the Discrete Approach

In the previous subsection, the honeycomb was considered as a structure that allowed an original discrete model to be proposed, based on the post-buckling phenomenon in stiffened structures. In this new subsection, this approach will be compared to direct indentation tests on a Nomex honeycomb without skins. The discrete approach is based on the assumption of independence of the response of the edges. Also, in a second step, the range of validity of this assumption will be sought.

2.2.1 Indentation with Spherical Indenters

The tests carried out for this study used one conical (half-angle 18°) and five spherical indenters with different radii (R = 57.25, 30.125, 21.75, 18.06, and 16.25 mm) but with the same overall diameter (see Fig. 19). Three tests were carried out with each indenter to observe the dispersion related to the impactor position at

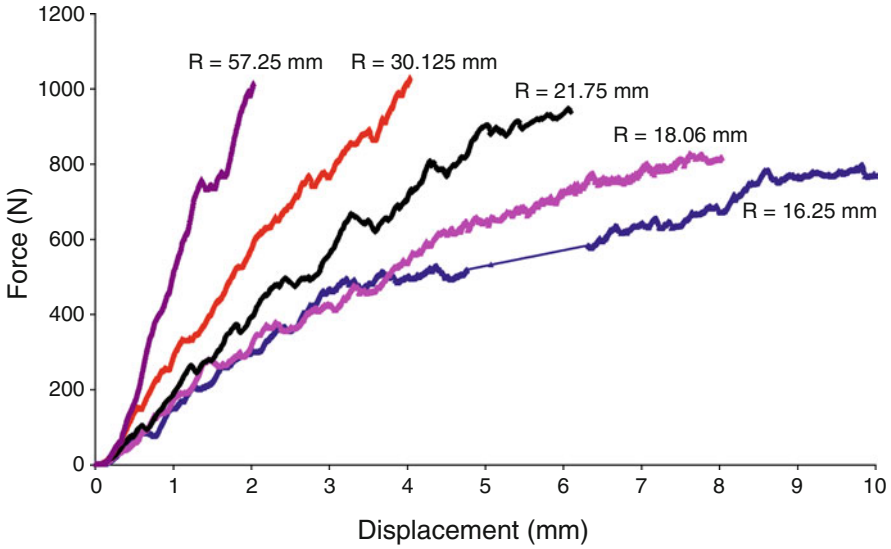


Fig. 20 Indentation test results for spherical indenters

the beginning of indentation (located at the center of the first cell in contact or not). Good test repetition was observed for each indenter.

The contact laws obtained from the tests can be seen in Fig. 20. A small undulation is visible, which corresponds to the drop in load of the vertical edges in the perimeter of the indenter. These undulations are less visible for larger impactor radii (R = 57.25 mm, Fig. 20) because the vertical edges inside the damaged surface are crushed at almost the same time. At the end of all tests, the final loading was identical (Fig. 20) except for tests with small impactor radii (R = 18.06 mm and R = 16.25 mm) (Fig. 21). It seems that this difference is due to the folding out of the vertical edges (instead of perfect vertical crushing) which begins from a certain depth of indentation. For the other tests, the same level of loading was reached at the same indentation displacement corresponding to the same number of folded vertical edges. During the tests, the honeycomb took the same shape as the surface of the indenter. The vertical edges situated just outside the crushed zone did not undergo any deformation, showing that there was no interaction between two neighboring vertical edges. These observations reconfirm the assumption that only the vertical edges "work" during indentation on a free-standing Nomex honeycomb structure.

The analytical calculation based on the discrete approach presented in Sect. 2.1.1 and the test results for the various indenters are compared in the following figures. A good correlation between calculation and test is obtained with a difference of less than 10% for all the indenters (Figs. 22, 23, 24), except those with the smaller

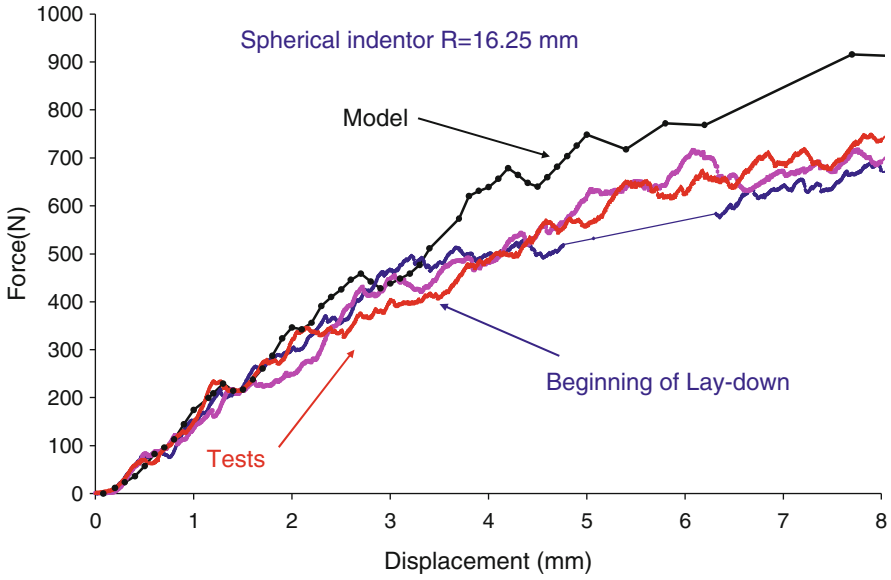


Fig. 21 Comparison between discrete model and test for a spherical indenter with a radius of 16.25 mm

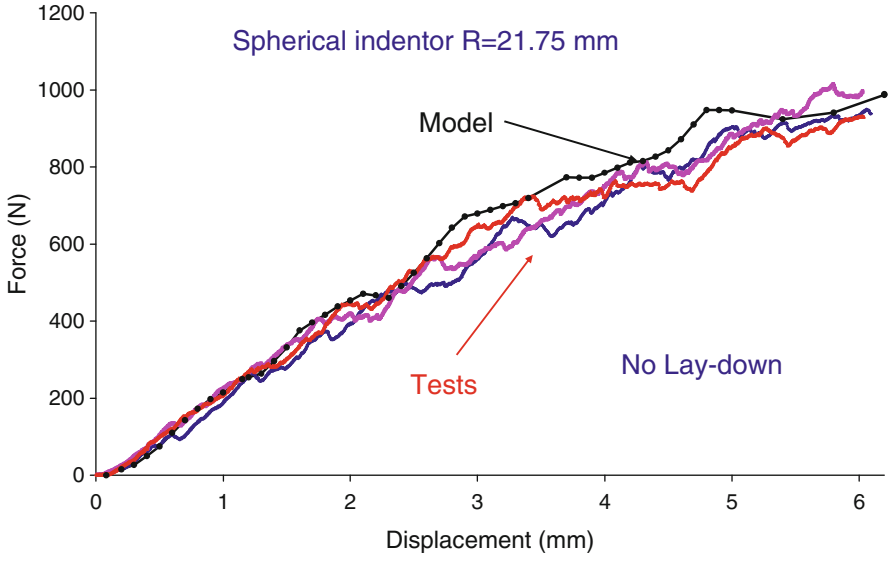


Fig. 22 Comparison between discrete model and test for a spherical indenter with a radius of 21.75 mm

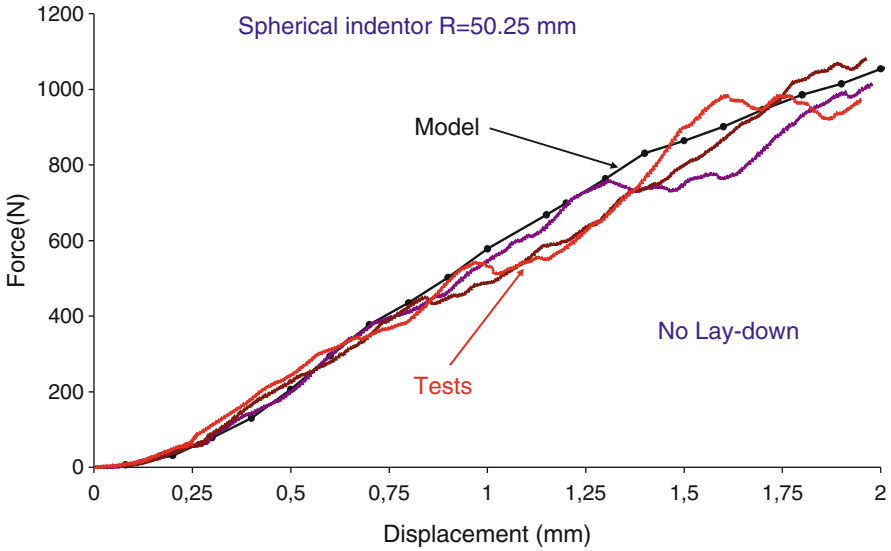


Fig. 23 Comparison between discrete model and test for a spherical indenter with a radius of 57.25 mm

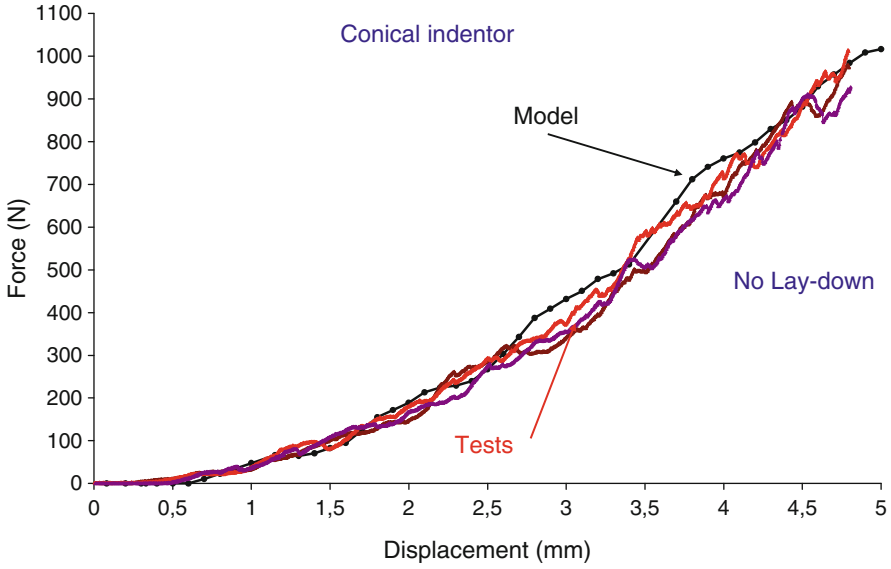


Fig. 24 Comparison between discrete model and test for a conical indenter

diameters because of the folding out phenomenon (Fig. 21). Moreover, we note that the model generates oscillations similar to those observed in the tests, which tends to show that the approach seizes the mechanical behavior of the crushing of the honeycomb core.

In this subsection, the discrete approach has been validated, confirming the assumptions and the methodology suggested previously. However, since the model is based on the independence of the cell edges' behavior, the limits of this assumption will be analyzed.

2.2.2 Verification of the Assumption of Independent Behavior of Edges

The crushing force of one edge is now formulated in the following way:

$$F = F_{crush}(w_i) + \sum_{i=1}^{3} F_{shear}.H(w_i - w_j - w_{\text{limit}}) \tag{5}$$

where w_i is the vertical depth of crushing of cell edge i. w_j, j = 1–3, are the crushing depths of the adjacent edges. $H(w_i\text{-}w_j\text{-}w_{Limit})$ is a Heaviside function with:

$$\mathrm{H}(\mathrm{w_i} - \mathrm{w_j} - \mathrm{w_{Limit}}) = \begin{cases} 0 & \text{if } w_i - w_j - w_{Limit} \leq 0 \\ 1 & \text{if } w_i - w_j - w_{Limit} > 0 \end{cases} \tag{6}$$

The influence of F_{shear} was investigated and w_{Limit} was determined from the results of tests using cylindrical indenters that created shear stress in the walls located in the circumferential zone of the indenter as explained by Wierzbicki et al [31]. Quasi-static tests using three different radii (8, 14.75 and 25 mm) of cylindrical indenters were conducted on the same honeycomb as in the previous subsection (see Fig. 25). Two tests were performed for each radius but only single-test curves are presented because the behavior hardly varied. The circumference of the cylindrical indenter can be observed to coincide either with a vertical edge (POINT 1, Fig. 25) or with a wall (POINT 2, Fig. 24). According to the position on the circumference, it can be assumed that either the edge is subjected to compression or the wall is under shear load.

Figure 26 compares the contact laws obtained from experiment and computation on the discrete model without taking the shear of the walls into account, for the three indenters, in terms of force versus indentation depth. The curves are nearly superimposed at the beginning and the difference starts to appear from a point corresponding to the shear of the wall in the circumferential zone. It is interesting to note that this difference begins to appear at indentation depths of about 0.32 mm independently of the indenter diameter. It should also be noted that the number of cell walls on the circumferential zone is proportional to the radius of the indenter. There were 18, 30 and 56 cells for radii of 8, 14.75 and 25 mm respectively (Fig. 27).

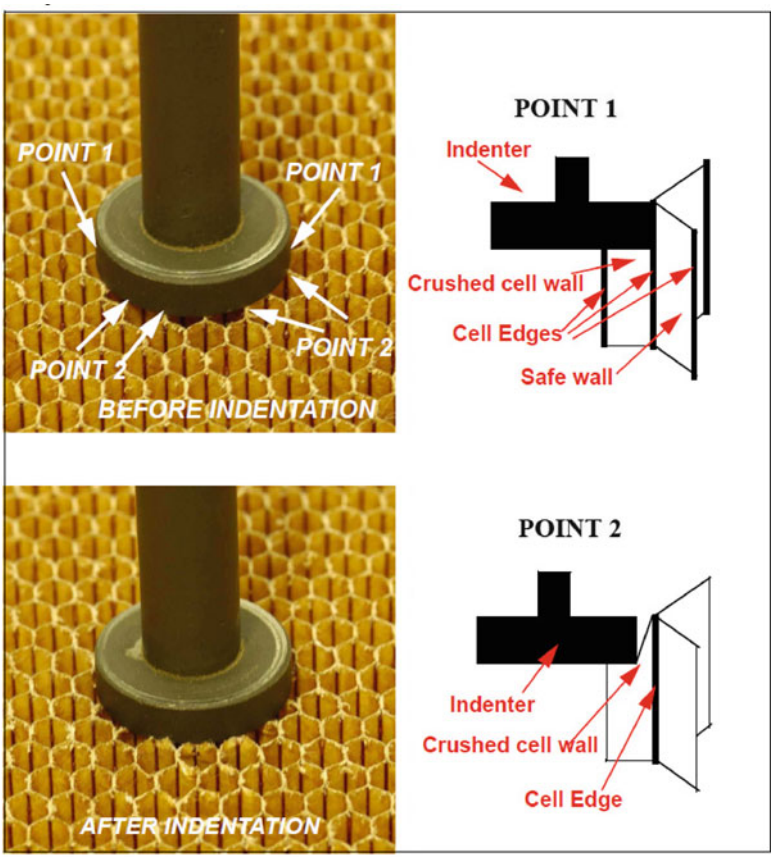


Fig. 25 Description of the indentation test with a cylindrical indenter

Since it is assumed that these walls are subjected to shear load, the shear force is also proportional to the indenter radius. This additional shear force, F_{Sup} can be expressed as

$$F_{Sup} = 2\pi r \cdot q_{shear}, \tag{7}$$

Where r is the radius of the cylindrical indenter and q_{shear} is the shear force per unit length in the circumferential zone.

The unit shear force q_{shear} can thus be obtained by dividing the difference between the computation and the test by $2\pi r$. Calculations show that the unit force q_{shear} is not very different for the three indenter radii (Fig. 26). However, the peak force is smaller for the 8 mm radius, possibly because of the greater dispersion due to the location of the indenter and the small number of walls subjected to shear load. This result globally confirms the hypothesis that the extra indentation force is taken

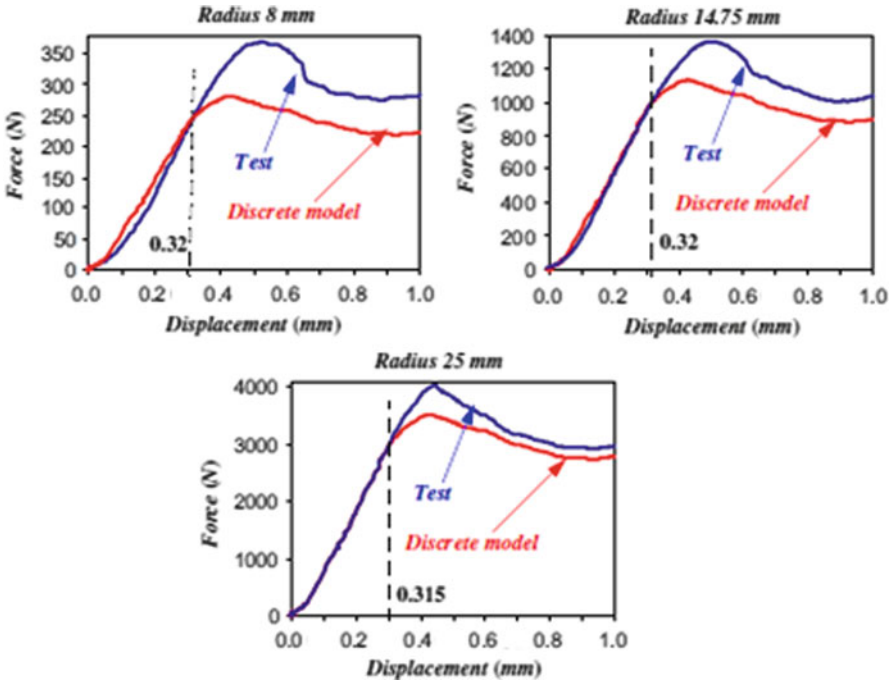


Fig. 26 Comparison of experimental contact law using cylindrical indenter and discrete model

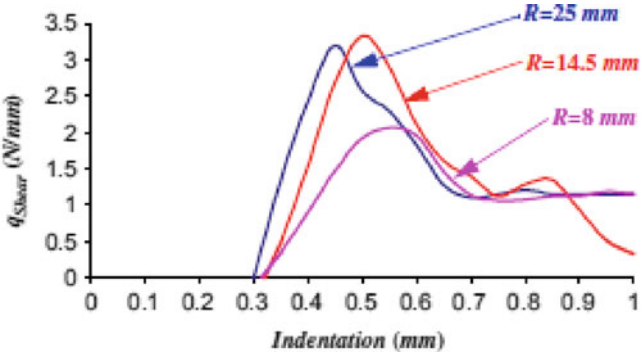


Fig. 27 Peripheral shear force per unit length

up by shear load at the periphery of indenter and is in agreement with Wierzbicki et al.'s results [31]. The results also demonstrate that the additional force, due to shear only, occurs from a certain indentation depth limit: $\Delta w_{Limit} \approx 0.32$ mm. Below this threshold, the error induced by assuming that the honeycomb can be modeled simply by its vertical edges, which behave independently of each other and are subjected only to compression load, seems to be negligible. A simple geometrical

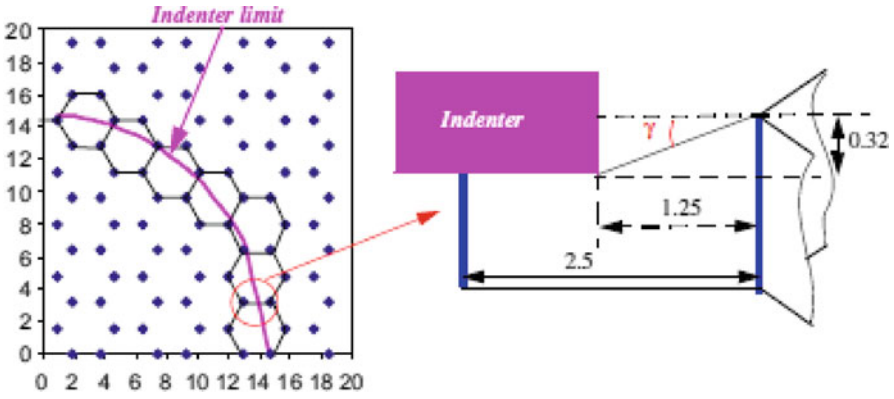


Fig. 28 Geometry for the computation of the limit γ

analysis (Fig. 28) shows that the corresponding limit angle is 0.27 rad, about 15°. This calculation was performed assuming that the circumference of the indenter passed through the middle of the cell, which avoided having to take the reaction of the vertical edge into account. It was then verified a posteriori that, in the case of experiments using spherical indenters, this limit was not reached. The limit angle varied between 0.007 rad (radius 57.25 mm) and 0.025 rad (radius 16.25 mm) which is well below the calculated threshold. To see if the angle obtained had a real physical meaning, a complementary test was carried out with a conical indenter of half-angle 18° (>15°) at the summit. It was observed that the edge-independence hypothesis still remained valid as the correlation between calculation and test results was very good (Fig. 24), which suggests that the actual threshold is little higher.

In consequence, for the indentation of a sandwich structure, it will be possible to model the honeycomb by its vertical edges alone if the deformation of the skin is not too pronounced and the difference in crushing between two neighboring edges does not exceed w_{Limit}, which is generally the case. For all our studies, $w_i - w_j$ was always less than w_{Limit}. Therefore, we did not try to determine the F_{shear} law because it is only needed for sharp projectiles acting on thin skins. In such cases, the skin is generally perforated, which is outside the scope of our research.

2.3 Conclusions

A phenomenological study of crushing has led us to propose an original model of Nomex honeycomb subjected to indentation loading. Because, in this study, we considered the honeycomb as a structure and not a material, it has been demonstrated that the compression load is essentially taken by the vertical edges of the hexagonal cell. This is the first step and the key-point in efficiently modeling

impacts on sandwich structures and setting up fast maintenance loops. Thus, the honeycomb can be represented by only its vertical edges, the crushing law for which can be obtained by a uniform compression test on a honeycomb block. It seems that the approach can be used for other honeycomb materials since the deformation mechanism is very similar. However a doubt exists for rigid walls, as in the case of aluminum core, because the buckling load of the wall is quite high and it is not sure that the post-buckling behavior occurs. Moreover, the hypothesis of edge independence would probably not be satisfied because of the stiffness of aluminum alloy. This key result allows the honeycomb to be modeled in indentation with a grid of nonlinear springs located exactly on the honeycomb vertical edges. The approach was then validated by experiments of indentation of Nomex honeycomb core with various conical and spherical indenters. By using a flat, cylindrical indenter, it was also demonstrated that the assumption of edge independence remains valid for not-too-sharp indenters. In the next section, this approach will be extended to sandwich structures with the same honeycomb core and metallic skins.

3 Impact on Sandwich Structures with Metallic Skins

In this section, a method is developed to model low-velocity/low-energy impacts on metal-skinned sandwich structures. Metal skins were used in order to avoid the complex failure damage mode of composite laminated skin. Experiments and numerical studies were carried out on sandwich structures with the same Nomex honeycomb core as described in the last section. Unlike classical modeling, which considers the core (honeycomb or foam) as a material and a continuum, the previous section has demonstrated the relevance of considering the honeycomb as a structure. Since it acts as a structure, the boundaries are important. So, in a first part, the interaction between the skin and the honeycomb core will be studied first by analyzing the indentation of a sandwich plate on a rigid foundation. Then, to overcome, the main limitation of a grid of vertical springs, which is not able to take the transverse shear in the core into account, a multi-level approach to the impact on a sandwich structure will be proposed.

3.1 Indentation of Sandwich Plates Supported by Rigid Foundation

In this subsection, indentation of sandwich plates with thin or thick skins is analyzed from an experimental and a numerical point of view. The approach proposed in the previous section is enhanced by taking the interactions between the skins and the honeycomb core into account.

Table 3 Detail of the sandwich specimens made

Sandwich materials	Skin thickness (mm)	Specimen size (mm)	Number
Skin: brass core: Nomex (HRH 78,1/8,3) 48 kg/m^3, 15 mm thick	0.1	100*100	6
	1	100*100	6
	1	220*100	6



Fig. 29 Description of the indentation tests on sandwich specimens

3.1.1 Experiments

Quasi-static indentation tests were carried out on 100 mm × 100 mm sandwich structures. Brass skins of 0.1 and 1 mm thickness were bonded to the Nomex honeycomb with a layer of REDUX 312/5 glue. Tension tests were performed on brass skin specimens for the two thicknesses. Brass was chosen because of its marked plastic behavior and its maximum strain, which avoid cracks appearing during the indentation. For the 0.1-mm specimen, the elastic modulus was 103,100 MPa and the yield stress was about 433 MPa. For the 1-mm specimen, the elastic modulus was 70,400 MPa and the yield stress was about 104 MPa. It should be noted that the two specimens had different alloy compositions. Several specimens were made, as listed in Table 3.

Indentation of all specimens was performed using the same INSTRON^{TM} machine and the same spherical indenters of different radii (57.25, 30.125 and 21.75 mm). Tests were performed at a speed of 0.5 mm/min, which can be considered as quasi-static loading. The specimens were fully supported on a rigid metal foundation (Fig. 29). The loads were measured by the machine's sensor but displacements were measured using a dial comparator positioned on the indenter. Three tests were completed for each type of sandwich structure (with thin or thick skin) and for each indenter.

Figure 30 shows the damage area after indentation for a specimen with a thickness of 0.1 mm. The cracks appear in the center of the damaged area for specimens indented by the 31.75 and 21.25 mm diameter indenters.

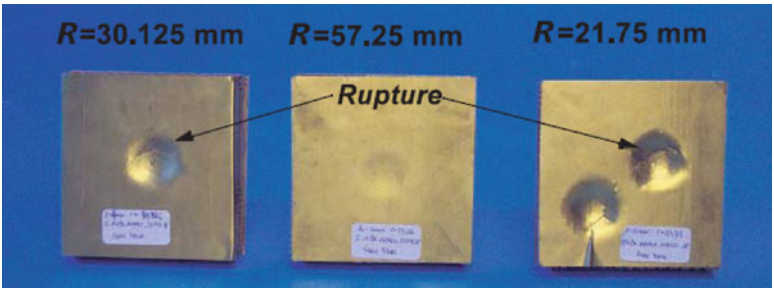


Fig. 30 Indentations on sandwich specimens

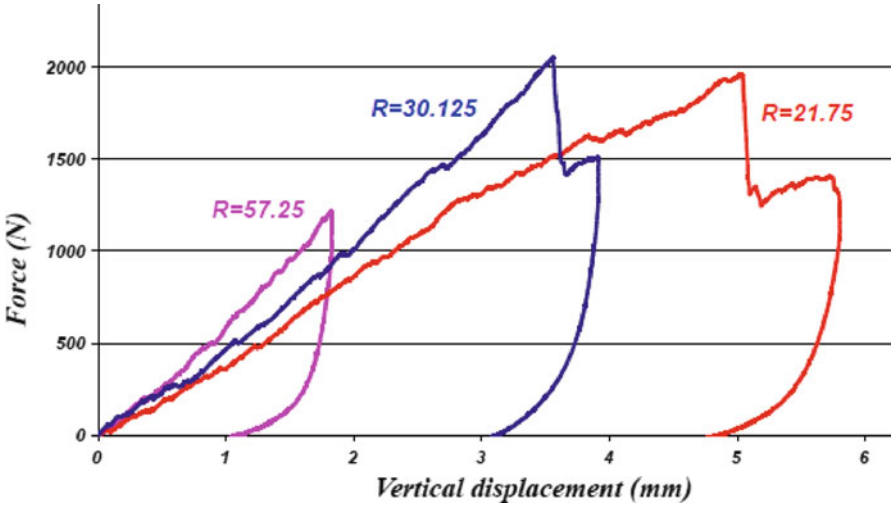


Fig. 31 Force/displacement curve for sandwich with brass skin thickness of 0.1 mm

The contact laws obtained showed low dispersion of the results except for extreme loads in the case of 0.1 mm thin skins. This seems to have been due to the appearance of cracks in the bottom of the indentation, in spite of the qualities of the alloy. Experimental contact laws are presented in Fig. 31 (skin 0.1 mm) and Fig. 32 (skin 1 mm). For specimens with skin thickness of 0.1 mm, the curves have no particularities except small undulations similar to those observed in the test with honeycomb alone. For sandwiches with skins 1 mm thick, the stiffness was very high at the beginning and lower thereafter. This qualitative change can be attributed to the collapse of the first cell of the honeycomb under the indenter as the change of slope occurs at a value of indentation displacement of 0.29 mm, which also corresponds to the transition from the "peak" (or maximum force) to the "plateau" zone of the honeycomb force-displacement curve obtained previously from uniform compression testing on a block of honeycomb alone. Moreover, a specific sound was heard at the same time.

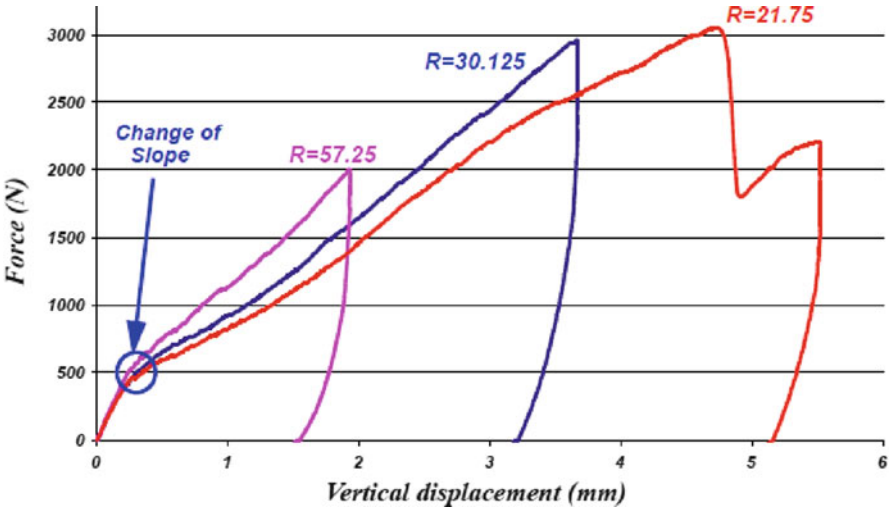


Fig. 32 Force/displacement curve for sandwich with brass skin thickness of 1 mm

The different behaviors observed with thick and thin skin suggests that the mode of folding of the vertical edges must be different. It is likely that the deflection of thin skin, which has a low bending stiffness, follows the shape of the indenter almost perfectly (Fig. 33) while the thick skin deforms differently (Fig. 33) because its quadratic bending moment is 1,000 times greater.

Thus the bending deflection of the thick skin imposes local rotations on the edges. Moreover, in the literature, experimental observations have shown that the edges remain perpendicular to the skin locally [32] due to a perfect honeycomb-skin bond. In addition, uniform compression tests with one or two skins showed the sensitivity of the folding mechanism to the boundary conditions. It is clear that this behavior involving the rotation of edges must be included in the model proposed previously. Therefore, an enhanced compression law is proposed in the next subsection. It is also important to note here that the conventional continuum solid modeling cannot take this sensitivity to boundary conditions in rotation into account.

3.1.2 Enhanced Compression law and Test/Numerical Model Comparison

As demonstrated in the previous part, the local rotations must be taken into account as they modify the crush law of a cell edge from a "with peak" law to a "no peak" law. So, the following form is proposed for a generalized crush law of a cell edge when there is no shear:

$$F = F_{crush}(w_i, \theta_i) \tag{8}$$

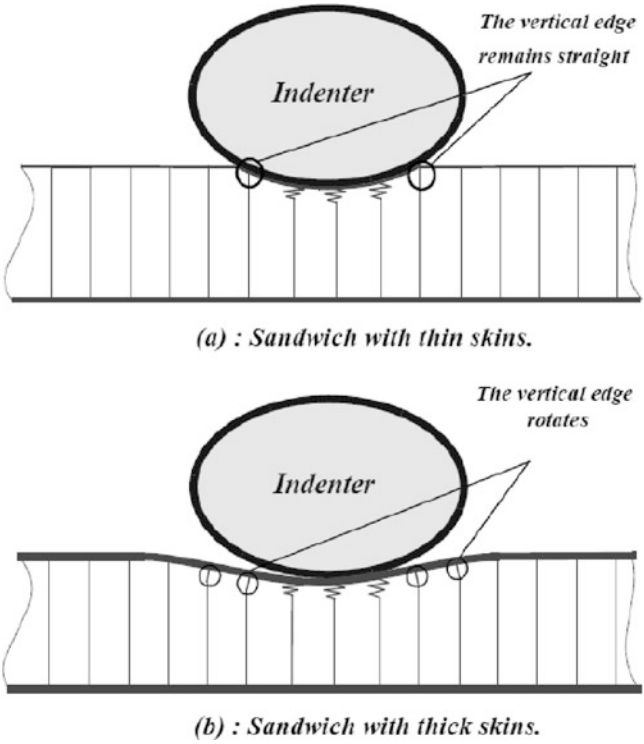


Fig. 33 Physical explanation of the different behavior between sandwiches with thin and thick skins

where w_i and θ_i are the vertical depth of crushing and the local rotation on the upper part of cell edge i. The function $F_{crush}(w_i, \theta_i)$ is plotted in Fig. 34. Three different crushing laws were used and are plotted in Fig. 34: "with peak" $F_{wp,}$ "no peak" F_{np} and an intermediate law F_i :

The choice between the different laws depends on the value of the local rotation at the interface between the core and the skin following these rules:

- *if* $\theta_i = 0$ *the experimental "with peak"* F_{wp} *law is used (see the "two-skins" curve Fig.*14*).*
- *if* $\theta_i \geq \theta_{critical}$ *a "no peak" law* F_{np} *is used.*
- *if* $0 < \theta_i < \theta_{critical}$ *an intermediate law* F_i *is defined (Fig.*35*).*

An implicit nonlinear finite element model was made (see Fig. 36). The software used was the SAMCEF™ code [33]. Nonlinear springs were placed at the same locations as the positions of the honeycomb cell angles.

The generalized law was implemented using special features of the software. The metal skins were modeled by Mindlin plate elements for thin skin (0.1 mm) specimens and by volume elements in the thickness for thick skins (1 mm). Using

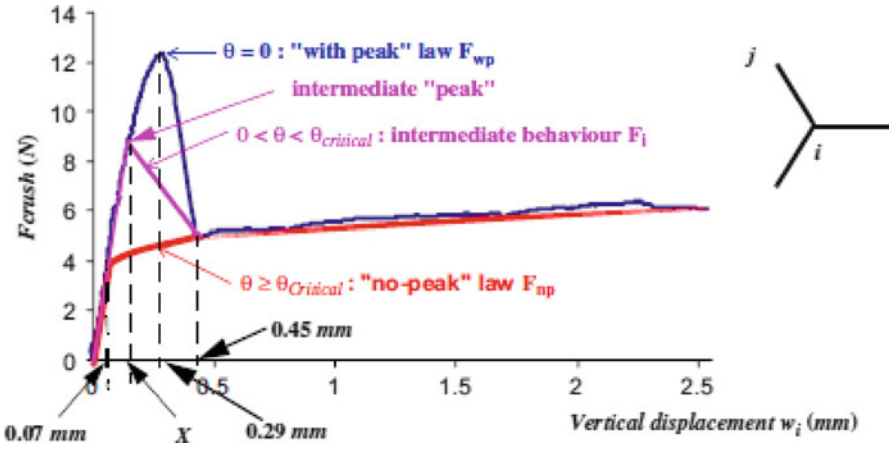


Fig. 34 *Generalized* crushing law $F_{crush}(w_i, \theta_i)$ of *cell edge i*

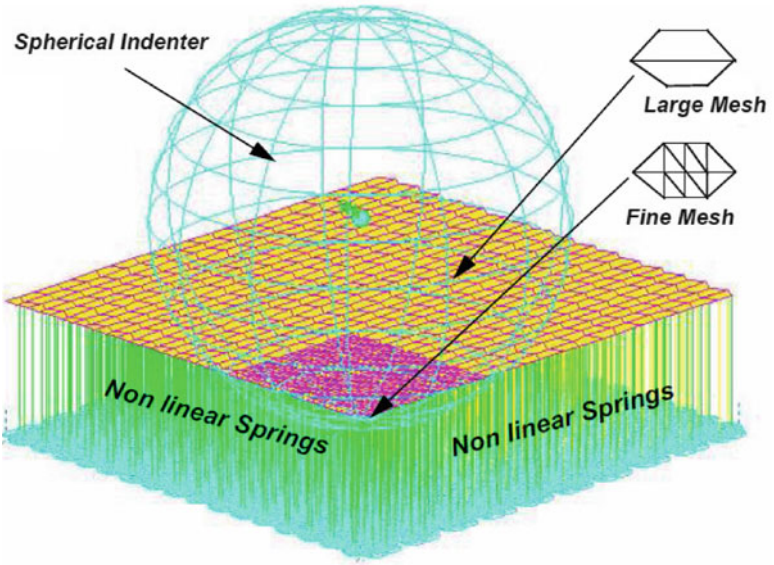


Fig. 35 Finite element modeling of the indentation problem on sandwich with thin metal skins

this method, the triaxial stress state of the metallic skin located directly below the indenter was modeled satisfactorily. A fine mesh was created in the contact area just under the indenter to generate a smooth contact law without any slope discontinuity. A sensitivity study of the mesh gave a convergence result if five volume elements through the thickness and 36 elements per cell in the contact area were used. The local rotation θ_i corresponded to the rotation of the upper node of the spring, which also belonged to the skin. This local rotation θ_i was obtained directly with Mindlin

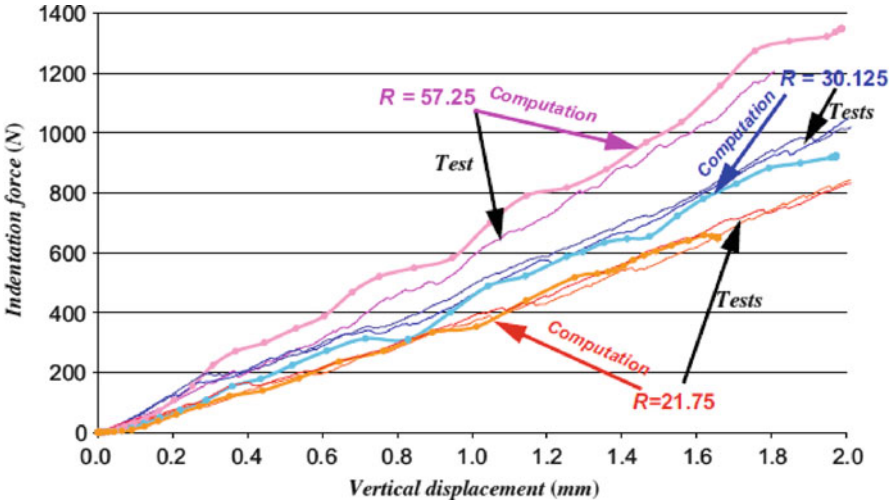


Fig. 36 Test/numerical model correlation in the case of sandwich with thin metal skins

plate elements but it had to be computed in the case of volume elements for the thick skin (more details can be found in [34]). In both cases, the rotation was assumed to be:

$$\theta_i = \sqrt{R_x^2 + R_y^2} \tag{9}$$

where R_x and R_y are the local rotations of the interface nodes between the skin and the spring. The angle $\theta_{critical}$ is found by analyzing the rotations obtained numerically on the edges of the first cell. After several numerical tests, we set $\theta_{critical} = 2.3°$ [35]. Different numerical tests were performed on the position of the connection point and the law of decrease between θ and $\theta_{critical}$ (linear or parabolic decrease). The computations showed less influence of these two parameters. The elastic–plastic behavior laws for brass skins were obtained from conventional tensile tests. Taking advantage of the symmetry of the structure, only one-quarter of the plate was modeled. The numerical simulation was limited to 2 mm of indentation, which largely exceeds the threshold value of detectability known as BVID (barely visible impact damage).

The results of computation were compared to the tests on sandwiches with thin skins (Fig. 36) and a good test/computation comparison was obtained for all three radii of indenter. Globally, the undulations observed during the test were also found numerically and corresponded to the drop in load after the peak load of each vertical edge located at the circumference of the indented area. For the thin skin, the rotation always proved to be less than 2.3°. It should therefore be possible to use the simple law with peak F_{wp} for all vertical edges. The good correlation between computational and experimental results was to be expected since the deformation

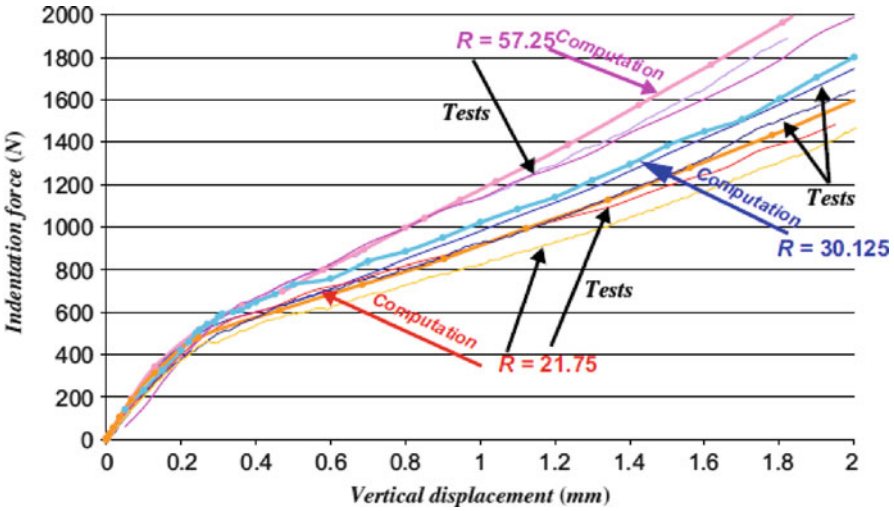


Fig. 37 Test/numerical model correlation in the case of sandwich with thick metal skins

of the thin skin exactly followed the indenter shape during indentation. Also, the phenomenon of folding back that was found from the indentation on the block of honeycomb alone using small indenter radii did not appear for the indentation on the sandwich structure. The good correlation is thus valid for any radius of indenter for the case of indentation of a sandwich structure with thin skin.

For thick skins, if the F_{wp} law was not corrected to take account of the rotation, there was a difference of about 15% between the computational and the experimental results. This can be explained by the fact that the rigid skin did not follow the shape of the indenter when it bent. The bend caused rotations at the menisci before the edges involved had reached peak load [34]. When the rotation is taken into account, the comparison for sandwich structures using thick skin gives a globally acceptable result considering the dispersion of test results (Fig. 37).

3.2 Impact on Sandwich Structure

In practice, impacted aeronautical sandwich structures are usually simply supported or clamped but are never fully supported by a rigid foundation. Moreover, one of the main limitations of the discrete approach at this stage of development is the impossibility to model the shear stresses in the core. Thus, in this subsection, a multi-level approach is proposed to overcome this difficulty [36].

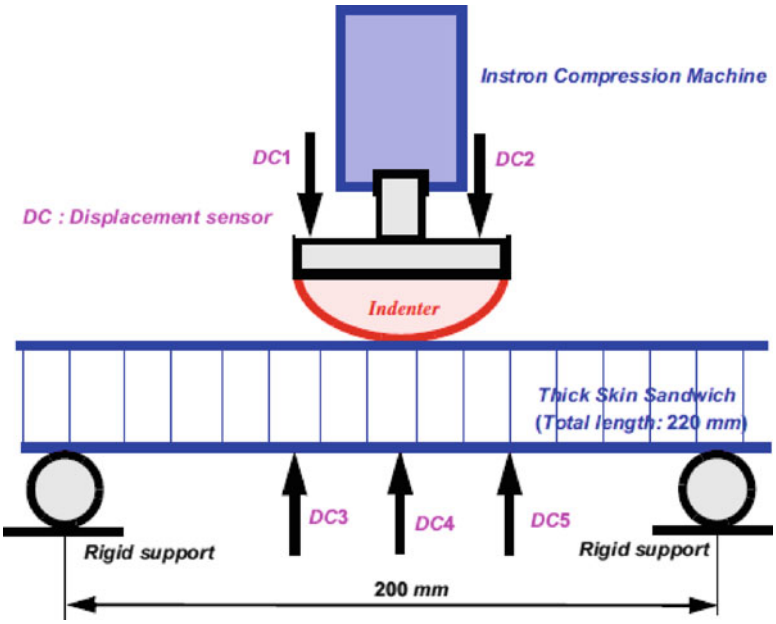


Fig. 38 Three-point bending test principle

3.2.1 Analysis of the Coupling Between Bending Stresses and Indentation

From a practical point of view, it is important to know whether or not a coupling effect exists between the indentation and the stress field generated by a bending load on a sandwich structure. It is the condition for eventually proposing a multi-level approach that separates the phenomena. Three Nomex honeycomb specimens measuring 220×100 mm with 1-mm-thick brass skins were produced (Table 3). Globally, the experimental procedure and the manufacturing of the specimen were the same as described previously.

The three-point bending test principle is shown in Fig. 38. The distance between the cylindrical steel supports was 200 mm and three displacement sensors (DC3–DC5) were located on the lower skin to measure the deflection of the specimen. Two displacement sensors (DC1 and DC2) were also located on the upper face of the indenter.

Three tests were completed with indenter radii of 21.75, 30.125 and 57.25 mm. The depth of indentation was obtained by calculating the difference in displacement between the points on the upper and lower skins just below the indenter [((DC1 + DC2)/2-DC4) in Fig. 37]. The force/indentation curves could then be directly compared with those obtained previously from the tests on rigid flat supports (Fig. 39) and it was seen that the force/indentation contact laws were

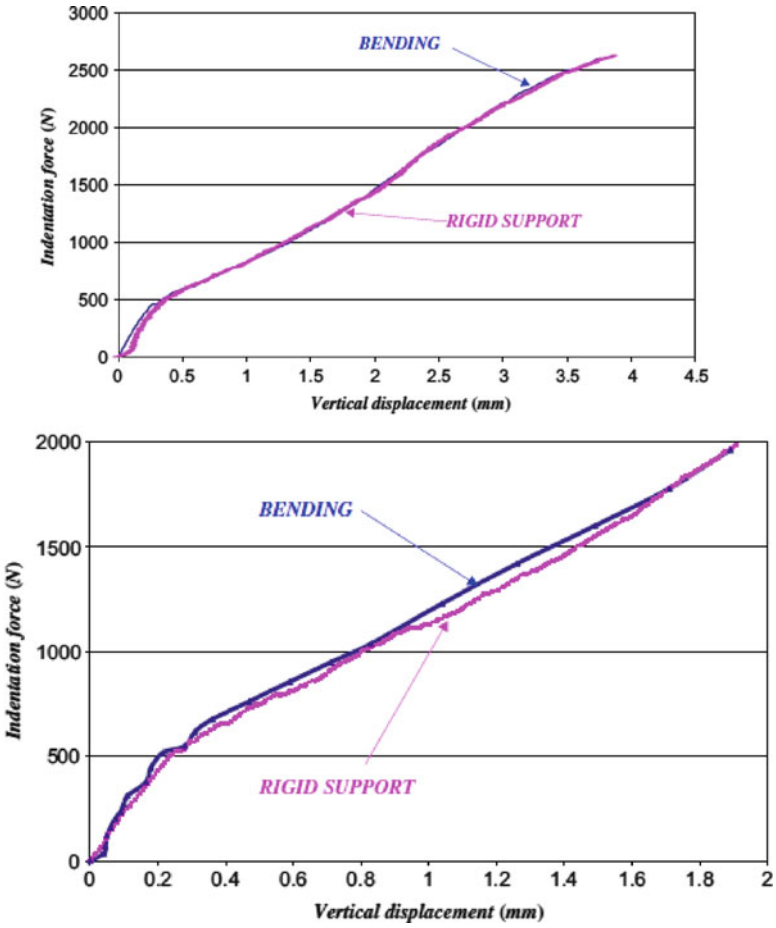


Fig. 39 Comparison of the force/crush experimental curves in the case of a rigid support and three-point bending, indenter R = 21.75 mm (*top*) or 57.25 mm (*bottom*)

superimposed. Experimentally, for the configuration tested, it appears that there is no nonlinear coupling and, consequently, there is a superimposition of global bending and local indentation effects.

When a honeycomb sandwich structure undergoes bending, the transverse shear of the core plays an important role in the deflection and has to be taken into consideration. It is obvious that the proposed modeling of the core by a series of nonlinear vertical springs cannot take this transverse shear stress into account. However, the bending and indentation effects seem to be uncoupled. So, to represent the bending effect of the sandwich, equivalent nodal compression loads were added laterally at the nodes located at the edge of the honeycomb block and at the indented skin side (Fig. 40). The computation result of this model was compared to the numerical simulations discussed in Sect. 3.1 and, as shown in Fig. 40, the results

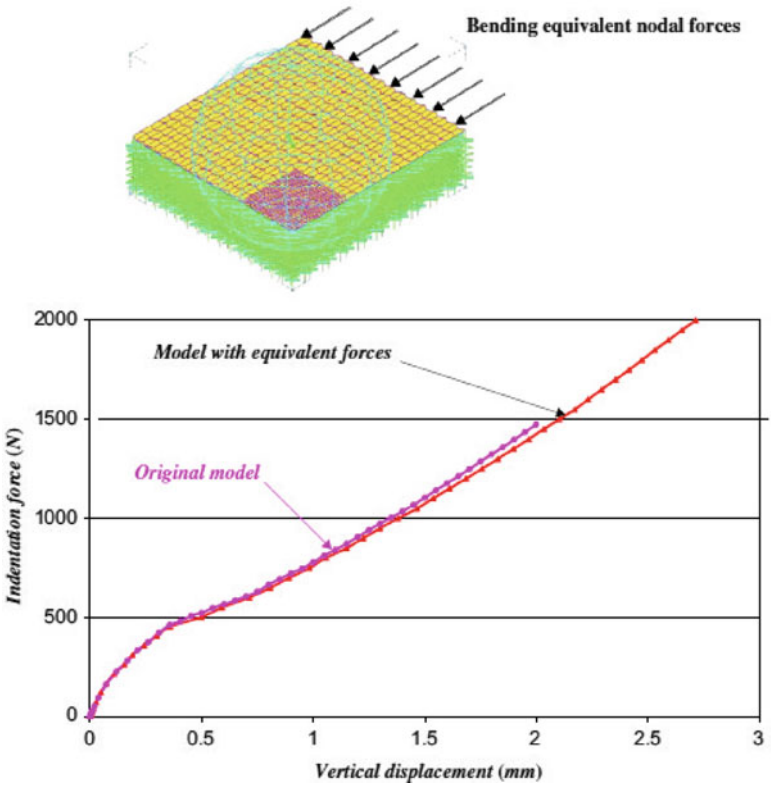


Fig. 40 Adapted indentation model for bending loads and comparisons between previous modeling and the model with nodal forces, for 21.75-mm indenter

were equivalent. This approach enables the practical problem of sandwich structure indentation to be represented, since the bending/indentation uncoupling is again present. Physically, this uncoupling can be attributed to the existence of a plasticized area under the indenter area, at a very early stage. This area becomes saturated in stress and insensitive to the loading increments on the sandwich skin. The only possible coupling must appear at the initiation of the indentation area, which must logically be earlier, when the skin is loaded under lateral compression. However, this phenomenon was not observable for the configuration tested.

At this stage of the study, it is possible to model the static indentation of metal-skinned sandwich structures and to propose a multi-level approach.

3.2.2 Multi-level Approach and Application to Dynamic Loading

In the previous subsection, the possibility of obtaining the static contact law numerically was demonstrated. However, in industrial cases, the geometry can be

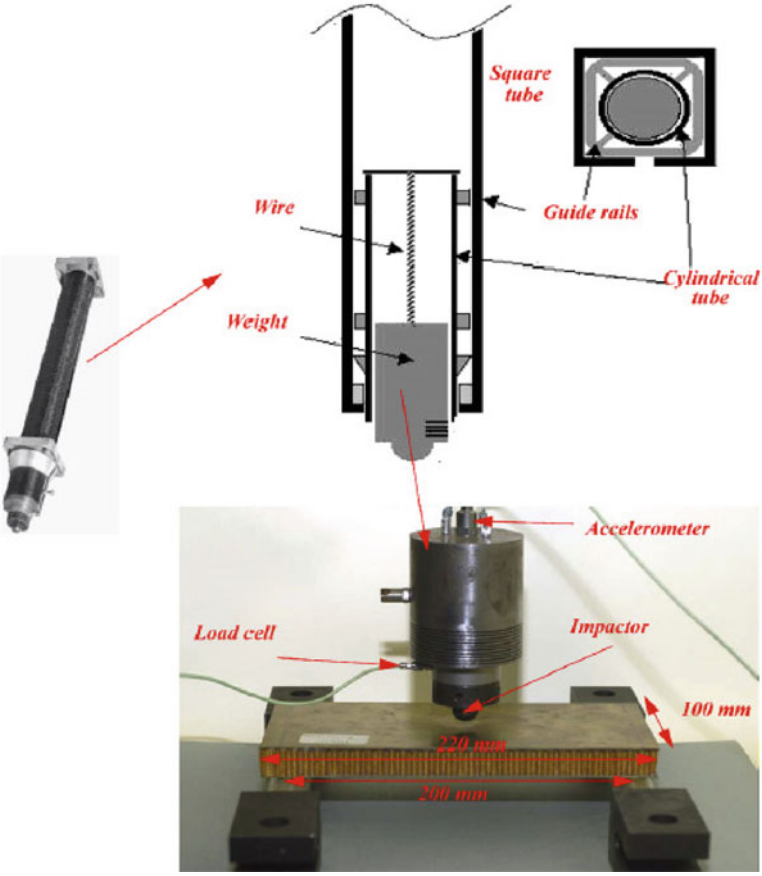


Fig. 41 Load drop test rig

more complex with various shapes and different local stiffnesses. So, the objective of this part of the study is to determine whether the approach developed in the last section is suitable for modeling the dynamic behavior of sandwich structures with metallic skins under low-velocity and low-energy impact. For this purpose, dynamic impact tests were performed using mass drop test equipment (see Fig. 41). The sandwich plates used for the experiments were of the same type as the ones for the three-point bending tests (100 mm $\times$ 220 mm, core thickness 15 mm and skin thickness 1 mm). The boundary conditions were also the same (see Fig. 38). The impactor having spherical tip of radius 30.125 or 57.25 mm, hit the center of the plate. The masses of the impactors were respectively 885 and 865 g. The impact speeds recorded were 2.58 and 2.80 m/s respectively. The impact energy was about 3 J. The impactor was equipped with a load cell and an accelerator to provide the deflection and the force during the impact. The redundancy of these two data items was voluntary. Nevertheless, practically, the force signal gave less interference and

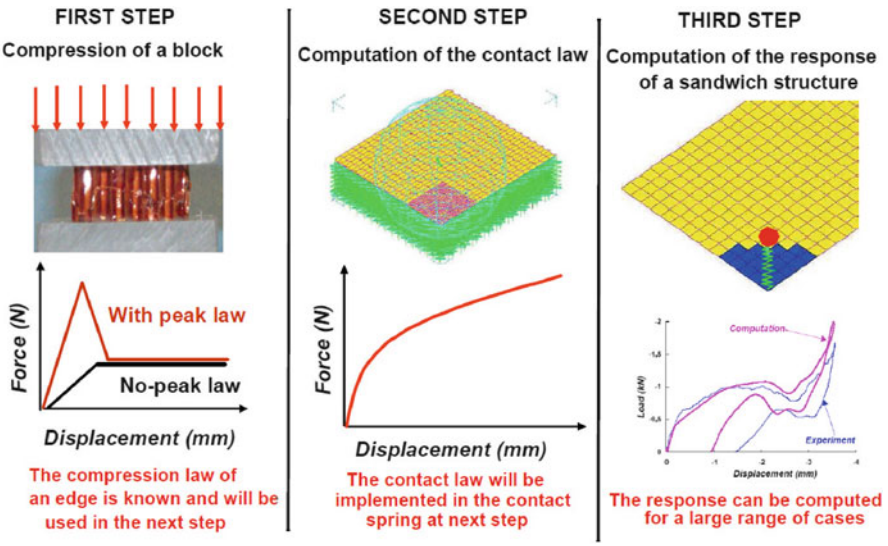


Fig. 42 Multi-level approach principle

it was the only information that was used to measure the force. The force/time and force/ displacement curves are shown in Fig. 44. The complex law of the dynamic contact force should, a priori, be the superimposition of the dynamic response of the sandwich structure and the local indentation.

To model the dynamic test, two assumptions were made:

- *The global behavior of the structure did not depend on the local response during impact. This hypothesis is in accordance with the local nature of the impact reported in the literature.*
- *The static/dynamic equivalence was assumed for the range of structures and impacts studied. Thus, it was possible to use the static contact law computed previously.*

With these assumptions, a multi-scale approach could be proposed (see Fig. 42). The local indentation law was computed first. The only parameter necessary was the crushing law for the spring, which was obtained simply by a basic uniform compression test on a block of honeycomb. As the local dynamic effects were neglected, a nonlinear spring was used to represent the contact law in the global model as shown in Fig. 42. The compression law for this spring was the indentation law previously computed in Sect. 3.1 This proposition is similar to the approach of Choi and Lim [37] for laminated plates.

An implicit finite element model was made. The sandwich structure was modeled by Mindlin plate finite elements (Fig. 43). The materials of the structure were assumed to be linearly elastic. The mass density of the brass skin and the Nomex were 8,000 and 48 kg/m^3 respectively. The transverse moduli of the core were

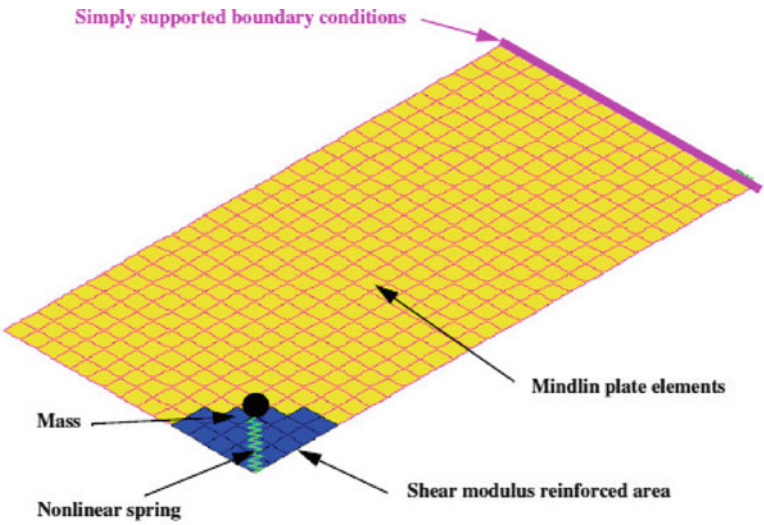


Fig. 43 Spring-mass finite element model

Gyz = 44, Gxz = 30 and Ezz = 120 MPa. Following the assumptions and to avoid local dynamic effects, it was decided to increase the transverse shear modulus of the core artificially on the right of the indenter with the following values: Gyz = Gxz = 5,000 MPa. Numerical tests were performed to demonstrate the little influence of the area dimension and the modulus of the local reinforcement on the global response of the structure. In our case, the nonlinear spring law was obtained numerically. The linear stiffness of the spring was 2.67 kN/mm, the yield stress corresponded to a force of 0.4 kN and the plastic stiffnesses were 0.714 and 0.93 kN/mm for the 30.125 and 57.25 indenters respectively. The initial velocities were those measured (2.58 and 2.80 m/s respectively). For the dynamic computation, a Hilbert–Hughes–Taylor algorithm with automatic time stepping (implicit predictor–corrector scheme) was selected.

In spite of the relative simplicity of the model used, the numerical simulations fit the experimental results correctly (Fig. 44). The maximum contact force was found, and will provide the damage area by a return to the indentation model. The static–dynamic equivalence for this range of structures and impacts, which was mainly observed experimentally, was also confirmed numerically. Besides, the possibility of making indentations on fully supported specimens was demonstrated. This result also globally validates the approach and the hypotheses made. The simplicity of the model should be an advantage in dealing with complex structures and multi-impact phenomena.

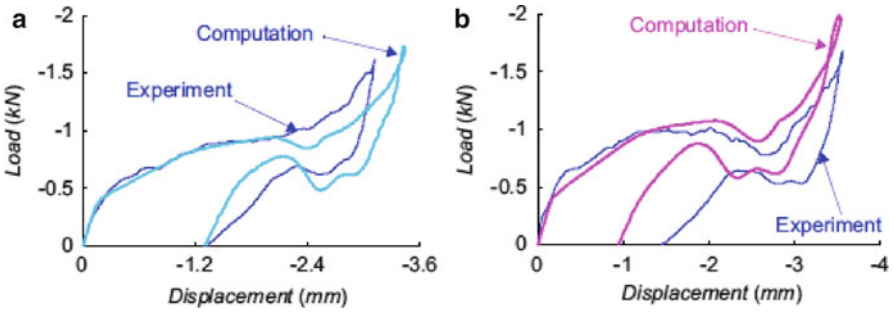


Fig. 44 Dynamic load–displacement law: (**a**) 30.125 mm and (**b**) 57.25 mm impactor

3.3 Conclusions

A method has been developed to model low-velocity/low-energy impacts on metal-skinned sandwich structures, and gives good correlation of contact laws. An analysis of the crushing from a structural point of view has enabled us to propose an original way of modeling Nomex honeycomb core using a grid of nonlinear springs. In practice, the springs in implicit finite elements provide a faster and a more robust computation, especially when the stiffness varies and decreases suddenly as is found to occur in brittle materials such as Nomex. The local rotation of the upper surface of the honeycomb that interfaces with the skin plays a role in the initiation of vertical edge buckling. This interface effect between skin and honeycomb is then taken into account in the model. Direct application of this modeling enables the contact law to be computed when metal-skinned sandwiches are quasi statically indented on a flat support. This approach gives highly accurate correlation with indentation tests on a flat support or under three-point bending. The proposed multi-level approach consists of three steps. First, a basic compression test must be performed on a block of honeycomb to obtain the initial crushing law. Second, using this law in nonlinear springs, it is possible to obtain the contact law using a finite element model and a nonlinear static computation. Finally, with the hypothesis of neglecting the dynamic effect at contact, a basic finite element spring-mass model using a nonlinear contact law computed in the last step is able to model a dynamic test.

As good correlation is obtained, the hypothesis of equivalence between static indentation and dynamic test is validated. This basic approach could be useful to model complex structures under impact or multi-impact. It is important to note again that the impact simulation is complete and is, finally, based only on a simple, economical compression test on a block of honeycomb core. It avoids the use of indentation tests on the complete structure to identify the Meyer's law coefficient [9]. It also shows that the phenomenon remains local and, for the range of structures studied, is independent of the boundary conditions and the dimension of the plate.

It would seem that the approach that has been developed can be used for other cellular cores made from other soft materials thanks to their similar and common crushing mechanism.

The use of metallic skin in this study enables a step-by-step approach to the modeling of the impact but this remains a limitation in practice since it is rare for sandwich structures to be made using metallic skin in industry nowadays. The real challenge will still be to couple this modeling approach with laminated skin. In this case, the plasticity behavior will be replaced by a determination of the damage state in both the honeycomb core and the composite skin and the possible coupling between the stress state of the global structure and the indentation phenomenon will have to be taken into account. Knowing the local state, it will then be possible to compute the residual strength by a second model. This approach will be developed in the next section.

4 Residual Dent and Post-impact Behavior

In this section, the discrete approach proposed in the previous section will be used to make a complete computation loop including indentation, computation of the residual print (or dent) geometry and computation of the compression after indentation (CAI) strength. In the first subsection, the approach is limited to a sandwich with metallic skins. Nevertheless, the discrete approach allows us to identify the failure mechanisms during CAI and the role of core crushing before the collapse of the sandwich panel. Thus, a core crush criterion can be identified [38]. This original criterion is then applied in the second subsection to determine the residual strength of impacted sandwich structures with composite skins [39].

4.1 Residual Dent and Compression After Impact on Sandwiches with Metallic Skins

Experiments have shown that the depth of residual dent will be different from the maximum static indentation [1, 19] because of “elastic” recovery. However, from the aviation regulations point of view, a limit of detectable print called barely visible impact damage (BVID) after impact is defined and, beyond this limit, the structure should be designed for damage tolerance [1, 40]. This threshold is based on visual inspection [40, 41]. Thus, it is important to be able to determine this residual print geometry first, which, as far as we know, has been the subject of only a small number of studies in terms of the numerical and analytical models that have been made. Palazotto [14] has proposed a finite elements model of impact using three loops of iterative computation to determine the damage on the honeycomb, the damage on the composite skin and the geometry of the print successively. Horrigan [19] has

proposed a continuum damage model to calculate the behavior of honeycomb. But, because of the continuum approach, the core damaged area could not be predicted correctly. Most authors, in particular in the case of foam cores [42, 43], separate the core into different regions (cavity, crushed or damaged, undamaged) to model the indentation and the compression after impact behavior. Destructive sectioning of sandwich panels is most often used to characterize the damaged or undamaged geometry for implementation in a finite element model. Concerning the strength of compression after impact, due to the weakness of the core after impact, several authors propose wrinkling models to compute the residual strength [44, 45]. Xie and Vizzini also couple this type of model with a skin failure criterion [46, 47].

Minakuchi et al. [48, 49] have proposed an efficient segment-wise analytical model using a discretization of the honeycomb similar to the discrete model approach proposed earlier [28]. This is used to compute the residual dent of a sandwich beam with laminated skins. A complete state-of-the art can also be found in [50].

In previous sections, honeycomb was represented by a grid of vertical springs in which the behavior law in compression was calibrated from uniform compressive loading experiments. In the following subsections, the law is developed further by integrating the cyclic behavior (compression loading and unloading) of honeycomb that allows the defect recovery of honeycomb after compression and the residual print geometry of the sandwiches structures after indentation to be simulated. The law is also used to compute the residual strength of an impacted sandwich plate subjected to edgewise compression.

4.1.1 Experimental Procedure and Test Results

Specimens (Fig. 45) were prepared by taking care to obtain high surface smoothness and high dimensional precision (± 0.01 mm), which are the necessary conditions to obtain a correct uniform compressive test. The standard dimension of the specimen was 150×100 mm. Two brass skins (thickness 0.5 mm) were bonded to Nomex honeycomb core HRH 78,1/4,3 (thickness 15 mm). Resins were molded into both extremities of each specimen. To transfer the compressive load properly, two plates of brass 1 mm thick were added as reinforcement in the resin–Nomex junction area.

These specimens were previously indented on a flat support (Fig. 29) and the indentation was carried out by imposing a displacement with a constant speed of 0.5 mm/mn. A spherical indenter made of steel with radius of 57.25 mm was used and several depths of maximum indentation $d = 0$, 0.5, 1, 1.5 and 2 mm were used to obtain different damage areas. For compression (CAI) tests after indentation, test supports and specimens corresponded to the AIRBUS standards so that we could compare the test results with industrial ones. To observe the evolution of damage geometry in terms of its depth and its form during compressive loading, a method of 3D Image correlation using two cameras was employed (Fig. 46). Strain gauges were also used to observe the distribution of compression flux on the two skins. The compressive load acting on the specimens was measured directly from the

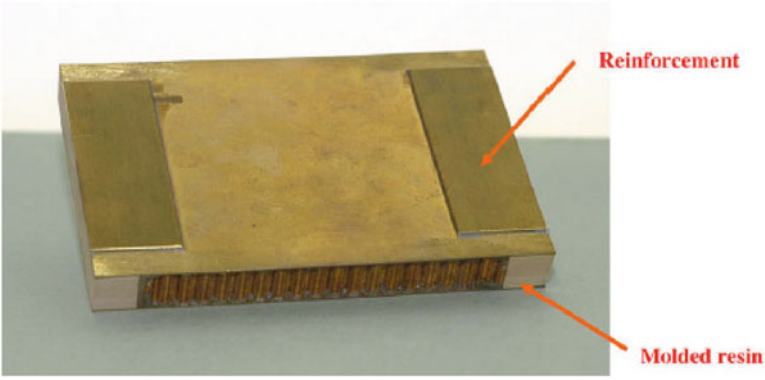


Fig. 45 Specimen for CAI tests

INSTRON machine and the displacement of the compression surface was measured using LVDT displacement measurement.

The experimental contact laws are plotted in Fig. 47. We note that the relaxation phenomenon is highly nonlinear and that the difference between the depth of the residual dent and the maximum depth of the indentation is significant. Qualitatively, although the depth of the residual print is very small, it can come from a significant indentation that has generated significant honeycomb crush. Furthermore, we observe that the relative difference is not constant and decreases as the depth of the indentation increases.

The shape of the residual imprint was also measured by 3D image correlation (Fig. 48). The radius of the surface of the residual dent increased with the depth of the indentation. The values measured in this way were consistent with the displacement of the indenter measured by lever comparators. Table 4 summarizes the values measured in each test and the relative differences.

The curves of compressive load as a function of its displacement for five indented specimens with different depths of indentation, d, are plotted in Fig. 49. For all the specimens, the initial stiffness was identical and corresponded to the elastic behavior of skins. Analytical calculation showed that the point where the slope changed just after the elastic behavior of skins coincided with the yield limit of the skin. Thus, it seems that, at the beginning of compression, the dimension of the damage area caused by indentation does not have a significant influence.

The second slope was also practically identical for all specimens. This slope seems to be controlled by the plastic behavior of the skins. As the force of compression increased, an inflexion was observed just after the passage of maximum force, which can be qualified as the residual strength of the indented structure. This residual strength depended on the depth of the maximum indentation, d. It decreased significantly with an increase of the maximum indentation depth, d, and hence the damage in the core due to indentation was greater (Fig. 50).

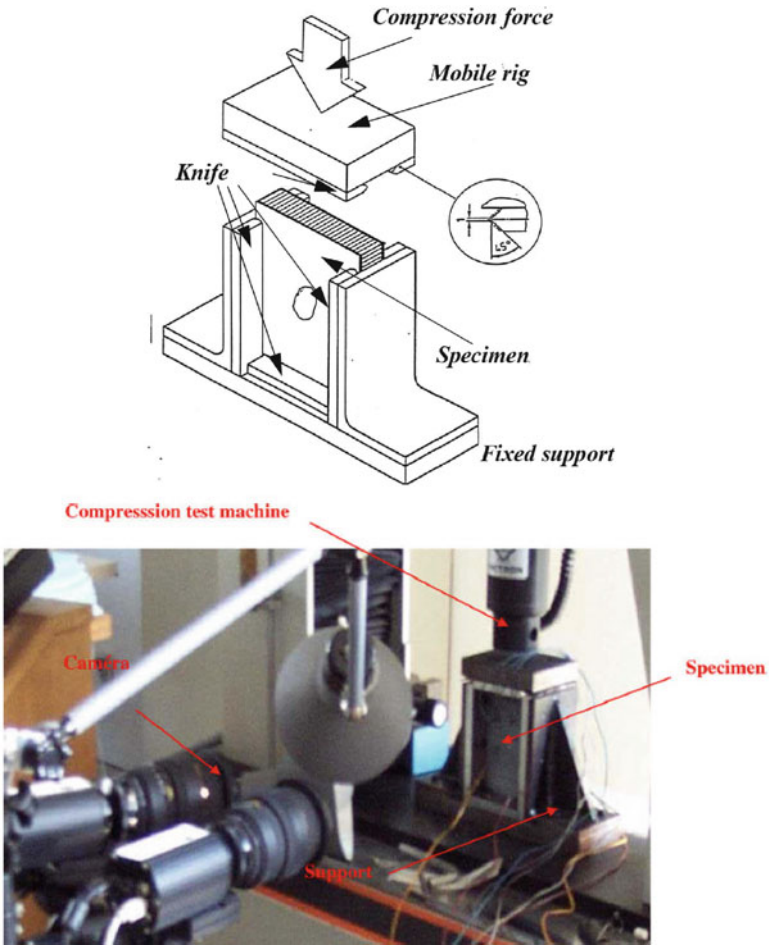


Fig. 46 CAI test device

The dent depth evolution of the residual print during loading is also drawn in Fig. 51.

By observation using Digital Image Correlation (DIC), the evolution of the damage area can be described as follows:

- *In the region of elastic behavior of the skins, the shape of the residual print geometry after indentation remains circular and its depth hardly varies.*
- *At the beginning of plastic behavior of the skins, the form of the print begins to become elliptical, progressively, in the direction of lateral axis a. At the same time, in the direction of longitudinal axis, b, no evolution is observed. The print depth is also observed to increase progressively.*

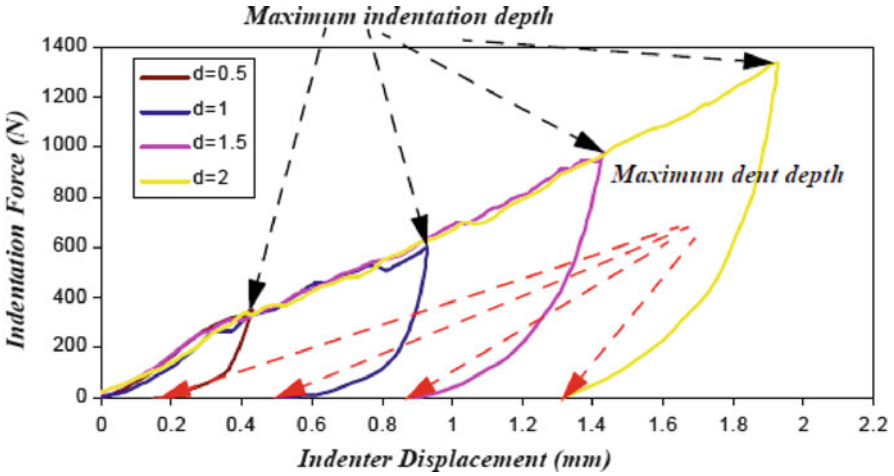


Fig. 47 Force/displacement curves using an indenter of radius R = 57.25 mm

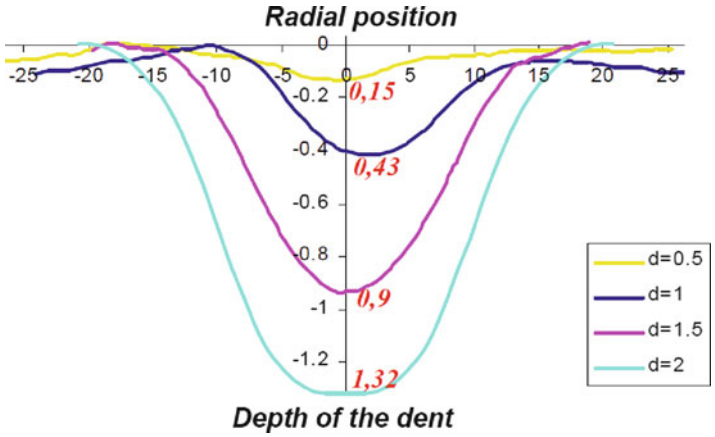


Fig. 48 Mapping of the residual dent profile (digital image correlation)

Table 4 Comparison of the depth of the indentation and the residual dent depth

Maximum indentation depth (mm)	0.5	1	1.5	2
Residual dent depth (mm)	0.15	0.43	0.9	1.32
Difference (%)	70	57	43	34

- *Approaching maximum compressive load (residual strength of the structure), the print depth increases abruptly. The same observation is also obtained for the evolution of radii about the lateral axis, a, which finally reach the edges of specimen. It is also interesting to note that the deflection of non-indented skin below the indented area also increases rather quickly.*

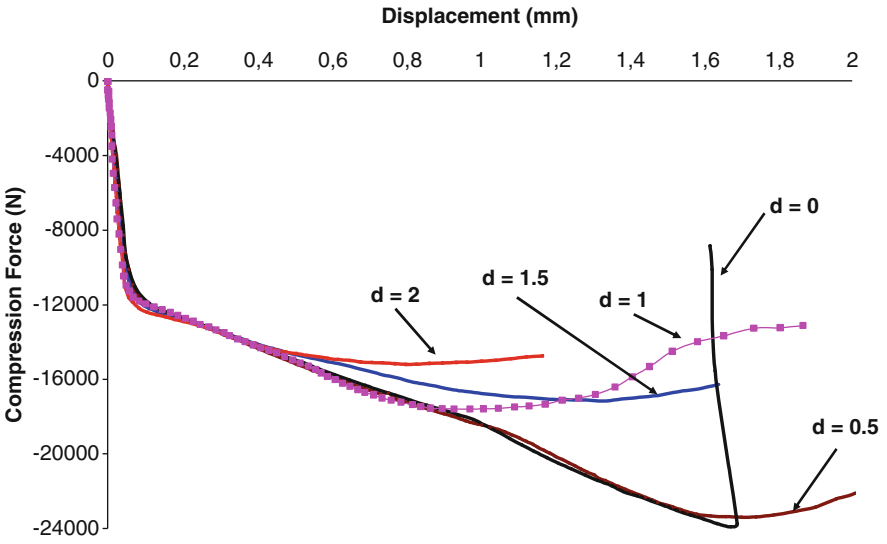


Fig. 49 Evolution of the dent under compression after impact loading for maximum indentation d_{max} from 0.5 to 2 mm

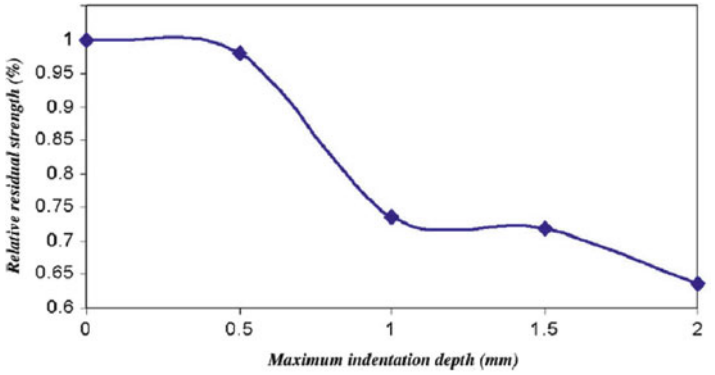


Fig. 50 Relative residual strength as a function of indentation depth

For the specimen that was indented only with maximum indentation depth d = 0.5 mm and which had a corresponding residual print depth of 0.1 mm, the evolution of the damage geometry was quite different. This specimen, with only 2% of decrease in terms of residual strength, behaved almost as a non-indented specimen. However, the elliptical evolution of the damage geometry was also observed with an abrupt progression when approaching the maximum compressive loading. This behavior was similar from all qualitative points of view to that observed for a thin composite skin [51].

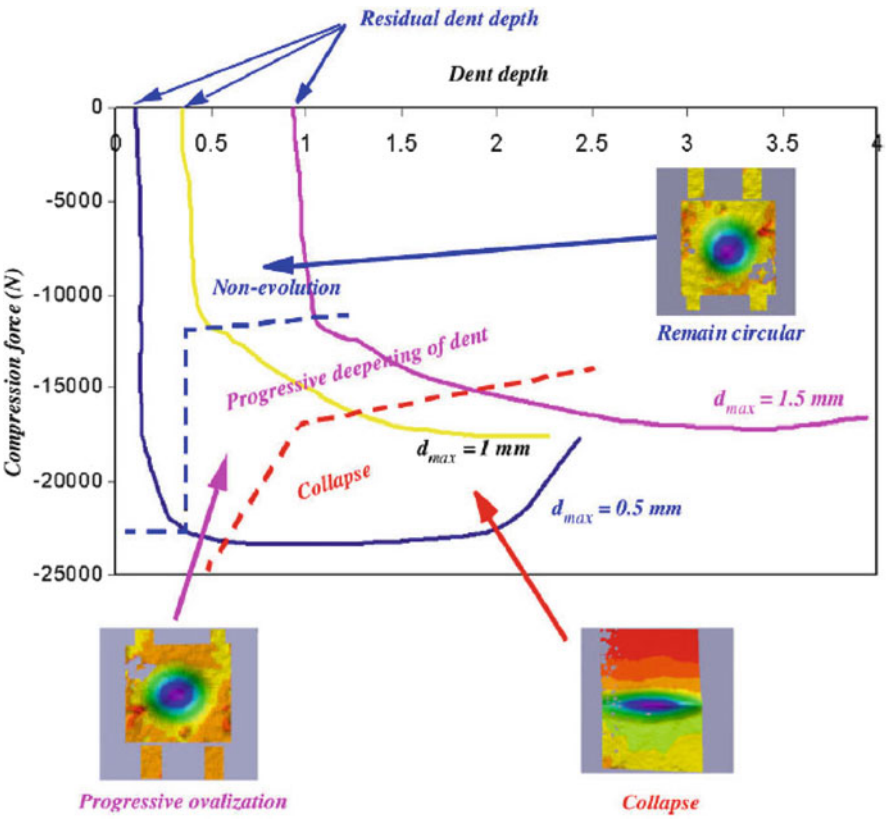


Fig. 51 Evolution of the dent under compression after impact loading for maximum dents d_{max} of 0.5, 1 and 1.5 mm and identification of different behaviors with the help of DIC

4.1.2 Application of the Discrete Approach

Globally, the same finite element model using implicit SAMCEF software that was used for the study of indentation was employed here (see Fig. 52).

The principles of the model are as follows*:*

- Indented skin is modeled by Mindlin-type elements. This skin has free boundary conditions except at the position of the CAI test supports (z-axis degree of freedom (d.o.f.) locked). These boundary conditions did not exist during indentation (Figs. 52 and 54). However, the literature shows that indentation causes a local damage area and, for the size of specimen used in this study, the boundary conditions are not sensitive. This insensitivity was confirmed by a posteriori numerical computation. The compression law for the brass skin was obtained from tests on a virgin (non indented) sandwich specimen and it appeared that the yield stress in compression was 110 MPa instead of the 100 MPa obtained for traction. Also, the hardening law was slightly different.

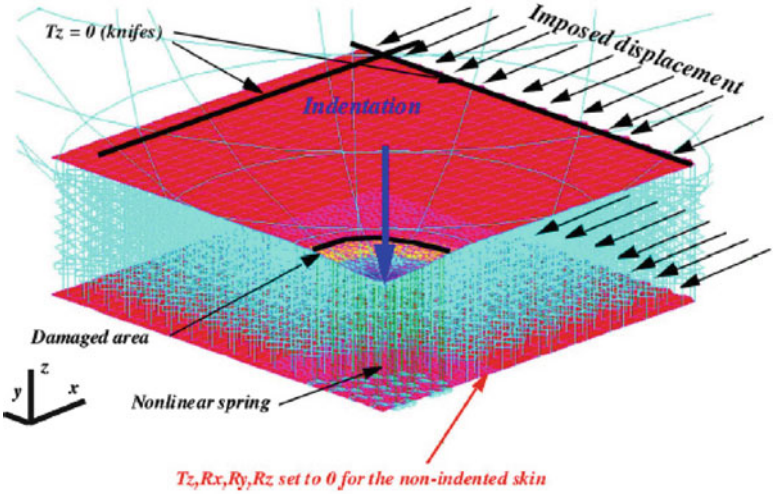


Fig. 52 Finite element model for compression after impact

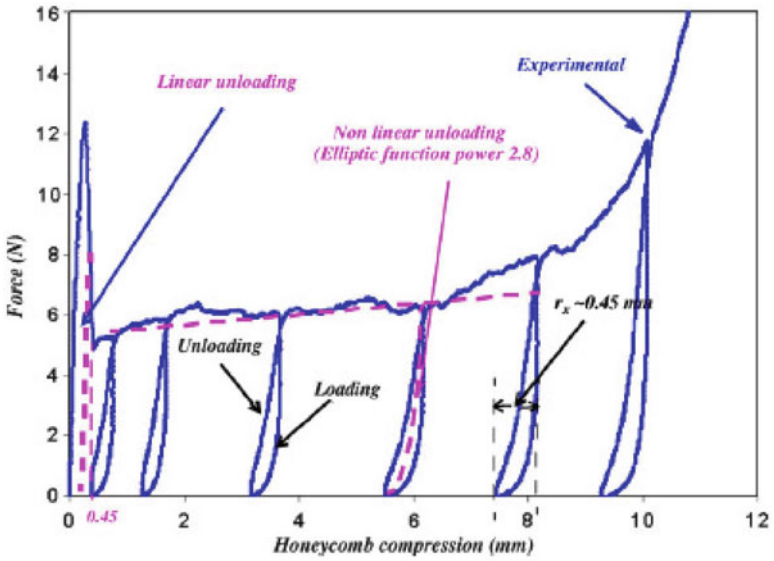


Fig. 53 Compression behavior of Nomex honeycomb with cycling

- Hexagonal Nomex honeycomb was modeled by a grid of non-linear vertical springs placed geometrically at the same positions as the honeycomb vertical edges. Its behavior law was obtained experimentally from a cycled compression uniform loading test on a small block of Nomex honeycomb (Fig. 53). Until 0.4 mm of displacement of the uniform compression surface, compression

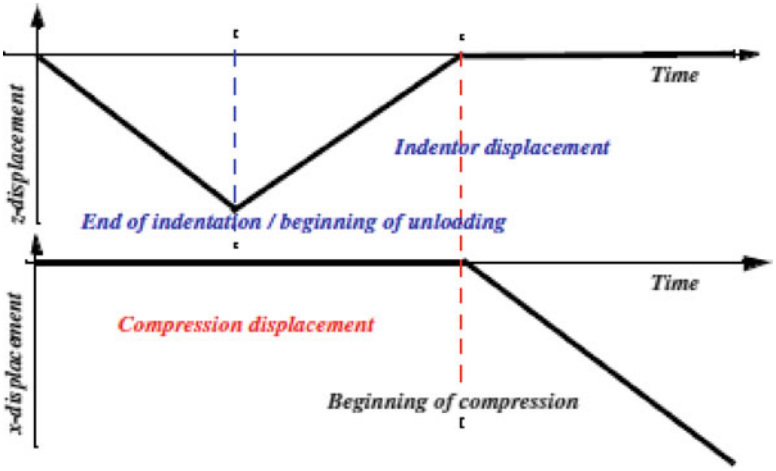


Fig. 54 Time–function displacement laws for compression after impact modeling. The first graph corresponds to the imposed displacement of the spherical indenter, the second to the displacement imposed on the upper skin

unloading gave a linear return of displacement with the same slope as the compression one. Beyond that displacement, the return was no longer linear (ellipse with a power of 2.8). The hysteresis behavior found from the test was assumed negligible and was not taken into account in the FEM computation.

- Non-indented skin had to be modeled with the same model as indented skin but almost all the degrees of freedom were blocked, except for its in-plane displacement (in this case translation in x and y) to allow non-indented skin to deform like a membrane during compression.

The lower skin was added because the distribution of the forces between the two skins varied as the defect progressed. It is obvious that the discrete model used before cannot directly represent the bending of the sandwich and, hence, the out-of-plane displacement of the non-indented skin. In fact, all the degrees of freedom of this skin were locked except for the displacements in the plane of the sandwich (x and y axis) so that the skin could deform during the compression. However, this assumption was justified because the deflection of non-indented skin below the indented area measured during tests was very small and became significant only when the compressive load approached the maximum one. Also, globally, the deflection of non-indented skin still remained negligible compared to the depth of the indented area. Moreover, the computation was more robust numerically when the boundary conditions were conserved for complete computation involving different phases. The load acting on a structure was simulated by imposing first a vertical displacement of the indenter towards negative Z (compression loading) and positive Z (compression unloading), then followed by imposing the displacement on the edges of the structure to simulate the lateral compression load (CAI) on the indented structure (Fig. 54).

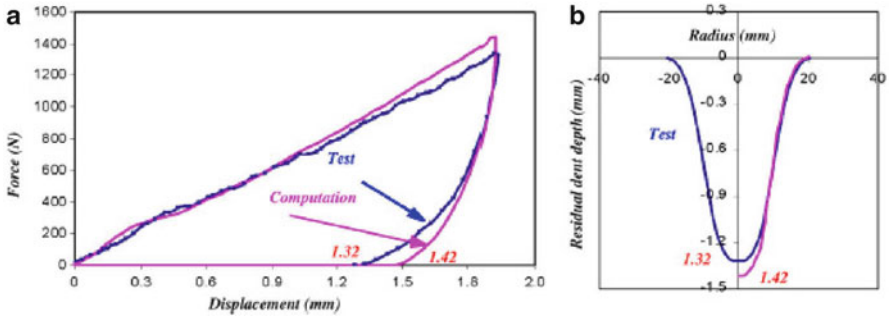


Fig. 55 Contact law and residual dent test compared with computation for a maximum indentation of 2 mm

4.1.3 Test/Numerical Model Comparison: Residual Dent and CAI

The comparison between test and computation during the indentation phase is described in Fig. 55 for the case of maximum indentation d = 2 mm. The curve of indentation force as a function of indenter displacement is plotted in Fig. 55a and the profile of the residual print about the longitudinal axis b is plotted in Fig. 55b. The depth of the residual print obtained from the computation is 1.42 mm whereas 1.32 mm is obtained from the test measurement, which gives the difference of 7%. For all specimens, the difference of residual print between computation and test varies from 25% for the smallest indentation depth (d = 0.5 mm) to 7% for the deepest one (d = 2 mm). The curves obtained from the indentation test are correctly simulated by computation [35] and also globally for the geometry of the residual print after indentation.

In the compressive loading after indentation phase, the evolution of the residual print was studied by analyzing two parameters: depth of residual print and profile about the major axis, a. The minor axis did not vary significantly. Test/computation comparisons for these two parameters are represented in Fig. 55 for the specimen indented with maximum indentation d = 1.5 mm. Globally, numerical computations give the same evolution as test results. The small difference at the beginning of the compression is due to the difference of residual print depth between computation and test from the previous phase. However, there is also a significant difference in terms of the final depth of the damage area (in the maximum compressive load region) because the out-of-plane deflection of the structure is not taken into account in the computation.

Nevertheless, the maximum compressive load, hence the residual strength of the indented sandwich structure, was perfectly simulated. Also, the evolution of the damage area in terms of its profile about the major axis was perfectly simulated by computation (Fig. 56). A good correlation between test results and computations in terms of print geometry evolution and maximum compressive load was obtained for almost all indented specimens except in the case of small indentation d = 0.5 mm (Fig. 57). For this test, the depth of the residual print was very small, only 0.15 mm.

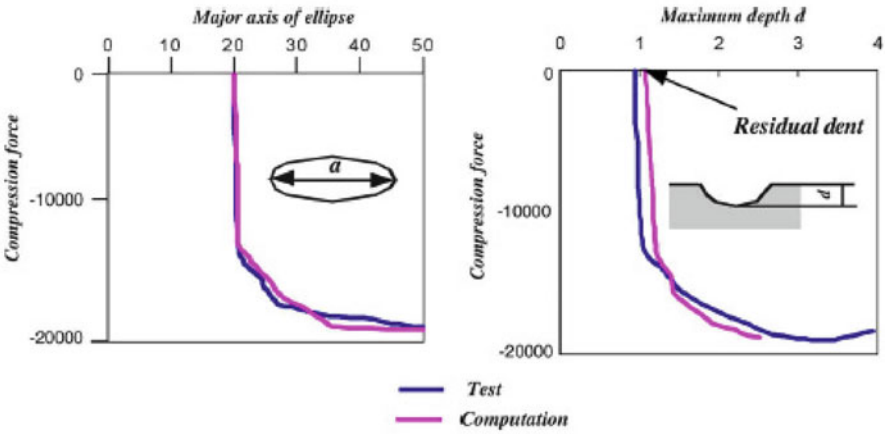


Fig. 56 Correlation of the maximum depth and the major axis of the ellipse of the dent during compression for the maximum indentation depth of 1.5 mm

Investigations were carried out to find out whether an initial geometry defect, such as skin curving, would stabilize the indented structure whereas this defect was not taken into account in computation. It was also possible that, regarding the smallness of residual print depth, the difference came from an insufficiently refined mesh that created early numerical instability. Globally, in this section, it has been shown that the discrete approach is also able to predict the residual dent after impact.

4.1.4 Failure Mechanisms and Core Crush Criterion

In this part, the reaction of the first uncrushed springs placed in the dent evolution direction about the major axis of the ellipse and in the circumference of the residual print (see Fig. 58) is analyzed. The force in these springs (1–3) is initially low and does not increase during the appearance and progressive extension of the ellipse. After a drop in the spring force, which is due to the appearance of a bump at the periphery of the ellipse that stretches the springs, a sudden increase in the compression force is observed until it reaches the critical force (the peak) for the first spring at the periphery (no. 1). The collapse of this first edge occurs only shortly before the abrupt progression of the ellipse, which takes place when the second edge (spring no. 2), situated on the major axis of the ellipse, collapses in turn. Numerically, it is shown here that the advance of the defect coincides with the physical phenomenon of local core crush. Therefore, ***the collapse of the first edge located on the major axis of the ellipse modeled by its spring can be proposed as the criterion for determining the computed residual strength***. Logically, this criterion should always underestimate the experimental residual strength, but not too much, since the ellipse generally appears just before the catastrophic failure of the specimens [50].

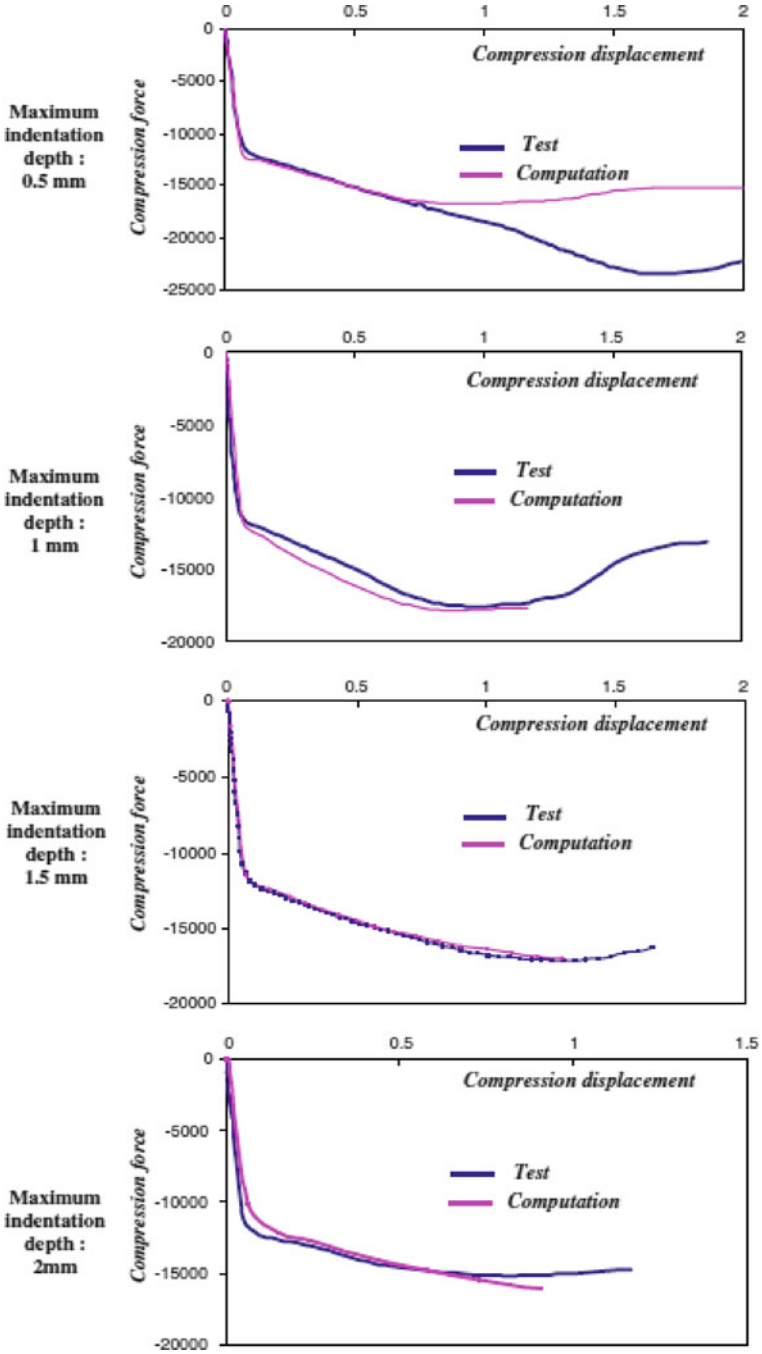


Fig. 57 Comparison of compression after impact: tests and modeling

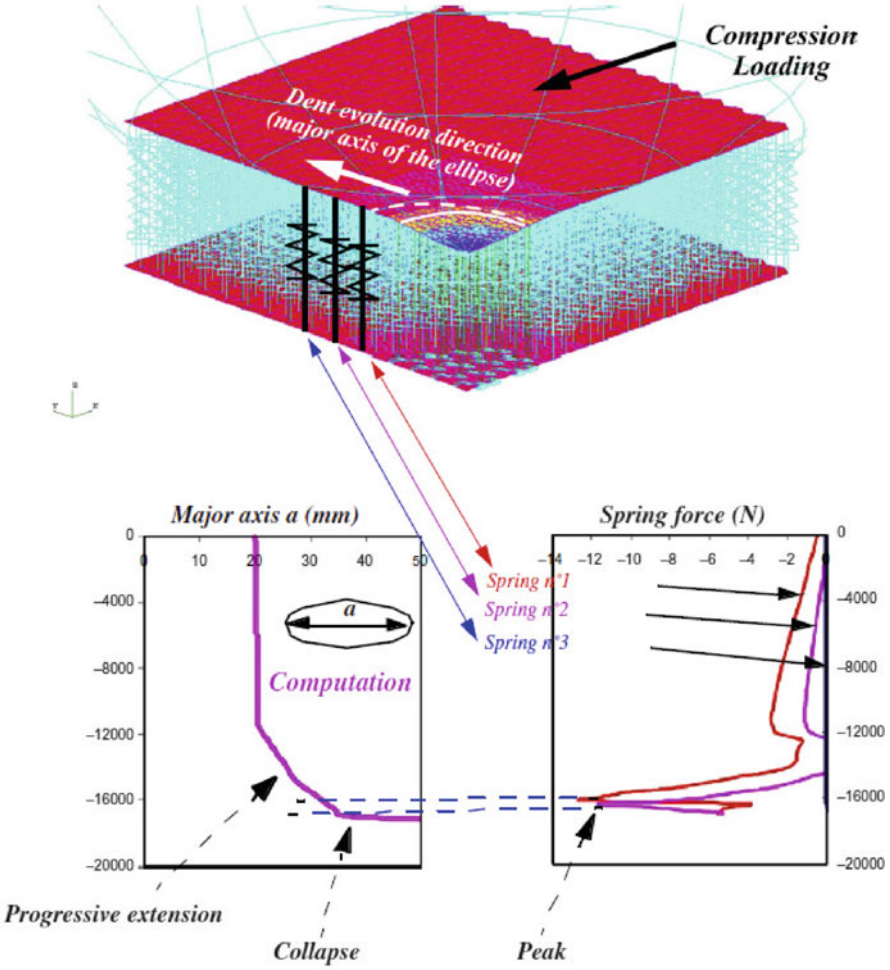


Fig. 58 Analysis of the collapse of pristine core after impact

Thus, the analysis of the tests combined with the discrete modeling of the core shows that the phenomenon occurring during CAI is due to interaction between three mechanical behaviors:

- A geometrical nonlinearity due to the skin's neutral axis offset in the dent area.
- A nonlinear response of the core due to the crushed state and the classic "with peak" response of the undamaged area.
- The response of the skin due to its type of damage after impact: plasticity for metallic skins and delamination or crack growth for laminated skins.

4.2 Application to Sandwich Structures with Composite Skins

In this section, the discrete model is applied to the case of compression after impact on sandwich structures with composite laminate skin. The core crush criterion presented in the previous subsection will be used to evaluate the CAI strength. The difficulty in modeling the phenomena lies in the determination, a priori, of the damage area of the core and the skin according to the delamination area and geometry of impact. In practice, these data could be the input recorded in parallel as explained in Sect. 1.1. The model developed here is inspired by the works of Lacy and Hwang [52, 53] which demonstrate the ability to model the behavior of laminate sandwich structures after impact globally. In this study, the initial damage geometry after impact was measured directly from the specimen using destructive and non-destructive inspection. A fixed behavior law for composite skins was also used on the impacted area (50% of module degradation). In the following subsections, the model used in this study will first be described and then a comparison will be made with the tests results provided by the same authors [52, 54].

4.2.1 Model Geometry and Assumptions

Only a quarter of the plate was modeled due to symmetries and the overall shape as shown in Fig. 58. Thus the model size area was 101.6×127 mm^2. The geometry parameters of the impact-damaged area are described in Fig. 59 using the same notations as in [52, 53]. For all specimens reported here, the thickness of the core t_c was 19.1 mm. The facesheet indentation depth, d_I, and radius, R_I, could be measured directly on specimens or on a real structure. In the new finite element model, the geometry of the dent is represented by Coons surfaces. The crushed core radius should be found by NDI techniques. It seems to be more difficult, in the case of sandwich structures, to determine the delaminated area precisely. Thus, the degraded facesheet radius R_F will be taken to be equal to:

$$R_F = \frac{R_I + R_C}{2} \tag{10}$$

The core used in [55] was made of Nomex honeycomb, 48 kg/m^3 and had a cell size of 4.76 mm and a transverse modulus E equal to 137.9 MPa. Its maximum compressive strength was 2.41 MPa and the plateau stress was 1.03 MPa. Knowing all these values, for a given surface, it was easy to transform the continuum values into discrete ones for the springs located at the corners of the cells. Law "A" for an intact honeycomb under compression is given in Fig. 60.

The peak force was found to be 23 N and the crush force was 9.86 N. The compression displacements were calculated directly from the strains given in [52]. This law was applied to the springs representing the pristine core, i.e. located at a radius $R > R_C$. For the springs representing the crushed core, law "B" was applied.

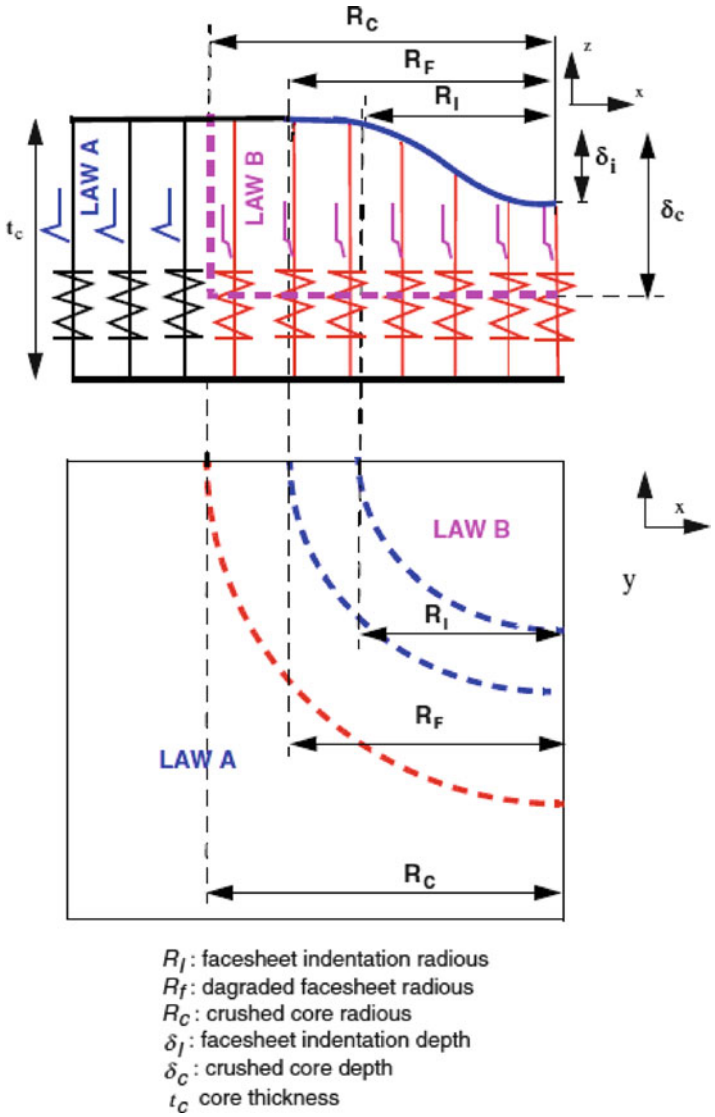


Fig. 59 Geometry of the impact-damaged region

These laws are of same type as in [52] and are in accordance with a previous cycling test performed by the authors on Nomex honeycomb (see Fig. 53 and [39]). The true value of the crushed core depth δ_C was, until now, obtained by destructive sectioning. In an initial approach, the values given in [52] will be taken and applied to all springs located in the crushed area (see Fig. 59). When this is done, the evolution of the crushed depth is not represented but an a posteriori sensitivity

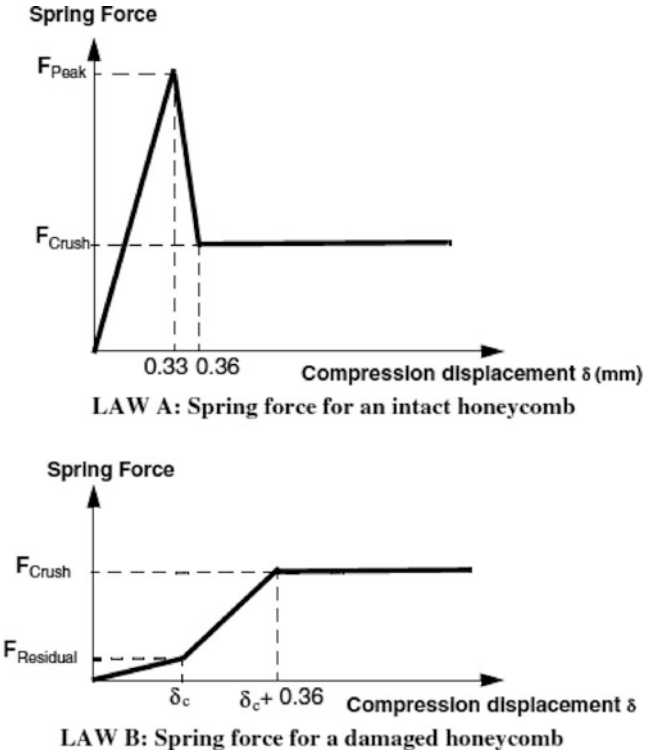


Fig. 60 Spring forces

analysis will demonstrate that the influence of this parameter is weak. The residual force $F_{Residual}$ is also a weak parameter and was set to 1 N, mainly for numerical stability reasons.

The skin was modeled by orthotropic Mindlin elements (see Fig. 58). The skins of the specimens tested by Tomblin et al. [54] were a laminate made of Newport NB321/3K70P plain wave carbon fabric. The stacking sequence was [90/45]n with n = 1,2,3. Thus the skin thickness was equal to 0.4, 0.8 or 1.2 mm. According to the material characteristics of the ply given in [54], the orthotropic equivalent moduli were calculated and implemented in the finite element model for the element located at a radius $R > R_F$: $E_1 = E_2 = 47{,}200$ MPa, $E_{12} = 17{,}800$ MPa, $G_{12} = 17{,}800$ MPa, $\nu_{12} = 0.328$. The same transverse characteristics as in [52] were implemented. For the damaged area, specific hypotheses were assumed concerning the stiffness matrix terms. For a given stacking sequence and for Mindlin's theory, this matrix can be written as:

$$\begin{bmatrix} A & B & 0 \\ B & D & 0 \\ 0 & 0 & K \end{bmatrix} \tag{11}$$

Table 5 Impact characteristics, damage dimensions (Reproduced from [52])

Test	Skin thickness (mm)	Impactor size (mm)	Energy (J)	$R_{Indented}$ (mm)	$R_{Crushed}$ (mm)	Indentation depth $\delta_{\chi\,(\mu\mu)}$	Crushed depth δ_c (mm)
1	0.4	25.4	6.7	10.2	15.2	2.3	5.9
2	0.04	76.2	7.2	15.9	25.4	0.4	6.2
3	0.8	25.4	6.7	3.2	15.9	0.8	3.8
4	0.8	25.4	20.3	12.7	21.7	3.2	7.8
5	0.8	76.2	7.2	9.5	28.6	0.4	4.5
6	0.8	76.2	28.2	34.4	48.7	4.2	6.6
7	1.2	25.4	6.7	9.5	19.1	0.6	4.1
8	1.2	76.2	11.1	12.7	28.6	0.6	4.8

[A] represents the membrane stiffness matrix. In the damaged area, this matrix should be affected by fiber breakages. Generally, these breakages are very localized at the center of the impact, thus the matrix [A] is not modified.

[D] represents the bending stiffness matrix. For thin skins, it is possible to assume the presence of a delamination located at the middle of the thickness and for $R < R_F$. This hypothesis leads to a decrease in bending stiffness equal to $1/(n+1)^2$ where n is the number of delaminations in the thickness. So, the bending stiffness matrix is divided by four here: [D]/4.

[B] represents the membrane-bending coupling stiffness matrix. When stacking sequences are symmetric with respect to the middle surface, its value is zero. This is not the case for the stacking of the specimen, thus the same hypothesis is used and the coupling stiffness matrix is also diminished: [B]/4.

[K] represents the transverse shear stiffness matrix. It should be affected by matrix cracking but the influence on the residual strength is weak and [K] is not modified.

During the loading, the skin remained linear elastic and no damage growth was modeled. A geometric nonlinear analysis was made using a line-search method. Different meshes were tested (quadrilateral cells or triangles) with different refinements showing a weak influence on the criterion. In the next paragraph, the model will be compared with eight tests performed by Tomblin et al. [54] for which all the data are available in [52].

4.2.2 Comparisons with Tests and Sensitivity Analysis Results

The data available in [52] are recalled in Table 5. Typical responses of the first uncrushed springs located on the major axis of the ellipse are given in Fig. 61 and are extracted from the computation of test case n° 4.

Springs representing the undamaged cells reach their peak forces one after another, showing the mechanism of extension of the dent. However, only the load corresponding to the first peak has a physical meaning since it is assumed that there is no damage growth in the skin or appearance of a crack before the dent progression.

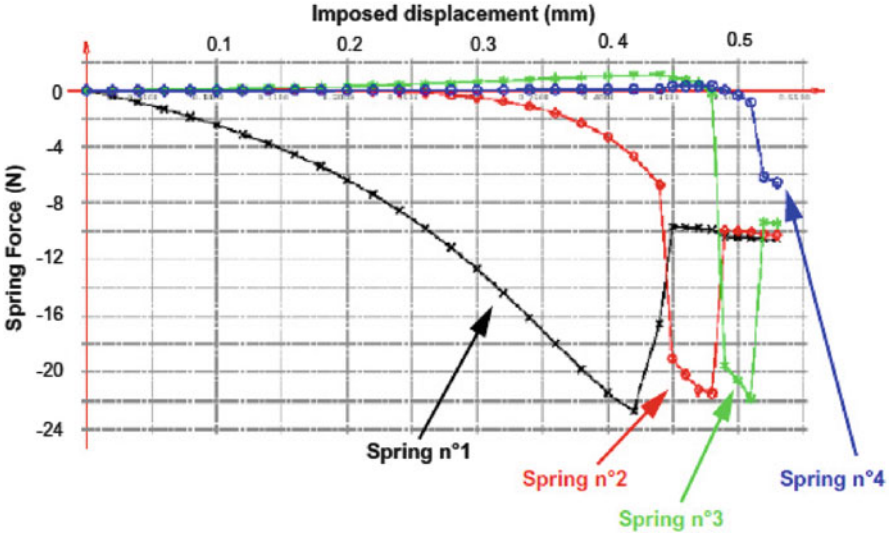


Fig. 61 Typical response given by the model (case no. 4)

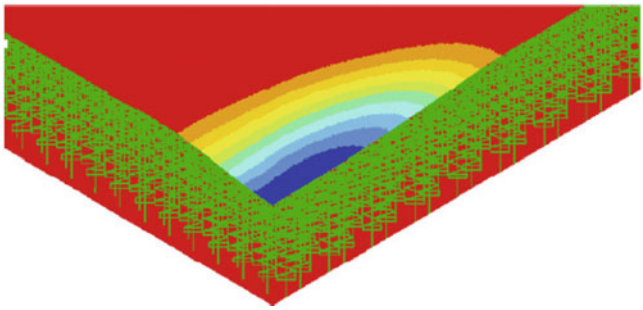


Fig. 62 Shape of the dent at the critical load

The load-displacement curve (not given) is globally linear and shows nothing in particular. When the first spring "crushes", the computed loading corresponding to the criterion is 291.5 N/mm. The second spring is crushed at 328 N/mm. The experimental failure of this sandwich was at 317.5 N/mm. Thus the criterion underpredicts the failure by about 8%.

The out-of plane displacement field for the load criterion can be seen in Fig. 62, showing an extension of the dent in an elliptical shape. It is interesting to see the maximum strain field for this load in Fig. 63. Although all the skin is in compression, at the apex of the dent, one face of the skin is under tension (see Fig. 62) due to local bending. The main strain reaches the very high level of 12,200 μstrains. Thus, this strain field implies that a crack could occur at this location, which is in agreement with the failure scenario identified by several authors [50, 51, 56]. The same order

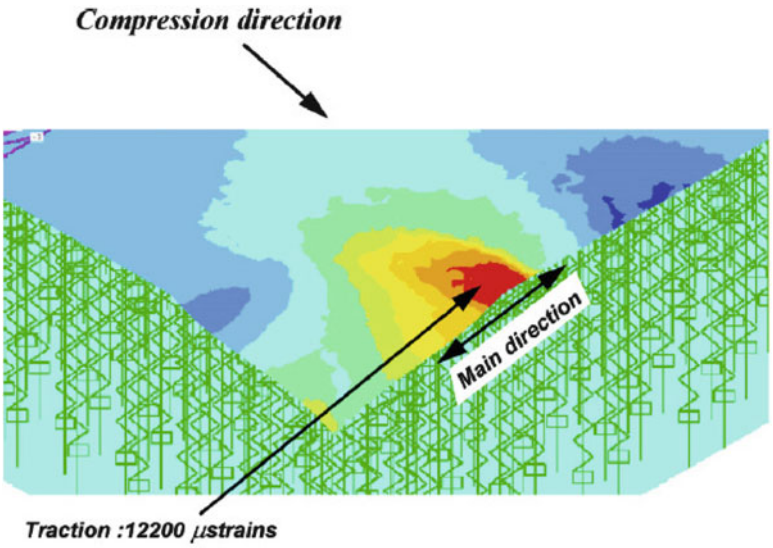


Fig. 63 Main strain field, lower skin, critical load 291.5 N/mm

of magnitude is frequently reached for thin skins of 0.4 and 0.8 mm but it becomes smaller for thicker skins of 1.2 mm (about 8,500 μstrains). A complementary analysis should be made on this point but the critical value of the crack opening for these materials remains to be found for this problem and cannot be provided by the authors.

In Table 6, the comparison is given for the eight cases proposed by Lacy and Hwang [52]. Globally, the comparison is good and the residual strength is under-predicted by 8–25%. In two cases (3 and 7), the criterion did not work and over-predicted the experiment by 16 and 25%. The approach seems not to work in the case of low energy impact with small indenters that cause too-small dents. The same behavior was pointed out in the case of metallic skins [38, 47]. Maybe, for small dents, the geometrical imperfections are of the same order of magnitude and should be taken into account. In case n° 5, the residual strength is under-predicted by 25%. The second spring collapses at a load of 315 N/mm (−11%) showing a very progressive extension of the dent. Moreover, for the criterion load, at the apex of the ellipse, the maximum tensile strain is only 8,870 μstrains, which suggests that no cracks appear at this load and could explain the value being under-predicted by 25%. In such cases, the analysis should be coupled with modeling of skin damage and failure estimation as proposed in [53] to improve the estimation. However, the present model has the advantage of giving results within 10 min on a personal computer thanks to the use of springs and the linear behavior in the skins. This approach is thus suitable for an industrial context where quick loops are required.

To validate the approach, a sensitivity study was also conducted [39] and showed the following points:

Table 6 Results given by the core crush criterion

Test	Impactor size (mm)	Energy (Joules)	CAI test (N/mm)	CAI criterion (N/mm)	Difference (%)
1	25.4	6.7	185.6	165	−12
2	76.2	7.2	165.5	150	−9.6
3	25.4	6.7	356	413	+16
4	25.4	20.3	317.5	291.6	−8.15
5	76.2	7.2	354.5	265	−25
6	76.2	28.2	236.9	196	−17.3
7	25.4	6.7	482.6	600	+25
8	76.2	11.1	429.6	398	−7.3

- The hypothesis on [A] is weak. If it is divided by 2, the differences on the computed residual strength are less than 10% and mostly situated between 0 and 5%.
- The hypotheses on [B] and [C] are also weak. Computations were made with no delamination, one delamination and three delaminations (Matrix [B] and [D] divided by 16). With no delamination, in comparison with one delamination, the residual strength given by the criterion is increased from 3 to 20% and with three delaminations the residual strength is decreased from 0.4 to 15%. The sensitivity is generally less than ±5% on thin skins (0.4 and 0.8 mm) and is higher for the 1.2 mm thick skin (cases 7 and 8). This hypothesis seems weak for skins less than 0.8 mm thick but will be more and more sensitive for thicker skins. However, for the cases analyzed, the proposed reduction in stiffness seems to be the better approximation.
- As it is not possible to measure the crushed depth, δ_c, in practice, a variation of ±50% was tested and the influence on the residual strength computed was less than 5% in most cases. Nevertheless, it is necessary to estimate the core depth to obtain accurate results [39]. In practice, this can be done by using the data already available in any aircraft company.
- A doubt also exists on the measurement by NDI of the core crushed radius R_C and the value finally used, especially for minor damage. A sensitivity study on this radius was carried out by varying the radius value by +/1 cell diameter (4.76 mm). Generally, the crushed core radius had an important influence on the strength given by the criterion and, thus, the given value has to be as close as possible to reality.

Overall, the strength given by the criterion is robust with respect to our hypotheses for the skin and the core. The main sensitivity was found for the crushed core radius and it has to be measured carefully. Moreover, by changing different parameters, the predicted strength evolves following the expected mechanical behavior and thus confirms the pertinence of the criterion.

5 Conclusions and Prospects

An original method for modeling the impact and post-impact behavior of sandwich structures has been proposed and validated. It is based on the demonstration that the Nomex honeycomb behaves in a post-buckling mode very early and that compression forces are taken up by the corners or vertical edges of honeycomb cells in the same way as by the stiffeners in aircraft structures. Thus it is possible to represent the honeycomb discretely by a grid of springs located at the six corners of the hexagonal cells. The only experimental characterization for this study is the uniform compression testing on a block of 100 cells to find the law of compression for each corner. This approach represents the phenomenon of indentation on honeycomb alone or on sandwiches very well. It has also been shown that local deformations of the skin under the indenter cause, via the meniscus of glue, local rotations of the core which significantly alter the compression response of the honeycomb. The limitations of this approach were sought in terms of independence of the behavior of edges. The hypothesis was verified for indenters that were not too sharp. However, the approach has not been validated for a comprehensive range of materials. It is not proved that this approach can be extended to cores with stiffer materials or thicker cell walls. Before applying this method to other cores, preliminary tests of indentation on the honeycomb core alone (as in Fig. 18) should be carried out.

Moreover, an important limitation of the approach is that the modeling of vertical springs makes it impossible to represent the transverse shear in the core. So it is, a priori, impossible to model the bending of a sandwich. To overcome this problem, a multi-level approach was proposed and validated by impact tests using a drop weight test on a sandwich plate supported by two pin supports. This approach should also allow the multi-impact phenomena of complex structures to be modeled easily. However, the study was limited to metallic skins because the behavior of laminated skins under impact is very complex. Two lines of research are therefore needed for this issue:

- The use of the discrete model proposed by Bouvet et al in this book to model the impacted skins.
- The modeling of the complex nonlinear behavior of the honeycomb cells. The model should be able to take account of the buckling and post-buckling of cells under compression and shear and eventually the coupling between these two modes.

The study also examined the post-impact behavior of these structures and the discrete approach demonstrated the mechanical phenomena at work in compression after impact. It was shown that the behavior was related to three nonlinearities:

- A geometrical nonlinearity due to the skin's neutral axis being offset in the dent area.
- A nonlinear response of the core due to the crushed state and the classical "with peak" response of the undamaged area.

- The response of the skin due to its type of damage after impact: plasticity for metallic skins and delamination or crack growth for laminated skins.

An original failure criterion was also proposed, based on the beginning of the extension of the damage dent that causes the destruction of some cells in the core. The study was carried out for metal and composite skins and the relevance of the criterion in compression after impact was demonstrated. However, it seems it would be appropriate to combine this criterion with a skin failure criterion (maximum strain for example). In some cases where the sandwiches are very damaged, extension of the defect takes place in a very progressive way. In these cases, the core crush criterion led to an underestimation of the residual strength of the structure. It is also important to note that the entire study is based on the compression after impact tests standardized by aircraft manufacturers. B. Castanié and al. [51] have conducted tests of compression /shear after impact on a specific test rig closer to real structures. In this configuration, under compression, the same initial evolution of the residual dent was observed but, in contrast to classical CAI test results, a slow progression of the crack initiated at the apex of the ellipse was observed. The shear behavior seems to be closer to that of drilled composite. In case of combined loading, the response is a mix of the two. It is important to note that these configurations give residual strengths higher than the conventional CAI tests.

Thus, the field of research is still open as far as combined loading after impact is concerned. This approach should also be combined with studies on impact with pre-loading. It is also important to use more realistic sizing of sandwich structures under impact load in order to obtain a better idea of the real margins.

References

1. Guedra-Degeorges D, Thevenet P, Maison S (1997) Damage tolerance of sandwich structures. Proceedings of the Euromech 360 colloquium. Kluwer Academic Publisher, Saint Etienne
2. Bernard ML (1987) Impact resistance and damage tolerance of composite sandwich plates. TELAC report 87-11. S.M thesis, MIT
3. Bernard ML, Lagace PA (1989) Impact resistance of composite sandwich plates. J Reinf Plast Compos 8(9):432–445
4. Llorente S, Weems D, Fay R (1990) Evaluation of advanced sandwich structure designed for improved durability and damage tolerance. In: American helicopter Society 46th annual forum proceedings, Washington, DC, pp 825–831
5. Caldwell MS, Borris PW, Falabella R (1990) Impact damage testing of bonded sandwich panels. In: 22nd international SAMPE technical conference, Boston, MA, USA, 6–8 Nov 1990
6. Sun CT, Wu CL (1991) Low velocity impact of composite sandwich panels. In: Proceedings of 32nd AIAA/ASME/ASCE/AHS/ASC structural, structural dynamic, materials conference, Baltimore, pp 1123–1129
7. Williamson JE (1991) Response mechanism in the impact of graphite/epoxy honeycomb sandwich panels. TELAC report 91-12, Technology for advanced composites, MIT
8. Williamson JE, Lagace PA (1994) Response mechanism in the impact of graphite/epoxy honeycomb sandwich panels. In: Proceedings of the 8th technical conference of the American Society for Composite, Cleveland, pp 287–297

9. Abrate S (1998) Impact on composite structures. Cambridge University Press, New York
10. Goldsmith W, Sackman J-L (1992) Experimental study of energy absorption in impact on sandwich plates. Int J Impact Eng 12(2):241–262
11. Jamjian M, Goldsmith W, Sackman JL (1994) Response of an infinite plate on a honeycomb foundation to a rigid cylindrical impactor. Int J Impact Eng 15(3):183–200
12. Wierzbicki T (1983) Crushing analysis of metal honeycomb. Int J Impact Eng 1:157–174
13. Ferri R, Sankar BV (1997) Static indentation and low velocity impact tests on sandwich plates. In: Proceedings of the 1997 ASME international mechanical engineering Congress and exposition, Dallas, vol 55, pp 485–490
14. Herup EJ, Palazotto AN (1997) Low-velocity impact damage initiation in graphite/epoxy/nomex honeycomb-sandwich plates. Compos Sci Technol 57:1581–1598
15. Swanson RS, Jongman K (2003) Design of sandwich structures under contact loading. Compos Struct 59:403–413
16. Soden P (1996) Indentation of composite sandwich beams. J Strain Anal 31(5):353–360
17. Olsson R, McManus HL (1996) Improved theory for contact indentation of sandwich panels. AIAA J 34(6):1238–1244
18. Besant T, Davies GAO, Hitchings D (2001) Finite element modelling of low velocity impact of composite sandwich panels. Compos Part A 32:1189–1196
19. Horrigan DPW, Aitken RR, Moltschaniwskyj G (2000) Modelling of crushing due to impact on honeycomb sandwich. J Sandw Struct 2:131–151
20. Palazotto AN, Herup EJ (2000) Finite elements analysis of low velocity impact on composite sandwich plates. Compos Struct 49:209–227
21. Heimbs S (2009) Virtual testing of sandwich core structures using dynamic finite element simulations. Comput Mater Sci 45:205–216
22. Giglio M, Manes A, Gilioli A Investigations on sandwich core properties through an experimental–numerical approach. Compos Part B. doi:10.1016/j.compositesb.2011.08.016
23. Singace AA (1999) Axial crushing analysis of tubes deforming in the multilobe mode. Int J Mech Sci 41:865–890
24. Wierzbicki T, Bhat T, Abramowicz W, Brodikin D (1992) A two fold elements model of progressive crushing of tubes. Int J Solid Struct 29(24):3269–3288
25. Wu E, Jiang W-S (1999) Axial crush of metallic honeycomb. Int J Impact Eng 19(5–6):439–456
26. Gupta NK (1999) Some aspects of axial collapse of cylindrical thin-walled tubes. Int J Mech Sci 41:865–890
27. Gupta NK, Husain A (2000) Mathematical modeling of axial crushing of cylindrical tubes. Thin-walled Struct 38:355–375
28. Aminanda Y, Castanié B, Barrau JJ, Thevenet P (2005) Experimental analysis and modeling of the crushing of honeycomb cores. Appl Compos Mater 12(3-4):213–227
29. Michael C, Yung N (1997) Airframe structural design. Conmilit Press, Hong Kong
30. Barrau JJ, Crézé S, Castanié B (2005) Buckling and post-buckling of beams with flat webs. Thin-Walled Struct 43(6):877–1002
31. Wierzbicki T, Alvarez ADL, Hoo Fatt MS (1995) Impact energy absorption of sandwich plates with crushable core. In: Proceedings of the joint ASME applied mechanical materials summer meeting, Los Angeles, vol 205, pp 391–411
32. Petras A, Sutcliffe MPF (2000) Indentation failure analysis for sandwich beams. Compos Struct 50:311–318
33. http://www.samtech.com/
34. Aminanda Y, Castanié B, Barrau JJ, Thevenet P (2005) Modélisation de l'indentation des structures sandwichs à peaux métalliques. Mécanique et Industrie 6:487–98
35. Yulfian Aminanda (2004) Contribution à l'analyse et à la modélisation de structures sandwichs impactées. PhD thesis, Ecole Nationale Supérieure de l'Aéronautique et de l'Espace
36. Castanié B, Bouvet C, Aminanda Y, Barrau JJ, Thevenet P (2008) Modelling of low energy/low velocity impact on nomex honeycomb sandwich structures with metallic skins. Int J Impact Eng 35:620–634

37. Choi IK, Lim CH (2004) Low-velocity impact analysis of composite laminates using linearized contact law. Compos Struct 66:125–32
38. Aminanda Y, Castanié B, Barrau JJ, Thevenet P (2009) Experimental and numerical analysis of the compression-after-impact of metal-skinned sandwich structures. Compos Sci Technol 69:50–59
39. Castanié B, Aminanda Y, Bouvet C, Barrau JJ (2008) Core crush criteria to determine the strength of sandwich composite structures subjected to compression after impact. Compos Struct 86:243–250
40. Fualdes C (2006) Composite@airbus. Damage tolerance philosophy. In: FAA workshop for composite damage tolerance and maintenance, Chicago, 19–21 July 2006
41. Lawrance Cook (2012) Visual inspection reliability for composite aircraft structures. PhD thesis Cranfield University, UK
42. Shipsha A, Hallstrom S, Zenkert D (2003) Failure mechanisms and modelling of impact damage in sandwich beams – A 2D approach: part II – analysis and modelling. J Sandw Struct Mater 5:33–51
43. Shipsha A, Zenkert D (2005) Compression-after-impact strength of sandwich panels with core crushing damage. Appl Compos Mater 12(3-4):149–164
44. Minguet PJ (1997) A model for predicting behavior of impact-damaged minimum gage sandwich panels under compression. In: Proceedings of the AIAA/ASME/ASCE/AHS/ASC 32nd structure, structural dynamics and material conference, St. Louis, pp 423–439
45. Thomson RS, Mouritz AP (1999) Skin wrinkling of impact damaged sandwich composite. J Sandw Struct Mater 1:299
46. Xie Z, Vizzini AJ (2005) Damage propagation in a composite sandwich panel subjected to increasing uniaxial compression after low-velocity impact. J Sandw Struct Mater 7:269
47. Xie Z, Vizzini AJ (2004) A feasible methodology for engineering applications in damage tolerance of composite sandwich structures. J Compos Mater 3(8):891
48. Minakuchi S, Okabe Y, Takeda N (2008) "Segment-wise model" for theoretical simulation of barely visible indentation damage in composite sandwich beams: Part I – Formulation. Compos Part A 39(1):133–144
49. Minakuchi S, Okabe Y, Takeda N (2007) "Segment-wise model" for theoretical simulation of barely visible indentation damage in composite sandwich beams: part II – experimental verification and discussion. Compos Part A 38(12):2443–2450
50. Tomblin J, Lacy T, Smith B, Hooper S, Vizzini A, Lee S (1999) Review of damage tolerance for composite sandwich airframe structures. DOT/FAA/AR-99/49
51. Castanié B, Barrau JJ, Jaouen JP, Rivallant S (2004) Combined shear/compression structural testing of asymmetric sandwich structures. Exp Mech 44(5):461–472
52. Lacy TE, Hwang Y (2003) Numerical modeling of impact-damaged sandwich composites subjected to compression-after-impact loading. Compos Struct 61:115–128
53. Thomas EL, Youngkeun Hwang (2007) Numerical estimates of the compressive strength of impact-damaged sandwich. J Compos Mater 41:367
54. Tomblin J, Raju KS, Acosta JF, Liew J, Smith JL (2002) Impact damage characterization and damage tolerance of composite sandwich airframe structures. DOT/FAA/AR-00/44
55. Baranger E, Cluzel C, Guidault P-A (2010) Modelling of the behaviour of aramid folded cores up to global crushing. Strain. doi:10.1111/j.1475-1305.2010.00753.x
56. Tsang PW, Lagace PA (1994) Failure mechanism of impact-damaged sandwich panels under uniaxial compression. In: Proceedings of the 35th AIAA/ASME/ASCE/AHS/ASC structural, structural dynamics, materials conference, Hilton Head, vol 2, pp 745–754

Foldcore Sandwich Structures and Their Impact Behaviour: An Overview

Sebastian Heimbs

Abstract This chapter gives a global overview on the family of foldcore sandwich structures with a special focus on their impact performance. Foldcore structures are produced by folding a flat sheet of material to three-dimensional zigzag structures in an origami-like manner. Relevant cell wall materials range from cardboard to plastics, from metals to composites. Different manufacturing processes and feasible cellular configurations are presented based on an extensive literature overview. The mechanical properties under compression and shear loads are assessed based on static and dynamic tests. The impact performance under low and high velocity impact with different projectiles ranging from hard body steel impactors to rubber fragments with subsequent damage assessment is addressed. In addition, a comprehensive overview on numerical modelling methods for foldcore sandwich analyses is given. Specific topics like cell wall material and imperfection modelling are discussed. Numerical foldcore geometry optimisation studies and impact simulations are presented and the robustness of such models and their relevance for industrial use is evaluated. Finally, an overview of current and potential applications of foldcore sandwich structures is given.

1 Introduction

Weight reduction is one of the main design drivers of modern engineering and transport structures for aerospace and automotive applications. In this context, the sandwich design principle is playing a major role, as it allows for much higher weight-specific bending stiffness compared to a monolithic structure. A sandwich structure typically consists of two thin and stiff skins, separated by a lightweight

S. Heimbs (✉)
EADS Innovation Works, 81663 Munich, Germany
e-mail: Sebastian.Heimbs@eads.net

S. Abrate et al. (eds.), *Dynamic Failure of Composite and Sandwich Structures*,
Solid Mechanics and Its Applications 192, DOI 10.1007/978-94-007-5329-7_11,
© Springer Science+Business Media Dordrecht 2013

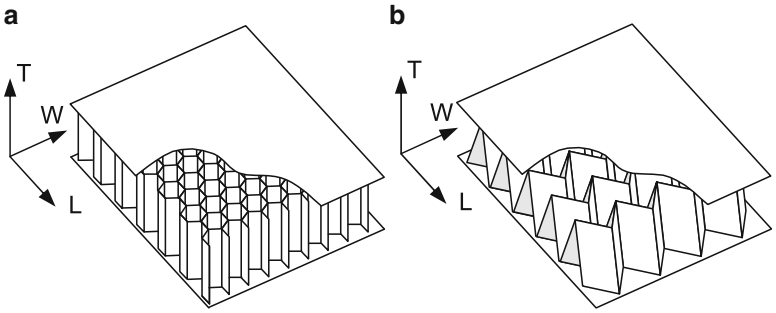


Fig. 1 Illustration of honeycomb and foldcore sandwich structures

cellular core. The main purpose of the core is to increase the bending stiffness by separating the skins, to carry transverse shear loads and to withstand compressive loads normal to the sandwich surface. In case of transversal impact loads, the core has to support the skins from local bending and it has to prevent major damage or penetration by a high energy absorption capability.

In aircraft design, sandwich structures can be found in numerous applications like control surfaces, fairings or in overhead stowage compartments or monuments inside the cabin (e.g. toilets or galleys), but also in primary load-carrying structures like passenger floor panels [1]. Sandwich fuselage structures have only been built for business jets but not yet for large airliners.

One traditional and established cellular core can be found in virtually all aircraft sandwich structures: hexagonal honeycomb core. This core, typically made from Nomex aramid paper or sometimes aluminium, offers higher weight-specific properties than all competing foam cores. However, one major drawback leads to a constant search for better, advanced core structures: water ingression. Condensing water can accumulate in the closed honeycomb cells during flight cycles, reducing the mechanical properties and increasing structural weight. If water begins to accumulate within the core, it will most likely never escape anymore except when the part is repaired or replaced. Although design guidelines to reduce the potential of water ingression exist, it is desirable to use a core structure where water accumulation simply does not occur.

During the search for an advanced cellular sandwich core that also has the potential to be used in primary sandwich fuselage structures of a large transport aircraft, one candidate has drawn most attention of international researchers within the last decade: folded cores (Fig. 1). Several names for this core exist, like foldcore, chevron core, folded core, origami core or Miura core, going back to one of the first researchers investigating this core type [2]. In this chapter, the term foldcore is used.

The basic principle of foldcores is that a flat sheet of material is folded to a three-dimensional structure in an origami-like manner without stretching the material (Fig. 2). The cell geometry can be selected and optimised according to the specific load case or application. Varying core heights or folding patterns can be generated, so that the core does not have to be machined like in case of honeycomb cores.

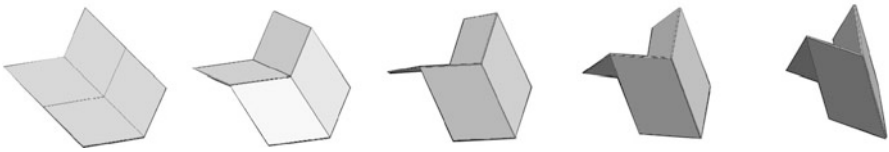


Fig. 2 Illustration of folding scheme to convert flat sheet into three-dimensional foldcore

Curved structures with single or double curvature can be folded without generating internal stresses. Furthermore, advanced continuous manufacturing processes can reduce the cost of such core structures compared to expensive honeycomb cores that are manufactured discontinuously. The major advantage of foldcores, making them especially interesting for the aircraft industry, is the ventability of the core, i.e. the cells are not closed and water is not trapped and can escape e.g. through drainage holes.

Although the first known patent for foldcores dates back to 1960 [3] and first publications by Miura on the manufacturing and properties of foldcore sandwich structures appeared in the early 1970s [2, 4], major interest in foldcore sandwich structures for engineering applications and extensive investigations on manufacturing techniques, possible geometries, mechanical behaviour and modelling methods began in the mid 1990s lasting until today. Although this core generation can still be seen as exotic, more than 120 research papers on foldcore structures are cited in this study, highlighting the high amount of research that has been conducted on foldcore sandwich structures so far.

The aim of the following chapter is two-fold. Firstly, it is intended to be a general review on foldcore structures, addressing all relevant topics of this core family from manufacturing to applications, from experimental to numerical investigations, presenting and citing all relevant research studies in an extensive literature overview. This literature overview is only focused on scientific publications, all patents related to foldcore sandwich structures that could eventually double the number of references, are not addressed here. Papers summarising numerous foldcore patents can be found in [5–8]. Secondly, the focus is on the impact performance of foldcore sandwich structures. The author has been working with sandwich structures under impact loads for many years and some of his research is presented in further details.

2 Foldcore Designs and Materials

The diversity of possible foldcore cell designs is almost unlimited, since the technique of origami folding allows even for very complex geometries [9]. However, most foldcore structures used in research works are made of relatively simple geometries with zigzag or chevron geometries or modifications of these (Fig. 3).

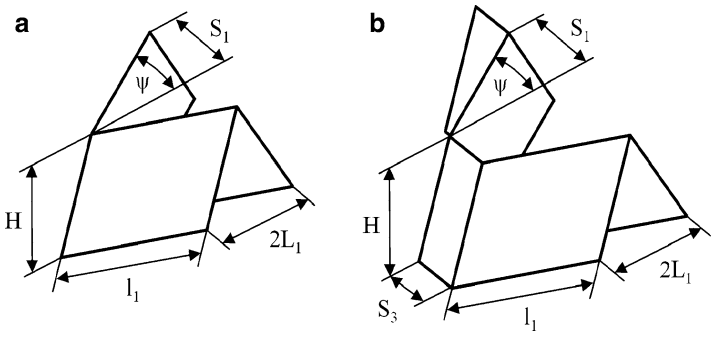


Fig. 3 Two foldcore unit cell geometries used in most research studies

Comprehensive overviews of possible foldcore geometries are given in [10–16]. The main geometrical possibilities are related to

- the unit cell geometry (Fig. 3),
- the folding of non-uniform or non-symmetric cores [12, 13] or curved folding lines [17],
- the folding of flat or curved or even doubly curved panels,
- the folding of wedge geometries with a decreasing height,
- the folding of spiral geometries [18].

Wedge-shaped cores are relevant for aerodynamic surfaces i.e. trailing edges of control surfaces like spoilers, flaps or rudders. The wedge shape of honeycomb cores is typically achieved by milling of a block of honeycomb core. This is not possible for foldcores, as the top folding lines would be removed and the core would loose structural integrity. Therefore, the core is directly folded to the wedge geometry. First simple solutions for wedge-shaped cores were developed in [10]. In an enhanced study in [19], it is demonstrated that it is important to partly fold the top folding edges back into the core in order to avoid a stepwise core height reduction and allow for a continuous attachment to the skins. The folding pattern for this advanced wedge-shaped core is given in [20], also describing the manufacturing process.

Possible cell wall materials for the foldcore are also manifold. In general, all materials can be used that can be folded, i.e. the material should not be too brittle like ceramics and it should not be too elastic like rubber. The following materials have been successfully used for foldcore sandwich structures so far (Fig. 4):

- Metals like aluminium, steel, titanium, copper, brass [2, 4, 10, 11, 21–23],
- plastics like PEEK, PC [11, 23–25],
- fibre-reinforced composites with unidirectional (UD) plies or woven fabric plies made of carbon fibre, glass fibre, aramid fibre or basalt fibre [10, 11, 26, 27],
- aramid paper (Nomex or Kevlar) with random fibres and phenolic resin [10, 25, 27],
- cardboard or Kraft paper [11, 22, 28, 29].

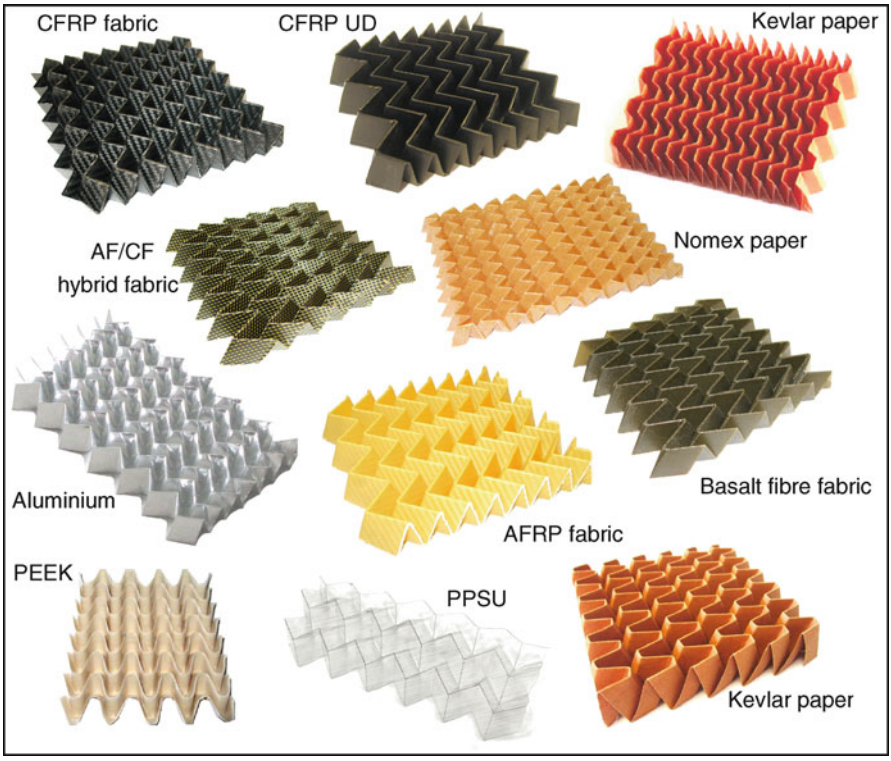


Fig. 4 Overview of different foldcore geometries and materials

Early studies indicated that the relatively large cell walls of the foldcore geometry lead to early stability failure under compression or shear loads. Therefore, different approaches were investigated to increase the stiffness of the cell walls. In [30] layered folded structures consisting of several core blocks were investigated. The authors in [13] propose geometrical modifications like grooved cell walls for increased stability and core strength or additional vertical cell walls for increased compressive strength by compacting defined rows of unit cells. In [31] the use of nanoparticles in the coating resin is investigated to increase the cell wall stability and strength. Further new materials and resin modifications for foldcore manufacturing with improved properties were investigated in [32].

Another design option is the dual-core or multi-core configuration. In [26, 33] a dual-core sandwich concept consisting of one layer of carbon fibre-reinforced composite (CFRP) and one layer of aramid fibre-reinforced composite (ARFP) separated by a third skin layer was investigated for a two-fold energy absorption process. The dual-core concept was used in [34] for a sound-absorbing application. Also in [32] a multi-core solution consisting of three foldcore layers was investigated for sound absorption purposes, where the vibrations of the outer skins are supposed to be uncoupled by the damping middle core layer.

3 Manufacturing

3.1 Overview of Manufacturing Processes in General

Numerous different approaches to manufacture foldcore structures exist. The basic principle of the folding technology is to fold or locally bend the material and not to elongate it. This makes it possible to use very thin sheet materials and imposes no restrictions with respect to the height of the folded structure. Since an efficient and robust manufacturing process is the key for new cellular core concepts to be interesting for industrial markets and widespread applications, a lot of research was conducted on foldcore manufacturing processes and many manufacturing patents have been published. One of the goals is to make the manufacturing process as efficient as possible in order to be able to compete with established core structures like honeycomb cores or even to be favourable in terms of lower manufacturing costs.

A good overview of foldcore manufacturing processes is given in [8], dividing the different approaches into 'synchronous', 'gradual' and 'pre-gathering' techniques. Also reference [7] gives a good overview, distinguishing between 'synchronous' and 'cyclic' manufacturing processes. In this current work, a short overview of different processes shall be given. For an easy understanding, 'discontinuous' and 'continuous' processes are distinguished.

3.1.1 Discontinuous Manufacturing Processes

The principle of discontinuous manufacturing is to produce a limited size of foldcore in a dedicated interrupted process. This technique was used in the beginning of foldcore research and is ideal for prototype foldcore structures or if the base material is not available on a coil for continuous supply. However, it cannot compete with continuous processes in terms of efficiency for industrial applications.

One established discontinuous foldcore manufacturing process is based on flexible, transformable dies (Fig. 5). This process is well described in further detail in [10, 22, 35]. Those dies consist of flexibly joined metal plates, representing the cell wall geometry, e.g. a simple zigzag pattern. Here, all foldcore cell walls have the geometrical shape of a parallelogram. Therefore, the metal plates of the transformable die are also parallelogram-shaped. The connection can either be achieved by cylindrical hinges or elastomeric membranes. These transformable dies can be stretched to complete flatness or folded to any degree of density. In the beginning of the folding process the sheet material is placed between the upper and lower dies. Those dies are not flat but compressed to a certain initial relief structure. In the next step they are compressed even more so that the prepreg in-between also deforms. In contrast to deep drawing, the material is simply folded without being elongated. The final foldcore geometry depends on the initial and final state of the transformable dies. The force, necessary for a uniform folding, can

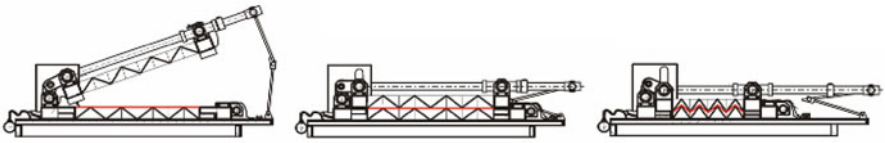


Fig. 5 Illustration of discontinuous foldcore manufacturing process [35]

either be applied by an external actuator or by using a vacuum bag and the physical pressure difference. If vacuum is used, then both the upper and lower dies are placed inside the vacuum bag. As this bag is evacuated, the forming takes places. This can be stopped mechanically at a required geometrical state by adjustable limiters. After opening the dies the folded core in its final shape can be taken out. In case of composite cell wall material like in this study, the folded core has to be cured in an autoclave afterwards, where it is placed on a rigid one-part or two-part mould. Another alternative is the use of slightly cross-linked polymers, which have to be heated prior to folding to be formable. After folding the polymer cools down inside the tool and can be taken out afterwards in a stable constitution. Composite foldcore structures manufactured with this process are treated in [26]. An adoption of this process for curved foldcore structures is given in [36].

A different method for discontinuous manufacturing is presented in [8], which is based on cold gas-pressure folding of metallic foldcores. Here, the folding pattern is transferred onto the metal sheet by perforation lines as a first step. Then, two of such metal sheets are placed in a sandwich manner around spacer plates consisting of the zigzag pattern of the foldcore. This combination is packed in an air-tight bag and is evacuated to near vacuum, leading to the folding of the plates. The folding process stops as soon as the top and bottom plate come into contact, controlled by the height of the spacers.

3.1.2 Continuous Manufacturing Processes

The continuous manufacturing of foldcore allows for higher efficiency. Ideally, the sheet of cell wall material is provided on a coil and can be fed into a machine, where the folding is performed continuously.

One way to produce foldcore structures continuously is to emboss the folding pattern into the sheet material with a robot, CNC-machine or roller (Fig. 6). Once the folding pattern is embossed, the structure can easily be folded to a three-dimensional geometry by adequate lateral forces. As another alternative for a continuous process, the sheet material can be bent along one axis in a first step to a certain wave-pattern. The bending along the second axis and final folding is then conducted in a second step using adequate dies. Many further details on continuous manufacturing processes for foldcore structures can be found in [10, 13, 17, 28, 32, 37–40].

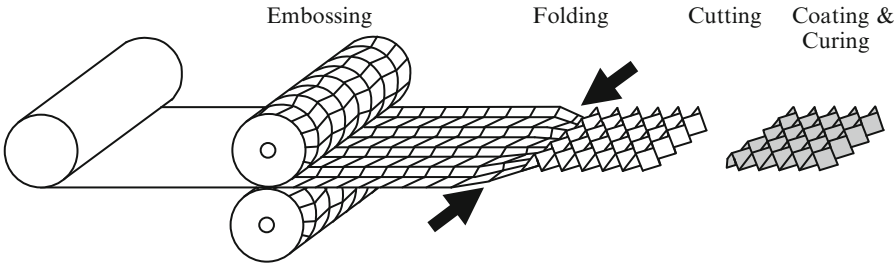


Fig. 6 Illustration of continuous foldcore manufacturing process

3.1.3 Fasteners

The topic of fastener installation in foldcore sandwich structures was investigated in [32, 41]. Potted inserts are typically used as load introduction points in sandwich structures, with a hole being drilled through the outer skin and core and an insert being fixed with epoxy adhesive. The core region at the position of the insert is typically filled with potting mass during sandwich manufacturing, i.e. the cells are filled with an epoxy-based compound to allow for an effective load distribution from the insert into both sandwich skins. As foldcore structures do not consist of closed cells as in case of honeycomb cores, the filling of the core with potting mass is difficult, as the mass would flow away during the curing process of the sandwich composite. Different concepts to prevent the potting mass from flowing, e.g. based on flexible mesh-like barriers, were developed in [32, 41]. The mechanical performance of inserts in the foldcore sandwich specimens was evaluated by pull-out and shear-out testing. Also repair methods for foldcore sandwich structures, which are related to the insert installation procedures, were investigated in [32].

3.2 Specimen Manufacturing in Present Study

The specimens that are described in further detail in this study and that were used for mechanical tests are based on composite foldcores made of unidirectional and woven carbon fibre (CF) and aramid fibre (AF) prepreg (Fig. 7). The woven fabrics consist of a 2/2 twill weave with an areal weight of 200 g/m^2 and were pre-impregnated with a bisphenol epoxy resin.

The foldcores were produced at the Kazan State Technical University with the discontinuous manufacturing process based on transformable dies as described before. After folding of the prepreg sheets in the transformable dies, the foldcore was cured in an autoclave at 120°C.

It has to be noted that for each foldcore three plies of unidirectional prepreg with the stacking sequence [0°, 90°, 0°] or two plies of woven fabric prepreg

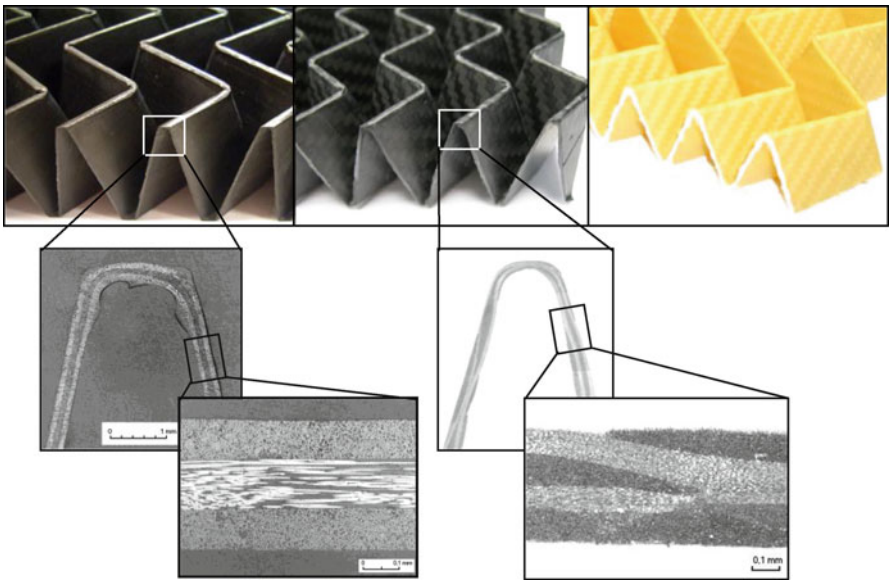


Fig. 7 Composite foldcore structures used in this study with micrographs of cell wall material: Carbon UD, carbon fabric and aramid fabric (from *left* to *right*)

have been used, leading to a final cell wall thickness of 0.35–0.5 mm. The fibre volume fraction was determined to be around $50 \pm 5\%$. Micrographs of the folded composite material are shown in Fig. 7. A curvature with a radius of about 0.5–0.6 mm could be measured. No fibre breakage was visible in these folding edges.

The folding pattern is a simple zigzag geometry, based on the unit cell geometry in Fig. 3a. Five configurations with different materials and geometries were investigated in this study, which are referred to in this chapter as type A, B, C, D and E (Fig. 8). The global densities vary from 102 to 119 kg/m^3. All geometrical details are given in the overview table in Fig. 8. The carbon foldcores type A and B and the aramid foldcore type C are based on the same geometry and have a height of 28 mm. The carbon foldcore type D has the same height and global density of type B, but the cell geometry with smaller cell walls and an orientation more parallel to the transverse direction aims at higher flatwise compressive properties. Type E is a dual-core configuration with a combination of a carbon foldcore and an aramid foldcore, each having the same zigzag pattern as type A but only half the height (14 mm). They are separated by a 1 mm thick Kevlar composite middle layer made from four plies of the same woven fabric prepreg as the aramid foldcore, stacked with the orientations $[0°/45°]_S$ with respect to each other. The global density and thickness is identical to the other types. The idea behind this dual-core configuration is based on the study of Weeks and Sun [42], who investigated the impact behaviour of multi-core sandwich structures and found these configurations to be superior to

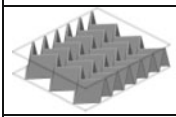
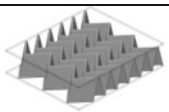
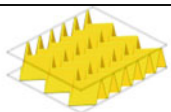
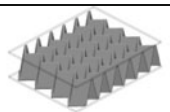
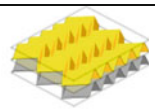
Type A: carbon UD	*Type B*: carbon fabric	*Type C*: aramid fabric	*Type D*: carbon fabric	*Type E*: dual-core aramid + carbon
				
Core geometry:				
l_1=29 mm, L_1=10 mm, S_1=20 mm			l_1=18 mm, L_1=7.5 mm, S_1=15.5 mm	l_1=29 mm, L_1=10 mm, S_1=20 mm
Core height *H*:				
28 mm				14 mm (AF) / 14 mm (CF)
Cell wall thickness *t*:				
0.35 mm	0.48 mm	0.40 mm	0.50 mm	0.40 mm (AF) / 0.52 mm (CF)
Core density ρ:				
102 kg/m³	113 kg/m³	103 kg/m³	114 kg/m³	109 kg/m³ (AF)/ 119 kg/m³ (CF)

Fig. 8 Different foldcore configurations investigated in this study with geometrical details

single-core structures in terms of impact resistance, extent of impact damage and residual strength after impact. The aim is to generate a two-phase impact behaviour with the ductile aramid core absorbing low impact energies, the stiff carbon core absorbing high impact energies and the Kevlar layer acting as an additional impact protection layer.

The sandwich skins in this study were made from unidirectional carbon/epoxy prepregs of type Cytec 977-2/HTS in a quasi-isotropic lay-up. The skin thickness was chosen to be 2 mm for types A–D (stacking sequence $[45°/90°/-45°/0°]_{2S}$) and 1.5 mm for the dual-core type E (stacking sequence $[60°/-60°/0°]_{2S}$), to be in a realistic range of aircraft exterior surfaces. The thickness is lower for type E in order to obtain a comparable total thickness and weight of the sandwich plates under consideration of the 1 mm thick middle layer mentioned before, although the comparability of the low velocity impact behaviour of the single- and dual-core specimens is made difficult, as the thinner outer skins surely lead to an earlier failure. The carbon/epoxy skins were cured in an autoclave for 2 h at 180°C and 7 bar. The final fibre volume fraction had a value of 65%.

The skins were bonded onto the core in a hot press using the epoxy-based structural adhesive Scotchweld 9323 B/A and a curing cycle of 80°C and 4 bar over 4 h.

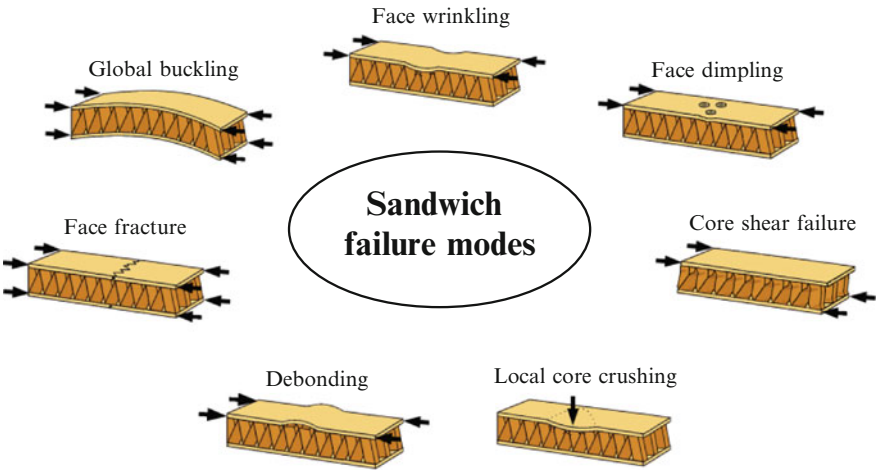


Fig. 9 Illustration of foldcore sandwich failure modes

4 Mechanical Properties

The classical way to determine the mechanical properties of sandwich core structures is mechanical testing. Information on the mechanical properties of several different foldcores can be found in the literature, which is presented as follows. Traditional tests of sandwich core specimens include flatwise compressive testing in order to identify the out-of-plane compressive properties and transverse shear testing in L- and W-direction. Further tests like bending tests, edgewise compression tests or debonding tests can also be found and are discussed later. The in-plane tensile behaviour of foldcore structures is characterised by a negative Poisson's ratio, which is referred to as an auxetic behaviour, i.e. the structure expands laterally under axial tensile loads [11, 43, 44].

The driver for cellular failure modes is primarily loss of stability due to the thin cell walls. Different failure modes can occur during mechanical testing or structural loading of a foldcore sandwich structure, which are illustrated in Fig. 9 [45].

4.1 Compression Testing

4.1.1 Quasi-Static Compression Testing

Quasi-static flatwise compression tests of foldcore structures are documented in several papers. Compression tests of aluminium foldcore are described in [21], of aramid paper foldcore in [1, 27, 46–49] and of carbon fibre foldcore in [1, 26, 27, 33, 46, 48, 50]. Different geometries of PEEK, PC and aramid paper foldcores were

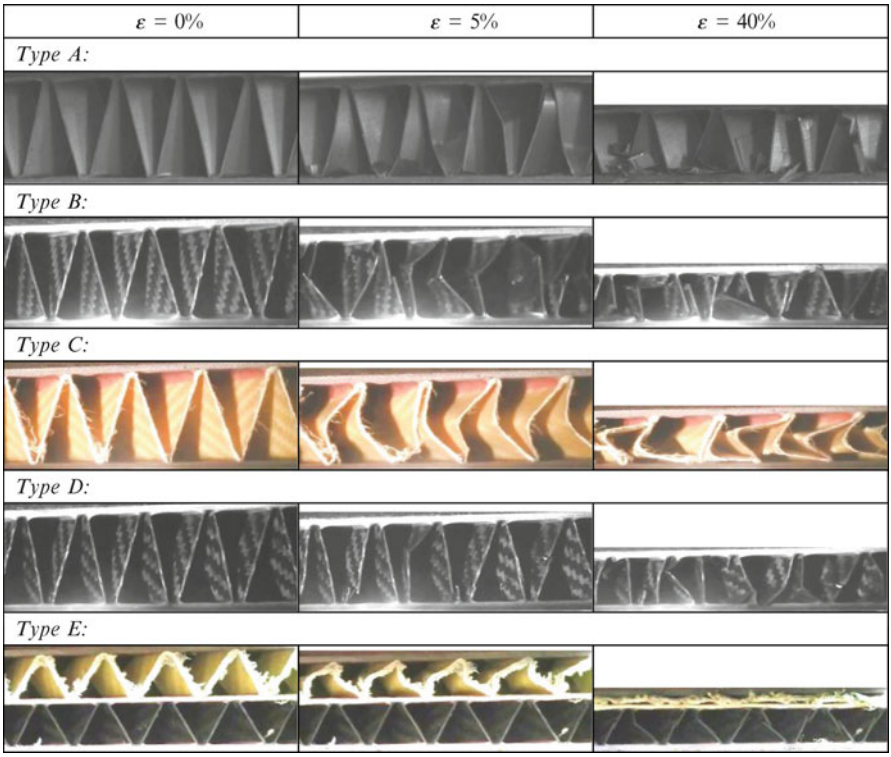


Fig. 10 Cell wall deformation behaviour of foldcore types under quasi-static compression

tested in [24, 25, 51] to identify the influence of geometrical parameters on the compressive response. Compression tests of wedge-shaped aramid paper foldcore samples are reported in [19].

In order to characterise and compare the compressive properties of the different foldcore types covered in this study, flatwise compression tests based on the standard DIN 53291 were conducted on sandwich specimens with a size of 150 mm × 150 mm. A laser extensometer was used for the displacement measurement between the upper and lower skin.

The compression tests gave valuable information on the cell wall deformation and failure mechanisms, shown in Fig. 10. The corresponding effective stress-strain curves are depicted in Fig. 11, each showing the typical characteristics of cellular structures with a stress peak, a plateau phase and a steep stress increase at densification.

The cell walls of the ductile aramid foldcore of type C buckle under compression and collapse under an average peak stress of about 3.2 MPa. Afterwards, the structure is folded up to the densification regime in a comparable way to aramid paper foldcores and Nomex honeycomb cores.

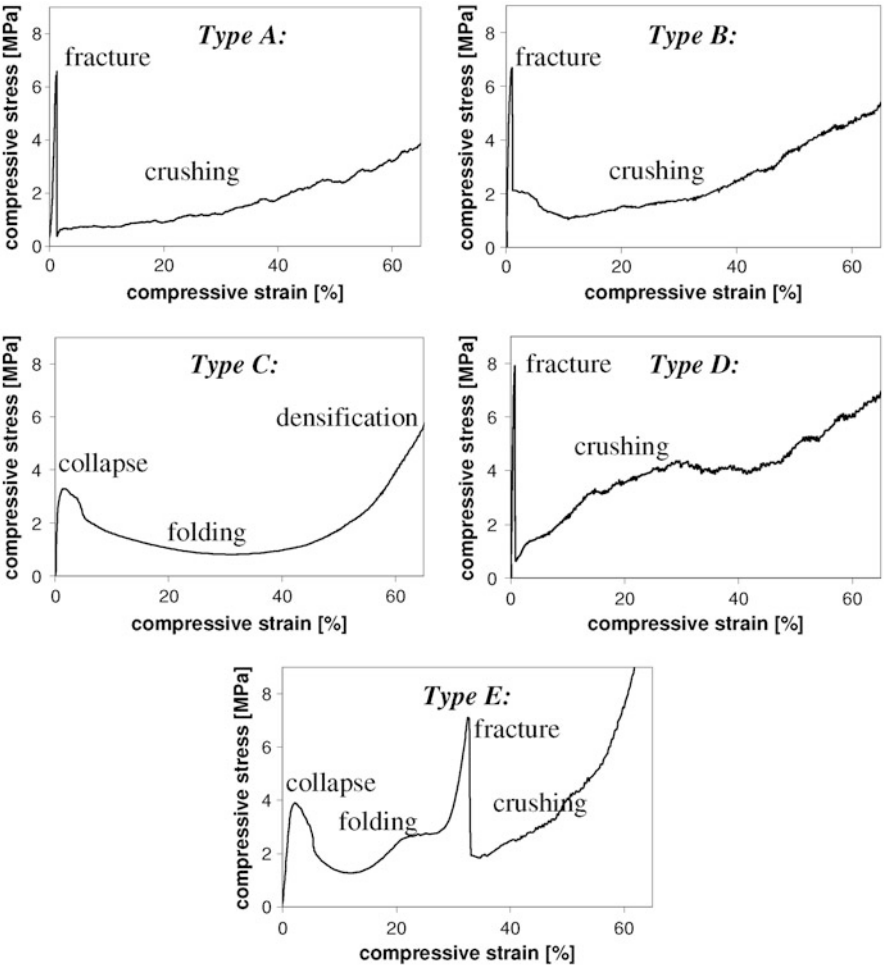


Fig. 11 Quasi-static compressive stress-strain diagrams of different foldcore types

In contrast, the carbon foldcores of types A, B and D show remarkably higher stiffness and strength properties, with maximum stresses of 6.7–8 MPa.

Also in this case the cell walls buckle before fracture. After fracture, the stress drops to a very low level and the cell walls are crushed as they come into contact with the opposite skin. Despite the same density, the compressive stiffness, strength and crushing stress of type D are significantly higher than the values of type B and, in terms of weight-specific properties, even higher than those of Nomex honeycomb cores of similar density. This is a good example of how the selection of the foldcore geometry can influence the mechanical properties and that the geometry can be tailored for specific requirements.

The dual-core type E shows a sequential two-phase behaviour. First the aramid foldcore fails in a ductile way. As soon as it is completely densified, the carbon foldcore fails in a brittle way. Since the orientation of the AFRP and CFRP foldcore in the dual-core sandwich with respect to each other may have an influence on the global behaviour, four different configurations were manufactured and tested.

No. #1 is a symmetrical alignment, No. #2 shows a longitudinal shift of half a cell size, No. #3 is based on a transversal shift of half a cell size and No. #4 shows a 90° rotation of the upper foldcore (Fig. 12). The middle layer was a 1 mm plate of aramid fibre prepreg in all cases. The results of the compressive tests showed only marginal differences between those four configurations. In general, the aramid foldcore is always compressed first until full compaction. Afterwards, the carbon foldcore is compressed. However, the overall surface under the load-displacement curve is the highest for #2, since here a bending deformation of the middle layer occurs that requires additional work. Therefore, this configuration was chosen for the impact plates described in a later paragraph.

A comparison of the specific absorbed energy of types A–E, which is the surface under the stress-strain curves divided by the core density showed that the difference is marginal for small compressive strains, but the dual-core type E and the carbon foldcore type D show the highest energy absorption potential for larger strains. Therefore, the specimens for the following impact study were only produced with type D and type E foldcore structures. A general comparison of weight-specific energy absorption capabilities under transverse compression loads until full compaction of these and other cellular core structures is given in [52]. It could be shown there that balsa and aluminium honeycomb cores offer the best weight-specific energy absorption potential, followed by CFRP foldcore and PMI foam.

4.1.2 High-Rate Dynamic Compression Tests

Quasi-static testing of foldcore structures might not be sufficient or representative for impact or energy-absorbing load cases. It is known that cellular structures can exhibit significant strain rate effects when loaded dynamically, especially when bending and folding of thin cell walls occurs and micro-inertia play a major role [53]. Also the constituent material of the cell walls may exhibit strain rate effects. However, dynamic compression test data are only rarely found in the literature [1, 50]. Dynamic compression testing of Kraft paper foldcore blocks for energy absorption purposes are documented in [28, 37, 39], covering the out-of-plane and also both in-plane directions of the cellular core. The tests were performed on a drop tower and indicate that the energy absorption of foldcores can exceed that of honeycomb cores made of the same Kraft paper material especially for higher impact speeds (9.1 m/s). Corrugated cells very similar to foldcore cells, made of CFRP in unidirectional and woven fabric configuration, were tested under high-rate compression in [54]. Dynamic tests were performed by firing rigid projectiles onto the core with a gas gun reaching velocities up to 50 m/s. A dynamic strengthening

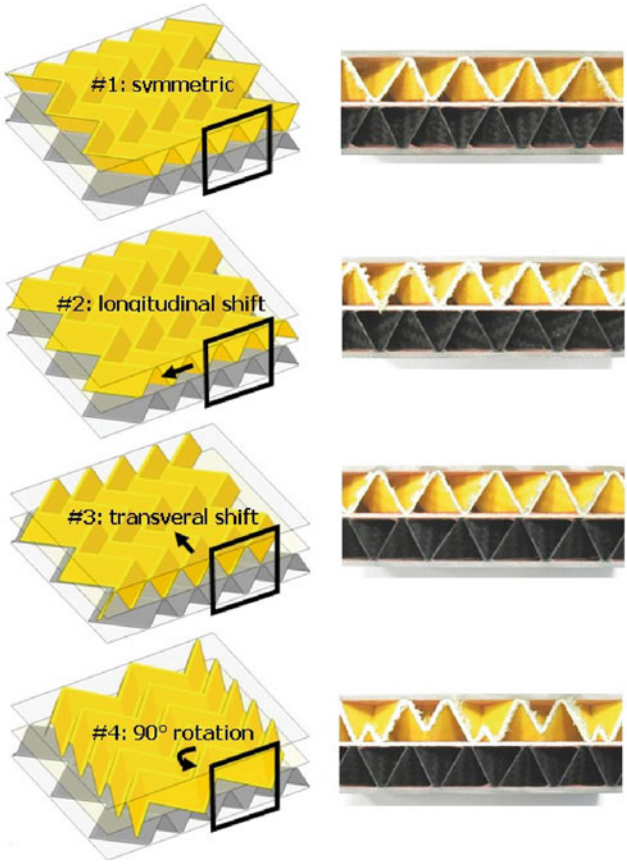


Fig. 12 Overview of four different foldcore orientations in the dual-core specimen

effect was observed with up to 12 times the static strength due to inertial effects. Global buckling of the whole cell wall occurred for low velocities of 5 m/s, local crushing at the top and no buckling occurred for high velocities of 50 m/s.

Also in the present study dynamic compression tests were performed with the CFRP foldcores of type A in addition to quasi-static testing. The tests were conducted on a drop tower facility and covered strain rates of 300 s^{-1} and 500 s^{-1} to investigate the strain rate-dependency of the compressive behaviour. However, no major strain rate effect occurred for the given velocities, i.e. the crushing stress level was not influenced by the loading rate (Fig. 13). This can be explained because cell wall folding, where micro-inertia are relevant, does not occur in this brittle foldcore that fails by crushing (Fig. 14). The crushing stress of CFRP at these strain rates is regarded as not or at most marginally rate-dependent [55–59].

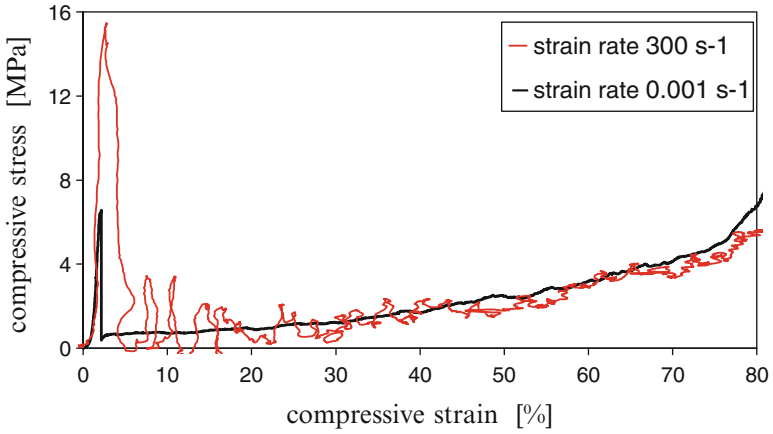


Fig. 13 Compressive stress-strain diagram of CFRP foldcore at 300 s^{-1}

4.2 Shear Testing

Transverse shear tests of aluminium foldcore [21], aramid paper foldcore [27, 47], carbon fibre foldcore [26, 50, 60] or PEEK and PC foldcores [24, 25, 51] are documented in the literature. Shear tests were even performed on wedge-shaped specimens made of aramid paper using a special test device [19]. The study in [61–63] investigated a combination of out-of-plane compression and transverse shear in order to allow for multiaxial stress states of Nomex paper foldcore. A multiaxial failure envelope was derived and used for material modelling. In contrast to conventional plate shear tests, the study in [49] used vibration tests of aramid paper foldcore sandwich samples to obtain the shear stiffness in L- and W-direction.

Since knowledge on the transverse shear behaviour of sandwich core structures is essential, shear tests based on the standard DIN 53294 have also been performed in the current study, using sandwich specimens of the size 150 mm × 150 mm. The compressive plate shear tests were performed in both L- and W-direction of the core types A–E, using metallic shear plates and a laser extensometer for the relative displacement measurement (Fig. 15).

During the testing it quickly turned out that the bondline between the sandwich skins and core was the weakest link, because it failed for all specimens as soon as the shear stress level exceeded 2–3 MPa. The core typically remained undamaged. This means that only the shear stiffness values as the initial slope of the effective shear stress-shear strain diagrams could be evaluated, the shear strength values could not be identified in these tests. Better adhesives or a better configuration of adhesive fillets are required to assess the full performance of composite foldcore under transverse shear loads.

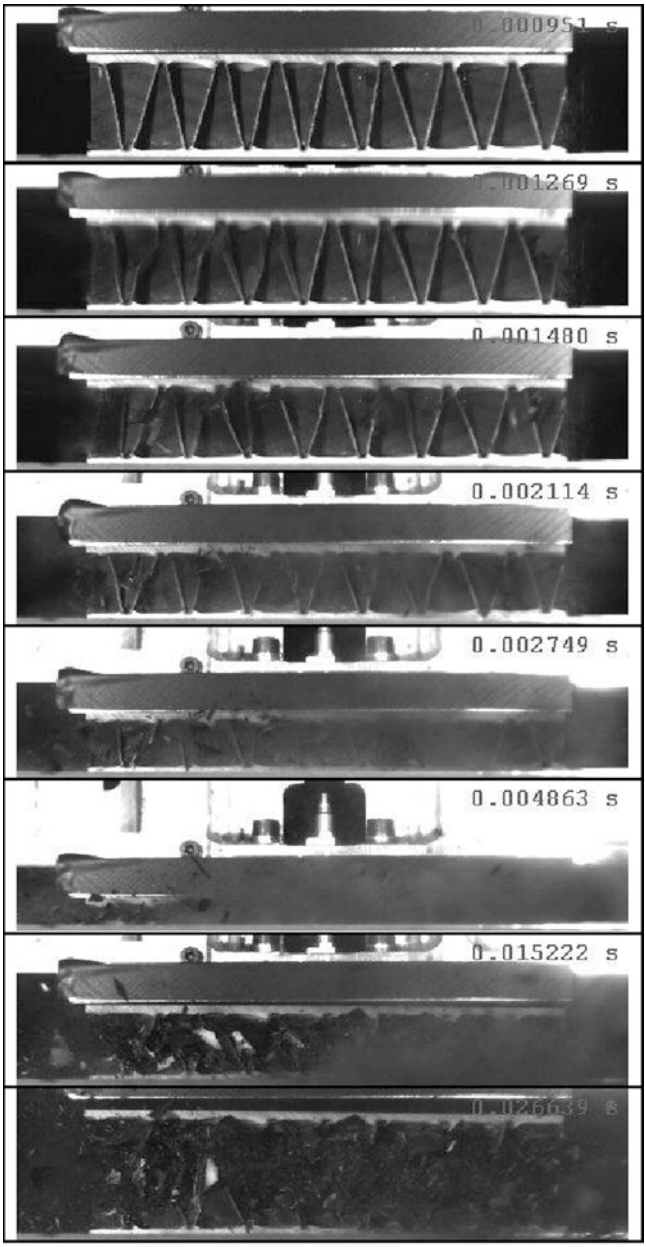


Fig. 14 Failure sequence of CFRP foldcore in dynamic compression (high-speed camera)

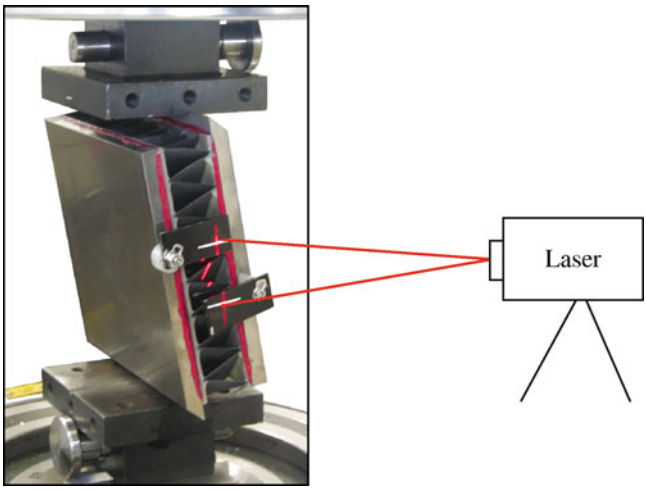


Fig. 15 Transverse shear test setup

4.3 Foldcore Sandwich Bending Tests

Bending tests of foldcore sandwich specimens were not part of the present study, but can be found in the following references. The study in [29] covers three-point bending tests of Kraft paper foldcore samples with a variation of foldcore geometry and orientation. Four-point bending tests of aramid paper foldcore with CFRP skins are presented in [64]. Such four-point bending tests of aramid paper foldcore with CFRP skins were also used in [65] to measure the residual strength after impact. In this test setup, a constant bending moment is introduced into the sandwich specimen between the inner supports, leading to compression loads in the impacted skin. With this testing procedure, the influence of impact damage on the bending strength was shown.

4.4 Skin-Core Debonding

Skin-core debonding is a typical failure mode of sandwich structures, representing the detachment of skin and core by failure of the adhesive bonding. Characteristic for foldcore structures is that the adhesive fillet only exists on one side of the cell wall (Fig. 16), which is in contrast to honeycomb core structures, where the fillet exists on both sides of the cell walls. A classical rule for design of aircraft sandwich structures requires that the bonding strength should be higher than the flatwise tensile strength of the core, so that debonding does not occur. However, as stated before, the tensile strength of most composite foldcore structures is so high, that most structural adhesives fail earlier [50].

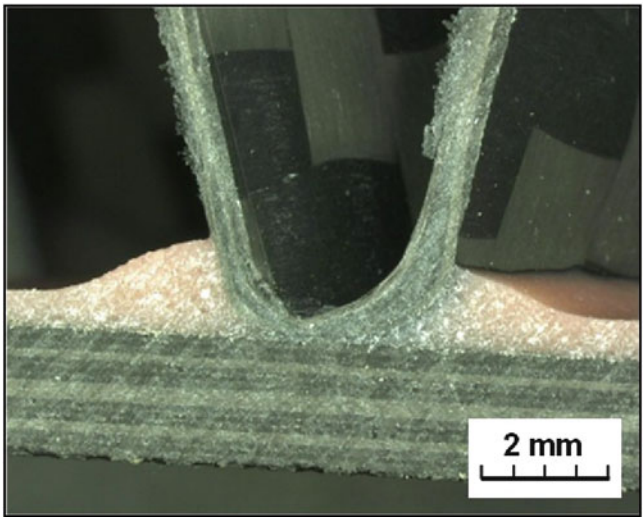


Fig. 16 Cross-section of bondline between CFRP foldcore and skin with adhesive fillets

Flatwise tensile tests of foldcore sandwich structures were performed in [32] to characterise the skin-core bonding strength. Different variants of foldcore paper and adhesive systems were investigated. A significant increase in bonding strength could only be achieved by an improved method to apply the adhesive film, leading to larger fillets. However, core tensile failure never occurred, it was always the adhesive layer or the paper coating that failed first. Also in [45] the paper coating failed first.

Another way to characterise the skin-core bonding strength is a climbing drum-peel test according to DIN EN 2243, where the skin is progressively peeled off the core. Climbing drum peel tests on aramid paper foldcore sandwich samples with glass fibre/epoxy skins for the prediction of global critical energy release rates were performed in [66]. The climbing drum peel tests in [32] were performed to identify measures to increase the bonding strength like perforation of the attached cell wall edges or larger fillets.

4.5 Analytical Approaches for Prediction of Mechanical Properties

Two other established approaches exist to identify the mechanical properties of cellular core structures besides classical experimental testing. One approach is virtual testing using finite element (FE) simulations, which is discussed in a later chapter, the other approach is a purely analytical prediction of the elastic and strength properties based on mathematical equations. The common aim is to predict

the mechanical properties of a prototype foldcore structure easily and efficiently just based on the geometrical data and cell wall material properties.

Analytical equations to predict the stiffness and strength of honeycomb structures can be found in numerous papers in the literature [1], but also for foldcore structures several analytical investigations have been conducted and published. First analytical estimations of foldcore shear stiffness and strength have already been developed by Miura in the early 1970s [2, 4]. Further mathematical analyses of foldcores and folding patterns can be found in [67, 68]. Equations to estimate the stiffness and strength of foldcores as a function of the core paper thickness are given in [69]. An analytical estimation of foldcore stiffness in thickness direction and buckling loads under transverse compression can be found in [70]. Analytical investigations of the saddle effect after bending of foldcore structures were performed in [71]. The publications in [6, 72, 73] present an analytical estimation of transverse shear moduli of homogenised foldcore sandwich structures. Despite the number of analytical equations that can be found in the literature, a large-scale validation study in order to validate the formulae or evaluate their accuracy is still missing.

5 Impact Performance Testing

The nature of sandwich structures with their relatively thin skins makes them especially vulnerable against transverse impact loads. Impact scenarios may range from low velocity impacts (LVI) (typically $v < 10$ m/s, e.g. tool drop on surface) over high velocity impacts (HVI) ($v < 1{,}000$ m/s, e.g. runway debris, hail or bird strike on aircraft structures) to hyper velocity impacts ($v > 1{,}000$ m/s, e.g. space debris on satellite structures). According to [74] the distinction of LVI and HVI is based on the relation of impact velocity to wave speed in thickness direction of the target structure. If this relation is higher than the failure strain of the material in thickness direction, then the incident is called high velocity impact, with local damage occurring before a global structural deformation is generated.

The impact performance of a sandwich structure, i.e. damage mechanisms and energy absorption capability, is strongly dependent on the skin material and thickness. However, the core – supporting the skins – also significantly influences the impact behaviour. Further influence factors are the sandwich thickness, boundary conditions, impactor geometry and stiffness, etc.

The impact performance of foldcore sandwich structures is one of the major topics of this study. The impact performance is also one of the major research topics related to foldcore sandwich structures that was addressed in various public research projects like CELPACT [75] or EMIR [76].

The following paragraphs give an overview on low velocity and high velocity impact test campaigns found in the literature and describe the impact performance of the foldcore structures that are in the focus of this study (types D and E).

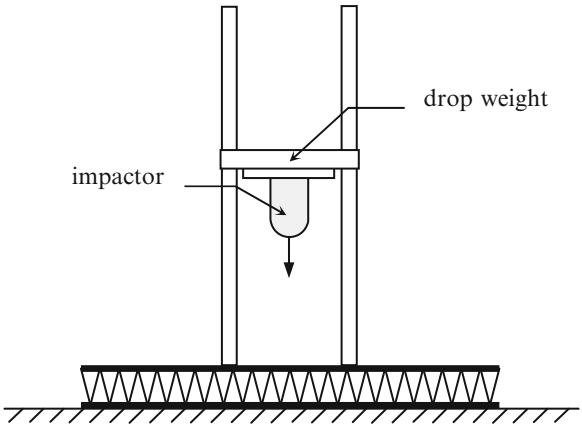


Fig. 17 Illustration of test setup for low velocity impact testing (drop tower)

5.1 Low Velocity Impact

Low velocity impact tests are typically conducted on a drop tower facility. The specimen is fixed underneath the drop tower and an impactor with defined mass and geometry is accelerated to fall on the specimen surface. LVI tests on different CFRP foldcore sandwich structures with CFRP skins using a 25.4 mm spherical impactor and energies of 2–75 J are documented in [26, 33, 50, 60, 77]. In [78] this study is extended with a variation of the impact point in relation to the zigzag pattern of the cell walls. The energy absorption was found to be nearly independent of the impact position. Aramid paper foldcore sandwich specimens were used for low velocity impact testing in [78–80] with a 50 mm steel sphere of 23.6 kg. The failure modes included impactor rebound, outer skin damage, core penetration, inner skin damage and inner skin penetration, depending on the impact energy. In [81] the specimens of this test series were analysed non-destructively using the X-ray-based technique of micro-computed tomography (micro-CT). In [82, 83] aramid paper foldcore sandwich specimens were impacted with a 25.4 mm steel sphere, followed by bending or compression-after-impact (CAI) tests in order to assess the residual strength. The study in [84] extends these tests and investigates the influence of compressive prestress on the LVI performance.

The LVI tests in this study were conducted on a drop tower (Fig. 17) with a hemi-spherical steel impactor of diameter 25.4 mm and total weight of 1.56 kg.

Foldcore types D and E were used for these tests. The sandwich plates with a size of 300 mm × 300 mm × 32 mm and composite skins as described before were fully supported on a rigid foundation in order to limit the complexity for modelling purposes. With such boundary conditions no energy can be absorbed through global bending of the sandwich panel. The impact location was chosen to be the middle of a foldcore cell wall, although further experiments proved that the influence of the impact location is negligible. Impact energies of 5 J ($v = 2.5$ m/s) to 60 J ($v = 9$ m/s) were tested. Additional tests with 2 J showed no significant skin or core damage

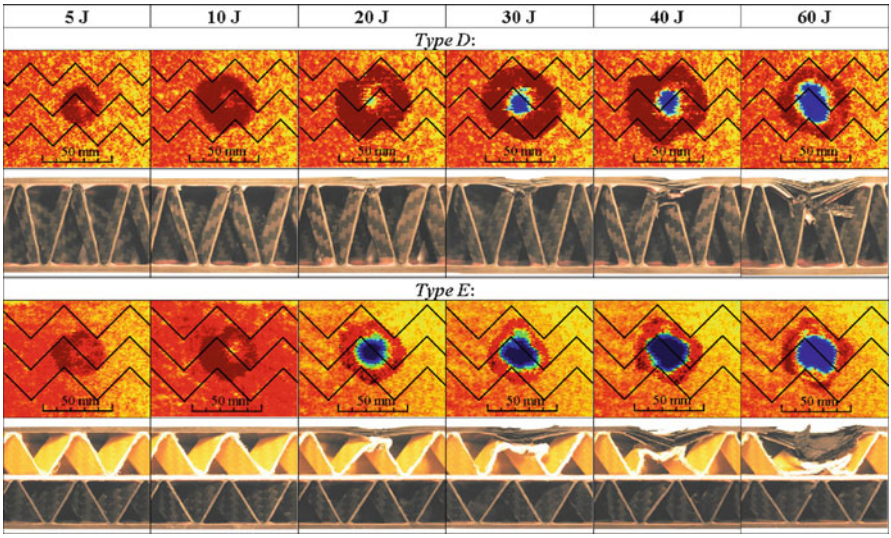


Fig. 18 LVI damage assessment of skin (ultrasonic C-scans) and core (cross-sections)

and hence are not shown here. The damage assessment of the upper skin was conducted in a non-destructive manner with ultrasonic C-scans. The core damage was evaluated by the destructive technique of cutting cross-sections (Fig. 18).

The corresponding impact force plots are shown in Fig. 19. A comparison of the curves for both foldcore types shows higher slopes and higher peak values for type D, which is primarily the result of the higher stiffness of the carbon foldcore and the 2 mm thick skin compared to the aramid foldcore and the 1.5 mm thick skins in the dual-core sandwich of type E. The oscillations in the curves mainly arise from vibrations in the system excited by the transient loading as well as damage in the sandwich structure. The carbon foldcore crushes very locally under the impact point with first damage already at 5 J, while the aramid foldcore of type E is compressed in a more ductile way. Skin damage is primarily based on delaminations as interlaminar failure with additional fibre and matrix breakage starting from 20 J as intralaminar failure modes. It is interesting to note that the neighbouring cell walls with their zigzag pattern act to a certain extent as delamination stoppers.

Due to the high stiffness of the adhesively connected foldcore cells, the bending deformation of the upper skin is very limited, impeding a propagation of delaminations across the edges of the neighbouring cells, which can be seen in Fig. 18. The highest impact energy of 60 J was just not high enough to evaluate the full potential of the dual-core configuration, since the impactor was stuck in the upper half of the sandwich structure with only a slight loading of the lower carbon foldcore (see the second increase in the 60 J force curve of type E in Fig. 19). All in all, the low velocity impact testing showed that the damaged region is very localised for both types and the amount of absorbed energy is comparable. However, as stated before, the comparability is limited, as the skin thickness is different between both types.

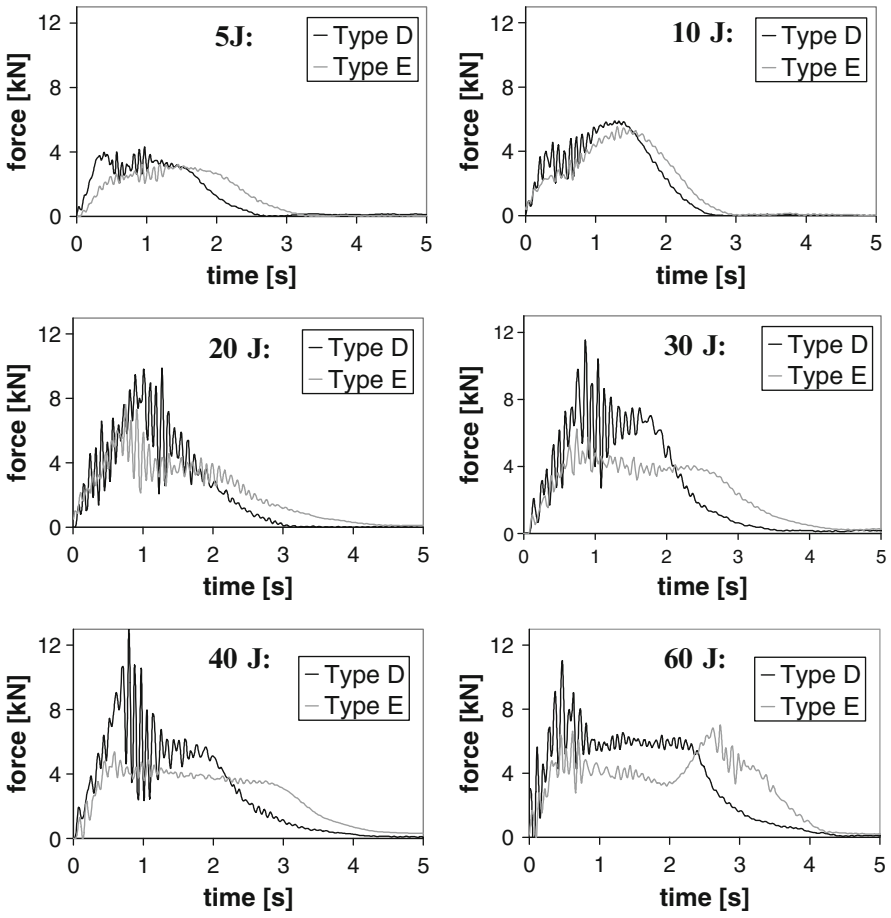


Fig. 19 Force plots of low velocity impact tests on fully supported type D and E foldcore sandwich specimens

Since the skins in the type E specimens are thinner, the extent of delaminations tends to be smaller, because the impactor penetrates earlier through the skins (already at 20 J). Once the impactor has penetrated, a significant growth of the delamination area in the upper skin does not tend to occur anymore.

5.2 High Velocity Impact

High velocity impact tests are typically performed with a gas gun, where the projectile is accelerated inside a metallic tube based on high gas pressure (Fig. 20). Different projectiles can be shot on such a facility, from small particles up to large birds. Different load cases are presented as follows.

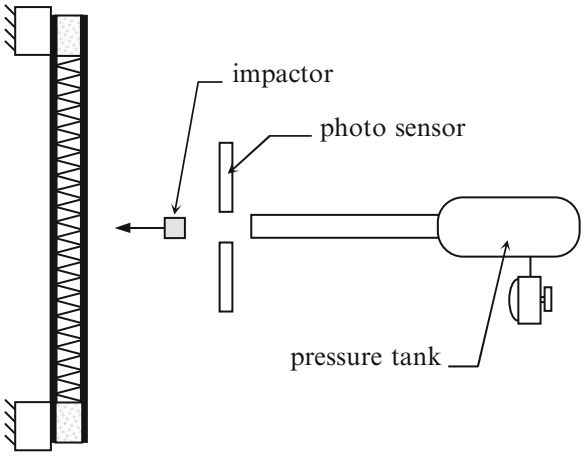


Fig. 20 Illustration of test setup for high velocity impact testing (gas gun)

5.2.1 Impact of Steel Cube

High velocity impact tests with steel cubes are documented in the literature for CFRP foldcore sandwich plates [26, 33, 85, 86] and aramid paper foldcore sandwich [87, 88]. The steel cubes are supposed to simulate the impact of debris, screws, screw nuts or small stones that could be lifted from the runway. In [87], additional protective layers were investigated to prevent the sandwich structure from impact damage.

A gas gun test apparatus was also used in the present study for the HVI tests, which were performed at the DLR labs. In this case, the sandwich plates with an identical configuration as in the LVI tests had a size of 400 mm × 400 mm × 32 mm, including a Rohacell foam core at all four edges for load introduction purposes (Fig. 20). The plates were simply supported at the edges to allow for bending deformation under impact load. The impactor was a 13.4 g steel cube with an edge length of 12 mm. The impact angle of the steel cube was 90°, i.e. perpendicular to the surface. Since some of the steel cubes were stuck in the sandwich core, the non-destructive technique of micro-CT was applied that allows for a three-dimensional look into the damaged core. In addition, cross-sections were cut from selected specimens in order to assess the damage patterns in detail.

The scope of the HVI testing covered the three characteristic load cases: (1) the impactor bounces back from the outer skin, (2) the impactor penetrates the outer skin and gets stuck in the core and (3) the impactor penetrates the whole sandwich structure. The velocity necessary to achieve this full penetration is generally referred to as the ballistic limit, characterising the impact resistance of protective structures.

The first load case with rebounding steel cube impactor occurred at velocities below 60 m/s (24 J) for type D and below 50 m/s (17 J) for type E, resulting from the different skin thickness. The steel cube got stuck in type D specimens for velocities below the ballistic limit of 130 m/s or energies of around 113 J. The ballistic limit of the dual-core configuration type E could not finally be identified

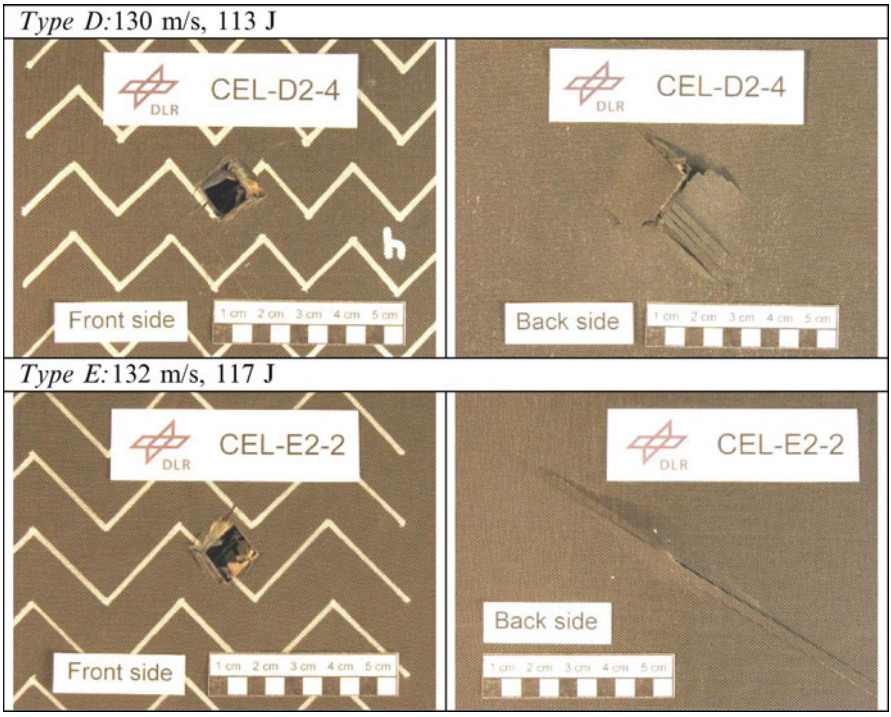


Fig. 21 Examples of HVI post-test images with 13.4 g steel cube projectile

due to limitations of the gas pressure. For the maximum velocity of 132 m/s the steel cube was still stuck in the sandwich structure, although a significant damage of the backside skin occurred (Fig. 21). This indicates the potential for an improved impact damage resistance of the multi-core concept with a further optimisation of the choice of middle layer and core types being worthwhile.

The assessment of the impact damage showed a remarkable extent of skin-core debonding of the backside skin, which can be seen in the micro-CT image in Fig. 22. This did not occur in the LVI tests due to the fully supported boundary conditions. Again, this is an indication of the weakness of the bondline under normal loads, which was already observed under shear loads in the transverse shear tests. The cross-sectional view of the impacted specimen in Fig. 23 shows further failure modes. Delamination occurs in the upper skin and part of the skin material and of the upper aramid foldcore are torn out by the impactor, which can be found at the bottom of the sandwich. The middle layer is penetrated and the lower carbon foldcore is crushed by the steel cube. The large-scale skin-core debonding at the backside can also be seen in this cross-section. All in all, this is a complex failure behaviour with various different failure modes, posing high demands on numerical models.

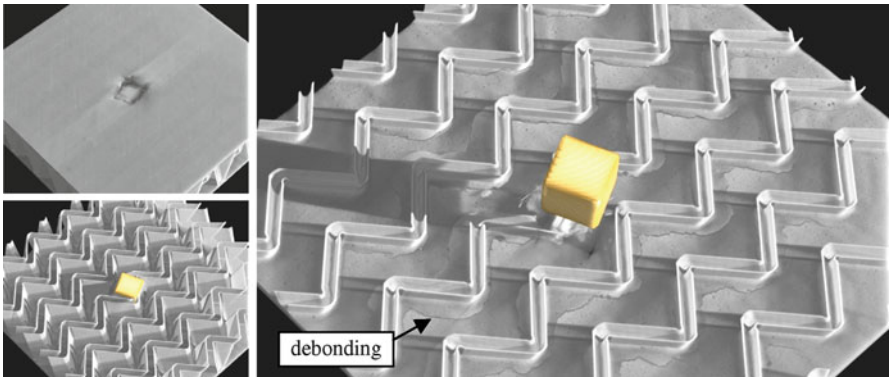


Fig. 22 Micro-CT scan of type D specimen with steel cube stuck in core (120 m/s, 96 J): extent of skin-core debonding is visible

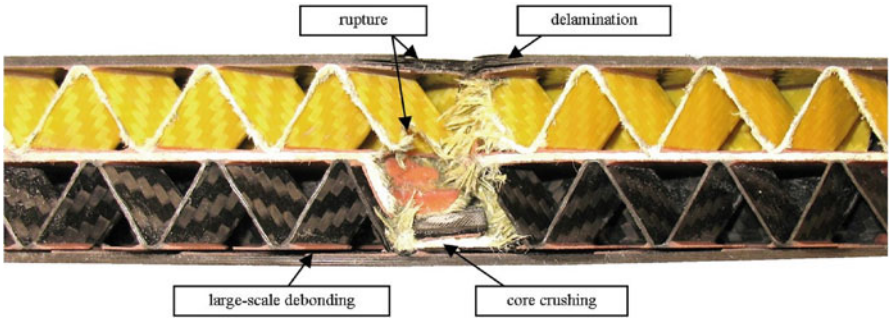


Fig. 23 Cross-section of type E specimen with steel cube stuck in core (132 m/s, 117 J): Different skin and core failure modes visible

5.2.2 Impact of Steel Bar

Furthermore, a small number of additional tests on similar foldcore sandwich specimens of types D and E were conducted in this study using a 100 g steel bar with the dimensions 109 mm × 30 mm × 4 mm, which reflects e.g. the load case of a released part of a turbine blade [26, 85].

For the steel bar an angle of 60° and velocities of 50–130 m/s were chosen. The tests with the steel bar impactor showed that for energies of approx. 140 J the steel bar was stuck in both type D and E specimens, although the backside skin was almost penetrated, which means that all kinetic energy was absorbed by the sandwich structure (Fig. 24).

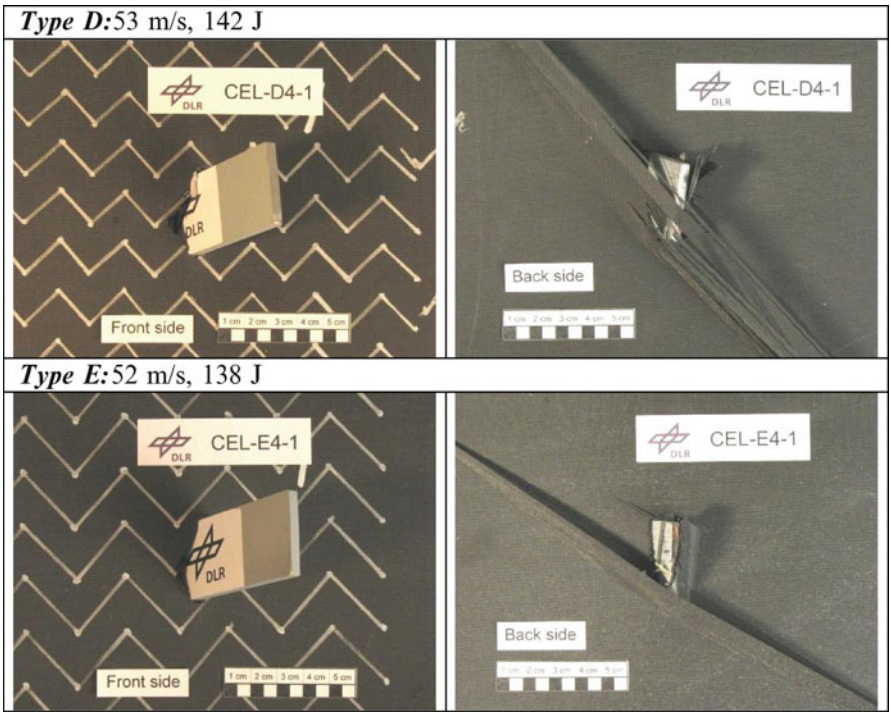


Fig. 24 Examples of HVI post-test images with 100 g steel bar projectile

5.2.3 Impact of Tire Rubber

High velocity impact of tire rubber is another important load case for aircraft structures as tire burst can occur during take-off or landing and rubber pieces can be thrown against the fuselage or surrounding aircraft structures. HVI tests with rubber projectiles have not been performed within this study. However, they were performed by DLR within the project CELPACT on sandwich panels with aramid paper foldcore and were reported in [88]. The rubber bar projectiles had a mass of 102.7 g and were shot with velocities from 97 to 135 m/s. During these tests with energies up to 937 J no visible skin damage occurred and only few foldcore cell walls showed irreversible kinking, which was assessed by micro-CT scans. This behaviour is caused by the hyperelastic constitutive performance of the rubber projectile, which can store a significant amount of kinetic energy as elastic strain energy, which is returned to the projectile during rebound and is not converted into damage of the structure.

5.2.4 Impact of Hailstones

The high velocity impact of ice or hailstones on foldcore sandwich panels was investigated in [89, 90]. Both hail on ground with hailstones up to 60 mm in diameter and $v = 30$–50 m/s as well as hail in flight with 20 mm diameter ice balls with velocities up to 180 m/s were addressed. Again, micro-CT scans were used for the damage assessment after impact and are shown for visualisation. Hailstones show a different mechanical behaviour compared to regular hard body impactors. In the moment of impact, micro-cracks are generated inside the brittle material and they propagate inside the ice. For high velocity impact, the material crushes and behaves in a fluid-like manner afterwards. The foldcore sandwich plate in the abovementioned study showed visible skin damage with partial core crushing after hail impact with 173 m/s using an 11 g ice ball.

6 Modelling and Simulation

Since experimental characterisations of innovative materials and structures like foldcores are time-consuming and expensive when it comes to the manufacturing of toolings, prototypes and test specimens as well as the testing itself and damage assessment, numerical simulations are an established efficient tool in the development process of engineering structures. The aim of the simulation activities in this study was to investigate the approach of virtual testing. The benefit of this approach is obvious: If the mechanical performance of a cellular structure can be obtained reliably with numerical simulations, testing efforts can be minimised and a large number of different core geometries can be characterised with a minor amount of time and cost. Models on different scales have been developed and are presented as follows. Meso-scale models are a detailed representation of the three-dimensional foldcore structure and are used for virtual compression or shear tests or for detailed impact simulations. Macro-scale models are a homogenisation of the core with continuum elements and are intended for large models where a detailed modelling approach would be too expensive.

6.1 Meso-Model

6.1.1 Parametric Foldcore Model

In order to be able to easily generate meso-scale foldcore unit cell models of different geometries, a parametric model was developed in this study in the pre-processing tool MSC. Patran using the command language PCL (Patran Command Language). The user input consists of

- foldcore geometry (cell wall dimensions and angles, cell wall thickness)
- model size (length, width, height or number of unit cells)
- element size and element type
- symmetry utilisation
- additional simulation controls (termination time, etc.)
- random imperfections.

The geometric model is defined by the foldcore height H, the zigzag opening angle ψ and the spacing parameters l_1 and L_1 (Fig. 3). In case of the CFRP folded core the top folding edge is modelled as a plateau and not as a sharp edge, which better represents the real geometry (Fig. 16). Inside the code a unit cell is generated from the geometry input and is duplicated in both in-plane directions as prescribed by the model size. Overlapping cell walls are trimmed. Two sandwich faces are generated on the upper and lower side of the foldcore, where the loads are applied. The whole model is meshed with four-node shell elements according to the defined element size and the core and the faces are connected by a contact formulation for simulations with the commercial simulation software LS-Dyna. The adhesive fillet between cell wall and skin and its stiffening effect are not covered by this model. Finally, the boundary conditions are applied to the face sheets. The user decides if half symmetry of the specimen is used to reduce computational cost. In that case the necessary boundary conditions are included at the symmetry surface. At the end a simulation input file for LS-Dyna is written, which can be used to perform virtual test simulations.

Further information on the parametric foldcore model and other developments in MSC. Patran and Ansys can be found in [46, 48, 70, 91–93]. Another parametric tool was developed at the Technical University of Dresden, which is called SandMesh [19, 30, 47, 94–96]. This tool is also able to generate parametric foldcore models for simulations with different codes.

6.1.2 Cell Wall Material Modelling

Cell wall material modelling is a crucial factor in the foldcore models, because it strongly influences the structure's elastic and failure behaviour. At the same time, however, it is very difficult to obtain the mechanical properties of the shell element's cell wall material.

In case of Nomex or Kevlar paper foldcores, the cell walls are made of phenolic resin-impregnated aramid fibre paper. Tsujii et al. [97] as well as Foo et al. [98] experimentally characterised Nomex cell wall material in tensile tests, providing stress-strain curves as well as stiffness and strength values. Tensile and bending tests of phenolic resin-impregnated Nomex paper for foldcores are presented in [45]. The material behaviour is very ductile and can be estimated by a bilinear elastic-perfect plastic material law. Furthermore, there is a difference in the properties of the machine direction and cross direction of the Nomex paper, which makes an orthotropic material model adequate.

The difference between machine direction and cross direction is much lower for the phenolic resin-impregnated Kevlar fibre paper. Such paper samples were tested in tension and compression in [19, 48] to obtain the material properties. The authors in [49, 99] performed bending tests and microscopic investigations of phenolic resin-impregnated Kevlar fibre paper to characterise the mechanical behaviour. In [100] this study was also enhanced by a block compression test to determine the compressive properties, where a block of 48 layers of aramid paper was compressed. Further extensive test series on phenolic/Kevlar paper with tensile tests, cylinder compression tests, strap crush tests with a free sample length of 0.7 mm, free vibration tests and bending tests are reported in [23, 101]. Simulations of these tests were performed to calibrate and validate the material model. Micrograph observations of phenolic resin-impregnated Kevlar paper in [27, 91] show strong inhomogeneity. The middle section mainly consists of randomly distributed fibres and phenolic matrix, the outside layers are poor in fibres and mainly made of phenolic resin. Bending and compression tests in both directions of the paper were found to be necessary. A multilayer modelling approach with an inner layer covering the material behaviour of the aramid fibre/phenolic resin composite and an outer layer with pure resin was proposed. A detailed discussion on the constitutive modelling of this material is also given in [1, 101].

A study on the influence of nanomodifying additives inside the phenolic coating of aramid paper is given in [31, 102], where the authors also performed tube compression tests and showed that the strength of the foldcore structure can be increased by such methods.

A different approach to determine the necessary material properties of the resin-impregnated Kevlar paper foldcore is given in [103, 104], using a parameter identification approach with the software LS-Opt. Flatwise compression and transverse shear tests of foldcore structures were simulated with a parametric material model. The initial values were taken from Nomex honeycomb paper, found in the literature [97]. During an optimisation study the parameters were adjusted automatically in such a way that the global response of the compression and shear tests of the foldcore matched with given test curves of the foldcore manufacturer.

In contrast to these resin-impregnated aramid fibre papers, other composite foldcore structures that are used in this study, are made of unidirectional laminates or woven fabric plies. Mechanical properties were taken from data-sheets of these materials and were validated with tensile and shear tests of such specimens [26]. The composite material models MAT54 (UD) and MAT58 (woven fabric) in LS-Dyna were used for the modelling of the plies. Each single layer is represented by one integration point through the shell thickness with the respective fibre orientation angle. The crush-front algorithm of MAT54 was also used, which reduces the strength of elements neighbouring eroded elements to facilitate the representation of pre-damage and progressing crushing of the brittle CFRP material.

Coupon tests of aluminium samples for aluminium foldcore modelling are reported in [21].

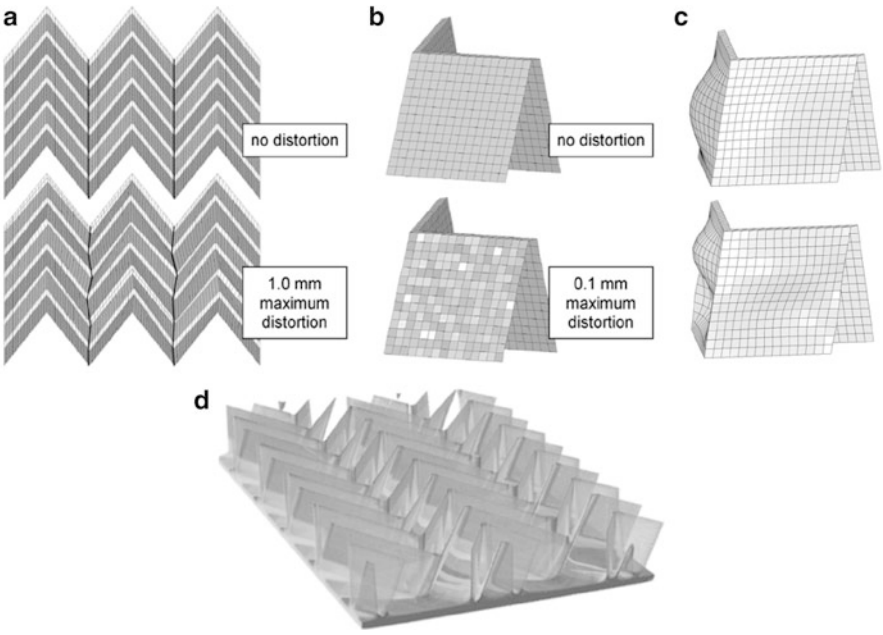


Fig. 25 Imperfection modelling through geometry distortion (**a**), node-shaking (**b**) and pre-buckling (**c**). (**d**) shows a sectional view through the CFRP foldcore using three-dimensional micro-CT data

6.1.3 Imperfections

So far the meso-scale models have a uniform, perfect geometry. In reality no cellular structure is either uniform in geometry or free of imperfections and irregularities. This affects the buckling load of the single cell walls and the whole structure's strength. Therefore, a meso-scale model without imperfections will always lead to an overestimation of stiffness and strength values. Neglect of imperfections can also lead to uniform unit cell behaviour, while in reality each cell may buckle or collapse in a different way, influencing the global response. In [19] compression test simulations were performed on an ideal foldcore model, which led to a significant overprediction of compressive stiffness that was attributed to missing imperfections.

In this work, several different approaches to account for imperfections in the FE models were investigated. Their effect on the stress-strain behaviour is explained as follows, for detailed stress-strain plots of each individual approach see [1].

One way is to include the actual imperfections in the mesh. Global geometric imperfections can be modelled by randomly distorting the core's geometry prior to meshing (Fig. 25a) [1, 46, 48, 91, 92]. Local imperfections like uneven cell walls can be represented by randomly modifying all nodes' coordinates ('node-shaking', Fig. 25b) [1, 33, 46, 48, 91–93]. Both features were included in the parametric model described before based on random numbers. The effect of this

approach was investigated in preliminary flatwise compression test simulations. In general, the foldcore structure first exhibits cell wall buckling as stability failure under compressive loads followed by cell wall fracture in case of brittle CFRP foldcore or a continuous folding pattern in case of ductile aramid paper cores. The random geometry distortion approach reduces the buckling load but not in a sufficient way for the simulation results of virtual compression tests to agree with experimental data. The influence of the node-shaking approach is slightly higher with a considerable decrease of the global compressive strength. However, compared to experimental stress-strain curves, which are still lower, not all imperfections can be covered by these approaches.

Another way to reduce the buckling load is to consider pre-buckling of the cell walls [92]. To achieve this, the first buckling modes – calculated within an implicit analysis – have to be superposed onto the unit cell's mesh, scaled to about 1–5% of the shell thickness (Fig. 25c).

A further method for including imperfections in the finite element mesh is to scan the real cellular core specimen in a micro-CT apparatus (Fig. 25d) and translate the three-dimensional X-ray data into a finite element mesh with special software tools. The result is a mesh of the actual specimen that covers all real geometrical imperfections [92, 93]. An optical scan of the real imperfect foldcore geometry using the 3D digitizer Atos by Gom was performed in [21, 24, 91]. The output data were polygons of measured lines, which were processed to NURBS surfaces that could be used for meshing. This was regarded in [105] as a good but expensive method.

Another interesting approach was investigated in [33]. The material orientation of the composite cell wall material was changed with angles of 2°, 5° and 10°. This was justified because an imperfection of the material angle could easily be detected in real foldcore samples with unidirectional and fabric composite cell walls. A significant influence on the foldcore stiffness and strength could be observed.

In [94] imperfections were incorporated into a numerical model by round-shaped folds and different wall thicknesses to account for accumulations of coating resin. These imperfections have shown to reduce the mechanical properties significantly.

Another way of imperfection modelling is to keep the ideal mesh and reduce the cell wall properties (material data and wall thickness), which can either be done uniformly for the whole model or stochastically distributed for individual elements [33, 92, 93]. This latter approach can also be implemented in the parametric model generation tool by defining a certain number of different parts with randomly reduced material properties and wall thicknesses in LS-Dyna and assigning these parts randomly to the elements. In case of a uniform reduction, a parameter identification procedure with LS-Opt as described before can be used. Within the parameter identification loop with LS-Opt, compression and shear test simulations are performed in order to determine the set of parameters with the best correlation to the target values. Hereby, the lack of imperfections in the FE model is compensated by the use of cell wall properties that are on purpose lower than in reality. This approach led to a very good correlation to the experimental stress-strain curves, while still maintaining a realistic buckling pattern in the simulation [104].

A further approach is presented in [91, 99, 105–107]. Here, the actual folding process of a flat sheet of paper is simulated using imperfect folding lines that can arise from the heterogeneity of the paper or the embossing process or kinematical incompatibilities during the folding process. Their model with these imperfections was very close to the experimental compression curve, while the model without imperfections strongly overpredicted both stiffness and buckling load.

Reality is a combination of the approaches presented here. There are geometrical imperfections in the cellular structure and there are variations in the material properties and the paper thickness, especially in case of impregnated aramid paper. The weakest or thinnest areas of a cell wall determine the global properties, since damage will start from these areas, which justifies the approach of locally reducing the properties in the model.

6.1.4 Skin and Bondline Modelling

For the modelling of the skin-core connection it is essential if debonding as a failure mode shall be represented in the model or not. If not, a simple tie contact or constraint can be used. If failure needs to be modelled, then cohesive elements or a contact formulation with failure is adequate. The contact interfaces between skin and core in the study [108] were based on a through-thickness tension/shear fracture criterion. In [33] a simple tie contact was used first. However, since debonding occurred in the test, the model was enhanced with a tiebreak contact in LS-Dyna using the mechanical properties of the adhesive film. This approach was also used in the models of this study. The idea of this contact formulation is to connect face and core segments until critical interface stresses are reached. For this purpose, maximum normal and shear interface stresses NFLS and SFLS need to be defined. Different failure criteria can be chosen in LS-Dyna, at which the connection fails, while the standard is a quadratic criterion:

$$\left(\frac{|\sigma|}{NFLS}\right)^2 + \left(\frac{|\tau|}{SFLS}\right)^2 \geq 1 \tag{1}$$

with σ and τ as the normal and shear interface stresses. As soon as the failure criterion is met, a relative movement of the connected nodes is allowed until a critical displacement CCRIT is reached, representing a continuous loss of connection on a linear basis. When CCRIT is reached, no load is transmitted anymore.

6.1.5 Simulation of Compression and Shear Testing

Meso-models of foldcore structures are ideal to perform virtual compression or shear tests. This has been performed for phenolic resin-impregnated Kevlar paper foldcores in [99, 106] with Abaqus, in [100, 101, 109] with Pam-Crash and in

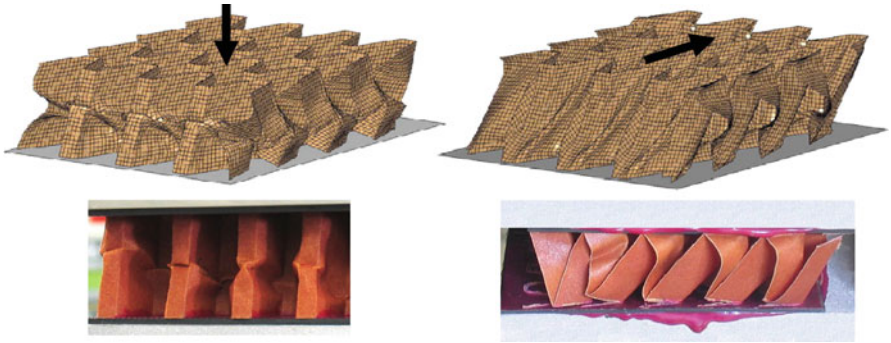


Fig. 26 Compression and shear test simulation of Kevlar paper foldcore with corresponding images from experimental tests

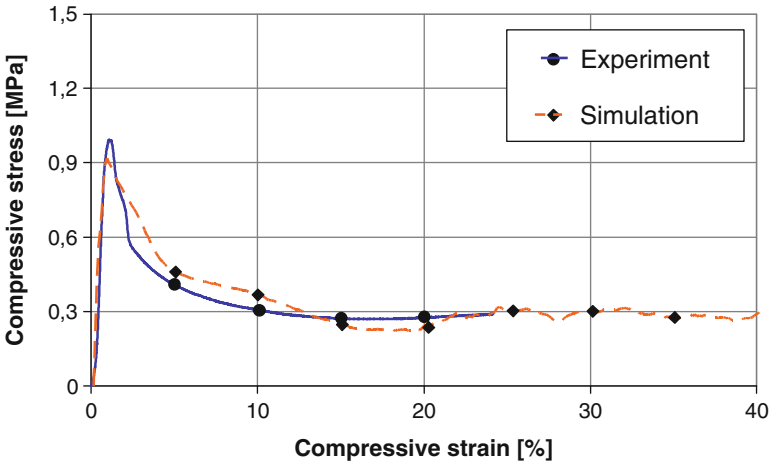


Fig. 27 Stress-strain curves of Kevlar paper foldcore under flatwise compression: comparison of test data and numerical prediction

[1, 45–48, 92, 93, 104] with LS-Dyna. Fig. 26 shows the compression and shear test simulations of a Kevlar paper foldcore with a very good representation of the cell wall deformation and buckling patterns as stability failure. The corresponding quantitative results in terms of stress-strain curves are depicted in Fig. 27 for the example of the Kevlar paper foldcore under flatwise compression. It can be seen that the stress-strain curve is accurately predicted by the numerical pre-test simulation model. The LS-Dyna simulations of foldcores under compression and shear in [19] also covered wedge-shaped specimens.

Implicit simulations with Nastran and Abaqus to determine the effective shear stiffness numerically have been performed in [21, 23, 24, 110] on Kevlar paper and aluminium foldcore.

In order to cover the strong nonlinearities and crushing of the foldcore, explicit FE codes are favourable for such simulations. Typical material tests are performed at a quasi-static loading rate. To perform the virtual tests in the simulation also quasi-statically would be very expensive, since the explicit integration scheme of dynamic simulation codes usually leads to very small time steps resulting in an immense computational time. Increasing the loading rate in the simulation has to be done with care, because the material behaviour of ductile cellular structures is typically rate-dependent due to micro-inertial effects and the results of a dynamic test may not be directly comparable to static test results. Since the time step of the simulation depends, amongst others, on the material density, a common technique to reduce the computational time for quasi-static explicit simulations is to increase the density of the materials in the model. This technique, known as mass-scaling, has also to be done very carefully, because an increased mass normally leads to a different structural behaviour due to inertial effects and an increased kinetic energy. Although the velocities in a quasi-static simulation are so small that a slight increase of the mass does not lead to a significant change in the system response, the engineer always has to check if the kinetic energy of the system is negligibly small after increasing the density. With this mass-scaling technique very low loading rates can be achieved in an acceptable computational time.

Several modelling parameters have an influence on the structural behaviour of the foldcore model and the respective simulation results, including not only the material model and geometry, but also the method of discretisation and boundary conditions: model size, element size, element type, loading rate and mass scaling. Those influences were investigated systematically by means of parameter studies [46, 48].

Challenging tasks arise regarding modelling of CFRP foldcore cell wall crushing in the post-failure region in a flatwise compression test of the foldcore [33, 50, 60, 70, 77, 92, 93]. First the cell walls slightly buckle, then the material fails under compression starting from the cell wall edges. The respective elements are eroded in a propagating horizontal crack. Once a complete row of elements is deleted, the compression force drops to zero. Due to the angular geometry of the folded core cell, the elements do not come into contact again. The force does not increase until the upper and lower halves of the failed foldcore have contact with the compression plates. Compression test simulations of dual-core sandwich structures of type E that were performed in the framework of this study are shown in Fig. 28 [85]. It can be seen that the failure sequence and local cell wall deformation mechanisms are accurately captured by the simulation model.

6.1.6 Foldcore Geometry Optimisation

The models described so far showed the potential to predict the mechanical response of cellular core structures in virtual test series with a high degree of accuracy. Therefore, the next step obviously is the utilisation of this method in the development process of new core geometries, tailored for specific applications.

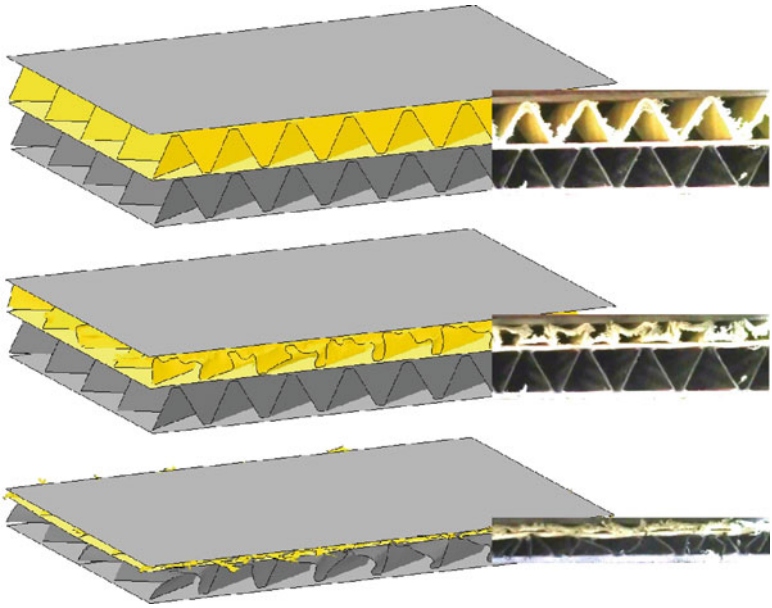


Fig. 28 Compression test simulation of dual-core sandwich type E

Based on the parametric model generation tool and the virtual testing simulations, this technique is much more efficient than producing core prototypes (and the respective toolings as well) and testing them in a lab.

In this study, such an optimisation of the core geometry for a specific target was performed for the CFRP foldcore. The target in this case was to maximise the compressive strength of the core structure while maintaining the global density of 102 kg/m^3 and the height of 28 mm from the reference geometry of type A. Additional requirements regarding the producibility of the structure with respect to a minimum cell wall size were also taken into account. The shear properties were allowed to be slightly lower.

In a first step, the aim was to investigate the influence of changing single geometric parameters (three different edge lengths l_1, l_2 and S_1 in Fig. 3) on the compressive properties. Therefore, the parameters were changed individually. The analysis of the resulting stress-strain curves, obtained in compression test simulations in LS-Dyna, was done after dividing them by the resulting density. This was necessary, since the parameter change affected the overall density, and the results had to be comparable.

In a second step, two parameters were changed at the same time, while the third one was kept constant. The other two were changed in such a way that the overall density always was constant. This was done using the following equations for the density of the CFRP foldcore according to Fig. 3.

$$\rho_{CFRP\ foldcore} = \frac{t \cdot \rho_{CFRP} \cdot (2 \cdot A_1 + A_2)}{S_1 \cdot l_2 \cdot h} \tag{2}$$

with

$$A_1 = \sqrt{q(q-a)(q-b)(q-c)} \tag{3}$$

$$A_2 = S_1 \cdot S_2 \tag{4}$$

$$q = \frac{a+b+c}{2} \tag{5}$$

$$a = l_1 \tag{6}$$

$$b = \sqrt{\mathrm{h}^2 + (\mathrm{l}_2 - \mathrm{S}_2)^2} \tag{7}$$

$$c = \sqrt{((\mathrm{l}_2 - \mathrm{S}_2) + \mathrm{V})^2 + {\mathrm{S}_1}^2 + \mathrm{h}^2} \tag{8}$$

With the help of this information an improved geometry could be defined, which led to the design of type D. Compared to the original geometry the cell walls are smaller, which corresponds to higher buckling loads, and the vertical angle is lower, which leads to a cell wall orientation more parallel to the transversal load direction. The experimental results of compression tests in Fig. 11 validated and confirmed this improvement. The optimisation was only performed with respect to the compressive behaviour. However, the effect on the shear behaviour was analysed in subsequent shear test simulations. In W-direction the transverse shear strength increased by 44% and the shear stiffness by 59%. In L-direction the transverse shear strength decreased by 33% and the shear stiffness by 37%.

Other studies, where the geometrical parameters were changed manually in order to improve the properties are provided in [19, 70, 92, 93, 111].

Also in [112] a foldcore geometry study was performed. The aim was to find the ideal cell geometry for a specific load case. Hyperworks and Optistruct were used as commercial software tools to optimise the geometry for stiffness and buckling loads under flatwise compression and transverse shear. The resulting geometry for compression was relatively dense, the cells were larger for shear. These load cases were treated separately and not combined. However, it is challenging to identify a geometry which is favourable both under compression and under transverse shear.

6.2 Macro-Model

Although meso-scale unit cell models are beneficial for local investigations like impact loadings or virtual compression and shear tests, they are numerically too

expensive to be used solely in FE models of large-scale sandwich structures. Therefore, a macro-scale modelling approach with a homogenised cellular foldcore was investigated as well. The basic idea of this homogenisation was to develop a constitutive law for continuum solid elements, so that the mechanical behaviour of these solid elements is equal to the effective mechanical behaviour of the foldcore structure. Only global behaviour can be represented with this approach, no local phenomena.

In most commercial codes like LS-Dyna or Pam-Crash there are material models existing for this purpose (e.g. honeycomb material models). The input of these models are the foldcore's six independent effective stress-strain curves, three for normal stresses and three for shear stresses in all three material directions, which were determined numerically using the meso-scale model [91]. In general, the mechanical behaviour for in-plane and transverse normal and shear stresses is treated as fully uncoupled.

The multi-model coupling (MMC) approach can combine the meso-scale unit cell model with the homogenised model and may be an efficient technique for impact simulations on large-scale sandwich structures. Typically, the detailed model is limited to the impact zone, where nonlinear effects like buckling and damage occur, and the homogenised model, which primarily covers the elastic foldcore behaviour, is used in the surrounding sandwich areas around the impact zone (Fig. 29). Each submodel may run at different time steps within the explicit calculation, which are determined by the individual smallest element size. The performance of the multiscale model depends strongly on the interface between meso-scale and homogenised model [91]. A constraint or contact formulation can be used, which is able to transfer forces and moments. The suitability of the respective interface to cover the correct global sandwich structure's stiffness was checked by three-point bending simulations and a global modal analysis.

The macro-modelling approach of foldcore sandwich structures was used in [1, 103, 104] for the modelling of a Kevlar paper foldcore sandwich fuselage under crash loads. The continuum elements of the foldcore were modelled based on tabular input of stress-strain curves determined with a meso-scale foldcore model and virtual tests.

In [108] a homogenised solid element modelling approach for foldcore structures is used in Pam-Crash for HVI impact simulations on foldcore sandwich. The orthotropic bi-phase solid element was used with a user-defined elastic-plastic material law and the parameters taken from flatwise compression tests.

Another approach of homogenised modelling of foldcore sandwich is to use one 2D shell element for the foldcore sandwich. The authors in [113, 114] describe the approach of developing a sandwich finite element for efficient prediction of impact damage in foldcore sandwich structures, using a three-layered shell element within a 3D stress analysis. In [1] a user-defined shell modelling approach is developed for foldcore sandwich structures subject to crash and impact load cases with complete nonlinear behaviour up to densification in all orthotropic directions, taking strain rate effects and realistic loading-unloading behaviour into account.

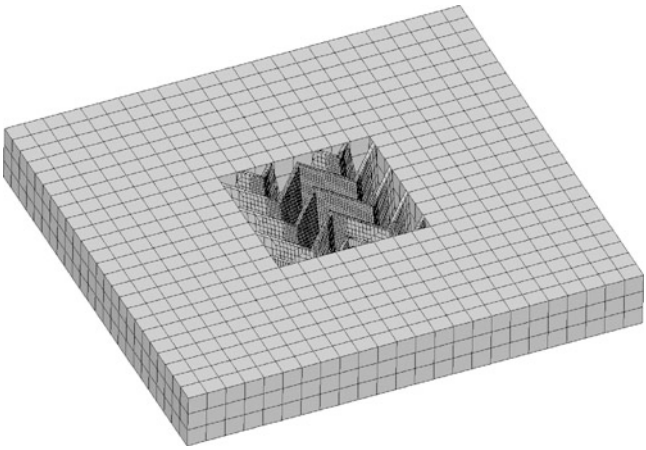


Fig. 29 Multi-model coupling with a meso foldcore model in the centre and macro model in the surrounding

6.3 Simulation of Low Velocity Impact

Low velocity impact simulations using a 25.4 mm spherical impactor have been performed in [26, 33, 50, 60, 77, 85] on CFRP and AFRP foldcore sandwich, in [30, 94, 95, 115] on Nomex paper foldcore sandwich and in [65, 83] on Kevlar paper foldcore sandwich, all using LS-Dyna. In the latter references, the model of the damaged structure after impact was used for post-impact four-point bending test simulations to assess the residual strength. Compared with results of non-impacted sandwich plates, a severe strength reduction was observed even for very low impact energies [91]. This study was extended in [116] so that CAI and four-point bending tests after impact were compared numerically, showing that CAI requires much higher forces and is more sensitive to changes in boundary conditions. The study in [84] covers LVI simulations with LS-Dyna on prestressed foldcore sandwich, which is loaded uniaxially under compression before impact. The LVI simulations in [79, 80, 91] use a 50 mm spherical impactor with a mass of 23.6 kg, Kevlar paper foldcore sandwich and Pam-Crash as the simulation code with a stacked shell modelling approach for the skins including three cohesive interfaces and a continuum damage mechanics (CDM) model for the composite plies.

The low velocity impact tests in this study were simulated using LS-Dyna and a rigid body for the spherical impactor and boundary conditions similar to the experiments. Both the foldcore and skins were modelled with 4-node Belytschko-Tsay shell elements with reduced integration and a uniform element size of 1 mm, which was the best compromise between calculation time and accuracy of the local material fracture representation.

For the textile-reinforced composite cell walls as well as the Kevlar middle layer of the multi-core sandwich structure (type E) the CDM-based material

model Mat_Laminated_Composite_Fabric (MAT58) was used. Adapted from the Matzenmiller-Lubliner-Taylor model [117], Schweizerhof et al. [118] extended and implemented this model for composite fabrics into LS-Dyna. This approach assumes nonlinear material behaviour with stiffness degradation based on a Weibull function resulting from internal defects and increased micro-damage during deformation of the material. Identical material behaviour in 1- and 2-direction of the lamina can be defined, which is important for fabrics, where no specific fibre and matrix direction exists. Element erosion after failure is controlled by the definition of maximum effective strain values.

The UD laminate of the skins was modelled with the composite material model Mat_Enhanced_Composite_Damage (MAT54). In contrast to the CDM model, this constitutive law assumes linear elastic behaviour until the Chang-Chang failure criteria are met [119]. Then, the stress level is kept constant until defined failure strains are reached. Element erosion is again controlled by failure strain values. The material properties are given in [26]. Since shell elements are unable to cover delamination failure, a stacked shell approach was applied for the upper skin. In this approach, two shell elements, each representing a sublaminate, i.e. half of the laminate, are connected by a delamination contact interface at the midplane, which allows for interlaminar failure and the separation of the sublaminates. The delamination tiebreak contact in this case is based on the cohesive zone model implemented into LS-Dyna by Borg et al. [120]. In these impact simulations no debonding between skin and core was allowed, since this also did not occur during the experiments. Therefore, a tie contact was used, which allows for the transfer of moments.

These LVI simulations are especially valuable as a quantitative comparison between experiments and simulations in terms of force and energy plots is possible – these data are not available for the HVI tests in this study.

The low velocity impact tests conducted experimentally covered the energy levels 2, 5, 10, 20, 30, 40, 50 and 60 J. To limit the number of comparisons, only the three representative energy levels 5, 30 and 60 J are treated here for the foldcore types D and E. The deformation and fracture behaviour in a cross-sectional view is compared as well as the energy and force curve plots.

Taking a look at the 5 J specimen of the single-core configuration type D in Fig. 30, the visual correlation of the core failure is good, since just some minor crushing in the upper part of the core appears with some elements eroded. The energy curve, which is calculated both in simulation and experiment from the kinetic energy of the impactor, can also be represented very well up to the rebound of the impactor. The total energy absorbed is higher in the real test since too much elastic energy is returned in the simulation model. Some differences can also be seen in the force curves, since the higher number of oscillations in the experiments – expected to be resulting from delaminations – is not covered by the simulation curve where only one delamination contact exists. However the overall correlation is satisfactory. A very good correlation can also be found for the dual-core specimen of type E and the 5 J impact (Fig. 31). The aramid foldcore buckles but behaves completely elastic with no elements eroded. The energy is absorbed mainly by delaminations and core

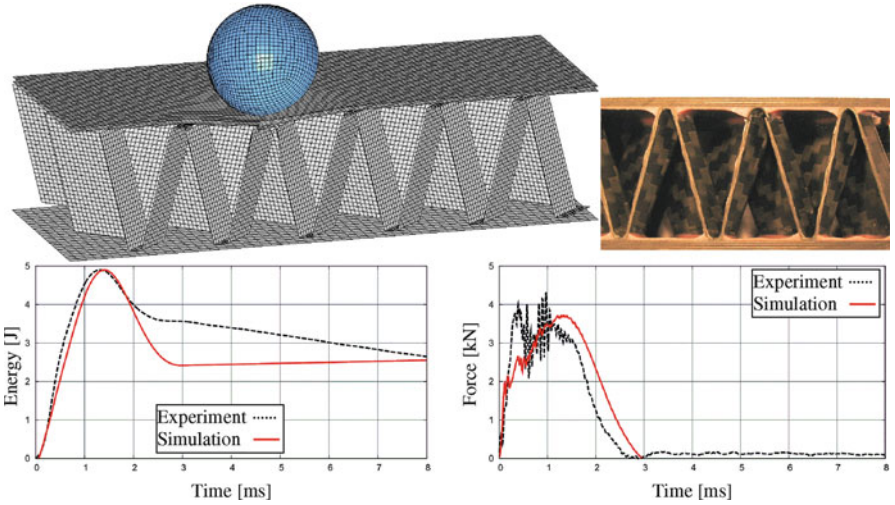


Fig. 30 Cell wall deformations, energy and force plot for 5 J impact on type D foldcore

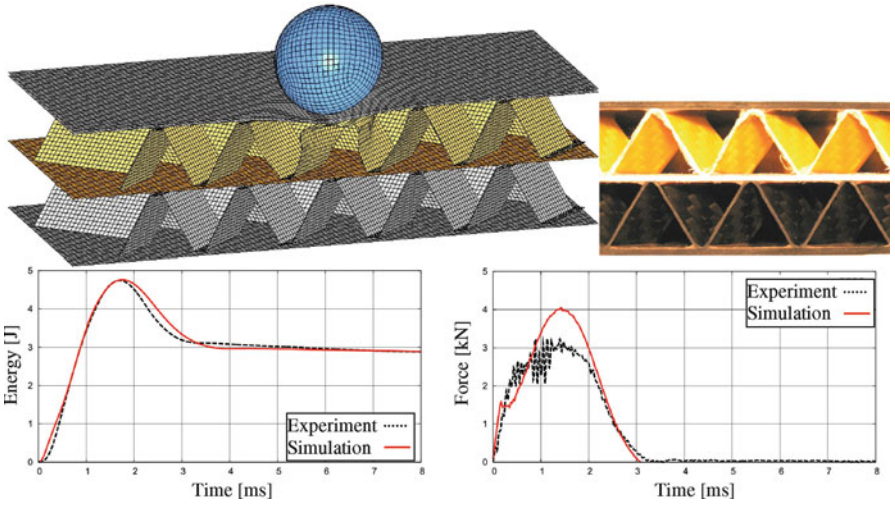


Fig. 31 Cell wall deformations, energy and force plot for 5 J impact on type E foldcore

deformation. The energy curves match almost exactly, some minor differences in the peak value of the force plot are visible, which result from too plastic skin behaviour.

For the 30 J impact the skin and core damage is much higher. The number of eroded elements in Fig. 32 is therefore also higher. For the single-core configuration type D the energy curves match quite well, but again the force peaks resulting from skin failure are not captured correctly. The same is true for the dual-core specimen

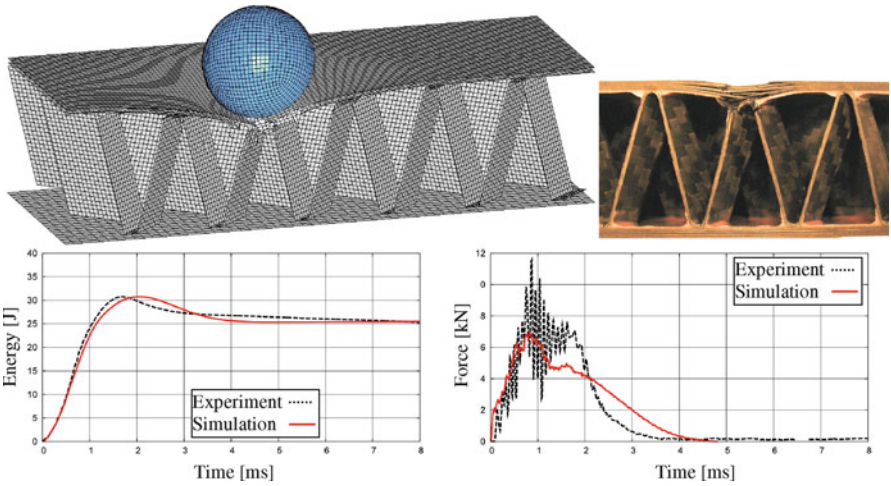


Fig. 32 Cell wall deformations, energy and force plot for 30 J impact on type D foldcore

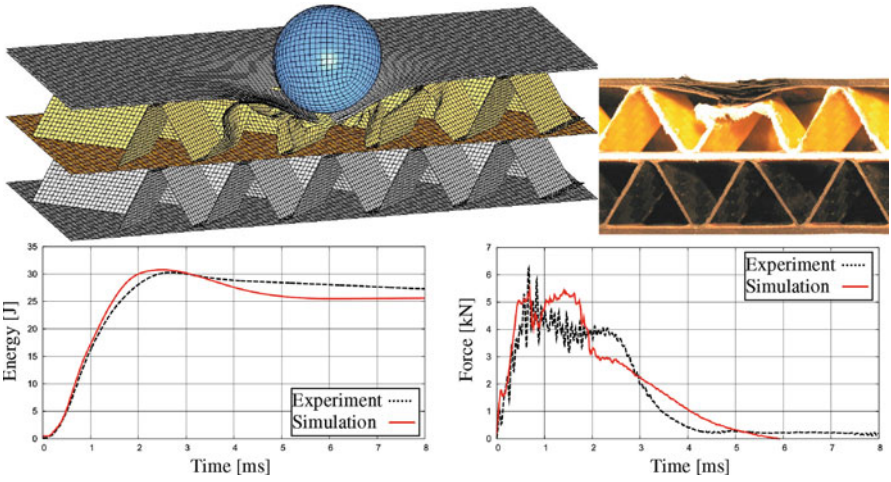


Fig. 33 Cell wall deformations, energy and force plot for 30 J impact on type E foldcore

in Fig. 33. The core behaviour is represented with a high degree of accuracy, the differences in the curves mainly arise from the skin behaviour, which is slightly too plastic in the simulation. However, making the skins more brittle leads to earlier element erosion and the impactor penetrates deeper, which also influences the core behaviour.

The maximum penetration depth during the 60 J impact on the single-core sandwich plate type D is almost equal in simulation and experiment (Fig. 34). However, some differences arise in the failure pattern of the upper skin, which lead

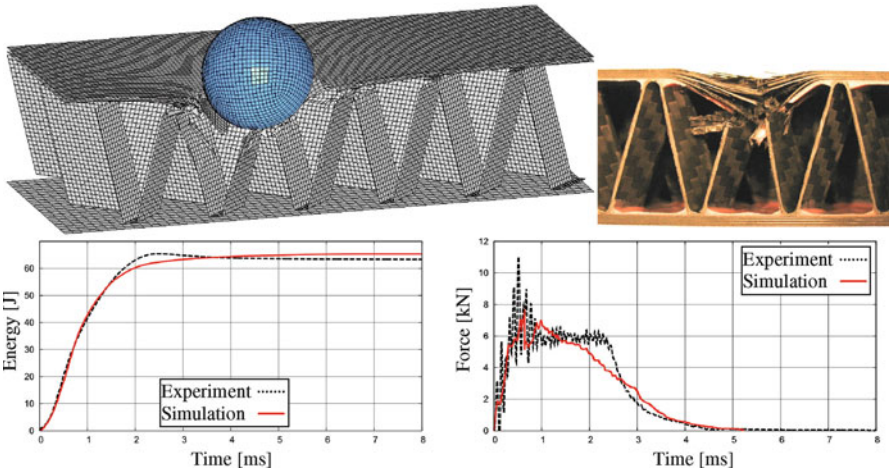


Fig. 34 Cell wall deformations, energy and force plot for 60 J impact on type D foldcore

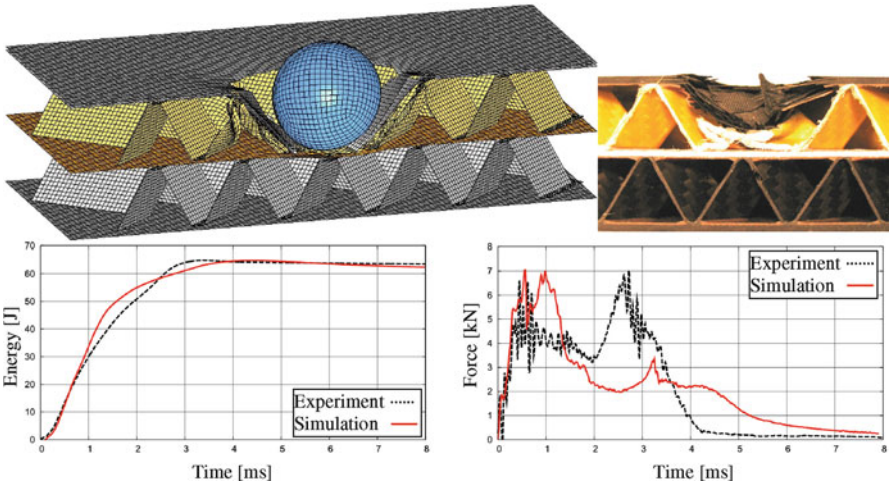


Fig. 35 Cell wall deformations, energy and force plot for 60 J impact on type E foldcore

to the early drop in the force curve, although the correlation in the first phase is very good. The increase of the force level after 3 ms is due to the friction between the impactor and the skin fragments. This situation is very similar for the dual-core specimen type E in Fig. 35 with some differences especially in the force plot. However, the overall correlation and the visual deformation behaviour can be represented to a good extent.

In summary, the qualitative correlation of the damage pattern and the indentation depth appear to be very good. Also the force and energy curves of most simulations

are consistent, although the expectation of a perfect correlation would not be justifiable due to the high complexity of the models and potential imperfections in the structure. One major issue in the simulation models is element erosion. On the one hand, it is necessary to delete failed elements at a certain point to generate cracks and to avoid severe mesh distortions that would reduce the explicit time step and would make the results inaccurate. On the other hand, the deletion of an element does not correspond to reality, as in the real structure the failed material is still existent, eventually just as fragments, interacting under friction with the impactor and the sandwich structure. Therefore, certain differences especially in the diagrams are inevitable. However, the general correlation can be judged as very satisfactory, making these models useful for parameter studies and their extension for HVI simulations.

6.4 Simulation of High Velocity Impact

The HVI simulations shown here are limited to the steel cube impactor, which was modelled as a rigid body with an initial velocity according to the experiments. The model of the sandwich structure was identical to the LVI simulations, except the connection of skin and core. Since skin-core debonding occurred in the test, a tiebreak contact interface with failure option was used for the connection of skin and core elements in the simulation model to allow for debonding.

Unlike in the LVI case, no force or energy data for a quantitative correlation of test and simulation are available, as their measurement was not possible in the HVI test. But this makes the evaluation of the numerical results especially helpful, as it allows for the analysis of data that are not available from the experiments.

This is shown in Figs. 36 and 37 for the two examples of a rebounding impactor on type D and a penetrating impactor in a type E foldcore model. First of all, the correlation of the damage pattern compared to the cross-sections of the real specimens is very good in both cases. A small amount of core damage occurs in Fig. 36 and the upper skin and middle layer are penetrated in Fig. 37 with a crushed carbon foldcore. The area of skin material that is separated by the impactor matches exactly the surface of the cube in experiment and simulation. The large area of skin-core debonding that is also visible in the cross-section in Fig. 37, is covered well by the simulation model.

Interesting is the evaluation of the impactor's kinetic energy plot in the simulation, as it allows to quantify, how much energy is absorbed by penetrating through the skin or by crushing the foldcore. Especially in Fig. 37 it can be seen that the skins absorb much more energy as for example the compression of the aramid foldcore between points (b) and (c). Almost all of the initial kinetic energy is absorbed by the sandwich structure, only a small amount is returned as elastic spring-back. This example shows the advantages of such numerical models in the detailed evaluation of result data, which are not available from the experimental tests.

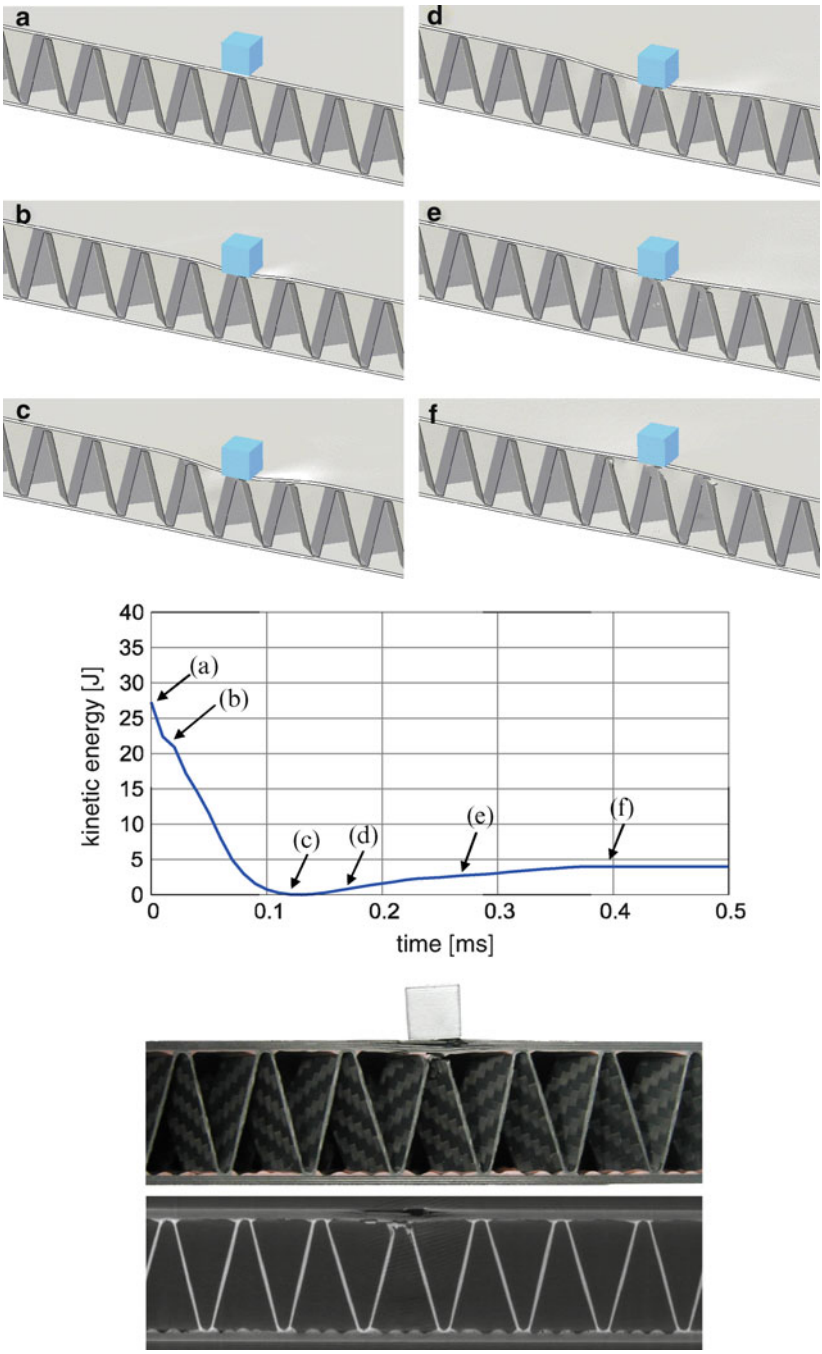


Fig. 36 High velocity impact simulation on type D sandwich structure with 64 m/s (27 J): deformation plots, kinetic energy curve of impactor and cross-section/micro-CT scan

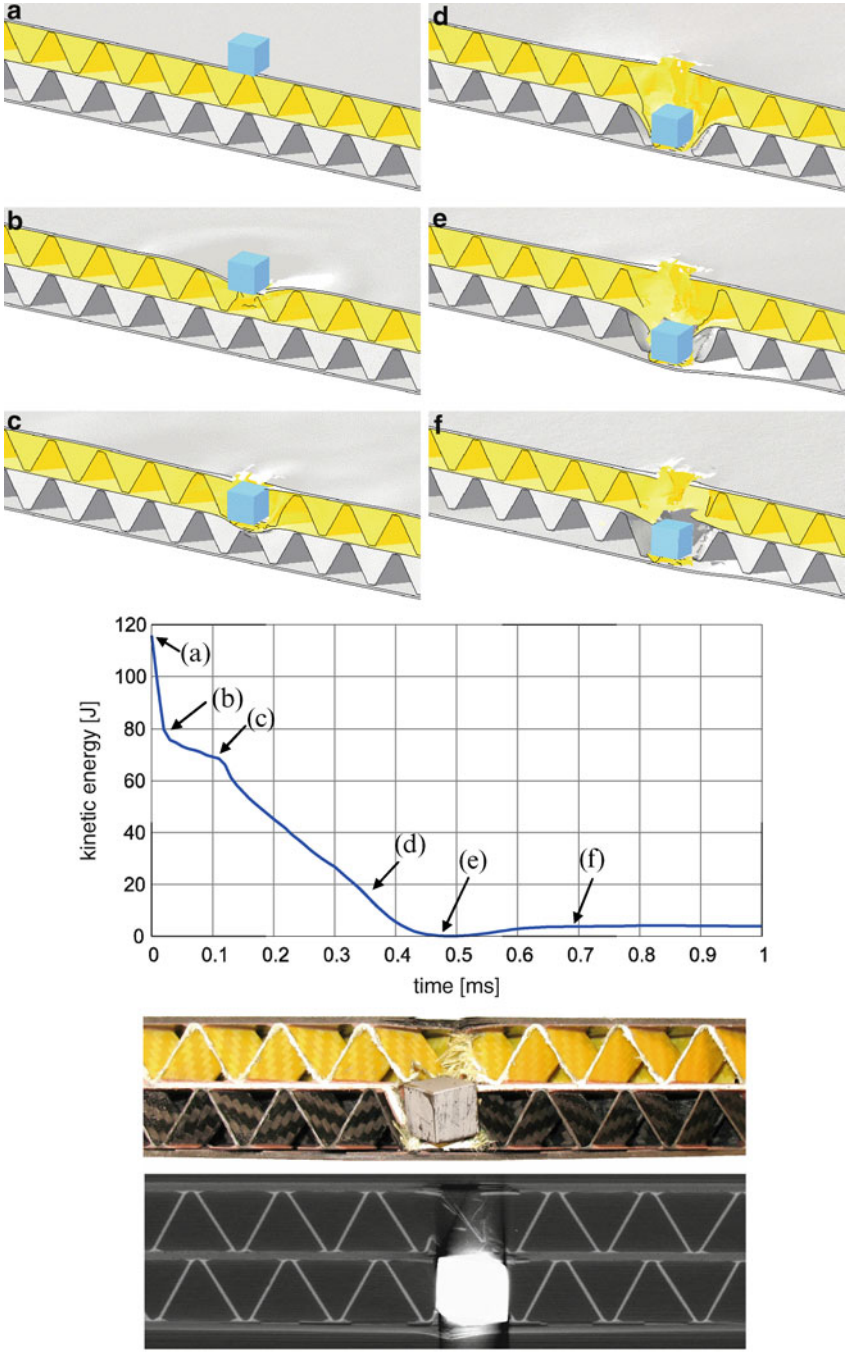


Fig. 37 High velocity impact simulation on type E sandwich structure with 132 m/s (117 J): deformation plots, kinetic energy curve of impactor and cross-section/micro-CT scan

7 Foldcore Applications

This chapter has shown how much work has been performed in the last years in order to identify suitable manufacturing methods for foldcore structure, to characterise their mechanical behaviour and to optimise their geometry for specific applications. The driver of these studies often were specific industrial needs. Starting from few relevant applications, numerous possible applications for foldcore structures have been identified in the meantime.

One major driver for these developments was the aircraft industry. Airbus has investigated foldcore sandwich structures on a research level for a long time as a potential candidate for an aircraft sandwich fuselage, where honeycomb is not applicable due to the water ingression issue [11, 103, 104, 121–132]. Curved foldcore structures are especially interesting for this fuselage application. Besides the sandwich fuselage, further applications for foldcore sandwich structures in the aircraft environment involve control surfaces with wedge-shaped core [19], in cargo compartment lining elements [133] and in sound-absorbing structures in the crew rest compartment [32]. For this purpose, the foldcore is modified by filling it with resin and rock flour. Also multi-layer sandwich configurations were proposed for acoustical decoupling. The soundproof characteristics of foldcore for sound insulation purposes using dual-core concepts were also investigated in [34]. The foldcore density and height were identified as the parameters affecting the soundproof characteristics the most. Another sound-absorbing application in an aircraft engine nacelle is proposed in [134].

Further applications include structural sandwich panels for civil engineering with heat- and sound-insulating properties [133] or panels for warehouse roofs, interior walls, bridges, or replacements for concrete decks [39]. Several papers propose the use of foldcore for filter elements [32, 39, 134]. Numerous further potential applications of foldcore structures are listed in [39], including shock-absorbing applications e.g. for air drop, packaging, automobile body structures, bumpers, hoods, crash-protecting car doors and highway crash barriers.

8 Conclusions

This chapter gave an overview on the research that has been conducted on foldcore sandwich structures over the last decades with an extensive literature overview and a focus on the impact performance of composite foldcore structures. It was shown that significant achievements were made in the field of efficient manufacturing processes, mechanical characterisation and analytical as well as numerical methods for the prediction of the properties. Foldcore structures are a core family that offer open cells for ventilation and the possibility to be folded from many different materials into arbitrary three-dimensional geometries without the need of

machining. The geometry or local reinforcements can be tailored to be suitable for specific applications.

This study was based on composite foldcores that offer even higher weight-specific mechanical properties than Nomex honeycomb cores of comparable density. The mechanical behaviour of such unidirectional and textile-reinforced composite foldcores with carbon/epoxy skins under compression, shear and impact loads was evaluated both experimentally and numerically. While foldcores made of woven aramid fibres show a rather ductile behaviour, carbon foldcores with their brittle nature absorb energy by crushing. Although the skins absorb most of the energy in the impact load case, the high stiffness of the foldcores lead to a very localised impact damage, since global bending of the skins is impeded. The stiff zigzag structure even acts like a delamination stopper. The carbon foldcore cells were locally crushed or fragmented under impact load, the ductile aramid foldcore cells were bent or folded.

In addition to regular single-core sandwich structures, a dual-core configuration with two foldcores and an aramid composite middle layer was also investigated, showing the potential of a two-phase energy absorption behaviour, which can be tailored by the choice of the constituents and the variation of the geometrical configuration. Confirming existing results in the literature, this multi-core configuration can lead to a beneficial impact performance in terms of absorbable impact energy and residual strength, but further research needs to be conducted in this direction.

Dynamic finite element simulations with LS-Dyna have shown to be an efficient tool in the development of such innovative structures that exhibit large design flexibility in terms of possible core geometries and materials. Although these models show a high degree of complexity due to the various skin/core failure modes that have to be captured, the results correlate well with experimental data, allowing for efficient parameter studies or detailed evaluations of damage patterns and energy absorption mechanisms.

Acknowledgments Part of this work has been performed within the framework of the EU FP6 project CELPACT. Sincere thanks are given to those who contributed either on the experimental or numerical side, i.e. Alastair Johnson and Sebastian Kilchert from DLR, Michael Klaus from RWTH, Torben Mehrens, Nikolai Voll, Christa Hampf and Jörg Cichosz from EADS.

References

1. Heimbs S (2008) Sandwichstrukturen mit Wabenkern: Experimentelle und numerische Analyse des Schädigungsverhaltens unter statischer und kurzzeitdynamischer Belastung. Dissertation, Technische Universität Kaiserslautern
2. Miura K (1972) Zeta-core sandwich – its concept and realization. ISAS Report 480, Institute of Space and Aeronautical Science, University of Tokyo
3. Rapp EG (1960) Sandwich-type structural element. US Patent 2,963,128
4. Miura K (1975) New structural form of sandwich core. J Aircraft 12:437–441
5. Hunt JF (2004) 3D structural panels: a literature review. In: Proceedings of the 7th Pacific Rim Bio-based composites symposium, vol II, Nanjing

6. Lebée A (2010) Thick periodic plates homogenization, application to sandwich panels including chevron folded core. Dissertation, Université Paris-Est
7. Khaliulin VI, Batrakov VV (2005) Technological schemes of zigzag crimp shaping. Izvestiya VUZ – Aviatsionnaya Tekhnika 48:68–73
8. Schenk M, Allwood JM, Guest SD (2011) Cold gas-pressure folding of miura-ori sheets. In: International conference on technology of plasticity (ICTP 2011), Aachen
9. Nojima T, Saito K (2006) Development of newly designed ultra-light core structures. JSME Int J A 49:38–42
10. Khaliulin VI, Batrakov VV, Menyashkin DG (2007) On structural and manufacturing capabilities of folded structures for use in sandwich panels. In: SAMPE Europe international conference, Paris, pp 141–148
11. Klett Y, Drechsler K, Kolax M, Wentzel H, Kehrle R (2007) Design of multifunctional folded core structures for aerospace sandwich applications. In: 1st CEAS European air and space conference, Deutscher Luft- und Raumfahrtkongress, Berlin, pp 903–908
12. Zakirov IM, Alexeev KA (2006) New folded structures for sandwich panels. In: SAMPE 2006, Long Beach, CA
13. Zakirov IM, Nikitin A, Alexeev K, Mudra C (2006) Folded structures: performance, technology and production. In: SAMPE Europe international conference, Paris, pp 234–239
14. Khaliulin VI (2005) A technique for synthesizing the structures of folded cores of sandwich panels. Izvestiya VUZ – Aviatsionnaya Tekhnika 48:7–12
15. Khaliulin VI (2003) Classification of regular row-arranged folded structures. Izvestiya VUZ – Aviatsionnaya Tekhnika 46:7–12
16. Khaliulin VI (1995) Geometrical modelling at synthesis of structures for folded fillers of multi-layer panels. Vestnik of KSTU 1:31–40
17. Drechsler K, Kehrle R (2004) Manufacturing of folded core-structures for technical applications. In: SAMPE Europe international conference, Paris, pp 508–513
18. Zakirov IM, Alekseyev KA (2005) Determination of four-beam spiral folded structure parameters. Izvestiya VUZ – Aviatsionnaya Tekhnika 48:57–61
19. Hähnel F, Wolf K, Hauffe A, Alekseev KA, Zakirov IM (2011) Wedge-shaped folded sandwich cores for aircraft applications: from design and manufacturing process to experimental structure validation. CEAS Aeronaut J. doi:10.1007/s13272-011-0014-8
20. Zakirov IM, Alekseev KA, Wolf K, Hähnel F (2010) Issues of design and manufacture of wedge-shaped folded cores. Modern technologies and materials – a key part in the revival of the domestic aviation industry. In: Proceedings of the international scientific-practical conference, vol 2, Kazan, pp 110–119
21. Fischer S, Drechsler K (2008) Aluminium foldcores for sandwich structure application. In: CELLMET2008, cellular metals for structural and functional applications, international symposium, Dresden
22. Khaliulin VI, Dvoyeglazov IV (2000) Experimental equipment for isometric shaping of thin-walled relief structures. In: Machine tools, automation and robotics in mechanical engineering, International Congress, Praha, pp 68–74
23. Fischer S, Drechsler K, Kilchert S, Johnson A (2009) Mechanical tests for foldcore base material properties. Composites A 40:1941–1952
24. Grzeschik M, Fischer S, Drechsler K (2009) Potential of high performance foldcores made out of PEEK polymer. In: SAMPE Europe technical conference, Bristol, pp 94–101
25. Grzeschik M, Drechsler K (2010) Experimental studies on folded cores. In: 9th international conference on dandwich structures, ICSS-9, Pasadena, CA
26. Heimbs S, Cichosz J, Klaus M, Kilchert S, Johnson AF (2010) Sandwich structures with textile-reinforced composite foldcores under impact loads. Compos Struct 92:1485–1497
27. Fischer S, Heimbs S, Kilchert S, Klaus M, Cluzel C (2009) Sandwich structures with folded core: manufacturing and mechanical behaviour. In: SAMPE Europe international conference, Paris
28. Basily BB, Elsayed EA (2004) Dynamic axial crushing of multi-layer core structures of folded chevron patterns. Int J Mater Prod Technol 21:169–185

29. Basily BB, Elsayed EA (2005) Design and development of lightweight sandwich structures with innovative sheet folded cores. Working papers, Department of Industrial and Systems Engineering, Rutgers University
30. Mudra C, Hachenberg D (2003) Alternative sandwich core structures – efficient investigation of application potential by using finite element modelling. In: SAMPE Europe international conference, Paris, 444–448
31. Zakirov IM, Alekseev KA, Kayumov RA, Gainutdinov IR (2009) Some possible techniques for improving the strength characteristics of folded cores from sheet composite materials. Russian Aeronaut (Iz VUZ) 52:347–350
32. Endres G, Luinge H, Meer T, Miletic A, Redmann D, Grzeschik M, Kehrle R, Klett Y, Wurzel R, Stierlen P, Wank M, Reiter K (2010) Innovative Faltstrukturen für Kernverbunde. Final report, BMBF-Project
33. Cichosz J (2009) Simulation des Impact-Verhaltens von Sandwichstrukturen mit Faltwabenkern. Diploma thesis, University of Stuttgart
34. Wang ZJ, Xu QH (2006) Experimental research on soundproof characteristics for the sandwich plates with folded core. J Vib Eng 19:65–69
35. Khaliulin VI, Dvoyeglazov IV (2001) On technological problems of fabrication of relief designs by isometric transformations of thin sheet. Trans Nanjing Univ Aeronaut Astronaut 18:11–16
36. Zakirov IM, Alekseyev KA (2004) Shaping of folded single-curvature cores. In: Proceedings of the all-union scientific-practical conference on aerospace technologies and equipment, Kazan, pp 5–9
37. Elsayed EA, Basily BB (2003) A continuous folding process for sheet materials. In: ICPR-17, conference proceedings, Blacksburg, VA
38. Zakirov IM, Nikitin A, Akishev N, Rückert C, Mudra C (2005) Technology research and equipment development for fabrication of folded structure sandwich core from new material. In: SAMPE Europe International Conference, Paris, pp 429–434
39. Elsayed EA, Basily BB (2004) A continuous folding process for sheet materials. Int J Mater Prod Technol 21:217–238
40. Zakirov IM, Alekseev KA (2007) Parameters of a creasing-bending machine as applied to the scheme of transverse rotary shaping of chevron structures. Russian Aeronaut (Iz VUZ) 50:186–192
41. Rosskamp S (2008) Integration von Befestigungselementen in Kernverbundbauteile und Charakterisierung des Versagensverhaltens. Diploma thesis, Universität Bremen
42. Weeks CA, Sun CT (1994) Multi-core composite laminates. J Adv Mater 25:28–37
43. Schenk M, Guest SD (2009) Folded textured sheets. In: Proceedings of the International Association for Shell and Spatial Structures (IASS) symposium 2009, Valencia
44. Schenk M, Guest SD (2010) Origami aolding: a structural engineering approach. In: Proceedings of the 5th international conference on origami in science, mathematics and education, Singapore
45. Drechsler K, Middendorf P, Van Den Broucke B, Heimbs S (2008) Advanced composite materials – technologies, performance and modelling. In: Guedra Degeorges D, Ladeveze P (eds) Course on emerging techniques for damage prediction and failure analysis of laminated composite structures. Cepadues Editions, Toulouse, pp 147–197
46. Heimbs S, Middendorf P, Kilchert S, Johnson AF, Maier M (2007) Numerical simulation of advanced folded core materials for structural sandwich applications. In: CEAS 2007, 1st European air and space conference, Deutscher Luft- und Raumfahrt Kongress, Berlin, pp 2889–2896
47. Hauffe A (2007) Theoretische/Numerische Bestimmung des CAI-Verhaltens von CFK-Sandwich. Report ILR-LFT/CR07-03/1, Technische Universität Dresden
48. Heimbs S, Middendorf P, Kilchert S, Johnson AF, Maier M (2007) Experimental and numerical analysis of composite folded sandwich core structures in compression. Appl Compos Mater 14:363–377

49. Cluzel C, Baranger E, Dorival O, Razzouck F (2011) Modelling and multiscale experimental identification of an origami-like sandwich core. JNC 17, 17èmes Journées Nationales sur les Composites, Poitiers
50. Heimbs S, Middendorf P, Hampf C, Hähnel F, Wolf K (2008) Aircraft sandwich structures with folded core under impact load. In: 8th international conference on sandwich structures (ICSS-8), Porto, pp 369–380
51. Fischer S, Grzeschik M, Drechsler K (2009) Experimental and numerical parameter study of foldcores. In: SAMPE Europe technical conference, Bristol, 2009
52. Foray PO (2011) Untersuchung der Energieabsorptionseigenschaften verschiedener zellulärer Kernstrukturen. Diploma thesis, Technische Universität München
53. Heimbs S, Schmeer S, Middendorf P, Maier M (2007) Strain rate effects in phenolic composites and phenolic-impregnated honeycomb structures. Compos Sci Technol 67: 2827–2837
54. Kazemahvazi S, Kiele J, Russell B, Deshpande V, Zenkert D (2010) Impact properties of corrugated composite sandwich cores. In: 9th international conference on sandwich structures (ICSS-9), Pasadena, CA
55. Mamalis AG, Yuan YB, Viegelahn GL (1992) Collapse of thin-walled composite sections subjected to high speed axial loading. Int J Vehicle Des 13:564–579
56. Thornton PH, Harwood JJ, Beardmore P (1985) Fiber-reinforced plastic composites for energy absorption purposes. Compos Sci Technol 24:275–298
57. Thornton PH (1979) Energy absorption in composite structures. J Compos Mater 13:247–262
58. Newill JF, Vinson JR (1993) Some high strain rate effects on composite materials. In: 9th international conference on composite materials (ICCM-9), Madrid, part 5, pp 269–277
59. Kawata K, Hashimoto S, Takeda N (1982) Mechanical behaviours in high velocity tension of composites. In: Progress in science and engineering of composites (ICCM-4), Tokyo, pp 861–870
60. Heimbs S, Middendorf P, Hampf C, Hähnel F, Wolf K (2009) Aircraft sandwich structures with folded core under impact load. Compos Solut Aero&Space 3:7–13
61. Kintscher M, Kärger L (2006) Versagen von Faltwaben- und Honigwabenkernen unter kombinierter Druck-Schub-Belastung. Report 131-2006/07, DLR Braunschweig, Institut für Faserverbundleichtbau und Adaptronik
62. Hartung D, Kintscher M, Kärger L, Wetzel A (2006) Stiffness and failure behaviour of folded sandwich cores under combined transverse shear and compression. In: CompTest 2006, composites testing and model identification, Porto
63. Kintscher M, Kärger L, Wetzel A, Hartung D (2007) Stiffness and failure behaviour of folded sandwich cores under combined transverse shear and compression. Composites A 38:1288–1295
64. Kehrle R (2006) 4-Punkt-Biegeversuch von Faltwaben-Sandwichstrukturen. Report, EMIR Project, IFB Stuttgart
65. Klaus M, Reimerdes HG (2009) Residual strength simulations of sandwich panels after impact. In: 17th international conference on composite materials (ICCM-17), Edinburgh
66. Baranger E, Cluzel C, Razzouk El Mohammadi F (2010) A multilevel approach for the prediction of skin/core debonding of foldcore sandwich structures. In: 14th European conference on composite materials (ECCM-14), Budapest
67. Khaliulin VI, Mardanova GN (1996) Construction of different configurations of light filler of z-corrugation type. Vestnik of KSTU 2:12–18
68. Kling DH (1997) Doubly periodic flat surfaces in three-space. Dissertation, Rutgers State University of New Jersey
69. Kayumov RA, Zakirov IM, Alekseev KP, Alekseev KA, Zinnurov RA (2007) Determination of load-carrying capacity in panels with chevron-type cores. Russian Aeronaut (Iz VUZ) 50:357–361
70. Voll N (2007) Charakterisierung und Optimierung von Wabenkernen für Sandwichstrukturen mit Hilfe der Finite-Elemente-Methode. Diploma thesis, Technische Universität Darmstadt

71. Zakirov IM, Katayev YP, Nikitin AV (2004) Folded-plate structures alteration when bent. Sci Tech J 'Polyot' ('Flight') 2:50–53
72. Lebee A, Sab K (2009) Transverse shear stiffness of a chevron folded core used in sandwich construction. In: JNC16, 16èmes Journées Nationales sur les Composites, Toulouse
73. Lebee A, Sab K (2010) Reissner-Mindlin shear moduli of a sandwich panel with periodic core material. In: Maugin GA, Metrikine AV (eds) Mechanics of generalized continua, advances in mechanics and mathematics, vol 21. Springer, New York, pp 169–177
74. Abrate S (1998) Impact on composite structures. Cambridge University Press, Cambridge
75. Johnson A (2009) Novel structural core sandwich materials for aircraft applications: CELPACT project overview. In: SAMPE Europe international conference, Paris
76. Engineering of multifunctional integrated CFRP structures – EMIR (2003–2007), Project Luftfahrtforschungsprogramm III, 20W0301A, Airbus Deutschland GmbH
77. Hampf C (2007) Experimentelle Ermittlung und numerische Simulation des mechanischen Verhaltens von Sandwichstrukturen mit Faltwabenkern unter Impactbelastung. Diploma thesis, Technische Universität Dresden
78. Labeas G, Johnson A, Mines R, Klaus M, Siviour C (2009) The impact performance of sandwich structures with innovative cellular metal and folded composite cores. In SAMPE Europe international conference, Paris
79. Kilchert S, Johnson AF, Voggenreiter H (2009) Modelling the impact behaviour of sandwich structures with folded composite cores. In: 15th international conference on composite structures (ICCS-15), Porto
80. Johnson AF, Kilchert S (2010) Modelling impact damage in sandwich structures with folded composite cores. In: 4th European conference on computational mechanics, ECCM 2010, Paris
81. Ullmann T, Jemmali R, Voggenreiter H (2008) Bauteiltest: 3D-Analyse prüft Vorhersagen von Simulationsmodellen. Konstruktion 5:12–14
82. Hähnel F, Weiße J (2007) Experimentelle Bestimmung des CAI-Verhaltens von CFK-Sandwich. Report ILR-LFT/CR07-02, Part 1, Technische Universität Dresden
83. Klaus M, Reimerdes HG (2010) Influence of delaminations in sandwich skins on residual strength after impact simulations. In: 9th international conference on sandwich structures (ICSS-9), Pasadena, CA
84. Weiße J, Hähnel F, Hauffe A, Wolf K (2008) Simulation des Impactverhaltens von CFK-Sandwichpanels unter Vorlast. In: 7th German LS-Dyna Forum, Bamberg
85. Heimbs S, Cichosz J, Kilchert S, Klaus M (2009) Sandwich panels with cellular cores made of folded composite material: mechanical behaviour and impact performance. In: 17th international conference on composite materials (ICCM-17), Edinburgh
86. Heimbs S (2011) Impact on sandwich structures with folded core. In: Workshop on dynamic failure of composite and sandwich structures, Toulouse, pp 141–144
87. Wachinger G, Angerer E, Middendorf P, Schouten M (2008) Impact protection structures for composite fuselage application. In: SAMPE Europe international conference, Paris, pp 271–277
88. Kilchert S, Johnson A, Reiter A, Jemmali R (2009) Gas gun impact tests on improved sandwich panels. Project report D32-5A/D33-2A, CELPACT, cellular structures for impact performance, EU FP7, Contract AST5-CT-2006-031038
89. Pentecote NT, Johnson AF, Ritt S, Voggenreiter H (2006) Impact-tolerante Leichtbaustrukturen. Konstruktion 9:19–21
90. Toso-Pentecote N, Johnson A (2007) Impact damage in sandwich composite structures from gas gun tests. In: Proceedings of the 13th international conference on experimental mechanics (ICEM13), Alexandroupolis
91. Heimbs S, Kilchert S, Fischer S, Klaus M, Baranger E (2009) Sandwich structures with folded core: mechanical modelling and impact simulations. In: SAMPE Europe international conference, Paris
92. Heimbs S (2009) Virtual testing of sandwich core structures using dynamic finite element simulations. Comp Mater Sci 45:205–216

93. Heimbs S (2008) Virtual testing of sandwich core structures with LS-Dyna. In: 26th CADFEM users' meeting, Darmstadt
94. Hachenberg D, Mudra C, Nguyen M (2003) Folded structures – an alternative sandwich core material for future aircraft concepts. Deutscher Luft- und Raumfahrt Kongress, Munich, pp 165–174
95. Nguyen MQ, Jacombs SS, Thomson RS, Hachenberg D, Scott ML (2005) Simulation of impact on sandwich structures. Compos Struct 67:217–227
96. Streubig M, Wolf K (2007) SAND-MESHplus – a parameter controlled finite element pre-processor for composite sandwich structures. In: 1st CEAS European air and space conference, Deutscher Luft- und Raumfahrtkongress, Berlin, pp 2227–2232
97. Tsujii Y, Tanaka K, Nishida Y (1995) Analysis of mechanical properties of aramid honeycomb core. Trans Jpn Soc Mech Eng 61:1608–1614
98. Foo CC, Chai GB, Seah LK (2007) Mechanical properties of Nomex material and Nomex honeycomb structure. Compos Struct 80:588–594
99. Baranger E, Cluzel C, Guidault PA (2011) Modelling of the behaviour of aramid folded cores up to global crushing. Strain 47:170–178
100. Fischer S, Drechsler K, Kilchert S, Johnson A (2008) Mechanical tests for foldcore base material properties. In: CompTest 2008, composite testing & model identification, Dayton, OH
101. Kilchert S, Johnson AF, Voggenreiter H (2008) Finite element modelling of phenolic resin impregnated aramid paper adopted in foldcore sandwich cores. In: Ninth international conference on computational structures technology (CST 2008), Athens
102. Zakirov IM, Alekseev KA, Movchan GV (2008) Influence of coating thickness on geometric parameters of a chevron core. Russian Aeronaut (Iz VUZ) 51:326–329
103. Mehrens T (2006) Simulation eines CFK-Sandwichrumpfes unter hochdynamischer Belastung. Diploma thesis, Hochschule für Angewandte Wissenschaften Hamburg
104. Heimbs S, Mehrens T, Middendorf P, Maier M, Schumacher A (2007) Numerical determination of the nonlinear effective mechanical properties of folded core structures for aircraft sandwich panels. In: 6th European LS-Dyna users conference, Gothenburg
105. Baranger E, Guidault PA, Cluzel C (2011) Numerical modelling of the geometrical defects of an origami-like sandwich core. Compos Struct 93:2504–2510
106. Baranger E, Cluzel C, Guidault PA, Allix O (2009) Modelling of the behaviour of aramid folded cores up to global crushing. In: 17th international conference on composite materials (ICCM-17), Edinburgh
107. Baranger E, Guidaut PA, Cluzel C (2010) A multiscale approach for the prediction of crushing of a folded core sandwich structure. In: 9th international conference on sandwich structures (ICSS-9), Pasadena, CA
108. Johnson AF, Pentecôte N (2005) Modelling impact damage in double-walled composite structures. In: Proceedings of the 8th international conference on computational plasticity (COMPLAS VIII), Barcelona
109. Johnson AF (2008) Novel hybrid structural core sandwich materials for aircraft applications. In: 11th Euro-Japanese symposium on composite materials, Porto
110. Fischer S, Drechsler K (2009) FE-simulation of foldcores made out of resin impregnated aramid fiber paper. In: SAMPE Europe international conference, Paris, pp 48–55
111. Heimbs S (2009) Eigenschaftsbestimmung zellulärer Wabenkernstrukturen anhand virtueller Tests. CADFEM Infoplaner 1:50–52
112. Bender B, Fischer S, Drechsler K (2011) Optimizing a foldcore concerning density specific stiffness properties. In: SAMPE Europe international conference, Paris
113. Kärger L (2004) Efficient impact damage prediction of composite sandwich structures. In: FENet technology workshop, Glasgow
114. Tessmer J, Kärger L, Wetzel A (2006) Simulation innovativer Sandwichbauteile. In: 12th national SAMPE symposium, Braunschweig
115. Mudra C (2002) Bestimmung mechanischer Eigenschaften von faserverstärkten Faltwaben unter Verwendung der Methode der finiten Elemente. Diploma thesis, Technische Universität Dresden

116. Klaus M, Reimerdes HG (2010) Numerical investigation of different strength after impact test procedures. In: Proceedings of the IMPLAST 2010 conference, Providence, RI
117. Matzenmiller A, Lubliner J, Taylor RL (1995) A constitutive model for anisotropic damage in fiber-composites. Mech Mater 20:125–152
118. Schweizerhof K, Weimar K, Münz T, Rottner T (1998) Crashworthiness analysis with enhanced composite material models in LS-DYNA – merits and limits. In: 5th international LS-DYNA users conference, Southfield, MI
119. Chang FK, Chang KY (1987) A progressive damage model for laminated composites containing stress concentrations. J Compos Mater 21:834–855
120. Borg R, Nilsson L, Simonsson K (2001) Simulation of delamination in fiber composites with a discrete cohesive failure model. Compos Sci Technol 61:667–677
121. Rückert C (2001) Der CFK-Rumpf – Anforderungen an Werkstoffe und Verfahren aus innovativen Bauweisen. Deutscher Luft- und Raumfahrtkongress, Hamburg, pp 277–280
122. Kupke M, Rückert C, Hachenberg D, Dolzinski WD, Kolax M (2002) Der CFK-Rumpf – Ergebnisse aus Bauweisenkonzeption und Wissenserwerb. Deutscher Luft- und Raumfahrtkongress, Stuttgart
123. Radmann T (2003) Fertigungstechnologien für CFK-Rumpfschalen. Deutscher Luft- und Raumfahrtkongress, Munich
124. Rückert C (2003) Validierung von Bauweisen für einen CFK-Rumpf – Werkstoff und Verfahrensauswahl. Deutscher Luft- und Raumfahrtkongress, Munich
125. Kupke M, Kolax M (2003) CFK-Rumpf: Zukunftssicherung mit Verbundwerkstoffen. Deutscher Luft- und Raumfahrtkongress, Munich
126. Kolax M (2003) Fortschrittliche Rumpfstrukturen aus Faserverbundwerkstoffen. Final report TN-ESD2-1209-1/2003, Luftfahrtforschungsprogramm, project 'CFK-Rumpf'
127. Rückert C (2004) Double skin composite fuselage design – materials & process approaches for test article realisation. In: SAMPE Europe international conference, Paris, pp 438–443
128. Kolax M (2004) Concept and technology: advanced composite fuselage structures. JEC Compos 10:31–33
129. Kupke M, Kolax M (2004) CFRP-fuselage – ensuring future competitiveness. In: SAMPE Europe international conference, Paris, pp 432–437
130. Kolesnikov BY, Herbeck L (2004) Carbon fiber composite airplane fuselage: concept and analysis. In: ILA international conference 'Merging the efforts: Russia in European research programs on aeronautics', Berlin
131. Kehrle R, Kolax M (2006) Sandwich structures for advanced next generation fuselage concepts. In: SAMPE Europe technical conference, Toulouse, pp 11–16
132. Drechsler K, Kehrle R, Klett Y, Thorsteinsson E (2006) Faltwabenkerne für multifunktionale Leichtbaustrukturen. In 2nd Materialica Composites-Congress 'Composites in automotive & aerospace', Munich
133. Zakirov IM, Alexeev KA (2008) Sandwich panels featuring chevron cores for airframe and building structures – properties and technology thereof. In: SAMPE Europe international conference, Paris, pp 201–205
134. Khaliulin VI, Batrakov VV (2004) Sound-absorbing structures and elements of folded structure filters. In: Proceedings of the all-union scientific-practical conference on aerospace technologies and equipment, Kazan, pp 115–117

Experimental and Numerical Study of Normal and Oblique Impacts on Helicopter Blades

J. Aubry, P. Navarro, I. Tawk, S. Marguet, J.F. Ferrero, S. Lemaire, and P. Rauch

Abstract This study is concerned with the understanding, analysis, and prediction of major damage mechanisms in helicopter blade components subjected to a high velocity impact load. Two types of impact are studied: the frontal impact, which corresponds to a normal impact on the leading edge, and the oblique impact on the skin of the lower surface of the blade.

Several tests are performed to identify the parameters that control the response of the structure and the chronology of damage development.

Dynamic finite element models of the phenomena observed experimentally are proposed. To overcome the problems related to the size of the modeled structure, original modeling strategies are developed to accurately represent the damage observed. The calculated impact behavior and amount of damage are validated by comparison with experimental test results.

1 Introduction

The objective of this work is to develop robust and efficient modeling capabilities for dynamic analysis of helicopter composite blades subjected to high-velocity impacts. The capabilities are focused on the understanding, analysis, and prediction of major

J. Aubry • P. Navarro (✉)
Université de Toulouse, ICA, ISAE, 10 Av E. Belin, 31055 Toulouse Cedex, France
e-mail: pablo.navarro@isae.fr

I. Tawk
University of Balamand – Deir El-Balamand, El-Koura, Lebanon

S. Marguet • J.F. Ferrero
Université de Toulouse/ICA/UPS, 118 Rte de Narbonne, 31062 Toulouse, France

S. Lemaire • P. Rauch
Eurocopter Marignane/ETMB–Aéroport Marseille P, 13725 Marignane, France

S. Abrate et al. (eds.), *Dynamic Failure of Composite and Sandwich Structures*,
Solid Mechanics and Its Applications 192, DOI 10.1007/978-94-007-5329-7_12,
© Springer Science+Business Media Dordrecht 2013

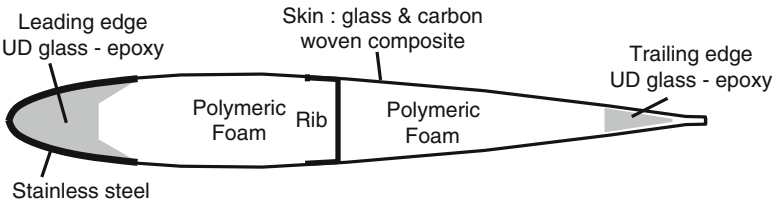


Fig. 1 Schematic section of the specimens and materials used

damage mechanisms in blade components. Due to a significant difference in the type of damage caused, two impact modes are addressed in this chapter: normal impact to the leading edge and oblique impact on the skin of the lower surface of the blade. In both cases, the approach is the same. At first an experimental study is performed. Analysis of the results allows the identification of the parameters that control the damage mechanisms. In a second step, a numerical model is developed. The modeling strategy is deduced from experimental observations.

Helicopter blades are large complex composite structures that operate in a severe dynamic environment. Typically, a blade is made up of a main spar with unidirectional glass-epoxy composite in the leading edge, a skin generally made of two or three plies of glass-epoxy and (or) carbon-epoxy woven fabrics, a polyurethane foam core, a glass-epoxy unidirectional composite trailing edge and a protection made of stainless steel that covers the leading edge. One or more composite carbon-epoxy ribs stabilize the skins (Fig. 1).

The impacting bodies can be birds, hailstones, small metal parts or other soft or hard bodies. The impact velocity is driven by the rotation of blades and is of the order of several hundred of meters per second.

A large number of research articles are available on impact and damage modeling, failure of composite laminates and sandwich composites. A comprehensive review by Abrate [1–3] discusses impact failure mechanisms and summarizes impact modeling approaches, based mainly on analytical models. Recent advances in understanding damage mechanisms of laminated composite [4–9] coupled with the development of the performance and capability of computers, offer the possibility of avoiding many experimental tests by using impact simulation. They must, in addition, be validated by experimental tests [10].

Very limited literature exists on the damage analysis of helicopter rotor blades. However, different approaches can be distinguished. Some works seek to develop a process capable of determining whether a critical impact has occurred, estimating the impact location, and quantifying impact amplitude, all while in-flight. Many methods for impact and, more generally, force identification have been developed over the years. Using physics-based or data-driven models, inverse methods are used to detect and locate loads and damage. Using a least squares method, Lui and Shepard [11] reproduce dynamic forces based on reconstructed frequency response

data. Many algorithms that are used for impact or damage identification require that extensive numbers of sensors be used. Modal-based damage location and detection techniques are investigated using several strain gauges on a beam by Kiddy and Pines [12]. An excellent review of localization and quantification of external impact loading on a structure is carried out by Inoue, Harrigan, and Reid [13].

Other works seek to develop analytical or F.E.M. models. Morozov et al. [14] study the impact damage tolerance of laminated composite helicopter blades using a simplified blade geometry. The effect of the projectile size on the damage tolerance of a composite blade is investigated and tolerable sizes of the defects estimated. Pawar and Ganguli [15–17] treat the helicopter blade as a thin walled composite beam taking into account transverse shear effect, elastic couplings and restrained warping. They study the effect of damage modes such as matrix cracking, debonding, and fiber breakage on the blade's response.

Recently Kumar et al. [18, 19] have studied low velocity impact loads and post impact behavior for ballistic impacts on the side of the blade. A general computational approach is developed to understand and quantify the effect of damage in composite rotor blades on their structural integrity. The approach is based on a multi-scale, non-linear finite element analysis (FEA) to capture the complexity of blade designs and to provide efficient engineering solutions.

Despite the diversity of the existing works, a predictive modeling of in-flight impacts on a representative blade is missing. Thus, the present study focuses on the understanding and the modeling of high velocity impacts on the leading edge and on the skin of the lower surface of the blade. Impact tests on structures similar to blade sections are performed. They are carried out with a steel ball for a wide range of speeds. An analysis of the specimens after impact is performed. This allows a greater understanding of the mechanisms of observable damage after a frontal or an oblique impact on a structure, as well as the identification of the various ruptures and kinematics of damage. A methodology of calculation that could be used by industry is proposed. It represents the phenomena observed experimentally and relies on a multi scale approach. The numerical model predicts the impact behavior of the blade, the amount of damage and the damage mechanisms. It is validated by comparison with experimental results.

2 Normal Impacts

Section 2 focuses on the study of normal impacts which correspond to a frontal impact on the leading edge as defined in Fig. 2.

Firstly, the experimental approach is developed. Various tests are carried out and analyzed to understand the damage mechanisms. Secondly, a numerical model is carried out to predict the damage induced by a normal impact on a blade.

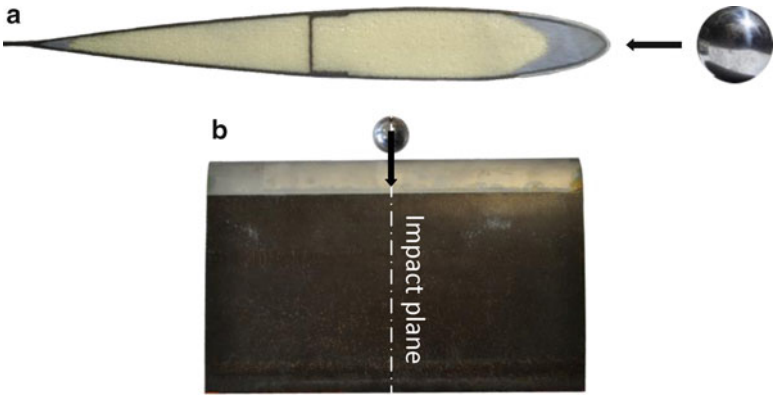


Fig. 2 Normal impact: *side view* (**a**) and *top view*, (**b**) of the blade and of the impactor

2.1 Experimental Study

As shown in Fig. 1, the studied specimens are composed of a main spar with unidirectional glass-epoxy, a skin, a rib with hybrid composite glass-epoxy and carbon-epoxy woven plies, a polyurethane foam core, and a 0.4 mm thick protective stainless steel leading edge. The skin is made up of three plies, a glass fabric oriented at 0°/90° and two carbon fabrics oriented at ±45°. The matrix is an epoxy resin. The length of the specimen is 378.2 mm, with a maximum thickness of 22 mm. The tests are conducted using a gas gun.

The projectiles are 30 mm diameter steel balls weighing 110 g. These steel balls are stabilized inside the gas gun by a polyurethane foam support. The impact speed is regulated by the control of the gas pressure. The specimen is positioned inside a safety box. It is placed directly in front of the end of the gun in a specific device (Fig. 3). It is free to move backwards during the impact.

A Fastcam Photron high speed camera is used to record the moment of the impact. The recording speed used is 30,000 fps (frames per second). The analysis of the photographs obtained with the high speed camera during the test is used to define the behavior of the blade and the damage mechanisms during the impact.

The photographs in Fig. 4 present the impact test for a specimen impacted with 550 J. The interval between two images is 66.6 μs. The projectile impacts the specimen and penetrates into the front edge (pictures 1–3). The local flexure of the stainless steel and the composite skin forms a wave at the impact point. This wave spreads up to the rib and propagates along the entire length of the specimen (pictures 4–8). Its propagation varies with the impact energy and corresponds to the separation of the skin from the foam. The wave arrives at the edges of the blade in 0.5 ms. Then, the specimen starts moving backward (picture 9). The observed bending of the front edge decreases after 0.5 ms due to the elastic recovery of the structure (pictures 9–15). The experimental tests carried out allow an understanding of the observable degradations on the test specimens after impact.

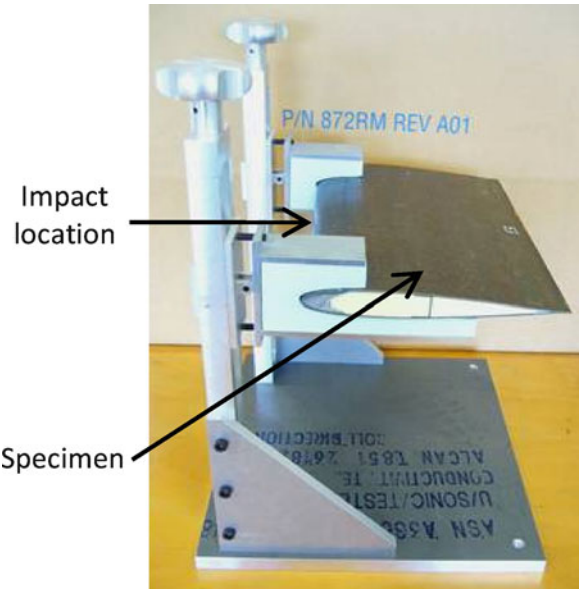


Fig. 3 Device supporting the specimen for a normal impact

Table 1 summarizes the impact characteristics and the energy balance established: impact energy (initial kinetic energy of the projectile), residual kinetic energy of the specimen, residual kinetic energy of the ball, and energy absorbed by the specimen. The energy absorbed by the specimen during the impact varies between 71 and 76% of the energy provided by the projectile. The duration of the contact between the projectile and the specimen ranges from 0.15 to 2.35 ms.

The depth of the residual deformation of the front edge is measured with a three-dimensional measurement machine (DEA-Hexagon Metrology). These measurements give the depth versus the impact energy (Fig. 5).

The behavior is quasi linear for all tests. To quantify the area of debonding between the skin and the foam, the tapping method is used on the two faces of the test specimens. The tapping method allows localization of areas of debonding in bonded assemblies. The principle is simple. It is to strike the considered surface with an acrylic head hammer at a constant interval. The response time or "bounce time" to physical shock depends on the stiffness of the material and it varies in the presence of defects. The detection of areas of delamination or defects is done through a comparison with the response obtained on a healthy area. Figure 6 shows the evolution of the delaminated area as the impact energy increases. The debonding surface increases linearly until it reaches the rib.

To analyze the internal damage of the structure, the test specimens are stabilized by inclusion in a resin, then cut every 10 mm parallel to the plane of symmetry of the specimen. The observation of the sections in the impact plane allows the determination of the damage induced.

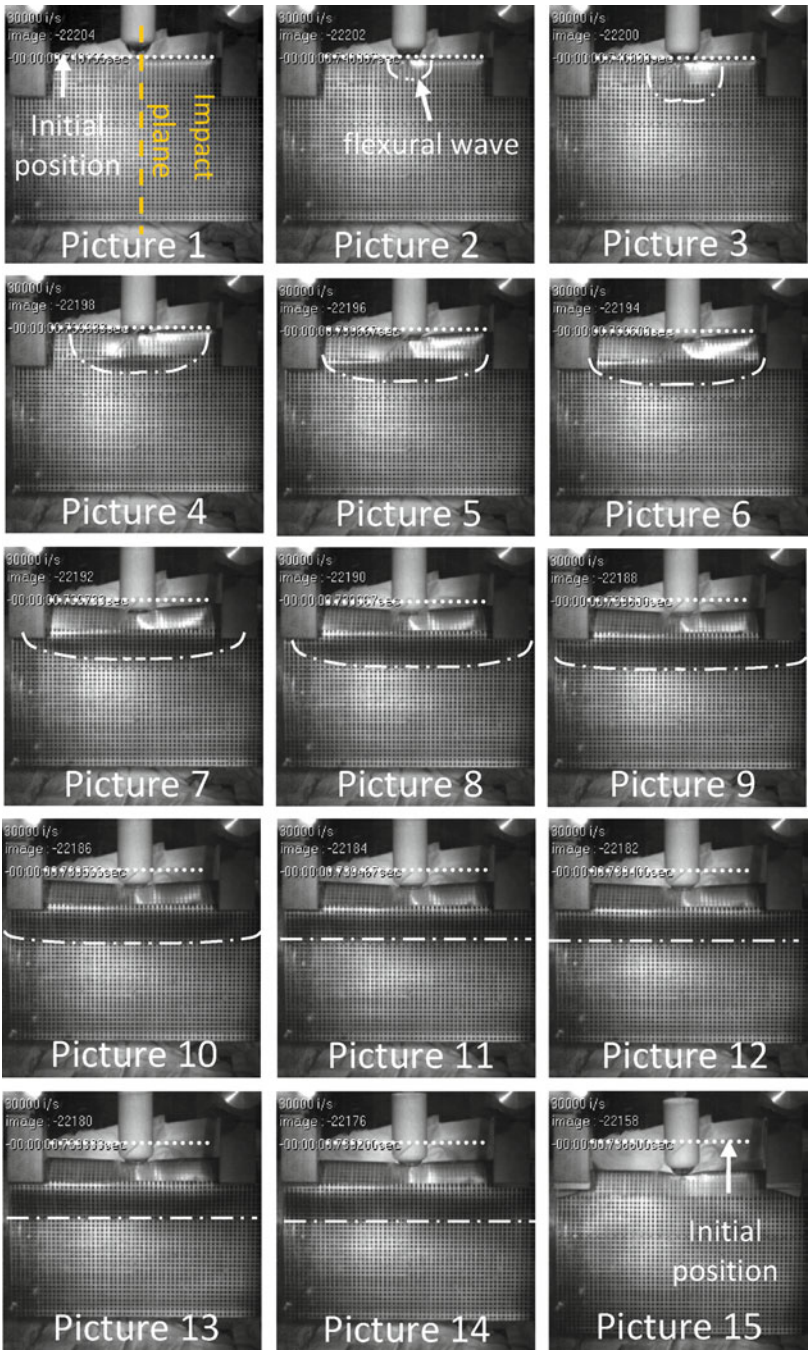


Fig. 4 *Top view* of a frontal impact at 550 J ($\Delta t = 66.6$ μs between each snapshot)

Table 1 Characteristics of normal impact tests

Mass of specimen (g)	Mass of projectile (g)	Impact speed (m/s) Impact Energy (J)	Residual kinetic energy of the specimen (J)	Residual kinetic energy of the ball (J)	Energy absorbed (%)
437.7	121.3	18.34	5.47	0	73.2
		20.42			
440.9	124.6	49.52	41.91	0	72
		152.77			
440	122.7	62.02	58.45	0.3	75
		235.98			
431.6	121.5	70.71	84.8	2.2	72.8
		303.74			
421	122.4	94.45	126.35	8.24	75.4
		545.95			
431	121	119	194.6	9.6	76
		855			
439.2	121.7	128	279	7.6	71.2
		997			
440.4	121	137	830.1	8.8	73.4
		1,144			

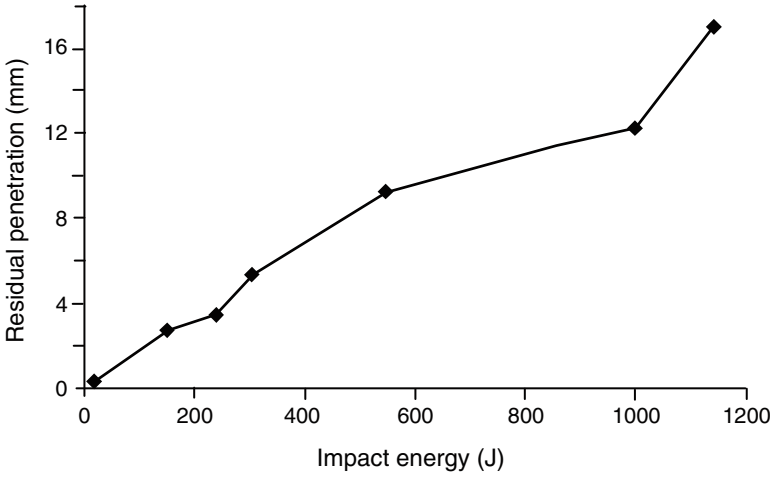


Fig. 5 Residual penetration in the leading edge versus impact energy

Figure 7 shows the cross section at the impact plane for different energy levels and a zoom on the roving.

For an impact energy of 20 J (Fig. 7), the damage generated in the structure is limited to a light indentation of the stainless steel protection under the impact point. The roving fissures at the contact area of impact, for a relatively low energy level. The indentation depth in the leading edge increases with the speed of the projectile. This results in a plastic deformation of the stainless steel protection, as well as a greater degradation of the roving.

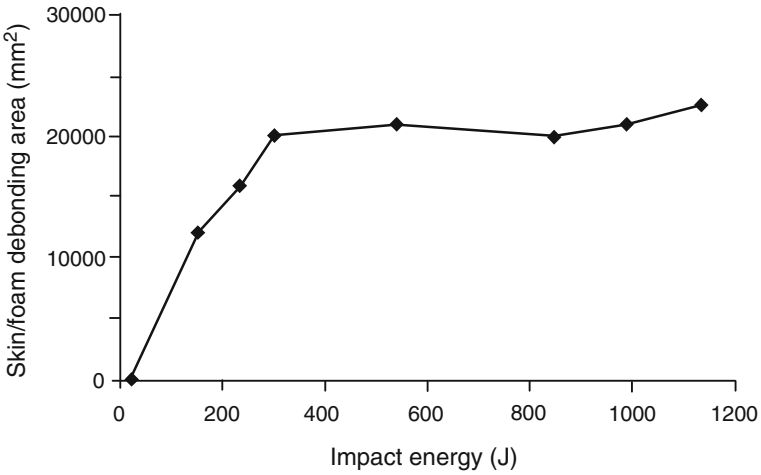


Fig. 6 Skin/foam debonding area versus impact energy

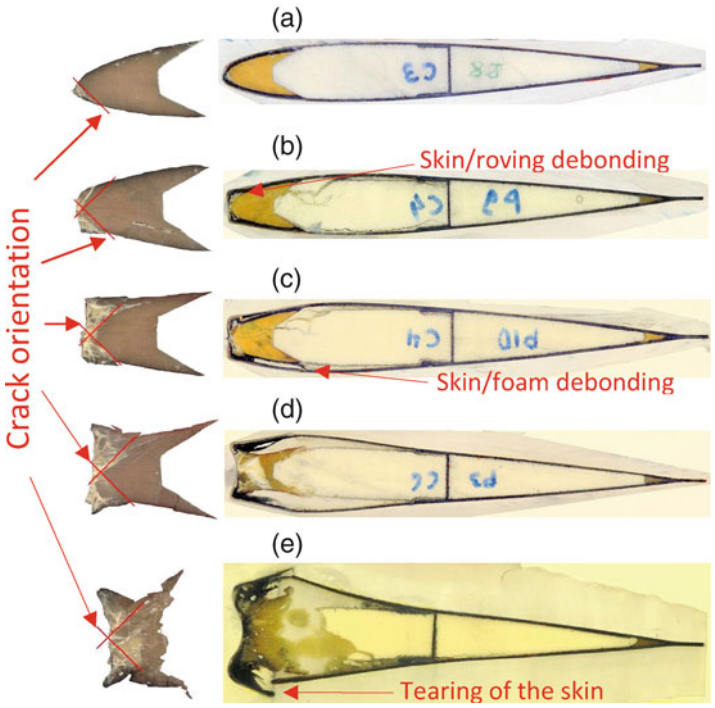


Fig. 7 Overview of cross sections in the plane of impact (**a**) 20 J, (**b**) 152 J, (**c**) 303 J, (**d**) 855 J, (**e**) 1,144 J

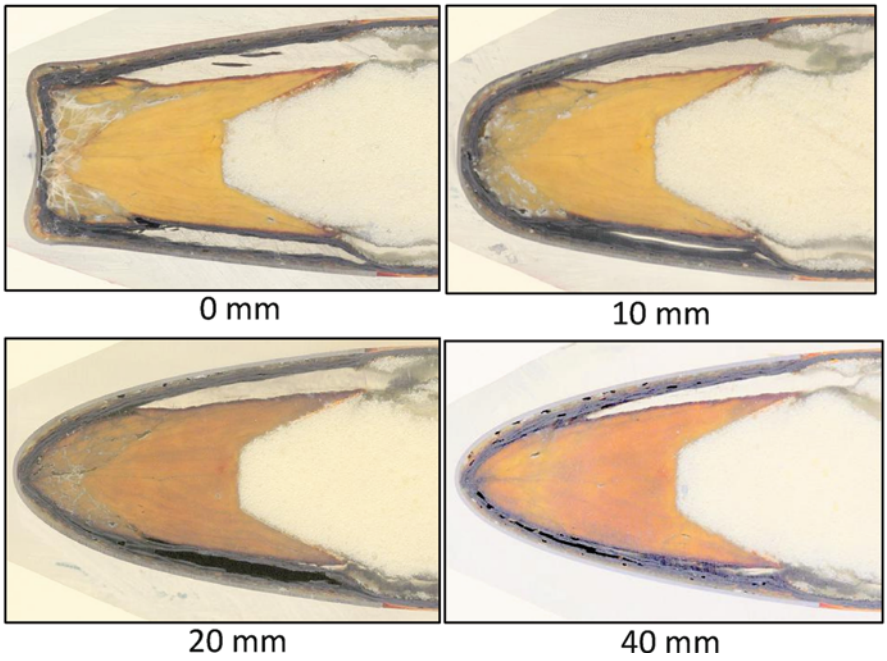


Fig. 8 Overview of roving sections located 0 −10 −20 et 40 mm from the impact plane (energy 303 J)

For an impact energy of 150 J, the cracks in the roving appear at 45° from the direction of impact (Fig. 7). The stainless steel opens and causes the debonding of the skin from the roving.

By increasing the impact velocity, the number of cracks in the resin increases while following an angle of 45° (Fig. 7). Packets of fibers thus move according to the direction of the cracks. This kinematics of displacement is found for all the impacted blades. The skin/roving separation spreads upwards to cause skin/foam separation. This phenomenon is due to the rupture of a small thickness of the foam bonded with the skin. It is necessary to reach an energy of 300 J to observe a separation between the stainless steel protection and the skin.

For an impact greater than 800 J (Fig. 7), local micro-fissuring of the resin and displacement of fiber packages located on the front of the spar are observed. More cracks appear on the rear area, which results in the complete rupture of the spar. The foam in contact with the spar is also severely damaged.

Figure 7 shows that for energies greater than 1,000 J, the skin is partly or completely torn in the zone located at the end of the stainless steel protection. Indeed, in this area, the skin undergoes a strong local curvature that lowers its strength.

The damage observed for roving sections located at 10, 20 and 40 mm from the plane of impact confirms these observations (Fig. 8). The degradation of the roving

in the form of micro-fissuring of the resin and rupture of the fiber plies keeps a local character limited to the zone located to the right of the impact point. Cracks and debonding propagates longitudinally and reaches the ends of the test specimens for a higher level of energy.

Various tests are carried out to analyze the influence of the components of the specimen's design on its resistance to a frontal impact and on the kinematics of the damage. Different stacking sequences of the skin and the design of the front edge as well as the rib are studied. The total geometry of the specimens, as well as the impactors, remains unchanged. The damage observed on the modified specimens is compared with that obtained in the tests carried out for the same impact energy, on the section of blade defined previously.

2.1.1 Influence of the Stacking Sequence

The influence of the removal of one ply of carbon fabric of the skin on the impact behavior is studied. A sample is built with a skin reinforced with one ply of glass fabric directed at 0°/90° and one ply of carbon fabric directed at ±45°. This test is carried out for an impact speed of 135 m/s and for an impact energy of 1,150 J.

The removal of a ply in the skin changes the behavior of the structure (Fig. 9). The sample is completely destroyed and separated into three pieces. The stainless steel protection is torn longitudinally at the point of impact, causing significant cracking of the resin and a rupture of the glass fiber. Damage to the front edge is significant, the skin being completely torn along the stainless protection and separated into two parts by the rupture of the rib-skin connection. The skin, made up of two fabric plies, tears in the zone located along the stainless steel protection. This is explained by the "S" shape of the skin as it passes under the stainless steel protection. An additional fabric ply provides an increase in the skin stiffness which prevents the tearing of the skin and preserves the integrity of the sample.

2.1.2 Influence of Front Edge

A sample with an entirely composite protection composed of three directed fabric carbon plies with 0°/90°, but no stainless steel protection, is tested (impact 360 J). The objective is to identify the role of protection in the kinematics of damage.

With a carbon fabric protection, the damage is located mainly at the point of impact (Fig. 10).

The impacted zone is significantly damaged. Around the point of impact, the plies constituting the protection, as well as the skin of the blade, are damaged and become detached from the structure causing the glass fibers to appear. Delamination of carbon fabric plies is observed. There is also a rupture of the glass fibers of the roving. The separation of the skin remains 30% weaker and is limited mainly to skin-foam separation.

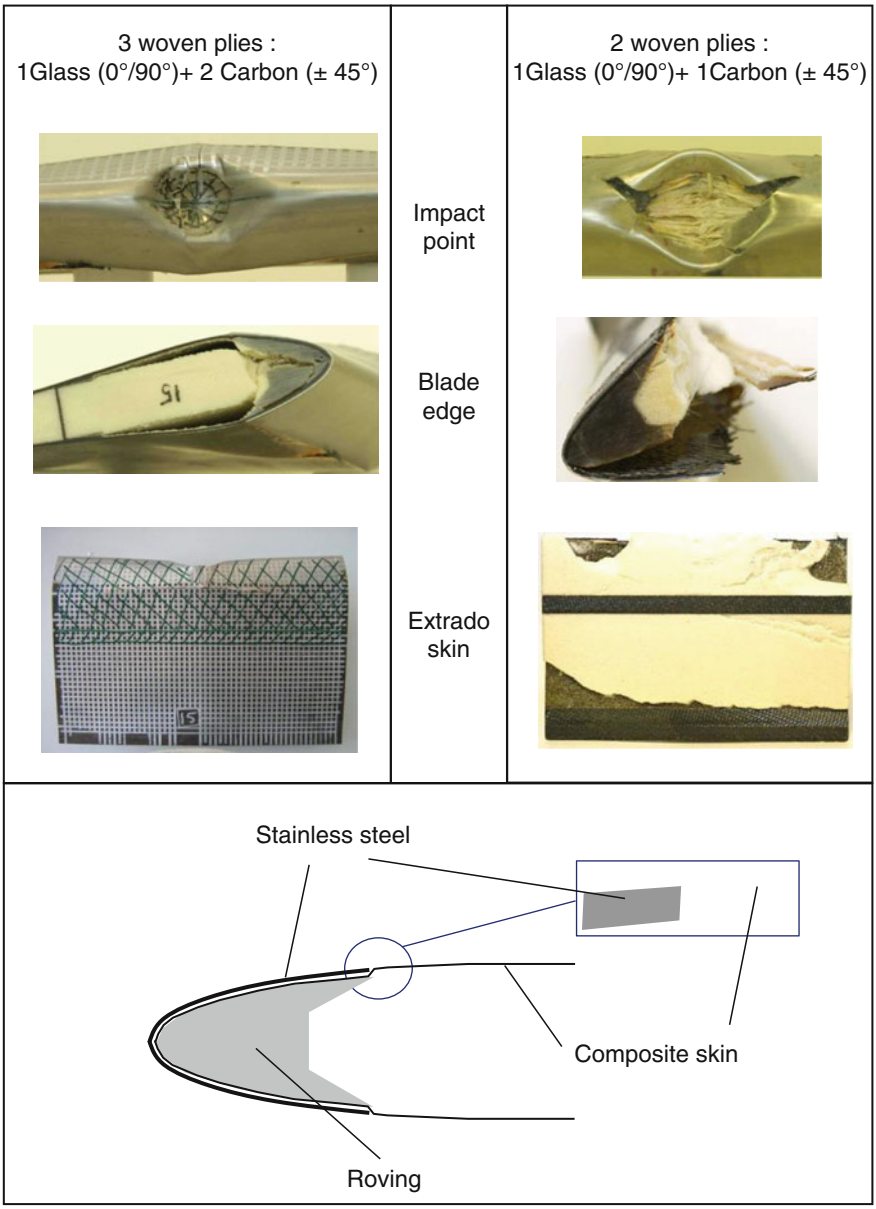


Fig. 9 Influence of the stacking sequence (Impact energy 1,150 J)

The analysis carried out on this test make it possible to identify the dominating role of the stainless steel protection in the damage mechanism. It partially protects the unidirectional fiber glass by absorbing part of the energy in plastic-deformation, but seems to cause skin-foam debonding. During the impact, the front edge becomes

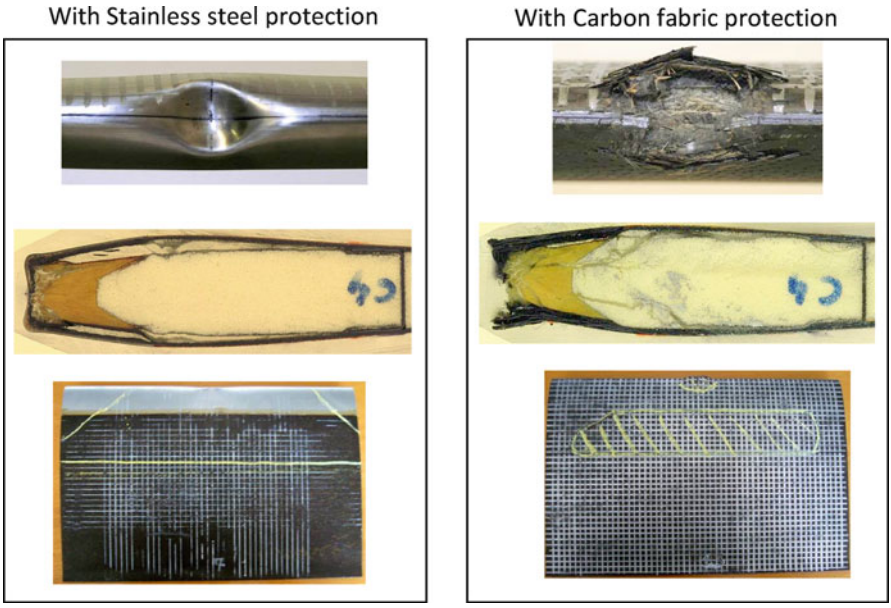


Fig. 10 Influence of front edge (impact 360 J)

deformed and swells, causing the detachment of the carbon skin from the roving. This displacement is controlled by the deformation of the stainless steel which also causes a more significant skin-foam debonding behind the front edge.

2.2 Numerical Model

F.E. model of impact on a blade structure is developed. It must be realistic in its representation of the physical phenomena observed in experiments for the whole blade. The difficulty results primarily in the compromise between mesh sizing and convergence/calculation time, which can be very prohibitive for the modeling of the complete blade. The complexity of the phenomena modeled and the different scales at which the phenomena of damage appear, require a very fine mesh and results in calculation times.

It is important to use effective modeling strategies at a macroscopic scale in order to model these phenomena without prohibitively fine mesh. This is implemented in the explicit code RADIOSS.

The impactor is modeled by a rigid body. The resin and the stainless steel protection are modeled by elastic–plastic properties with isotropic damage. The composite skin is modeled as a conventional orthotropic shell. The rupture criterion is based on a failure strain. The foam is modeled by a user law, which makes it possible to differentiate the compression and the traction behaviors. Three

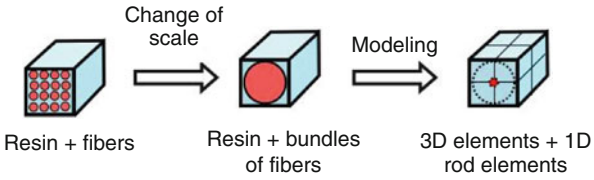


Fig. 11 Modeling strategy for the roving

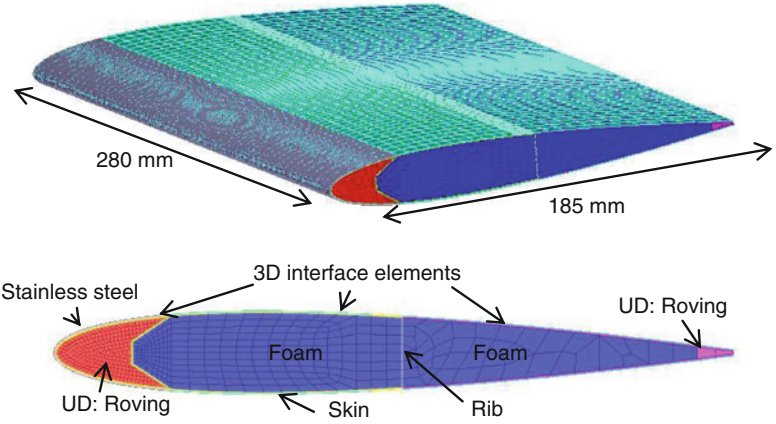


Fig. 12 principle of the modeling

dimensional specific elements are used to represent the debonding of the interface between the skin and the foam and between the stainless steel protection and the skin.

The main originality of the developed model is in the way the roving is modeled. The model must represent the damage of the resin and the decohesion of fibers and bundles of fibers. The fibers can be damaged or intact. The idea is to model the matrix using three dimensional elements and the bundles of fibers using unidimensional elements (Fig. 11). The diameter of the rods is 0.9 mm. It corresponds to the average diameter measured experimentally for the bundles of fibers. The fiber area represents 65% of the spar area which is the conventional percentage of fiber. The displacement of fibers is managed by the slipping and the contact between the unidimensional elements. An equivalent Young modulus of the glass fibers is obtained by applying the homogenization laws.

During an impact, the matrix is damaged independently. An elastic–plastic law, with damage, is used to model the resin. To correctly represent the quasi linear behavior until rupture of the fibers, a bilinear law with damage and strain rupture is defined. The definite numerical model (Fig. 12) is made up of 104,810 nodes, 53,408 solid elements, 8,819 shell elements and 20,509 bar elements. The dimensions are given Fig. 12. The definition of different interfaces allows the automatic management of the contacts.

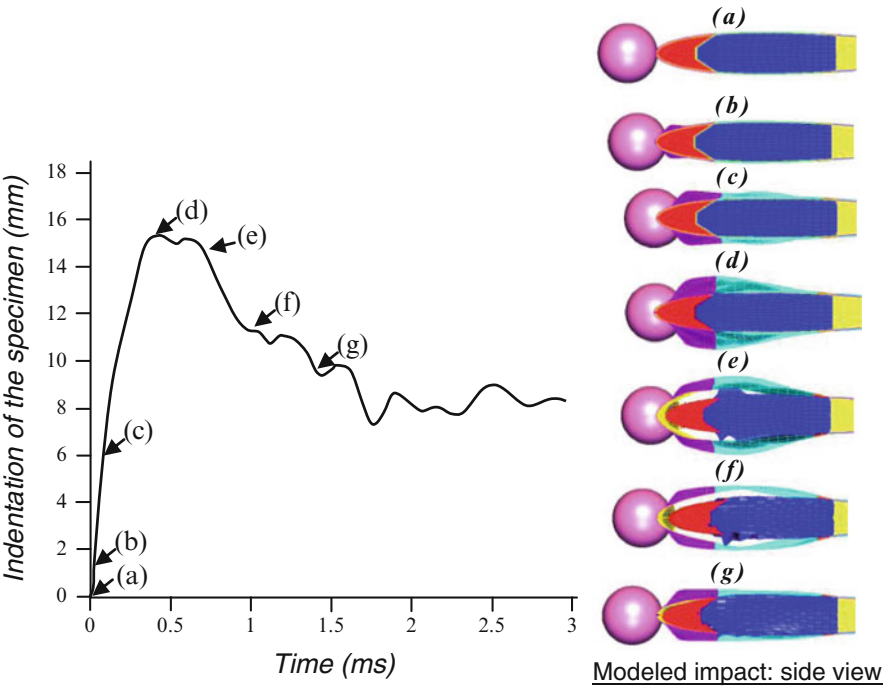


Fig. 13 Behavior of the blade during the impact (**a**) T = 0 ms, (**b**) T = 0.06 ms, (**c**) T = 0.16 ms, (**d**) T = 0.38 ms, (**e**) T = 0.68 ms, (**f**) T = 1 ms, (**g**) T = 1.4 ms

Figure 13 shows the behavior of the blade cross section during the impact for an energy of 550 J. The penetration of the front edge at the point of impact is represented on the curve as a function of time.

The image at t = 0.06 ms shows the bending of the stainless steel on the front edge caused by the contact with the steel ball. The amplitude of this deformation increases and a wave due to the flexure of the skin propagates in the direction of the impact and towards the two ends of the blade. This behavior involves a swelling of the structure and leads to delamination skin-roving and skin-foam.

On the curve, four zones can be observed. A first zone of load increasing during 0.35 ms, which corresponds to the local phase of damage. The penetration of the ball involves the rupture of the resin, the plastic deformation of the stainless steel and then, delamination between the skin and the roving which generates a swelling of the section. The maximum swelling is reached at approximately 0.38 ms. A second zone, where the penetration of the front edge stabilizes for a duration of 0.25 ms. During this time, delamination propagates throughout the area between the front edge and the rib. A third zone during the next 1 ms which represents the elastic recovery of the structure. A fourth zone where the blade takes its final form.

To validate the model, the results obtained numerically are compared with experimental measurements.

Figure 14 presents the speed of the blade after impact, the depth of penetration, the length of the residual deformation in the front edge, as well as the surface of delamination as a function of impact energy. The results obtained are rather close. The maximum relative error for the blade speed after impact is 8.48%, for an impact energy of 854 J (V = 119 m/s), 5.68% for the penetration in the front edge, 4% for the length of residual deformation of the front edge and finally, 7.5% for the delamination area.

The analysis of results obtained from the achieved model allows a greater understanding of the kinematics of the impact. These results show that the strategy used for the model is correct and that the model allows a good representation of the experimental ruptures for energy levels less than 1,000 J.

3 Oblique Impact

Section 3 focuses on the study of oblique impacts. This kind of impact is characterized by the angle of incidence of the impactor, generally between 10° and 20°, caused by the inclination of the blade in flight. Given the geometry of the impacted area, the blade can be assimilated to a sandwich structure made up of a foam core and a skin built up of two plies of woven glass/epoxy composite [20, 21].

3.1 Experimental Test

High velocity oblique impact tests are performed in order to identify the chronology of the damage mechanisms for the thin woven composite skin. These tests are carried out with an air gun. The impactor is a 19 mm diameter steel ball with a mass of 28 g. The impacted panels are composed of an aeronautical foam (Rohacell A51), and two skins of two plies of pre-impregnated glass/epoxy woven fabric (7781/913) oriented at 0–90° from the firing direction. Special attention is taken to balance the proportions of warp and weft fibers in each direction. The composite skin thickness is 0.7 mm. The material characteristics are shown in Table 2.

The specimens are square, 200 mm on each side and 20 mm thick. The sample is placed on a table tilted at 15° from the impact axis (Fig. 15). This value is chosen to reproduce the flight conditions of the helicopter blade. The impact velocity varies from 60 to 130 m/s, which corresponds to impact energies evolving from 50 to 230 J.

These tests show two states of damage to the woven skin depending on the impact energy (Fig. 16). The first state of damage is observed under the lowest impact energies (lower than 85 J). Micro cracking of the resin is visible using a scanning electron microscope, however, no failure of the bundles is observed. The impactor rebounds during the impact. The second level of damage, obtained for impact energies greater than 85 J, is characterized by the damage of the resin and the breakage of the fibers. For these energies, the impactor either rebounds or perforates

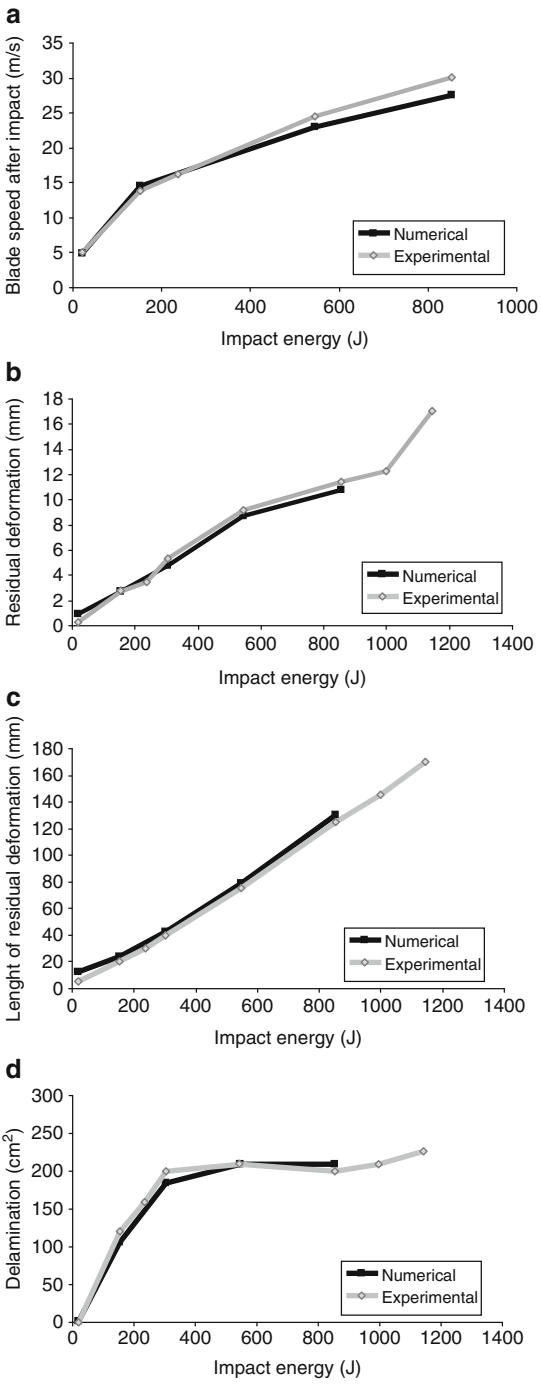


Fig. 14 Numerical/experimental comparison of (**a**) the blade speed after impact, (**b**) the residual deformation at the impact point, (**c**) the length of the residual deformation and (**d**) the delamination

Table 2 Characteristics of the materials

Woven fabric (7781/913)		Foam (Rohacell A51)	
Density (kg/m^3)	1,900	Density (kg/m^3)	52
Elastic modulus (MPa) $E_x = E_y$	17,000	Elastic modulus (MPa)	70
Shear modulus (MPa)	3,000	Shear modulus (MPa)	19
Poisson ratio	0.13	Compressive strength (MPa)	0.9
Tensile strain limit	0.025	Tensile strength (MPa)	1.9

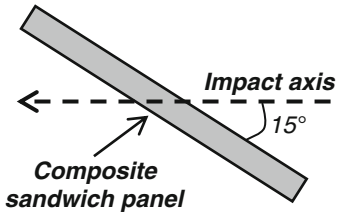


Fig. 15 Presentation of the oblique impact tests

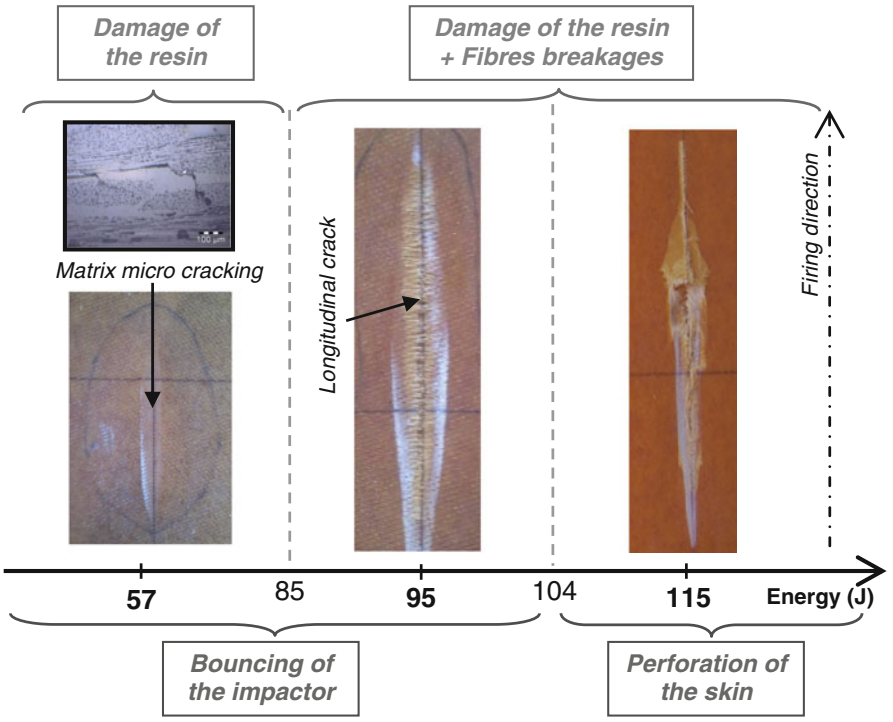


Fig. 16 Influence of the impact energy on the damage of the skin

the skin. If the steel ball rebounds, the resulting fracture surface can be seen as a longitudinal crack oriented along the firing axis. For a given configuration of the sample, the thresholds between these different states of the skin depends on the impact angle and on the mass and velocity of the impactor.

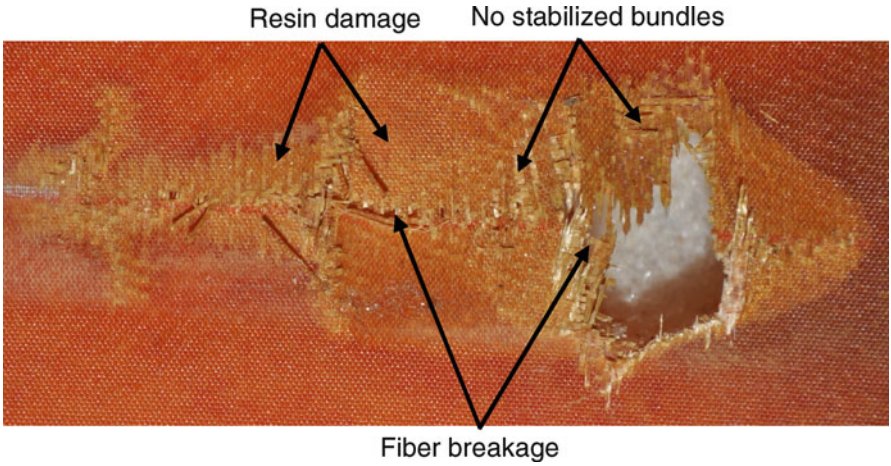
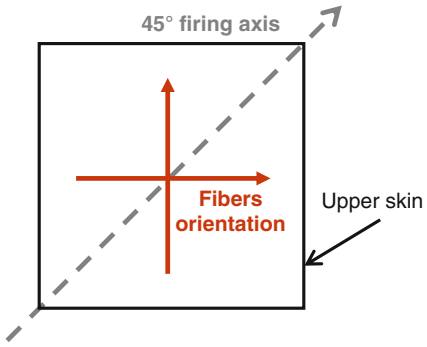


Fig. 17 Damage mechanisms of the woven skin

Fig. 18 Description of the 45° firing axis



The analysis of the test results brings to light the mechanisms of damage of the thin woven composite skin (Fig. 17). Firstly, the skin damage begins with the apparition of micro cracks in the matrix resin. Once the resin is totally damaged, the bundles, which are no longer stabilized, carry the whole load. Finally, when the strain in the fibers reaches the ultimate tensile strain, the fibers break and the skin tears. As the skin is made up of two woven composite layers, no delamination is observed.

Furthermore, a study of the influence of the orientation of the impact axis is carried out. Impact tests are performed for a firing axis orientation of 45° from the fiber orientation. As the skins are in woven composite, the fibers are oriented at both 0° and 90° (Fig. 18). The same impact energies in the previous tests are used; varied from 50 to 230 J.

For the lower energies only a micro-cracking of the resin is observed. No influence of the firing axis orientation on the type and on the level of the damage

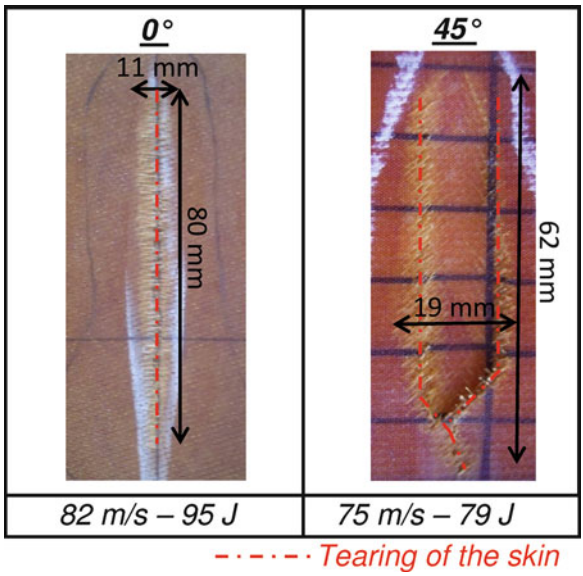


Fig. 19 Fracture surfaces and tearing energy thresholds

onset is noticed. Figure 19 shows the fracture surface of the skin, and the minimal value of the impact velocity which lead to the fiber breakage for an impact along the fibers, and oriented at 45° from the fibers.

The impact energy threshold necessary to tear the skin is 16% higher when the impact is along the fiber direction. For a firing axis oriented at 45°, the fracture surface is separated into two parts. In the area of the initiation of the tearing, the shape of the fracture can be seen as a "V". In the area of the propagation of the tearing, the presence of two lines of fiber breakage oriented in the direction of the trajectory of the projectile is observed. The resin located between these two cracks is damaged. Thus, the angle between the fibers orientation and the impact direction has an influence, firstly, on the shape of the fracture surface and, secondly, on the initiation threshold.

To optimize the oblique impact response of a helicopter blade, a study of the influence of the various parameters (materials and impact conditions) on the amount of damage must be carried out. Therefore, a numerical modeling is developed.

3.2 Numerical Model

3.2.1 Presentation and Formulation

A semi-continuous model for the thin woven composite blade skin is selected. It relies on the chronology identified experimentally. The idea is to build a model which can represent the behavior of the undamaged woven skin (a continuous

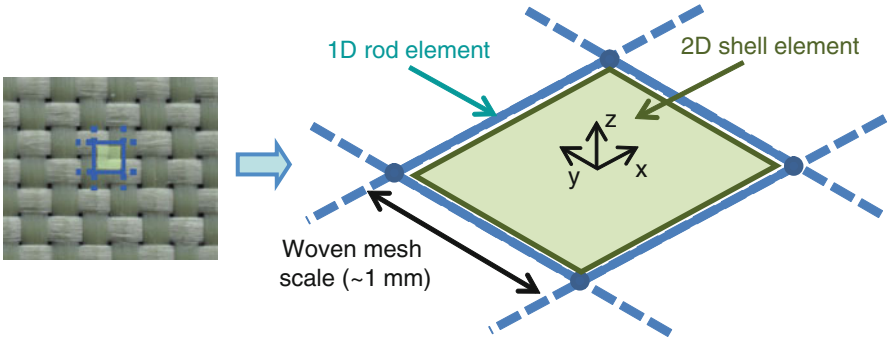


Fig. 20 Modeling of the skin

panel) as well as that of the damaged skin (non-stabilized bundles). Therefore, the model is developed at the woven fabric mesh scale. As a consequence of the same warp and weft distribution, no distinction is made between the modeling of the two membrane directions. As delamination is not predominant, only one element is taken through the thickness. The bundles are represented by the use of unidimensional rod elements. This truss structure is stabilized by a damageable bidimensional element, which is fully developed (Fig. 20).

The plate theory gives the normal forces per unit length (vector N) and the bending moments per unit length (vector M) of the woven skin. They are obtained from the membrane and bending strains (respectively vectors ε and k) by the introduction of three constitutive matrices A, B and D (1):

$$\begin{Bmatrix} N \\ M \end{Bmatrix} = \begin{bmatrix} A & B \\ B^t & D \end{bmatrix} \begin{Bmatrix} \varepsilon \\ k \end{Bmatrix}$$
$$with \quad N = \begin{Bmatrix} N_{xx} \\ N_{yy} \\ N_{xy} \end{Bmatrix}, \; M = \begin{Bmatrix} M_{xx} \\ M_{yy} \\ M_{xy} \end{Bmatrix}, \; \varepsilon = \begin{Bmatrix} \varepsilon_{xx} \\ \varepsilon_{yy} \\ \varepsilon_{xy} \end{Bmatrix}, \; k = \begin{Bmatrix} k_{xx} \\ k_{yy} \\ k_{xy} \end{Bmatrix} \tag{1}$$

Where A is the constitutive matrix of the membrane behavior and D the constitutive matrix of the bending behavior. B represents the extension-bending coupling. In this study, the skin is a balanced woven laminate, so that $B = 0$.

For the membrane loading, the stiffness of the woven skin is represented by both the rods and the shell elements. However, for the bending loading, the rods do not have any influence (2):

$$\begin{aligned} A &= A_{shell} + A_{rod} \\ D &= D_{shell} \end{aligned} \tag{2}$$

where A_{shell} and D_{shell} are respectively the constitutive matrix of the membrane behavior and the bending behavior of the shell element. A_{rod} is the stiffness of the rod elements. Thus, the characteristics inserted in the matrix A_{shell} are those of the

resin. The matrix D_{shell} represents the stiffness of the whole skin. All the damage mechanisms (micro cracking of the resin between and inside the bundles) are taken into account by damaging the matrices A_{shell} and D_{shell}.

The connection between the unidimensional and bidimensional elements is made at the nodes and the interaction between the bundles and the resin is neglected.

The specific shell element is developed from Belytschko's formulation [22]. To increase stability and to avoid hourglass strain modes, the element incorporates four integration points. As this bidimensional element is considered as homogenous in the thickness, the transverse shear is calculated using Hencky-Mindlin's theory of bending of shells. The behavioral distinction of membrane/bending/shear is made when choosing the values of the corresponding elastic modulus, respectively E_M, E_F and G_T. The normal forces per unit length and the bending moments per unit length are calculated using the constitutive matrix for a plane stress state. An explicit code is used for the modeling. Equation (3) shows the values of the forces and moments at the iteration $t + \Delta t$, which are calculated from their values at the previous iteration :

$$\begin{bmatrix} N_{xx}(t+\Delta t) \\ N_{yy}(t+\Delta t) \end{bmatrix} = \begin{bmatrix} N_{xx}(t) \\ N_{yy}(t) \end{bmatrix} + \frac{e.E_M(t).\Delta t}{1-\nu^2} \begin{bmatrix} 1 & \nu \\ \nu & 1 \end{bmatrix} \begin{bmatrix} \dot{\varepsilon}_{xx} \\ \dot{\varepsilon}_{yy} \end{bmatrix}$$

$$\begin{bmatrix} M_{xx}(t+\Delta t) \\ M_{yy}(t+\Delta t) \end{bmatrix} = \begin{bmatrix} M_{xx}(t) \\ M_{yy}(t) \end{bmatrix} + \frac{e^3.E_F(t).\Delta t}{12(1-\nu^2)} \begin{bmatrix} 1 & \nu \\ \nu & 1 \end{bmatrix} \begin{bmatrix} \dot{k}_{xx} \\ \dot{k}_{yy} \end{bmatrix}$$

$$\begin{bmatrix} Q_{xx}(t+\Delta t) \\ Q_{yy}(t+\Delta t) \end{bmatrix} = \begin{bmatrix} Q_{xx}(t) \\ Q_{yy}(t) \end{bmatrix} + \Delta t.K_y.G_T(t).e \begin{bmatrix} 1 & 0 \\ 0 & 1 \end{bmatrix} \begin{bmatrix} 2\dot{\varepsilon}_{xz} \\ 2\dot{\varepsilon}_{yz} \end{bmatrix} \tag{3}$$

where $\dot{\varepsilon}_{ij}$ and $\dot{k}_{ij}$ represent respectively the strain rates in membrane and bending, Q_{ij} is the transverse shear, e the thickness of the panel, υ the Poisson's ratio of the fabric and Δt the time step. The elastic modulus E_F, which represents the bending stiffness, is that of the woven composite oriented at 0°/90°. E_M is the elastic modulus of the resin and G_T is the transverse shear modulus of the whole skin. These two moduli are given by the manufacturer of the woven fabrics. K_y is a transverse shear correction factor. The value is set to 5/6.

The response of woven fabric laminates under in-plane shear loading conditions is highly non-linear. This behavior is usually represented with a plasticity model [23]. The in-plane shear forces per unit length are calculated from the in-plane shear elastic strain (4):

$$\begin{cases} N_{xy}(t) = e.\Delta t.G_M.2.{\varepsilon_{xy}}^e \\ M_{xy}(t) = \dfrac{e^3}{6}.\Delta t.G_M.{k_{xy}}^e \end{cases} \quad with \quad \begin{cases} {\varepsilon_{xy}}^e = {\varepsilon_{xy}}^t - {\varepsilon_{xy}}^p \\ {k_{xy}}^e = {k_{xy}}^t - {k_{xy}}^p \end{cases} \tag{4}$$

where G_M is the in-plane shear modulus. It is given experimentally by a tensile test of the woven fabric oriented at ±45°. $({\varepsilon_{xy}}^e, {k_{xy}}^e)$ are the in-plane shear elastic strains, $({\varepsilon_{xy}}^t, {k_{xy}}^t)$ the in-plane shear total strains and $({\varepsilon_{xy}}^p, {k_{xy}}^p)$ the in-plane shear plastic strains.

At each time step, the calculation of these strains is carried out in two principal steps. Firstly, in an elastic prediction step, the strain increment is assumed to be purely elastic. Secondly, Eq. (5) is used to verify the nature of the stress computed under the elastic prediction:

$$f = \left|\sigma_{xy}\right| - R - \sigma_0 \tag{5}$$

Where σ_{xy} is the in-plane shear stress, σ_0 the plastic strength and R the hardening variable. If $f > 0$, a plastic correction is carried out using a Newton–Raphson iterative scheme to find the value of the plastic strain, as defined in [24].

The micro cracking of the resin is represented by the degradation of the 2D elements. Because the skin is thin, damage is assumed to be the same throughout the thickness. The evolution of the membrane, bending and transverse shear modulus due to damage is described by a single parameter *(d)*. As developed by Coutellier and Rozycki [25], *(d)* is a function of the energy release rate Y, obtained by differentiating the elastic energy W_e with respect to the damage, as shown in Eq. (6):

$$\begin{aligned} E_M(t) &= (1-d).E_M \\ E_F(t) &= (1-d).E_F \\ G_T(t) &= (1-d).G_T \end{aligned} \tag{6}$$

$$Y = -\frac{1}{2}\frac{\partial W_e}{\partial d}; \quad d = \frac{\langle Y - Y_0 \rangle_{\geqslant 0}}{Y_c}$$

where Y_0 controls the damage initiation and Y_c the damage evolution from the initiation to the failure, as defined by Ladeveze and Ledante [26]. Classically (d) varies between 0 (no damage) and 1, (entirely damaged).

The fibers is modeled using rods elements, which are integrated in the formulation of the bidimensional specific element. A linear elastic material law with brittle failure in tension is chosen. As shown in [27], tensile failure properties for woven fabric glass/epoxy composite are highly dependent of the strain rate. Thus the strain to failure ε_r implemented increases according to the strain rate. In order to represent the behavior of the non-stabilized bundles, the compression stiffness of the rod is set to zero when the resin is totally damaged.

This element is implemented in the F.E. explicit software RADIOSS (Altair Hyperworks) using USERS elements and USERS material laws.

3.2.2 Identification

The matrix modulus E_M is a material property given by the fabric's manufacturer. The other parameters are identified with a reverse engineering method which consists of minimizing the difference between experimental and computed

Table 3 Identified parameters for the modeling of the woven fabrics (7781/913)

E_{fiber} (MPa)	40,000	G_M (MPa)	4,500
E_M (MPa)	3,000	σ_0 (MPa)	40
E_F (MPa)	17,000	R (MPa)	220

load/displacement curves. This optimization is carried out using the numerical tool Cobyla, which is an implementation of Powell's nonlinear derivative–free constrained optimization that use a linear approximation approach [28].

With this approach:

- quasi-static tensile tests are performed on the woven fabric oriented at 0°/90° in order to determine the tensile modulus E_F. The stiffness E_{Fiber} of the rods is then deduced from E_F and E_M from the classic rules of mixture.
- the influence of the strain rate upon the strain to failure ε_r of the rods is identified with dynamic tensile tests on 0°/90° specimens.
- the parameters governing the in-plane shear behavior (G_M, σ_0 and R) are identified by performing tensile tests on the same woven fabric oriented at ±45°.
- the evolution of the damage parameter (d) is calculated from static and dynamic indentation tests.

The identified parameters for the model are given in Table 3:

3.2.3 Validation and Discussion

In order to validate the strategy of modeling of the woven composite skin, the high velocity oblique impact tests previously presented are modeled. To optimize the calculation time, the developed formulation is used only in the area located below the indentor. The other part of the skin is modeled with classic composite shell elements (Fig. 21).

The mesh size in the impacted region is 1 mm × 1 mm. The other part of the skin is modeled with classic composite shell elements, with an edge length varying from 1 to 20 mm. Three dimensional elements are used to model the 20 mm thick foam core. There are seven elements in the thickness and their heights varie from 1 to 5 mm. The bottom face of the panel is embedded. The indentor is modeled using a rigid body, which is an undeformable solid. This model contains approximately 5,000 specific shell elements, 10,000 rod elements, 6,000 composite shell elements and 80,000 volume elements.

The foam core is modeled by a constitutive law implemented in RADIOSS. This law gives a good representation of the elastic behavior and the crushing of the foam by using an elasto-plastic law. The densification of the foam is carried out by adding to the stresses, a term of pressure (P) depending on the volumetric strain (7):

$$P = -\frac{P_0 \cdot \gamma}{1 + \gamma - \Phi} \quad with: \ \gamma = \frac{V}{V_0} - 1 + \gamma_0 \tag{7}$$

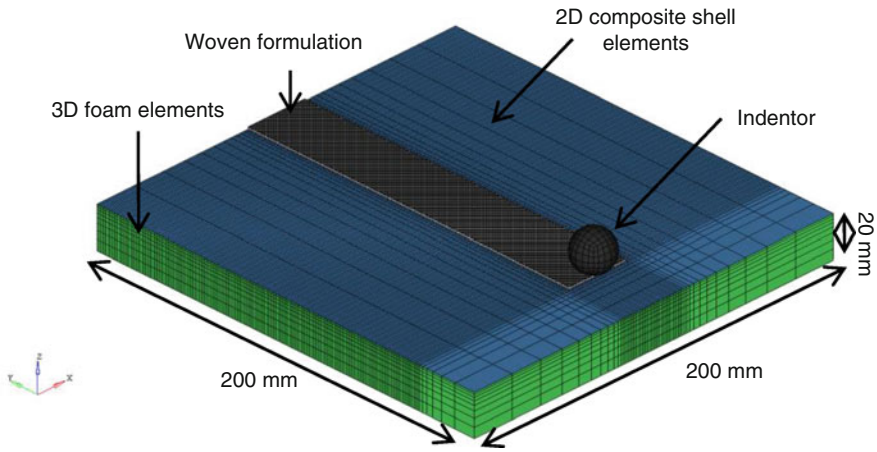


Fig. 21 Finite element modeling of a high velocity oblique impact

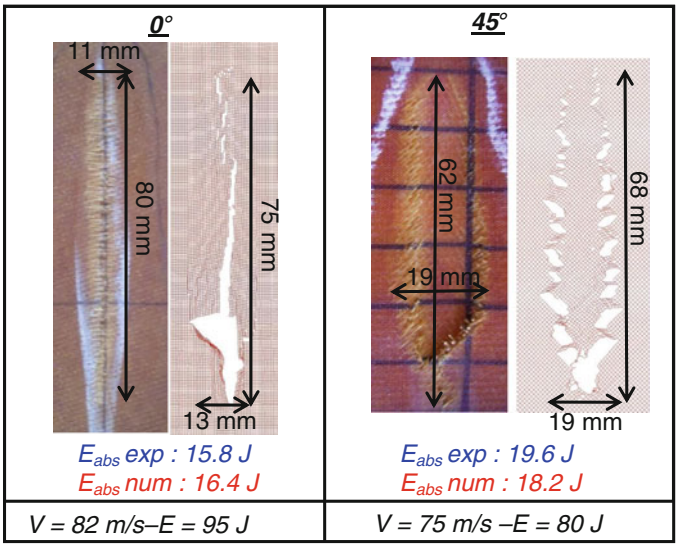


Fig. 22 Experimental and numerical fracture surfaces

where γ is the volumetric strain, Φ the porosity, P_0 the initial air pressure, γ_0 the initial volumetric strain, V the volume of the element and V_0 the initial volume of the element.

Two oblique impact tests corresponding to an impact axis at 0° and an impact axis at 45° from the fiber orientation are modeled. The two fracture surfaces previously described are well represented (Fig. 22).

For the impact along the fibers' direction, the fracture surface and the fiber breakage given by the calculation corelates with the experimental observations.

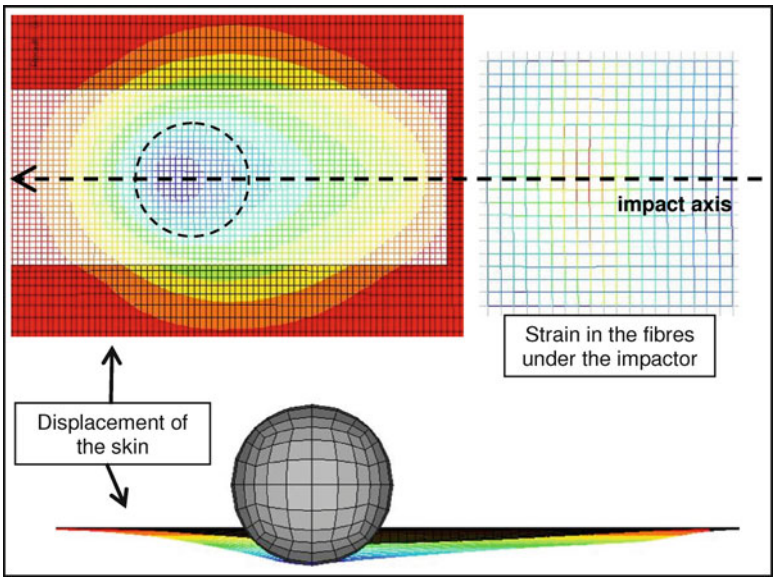


Fig. 23 Displacement of the skin and bundles strains

The length of the crack obtained numerically is 6% smaller than that observed in the experimental measurements. The numerical absorbed energy is 4% greater than the experimental absorbed energy. For a firing axis oriented at 45°, the initiation of the tearing is "V" shaped. Multiple small cracks oriented at 45° are noticed. These cracks are disposed along two axes both parallel to the projectile trajectory. This correlates well with the experimental observations. The dimensions of the calculated fracture surface are 12% greater than the experimental measures. The absorbed energy is 7% lower than that obtained in the tests. The model reproduces the global shape of the fracture surface, and predicts the energy absorbed and the fiber breakage energy threshold.

One of the main difficulties in studying this kind of impact is that the only experimental data available is the post-mortem analysis of the impacted panels. Thus, the results given by the model are analyzed in order to provide a better understanding of the failure mechanisms of the woven skin during the impact, for each orientation.

Firstly, for the firing axis oriented along the direction of the fibers, the shape of the out-of-plane displacement of the skin is observed (Fig. 23). It is maximum directly under the impactor. Since the foam is permanently crushed when compressed by the steel ball, the flexure of the skin is elongated in the direction of the firing axis. The radius of curvature of the skin is smaller in the perpendicular direction. The consequence is that the bending moment is greater in that direction. Thus, under the projectile in the rods perpendicular to the impact axis, the tensile strain in the fibers is greater.

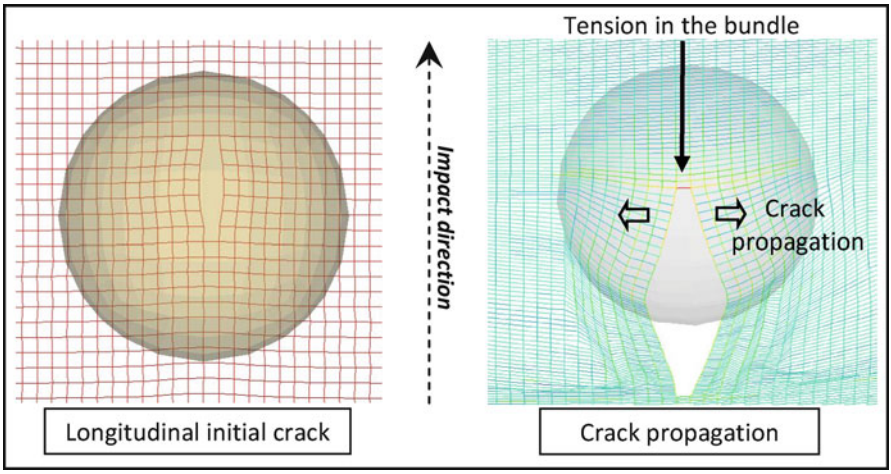


Fig. 24 Initiation and propagation of the crack

When the strain in the rods reaches the ultimate strain of the material, the crack starts to form in the direction of the impact axis (Fig. 24). The impactor opens the crack whilst moving along the firing axis. The bundles in the front of the crack are mainly loaded in tension. The failure of these bundles causes the crack to propagate in the impact direction, until either the steel ball rebounds or penetrates.

Concurrently, another phenomenon observed numerically is the damage of the resin in the contact area. According to the calculation results 87% of the damage is due to bending and 13% to the transverse shear. The damaged area is characterized by numerous lines of damaged resin perpendicular to the trajectory of the steel ball. This represents micro cracking propagations in the matrix due to the local bending induced by the impactor (Fig. 25).

The consequence of the resin damage is an increase of the stress and strain on the rods. Indeed, Fig. 26 shows the evolution of the strain versus time on the same impacted rod for two different calculations: one with the damage of the resin taken into account and the other with no matrix damage. The value of the strain in the rods is 13% higher when the matrix is damaged.

Thus, the initiation and propagation of the crack in the skin depends simultaneously on the bending stiffness of the skin, the material properties of the foam, the failure strain of the fibers and the damage of the resin.

Damage mechanisms for a firing axis oriented at 45° are analyzed. Similar to the behavior of the skin for a firing axis oriented at 0°, the damage to the resin is observed in the contact area at the beginning of the loading. This leads to an increase in stress and strain in the rods. The fracture of the woven skin begin when the extension of the rods reaches the tensile failure strain value.

The initiation of the crack is cross-oriented at 45° (Fig. 27). The steel ball follows its path along the firing axis, presses the front part of the woven skin and loads

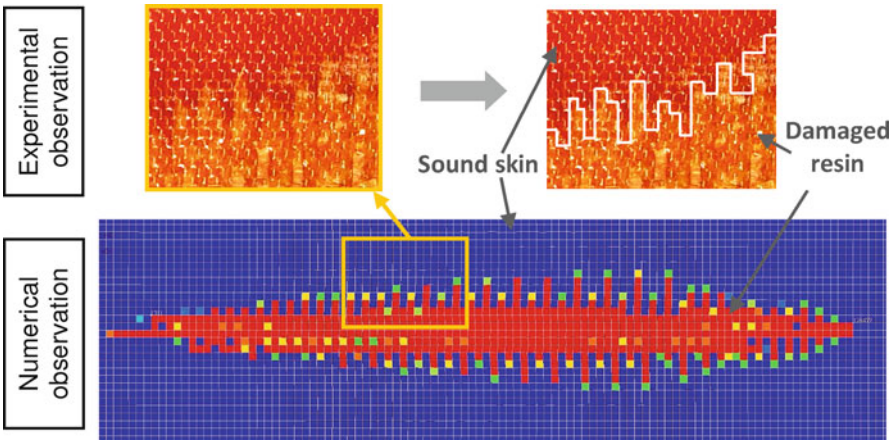


Fig. 25 Damaged area and transverse micro cracking of the matrix (numerical and experimental observations)

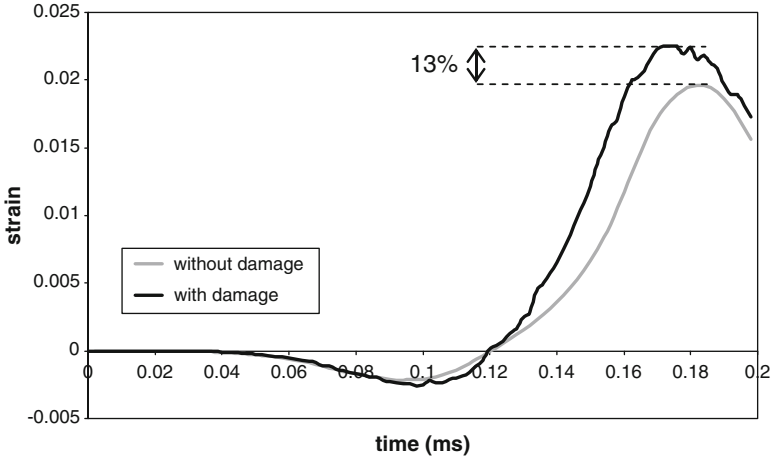


Fig. 26 Strain on an impacted rod with and without taking into account resin's damage

it in bending. The stress is at its maximum at the end of the cracks. There the resin is damaged along a line oriented at ±45° and perpendicular to each crack (Fig. 27). This local degradation of the bidimensional specific elements leads to a significant increase of the strain in the rods located in the damaged area. If the loading is sufficient, these rods break in tension, leading to the apparition of two small cracks oriented at ±45° and parallel to the initial cracks. While the steel ball continues moving forward, the same mechanisms, described before, are observed. The fracture surface obtained by the calculation forms two parallel lines of small cracks oriented at 45° (Fig. 27).

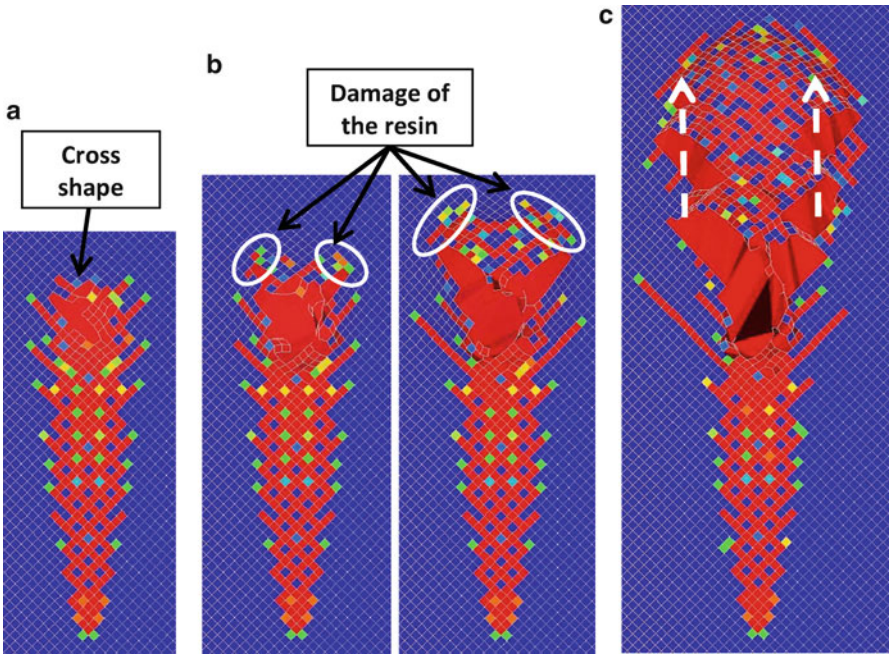


Fig. 27 Failure mechanisms for an impact at 45° (**a**) initialisation of the crack, (**b**) damage of the resin at the end of the cracks, (**c**) propagation of the cracks

The behavior between an impact oriented along the fibers and an impact at 45° is compared. Figure 28 gives the evolution of the damage parameter *(d)* for an element located in the first contact area for an impact at 0° and an impact at 45°. The loading for both elements begins at $t = 0.056$ ms.

Owing to the relative orientation of the fibers from the direction of the impact loads, the resin is damaged more quickly for an impact at 45°. Thus, for an impact at 0° the fibers remain stabilized longer. These numerical observations explain why the tearing energy threshold is higher for an impact in the direction of the fibers.

4 Conclusion

Many experimental tests were carried out to further understand the phenomena concerned during a front and oblique impact to a blade. Failure mechanisms were defined. For normal impact, the front edge is the first element to be damaged, then the increase in the impact energy level causes a plastic deformation of the stainless steel protection, which drives the skin-foam debonding of the structure. Moreover, the penetration of the projectile damages the roving by cracking the resin, which causes the slipping of the packages of fibers on both sides of the impacted zone.

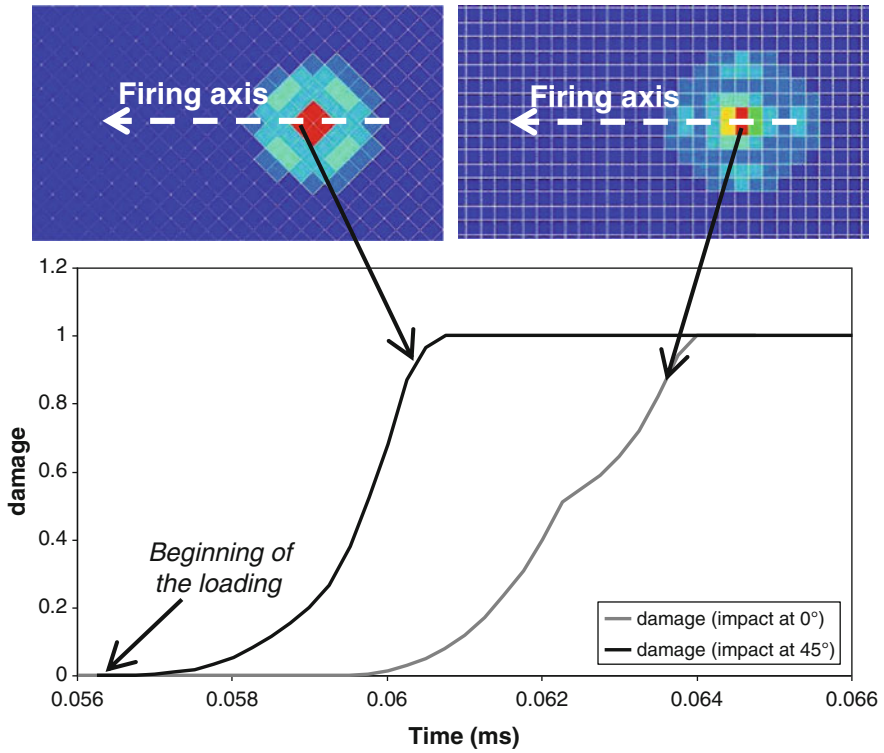


Fig. 28 Evolution of the damage in the first contact area

An original approach for the modeling of the impact on blades is proposed. This strategy consists of representing the roving by the superposition of three dimensional and unidimensional elements. The three dimensional elements represent the epoxy's resin, while the rods represent the packages of fibers. The change of the modeling scale can correctly represent the separation of the roving into packs of fibers. At the onset, only the element representing the three dimensional resin is damaged. The rod element, which represents a fiber package, may continue to transmit loads by contact with the other elements. The roving damage can spread to neighbouring elements. This new approach was validated by the results obtained in the modeling of the impact of the blade at various speeds. These results are satisfactory. The developed model allows a good representation of all the experimental ruptures for energy levels less than 1,000 J. It can be used industrially in the phase of pre-dimensioning to model the behavior of the blade to an impact.

For oblique impacts, an experimental study was performed on a sandwich structure made up of a foam core and a thin woven composite skin. The impact energies were varied from 50 to 230 J to observe the chronology of the damage. For the lower energies, only the resin was damaged. For greater energies, fiber breakages could lead to skin perforation. Moreover, a high influence of the angle between the

firing axis and the fibers' orientation on the shape of the fracture surface, and on the tearing energy threshold, was observed.

A numerical model of the skin has been developed at the woven pattern scale in order to reproduce the behavior of the woven skin under this kind of loading. This modeling relies on the analysis of the damage observed experimentally. The idea consists of separating the functions of the fibers from those of the resin in order to damage only the resin. This modeling allows a good reproduction of the chronology of the resin's damage. Calculation results correlate accurately with the experimental results. The analysis of the numerical results permits a better understanding of the mechanisms involved in the response of the woven skin.

Work is currently being developed in order to allow the simulation of impacts on thicker woven skins or skins made up of two plies with different orientations.

Acknowledgement This work was granted access to the HPC resources of CALMIP under the allocation 2012-[09105].

References

1. Abrate S (1991) Impact on laminate composites. Appl Mech 44:155–190
2. Abrate S (1997) Impact on laminate composites, recent advances. Appl Mech 47:517–544
3. Abrate S (1998) Impact on composite structures. Cambridge University Press, Cambridge
4. Talreja R (2008) Damage and fatigue in composites – a personal account. Compos Sci Technol 68:2585–2591
5. Jonhson AF, Pickett AK, Rozycki P (2001) Computational methods for predicting impact damage in composite structure. Compos Sci Technol 61:2183–2192
6. Hu N, Zemba Y, Okabe T, Yan C, Fukunaga H, Elmarakbi AM (2008) A new cohesive model for simulating delamination propagation in composite laminates under transverse loads. Mech Mater 40:920–935
7. Tawk I, Navarro P, Ferrero JF, Barrau JJ, Abdullah E (2010) Composite delamination modeling using a multi layered solid element. Compos Sci Technol 70:207–214
8. Tay TE, Liu G, Tan VBC, Sun XS, Pham DC (2008) Progressive failure analysis of composites. J Compos Mater 42:1921–1966
9. Fleming DC (1999) Delamination modeling of composites for improved crash analysis. NASA CR-1999-209725, http://ntrs.nasa.gov/search.jsp?R=19990110662
10. Kim H, Welch DA, Kedward KT (2003) Experimental investigation of high velocity ice impacts on woven carbon/epoxy composite panels. Compos Part A 34:25–41
11. Liu Y, Shepard WS (2005) Dynamic force identification based on enhanced least squares and total least-squares schemes in the frequency domain. J Sound Vib 282:37–60
12. Kiddy J, Pines D (2001) Experimental validation of a damage detection technique for helicopter main rotor blades. J Syst Control Eng 215:209–220
13. Inoue H, Harrigan JJ, Reid SR (2001) Review of inverse analysis for indirect measurement of impact force. Appl Mech Rev 54:503–524
14. Morozov EV, Sylantiev SA, Evseev EG (2003) Impact damage tolerance of laminated composite helicopter blades. Compos Struct 62:367–371
15. Pawar PM, Ganguli R (2005) On the effect of matrix cracks in composite helicopter rotor blade. Compos Sci Technol 65:581–594
16. Pawar MP, Ganguli R (2007) On the effect of progressive damage on composite helicopter rotor system behavior. Compos Struct 78:410–423

17. Pawar MP, Ganguli R (2006) Modeling progressive damage accumulation in thin walled composite beams for rotor blade applications. Compos Sci Technol 66:2337–2349
18. Kumar RS, Gurvich MR, Urban MR, Cappelli MD (2010) Structural integrity of composite rotor blades with service and ballistic damage. In: Proceedings of the American helicopter society 66th annual forum, Phoenix, AZ
19. Kumar RS, Gurvich MR, Urban MR, Cappelli MD (2011) Dynamic modeling and analysis of composite rotor blades under low velocity impact loads. In: Proceedings of the American Helicopter Society 67th Annual Forum, Virginia Beach, VA
20. Navarro P, Aubry J, Marguet S, Ferrero JF, Lemaire S, Rauch P (2012) Experimental and numerical study of oblique impact on woven composite sandwich structure: influence of the firing axis orientation. Compos Struct 94(6):1967–1972
21. Navarro P, Aubry J, Marguet S, Ferrero JF, Lemaire S, Rauch P (2012) Semi-continuous approach for the modeling of thin woven composite panels applied to oblique impacts on helicopter blades. Compos Part A 43(6):871–879
22. Belytschko T, Lin JI, Tsay CS (1984) Explicit algorithms for the nonlinear dynamics of shells. Comput Methods Appl Mech Eng 42:225–251
23. Marguet S, Rozycki P, Gornet L (2006) A rate dependent constitutive model for carbon-fibre/epoxy-matrix woven fabrics submitted to dynamic loadings. In: IIIrd European conference on computational mechanics, Lisbon, Portugal, 5–8 June 2006, p 75
24. Simo JC, Hugues TJR (2000) Computational inelasticity. Springer, New York
25. Coutellier D, Rozycki P (2000) Multi-layered multi-material finite element for crashworthiness studies. Compos Part A Appl Sci Manuf 31:841–851
26. Ladeveze P, Le Dantec E (1992) Damage modeling of the elementary ply for laminated composites. Compos Sci Technol 43:257–267
27. Naik NK, Yernamma P, Thoram NM, Gadipatri R, Kavala VR (2010) High strain rate tensile behavior of woven fabric E-glass/epoxy composite. Polym Test 29:14–22
28. Powell MJD (1994) A direct search optimization method that models the objective and constraint functions by linear interpolation. In: Advances in optimization and numerical analysis: proceedings of the Sixth Workshop on Optimization and Numerical Analysis, Oaxaca, Mexico – Key: citeulike:7297019, pp 51–67

Energy Absorbing Sacrificial Structures Made of Composite Materials for Vehicle Crash Design

G. Belingardi, S. Boria, and J. Obradovic

Abstract Nowadays thin-walled components in CFRP composite materials are considered in order to progressively replace metals for crashworthy applications in the automotive industry, thanks to their undoubted advantages such as high strength to weight ratio.

The present chapter is dealing with the lightweight design and the crashworthiness analysis of a composite nose cone as the Formula SAE racing car front impact attenuator. The analysis of the crash behaviour was conducted both numerically, using explicit FE codes as LS-DYNA and Radioss, and experimentally, by means of a drop weight test machine.

In order to assess the quality of the simulation results, initially a complete comparative analysis with material characterization was developed on simple CFRP composite tubes subjected to dynamic axial impact loading. After quasi-static and dynamic experimental crash tests on the composite nose cone were performed. These experimental results are reported together with numerical simulation ones. The main idea of the research was to demonstrate energy absorbing capabilities of a thin-walled crash box during the frontal impact, with the lowest initial deceleration. In order to initialize the collapse in a stable way, the design of the composite impact attenuator has been completed with a trigger which consists of a very simple smoothing (progressive reduction) of the wall thickness. Initial requirements were set in accordance with the 2008 Formula SAE rules and they were satisfied with the final configuration.

G. Belingardi (✉) • J. Obradovic
Department of Mechanics (DIMEC), Politecnico di Torino, Duca degli Abruzzi, 24, 10129 Torino, Italy
e-mail: giovanni.belingardi@polito.it; jovan.obradovic@polito.it

S. Boria
School of Science and Technology, University of Camerino, Madonna delle Carceri, 9, 62032 Camerino, Italy
e-mail: simonetta.boria@unicam.it

S. Abrate et al. (eds.), *Dynamic Failure of Composite and Sandwich Structures*, Solid Mechanics and Its Applications 192, DOI 10.1007/978-94-007-5329-7_13,
© Springer Science+Business Media Dordrecht 2013

Keywords Carbon fibre • Composites • Crashworthiness • CFRP • Axial compression

1 Introduction

Racing cars demonstrate maximum vehicle driving performance resulting from high-tech developments in the area of lightweight materials and aerodynamic design. Since extreme racing speeds may lead to severe accidents with high amounts of energy involved, special measures are taken in order to ensure the drivers safety in case of high-speed crashes. Besides the driver's protective equipment (like helmet, harness or head and neck support device) and the circuit's safety features (like run-off areas and barriers), the race car itself is designed for crashworthiness and possesses special sacrificial impact structures that absorb the race car's kinetic energy and limit the decelerations acting on the human body.

The main scope of the strict crashworthiness regulations, imposed by race governing bodies, is to assure that the driver is enclosed within a strong survival cell, surrounded by energy absorbing structures in the front, back and sides. The passenger survival space concept, introduced in 1970s, requires that, during standard crash tests, the passenger compartment remains nearly non deformed and non intruded by other structural parts of the vehicle itself, while the front structure deforms and thus absorbs the needed amount of energy. Besides static tests (nose push-off tests, side intrusion tests etc.), the vehicle structure has to withstand dynamic impact tests (frontal impact test, rear impact test, side impact test and steering column test).

For the passenger safety it is fundamental the progression of the energy absorption phenomena. It is also essential that the accelerations and the forces that the different parts of the human body are submitted to do not exceed the tolerability values that are typical of the human body, i.e. limits over which permanent injuries or even the death are caused.

With this scope, the vehicle body structure is designed in order to get a vehicle deceleration history that has the desired characteristic of progression. For formula racing cars, due to their smaller transversal dimensions, the front structure can be quite different. This is mainly due to the fact that the engine is placed in the rear part of the vehicle and the impact velocity that should be considered is higher than in the urban use of the vehicle.

During the impact, the vehicle's kinetic energy is absorbed by plastic deformation of the structure if it is made out of metal, or by fracture and fragmentation if it is made out of brittle plastic materials such as composite materials with polymeric matrix.

To reduce the development and testing costs of a new safety design, it is recommendable to use computational crash simulations for early evaluation of safety behaviour under vehicle impact test. Without a doubt, the validation of numerical models for accurate simulation of structural response to crash impacts



Fig. 1 The racing car of Politecnico di Torino – season 2008

is an important aspect of crashworthiness research. Indeed, they constitute the necessary tools for the designer to study the response of the specific structures to dynamic crash loads, to predict global response to impact, to estimate probability of injury and to evaluate numerous crash scenarios, not economically feasible with full scale crash testing.

Recent race cars and dream cars present many components made of composite materials, thanks to their low density and high strength. In particular specific composite structures are integrated into cars in order to increase their crashworthiness. Excellent performance of composites, sometimes better than those of the metallic similar structures, can be obtained by choosing appropriately the mechanical (the stacking sequence, the number of layers, the type and quantity of fibres and matrix) and geometrical (the beam section shape, the wall thickness, the extremity joints) design parameters [1].

The present work analyses the steps to follow during the design of the lightweight composite frontal structure of formula SAE vehicle, developed by the Politecnico di Torino team. Composite materials are considered as an alternative to metal in order to match both lightweight and energy absorption in case of impact requirements. Figure 1 shows the final solution of the auto-cross racing car with small formula style that was produced in the collaboration with partner enterprises in Turin and successfully demonstrated in several racing competitions in Italy and Europe. The production strategy of this car consists in a concurrent analytical and experimental development, from the initial conceptual design and coupon testing, through the stages of element and subcomponent engineering, to final component manufacturing.

Design, manufacture and predict the behaviour of composite structures under impact loading is difficult because of their different failure modes that govern energy absorption and the anisotropy that considers a complex material characterization.

Therefore, in a first stage, CFRP thin-walled tubular structures are analysed both numerically and experimentally. The numerical analysis is conducted through the non-linear dynamic code LS-DYNA, while the experimental one with a dynamic drop weight test.

Thin-walled tubular structures made of composite material, found interesting applications as frontal energy absorbing parts, implemented in the design of urban vehicle's body-in-white. Instead, in the case of size vehicles, such as sport cars, it is predominantly used the conical absorbing structure [2].

The next step is to perform quasi static and dynamic tests and numerical analyses of truncated pyramidal impact attenuator, which is the main absorbing structure of formula SAE during the impact event. In this case, the numerical analysis is performed by use both of LS-DYNA and Radioss explicit nonlinear codes. The particular intention is put on the design of triggering mechanism that is providing better crashworthiness.

Finally, the explicit codes were able to predict experimental results regarding both crash behaviour and absorbing mechanism of the impact attenuator structure and CFRP tubes. Force versus displacement diagrams confirm that experimental and numerical results are almost the same. Thus confirms the quality of the used methodology and approach for the design of racing car impact attenuator.

2 Crashworthiness of Automotive Composite Energy Absorber

Carbon fibre composites have been shown to perform extremely well in case of a crash, and are used to manufacture dedicated energy-absorbing components, both in the motor sport world and in the construction of mass production vehicles [3, 4]. In case of impact, the kinetic energy of the vehicle should be dissipated in a very fast but stable and controlled way so that passengers can survive. In metallic structures, this energy absorption is achieved by plastic deformation, while in composite structures it relies on the material diffuse fracture: i.e. on a completely different mechanism.

During the development phase of the research, the structure designer has to take into account that, even along the composite fiber direction, the laminate elastic modulus is usually lower than the corresponding values of steels while the tensile strength is comparable. Therefore, in order to match the structure targets in terms of stiffness, the use of composite materials leads to increase the wall thickness of the structural members with respect to the corresponding steel members.

The different collapse mechanisms of thin walled members made of composite material have to be taken into account. In particular, the composite structure may fail due to compression strength or to bending strength, in both cases the local wall behaviour has to be considered. The limit compression load per unit length can be evaluated as $F_{comp} = \sigma_{lam,comp}\ h$, where $\sigma_{lam,comp}$ is the limit compression strength of the laminate, according to the considered loading direction, and h is the wall thickness. The limit bending moment, valid for the bending of a rectangular beam, can be evaluated as $M_{lim} = \sigma_{lam,bend}\ h^2/6$, where $\sigma_{lam,bend}$ is the limit bending strength of the laminate, according to the considered loading direction [2]. This

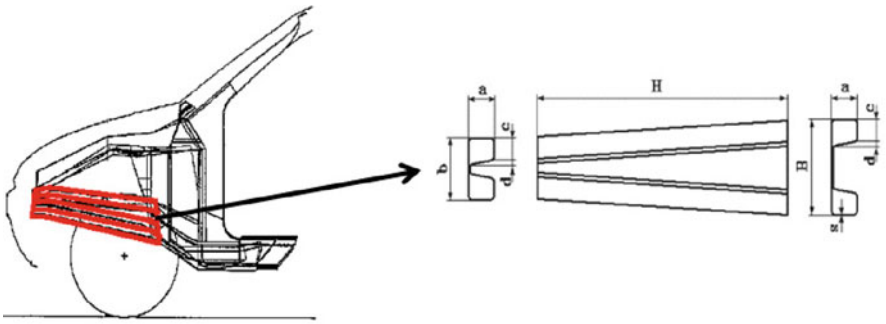


Fig. 2 Composite front beam in the vehicle front structure

formula for the limit bending moment takes into account that, generally, composite material laminas have not substantial plastic deformation, as steels have, but, in the fiber direction, behave elastically up to fracture. For both the collapse mechanisms, the increment of the wall thickness, consequent to the adoption of composite materials, is favourable for the crash behaviour, leading to an increment of the structure crush strength.

Furthermore, it should be noted that the energy absorption mechanism in the composite front longitudinal beams of the vehicle is material progressive fragmentation consequent to axial compression and therefore the compression failure mechanism may prevail on the bending one. Figure 2 shows the front structure of a composite material vehicle designed within the framework of a national research program devoted to evaluate the suitability of composite longitudinal beams for the vehicle crash performance [2]. The presented base geometry is a thin-walled beam composed of two prismatic square section tubes connected by a flat vertical plate. The two tubes are disposed with their axis converging toward the front of the vehicle so that there is a progressively increasing resisting cross-section starting from the first impact point and moving backward to the passenger compartment. This tapered shape has been chosen to obtain also a proper value of the bending stiffness and strength: in this application, this beam is loaded in bending and torsion both by the engine mounting reactive loads and by the vehicle suspension loads.

Quasi-static axial loading tests were performed using a standard material testing machine. Results show that the force at collapse initialisation is reduced approximately to the mean force value due to the proper design of the crush trigger. Also, the mean load is only slightly lower than the maximum load and the load uniformity parameter (defined as the ratio of these two values $LU = L_{max}/L_{mean}$) is close to one (one is the value that characterize the ideal energy absorber). A narrow range of variation of the force opposed by the beam during the crush means both a stable, progressive collapse mechanism and a nearly constant deceleration for the vehicle.

Besides material progressive fragmentation, two other energy absorbing mechanisms are present and dissipate a significant portion of the energy: delamination and friction between different fronds and between fronds and the target. Figure 3

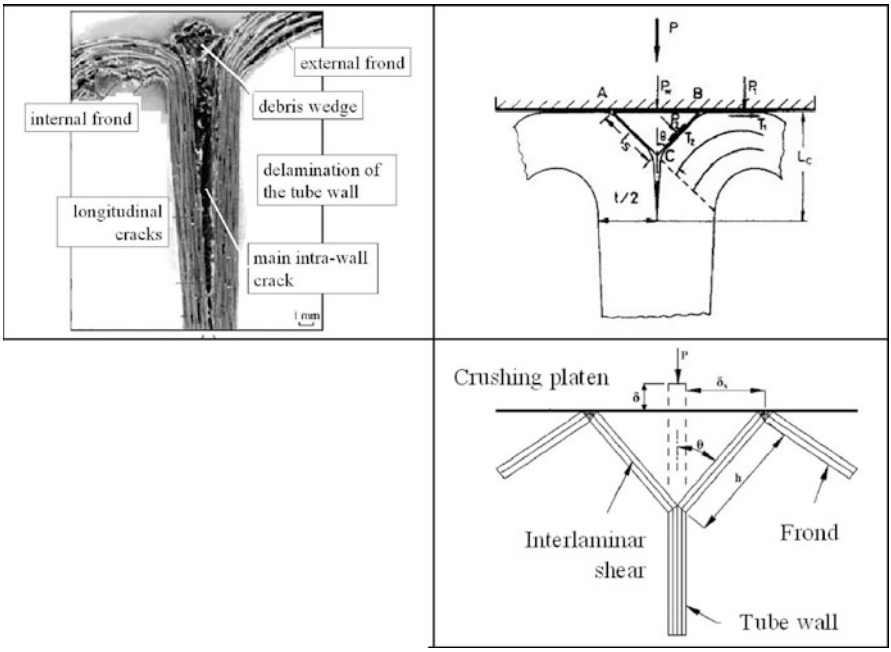


Fig. 3 Failure mechanisms with formation of fronds and debris wedge in the axial collapse of a composite column

shows a synthesis of the failure mechanisms that take place in the axial collapse of a composite column. In the figure there are: a micrograph of the crushed tube [5], a draft of the crush zone [6] and a mechanical model for the analysis of the energy absorption [7].

According to this model the concurring energy terms are the following six:

(i) external work done by the crushing platen,
(ii) energy dissipated during circumferential delamination,
(iii) energy dissipated during frond formation (axial cracks),
(iv) energy dissipated on bending of fronds,
(v) energy dissipated through interlaminar shear deformation in the fronds during bending,
(vi) energy dissipated due to friction between crushing platen and fronds.

Furthermore, Hull [8] and Sigalas et al. [9] discuss failure mechanisms for composite tubes in detail and comment upon the influence of geometry and material composition on structural performance. Hull's paper is based on experimental work on the axial collapse of tubes (made from a variety of composite materials) by failure of the centre of the column away from the ends and by progressive crushing from one end (progressive crush failure). Four examples of centre failure are illustrated in Fig. 4. The only significant difference between used materials is the arrangement

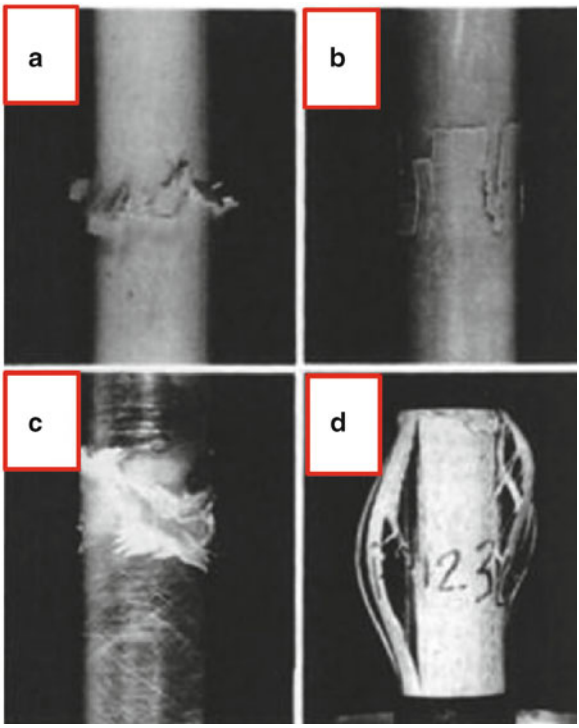


Fig. 4 Examples of central fracture: (**a**) sheet moulding compound (SMC), 4 mm s^{-1}; (**b**) woven cloth, 1 m s^{-1}; (**c**) helically wound, 4 mm s^{-1}; (**d**) pultruded, 4 mm s^{-1} [8]

and volume fraction of the glass fibres. However, it is clear that these differences have resulted in large difference in the failure modes. Progressive crush failure of composite tubes is shown in Fig. 5. The crushed materials spreads out on both sides of the tube wall. The material on the inside of the tube is further compacted and is constrained to fold inwards whereas the material on the outside tends to splay into a mushroom shape. Also, the behaviour of the reinforcing fibres depends on their orientation. Fibres aligned axially bend inwards and outwards with or without fracturing, depending on their flexibility and the constraints produced by other fibres.

Also, Hull [10] summarised the forces acting at various locations in the progressive crush wedge. A detailed description is given of the effect of fibre arrangement on progressive crushing in carbon fibre-epoxy unidirectional laminated tubes, woven glass cloth-epoxy tubes, filament-wound angle-ply glass fibre-polyester tubes and inplane random chopped glass fibre-polyester tubes. Transition between splaying and fragmentation modes are identified and related to the force-displacement response. Similar transitions have been reported with other variables, such as fibre and matrix properties, dimensions and shape of tubes, speed and temperature effects, and trigger geometries. Warrior et al. [11] investigated the influence of increasing the inter-laminar properties of the composite on the crushing strength of the tube. Methods for increasing the inter-laminar properties of the composite included a toughened resin and inter-laminar stitching. The research

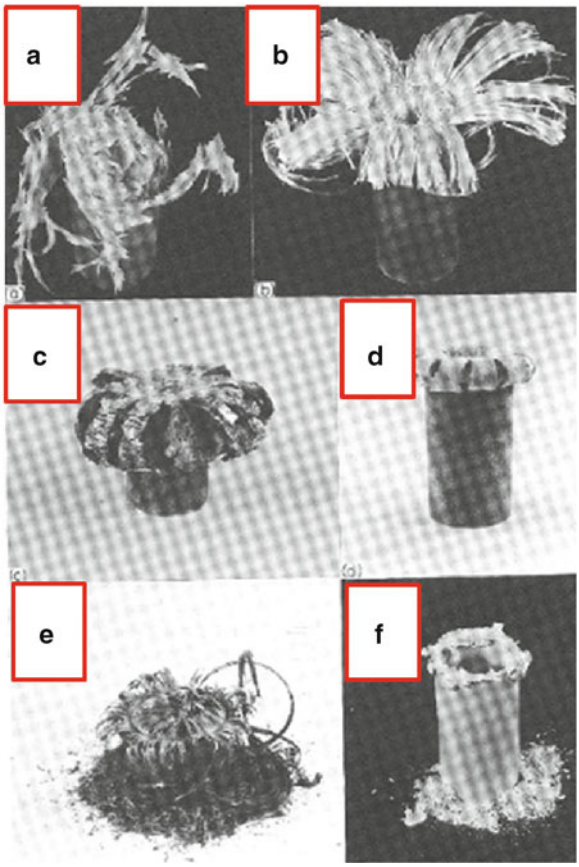


Fig. 5 Typical examples of progressive crush failure: (**a**) helically wound glass-polyester, 4 mm s^{-1}; (**b**) 0/90 glass-polyester, 4 m s^{-1}; (**c**) mica-shellac laminated, 1 mm s^{-1}; (**d**) woven cloth glass-epoxy, 4 m s^{-1}; (**e**) 0/90 carbon-epoxy, 4 m s^{-1}; (**f**) dough moulding compound DMC, 2 m s^{-1} [8]

found that using a toughened resin was the best method for increasing the crushing strength of the tube. Inter-laminar stitching and using thermoplastic interleaves actually decrease the crushing strength due to reduction in the in-plane properties and contact frictions.

Crash investigations on composite structures reported in the literature are mainly based on small plates submitted to bending impact and on simple bars, of circular or rectangular cross section, of prismatic or tapered shape, submitted to axial impact. Most of the research on the energy absorption of composite materials has been limited to the axial compression of tubular structures and has been based on experimental test analysis [12, 13]. Until now only few analytical models, with some simplifications, have been proposed to predict the energy absorption characteristics of thin-walled tubular structures [14–18]. The tubular devices have been shown to perform at their best when geometric, material and loading conditions are such that axial failure of the tubes is characterized by the progression of a destructive zone of constant size at the loaded end, called "crush zone". The design challenge is to arrange the composite material column such that the destructive zone can progress

in a stable manner. The energy absorption must be as high as possible by allowing the development of a sustained high level crushing force, with little fluctuation in amplitude as the progress zone travels along the component's axis.

A representative pioneering work to study the crush behaviour of composite tubes submitted to axial load has been done by Thornton [19].

Thornton studied the behaviour of various composite tubes, taking into account difference in fiber type (glass, carbon and aramid fibers), different lay-ups and different t/D thickness to diameter ratio. Energy absorption characteristic was found to be largely affected by the fiber type and by the lay-up, while results are less sensitive to t/D ratio than for metal tubes. Further rectangular and square section tubes were considered, experimental results showed that these sections are less effective in energy absorption than circular sections.

Farley and Jones [20] studied the effect of crushing velocity on the energy absorbing characteristic of circular tubes made with aramid fibers and carbon fibers in epoxy matrix, with different lay-ups. For carbon/epoxy tubes with $[0/\pm\theta]$ fibers, the specific energy does not vary with the crushing velocity, whereas with $[\pm\theta]$ fibers (they considered only two cases: θ equal to 45° and 75°) it increases with the increase of the crushing speed. With the aramid/epoxy tubes the energy absorption characteristic increases in all the considered cases.

For tubes with structures other than circular, the crushing behaviour has been shown to be improved when the corners of polygonal thin-walled sections are rounded so as to represent segments of circular tubes. For square sections, the greater the corner radius, the higher will be the efficiency of energy absorption [21]. Rounded corners prevent flat segments from failing by local plate buckling, with associated plate strip buckling and much lower specific energy absorption.

Boria and Belingardi [22] analyzed CFRP collapsible energy absorbers by presenting the results of experimental tests on circular and square tubes made of woven fabric in epoxy resin that were submitted to dynamic compressive loading. Moreover, the explicit FE code LS-DYNA is used to investigate the impact energy absorption characteristics and in order to compare the numerical results with the experimental data. To set up the numerical models of the energy absorbers, tensile static tests were performed on simple strips of fabric at various orientations was at first performed. Due to the typical energy absorbing mechanism for the composite material, the section shape seems to have no evident influence on the results.

Composite structures are characterized by complex failure events such as lamina bending, transverse shear, local fibre buckling, and inter-laminar or intra-laminar cracks that are difficult to predict. That is why the literature on "real structures", and not only simple composite columns, is not widespread. In order to fit Formula One regulations about energy absorbers, results reported by Bisagni et al. [23] indicate that hollow truncated cones can be an interesting solution to match the regulation requirements, provided that the wall thickness, the cross section dimensions and the semi-apical angle are chosen in an appropriate relationship. The goal of this cone geometry is to obtain a stable progressive collapse (as shown in Fig. 5), avoiding a catastrophic failure (total collapse without desired energy absorption). Ref. [23] describes an experimental and numerical investigation on energy absorbers

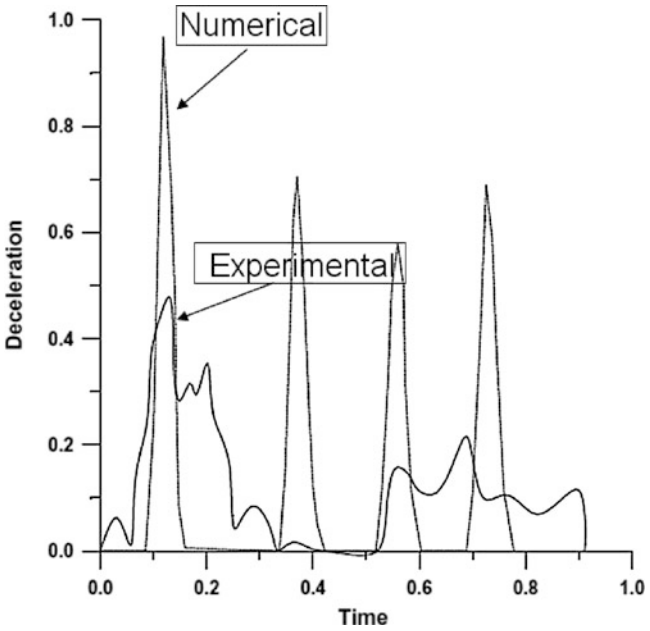


Fig. 6 Numerical and experimental load-shortening diagrams of the steering column [23]

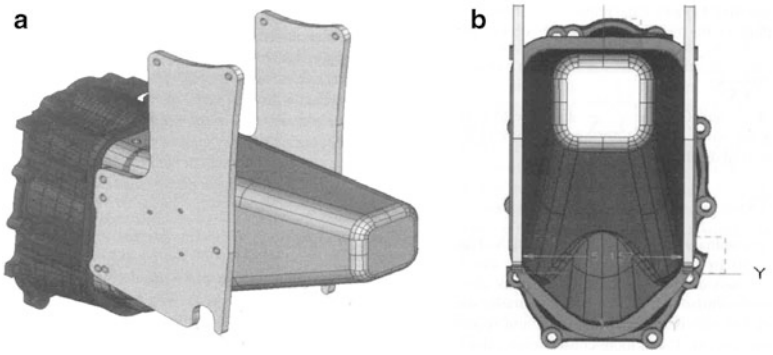


Fig. 7 Views of CAD model of the RIMP structure [24]

for Formula One side impact and steering column impact. Comparing the numerical data to the experimental results, the differences are around 20% for the peak load and around 10% for the specific absorbed energy. The final element model is not able to simulate correctly only the first phase of the steering column impact (Fig. 6); consequently the maximum deceleration is about 50% higher than the measured one.

The final design of the rear impact absorbing structure (RIMP) of the Star Mazda race car reported by Feraboli et al. [24], has been defined as a truncated pyramid having the minor base nearly parallel to the major base (Fig. 7). The minor

base has the square section while the major base is roughly rectangular in shape. Composite materials made with either commercial grade and high modulus fibres and with commercial grade epoxy resins have been considered. The selection of the epoxy resin has taken into account both the requirement of a tough resin, in order to optimise the energy absorption capability, and the requirement of quite high operating temperature, due to the proximity to the engine. Therefore, a rubber modified epoxy has been discarded in favour of a more brittle, higher temperature epoxy matrix.

Two different designs of the composite material laminate have been considered, both fabric and tape prepregs are used. The first design is based on a quasi–isotropic lay-up (it has been referred as FQI lay-up) with axial, angle and hoop plies, the second design has a greater content of angle plies but no fibres in the hoop direction (it has been referred as K0/45 lay-up). This latter laminate results to have a easier manufacturability thanks to its simpler staking sequence. Both designs have trigger in order to initialise the collapse of the structure by the conical shape of the component and also by the progressive reduction of the wall thickness along the cone axis from the major to the minor bases. However, the adopted strategies for thickness reduction are different in the two designs.

The cones have been submitted to quasi-static and dynamic crush tests, the dynamic test was conducted according to the FIA regulation. Quasi-static crush testing has shown to lead to greatly non conservative estimates of the SEA characteristics of the rear impact absorbing structure, although fairly good agreement between quasi-static and dynamic tests was observed in terms of overall load-stroke response and failure behaviour. Since the design of the K0/45 cone appears to be more effective than the FQI cone in terms of capability of energy absorption, it is concluded that wall thickness and shear modulus have greater influence than ply schedule and circumferential modulus on the energy absorption capabilities of the structure.

The sacrificial structure, that constitute the main safety device in case of frontal impact for Formula one racing car, is nowadays generally made of various types of a sandwich structure. The numerical simulation of the crash behaviour of this structure by finite element modelling could be of great interest in order to optimise its performance and weight.

Boria [25] presented the prediction of dynamic behaviour of an impact attenuator for a Formula SAE car under frontal impact conditions by using numerical and experimental approaches. A truncated pyramidal shaped impact attenuator is a combination of sandwich panels with hexagonal core and aluminium inner sheets assembled by using rivets between the two panels. These membranes create higher stiffness areas and consequently trigger the instability and folding of the sandwich structure. Firstly, the analysis of sandwich structures is carried out to better understand their behaviour and model them properly in the numerical simulation using LS-DYNA. The material characteristics are defined by combining the experimental tests on the sandwich structures with simple numerical models. In order to obtain the best configuration for the impact attenuator in terms of maximum absorbed energy, minimum deceleration and weight saving, its length and the number of inner sheets are optimised. The impact attenuator of 300 mm long and six inner

sheet is considered to be the best choice based on the deceleration and force versus displacement (measure of energy absorption capacity) responses. Finally, a crash-test is performed on this impact attenuator configuration to compare the experimental results with the numerical ones.

The velocity and the displacement responses from the crash test data have shown good agreement with the FE simulation results. The maximum force and the absorbed energy from the FE analysis correlate well with the experimental ones. The different trend of force versus displacement curves is due to the simple idealisation of the impact attenuator and the maturity if contact characteristics. The first peak in the experimental data is dominated by the buckling of the top plate. This peak is not observed in the numerical results as the top plate is not idealised in the FE model. Also, the FE analysis is able to reproduce the progressive crushing of the impact attenuator. The average deceleration from simulation (12.1 g) is higher 23% than the experimental one (9.81 g), but both are satisfying standard required average deceleration that should be less than 20 g.

Heimbs et al. [26] studied the crushing simulation of a F1 racing car front impact structure in a frontal crash against rigid wall. The honeycomb composite structure consists mainly of the nose box, which is mounted to the chassis. Attached are the nose tip and the representative front wing with certain wing pillars. The focus of the work is on the modelling of the composite material crushing by use of LS-DYNA non linear explicit code. The modelling approach used in this study is to model the whole sandwich structure within a multi-layered shell element ('layered shell' approach). Simulation results are compared to experimental test data in a qualitative and quantitative way with respect to crush front propagation and deceleration curves. A comparison of the deceleration curves versus crushing displacement shown a good quantitative correlation between numerical simulation and crush test. Also, the qualitative correlation appears to be very good. The front impact crush simulation begins with the nose tip hitting the wall, being compressed and partly being fractured. Then the lower structure of the nose tip and the wing pillar are detached through a debonding failure under shear loads. Afterwards, the nose box strikes the wall and is crushed continuously until all kinetic energy is absorbed. Authors also shown for comparison reasons, a sequence of images taken from the high speed film in the crash test at corresponding time steps and the qualitative correlation appears to be very good.

Anghileri, Chirwa and co-workers [27], present an interesting procedure. The identification of the parameters of the constitutive equation with particular reference to the damage initiation and evolution for the considered composite material can be performed by means of an inverse approach base on an optimisation technique. The objective function of the optimisation is the minimisation of the distance of the load–displacement curve obtained through the numerical simulation with respect to the experimental one, the design variables are the parameters to be evaluated. Anghileri and co-workers base the identification on the behaviour of a cylindrical composite tube with two different stacking sequences. Then a conical tube made of the identified material has been submitted to axial crushing load both in the laboratory and in the virtual test environment in order to get a confirmation of the

validity of the identification approach and the suitability of the parameter values. Finally, the results are reported in terms of the axial crushing force – displacement curves. Although there are still some differences between the experimental and the numerical optimised curves, the quality of the obtained results is remarkable.

Then, Anghileri and co-workers simulate the axial impact of the frontal sacrificial structure for a Formula racing car. The shape of the structure consists of two truncated pyramidal shells of carbon fibre/epoxy matrix composite with a foam core. In the finite element model the foam has been substituted by a number of webs that act as spacers between the two shells, with an appreciable simplification of the model that thus avoid the well known problems connected with the numerical simulation of foams when very large compression deformations take place. Finally, figures show the shape of the collapsed shells at three subsequent times. The figures include also information on the evolution of the damage level for the composite material. For the deceleration time history, a comparison between experimental results and the numerical simulation shows good agreement.

Lanzi et al. [28] investigate the effect of the shape on the crash behaviour of conical composite absorbers with elliptical cross-sections and, eventually, to find that better suites specific crashworthiness requirements through an optimisation process. The optimisation results show how the presence of moderate eccentricity and conicity leads to high efficiency structures characterised by stable crash fronts and good absorption capabilities both considering ideal vertical and inclined crash conditions. Finally, a minimum weight optimization is performed fixing the minimum energy values to be absorbed under vertical and inclined impact conditions. The performance of the final configuration, identified using optimisation functions, is validated by finite element analysis with an accuracy within 3%.

Producing a structure from composite materials can be achieved in different ways, for example by resin infusion of dry fabrics or the use of pre-impregnated plies to form laminates that are cured in an autoclave. Resin transfer moulding (RTM) infusion methods require a manufacturer to arrange the fabric in the desired shape using a mould and then infuse with a resin. The benefits of RTM include the production of a safe manufacturing environment due to enclosure of the mould and increased flexibility in defining the component shape. The disadvantages include the expense of mould manufacture and control over the component quality, such as resin voids, when compared with pre-impregnated composite components. RTM developed components are being introduced to an increasing number of aerospace and automotive applications, such as the bumper tube shown in Fig. 8 used to absorb the energy from a frontal crash.

3 Material Characterization Tests

The carbon fibre type material used to manufacture thin-walled cylindrical specimens and the impact attenuator is plain weave prepreg GG203PIMP530R-42. The matrix type is resin epoxy and it is developed for the automotive sector, in particular

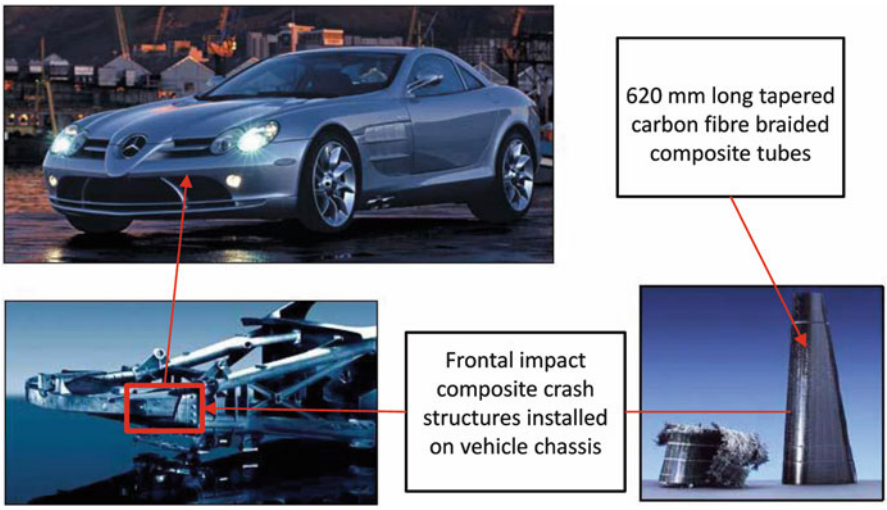


Fig. 8 McLaren Mercedes SLR bumper tube [29]

for sport applications. It is characterized by good impact resistance properties and quality surface finish and is adapted for high speed cold stamping. The resin content is $42\% \pm 3\%$.

To obtain appropriate input data for the simulation of the composite components and for the validation of the numerical material model, standard static coupon tests were performed at Politecnico di Torino laboratory. The material characterisation tests were performed in tension, according to ASTM Standard D3039, with the warp direction aligned with the test direction (0° tests) and also according to ASTM Standard D3518 with fibers aligned at 45° to the test direction. Coupon tests were performed up to material failure; Young's modulus, Poisson's ratio, yield stress and strain in the warp direction were obtained from the 0° tests, while the shear properties were extracted from the 45° tests. The flat specimens, used to measure these properties, were made from one ply of prepreg sheet, 200×10 mm^2, and composite end tabs were bonded at each end. Tensile tests were conducted with an electromechanical Zwick Z100 machine at a crosshead speed of 0.05 mm/s. Two strain gages (Micro-Measurements EP-08 250BG-120 and 125DQ-120) were bonded onto one side of the specimen, in order to acquire longitudinal and transversal strains, respectively. The testing machine and some plain specimens after tensile tests are shown in Fig. 9.

After careful analysis, it is noticed that the material characteristics obtained are similar to properties of CFS003/LTM25 carbon-epoxy prepreg. In the model, the properties obtained from tests are completed with material compression parameters of CFS003/LTM25 carbon-epoxy prepreg available in the literature. Although this material is twill weave, in numerical simulations it is modelled as plain weave. The mechanical properties, for considered material, are given in Table 1.

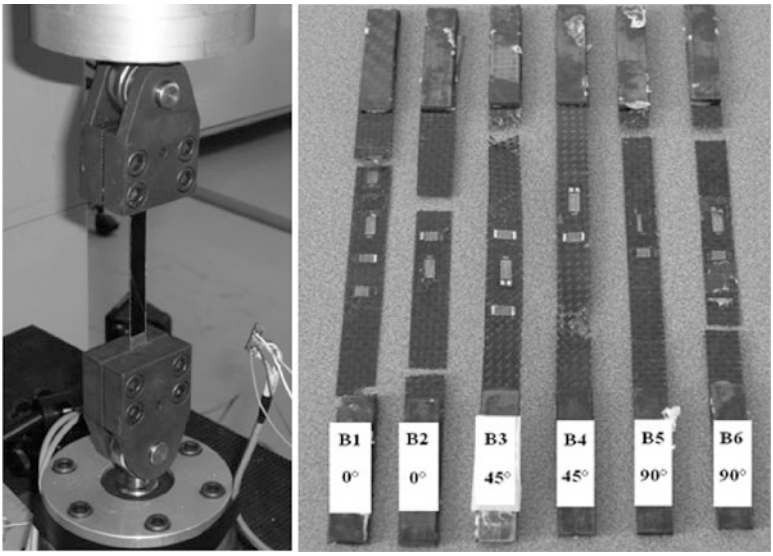


Fig. 9 The testing machine and some specimens after tensile tests

Table 1 Material properties for used prepreg

Property	Composite CFS003/LTM25 carbon-epoxy fabric prepreg
Density	$1.45 * 10^{-3}$ g/mm ^{3}
Young modulus in fibre longitudinal direction	53.6 GPa
Young modulus in transverse direction	55.2 GPa
Poisson's ratio	0.042
Shear modulus in direction 12	2.85 GPa
Shear modulus in direction 23	1.425 GPa
Shear modulus in direction 31	2.85 GPa
Longitudinal tensile strength	0.618 GPa
Transverse tensile strength	0.652 GPa
Longitudinal compressive strength	0.642 GPa
Transverse compressive strength	0.556 GPa
Compressive strength in direction 12	0.084 GPa
In plane shear strength	0.084 GPa

4 Definition of Energy Absorbing Structures

It is good to analyze the impact phenomenon from the two points of view initially for simple structures, such as cylindrical tubes, before proceeding with a more complex geometry, such as the Formula SAE impact attenuator.

The geometrical dimensions of the analysed cylindrical tubes are given in Table 2.

Table 2 Geometrical dimensions of cylindrical tubes

Internal diameter (mm)	Wall thickness (mm)	Length (mm)	Number of plies	Fiber orientations
80	2.5	200	10	Prepreg 0–90°
80	2	200	8	Prepreg 0–90°
80	1.5	200	6	Prepreg 0–90°
50	2.5	200	10	Prepreg 0–90°
50	2	200	8	Prepreg 0–90°
50	1.5	200	6	Prepreg 0–90°

The Society of Automotive Engineers has introduced a series of regulations to ensure that race cars conform to stringent safety requirements and build quality, in order to be granted race-worthiness certification. These criteria include a series of static loads applied to the chassis, which guarantee the strength and integrity of the survival cell and a series of requirements on the location and impact characteristics of the energy-absorbing device. Each year the number and severity of these requirements increases in line with ongoing research and development in crashworthiness or in response to real life accidents [30].

In order to meet the competition requirements of Formula SAE 2008, the attenuator must guarantee specific performances in terms of average deceleration values which must not exceed 20 g. Moreover the assembly of the sacrificial structure is subjected to the following conditions according to reference [30]:

- The impact attenuator must be installed in front of the bulkhead;
- It must be at least 200 mm long (along the main axis of the frame), 200 mm wide and 100 mm high;
- It must not penetrate the front bulkhead in case of impact;
- It must be attached to the front bulkhead by welding, or at least, four bolts (M8, grade 8.8);
- It must guarantee safety in case of off-axis impact (when the overlap between impact attenuator and barrier is less than 100%);

The energy absorber (Fig. 10) consists of a truncated pyramidal structure with an almost rectangular section. The pyramidal structure makes it possible to obtain a major stability during progressive crushing, while the rectangular section has rounded edges to avoid stress concentrations [31]. The design of sacrificial structure has been completed with a trigger which consists in a smoothing (progressive reduction) of the wall thickness in order to reduce the resisting section locally. This trigger is intended both to reduce the value of the force peak and to initialize structure collapse in a stable way.

Considering literature resources [24] and in order to implement proper triggering mechanism, it is decided to design three different wall thickness zones, presented in Fig. 10. Also, during the production process, the attenuator structure was made in two pieces that were later bonded together.

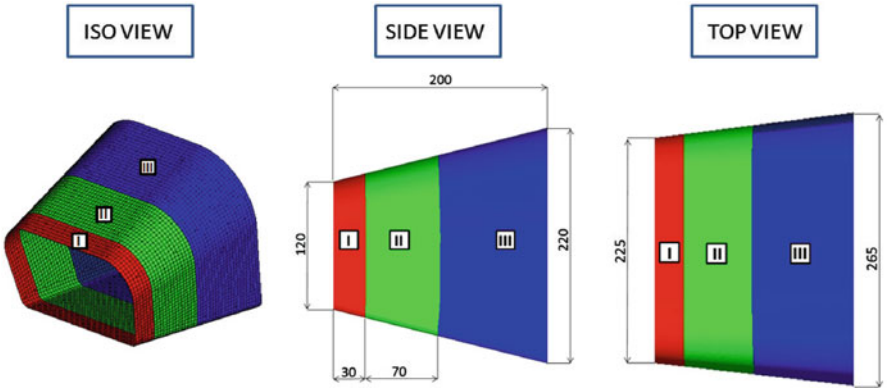


Fig. 10 *Isometric*, *side* and *top view* of FE model of produced composite impact attenuator with dimensions and different wall thickness zones

In order to analyze the effect of different thickness of the attenuator wall on resistance properties, the sacrificial structure has been produced in two versions as reported below:

Version 1:

- First zone – length = 30 mm, laminate thickness = 0.8 mm simulated with 4 plies
- Second zone – length = 70 mm, laminate thickness = 1.3 mm simulated with 6 plies
- Third zone – length = 100 mm, laminate thickness = 1.4 mm simulated with 7 plies

Version 2:

- First zone – length = 30 mm, laminate thickness = 1.68 mm simulated with 7 plies
- Second zone – length = 70 mm, laminate thickness = 2.16 mm simulated with 9 plies
- Third zone – length = 100 mm, laminate thickness = 2.4 mm simulated with 10 plies

5 Numerical Modelling

Before manufacturing and testing the cylindrical specimens and the impact attenuator, FE analyses were performed using the commercial solvers LS-DYNA and Radioss, which have been developed specifically for impact and non-linear dynamic simulations. In this way, it is possible to evaluate the impact attenuator crashworthiness by use of two different solvers, and after to compare these numerical simulations with experimental results.

The tubes are modeled in LS-DYNA by four-node shell elements with Belytschko-Tsay formulation. A multi-layered shell is used with one integration point per layer. To present composite numerical model, it is used the laminate with a thickness defined by the sum of each individual layer. Laminate theory is also activated with LAMSHT parameter in control card, to correct for the assumption of a uniform constant shear strain through the thickness of the shell. A moving rigid wall with a finite mass of 294 kg and an initial velocity of about 4 m/s represents the impacting mass. A master-surface to slave-node contact is defined between the impact surface and the nodes of the tubes. Then a self-contact algorithm based on the penalty formulation is defined on the tube surface to provide the friction effect between its parts during deformation and to prevent the elements penetration.

The impact attenuator, instead, has been modelled both in LS-DYNA and in Radioss, in order to capture the differences of the two codes. In the case of LS-DYNA modelling, it is implemented the same procedure that was used for cylindrical tubes.

In the case of Radioss numerical model, a rigid wall with a finite mass of 300 kg is added and it represents the obstacle that is impacting the attenuator during the test with initial velocity of 7 m/s. There is the friction between the rigid wall and attenuator. The friction coefficient has the value of 0.2 between the different parts of the attenuator itself and 0.4 between rigid wall and attenuator. Furthermore, the nose cone is supported by a rigid plate, characterized by particular material card and friction coefficient of 0.4. The element property type is Type10-Composite Shell.

Regarding the LS-DYNA numerical model of impact attenuator, it is implemented the “rigid wall planar moving forces” card with a mass of 300 kg, which is presenting the obstacle that is impacting the attenuator with the initial velocity of 7 m/s. The support of the attenuator is modelled as “rigid wall planar”, with prescribed friction coefficient equal to 0.4. Then, a self-contact algorithm, based on the penalty formulation, is defined on the attenuator surface to provide the friction between its parts during the deformation and to prevent the elements penetration.

Particular attention was given to the material definition of composites. The codes, in fact, contain different materials models that implement composite fabric with various failure criteria.

In particular, for the LS-DYNA library the material types 54 and 55, that implement the Chang-Chang and Tsai-Wu criteria, were used for modelling of composite tubes and impact attenuator, thanks to their ability to give a numerical behaviour near to the experimental ones [32]. To avoid ductile behaviour with folding, it is important to change the element strength at some point of the collapse evolution. This is obtained thanks to a time-step failure parameter (TFAIL), which defines a limit to the element effective strain. This allows to reproduce the brittle behaviour of the material and, at the same time, to control the time-step value and therefore to reduce the analysis CPU time. After sensitivity analyses a TFAIL parameter equal to 0.8 was chosen for most of the herein performed calculations.

Instead for RADIOSS the orthotropic composite material law COMPSH (25) was used which is based on a visco-elasto-plastic modelling of composites with

non-linear and strain rate dependent behaviours. Besides, the plasticity model is based on the Tsai-Wu criterion which allows to model the yield and failure phases. Regarding rupture, two types of failure criterions are available for composite materials in the Radioss solver. The first one is based on tensile failure strains in the fibers (for fabrics) or transverse (for unidirectional) directions (i = 1,2), representative of the typical brittle elastic behaviour of composite materials in these directions. The second one is based on an energy criterion involving the maximum plastic work $W_{\max}^{p}$ [33]. Once reached the material limit strength, these criteria lead to the progressive degradation of the mechanical properties of the composite ply, in the failed direction. In particular, the model allows to simulate the brittle failure by formation of cracks. The cracks can either be oriented parallel or perpendicular to the orthotropic reference frame (or fiber direction). For plastic failure, if the plastic work is larger than the maximum value $W_{\max}^{p}$ for a given element, then the element is considered to be ruptured. The final deletion of the multi-layer element is controlled by the global failure parameter Ioff (integer from 1 to 6), which activates the element deletion according to the number of failed plies and their failure mode [34]. In the current analysis, Ioff = 0 (element deleted once one ply has failed after reaching maximum work), and $W_{\max}^{p} = 0.1$ GPa are used. A delamination of chosen material law is handled mainly by delamination damage factor that permits to penalize the out-of-plane shear characteristics. The damage evolution law is linear with respect to the shear strain. In actual simulation, delamination is not considered.

6 Experimental Quasi-Static and Dynamic Tests

This section summarizes the experimental campaign conducted during this research work; in particular the first part describes the dynamic tests on simple cylindrical tubes, while the second one the quasi-static and dynamic tests on the impact attenuator with a more complex geometry. In order to assess the quality of the research results, initially a complete comparative analysis was developed on simple CFRP composite tubes. Only then it was analyzed the impact attenuator.

6.1 Experimental Dynamic Tests on Cylindrical Tubes

All the dynamic experimental tests reported in this paper were performed at the Picchio S.p.A. plant in Ancarano (TE, Italy) using a drop weight test machine (Fig. 11a) with a 6 m free-fall height and a maximum mass of 413 kg. For the experimental tests on cylindrical tubes was used an impact mass of 294 kg and an initial velocity of about 4 m/s. During the tests every tube was supported at the bottom edge on a metallic base with air holes. The acceleration of the mass and the velocity at impact were measured using an accelerometer with 180 g full-scale and a photocell, respectively (Fig. 11b, c).



Fig. 11 Drop tower (**a**), accelerometer (**b**) and photocell (**c**)

All the tubular specimens were manufactured with an outside chamfer, added by the manufacture manually, so that the crushing begins in the highly stressed region at the tip of the chamfer and this develops into a stable crush zone.

After the tests, the diagrams representing the variation of the acceleration with the time are analyzed and filtered with a CFC60 filter, in accordance with SAE J211.1 (Fig. 12). CFC is the abbreviation for Channel Frequency Class and this type represents a 4th-order Butterworth low pass phaseless digital filter with a 3 dB limit frequency of 100 Hz. The filter was used to eliminate the high frequency content introduced by vibration and noise and to give a relatively smooth trace that can be replicated. Moreover some important parameters for crash resistance characterisation have been computed and reported in Table 3. In particular the peak deceleration is the maximum filtered deceleration, the average deceleration is obtained from the beginning of the impact to the instant when the velocity vanishes, the absorbed energy corresponds to the area under the load-shortening diagram, residual height is the height of the crushed tube, the crash load efficiency (η_c) is

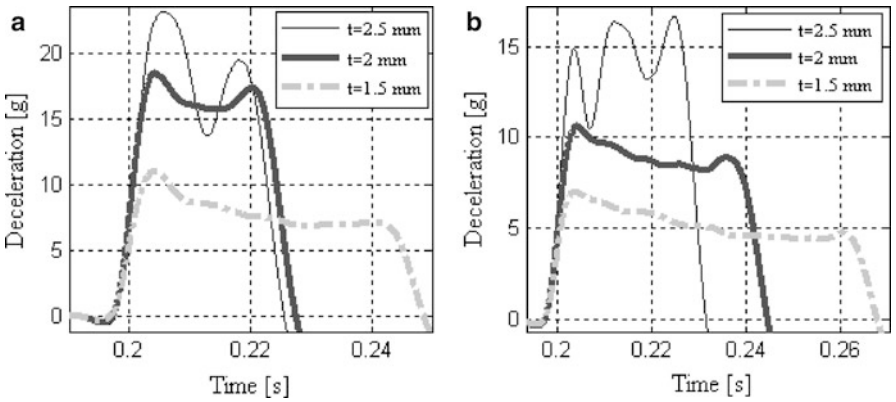


Fig. 12 Deceleration-time diagrams for tubular specimens: (**a**) diameter 80 mm, (**b**) diameter 50 mm

Table 3 Experimental crash-tests results of tubular specimens

Diameter (mm)	Thickness (mm)	Impact velocity (m/s)	Peak deceleration (g)	Average deceleration (g)	Absorbed energy (kJ)	Residual height (mm)	Load efficiency ηc	$\sigma_{average}$ (MPa)	SEA (kJ/kg)
80	2.5	3.7	23.10	16.18	2.02	165	0.70	73.41	65
80	2	3.6	18.81	14.51	1.96	156	0.77	82.83	65
80	1.5	4	11.01	7.55	2.35	115	0.68	57.80	54
50	2.5	3.9	16.68	12.59	2.24	146	0.75	89.84	76
50	2	4.2	10.62	8.46	2.59	120	0.79	76.06	76
50	1.5	4.2	7.01	5.14	2.59	73	0.73	62.19	63

defined as the ratio between average load $F_{average}$ and peak load F_{max}, the axial average strength ($\sigma_{average}$) is the ratio between average load and cross section and the specific energy absorption (SEA) is the ratio between absorbed energy and mass of damaged material.

From the deceleration versus time diagram, with a double integration and multiplying deceleration by mass, it is possible to obtain the load versus stroke trend. As indicated before, the area under this load-shortening diagram is the absorbed energy by the tube. Obviously the internal energy trend during crushing is of linear type, starting from a zero value before the impact until it reaches the maximum when the phenomenon it was concluded. The theoretical absorbed energy is obtained roughly as the product among SEA, density, cross sectional area and total crush length.

In particular for the tube with 50 mm of diameter and 2 mm of thickness the plots of the velocity and stroke versus time (Fig. 13a) and of the measured and theoretical absorbed energy versus stroke (Fig. 13b) are reported. Considering the

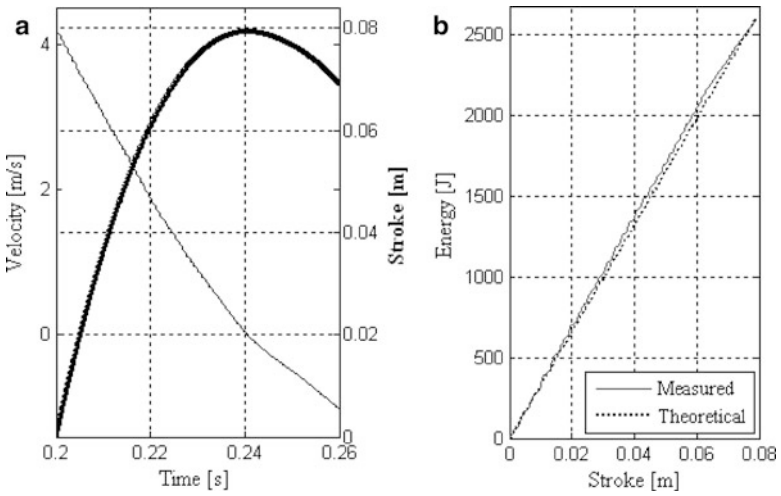


Fig. 13 Velocity and stroke versus time (**a**), measured and theoretical absorbed energy versus stroke (**b**)

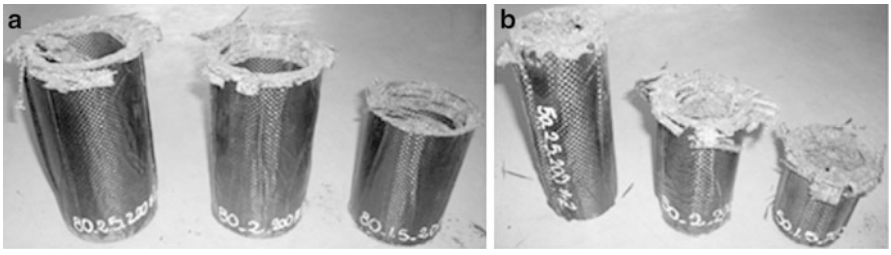


Fig. 14 Failure modes of the cylindrical tubes tested: (**a**) diameter 80 mm, (**b**) diameter 50 mm

results obtained for value of SEA of 76 kJ/kg, in Fig. 13b very good agreement can be observed between the theoretical (dot line) and the measured (thin line) curves.

The tested CFRP tubes absorbed impact energy by a progressive crushing process, through various combinations of failure mechanisms (Fig. 14). The specimens have shown two different crushing modes: splaying with axial splitting and fragmentation with debris compacted inside the tube and preventing further crushing (Fig. 15). In the first case, the axial fibres have splayed in a series of fronds to the outside and inside of the tube and a crack has formed along the centre of the wall. The second case, involves the formation of fragments in the crush zone which are forced to the inside and outside of the tube before complete separation from the wall. Only for the pair of specimens with thickness 1.5 mm it is possible to notice the difference in the absorption. However, in all configurations, the remaining part of tubes results intact.

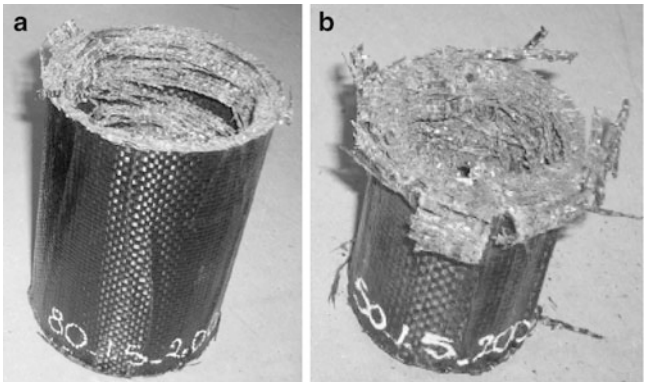


Fig. 15 Different failure modes of the cylindrical tubes: (**a**) fragmentation with debris, (**b**) splaying with axial splitting

6.2 Experimental Quasi-Static and Dynamic Tests on Impact Attenuator

The two competing nose cone designs, discussed in Sect. 4, are tested in quasi-static axial compression. The tests are conducted with an electromechanical Zwick Z100 machine at a crosshead speed of 0.5 mm/s. The compression is performed with upper moving plate and the load is measured by the load cell.

The thinner nose cone (version 1) is tested up to the displacement in axial direction of 100 mm. The structure with thicker wall (version 2) is tested up to the displacement of 160 mm. The thinner impact attenuator, at two subsequent stages of the test i.e. before quasi-static test and after the displacement of 100 mm, is shown in Fig. 16. The failure mode of the impact attenuator and cylindrical tubes (Fig. 15b) are very similar, i.e. splaying with axial splitting. Cracks propagate along the bonding line of two parts of impact attenuator. The crack did not propagated to the end of attenuator, since the test was interrupted.

Figure 17 compares the force versus displacement for two different impact attenuator designs the trend is the same and the desired smooth curve behaviour is obtained for both cases. After the initial peak, the second force peak at the displacement of 30 mm and the third one at the displacement of about 100 mm. This is because of the wall thickness change (Fig. 10). The wall thickness change is a very sensitive parameter and in order to decrease force peaks, the difference in ply thickness between different impact attenuator zones should be as small as possible.

The dynamic experimental tests were performed using a drop tower test machine presented previously. Considering initial conditions, set according to SAE 2008 rules, the nose cone is impacted with the mass of 300 kg which has the initial velocity of 7 m/s. The calculated kinetic energy is 7,350 J. Structural crashworthiness of the composite impact attenuator is affected by the manufacturing. The

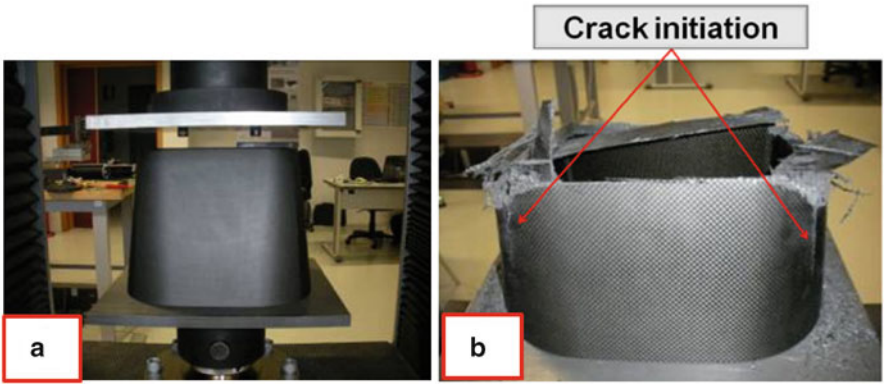


Fig. 16 Quasi-static test: (**a**) Initial position of attenuator; (**b**) and after the performed test

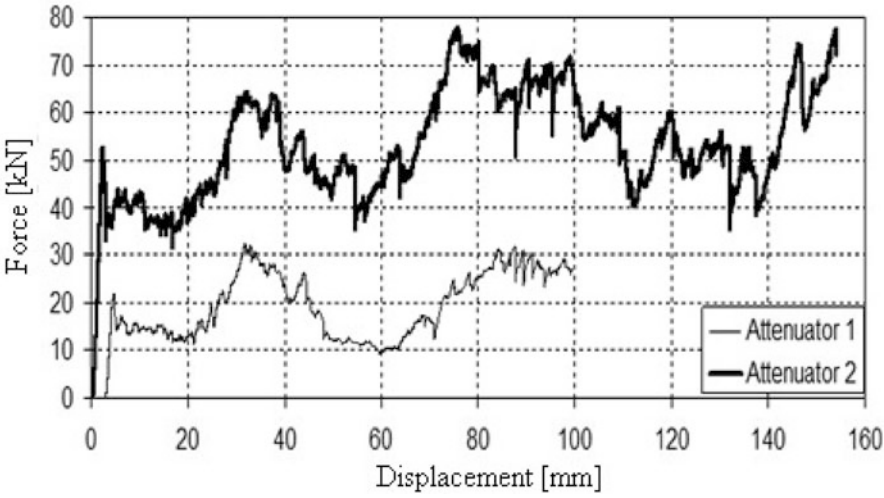


Fig. 17 Quasi-static test: comparison of force versus displacement diagram of two attenuators

impacted sacrificial structure has a brittle failure up to some point, after which it is predominant the detachment of the fabric laminates exactly along the bonding line of two parts of impact attenuator (Sect. 4). That causes the loss of the attenuator's strength and stability and the collapse of the structure, which is not able to show the real resistance and crash impact behaviour. Figure 18a shows the nose cone after the dynamic impact. Almost half of the attenuator material remained undamaged, i.e. the energy absorption capability is lower than in the case of quasi-static test, when the main damage mechanism is a complete diffuse brittle failure. In Fig. 18b the nose cone with higher value of wall thickness and the pieces of crashed thinner attenuator positioned on it. This allows us to distinguish the laminate detachment along the bonding line. The same type and position of laminate detachment is present also,

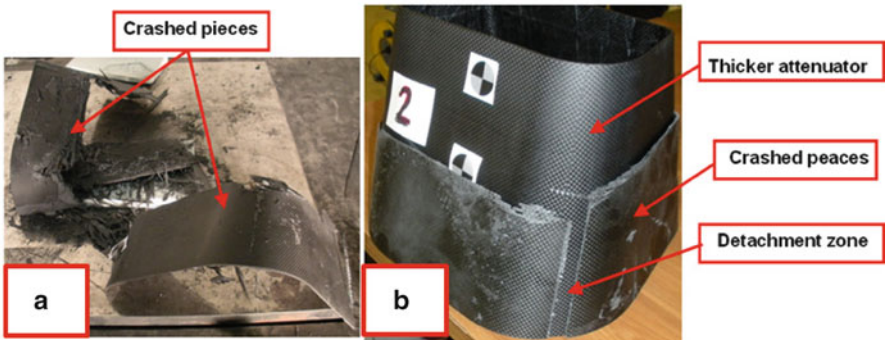


Fig. 18 Dynamic crash test: (**a**) attenuator after the crash; (**b**) laminate detachment zone

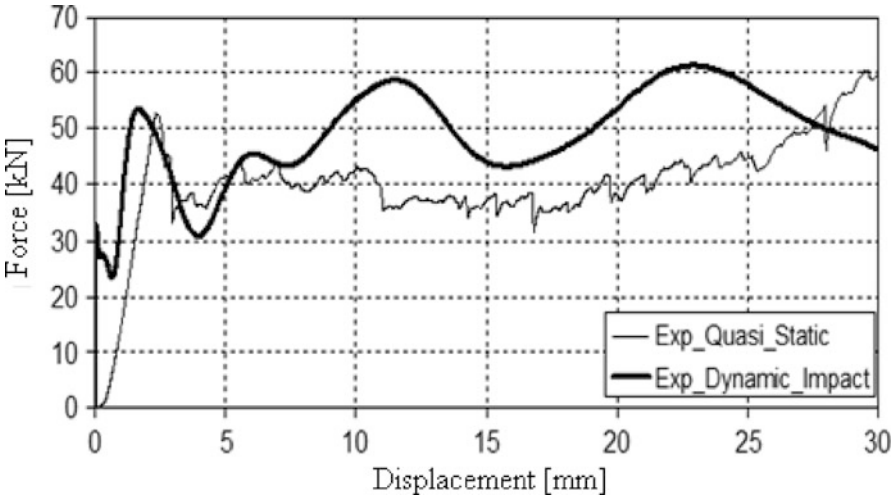


Fig. 19 Dynamic test versus quasi-static experimental test: comparison of force versus displacement

after carrying out the dynamic impact of thicker attenuator. This type of debonding laminate behaviour was also noticed during the static tests (Fig. 16b).

Figure 19 compares the force versus displacement curves of quasi-static and dynamic tests of impact attenuators with higher wall. The trend of curves up to the displacement of 30 mm is analysed. After this value, attenuator collapses during dynamic crash due to laminate detachment. The first peak in the diagram, has approximately the same value in both cases of dynamic and quasi-static tests. The trend of curves is almost the same, although it appears that in dynamic impact the structure has higher load carrying capacity. The final evaluation of the attenuator design and crashworthiness is performed according to Formula SAE requirements (particular attention is put on average deceleration of the vehicle), and this will be discussed in Sect. 7.2.

7 Comparison Between Numerical and Experimental Results

This section compares numerical and experimental results, for simple tubes and for the more complex impact attenuator under all load conditions. The numerical model is able to reproduce the response of such structures to crash.

7.1 Cylindrical Tubes

After a mesh sensitivity analysis, a uniform mesh with elements of about 2 mm per side has been chosen. A sequence of deformed shapes of a fabric tube (diameter 50 mm and thickness 2 mm) at different simulation times, is shown in Fig. 20. Also, it is visible fragmentation of composite tubes, achieved by implementation of failure criteria.

The numerical and experimental deceleration versus shortening curves for the tube with diameter 50 mm and thickness 2 mm are compared in Fig. 21, while some crash parameters obtained from experimental tests are reported together with numerical results in Table 4 for all specimens. As the experimental data, also the numerical ones are filtered with the same filter CFC60. The conditions for the test are obviously the same, then an impacting mass of 294 kg with an initial velocity of 4.2 m/s.

These results indicate that the FE model can simulate the brittle composite material behaviour with material separation from the specimens and consequently approximate the absorbed energy and the actual crushing with good accuracy.

In all cases the difference between numerical and experimental results is lower than 12%. It is mainly due to the complexity to simulate the initialization of the fragmentation phase and defects in the construction of the tubes.

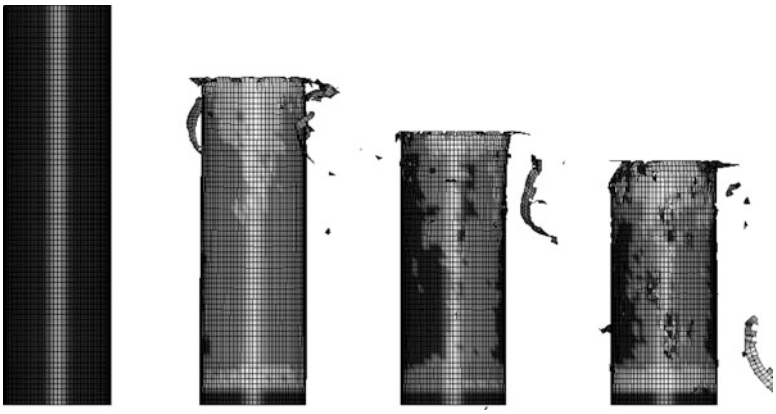


Fig. 20 Sequence of deformation for tube with 50 mm diameter and 2 mm thickness

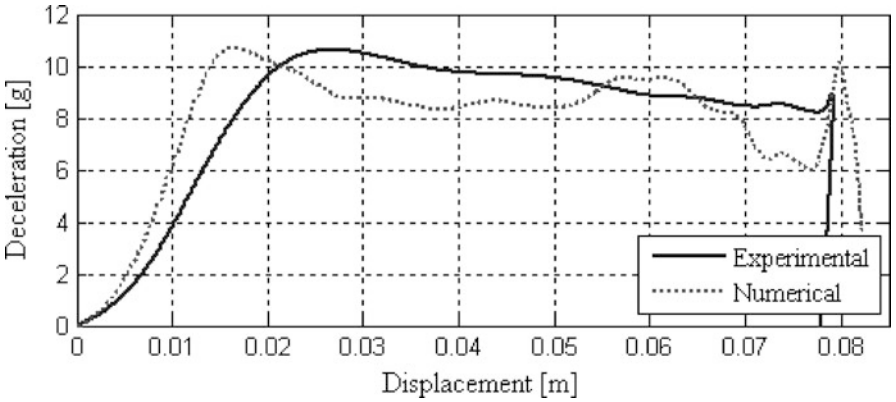


Fig. 21 Numerical and experimental deceleration-shortening diagram for the cylindrical tube with diameter 50 mm and thickness 2 mm

Table 4 Numerical and experimental results for all tubular specimens

Specimen	FE model		Experimental test		Error % on crushing
Diameter – thickness (mm)	Absorbed energy (kJ)	Crushing (mm)	Absorbed energy (kJ)	Crushing (mm)	FE vs. experimental difference %
80 – 2.5	2.01	38	2.02	35	8.5
80 – 2.0	2.01	45	1.96	44	2.2
80 – 1.5	2.01	87	2.35	85	2.3
50 – 2.5	2.01	53	2.24	54	1.8
50 – 2.0	2.47	82	2.59	80	2.5
50 – 1.5	2.01	132	2.59	127	3.9

7.2 Impact Attenuator

Figure 22 compares the kinetic energy histories of the impact attenuator modelled by LS-DYNA and by Radioss. Both curves are starting from the initial energy value of 7,350 J. The trend of both structures is almost the same, but the kinetic energy calculated by Radioss is decreasing slower than the one calculated by LS-DYNA during the crash event. That means that Radioss code is giving more progressive collapse, but in any case the difference is very small.

Figure 23 shows the evolution of decelerations during the time, predicted by both solvers. The first peak of the impact attenuator is due to the initialization of structural collapse. The decrease of the initial peak values can be obtained by a proper modification of impact attenuator structure that includes crush initialisation triggers. After the initial peaks, a stable propagation of the deceleration curve is obtained as expected. The results obtained by the two performed simulations are very close to each other up to 25 ms then a divergence is visible. In particular in the

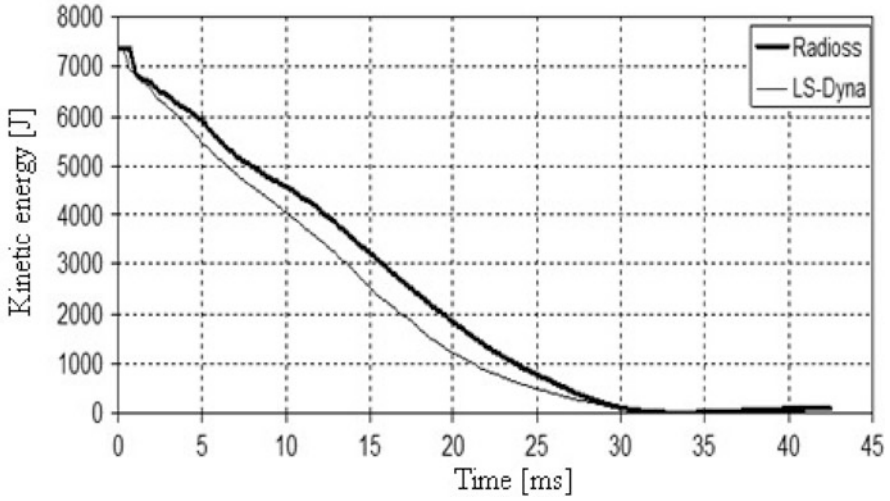


Fig. 22 Comparison of simulation results of kinetic energy versus time obtained by Radioss and LS-DYNA

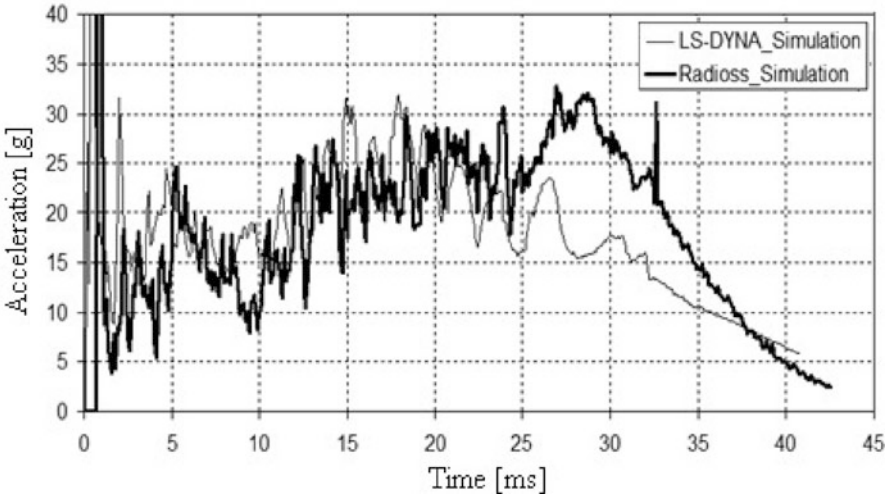


Fig. 23 Comparison of decelerations of the attenuator modeled by Radioss and LS-DYNA

case of LS-DYNA simulation, the structure has a lower load carrying capacity than the one modelled with Radioss code. The diagram of Fig. 24 compares results from numerical simulations performed using Radioss with tests results up to 22 ms. The same trend of curves is confirmed, and the predictions are in good agreement with experimental results. The high value of the initial peak is a numerical problem that doesn't appear in the case of experiments. Also, it is recommended in SAE rules

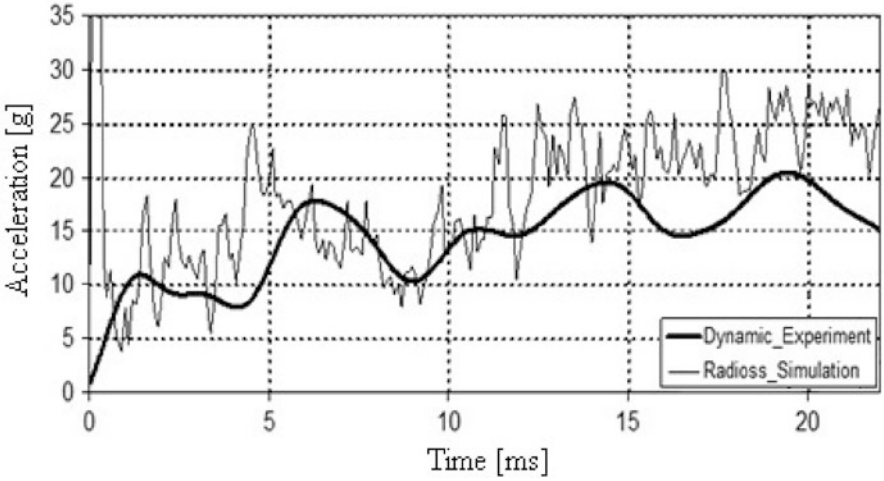


Fig. 24 Comparison of decelerations obtained by Radioss code and dynamic crash experiment

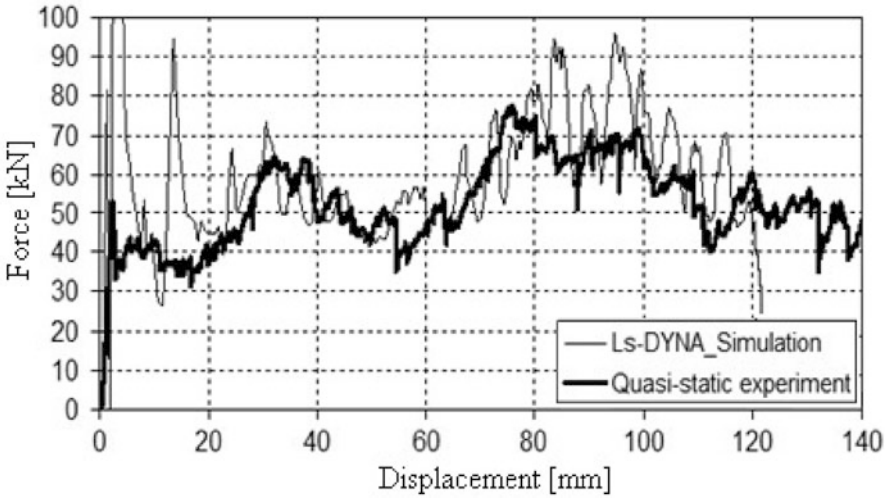


Fig. 25 Comparison of force versus displacement curves obtained by LS-DYNA code and quasi-static experiment

that "average deceleration of the vehicle must not exceed 20 g". This constraint is satisfied both in experimental and numerical circumstances.

Figures 25 and 26 compare force versus displacement curves obtained by experimental quasi-static tests and crash dynamic simulations carried out using LS-DYNA and Radioss. As mentioned before, the first critical peak is mostly a numerical problem that does not appear in the experiment. This numerical peak is mostly due to the model that is used to describe the specific contact between the rigid

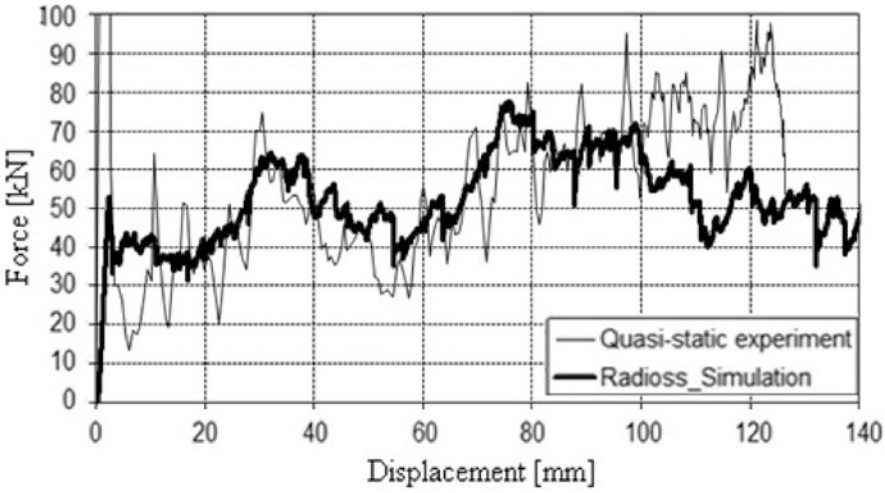


Fig. 26 Comparison of force versus displacement curves obtained by Radioss code and quasi-static experiment

wall and the attenuator, since the stiffness difference between the two impacting bodies is very high the model gives this unrealistic peak. Further, geometrical and material imperfections of the impact attenuator, that are in the manufactured part but not in its numerical model, are contributing to decrease the initial peak value. During the quasi static test, the first maximum peak of the force is 52 kN. The trend of curves is almost the same in the case of both FE codes. A stable propagation of the impact force is obtained, which means a nearly constant value of the deceleration, as visible also in Fig. 23. At the end of the simulation, the structure modelled in Radioss has a larger load carrying capacity than the impact attenuator used in experiment.

Figure 27a, shows the bending of the wall of the composite impact attenuator under quasi-static loading conditions. This behaviour is well visible after the displacement of 100 mm, which corresponds to the half of the attenuator length. Numerical simulations performed with Radioss and LS-DYNA are shown in Fig. 27b, c. The flexion of the wall after a displacement of 100 mm during quasi-static test is confirmed by simulations.

8 Conclusions

The present chapter describes the numerical and experimental investigation on the energy absorbing mode of composite structures, initially of simple tubular shape and then of more complex geometry. This in order to develop a methodology to follow during the design of a lightweight impact attenuator that must pass well

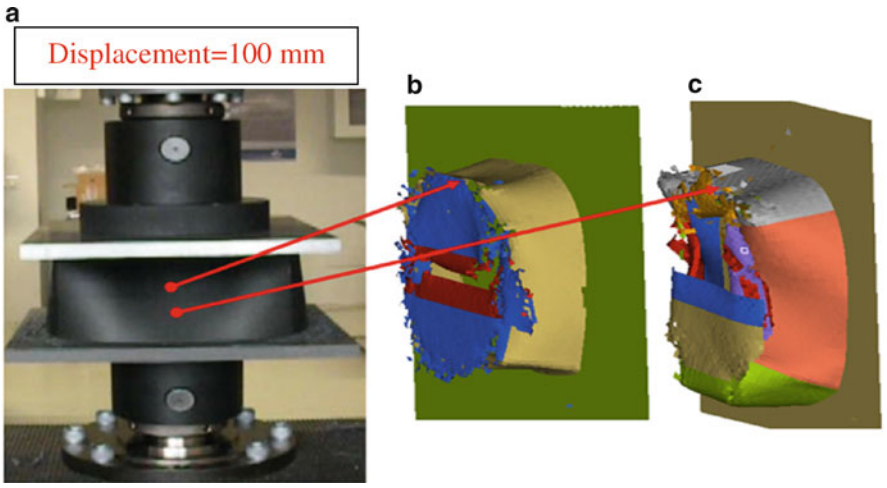


Fig. 27 Flexion of the attenuator wall subjected to quasi-static compression test-comparison of experimental and numerical results. (**a**) Quasi-static compression experimental test, (**b**) Radioss simulation, (**c**) LS-DYNA simulation

defined homologation tests. The attention was focused on the lightweight frontal safety structure of a Formula SAE vehicle.

Initially, to calibrate the numerical models, tensile tests were conducted to characterize the constitutive behaviour of the composite material under different loading conditions and CFRP tube crushing experiments were performed to determine the global failure modes in a crash and to understand the numerical parameters. The FE models were developed using the two dynamic solvers LS-DYNA and Radioss. Crash-tests were performed using a drop test machine, measuring the deceleration-time diagram and, after integration processes, load-shortening trend and energy absorbed by the structure.

Despite the complexity of the fracture phenomenon, a good agreement between numerical and experimental results has been achieved for simple tubular structures. The FE model is able to simulate the brittle composite material behaviour with material separation from the specimens and consequently approximate the absorbed energy and the actual crushing with an accuracy of about 90%.

A careful analysis of the crash behavior of the impact attenuator structure that has been designed to equip the formula SAE car of the Politecnico di Torino racing team was performed. Experiments confirmed the stable behaviour of the sacrificial structure with flat, almost constant force versus displacement curves and acceleration limit below 20 g. This value fits well with the requirements of SAE 2008 rules, as they require that the solution adopted leads to an average deceleration lower than 20 g.

Explicit FE solvers LS-DYNA and Radioss, were able to predict experimental results regarding both stiffness and progressive collapse mechanism of the impact

attenuator. Beside the appropriate choice of a trigger mechanism, the failure criteria was the most important parameter of the modeling of composite structure in order to predict brittle collapse of the nose cone. Force-displacement diagrams confirm that experimental and numerical results are almost the same. Also, the absorption of the kinetic energy of the composite attenuator shows stable behaviour.

References

1. Belingardi G, Obradovic J (2011) Crash analysis of composite sacrificial structure for racing car. Mobil Veh Mechan 37:41–55. ISSN: 1450–5304
2. Belingardi G, Chiandussi G (2011) Vehicle crashworthiness design – general principles and potentialities of composite material structures. In: Abrate S (ed) Impact engineering of composite structures. Springer, Wien, pp 193–264. ISBN 9783709105221
3. Feraboli P, Masini A (2004) Development of carbon/epoxy structural components for a high performance vehicle. Compos Part B 35:323–330
4. Ickert L (2010) Load adapted automotive lightweight structures in composite design. In: 4th international CFK-Valley Stade convention, Stade
5. Mamalis AG, Manolakos DE, Ioannidis MB, Papapostolou DP (2004) Crashworthy characteristics of axially statically compressed thin-walled square CFRP composite tubes: experimental. Compos Struct 63:347–360
6. Mamalis AG, Manolakos DE, Ioannidis MB, Papapostolou DP (2006) The static and dynamic axial collapse of CFRP square tubes: finite element modeling. Compos Struct 74:213–225
7. Solaimurugan S, Velmurugan R (2007) Influence of fibre orientation and stacking sequence on petalling of glass/polyester composite cylindrical shells under axial compression. Int J Solids Struct 44:6999–7020
8. Hull D (1983) Axial crushing of fibre-reinforced composite tubes. In: Jones N, Wierzbicki T (eds) Structural crashworthiness. Butterworths, London, pp 118–135
9. Sigalas I, Kumosa M, Hull D (1991) Trigger mechanisms in energy absorbing glass cloth/epoxy tube. Compos Sci Technol 40:265–287
10. Hull D (1991) A unified approach to progressive crushing of fibre-reinforced composite tubes. Compos Sci Technol 40:377–421
11. Warrior NA, Turner TA, Robitaille F, Rudd CD (2004) The effect of interlaminar toughening strategies on the energy absorption of composite tubes. Compos Part A 35:431–437
12. Mamalis AG, Manolakos DE, Demosthenous GA, Ioannidis MB (1998) Crashworthiness of composite thin-walled structural components. CRC Press, Lancaster
13. Mamalis AG, Manolakos DE, Demosthenous GA, Ioannidis MB (1996) Analysis of failure mechanisms observed in axial collapse of thin-walled circular fiberglass composite tubes. Thin Wall Struct 24:335–352
14. Mamalis AG, Manolakos DE, Demosthenous GA, Ioannidis MB (1996) Energy absorption capability of fiberglass composite square frusta subjected to static and dynamic axial collapse. ThinWall Struct 25(4):269–295
15. Mamalis AG, Manolakos DE, Demosthenous GA, Ioannidis MB (1997) Analytical modeling of the static and dynamic axial collapse of thin-walled fiberglass composite conical shells. Int J Impact Eng 19(5–6):477–492
16. Gupta NK, Velmurugan R (1999) Analysis of polyester and epoxy composite shells subjected to axial crushing. Int J Crashworthiness 5(3):333–344
17. Zhang X, Cheng G, Zhang H (2009) Numerical investigations on a new type of energy absorbing structure based on free inversion of tubes. Int J Mech Sci 51(1):64–76
18. Zhang A, Suzuki K (2007) A study on the effect of stiffeners on quasi-static crushing of stiffened square tube with non-linear finite element method. Int J Impact Eng 34(3):544–555

19. Thornton PH, Edwards PJ (1982) Energy absorption in composite tubes. J Compos Mater 16:521–545
20. Farley GL, Jones RM (1992) Crushing characteristics of continuous fiber-reinforced composite tubes. J Compos Mater 26(1):37–50
21. Savage G, Bomphray I, Oxley M (2004) Exploiting the fracture properties of carbon fibre composites to design lightweight energy absorbing structures. Eng Fail Anal 11:677–694
22. Boria S, Belingardi G (2012) Numerical investigation of energy absorbers in composite materials for automotive applications. Int J Crashworthiness 17(4):345–356. doi:10.1080/13588265.2011.648516
23. Bisagni C, Di Pietro G, Fraschini L, Terletti D (2005) Progressive crushing of fiber-reinforced composite structural components of a formula one racing car. Compos Struct 68:491–503
24. Feraboli P, Norris C, McLarty D (2007) Design and certification of a composite thin-walled structure for energy absorption. Int J Veh Des 44(3–4):247–267
25. Boria S (2010) Behaviour of an impact attenuator for formula SAE car under dynamic loading. Int J Veh Struct Syst 2(2):45–53
26. Heimbs S, Strobl F, Middendorf P, Gardner S, Eddington B, Key J (2009) Crash simulation of an F1 racing car front impact structure. In: 7th European LS-DYNA users conference, Salzburg
27. Anghileri M, Chirwa EC, Lanzi L, Mentuccia F (2005) An inverse approach to identify the constitutive model parameters for crashworthiness modelling of composite structures. Compos Struct 68:65–74
28. Lanzi L, Castelletti L, Anghileri M (2004) Multi-objective optimisation of composite absorber shape under crashworthiness requirements. Compos Struct 65:433–441
29. Lamb AJ (2007) Experimental investigation and numerical modelling of composite-honeycomb materials used in Formula 1 crash structures. PhD dissertation, Cranfield University
30. Formula SAE rules (2008). http://students.sae.org/competitions/formulaseries/rules/rules.pdf
31. Belingardi G, Obradovic J (2010) Design of the impact attenuator for a formula student racing car: numerical simulation of the impact crash test. J Serbian Soc Comput Mech 4(1):52–65. ISSN: 1820–6530
32. LS-DYNA keywords user's manual, version 971 BETA 4, June (2009)
33. RADIOSS theory manual, version 10.0, January (2009)
34. Delsart D, Joly D, Mahe M, Winkelmuller G (2004) Evaluation of finite element modelling methodologies for the design of crashworthy composite commercial aircraft fuselage. In: 24th international congress of the aeronautical sciences, Yokohama

Composites and Dynamic Failures: Experimental and Numerical Solving Strategies and Solutions

Daniel Coutellier

Abstract The constraints related to structures design in the field of transportation are increasingly complex in order to comply with safety standards. Composite materials being increasingly widespread within these structures, their behavior must therefore be more accurately mastered. Current numerical tools can now permit an accurate simulation in the static field, but concerning fast transient problems, the available numerical methods are not optimal yet. Starting from concrete cases, this chapter introduces problem solving strategies. A procedure is then presented to improve numerical simulations in the field of rapid dynamics. It includes the establishment of experimental protocols to assist in a thorough understanding of materials behavior. These experimental studies can then provide models, laws and methodologies to better simulate the behavior of composite structures under dynamic load. However experimentation is sometimes complicated by the size of structures. The similitude techniques can then provide a solution. Similitude techniques are used to study composite materials subjected to impact. We propose here an approach allowing modeling and numerical simulation validated on an industrial case.

Keywords Rapid dynamics • Composite • Damage • Scale effect

1 Introduction

Structural design in the transportation field must comply with numerous constraints in order to meet both environmental and recycling criteria. Increasingly integrating features within components contributes to on-going weight reduction

D. Coutellier (✉)
LAMIH UMR CNRS 8201, University Lille Nord de France, Valenciennes, France

University of Valenciennes, F-59313 Valenciennes, France
e-mail: daniel.coutellier@univ-valenciennes.fr

S. Abrate et al. (eds.), *Dynamic Failure of Composite and Sandwich Structures*,
Solid Mechanics and Its Applications 192, DOI 10.1007/978-94-007-5329-7_14,
© Springer Science+Business Media Dordrecht 2013

in order to increase the capacities and reduce consumption while retaining, or even improving, the mechanical performance. These primary objectives result in increased use of composite materials, plastics and alternative new materials and sandwich construction. Even though those materials have been used in aeronautics for quite a long time featuring some 15% (in mass) of composites on the A320 since 1988 and 25% for the Airbus A380. The new Boeing 787 and the future Airbus A350 reach the ratio of 50%. In the automotive field, the 25% score has by now been reached on some space-wagons. And today, the **ULIMAT** project (***Innovative Use of New Materials in Railway Design***) of the **Itrans** cluster, on a global scale, aims at validating the use of new materials (Composites, foams, metallic materials, brand new steels, steel/polymers sandwich structures) in order to build up a multi-material body-shell aiming at using the most adapted material for a specific function in order to reach a 20% mass reduction, a 20% reduction in the number of parts making up a body and a 50% decrease in the assembly-time. As regards the behavior field in rapid dynamics, the solutions available are not perfect yet. Right now major research and development themes in this domain are studied [1–3]. A procedure proposed to help improve the numerical simulation tools in the field of rapid dynamics is then introduced for 2D composites. It includes the establishment of experimental protocols to assist in a thorough understanding of materials behavior. However experimentation is sometimes complicated by the size of structures. Similitude techniques can then provide a solution to reduce the cost and study time. First, we present a variant of the similitude techniques for the study of composite materials subjected to impact. Introduced by Jackson [4] and Simitses [5] for linear cases, this method has been extended for rapid dynamic cases [6]. In the second part, we propose an approach for the numerical simulation of rapid dynamic phenomena. The modeling of damage, of delamination, of strain rates is proposed here and contributes to the simulation of complex phenomena. The application to an industrial case of a composite bonnet allows to validate this approach.

2 A Few Examples of Fracture of Composites Materials

The study of structures submitted to shocks and impact is rather complex whenever the materials used are composites. Indeed, the failure modes encountered are wide-ranging and mainly depend upon the choice of the material and its components. As a result, they are still poorly mastered and are right now difficult to reproduced in terms of numerical simulation. Figure 1 displays the complexity of the fracture modes encountered in the case of energy absorbers, in-built within the floor of aeronautic structures submitted to axial compression [7, 8]. Delamination between the laminated material plies, fiber splitting within the same ply present many difficulties in terms of repeatability in numerical models in order to determine exactly the value of the energy absorbed by overall deformation. With composite structures, the assembly areas are equally critical and complex. Figure 2 (Postec

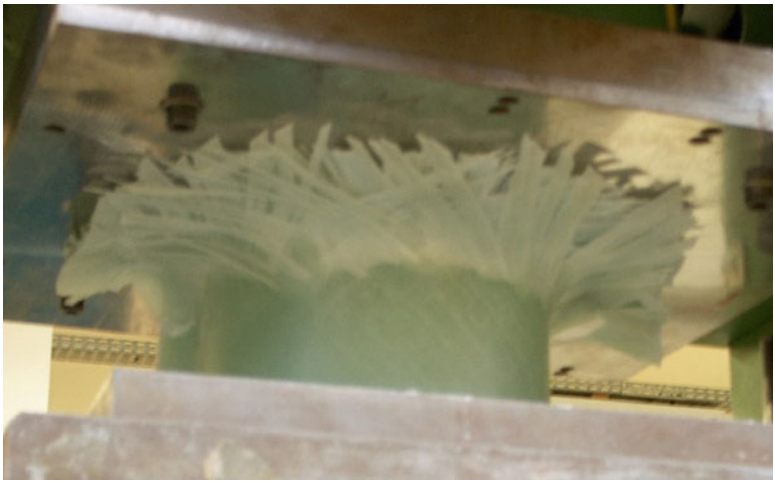


Fig. 1 Fracture mode of an energy absorber

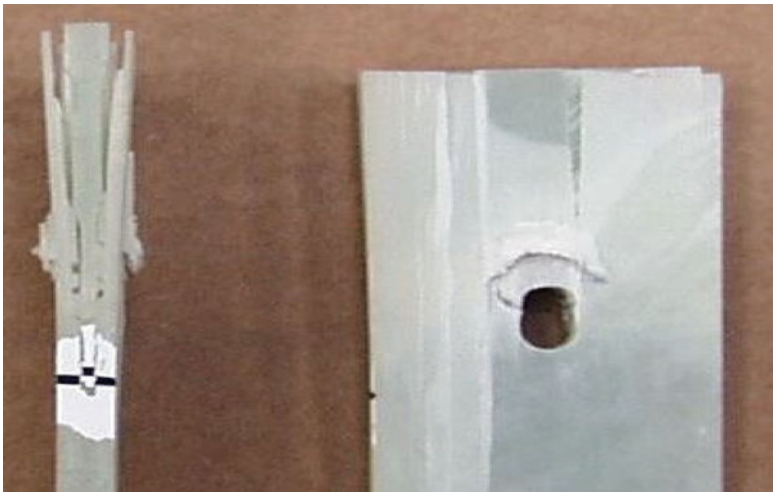


Fig. 2 Fracture mode during the bearing process of a $[0/45/90/-45]_s$ composite assembly

et al. [9]) shows the desirable fracture mode via bearing rupture in order to consume little energy within link fracture. Figure 3 (Provost et al. [10]) shows the fracture mode after impact behavior of a composite solution made with warp interlock fabric used in hard protection as armored shield of vehicles. The assumed delamination process of the 3D textile structure tends to be more complex. This failure kinematics is paramount in order to contribute to an overall prediction of the failure process. It is therefore essential not only to be able to reproduce it in numerical simulations but also first and foremost to understand it. Many other

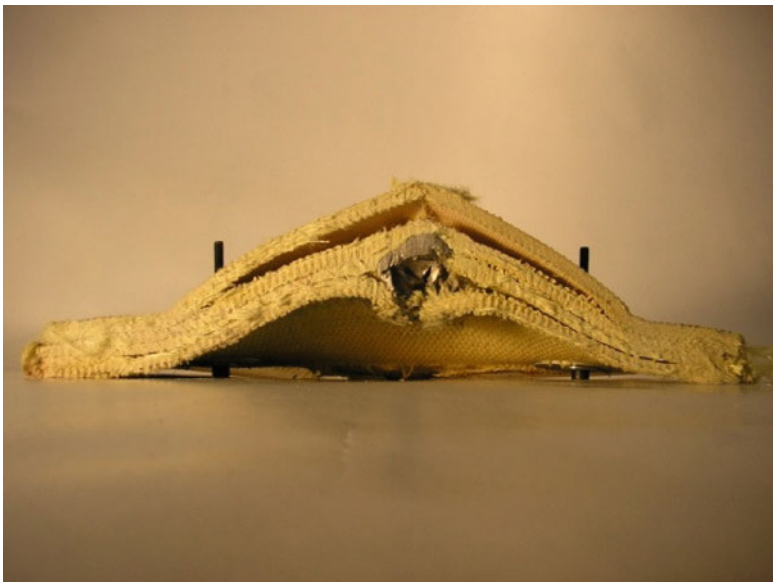


Fig. 3 Fracture mode after impact behavior of a warp interlock fabric composite

examples might be given in all fields and the limits are often associated with the development tools available during the design phase [11–13]. For instance, some car manufacturers are now considering multi-material composite bonnets which would permit to reduce injuries, more particularly, head-injuries in the case of an impact, in their efforts to anticipate new regulations. Again, the simulation softwares are far from being efficient and, right now, numerous tests [14] (Fig. 4) are required in order to permit the test/computations calibration to refine the technological developments. The tendency to lighten structures requires to use more composite materials in the future design.

The composite material complexity is due not only to its components structure but also to its various processes, to its durability, to its deformation, damage and fracture modes in the case of an impact or a crash. In order to master these phenomena, experimental campaigns are necessary. They represent a non-negligible cost and they may be somehow difficult to implement should the structure size be important and the price of the structure. Indeed, if it is fairly easy and usual to crash-test an automobile, it is quite a different story for a train-coach or a plane. In this particular case-study, a scaled-down test helps reduce the costs under the condition that it is possible to reproduce the accurate behavior, which is here far from being valid whenever the structures are made up with composites and the loading mode is rapid dynamics, therefore restricted to the non-linear field. For over a decade, studies have been carried out at the **LAMIH** in order partly to answer the questions arising during the crash, in the field of metallic/composite materials behavior, while developing similitude applications. For composite materials, specific items have

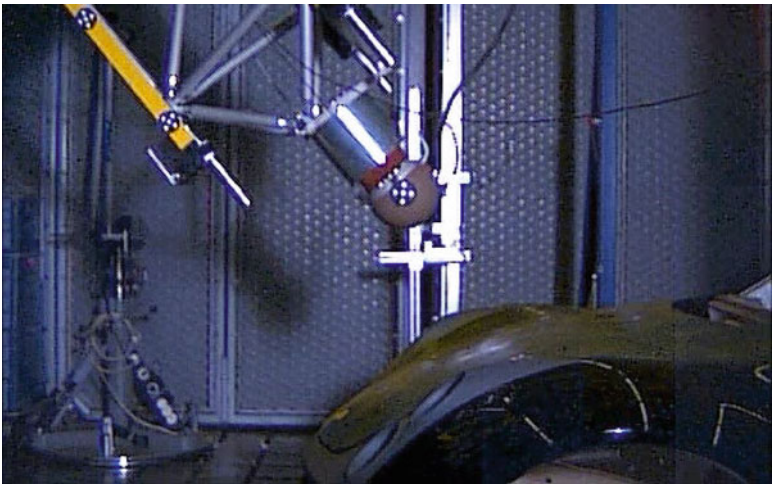


Fig. 4 Example of a pedestrian collision test on bonnet (Courtesy: Daimler)

been developed in industrial codes [15, 16], methodologies have been implemented in order to integrate precise damage modes [17], similitude methodologies have been suggested in order to permit the study of scaled-down composite structures [18]. Those studies are still going on in order to bring a contribution to the improvement of virtual prototyping tools and we hereby present two examples of resulting applications. One concerns the development of a similitude method to determine the real scale behavior starting from scaled-down structures. The second concerns the studies carried out with a car-manufacturer for the analysis of a pedestrian's head impact onto a front car-bonnet.

3 Analytical Model for Similitude Analysis

Despite recent improvements achieved in numerical simulation [19–21], such phenomena as delamination or strain rate influence are still poorly represented and are the aims of numerous studies nowadays. Experimentation is consequently the only reliable validation method but its setting up can give rise to some problems of cost, of place or of equipment especially for airplane or railway structures. Tests on scaled down structures seem to be the obvious solution. But it also leads to a lot of problems such as the preservation of the assembly way, of the manufacturing process and of the mechanical properties. Similarity laws already exist for traditional materials [22] but there is nothing about composite materials under dynamic loading. However laminated composites still present an issue: to preserve the ply material and reduce the specimen thickness, it is unavoidable to reduce the number of plies. Some re-arrangement techniques exist for this thickness



Fig. 5 Structures featuring three different scales (1; 1/2; 1/4)

reduction [4, 5] but they originate only from geometrical considerations, they are not applicable to the whole stacking sequences and they do not preserve all the mechanical properties of the structure. Moreover, modifying the ply number makes it impossible to use total similarity (there is a distortion between the prototype ply number and the scaled down model one). So, the aim is to apply partial similarity on a determined structure under a specific loading minimising the distortion effects, and then, to extend the method to more complex structures. Static and dynamic tests have been performed on specimens (Omega structure (Fig. 5)) currently used in the design of aeronautic structures to absorb energy.

The objective of these techniques is a structure scale reduction; however, within our study, these techniques have been used in an inverse way, that is to say applied gradually on the 1/4 scaled models then on the 1/2 scaled models and finally on the prototype. The similitude techniques, developed initially by Jackson [4] are the following ones:

- the first one, consists in defining a first stacking sequence made of n plies $[+\theta/-\theta]$, then defining the following one by doubling each ply in order to obtain a final laminate made of 2n plies $[+\theta_2/-\theta_2]_s$. This similitude is very interesting because it permits directly to have consistent stiffness (in-plane tension and compression) and flexion modulus,
- the second one, consists in symmetrising the initial stacking sequence,
- the third one, leading from the laminate $[+\theta/-\theta]_s$ to the final laminate $[+\theta/-\theta]_{2s}$, is performed by symmetrising the initial sequence twice. As for the first technique, it allows a correct setting of the in-plane modulus, but not of the bending modulus.

A static INSTRON machine can be used as well in traction as in compression. Its load capacities are adaptable (2, 5, 10, 20, 50, 100 kN) according to the testing speeds applied (0.1 mm/min until 500 mm/min). An in-house developed hydraulic



Fig. 6 Comparison of fracture modes at different scales

press has been used for the one half and one scaled specimens. This machine has a 1,000 kN compression load capacity and is composed of a hydraulic jack with a maximum 100 mm displacement; that explains why the total crush displacement is limited to this value. Its speed range extends from 10 to 100 mm/min.

For the one-fourth scaled specimens, dynamic tests have been performed on an in-house designed hydraulic machine composed of a dynamic jack supplied by a pressure of 350 bars and a 150 l/h flow rate. Its load capacities are 50 kN in dynamics and 69 kN in statics. Its maximal speed reaches 10 m/s for a maximum 250 mm displacement. For larger specimens (scale 1/2 and 1), tests have been carried out in a drop tower designed by **C3T** (University of Valenciennes) and permits to test in free fall conditions, a maximum mass ranging from 100 to 700 kg, from a variable height between 80 cm and 4 m.

For each laminate or test speed tested, at least three tests has been performed. The main fracture mode observed in the tests performed consists of a peeling mode. Plies progressively and symmetrically separate in most cases, on both sides of the middle-plan of the structure. This mode has already been described in previous studies [5, 23–25]. This fracture mode, specific to composites, has been shown not to be influenced either by the structure dimensions or by the loading speed and by the stacking sequence tested. The Fig. 6 presents a comparison between different scales.

This research on similitude uses the dimensional analysis approach coupled with experimental observations for distortion detection. An empirical polynomial model was developed to predict the evolution of the result as a function both

of the scale and of the distorted parameters. This approach seems to be feasible since studies about the scale-effects, available in literature, describe their evolution as being both monotonous and continuous if the latter is not linked with the emergence of the phenomenon for a specific scale which goes unobserved in all other cases. Therefore, this method consists in carrying out the scaled-down models and experimental conditions dimensioning starting from a dimensional analysis. The latter permits the detection of parameters failing to be scaled up. Then, starting from tests on scaled-down models, a polynomial is identified by performing an extrapolation using the distorted parameters as well as the overall (geometric) scale factor, as unknown factors, in order to bring to the fore the scale effects. This step requires to carry out tests on several configurations and several scales of scaled-down models. The number of tests to be performed mainly depends on the polynomial degree for each unknown factor and therefore on the phenomena brought into play. However, the dimensional analysis provides the polynomial degree for a distortion-free scale factor and it therefore makes sense to suppose that this degree is but slightly changed by the distortion effect. Furthermore, a phenomenological study may enable to put forward hypotheses as regards the evolution of the result in function of the distorted parameters as it is the case for energy absorbers (Figs. 1 and 6) with a+ or –45° configuration.

Generally speaking, there are two main methods to determine similarity relations between a scale 1 prototype and a scaled-down model. The *direct method* consists in using an analytical model representing the test. Comparing the equations colloquial with the parameters of the prototype and those of the scaled-down model, relations which directly link the two structure scales are obtained. In this case the phenomena are too complex and, as a result, there does not exist any really reliable analytical model. So, this method is not usable for this kind of structures. The second method consists in identifying all the parameters likely to exert an influence. Then, we apply the Vashy-Buckingham Π theorem [26]: "an equation (E) linking (n) physical quantities can be transformed into an equation (E′) linking (n–p) dimensionless quantities π, where p is the maximum number of quantities dimensionally independent in (E) considered." The similarity relations are obtained equalizing each π number from the prototype and the scaled-down model. Generally, during the setting up of the π numbers, an effort is made to use specified ones with a particular meaning. In the case of a structure crash, Cauchy's number allows to conserve the proportions between the inertial effects and the elastic forces.

$$\Pi_{Cauchy} = \frac{\rho V^2}{E} \tag{1}$$

The problem in this case is the very large number of parameters and the fact that influent parameters are very difficult to identify. However, a dimensional analysis of the main parameters, supposed to be the most influent, has permitted not only to dimension the specimens but also to make a first comparison of the experimental results.

Table 1 Evolution of some quantities from Cauchy's similarity law

Variables	Prototype	Model
Acceleration	A	A/β
Stress	σ	σ
Strain	ε	ε
Density	ρ	ρ
Displacement	δ	βδ
Length	L	βL
Kinetic energy	Ec	β^3Ec
Force	F	β^2F
Mass	m	β^3m
Young modulus	E	E
Time	T	βT
Impact velocity	V	V

The use of the Vashy-Buckingham Π theorem permits to obtain several π numbers including Cauchy's one. For each X parameter, a scale factor is defined as follows:

$$\beta_X = \frac{X_{\text{mod } el}}{X_{prototype}} \tag{2}$$

The equalization of the π numbers from the prototype and the scaled-down model permits to express the scale factors relative to all parameters in function of one of them. Generally, the parameter chosen is the length and its scale factor is simply noted β. Some examples of relations obtained are plotted in Table 1. It is interesting to see that, in this case, the test velocity is not modified by the scale change.

Cauchy's similarity law foresees to conserve all mechanical properties which suggests to keep the same material with the same fibre rate to manufacture both the prototype and the scaled-down models. This induces ply thickness conservation. So, the first distortion is obvious because there is an un-scalable geometrical parameter. Consequently, the only way to reduce the stratified structure thickness is to reduce the ply number. The dimensionless numbers such as the ply number or the interface number between plies with different orientations are directly π numbers. They should be the same both for the prototype and the scaled-down models. The standard choice is to conserve the material making up plies and to modify the ply number and therefore the stacking sequence. This modification can also induce a modification of the non-linear behavior of the composite. A second more specific distortion for tests carried out with the drop tower has been detected: the gravity acceleration cannot be modified. But some tests carried out at 4 m/s with one fourth scale specimens with a 12.9 and a 21.5 kg dropped mass have shown there is no influence of the impactor weight on the force plateau. To sum up, some distortions have been detected between the prototype and the scaled-down models but they seem to be unavoidable. In addition, without equations describing the system, it is impossible

to determine exactly the effects of these distortions. As a consequence, another approach is necessary to obtain relations permitting to foresee the results of a composite material structure crash from those of crashes of scaled-down models.

3.1 Polynomial Construction for Omega Structure Crashes

The dimensional analysis has brought to the fore a ply-number distortion (hereby, the structure is studied at a mesoscopic scale) which results most of the time into a distortion at the interface level between +45°/−45° oriented plies. Those interfaces are generally the delamination location since they undergo shearing constraints due to the orientation difference of the adjacent ply fibers, which favors its initiation. In addition, the branch flexion makes the surfaces thus created relatively slide, thus inducing frictional forces. The delamination and the frictional phenomena between delaminated plies contribute towards energy absorption, therefore the effort withstanding the structure crunch must linearly depend on the interface-number between differently oriented plies. As a result, the medium level effort value can then be stated via the following formula:

$$F_{pal} = A_0 n + B_0 \tag{3}$$

Where n stands for the interface number between +45°/−45° oriented plies, A_0 and B_0 are empirical coefficients depending on the scale. By studying the A_0 coefficients relative to each scale, the terms seemingly evolve with the overall squared scale factor. This dependence in β^2 does not come as a surprise since β^2 is the force scale factor according to Cauchy's similitude law. The efforts related to frictions between adjacent plies together with the effort linked with the inter-laminar cracking is unaffected by distortions. The interface and the frictional coefficients are indeed retained by the scale change since the material making up the plies is quite identical. It is therefore quite predictable that those phenomena do not entail a scale effect. The Eq. (3) can therefore be re-formulated as follows:

$$F_{pal} = An\beta^2 + B_0 \tag{4}$$

The A coefficient, thus determined, features a weak amplitude variation in function of the scales of the structure under study, which may be accounted for by the experimental scattering. By imposing the A coefficient the determined value by averaging the A coefficients relative to the series of points originating from each scale, a linear increase of B_0 term in function of the overall scale factor can be highlighted.

The Eq. (4) thus becomes:

$$F_{pal} = An\beta^2 + B\beta - C \tag{5}$$

A, B and C being empirical coefficients independent from n and β, are therefore constant whatever the stacking sequences and the omega structures scales (Fig. 5) Some phenomena can be related to the different polynomial coefficients (5). Indeed, the resistance efforts corresponding to the phenomena cropping up at the interface level, such as de-lamination or inter-ply friction, are related to A term as above demonstrated. The other main phenomenon in the energy absorption process being the resistance to ply-bending. It seems therefore logical to associate it with B and C terms, more particularly as the latter feature a scale effect. Now, the distortion over the interface number must entail consequences on the resistance of samples subjected to flexion. However, those terms remain constant whatever the interface number. The inter-laminar crack number still alters the structure resistance in flexion by splitting the structure into several independent ply clusters, within the material thickness. Also included in A terms an item corresponding to the effort collapse related to delamination. In other words, A term corresponds to the sum of the effort connected with delamination, of the one related with friction and to the resistance collapse in bending triggered by delamination, whereas B and C coefficients correspond to the maximum resistance in bending of the delamination-free plies, to the impactor/structure friction and to the longitudinal cracking process. The scale effect therefore concerns the ply resistance in bending or the longitudinal cracking process. Now, both phenomena certainly feature a strong interaction since the ply cracking cuts the structure into strips, which alters it quadratic moment and therefore its resistance in flexion. Likewise, longitudinal cracking is caused by tensile/compression constraints which appear whenever the branches bend. Consequently, whatever the phenomenon submitted to this scale effect, the ply resistance in bending is necessarily affected. Whatever the approach, even though some observations still remain difficult to explain, the methodology explained throughout this paragraph has permitted to reach polynomial relation (6). This empirical expression cannot be explicitly connected with the samples' geometrical properties or with the material mechanical properties. Yet, it can be used in order to determine the step by step real-scale sample efforts since it provides this value in function of parameters characterizing the samples.

3.2 Scale Change Relation Determination

In the previous paragraph, a polynomial was built up starting from the basis of a dimensional analysis, of phenomenological observations and from measurement performed on scaled-down models. This polynomial (5) permits the direct computation of the step effort average values whatever the interface number featured by the laminated material stacking sequence and the structure scale under study. In addition, by using this direct method, this polynomial can be used to determine the scale change relations which will then be applied to the force/displacement graphs recorded during tests on scaled-down models in order to obtain those

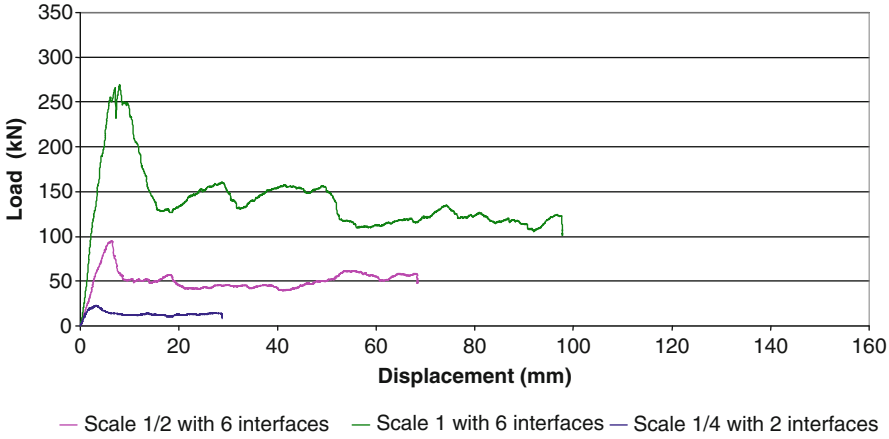


Fig. 7 Experimental curves for three scales

of the prototype. Let $F_{pal}[\beta,n]$ and $F_{pal}[\beta°,n°]$ be the polynomial expressions corresponding to a β scale structure, respectively β°, and featuring n interfaces, respectively n°, between ±45° oriented plies. The polynomial relative to one configuration can then be expressed in function of the one corresponding to the other configuration, as follows:

$$F_{pal}[\beta°, n°] = F_{pal}[\beta, n]\left(\frac{\beta°}{\beta}\right)^2 + A\beta°^2\left(n° - n\right) + B\beta°\left(1 - \frac{\beta°}{\beta}\right) - C\left(1 - \left(\frac{\beta°}{\beta}\right)^2\right) \quad (6)$$

It is worth noting that in expression (6), the first term is identical to the one appearing within the Cauchy similitude application, the second term is used to somehow correct the distortion concerning the interface number and the last two terms permit to take into account the scale effect related with the structure crunch resistance. The prototype configuration being sought for is a priori known. It is therefore possible to apply this polynomial expression (6) to an effort/time or effort/displacement curve. The x-axis can then be scaled by using the scale-factors resulting from the Cauchy similitude law since neither time nor displacements are affected by distortions. Figures 7 and 8 are a perfect illustration of the axial compression study-case of the energy absorbers tested in real scale.

In this part, a similitude technique was proposed to allow the study of a structure of big size with a reduced mock-up. The global behavior of structures can thus be studied. In the following part, the study of behavior of structures by numerical simulation will be proposed. For that, a methodological approach will be presented using many simple tests, by identifications and to permit the development of tools for numerical simulation.

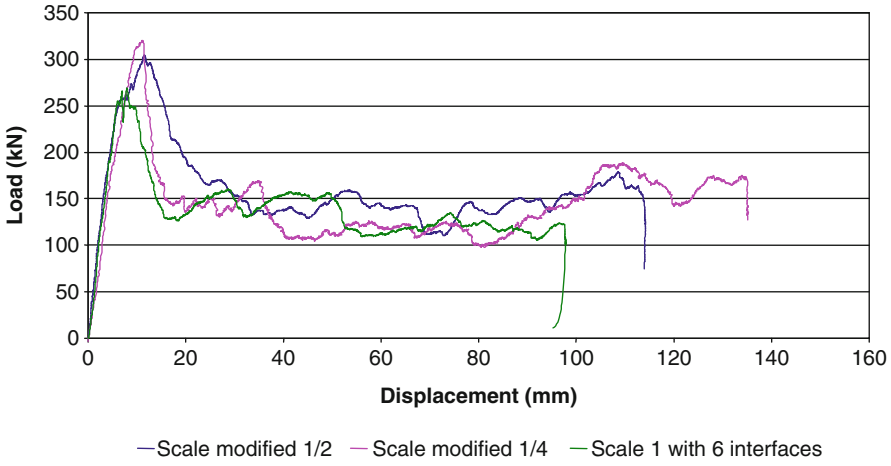


Fig. 8 Curves after similitude application

4 Pedestrian Impact Modelling onto a Composite Bonnet

The issues linked with numerical simulation use for severe impacts are mainly due to the complexity of the composite material. Indeed, the behavior of each composite material is specific and its thorough knowledge is paramount for a better integration into the models. On the other hand, in order to achieve a suitable composite material behavior modeling, a sufficiently significant representation scale definition (Macro, Meso, Micro) is of primary importance. In order to permit both the improvement and the development of innovative tools, for a better contribution towards an improved approach to design via numerical simulation, it seems to be a prerequisite to have an in-depth understanding of the associated physical phenomena in order to reduce the real practical tests. The methodology generally used is based upon an accurate knowledge of the composite materials, reached through experimental campaigns on simple-shaped samples, thus permitting the development of data-bases on materials. Tests are sometimes necessary when more complex behavior in 3D can be complex [27]. For example in a static case on Fig. 9, we present results obtained from the experimental study on the behavior of glass/epoxy butterfly-shaped specimens tested under pure shear and biaxial loadings using an Arcan device [28]. Notch-to-notch longitudinally and perpendicularly oriented fiber samples, respectively referred to as Mat31 and Mat32 ones have been tested with different loading angles ranging from 0° to 90°. Figure 10 presents the test configuration. A thorough analysis of the results, aimed at better understanding and explaining the fracture and damage phenomena, thus contributes to implement knowledge bases.

Those phenomena then must be translated into an already-existing or new behavior model. Thus, innovative features are defined in terms of behavior laws, of specific items or even in terms of methodologies. The validation phase is essential.

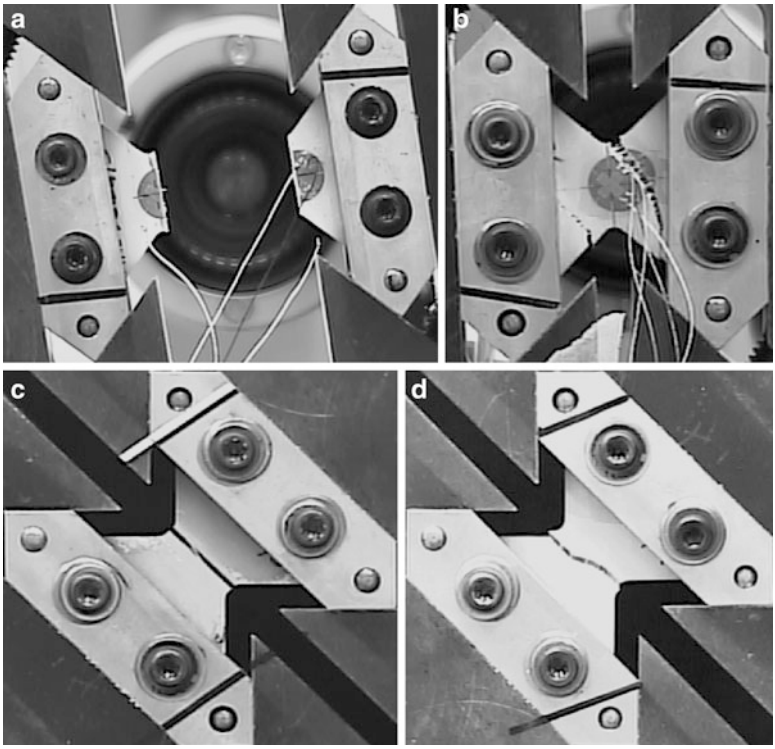


Fig. 9 Photos of fractured samples under pure shear loading of Mat31 (**a**) and Mat32 (**b**) obtained by Arcan tests Photos of fractured samples under biaxial loading ($\alpha = 45°$) of Mat31 (**c**) and Mat32 (**d**) obtained by Arcan tests

It permits, in the first instance and within the sample scale, to reproduce the elementary material behavior. Then comes the time for validation at the scale of either a component or a structure.

4.1 The Mechanisms Encountered During the Deformation of Composite Materials

There are three fundamental damage mechanisms that are frequently encountered in the plies of a laminated material (resin-fiber); these are: fiber-matrix debonding, cracking of the matrix and the failure of fibres (Fig. 11). Between differently oriented plies these primary mechanisms generate another type of mechanism, known as delamination, which causes interlaminar cracking.

These mechanisms can be incorporated into computation codes in several ways. One possibility is a macromechanical approach in order to deal with the overall

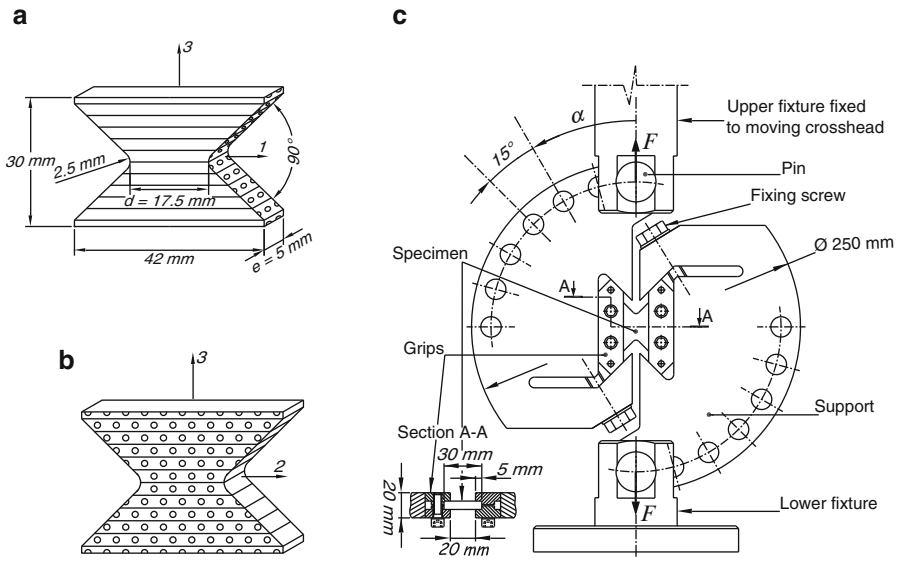


Fig. 10 Schematics of Mat31 (**a**) and Mat32 (**b**) specimens: notations with stacking orientation and local coordinates. Arcan test setup in pure shear mode (**c**)

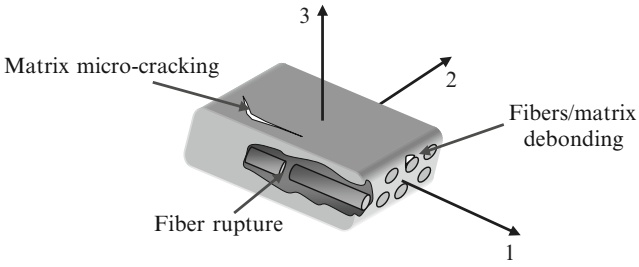


Fig. 11 Damaging modes within the elementary ply

processes taking place. A micromechanical approach can also be considered which provides a detailed understanding of localized phenomena. The approach adopted here is based on a mésomodèle [29], which means that the phenomena can be homogenized at the ply level. The basic model which is implemented within the computation code is that developed by Ladevèze [29]. Originally, this expressed fiber-matrix debonding and the cracking of the resin respectively by means of two damage variables associated with the shear and transverse moduli. A third parameter was then introduced that defined the yield point of the fibers. Depending on the materials used to make the composite (kind of fiber, resin, manufacturing process...), it was then necessary to introduce other characteristics, for example the anelastic effect of the resin, the effects of strain rate, the difference in tensile and compressive behaviour, etc. The research conducted at **LAMIH** has made a

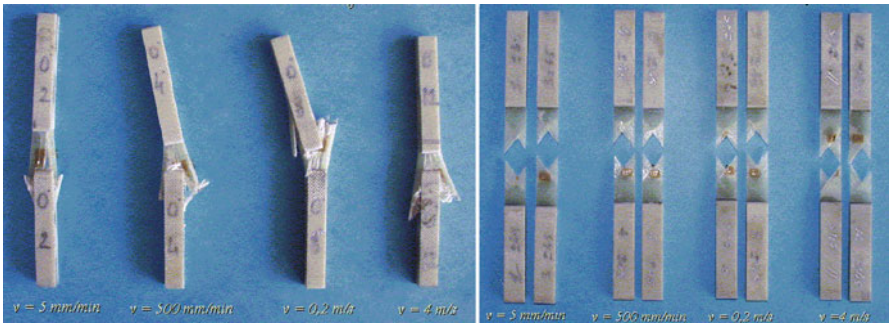


Fig. 12 Examples of failure of specimens tested experimentally (compression and tensile tests on different specimens)

significant contribution to the original mesomodel. The detailed account of these contributions with regard to the points mentioned above is to be found in a number of theses [30–32].

4.2 Experimental Characterization

To supply the models and methodologies with data, an experimental characterization campaign was required, with the aim of understanding the behavior of the composite and the associated damage processes. Static and dynamic studies were conducted on configurations of laminates of specified orientation in order to ascertain the tensile and compressive behavior of the material and its components (Fig. 12). Between three and five specimens were prepared and tested for each test, so as to ensure a minimum amount of dispersion and the validity of the values obtained. The dynamic tests were generally performed at different velocities of loading, so it was possible to quantify the influence of the strain rate, which is often important in the case of crash phenomena.

Strength tests were also performed on the interfaces between plies ARCAN test (Fig. 9) and DCB type test (Fig. 13) to characterize the interface and provide an insight into delamination phenomena [33]. These tests, which were also conducted on several specimens, had to be performed with great care and it was important for the specimens to resemble real materials, in particular resulting from the same manufacturing processes.

4.3 New Possibilities Provided by the Behavior Models

The research conducted in the laboratory was the outcome of work on the modeling of multimaterials (GLARE) that were in use a few years ago for aeroplane fuselages.

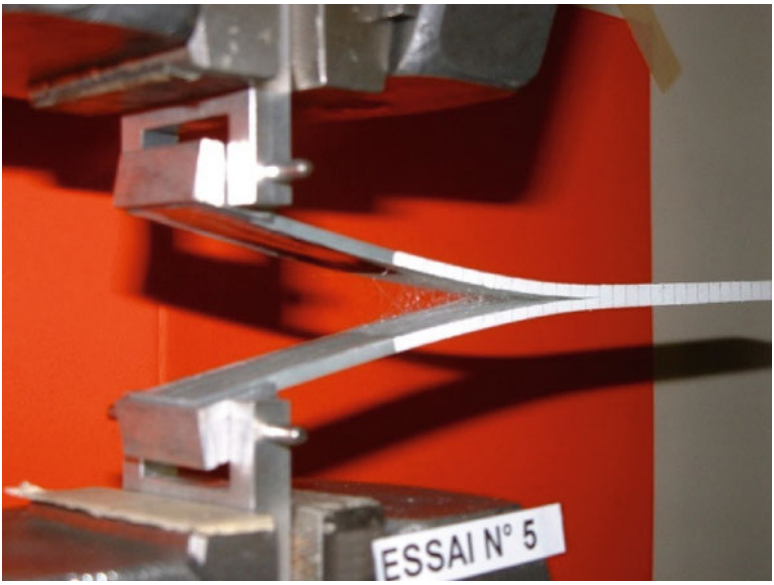


Fig. 13 DCB test

Composite structures are very frequently subjected to severe local stresses which do not necessarily cause visible damage of the surface of the material but which lead to major internal damage which often endangers safety and the survival of components. It was in order to provide a partial solution to this problem that a multi-layer multimaterial element was developed [15], for the impact modelling of laminates made up of materials which differ very greatly in their behavior. The multi-layer element is based on a Mindlin-Reisser finite element shell taking into account the effect of transverse shear and with bilinear interpolation functions. Between one and four integration points can be used in each ply. Many studies [30] have validated this finite element, which has been incorporated into the **PAMCRASH**™ industrial software. After this initial stage, in order to make improvements which take account of the principal behaviors of a composite material consisting solely of fibers and an organic matrix, the basic models [29] in the computation code were extended in order to reproduce behaviors which are close to reality. This illustrates the influence of taking certain phenomena into account or not.

Damage is taken into account by two scalar variables (d and d'). The parameter d quantifies the damage which comes from the dissociation between fibers and matrix whereas the parameter d' is related to the damage due to the micro-cracking of matrix parallel to the direction of fibers (Fig. 11). That is the reason the parameters d and d' are applied respectively to shear and transverse modulus. However, distinguishing between tensile and compressive transverse responses is required. Indeed, micro-cracks grow when the composite ply is under tensile transverse loading, but they close up in the other case. Moreover, modeling also includes the

rupture of fibers. Nevertheless, this rupture rate is determined by considering the longitudinal strain limit because rupture of representative layers is brittle in most cases. So the assigned moduli are calculated from the initial shear modulus G_{12}^0 and initial transverse modulus E_{22}^0 according to:

$$\begin{cases} E_{22} = E_{22}^0(1-d') & \text{if} \quad \sigma_{22} > 0 \\ E_{22} = E_{22}^0 & \text{if} \quad \sigma_{22} \leqslant 0 \end{cases}$$
$$G_{12} = G_{12}^0(1-d) \tag{7}$$

Expression of the elementary ply behaviour is given by (8).

$$\begin{Bmatrix} \varepsilon_{11} \\ \varepsilon_{22} \\ 2\varepsilon_{12} \end{Bmatrix} = \begin{bmatrix} \frac{1}{E_{11}^0} & -\frac{\nu_{12}^0}{E_{11}^0} & 0 \\ -\frac{\nu_{12}^0}{E_{11}^0} & \frac{1}{E_{22}^0(1-d')}\frac{\langle\sigma_{22}\rangle_+}{|\sigma_{22}|} + \frac{1}{E_{22}^0}\frac{\langle\sigma_{22}\rangle_-}{|\sigma_{22}|} & 0 \\ 0 & 0 & \frac{1}{G_{12}^0(1-d)} \end{bmatrix} \begin{Bmatrix} \sigma_{11} \\ \sigma_{22} \\ \sigma_{12} \end{Bmatrix}$$
$$\text{where} : \quad \langle a\rangle_+ = \begin{cases} a \; if \; a > 0 \\ 0 \; if \; a < 0 \end{cases} \quad \text{and} \quad \langle a\rangle_- = \begin{cases} 0 \; if \; a > 0 \\ a \; if \; a < 0 \end{cases} \tag{8}$$

The non-damaging thresholds ($\underline{Y}$ and $\underline{Y'}$) for the elementary layer are given by (9). The multiplication factor b from (9), allows the representation of coupling between shear and transverse effects.

$$\underline{Y}(t) = Sup_{\tau \leqslant t} \sqrt{\frac{1}{2}\frac{\sigma_{12}^2}{G_{12}^0(1-d)^2} + b\frac{1}{2}\frac{\langle\sigma_{22}^2\rangle_+}{E_{22}^0(1-d')^2}}$$
$$\underline{Y'}(t) = Sup_{\tau \leqslant t} \sqrt{\frac{1}{2}\frac{\langle\sigma_{22}^2\rangle_+}{E_{22}^0(1-d')^2}} \tag{9}$$

Moreover, laws of the damage evolution are chosen as being linear:

$$d = \frac{\langle \underline{Y} - Y_O\rangle_+}{Y_C} \quad \text{if} \quad d < 1 \quad \text{and} \quad \underline{Y'} < Y'_S \quad \text{and} \quad \underline{Y} < Y_R \quad \text{else} \quad d = 1$$
$$d' = \frac{\langle \underline{Y'} - Y'_O\rangle_+}{Y'_C} \quad \text{if} \quad d' < 1 \quad \text{and} \quad \underline{Y'} < Y'_S \quad \text{and} \quad \underline{Y} < Y_R \quad \text{else} \quad d' = 1. \tag{10}$$

Y'_S and Y_R have been introduced to limit the evolution of non-damaging thresholds $\underline{Y}$ and $\underline{Y'}$, in time. Indeed, ruptures can be reached even before d and d' reach "one" value.

Elastic characteristics (Young's modulus, shear modulus, Poisson's ratio) and parameters Y_0, Y_C, Y'_0, Y'_C, Y_R, Y'_S and b result from four experimental characterization tests.

In some cases of stacking, loading, etc. the ductility of resin can have a strong effect on composite behavior. For example, if experimental conditions let a weak loading of fibers, the behavior of the resin "will be prevalent". Moreover, some studies on strain rate dependency are carried out parallel. The first conclusions point to the high sensitivity of strain rate in previous cases where ductility of resin is dominant. It motivates the search of a better description for composite ply behavior before the introduction of strain rate sensitivity. It has also decided to introduce the asymmetrical behavior frequently noticed for tensile and compressive loading in the direction of fibers. Indeed, this could provide a difference in longitudinal Young's modulus because of fiber micro-buckling, micro-defaults at matrix/fibers interface, fibers misalignments... The integration of plasticity is proposed in the following parts as well as an account of asymmetrical tension/compression behavior. Studies concerning the plasticity of the elementary ply still draw inspiration from the modeling developed by Ladevèze [29]. The elastic damage model is identical to the previously described model. However, here, the total strain is composed as a sum of elastic strain and plastic strain:

$$\varepsilon^{\text{total}} = \varepsilon^{\text{elastic}} + \varepsilon^{\text{plastic}} \tag{11}$$

Elastic domain is described owing to a criteria function f chosen under a general form of Von Mises criteria, which is related to anisotropic materials. This function depends a priori on principal stresses. However, high rigidity of fibers locks plastic flow in their direction. Therefore, criteria function depends only on transverse and shear stresses. Effective stresses permit an agreement to plasticity/damage coupling:

$$\begin{aligned} \tilde{\sigma}_{11} &= \sigma_{11} \\ \tilde{\sigma}_{22} &= \frac{\langle \sigma_{22} \rangle_+}{1 - d'} + \langle \sigma_{22} \rangle_- \\ \tilde{\sigma}_{12} &= \frac{\sigma_{12}}{1 - d} \end{aligned} \tag{12}$$

Plastic strain evolution is described in accordance with an isotropic hardening law (13). This choice is arbitrary but it allows the evaluation of resin ductility at the first approximation for dynamic studies. Moreover, it permits the simplifying of experimental characterization for newly introduced parameters.

$$R = \beta p^m + R_0 \qquad \begin{cases} \beta, m\text{: material constants} \\ p\text{: effective plastic strain} \\ R_0\text{: initial yield stress} \end{cases} \tag{13}$$

In consequence, criteria function is:

$$f = f(\tilde{\sigma}, R) = \sqrt{\tilde{\sigma}_{12}^2 + a^2\tilde{\sigma}_{22}^2} - R \tag{14}$$

β, m, a^2, and R_0 parameters are characteristics depending on materials and evaluated experimentally.

The choice of isotropic hardening law implies that it is not necessary to add extra experimental tests. Even, R_0, β, and m are found from the existing test on laminate $[\pm 45]_{2S}$, which is a "quasi-pure" shear case. So, from each load/unload cycles, R and p (by integration) can be found simply (15). Then linear interpolation of the curve Log R versus Log p gives the necessary coefficients of the hardening law.

$$\begin{aligned} R &= \frac{\sigma_{12}}{(1-d)} - R_0 \\ \dot{p} &= \dot{\varepsilon}_{12}^p (1-d) \end{aligned} \tag{15}$$

As for weighting between transverse and shear stresses (a^2), the different load and unload values from the cyclic tensile test on the laminate $[+45]_8$ allow its calculation:

$$a^2 = \frac{\dot{\varepsilon}_{22}^p (1-d')^2}{2\dot{\varepsilon}_{12}^p (1-d)^2} \tag{16}$$

During compressive loading, laminates can suffer from non-linear rigidity losses. This is generally a consequence of micro-buckling of fibres. Indeed, the misalignment of fibers or the micro-defaults at fibers/matrix interface can strongly influence the emergence of micro-buckling. Therefore, compressive behaviour must be distinguished from tensile behaviour.

Drop in Young's modulus – or secant modulus because any damage appears in this direction – is a linear function of compressive stress. The linear coefficient is called γ. A similar approach has been introduced using the longitudinal strain:

$$E_{11}^{compression} \approx E^{secant} = E_{11}^{initial\ compression}(1 + \gamma E^{secant}\varepsilon_{11}) \tag{17}$$

Therefore, Young's modulus is given by (16) if during calculation, a compressive load is detected.

$$E_{11}^{compression} \approx E^{secant} = \frac{E_{11}^{initial\ compression}}{1 - \gamma E_{11}^{initial\ compression}\varepsilon_{11}} \tag{18}$$

Finally, the fact that the strain of rupture could be different in both cases of loading is also taken into account. Consequently, a new parameter is added to measure this compressive rupture strain rate.

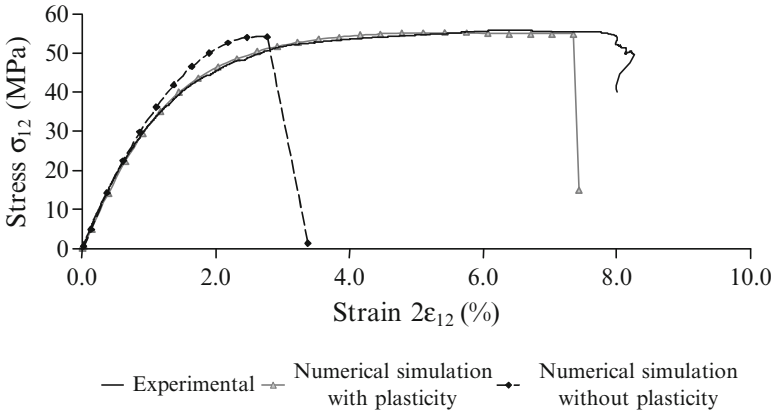


Fig. 14 Tensile comparisons on $[\pm 45]_{2S}$

The three sections that follow give three examples which explain the possible benefits of including one or other of the above improvements in the computation model for an application involving laminated components (fiber-matrix).

4.4 Modeling the Ductility of the Resin in a Laminate

The aim in this example is to visualize numerically the influence of matrix ductility on the overall behavior of a laminate [23]. On the basis of a tensile test performed on a glass E/epoxy $[\pm 45]_{2S}$ laminate with a fiber content of 60%, we have compared, in the case where the strength of the matrix is dominant, the experimental stress/strain plot to a model for a composite material that includes elastic with damage behavior and a model which includes anelastic effects due to the ductility of the resin (Fig. 14). It is apparent that if anelastic phenomena are ignored, there is an error of approximately 50% in the shear strain. This case is an extreme one as the stacking of the studied material augmented shearing effects.

4.5 Modeling the Effects of Strain Rate on the Behavior of the Laminate

Tests [32] were performed to test the influence of the velocity of loading on a composite consisting of glass-E embedded in epoxy resin with 60% of fibres by volume. The several types of tests are: a tensile test on a $[0]_4$ laminate, a tensile test on a $[\pm 45]_S$ laminate, a tensile test on a $[\pm 67.5]_S$ laminate, a tensile test on a $[45]_4$ laminate and a compressive test on a $[0]_6$ laminate. The experimental

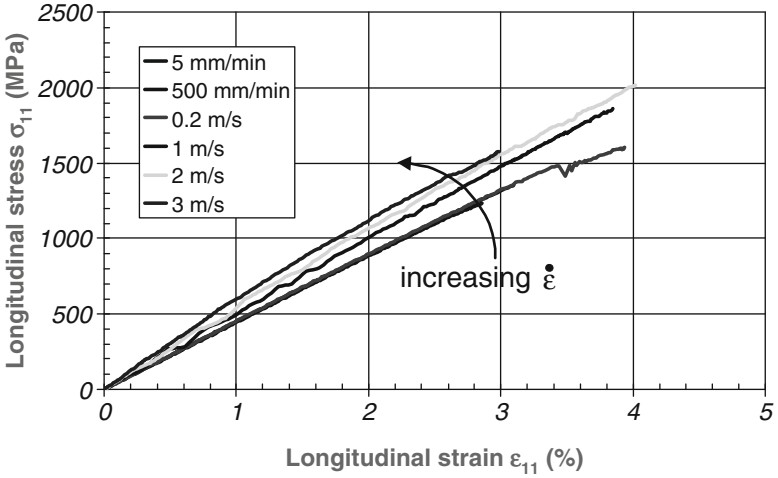


Fig. 15 Dynamic tensile tests on laminate $[0]_4$

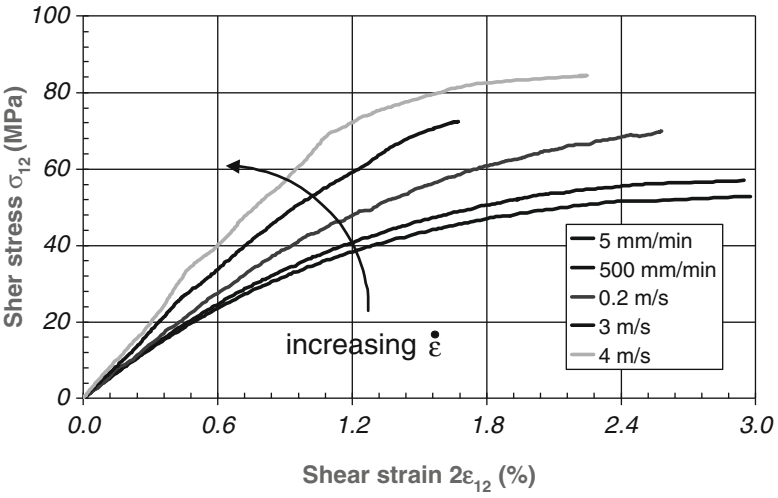


Fig. 16 Dynamic tensile tests on laminate $[\pm 45]_S$

device used was a hydraulic jack. For each type of test, four velocities of loading were principally applied: 5, 500 mm/min, 0.2 and 4 m/s. In this case, two essential conclusions resulted from the experimental tests. As shown in Figs. 15 and 16, the elastic moduli, the initial plastic flow stress and the failure stresses increase significantly beyond a certain strain rate threshold. These increases are of the order of between 30 and 300% depending on the parameters. In the direction of the fibers (Fig. 15), brittle-elastic behavior is conserved, but the modulus also changes significantly. In the other cases, there is a tendency for elastic-damage behavior to appear as a result of the influence of the strain rate.

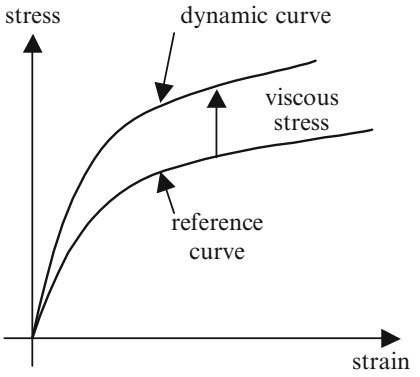


Fig. 17 Definition of viscous stress

Consequently, the behavior may be in general described as elastic plastic viscous damage, on the basis of a reference behavior model. It is difficult to identify the type of behavior observed experimentally: it is neither, strictly speaking, viscoelastic nor viscoplastic. The proposed model has been combined with the viscous fluids approach [34]: the *pseudo-viscoelasticity* of the resin (in this case of the laminated composite) is taken into account using viscous stress which is added to the computed stress (Fig. 17). The behaviour is considered to be known at a reference rate.

The type of behavior observed in experiments is not easily identifiable: it represents neither visco-elasticity nor visco-plasticity. However, it is possible to approach the definition suggested by Lemaître and Chaboche [35] with regard to viscous fluids.

Indeed, epoxy resins, and more generally reticulate polymers, are sensitive to the strain rate during loads [36] viscosity primarily comes from the chain segment movements through barriers of energy potentials. These phenomena are all the more active (since they are thermally activated) as the vitreous transition temperature from epoxy resin is relatively low (between 50 and 150 °C). We can be led to think that this rise in temperature, as a function of strain rate, brings about some micro-changes in resin phases, which thus tend to become "soft" solids.

However, it should be noticed that strain rate influence on material behavior is certainly related to the resin dependence with respect to this strain rate, but is also closely related to the choice of components. Some studies on carbon/epoxy unidirectional laminates [37] have shown a strain rate insensitivity of the elastic moduli: carbon fibers have a Young modulus on average three times higher than that of glass-E fibers and thus inhibit the viscous effects of resin (in the elastic range).

Modeling results from the approach of viscous fluids [32]: the "pseudo-visco-elasticity" of resin (and in fact of laminated composite) are taken into account using a viscous stress, which is itself combined with the elastic stress (Fig. 17). Indeed, in experiments, it is always possible to determine the behavior at a given strain rate according to behavior at a reference strain rate.

In order to integrate the pseudo-visco-elastic nature of resin, the idea is to consider that dissipation's potential form is identical to the thermodynamic potential

one, with the help of some characteristic functions of resin viscosity. Therefore, the stress tensor becomes as Eq. (19) according to the state law and the complementary law.

$$\underline{\underline{\sigma}} = C^0 : \underline{\underline{\varepsilon}}^e + \Theta : \dot{\underline{\underline{\varepsilon}}}^e \quad (\Theta : \textit{viscous tensor}) \tag{19}$$

The development of Eq. (19) for longitudinal, transverse and shear direction results in a description of elastic range. However, it is simplified owing to the approximation due to the dynamic rapid load type we are faced with. It can then be attributed to this general equation describing the elastic range:

$$\underline{\underline{\sigma}} = C^0 (I + F) : \underline{\underline{\varepsilon}}^e \quad (F : \textit{viscous functions}) \tag{20}$$

In a phenomenological way, the material state (resin or composite) can always be given starting from its state in the reference configuration. We can thus suppose that the state for a given strain rate corresponds to the quasi-static state of another glass E/epoxy composite material from which material characteristics are different. Since the elastic moduli can increasingly evolve with the strain rate, this assumption results in postulating a damage progress faster than that of the reference case. It is possible to show that the constant damage evolution intrinsic to modeling [32], is a function root of the viscosity shear function:

$$Y_{ij}(\dot{\varepsilon}) \approx \sqrt{(1 + F_{12}(\dot{\varepsilon}))} Y_{ij}$$
$$\textit{where } Y_{ij} \textit{prepresent each damage parameter} \tag{21}$$

The previous assumption also suggests that the plasticity field moves accordingly (with an evolution of initial yield stress). Indeed, the initial yield stress undergoes an evolution of the same type as the elasticity moduli (22). Resin plasticity is coupled with the model by supposing that the plastic strain evolution is similar to the reference case. However, they are delayed since the material becomes increasingly "rigid".

$$R_0(\dot{\varepsilon}) = (1 + F_R(\dot{\varepsilon})) R_0 \tag{22}$$

Finally, we put forward the additional assumption that the energy rate required to break the laminate (in the transverse and/or shear directions) is insensitive to the strain rate.

To verify that the *primary* theoretical behaviors had been accurately represented, so-called elementary validation was performed. This consisted of simulating the experimental tensile or compressive tests conducted under static and dynamic conditions. Figures 18 and 19 show the procedure and provide satisfactory correlation with the experiment.

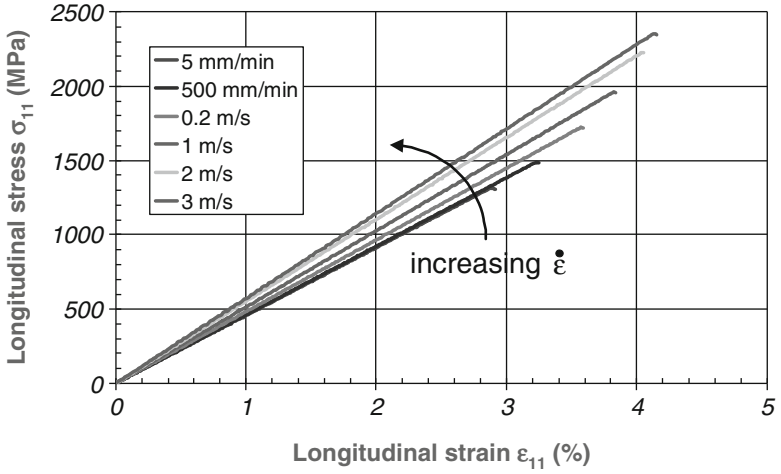


Fig. 18 Numerical dynamic tensile tests on laminate $[0]_4$

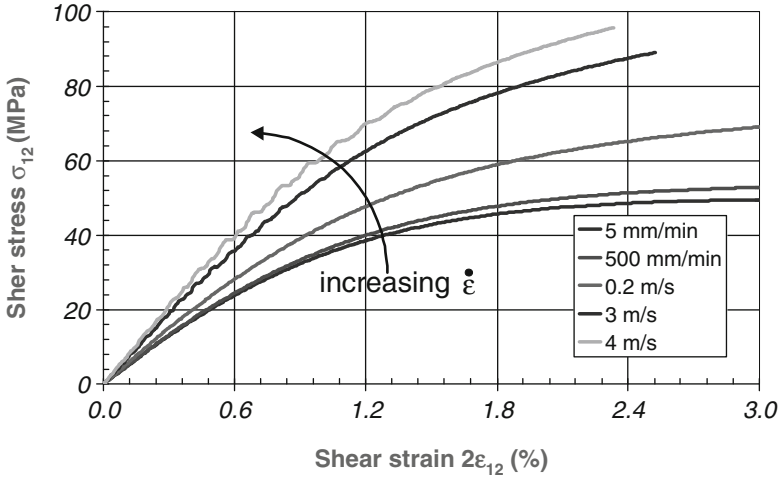


Fig. 19 Numerical dynamic tensile tests on laminate $[\pm 45]_S$

4.6 Taking Delamination into Account

The above effects take place within the ply. However, as has been stated above, damage within the plies generates inter-ply cracking which greatly reduces the stiffness of the material. A methodology [38] was therefore developed which enables these effects to be included in a comprehensive impact calculation for multi-material composites and organic matrix laminates. The approach involves two stages. Initially, delamination in thin laminate structures is detected. The models

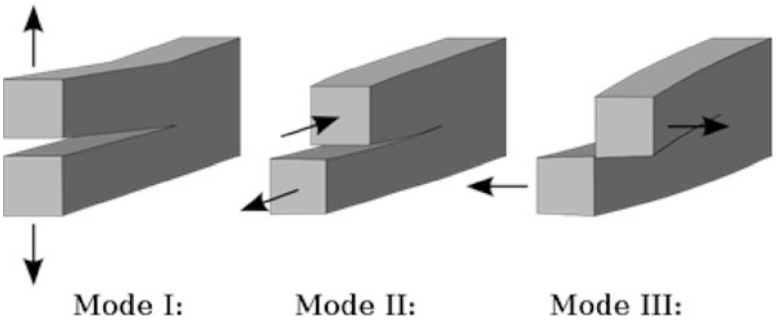


Fig. 20 Different fracture modes

which deal in a general manner with interface failures are very often 3D and model each ply with an element. The interface is also modeled by a variety of techniques depending on the method. In the case of large structures, these calculations require too many elements and are therefore too demanding of computing time. Our approach, which is based on a single multi-layer shell element developed previously, provides a powerful and effective alternative. While it is true that the method is unable to take account of mode I opening (Fig. 20), because the stress which is normal to the surface of the element is not considered, this problem is a minor problem as in the case of most impact problems it is shear delamination which dominates.

The original feature of this research is the development of a numerical methodology which is able to detect delamination within a multi-layer shell element. The first stage is to introduce a thin layer with the characteristics of the resin used between the composite plies which are likely to undergo delamination. This layer, which is thin in relation to the plies in question, is considered as an interface which permits the application of criteria for the localization of delamination. Various concepts are used in order to analyze failure, namely the energy density at the epoxy interface, computed using the local stress tensor at the interface, and the Tsai-Hill criterion which can be applied for the stress tensor of the different layers. As delamination at the interface is very closely related to the damage of the adjacent composite plies, criteria of the same type as the Tsai-Hill criterion have been added in order to identify the different failure modes of the composite plies (cracking of the matrix, fibre/matrix shear) in both tensile and compression. The developed methodology consists of combining different criteria identified at the interfaces and in the associated plies. For the interface, the change in the energy density is computed during load application. In the event of a major reduction in this density (estimated on the basis of a percentage of the maximum amplitude by experimental calibration) and if the computed Tsai-Hill criterion is significant, the interface of the element is considered to have failed. Likewise, specific criteria are applied to the plies such that, if failure is detected in adjacent plies, the interface is automatically considered to have failed. This methodology takes account of the fact that interfacial damage

depends on the cracking in the associated composite plies and that delamination is considered as an energy dissipation phenomenon as in fracture mechanics. This numerical processing has been applied to all the shell elements in stressed areas of the mesh at different time steps. The methodology also makes it possible to determine the critical stress level at which the interface fails in each element. The results take the form of a modification of the damaged surface within the structure over the course of time. The precision with which propagation of delamination is detected depends on the size of the constituent elements. A compromise must be made between the geometry of the shell element and the precision with which the model detects damage. Numerical processing was then applied in order to reproduce the mechanical effects generated by damage of the interface and the associated plies. This processing is based on a local modification of the mechanical characteristics of elements whose plies the methodology considers to be fractured. Effects are included in the code in a sequential manner: for each critical level of deflection that is attained, the elements whose plies have been identified as fractured have their characteristics modified. Computation then continues until the next critical deflection, which corresponds to fracture within other elements. Thus, by a cascade of localized reductions in the characteristics of the material, the aim is to influence the overall stiffness of the structure in order to ascertain the influence of these characteristics on the behavior of the structure as a whole. This modification in the critical phases of debonding causes fluctuations on the plots which may be filtered out subsequently. The ultimate objective is to obtain a good evaluation of the energy which is absorbed during impact. All the criteria-based analyses were processed using **Mathlab**, in this case combined with the **PAMCRASH**™ software which takes account of the modifications of the characteristic properties of the composite. Explicit formulation has been used to perform the finite element computation.

Various tests were conducted [31], in particular dynamic three point bending tests in the case of the laminated plates. A test conducted on a $[90_2/0_4/90_2]$ glass E/epoxy plate is presented here (Figs. 21 and 22). A velocity controlled jack was used for the dynamic experimental study. The damage mechanisms were validated by observations conducted with a high speed camera, strain gauges and displacement sensors. Two types of calculation were performed in order to demonstrate the validity of the developments. The first, which we have named *comprehensive*, does not take account of the mechanisms detected by the methodology in post-processing, while the second, known as *sequential*, includes modifications of the intrinsic characteristics of the layers. The stress/strain curves shown on Fig. 23 are for a loading velocity of 5 m/s. The difference between the comprehensive calculation and the experimental result is considerable. The sequential calculation which includes the developments is already a considerable improvement as regards the estimation of the changes in energy. Its value is obvious in the case of the prediction of the overall behavior of the structure at the end of impact. It provides a very accurate estimate of the amount of energy absorbed, which is a fundamental variable in the framework of the impact design of structures.

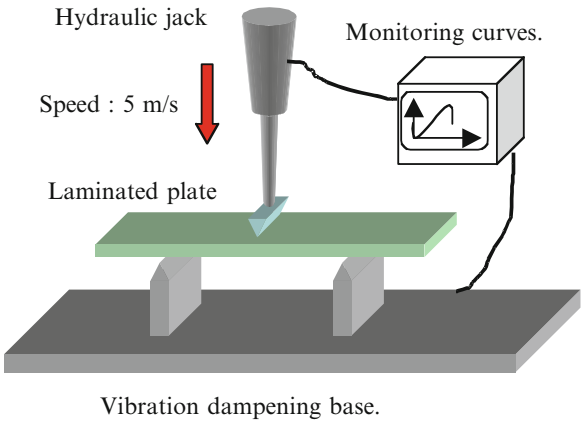


Fig. 21 Three point bending test

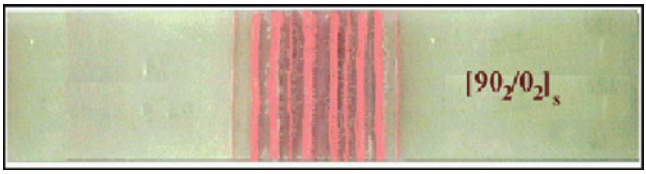


Fig. 22 Transverse stripes delamination (*in red*) of $[90_2/0_4/90_2]$ (*top view*)

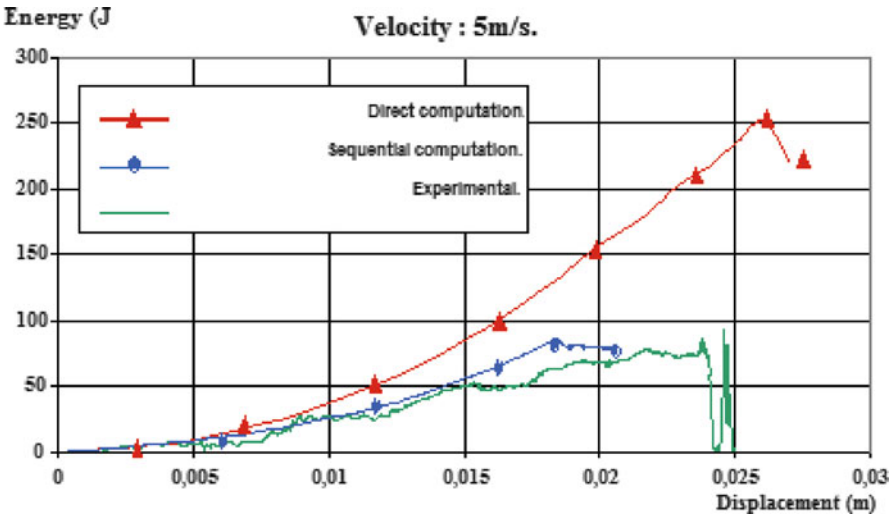


Fig. 23 Different curves of methodologies with or without delamination included compared to the experimental

4.7 Validation on a Composite Bonnet

In order to illustrate this part, simulations of a pedestrian's head impact onto the front bonnet of a car (Fig. 4) have been achieved with a particular composite material [14]. Euro NCAP procedures exist now to measure the pedestrian safety. Euro NCAP's aim is to provide motoring consumers both drivers and the automotive industry with a realistic and independent assessment of the safety performance of some of the most popular cars sold in Europe. In this particular test studied here on a car bonnet, the objectives aimed are in fact to:

- Assure a minimal deflection of the engine hood during the head impact,
- Obtain an Head Injury Criteria (HIC) lower than 1,000 on the 2/3 of the area of the engine hood and lower than 2,000 on 1/3 of the area when a specific head impactor hits the engine hood,
- Minimize the weight of the engine hood,
- Improve the numerical model of the engine hood by considering material damage or material strain rates.

Fiber Reinforced Plastic has been used for improving the pedestrian safety and permitting less injury. To design and optimize the shape of an engine hood, numerical simulations are widely used. Because of the entirely different material behavior of Fiber Reinforced Plastics compared with metals, new material models have to be used in the crash simulations. Existing material models for these materials show some deficits and therefore have to be improved. The strain rate material dependency and the delamination of the composite are implemented in the numerical simulation to obtain more accurate results. The influence on the results of secondary contacts between the hood and the engine which could happen during the impact with a pedestrian is also studied to forecast the potential damages on the hood. The experimental measurements have permitted to define the displacement values and, starting from decelerations, the HIC have been determined. The HIC is a measure of the likelihood of head injury arising from an impact. The HIC is used to assess safety related to vehicles. The variable is derived from the acceleration/time history of an accelerometer mounted at the centre of gravity of a dummy's head, when the dummy is exposed to crash forces. Figure 24 displays the experimental and numerical curves with and without the incidence of the strain rates for a given load case. The results are in perfect adequacy. In addition, taking into account the delamination, the damaged areas location have also been identified (Fig. 25).

The introduction of material laws optimized, of strain rates and of delamination contributes by numerical simulation to obtain a good behavior on the real industrial case.

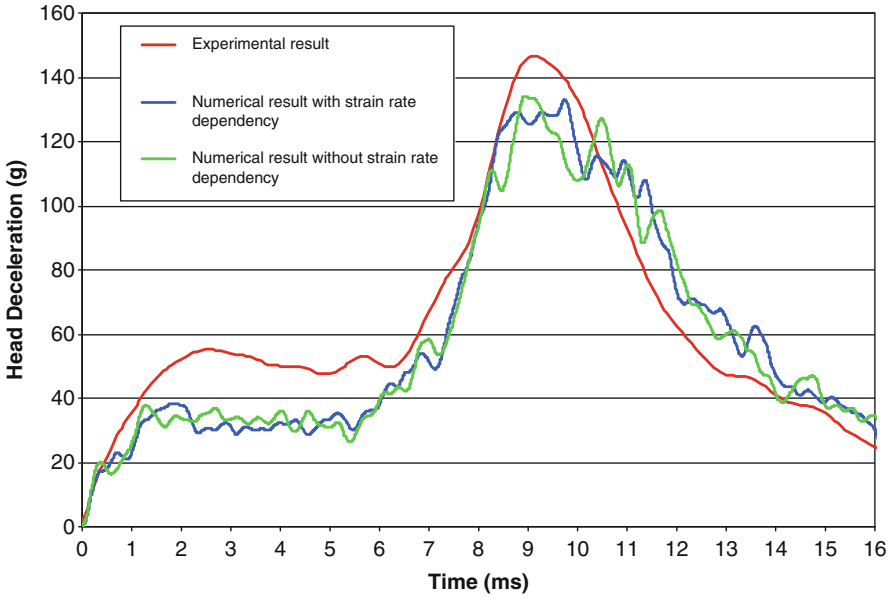


Fig. 24 Head impact deceleration curves (Courtesy: Daimler)

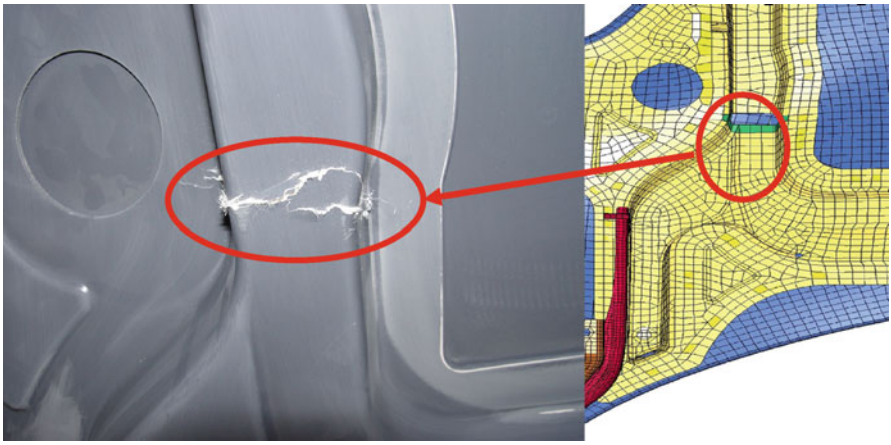


Fig. 25 Failure zone located on bonnet of a car (Courtesy: Daimler)

5 Conclusion

The few problem solving strategies hereby mentioned in this article illustrate the representation complexity in the field of composite materials simulation models whenever these are subjected to severe loadings such as impacts or shocks. Indeed, both the economic and normative constraints are to contribute, within the few years

to come, to the general use of composite materials in the fields of transportation whatever they are. It therefore becomes a topical top-priority to bring about answers to contribute to the development of new tools or to the improvement of already-existing items. A few examples have demonstrated the necessity to work at different levels and they have also permitted to illustrate the relevance of the developed models. Those studies are still going on in order to bring a contribution to the improvement of virtual prototyping tools and we hereby present two examples of resulting applications. One concerns the development of a similitude method to determine the real scale behavior starting from scaled-down structures. The first innovation is important. It allows us to study experimentally the large structures with scaled-down mock-up. This reduces costs. The second concerns the studies carried out with a car-manufacturer for the analysis of a pedestrian's head impact onto a front car-bonnet. This application demonstrates the relevance of developments made to allow better simulation of fracture phenomena in composite materials. An approach based on experimental campaigns led to the identification of material behaviors. This knowledge was then used to propose models capable of reproducing the phenomena.

Acknowledgements This research work results from numerous industrial cooperative schemes in the fields of aeronautic, automotive and railway technologies, more particularly with Daimler and ONERA, the European Community, the Ministry of Education, Research & Technology, the North-Pas De Calais Region and the National Board for Scientific Research (CNRS) have also brought about a significant contribution to the development of this research work.

References

1. Corigliano A, Mariani S, Pandolfi A (2006) Numerical analysis of rate-dependent dynamic composite delamination. Compos Sci Technol 66(6):766–775
2. Flesher ND, Herakovich CT (2006) Predicting delamination in composite structures. Compos Sci Technol 66(6):745–754
3. Li S, Reid SR, Zou Z (2006) Modelling damage of multiple delaminations and transverse matrix cracking in laminated composites due to low velocity lateral impact. Compos Sci Technol 66(6):827–36
4. Jackson KE (1994) Workshop and scaling effects on composite materials and structures, Rapport NASA, Langley Research Center, Hampton, VA, NASA conference publication 3271
5. Simitses GJ (2001) Structural similitude for flat laminated surfaces. Compos Struct 51(2):191–194
6. Dormegnie D (2001) Contribution à l'étude de lois de similitude applicables au crash de structures composites stratifiées du type absorbeur d'énergie. Thèse de doctorat, Université de Valenciennes et du Hainaut-Cambrésis
7. Delsart D, Dormegnie D, Lassus V, Coutellier D (2002) Résistance au crash des structures d'hélicoptères, vers la réduction des coûts de conception. Revue Scientifique et Technique de la Défense 56:28–33
8. Dormegnie D, Coutellier D, Delsart D, Deletombe E (2003) Studies of scale effects for crash on laminated structure. Appl Compos Mater 10:49–61
9. Postec M, Deletombe E, Delsart D, Coutellier D (2008) Study of the influence of the number of inter-ply interfaces on the bearing rupture of riveted composite assemblies. Compos Struct 84:99–113

10. Provost B, Boussu F, Coutellier D, Vallee D, Rondot F, Nussbaum J (2012) Comparison of Damages on 2D and 3D warp interlock fabric composite due to high velocity impact. International conference on mechanics of nano, micro and macro composite structures that will be held at the Politecnico di Torino, Department of Aeronautics and Space Engineering, Italy, 18–20 June 2012
11. Johnson AF, Holzapfel M (2006) Influence of delamination on impact damage in composite structures. Compos Sci Technol 66(6):807–815
12. Greve L, Pickett AK (2006) Delamination testing and modelling for composite crash simulation. Compos Sci Technol 66(6):816–826
13. Guédra-Degeorges D (2006) Recent advances to assess mono- and multi-delaminations behaviour of aerospace composites. Compos Sci Technol 66(6):796–806
14. Chick L (2006) Numerical simulation of advanced engine hoods with improved pedestrian safety, Diplôme de Recherche Technologique, Université de Valenciennes with Daimler AG
15. Coutellier D, Gauthier C, Rozycki P, Ravalard Y (1998) Numerical simulation of the tensile behaviour of multilayered multi-materials within an explicit software code. Eur J Mech Environ Eng 43(2):51–60
16. Coutellier D, Rozycki P (2000) New functionalities for PAMCRASH™ multi-layered multi-material element. Compos Part A 31(8):841–851
17. Coutellier D, Geoffroy P, Walrick JC (2006) Presentation of a methodology for delamination detection within laminated structures. Compos Sci Technol 66(6):837–845
18. Grenêche R, Coutellier D, Ravalard Y (2005) A method for crash tests on laminated composite scaled down models. Appl Compos Mater 12(6):355–368
19. Allix O, Blanchard L (2006) Mesomodeling of delamination: towards industrial applications. Compos Sci Technol 66(6):731–744
20. Ladevèze P, Lubineau G, Marsal D (2006) Towards a bridge between the micro- and mesomechanics of delamination for laminated composites. Compos Sci Technol 66(6):698–712
21. De Borst R, Remmers J (2006) Computational modelling of delamination. Compos Sci Technol 66(6):713–722
22. Dacheux F (1993) Développement d'une technique de similitude indirecte sur modèles réduits; Application à l'étude du comportement en collision des véhicules de transport guidés, Thèse de Doctorat, Université de Valenciennes et du Hainaut Cambrésis
23. Farley GL, Wolterman RL, Kennedy JM (1992) The effects of crushing surface roughness on the crushing characteristics of composite tubes. J Am Helicop Soc 38:53–59
24. Hull D (1991) A unified approach to progressive crushing of fibre-reinforced composite tubes. Compos Sci Technol 40(4):377–421
25. Thornton PH (1979) Energy absorption in composite structures. J Compos Mater 13:247–262
26. Buckingham E (1914) On physically similar systems; illustration of the use of dimensional equations. Phys Rev 4:345
27. Gning P-B, Delsart D, Mortier J-M, Coutellier D (2010) Through-thickness strength measurements using Arcan's method. Compos Part B 41:308–316
28. Arcan M, Hashin Z, Voloshin A (1978) A method to produce uniform plane-stress states with applications to fiber reinforced materials. Exp Mech 18(2):141–146
29. Ladevèze P (1986) Sur la mécanique de l'endommagement des composites, JNC 5. Ed Pluralis, Paris, pp 667–683
30. Gauthier C (1996) Contribution à la modélisation du comportement en crash des structures stratifiées métal/composite. Développement d'un élément de coque multicouches multi-matériaux, thèse de l'Université de Valenciennes et du Hainaut-Cambrésis
31. Walrick JC (1999) Contribution au développement d'une nouvelle méthodologie pour l'étude du délaminage dans les structures stratifiées composites: application à l'impact basse vitesse, thèse de l'Université de Valenciennes et du Hainaut-Cambrésis, Valenciennes
32. Rozycki P (2000) Contribution au développement de lois de comportement pour matériaux composites soumis à l'impact, Thèse de doctorat, Université de Valenciennes et du Hainaut Cambrésis

33. Devillers JC, Coutellier D, Delsart D (2003) Determination of the interface characteristics of a glass-epoxy laminated composite by means of the ARCAN test procedure. 2nd international crashworthiness and design symposium 2003, vol 3, Lille, pp 1177–1186
34. Rozycki P, Coutellier D (2003) Improvement of the simulation tools dedicated to composite structures subjected to crash loads. In: Gogu G, Coutellier D, Chedmail P, Ray P (eds) Recent advances in integrated design and manufacturing in mechanical engineering. Kluwer Academic, Dordrecht, pp 105–116
35. Lemaitre J, Chaboche JL (1985) Mécanique des matériaux solides. Ed Dunod, Paris, Chapitre 1: pp 26–31, chapitre 4: pp 145–148
36. Chaboche JL (1995) Formalisme général des lois de comportements: applications aux métaux et polymères. In G'sell C, Haudin JM (eds) Introduction à la mécanique des polymères, Nancy, pp 119–140
37. Allix O, Deü JF, Ladevèze P (1999) A delay-damage meso-model for the prediction of localisation and fracture of laminates subjected to high-rate loading. European conference on computational mechanics, München, Germany
38. Coutellier D (2005) Innovation towards improved laminated structures design aid tools. In: Bramley A, Brissaud D, Coutellier D, McMahon C (eds) Advances in integrated design and manufacturing in mechanical engineering. Springer, Dordrecht, pp 269–280. ISBN 1-4020-3481-4